RIKEN Accelerator Progress Report

2002

vol. 36

理化学研究所
RIKEN (The Institute of Physical and Chemical Research)

RIKEN Accelerator Progress Report
January-December 2002

vol. 36

理化学研究所
RIKEN (The Institute of Physical and Chemical Research)
Wako, Saitama, 351-0198 JAPAN

CONTENTS

2. Atomic and Solid-State Physics

3. Radiochemistry and Nuclear Chemistry

IV. DEVELOPMENT OF ACCELERATOR FACILITIES

I. PREFACE

This issue of RIKEN Accelerator Progress Report reports research activities of the RIKEN Accelerator Research Facility (RARF) during the calendar year of 2002. The research programs have been coordinated in the framework of the project entitled Multidisciplinary Researches on Heavy-Ion Science. The project involves a variety of fields such as nuclear physics, nuclear astrophysics, atomic physics, nuclear chemistry, radiation biology, condensed matter physics in terms of accelerator or radiation application, plant mutation, material characterization, application to space science, accelerator physics and engineering, laser technology, and computational technology.

These activities involved ten laboratories, five Centers involving seven divisions, the RIKEN-RAL Center, and the RBRC (RIKEN BNL Research Center), and more than 350 researchers from domestic and foreign institutions. Thirty-six universities and institutes from within Japan and 33 institutes from 10 countries are also involved.

Major research activities of the RARF are based on the heavy-ion accelerator complex consists of the K= 540 MeV RIKEN Ring Cyclotron (RRC), the energy-variable heavy-ion linear accelerator (RILAC), and the K=70 MeV azimuthally varying field cyclotron (AVF), which have altogether provided a beam time (on the target) of about 7800 hours through the year. The RILAC beam line and the experimental room are remodeled, thus providing extra opportunity for using high-intensity low-energy beams. The three accelerators deliver heavy-ion beams of a variety of elements with energies ranging from a few A MeV to 135A MeV. The two-injector machines (AVF and RILAC) are equipped with ECR heavy-ion sources. The AVF is additionally equipped with a polarized ion source for vector and tensor polarized deuterons. The three accelerators have been used in various configurations. The RRC operates either with the AVF or the RILAC as the injector. The AVF has been providing beams of ions of mass numbers up to 60. The energy booster for the RILAC has been installed so that the maximum beam energy from the RILAC has been raised to 6A MeV. High-intensity beams of intermediate-mass ions have been delivered. Taking advantage of the intensity an experiment on searching superheavy elements has been started. This also enabled to deliver high-intensity beams of intermediate-mass elements such as Ni and Kr up to 85A MeV from RRC. In addition, the AVF and the RILAC are used separately, when they are not used as the injector, for low-energy applications. Two thirds of the RRC research beam time (~4470 hours is the total RRC run time) is used for nuclear physics and nuclear astrophysics, and remaining one third is used for atomic physics, material science, nuclear chemistry, radiation biology and others. While, the AVF beam time was also used for fields other than nuclear physics. Studies with low-energy RI beams have been started. The research beam time at the AVF was 476 hours and it was 2880 hours at the RILAC.

The RARF carries many international collaborations. Among them are two large-size international-collaboration programs using overseas accelerator facilities: one is the muon science project at ISIS in collaboration with the Ratherford-Appleton Laboratory (RAL), and the other is the spin physics program at the RHIC in collaboration with the Brookhaven National Laboratory (BNL). The pulsed muon-beam facility at ISIS has been operating steadily. At the RHIC facility, the first heavy-ion beam and the first polarized proton beams have been successfully accelerated. The first data with polarized-proton collider have been accumulated. Other smaller collaborations using foreign facilities are underway on at Lanzho (China), Dubna (Russia), CERN, GSI (Germany), and TRIUMF (Canada).

We have collaborated with the CNS of the University of Tokyo for installing the new low-energy RI beam separator (CRIB) to use the low-energy beam from the AVF. High-quality low-energy RI beams are now available as a CNS/RIKEN facility. Several experiments have been completed this year.

One of the highlights of the year is the starting of the Superheavy element search. (1) Using high-intensity beams from the RILAC to the GARIS (Gas Filled Recoil Ion Separator) an isotope of element [110] has been produced. This experiment, observing 14 sets of alpha-decay chains, gave the first confirmation of ^{271}[110] that was observed so far only at GSI. New transuranium heavy isotopes ^{230}Am and ^{234}Bk have been discovered with the same system. (2) Concerning the new isotopes, the nuclear chart in light nucleus has been expanded to more neutron-rich nuclei. New isotopes of ^{34}Ne, ^{37}Na, and ^{43}Si have been discovered using high-intensity ^{48}Ca beam. (3) A clear evidence of proton skin has been observed from the interaction-cross-section measurement of Ar isotopes. (4) An rf deflector has been newly installed at the RI beam separator RIPS. This deflector adds a separation by the TOF of a secondary nucleus between the production target and the deflector. Orders of magnitude reduction of admixtures in secondary beams has

been achieved. (5) The gas-filled rf-ion guide and trap of the RI beams has being developed. High collection efficiency has been achieved.

The RI beam factory project is progressing well. The building for the cyclotrons and the separators will be completed soon. The construction of the experimental facility building has been started. This building will be completed in 2005.

I. Tanihata
Director, Experimental System Group
RIKEN Accelerator Research Facility

II. OPERATION OF ACCELERATORS

RILAC operation

E. Ikezawa, M. Kase, S. Kohara, O. Kamigaito, T. Nakagawa, M. Fujimaki, M. Nagase, T. Kageyama, N. Fukunishi, N. Sakamoto, H. Okuno, N. Inabe, M. Wakasugi, M. Kobayashi-Komiyama, M. Kidera, S. Yokouchi, A. Yoneda, H. Akiyoshi, M. Hemmi, I. Yokoyama, S. Numata, Y. Higurashi, T. Aihara,* T. Ohki,* H. Hasebe,* H. Yamauchi,* A. Uchiyama,* K. Oyamada,* A. Goto, and Y. Yano

In the previous year, an energy upgrade program of RILAC from 4 to 6 MeV/nucleon in collaboration with the CNS (Center for Nuclear Study, University of Tokyo) was completed.[1] In the beginning of 2002, we obtained an official license for the new RILAC performance and started the RILAC operation after an eighteen-month shutdown.

Table 1 shows the statistics of the RILAC operation from January 1 through December 31, 2002. Table 2 summarizes the number of days allotted to different research groups. The percentage of beam time used by the RIKEN Ring Cyclotron (RRC) was approximately 32% of the total. The ^{4}He, ^{58}Ni, ^{84}Kr, ^{136}Xe, ^{181}Ta, and ^{209}Bi ions accelerated by RILAC were injected into RRC. Among these, the ^{86}Kr and ^{48}Ca ions were accelerated by RILAC together with the charge-state multiplier (CSM) A1 and A2 cavities and injected into RRC with a harmonic number of 8.

Various experiments have been carried out routinely since spring 2002 using the new six beam lines (e1–e6) of the RILAC experimental hall.

Research experiments on superheavy elements began in March 2002 with a gas-filled recoil isotope separator (GARIS) at the e3 beam line.[2–6] In order to study the characteristics of the GARIS, the beams of ^{40}Ar, ^{48}Ca, and ^{58}Fe with energies of 4.6–4.9 MeV/nucleon were used. Since July 2002, a confirmation experiment on the synthesis of element 110 using a ^{64}Ni ion beam with an energy of 5.0 MeV/nucleon has been performed. A total of 14 atoms of the ^{271}110 isotope were successfully observed so far. The total service time for the experiments was 1403.7 hours. The 18 GHz ECR ion source with the MIVOC method and the new six cavities of CSM worked actively to provide these beams with a high stability and a strong intensity for a very long time.

The CNS group performed beam-plasma interaction experiments related to heavy-ion inertial confinement fusion research experiments at the e4 beam line.[7] The stopping power in a plasma was measured by the time-of-flight method. Now the group is measuring the charge state distribution of the projectile passing through the plasma using a magnetic spectrometer and MCP. The ion beams ^{84}Kr, ^{136}Xe, and ^{181}Ta, with an energy of 1.0 MeV/nucleon were used. The total service time for the experiments was 144.7 hours.

Tables 3 and 4 show the statistics of the number of days of the RILAC ion beams delivered using the Cockcroft-Walton injector with an 8 GHz ECR ion

Table 1. Statistics of RILAC operation from January 1 through December 31, 2002.

	No. of Days	%
Beam time	187	51.2
Overhaul and improvement	77	21.1
Periodic inspection and repair	33	9.0
Scheduled shutdown	68	18.6
Total	365	100

Table 2. Beam time allocated for different research groups.

	No. of Days	%
Atomic physics	11	5.9
Nuclear physics	83	44.4
Radiation chemistry	13	7.0
Material analysis and development	12	6.4
Accelerator research	8	4.3
Beam transport to RRC	60	32.1
Total	187	100

* SHI Accelerator Service, Ltd.

Table 3. Statistics of the RILAC ion beams delivered using the Cockcroft-Walton injector with an 8 GHz ECR ion source (NEOMAFIOS).

Ion	Mass	Charge state	No. of Days
Ar	40	8	2
Ni	58	9	3
Kr	84	8	2
Bi	209	16	2
	Total		9

Table 4. Statistics of the RILAC ion beams delivered using the RFQ injector with an 18 GHz ECR ion source.

Ion	Mass	Charge state	No. of Days
He	4	2	2
Ar	40	8, 11	40
Ca	48	11	17
Fe	58	13	9
Ni	58	9	6
Ni	64	13, 14	52
Kr	84	17, 19, 20	7
Kr	86	20	9
Xe	136	18, 20, 27	31
Ta	181	20	5
	Total		178

source (NEOMAFIOS) and those delivered using the RFQ injector with an 18 GHz ECR ion source, respectively. The ion beams of 11 elements were used for the experiments and beam acceleration tests.

We carried out the following machine improvements during this reporting period.

(1) A solenoid magnet was installed between RIKEN 18 GHz ECRIS and the analyzing magnet.[8] The maximum magnetic field on the axis is 0.65 T. As the result, the beam intensity compared with that without the magnet increased by about 50% at the exit of the analyzing magnet.
(2) A turbomolecular pump of 2400 l/s for the No. 6 RILAC cavity was replaced with a cryogenic pump of 13000 l/s. As the result, the operating pressure decreased from 1×10^{-4} Pa to 4×10^{-5} Pa.
(3) To obtain a stable operation, the phase controllers of the six rf systems and the amplitude controllers of the No. 5 and No. 6 rf systems were replaced with newly designed ones.[9] The basic design is similar to that of RRC. The new controllers and the existing automatic tuning and amplitude controllers were connected to programmable logic controllers by InTouch software.
(4) A Mitsubishi M60/500 minicomputer, which has been used for the RILAC operation since 1986, was completely replaced with an experimental physics and industrial control system (EPICS).[10]

We experienced the following machine problems during this reporting period.

(1) The No. 6 rf power amplifier had troubles. A parasitic oscillation with a frequency of 105 MHz was detected at the final amplifier. This parasitic mode was suppressed by mounting dumping resistors on the circuit.
(2) The No. 4 rf power amplifier was splashed with water due to a small hole in the cooling pipe inside the grid stub. We replaced the grid stub with a spare one.
(3) In the No. 5 and No. 6 cavities, a thin copper sheet (10 cm wide, 7 cm long, and 0.3 mm thick) used for electric contact melted due to the excessive rf current and parasitic oscillation.

References

1) E. Ikezawa et al.: RIKEN Accel. Prog. Rep. **35**, 3 (2002).
2) K. Morita et al.: RIKEN Accel. Prog. Rep. **36**, 90 (2003).
3) K. Morita et al.: RIKEN Accel. Prog. Rep. **36**, 91 (2003).
4) K. Morita et al.: RIKEN Accel. Prog. Rep. **36**, 196 (2003).
5) K. Morimoto et al.: RIKEN Accel. Prog. Rep. **36**, 89 (2003).
6) D. Kaji et al.: RIKEN Accel. Prog. Rep. **36**, 88 (2003).
7) A. Sakumi et al.: RIKEN Accel. Prog. Rep. **36**, 104 (2003).
8) Y. Higurashi et al.: RIKEN Accel. Prog. Rep. **36**, 277 (2003).
9) N. Sakamoto et al.: RIKEN Accel. Prog. Rep. **36**, 283 (2003).
10) M. Kobayashi-Komiyama et al.: RIKEN Accel. Prog. Rep. **36**, 281 (2003).

RRC and AVF operation

M. Kase, T. Kageyama, M. Nagase, S. Kohara, T. Nakagawa, E. Ikezawa, M. Fujimaki, H. Akiyoshi, N. Inabe, H. Okuno, O. Kamigaito, M. Kidera, M. Kobayashi-Komiyama, N. Fukunishi, N. Sakamoto, M. Wakasugi, Y. Ohshiro,[*1] S. Yokouchi, A. Yoneda, Y. Higurashi, I. Yokoyama, S. Numata, H. Isshiki,[*2] K. Takahashi,[*2] H. Akagi,[*2] N. Tsukiori,[*2] T. Maie,[*2] R. Ohta,[*2] K. Kobayashi,[*2] M. Nishida,[*2] A. Goto, and Y. Yano

The statistics of operation of the RIKEN Ring Cyclotron (RRC) in 2002 is shown in Table 1. The RRC together with the AVF and the RILAC have routinely provided a beam time of more than 4400 hr throughout the year 2002. The beam time had decreased by 15% in the previous year due to the RIBF construction work but it recovered this year up to a regular level of the RRC operation history.

Table 2 shows the statistics of beam time used for each beam course. Ninety-three experiments were carried out in 2002 using the RRC beams. Among these, thirty-one RIPS experiments were carried out in the E6 room and they used a total beam time of 3113 hr, that is, 70% of the total beam time in 2002. Each RIPS experiment normally required a preparation time of a week at least. In order to use a beam time more efficiently, an increase in number of experiments, other than RIPS experiments, is desired, which can be scheduled during the preparation time. In fact, the RRC operation was interrupted for two weeks in April and May due to the installation of RIPS experimental devices. An rf deflector was installed in the RIPS beam line, which gives an additional separation power of RI beams to the RIPS.

Table 1. Statistics of RRC & AVF operation from Jan. to Dec. 2002.

Operation time of RRC	6058	hr
Beam Service Time	4399	hr
Mchine troubles	172	hr
Nuclear Physics Experiment	78%	
Non-Nuclear Physics Experiment	22%	
RILAC-RRC Operation	11%	
AVF-RRC Operation	89%	
Operation time of AVF standalone	670	hr
Beam Service Time	476	hr

Table 2. Beam time for each beam course in 2002.

Target room	Total time (hr)	No. of experiments
E1	257	6
E2	157	4
E3	275	15
E4 (SMART)	327	5
E5	273	29
E6 (RIPS)	3114	31
E7 (CRIB)	476[†]	8[†]

[†] AVF stand-alone only, and used for CNS of Univ. Tokyo.

*1 Center for Nuclear Study, University of Tokyo
*2 SHI Accelerator Service, Ltd.

The official license grounded on the radiation-protection law was obtained for the upgrade of the RILAC in February 2002, and then some high-intensity beams became available in use of the new acceleration scheme. The harmonics of the rf system of the RRC is designed to be 9 when the RILAC is used as an injector. The additional velocity gain through the Charge-State Multiplier (CSM) after the RILAC makes it possible to operate the RRC in the harmonics of 8, which indicates that the extraction velocity can be boosted by a factor of 9/8 at the same rf-frequency. This energy gain is very useful to produce more intense radioactive beams far from stability. This new acceleration scheme for the RILAC, CSM and RRC was successfully tested using a 63 MeV/u ^{86}Kr beam. More than 100 pnA of ^{48}Ca beam was accelerated up to 63 MeV/u in order to apply to new isotope search, resulting in discoveries of the new isotopes of ^{34}Ne, ^{37}Na and ^{43}Si. The data of these beams are listed in Table 3. As shown in the table, the new scheme gives much more intense beams than the traditional one, although their energies are slightly lower. These results are mainly due to the following two facts. The 18 GHz-ECR ion source gives more intense beam than 10 GHz-ECR ion source. The transmission of the RILAC is more efficient than that of the AVF.

A total beam time of 480 hr is used by the Center for Nuclear Study (CNS) of the University of Tokyo in 2002, that is, the third year after the CNS/RIKEN collaboration started. Their experiments using the low-energy RI-beam separator (CRIB) in the E7 target room were running well. As the first trial for RARF, the physics experiments for university students started this year. A total of 4 days was spent for nuclear physics experiments as a regular course for third-year students of the University of Tokyo along the CNS-RIKEN collaboration agreement. Twenty-four students carried out measurements about elastic scattering and gamma-ray spectroscopy using an alpha beams from the AVF.

A new management system started this year. One of the nine young accelerator physicists is in charge of the operation of the accelerators for a week in rotation. He manages every matter including machine conditions and user's requirements for a week of his duty. It is helpful for him to know the realistic performance of

Table 3. Comparison of beams accelerated in two acceleration shcemes.

10GHz-ECR ⇨ AVF ⇨ RRC

Ion	Energy	F for RRC	h for RRC	Charge	Intensity	Date
^{86}Kr	66MeV/u	24.1MHz	5	20+ ⇨ 31+	1pnA	Oct. 2000
^{48}Ca	70MeV/u	24.6MHz	5	11+ ⇨ 18+	6.5pnA	May 1998

18GHz-ECR ⇨ RFQ ⇨ RILAC ⇨ CSM(A1 and A2) ⇨ RRC

Ion	Energy	F for RRC	h for RRC	Charge	Intensity	Date
^{86}Kr	63MeV/u	37.8MHz	8	20+ ⇨ 30+	83pnA	Dec. 2002
^{48}Ca	63MeV/u	37.8MHz	8	11+ ⇨ 17+	110pnA	Feb. 2002

the RARF accelerators, which will be used as injector for the RIBF.

The control system of the RRC vacuum system was renewed in the summer of 2002. A very old sequencer in the system was completely converted into a modern device, which is matched to the control system of new cyclotrons in the RIBF. At the same time, four sets of turbo-molecular pumps for each sub-vacuum chamber in the RRC sector magnet were also renewed.

The hyper-ECR ion source had been installed in the ion source room of the AVF in the preceding year in collaboration with the CNS of the University of Tokyo, and then an alternate use of the two ion sources (10 GHz-ECR and hyper-ECR) became available for the injection into the AVF with a mechanically switching bending magnet. The hyper-ECR ion source has been used to provide beams such as ^{12}C, ^{14}N, ^{16}O, ^{20}Ne, which are required frequently by users, and also to provide a beam for the CRIB experiment. During an operation of the hyper-ECR ion source, maintenance of the 10 GHz ECR ion source can be carried out.

A flat top rf system was added to the cavities of the AVF. The beam test with $^{14}N^{6+}$ ion was carried out to investigate the improvement of beam quality by the flat-top system. It was found out that the turn separation of the beam orbit in the cyclotron was enlarged. This indicates that the momentum spread of the beam has been successfully reduced. Moreover a beam transmission efficiency, *i.e.*, the ratio of the extracted beam current to the injected beam current of the RRC, was also improved by more than 10%.

Operation of the tandem accelerator

T. Kobayashi and K. Ogiwara

The 1.7 MeV tandem accelerator (pelletron) was operated for a total of 97 days for experiments, except for the time required for machine inspection and beam test (34 days), during the annual reporting period from Nov. 1, 2001 to Oct. 31, 2002. The system was shut down from April 1 to June 13 due to the deconstruction work on the plasma building.

Experimental studies on the following subjects were performed, and are still in progress except for those mentioned in (3)-(b).

(1) Nuclear reaction analysis (NRA) (53 days)
  (a) Lattice location of hydrogen in alloys by means of the channeling method
(2) Particle-induced X-ray emission (PIXE) (31 days)
  (a) Development of a highly sensitive high-resolution in-air PIXE system for chemical state analysis
  (b) Trace element analysis of biological and environmental samples using energy dispersive X-ray spectrometry
  (c) Characterization of the II-VI ternary semiconducting crystals
(3) Rutherford backscattering spectroscopy (RBS) (12 days)
  (a) RBS analysis of polymers and carbon materials containing metallic nanoparticles
  (b) Channeling analysis of interstitial atoms in ceramics and dopants in semiconductor materials

The total time in days, which was spent for each experiment, is shown in parentheses.

III. RESEARCH ACTIVITIES

1. Nuclear Physics

Nuclidic mass formula on a spherical basis with an improved even-odd term†

H. Koura,[*1] T. Tachibana,[*1] M. Uno,[*2,*1] and M. Yamada[*1]

[Binding energies and masses]

A nuclear mass formula with an improved even-odd term is presented as a revised version of our previous mass formula published in 2000.[1] The even-odd term is determined by considering the experimental even-odd properties which are different between neutrons and protons.[2] The shell energies of our method are calculated based on a spherical basis, that is, the spherical shell energies are calculated from spherical single-particle potentials, and the shell energy for a deformed nucleus is calculated from the superposition of spherical shell energies with appropriate weights. The obtained mass formula is applicable to nuclei with Z and $N \geq 2$. The root-mean-square (RMS) deviation from experimental masses[3] is 657.7 keV, which is less than that of our previous mass formula and is comparable or less than those of other two mass formulas having similar applicabilities, as shown in Table 1. The RMS deviations of some separation energies for the above mass formulas are also shown in Table 2, and our deviations are significantly smaller than those of other mass formulas.

Figure 1 shows the two-neutron separation energies S_{2n} for the experimental data (upper) and our results (lower). The solid lines connect nuclei with the same N. In such a figure, magicities are seen as large gaps between two lines. In general, the lines have similar smoothness, and large gaps are seen at $N = 8$, 14, 20, 28, 50, 82 and 126 around $S_{2n} = 10$–20 MeV. In the neutron-rich region, in which the lines go to the zero-line, large gaps of ours decrease in size at $N = 14$, 20, 28, 50, while they become larger than the neighboring ones at $N = 16$, 32 (or 34) and 58.

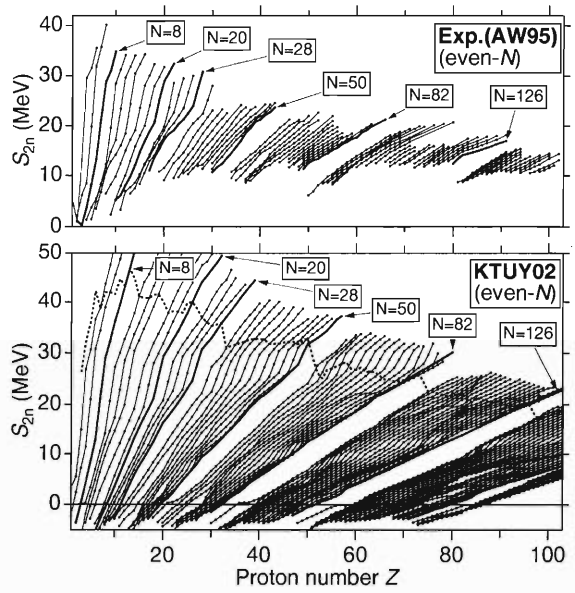

Fig. 1. Two-neutron separation energies S_{2n} of experimental data (upper) and this study (lower) for even-N. Solid lines connect nuclei with the same N and dashed lines connect proton-drip nuclei.

Table 1. RMS deviations of mass formulas in keV.

Mass formula	$Z, N \geq 2$ (1835 nuclei)	$Z, N \geq 8$ (1768 nuclei)
KTUY02 (this work)	657.7	640.8
KUTY00[1]	680.2	656.1
FRDM[4]	—	678.3
HFBCS-1[5]	—	718.0

Table 2. RMS deviations for separation energies in keV. Values in parentheses are the numbers of nuclei.

Mass formula	Neutron		Proton	
	S_n	S_{2n}	S_p	S_{2p}
$Z, N \geq 2$	(1648)	(1572)	(1592)	(1483)
KTUY02	361.7	466.0	403.1	542.0
$Z, N \geq 8$	(1585)	(1515)	(1527)	(1424)
KTUY02	319.1	391.9	344.4	465.8
FRDM[4]	416.7	551.6	409.0	514.2
HFBCS-1[5]	464.6	506.1	483.3	529.0

We tabulate ground-state masses, deformation parameters α_2, α_4, α_6, shell energies, one- and two-neutron separation energies, and one- and two-proton separation energies for 9432 nuclei ranging from $Z \geq 2$ and $N \geq 2$ to $Z \leq 130$ and $N \leq 200$.

† Condensed from the article in At. Data Nucl. Data Tables, submitted for publication

*1 Advanced Research Institute for Science and Engineering, Waseda University

*2 Ministry of Education, Culture, Sports, Science and Technology

References

1) H. Koura et al.: Nucl. Phys. A **674**, 47 (2000).
2) H. Koura et al.: RIKEN Accel. Prog. Rep. **36**, 10 (2003).
3) G. Audi et al.: Nucl. Phys. A **595**, 409 (1995).
4) P. Möller et al.: At. Data Nucl. Data Tables **59**, 185 (1995).
5) S. Goriely et al.: At. Data Nucl. Data Tables **77**, 311 (2001).

Properties of "experimental" even-odd term†

H. Koura,*1 T. Tachibana,*1 M. Uno,*2,*1 and M. Yamada*1

[Binding energies and masses]

To determine the even-odd term in the mass formula, we investigate the properties of "experimental" even-odd term. We take the form of the mass formula as

$$M(Z,N) = M_{\rm gsh}(Z,N) + M_{\rm eo}(Z,N), \quad (1)$$

where $M_{\rm gsh}$ represents both of a gross feature expressed as a smooth function of proton number Z and neutron number N, and a shell structure including the deformation effect. $M_{\rm eo}$ is an even-odd term and expressed as

$$M_{\rm eo} = M_{{\rm odd}Z}(Z,N)\delta_{{\rm odd}Z} + M_{{\rm odd}N}(Z,N)\delta_{{\rm odd}N} - M_{\rm oo}(Z,N)\delta_{{\rm odd}Z}\delta_{{\rm odd}N} \quad (2)$$

with

$$\delta_{{\rm odd}Z} = \begin{cases} 0 & \text{for } Z\text{-even}, \\ 1 & \text{for } Z\text{-odd}, \end{cases} \quad (3)$$

$$\delta_{{\rm odd}N} = \begin{cases} 0 & \text{for } N\text{-even}, \\ 1 & \text{for } N\text{-odd}. \end{cases} \quad (4)$$

When taking even-Z and odd-N, we obtain

$$M(Z,N-1) = M_{\rm gsh}(Z,N-1), \quad (5)$$
$$M(Z,N) = M_{\rm gsh}(Z,N) + M_{{\rm odd}N}(Z,N), \quad (6)$$
$$M(Z,N+1) = M_{\rm gsh}(Z,N+1). \quad (7)$$

Now we regard M as the experimental mass $M^{\rm exp}$, and obtain the "experimental" odd-N term as

$$M^{\rm exp}_{{\rm odd}N}(Z,N) = M^{\rm exp}(Z,N) - M_{\rm gsh}(Z,N) - \frac{1}{2}[M^{\rm exp}(Z,N-1) - M_{\rm gsh}(Z,N-1)] - \frac{1}{2}[M^{\rm exp}(Z,N+1) - M_{\rm gsh}(Z,N+1)]. \quad (8)$$

We take the above equation from Eqs. (5)–(7) instead of

$$M^{\rm exp}_{{\rm odd}N}(Z,N) = M^{\rm exp}(Z,N) - M_{\rm gsh}(Z,N) \quad (9)$$

because we take $M_{\rm gsh}$ from the current mass fromulas having deviations of several hundred keV and the magnitudes of $M_{{\rm odd}N}$ are comparable to these deviations.

We also obtain the "experimental" odd-Z term as

$$M^{\rm exp}_{{\rm odd}Z}(Z,N) = M^{\rm exp}(Z,N) - M_{\rm gsh}(Z,N) - \frac{1}{2}[M^{\rm exp}(Z-1,N) - M_{\rm gsh}(Z-1,N)] - \frac{1}{2}[M^{\rm exp}(Z+1,N) - M_{\rm gsh}(Z+1,N)]. \quad (10)$$

It is interesting to compare the magnitudes of the "experimental" $M_{{\rm odd}Z}$ and $M_{{\rm odd}N}$ between mirror nuclei. These magnitudes are expected to be similar because of the charge symmetry of the nuclear force. As $M_{\rm gsh}$, we take the KUTY gross and shell term,[1] in which the charge symmetry has been carefully treated. In Fig. 1, $M_{{\rm odd}N}(a,b) - M_{{\rm odd}Z}(b,a)$ values for mirror nuclei[2] are shown. Almost all the values are positive and the average is about 100 keV, which is considerably smaller than the average of the even-odd term itself in this mass region (a few MeV). This means that the even-odd term for a proton is smaller than that for a neutron.

There may be no doubt that the main reason of this is the Coulomb repulsive force between protons. We think that the positiveness is brought about through two mechanisms. One is that the single-proton potential, which is composed of an averaged nuclear potential and a Coulomb potential, is broader than the single-neutron potential. Thus the single-particle level spacing for a proton is narrower than that for a neutron. Another is related to the proton-proton interaction. When two protons form a pair, the Coulomb repulsive force between them counteracts the two-body nuclear force in the isospin-triplet spin-singlet state, therefore the even-odd effect decreases.

Considering the above features of the "experimental" even-odd term, we have developed the functional form of the even-odd term in our mass formula.

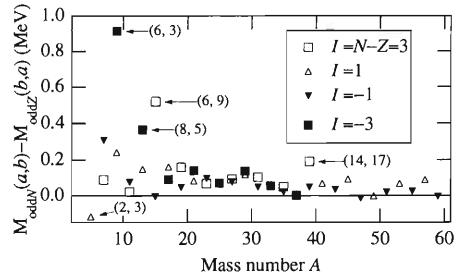

Fig. 1. Differences in "experimental" even-odd term between mirror nuclei. Some sets are indicated by (Z,N).

† Extracted from the article in At. Data Nucl. Data Tables, submitted for publication

*1 Advanced Research Institute for Science and Engineering, Waseda University

*2 Ministry of Education, Culture, Sports, Science and Technology

References

1) H. Koura et al.: Nucl. Phys. A **674**, 47 (2000).
2) G. Audi et al.: Nucl. Phys. A **595**, 409 (1995).

Fusion theory for superheavy elements

C. W. Shen,[*1] G. Kosenko,[*2] and Y. Abe[*3]

[Theory of fusion, Superheavy element]

The two-step model for fusion of massive heavy ions which was proposed by the present authors[1] is applied to ^{48}Ca + actinide target systems. There, the fusion process is divided into two steps; collisions of the incident ions which determine the sticking probability $P_{\rm stick}$ and evolution of the amalgamated nucleus which determines the formation probability $P_{\rm form}$. Thus, the fusion probability is given by the product of the sticking probability and the formation probability.

$$P^J_{\rm fusion}\left(E_{\rm c.m.}\right) = P^J_{\rm stick}\left(E_{\rm c.m.}\right) \cdot P^J_{\rm form}\left(E_{\rm c.m.}\right). \qquad (1)$$

The sticking probability is obtained by solving the approaching phase up to the point of contact of the incident ions where the surface friction model[2] is employed with an extention including random forces. The formation probability is obtained by solving a Langevin equation which describes shape evolution to the spherical shape, starting from the contact configuration.[3] The shapes are described by the Two-Center Parameterization.[4] As dynamical variables, we only use the distance between two centers and the mass asymmetry. The deformations of the ions are taken to be zero, while the neck parameter is taken to be 0.8. Since the incident ions are expected to be excited in the approaching phase up to the contact point, the shell correction energy of the amalgamated system is not taken into account, *i.e.*, LDM energy is used as a potential energy for the collective shape motion. As friction for the shape evolution, we employ the One-Body Wall-and-Window formula.[5]

With the fusion probability thus obtained, fusion cross sections are calculated as usual,

$$\sigma_f\left(E_{\rm c.m.}\right) = \pi \lambda\!\!\!^{-2} \bar{\Sigma}\,(2J+1) \cdot P^J_{\rm fusion}\left(E_{\rm c.m.}\right), \qquad (2)$$

where $\lambda\!\!\!^{-}$ denotes the wavelength divided by $2 \cdot \pi$ of the incident channel.

Results are shown in Fig. 1, together with the available experimental data from GSI[6] and from Dubna.[7] It is remarkable that the calculations reproduce very well the measured excitation functions systematically over three ^{48}Ca + actinide target systems.

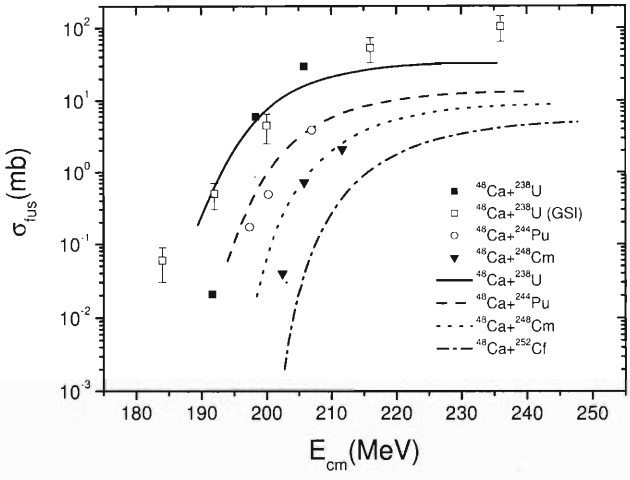

Fig. 1. Calculated fusion excitation functions for four systems of ^{48}Ca + actinide targets are compared with the available experimental data from GSI[6] and Dubna.[7]

Furthermore, a prediction is made for the ^{252}Cf target case which is to be tested by experiment.

Systematic studies of residue cross sections for the superheavy elements are being carried out, combined with a new statistical code KEWPIE.[8]

References

1) C. W. Shen et al.: Phys. Rev. C **66**, 061602 (R) (2002); Y. Abe et al.: Prog. Theor. Phys. Suppl. No. 146, 104 (2002); Y. Abe et al.: to be published in Proc. DANF01, Casta-Papiernicka, Slovakia, 2001-10 (World Scientific Inc., 2001).
2) D. H. E. Gross and H. Kalinowski: Phys. Rep. **45**, 175 (1978).
3) Y. Abe et al.: J. de Phys. **47**, C4-329 (1986); Y. Abe et al.: Phys. Rep. **275**, No. 2/3 (1996).
4) K. Sato et al.: Z. Phys. A **290**, 145 (1979).
5) J. Blocki et al.: Ann. Phys. (NY) **113**, 330 (1978).
6) W. Q. Shen et al.: Phys. Rev. **36**, 115 (1987).
7) M. G Itkis et al.: Nuovo Cimento A **111**, 783 (1998).
8) B. Bouriquet et al.: in preparation.

*1 Laboratori Nazionale di Sud, Istituto Nazionale di Fisica Nucleare, Italy
*2 Department of Physics, Omsk University, Russia
*3 Yukawa Institute for Theoretical Physics, Kyoto University

Saturation of nuclear matter and radii of unstable nuclei

K. Oyamatsu* and K. Iida

[Dense matter, Saturation, Unstable nuclei]

We systematically examine relationships among the parameters characterizing the phenomenological equation of state (EOS) of nearly symmetric, uniform nuclear matter near the saturation density by comparing macroscopic calculations [1] of radii and masses of stable nuclei with the experimental data.

We may generally express the energy per nucleon near the saturation point of symmetric nuclear matter of nucleon density n and proton fraction x as

$$w = w_0 + \frac{K_0}{18n_0^2}(n-n_0)^2 + \left[S_0 + \frac{L}{3n_0}(n-n_0)\right]\alpha^2. \quad (1)$$

Here, w_0, n_0, and K_0 are the saturation energy, the saturation density, and the incompressibility of symmetric nuclear matter, respectively, and $\alpha = 1-2x$ is the neutron excess. L and S_0 are associated with the density-dependent symmetry energy $S(n)$; S_0 is the symmetry energy at $n = n_0$, and $L = 3n_0(dS/dn)_{n=n_0}$ is the symmetry energy density-derivative coefficient. As the neutron excess increases from zero, the saturation point moves in the density versus energy plane. This movement is determined mainly by the parameters L and S_0. The slope, y, of the saturation line near $\alpha = 0$ ($x = 1/2$), expressed as

$$y = -\frac{K_0 S_0}{3n_0 L}, \quad (2)$$

characterizes the EOS of asymmetric matter as shown in Fig. 1.

We estimate a range of (K_0, L) from the empirically reasonable values of the slope of the saturation line, and find a strong correlation between S_0 and L. In the light of the uncertainties in the values of K_0 and L, we macroscopically calculate the radii of unstable nuclei as expected to be produced in future facilities. The results for Ni and Sn isotopes are plotted in Fig. 2. We find that the matter radii depend appreciably on L while being almost independent of K_0, a feature that may help to determine the L value via systematic measurements of nuclear size.

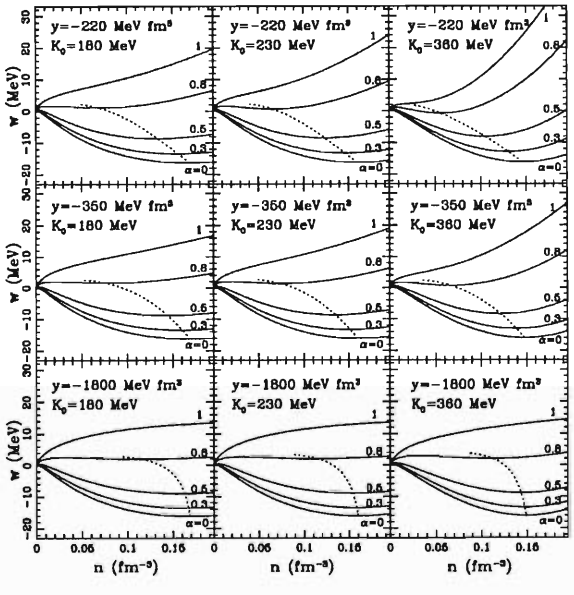

Fig. 1. Energy per nucleon as a function of nucleon density at $\alpha = 0, 0.3, 0.5, 0.8, 1$ (from bottom to top), plotted for combinations of $y = -220, -350, -1800\,\mathrm{MeV\ fm^3}$ and $K_0 = 180, 230, 360\,\mathrm{MeV}$. Dotted lines denote the saturation lines.

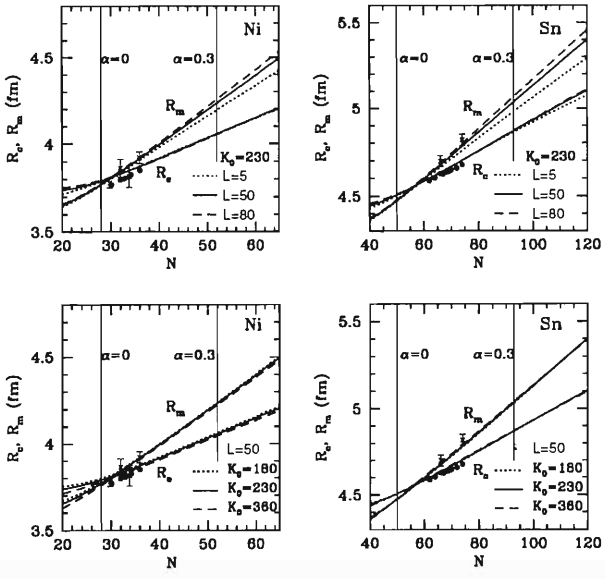

Fig. 2. Root-mean-square charge and matter radii of Ni and Sn isotopes for combinations of $L = 5, 50, 80\,\mathrm{MeV}$ and $K_0 = 180, 230, 360\,\mathrm{MeV}$. Experimental data on the root-mean-square charge radii [2] (dots) and matter radii [3] (crosses) are also plotted.

* Department of Media Production and Theories, Aichi Shukutoku University

References

1) K. Oyamatsu: Nucl. Phys. A **561**, 431 (1993).
2) H. de Vries, C. W. de Jager, and C. de Vries: At. Data Nucl. Data Tables **36**, 495 (1987).
3) C. J. Batty, E. Friedman, H. J. Gils, and H. Rebel: Adv. Nucl. Phys. **19**, 1 (1989).

Patterns of r-process nucleosynthesis in supernova explosions

K. Sumiyoshi,[*1] M. Terasawa,[*2] H. Shen,[*3] S. Yamada,[*4] H. Suzuki,[*5] T. Kajino,[*2] and H. Toki[*6]

[R-process, Unstable nuclei, Supernova, EOS]

Recent increase of observational data of r-process elements in extremely metal-poor stars[1] has supported the idea that such r-process elements are produced with the solar abundance pattern in massive stars having a short life, such as supernovae. Moreover, it revealed that there is more than one site that produces universal patterns for light and heavy r-process elements. Therefore, it is very interesting to seek the astrophysical r-process sites, which produce universal but different abundance patterns. One answer to the puzzle of the multiple r-process sites is to consider the mass range of pre-supernova stars, which is related to the explosion mechanism (See Fig. 1).

Typical supernovae from most massive stars explode with a delayed explosion mechanism due to a large Fe core mass. After the birth of a nascent neutron star, neutrino-driven winds occur with the neutrino heating of the neutron star surface. The r-process elements are produced during the rapid expansion of alpha-rich material with neutrons in the neutrino-driven wind. On the other hand, low-mass stars ($\sim 10\,M_{\odot}$), having a rather small Fe core mass, may explode hydrodynamically after the bounce of the central core. This so-called prompt explosion is energetic and the neutron-rich material close to the nascent neutron star can be ejected dynamically to produce the r-process elements.

In order to determine the r-process patterns from each supernova event in different mass ranges of pre-supernova stars, we perform hydrodynamical simulations of the r-process in the prompt explosion[2] and in the neutrino-driven winds[3–5] by adopting the latest information of the equation of state (EOS)[6] and the extended nuclear reaction network with 3000 nuclear species.[7] The table of relativistic EOS[8] is derived by the relativistic mean field theory based on the experimental masses and radii including the data of unstable nuclei. The extended nuclear reaction network includes the reactions of unstable nuclei in the light mass region up to the drip line. Those light neutron-rich nuclei may play important roles in the r-process[7] and thus the systematic measurement of nuclear reactions is necessary.

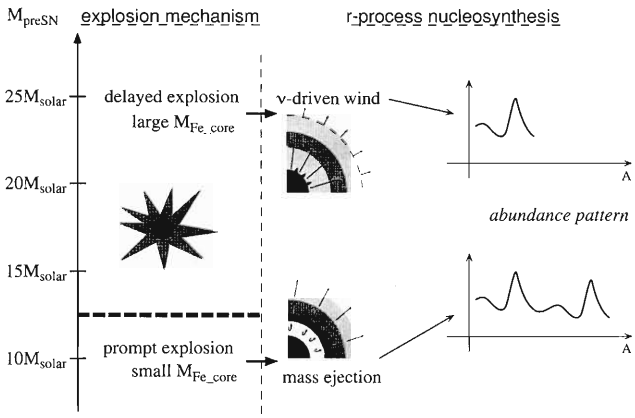

Fig. 1. Schematic diagram displays the relation between the supernova mechanism and the r-process nucleosynthesis as a function of the mass of presupernova star.

By performing the numerical simulations of hydrodynamics coupled with the nuclear reaction network, we have shown that the two scenarios of the r-process in supernovae are viable, depending on the mass of pre-supernova stars and the explosion mechanism.[9] Comparisons of abundance patterns to distinguish the two scenarios are important for cosmochronology using Th-U and future observations of the r-process elements.

Numerical studies of supernova explosions by general relativistic hydrodynamics with neutrino-transfer are now under way using the relativistic EOS table. We will examine the possible mass ejection in prompt explosions and the environment of the neutrino-driven winds above proto-neutron stars in delayed explosions. Further careful studies on the reaction rates of electron captures on neutron-rich nuclei and neutrino scatterings in dense matter in the light of radioactive nuclear beam experiments are necessary for these new supernova simulations.

*1 Numazu College of Technology
*2 National Astronomical Observatory
*3 Department of Physics, Nankai University, China
*4 Department of Physics, Waseda University
*5 Faculty of Science and Technology, Tokyo University of Science
*6 Research Center for Nuclear Physics, Osaka University

References

1) C. Sneden et al.: Astrophys. J. **467**, 819 (1996).
2) K. Sumiyoshi, M. Terasawa, G. J. Mathews, T. Kajino, S. Yamada, and H. Suzuki: Astrophys. J. **562**, 880 (2001).
3) K. Otsuki, H. Tagoshi, T. Kajino, and S. Wanajo: Astrophys. J. **533**, 424 (2000).
4) K. Sumiyoshi, H. Suzuki, K. Otsuki, M. Terasawa, and S. Yamada: Pub. Astron. Soc. J. **52**, 601 (2000).
5) M. Terasawa, K. Sumiyoshi, S. Yamada, H. Suzuki, and T. Kajino: Astrophys. J. Lett. **578**, L137 (2002).
6) H. Shen, H. Toki, K. Oyamatsu, and K. Sumiyoshi: Nucl. Phys. A **637**, 435 (1998).
7) M. Terasawa, K. Sumiyoshi, T. Kajino, G. J. Mathews, and I. Tanihata: Astrophys. J. **562**, 470 (2001).
8) H. Shen, H. Toki, K. Oyamatsu, and K. Sumiyoshi: Prog. Theor. Phys. **100**, 1013 (1998).
9) K. Sumiyoshi: Nucl. Phys. A, (2003), in press.

^{40}K electron capture decay at ultrahigh pressures

Y. Mochizuki, K. Takahashi,[*1] and T. Izuyama[*2]

[first-forbidden-unique transition, ^{40}K/^{40}Ar dating method, ultrahigh pressure earth science]

The suggestion that the decay constants of certain radioactive nuclides might be altered by varying the electron density near their nuclei was proposed independently by Daudel [1] and Segrè [2] more than half a century ago. Attempts have been made to observe this effect, by changing either the chemical or the physical environment of nuclides that decay by electron capture or internal conversion.[3]

As a radioactive nuclide undergoing electron capture decay, ^{40}K is of great interest for such study, since a slight change in the decay rate may have a great influence on earth science. The electron capture decay of ^{40}K to the 1461 keV level in ^{40}Ar is a first-forbidden-unique transition with a Q value of only 44 keV. This decay mode is the basis for the ^{40}K/^{40}Ar dating technique. Because K-containing minerals were subjected to high pressures during their geological history, the ages of these materials determined by the conventional dating method might be overestimated if the decay rate is increased with pressure. Also, the amounts of ^{40}K and ^{40}Ar may constrain recycling continental crust into the mantle.[4]

Very recently, Liu *et al.* [5] measured the effect of pressure on the decay rate of ^{7}Be, the lightest electron capture decay nuclide, using diamond-anvil pressure cells. They found that the decay constant of ^{7}Be increases by about 1% at 40 GPa.[a] This suggests that the pressure-induced change in the electron capture decay would also be expected in ^{40}K. Furthermore, the equation of state (EOS; the relation between atomic volume and pressure) of potassium metal was studied with diamond-anvil cells by energy-dispersive X-ray diffraction with synchrotron radiation at room temperature up to 50 GPa.[6] As for the influence of chemical forms on the decay rate of ^{40}K, Norman *et al.* [7] found no evidence of the change to within their measurement precision ±1%.

In this article, we estimate the pressure-induced change of the electron capture decay rate of metallic ^{40}K, because we already know its experimental EOS up to 50 GPa. It is worth noting here that the pressure inside the earth attains 23 GPa at the boundary of the upper and lower mantles (660 km in depth), and 136 GPa at the core-mantle boundary (CMB; 2890 km in depth). The current diamond-anvil technique can provide pressures up to 100 GPa. At the CMB, ^{40}K is expected to be included in the form of $KAlSi_3O_4$, the so-called hollandite structure. As a crude estimate, the pressure-induced change in the decay rate of metallic ^{40}K will give the upper limit of that of ^{40}K in hollandite, since the hollandite structure is found to be less compressible compared to potassium metal up to 5 GPa.[8]

In our calculation, we confine 18 bound electrons and a free (conduction) electron within a rigid sphere, surrounding a finite ^{40}K nucleus at its center. We have solved the field of an ion self-consistently using relativistic, Dirac-Slater method with a new Kohn-Sham potential to describe interelectron interaction correctly. We then obtain radial orbital wave functions for bound electrons and their binding energies. With these values the electron capture decay rate is computed as the summation of the contribution from each orbital electron. The nature of the unique first forbidden decay of ^{40}K has been treated carefully, including the nuclear shape factor, for the first time.

Our preliminary result suggests the enhancement of the electron capture decay rate in the order of 10^{-5} relative to its atmospheric value in the range of pressures of interest. This difference is smaller than the accuracy, 10^{-4}, of decay constant measurements that are the most accurate at this moment. It should be noted, however, that the lattice effect is not taken into account in our calculation presented here. This may cause an increase in the decay rate and should be examined in the future.

References

1) R. Daudel: Rev. Sci. **85**, 162 (1947).
2) E. Segrè: Phys. Rev. **71**, 274 (1947).
3) G. T. Emery: Ann. Rev. Nucl. Sci. **22**, 165 (1972).
4) N. Coltice et al.: Science **288**, 845 (2000).
5) L. Liu et al.: Earth Planet. Sci. Lett. **180**, 163 (2000).
6) M. Winzenick et al.: Phys. Rev. B **50**, 12381 (1994).
7) E. B. Norman et al.: Phys. Lett. B **519**, 15 (2001).
8) J. Zhang et al.: Am. Mineral. **78**, 493 (1993).

*1 Max-Planck Institute for Astronomy, Germany
*2 Department of Physics, Toho University

a) The pressure 1 GPa corresponds to 10 kbar.

Three-dimensional TDHF calculation on reactions of unstable nuclei

K.-H. Kim, T. Otsuka,[*1] and P. Bonche[*2]

[NUCLEAR REACTION, Unstable nuclei]

Recent developments in experiments with radioactive nuclear beams enable us to study nuclei far from the β-stability line, *i.e.*, unstable nuclei. Characteristic features of the structure of unstable nuclei, such as a neutron halo and neutron skin, have attracted much interest not only in themselves but also in their effects on reactions. We study here the reactions of unstable nuclei with neutron skin.

We have applied here the time-dependent Hartree-Fock (TDHF) method[1)] in three dimensions with the full Skyrme interaction[2)] to study the reactions of unstable nuclei. We mention that, at present, the TDHF is probably the only possible and practical means of describing massive transfer and fusion of nuclei with neutron skin where the density, mean potential and shape of the nuclei may change much more significantly than those of stable nuclei and the core part of halo nuclei in an unexpected way.

We have already studied the reactions of ^{28}O as an example of unstable nuclei with neutron skin.[1)] In the case of the reactions between a stable nucleus and an unstable nucleus with neutron skin, it is interesting whether the neutron skin enhances the fusion cross section or not. In the case of the ^{28}O+^{16}O and ^{28}O+^{40}Ca reactions, an enhancement of the fusion cross section is not observed compared with the reaction between stable nuclei, such as ^{16}O+^{16}O and ^{16}O+^{40}Ca. These results are consistent with the results of the two-dimensional one.[3)] Since in the case of light nuclei, the number of neutrons in the neutron skin is not large, for example it is four in ^{28}O, and they are all loosely bound, neutron transfer can easily occur compared with the case of stable nuclei, although the separation of these neutrons from the core can easily occur simultaneously compared with the case of stable nuclei. Therefore, neutron transfer does not enhance the fusion cross section directly, but massive transfers are seen both for neutrons and protons.

The situation is changed in the case of reactions of heavier unstable nuclei. We have considered the reactions of ^{60}Ca as a heavier unstable nucleus with neutron skin. Similarly to the reactions of ^{28}O, a significant difference in the fusion cross section between the ^{60}Ca+^{40}Ca and ^{40}Ca+^{40}Ca reactions is not seen. In the former reaction, massive transfers are seen both for neutrons and protons, similarly to the reactions of ^{28}O. The cross section of one nucleon transfer becomes larger than the case of ^{28}O, because ^{60}Ca has much more neutrons in the neutron skin.

In the case of the ^{60}Ca+^{16}O reaction, on the other hand, the fusion cross section becomes larger compared with the ^{40}Ca+^{16}O reaction. We can also see that the cross section of the neutron transfer for this reaction is not as large as that of the ^{60}Ca+^{40}Ca reaction. In this case, neutron flow still occurs easily due to the difference in the neutron Fermi energies between ^{60}Ca and ^{16}O, similar to the ^{60}Ca+^{40}Ca reaction, although the channels of the neutron transfer are not so favored due to energy constraints.

We also see the situation is similar in the case of protons, too. The cross section of the proton transfer for the ^{60}Ca+^{16}O reaction is much smaller than that for the ^{60}Ca+^{40}Ca reaction. It is easy to understand that the channels of such reactions are not favored due to energy constraints, since transfer of both neutrons and protons generates another neutron-rich unstable nucleus for ^{16}O. Because neutrons and protons can easily move between ^{60}Ca and ^{16}O, and the transfer of these nucleons is difficult for these nuclei, the nucleon flow enhances the fusion in the case of this reaction.

We can study more reactions taking various stable nuclei in the case of reactions of heavier unstable nuclei with neutron skin. It is interesting to see the relation between the nucleon transfer and the fusion for such reactions.

References

1) K.-H. Kim, T. Otsuka, and P. Bonche: J. Phys. G: Nucl. Part. Phys. **23**, 1267 (1997).
2) E. Chabanat, P. Bonche, P. Hansel, J. Meyer, and R. Schaeffer: Phys. Scr. T **56**, 31 (1995).
3) K.-H. Kim, T. Otsuka, and M. Tohyama: Phys. Rev. C **50**, R566 (1994).

*1 Department of Physics, University of Tokyo
*2 Service de Physique Théorique, CE Saclay, France

Dependence of density-distribution analyses on the choice of basis functions

A. Kohama, R. Seki,* A. Arima, and S. Yamaji

[NUCLEAR REACTION: matter density distribution of nuclei, least-squares fitting, proton-nucleus elastic scattering]

Neutron-rich nuclei have received much attention since their discovery in the mid-80s. Their one-body matter density distributions, particularly in the surface region, are appropriate quantities to explore, because the presence of a halo structure is expected to be one of their interesting features. Such measurements are planned for in the upcoming experiments at the Radioactive Ion Beam Factory (RIBF) of RIKEN.

From this viewpoint, we showed that the matter density distribution of neutron-rich nuclei in the surface region can be determined well using a relatively low-intensity beam on the order of 10 [sec^{-1}], which is the expected intensity of the ^{78}Ni beam at the RIBF.[1] In our simulations, the density distributions are determined in a model-independent way [1,2] by generating pseudodata and performing error analysis. The density distributions are expanded in a linear combination of Gaussian basis functions,[3] and their coefficients are determined by least-squares fitting with the pseudodata of the cross sections.

Here we report that we have confirmed our conclusion above by comparing the error distributions calculated from two different basis functions. The dependence of the density distribution in the surface region on the choice of basis functions is found to be very weak.[1] We introduce the statistical and systematic errors for the fitted density distributions: The statistical error shows how large the fitted results fluctuate around the sample mean, while the systematic error shows the deviation of the sample means from the true value.[4] The numerical results are shown in the figures. Each curve represents the relative error, because the results are divided by $\rho_{\rm true}(r)$ which is used to generate the pseudodata. Figure 1 (a) shows that the matter density distribution in the surface region can be determined well using our Gaussian basis functions, and the results in Fig. 1 (b) confirm this statement based on the well-established Fourier-Bessel basis functions,[2] because each basis function shows similar types of behaviors in the surface region.

References

1) A. Kohama, R. Seki, A. Arima, and S. Yamaji: nucl-th/0211025.
2) J. L. Friar and J. W. Negele: Adv. Nucl. Phys. **8**, 219 (1975).
3) M. Kamimura: Phys. Rev. A **38**, 621 (1988).
4) G. Cowan: *Statistical Data Analysis* (Clarendon Press, Oxford, 1998).

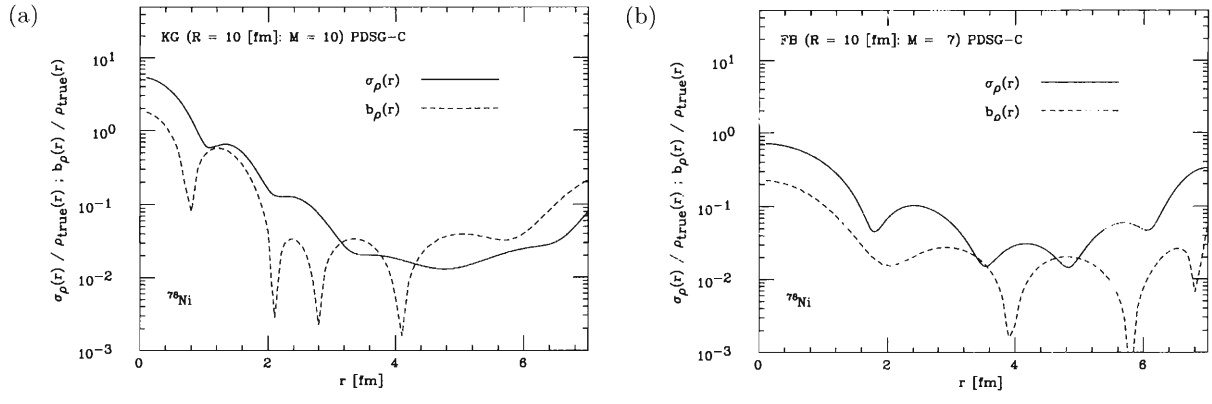

Fig. 1. Statistical and systematic errors of the 25 fitted density distributions for the pseudodata set group C (PDSG-C) of ^{78}Ni for (a) our Gaussian basis functions ($M = 10$) [3] and (b) the Fourier-Bessel basis functions ($M = 7$).[2] The solid curve is the statistical error and the dashed one is the systematic error. R (= 10 [fm]) is the maximum distance to probe nuclei by the experiment, and M is the number of basis functions. Each M is the best choice for this pseudodata set group corresponding to a nuclear beam intensity of 10 [sec^{-1}] at the RIBF.

* Department of Physics and Astronomy, California State University, Northridge, and W. K. Kellogg Radiation Laboratory, California Institute of Technology, USA

Cross section calculations in Glauber model: I. Core plus one-nucleon case†

B. Abu-Ibrahim,[*1] Y. Ogawa,[*2] Y. Suzuki,[*3] and I. Tanihata

[Glauber model, One-nucleon halo, Reaction cross section, Nucleon-removal cross section, Momentum distribution, Elastic differential cross section]

We have developed a computer code to calculate the inclusive cross sections for various reactions between composite particles in the framework of the Glauber model. This code gives the reaction cross section, one-nucleon removal cross section, momentum distribution, and elastic differential cross section. These quantities have played an important role in revealing nuclear structure and the measurement of these cross sections is now a standard work for the study of the structure of unstable nuclei, particularly the halo structure near the drip-line.[1–3)]

The phase-shift function which appears in the calculation for these cross sections based on the Glauber model[4)] is given by

$$e^{i\chi_{PT}(\boldsymbol{b})} = \left\langle \Psi_0\Theta_0 \left| \prod_{i\in P}\prod_{j\in T} \left[1-\Gamma\left(\boldsymbol{b}+\boldsymbol{s}_i^P-\boldsymbol{s}_j^T\right)\right] \right| \Psi_0\Theta_0 \right\rangle . \quad (1)$$

Equation (1) includes a very complicated multidimensional integration. This integration is usually reduced to a much simpler one by introducing the optical-limit approximation (OLA). The OLA, however, truncates the significant part of the breakup effects which plays an important role in the reaction of weakly bound nuclei.[5,6)] In this code, to take into account the breakup effects, we perform the integration for the valence-nucleon coordinate without any approximation as follows,[6–8)]

$$e^{i\chi_{PT}(\boldsymbol{b})} \to \langle\varphi_0|e^{i\chi_{CT}(\boldsymbol{b}_C)+i\chi_{NT}(\boldsymbol{b}_C+\boldsymbol{s})}|\varphi_0\rangle. \quad (2)$$

The projectile nucleus is assumed to be a system of a core nucleus coupled with a valence-nucleon, in which the valence-nucleon is described with a pure configuration $nljm$,

$$\Psi_0 = \varphi_{nljm}(\boldsymbol{r})\Phi(\text{core}). \quad (3)$$

The profile function Γ is determined so as to fit empirical nucleon-nucleon scattering amplitudes and is assumed to have one-range Gaussian form or zero-range delta form. The phase-shift functions between the core and the target, χ_{CT}, and between the valence-nucleon and the target, χ_{NT}, are calculated in the optical limit and are calculated through the relevant core and target densities.

The integration over the valence-nucleon coordinates (from 4 to 6 dimensions) is performed by Monte Carlo quadrature with Metropolis algorithm,[9)] while the integration over the impact parameter is performed with a trapezoidal rule. In the Monte Carlo integration, a set of configuration or integration points is generated according to a suitably chosen guiding function $w(\boldsymbol{x})$. In order to obtain the result with much higher precision, the integration points are concentrated about the values of $\boldsymbol{x}$ where the guiding function or integrand is large, while the computing power is decreased for the values of $\boldsymbol{x}$ where the guiding function or integrand is small. These generated random points are used to perform the multidimensional integration for all impact parameter values. In this code, a user is advised to make sure the convergence of the Monte Carlo integration by changing the number of integration points and the step size of the random work which control the accuracy of the present method.

The running times, in the case with two-range Gaussians for the core and target densities and with 500,000 integration points, are as follows; 5 min for the total reaction cross section, 5 min/point for the elastic differential cross section, and 10 min/point for the momentum distribution on a Digital Unix computer at RIKEN (Alpha Server ES40, 2048 MB Memory, True 64 Unix 4.0 G). The details for the program description and how to run the code are given in an article shown in the footnote.

† Condensed from the article in Comput. Phys. Commun., in Press

*1 Department of Physics, Cairo University, Egypt
*2 Research Center for Nuclear Physics, Osaka University
*3 Department of Physics, Niigata University

References

1) I. Tanihata et al.: Phys. Rev. Lett. **55**, 2676 (1985).
2) T. Kobayashi et al.: Phys. Rev. Lett. **60**, 2599 (1988).
3) A. Ozawa et al.: Nucl. Phys. A **693**, 32 (2001).
4) R. J. Glauber: in *Lectures in Theoretical Physics, Vol. 1*, edited by W. E. Brittin and L. C. Dunham (Interscience, New York, 1959), p. 315.
5) K. Yabana, Y. Ogawa, and Y. Suzuki: Phys. Rev. C **45**, 2909 (1992).
6) G. F. Bertsch, H. Esbensen, and A. Sustich: Phys. Rev. C **42**, 758 (1990).
7) Y. Ogawa, K. Yabana, and Y. Suzuki: Nucl. Phys. A **543**, 722 (1992).
8) J. S. Al-Khalili and J. A. Tostevin: Phys. Rev. Lett. **76**, 3903 (1996).
9) N. Metropolis, A. Rosenbluth, M. Rosenbluth, A. Teller, and E. Teller: J. Chem. Phys. **21**, 1087 (1953).

Disappearance of the $N = 20$ magic structure studied using nuclear moments of Na isotopes

Y. Utsuno,[*1] T. Otsuka,[*2] T. Mizusaki,[*3] and M. Honma[*4]

[Nuclear structure, Shell model, Unstable nuclei]

Over the last two decades, it has been well established that the $N = 20$ magic structure disappears in the neutron-rich region indicated, for instance, by a large $B(E2; 0_1^+ \rightarrow 2_1^+)$ value of ^{32}Mg.[1] As for the boundary of which the magic number disappears, a clear answer has not yet been given by many experimental and theoretical studies. In the present study, we theoretically investigated the boundary, focusing on the electric quadrupole and magnetic dipole moments of Na isotopes. The Monte Carlo shell model (MCSM)[2] was used for a large-scale shell-model calculation performed in part with the Alphleet and Alphleet-2 computer systems in RIKEN.

The model space and the effective interaction are the same as those in our previous study.[3] The Na isotopes have an odd Z number, for which the feasibility of the MCSM calculation was confirmed.[4] In a similar manner, the moments of Na isotopes are calculated and compared with experimental values[5] in Fig. 1. Up to $N = 18$, the *sd*-shell calculation well reproduces experimental quadrupole and magnetic moments, whereas a large discrepancy between them is seen for $N = 19$ and 20. On the other hand, the MCSM including the *pf* shell succeeds in reproducing all of them. In the decomposition of the ground-state wave function obtained by the MCSM into *np-nh* configurations ($n = 0, 2, 4, \ldots$), it is observed that ^{30,31}Na are dominated by the 2*p*-2*h* configurations. Namely, for Na isotopes the closed-shell structure is completely broken at $N = 19$, which is not shown by previous shell-model calculations.

Based on the agreement of the moments, we shall discuss the mechanism of the disappearance of the $N = 20$ magic number in neutron-rich nuclei. Recently, it has been suggested by our group[6] that a strong spin-isospin dependence in the NN interaction induces that the so-called *effective single-particle energy*[3] between the *sd*- and *pf*- shells becomes narrower for smaller Z. Due to this effect, the disappearance can occur for isotopes lighter than $N = 20$. In order to confirm whether or not this is essential, the effective $N = 20$ energy gap is artificially widened by shifting the monopole interaction, and we examine the ground-state properties. As a result, the disappearance of $N = 19$ never occurs with aneffective shell gap wider than $\sim$4 MeV, and ^{31}Na with $N = 20$ is still dominated by the 2*p*-2*h* configurations. The quadrupole and magnetic moments of ^{30}Na move from near the experimental value to the *sd*-shell value simultaneously. Note that the $N = 20$ shell gap around a stable nucleus ^{40}Ca is about 6 MeV. It is thus concluded that the single-particle structure in the neutron-rich region is indeed different from that of stable nuclei, and that this narrow shell gap plays an important role in the disappearance.

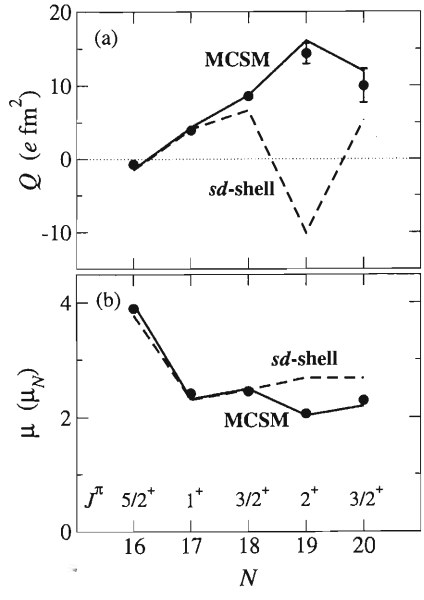

Fig. 1. (a) Electric quadrupole and (b) magnetic dipole moments of Na isotopes compared between experiment[5] (symbols) and shell-model calculations (lines). The solid and dashed lines respectively stand for the MCSM and *sd*-shell model.

*1 Japan Atomic Energy Research Institute
*2 Department of Physics, University of Tokyo
*3 Institute of Natural Sciences, Senshu University
*4 Center for Mathematical Sciences, University of Aizu

References

1) T. Motobayashi et al.: Phys. Lett. B **346**, 9 (1995).
2) T. Otsuka, M. Honma, T. Mizusaki, N. Shimizu, and Y. Utsuno: Prog. Part. Nucl. Phys. **47**, 319 (2001).
3) Y. Utsuno, T. Otsuka, T. Mizusaki, and M. Honma: Phys. Rev. C **60**, 054315 (1999).
4) Y. Utsuno, T. Otsuka, T. Mizusaki, and M. Honma: Phys. Rev. C **64**, 011301(R) (2001).
5) M. Keim et al.: Eur. Phys. J. A **8**, 31 (2000).
6) T. Otsuka, R. Fujimoto, Y. Utsuno, B. A. Brown, M. Honma, and T. Mizusaki: Phys. Rev. Lett. **87**, 082502 (2001).

Monte Carlo shell model description of ^{136}Te

N. Shimizu, T. Otsuka,[*1] T. Mizusaki,[*2] and M. Honma[*3]

[Nuclear Shell Model, Quadrupole Collective States]

The nuclear collective motion has been one of the most intriguing and unique problems of many-body physics. It is unique in the sense that the nucleus is a truly quantum system and, at the same time, one can discuss its "shape." The nuclear shell model is one of the most useful tools for studying the nuclear structure microscopically. However, the large dimensions of the Hilbert space prevent us from diagonalizing its Hamiltonian matrix, especially for the medium-heavy nuclei. In order to overcome such difficulty, the Monte Carlo Shell Model (MCSM) has been proposed,[1] which enabled us to apply the nuclear shell model to the collective states of the medium-heavy nuclei.[2]

Recently, the anomalously small B (E2) value of ^{136}Te has been observed by Radford *et al.*[3] Here, we discuss the structure of ^{136}Te using the nuclear shell model. Because the quadrupole collective states have already been discussed at the microscopic level using the MCSM, we use the same effective Hamiltonian and effective charges, which can reproduce the spherical to deformed phase transition of Ba isotopes.[2]

Figure 1 shows the E2 transition probabilities of Sn, Te, Xe, and Ba isotopes obtained by experiments and by calculation using the MCSM. One sees a good agreement between the experiments and the present calculations even in terms of the B (E2) value of ^{136}Te, the neutron number of which is 84.

The anomalous value is due to the low 2_1^+ level of ^{134}Sn (its excitation energy is 0.725 MeV), in comparison with the 2_1^+ level of ^{134}Te (1.280 MeV). The 2_1^+ level of ^{134}Sn is mainly dominated by a 2^+ state of two neutrons, called D_ν, and that of ^{134}Te of a 2^+ state of two protons, called D_π. The 2^+ state of ^{136}Te (0.606 MeV) is mainly dominated by the product of $S_\pi \times D_\nu$, because the other product has an excitation energy of nearly twice higher. This means that the quadrupole collectivity is not sufficiently strong. Results of studying the wave function indicate that the probability ratio of $S_\pi \times D_\nu$ is larger than the ratio of $D_\pi \times S_\nu$ in ^{136}Te by a factor of approximately four. This structure is the main reason for the small B (E2) value of ^{136}Te. Generally, these ratios are equally important.

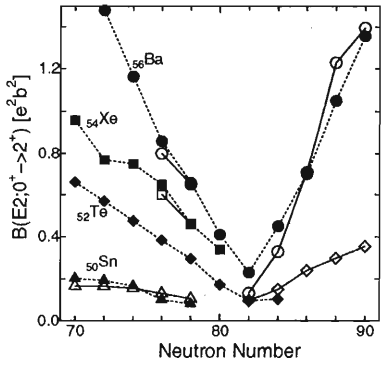

Fig. 1. B (E2;$0_1^+ \rightarrow 2_1^+$) values obtained by experiments[3] (solid symbols) and calculation using MCSM (blank symbols). The circle, square, diamond, and triangle symbols correspond to the B (E2) values of Ba, Xe, Te, and Sn isotopes, respectively.

It is shown that even such an anomalous feature can be reproduced consistently with the description of the spherical to deformed phase transition.

References

1) T. Otsuka, M. Honma, T. Mizusaki, N. Shimizu, and Y. Utsuno: Prog. Part. Nucl. Phys. **47**, 319 (2001) and references therein.
2) N. Shimizu, T. Otsuka, T. Mizusaki, and M. Honma: Phys. Rev. Lett. **86**, 1171 (2001).
3) D. C. Radford et al.: Phys. Rev. Lett. **88**, 222501 (2002).

*1 Department of Physics, University of Tokyo
*2 Institute of Natural Science, Senshu University
*3 Center for Mathematical Sciences, University of Aizu

Extension of massive parallel computer for nuclear study

N. Shimizu, T. Otsuka,[*1] T. Mizusaki,[*2] M. Honma,[*3] Y. Utsuno,[*4] and S. Shimoura[*5]

[Nuclear Shell Model, Computational Physics]

The nuclear shell model is one of the most useful tools for studying the nuclear structure microscopically. However, the huge dimension of the Hilbert space prevents us to diagonalize its Hamiltonian matrix, especially for the medium-heavy nuclei and the nuclei near the drip line. In order to overcome such difficulty, the Monte Carlo Shell Model (MCSM) has been introduced.[1] Although the MCSM is useful for extending the applicable region of the nuclear shell model, it requires a large amount of floating-point calculation. Since it is difficult to vectorize the MCSM calculation that has a long loop, the MCSM calculation has an advantage of using a massive parallel computer.

In 1999, we built a workstation farm named "Alphleet," which consists of 146 COMPAQ's "Alpha" 21264 500 MHz CPUs similar to a "fleet," as part of the RIKEN RI-Beam Factory Project for the MCSM calculation.[2] In order to cope with the recent marked increase in the demand of computational performance, we began to introduce a new massive parallel computer named "Alphleet-2" as a joint project of RIKEN, the nuclear theory group of Univ. of Tokyo, and Center for Nuclear Study of Univ. of Tokyo in 2002.

We briefly describe the outline of the Alphleet-2 system shown in Fig. 1. The basic concept and the structure of this system are almost the same as those of the Alphleet system. It consists of one front-end cluster server, 12 parallel nodes (48 CPUs), and one node with large main memory and hard disk. Because floating-point calculations are important for the MCSM calculation, Compaq Alpha 21264 CPU (1 GHz) is selected for the parallel nodes. We plan to add about 100 CPUs for parallel computing within the next two years. All the parallel nodes are connected to each other with both Myrinet network and 100BaseT Ethernet. The only front-end server, consisting of three computers, can be accessed directly from the internet, and can always monitor the condition of all the other nodes. A storage system (180 GB, RAID-5) is prepared outside these networks.

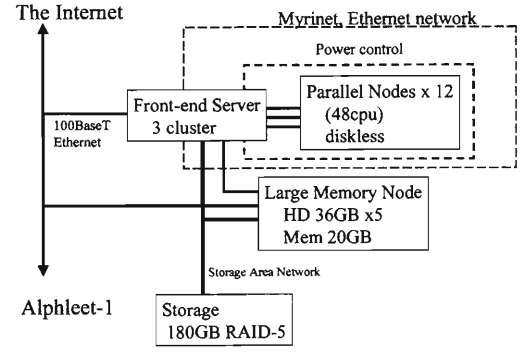

Fig. 1. A schematic diagram of the Alphleet-2.

It is our goal to maximize the performance of the system for the MCSM calculation with small management task. In order to simplify the administration, we decided to use parallel nodes without a hard disk but connected with power controllers, which are managed by the front-end server. Because we can supply and cut off the power of each node using the power controllers, any node can be rebooted remotely even when it hangs up without any response.

The Alphleet-2 system provides us high computer performance with low management cost, and contributes to the study of nuclear structure significantly.

References

1) T. Otsuka, M. Honma, T. Mizusaki, N. Shimizu, and Y. Utsuno: Prog. Part. Nucl. Phys. **47**, 319 (2001) and references therein.
2) Y. Watanabe, N. Shimizu, S. Haruyama, M. Honma, T. Mizusaki, A. Taketani, Y. Utsuno, and T. Otsuka: Prog. Theor. Phys. Suppl. No. 138, 43 (2000).

*1 Department of Physics, University of Tokyo
*2 Institute of Natural Sciences, Senshu University
*3 Center for Mathematical Sciences, University of Aizu
*4 Japan Atomic Energy Research Institute
*5 Center for Nuclear Study, University of Tokyo

A search for a unified effective interaction for Monte Carlo shell model calculations (IV)†

M. Honma,*1 T. Otsuka,*2 B. A. Brown,*3 and T. Mizusaki*4

[Nuclear structure, Shell model, Effective interaction]

The Monte Carlo shell model [1] has enabled us to study various nuclear structures in the full pf-shell. For this purpose, we have developed an effective interaction GXPF1.[2] In this report we discuss several important results and predictions obtained by this interaction.

The first 2^+ energy level of even-even nuclei is a good systematic measure of the structure. The left panel of Fig. 1 shows the 2^+ energy levels of Ca, Ti, Cr, Fe, and Ni isotopes. The lightest nucleus in each isotope chain corresponds to $N = Z$ because of the mirror symmetry. The energies are computed by the few-dimensional basis approximation (FDA*) [3] and by exact or nearly exact conventional shell-model calculations by the code MSHELL.[4] The overall description of the 2^+ energy level is quite successful throughout these isotope chains. In all cases, the energy jump corresponding to $N = 28$ shell closure is well reproduced.

The basic aspect of the effective interaction is provided by the effective single-particle energies (ESPEs).[7] In the right panel of Fig. 1, ESPEs of the neutron orbits are shown. A large energy gap ($\sim$4.1 MeV) between $p_{1/2}$ and $f_{5/2}$ can be seen in the ESPE for Ca and Ti isotopes. As predicted,[8] due to large attractive proton-neutron matrix elements, the ESPE of the $\nu f_{5/2}$ orbit decreases as the $\pi f_{7/2}$ orbit is occupied, reducing the subshell gap. This means that the $N = 34$ magic number arises only in neutron-rich Ca and Ti isotopes, and disappears in stable nuclei.

In the Ca isotopes, a prominent peak in the calculated 2^+ excitation energy can be seen at $N = 34$, which is definitely due to the $N = 34$ subshell closure discussed above. This gap is small with the FPD6 interaction.[9] Thus the experimental energy of the 2^+ state in ^{54}Ca is an important test of the pf-shell Hamiltonians. In the Ni isotopes, both experimental and theoretical 2^+ excitation energies decrease at N=34, where the ESPEs of $\nu p_{1/2}$ and $\nu f_{5/2}$ are almost degenerate and therefore the collectivity is enhanced. It is remarkable that the drastic change of the structure among those nuclei can be described by a single effective interaction.

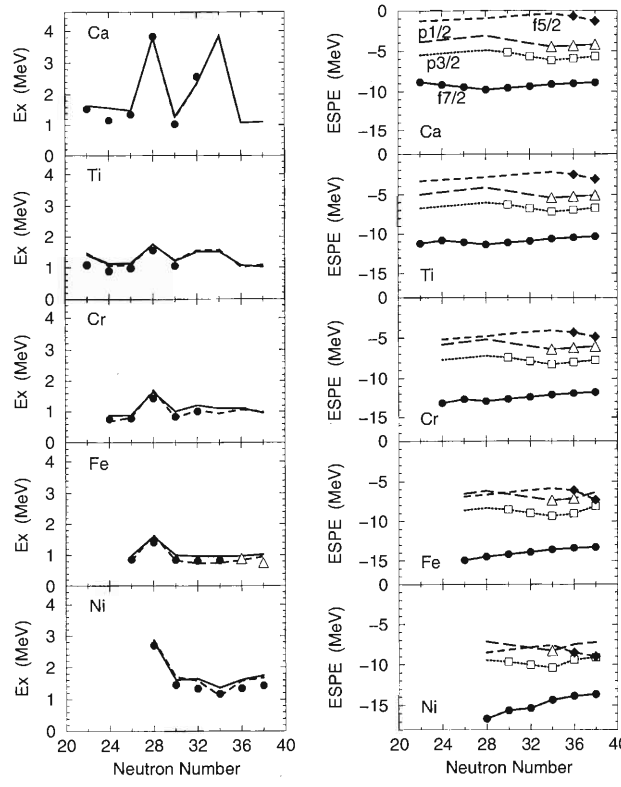

Fig. 1. (Left) First 2^+ energy levels as a function of the neutron number N. Experimental data are shown by filled circles [5] and open triangles.[6] Solid lines show results of conventional calculations: the maximum number of nucleons excited from $f_{7/2}$ to $p_{3/2}$, $p_{1/2}$ or $f_{5/2}$ is 5 for ^{56}Fe and ^{58,60,62}Ni, 6 for ^{52,54}Fe and ^{56}Ni, and 7 for ^{58,60}Fe. Dashed lines imply FDA* results. (Right) Effective single-particle energies for neutron orbits. Symbols indicate that the corresponding orbit is occupied by at least one nucleon in the lowest filling configuration.

† Condensed from the article in Phys. Rev. C **65**, 061301 (R) (2002)

*1 Center for Mathematical Sciences, University of Aizu
*2 Department of Physics, University of Tokyo
*3 National Superconducting Cyclotron Laboratory and Department of Physics and Astronomy, Michigan State University, USA
*4 Institute of Natural Sciences, Senshu University

References

1) T. Otsuka et al.: Phys. Rev. Lett. **81**, 1588 (1998).
2) M. Honma et al.: RIKEN Accel. Prog. Rep. **33**, 16 (2000); RIKEN Accel. Prog. Rep. **34**, 15 (2001); RIKEN Accel. Prog. Rep. **35**, 12 (2002).
3) M. Honma et al.: Nucl. Phys. A **704**, 134c (2002).
4) T. Mizusaki: RIKEN Accel. Prog. Rep. **33**, 14 (2000).
5) R. B. Firestone et al. (ed.): *Table of Isotopes* (Wiley, New York, 1996).
6) M. Hannawald et al.: Phys. Rev. Lett. **82**, 1391 (1999).
7) Y. Utsuno et al.: Phys. Rev. C **60**, 054315 (1999).
8) T. Otsuka et al.: Phys. Rev. Lett. **87**, 082502 (2001).
9) W. A. Richter et al.: Nucl. Phys. A **523**, 325 (1991).

Non empirical extrapolation method for large-scale shell model diagonalization

T. Mizusaki*

[Shell Model, Extrapolation method]

A quest for numerical algorithms to solve nuclear shell model problems has been one of the most intriguing issues in nuclear structure physics. In past decades, diverse numerical methods were proposed. Among them, in order to enhance a limited power of Lanczos shell model calculations, several extrapolation methods [1-4] were advocated. We proposed a new shell model method,[3] combining the Lanczos shell model diagonalization with a non-empirical extrapolation technique, which was invented in strongly correlated electron systems in a lattice.[5,6] Moreover, we developed a quadratic extrapolation formula for more precise estimation of the shell model energy.[4] This new shell model approach succeeded in improving the feasibility of shell model calculations.

We consider a scaling property between the energy difference δE (energy eigenvalue in a given truncated space - true energy eigenvalue) and energy variance ΔE in the truncated spaces. If the truncated spaces become sufficiently large, we can derive a linear relation.[5,6] Moreover we can derive a quadratic relation by considering a higher order effect,[4] the details of which are discussed in Ref. 4. Such scaling properties can be utilized for extrapolating energies and other physical quantities of various truncated shell model spaces into zero energy variance. Therefore we can evaluate true values by such extrapolations.

Quite recently other extrapolation methods have been utilized for Lanczos shell model calculations,[1,2] however, such methods assume *empirical* functional forms for the extrapolation region. On the other hand, the present extrapolation method has a *non empirical* functional form based on quantum mechanics. This point is crucial in the theoretical framework point of view and in practical applications.

Here we show its feasibility by taking some examples of state-of-the-art large-scale shell model calculations. In Fig. 1, we show quadratic extrapolations for energies of ^{50}Mn and ^{52}Fe, where fp shell model space and KB3 interaction [7] are taken. The t values specify the truncation spaces. As t increases, the size of the truncated spaces increases. Energies of truncated spaces are well described by quadratic curves. Therefore, we can definitely extrapolate them into zero energy variance. The extrapolated energy agrees with the exact one.

In summary, we propose a new Lanczos shell model method with an extrapolation method [3] or an improved extrapolation method,[4] which can improve the feasibility of the Lanczos shell model calculations. The non empirical nature of the present extrapolations is crucially important for reliability of extrapolated energy. Furthermore, we would like to note that the present extrapolation technique has a possibility to be applied to various approaches in nuclear structure physics.

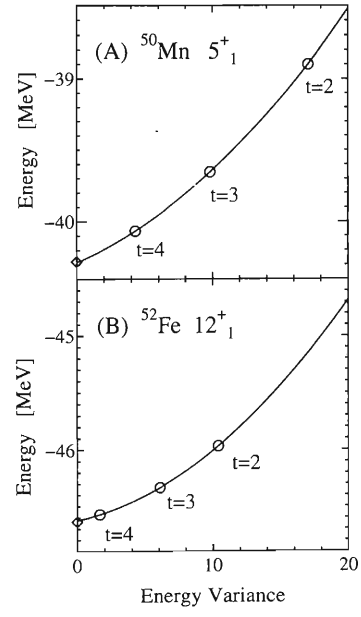

Fig. 1. Quadratic extrapolations of shell model energies into zero energy variance; (A) for 5^+_1 state of ^{50}Mn, and (B) for 12^+_1 state of ^{52}Fe. Open circles are energies for the truncated shell model spaces. Exact ground-state energies are shown by diamonds.

This work was supported in part by a Grant-in-Aid for Scientific Research (A) (2) (10304019), and that for Specially Promoted Research (13002001) from the Ministry of Education, Science and Culture.

References

1) M. Horoi et al.: Phys. Rev. Lett. **82**, 2064 (1999).
2) E. Caurier et al.: Nucl. Phys. A **654**, 747c (1999).
3) T. Mizusaki and M. Imada: Phys. Rev. C **65**, 064319 (2002).
4) T. Mizusaki and M. Imada: Phys. Rev. C, submitted.
5) M. Imada and T. Kashima: J. Phys. Soc. Jpn. **69**, 2723 (2000).
6) S. Sorella: Phys. Rev. B **64**, 024512 (2001).
7) A. Poves and A. P. Zuker: Phys. Rep. **70**, 235 (1981).

* Institute of Natural Sciences, Senshu University

Role of proton-neutron interactions in ^{64}Ge†

K. Kaneko,*1 M. Hasegawa,*2 and T. Mizusaki*3

[NUCLEAR STRUCTURE, Shell model, Unstable nuclei]

The $N = Z = 32$ nucleus $^{64}_{32}Ge_{32}$ is a typical example showing a γ-soft structure in $N = Z$ proton-rich unstable nuclei, according to theoretical calculations based on the mean-field approximation.[1] The calculations predict an almost γ-instability in the ground state, and triaxiality at the excited states, giving the quadrupole deformations $\beta_2 \sim 0.22$ and $\gamma \sim 27°$. The spherical shell model approach could be more appropriate for describing various aspects of a nuclear structure. In Fig. 1, we show the results of the shell model calculation with the model space in the $p_{3/2}$, $f_{5/2}$, $p_{1/2}$, and $g_{9/2}$ orbitals with a recently developed shell model code.[2] Then we adopted an extended $P + QQ$ force[3] recently applied to the $f_{7/2}$-shell nuclei, which is schematic but works remarkably well. Two side bands are shown in addition to the ground-state band, *i.e.*, the gamma band on the band head 2^+ and the octupole band on the band head 3^-.

Since protons and neutrons in the $N = Z$ nuclei occupy the same levels, one would expect strong proton-neutron (p-n) interactions.[4] In particular, one of the most interesting questions in studying the nuclear structure is what roles the p-n interactions play in the nuclear deformation. The long-range p-n isoscalar ($T = 0$) interaction between valence nucleons has been suggested to be a source of the nuclear deformation.[5] On the other hand, the isoscalar QQ interaction used in the $P + QQ$ force model has a very strong p-n component Q_pQ_n, which gives rise to nuclear quadrupole deformation.[6] The Q_pQ_n interaction is expected to be important for quadrupole deformation and γ-softness (triaxiality) in ^{64}Ge.

In this study, we have examined the γ-soft structure in the even-even $N = Z$ nucleus ^{64}Ge by spherical shell model calculations. The $P + QQ$ force model including the octupole interaction and monopole corrections, which are schematic but reproduce experiments, was adopted for describing the quadrupole correlations. It was shown that ^{64}Ge is an unstable nucleus with respect to the quadrupole deformations. The present results reveal that the p-n QQ interaction (Q_pQ_n) induces the onset of quadrupole deformation and γ-softness (triaxiality) estimated from $E2$ transitions (Fig. 2). The Q_pQ_n interaction can be expected to play an important role in the prolate-oblate shape coexistence of the neighboring even-even $N = Z$ nucleus ^{68}Se, which has been recently observed.[7]

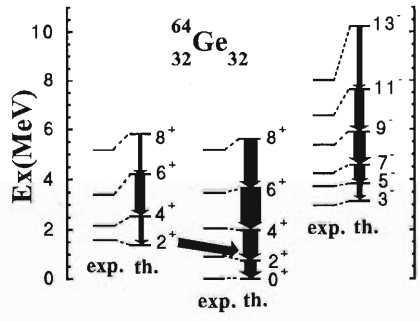

Fig. 1. Comparison of experimental and calculated energy levels of ^{64}Ge. The arrows indicate $E2$ transitions with the calculated $B(E2)$ values indicated by their widths.

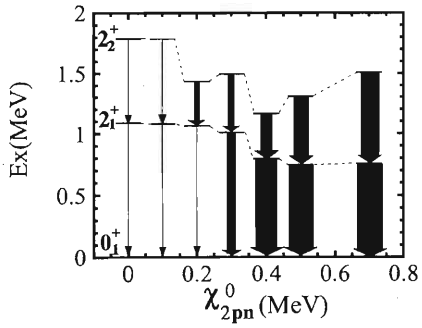

Fig. 2. Excitation energies of the first and second excited 2^+ states as a function of the p-n quadrupole force strength χ^0_{2pn}. The arrows indicate $E2$ transitions with the calculated $B(E2)$ values indicated by their widths.

References

1) P. J. Ennis et al.: Nucl. Phys. A **535**, 392 (1991).
2) T. Mizusaki: RIKEN Accel. Prog. Rep. **33**, 14 (2000).
3) M. Hasegawa, K. Kaneko, and S. Tazaki: Nucl. Phys. A **674**, 411 (2000); Nucl. Phys. A **688**, 765 (2001).
4) A. L. Goodman: Adv. Nucl. Phys. **11**, 263 (1979).
5) P. Federman and S. Pittel: Phys. Rev. C **20**, 820 (1979).
6) J. Dobaczewski et al.: Phys. Rev. Lett. **60**, 2254 (1988).
7) S. M. Fischer et al.: Phys. Rev. Lett. **84**, 4064 (2000).

† Condensed from the article in Phys. Rev. C **66**, 051306(R) (2002)

*1 Department of Physics, Kyushu Sangyo University
*2 Laboratory of Physics, Fukuoka Dental College
*3 Institute of Natural Sciences, Senshu University

Negative-parity states in the island of inversion

M. Kimura and H. Horiuchi

[nuclear structure, unstable nucleus]

The vanishing of the magic number $N = 20$ is a great interest in the unstable nuclear physics. Large deformation of ^{32}Mg has been confirmed by the observations of the small excitation energy of the 2^+ state and the large $E2$ transition probability. Shell model studies[1] have predicted these observed values of ^{32}Mg and neighboring nuclei by including the neutron $2p$-$2h$ and $4p$-$4h$ configurations, which are beyond the neutron magic number $N = 20$, in the model space. In this study, we focus on the negative-parity states and the cluster structure. The vanishing of the magic number $N = 20$ implies that neutrons can be easily promoted into the pf-shells. Thus we can expect that the negative-parity states have small excitation energies and are sensitive to the shell gap energy between sd- and pf-shells. As is well known, the low-lying states of ^{20}Ne have an α-^{16}O cluster structure and it is conceivable that the cluster structure plays an important role in some states of neutron-rich Ne isotopes.

To study the above-mentioned points, we have applied a new version of antisymmetrized molecular dynamics (deformed base AMD) to the low-lying positive- and negative-parity states of ^{26,28,30}Ne and ^{32}Mg. By using this new method, we can describe the single particle motion in the deformed mean-field as well as in the cluster structure. Details of this method are presented in Ref. 2.

The calculated level schemes of ^{26,28,30}Ne and ^{32}Mg are shown in Fig. 1. We mention that the ground states of ^{30}Ne and ^{32}Mg have neutron $2p$-$2h$ configurations and the observed values of the excitation energy of 2^+_1 states of these isotopes and the $E2$ transition probability $B(E2; 0^+_1 \rightarrow 2^+_1)$ of ^{32}Mg are well described.[2] The negative-parity states of both nuclei have very small excitation energies and have neutron $3p$-$3h$ configurations. This is quite in contrast to those of stable $N = 20$ isotones. For example, ^{40}Ca has the lowest negative-parity 3^- state at 3.7 MeV, which is much higher than the 1^- states of ^{30}Ne and ^{32}Mg. However, this result is a natural consequence of the vanishing $N = 20$ shell gap. In ^{30}Ne and ^{32}Mg nuclei, the shell gap energy between the pf- and sd-shells are very small even in the negative-parity states and thus neutrons can jump to the pf-shell much more easily than those in the stable $N = 20$ isotones. Therefore, three neutrons can be promoted into the pf-shell with small excitation energy.

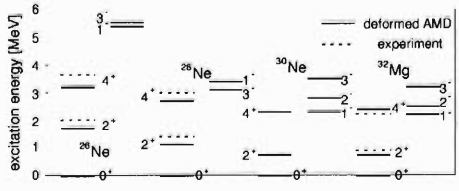

Fig. 1. Level scheme of ^{26,28,30}Ne and ^{32}Mg. Compared with the experiments. Only the ground band and the lowest negative-parity band are shown.

We have also calculated the low-lying positive- and negative-parity states of ^{26}Ne and ^{28}Ne. In the case of ^{26}Ne, the calculated ground state has an ordinary $0\hbar\omega$ configuration, and the $N = 20$ shell gap energy is larger than that in the case of ^{30}Ne. This characteristic is directly attributed to the excitation energy of the negative-parity states. The lowest negative-parity state has a much larger excitation energy (5.4 MeV). The negative-parity state of ^{28}Ne is a 3^- state and has also a structure with one neutron promoted to the pf-shell. The excitation energy of the lowest 3^- state is larger than those of ^{30}Ne and ^{32}Mg, but much smaller than that of ^{26}Ne. ^{28}Ne exhibits an intermediate characteristic between ^{30}Ne and ^{26}Ne.

We have calculated the overlap of the proton wave functions between the AMD wave functions and $\alpha + {}^{16}$O cluster wave functions to evaluate the existence of the cluster core in these neutron-rich Ne isotopes (Table 1). The overlap N_p, which indicates the amount of the $\alpha + {}^{16}$O component in the proton wave function, is defined as $N_p = \sum_k |\langle \phi^{J=0^+}_{AMD}(proton) | \varphi_k(\alpha + {}^{16}\mathrm{O})^{J=0^+}(proton) \rangle|^2$. Here, $\varphi_k(\alpha + {}^{16}\mathrm{O})$ is the complete set of the $\alpha + {}^{16}$O cluster wave function. It is found that the ground state and the 0^+_3 state have some amount of $\alpha + {}^{16}$O cluster core component. In particular, the 0^+_3 state has almost the same amount of $\alpha + {}^{16}$O component as that of ^{20}Ne ground state and is expected that the cluster core exists in this state.

Table 1. The overlaps of the proton wave functions between the AMD and $\alpha + {}^{16}$O model space.

State	^{20}Ne	^{30}Ne g.s.	^{30}Ne 0^+_2	^{30}Ne 0^+_3
N_p	0.79	0.38	0.16	0.71

References

1) N. Fukunishi et al.: Phys. Lett. B **296**, 279 (1992); Y. Utsuno et al.: Phys. Rev. C **60**, 054315 (1999).
2) M. Kimura and H. Horiuchi: Prog. Theor. Phys. **107**, 33 (2002).

Clustering aspect and triaxially superdeformed band in ^{44}Ti

M. Kimura and H. Horiuchi

[nuclear structure, cluster structure, superdeformation]

Recently, many rotational spectra associated with superdeformed (SD) bands have been observed in the mass $A \sim 40$ nuclei such as ^{36}Ar, ^{40}Ca and ^{44}Ti. In the case of ^{44}Ti, it is built upon the excited 0_2^+ state at 1.905 MeV and is observed up to $J^\pi = 12^+$ ($K^\pi = 0_2^+$ band). Furthermore, since there is also a $K = 2^+$ band, we can expect the triaxial deformation of this SD band and we have to study without assuming axial symmetry. Besides the SD structure, the existence of the $\alpha + ^{40}$Ca cluster structure has been discussed as an analogy to the $\alpha + ^{16}$O cluster structure in ^{20}Ne. Experimentally, negative parity states which have large α-spectroscopic factors are observed. They are considered as the candidate of the $K = 0^-$ band members which arise as a result of the $\alpha + ^{40}$Ca cluster structure of the intrinsic state. However, in both theoretical and experimental studies, the cluster structure of this nucleus is still unclear, because the deformation of the mean-field and the strong effect of the spin-orbit force, which become more important as the mass number increases, act to dissolve the cluster structure. Therefore, it is neccecary to investigate these effects as well as the cluster structure in the cluster study of heavier isotopes.

In this study, we have investigated the low-lying states of ^{44}Ti within a deformed base AMD framework. In this framework, by using the triaxially deformed Gaussians as the single particle wave packets, we can describe the triaxially deformed system and can include both the cluster structure and the deformed mean-field structure into the model space.

In Fig. 1, the energy surface of the positive parity state is given. In the small deformed region ($\beta < 0.35$), the nucleus has a $0\hbar\omega$ structure. After the generator coordinate calculation (GCM calculation), this part composes the ground band (Fig. 2). We have also found the $K = 0^-$ band which has a $\alpha + ^{40}$Ca cluster structure about 9.0 MeV above the ground state which corresponds to the observed $K = 0^-$ band. These two bands (the ground band and $K = 0^-$ band) are supposed to be the parity doublet bands which arise from the $\alpha + ^{40}$Ca cluster structure, though in the ground band, the cluster structure is not so clear and is distorted by the deformed mean-field. In the medium deformed region ($0.35 < \beta < 0.6$), it has a $4\hbar\omega$ structure and has a triaxially deformed form ($\gamma = 0.25°$). After the GCM calculation, these states compose the superdeformed band built upon the 0_2^+ states and $K = 2^+$ side band. The triaxial deformation of this nuclei has been discussed, since the triaxially

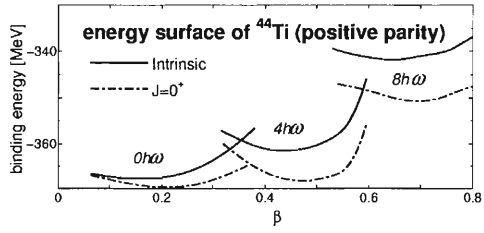

Fig. 1. Energy surface as a function of the deformation parameter β for the positive parity state of ^{44}Ti. Solid lines (dashed lines) are for the intrinsic states ($J = 0^+$ states).

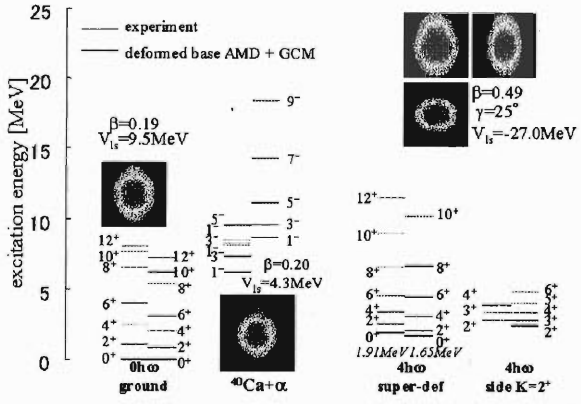

Fig. 2. Low-energy level scheme of ^{44}Ti. Only the ground band, $K = 0^-$ band ($\alpha + ^{40}$Ca), $K = 0_2^+$ band (super-def) and $K = 2^+$ band (side) are shown. Left lines (right lines) in each band are experimental (calculated) results. Density distributions of the intrinsic states are also shown for each band head state.

deformed rotator + vibration model gives rough comprehension of the excitation energy and $E2$ transition probabilities of the ground band, $K = 0_2^+$ (SD band) and $K = 2^+$ side band. However, in our calculation, the ground band and SD band have different intrinsic structures. The ground band and $K = 0^-$ band have the $\alpha + ^{40}$Ca cluster nature, though the cluster structure is distorted in the ground band. The SD band has a triaxially deformed intrinsic structure. From this triaxial deformation, $K = 2^+$ band also arises.

We have also found a $8\hbar\omega$ state at a large deformed region which composes the hyper-deformed band, details of this band will be given elsewhere.

Shape coexistence in $N = 14$ isotones: ^{19}B, ^{24}Ne and ^{28}Si

Y. Kanada-En'yo*

[NUCLEAR STRUCTURE, Shape coexistence, Unstable nuclei]

Shape coexistence phenomena have been suggested to occur in many *sd*-shell nuclei.[1] A famous shape coexistence is known in ^{28}Si, in which the ground band is oblate and an excited band starting from the 0^+_3 state at 6.691 MeV is considered to be prolate. It is a challenging problem to determine whether or not the shapes coexist in other $N = 14$ nuclei. We are also interested in the deformations of proton and neutron density distributions in unstable $N = 14$ nuclei. We study the structures of $N = 14$ isotones, and discuss the intrinsic shapes while relating the deformations to observable properties such as electric moments and transition strengths.

We apply a microscopic method of antisymmetrized molecular dynamics[2,3] to study the structures of $N = 14$ isotones: ^{28}Si, ^{19}B and ^{24}Ne. In the results for ^{28}Si, an oblate state and a prolate state are obtained as local minima. The significance of the AMD results is that the energy difference between the oblate ground band and the excited prolate band is well reproduced with strong spin-orbit forces. Using this set of interaction parameters, the shape coexistence problems in ^{19}B and in ^{24}Ne are investigated.

Deformation parameters β_n and γ_n for neutron densy distributions are presented in Fig. 1. In ^{19}B, the states with oblate and prolate neutron densities coexist in the low-energy region. In the present calculations, the oblate state is the ground state of ^{19}B. It is interesting that the oblate ground state is inconsistent with the predicted prolate neutron deformations in the ground states of ^{15}B and ^{17}B. The Q-moment of ^{19}B in the present calculation is almost equal to that of ^{17}B. This result differs from that of previous AMD calculations for B isotopes,[4] in which the prolate ground state of ^{19}B and its large Q-moment were suggested. This inconsistency arises because the spin-orbit force adopted in the previous study was too weak, because we did not take account of the shape coexistence in ^{28}Si. In fact, in the AMD calculations for ^{28}Si with weak spin-orbit forces, a prolate ground state was obtained although the ground state of ^{28}Si is experimentally known to be oblate. In the present results for ^{19}B, the prolate deformed band appears 2 MeV above the ground band. In the prolately deformed states, a cluster structure of ^{8}He + ^{11}Li develops due to the highly deformed neutron density distribution.

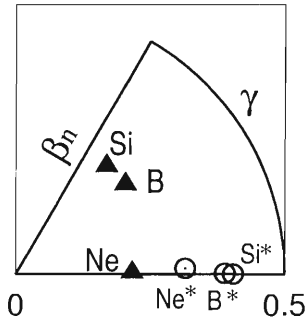

Fig. 1. Deformation parameters for neutron densy distributions of ^{28}Si, ^{24}Ne and ^{19}B. Triangles (circles) correspond to the lowest (excited) states.

As seen in Fig. 1, the neutron deformations in the oblate ground state and in the prolate excited states of ^{19}B are similar to those of ^{28}Si. On the other hand, the shape coexistence in ^{24}Ne differs from that in ^{28}Si. Also in ^{24}Ne, two neutron shapes are found in the present results. One is a smaller prolate deformation in the lowest band, and the other is a larger prolate shape in the excited band. We conjecture that the oblate structure of 14 neutrons seen in ^{28}Si is changed into the smaller prolate deformed structure following the trend of the prolately deformed proton structure in Ne isotopes. In the lowest band of ^{24}Ne, the deformation parameters for the proton and neutron densities are $\beta_p = 0.3$ and $\beta_n = 0.2$, which indicate a difference between the proton and neutron deformations. The theoretical values of $B(E2; 2^+_1 \rightarrow 0^+_1)$ for protons and neutrons are $B_p(E2) = 37$ (e^2fm^4) and $B_n(E2) = 38$ (e^2fm^4), respectively. In spite of the large number of valence neutrons, the strength for neutrons $B_n(E2_n)$ is not so high due to the small deformation of the neutron density distribution in the ground band.

In summary, the theoretical results suggest shape coexistence in ^{19}B and ^{20}Ne. The oblate and prolate shapes of the neutron densities in ^{19}B are similar to those in ^{28}Si, while the feature of shape coexistence in ^{24}Ne seems to be different from those in ^{19}B and ^{28}Si.

References

1) J. L. Wood, K. Heyde, W. Nazarewicz, P. Van Duppen, and M. Huyse: Phys. Rep. **215**, 101 (1992).
2) Y. Kanada-En'yo and H. Horiuchi: Phys. Rev. C **52**, 628 (1995).
3) Y. Kanada-En'yo and H. Horiuchi: Prog. Theor. Phys. Suppl. No. 142, 205 (2001).
4) Y. Kanada-En'yo and H. Horiuchi: Phys. Rev. C **52**, 646 (1995).

* Institute of Particle and Nuclear Studies, High Energy Accelerator Research Organization (KEK)

Trial of direct treatment of tensor force with antisymmetrized molecular dynamics

A. Doté,[*1] H. Horiuchi,[*2] Y. Akaishi,[*1] and K. Ikeda

[NUCLEAR STRUCTURE, Cluster, Tensor force, Unstable nuclei]

The tensor force is the most important ingredient in nuclear forces. For example, it is well known that the deuteron cannot be bound without the tensor force. But microscopic "model" approaches have avoided treating it directly due to the difficulty of its treatment, and alternatively, have employed the effective central force in which the tensor force is incorporated. Certainly many models, for instance Hartree-Fock and Antisymmetrized Molecular Dynamics (AMD), have succeeded in studying nuclear structures without the tensor force. However, there still remain some unanswered questions: How does the most important force, *i.e.* tensor force, work in real nuclei? How does it contribute to nuclear structures?

In order to treat the tensor force directly, we include the following three requirements in the model: i) In the mean-field-like treatment, the tensor force is roughly represented as $\tau_1(\boldsymbol{\sigma}_1 \cdot \mathbf{r})\langle\tau_2(\boldsymbol{\sigma}_2 \cdot \mathbf{r})\rangle = U\tau_1(\boldsymbol{\sigma}_1 \cdot \mathbf{r})$. If a single particle wave function for calculating the expectation value of this operator is the eigen-state of parity, apparently the value is zero. Therefore we prepare a parity-violating single particle state, namely *parity-violating mean field.* ii) The tensor force contains the operator $(\boldsymbol{\sigma} \cdot \mathbf{r})$. It indicates a *strong correlation between spin and space.* The model should treat such a correlation. iii) The tensor force contains the operator $(\boldsymbol{\tau}_1 \cdot \boldsymbol{\tau}_2)$, which can *change the isospin state of a single particle.* Therefore the model should have flexibility concerning the isospin.

We start our study from AMD. AMD has already satisfied the requirement i), because its trial wave function has the form $|\Phi^{\pm}\rangle = |\Phi\rangle \pm |\mathcal{P}\Phi\rangle$ and its intrinsic wave function $|\Phi\rangle$ can describe the parity-violating state. To satisfy the other requirements, we improve the AMD single particle wave function $|\varphi_i\rangle$ as follows:

$$|\varphi_i\rangle = \sum_{\alpha=1}^{N} C_\alpha^i \exp\left[-\nu\left(\mathbf{r} - \frac{\mathbf{Z}_\alpha^i}{\sqrt{\nu}}\right)^2\right]|\sigma_\alpha^i\rangle|\tau_\alpha^i\rangle. \quad (1)$$

$|\varphi_i\rangle$ is represented by the superposition of several Gaussian packets, whose positions $(\mathbf{Z}_\alpha^i)$ are different from each other, and the spin wave function $|\sigma_\alpha^i\rangle$ can change in each wave packet. Although the isospin wave function $|\tau_\alpha^i\rangle$ has been fixed to a proton or neutron so far, it can also change by introducing a variational parameter as well as $|\sigma_\alpha^i\rangle$. Thus, employing Eq. (1), we can make AMD satisfy all the above requirements.

*1 Institute of Particle and Nuclear Studies, High Energy Accelerator Research Organization (KEK)
*2 Department of Physics, Kyoto University

We have performed tests to investigate to what extent our model can pick up the contribution of tensor force. Here we have employed Furutani potential[1)] which has tensor force. The results of deuteron and ^{4}He are summarized in Table 1. This table shows that our concept for improvement is reasonable. The result shown in the left-most column is obtained without any improvement and that shown in the right-most column is obtained with full improvements. Apparently, in both cases of deuteron and ^{4}He, the calculation with full improvements picks up the contribution of the tensor force more effectively than that without any improvement. In addition, by analyzing single particle levels, we have confirmed that the effect of the requirement i) appears in the solution of ^{4}He with full improvement. Two of the single particle levels in it are found to be in the *parity-mixed* state.

Hence we have completed the improvement of AMD to treat tensor force directly. However, we did not show the final results since we failed to reproduce basic quantities such as binding energy and radius. This is due to the fact that in the Furutani potential, the main part of tensor force is already incorporated into the central force. We have a future plan as follows: One of the authors (Y.A.) derived an effective interaction in which tensor force is not incorporated into the central force. Hereafter, by using his effective interaction in our framework, first we will try to reproduce the basic properties of deuteron and ^{4}He. Then we will investigate the relationship between tensor force and nuclear structure (especially *clustering structure*) systematically, of unstable nuclei as well as stable nuclei, and of the excited state as well as the ground one.

Table 1. Contribution of tensor force in deuteron and ^{4}He. V_T: $\langle\hat{V}_T\rangle$. L^2: $\langle\hat{L}^2\rangle$, where $\hat{L}$ is orbital angular momentum operator. "N": the number of wave packets as shown in Eq. (1). In "isospin fix" case, we ignore the requirement iii).

(N, isospin)		(1, fix)	(4, fix)	(4, free)
^{2}H	V_T	−1 MeV	−10 MeV	−21 MeV
	L^2	0.01	0.5	0.5
^{4}He	V_T	−1 MeV	−3.3 MeV	−22.4 MeV
	L^2	0.01	0.06	0.4

References

1) H. Furutani, H. Horiuchi, and R. Tamagaki: Prog. Theor. Phys. **62**, 981 (1979).

High-density $\bar{K}$ nuclear systems with isovector deformation

A. Doté,[*1] H. Horiuchi,[*2] Y. Akaishi,[*1] and T. Yamazaki

[kaonic nuclei, dense nuclei]

Recently, exotic nuclear systems involving a $\bar{K}$ (K^- or $\bar{K}^0$) as a constituent have been studied theoretically by Akaishi and Yamazaki (AY),[1] who constructed $\bar{K}N$ interactions phenomenologically so as to reproduce low-energy $\bar{K}N$ scattering data, kaonic hydrogen atom data and the binding energy and decay width of $\Lambda(1405)$. These interactions are characterized by a strongly attractive isoscalar ($I = 0$) part. With these interactions, they calculated the bound systems of ppnK^-, pppnK^- and ^{8}BeK^-, showing the following characteristics: i) The $I = 0$ $\bar{K}N$ interaction is strong enough to shrink the nucleus against the nuclear incompressibility. ii) The binding energies are extremely large due to the strong $I = 0$ interaction supported by the nuclear shrinkage effect so that the bound states lie below the threshold of the main decay channel to $\Sigma\pi$, thus inferring the presence of quasi-stable discrete bound states (width (Γ_K) < binding energy (B_K)). Furthermore, they have shown[2] that the (K^-, π^-) reaction as a source of Λ^* can produce various exotic $\bar{K}$ bound states in non-existing proton-rich nuclei, such as p^2 (^{2}He), p^3 (^{3}Li), p^3n (^{4}Li), p^4n^2 (^{6}Be) and p^5n^4 (^{9}B).

Since the presence of a K^- in nuclei is expected to cause a drastic change in nuclear systems, it is important to perform theoretical studies of such exotic systems without any constraint from the existing common knowledge of nuclear physics. Thus, we started a series of calculations,[3] employing the method of Antisymmetrized Molecular Dynamics (AMD),[4,5] based on the AY $\bar{K}N$ interactions.[1]

Table 1. Summary of present calculations.

	B.E. [MeV]	Γ_K [MeV]	$\rho(0)$ [fm^{-3}]	R_{rms} [fm]	ν [fm^{-2}]	β
^{3}He	5.95	—	0.14	1.59	0.20	0.0
ppnK^-	113	**24**	1.39	0.72	1.12	0.19
ppnK^{-f}	116	**20**	1.10	0.97		
^{8}Be	48.72	—	0.10	2.46	0.205	0.63
^{8}BeK^-	159	43	0.76	1.42	0.52	0.55
^{8}BeK^{-f}	168	38	~ 0.85			

$\rho(0)$: nucleon density at the center of the system. R_{rms}: root-mean-square radius of the nucleon system. ν: width parameter of a Gaussian wave packet used in the calculation. β: deformation parameter for the nucleon system. ppnK^{-f} and ^{8}BeK^{-f}: Akaishi and Yamazaki's results.

*1 Institute of Particle and Nuclear Studies, High-Energy Accelerator Research Organization (KEK)
*2 Department of Physics, Kyoto University

Our calculations show that strongly bound kaonic nuclear systems with unusual exotic structures are formed around the K^-, which attracts the surrounding nucleons (preferentially protons) to an extremely high-density assembly thereby inducing a proton-neutron separation, "isovector deformation." These results are shown in Table 1 and are in good agreement with those of Akaishi and Yamazaki.[1] The density contours of ^{8}Be and ^{8}BeK^- are shown in Fig. 1. It is interesting that the two alpha clusters in ^{8}Be are shrunk to a high density (about 4 times the normal nuclear density) in ^{8}BeK^-, yet preserving their cluster structure.

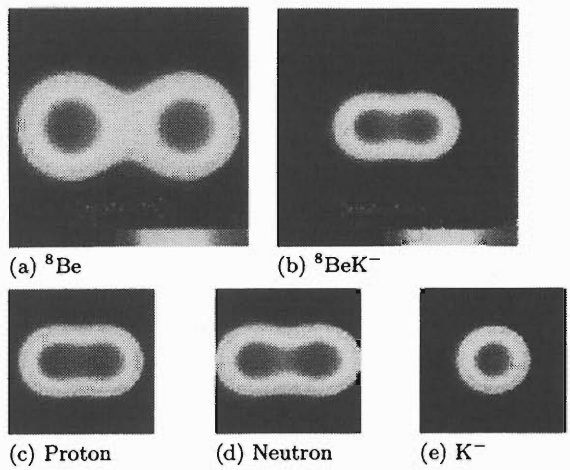

Fig. 1. Calculated density contours of ^{8}BeK^-. Comparison of density distributions between (a) usual ^{8}Be and (b) ^{8}BeK^- is shown at a size of $7 \times 7\,\mathrm{fm}^2$. Individual contributions of (c) proton, (d) neutron and (e) K^- are given at a size of $4 \times 4\,\mathrm{fm}^2$.

References

1) Y. Akaishi and T. Yamazaki: Phys. Rev. C **65**, 044005 (2002).
2) T. Yamazaki and Y. Akaishi: Phys. Lett. B **535**, 70 (2002).
3) A. Doté, H. Horiuchi, Y. Akaishi, and T. Yamazaki: arXiv:nucl-th/0207085.
4) Y. Kanada-En'yo, H. Horiuchi, and A. Ono: Phys. Rev. C **52**, 628 (1995); Phys. Rev. C **52**, 647 (1995); Y. Kanada-En'yo: Phys. Rev. Lett. **81**, 5291 (1998).
5) A. Doté, Y. Kanada-En'yo, and H. Horiuchi: Phys. Rev. C **56**, 1844 (1997); A. Doté and H. Horiuchi: Prog. Theor. Phys. **103**, 91 (2000); Prog. Theor. Phys. **103**, 261 (2000).

Mirror symmetry breaking between ^{10}Be and ^{10}C

N. Itagaki,[*1] T. Otsuka,[*1] S. Okabe,[*2] and K. Ikeda

[NUCLEAR STRUCTURE, Cluster model, Unstable nuclei]

We introduced a microscopic $\alpha+\alpha+N+N$ model for ^{10}Be and ^{10}C.[1] The total wave function was fully antisymmetrized and expressed as a superposition of Slater determinants with various configurations of the valence neutrons. The Slater determinants were also superposed with respect to different relative distances between the two α clusters. The projection to the eigen states of angular momentum J was numerically performed. The configurations of valence nucleons were introduced based on the molecular orbit (MO) picture.[2] In the MO model, the states of the valence neutrons are expressed by a linear combination of orbits around two α clusters. The lowest orbit has one node and negative parity, that is, the p-orbit, and we constructed MO from these p-orbits. The effective nucleon-nucleon interactions were Volkov No.2 for the central part and the G3RS spin-orbit term for the spin-orbit part.

Using this framework, the threshold energy of $\alpha+\alpha+N+N$ becomes -55.0 MeV. For ^{10}Be, at $K=0$ state, the ground 0^+ state was calculated at -60.5 MeV, and the 2^+ state appeared at $E_x=3.6$ MeV, where the dominant component was $(3/2^-)^2$ for the two valence neutrons. At $K=2$ state, the 2^+ and 3^+ states appeared at $E_x=5.6$ MeV and $E_x=9.4$ MeV, respectively, the dominant component of which was $(3/2^-)(1/2^-)$ for the two valence neutrons.

The electromagnetic transition rate, B(E2) values among these states are summarized in Table 1, together with those of ^{10}C. Using the Davydov-Filippov model,[3] we can estimate the degree of the triaxiality as a function of the γ angle. The ratio $\frac{\mathrm{B(E2:}\ 2_2^+\to 2_1^+)}{\mathrm{B(E2:}\ 2_1^+\to 0_1^+)}$ becomes 0.34 in our calculation, and it has a crossing point with the Davydov-Filippov model around $\gamma=19^o$. Although the α-α core is of axial symmetry and electric charges are only in the α's, the recoil effect gives rise to a change from the axial symmetry to the triaxial shape.

Table 1. The B(E2) values (e^2fm^4). ^{10}C(p) and ^{10}Be(p) are proton B(E2) values calculated with the charge value of $(p,n)=(e,0)$, whereas ^{10}C(n) and ^{10}Be(n) are neutron B(E2) values calculated with the charge value of $(p,n)=(0,e)$. The values in parenthesis are experimental values.

B(E2)	^{10}C(p)	^{10}C(n)	^{10}Be(p)	^{10}Be(n)
$2_1^+\to 0_1^+$	12.8 (12.3)	12.1	11.8 (10.04)	11.4
$2_2^+\to 0_1^+$	1.3	1.1	0.7	1.7
$2_1^+\to 2_2^+$	17.0	6.2	4.0	13.7

*1 Department of Physics, University of Tokyo
*2 Center for Information and Multimedia Studies, Hokkaido University

The ground 0^+ state of ^{10}C was calculated at -56.3 MeV, higher by 4.2 MeV than that of ^{10}Be (experimentally 4.66 MeV), and as a result of the K-mixing effect, two 2^+ states appeared at $E_x=3.5$ MeV (Exp. $E_x=3.35$ MeV) and $E_x=6.0$ MeV. We compare the calculated proton B(E2) value of ^{10}C with neutron B(E2) of ^{10}Be. The proton B(E2) value of ^{10}C (12.8 e^2fm^4) is almost the same as the neutron B(E2) of ^{10}Be (11.9 e^2fm^4), and mirror symmetry seems to hold judging from the transition probability between the yrast states. However, the interband transition, B(E2: $2_1^+\to 2_2^+$) values show a significant difference. The neutron B(E2: $2_1^+\to 2_2^+$) value of ^{10}C was calculated to be 6.2 e^2fm^4, which is about 1.5 times larger than the proton B(E2) of ^{10}Be (4.0 e^2fm^4). Also, the proton B(E2: $2_1^+\to 2_2^+$) value of ^{10}C (17.0 e^2fm^4) is larger than neutron B(E2) of ^{10}Be (13.7 e^2fm^4). If the system is axially symmetric, the transition between different K-values is more suppressed. Since the present value is much larger than that of ^{10}Be, the triaxiality of ^{10}C is considered to be much larger than that in ^{10}Be. Using the Davydov-Filippov model, our proton B(E2) values correspond to the γ deformation of $\gamma=28^o$.

This result indicates that the interband transition, which appears as a result of mixing different K-values, is a good tool to observe the mirror symmetry breaking of the triaxiality. In the present case, due to the Coulomb energy shift of about 4 MeV, the valence protons of ^{10}C are more weakly bound, and contribution of the spin-orbit interaction from the core nucleus becomes weaker. Therefore, the di-nucleon component of the valence nucleons mixes more in ^{10}C and the system becomes more triaxial in shape ($\alpha+\alpha+$ di-nucleon). Recently, mirror symmetry breaking between ^{10}C and ^{10}Be was experimentally discussed through the β-decay probability to ^{10}B.[4] The transition strength from the 2^+ states of ^{10}Be and those from ^{10}C show significant difference, which is consistent with our analysis.

References

1) N. Itagaki, S. Hirose, T. Otsuka, S. Okabe, and K. Ikeda: Phys. Rev. C **65**, 044302 (2002).
2) Y. Abe, J. Hiura, and H. Tanaka: Prog. Theor. Phys. **49**, 800 (1973).
3) A. S. Davydov and G. F. Filippov: Nucl. Phys. **8**, 237 (1958).
4) I. Daito et al.: Phys. Lett. B **418**, 27 (1998).

New cluster model based on the generator coordinate method

M. Ito,* K. Katō,* and K. Ikeda

[NUCLEAR STRUCTURE, Cluster model, Unstable nuclei]

Recently, the breakup experiment of ^{12}Be into ^{6}He + ^{6}He has been performed using a 378 MeV ^{12}Be beam inelastically excited by ^{12}C and proton targets.[1] The results strongly indicate the existence of the exotic "^{6}He + ^{6}He molecular states" in the 10 to 25 MeV excitation energy interval, with spins in the range of $4\hbar$ to $8\hbar$.[1] In not only the ^{12}Be nucleus but also in other Be isotopes such as ^{10}Be and ^{14}Be, similar molecule-like states with the α + ^{6}He and ^{6}He + ^{8}He configurations have been observed in recent experiments.[2]

In order to study such exotic molecule-like states, we proposed a new approach based on the so-called coupled-channel generator coordinate method[3] and applied it to the α + ^{6}He system with the $J^{\pi} = 0^{+}$ state as a simple example. In this approach, the intrinsic states of the total system are defined in terms of a linear combination of α + ^{6}He with different channels. Internal states of ^{6}He are expressed by the $(0s)^4(0p)^2$ configuration in the harmonic oscillator, in which the two valence neutrons take p-orbitals with different "directions" such as $0p_x$, $0p_y$, $0p_z$ around an α cluster.

The total Hamiltonian is diagonalized after we perform the angular momentum and parity projection of the total intrinsic-system. This procedure leads to that the mixing of different p-orbitals in ^{6}He is optimized depending on the relative distance between α and ^{6}He. Regarding the NN interaction, we adopted the Volkov No. 2 interaction. In Fig. 1, the white circles show the energy surfaces obtained by the coupled-channel calculation. To confirm the asymptotic states generated by the channel-coupling effects, we artificially constructed the weak-coupling states, in which the ^{6}He nucleus had a definite intrinsic spin and coupled with the α particle with an α–^{6}He relative angular momentum.

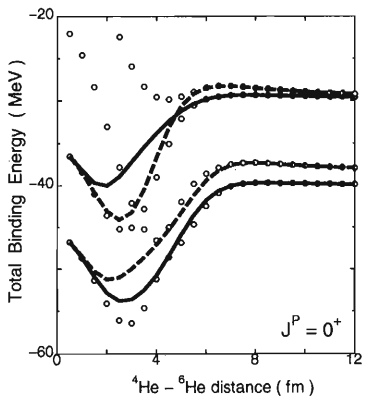

Fig. 1. Comparison between the energy surfaces of the coupled-channel calculation (white dots) and those of the weak-coupling states (solid and dashed curves).

Both solid curves show the surfaces of the weak-coupling states in which ^{6}He has the 0^{+} intrinsic spin. In the lower solid curve, the two valence neutrons in ^{6}He have the $L = S = 0$ configuration, where L and S denote the valence neutron's total orbital-angular-momentum and their total intrinsic-spins, respectively. On the other hand, in the upper solid curve, they are in the $L = S = 1$ configuration, which couple with the 0^{+} spin. In a similar way, the two dashed curves correspond to the weak-coupling states in which the ^{6}He nucleus forms the 2^{+} states. The lower dashed-surface and upper one correspond to the $L = 2$, $S = 0$ configuration and the $L = S = 1$ one, respectively. It is important to note that the energy surfaces of the coupled-channel calculation are completely the same as those of the weak-coupling states in the asymptotic region. This means that the channel coupling effect exactly generates the weak-coupling states in the asymptotic region.

At a short distance, however, the coupled-channel solutions are different from the weak-coupling states. Therefore, ^{6}He hardly keeps the asymptotic states with the definite spins in the case that the ^{6}He nucleus and the α particle becomes much closer. In such a short distance, we found that the two valence neutrons in ^{6}He occupy definite directions such as $(0p_x)^2$, $(0p_z)^2$ and so on. That is, the total system becomes a strong-coupling state such as a rigid-rotor in which ^{6}He has a definite geometrical configuration.

In conclusion, the present model will be a powerful tool for studies on the molecular resonances in the neutron-rich Be isotope because the model quite naturally generates both the weak-coupling states at an asymptotic distance and the strong-coupling ones at a small distance. The inclusion of the ^{5}He + ^{5}He channel is currently being performed.

References

1) M. Freer et al.: Phys. Rev. Lett. **82**, 1383 (1999).
2) A. Saito et al.: Proc. Int. Symp. on Clustering Aspects of Quantum Many-Body Systems, Kyoto, 2001-11 (World Scientific, 2001), p. 39.
3) H. Horiuchi et al.: Suppl. Prog. Theor. Phys. **62**, 1 (1977) and references therein.

* Division of Physics, Graduate School of Science, Hokkaido University

Extended ^{9}Li + n + n three-body model of ^{11}Li with a pairing correlation in ^{9}Li†

T. Myo,[*1] S. Aoyama,[*2] K. Katō,[*1] and K. Ikeda

[NUCLEAR STRUCTURE, Unstable nuclei, Cluster model]

The ^{11}Li nucleus is well known as a typical two-neutron halo system with a small amount of two-neutron separation energy, 0.31 MeV and a large matter radius. Related to the anomalous properties of ^{11}Li, the existence of 1s-wave states in ^{10}Li has also been discussed. The key to understanding the structures of ^{11,10}Li is the 1s-wave component in valence neutrons. However, the essential mechanism to lower the energy of the 1s-wave in these nuclei is still unclear.

In most of the theoretical studies of ^{11}Li based on the ^{9}Li+n+n three-body model, the ^{9}Li core is treated as inert and a state-dependent ^{9}Li-n interaction is often used in both the calculations for ^{11}Li and ^{10}Li. Although the obtained properties of ^{11}Li and ^{10}Li are consistent with experimental results, the mechanism that can account for the state dependence of the ^{9}Li-n interaction and the reliability of using the same interaction for both two nuclei have not yet been realized.

In this report, we propose the extended ^{9}Li + n + n three-body model, in which we adopt a multi-configuration representation for the ^{9}Li core in order to take into account the p-shell neutron pairing correlation in ^{9}Li. We analyze the structure of the ^{11}Li ground state and also the structure of ^{10}Li as ^{9}Li+n. The folding potential is used for a ^{9}Li-n interaction. Two cases with different strengths of neutron pairing correlation are considered in ^{9}Li: mixing of the $(0p_{3/2})^2_\nu(0p_{1/2})^2_\nu$ configuration in addition to the $(0p_{3/2})^4_\nu$ one is set to 15% (weak; PC-W) or 25% (strong; PC-S). In ^{10}Li, the pairing correlation in ^{9}Li produces the pairing-blocking effect which degenerates 1s- and p-wave states in the PC-S case shown in Table 1.

For ^{11}Li, the effect of the pairing correlation resolves the underbinding problem given in Table 2. The calculated binding energy depends on the strength of the pairing correlation in ^{9}Li and the $(s_{1/2})^2$ probability is too small to reproduce the halo structure for any two cases. This result differs from that for ^{10}Li and is due to the additional valence neutron in ^{11}Li. Due to the additional valence neutron, the pairing-blocking effect on the pairing correlation in ^{9}Li is overwhelmed by the attractive ^{9}Li-n interaction for the $p_{1/2}$-orbit in ^{11}Li. From this study, we can conclude that the effects of the pairing correlation differ in the cases of ^{10}Li and ^{11}Li. This indicates that one must be careful in using the state-dependent ^{9}Li-n potential in the calculations of both ^{10}Li and ^{11}Li.

Table 1. Spectroscopic properties of ^{10}Li. The units are MeV for energies and fm for scattering lengths.

	$1^+(E_r, \Gamma)$	$E(2^-)$	$a_s(2^-)$
PC-W	(0.42, 0.22)	—	+0.2
PC-S	(0.42, 0.16)	−0.38	−5.0
PC-W+Tail	(0.42, 0.43)	−0.04	−14.8
Exp.	(0.42, 0.15)[1)]	—	—

Table 2. Ground state properties of ^{11}Li. The units are MeV for binding energy and fm for matter radius.

	$E_{g.s.}$	$P[(s_{1/2})^2]$	R_m	α_{s-p}
PC-W	−0.50	1.8 %	2.69	1
PC-S	−2.67	1.9 %	2.49	1
PC-W+Tail	−0.31	25.1%	3.47	2.8
Exp.	−0.31	—	3.12 ± 0.16[2)] 3.53 ± 0.06[3)]	

We further improve the tail behaviour in the ^{9}Li-n interaction, and also introduce a parameter α_{s-p} to enhance the $(0p)^2$-$(1s)^2$ pairing coupling for valence neutrons; $\langle(0p)^2|v_{nn}|(1s)^2\rangle \rightarrow \alpha_{s-p}\ \langle(0p)^2|v_{nn}|(1s)^2\rangle$ where Minnesota interaction is used for v_{nn}, the interaction between valence neutrons. It might be expected that the pairing correlation can be changed in ^{11}Li due to the coupling of two kinds of neutron pairings of ^{9}Li and the valence parts.

For ^{11}Li, the $(s_{1/2})^2$ probability in the ground state increases sufficiently to be consistent with the experimental matter radius. It should be mentioned that the tail interaction plays an important role in lowering the energy of the $(s_{1/2})^2$ component with respect to that of the $(p_{1/2})^2$-component for ^{11}Li. As a result, the $(s_{1/2})^2$ and $(p_{1/2})^2$ components can be easily made to couple in the ^{11}Li ground state. It is found that the values of α_{s-p} are larger than unity. This might indicate the enhancement of the pairing correlation due to the coupling of neutrons between valence and core parts.

† Condensed from the article in Prog. Theor. Phys. **108**, 133 (2002)

*1 Division of Physics, Graduate School of Science, Hokkaido University

*2 Information Processing Center, Kitami Institute of Technology

References

1) H. G. Bohlen et al.: Z. Phys. A **344**, 381 (1993).
2) I. Tanihata et al.: Phys. Lett. B **206**, 592 (1988).
3) J. A. Tostevin and J. S. Al-Khalili: Nucl. Phys. A **616**, 418c (1997).

Three-body coulomb breakup of ^{11}Li in the complex scaling method

T. Myo,[*1] S. Aoyama,[*2] K. Katō,[*1] and K. Ikeda

[NUCLEAR STRUCTURE, Unstable nuclei, Cluster model]

The structure of the ^{11}Li nucleus is one of the interesting objects in unstable nuclear physics. The most typical feature observed in ^{11}Li is a neutron halo structure which is related to a small binding energy (0.31 MeV) against two-neutron emission. The weak-binding energy of this nuclei is also responsible for large breakup cross section. Through the breakup reactions involving neutron halo nuclei, one obtains important information not only about the ground-state properties, but also about the fundamental excitation mechanism of unstable nuclei above the threshold energy, such as the soft dipole resonance.

The breakup reactions of two-neutron halo nuclei provide us with much information on the strength distribution of various kinds of three-body configuration. In observing those responses theoretically, it is important to decompose the transition strengths into the components of every resonant and continuum states. For this purpose, we adopt the complex scaling method (CSM).[1] In this report, we discuss the excitation mechanisms of ^{11}Li through its three-body breakup in the Coulomb excitation with CSM.

First, we describe ^{11}Li with an extended $^{9}\mathrm{Li}+n+n$ three-body model.[2] We adopt a multiconfiguration representation for the ^{9}Li nucleus in order to take into account the neutron pairing correlation for ^{9}Li in addition to that for two valence neutrons. In this model, the underbinding problem of the ^{11}Li ground state is solved and its halo structure is also reproduced.

Second, we use CSM to separate the strength distribution to a scattering state into the following terms; (i) three-body resonances, (ii) two-body continuums corresponding to the sequential breakup via $^{10}\mathrm{Li}^{(*)}+n$, (iii) three-body continuums corresponding to the direct breakup into $^{9}\mathrm{Li}+n+n$. We determine which process determines the structures of the strength distribution.

We first determine the resonance for dipole excited states ($1/2^+$, $3/2^+$, $5/2^+$) of ^{11}Li in CSM, but we cannot find any three-body resonance having a small decay width. This implies that the dipole strengths are exhausted by the continuum components of the ^{11}Li. Figure 1 (a) shows the calculated cross section of ^{11}Li breakup using the virtual photon number, where the $(s_{1/2})^2$ probability in the ^{11}Li ground state is set to be 30%. The strength shows low-energy enhancement

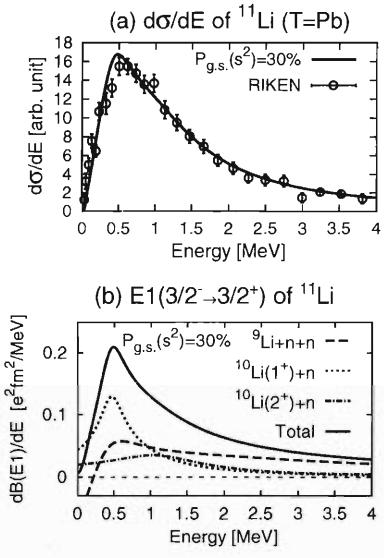

Fig. 1. (a) Calculated cross section compared with experimental data.[3] (b) Separation of $E1$ strength.

which is very sensitive to the $(s_{1/2})^2$ probability of the ^{11}Li ground state. Then, this low-energy enhancement may be interpreted as the threshold effect and reflect the halo structure of ^{11}Li.

Figure 1 (b) shows the result of the separation of $E1$ strength where the $(s_{1/2})^2$ probability is 30%. It is found that the each continuum component contributes to the strength comparably. The ratios of the integrated strength of each continuum component to the total integrated strength are 42%, 36% and 22% for $^{9}\mathrm{Li}+n+n$, $^{10}\mathrm{Li}(1^+)+n$ and $^{10}\mathrm{Li}(2^+)+n$ continuum states, respectively. This means that there are two kinds of breakup process of a three-body direct one and a sequential one through $^{10}\mathrm{Li}^{(*)}+n$ components. In particular, the $^{9}\mathrm{Li}+n+n$ three-body continuum component is sensitive to the halo structure of ^{11}Li.

References

1) T. Myo, K. Katō, S. Aoyama, and K. Ikeda: Phys. Rev. C **63**, 054313 (2001).
2) T. Myo, S. Aoyama, K. Katō, and K. Ikeda: Prog. Theor. Phys. **108**, 133 (2002).
3) S. Shimoura et al.: Phys. Lett. B **348**, 29 (1995).

*1 Division of Physics, Graduate School of Science, Hokkaido University
*2 Information Processing Center, Kitami Institute of Technology

Coupled channel study of O-isotopes with core plus valence neutron model

H. Masui,* T. Myo,* K. Katō,* and K. Ikeda

[Nuclear structure, Unstable nuclei, Cluster model]

In recent years, there has been much interest in the study of unstable nuclei.[1,2] Neutron-rich nuclei have unique features, such as a halo structure. Among these nuclei, ^{23}O and ^{24}O have a possibility of becoming halo nuclei, *i.e.*, one- and two-neutron halo nuclei, respectively. From the theoretical point of view, the concept of the "core plus valence neutron(s)" is a good assumption and well describes the property of loosely bound nuclei. The procedure of such calculation has been developed and improved in light unstable nuclei, *e.g.*, He, Li, and Be, not only for bound states but also for resonant states.

In this work, we investigate the O-isotopes in the "core plus valence neutron(s)" model. Here the dynamics in the core, which is the pairing excitation of neutrons inside the core, and the exchange effect from the RGM-kernel are investigated. As the first example, we perform a coupled-channel calculation for the $^{16}\mathrm{O}+n$ system (^{17}O), and investigate the $^{16}\mathrm{O}+n+n$ system (^{18}O) by using the same interaction. The core-n potential is made by folding the effective NN-interaction. The LS potential is taken as a density-derivative type. The other contributions, such as those from the tensor force, are neglected in this stage. In this framework, the pairing excitation of the neutrons in the ^{16}O is produced as a coupled-channel model between the different configurations in the core.

First, we study ^{17}O. For the low-lying positive-parity states, $5/2^+$, $1/2^+$ and $3/2^+$, we apply the exchange kernel of RGM (the resonating group method), using it's knock-on exchange kernel (model-K kernel).[3] Since the exchange effect is stronger for the d-wave than that for the s-wave, we can obtain the state-independent interaction (parameter set) to reproduce the positive-parity states.

Next, we investigate the negative-parity state $1/2^-$, which can be considered the one neutron-hole state in the $0p_{1/2}$-orbit. We perform a coupled-channel calculation of two different configurations in the core nucleus. The ground-state configuration is $(0p_{1/2})^2_\nu$ and the first excited one is $(0d_{5/2})^2_\nu$ for the last two neutrons in ^{16}O. In this calculation, we use the same potential as that of the positive-parity states, but change the energy difference of the core between the $0p_{1/2}$- and the $0d_{5/2}$-orbits, which corresponds to the single particle energy (SPE) in the shell model picture. We confirm that the obtained SPE is comparable to that of the shell model calculation (11.63 MeV).[4]

For ^{18}O, we perform the three-body calculation using the $^{16}\mathrm{O}+n+n$ model. As the first step, we only use the COSM (cluster orbital shell model) basis sets. Figure 1 shows the calculated results by using the RGM kernel. The energy levels still deviate from the experimental ones. To improve the lack of binding energy for the ground state, the inclusion of the ECM (extended cluster model) basis set is necessary. Also, the coupled-channel treatment in the core-n interaction will be important in the ^{18}O system.

To summarize, we study the low-lying states of ^{17}O in the core + n model by including the model-K RGM kernel.[3] For the positive-parity states, the exchange kernel can reproduce the levels of the low-lying states in a state-independent manner. By using such state-independent potentials and kernels, we calculate the lowest negative-parity state $1/2^-$. The coupled-channel calculations show that the energy difference in the core states is comparable to the SPE of the shell model calculation.[4] For the ^{18}O system, by using the core + n + n three-body model, the effect of the non-local kernel seems to be important. In the future, we will proceed to study heavier oxygen isotopes.

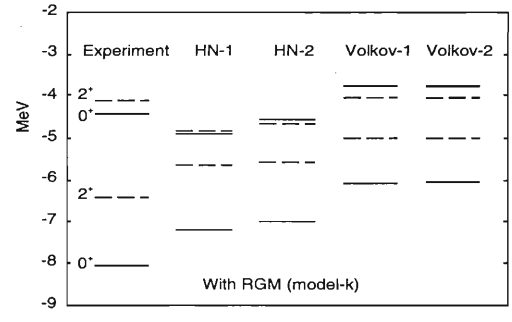

Fig. 1. Energy levels of ^{18}O.

References

1) I. Tanihata et al.: Phys. Lett. B **160**, 380 (1985); Phys. Rev. Lett. **55**, 2676 (1985).
2) A. Ozawa et al.: Nucl. Phys. A **691**, 599 (2001).
3) T. Kaneko, M. LeMere, and Y. C. Tang: Phys. Rev. C **44**, 1588 (1991).
4) E. K. Warburton and B. A. Brown: Phys. Rev. C **46**, 923 (1992).

* Department of Physics, Hokkaido University

The microscopic description of nuclear shell structures with modern nucleon-nucleon interactions

S. Fujii, R. Okamoto,* and K. Suzuki*

[Shell structure, Magic number, Effective interaction]

The shell structure is one of the important features of the nucleus. The fundamental quantities in the nucleus such as the spin-orbit splitting and the magic numbers are closely related to the shell structure. Recently, it has been discussed that the magic numbers in the neutron-rich region should be modified due to the change of the shell structure.[1)]

The derivation of new magic numbers from a microscopic structure calculation is a challenging problem in the theoretical studies of nuclei. We are now trying to describe shell structures in a wide range of mass numbers systematically and microscopically, starting from modern nucleon-nucleon interactions such as the charge-dependent Bonn (CD Bonn) and the Argonne V18 potentials. In such structure calculation, we need to derive an effective interaction from a bare interaction due to the limitation of the computer power, except for the calculation of very light nuclei.

The unitary-model-operator approach (UMOA) is very useful for this problem. The UMOA is a many-body theory that leads to a Hermitian and energy-independent effective interaction. This type of effective interaction is suitable for the structure calculation. The shell-model calculation using the effective interaction derived within the framework of the UMOA has recently been performed for the Λ hypernucleus ${}^{16}_{\Lambda}$O.[2)]

We are now developing a method of structure calculation to obtain properties of nuclei near the drip line. Several important developments are as follows. First, the effective interaction is derived in terms of the particle basis. The particle basis means that the proton and neutron are treated independently. The advantage of the description by the particle basis is that the Coulomb force can be treated only for the proton-proton channel. The second is that three-body cluster terms are derived by the particle basis. This effect is considered to be very important for particle states in neutron-rich nuclei.

At the present stage, we have finished the derivation of the numerical formulae needed in the actual calculation and are developing the computer program. Some preliminary calculations in a restricted model space are in progress.

In Fig. 1, calculated single-particle levels for hole states in ^{16}O (a) and ^{24}O (b) using the CD Bonn potential are shown. In these calculations, the effective interaction is derived in the model-space size $N_{\max} = 8\hbar\omega$ with the harmonic-oscillator frequency $\hbar\omega = 14$ MeV.

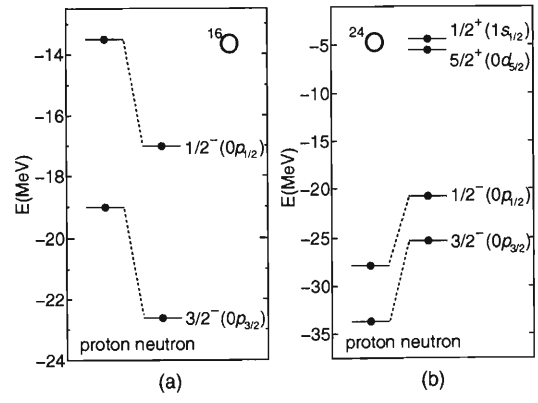

Fig. 1. Calculated single-particle levels for hole states in ^{16}O (a) and ^{24}O (b). The results are for $\hbar\omega = 14$ MeV and $N_{\max} = 8\hbar\omega$. The CD Bonn potential is employed.

The results include the effects of the one-particle two-hole contributions and the three-body cluster terms in this model-space size.

A fairly good result of the spin-orbit splitting is obtained as shown in Fig. 1 (a), where the experimental value is about 6.2 MeV. The remaining disagreement between the calculated and the experimental values may be compensated by the inclusion of three-or-more-body interactions and/or some relativistic effects. It should be noted that the magnitude of the proton-neutron difference for the $0p_{1/2}$ state is in good agreement with the experimental value, namely, the mass difference between ^{15}N and ^{15}O which is 3.54 MeV.

In Fig. 1 (b), the single-particle levels including the *sd* shells for the neutron are shown. These levels were obtained for the first time in the fully microscopic calculation using the CD Bonn potential. The calculation of the $0d_{3/2}$ state which is the particle state of the neutron is in progress, which is very important to theoretically confirm the new magic number $N = 16$.

The final results of the calculations in a larger model space for oxygen isotopes will be reported elsewhere in the near future.

References

1) A. Ozawa, T. Kobayashi, T. Suzuki, K. Yoshida, and I. Tanihata: Phys. Rev. Lett. **84**, 5493 (2000).
2) S. Fujii, R. Okamoto, and K. Suzuki: Phys. Rev. C **66**, 054301 (2002).

* Department of Physics, Kyushu Institute of Technology

Shell-model description of $^{16}_{\Lambda}$O with Σ degrees of freedom†

S. Fujii, R. Okamoto,* and K. Suzuki*

[Hypernuclei, Effective interaction, Shell model]

Shell-model calculations for $^{16}_{\Lambda}$O in a large model space have been performed. By introducing a new model space including ΣN states, we have calculated effective interactions which include the ΣN-ΛN coupling terms. As far as we know, the degrees of freedom of Σ in addition to Λ and nucleons have been explicitly introduced in the shell-model calculations for the first time. The effective interactions and the single-particle energies employed in the shell-model calculations have been microscopically derived from the Nijmegen soft-core (NSC) 97a-f and NSC89 *YN* interactions and the Paris *NN* interaction within the framework of the unitary-model-operator approach (UMOA).[1)]

It has been found that a drastic change in the structure of $^{16}_{\Lambda}$O induced by the Σ degrees of freedom does not occur as long as we employ the NSC97a-f potentials. The Σ degrees of freedom give rise to a small effect on the first-excited doublet $(1^-_2,\ 2^-_1)$ in $^{16}_{\Lambda}$O. However, if we use the NSC89 potential which has a strong ΣN-ΛN interaction, the splittings of the ground and first-excited doublets, respectively, $(0^-_1,\ 1^-_1)$ and $(1^-_2,\ 2^-_1)$ are enlarged. The magnitude of the splitting of the ground-state doublet gradually decreases from 0.69 MeV to 0.11 MeV from NSC97a to NSC97f, respectively. We should note that the 0^-_1 state lies below the 1^-_1 state in energy for the NSC97 models. On the other hand, the 1^-_1 state is below the 0^-_1 state for the NSC89. In the E930 experiment at BNL, the magnitude of the ground-state doublet should be determined in the near future, which would give useful information on the underlying properties of the *YN* interaction.

Effects of the parity-mixing intershell coupling on $1\hbar\omega$ excited states have been investigated. It has been found that the parity-mixing intershell coupling plays an important role in the structure of the 0^+_1 and 1^+_1 states in $^{16}_{\Lambda}$O with the help of the *NN* effective interaction. As a result, the 0^+_1 and 1^+_1 states have complex structures. On the other hand, the parity-mixing intershell coupling on the 2^+_1 state is less active than the 0^+_1 and 1^+_1 states.

In conclusion, the present shell-model results, in particular, the excitation spectra are in good agreement with the experimental levels on the whole, even though our calculation method is fully microscopic and does not include any experimental values and adjustable parameters. The experimental levels are between the two results for the NSC97f and NSC89. In the near future, some fine structures of Λ hypernuclei reflecting the properties of the underlying *YN* interaction could be revealed experimentally. We hope that our method will help to bridge the *YN* interaction and the Λ hypernuclear structure microscopically, and give a useful constraint to determine *YN* interactions more realistically.

The final results of the calculations are summarized in Fig. 1 and Table 1.

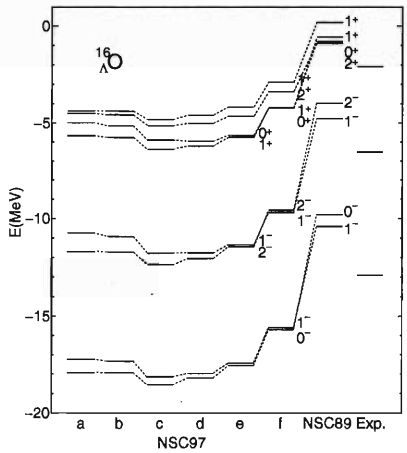

Fig. 1. Calculated energy levels in $^{16}_{\Lambda}$O using the NSC97a-f and NSC89 *YN* potentials. The Paris potential is employed for the *NN* interaction. The experimental levels are also shown.

Table 1. The percentage analysis of the low-lying positive parity states. The percentage for each configuration denotes the probability, namely, the square of mixing amplitude. The NSC97f and the Paris potentials are employed for the *YN* and *NN* interactions, respectively.

Configuration	0^+_1	1^+_1	2^+_1
$[0p^{\Lambda}_{1/2}, 0p^{-1}_{1/2}]$	30.1%	1.9%	0%
$[0p^{\Lambda}_{3/2}, 0p^{-1}_{1/2}]$	0%	37.8%	65.6%
$[0s^{\Lambda}_{1/2}, 0s^{-1}_{1/2}]$	12.1%	9.0%	0%
$[0s^{\Lambda}_{1/2}, 0d_{5/2}, 0p^{-1}_{3/2}, 0p^{-1}_{1/2}]$	33.0%	26.6%	6.9%

References

1) S. Fujii, R. Okamoto, and K. Suzuki: Prog. Theor. Phys. **104**, 123 (2000).

† Condensed from the article in Phys. Rev. C **66**, 054301 (2002)

* Department of Physics, Kyushu Institute of Technology

Relativistic mean field theory with the pion for finite nuclei II

S. Sugimoto, H. Toki,* and K. Ikeda

[Nuclear structure, Pion, Mean field model]

We are developing a mean field framework for the nuclear structure which treats the finite pion mean field on the same footing as other mesons. It is well-known that the pion is one of the most important mesons in nuclear physics. The pion mainly produces the tenor interaction between two nucleons, which plays significant roles in the nuclear structure.

Although we know well the pion is the essential ingredient of the nuclear structure, many nuclear models, particularly mean field models, do not treat the pion or the tenor force explicitly. The effect of the pion is incorporated by renormalizing the other parts of the nuclear interactions as central and LS forces. However, considering the important role of the pion, it is of interest to establish a mean field framework which includes the effect of the pion explicitly. To achieve this we need to break parity symmetry of a nuclear mean field. It means that a single-particle state in the mean field is a parity-mixed state. We show in the recent study[1] that we can incorporate the finite pion mean field into the nuclear mean field by using such parity-mixed single-particle states.

Our model is in a developing stage and we have many improvements to make. In the previous work[1] we adopted the mean field approximation (Hartree approximation) as usually done in the relativistic mean field (RMF) theory. It means that we neglect the exchange (Fock) term, which is very important because the antisymmetrization plays an essential role in nuclear physics. In the relativistic Hartree-Fock approximation with no parity-mixing, the pion contributes greatly to the binding energy in finite nuclei and nuclear matter.[2] Therefore, we must improve our model from the Hartree approximation to the Hartree-Fock one and study the effect of the exchange term in our framework.

The Hamiltonian adopted here has the following form,

$$
\begin{aligned}
H = & \int d^3x \psi^\dagger(\boldsymbol{x}) \left(-i\boldsymbol{\alpha}\cdot\nabla + \gamma^0 M\right) \psi(\boldsymbol{x}) \\
& + \frac{1}{2}\int d^3x \int d^3y \psi^\dagger(\boldsymbol{x})\psi^\dagger(\boldsymbol{y}) \\
& \times \left[-\gamma^0_{\boldsymbol{x}}\gamma^0_{\boldsymbol{y}} \frac{g_\sigma^2 e^{-m_\sigma|\boldsymbol{x}-\boldsymbol{y}|}}{4\pi|\boldsymbol{x}-\boldsymbol{y}|} + \frac{g_\omega^2 e^{-m_\omega|\boldsymbol{x}-\boldsymbol{y}|}}{4\pi|\boldsymbol{x}-\boldsymbol{y}|} \right. \\
& \left. - \left(\gamma^0\gamma^i\gamma_5\right)_{\boldsymbol{x}} \nabla^i_{\boldsymbol{x}} \left(\gamma^0\gamma^i i\gamma_5\right)_{\boldsymbol{y}} \nabla^i_{\boldsymbol{y}} \frac{f_\pi^2}{m_\pi^2} \frac{e^{-m_\pi|\boldsymbol{x}-\boldsymbol{y}|}}{4\pi|\boldsymbol{x}-\boldsymbol{y}|} \right] \\
& \times \psi(\boldsymbol{y})\psi(\boldsymbol{y}), \qquad (1)
\end{aligned}
$$

where the sigma (σ) meson, the time component of omega (ω), and the pi (π) meson are included. We obtain this Hamiltonian from the usual RMF Lagrangian. By varying the expectation value of the Hamiltonian with respect to a single Slater determinant, we obtain the relativistic Hartree-Fock (H-F) equation.[2] We take parity-mixed single particle states as trial functions and solve the H-F equation self-consistently.

We show the very preliminary result for ^{40}Ca, where we only include the π^0 meson and the time component of the omega meson (ω^0) in both the direct and the exchange terms. We adopt the parameters for the meson-nucleon coupling constants from A. Bouyssy *et al.*[2] The parameters are labelled as (c) in the paper and include the sigma, the omega, and the pi meson-nucleon couplings. In Table 1, we show the results obtained with the Hartree-Fock (H-F) and the Hartree (H) approximations. We give the potential energy from each meson and the contribution from the direct term in parentheses for the H-F case. From the results we can see that the exchange contribution is not small and that, more interestingly, in the Hartree-Fock approximation the contribution of the pion is larger, compared to that in the Hartree approximation. We need to carry more elaborate work to confirm this but we can say that the exchange term is important in our framework.

In addition to the inclusion of the exchange terms, there are many improvements which should be made to establish our model as written in our recent paper.[1] Through this model we want to reveal remarkable phenomena induced by the pion in nuclear structure in the near future.

Table 1. The result with Hartree-Fock (H-F) and Hartree (H) approximation for the potential energy from the sigma (V_σ), the omega (V_ω), and pi (V_π) meson. In the parentheses, the contribution from the direct (Hartree) term is given for the H-F case. We also give the kinetic energy and the total binding energy. The unit for all entries is MeV.

	V_σ	V_ω	V_π	KE	BE
H-F	−3818 (−5929)	3127 (5474)	−275 (−477)	760	214
H	−5224	4439	−59	521	331

* Research Center for Nuclear Physics, Osaka University

References

1) H. Toki, S. Sugimoto, and K. Ikeda: Prog. Theor. Phys. **108**, 903 (2002).
2) A. Bouyssy, J.-F. Mathiot, N. V. Giai, and S. Marcos: Phys. Rev. C **36**, 380 (1987).

Relativistic mean field theory with the pion for finite nuclei III

K. Ikeda, S. Sugimoto, and H. Toki*

[Nuclear structure, Pion, Mean field model]

We have studied the possible existence of a finite pion mean field in finite nuclei by introducing a pion field into the relativistic mean field (RMF) theory.[1] To accommodate the finite pion mean field, we have extended the RMF theory by introducing the parity-mixed single-particle basis. With the use of the pion coupling constant in free space, we have carried out calculations for $N = Z$ closed shell nuclei and shown the actual appearance of a finite pion mean field. We have demonstrated that the potential energy associated with the pion behaves roughly proportional to the nuclear surface. For this reason, we refer to the onset of the finite pion mean field as "surface pion condensation."

We have seen[1] that there is a critical value of pion coupling constant, $g_\pi = g_\pi^{\rm cr}$, at which there arises a finite pion mean field. The critical values for various nuclei are distributed in the region satisfying $0.92 g_\pi^0 \leq g_\pi^{\rm cr} \leq 0.97 g_\pi^0$ except for ^{12}C. This finding indicates that the symmetry breaking mean field is fragile and that various effects, which are not taken into account in the previous study, could influence the realization of the finite pion mean field in finite nuclei. Therefore, in order to establish the mean field theory with the inclusion of the pion, we must improve the approximations employed in the RMF theory.

One of the important problem is the improvement of the many-body treatment which is necessarily demanded. We should work out the exchange terms, *i.e.*, the Fock terms in the many-body theory. In addition, we have to recover the parity symmetry in the total system since the finite pion mean field breaks the parity symmetry of the intrinsic state. Therefore, we should further perform the study of the parity projection in the framework of the variation after projection (VAP) to compare the theoretical consequences of the finite pion mean field with the experimental phenomena.

We employ the variational wave functions $\Psi^{(\pm)}$ which are projected out from a Slater determinant $\Phi = \det\{\phi_1, \phi_2, \ldots, \phi_A\}$ composed of the set of the parity-mixed single-particle wave functions $\{\phi_i(\xi),\ i = 1, \ldots, A\}$. We obtain the equations for the single-particle states from the variation of the energy functional of the expectation value under the conditions $\langle\phi_i|\phi_j\rangle = \delta_{ij}$. We call these equations the parity projected Hartree-Fock (PPHF) equations for $J^\pi = 0^\pm$, which are of the same form as the equations given by Yabana *et al.* for the case of using of the Skyrme interactions.[2]

$$\hat{h}_{\rm HF}(\xi,\xi')\,\phi_i(\xi') \pm n^{(P)}\Big\{\hat{h}_{\rm HF}^{(P)}(\xi,\xi')\,\tilde{\phi}_i^{(P)}(\xi') - \sum_j \left\langle \phi_j \middle| \hat{h}_{\rm HF}^{(P)} \middle| \tilde{\phi}_i^{(P)}(\xi) \right\rangle \tilde{\phi}_j^{(P)}(\xi)\Big\} + \left(E^\pm - E^0\right)\tilde{\phi}_i^{(P)}(\xi) = \sum_j \epsilon_{ij}\phi_j(\xi), \tag{1}$$

$$\tilde{\phi}_i^{(P)}(\xi) = \sum_j \phi_j(-\vec{r},\eta)\left(B^{(P)^{-1}}\right)_{ji}, \tag{2}$$

$$B_{ij}^{(P)} = \left\langle \phi_i \middle| \hat{p} \middle| \phi_j \right\rangle, \quad n^{(P)} = \det B^{(P)}. \tag{3}$$

Here, $\hat{h}_{\rm HF}$ is the HF single-particle Hamiltonian operator, and $\hat{h}_{\rm HF}^{(P)}$ is the single-particle coupling Hamiltonian operator with a form similar to $\hat{h}_{\rm HF}$, which combines $\{\phi_i\}$ with the parity-transformed single-particle states $\{\tilde{\phi}_i{}^{(P)}\}$ defined in Eq. (2). We could solve the PPHF equations self-consistently in the same manner as we do for the HF equations.

The PPHF equations give us not only the single-particle energies, $\epsilon_i \equiv \epsilon_{ii}$ $(i = 1, \ldots, A)$, but also the energy difference $E^\pm - E^0$, where $E^\pm$ are the energy expectation values of the parity-projected states $\Psi^\pm$ for $J^\pi = 0^\pm$ and E^0 that of the nonprojected state Φ. Thus, we could obtain the finite energy gap between the ground 0^+ state and the excited 0^- state as

$$E^- - E^+ = \Delta E^- - \Delta E^+ + \left(E^{0-} - E^{0+}\right), \tag{4}$$

with $\Delta E^\pm = E^\pm - E^{0\pm}$. Here, we note that the expectation value of nonprojected wave function Φ (Hatree-Fock energy), E^0, is different between the states with $J^\pi = 0^\pm$ because the coupling terms in Eq. (1) have opposite signs. Therefore, the difference of the Hartree-Fock energies, $(E^{0-} - E^{0+})$, contributes to the energy gap as shown in Eq. (4), which is *a priori* assumed to be zero under the H-F approximation. We expected that the solutions of Eq. (1) will clarify the relationship of the surface pion condensation with the finite energy gap between the 0^+ and 0^- states.

We are now studying the PPHF equations for the doubly closed-shell nuclei studied in the previous paper.[1]

* Research Center for Nuclear Physics, Osaka University

References

1) H. Toki, S. Sugimoto, and K. Ikeda: Prog. Theor. Phys. **108**, 903 (2002).
2) S. Takami, K. Yabana, and K. Ikeda: Prog. Theor. Phys. **96**, 407 (1996).

Energies of ground state and first excited 0^+ state in an exactly solvable pairing model†

N. Dinh Dang

[NUCLEAR STRUCTURE, BCS theory, Lipkin-Nogami method, boson formalism, superfluid - normal phase transition, random-phase approximation]

The random-phase approximation (RPA)[1,2] is one of the most popular methods used in the theoretical microscopic study of the nuclear structure. It includes the correlations beyond the mean field models such as the Hartree-Fock (HF) approximation with phenomenological interactions. It serves as a powerful tool for treating all the excited states in nuclei, which are beyond the reach of the full diagonalization within a shell-model basis. The quasiparticle RPA (QRPA), in which quasiparticle correlations and excitations are considered, has shown its prominent role in treating open-shell nuclei, where superfluid pairing correlations are important. Recently, the accuracy of the RPA in describing binding energies has been tested using HF+RPA calculations within schematic exactly solvable models[3] as well as for nuclei throughout the *sd*-shell and the lower *pf*-shell.[4] The test using exactly solvable Lipkin models[3] has shown that the HF+RPA (QRPA) calculations yield a very good ground-state energy except for the region of pairing interaction around the point where the pairing gap collapses. Meanwhile, tests using a more realistic shell-model Hamiltonian have shown that the binding energy predicted by the RPA is generally, but not always, satisfactory.[4,5] A number of suggestions have been made to improve the reliability of the RPA.

Since the RPA is a theory of excited states, an improvement of the accuracy of the RPA should provide, as a first step, a better description for both of the energies of ground state and the first excited state simultaneously. In the present paper, a recipe is proposed for such improvement using existing approximation schemes, namely the Lipkin-Nogami (LN) method for the pairing gap[6] and the renormalized RPA (renormalized QRPA) to treat the ground-state correlations beyond the RPA.[7,8] The BCS approximation (BCS), LN method, RPA, QRPA, the RRPA, and RQRPA are tested by calculating the ground-state energy and the energy of the first excited 0^+ state using a well-known exactly solvable two-level model[9] (Fig. 1). It is shown that, in the strong-coupling regime, the QRPA which excludes the scattering term of the model Hamiltonian yields the best fit to the exact solutions. A combination of the RRPA and RQRPA with the pairing gap given by the LN method has been proposed to avoid the superfluid-normal phase transition, and achieve a reasonably good description for both the ground-state energy and the energy of the first excited 0^+ state.

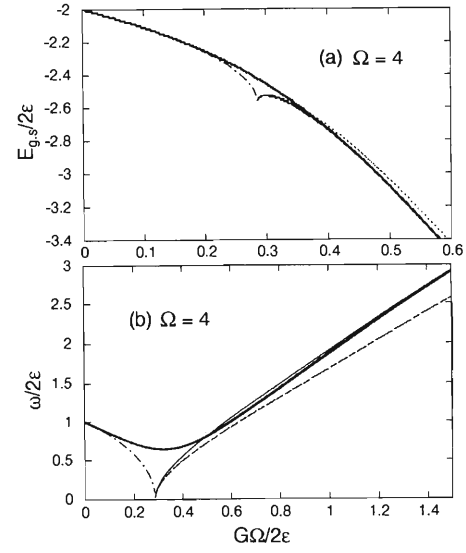

Fig. 1. Ground-state energy (a) and energy of the first excited state (b) (in units of 2ϵ) as functions of $G\Omega/(2\epsilon)$. The thick solid line is the exact result. The thin solid line shows the QRPA result excluding the scattering term in the pairing Hamiltonian within the quasiparticle representation. The dashed line denotes the QRPA result shown in Ref. 3. The dotted line represents the result obtained using the exact commutation relations between the quasiparticle-pair operators for evaluating the contribution of the scattering term. The dash-dotted line represents the RPA result.

† Condensed from the article in Eur. Phys. J. A **16**, 181 (2003)

References

1) D. J. Rowe: Phys. Rev. **175**, 1293 (1968); Rev. Mod. Phys. **40**, 153 (1968); Nucl. Phys. A **107**, 99 (1968).
2) P. Ring and P. Schuck: *The Nuclear Many-Body Problem* (Springer-Verlag, New York, 1980).
3) K. Hagino and G. F. Bertsch: Nucl. Phys. A **679**, 163 (2000).
4) I. Stetcu and C. W. Johnson: Phys. Rev. C **66**, 034301 (2002).
5) N. Ullah and D. J. Rowe: Phys. Rev. **188**, 1640 (1969).
6) H. C. Pradhan, Y. Nogami, and J. Law: Nucl. Phys. A **201**, 357 (1973).
7) K. Hara: Prog. Theor. Phys. **32**, 88 (1964); K. Ikeda, T. Udagawa, and H. Yamamura: Prog. Theor. Phys. **33**, 22 (1965).
8) F. Catara, N. Dinh Dang, and M. Sambataro: Nucl. Phys. A **579**, 1 (1994).
9) J. Högaasen-Feldman: Nucl. Phys. **28**, 258 (1961).

Strength of the double-phonon state in an exactly solvable model†

N. Dinh Dang

[NUCLEAR STRUCTURE, double-phonon excitations, energy-weighted sum rule]

The double giant dipole resonance (DGDR) has been observed recently in the relativistic heavy-ion reactions via Coulomb excitation[1–3] and pion-induced charge-exchange reactions. The results of these experiments are rather controversial with respect to conventional understanding of multiphonon resonances within the independent-phonon picture (also called the harmonic limit). According to the latter, a DGDR is assumed to be a two-dipole-phonon resonance, which is a giant dipole resonance (GDR) built on top of another GDR. As such, the DGDR parameters can be calculated by folding two independent GDRs.[4] Hence, the DGDR energy $E_{\rm DGDR}$ is expected to be $2E_{\rm GDR}$ ($E_{\rm GDR}$ is the GDR energy), and the DGDR full width at the half-maximum (FWHM) $\Gamma_{\rm DGDR}$ is equal to $2\Gamma_{\rm GDR}$ ($\Gamma_{\rm GDR}$ is the GDR FWHM), if folding Lorentzian photoabsorption cross sections is used, or to $\sqrt{2}\Gamma_{\rm GDR}$, if Gaussians are folded. In reality, because of the anharmonicities, the energy and width of DGDR will differ slightly from these values. This feature has been observed in experiments,[2,3] where it has been found that the energy shift $\Delta E \equiv 2E_{\rm GDR} - E_{\rm DGDR}$ is few hundred keV for ^{136}Xe, while the relation $\sqrt{2}\Gamma_{\rm GDR} \leq \Gamma_{\rm DGDR} \leq 2\Gamma_{\rm GDR}$ holds. However, the controversy is seen in the value of the experimentally extracted cross section of electromagnetic (EM) (or Coulomb) excitation for the DGDR, which turns out to be much larger than that given by the folding model. The "enhancement" is found to be around 178–200% in the reactions with ^{136}Xe projectiles at 700 MeV/nucleon kinetic energy,[3] and around 133% using ^{208}Pb projectiles at 640 MeV/nucleon kinetic energy, bombarding the ^{208}Pb target.[2] Several microscopic approaches have been recently developed to study the multiphonon giant resonances.[5] However, none of them can describe the "enhancement" of the DGDR cross section without artificially increasing the GDR integrated strength to a value much higher than the experimental one. Recently, the phonon damping model (PDM), proposed in Ref. 6, has been applied to calculate the multiple-phonon resonances.[7–9] The PDM can describe the EM cross sections of DGDR simultaneously for both of ^{136}Xe and ^{208}Pb cases along with the DGDR width and energy.[9] Since the PDM uses two phenomenological parameters to reproduce the GDR, a question still remains about the reason why the other microscopic models significantly underestimate the EM cross section of the DGDR. The aim of the present work is to shed light on this issue. For a clear the answer, it is desirable to use a simple yet exactly solvable model, with which the results of well-established microscopic approaches such as the random-phase approximation (RPA) can be compared with. A candidate is the Lipkin-Meskov-Glick (LMG)[10] model, which has been widely reported in the literature for testing the validity of various many-body approximation methods.

In this work, the deviation of the energy-weight sum rule (EWSR) and the energy shift for the two-phonon state from the prediction of the independent-phonon picture are studied within the exactly solvable LMG model. The exact results are used to compare with the estimations given within the random-phase approximation (RPA) and the renormalized RPA (RRPA). The analysis of the numerical results shows that the source of the "enhancement" of the two-phonon ESWR compared to the value given by the harmonic limit is in violation of the condition $[\hat{D},[\mathcal{V},\hat{D}]] = 0$ for the interaction part $\mathcal{V}$ of the model Hamiltonian and the operator $\hat{D}$ generating the electromagnetic transition. As a result, the EWSR for the two-phonon excitation exceeds its value in the harmonic limit by a factor of $\sim$ 1.8 at $N \simeq 136$ and $\chi = 0.8$. It is also shown that the energy shift of the two-phonon energy compared to its value in the harmonic limit decreases with increasing the particle number N following a power law, which is more complicated than the simple approximation $\sim N^{-x}$. The RPA and RRPA underestimate the exact EWSR of the two-phonon excitation by about 30% at a given interaction in the region where the RPA is valid.

† Condensed from the article in Phys. Rev. C **65**, 034325 (2002)

References

1) R. Schmidt et al.: Phys. Rev. Lett. **70**, 1767 (1993).
2) K. Boretzky et al.: Phys. Lett. B **384**, 30 (1996).
3) A. Grünschloß et al.: Phys. Rev. C **60**, 051601 (1999).
4) W. J. Llope and P. Braun-Munzinger: Phys. Rev. C **41**, 2644 (1990).
5) T. Aumann, P. F. Bortignon, and H. Emling: Ann. Rev. Nucl. Part. Sci. **48**, 351 (1998).
6) N. Dinh Dang and A. Arima: Phys. Rev. Lett. **80**, 4145 (1998); Nucl. Phys. A **636**, 443 (1998).
7) N. Dinh Dang, K. Tanabe, and A. Arima: Phys. Rev. C **59**, 3128 (1999)
8) N. Dinh Dang, K. Tanabe, and A. Arima: Nucl. Phys. A **675**, 531 (2000).
9) N. Dinh Dang, V. K. Au, and A. Arima: Phys. Rev. Lett. **85**, 1827 (2000).
10) H. J. Lipkin. N. Meshkov, and A. J. Glick: Nucl. Phys. **62**, 188 (1965).

Thermal quasiparticle correlations and continuum coupling in nuclei far from stability†

N. Dinh Dang and A. Arima

[NUCLEAR STRUCTURE, finite-temperature BCS theory, superfluid-normal phase transition]

The contributions of quasiparticle correlations and of continuum coupling to the superfluid properties of neutron-rich Ni isotopes are studied within the modified Bardeen-Cooper-Schriffer (MBCS) approximation at finite temperature.[1] The effect of quasiparticle correlations is included using a secondary Bogoliubov canonical transformation explicitly involving the quasiparticle occupation numbers at the temperature T. The effect of continuum coupling is taken into account via the finite widths of the resonant states.[2]

It is shown that the combined effect of thermal quasiparticle correlations and continuum coupling washes out the sharp superfluid-normal phase transition given by the standard finite-temperature BCS calculations (Fig. 1 (a)). Within the proposed resonant-continuum MBCS approximation the fluctuations of particle number also become more suppressed particularly at high temperature for nuclei closer to the drip line. It is also found within the same approximation that the two-neutron separation energy for ^{84}Ni drops to zero at $T \simeq 0.8$ MeV (Fig. 1 (b)). A slope is seen in the two-neutron separation energy between $A = 78$ and $A = 80$ at $T = 0.3$ MeV due to the large gap of around 3.6 MeV between the $1g_{9/2}$ orbit of the 28–50 shell and the $2d_{5/2}$ orbit of the 50–82 shell when moving from the double-magic nucleus ^{78}Ni to ^{80}Ni. This slope is smoothed out with increasing T. Finally, the self-consistent calculations of quasiparticle occupation numbers within the MBCS and modified quasiparticle random-phase approximations were also carried out. The results show that, within the model Hamiltonian with pairing interaction leading to the Cooper pairs, the quasiparticle occupation number at a finite temperature can be well approximated by the Fermi-Dirac distribution of noninteracting quasiparticles.

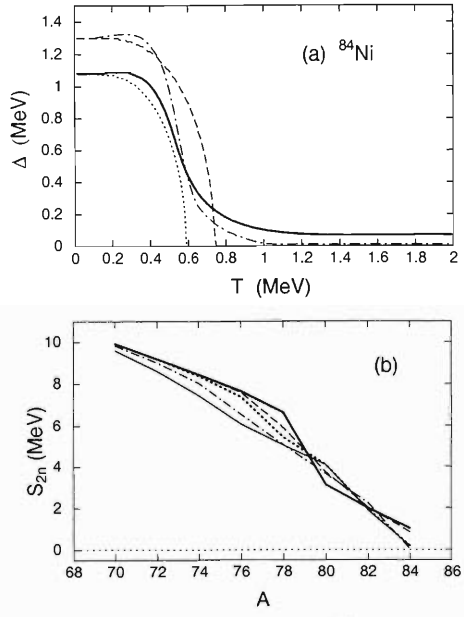

Fig. 1. (a) Neutron pairing gap for ^{84}Ni as a function of temperature. The dashed, dotted, dash-dotted, and solid lines are results given by the quasibound BCS, resonant-continuum BCS, quasibound MBCS, and resonant-continuum MBCS, respectively. (b) Two-neutron separation energies as a function of the mass number A for Ni isotopes obtained within the resonant-continuum MBCS at temperatures $T = 0.3$ (thick solid line), 0.5 (dashed line), 0.6 (dotted line), 0.8 (dash-dotted line), and 1 MeV (thin solid line).

References

1) N. Dinh Dang and V. Zelevinsky: Phys. Rev. C **64**, 064319 (2001).
2) N. Sandulescu, O. Civitarese, and R. J. Liotta: Phys. Rev. C **61**, 044317 (2000).

† Condensed from the article in Phys. Rev. C **67**, 014304 (2003)

Effective field theory of halo nuclei†

U. van Kolck*

Great progress has been made over the last few years in the development of an effective field theory (EFT) of nucleons that is consistent with QCD.[1] Many observable quantities in two- and three-nucleon systems have been successfully calculated, and the four-body problem will be addressed in the near future. The ultimate goal of this program is to describe the hadronic phase of nuclear matter at finite temperatures.

As a preliminary step in the study of more complex nuclei, we have recently constructed an EFT for halo nuclei.[2] Halo nuclei are particularly simple because they contain, in addition to the typical nuclear scale $M \sim 100\,\mathrm{MeV}$ characterizing a core of nucleons, also a low-momentum scale $\aleph \ll M$ associated with the small energy required to remove "halo" nucleons. Physics at a momentum scale $Q \sim \aleph$ can be treated in a systematic Q/M expansion if we consider all possible (contact) interactions among nucleon and core fields.

As an example, we have applied this framework to $n\alpha$ scattering. Although there is no bound state in this system, there exists a resonance in the $p_{3/2}$ channel at $\aleph \sim 30\,\mathrm{MeV}$. An illustration of our results can be found in Fig. 1, where the convergence of the expansion towards data is obvious. We are currently working on extensions to other systems, particularly the Borromean ^{6}He nucleus.[3]

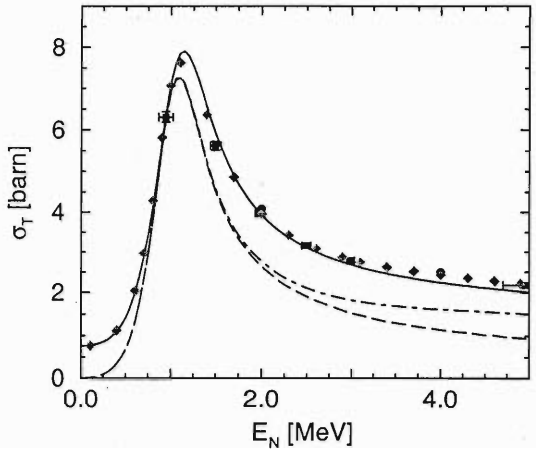

Fig. 1. Total cross section for $n\alpha$ scattering as a function of the lab kinetic energy. The dashed and solid lines are the leading- and next-to-leading-order EFT results, respectively, while the dash-dotted line shows the effects of some higher-order terms. Diamonds and black squares represent data. See Ref. 2 for details.

References

1) P. F. Bedaque and U. van Kolck: Ann. Rev. Nucl. Part. Sci. **52**, 339 (2002).
2) C. A. Bertulani, H. W. Hammer, and U. van Kolck: Nucl. Phys. A **712**, 37 (2002).
3) H. W. Hammer and U. van Kolck: in progress.

† This research was supported in part by a DOE OJI Award and an Alfred P. Sloan Research Fellowship
* University of Arizona, USA

Hydrodynamic evolution near the QCD critical end point and its consequences

C. Nonaka,[*1] M. Asakawa,[*2] and S. Muroya[*3]

[Relativistic heavy-ion collisions, Hydrodynamic models, Critical point phenomena]

Recently, the possibility of the existence of a critical end point (CEP) in the QCD phase diagram has attracted a lot of attention and several experimental signatures have been proposed for it.[1] Since at the critical end point the order of phase transition changes from first to cross over, thermodynamical quantities such as specific heat show a singular behavior. The existence of the critical end point was reported by Asakawa and Yazaki for the first time by NJL model with two flavors.[2] Furthermore, Fodor and Katz found the critical end point in phase diagram by a lattice QCD calculation.[3]

However, there has seen, so far, no quantitative study on the hydrodynamic evolution near CEP. Berdnikov and Rajagopal discussed the growth of the correlation length near the critical end point in heavy-ion collision from the schematic argument.[4] Here we quantitatively evaluate the effect of the critical end point on the observables using the 3D full hydrodynamical model. We construct an equation of state (EOS) that includes CEP. Here we assume that the critical behavior of phase transition from the hadron phase to the quark-gluon plasma phase near CEP belongs to the same universality class as the 3-d Ising model. We then carry out an extensive study of the hydrodynamical evolution of a system that passes near CEP, using the above EOS and a full 3D hydrodynamics code. Since our code is based on Lagrangian hydrodynamics, it is possible to follow the time evolution of each volume element on the T-μ plane and detect the influence of the phase transition on physical quantities.[5] Taking advantage of this feature, we shall in particularly discuss the focusing of the time evolution trajectories on the T-μ plane, caused by the critical behavior of the thermodynamical quantities near CEP and its possible relevance to the HBT puzzle and apparently low kinetic freezeout temperature at RHIC.

Here we construct the EOS which includes the critical end point as follows. First we construct the EOS of the 3-d Ising model as a function of r and h, assuming the singular part of QCD EOS has the same universality class as the 3-d Ising model. Here r is defined as $(T - T_c)/T_c$ and h is the external field. Second, the Ising model is mapped to the T-μ plane. Third, we match this singular part of EOS with a nonsingular part of EOS such as QCD and hadron EOS. The EOS of the 3-d Ising model is given by the parametric representation.[6]

Figure 1 shows the trajectories of the ratio of baryon number density to entropy density (n_B/s) in the r-h plane, which is mapped to the T-μ plane as in the upper figure. We can see the strong focusing effect of the critical end point on them. The trajectories concentrate each other after passing through the critical end point. This means that the fine-tuning of the collision energy is not needed in the survey of the critical end point in heavy-ion collisions. This tendency results from the singular part of EOS near the QCD critical point. Furthermore, this result suggests the uniform final state in the T-μ plane, similar final states in central peripheral regions, the freeze out approximately all together, and a larger correlation than Berdnikov-Rajagopal's estimate. A realistic hydrodynamical calculation with matched EOS is in progress. Using the realistic hydrodynamical calculation we can discuss the deformation effect on critical correlation, modification of EOS due to dynamical phase transition and effects of the critical end point on experimental observables.

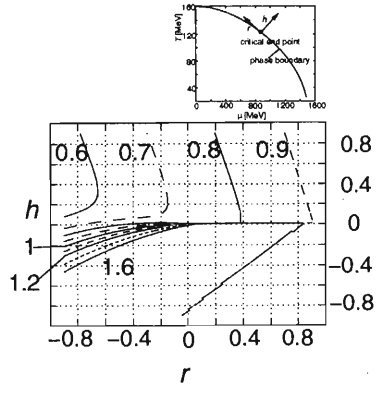

Fig. 1. Trajectories of n_B/s in phase diagram.

*1 Department of Physics, Duke University, USA
*2 Department of Physics, Kyoto University
*3 Tokuyama Women's College

References

1) M. Stephanov, K. Rajagopal, and E. Shuryak: Phys. Rev. Lett. **81**, 4816 (1998).
2) M. Asakawa and K. Yazaki: Nucl. Phys. A **504**, 668 (1989).
3) Z. Fodor and S. D. Katz: JHEP **0203**, 014 (2002).
4) B. Berdnikov and K. Rajagopal: Phys. Rev. D **61**, 105017 (2000).
5) C. Nonaka, E. Honda, and S. Muroya: Eur. Phys. J. C **17**, 663 (2000).
6) R. Guida and J. Zinn-Justin: Nucl. Phys. B **489**, 626 (1997).

Color SU(2) lattice QCD at finite density†

S. Muroya,*1 A. Nakamura,*2 and C. Nonaka*3

[Lattice gauge theory, Finite density QCD]

Lattice QCD is expected to provide nonperturbative information of the hadronic world at finite density as the first-principles calculation.[1] However, numerical study of lattice QCD with chemical potential is extremely difficult, because at finite μ, the fermion matrix does not satisfy the usual condition, $D^\dagger = \gamma_5 D \gamma_5$, and the fermion determinant $\det D$ becomes complex. In order to circumvent the above difficulty, two-color QCD has been investigated.[2–6] We report here, for the first time, a lattice study of hadron propagators together with thermodynamical quantities for finite density SU(2) QCD with Wilson fermions ($N_f = 2$).

Here we employ an algorithm in which the ratio of the determinant is evaluated explicitly in each Metropolis update process. For details of the algorithm, see Refs. 7–10. Using this algorithm, we first investigate the relevant parameter space. For the gauge action, we employ the Iwasaki improved action. We set $\beta = 0.7$ from the measurement of the Polyakov line for $\mu = 0$ and $\kappa = 0.150$ on a 4^4 lattice. At this β value, we measure the Polyakov line, its susceptibility, the gluon energy density and the number density as functions of μ and κ. They increase as μ increases and show deconfinement behavior (Fig. 1).

We calculate correlations of color singlet hadron operators, $M(x) = \bar{\psi}^a_\alpha(x)\Gamma_{\alpha\beta}\psi^a_\beta(x)$ and $B(x) = \epsilon^{ab}\psi^a_\alpha(x)(C\Gamma)_{\alpha\beta}\hat{\tau}\psi^b_\beta(x)$, where Γ is the product of Dirac matrices and $\hat{\tau}$ is a Pauli matrix acting on flavor indices. C is the charge conjugation matrix and a and b are color indices. From hadron propagators we evaluate the chemical potential effect on hadron masses qualitatively, and in Fig. 2 we plot the scalar and vector meson masses together with those of corresponding baryons, as functions of the chemical potential. We find that the vector meson mass drops as μ reaches the critical region. In order to check this unexpected result, we calculate both periodic and antiperiodic spatial boundary conditions and several κ's ($\kappa = 0.150$, 0.160, 0.175); the reduction of vector meson mass is always observed. Indeed, there are several conjectures in the literature about the behavior of vector meson mass in the medium.[10] There have been experiments which suggest that vector meson masses are modified at finite density.[11,12]

We find that the vector meson propagators are strongly modified in large μ regions, indicating the reduction of the mass. This anomalous behavior of the vector meson is observed for the first time in lattice QCD. As an urgent project, we will perform simulations on larger lattices, which will allow us to perform the chiral limit extrapolation to estimate the physical scale. It is interesting to compare our results to those of the effective theory and discuss the behavior of the vector meson mass at finite density in color SU(3).

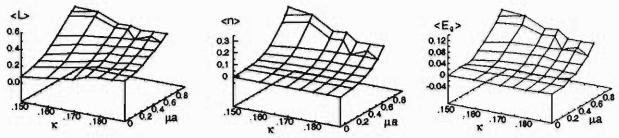

Fig. 1. The Polyakov line $\langle L \rangle$, the number density $\langle n \rangle$ and the gluon energy $\langle E_g \rangle$ as functions of κ and μ. Lattice size is 4^4.

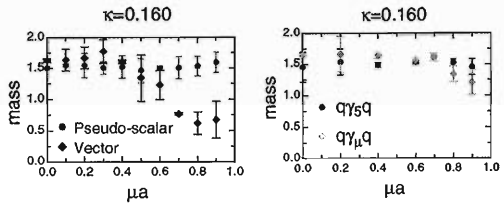

Fig. 2. Meson mass (left) and diquark mass (right) as functions of μ at $\kappa = 0.160$ under the periodic boundary condition.

References

1) P. Hasenfratz and F. Karsch: Phys. Lett. B **125**, 308 (1983).
2) A. Nakamura: Phys. Lett. B **149**, 391 (1984).
3) S. Hands, I. Montvay, S. Morrison, M. Oevers, L. Scorzato, and J. Skullerud: Eur. Phys. J. C **17**, 285 (2000).
4) J. Kogut, D. Toublan, and D. Sinclair: Phys. Lett. B **514**, 77 (2001).
5) J. Kogut, D. Sinclair, S. Hands, and S. Morrison: Phys. Rev. D **64**, 094505 (2001).
6) J. Kogut, D. Toublan, and D. Sinclair: hep-lat/0205019.
7) I. Barbour et al.: J. Comput. Phys. **68**, 227 (1987).
8) A. Nakamura et al.: Comput. Phys. Commun. **51**, 301 (1988).
9) Ph. de Forcrand et al.: Phys. Rev. Lett. **58**, 2011 (1987).
10) G. E. Brown and M. Rho: Phys. Rev. Lett. **66**, 2720 (1991).
11) CERES/NA45 Collaboration, G. Agakichiev et al.: Phys. Lett. B **422**, 405 (1998); R. Rapp and J. Wambach: Adv. Nucl. Phys. **25** (2000).
12) K. Ozawa et al.: Phys. Rev. Lett. **86**, 5019 (2001).

† Condensed from the article in Phys. Lett. B **551**, 305 (2003)

*1 Tokuyama Women's College
*2 Information Media Center, Hiroshima University
*3 Department of Physics, Duke University, USA

Chiral symmetry on light cone

F. Lenz,[*1] M. Thies,[*1] K. Ohta,[*2] and K. Yazaki[*3]

[HADRON PHYSICS, Chiral Symmetry, Light Cone]

The description of the dynamical chiral symmetry breaking on a light cone has several problems due to the reduction of the number of dynamical degrees of freedom and the triviality of the vacuum. We discuss here one of the problems related with the chiral Ward-Takahashi identity (C.W-T.I). In ordinary coordinates, the pion dominance in the C.W-T.I. at $p = 0$ enables us to determine the pion B.S. amplitude in the chiral limit.[1)] We examine the possibility of a similar pion dominance on light cone which will determine the pion light-cone wave function.

The C.W-T.I. on a light cone in the chiral limit can be expressed as

$$ip^\mu F^5_{\mu\alpha\beta}(p,q) = (\sigma_3)_{\alpha\beta}\big(G(q-p) - G(q)\big), \tag{1}$$

where the vertex function, $F^5_{\mu\alpha\beta}$, and the Green's function, G, are defined by

$$F^5_{\mu\alpha\beta}(p,q) \equiv \int d^4x\, d^4y\, e^{-i(px-qy)} \langle 0|T(j^5_\mu(x)\varphi^\dagger_\beta(0)\varphi_\alpha(y))|0\rangle, \tag{2}$$

and

$$\delta_{\alpha\beta}G(q) \equiv \int d^4y\, e^{iqy}\langle 0|T(\varphi_\alpha(y)\varphi^\dagger_\beta(0)|0\rangle. \tag{3}$$

j^5_μ is the axial vector current and φ_α is one of the two "good" components of the fermion (quark) on the light cone. The number of flavors is assumed to be one for simplicity. The l.h.s. of Eq. (1) can be expressed as a sum over mesonic states, *i.e.*,

$$\begin{aligned} &p^\mu F^5_{\mu\alpha\beta}(p,q) \\ &= p^\mu \int d^4x\, d^4y\, e^{-i(px-qy)}\theta(y^+ - x^+)\theta(-x^+) \\ &\quad \times \langle 0|T(\varphi^+_\beta(0)\varphi_\alpha(y))j^5_\mu(x)|0\rangle \\ &= \sum_n \frac{p^\mu}{2p_-}\int dx^+ \int d^4y\, e^{-i(p_+ - p_{n+})x^+ + iqy} \\ &\quad \times \theta(y^+ - x^+)\theta(-x^+) \\ &\quad \times \langle 0|T(\varphi^+_\beta(0)\varphi_\alpha(y))|n(\vec{p})\rangle\langle n(\vec{p})|j^5_\mu(0)|0\rangle, \end{aligned} \tag{4}$$

where $|n(\vec{p})\rangle$ is a mesonic state with mass, m_n, and momentum, $\vec{p}$, and

$$p_{n+} = \frac{\vec{p}_\perp^{\,2} + m_n^2}{2p_-}.$$

Integration over x^+ yields

$$\begin{aligned} &p^\mu F^5_{\mu\alpha\beta}(p,q) \\ &= i\sum_n \frac{p^\mu\langle n(\vec{p})|j^5_\mu(0)|0\rangle}{p^2 - m_n^2 + i\varepsilon}\int d^4y\, e^{iqy} \\ &\quad \times \Big\{\theta(-y^+)\langle 0|\varphi^+_\beta(-y)\varphi_\alpha(0)|n(\vec{p})\rangle e^{-ipy} \\ &\quad - \theta(y^+)\langle 0|\varphi_\alpha(y)\varphi^+_\beta(0)|n(\vec{p})\rangle\Big\}. \end{aligned} \tag{5}$$

We now examine the pion dominance in the sum over n by studying the matrix element, $p^\mu\langle n(\vec{p})|j^5_\mu(0)|0\rangle$. The current conservation, $\partial^\mu j^5_\mu(x) = 0$ implies

$$\langle n(\vec{p})|p^\mu_n j^5_\mu(0)|0\rangle = 0, \tag{6}$$

where $\vec{p_n} = \vec{p}$ and p_{n+} is the same as that given above. We note that, due to the covariance, only pseudo-scalar (0^-) or axial vector (1^+) states can contribute to the sum. For p.s. states, we have

$$\langle n(\vec{p})|j^5_\mu(0)|0\rangle = 2if_n p_{n\mu}. \tag{7}$$

Equation (6) then gives

$$p^\mu_n\langle n(\vec{p})|j^5_\mu(0)|0\rangle = 2iF_n p_n^2 = 2iF_n m_n^2 = 0.$$

Thus $f_n = 0$ unless $m_n = 0$ and only the pion ($m_n = 0$) contributes to the sum.

The pion dominance is thus proved for p.s. states. For a.v. states, however, we have

$$\langle n(\vec{p})|j^5_\mu(0)|0\rangle = 2i(f_n p_{n\mu} + g_n\varepsilon_\mu),$$

where ε_μ is the polarization vector for a.v. states. Equation (6) gives

$$p^\mu_n\langle n(\vec{p})|j^5_\mu(0)|0\rangle = 2i(f_n m_n^2 + g_n p^\mu_n\varepsilon_\mu) = 0.$$

Since $p^\mu_n\varepsilon_\mu = 0$, $f_n = 0$ for $m_n^2 \neq 0$ but $g_n \neq 0$ generally and $p^\mu\varepsilon_\mu \neq 0$ because $p_+ \neq p_{n+}$. Thus a.v. states can contribute to the sum and the pion dominance generally does not hold.

We are now studying a different form of the chiral transformation and the corresponding C.W-T.I. for which we can attain the pion dominance in the chiral limit.

References

1) T. Hatsuda and T. Kunihiro: Phys. Rep. **247**, 221 (1994).

*1 Institute for Theoretical Physics, University of Erlangen, Germany
*2 Institute of Physics, University of Tokyo
*3 College of Arts and Sciences, Tokyo Woman's Christian University

Rate of electron cooling with inclusion of Coulomb logarithm

H. Amemiya, H. Tsutsui,* and T. Katayama

[Electron cooling, Cooling rate, Ion beam, Coulomb logarithm]

In previous papers on electron cooling,[1,2] the Coulomb logarithm was assumed to be constant. In our recent report,[3] the cooling rate was calculated by taking the Coulomb logarithm into account. Rates of energy cooling and broadening, dE_p/dt and dE_t/dt, for an ion moving with a velocity V are given by

$$dE_p/dt = -C\alpha\{(L_o+2)\nabla_\alpha\phi_1(\alpha) + \nabla_\alpha\phi_2(\alpha)\}, \quad (1)$$

$$dE_t/dt = -C(m/M)\{L_o\phi_1(\alpha) + \phi_2(\alpha)\}, \quad (2)$$

where $\alpha = V/s$, $C = 4\pi Q/ms$, $Q = N_e Z^2 e^4/(4\pi\varepsilon_0)^2$, Z: ion charge, $L_o = \ln(6N_D/Z)$, $N_D = (4\pi/3)N_e\lambda^3$, N_e: electron density, λ: Debye length, $1/m = 1/m_e + 1/M$, m_e and M: electron and ion masses, respcetively and $s = (2\kappa T_e/m)^{1/2}$. ϕ_1 and ϕ_2 are respectively

$$\phi_1(\alpha) = -\int \frac{1}{(U/s)} f(\boldsymbol{v})d\boldsymbol{v}; \quad (3a)$$

$$\phi_2(\alpha) = -\int \frac{\ln(U/s)^2}{(U/s)} f(\boldsymbol{v})d\boldsymbol{v}, \quad (3b)$$

where $f(\boldsymbol{v})$ is the electron velocity distribution, and U is the relative velocity between an electron and an ion. ϕ_1 and ϕ_2 have been calculated for isotropic velocity distributions with temperature T_e.

The cooling rate is obtained by integrating (1) and (2) over the ion velocity distribution $F(V)$, which is assumed to be Maxwellian with a temperature T_i, as

$$F(\alpha)d\alpha = 4\xi^3\alpha^2/\sqrt{\pi}\exp(-\xi^2\alpha^2)d\alpha, \quad (4)$$

where $\xi = s_e/s_i$, $s_i = (2\kappa T_i/M)^{1/2}$.

Cooling and heating rates, W_p and W_t, become respectively

$$W_p = CL_o[W_{p1} + (2W_{p1} + W_{p2})/L_o], \quad (5)$$

$$W_t = CL_o(m/M)[W_{t1} + W_{t2}/L_o], \quad (6)$$

where $W_{p1,2}$ and $W_{t1,2}$ are given by putting $x = \alpha\xi$ as

$$W_{p1,2} \equiv (4/\sqrt{\pi})\int_0^\infty \phi_{1,2}(x/\xi)(3x^2 - 2x^4)\exp(-x^2)dx, \quad (7)$$

$$W_{t1,2} = (4/\sqrt{\pi})\int_0^\infty \phi_{1,2}(x/\xi)x^2\exp(-x^2)dx. \quad (8)$$

Substituting $\phi_1 = -\mathrm{Erf}(\alpha)/\alpha$, we obtain previous results.[1,2]

For ϕ_2, we consider two limiting cases.

(1) $\xi < 0.2$: high ion temperature

Putting $\exp(-\alpha^2\xi^2) = 1$ and substituting $\phi_2 \sim -\ln(\alpha^2)/\alpha$, we obtain

$$W_{p2} \simeq \frac{4\xi}{\sqrt{\pi}}\left[\ln(\xi) + \frac{\gamma+2}{2}\right];$$

$$W_{t2} \simeq -\frac{4\xi}{\sqrt{\pi}}\left[\ln(\xi) + \frac{\gamma}{2}\right]. \quad (9)$$

(2) $\xi > 5$: low ion temperature

Taylor expansion $\phi_2 \sim 2/\pi^{1/2}[\gamma - (2+\gamma)\alpha^2/3 + \ldots)$ gives

$$W_{p2} \simeq \frac{1}{\sqrt{\pi}}\left[\frac{2(\gamma+2)}{\xi^2} - \left(\gamma + \frac{8}{3}\right)\frac{3}{\xi^4}\right], \quad (10)$$

$$W_{t2} \simeq \frac{1}{\sqrt{\pi}}\left[-2\gamma + \frac{\gamma+2}{\xi^2} - \left(\gamma + \frac{8}{3}\right)\frac{3}{4\xi^4}\right]. \quad (11)$$

W_{p2} and W_{t2} for medium ξ have been calculated numerically. Figure 1 shows the result.

The overall cooling rate $d(\kappa T_i)/dt$ is given by the sum of W_{p1}, W_{p2}, W_{t1} and W_{t2}. Namely,

$$d\kappa T_i/Cdt = L_o(W_{p1} + \varepsilon W_{t1}) + (2W_{p1} + W_{p2} + \varepsilon W_{t2}), \quad (12)$$

where $\varepsilon = m/M$. The correction term should be taken into account because L_o is not always large ($\sim$5) for heavy ions such as ^{238}U ($Z = 92$). Cooling time is obtained by the integration of (12).[4]

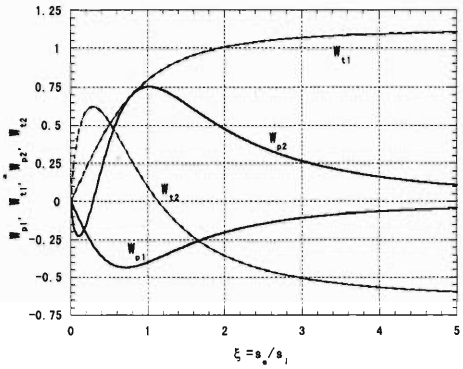

Fig. 1. Cooling rates W_{p1}, W_{p2} (solid curves) and heating rates W_{t1}, W_{t2} (dotted curves) *vs.* $\xi = s_e/s_i$.

* Sumitomo Heavy Industries, Ltd.

References

1) H. Poth: Phys. Rep. **196**, 135 (1990).
2) I. N. Meshkov: Phys. Part. Nucl. **25**, 631 (1994).
3) H. Amemiya, T. Tanabe, and T. Katayama: RIKEN Accel. Prog. Rep. **35**, 38 (2002).
4) H. Amemiya, T. Tsutsui, and T. Katayama: RIKEN Accel. Prog. Rep. **36**, 46 (2003).

Time of electron cooling with inclusion of Coulomb logarithm

H. Amemiya, H. Tsutsui,* and T. Katayama

[Electron cooling, Cooling time, Ion beam, Coulomb logarithm]

According to the result,[1] the temporal change of the cooling of an ion beam with a temperature T_i is given by using the characteristic time $t_o = (\kappa T_e/CL_o)(M/m)$ as

$$\frac{\mathrm{d}\xi^{-2}}{\mathrm{d}\tau} = W_{p1} + \varepsilon W_{t1} + \frac{2W_{p1} + W_{p2} + \varepsilon W_{t2}}{L_o}, \qquad (1)$$

where $\tau = t/t_o$, $\varepsilon = m/M$, $\xi^{-2} = (T_i/T_e)/(m/M)$, and $W_{p1,2}$ and $W_{t1,2}$ are the cooling and heating rates.

The cooling rate is calculated as follows.

(1) small ξ ($\xi < 0.2$): high T_i

Substituting W_{p1}, W_{p2} and W_{t1}, W_{t2} from the foregoing result[1] into Eq. (1), we obtain

$$\tau = \frac{\sqrt{\pi}}{(1-\varepsilon)} \int_{\xi_o}^{\xi} \frac{\mathrm{d}\xi}{\xi^4[1 + (\gamma + 2\ln\xi)]}. \qquad (2)$$

The integration gives by defining $z = 3\ln(\xi) - 3(L_o - \gamma)/2$

$$\tau = H(\xi,\varepsilon) - H(\xi_o,\varepsilon), \qquad (3)$$

$$H(\xi,\varepsilon) = \frac{\sqrt{\pi}L_o}{2(1-\varepsilon)} \exp\left[-\frac{3(L_o-\gamma)}{2}\right][-\mathrm{Ei}(-z)], \qquad (4)$$

where $\mathrm{Ei}(-z)$ is the exponential integral.

When $L_o \gg 1$ and $\varepsilon = 0$, Eq. (4) is reduced to

$$H_o(\xi,0) = \frac{\sqrt{\pi}}{2}\left\{-\left(\frac{2}{3\xi^3} + \frac{8}{3\xi}\right)\sqrt{\xi^2+1} + 2\sinh^{-1}(\xi)\right\}. \qquad (5)$$

(2) large ξ ($\xi > 5$): low T_i

Using approximate forms of W_{p1}, W_{t1} and W_{p2}, W_{t2} from (9), (11) in Ref. 1, we obtain

$$\tau = \left(\sqrt{\pi}/D\right)\int_{\xi_o}^{\xi} \xi(-a\xi^4 + \xi^2 + b)^{-1}\mathrm{d}\xi, \qquad (6)$$

$$a = \varepsilon(1 - \gamma/L_o)/D, \quad b = B/D,$$

$$D = 1 + \varepsilon/2 - \gamma/L_o,$$

$$B = -3(1 + \varepsilon/4)/2 + (1 + 3\gamma/2)/L_o, \qquad (7)$$

where $\varepsilon/L_o \ll 1$ is assumed. Denoting $\eta = \xi^2$, we obtain

$$H(\xi) = \frac{\sqrt{\pi}}{2D}\int^{\eta}(-a\eta^2 + \eta + b)^{-1}\mathrm{d}\eta. \qquad (8)$$

For the case of $L_o \gg 1$, we have $a \sim \varepsilon$, $D \sim 1$. Hence,

$$H(\xi) \simeq \frac{\sqrt{\pi}}{2}\left\{\ln(\xi^2) + \ln\frac{1}{1-\varepsilon\xi^2}\right\}; \qquad (9)$$

which corresponds to the previous results.[2,3] The cooling time becomes longer near the thermal equilibrium, $\varepsilon_1\xi = 1$ or $T_i = T_e$. Equation (1) has been numerically calculated for several values of L_o.

Figure 1 (a) and (b) shows $H(\xi)$ *vs.* ξ at $H < 0$ and $H > 0$ for some values of L_o. The dependence of $H(\xi)$ on L_o indicates that the effect of Coulomb logarithm or ϕ_2 is important for small L_o. For large L_o, Eq. (9) holds, where only W_{p1} and W_{t1} are important.[2,3]

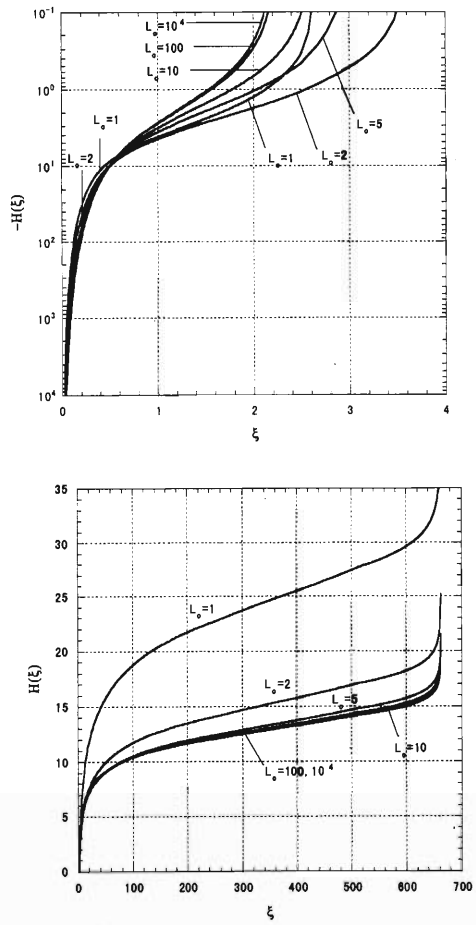

Fig. 1. Electron cooling function $H(\xi)$ *vs.* ξ ($= s_e/s_i$). (a) $H < 0$, (b) $H > 0$.

* Sumitomo Heavy Industries, Ltd.

References

1) H. Amemiya, T. Tsutsui, and T. Katayama: RIKEN Accel. Prog. Rep. **36**, 45 (2003).
2) H. Poth: Phys. Rep. **196**, 135 (1990).
3) I. N. Meshkov: Phys. Part. Nucl. **25**, 631 (1994).

New mathematical tools for electron cooling

H. Amemiya, H. Tsutsui,* and T. Katayama

[Electron cooling, Cooling rate, Logarithmic-elliptic integral, Ion beam, Coulomb logarithm]

In a previous report,[1)] the electron-cooling rate for ion beams with an isotropic electron velocity distribution $f(\boldsymbol{v})$ was described using potentials ϕ_1 and ϕ_2 by taking the Coulomb logarithm into account, where notations are given elsewhere.[1,2)] The Maxwellian and two temperature distributions have been assumed for $f(\boldsymbol{v})$ depending on low and high energy beams. In the latter, we introduce the velocity anisotropy as η.

ϕ_1 and ϕ_2 are triple integrals over axial, radial and angular directions. Using elliptic and logarithmic- elliptic integrals for the angular component, they are reduced to single integrals for isotropic $f(\boldsymbol{v})$. They remain double integrals for a flat $f(\boldsymbol{v})$ but can be reduced to single integrals for $f(\boldsymbol{v})$ of completely flat ($\eta = 0$) and even for $f(\boldsymbol{v})$ with a small η if the Taylor expansion is made with η. Then, ϕ_1 and ϕ_2 as well as the gradients and derivatives can be expressed by the combination of the following functions.

1. Functions related to complete elliptic integrals of first and second kinds, $K(k)$ and $E(k)$, defined as

$$K_{2J-1}(k) \equiv \int_0^{\pi/2} \frac{\mathrm{d}\psi}{(1-k^2\sin^2\psi)^{(2J-1)/2}}; \quad J = 0, 1, 2, \ldots, \tag{1}$$

$$KS_{2J+1}(k) \equiv \int_0^{\pi/2} \frac{\sin^2\psi \mathrm{d}\psi}{(1-k^2\sin^2\psi)^{(2J+1)/2}} = \frac{K_{2J+1} - K_{2J-1}}{k^2}, \tag{2}$$

where $K_1 = K$ and $K_{-1} = E$. Polynomial expressions of K and E are already known.[3)] It is possible to calculate K_{2J+1} and KS_{2J+1} from K and E.

2. Logarithmic-elliptic integrals and related functions

$$M(k) \equiv \int_0^{\pi/2} \ln(1-k^2\sin^2\psi)\cdot\sqrt{1-k^2\sin^2\psi}\mathrm{d}\psi \tag{3}$$

$$\simeq \left[\ln(4) - 2 + a_1 {k_c}^2 + a_2 {k_c}^4 + a_3 {k_c}^6 + a_4 {k_c}^8\right] + \left[b_1 {k_c}^2 + b_2 {k_c}^4 + b_3 {k_c}^6\right]\ln({k_c}^2),$$

$a_1 = 4.0848,\ a_2 = 6.6498,\ a_3 = -8.7378,$

$a_4 = -1.3833;\ {k_c}^2 = 1 - k^2,$

$b_1 = 1.3664,\ b_2 = 7.313,\ b_3 = 6.4623.$

$$L_{2J-1}(k) \equiv \int_0^{\pi/2} \frac{\ln(1-k^2\sin^2\psi)\mathrm{d}\psi}{(1-k^2\sin^2\psi)^{(2J-1)/2}}, \quad J = 0, 1, 2, \ldots, \tag{4}$$

where $L_1 = L$ and $L_{-1} = M$. L is expressed by

$$L \simeq \left[a_1 {k_c}^2 + a_2 {k_c}^4 + a_3 {k_c}^6 + a_4 {k_c}^8\right] + \left[\ln(2) + b_1 {k_c}^2\right]\ln({k_c}^2) + \left[-\frac{1}{4} + b_2 {k_c}^2\right]\left[\ln({k_c}^2)\right]^2,$$

$a_1 = -0.082545,\ a_2 = 0.0967808,\ a_3 = -0.0168824,$

$a_4 = 0.0026424,\ b_1 = 0.021328,\ b_2 = -0.064928,$

For $k \leq 0.1$, Taylor expansions are more accurate. L_{2J+1} can be expressed by K, E, M and L using

$$L_{2J+1} = LS_{2J+1} + \frac{2J-2}{2J-1}L_{2J-1} - \frac{2J-3}{2J-1}LS_{2J-1} + \frac{2k^2}{2J-1}\cdot\frac{2KS_{2J-1} - K_{2J-1}}{(2J-1)k^2}, \tag{5}$$

$$LS_{2J+1}(k) \equiv \int_0^{\pi/2} \frac{\sin^2\psi\ln(1-k^2\sin^2\psi)\mathrm{d}\psi}{(1-k^2\sin^2\psi)^{(2J+1)/2}} = \frac{L_{2J+1} - L_{2J-1}}{k^2}. \tag{6}$$

Figure 1 shows functions M, L, L_3, L_5, L_7 *vs.* k^2. All the functions start with 0 at $k = 0$ and tend to infinity at $k = 1$ except M which is $\ln(4) - 2$.

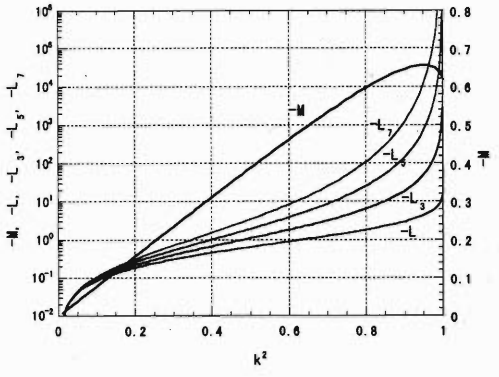

Fig. 1. Functions M, L, L_3, L_5, L_7 *vs.* k^2.

References

1) H. Amemiya, T. Tanabe, and T. Katayama: RIKEN Accel. Prog. Rep. **35**, 38 (2002).
2) H. Amemiya, T. Tsutsui, and T. Katayama: RIKEN Accel. Prog. Rep. **36**, 45 (2003); RIKEN Accel. Prog. Rep. **36**, 46 (2003).
3) M. Abramovitz and I. A. Stegun: *Handbook of Mathematical Functions with Formulas, Graphs and Mathematical Tables*, 9th ed. (Dover Publications, New York, 1970).

* Sumitomo Heavy Industries, Ltd.

Polarized solid proton target for the RI beam experiments

M. Hatano,[*1] T. Wakui,[*2] H. Sakai,[*1,*2] T. Uesaka,[*2] and A. Tamii[*1]

[polarized proton target]

We are developing a new spin polarized solid proton target which is applicable in a low magnetic field and at a high temperature.[1)] The target system is mainly for the RI-beam experiments, for example, $\vec{p}$+ unstable nuclei elastic scattering under the inverse kinematics condition. In a conventional polarized proton target system, protons are polarized by means of dynamic nuclear polarization (DNP).[2)] In the DNP method, thermal electron polarization is transferred to the proton polarization. Therefore, to obtain high proton polarization, a high magnetic field of higher than 1 T and a very low temperature of lower than 1 K are required. In our case, to investigate forward scattering at the center of the mass system, detection of low-energy protons emitted at nearly 90° in the laboratory system is necessary. In this respect, the polarized proton target which does not require a high magnetic field and/or a cryostat for the low temperature around the target is suited for such an experiment.

As a target material we use a highly purified single crystal of naphthalene ($C_{10}H_8$) doped with 0.01 mol% pentacene ($C_{22}H_{14}$). Protons in the crystal are polarized in a magnetic field of 8.5×10^{-2} T and at a temperature of 90 K by means of the pulsed DNP technique.[3)] In this method, an electron alignment is induced in the lowest triplet state of pentacene molecule through optical pumping. Subsequent sweeping of a magnetic field under microwave irradiation transfers the alignment to proton polarization. The ideal maximum value of the proton polarization is 73%.

Until now, test experiments for the proton polarization have been carried out by using a small sized prototype system.[1,4)] Recently, the development of ion beam injection experiments has been started. In this paper the present status of the development and a test experiment with α beam of 80 MeV/A are reported.

A large-sized C-type magnet is introduced for the external magnetic field of 8.5×10^{-2} T. The pole gap is designed to be 100 mm for a scattering chamber which is placed in the gap. The field uniformity is required to be smaller than the internal magnetic field of the crystal (1×10^{-3} T). To fulfill the requirement, the diameter of the pole is designed to be 220 mm. The measured field uniformity around the center region of $20 \times 20 \times 20\,\mathrm{mm}^3$ is 3.4×10^{-4} T at 0.3 T.

Figure 1 shows a schematic view of the scattering chamber. The target crystal is placed inside the cooling chamber and is maintained at a temperature lower than 90 K by cold N_2 gas flow. The cooling chamber is housed inside the vacuum chamber and is thermally isolated from the environment at a room temperature. The flow of the cold N_2 gas is controlled with a heater placed inside the liquid N_2 tank. Both of the chambers have glass ports for the laser irradiation and windows of kapton films for incident and outgoing particles. Around the target, devices for the pulsed DNP are mounted. They are a microwave resonator, a field modulation coil, and an NMR coil. As a microwave resonator a cylindrical loop-gap resonator (LGR)[5)] is introduced instead of a microwave cavity to reduce materials in the path of the low-energy recoiled protons. The LGR is made of a coupling coil and 25-μm-thick Teflon coated on both sides with 4.4 μm copper. The resonance frequency is 3.2 GHz which corresponds to an electron spin resonance of a pentacene molecule in 8.5×10^{-2} T. The LGR is inductively coupled to the microwave circuit through a coupling coil. The coupling is adjusted by moving the coil. For field modulation, a Helmholtz coil (50 mm ϕ) is used. It produces a $\pm 3.0 \times 10^{-3}$ T field sweep around the target. As shown in Fig. 1, an ion beam is incident on the target through a kapton film. Recoiled protons pass out of the scattering chamber through the LGR and two kapton films. Scattered particles pass out through the two kapton films. The pulsed laser system is reported in detail in reference.[4)]

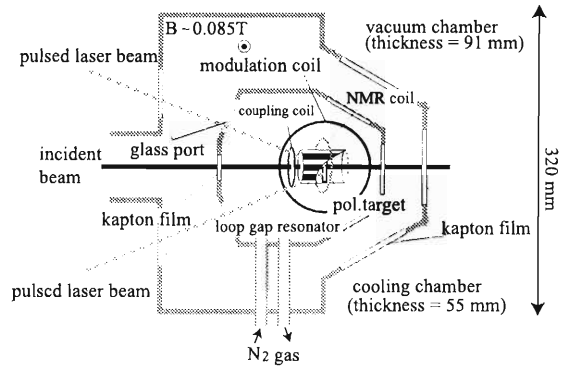

Fig. 1. Schematic view of scattering chamber.

We have tested a small-sized LGR (8 mm ϕ) with a small-sized crystal ($4 \times 4\,\mathrm{mm}^2$, 1 mm thickness). We have succeeded in obtaining an enhancement of the proton polarization (Fig. 2). The laser power was 8 W in CW-mode. The relaxation time of the crystal was 17.9 hours.

Although we have observed the enhancement of the

*1 Department of Physics, University of Tokyo
*2 Center for Nuclear Study, Graduate School of Science, University of Tokyo

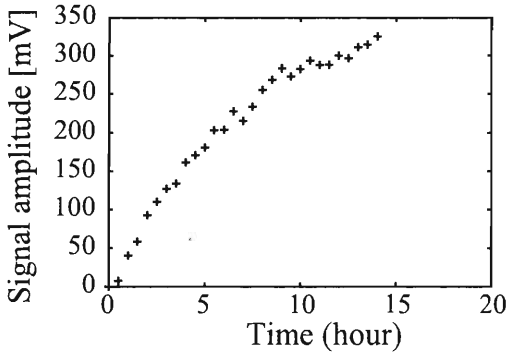

Fig. 2. Build up of the proton polarization.

proton polarization, there remain several unsolved issues: an absolute value of the proton polarization cannot be estimated, because a thermal NMR signal cannot be observed by the present NMR coil. The absolute value will be calibrated after an improvement of the NMR coil sensitivity by measuring the thermal NMR signal. In the present condition, the NMR coil is fixed around the LGR. To improve the sensitivity of the NMR coil, we should place the coil inside the LGR and make the diameter of the coil almost the same as that of a target crystal. However, if the NMR coil is inside the LGR, the LGR cannot be coupled to the coupling coil. (Even if the NMR coil is placed outside the LGR, because the microwave radiates to the surrounding metals, some of the microwave power breaks out through the LGR.) Another problem is that the resonance frequency changes about 1% when the LGR is cooled from room temperature to 90 K. In the present condition, since the LGR and the coupling coil are fixed, the coupling cannot be readjusted at a low temperature. To overcome these problems, we will make the NMR coil and the coupling coil adjustable.

The test experiment using an α beam of 80 MeV/A for background estimation was carried out by using a small-sized crystal without proton polarization. One can reduce most of the background which mainly comes from carbon in the target by detecting the scattered α nucleus and the recoiled proton in coincidence. The beam intensity was 10^5 particles/sec, the same as in the main RI-beam experiments. Figure 3 shows the schematic view of the experimental setup. For detection of a recoil proton, we used a plastic scintillator with a thickness of 55 mm (5.7 g/cm^2). To select the recoiled proton of scattering angle 49° (80° in the center of mass system), we used a brass collimater. For detection of the α particle, we used two layers of plastic scintillators with thickness of 30 mm (3.1 g/cm^2). The data analysis is now in progress.

The first experiments with the RI-beam will be carried out in 2003. We are planning an analyzing power measurement in $\vec{p}+{}^6$He, 71 MeV/A elastic scattering. This experiment aims at determining the spin-orbit potential between proton and ^{6}He.

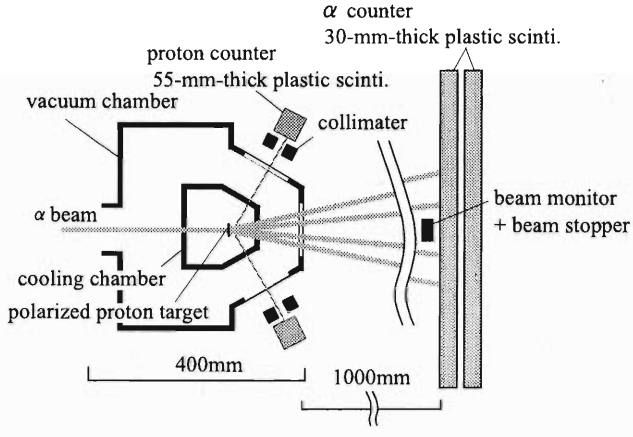

Fig. 3. Experimental setup for the test experiment (see text for details).

References

1) T. Wakui et al.: RIKEN Accel. Prog. Rep. **35**, 149 (2002).
2) A. Abragam: *The Principles of Nuclear Magnetism* (Clarendon Press, Oxford, 1961).
3) M. Iinuma et al.: Phys. Rev. Lett. **84**, 171 (2000).
4) T. Wakui et al.: RIKEN Accel. Prog. Rep. **36**, 171 (2003).
5) B. T. Ghim et al.: J. Magn. Reson. A **102**, 72 (1996).

Three-body dN interaction in the analysis of the $^{12}C(\vec{d}, d')$ reaction at 270 MeV†

Y. Satou,[*1] S. Ishida,[*2] H. Sakai,[*3] H. Okamura,[*4] N. Sakamoto, H. Otsu,[*5] T. Uesaka,[*4] A. Tamii,[*3] T. Wakasa,[*6] T. Ohnishi, K. Sekiguchi, K. Yako,[*3] K. Suda,[*4] M. Hatano,[*3] H. Kato,[*3] Y. Maeda,[*3] J. Nishikawa,[*4] T. Ichihara, T. Niizeki,[*7] H. Kamada,[*8] W. Glöckle,[*8] and H. Witała[*9]

[(d, d') reaction, DWIA analysis, Three-nucleon t-matrix]

Light-ion-induced inelastic scattering at bombarding energies above 100 MeV/nucleon is an attractive probe for application to nuclear structure due to the simple reaction mechanism. In such an energy domain, the reaction proceeds predominantly through a single step, and the distorted-wave impulse approximation (DWIA) gives a reasonable starting point for the theoretical description of data. In the IA for the (p, p') reaction, the effective interaction between a projectile nucleon and a target nucleon is taken to be the free nucleon-nucleon (NN) t-matrix. For the (d, d') reaction, the situation is not as simple as that for the nucleon case because the structure of the deuteron must be considered. Recently, the Orsay group developed a DWIA model[1] using the double-folding method to calculate the deuteron inelastic scattering at intermediate energies. In previous applications,[1,2] the deuteron-nucleus (dA) transition matrix was calculated, first by folding the on-shell NN t-matrix with the deuteron wave function to yield the deuteron-nucleon (dN) t-matrix, and then by folding it with the target transition density. In a comparison between model predictions and data, however, it was found that the d+N elastic differential cross sections were overestimated by the first folding, leading to too large dA cross sections by factors of 1.2–2.0.[2]

Present day state-of-the-art three-nucleon ($3N$) Faddeev calculations have made it possible to describe $3N$ scattering processes at intermediate energies with a reliable accuracy using modern NN potentials.[3] Since the dN t-matrix obtained from the rigorous $3N$ Faddeev calculations helps reduce uncertainties involved in the folding dN t-matrix, it is quite conceivable that the Faddeev amplitude, when used as an effective interaction, provides a more precise DWIA description of the (d, d') reaction. Such rigorous $3N$ amplitudes have recently been successfully employed in a PWIA model for interpreting analyzing power data of the $^3He(\vec{d}, p)^4He$ reaction.[4] They would also facilitate the analysis of deuteron spin-flip data taken in search for isoscalar single- and double-spin-flip excitations.[5]

We have measured the cross sections and analyzing powers A_y and A_{yy} for the elastic and inelastic scattering of deuterons from the 0^+ (g.s.), 2^+ (4.44 MeV), 3^- (9.64 MeV), 1^+ (12.71 MeV), and 2^- (18.3 MeV) states in ^{12}C at an incident energy of 270 MeV. The data are compared with microscopic distorted-wave impulse approximation calculations where the projectile-nucleon effective interaction is determined from the three-nucleon t-matrix given by rigorous Faddeev calculations presently available at intermediate energies. It is found that the agreement between theory and data compares well with that for the (p, p') reactions at comparable incident energies/nucleon.

References

1) J. Van de Wiele, A. Willis, and M. Morlet: Nucl. Phys. A **588**, 829 (1995).
2) F. T. Baker et al.: Phys. Rep. **289**, 235 (1997).
3) W. Glöckle, H. Witała, D. Hüber, H. Kamada, and J. Golak: Phys. Rep. **274**, 107 (1996).
4) H. Kamada et al.: Prog. Theor. Phys. **104**, 703 (2000).
5) Y. Satou et al.: Phys. Lett. B **521**, 153 (2001).

† Condensed from the article in Phys. Lett. B **549**, 307 (2002)

*1 Department of Physics, Tokyo Institute of Technology
*2 Soei International Patent Firm
*3 Department of Physics, University of Tokyo
*4 Department of Physics, Saitama University
*5 Department of Physics, Tohoku University
*6 Research Center for Nuclear Physics, Osaka University
*7 Faculty of Home Economics, Tokyo Kasei University
*8 Institut für Theoretische Physik II, Ruhr-Universität, Germany
*9 Institute of Physics, Jagiellonian University, Poland

Model-independent spin-parity determination by the $(d, {}^2\mathrm{He})$ reaction and possible evidence for a 0^- state in ^{12}B†

H. Okamura,[*1] T. Uesaka,[*2] K. Suda,[*1] H. Kumasaka,[*1] R. Suzuki,[*1] A. Tamii,[*3] N. Sakamoto, and H. Sakai[*3]

[NUCLEAR REACTIONS, $(d, {}^2\mathrm{He})$, $E_d = 270$ MeV, spin-flip dipole]

A method of model-independent spin-parity determination is proposed for the $(d, {}^2\mathrm{He})$ reaction by using the tensor analyzing power A_{zz} at $\theta = 0°$, which is expected to have extreme values for some states solely by parity-conservation:

$$A_{zz}(0°) = \begin{cases} -2, & \text{if } I^\pi = 0^-, \\ +1, & \text{if } \pi = (-)^I \text{ (natural parity).} \end{cases}$$

This method has been applied to the ^{12}C$(d, {}^2\mathrm{He})^{12}$B reaction at $E_d = 270$ MeV. The polarization axis (Z) was aligned parallel to the beam axis (z) in order to enhance the sensitivity of the cross section to A_{zz}. Figure 1 (a) shows ^{12}B excitation-energy spectra obtained by using the beams having positive and negative tensor polarizations (p_{ZZ}). A negative large value of A_{zz} is observed at $E_x = 9.3$ MeV (Fig. 1 (c)), suggesting large contributions from the 0^- states. Figure 2 shows angular distributions of A_{zz} for this peak, as well as that for the bump at $E_x = 7.5$ MeV and the ground state, compared with a theoretical calculation. A possible indication of a 0^- state in ^{12}B has been found for the first time at $E_x = 9.3$ MeV. Also the bump at $E_x = 7.5$ MeV appears to have more 2^- strength than 1^- strength at $\theta \sim 0°$, supporting our reported results for a previous study.[1)]

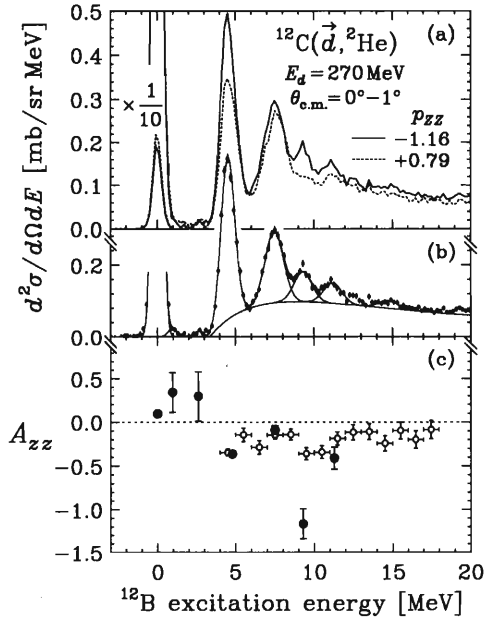

Fig. 1. Double differential cross sections at $\theta_{c.m.} = 0°$–1° plotted as a function of ^{12}B excitation energy (a), a result of peak-fitting for the spectrum with $p_{ZZ} = -1.16$ (b), and the corresponding A_{zz} spectra (c). A_{zz} for each peak obtained by the fitting is shown by the closed circle, while A_{zz} for the continuum binned in 1 MeV is shown by open circles.

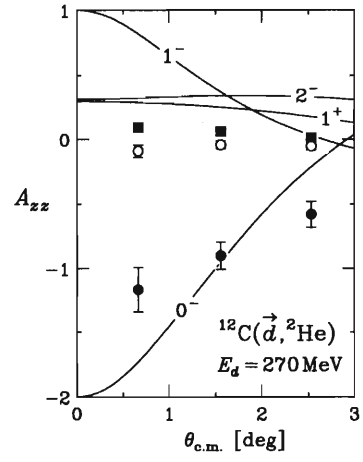

Fig. 2. Angular distributions of A_{zz} for the ground (closed square), $E_x = 7.5$ MeV (open circle), and $E_x = 9.3$ MeV (closed circle) states. Results of calculation[2)] for Gamow-Teller (1_1^+) and spin-dipole $(0_2^-, 1_1^-$, and $2_2^-)$ states are also shown by solid curves.

References

1) H. Okamura et al.: Phys. Lett. B **345**, 1 (1995).
2) H. Okamura: Phys. Rev. C **60**, 064602 (1999).

† Condensed from the article in Phys. Rev. C **66**, 054602 (2002)

*1 Department of Physics, Saitama University
*2 Center for Nuclear Study, University of Tokyo
*3 Department of Physics, University of Tokyo

Determination of the sub-threshold state contribution in $^{13}C(\alpha,n)^{16}O$, the main neutron-source reaction of the s-process

S. Kubono,[*1] K. Abe,[*2] S. Kato,[*2] T. Teranishi,[*1] M. Kurokawa,[*1]
X. Liu,[*1] N. Imai,[*3] K. Kumagai,[*4] P. Strasser, M. H. Tanaka,[*5]
Y. Fuchi,[*5] C. S. Lee,[*6] Y. K. Kwon,[*6] L. Lee,[*6] J. H. Ha,[*6] and Y. K. Kim[*6]

[direct alpha-transfer reaction, nucleosynthesis, s-process]

Roughly a half of heavy elements in the universe is considered to have been produced through a process, called the slow (s) - process,[1,2] which basically includes neutron-induced capture reactions and beta decays in relatively quiescent sites in the universe. The neutron source for this process is not well understood yet, and is one of the crucial issues in nuclear astrophysics. In low-mass stars at the asymptotic giant branch (AGB), the $^{13}C(\alpha,n)^{16}O$ reaction is considered to be the main source of neutron production for the s-process[3–6] at low temperatures, typically $T = 10^8$ K.

The reaction rate of the $^{13}C(\alpha,n)^{16}O$ reaction, however, has not been not determined at this temperature region. The cross section was measured only down to 270 keV, but no data below. The lowest energy data suggests a rapid increase of the cross sections toward zero energy,[7–10] due to a contribution of the sub-threshold state at 6.356 MeV, 3 keV below the α threshold in ^{17}O.

The α width Γ_α is related to the α-spectroscopic factor S_α by $\Gamma_\alpha = 3\hbar^2 k_\alpha/(\mu R) P_l S_\alpha$, where μ is the reduced mass, $R = r_0(A_1^{1/3} + A_2^{1/3})$, and P_l the penetrability. Then, the cross section of the $^{13}C(\alpha,n)^{16}O$ reaction through the tail of the sub-threshold resonance can be calculated using the Breit-Wigner single-level formula.[11]

Since the total width of the sub-threshold state at 6.356-MeV is known to be 124 ± 12 keV from the $^{16}O(n,n)$ resonance study,[12] the most critical parameter that determines the reaction rate of the stellar reaction $^{13}C(\alpha,n)$ is the α-width. Thus, the sub-threshold contribution to the reaction rate can be determined using the α-spectroscopic factor S_α of the state. Most s-process models use about $S_\alpha = 0.3$–0.7,[3–6] which implies that the state should have a well developed α-cluster structure. Therefore, it is of critical importance to check experimentally the property of the subthreshold state in order to study the reaction rate of $^{13}C(\alpha,n)$ at low energies.

Thus, we have decided to determine the S_α of the 6.356-MeV state in ^{17}O by the $^{13}C(^6Li,d)^{17}O$ reaction.

*1 Center for Nuclear Study, University of Tokyo
*2 Yamagata University
*3 University of Tokyo
*4 Tohoku University
*5 Institute of Particle and Nuclear Studies, High-Energy Accelerator Research Organization (KEK)
*6 Chung-Ang University, Korea

Isotopically enriched ^{13}C self-supporting targets (enriched to about 99.9%) with thicknesses of 140, 300 and 520 μg/cm^2 and a mylar foil of 3 μm were bombarded with a 60-MeV ^6Li beam from the AVF cyclotron. The reaction products were momentum analyzed by a QDD type magnetic spectrograph.[13] and detected by a position-sensitive gas proportional counter[14] together with a plastic scintillator on the focal plane. Particle identification was made unambiguously using ΔE, E, and TOF. The overall energy resolution was about 170 keV with an aperture of 5 msr for the spectrograph.

Figure 1 shows a typical deuteron spectrum from the $^{13}C(^6Li,d)^{17}O$ reaction obtained at 30°. The peak for the 6.356 MeV state in ^{17}O was separated at large scattering angles $\theta \geq 25°$, but it was not separated at smaller angles. The contribution from the carbon contamination in the target was subtracted at small angles by measuring the cross sections of $^{12}C(^6Li,d)^{16}O$ (6.917 MeV) with the same setup using the mylar foil mentioned above. The amount of subtraction was determined with the yield ratio to the transition to the ground state in ^{16}O which was clearly separated at all angles. The differential cross sections for elastic scattering of ^{13}C + ^6Li were also measured to determine the amount of the contamination as well as to check the optical potential parameters for the incident channel.

The uncertainties in the experimental data are

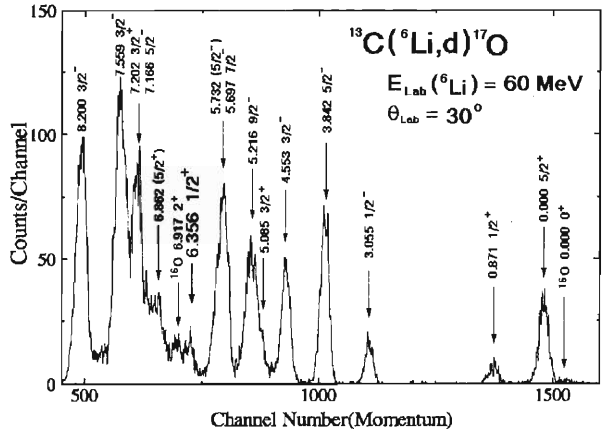

Fig. 1. Momentum spectrum of deuterons from the $^{13}C(^6Li,d)^{17}O$ reaction, measured at $\Theta_{Lab} = 30°$ with a 60-MeV ^6Li beam.

mainly due to the subtraction of the contamination contributions to the 6.356-MeV state. The transition to the 0,871-MeV $1/2^+$ state has a similar shape because it has the same transferred angular momentum of $L = 1$. The exact finite-range DWBA calculations have been made by a computer code, TWOFNR,[15] where the optical potential parameter sets were obtained from fitting the elastic scattering data for the incident channel, and the ones for the exit channel were taken from Refs. 16 and 17. The bound-state potential parameters were set to be $r_0 = 1.lpq - P25$ fm and $a = 0.65$ fm, and the depth was searched to reproduce the separation energy as is often adopted.

Since DWBA calculations for α transfer reactions usually explain well relative spectroscopic factors, we adopt here a normalization factor.[18] A normalization factor has been obtained so that the DWBA cross sections for the transition to the 3.055-MeV $1/2^-$ state, which is known to be a good α cluster state, has $S_\alpha = 0.25$.[19] The normalized α-spectroscopic factor for the 6.356-MeV state is $S_\alpha = 0.011$. This S_α value changes about 5% or less due to a different combination of the optical potential sets. Here, the optical potential sets SET1 and SET2 were chosen since the DWBA calculation gives an overall fit to the data. This S_α-factor is much smaller than predicted in a recent compilation of reaction rates, where about $S_\alpha = 0.7$ was used.[8,9] From the present experimental result, it can be concluded that the 6.356-MeV state is not a state that has a large S_α amplitude, and thus would not enhance so much the astrophysical S-factor at the Gamow energy region, which is marked in Fig. 2. Note that even if the measured S_α is as large as 1.0 for the 3.055 MeV state, the normalized S_α for the 6.356 MeV state can be 0.044 at most. Thus, we can conclude that the S_α for the 6.356 MeV state is much smaller than predicted before.

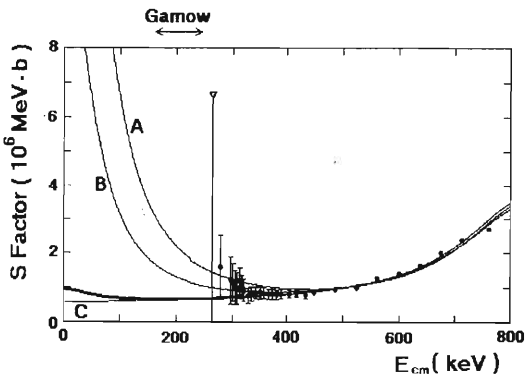

Fig. 2. The astrophysical S-factors of the $^{13}C(\alpha,n)^{16}O$ stellar reaction together with the experimental data taken from Ref. 3. The thick solid line is the result derived here, including the sub-threshold resonance contribution. The curves A, B, and C are the results with $S_\alpha = 0.7$, 0.3 and 0.0, respectively. See text for details.

By taking the experimental value of $\Gamma_{tot} = 124$ keV, the astrophysical S-factor of the $^{13}C(\alpha,n)^{16}O$ reaction was calculated. Figure 2 displays the energy dependence of the S-factor, which is the sum of the non-resonant contribution and the tail contribution of the sub-threshold state.

The present reaction rate is much smaller than the one in Refs. 8 and 9 which is shown by the line A in Fig. 2, and that suggested in Ref. 3 by the line B. The present rate is rather similar, at the Gamow window region, to the old rate that did not include the sub-threshold state contribution.[20]

In summary, it is found that there would be no such large enhancement of neutron productions due to the sub-threshold state at 6.356 MeV in ^{17}O at low temperatures for the s-process. It should be of great interest to determine the effect of the new reaction rate in the s-process models.

References

1) A. G. W. Cameron: Astrophys. J. **121**, 144 (1955).
2) I. Iben, Jr.: Astrophys. J. **395**, 202 (1976).
3) R. Gallino et al.: Astrophys. J. **497**, 388 (1998).
4) M. Busso, R. Gallino, and G. J. Wasserburg: Ann. Rev. Astron. Astrophys. **37**, 239 (1999).
5) M. Lugaro and F. Herwig: Proc. Nuclei in the Cosmos 2000, Aarhus, Denmark, 2001-6 (2001), edited by J. Christensen-Dalsgaard and K. Langanke; Nucl. Phys. A **688**, 201c (2001).
6) S. Goriely and L. Siess: Astron. Astrophys. **378**, L25 (2001).
7) H. W. Drotleff et al.: Astrophys. J. **414**, 735 (1993) and the references therein for the previous experiments.
8) G. M. Hale: Nucl. Phys. A **621**, 177c (1997).
9) C. Angulo et al.: Nucl. Phys. A **656**, 3 (1999).
10) M. Dufour and P. Descouvemont: Nucl. Phys. A **694**, 221 (2001).
11) C. E. Rolfs and W. S. Rodney: *Cauldrons in the Cosmos*, edited by C. E. Rolfs and W. S. Rodney (The University of Chicago Press, Chicago, 1988).
12) F. Ajzenberg-Selove: Nucl. Phys. A **460**, 1 (1986).
13) S. Kato, T. Hasegawa, and M. Tanaka: Nucl. Instrum. Methods **154**, 19 (1978).
14) M. H. Tanaka, S. Kubono, and S. Kato: Nucl. Instrum. Methods **195**, 509 (1982).
15) M. Igarashi: private communication.
16) G. Mairle, U. Schmidt-Rohr, and G. J. Wagner: Nucl. Phys. A **111**, 265 (1968).
17) M. D. Cooper, W. F. Hornyak, and P. G. Roos: Nucl. Phys. A **218**, 249 (1974).
18) A. Arima and S. Kubono: in *Treatise on Heavy-Ion Science*, Vol. I, edited by A. Bromely (Plenum, New York 1984) p. 617.
19) H. Furutani et al.: Prog. Theor. Phys. Suppl. No. 68, 193 (1980).
20) G. R. Caughlan and W. A. Fowler: At. Data Nucl. Data Tables **40**, 283 (1988).

Study of spin-isospin excitation in doubly magic nucleus ^{16}O

K. Suda,[*1] H. Okamura,[*1] H. Kumasaka,[*1] R. Suzuki,[*1] T. Ikeda,[*1] K. Itoh,[*1] H. Sakai,[*2] A. Tamii,[*2] M. Hatano,[*2] Y. Maeda,[*2] T. Saito,[*2] H. Kuboki,[*2] T. Uesaka,[*3] K. Yako,[*3] Y. Satou,[*4] N. Sakamoto, and K. Sekiguchi

[NUCLEAR REACTIONS ^{16}O$(d, d^*_{singlet})^{16}$O*, ^{16}O(polarized d,^{2}He)^{16}N, $E_d = 270$ MeV]

The spin-isospin excitation in nuclei is one of the fundamental modes of nuclear oscillation. The Gamow-Teller resonance has been extensively studied experimentally and theoretically. However, the spin-dipole resonance (SDR), which is the spin-coupled analog state of giant dipole resonance, is not extensively investigated due to its three different spin-parity states, $J^\pi = 2^-, 1^-$ and 0^-. Among the possible targets of the study of SDR, the ^{16}O nucleus is particularly attractive because not only it is a doubly magic nucleus, but also it is considered to be a possible detector material for ν_μ and ν_τ emitted by supernova explosion.[1] The detection scheme is as follows. Such neutrinos with an average energy of 25 MeV excite the SDR state of ^{16}O via the neutral current reaction. ^{16}O* decays mainly into ^{15}N and ^{15}O by proton and neutron emissions, respectively. If ^{15}N and ^{15}O are in an excited state below the particle threshold, they deexcite and emit photons, which can be detected by Superkamiokande. In this scheme, the cross sections of neutrino-induced reaction on ^{16}O are important and should be estimated and possibly confirmed experimentally. Thus, we measured the cross sections of SDR in ^{16}O by the $(d, d^*_{singlet})$ reaction at an intermediate energy. Here, $d^*_{singlet}$ denotes an unbound system of a proton and a neutron coupled to ^{1}S$_0$ state. The SDR state can be selectively excited by this reaction, which essentially involves spin-flip ($\Delta S = 1$) and isospin-flip ($\Delta T = 1$) transitions.

Another powerful probe for SDR is the $(d, ^2$He) reaction, where ^{2}He denotes a pair of protons coupled again to ^{1}S$_0$ states. This reaction also have the same selectivity for spin and isospin as that of the $(d, d^*_{singlet})$ reaction. The advantage of this reaction is its ability to determine J^π model-independently using the tensor analyzing power A_{zz} at 0°.[2]

The experiment was performed using a 270-MeV-polarized deuteron beam at RARF. The ^{16}O$(d, d^*_{singlet})^{16}$O* and ^{16}O$(d,^2$He$)^{16}$N reactions were measured at 0°. The newly developed solid oxygen target with a thickness of a few tens of mg/cm^2 was employed.[3] The $d^*_{singlet}$ was measured in coincidence with a proton and a neutron. Protons were momentum-analyzed by the magnetic spectrograph SMART, and detected using one pair of multiwire drift chambers and a trigger scintillator hodoscope at the first focal plane (F1) of the SMART. Neutrons were detected by the neutron counter newly developed and installed in the TOF beam line with a flight length of 21 m.[4] The neutron counter consists of segmented plastic scintillators with a total dimension of $60 \times 60 \times 24$ cm^3. On the other hand, the ^{2}He was measured in coincidence with two protons by the same detectors at F1. The $(d, ^2$He) reaction can be measured simultaneously with the $(d, d^*_{singlet})$ reaction, and therefore served as a thickness monitor for the oxygen target during the experiment. The average beam current was 0.3 nA.

Data analysis is in progress.

References

1) K. Langanke et al.: Phys. Rev. Lett. **76**, 2629 (1996).
2) H. Okamura et al.: RIKEN Accel. Prog. Rep. **36**, 51 (2003).
3) R. Suzuki et al.: RIKEN Accel. Prog. Rep. **36**, 188 (2003).
4) H. Kumasaka et al.: RIKEN Accel. Prog. Rep. **36**, 164 (2003).

*1 Department of Physics, Saitama University
*2 Department of Physics, University of Tokyo
*3 Center for Nuclear Study, University of Tokyo
*4 Tokyo Institute of Technology

Isovector quadrupole resonance observed in the ^{60}Ni(^{13}C, ^{13}N)^{60}Co reaction at $E/A = 100$ MeV†

T. Ichihara, M. Ishihara, H. Ohnuma,[*1] T. Niizeki,[*2] Y. Satou,[*3] H. Okamura,[*4] S. Kubono,[*3] M. H. Tanaka,[*5] and Y. Fuchi[*5]

[giant resonance, isovector, quadruple, charge-exchange reaction, intermediate energy]

Giant resonances (GR) represent major modes of collective motion, which dictate the dynamical properties of nuclei. Among the isovector non-spin-flip modes, the dipole resonance (IVGDR; $L = 1$) has been explored most extensively and is known to prevail over the nuclear chart. On the other hand, only limited information has been so far obtained for the monopole (IVGMR; $L = 0$) and quadrupole (IVGQR; $L = 2$) resonances.

In recent years, several attempts have been made to locate these high-lying resonances by employing charge-exchange reactions. Among those studies, measurements with reactions of (π^-, π^0)[1] and (^{7}Li, ^{7}Be),[2] provided strong indications for the existence of the IVGMR. On the other hand, clear observation of an IVGQR has been so far unsuccessful.

In this paper we report on the first clear identification of the IVGQR in the ^{60}Ni(^{13}C, ^{13}N)^{60}Co reaction at $E/A = 100$ MeV.[3]

The measurements were performed using $E/A = 100$ MeV ^{13}C and $E/A = 135$ MeV ^{12}C beams from the K540 RIKEN Ring Cyclotron and the spectrograph SMART with a QQDQD-configuration. Figure 1 shows typical energy spectra of the ^{60}Ni(^{13}C, ^{13}N)^{60}Co reaction at $E/A = 100$ MeV. Besides the IVGDR at $E_x = 8.7$ MeV, a significant peak was observed at $E_x = 20$ MeV with a width of 9 MeV. The extracted angular distributions for these two states are plotted in Fig. 2.

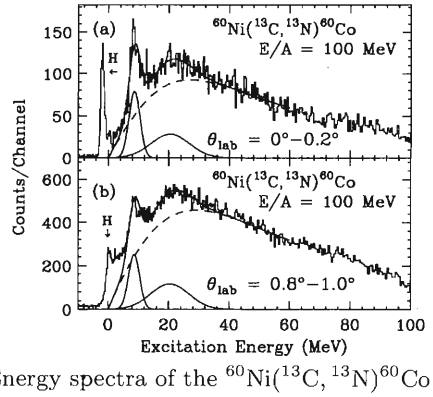

Fig. 1. Energy spectra of the ^{60}Ni(^{13}C, ^{13}N)^{60}Co reaction.

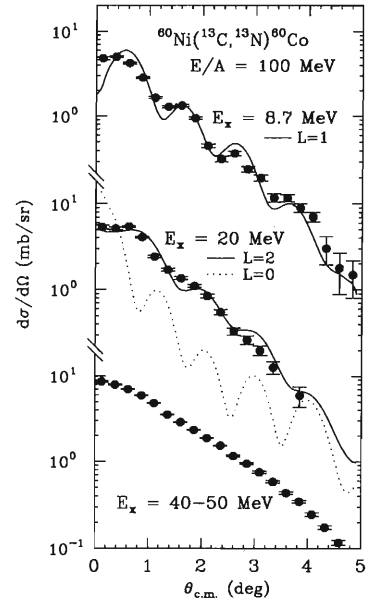

Fig. 2. Differential cross sections for the $E_x = 8.7$ MeV and $E_x = 20$ MeV states of the ^{60}Ni(^{13}C, ^{13}N)^{60}Co reaction at $E/A = 100$ MeV.

In order to determine the multipolarity (L) of the resonances, microscopic DWBA calculations were performed. The curves in Fig. 2 represent the results of the DWBA calculations. For the $E_x = 8.7$ MeV state, an IVGDR was assumed. Hence the $L = 1$ form factor was taken. Indeed, a very good fit has been obtained, justifying the validity of the DWBA analysis. For the $E_x = 20$ MeV state, we have studied two cases, with the $L = 0$ IVGMR and $L = 2$ IVGQR form factors.

The calculated angular distribution for the $L = 0$ IVGMR exhibits a steep rise at 0° and the first minimum near the $\theta_{cm} = 0.8°$. However, these distinctive features are hardly manifested in the observed angular distribution. On the other hand, an excellent fit has been obtained with the calculated distribution for the $L = 2$ IVGQR excitation. This result strongly indicates that the resonance state observed at $E_x = 20$ MeV is an IVGQR rather than an IVGMR. The present DWBA analysis further indicates that the observed peak exhausts approximately 50% strength of the isovector $L = 2$ classical energy-weighted sum rule.

† Condensed from the article in Phys. Rev. Lett. **89**, 142501 (2002)

*1 Department of Physics, Chiba Institute of Technology
*2 Faculty of Home Economics, Tokyo Kasei University
*3 Center for Nuclear Study, University of Tokyo
*4 Department of Physics, Saitama University
*5 High Energy Accelerator Research Organization (KEK)

References

1) A. Erell et al.: Phys. Rev. C **34**, 1822 (1986).
2) S. Nakayama et al.: Phys. Rev. Lett. **83**, 690 (1999).
3) T. Ichihara et al.: Phys. Rev. Lett. **89**, 142501 (2002).

Production of projectile-like fragments at intermediate energies†

S. Momota,[*1] M. Notani,[*2] S. Ito, A. Ozawa, T. Suzuki,[*3] I. Tanihata, N. Aoi,[*2] H. Sakurai,[*2] T. Teranishi,[*2] Y. Watanabe, A. Yoshida, N. Inabe, T. Kubo, H. Okuno, N. Fukuda, H. Iwasaki,[*2] K. Yoneda, H. Ogawa, A. Kitagawa,[*4] M. Kanazawa,[*4] M. Torikoshi,[*4] M. Suda,[*4] and A. Ono[*5]

[Nuclear reaction, Projectile fragmentation, Production cross section]

Momentum distribution and a production cross section of projectile-like fragments (PLF's) provide information on the mechanism of the nuclear reaction through which fragments are produced. In this article, we report on the transverse momentum (P_T) distribution and the production cross sections (σ(prod.)'s) of PLF's at an intermediate energy $E/A \sim 100$ MeV.

The experiment was performed at the RIPS beam line. An ^{40}Ar beam at $E/A = 90$ MeV accelerated by RIKEN Ring Cyclotron impinged on a 0.5-mm-thick ^{9}Be target. Produced PLF's were separated and identified by RIPS. The acceptance of RIPS was set to $\Delta P/P = \pm 0.5\%$ and ± 12.5 mrad for θ_x and θ_y, respectively. The incident angle of ^{40}Ar beam was deflected by the RIPS swinger magnet located in front of the target and the scattering angle of PLF's was selected by a 4-direction slit located immediately after the target. The P_T distribution was observed at the magnetic rigidity $B\rho = 3.71$ Tm. To derive σ(prod.), $B\rho$ of RIPS was varied stepwise over a range of 2.52–4.14 Tm. In addition, another experiment was performed at the NIRS-HIMAC. An ^{16}O beam at $E/A = 290$ MeV accelerated by HIMAC impinged on a 1.0-mm-thick ^{12}C target. The acceptance of the separator was set to $\Delta P/P = \pm 2.5\%$ and ± 13.0 mrad for θ_x and θ_y, respectively. $B\rho$ of the separator was varied stepwise over a range of 2.36–7.06 Tm.

In both experiments, the beam current was monitored by detecting the radiation induced by beam. The particle was identified by measuring time-of-flight and energy loss in the Si detector event-by-event.

The P_T distribution of PLF's measured at RIKEN was fitted by Gausssian functions and their standard deviations (σ_T's) were derived. The correlation between σ_T and P_L/A was observed. By subtracting the contributions of σ(Fermi)[1] and σ(def.)[2] as

$$(\Delta\sigma_T)^2 = \sigma_T^2 - \left(\sigma(\text{Fermi})^2 + \sigma(\text{def.})^2\right), \qquad (1)$$

this correlation can be extracted more clearly as shown in Fig. 1. The enhancement of σ_T at a low momentum region implies the contribution of the multistep process. To understand this correlation, this reaction

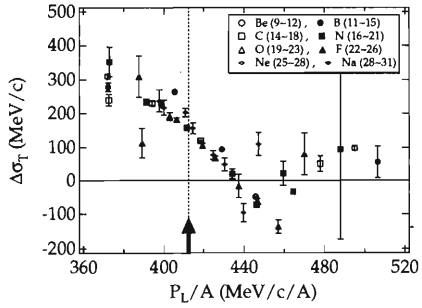

Fig. 1. Observed σ_T as a function of P_L/A.

was simulated by antisymmetrized molecular dynamics (AMD). σ_T derived from AMD calculation does not show any enhancement at the low momentum region.

By integrating observed production rates over P_L and P_T, σ(prod.) was derived (Fig. 2). σ(prod.)'s of PLF's estimated by EPAX2[3] agree well with the present results. Comparing with σ(prod.)'s measured in a similar experiment at MSU,[4] a rather good agreement is found for nuclei near the stable line but not for neutron-rich nuclei.

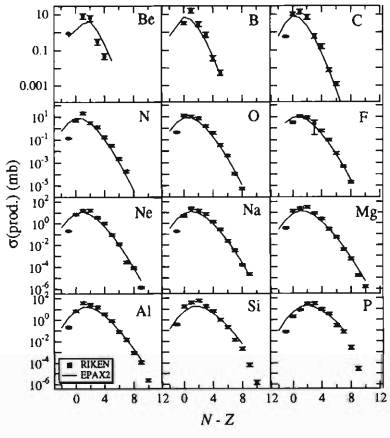

Fig. 2. σ(prod.) of PLFs measured at RIKEN.

† Condensed from the article in Nucl. Phys. A **701**, 150c (2002)

*1 Kochi University of Technology
*2 University of Tokyo
*3 Niigata University
*4 National Institute of Radiological Sciences (NIRS)
*5 Tohoku University

References

1) A. S. Goldhaber: Phys. Lett. B **53**, 306 (1974).
2) K. Van Bibber et al.: Phys. Rev. Lett. **43**, 840 (1979).
3) Sümmerer and B. Blank: Phys. Rev. C **61**, 034607 (2000).
4) M. Fauerbach et al.: Phys. Rev. C **53**, 647 (1996).

Momentum distribution of projectile fragments at intermediate energies

S. Momota,[*1] I. Tanihata, A. Ozawa, K. Yoshida, K. Morimoto, T. Onishi, T. Yamaguchi, A. Yoshida, Y. X. Watanabe,[*2] Z. Liu, M. Notani,[*3] and Y. Nojiri[*1]

[Nuclear reaction, Projectile fragmentation, Momentum distribution]

Nuclear reactions at intermediate energies, $E_i \sim 100\,\mathrm{MeV/A}$, involve multistep processes as well as direct processes, for example, projectile fragmentation. The former becomes important for fragments whose velocity is lower than the incident-beam velocity and the later is dominant for fragments with the velocity equal to the beam velocity. The correlation between the transverse momentum (P_T) distribution and longitudinal momentum (P_L) of projectile-like fragments (PLF's) described in the previous study[1] may be caused by this reaction mechanism. To observe the correlation more clearly, P_T distribution of PLF's was observed as a function of P_L. The systematic measurements of P_T distributions are also required for the application of the RI beam.

An ^{40}Ar beam accelerated up to $E/A = 95\,\mathrm{MeV}$ by the RIKEN Ring Cyclotron impinged on a 0.5-mm-thick ^{9}Be target. The PLF's produced were separated and identified by the isotope separator RIPS. The momentum acceptance was set to $\Delta P/P = \pm 0.5\%$ and the angular acceptance was set to ± 7.5 mrad and ± 12.5 mrad for θ_x and θ_y, respectively. The incident angle of the ^{40}Ar beam was deflected by the RIPS swinger magnet located in front of the target and the scattering angle of PLF's was selected by the 4-direction slit located just after the target. The angular distribution within $\theta_\mathrm{x} = 0 - 90$ mrad was observed upon varing the magnetic rigidity of the RIPS stepwise over the range $B\rho = 3.24 - 3.96$ Tm. Particle identification was performed by simultaneous event-by-event measurements of the time of flight (TOF) and the energy loss in two silicon detectors (ΔE). The production rate of each fragment was derived by normalizing the observed count by the beam current monitored by two sets of monitor counters consisting of three plastic scintillators. The typical error of the production rate derived from experimental results was about 10%. The main part of this error originated from the ambiguity in the beam-current monitor and the statistics of observed counts.

The P_T distributions of ^{20}O observed in the present experiment are shown in Fig. 1. As shown in the figure, the observed distribution, except for a few isotopes, are reproduced well using integrated Gaussian functions and their standard deviations (σ_T's) are derived. σ_T's of PLF's are shown as a function of P_L/A in Fig. 2 and an interesting correlation between σ_T and P_L/A is seen. σ_T decreases with increasing P_L/A. This correlation depends on the mass of PLF. σ_T coincides with that derived from the model in which the contributions of the Fermi momentum of removed nucleons[2] and the deflection of the projectile in the field of the target nucleus[3] are considered.

The mechanism of nuclear reactions in this energy region will be discussed on the basis of these results.

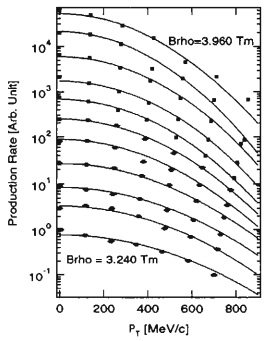

Fig. 1. Observed P_T distributions of ^{20}O. The values plotted at the upper region were measured at higher momentum. The solid lines are results of fitting using integrated Gaussian functions.

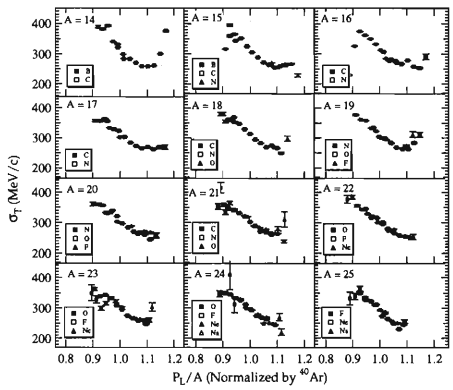

Fig. 2. Correlation between σ_T and P_L/A.

References

1) S. Momota et al.: Nucl. Phys. A **701**, 150c (2002).
2) A. S. Goldhaber: Phys. Lett. B **53**, 306 (1974).
3) K. Van Bibber et al.: Phys. Rev. Lett. **43**, 840 (1979).

*1 Faculty of Engineering, Kochi University of Technology
*2 Institute of Particle and Nuclear Studies, High-Energy Accelerator Research Organization (KEK)
*3 Center for Nuclear Study, University of Tokyo

Breakup reaction of ^{11}Be

N. Fukuda, T. Nakamura,[*1] T. Kobayashi,[*2] H. Otsu,[*2] N. Aoi,[*3] N. Imai,[*3] H. Iwasaki,[*4] T. Kubo, A. Mengoni,[*5] M. Notani,[*5] H. Sakurai,[*3] S. Shimoura,[*4] T. Teranishi,[*4] Y. X. Watanabe,[*6] K. Yoneda, and M. Ishihara

[NUCLEAR REACTIONS: ^{208}Pb,^{12}C(^{11}Be,^{10}Be+n)X; Coulomb breakup, Nuclear breakup, Diffraction dissociation]

We report the preliminary results of the breakup experiment of the one-neutron halo nucleus ^{11}Be. The breakup reaction is an efficient means of determining the structure of neutron-rich nuclei. The Coulomb breakup induced by a high-Z target has been utilized to determine the E1 transition strength which contains information on the nuclear structure. This reaction has also been applied to the determination of an astrophysical S-factor. On the other hand, the nuclear breakup induced by a low-Z target can possibly be used in investigating resonant states. When we employ breakup reactions for such spectroscopic purpose, we need to control Coulomb and nuclear contributions. To this end, we compared the excition energy distribution and the angular distribution between measurement with a light-Z target (^{12}C) and that with a high-Z target (^{208}Pb). In this report, the results for the ^{12}C target are presented.

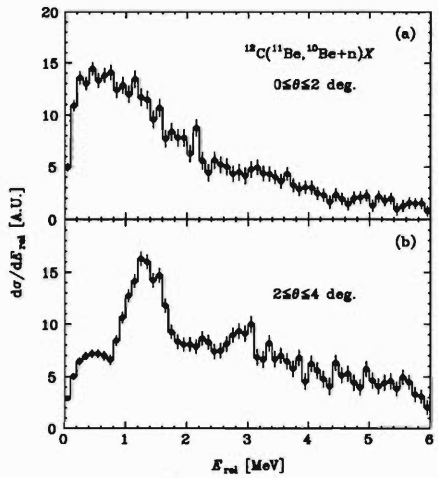

Fig. 1. Breakup reaction cross section as a function of $E_{\rm rel}$ for ^{12}C target. (a) and (b) show the distributions for angular regions of $0^\circ \leq \theta \leq 2^\circ$ and $2^\circ \leq \theta \leq 4^\circ$, respectively.

*1 Department of Physics, Tokyo Institute of Technology
*2 Department of Physics, Tohoku University
*3 Department of Physics, University of Tokyo
*4 Center for Nuclear Study, University of Tokyo
*5 Applied Physics Division, Italian National Agency for New Technologies, Energy and the Environment, Italy
*6 Institute of Particle and Nuclear Studies, High-Energy Accelerator Research Organization (KEK)

The experiment was performed at the RIPS[1] beam line at the RIKEN Accelerator Research Facility. Details of the experimental setup are described in Ref. 2.

In Fig. 1, the breakup reaction cross sections at different scattering angles, $\theta_{\rm cm}$, are plotted as a function of neutron-^{10}Be relative energy, $E_{\rm rel}$. For $0^\circ \leq \theta_{\rm cm} \leq 2^\circ$ (a), a nonresonant state has been observed which is possibly caused by diffraction dissociation.[3] For $2^\circ \leq \theta_{\rm cm} \leq 4^\circ$, the known resonant state[4] at $E_{\rm rel} = 1.25$ MeV with a spin-parity of $5/2^+$ has been observed. Figure 2 shows the angular distributions for the regions of the nonresonant state (a) and the resonant state (b). For the resonance region, a typical $\Delta L = 2$ diffraction pattern is observed. On the other hand, the distribution for the nonresonance region is as yet unknown. Further study is now in progress.

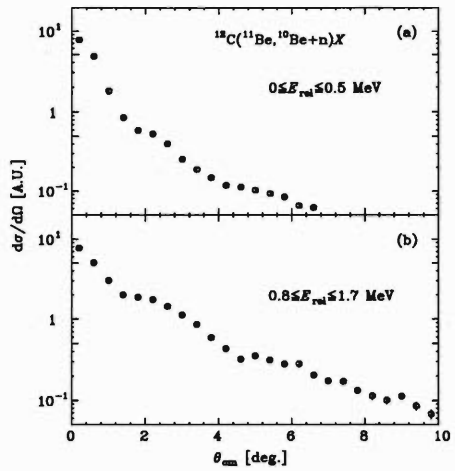

Fig. 2. Angular distributions for different $E_{\rm rel}$ regions. The regions of 0 MeV $\leq E_{\rm rel} \leq$ 0.5 MeV (a) and 0.8 MeV $\leq E_{\rm rel} \leq$ 1.7 MeV (b) correspond to the nonresonant and resonant states, respectively.

References

1) T. Kubo et al.: Nucl. Instrum. Methods Phys. Res. B **70**, 309 (1992).
2) N. Fukuda et al.: RIKEN Accel. Prog. Rep. **32**, 74 (1998).
3) F. Barranco and P. G. Hansen: Eur. Phys. J. A **7**, 479 (2000).
4) G.-B Liu and H. T. Fortune: Phys. Rev. C **42**, 168 (1990).

Measurement of the transfer differential cross section for ^{6}He on Be target

Y. Ye,[*1] D. Jiang,[*1] T. Zheng,[*1] Q. Wang,[*1] Y. Ge,[*1] Z. Li,[*1] X. Li,[*1] A. Ozawa, R. Kanungo, Y. Yamaguchi,[*2] C. Wu, D. Fang, and I. Tanihata

[^{6}He; Be target; neutron transfer; elastic scattering]

In order to fully understand the internal structure of exotic nuclei, more experiments are needed. Among those experiments, the transfer and breakup measurements are sensitive tools for testing the surface nucleon distribution for light exotic nuclei.[1–4)]

^{6}He is recognized as a typical neutron halo nucleus. Nevertheless the real internal structure is still quite confusing. For instance ^{6}He may be treated as an alpha particle core plus two surrounding neutrons, or as two triton clusters, each with certain probability.[5)] The transfer of 1n and 2n processes and accompanying 2t breakup process are sensitive to these kinds of clustering structures. Over the last few years some transfer experiments were performed on ^{6}He a Hydrogen target and very interesting results were obtained.[2–4,6)]

In the present experiment, the differential cross section for the neutron transfer from ^{6}He projectiles to a Be target as well as the elastic scattering were measured. The experiment was performed at the RIKEN projectile-fragment separator (RIPS) at RIKEN. ^{13}C of 70 A MeV was used to bombard the Be target to produce ^{6}He through the projectile fragmentation procedure. The primary target was ^{9}Be of 8 mm in thickness. By the Bρ-ΔE-TOF method, where TOF denotes the time-of-flight, the ^{6}He beam ($\sim$25A MeV) was identified and separated from other secondary beams. Two plastic scintillation counters (0.5 mmt at F2, 0.3 mmt at F3) were used to measure the TOF and the energy loss (ΔE). The purity of ^{6}He was better than 99%.

The secondary target was ^{9}Be of 100 μm in thickness, which was chosen due to the consideration of the reaction channel independence and the feasibility of the target film for light mass nucleus. The target was tilted 45°. The effective area of the target was 30 × 30 mm^2. Two parallel-plate avalanche counters (PPAC) of delay-line (DL) type were placed in front of the target to track the incident ^{6}He particles. In order to get higher detection efficiency, the octafluoropropane gas pressure was 30 torr and the high voltage was $\sim$1650 V. The outgoing charged particles from the Be target were detected by 6 telescopes, each composed of a PSD, a large area Si detector and a CsI scintillator, as shown in Fig. 1. The setup of the detector is based on the detailed kinematics calculation for coincidence measurement of the transfer products.

*1 Department of Technical Physics, Peking University, China
*2 Department of Physics, Niigata University

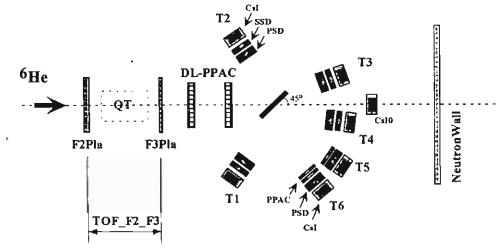

Fig. 1. The experimental setup.

From the preliminary result of data analysis, several thousand satisfactory Be events were observed, which corresponded to elastic recoiling, transfer and other reaction channels. A few ^{11}Be events were observed. It was also very interesting to observe some Li events. The particle identification carried out using one of the telescopes is shown in Fig. 2. Further data analysis is going on.

The authors gratefully acknowledge all of the staff at the RIKEN Ring Cyclotron for their perfect work. We are grateful to Dr. N. Fukuda for helping us to operate the Neutron Wall and to all the other people who provided help during the experiment.

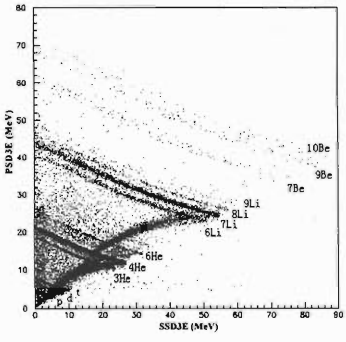

Fig. 2. The particle identification by No.3 telescope.

References

1) F. Negoita et al.: Phys. Rev. C **59**, 2082 (1999).
2) R. Raabe et al.: Phys. Lett. B **458**, 1 (1999).
3) G. M. Ter-Akopian et al.: Phys. Lett. B **426**, 251 (1998).
4) E. F. Aguilera et al.: Phys. Rev. Lett. **84**, 5058 (2000).
5) K. Arai et al.: Phys. Rev. C **59**, 1432 (1999).
6) K. Rusek et al.: Phys. Rev. C **64**, 044602 (2001).

Lifetime of isomeric 0_2^+ state in ^{12}Be

K. Demichi,[*1] S. Shimoura,[*2] T. Motobayashi, N. Aoi,[*3] H. Baba,[*1] Z. Elekes, T. Fukuchi,[*4] T. Gomi,[*1] H. Hasegawa,[*1] E. Ideguchi, M. Ishihara, N. Iwasa,[*5] H. Iwasaki,[*2] S. Kanno,[*1] S. Kawai,[*1] S. Kubono,[*2] N. Kuboshima,[*1] K. Kurita,[*1] M. Kurokawa,[*2] Y. U. Matsuyama,[*1] S. Michimasa,[*2] K. Miller,[*6] T. Minemura, T. Murakami,[*7] M. Notani,[*2] A. Odahara,[*8] S. Ota,[*7] A. Saito,[*1] H. K. Sakai,[*1] H. Sakurai,[*3] E. Takeshita,[*1] S. Takeuchi, M. Tamaki,[*2] T. Teranishi,[*2] Y. Togano,[*1] K. Yamada,[*1] and Y. Yanagisawa

[Isomeric state, Radioactive beam experiment]

The neutron-rich nucleus ^{12}Be has attracted much attention, since it was suggested that the $N = 8$ shell closure may be broken in neutron-rich Be isotopes. The neighboring nucleus ^{11}Be has the ground state of $1/2^+$ 320 keV below the $1/2^-$ state, indicating that the gap between p- and sd-shells is strongly quenched and the $p_{1/2}$ and $s_{1/2}$ orbitals almost degenerate. The spectroscopic factor of the n + ^{11}Be$(1/2^+)$ for the ground state of ^{12}Be has been extracted to be about 50% in studies of the neutron knockout reaction ^{9}Be(^{12}Be, ^{11}Be + γ)X.[1,2] A large deformation of ^{12}Be has been found in an experiment of the ^{12}Be(p, p′)^{12}Be$^*(2^+)$ reaction.[3] Together with these results, the finding of a low-lying intruder 1^- state at $E_x = 2.7$ MeV populated by Coulomb excitation[4] supports the picture that p- and s-shells almost degenerate also in ^{12}Be. This indicates that a break of the $N = 8$ shell closure is seen in ^{12}Be as well as in ^{11}Be. Recently an isomeric 0_2^+ state in ^{12}Be was found at $E_x = 2.24$ MeV by measuring coincident two γ rays from in-flight ^{12}Be nuclei, ^{12m}Be $\rightarrow$ ^{12}Be* $(2_1^+ \rightarrow {}^{12}\mathrm{Be}_{g.s.})$.[5] The decay branches of the E2 transition to the 2_1^+ state and the E0 (pair) decay to the $0_{g.s.}^+$ are extracted to be 17 ± 2 and 83 ± 2%, respectively. However, the experiment could deduce only the lower and upper limits of the mean-life τ to be 50 ns $< \tau <$ 11 μs. Lifetime determination is required to understand the nuclear structure more precisely.

The experiment was performed at the RIKEN Acceleator Reserach Facility using a 100 A MeV ^{18}O primary beam. We used three targets, 10-mm-thick Be, 3-mm-thick Nb and 8-mm-thick Be. The $^{12(m)}$Be nuclide at 52 A MeV was selected through the RIKEN Projectile Fragment Separator (RIPS). Two plastic scintillators at the second (F2) and the third (F3) focal planes of the RIPS were used for event-by-event identification of ^{12}Be fragments with the time-of-flight (TOF) between the two scintillators and the energy losses in the scintillators. The beam which includes the isomeric 0_2^+ state was incident on a $4 \times 4 \times 4$ cm^3 polyethylene block stopper. ^{12m}Be stopped in the stopper decayed through γ emission to the 2_1^+ state, which was followed by a cascade γ decay to the ground state, or directly to the ground state by emission of an e^-e^+ pair. In the latter case, annihilation γ rays are radiated from the stopper. Gamma rays were detected by an array of 75 NaI(Tl) scintillators and 6 Ge detectors positioned around the stopper. Each NaI(Tl) crystal had an active volume of $4 \times 8 \times 16$ cm^3. The typical energy and time resolution of each scintillator were 8.8% for the 662 keV γ ray and about 1 ns (1σ).

Figure 1 shows a decay curve of the 511 keV γ rays from the isomeric 0_2^+ state measured by the NaI(Tl) array. The horizontal axis indicates the interval between the time when ^{12m}Be reaches the stopper and one of the detecting γ rays by the NaI(Tl) scintillators. The solid line is the result of a fit with a functional form of a single exponential. Assuming that all the observed annihilation γ rays originate from the isomeric state, the value of the half-life $T_{1/2}$ is extracted to be 218 ± 13 ns as a preliminary result. Analysis of the data for 140 keV and 2100 keV γ rays is now in progress.

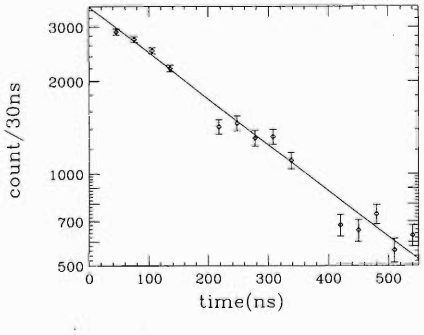

Fig. 1. The decay curve of the 511 keV γ rays. The solid line is the result of a fit with a functional form of a single exponential.

*1 Rikkyo University
*2 Center for Nuclear Study, University of Tokyo
*3 University of Tokyo
*4 Kyushu University
*5 Tohoku University
*6 Michigan State University, USA
*7 Kyoto University
*8 Nishinippon Institute of Technlolgy

References

1) A. Navin et al.: Phys. Rev. Lett. **85**, 266 (2000).
2) F. Nunes et al.: Nucl. Phys. A **609**, 43 (1996).
3) H. Iwasaki et al.: Phys. Lett. B **491**, 7 (2000).
4) H. Iwasaki et al.: Phys. Lett. B **491**, 8 (2000).
5) S. Shimoura et al.: RIKEN Accel. Prog. Rep. **35**, 54 (2002).

Measurement of ^{4}He(^{12}Be,^{13}Bγ) at 50 MeV/nucleon

S. Ota,[*1] K. Demichi,[*2] S. Shimoura,[*3] H. Iwasaki,[*3] M. Kurokawa,[*3] S. Michimasa,[*3] S. Kubono,[*3] T. Teranishi,[*3] M. Notani,[*3] M. Tamaki,[*3] T. Murakami,[*1] N. Iwasa,[*4] T. Motobayashi, Y. Yanagisawa, T. Minemura, S. Takeuchi, T. Gomi,[*2] K. Yamada,[*2] A. Saito,[*2] H. Baba,[*2] Y. U. Matsuyama,[*2] S. Kanno,[*2] E. Takeshita,[*2] H. Hasegawa,[*2] K. Kurita,[*2] H. Sakurai,[*5] N. Aoi,[*5] E. Ideguchi, A. Odahara,[*6] T. Fukuchi,[*7] K. Miller,[*8] Z. Elekes, Y. Togano,[*2] S. Kawai,[*2] N. Kuboshima,[*2] H. K. Sakai,[*2] and M. Ishihara

[NUCLEAR REACTIONS, ^{4}He(^{12}Be,^{13}Bγ), Nucleon transfer]

The disappearance of regular magic numbers in neutron-rich nuclei has been one of the most interesting phenomena to be studied in order to clarify the basic mechanism responsible for the nuclear structure of unstable nuclei far from stability. As an example of neutron-rich nuclei with magic numbers, we have studied ^{13}B with $N = 8$, where the spin assignments for low-lying states have not been determined.[1] In the present study, we are aiming at extracting information on spin and parity of these states in ^{13}B by measuring the angular distribution of the one-nucleon transfer reaction, ^{4}He(^{12}Be,^{13}Bγ). Here we report the experimental arrangement.

A ^{12}Be beam was produced by the projectile fragmentation of a 100 MeV/nucleon ^{18}O primary beam incident on a 1.85 g/cm^2-thick Be target and separated by the RIKEN Projectile-fragment Separator (RIPS).[2] The intensity of secondary beam was a few hundreds of thousands counts per second with the momentum spread ±1%. Two plastic scintillators (PL) were located at the first achromatic focal plane (F2) of RIPS and the final focal plane (F3). The particle identification of the incident beam was carried out event-by-event with the time-of-flight (TOF) measurement. The TOF was determined between F2-PL and F3-PL timings. Two parallel plate avalanche counters (PPACs) were located in F3 to determine the angle of incident beam.

Figure 1 shows the schematic view of the experimental setup for the ^{4}He(^{12}Be,^{13}Bγ) reaction.

Excited ^{13}B was populated by the transfer reaction of ^{12}Be at around 50 MeV/nucleon on a 120 mg/cm^2-thick liquid-helium target located 1.3 m downstream of F3-PL. The scattered ^{13}B was detected by a hodoscope located 4.8 m downstream of the target. The hodoscope consists of 5-mm-thick ΔE and 60-mm-thick E plastic scintillators. The particle was identified performed using ΔE-TOF and E-TOF information. The TOF between the target and hodoscope was evaluated by timing the signals of F2PL, F3PL and hodoscope. The scattered angle of ^{13}B was determined by the hit position on PPACs and the hodoscope.

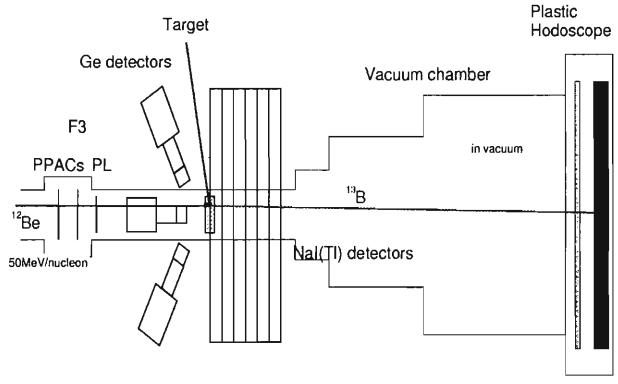

Fig. 1. The schematic view of the experimental setup.

The de-excitation γ rays from excited ^{13}B were measured by the hybrid array, which consists of six segmented Ge detectors and 75 pieces of NaI(Tl) detectors. The NaI detectors[3] were set downstream of the target, while Ge detectors were set upstream. Each Ge detector consists of two planar-type crystals, which are of a cylindrical shape with a size of 6 cmϕ × 2 cm. One base of the crystal is a cathode divided into nine segments.[4] By applying the pulse-shape analysis of nine outputs from the cathode, the position resolution along the depth of the crystal is estimated to be about 1 mm FWHM, which allows us to measure 3.7 MeV γ rays from ^{13}B[1] at the energy resolution of 15 keV (FWHM).[4]

Data analysis, in particular pulse-shape analysis to improve γ-ray energy resolution, is now in progress.

*1 Department of Physics, Kyoto University
*2 Department of Physics, Rikkyo University
*3 Center for Nuclear Study, University of Tokyo
*4 Department of Physics, Tohoku University
*5 Department of Physics, University of Tokyo
*6 Nishinippon Institute of Technology
*7 Department of Physics, Kyushu University
*8 Michigan State University, USA

References

1) F. Ajzenberg-Selove, E. R. Flynn, and O. Hansen: Phys. Rev. C **17**, 1283 (1978).
2) T. Kubo et al.: Nucl. Instrum. Methods Phys. Res. B **70**, 309 (1992).
3) S. Takeuchi et al.: RIKEN Accel. Prog. Rep. **36**, 148 (2003).
4) M. Kurokawa et al.: Conf. Rec. 2002 IEEE Nuclear Science Symp. and Medical Imaging Conf., Norfolk, USA, 2002-11, in press.

Molecular states in ^{12}Be and ^{14}Be

A. Saito,[*1] S. Shimoura,[*2] S. Takeuchi, T. Motobayashi, H. Akiyoshi, Y. Ando,[*1] N. Aoi,[*3] Zs. Fülöp,[*4] T. Gomi,[*1] Y. Higurashi, M. Hirai,[*5] N. Iwasa,[*6] H. Iwasaki,[*2] Y. Iwata,[*5] H. Kobayashi,[*1] M. Kurokawa,[*2] Z. Liu,[*7] T. Minemura, S. Ozawa, H. Sakurai,[*3] M. Serata,[*1] T. Teranishi,[*2] K. Yamada,[*1] Y. Yanagisawa, and M. Ishihara

[NUCLEAR REACTIONS: ^{14}Be(^{12}C, X)^{12,14}Be $\rightarrow$ ^{6}He + ^{6}He, ^{6}He + ^{8}He, 75 A MeV]

Excited states in ^{12}Be and ^{14}Be were investigated by measuring the ^{6}He + ^{6}He and ^{6}He + ^{8}He breakup channels in the two-neutron removal and the inelastic scattering of an exotic ^{14}Be beam, respectively.[1)]

The experiment was carried out at RIPS. Excited states in ^{12}Be and ^{14}Be were populated in the final state of the ^{14}Be + CH_2 and ^{14}Be + C interactions at an incident energy of 75 A MeV. The reaction products were measured and identified using a hodoscope of a plastic scintillator array with an active area of 1×1 m^2 located 4.9 m downstream of the target. The decay energies for ^{12}Be $\rightarrow$ ^{6}He + ^{6}He and ^{14}Be $\rightarrow$ ^{6}He + ^{8}He were extracted by the invariant-mass method.

Figure 1 shows the decay-energy spectra for the breakup channels of (a) ^{12}Be and (b) ^{14}Be. Mixed-event analyses were attempted in order to estimate the continuum structure of the backgrounds. Solid curves are the results of fitting with the mixed events and resonances. Dashed and dotted ones represent their contributions. For the ^{6}He + ^{6}He channel (a), the levels at 3.1, 4.8, and 6.0 MeV reported from the ^{12}Be + ^{12}C $\rightarrow$ ^{6}He + ^{6}He + ^{12}C experiment[2)] are taken into account. New levels are observed at 1.7 MeV and 2.7 MeV for ^{6}He + ^{6}He, and 1.4 MeV and 2.2 MeV for ^{6}He + ^{8}He. Peak-to-background ratios are determined for each peak according to the fitting results.

Angular-correlation analyses are attempted for the newly observed peaks (Fig. 2). ψ is defined as the angle of the relative velocity of the decay particles with respect to the beam direction.[3)] Figure 2 shows results of the χ^2-fitting with the fixed peak-to-background ratios for the peaks at 1.7 MeV in ^{6}He+^{6}He (a), and 1.4 MeV (b) and 2.2 MeV (c) in ^{6}He + ^{8}He. The χ^2 values are summarized in Table 1. By comparing the χ^2 values, $J = 0$ is a candidate of the spin for the 1.7 MeV state in ^{12}Be, which is a possible member of the ^{6}He-^{6}He rotational band.[2)] In the same way, the correlation for the 1.4 MeV peak in ^{14}Be was well reproduced by the $J = 0$ curve (Fig. 2 (b)). For the 2.2 MeV peak in ^{14}Be, $J = 0$ and 4 are favored.

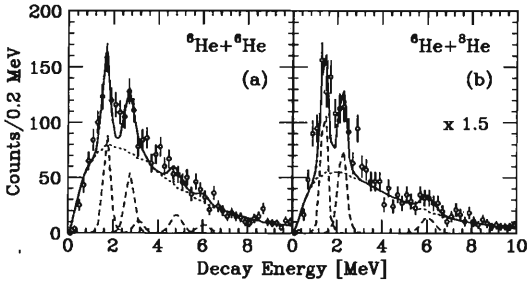

Fig. 1. Decay-energy spectra of (a) ^{12}Be* $\rightarrow$ ^{6}He+^{6}He and (b) ^{14}Be* $\rightarrow$ ^{6}He + ^{8}He.

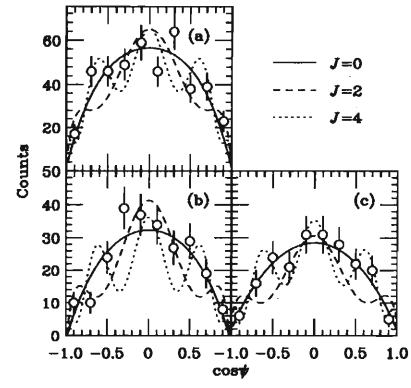

Fig. 2. Angular correlations for observed peaks at (a) 1.7 MeV in ^{6}He+^{6}He, and (b) 1.4 MeV and (c) 2.2 MeV in ^{6}He + ^{8}He.

Table 1. The χ^2 values of fitting results in Fig. 2.

	E_d [MeV]	E_x [MeV]	J 0	2	4
(a) ^{12}Be	1.7	11.8	1.4	2.9	2.7
(b) ^{14}Be	1.4	10.7	1.3	2.4	5.1
(c) ^{14}Be	2.2	11.5	0.4	3.7	0.9

*1 Department of Physics, Rikkyo University
*2 Center for Nuclear Study, University of Tokyo
*3 Department of Physics, University of Tokyo
*4 ATOMKI, Hungary
*5 National Institute of Radiological Science
*6 Department of Physics, Tohoku University
*7 Institute of Modern Physics, China

References

1) A. Saito et al.: RIKEN Accel. Prog. Rep. **35**, 55 (2002).
2) M. Freer et al.: Phys. Rev. Lett. **82**, 1383 (1999); M. Freer et al.: Phys. Rev. C **63**, 034301 (2001).
3) M. Freer: Nucl. Instrum. Methods Phys. Res. A **383**, 463 (1996).

Measurement of mean lives of ^{12}Be(2_1^+) and ^{16}C(2_1^+)

N. Imai,[*1] H. J. Ong,[*1] N. Aoi,[*1] H. Sakurai,[*1] K. Demichi,[*2] H. Kawasaki,[*2] H. Baba,[*2] Zs. Dombrádi,[*3] Z. Elekes, N. Fukuda, Zs. Fülöp,[*3] A. Gelberg,[*4] T. Gomi,[*2] H. Hasegawa,[*2] K. Ishikawa,[*5] H. Iwasaki,[*6] E. Kaneko,[*2] S. Kanno,[*2] T. Kishida, Y. Kondo,[*5] T. Kubo, K. Kurita,[*2] S. Michimasa,[*6] T. Minemura, M. Miura,[*5] T. Motobayashi, T. Nakamura,[*5] M. Notani,[*3] T. K. Onishi,[*1] A. Saito,[*2] S. Shimoura,[*6] T. Sugimoto,[*5] M. K. Suzuki,[*1] E. Takeshita,[*2] S. Takeuchi, M. Tamaki,[*6] K. Yoneda, H. Watanabe, and M. Ishihara

[NUCLEAR REACTIONS: ^{197}Au(^{12}Be, ^{12}Be*)^{197}Au $E = 40.3$ MeV/u, ^{9}Be(^{16}C, ^{16}C*)^{9}Be $E = 43.8$ MeV/u, ; DSA]

We applied the Doppler-shift attenuation method at intermediate energy[1)] to measure the mean lives of ^{12}Be(2_1^+) and ^{16}C(2_1^+). The mean life is directly related with the B($E2$) value of the nucleus, which reflects the deformation of proton distribution of the ground state. We can deduce neutron and proton deformation separately together with the nuclear deformation parameter obtained from proton inelastic scattering which is sensitive to the neutron deformation. These can reveal exotic structures of different deformations between neutrons and protons, which may be related to the melting magicity of $N = 8$.

In this experiment, we used a thick target where the projectile was excited and its velocity was degraded in the target. Accordingly, the Doppler shifted γ-ray energy was spread over a certain region. The energy of the γ ray emitted inside the target was distributed continuously, while the one emitted outside the target was constant since the projectile did not change its velocity anymore. Therefore, if we properly chose the target thickness and the projectile energy so that the time for the projectile to pass through the target would be comparable with the mean life of its excited state, the mean life can be determined from the shape of the energy spectrum of 500 γ-ray events with $\pm$10% uncertainty.

Radioactive beams of ^{12}Be and ^{16}C were produced by the projectile fragmentation of a 100 MeV/u ^{18}O beam with a 1850 mg/cm^2 thick Be target. Particle identification of secondary beams was carried out using the energy deposit in a plastic scintillator (PL) placed in the F3 chamber and the time difference between the RF signals of the accelerator and the plastic scintillator. The ^{12}Be and ^{16}C beams were separated by the RIPS beam line[2)] and bombarded on a 1930 mg/cm^2 thick Au target or a 370 mg/cm^2 thick Be target, respectively. Figure 1 shows a schematic view of the experimental setup. At the final focal plane of RIPS, the energies of beams were 40.3 and 43.8 MeV/u, respectively. The typical secondary beam intensity was 400 kHz. The de-excitation γ rays from the inelastically excited ^{12}Be and ^{16}C nuclei were detected by four clover Ge detectors (Clovers). Each Clover was located 30 cm upstream from the target at 150 degrees with respect to the beam direction. In order to measure the excitation cross sections, an array of 32 NaI(Tl) scintillators was also placed around the target at about 90 degrees with respect to the beam axis.

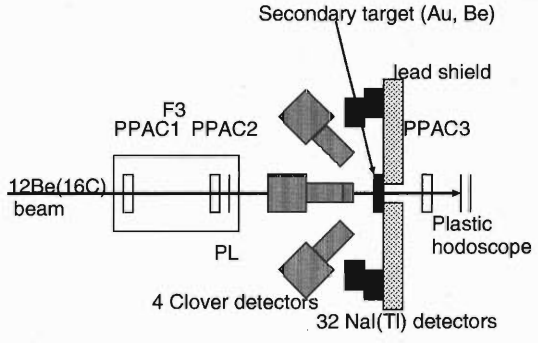

Fig. 1. Layout of the detection system. See text for details.

The observed Doppler-shifted γ-ray energy was spread due to the finite angular acceptance and the change in the velocity. The spread due to the angular acceptance was about 25 keV, while the energy spread by the velocity change was 150 keV. Based on these, we can distinguish between a γ ray from outside the target and that from inside. The scattering angle was measured by three parallel plate avalanche counters, two of which were located upstream and the third one downstream of the target. Identification of the scattered particle was carried out with a plastic scintillator hodoscope. It consisted of a 2-mm-thick ΔE plane and a 5-mm-thick E plane. In order to prevent the background γ rays from the particles which stopped at hodoscope, we put a 5-cm-thick lead shield between the Clovers and the hodoscope (See Fig. 1). Data analysis is in progress.

*1 University of Tokyo
*2 Rikkyo University
*3 ATOMKI, Hungary
*4 University of Cologne, Germany
*5 Tokyo Institute of Technology
*6 Center for Nuclear Study, University of Tokyo

References
1) N. Imai et al.: RIKEN Accel. Prog. Rep. **35**, 49 (2002).
2) T. Kubo et al.: Nucl. Instrum. Methods Phys. Res. B **70**, 309 (1992).

Astrophysical rate for the ^{8}B(p,γ)^{9}C reaction

T. Motobayashi, I. Hisanaga,[*1] H. Akiyoshi, Y. Ando,[*1] H. Fujiwara,[*1] N. Fukuda,[*2] Zs. Fülöp,[*3] T. Gomi,[*1] K. I. Hahn,[*4] Y. Higurashi, M. Hirai,[*2] M. Ishihara, N. Iwasa,[*5] H. Iwasaki,[*2] Y. Iwata,[*1] T. Kijima,[*1] S. Kubono,[*2] T. Minemura, T. Nakamura,[*6] M. Notani,[*2] S. Ozawa, H. Sakurai, S. Shimoura,[*2] S. Takeuchi, T. Teranishi,[*2] and Y. Yanagisawa

[NUCLEAR REACTIONS: Pb(^{9}C,p^{8}B), ^{12}C(^{9}C,p^{8}B)^{12}C, E = 65 A MeV; measured projectile-Coulomb breakup σ, Astrophysical reaction rate for ^{8}B(p,γ)^{9}C]

The low-energy behavior of the ^{8}B(p,γ)^{9}C reaction was studied by Coulomb and nuclear dissociation measurements. In hot pp chain hydrogen burning, this reaction plays a role at a temperature above approximately 10^8 K and a density higher than 10^5 g/cm^3 in hydrogen-rich supermassive objects.[1] This reaction is also important in estimating the ^{7}Li production in novae.[2] Direct measurements of the reaction are difficult because of the short half-life of ^{8}B (770 ms). We made an attempt to determine its cross section indirectly using fast radioactive ^{9}C beams.

The process ^{9}C $\rightarrow$ ^{8}B + p was studied with carbon and lead targets at $E_{\rm in}$ = 65 A MeV. Details of the experiment and preliminary results are given in previous reports.[3,4] The experimental p-^{8}B relative-energy spectrum consisted of contributions from the resonance at 0.922 MeV and a continuum without structure. With a small correction due to the ℓ = 2 contribution estimated from the data obtained with the carbon target, astrophysical S factors were extracted, where ℓ denotes the angular momentum transfer. The result, 77 $\pm$ 15 eV-b as an average in the energy region from 200 keV to 600 keV, is considerably smaller than that estimated by Wiescher *et al.*, 210 eV-b,[1] whereas it is consistent with that theoretically predicted by Descouvemont.[5]

By comparing the spectra taken with the carbon and lead targets, radiative widths of the resonance could be extracted as Γ_γ(M1) = 21 $\pm$ 6 meV and Γ_γ(E2) = 4.3$\pm$1.0 μeV. They are consistent respectively with the predictions 34 meV by Wiescher *et al.*[1] and 4.6 μeV by Kanada-En'yo and Horiuchi.[6]

By using the present results, the astrophysical rate for the ^{8}B(p,γ)^{9}C reaction was obtained. Astrophysical reaction rate is defined as the rate of the relevant reaction per unit volume, time, and densities of particles in its incident channel. It is the product of the cross section and the relative velocity averaged by the Maxwell-Boltzmann distribution, and is often expressed as $N_{\rm A}\langle\sigma{\rm v}\rangle$, where $N_{\rm A}$ represents the Avogadro number. Figure 1 shows the astrophysical reaction rates for the ^{8}B(p,γ)^{9}C reaction. The solid curve is obtained by the present results. The rate is smaller by a factor of about three than the one evaluated by Wiescher *et al.*,[1] reflecting the difference in the S factors. The dash-dotted curve shows the contribution of the resonant state, which has only a minor contribution in the full temperature range from T_9 = 0.05 to 10, where T_9 is the temperature measured in the unit of 10^9 K.

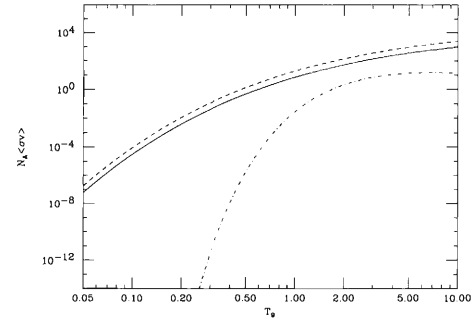

Fig. 1. Astrophysical reaction rate for the ^{8}B(p,γ)^{9}C reaction.

Recently, astrophysical S factors of the same reaction have been determined by experiments with the ANC method. The extracted values, 45 $\pm$ 13 eV-b[7] and 46 $\pm$ 6 eV-b,[8] are slightly smaller than the present result. However, this difference does not significantly affect the reaction rate. Astrophysical network calculations for the hot pp chain nuclear burning[1] and the ^{7}Li production in novae[2] are now firmly supported. The present results also demonstrate that a combination of Coulomb and nuclear dissociation measurements is a powerful tool for spectroscopy of unstable nuclei.

*1 Rikkyo University
*2 University of Tokyo
*3 ATOMKI, Hungary
*4 Ewha Womens University, Korea
*5 Tohoku University
*6 Tokyo Institute of Technology

References

1) M. Wiescher, J. Görres, S. Graff, L. Buchmann, and F.-K. Thielemann: Astrophys. J. **343**, 352 (1989).
2) H. M. J. Boffin, G. Paulus, M. Arnould, and N. Mowlavi: Astron. Astrophys. **279**, 173 (1993).
3) T. Motobayashi et al.: RIKEN Accel. Prog. Rep. **33**, 60 (2000).
4) I. Hisanaga et al.: RIKEN Accel. Prog. Rep. **31**, 162 (1998).
5) P. Descouvemont: Astrophys. J. **405**, 518 (1993); Nucl. Phys. A **646**, 261 (1999).
6) Y. Kanada-En'yo and H. Horiuchi: Phys. Rev. C **55**, 2860 (1997).
7) D. Beaumel et al.: Phys. Lett. B **514**, 226 (2001).
8) L. Trache, F. Carstoiu, A. M. Mukhamedzhanov, and R. E. Tribble: Phys. Rev. C **66**, 035801 (2002).

In-beam γ spectroscopy of neutron-rich B isotopes

Y. Kondo,[*1] T. Nakamura,[*1] N. Fukuda, T. Sugimoto,[*1] M. Miura,[*1] N. Aoi,[*2] N. Imai,[*2] T. Kubo, T. Kobayashi,[*3] T. Gomi,[*4] A. Saito,[*4] H. Sakurai,[*2] S. Shimoura,[*2] D. Bazin,[*5] H. Hasegawa,[*4] H. Baba,[*4] T. Motobayashi, T. Yakushiji,[*3] Y. Yanagisawa, K. Yoneda, K. Watanabe,[*3] Y. X. Watanabe,[*6] and M. Ishihara

[NUCLEAR REACTIONS: ^{12}C(^{17}B,^{15,17}B*), in-beam γ spectroscopy]

We investigated excited states in neutron-rich boron isotopes by in-beam γ spectroscopy through the breakup and inelastic scattering of ^{17}B. Neutron-rich B isotopes are considered to have a unique feature such as a halo or a cluster. In a previous theoretical study, it was predicted that, with increase in neutron number, B isotopes have a clustering structure.[1] In a recent experiment, a two-neutron halo structure in ^{17}B was observed.[2]

The experiment was performed at the in-flight radioactive-isotope beam separator, RIPS. A ^{22}Ne beam at 110 MeV/u was bombarded on a Be target with 6 mm thickness to produce a secondary ^{17}B beam. The intensity of the secondary beam separated by RIPS was about 700 cps. The purity of the ^{17}B beam was 85%. Particle identification of the secondary beam was carried out event-by-event using the time-of-flight (TOF) information between the cyclotron RF and a plastic scintillator with 1 mm thickness placed at the second focal point (F2). A ^{12}C target with a thickness of 377 mg/cm^2 was placed downstream of the third focal point (F3), and used for generating excited B isotopes by the breakup or inelastic scattering of ^{17}B. The energy of the ^{17}B beam was about 73 MeV/u at the middle of the ^{12}C target. The position and the incident angle of the secondary beam at the ^{12}C target were measured using two sets of parallel-plate avalanche counters (PPACs) placed at F3.

The outgoing B isotopes downstream of the ^{12}C target were analyzed using a magnetic spectrometer equipped with two drift chambers (FDC1 and FDC3) and a plastic scintillator hodoscope. Particle identification of outgoing B isotopes was performed by combining the ΔE and TOF information from the hodoscope, and the magnetic rigidity information from the drift chambers.

Thirty-six blocks of NaI(Tl) scintillators surrounded the ^{12}C target in order to measure γ rays. Each scintillator crystal had a size of $6 \times 6 \times 12$ cm^3. Doppler shift was corrected using the detector angle in the beamdirection and the velocity ($\beta \approx 0.37$) of outgoing B isotopes.

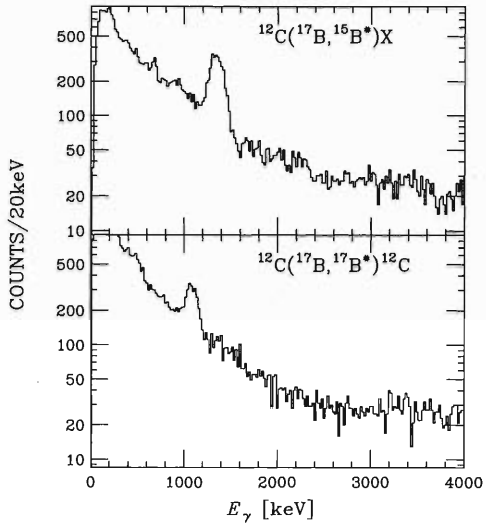

Fig. 1. Doppler-corrected energy spectra of γ rays coincidence with ^{15}B (upper) and ^{17}B (lower).

Figure 1 shows the preliminary γ-ray energy spectra obtained coincidence with outgoing ^{15}B and ^{17}B from the ^{12}C target. A peak is clearly observed at 1.3 MeV in the case of ^{15}B, and at 1 MeV in the case of ^{17}B. Assignments of these multipolarities of transitions were not made. We also measured ^{12}C(^{15}B,^{15}B*) using the secondary ^{15}B beam. Thus, we expect to assign the multipolarities based on angular distributions of ^{15}B and ^{17}B scattered inelastically. Further analysis is now in progress.

References

1) Y. Kanada-En'yo and H. Horiuchi: Phys. Rev. C **52**, 647 (1995).
2) T. Suzuki et al.: Phys. Rev. Lett. **89**, 12501 (2002).

*1 Tokyo Institute of Technology
*2 University of Tokyo
*3 Tohoku University
*4 Rikkyo University
*5 National Superconducting Cyclotron Laboratory, Michigan State University, USA
*6 High Energy Accelerator Research Organization (KEK)

Momentum distribution of ^{15}B fragments from the breakup of ^{17}B†

T. Suzuki,[*1] Y. Ogawa,[*2] M. Chiba,[*3] M. Fukuda,[*2] N. Iwasa,[*3] T. Izumikawa,[*4] R. Kanungo, Y. Kawamura,[*1] A. Ozawa, T. Suda, I. Tanihata, S. Watanabe,[*1] T. Yamaguchi, and Y. Yamaguchi[*1]

[Neutron halo, Fragmentation cross section, Unstable nuclei]

Halo nuclei are characterized by weak binding of the last bound nucleon (or nucleons), large reaction cross sections, large *r.m.s.* matter radii, narrow momentum distributions following fragmentation and concentration of the dipole breakup strengths at low continuum energies. These features are most clearly seen for the last two neutrons in ^{6}He and ^{11}Li and for the last neutron in ^{11}Be and ^{19}C. The neutron-rich nuclei ^{14}Be and ^{17}B have been considered to be "candidate" halo systems since the observation of their large matter radii.[1] ^{17}B has bulk properties similar to those of ^{14}Be. The matter radius[2] and the two-neutron separation energy (S_{2n})[3] are reported to be 3.10 ± 0.15 fm and 1.34 ± 0.11 MeV for ^{14}Be and 2.99 ± 0.09 fm and 1.39 ± 0.14 MeV for ^{17}B, respectively. The radii of ^{14}Be and ^{17}B are much larger than those of ^{12}Be (2.59 ± 0.06 fm[1]) and ^{15}B (2.59 ± 0.03 fm[4]).

Both the angular distribution of neutrons[5] and the longitudinal momentum distribution[6] of ^{12}Be produced by the breakup of ^{14}Be exhibit narrow widths indicative of a halo structure in ^{14}Be. Recently, an experiment on ^{14}Be has been performed by Labiche *et al.*[7] The two-neutron removal cross section (σ_{-2n}), neutron angular distributions and invariant mass spectra characteristic of a halo structure were observed, thus establishing a halo structure in ^{14}Be. However, little is known about ^{17}B aside from its matter radius, and therefore it is important to measure the longitudinal momentum ($p_{\parallel}$) distribution for ^{15}B fragments from the breakup of ^{17}B,[8] in order to obtain more detailed structure information. In this letter, we report the new results obtained from measurements of the $p_{\parallel}$ distribution and σ_{-2n} of ^{17}B after breakup on a Be target at 70 A MeV incident energy, performed at the RIken Projectile fragment Separator (RIPS).[9]

The ^{17}B beam (~30 pps) was delivered from the RIPS as follows: A 110A MeV ^{22}Ne primary beam was used to bombard a Be (920 mg/cm^2) production target. A thick, wedge-shaped Al degrader was placed at the first focal plane (F1) of the RIPS. The momentum spread in a beam of $\pm 0.25\%$, determined by the slit at F1, was measured by the time-of-flight (TOF) between plastic scintillators (0.5 mm thick) located at F1 and at the achromatic focus (F2). The distance between these foci was 10.8 m. Particles were identified by the $B\rho$-TOF-ΔE technique. The energy loss was measured in a Si-detector (350 μm thick) at F2 as well as in the scintillators. Additionally, the TOF with the rf signal from the accelerator was used. The impurity in the ^{17}B beam was reduced to less than one part in 10^5 in the off-line analysis. The mean energy of the beam was 70A MeV at the midpoint of the secondary reaction target (Be; 277 mg/cm^2 × 30 mmϕ) placed at F2. The beam position at the reaction target was restricted by a collimator ($\pm$10 mm) located 10 cm upstream from the reaction target, and was measured using a parallel-plate avalanche counter (PPAC).

The charged fragments from the breakup were transported to the final focus (F3) through triplet Q magnets, located 1.5 m downstream from the reaction target with an opening of 17.2 cmϕ. Particles were tracked by PPACs and identified using a large-area Si-NaI telescope (three layers of Si 5 × 5 cm^2 × 500 μm, and NaI 3"ϕ × 6 cm). The velocity of a fragment was determined by the TOF between F2 and F3 with a path length of 6.0 m. A TOF calibration was performed for section F1-F2 using primary beams with energies of 110 A, 84.6 A, and 59.8 A MeV and for section F2-F3 by changing the magnetic field of the second dipole magnet by $\pm$2.5%. The total momentum resolution of the system was 33 MeV/c (0.6%) in FWHM or 14 MeV/c in σ.

The background-subtracted distribution, which is in the projectile rest frame, is characterized by a FWHM of 80 ± 10 MeV/c for ^{15}B. The two-neutron removal cross section (σ_{-2n}) is found to be 0.22 ± 0.05 b. A Glauber-type analysis of the data provides clear evidence of a two-neutron halo structure in ^{17}B.

References

1) I. Tanihata et al.: Phys. Lett. B **206**, 592 (1988).
2) T. Suzuki et al.: Nucl. Phys. A **658**, 313 (1999).
3) G. Audi, O. Bersillon, J. Blachot, and A. H. Wapstra: Nucl. Phys. A **624**, 1 (1997).
4) A. Ozawa et al.: Nucl. Phys. A **608**, 63 (1996).
5) K. Riisager et al.: Nucl. Phys. A **540**, 365 (1992).
6) M. Zahar et al.: Phys. Rev. C **48**, R1484 (1993).
7) M. Labiche et al.: Phys. Rev. Lett. **86**, 600 (2001).
8) I. Tanihata: J. Phys. G: Nucl. Part. Phys. **22**, 157 (1996).
9) T. Kubo et al.: Nucl. Instrum. Methods Phys. Res. B **70**, 309 (1992).

† Condensed from the article in Phys. Rev. Lett. **89**, 12501 (2002)

*1 Department of Physics, Niigata University
*2 Department of Physics, Osaka University
*3 Department of Physics, Tohoku University
*4 Radio-Isotope Center, Niigata University

Breakup reaction of ^{17}B

T. Sugimoto,[*1] T. Nakamura,[*1] N. Fukuda, M. Miura,[*1] Y. Kondo,[*1] N. Aoi,[*2] N. Imai,[*2] T. Kubo, T. Kobayashi,[*3] T. Gomi,[*4] A. Saito,[*4] H. Sakurai,[*2] S. Shimoura,[*5] D. Bazin,[*6] H. Hasegawa,[*4] H. Baba,[*4] T. Motobayashi, T. Yakushiji,[*3] Y. Yanagisawa, K. Yoneda, K. Watanabe,[*3] Y. X. Watanabe,[*7] and M. Ishihara

[NUCLEAR REACTIONS: ^{208}Pb, ^{12}C(^{17}B, ^{12,13,14,15}BX), Coulomb dissociation, Nuclear breakup]

To investigate low-lying excited states of ^{17}B and its cluster structure in the ground state, we have measured the Coulomb and nuclear breakup reactions.[1] For the first objective, we study the correlation between the core nucleus and neutrons[2] such as the ^{15}B + 2n system. This study will give us an insight into the halo structure of ^{17}B. For the latter one, we study the systematics of the cross sections for different fragments produced from ^{17}B. These fragments are considered to be reflecting the cluster structure of the nucleus.[3]

The experiment was performed at the RIKEN Accelerator Research Facility. A 6-mm-thick Be production target was bombarded with a beam of 110 MeV/nucleon ^{22}Ne. The secondary ^{17}B beam was selected by the RIKEN Projectile-fragment Separator (RIPS).[4] The energy of ^{17}B beam was 75.0 MeV/nucleon on the secondary target, the intensity was about 700 cps, and the purity was 85%. Using this beam, we measured the cross sections of ^{208}Pb(^{17}B, $^{12-15}$B X) and ^{12}C(^{17}B, $^{12-15}$B X).

The momentum vectors of the secondary beam were obtained by tracing the trajectory using two parallel plate avalanche counters, and by measuring the time of flight (TOF) between cyclotron RF signal and a 1.0-mm-thick plastic scintilllation counter (SF2) located downstream of the RIPS F2 focal point. The secondary lead (346 mg/cm^2) and carbon (377 mg/cm^2) targets were bombarded by the ^{17}B beam. The outgoing charged fragment was bent by the dipole magnet and measured using the drift chamber placed at the exit of the magnet. The TOF was measured by the hodoscope located downstream of the drift chamber. The hodoscope was composed of seven plastic scintillators, each having a thickness of 1.0 cm. Neutrons were measured by 54 rods of plastic scintillation counters. These rods were arranged into two walls. Each wall is placed at 4.7 m and 5.8 m downstream from the secondary target. The measured TOF of neutrons and hit position were used to reconstruct momentum vectors of neutrons.

In the analysis, ^{17}B was identified using the TOF of the incident ion and the pulse height of SF2. The charge of the fragment was identified using the pulse height of the hodoscope, and the mass was identified using the TOF and the track of the drift chamber.

Figure 1 shows the preliminary result of neutron removal cross sections for ^{208}Pb, ^{12}C(^{17}B, $^{12-15}$B n X). The efficiency and the acceptance are not incorporated. For both of the targets, the breakup cross sections for ^{13}B and ^{15}B are larger than those of ^{12}B and ^{14}B. The cross sections for ^{13}B and ^{15}B with a lead target are higher than those with a carbon target. We have also deduced the inclusive cross section of ^{17}B $\rightarrow$ ^{15}B + X, which is consistent with the report in Ref. 5.

We will analyze the momentum vectors of charged particle and neutrons, and deduce the mass spectrum of ^{15}B + n and ^{15}B + 2n.

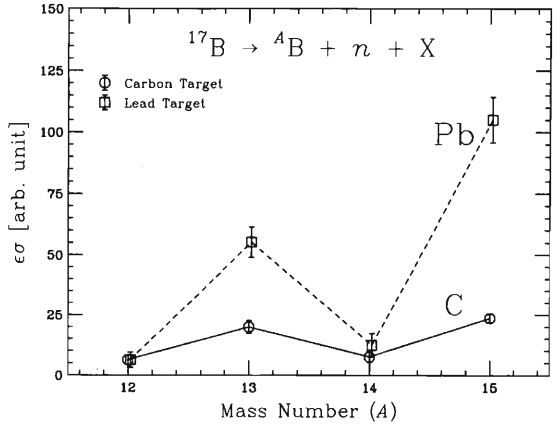

Fig. 1. Neutron removal cross sections of ^{17}B $\rightarrow$ $^{12-15}$B + n + X by Coulomb and nuclear breakup reaction. The efficiency and the acceptance are not incorporated.

*1 Tokyo Institute of Technology
*2 University of Tokyo
*3 Tohoku University
*4 Rikkyo University
*5 Center for Nuclear Study, University of Tokyo
*6 National Superconducting Cyclotron Laboratory, Michigan State University, USA
*7 Institute of Particle and Nuclear Studies, High Energy Accelerator Research Organization (KEK)

References

1) T. Nakamura et al.: RIKEN Accel. Prog. Rep. **35**, 57 (2002).
2) M. Labiche et al.: Phys. Rev. Lett. **86**, 600 (2001).
3) Y. Kanada-En'yo and H. Horiuchi: Phys. Rev. C **52**, 647 (1995).
4) T. Kubo et al.: Nucl. Instrum. Methods Phys. Res. B **70**, 309 (1992).
5) T. Suzuki et al.: Phys. Rev. Lett. **89**, 12501 (2002).

Proton inelastic scattering of ^{16}C

H. J. Ong,[*1] N. Imai,[*1] N. Aoi,[*1] H. Sakurai,[*1] Zs. Dombrádi,[*2] A. Saito,[*3] Z. Elekes,[*4] H. Baba,[*3] K. Demichi,[*3] Zs. Fülöp,[*2] J. Gibelin,[*5] T. Gomi,[*3] H. Hasegawa,[*3] M. Ishihara, H. Iwasaki,[*6] S. Kanno,[*3] S. Kawai,[*3] T. Kubo, K. Kurita,[*3] Y. U. Matsuyama,[*3] S. Michimasa,[*6] T. Minemura, T. Motobayashi, M. Notani,[*6] S. Ota,[*7] H. K. Sakai,[*3] S. Shimoura,[*6] E. Takeshita,[*6] S. Takeuchi, M. Tamaki,[*6] Y. Togano,[*3] K. Yamada,[*3] Y. Yanagisawa, and K. Yoneda

[NUCLEAR REACTION: ^{16}C(p,p'), 47AMeV, Inelastic Scattering, Cross Section]

One of the exotic phenomena predicted for unstable nuclei is the differences of deformation parameters between proton and neutron matters.[1,2] The combination of electromagnetic and nuclear excitations from the ground states to the first 2^+ states leads to a possible determination of the deformation parameters for each matter.[3–5] In this respect, the proton inelastic scattering at intermediate energies is a powerful tool for probing the neutron matter because of its high sensitivity to neutrons.[6]

We have performed an experiment at RIKEN to measure the inelastic proton-scattering cross section on ^{16}C. A primary beam of ^{40}Ar at 94 A MeV bombarded ^{9}Be target of 744 mg/cm^2 thickness, producing the ^{16}C beam which was later separated from the other beams by the RIKEN Projectile-fragment Separator (RIPS).[7] The energy of ^{16}C was 47A MeV at the final focal plane, F3, and the momentum acceptance was set at 1%.

The secondary beams were identified by time-of-flight information between two plastic scintillators of 1 mm thickness, placed at F2 and F3. The ^{16}C beam bombarded a liquid hydrogen target with an average thickness of 210 mg/cm^2. The angular distribution for the inelastic scattering was measured by three parallel-plate avalanche counters, two of them placed upstream and the remaining one placed downstream of the target.

Particle identification of the scattered particles was performed using a four-layer-silicon-telescope. Each layer has four silicon detectors, each with an effective detection area of 50×50 mm^2, placed in a 2×2 matrix. The thicknesses of the silicon detectors placed in the first, second, third and fourth layer are 0.5, 0.5, 1.0 and 0.5 mm, respectively. The ^{16}C nuclei were stopped in the third layer of the silicon detectors and were identified by the $\Delta E - E$ method.

Instead of measuring scattered protons, we detected de-excitation γ-rays emitted in coincidence with the scattered ^{16}C's. The de-excitation γ-rays from the first excited state of ^{16}C were detected by the DALI2 detector array,[8] consisting of 116 NaI(Tl) scintillators with a size of $40 \times 80 \times 160$ mm^3, plus 30 additional NaI(Tl)'s of the size $60 \times 60 \times 120$ mm^3. Both of them were placed around the secondary target.

Figure 1 shows a Doppler shift corrected γ-spectrum detected by NaI(Tl)'s. The peak around 1.77 MeV corresponds to the γ-ray from the first excited state. Further analysis is in progress.

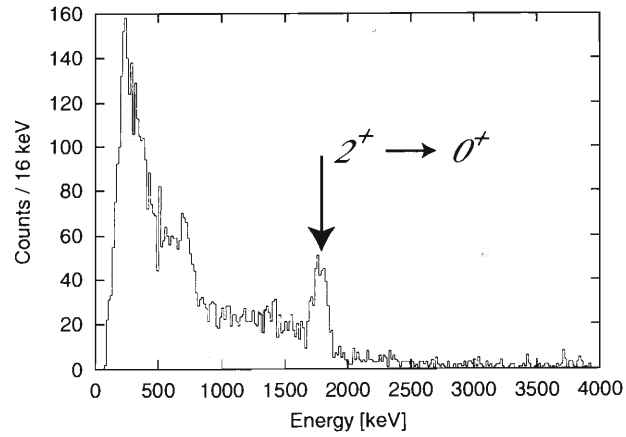

Fig. 1. Doppler-shift corrected γ-ray energy spectrum for ^{16}C.

*1 Department of Physics, University of Tokyo
*2 ATOMKI, Hungary
*3 Department of Physics, Rikkyo University
*4 On leave from ATOMKI, Hungary
*5 Institut de Physique Nucléaire, France
*6 Center for Nuclear Study, University of Tokyo
*7 Department of Physics, Kyoto University

References

1) H. Horiuchi and Y. Kanada-En'yo: Nucl. Phys. A **616**, 394c (1997).
2) Y. Kanada-En'yo and H. Horiuchi: Phys. Rev. C **55**, 2860 (1997).
3) J. H. Kelley et al.: Phys. Rev. C **56**, R1206 (1997).
4) A. Krasznahorkay et al.: RIKEN Accel. Prog. Rep. **34**, 67 (2001).
5) N. Imai et al.: RIKEN Accel. Prog. Rep. **36**, 63 (2003).
6) H. Iwasaki et al.: Phys. Lett. B **481**, 7 (2000).
7) T. Kubo et al.: Nucl. Instrum. Methods Phys. Res. B **70**, 309 (1992).
8) H. Hasegawa et al.: RIKEN Accel. Prog. Rep. **35**, 169 (2002).

Measurement of reaction cross section for ^{16}C and finite-range Glauber model analysis†

T. Zheng,[*1,*2] T. Yamaguchi,[*3] A. Ozawa, M. Chiba,[*4] R. Kanungo, T. Kato, K. Katori, K. Morimoto, T. Ohnishi, T. Suda, I. Tanihata, Y. Yamaguchi,[*5] A. Yoshida, K. Yoshida, H. Toki,[*6] and N. Nakajima[*6,*7]

[^{16}C, TOF-ΔE-E method, measured reaction cross section, finite-range Glauber-model calculation, effective range parameter, deduced effective density of ^{16}C]

Motivated by the measurement of the interaction cross section for carbon isotopes at energy ~960 A MeV,[1] the reaction cross section for ^{16}C was measured at the energy of 83 A MeV.[2] The large enhancement of the ^{16}C reaction cross section at the low energy was considered in the study of the density distribution of ^{16}C.

The experiment was performed at the RIKEN projectile-fragment separator (RIPS) in the RIKEN Accelerator Research Facility in July 2001. Secondary ^{16}C beams were produced *via* the projectile fragmentation of a ^{22}Ne primary beam that was accelerated to ~110 A MeV by the RIKEN Ring Cyclotron (RRC). The beryllium production targets of 2 and 4 mm thicknesses were used.

Before a secondary reaction target, ^{16}C was identified and isolated from the other nuclei by the Bρ-ΔE-TOF method. The reaction target was a carbon plate of 370 mg/cm^2 thickness, which was placed at F2. After the reaction target, the particles were identified with the TOF-ΔE-E method, which was a new method for the reaction-cross-section measurement. In addition to the usual ΔE-E measurement, the present method also measured the time-of-flight. The reaction products were transported downstream of the beam line by the last quadrupole triplet. Detectors were placed at the final focus F3 of the RIPS. The TOF was measured by the timing difference of the F2 plastic counter and F3 plastic counter. The energy loss (ΔE) was measured by three silicon detectors (50×50 mm$^2 \times 150$ μm). The total energy (E) was measured by a NaI(Tl) detector (3"$\phi \times 60$ mm). This method overcame the shortcomings of the conventional ΔE-E method by which it was difficult to separate the reactions in the target from those in the detectors. By the present experimental system, the reactions that occurred at different places were well separated because they gave different TOF values. In order to obtain the σ_R value of ^{16}C, the number of inelastically scattered ^{16}C was subtracted from the total number of ^{16}C. The measured reaction cross section is shown in Fig. 1 as a solid circle.

The finite-range Glauber-model calculation[3] was introduced to determine the structure of ^{16}C. The range parameters β_{ij} were fixed by fitting the ^{12}C+^{12}C reaction cross sections from 30 A MeV to 1 A GeV. This method was confirmed to be efficient in reproducing the ^{14}C+^{12}C reaction cross section. Based on the assumption that ^{16}C was a three-body system composed of a core (^{14}C) and two valence neutrons, the possible halo structure of ^{16}C was studied. The $s_{1/2}$ configuration of the valence neutrons was found to be dominant.

Assuming the density distribution was HO-type density distribution with a Yukawa-square tail, the effective density of ^{16}C was obtained through the χ^2-fitting procedure. The result showed that a long low-density tail was necessary to reproduce the cross sections with minimal assumptions. This observation suggested the formation of a neutron halo in the ^{16}C nucleus.

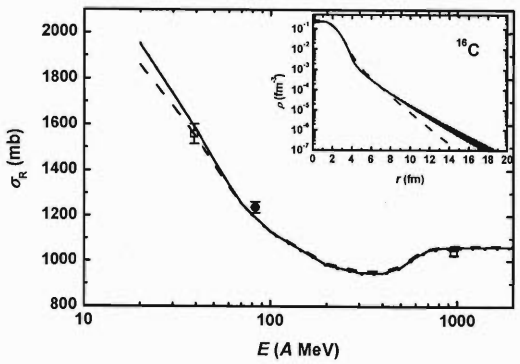

Fig. 1. Reaction cross section for ^{16}C on carbon target. The finite-range Glauber-model calculation using the HO+Yukawa-square density, while all the parameters were determined by the best fitting to the experimental data, is shown in the figure by the solid line. For comparison, the calculation using a density of core+$(2s_{1/2})^2$ is also shown by the dashed line. The densities are shown in the inset using the same denotations.

† Condensed from the article in Nucl. Phys. A **709**, 103 (2002)

*1 Department of Physics, Tokyo University of Science
*2 Department of Technical Physics, Peking University, China
*3 Present address; KPII, GSI, Germany
*4 Department of Physics, Tohoku University
*5 Department of Physics, Niigata University
*6 Research Center for Nuclear Physics, Osaka University
*7 Present address; Kochi Medical School

References

1) A. Ozawa et al.: Nucl. Phys. A **691**, 599 (2001).
2) T. Yamaguchi et al.: RIKEN Accel. Prog. Rep. **35**, 64 (2002).
3) Y. Ogawa et al.: Nucl. Phys. A **543**, 722 (1992), and references therein.

Momentum distributions of ^{14}C and ^{15}C fragments from ^{16}C breakup

T. Yamaguchi,[*1] T. Zheng,[*2,*3] A. Ozawa, M. Chiba,[*4] R. Kanungo, T. Kato, K. Morimoto, T. Ohnishi, T. Suda, Y. Yamaguchi,[*5] A. Yoshida, K. Yoshida, and I. Tanihata

[NUCLEAR REACTIONS: C(^{16}C, ^{15}C), C(^{16}C, ^{14}C), $E = 83$ A MeV; measured longitudinal momentum distributions; few-body Glauber calculations]

Recently, the reaction cross section of ^{16}C has been measured at 83 A MeV.[1] In spite of the relatively large separation energy, $S_n = 4.25$ MeV, the reaction cross section showed anomalously large enhancement. This could be explained with a halo-like s-wave component in the ^{14}C + 2n model.[1] In the present study, we have simultaneously measured the longitudinal momentum distributions of ^{14}C and ^{15}C fragments from ^{16}C breakup at 83 A MeV, to investigate the configuration of valence neutrons more quantitatively.

The experiment was performed at the RIKEN Projectile fragment Separator (RIPS) using the newly developed time-of-flight (TOF) technique.[2,3] ^{22}Ne of 110 A MeV bombarded a Be target to produce ^{16}C through the projectile fragmentation. The separation technique of the secondary beam was based on the combination of magnetic rigidity selection and energy loss analysis. We set a carbon target (370 mg/cm^2) as a reaction target at the achromatic focus F2. The fragments produced in the carbon target were transported 5.5 m downstream and focused by a quadrupole triplet at the final focus F3. The fragments were identified with the TOF-ΔE-E method. Ultrafast plastic scintillation counters[2] (0.5 mm thick at F2, 1.5 mm thick at F3) were used for TOF measurement to obtain the fragment momentum. The momentum resolution was estimated to be 25 MeV/c in σ. Three Si detectors (50×50 mm^2, 150 μm thick) were used to identify the charge of the fragments, and a NaI(Tl) detector (3"$\phi \times$ 60 mm) was used to measure the total energy.

The obtained momentum distributions of ^{15}C and ^{14}C are shown in Fig. 1 (a) and (b), respectively. We fitted these spectra by Lorentzian functions folded by the system resolution. The fits resulted in the widths of 90 ± 9 MeV/c and 142 ± 14 MeV/c in FWHM for ^{15}C and ^{14}C, respectively.

A few-body Glauber analysis[4] was performed for the ^{15}C distribution. We applied ^{15}C + n structure for ^{16}C. The wavefunction of the valence neutron was obtained by solving the eigenvalue problem in a Woods-Saxon potential for $s_{1/2}$ or $d_{5/2}$. The depth of the potential was adjusted to reproduce the experimental one neutron separation energy. For $d_{5/2}$, the core of ^{15}C is assumed to be in its first excited state. A harmonic-oscillator-type ^{15}C core density profile was calculated so as to reproduce the interaction cross section at $\sim$ 950 A MeV.[5] We performed χ^2-fitting by adjusting the mixing ratio of the s- to d-components. The best fit resulted in the s-wave component of 35 ± 20%, which is consistent with the ones reported by Sauvan *et al.*[6] and Maddalena *et al.*[7]

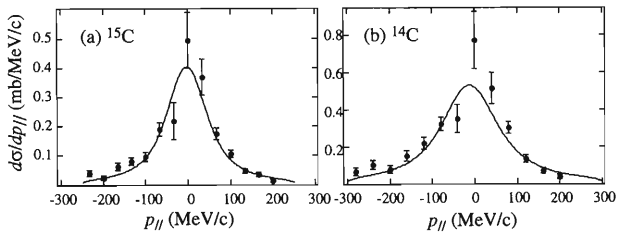

Fig. 1. Longitudinal momentum distributions of ^{15}C and ^{14}C from ^{16}C breakup.

For the ^{14}C distribution, we introduced a phenomenological method. We assumed a ^{14}C + 2n structure for ^{16}C. The wavefunctions of the valence neutrons were obtained similarly to the one mentioned above. The separation energy was taken as $S_{2n}/2$ for one neutron. The ^{14}C core density profile was determined so as to reproduce the interaction cross section.[5] After calculating the momentum distribution of one neutron removal, the effect of the motion of the second neutron was included by folding. χ^2-fitting resulted in the s-wave component of 31 ± 18%. The s-wave components of ^{14}C and ^{15}C are thus in agreement with each other and are around 30%. The contribution of s-wave of valence neutrons in ^{16}C is smaller than that in halo nucleus ^{15}C where the s-wave component is dominant. This suggests that ^{15}C in ^{16}C is not the same as that in free space. However, the present result indicates a discrepancy with that of the reaction cross sections. Further theoretical developments are necessary.

*1 Present address; KP2, GSI, Germany
*2 Department of Physics, Tokyo University of Science
*3 Department of Technical Physics, Peking University, China
*4 Department of Physics, Tohoku University
*5 Department of Physics, Niigata University

References
1) T. Zheng et al.: Nucl. Phys. A **709**, 103 (2002).
2) R. Kanungo et al.: Phys. Rev. Lett. **88**, 142502 (2002).
3) T. Suzuki et al.: Phys. Rev. Lett. **89**, 12501 (2002).
4) Y. Ogawa et al.: Prog. Theor. Phys. Supple., No. 142, 157 (2001).
5) A. Ozawa et al.: Nucl. Phys. A **691**, 599 (2001).
6) E. Sauvan et al.: Phys. Lett. B **491**, 1 (2000).
7) V. Maddalena et al.: Phys. Rev. C **63**, 024613 (2001).

Measurement of longitudinal momentum distribution of ^{19}C

M. Chiba,[*1] R. Kanungo, B. Abu-Ibrahim, S. Adhikari,[*2] D. Q. Fang, N. Iwasa,[*1] K. Kimura,[*3] K. Maeda,[*1] S. Nishimura, T. Ohnishi, A. Ozawa, C. Samanta,[*2] T. Suda, T. Suzuki,[*4] Q. Wang, C. Wu, K. Yamada,[*5] Y. Yamaguchi,[*4] A. Yoshida, T. Zheng,[*6] and I. Tanihata

[NUCLEAR STRUCTURE, ^{19}C, Momentum distiribution, TOF]

We have measured the one- and two-neutron removal cross sections and longitudinal momentum distribution of ^{19}C. Several experiments suggested that ^{19}C has a one-neutron halo structure.[1-3] This attracted much attention as this indicates that ^{19}C is a one-neutron halo candidate as is ^{11}Be.[4] Recently Kanungo *et al.*[5] analyzed the interaction cross section and the one-neutron removal momentum distribution data of ^{19}C in a few-body Glauber model, and found it difficult to describe both sets of data consistently. To probe the cause for this anomaly we have measured the two-neutron removal momentum distribution and removal cross section in addition to the one-neutron removal distribution and cross section. Multi-nucleon removal momentum distribution and cross section can be a tool to investigate the orbital configuration of core and valence neutrons.[6]

We have measured the time-of-flight (TOF) of fragments to determine their longitudinal momenta. Owing to the large momentum acceptance, the tail of the fragmentaion peak in the momentum distribution is covered in a single experimental setting.

The experiment was performed using the RIKEN projectile fragment separator (RIPS). A primary ^{22}Ne beam at $\sim$100 A MeV was impinged on a 462 mg/cm^2 Be target to produce a ^{19}C secondary beam. A 1244 mg/cm^2 aluminum wedge degrader was placed at the dispersive focus of RIPS. The momentum acceptance of RIPS was restricted to $\pm$1.25%. We installed a 1.0-mm-thick plastic scintillator at the dispersive focus, F1. A system consisting of a 7×7 cm^2 BICRON BC420 plastic scintillator and a HAMAMATSU R4998 phototube gave a very fast timing response, and a typical time resolution of $\sim$30 ps in FWHM was achieved. The typical primary beam intensity was $\sim$1.0 eμA just before F0.

At the first achromatic focus (F2), we installed a 350 mg/cm^2 Si detector. Following that was installed a 370 mg/cm^2 Be target whose diameter was 50 mm. For beam tracking, two PPACs were installed in front of the target and one PPAC after the target. We also installed a 0.5-mm-thick plastic scintillator just after the target. The energy of ^{19}C incident on the target was $\sim$70 A MeV.

Another 1.5-mm-thick scintillator was located 5.5 m downstream at the final achromatic focus (F3). Two PPACs located upstream of the plastic tracked particles. An ionization chamber and a 3"$\phi \times$ 6 cm NaI(Tl) crystal were also installed at F3. The ionization chamber provides ΔE information. The NaI(Tl) scintillator was used as a total energy detector and was surrounded by thick plastic scintillators which were used for estimating nuclear reaction events in NaI(Tl).[7] The reaction in the NaI(Tl) is the major source of background in this measurement. The use of the plastic veto detectors provided a $\sim$90% rejection efficiency.

Particle identification (PID) of the secondary beam was performed by the magnetic rigidity (Bρ)-ΔE-TOF method. The ratio of impurity in the ^{19}C beam was estimated to be $\sim 10^{-5}$ after the PID. After the secondary target, reaction products were identified by the ΔE-TOF-E method as shown in Fig. 1. Momentum resolution in this experiment was estimated to be $\sim$10 MeV/c. Further analysis is in progress.

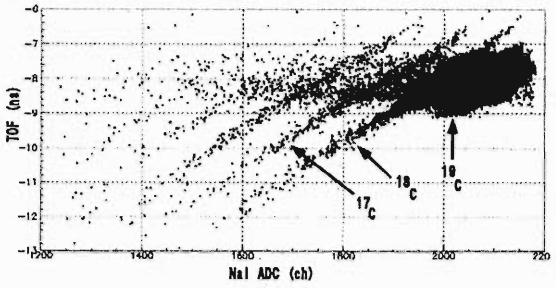

Fig. 1. Particle identification plot at F3. Fragments of ^{19}C are clearly identified.

References

1) D. Bazin et al.: Phys. Rev. C **57**, 2156 (1998).
2) T. Baumann et al.: Phys. Lett. B **439**, 256 (1998).
3) T. Nakamura et al.: Phys. Rev. Lett. **83**, 1112 (1999).
4) I. Tanihata et al.: Phys. Lett. B **206**, 4 (1988).
5) R. Kanungo et al.: Nucl. Phys. A **677**, 171 (2000).
6) R. Kanungo et al.: Phys. Rev. Lett. **88**, 142502 (2002).
7) T. Suda et al.: RIKEN Accel. Prog. Rep. **35**, 171 (2002).

*1 Tohoku University
*2 Saha Institute of Nuclear Physics, India
*3 Nagasaki Institute of Applied Science
*4 Niigata University
*5 Rikkyo University
*6 Peking University, China

Study of spin polarization of ^{19}C and ^{19}N for g-factor measurement

D. Kameda,* H. Ueno, K. Asahi, A. Yoshimi, W. Sato, H. Miyoshi,* H. Watanabe, J. Murata, Y. Kobayashi, J. Kaihara,* and K. Shimada*

[NUCLEAR STRUCTURE, ^{19}C, ^{19}N, Spin polarization, β-NMR method]

The magnitude of the spin polarization of ^{19}C and ^{19}N was studied in order to measure the g factor by means of the β-NMR method.[1] The magnitude strongly depends on two physical processes, induction of the spin polarization in the fragmentation reaction and preservation of the spin polarization in the stopper material in which these nuclei are implanted. The purpose of this study is to investigate suitable production targets and stopper conditions for obtaining a sufficiently large magnitude of spin polarization for g-factor measurements.

^{19}C was obtained from the fragmentation of ^{22}Ne projectiles at an energy of 110 MeV/nucleon on two types of target, $^{12}C_{nat}$ of 546 mg/cm^2 thickness and ^{93}Nb of 778 mg/cm^2 thickness. The fragment was isotope-separated and accepted by RIPS at optimized emission angle and momentum for the induction of spin polarization, as summarized in Table 1. It is noted that the momentum acceptance was taken from the peak of the momentum distribution of the fragment to the high momentum which is 6% larger than the peak. ^{19}N was obtained by the same procedure as in the case of ^{19}C. These fragments were then implanted in a stopper material to which a magnetic field of $B_0 = 40.07$ mT was applied. For the preservation of the spin polarization, appropriate stopper materials should be chosen so that they can provide a sufficiently long relaxation time compared with the β-decay lifetime of each nucleon. In the case of $J^\pi(^{19}C_{g.s.}) = 1/2^+$, graphite can be used because of the long relaxation time observed in the research of $^{15}C(J^\pi = 1/2^+)$.[1] This material, however, might not be applicable for the cases of $J^\pi(^{19}C_{g.s.}) = 3/2^+$ and $5/2^+$ because of the effect of ^{19}C quadrupole relaxation. Pt is known to be applicable to these cases based on results of the g-factor measurement of ^{17}C.[2] In this study, the preservation of spin polarization can be achieved using both stoppers in each target.

We can measure the magnitude under each condition by observing the β-ray asymmetry change when the nuclear spin in a stopper is flipped by the adiabatic field rotation method.[3] This technique has the great advantage of causing an asymmetry change without any information concerning the NMR parameters, including the g factor. The experimental results are summarized in Table 2 together with those of a previous study[4] using a Be target.

The experimental result of ^{19}C shows that $A_\beta P$ of ^{19}C is significantly small without ambiguity of the relaxation time in the stopper material. The result indicates that either the spin polarization that is induced in the fragmentation reaction is very small or the analyzing power of ^{19}C, which is still unknown, is very small or both are small. On the other hand, we found sufficient magnitude in the ^{19}N case in which a cooled Pt stopper is used. The first g factor measurement was performed. This analysis is now in progress.

Table 1. Parameters for RIPS acceptance.

Nucleon	Target	θ	p (GeV/c)
^{19}C	C_{nat}	1.2°–5.9°	7.93–8.42
	Nb	0.3°–6.0°	7.90–8.52
^{19}N	C_{nat}	2.6°–6.0°	8.15–8.73
	Nb	1.6°–6.0°	8.24–8.53

Table 2. $A_\beta P$ is the β-ray asymmetry change, where P is the spin polarization and A_β is the analyzing power. The Pt stopper is cooled at 22 (15) K for a long relaxation time in ^{19}C(^{19}N) measurement. The experimental result of using the Be target is cited from Ref. 4. In Ref. 4, a Pt stopper was used at room temperature (r.t.).

Nucleon	Target	Stopper	$A_\beta P$ (%)
^{19}C	C_{nat}	Graphite	-0.19 ± 0.16
		Pt (22 K)	-0.16 ± 0.11
	Nb	Graphite	0.40 ± 0.28
		Pt (22 K)	0.05 ± 0.18
	Be	Graphite	-0.29 ± 0.17
		Pt (r.t.)	-0.18 ± 0.26
^{19}N	C_{nat}	Graphite	0.00 ± 0.08
		Pt (15 K)	-0.28 ± 0.09
	Nb	Graphite	-0.01 ± 0.15
		Pt (15 K)	-0.39 ± 0.09

* Department of Physics, Tokyo Institute of Technology

References

1) H. Ogawa et al.: RIKEN Accel. Prog. Rep. **34**, 66 (2001).
2) D. Kameda et al.: RIKEN Accel. Prog. Rep. **34**, 70 (2001).
3) H. Ogawa et al.: Phys. Lett. B **451**, 11 (1999).
4) D. Kameda et al.: RIKEN Accel. Prog. Rep. **35**, 65 (2002).

Study of resonance states in ^{12}N by elastic resonance scattering of ^{11}C+p

T. Teranishi,[*1] S. Kubono,[*1] S. Shimoura,[*1] M. Notani,[*1] Y. Yanagisawa, S. Michimasa,[*1] K. Ue,[*2] H. Iwasaki,[*1] M. Kurokawa,[*1] Y. Satou,[*3] T. Morikawa,[*4] A. Saito,[*5] H. Baba,[*5] J. H. Lee,[*6] C. S. Lee,[*6] Zs. Fülöp,[*7] and S. Kato[*8]

[Unstable nuclei, Nuclear astrophysics]

Proton elastic resonance scattering with low-energy radioactive beams is useful for studying resonance states in unstable nuclei. We have performed an experiment of the ^{11}C+p elastic resonance scattering using a radioactive beam of ^{11}C. A major goal of this study is to determine spin-parity (J^π) values, which have not been clearly determined yet for some levels in ^{12}N. It is also important to examine the resonance energies and proton widths of known levels, which may play a crucial role in the stellar reaction process of ^{11}C(p,γ)^{12}N in metal-deficient massive stars.[1,2]

The radioactive beam ^{11}C was produced by the CNS low-energy Radioactive Ion Beam separator (CRIB)[3,4] installed at the E7 room in the RIKEN Accelerator Research Facility. The beam had an energy of 3.4 MeV/nucleon and an intensity of 1.7×10^4 particles/sec. The elastic scattering was observed by the thick target method[5,6] using a $(CH_2)_n$ target (8.0 mg/cm^2). The recoil protons were detected by a set of ΔE-E silicon detectors at forward angles of 0–5° in the laboratory frame. Figure 1 shows the preliminary result of the proton energy (E_p) spectrum for ^{11}C+p. As compared with the spectrum previously reported,[7] the present spectrum has a better quality in terms of statistics and larger detection efficiencies at $E_p < 3$ MeV; these are due to a longer beam time and improvements of the detector system, respectively.

The spectrum covers a region of $E_x = 0.9$–3.7 MeV in ^{12}N. There are several known levels in this region. The spectrum was fitted to an R-matrix resonance formula as indicated by the solid line in Fig. 1. The energies and widths of the levels determined by the present experiment are consistent with the known values. The large peak seen in the spectrum at $E_p \sim 8.6$ MeV corresponds to the 3.13-MeV level, whose J^π value has not been clearly determined yet.[8] From the shape and width of the peak, the peak should be attributed to a d-wave resonance, which indicates the negative parity

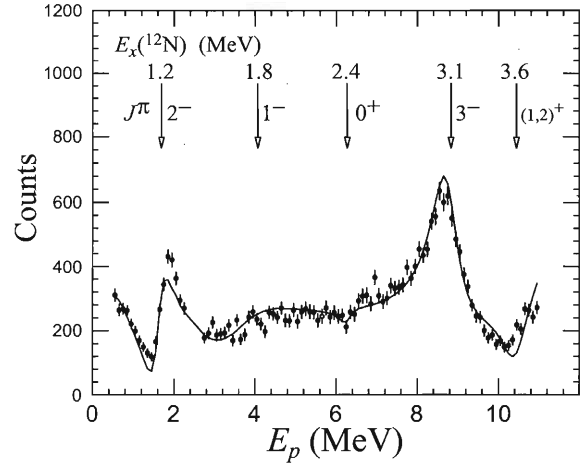

Fig. 1. Preliminary experimental result of the proton energy spectrum for the elastic resonance scattering of ^{11}C+p.

of the level. The height of the peak depends on J and is consistent with $J = 3$. Therefore, we made a tentative assignment of $J^\pi = 3^-$ for the level at $E_x = 3.13$ MeV in ^{12}N. This analysis is in the process of refinement.

References

1) M. Wiescher et al.: Astrophys. J. **343**, 352 (1989).
2) R. Mitalas: Astrophys. J. **290**, 273 (1985).
3) S. Kubono et al.: Eur. Phys. J. A **13**, 217 (2002).
4) Y. Yanagisawa et al.: RIKEN Accel. Prog. Rep. **34**, 183 (2001).
5) K. P. Artemov et al.: Sov. J. Nucl. Phys. **52**, 408 (1990).
6) S. Kubono: Nucl. Phys. A **693**, 221 (2001), and references therein.
7) T. Teranishi et al.: RIKEN Accel. Prog. Rep. **35**, 60 (2002).
8) F. Ajzenberg-Selove: Nucl. Phys. A **506**, 1 (1990).

*1 Center for Nuclear Study, University of Tokyo
*2 Department of Physics, University of Tokyo
*3 Department of Physics, Tokyo Institute of Technology
*4 Department of Physics, Kyushu University
*5 Department of Physics, Rikkyo University
*6 Department of Physics, Chun-Ang University, Korea
*7 Institute of Nuclear Research (ATOMKI), Hungary
*8 Department of Physics, Yamagata University

Development of a ^{17}N secondary beam

A. Odahara,[*1] T. Teranishi,[*2] M. Notani,[*2] S. Kubono,[*2] S. Michimasa,[*2] J. J. He,[*2] Y. Yanagisawa, H. Iwasaki,[*2] S. Shimoura,[*2] H. Watanabe, T. Kishida, T. Fukuchi,[*3] T. Sasaki,[*3] Y. Wakabayashi,[*3] N. Hokoiwa,[*3] M. Kibe,[*3] Y. Gono,[*3] S. Kato,[*4] and D. Beaumel[*5]

[RI beam, γ-ray spectroscopy, nuclear structure]

A secondary beam of ^{17}N was developed using the low-energy radioisotope beam separator (CRIB)[1] of the Center for Nuclear Study (CNS), University of Tokyo, in order to search for high-spin isomers in $N = 51$ isotones.

Configurations of these isomers are considered to be $[\nu(d_{5/2}g_{7/2}h_{11/2})\pi g_{9/2}{}^2]_{39/2}{}^-$ for odd nuclei and $[\nu(d_{5/2}g_{7/2}h_{11/2})\pi(p_{1/2}g_{9/2}{}^2)]_{20}{}^+$ for odd-odd nuclei. High-spin isomers are expected to be of stretch coupled configurations resulting from the breaking of a neutron magic 50 core and to be shape isomers caused by the sudden shape change from near spherical to an oblate shape because the same type of isomerism appeared in $N = 83$ isotones.[2]

Since the nuclei with $Z < 40$ in $N = 51$ isotones are close to the stability line, it is difficult to produce nuclei exciting high-spin states using reactions by combinations of stable beams and targets. Therefore, it is very effective to use the radioisotope beam. As the number of nuclei produced by a secondary fusion reaction is estimated to be low, the CNS Ge array[3] is suitable for use. This array was developed by CNS and consists of planar type Ge detectors of two cylindrical crystals divided into nine segments. By using the delayed coincidence method, high-spin isomers can be searched for in the nuclei of ^{90}Y, ^{89}Sr and ^{88}Rb produced by the α5n, αp5n and 2α3n channels of the ^{82}Se + ^{17}N reaction, respectively.

Development of a secondary ^{17}N beam was carried out using the CNS CRIB beam line which consists of two dipole (D1, D2), three quadrupole (Q1, Q2, Q3) and small correction magnets (M1, M2).[1] The ^{17}N beam was produced by the transfer reaction of ^{9}Be(^{18}O,^{17}N)^{10}B. A ^{9}Be target of 1.35 mg/cm^2 was bombarded by a ^{18}O^{8+} primary beam of 109.4 MeV which was provided by the AVF cyclotron in RIKEN. The beam intensity was 0.2 pμA. A parallel plate avalanche counter (PPAC) was set at a dispersive focal plane (F1) for beam monitoring. In order to identify reaction products, two PPACs and one Si detector were installed at an achromatic focal plane (F2). Two PPACs at F2 were located at 184 and 726 mm downstream of F2. A Si detector of 1.5 mm thickness and a catcher foil of 0.1 mm Ta were placed 985 and 1545 mm downstream of F2, respectively. A HPGe detector was placed at 80 mm apart from the catcher position to measure γ-rays emitted after a β-decay of ^{17}N. The acceptance solid angle was set to 5.6 msr, which was a maximum setting by a slit at F0. The energy of ^{17}N recoiling out of a primary target was 94.4 $\pm$ 1.1 MeV. A $B\rho$ volume of D1 was set to be 0.8240 Tm to select a ^{17}N^{7+} beam. Momentum acceptance was restricted to 2.2% by a rectangular slit at F1. The ^{18}O primary beam was stopped by the slit at F1. An energy degrader of a 10 μm mylar foil was placed at F1 to improve the purity of the ^{17}N beam. The $B\rho$ value of a second dipole magnet D2 was 0.7975 Tm.

Particle identification was made by using energies of reaction products and time-of-flight (TOF) between two PPACs at F2. The particle energies were measured by the Si detector mentioned above.

The intensity of ^{17}N at F2 was (5.1 $\pm$ 1.0) $\times$ 10^3 particles/s. The purity of the ^{17}N beam detected by F2-PPACs was 10% without the degrader. The purity was improved to 29% by using the degrader. However the beam spot size was deteriorated by the degrader. The intensity of ^{17}N obtained at the catcher, which was located in the secondary target position, was estimated to be 1.4 $\times$ 10^3 particles/s by measuring the γ-rays of the ^{17}N β decay. A decrease of the ^{17}N intensity by a factor 4 from F2 to the catcher was caused by a collimator of ϕ13 mm which was set to restrict the beam spot size at a secondary target position within a target size of ϕ20 mm.

In order to obtain enough statistics of γ-rays in the experiment using ^{17}N induced reactions, more than 10^4 particles/s of ^{17}N are required. The increase of the ^{17}N beam intensity is expected, (1) by a factor of 4 by bringing the secondary target to a closer position from F2, (2) by a factor of 2 by increasing the primary target thickness and (3) by a factor of 5 by an increase of the primary beam to 1 pμA. The expected beam intensity resulting from these improvements is 6 $\times$ 10^4 particles/s.

*1 Nishinippon Institute of Technology
*2 Center for Nuclear Study, University of Tokyo
*3 Kyushu University
*4 Yamagata University
*5 Institut de Physique Nucléaire, Orsay, France

References

1) Y. Yanagisawa et al.: RIKEN Accel. Prog. Rep. **34**, 183 (2001).
2) Y. Gono et al.: Eur. Phys. J. A **13**, 5 (2002) and references therein.
3) S. Shimoura et al.: CNS Ann. Rep. **5** (2001).

Inelastic α scattering on ^{14}O

H. Baba,[*1] S. Shimoura,[*2] T. Minemura, Y. U. Matsuyama,[*1] A. Saito,[*1] H. Akiyoshi, N. Aoi, T. Gomi,[*1] Y. Higurashi, K. Ieki,[*1] N. Imai,[*3] N. Iwasa,[*4] H. Iwasaki,[*2] S. Kanno,[*1] S. Kubono,[*2] M. Kunibu,[*1] S. Michimasa,[*2] T. Motobayashi, T. Nakamura,[*5] H. Sakurai,[*3] M. Serata,[*1] E. Takeshita,[*1] S. Takeuchi, T. Teranishi,[*2] K. Ue,[*3] K. Yamada,[*1] and Y. Yanagisawa

[NUCLEAR REACTIONS: ^{4}He(^{14}O,p^{13}N), 60 A MeV; Inelastic α Scattering]

Intermediate-energy radioactive isotope (RI) beams enable us to excite unstable nuclei by using inverse kinematics and measuring decaying particles. Coulomb dissociation and (p, p′) reactions for unstable nuclei have been successfully employed for the E1 and E2 excitation in the past decades. As another probe for excitation, inelastic α scattering is useful for exciting natural parity states including isoscalar monopole states, which are related to density oscillations of nuclei, because of its selection rules. In order to measure (α, α') reactions systematically, we developed a liquid helium target.[1)] Here, we report the measurement of inelastic α scattering on the unstable nuclei ^{14}O as the first series in our experiment. The present experiment was aimed at measuring the cross sections in the known 0^+ state and other states, and obtaining higher excitation energy spectra by applying the invariant mass method to various particle decay channels.

The experiment was performed at the RIKEN projectile fragment separator (RIPS). A beam of ^{14}O was produced by the fragmentation of a 135 A MeV ^{16}O beam in a ^{9}Be target with a 1.3 g/cm^2 thickness. The ^{14}O particles were identified event-by-event by the time-of-flight (TOF) measured by two 0.5-mm-thick plastic scintillators placed 5.3 m apart. An ^{14}O beam bombarded a 100 mg/cm^2 thick liquid-helium target. The incoming angle and position on the target were measured using two sets of Parallel Plate Avalanche Counters (PPAC's) installed upstream of the target. Reaction products were measured using a ΔE-E plastic hodoscope[2)] located 4 m downstream from the target. The hodoscope consisted of ΔE and E walls 5 and 60 mm thick, respectively. The ΔE (E) wall was divided horizontally (vertically) into 16 (13) plastic scintillators. The momenta and scattering angles of the reaction products were determined by measuring TOF between the target and the hodoscope, and based on the segmented detector positions, respectively.

Decay energy spectra were constructed from the momentum vectors of decay products. The preliminary decay energy spectrum of the $^{14}\mathrm{O} \rightarrow {}^{13}\mathrm{N} + \mathrm{p}$ is shown in Fig. 1. The peaks observed at 0.54 MeV, 3.09 MeV and about 1.8 MeV correspond to the known 1^-, 2^+ and the mixture of the known 3 states (0^+, 3^- and 2^+) which overlap because of the present experimental resolution.

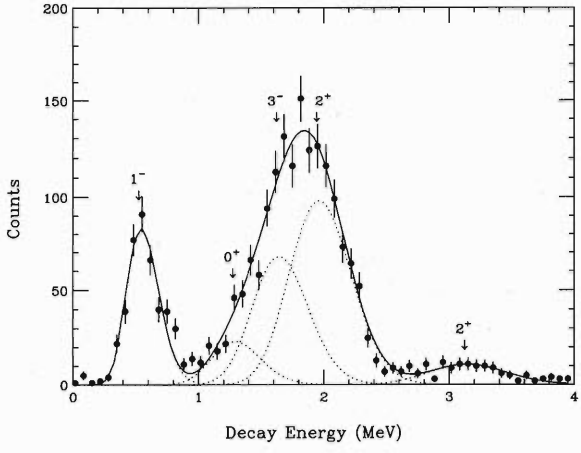

Fig. 1. Decay energy spectrum for the inelastic α scattering on ^{14}O. The solid curve represent the fitted observed data that contains the sum of the 5 known states (dotted curves) including experimental resolution.

Analyses of the angular distribution of the center of mass of the $^{13}\mathrm{N} + \mathrm{p}$ system, *i.e.*, $^{14}\mathrm{O}^*$, and angular correlation between decaying particles are now in progress to investigate the excitation mechanism of the 1^- state of the $T \neq 0$ even-even nuclei by isoscalar spin-0 particle (α). Angular distributions for the other states will be obtained using the known energies of the states and the experimental resolution for the decay energies, which is expected to have characteristics of the transferred angular momenta.

References

1) H. Akiyoshi et al.: CNS Report (2001), p. 73; RIKEN Accel. Prog. Rep. **34**, 193 (2001).
2) I. Hisanaga et al.: RIKEN Accel. Prog. Rep. **31**, 162 (1998).

*1 Department of Physics, Rikkyo University
*2 Center for Nuclear Study, University of Tokyo
*3 Department of Physics, University of Tokyo
*4 Department of Physics, Tohoku University
*5 Department of Applied Physics, Tokyo Institute of Technology

Study of resonance scattering of $^{14}O + \alpha$ using a cold helium gas target

M. Notani,[*1] T. Teranishi,[*1] J. J. He,[*1] T. Minemura, Y. Yanagisawa, S. Michimasa,[*1] H. Iwasaki,[*1] S. Shimoura,[*1] K. Ue,[*1] E. K. Lee,[*2] K. I. Hahn,[*2] Zs. Fülöp,[*3] A. Odahara,[*4] T. Sasaki,[*5] Y. Wakabayashi,[*5] Y. Gono,[*5] S. Kato,[*6] and S. Kubono[*1]

[NUCLEAR REACTIONS ^{1}H(^{14}N,^{14}O)n, Unstable nuclei, Nuclear astrophysics]

Low-energy RI beams ($\leq$ 10 A MeV) produced by an in-flight method are useful in studying resonance states in unstable nuclei, which are of great interest in the field of nuclear structure and nuclear astrophysics. This report describes an experiment to study resonance states in unstable nuclei, ^{18}Ne, *via* resonance scattering $^{14}O + \alpha$. Data for the resonance states in ^{18}Ne are important to understand the breakout process from the hot CNO cycle. The measurement of the excitation function of the resonance scattering was performed using the thick-target method.[1,2] To apply this method to the present experiment, we used a helium gas target cooled to 30 K to obtain the thickness of the gas target. Here, we report the results of the first experiment with the ^{14}O beam.

The experiment was performed at the CRIB beam line[3] in E7. A primary beam of ^{14}N was accelerated up to an energy of 8.4 A MeV at the RIKEN AVF cyclotron. The maximum intensity of the beam was 180 pnA. A secondary beam of ^{14}O was produced by the ^{1}H(^{14}N,^{14}O)n reaction. The production target was CH_4 gas with a thickness of 1.3 mg/cm^2 in a cell.

The reaction fragments were separated by the CRIB with an energy degrader of 10-μm mylar foil at the dispersive focal plane (F1). The momentum acceptance was set to be 1% by using a rectangle slit at F1.

At the achromatic focal plane (F2), the secondary beam was monitored with two parallel-plate avalanche counters (PPACs).[4] Particle identification was performed for each event on the basis of time of flight (TOF) between the two PPACs. The purity of the ^{14}O beam was 85% at F2.

A cold helium gas target was bombarded with the ^{14}O beam. He gas was confined in a small cell of 50 mm length with two windows of 2.2-μm Havar foils. It was kept at a pressure of 0.4 atm and was cooled to 30 K. The effective thickness of ^{4}He was about 3.1 mg/cm^2. The target thickness was chosen as thin as possible, however, enough for the ^{14}O nuclei to stop in the target. The reaction products from the helium target were identified by the ΔE-E method using a telescope with three Si detectors at 0°. The thicknesses of the Si detectors were 20 μm, 70 μm and 1500 μm, respectively.

Figure 1 shows a two-dimensional plot of energy deposit in the second and third Si detectors, obtained from the data accumulated in 0.6 hours. Protons and α particles produced in the helium target were clearly observed.

In this experiment, the ΔE-E plot of protons and α particles originating from the resonance scattering of $^{14}O + \alpha$ was obtained. An extensive experimental run is being planned based on the present result.

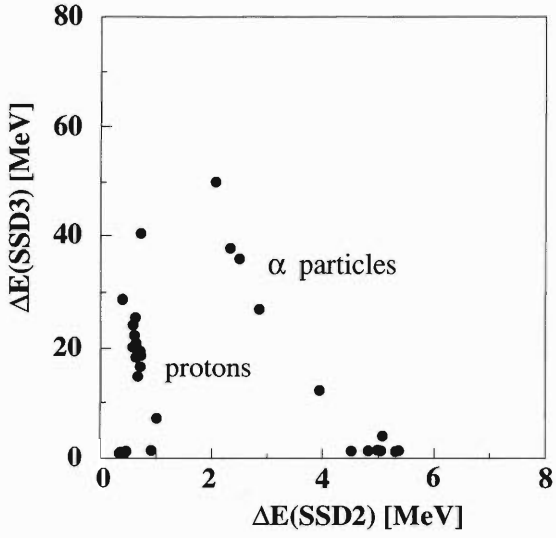

Fig. 1. Two-dimensional energy-deposit plot for SSD2 and SSD3, which was obtained in the resonance scattering of a 5.1 A MeV ^{14}O beam on a helium target.

References

1) K. P. Artemov et al.: Sov. J. Nucl. Phys. **52**, 408 (1990).
2) S. Kubono et al.: Nucl. Phys. A **693**, 221 (2001).
3) Y. Yanagisawa et al.: RIKEN Accel. Prog. Rep. **34**, 183 (2001).
4) S. Kumagai et al.: Nucl. Instrum. Methods Phys. Res. A **470**, 562 (2001).

*1 Center for Nuclear Study, University of Tokyo
*2 Ewha Womans University, Korea
*3 ATOMKI, Hungary
*4 Nishinippon Institute of Technology
*5 Kyushu University
*6 Yamagata University

Gamma spectroscopy of exotic nuclei *via* (p,p′) reaction

Zs. Dombrádi,[*1] Z. Elekes, A. Saito,[*2] N. Aoi,[*3] H. Baba,[*2] K. Demichi,[*2] Zs. Fülöp,[*1] J. Gibelin,[*4] T. Gomi,[*2] H. Hasegawa,[*2] N. Imai,[*3] M. Ishihara, H. Iwasaki,[*3] S. Kanno,[*2] S. Kawai,[*2] T. Kishida, T. Kubo, K. Kurita,[*2] Y. U. Matsuyama,[*2] S. Michimasa,[*3] T. Minemura, T. Motobayashi, M. Notani,[*3] T. Ohnishi,[*3] H. J. Ong,[*3] S. Ota,[*5] A. Ozawa, H. K. Sakai,[*2] H. Sakurai,[*3] S. Shimoura,[*3] D. Sohler,[*1] E. Takeshita,[*2] S. Takeuchi, M. Tamaki,[*3] Y. Togano,[*2] K. Yamada,[*2] Y. Yanagisawa, and K. Yoneda

[Nuclear structure, Unstable nuclei]

We studied the excited states of neutron-rich nuclei *via* (p,p′) reaction. Experimental information on neutron-rich nuclei provides a bench mark test for theoretical approaches to the neutron-rich nuclei, such as the quantum Monte Carlo Shell Model (MCSM) calculation. Recent MC shell calculations[1,2] revealed that intruder and higher intruder configurations are enhanced due to the narrowing of the $N = 20$ shell gap toward smaller Z. However, experimental data on the structure of those exotic nuclei is very limited, mainly because of the small intensities of radioactive beam available.

In a recent experiment in RIKEN[3] the first excited state of ^{30}Ne was studied by means of proton inelastic scattering in inverse kinematics using a ^{30}Ne beam intensity less than 1/s. In the present experiment we extended the investigation of $N \sim 20$ nuclei by using a radioactive beam cocktail of several exotic nuclei.

The experiment was performed at RIKEN. A ^{40}Ar primary beam of 94 A MeV energy and 60 pnA intensity bombarded a 0.5-mm-thick natural Tantalum target. According to previous studies[4] the yield of neutron rich nuclei is higher for Ta than for the Be primary target. The cocktail, consisting of neutron rich ^{24}O, ^{25,26,27}F, ^{27,28,29,30}Ne, ^{29,30,31,32}Na isotopes, was separated by the RIPS fragment separator operated at 6% momentum acceptance. The total beam intensity was about 100 cps, while the fraction of individual isotopes varied in the range of 1–10%. The particle identification of the secondary beam was made by using the information on the beam energy loss in 350-μm-thick silicon detectors, the particle time-of-flight between plastic scintillators and the fragment positions measured by PPAC's at the momentum dispersive focal plane (see Fig. 1). The beam position on the target was monitored by two PPAC's upstream from the target. The beam cocktail bombarded liquid hydrogen target with a minimum 140 mg/cm^2 thickness developed in RIKEN.[5] The scattered particles were detected by a PPAC (position) and a 2 × 2 silicon telescope matrix (particle identification). An array of NaI(Tl) detectors[6] was placed around the target to detect the gamma-rays emerging from the inelastically scattered beam particles. The efficiency of the array is around 15% for $E_\gamma = 1.5$ MeV.

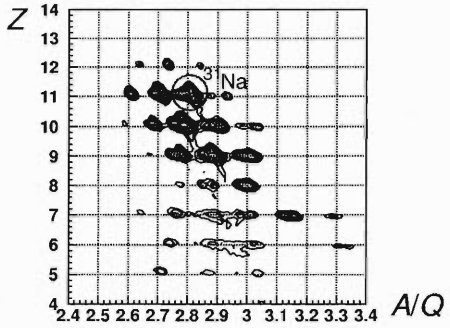

Fig. 1. A/Q *vs.* Z secondary beam particle identification plot. See text for details.

The overall efficiency of the experimental setup and the high reaction cross section allow gamma spectroscopy investigation at the level of 1–10 cps radioactive beam intensity. An example of the preliminary results is shown in Fig. 2 for ^{31}Na. The analysis of the collected $\sim 10^6$ beam events is in progress.

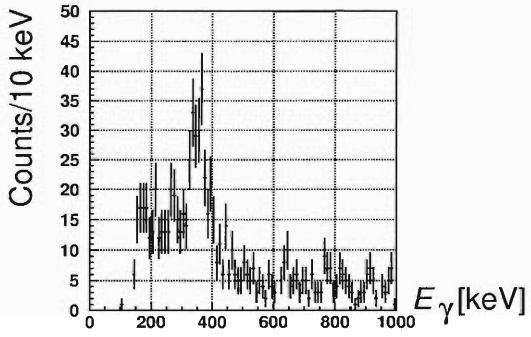

Fig. 2. Doppler corrected γ-ray spectrum from the (p, p′) reaction induced by ^{31}Na beam.

*1 ATOMKI, Hungary
*2 Rikkyo University
*3 University of Tokyo
*4 Institut de Physique Nucléaire, France
*5 Kyoto University

References

1) Y. Utsuno et al.: Phys. Rev. C **64**, 011301 (2001).
2) Y. Utsuno et al.: Phys. Rev. C **60**, 054315 (1999).
3) Y. Yanagisawa et al.: RIKEN Accel. Prog. Rep. **35**, 71 (2002).
4) M. Notani et al.: RIKEN Accel. Prog. Rep. **29**, 50 (1996).
5) H. Akiyoshi et al.: RIKEN Accel. Prog. Rep. **32**, 167 (1999).
6) H. Hasegawa et al.: RIKEN Accel. Prog. Rep. **35**, 169 (2002).

Two-proton halo in ^{17}Ne

R. Kanungo, M. Chiba, S. Adhikari,[*1,*2] D. Fang, N. Iwasa,[*3] K. Kimura,[*4] K. Maeda,[*3] S. Nishimura, Y. Ogawa,[*5] T. Ohnishi, A. Ozawa, C. Samanta,[*1,*2] T. Suda, T. Suzuki,[*6] Q. Wang,[*7] C. Wu, Y. Yamaguchi,[*6] K. Yamada, A. Yoshida, T. Zheng, and I. Tanihata

[Halo, Momentum distribution, Proton removal cross section]

Over the past decade studies of unstable nuclei led to the discovery of nuclear halo structures close to the neutron drip line. Investigations around the proton drip line in search of such structures are however few, particularly for two-proton halos. Their existence seem a rare possibility owing to the Coulomb barrier.

The ^{17}Ne nucleus poses to be a promising candidate for searching a possible two-proton halo with its borrowmean character and small two-proton separation energy $S_{2p} = 0.94$ MeV. Furthermore, the observed enhanced interaction cross section for this nucleus suggets an anomalous structure,[1] though this alone is not a confirmation of the halo formation. However, recent theoretical investigations present a contradictory picture suggesting the two protons in ^{17}Ne to be predominantly in the $1d_{5/2}$ orbital.[2]

The first measurements of the two-proton removal momentum distribution and cross section of ^{17}Ne with a Be target at 66 A MeV performed at RRC, RIKEN are reported here. A Glauber model analysis of available experimental information clearly indicates the possibility of a two-proton halo in ^{17}Ne.

The secondary beam of ^{17}Ne with an average intensity of 120 pps was produced from a 135 A MeV ^{20}Ne primary beam interacting with a Be target. The produced ^{17}Ne further interacted with a 0.5 mm Be reaction target placed at the achromatic focus F2. Details of the experimental setup and particle identification are the same as in Ref. 3.

The measured two-proton removal momentum distribution has a width of 153 ± 3 MeV/c in a Lorentzian fitting. The two-proton removal cross section has been measured to be 191 ± 48 mb. We performed an analysis of the interaction cross section of $^{17}\mathrm{Ne} + ^{12}\mathrm{C}$ data[1] at 700 A MeV, the longitudinal momentum distribution, and the two-proton removal cross section at 66 A MeV in a few-body Glauber model approach. Three possibilities of the two-proton emission process have been considered. Firstly, we consider ^{17}Ne as a ^{15}O-core-plus two-uncorrelated protons. Secondly, a core-plus di-proton model is considered for ^{17}Ne. Lastly the emission of two protons thorugh the unbound resonances in ^{16}F have been considered.

The process that can consistently describe all three observables turns out to be the one with a core-plus-two uncorrelated proton picture where the protons dominantly occupy the $2s_{1/2}$ orbital. This is thus indicative of the presence of a two-proton halo in ^{17}Ne. Furthermore, it also shows the existence of mirror nuclei ^{17}Ne and ^{17}N whose ground states are quite different, because in ^{17}N the valence neutrons mainly occupy the $1d_{5/2}$ orbital.

References

1) A. Ozawa et al.: Phys. Lett. B **334**, 18 (1994).
2) H. T. Fortune and R. Sherr: Phys. Lett. **503**, 70 (2001).
3) R. Kanungo et al.: Phys. Rev. Lett. **88**, 142502 (2002).

*1 Physics Department, Virginia Commonwealth University, USA
*2 Saha Institute of Nuclear Physics, India
*3 Department of Physics, Tohoku University
*4 Department of Electric, Electronics and Computer Engineering, Nagasaki Institute of Applied Science
*5 Research Center for Nuclear Physics, Osaka University
*6 Department of Physics, Niigata University
*7 Department of Technical Physics, Peking University, China

Transient field in Gd foils acting on ^{22}Ne ions at the Bohr velocity

H. Ueno, W. Sato, H. Watanabe, A. Yoshimi, Y. Kobayashi, T. Saito,[*1]
J. Murata, H. Miyoshi,[*2] K. Shimada,[*2] and K. Asahi

[Transient magnetic field, Coulomb excitation]

For g-factor measurements of the excited states of unstable nuclei, we have been developing a setup for the transient-field (TF) experiment. The TF technique has been applied to the measurement of the g-factors of short-lived nuclear states at only low beam velocities. However, taking into account the fact that RI beams produced in the projectile fragmentation reaction have very high velocities compared to the Bohr velocity, it is important to know the TF strength at that velocity. Theoretically, no successful quantitative description of the TF from first principles has been given so far. The earlier models lead to the expectation of a strong decrease of TF as the velocity increases whereas the recent model predicts the rather constant or even increasing trend of the TF with increasing velocity.[1] To investigate this experimentally several experiments have been carried out recently at high velocities.[2,3]

For the measurement of the TF strength at very high velocities we have improved the experimental setup described in the previous report.[4] At high beam velocities, the elastic scattering of beams must be a serious background during particle detection. In order to distinguish the Coulomb excitation from this large background, the segmented plastic scintillators, consisting of thirty plastic scintillators mounted cylindrically 7.5 cm from the beam axis, were chosen as fast-response particle counters. In addition, to reduce the ambiguities in the scattering angle of the particle, which is important to determine the particle-γ angular correlation, the particle-detector system is placed inside the vacuum chamber. The schematic layout of the new setup is shown in Fig. 1.

An experiment was performed using the RIKEN AVF cyclotron. The $J^\pi = 2^+$ and $E_x = 1.275$ MeV first excited state of a ^{22}Ne beam, whose magnetic moment and lifetime are known to be $\mu = +0.65(2)\,\mu_N$ and $\tau = 3.63(5)$ ps, respectively, was populated by the scattering from a target consisting of two layers, Au and Gd, with thicknesses of 21.4 and 6.4 mg/cm^2, respectively. The averaged energy of the ^{22}Ne beam was $E = 4.9\,A$ MeV, which corresponds to a beam velocity of $v = 14\,v_0$, where v_0 is the Bohr velocity. The γ-rays emitted from the excited projectiles were detected with the four NaI(Tl) detectors placed at the angles $\theta_{Lab} \sim \pm 53°$ and $\pm 100°$ relative to the beam axis. In coincidence with the γ rays, the projectiles scattered from the target were detected for the measurement of particle-γ angular correlation. The

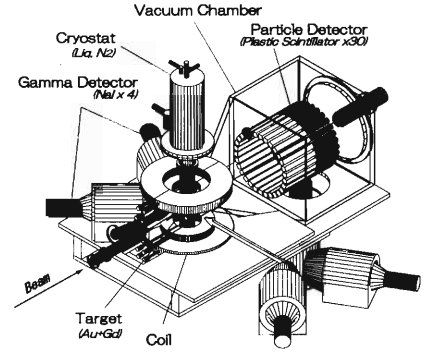

Fig. 1. Schematic layout of the setup for the transient field experiments.

measured particle-γ angular correlations are shown in Fig. 2. For small precession of the nuclear moment, the strength B_{TF} can be obtained from a double ratio of photo-peak counting rates measured using the pair of NaI detectors under external magnetic field $B_{ext} = 450$ Gauss in the "up" and "down" directions, which was changed periodically every 15 seconds to reduce the systematic error. With the above-obtained angular correlation we determined a preliminary value of $B_{TF} = 3.2(10)$ kT. We confirm that the effect is caused not by the direction change of external magnetic field but by the TF, since no such effect is found in the value $B_{TF} = 0.9(14)$ kT that was obtained without the Gd layer.

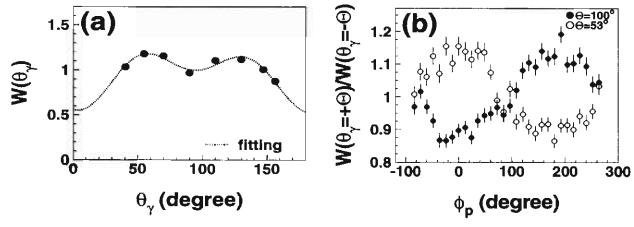

Fig. 2. Particle-γ angular correlations measured as the function of (a) the γ-ray emission angle and (b) the azimuth angle of particle detection for the de-excitation γ rays from the ^{22}Ne(2_1^+) state after Coulomb excitation.

*1 Department of Chemistry, Tokyo University of Science
*2 Department of Physics, Tokyo Institute of Technology

References
1) F. Hagelberg, T. P. Das, and K.-H. Speidel: Phys. Rev. C **48**, 2230 (1993).
2) K.-H. Speidel et al.: Z. Phys. A **339**, 265 (1991).
3) J. Cub et al.: Nucl. Phys. A **549**, 304 (1992).
4) H. Ueno et al.: RIKEN Accel. Prog. Rep. **34**, 190 (2001).

Production and identification of new neutron-rich nuclei ^{34}Ne, ^{37}Na, and ^{43}Si with a 64A MeV ^{48}Ca beam†

M. Notani,[*1] H. Sakurai,[*2] N. Aoi,[*2] Y. Yanagisawa, A. Saito,[*3] N. Imai,[*2] T. Gomi,[*3] M. Miura,[*4] S. Michimasa,[*1] H. Iwasaki,[*1] N. Fukuda, M. Ishihara, T. Kubo, S. Kubono,[*1] H. Kumagai, S. M. Lukyanov,[*5] T. Motobayashi, T. K. Onishi,[*2] Yu. E. Penionzhkevich,[*5] S. Shimoura,[*1] T. Teranishi,[*1] K. Ue,[*1] V. Ugryumov,[*5] and A. Yoshida

[NUCLEAR REACTIONS: ^{181}Ta(^{48}Ca,X), E(^{48}Ca) = 64A MeV; Evidence for ^{34}Ne, ^{37}Na, and ^{43}Si]

The results of an experiment to synthesize new neutron-rich nuclei in the $10 \leq Z \leq 14$ region are presented. The experiment was performed using an intense ^{48}Ca beam at RIKEN Accelerator Research Facility. In this work, the maximum beam intensity of the ^{48}Ca beam of 140 pnA was achieved via a new acceleration scheme at RIKEN, in which the linear accelerator complex of the RFQ + RILAC + CSM newly developed was used as an injector to the RIKEN Ring Cyclotron (RRC), where CSM was introduced by CNS. Here, we report the first production and identification of new neutron-rich nuclei ^{34}Ne, ^{37}Na and ^{43}Si.

The ^{48}Ca ions were produced at the 18 GHz ECR,[1] where the 64% enriched ^{48}Ca oxide powder was used. The ^{48}Ca beam accelerated up to an energy of 64 A MeV at the RRC reacted with a 336-mg/cm^2-thick ^{181}Ta target. In order to avoid melting of the production target, a water-cooled rotating target system was developed and used in this experiment.[2]

The reaction fragments were collected and analyzed using an RIPS spectrometer[3] operated in an achromatic mode. The intense primary beam may cause an increase of background rates and piled-up events. To reduce the relative rates of light isotopes, an aluminum wedge degrader with a mean thickness of 64 mg/cm^2 was installed at the momentum dispersive focal plane (F1). Particle identification was performed event-by-event by a standard method[4] on the basis of energy loss (ΔE), total kinetic energy (TKE), time-of-flight (TOF) and magnetic rigidity ($B\rho$) measured for each fragment. In order to determine the $B\rho$ values, the positions of the fragments at F1 were measured using a parallel-plate avalanche counter (PPAC). The TOF of each fragment was determined from a set of two plastic scintillation counters with a thickness of 0.5 mm, one of which was placed at the first achromatic focal plane (F2) and the other, at the final focal plane (F3) of the RIPS spectrometer. A telescope of eight silicon detectors was installed behind the plastic counter at F3. The thicknesses of the silicon detectors were 0.35, 0.35, 1, 1, 2, 2, 0.35 and 2 mm. Each silicon detector provided independent energy-loss values (ΔE), while the whole telescope provided the TKE measurement. The accuracy in the Z determination was about 0.7% (r.m.s.) for the sodium isotopes, while the mass-to-charge ratio (A/Q) was determined at an accuracy of 0.2%.

Figure 1 (a) shows a two-dimensional plot of A/Z versus Z, obtained from the data accumulated for the ^{40}Mg $B\rho$ setting, while Fig. 1 (b) shows that for the ^{43}Si setting. The integrated beam intensities for the two settings are 6.9×10^{16} and 1.7×10^{15} particles, respectively. Significant numbers of events were observed for three new isotopes, ^{34}Ne (2 events), ^{37}Na (3 events) and ^{43}Si (4 events). However, the ^{33}Ne, ^{36}Na and ^{39,40}Mg isotopes were not observed in this experiment.

For the first time, by this experiment we produced and identified the new neutron-rich nuclei ^{34}Ne, ^{37}Na and ^{43}Si, and showed that these nuclei are particle-stable nuclei.

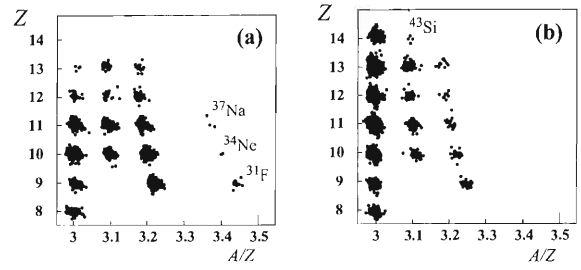

Fig. 1. Two-dimensional A/Z versus Z plot, which was obtained in the reaction of a 64 A MeV ^{48}Ca beam on a 336 mg/cm^2 tantalum target. (a) was measured with the ^{40}Mg $B\rho$ setting and (b) with the ^{43}Si setting. The new isotopes, ^{34}Ne, ^{37}Na and ^{43}Si, are clearly separated and visible.

References

1) T. Nakagawa et al.: Nucl. Instrum. Methods Phys. Res. A **396**, 9 (1997).
2) A. Yoshida et al.: RIKEN Accel. Prog. Rep. **34**, 188 (2001).
3) T. Kubo et al.: Nucl. Instrum. Methods Phys. Res. B **70**, 309 (1992).
4) H. Sakurai et al.: Phys. Lett. B **448**, 180 (1999).

† Major part is published in Phys. Lett. B **542**, 49 (2002)

*1 Center for Nuclear Study, University of Tokyo
*2 University of Tokyo
*3 Rikkyo University
*4 Tokyo Institute of Technology
*5 Joint Institute for Nuclear Research, Russia

Development of ^{22}Mg RI beam with CRIB

J. J. He,* S. Kubono,* T. Teranishi,* M. Notani,* S. Michimasa,* H. Iwasaki,* and Y. Yanagisawa

[Unstable nuclei, Nuclear Astrophysics]

A ^{22}Mg radioactive ion beam was developed with CRIB[1,2] using the inverse kinematics reaction ^{3}He(^{20}Ne,^{22}Mg)n. The ^{22}Mg RI beam can be used for investigating the excited states in ^{23}Al *via* the elastic scattering of ^{22}Mg+p. The resonance states in ^{23}Al are relevant to the reaction rate of astrophysical reaction ^{22}Mg(p,γ)^{23}Al.[3,4] This proton capture reaction is very important in the Hot NeNa cycle, because it possibly influences the nucleosynthesis of the γ emitter ^{22}Na in Ne-rich novae[5] and may help us to understand the observed large enhancements of element abundances beyond CNO nuclei in nova ejecta.[6]

A primary beam of ^{20}Ne^{7+} was accelerated up to 6.464 MeV/nucleon by the AVF cyclotron, and bombarded on a 0.25-mg/cm^2 ^{3}He gas target. At the momentum-dispersive focal plane (F1), a 3.1-μm mylar foil corresponding to $d/R = 0.05$ (d - thickness of degrader, R - range of ^{22}Mg particle in the material) was used as a homogeneous energy degrader, which can be moved in or out by remote control. The ^{22}Mg RI beam was distinguished from the products at the achromatic focal plane (F2), where two delay-line type PPACs and a Si detector (1500 μm) were installed to measure the positions and the energies of the particles.

The plots of particle identification are shown in Fig. 1, in which ^{20}Ne and ^{21}Na particles were the main contaminants. The purities of ^{22}Mg were about 1.5–2.7% as shown in Table 1. Here, the ^{20}Ne contaminant was produced by the primary beam scattered along the beam pipe, the edge of the target holder and the inner walls of D1 magnet, while the ^{21}Na contaminant was produced *via* the ^{3}He(^{20}Ne,^{21}Na)^{2}H reaction.

The ^{20}Ne contaminant can be eliminated mainly by increasing the quality of the primary beam, increasing the thickness of the degrader and setting slits properly in the next experiment. As for the ^{21}Na contaminant, there is no better method of reducing it from ^{22}Mg with the present setup, and this will be the major limitation for increasing the purity of ^{22}Mg. The production ratio of ^{21}Na and ^{22}Mg was about 9 : 1. Therefore, the maximum purity for ^{22}Mg will be about 10% under the most ideal case. In fact, the ^{21}Na contaminant is also very useful as a RI beam for investigating the excited states of ^{22}Mg, which are related to the astrophysical ^{21}Na(p,γ)^{22}Mg reaction. The properties of the ^{21}Na RI beam are also presented in Table 1.

In the next proposed experiment, the ^{22}Mg RI beam will be tuned at its maximum purity to investigate the excited states of ^{23}Al *via* the elastic scattering of ^{22}Mg + p, and as a byproduct, the elastic scattering of ^{21}Na + p will be measured at the same time.

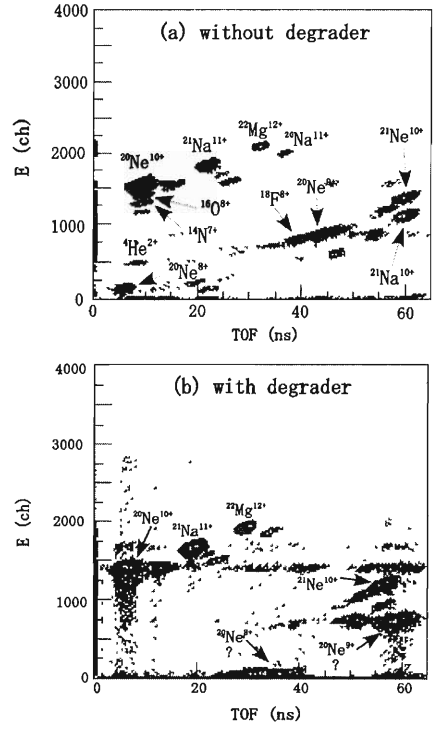

Fig. 1. Plots of particle identification (a) without degrader and (b) with degrader.

Table 1. Properties of ^{22}Mg and ^{21}Na RI beam. The maximum intensity of the ^{20}Ne primary beam is 130 pnA. (Where, w/o: without degrader; w: with degrader.)

	^{22}Mg^{12+}		^{21}Na^{11+}	
	w/o	w	w/o	w
Purity (%)	1.5	2.7	19.6	26.2
Intensity (cps/pnA)	16	30	200	290
Beam spot (mm)	10	14	12	13

References

1) S. Kubono et al.: Eur. Phys. J. A **13**, 217 (2002).
2) T. Teranishi et al.: CNS-REP-39 (2001).
3) M. Wiescher et al.: Nucl. Phys. A **484**, 90 (1988).
4) J. A. Caggiano et al.: Phys. Rev. C **64**, 025802 (2002).
5) H. Schatz et al.: Phys. Rev. Lett. **79**, 3845 (1997).
6) M. Wiescher et al.: Astron. Astrophys. **160**, 56 (1986).

* Center for Nuclear Study, University of Tokyo

Coulomb dissociation of ^{23}Al and ^{27}P

T. Gomi,[*1] T. Motobayashi, Y. Ando,[*1] N. Aoi,[*2] H. Baba,[*1] K. Demichi,[*1] Z. Elekes,[*3] N. Fukuda, Zs. Fülöp,[*3] U. Futakami,[*1] H. Hasegawa,[*1] Y. Higurashi, K. Ieki,[*1] N. Imai,[*2] M. Ishihara, K. Ishikawa,[*4] N. Iwasa,[*5] H. Iwasaki,[*6] S. Kanno,[*1] Y. Kondo,[*4] T. Kubo, S. Kubono,[*6] M. Kunibu,[*1] K. Kurita,[*1] Y. U. Matsuyama,[*1] S. Michimasa,[*6] T. Minemura, M. Miura,[*4] H. Murakami,[*1] T. Nakamura,[*4] M. Notani,[*6] S. Ota,[*7] A. Saito,[*1] H. Sakurai,[*2] M. Serata,[*1] S. Shimoura,[*6] T. Sugimoto,[*4] E. Takeshita,[*1] S. Takeuchi, Y. Togano,[*1] K. Ue,[*2] K. Yamada,[*1] Y. Yanagisawa, K. Yoneda, and A. Yoshida

[NUCLEAR REACTIONS: ^{208}Pb(^{23}Al,p^{22}Mg)^{208}Pb, ^{208}Pb(^{27}P,p^{26}Si)^{208}Pb, Coulomb dissociation]

We have performed an experiment to study the rate of stellar ^{22}Mg(p,γ)^{23}Al and ^{26}Si(p,γ)^{27}P reactions using the Coulomb-dissociation method. These reactions are relevant to the nucleosynthesis of the γ-ray emitters ^{22}Na and ^{26}Al in Ne novae.

The observed abundance of ^{22}Na and ^{26}Al in novae is not reproduced by network calculations.[1–4] One reason for this might be the large ambiguity in the reaction rates. ^{22}Na is expected to be produced in the reaction sequence ^{20}Ne(p,γ)^{21}Na(p,γ)^{22}Mg($\beta^+\nu$)^{22}Na.[5,6] The ^{22}Na yield is reduced if an escape from the reaction sequence takes place *via* the ^{22}Mg(p,γ)^{23}Al reaction. As for ^{26}Al, it is expected to be produced by the reaction sequence ^{23}Mg(p,γ)^{24}Al($\beta^+\nu$)^{24}Mg(p,γ)^{25}Al($\beta^+\nu$)^{25}Mg(p,γ)^{26}Al.[2,4] In this case, it can be bypassed by ^{25}Al(p,γ)^{26}Si(p,γ)^{27}P. The ^{25}Al(p,γ)^{26}Si reaction rate can be evaluated from experimental data,[7] while the ^{26}Si(p,γ)^{27}P reaction is poorly known. In the energy region of astrophysical interest, the first excited states of ^{23}Al and ^{27}P were measured at excitation energies of 0.528 MeV and 1.199 MeV, respectively.[8] However, there is no experimental data for the strength of the resonant captures through these first excited states. In the present work, we aimed at determining the radiation widths of these resonant states.

The experiment was performed at the RIPS beam line. The secondary beams of ^{23}Al at 50 MeV/nucleon and ^{27}P at 57 MeV/nucleon were produced by the projectile fragmentation of 135 MeV/nucleon ^{28}Si and 115 MeV/nucleon ^{36}Ar in a ^{9}Be target, respectively. The beam of ^{23}Al bombarded an 88 mg/cm^2 Pb or a 58 mg/cm^2 Nb target. A typical intensity and the resultant purity of the ^{23}Al beam were 10 kcps and 7%, respectively. The ^{27}P beam bombarded a 125 mg/cm^2 Pb or an 88 mg/cm^2 C target. A typical intensity and the resultant purity of the ^{27}P beam were 1.5 kcps and 1%, respectively. The experimental setup was almost the same as that of the previous experiment.[9,10] The schematic of the setup is given in Fig. 1. The products of the breakup reaction, ^{22}Mg (or ^{26}Si) and a proton, were detected respectively using silicon counter telescopes and a plastic scintillator hodoscope located 50 cm and 3 m downstream of the target. We achieved good angular resolution and wide acceptance for the products, compared with those in the previous experiment. Because we determine the position or the angle of the products from the hit pattern on position-sensitive silicon detectors with strips of 5 mm width instead of on single-element silicon detectors, the resolution of the opening angle between ^{22}Mg (or ^{26}Si) and a proton is expected to be 1.5° (FWHM) in contrast with 4° in the previous experiment. The acceptance of the products increased 1.5 times with shortening of the distance between the target and detectors. A stack of sixty-eight NaI(Tl) scintillators (DALI) was placed around the target to measure deexcitation γ-rays from ^{22}Mg (or ^{26}Si) in its excited states, the contribution of which should be subtracted to extract the Coulomb dissociation cross section of interest. Data analysis is now in progress.

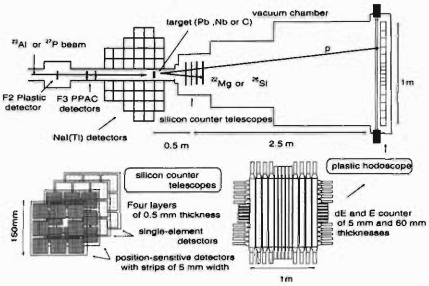

Fig. 1. Schematic depiction of the experimental setup.

*1 Rikkyo University
*2 University of Tokyo
*3 ATOMKI, Hungary
*4 Tokyo Institute of Technology
*5 Tohoku University
*6 Center for Nuclear Study, University of Tokyo
*7 Kyoto University

References
1) A. F. Iyudin et al.: Astron. Astrophys. **300**, 422 (1995).
2) N. Prantzos et al.: Phys. Rep. **267**, 1 (1996).
3) H. Schatz et al.: Phys. Rev. Lett. **79**, 3845 (1997).
4) J. Jose et al.: Astrophys. J. **520**, 347 (1999).
5) S. Schmidt et al.: Nucl. Phys. A **591**, 227 (1995).
6) F. Stegmüller et al.: Nucl. Phys. A **601**, 168 (1996).
7) C. Iliadis et al.: Phys. Rev. C **53**, 475 (1996).
8) J. A. Caggiano et al.: Phys. Rev. C **64**, 025802 (2001).
9) T. Gomi et al.: RIKEN Accel. Prog. Rep. **34**, 73 (2001).
10) T. Gomi et al.: RIKEN Accel. Prog. Rep. **35**, 69 (2002).

Measurements of interaction cross sections for Ar and Cl isotopes†

A. Ozawa, T. Baumann,*1 L. Chulkov,*2 D. Cortina,*3 U. Datta,*1 J. Fernandez,*4 H. Geissel,*1 F. Hammache,*1 K. Itahashi, M. Ivanov,*5 R. Janik,*5 T. Kato,*6 K. Kimura,*4 T. Kobayashi,*7 K. Markenroth,*8 M. Meister,*8 G. Münzenberg,*1 T. Ohtsubo,*6 S. Ohya,*6 T. Okuda,*7 A. A. Ogloblin,*2 V. Pribora,*2 S. Sekiguchi,*7 B. Sitár,*5 P. Strmen,*5 S. Sugimoto, K. Sümmerer,*1 T. Suzuki,*6 I. Tanihata, and Y. Yamaguchi*6

[NUCLEAR REACTIONS: ^{12}C($^{31-40}$Ar, $^{31-40}$Ar), ^{12}C($^{31-37}$Cl, $^{31-37}$Cl) $E = 950$ A MeV]

One of the most interesting features of unstable nuclei is the existence of skins. Evidence for neutron skins in unstable nuclei has been collected for ^{6}He and ^{8}He for the first time.[1] Measurements of interaction cross sections ($\sigma_{\rm I}$) for Na isotopes have revealed a monotonic increase in the neutron skin thickness with increasing neutron number.[2] However, no clear experimental evidence for proton skins has been obtained so far. Argon isotopes can provide quantitative information on proton skins, since their charge radii of $^{32-40}$Ar have been studied by optical isotope shift measurements.[3]

The experiment was performed at the projectile-fragment separator at GSI. Secondary beams of $^{31-35}$Ar ($^{36-39}$Ar) and $^{31-33}$Cl ($^{34-37}$Cl) were produced via the projectile fragmentation of ^{36}Ar (^{40}Ar) primary beam accelerated to around 1A GeV by the heavy-ion synchrotron SIS. The data-analysis method for obtaining $\sigma_{\rm I}$ was the same as that in our previous experiments.

The effective root-mean-square (RMS) matter radii of the nucleon distributions were deduced from $\sigma_{\rm I}$ using the Glauber model in the optical-limit approximation. Glauber model calculations require that the functional form of the density distribution is specified. We assumed a Fermi-type distribution for the densities, where the radius and the diffuseness parameters should be fixed. Since we measure only one observable ($\sigma_{\rm I}$), we have chosen to set the diffuseness to the value obtained for stable ^{36}Ar (0.507 fm) and vary the radius parameter.

In order to extract numerical values for the proton skin thickness, we used the following equation for the matter radii: $(\text{RMS\_m})^2 = (Z/A)(\text{RMS\_p})^2 + (N/A)(\text{RMS\_n})^2$, where RMS_m, RMS_p and RMS_n are the RMS matter, proton and neutron radii, respectively. By optical isotope shift measurements, relative differences of the mean-square charge radii have been determined for $^{32-40}$Ar.[3] We normalized the ^{36}Ar radius to a value determined by electron scattering. Thus, we obtained the RMS charge radii (RMS_ch) for $^{32-40}$Ar. The RMS_p radii were deduced from the RMS_ch radii by the relation: $(\text{RMS\_p})^2 = (\text{RMS\_ch})^2 - 0.64$ (fm^2).[4] To obtain the RMS_n radii, we subtracted the deduced RMS_p from our RMS_m. The proton skin thickness is given by (RMS_p − RMS_n) as visualized in Fig. 1. The errors of the skin thicknesses are dominated by the errors of the RMS_m. We demonstrate for the first time a monotonical increase in the thickness of proton skins. For a comparison, we also plot in Fig. 1 the proton skin thicknesses obtained by RMF calculations with the NL3 parameter set.[5] The RMF calculations reproduce the observed trend very well.

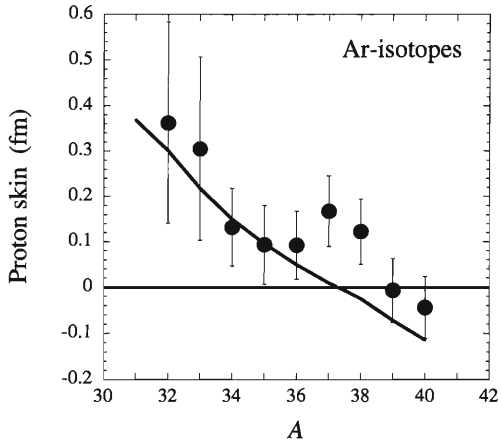

Fig. 1. Mass number dependence of proton skin thickness in Ar isotopes. The solid line shows radii calculated by RMF calculations with NL3 parameterization.[4]

References
1) I. Tanihata et al.: Phys. Lett. B **289**, 261 (1992).
2) T. Suzuki et al.: Phys. Rev. Lett. **75**, 3241 (1995).
3) A. Klein et al.: Nucl. Phys. A **607**, 1 (1996).
4) I. Tanihata et al.: Phys. Lett. B **206**, 592 (1988).
5) G. Lalazissis et al.: Phys. Rev. C **55**, 540 (1997).

† Condensed from the article in Nucl. Phys. A **709**, 60 (2002)

*1 GSI, Germany
*2 Kurchatov Institute, Russia
*3 Universidad de Santiago de Compostela, Spain
*4 Nagasaki Institute of Applied Science
*5 Comenius University, Slovakia
*6 Niigata University
*7 Tohoku University
*8 Chalmers University, Sweden

Beta decay of ^{46}Cr

T. K. Onishi,[*1] A. Gelberg,[*2] H. Sakurai,[*1] K. Yoneda, N. Aoi,[*1] N. Imai,[*1] H. Baba,[*3] P. von Brentano,[*2] N. Fukuda, Y. Ichikawa,[*1] M. Ishihara, H. Iwasaki,[*1] D. Kameda,[*4] T. Kishida, H. J. Ong,[*1] M. Osada,[*1] M. K. Suzuki,[*1] K. Ue,[*1] and H. Watanabe

[^{46}Cr, Gamow-Teller β decay]

It is well known that even-even nuclei with $N = Z - 2$ and $A = 4n + 2$, where n is an integer, decay to odd-odd $N = Z$ nuclei through favoured Gamow-Teller (GT) transitions. In particular, it is important to obtain information on the GT strength (B(GT)) in the p-f shell, because this will indicate the degree to which the Wigner SU(4)[1] symmetry is broken. ^{46}Cr is one of the candidates for such nuclei. In the β decay of ^{46}Cr no GT transitions have ever been observed.[2] However, very recently, a 1^+ excited state at 993 keV in ^{46}V has been observed.[3] Then, ^{46}Cr can decay to the 1^+ state in ^{46}V by GT transition with a significant branching ratio. In this work, we aimed to observe the GT transition, and to determine the B(GT) value from measurements of the half-life and the branching ratio.

The experiment was carried out at RIPS.[4] A ^{46}Cr beam was produced from the fragmentation of ^{50}Cr with a ^{9}Be target of 139 mg/cm^2. The energy of ^{50}Cr primary beam was 80 MeV/u and the intensity was 5 pnA. The obtained purity of ^{46}Cr was 0.1% and the rate was 66 cps at the final focal plane of RIPS. They were much smaller than the estimations using EPAX-2 with a modification in low momentum tails by 1/20. The ^{46}Cr ions were implanted into a plastic scintillator (stopper) with 5 mm thickness in order to determine the total beam intensity. The number of ^{46}Cr implanted in the stopper was determined by the purity of ^{46}Cr and the total beam intensity instead of identifying ^{46}Cr event-by-event. For measuring the half-life of ^{46}Cr, we used a pulsed beam with beam-on (500 ms) and beam-off (790 ms) periods. The β-rays from ^{46}Cr were detected by two sets of ΔE-ΔE-E plastic scintillators placed above and below the stopper. Each ΔE counter had a size of $200 \times 200 \times 2$ mm^3 and each ΔE counter closer to the stopper covered 42% of the solid angle. β-delayed γ-rays were detected by 4 Ge detectors (Clover type). The distance between the stopper and each clover was 120 mm. Each clover was used in the add-back mode, because the photopeak efficiency and the signal-to-background ratio became better. The total photopeak efficiency in the add-back mode was 1.4% for 1 MeV γ-rays. We measured the single γ and β-γ coincident spectrum for identifying β-delayed γ-rays and the γ-γ coincident spectrum for observing cascade transitions.

Figure 1 shows the γ-ray energy spectrum coincident with β-rays. The strong γ lines observed at 437 keV, 1228 keV, and 1525 keV are β-delayed γ-rays of ^{42}Sc which was a contaminant of the ^{46}Cr beam. Figure 2 shows the γ-ray energy spectrum around 1 MeV. The bump around 1015 keV has not been identified yet. The observed line at 992.3 ± 0.9 keV corresponds to the transition from the 1^+ state to the ground state of ^{46}V. Thus, we observed the GT decay of ^{46}Cr for the first time. Data analysis is now in progress.

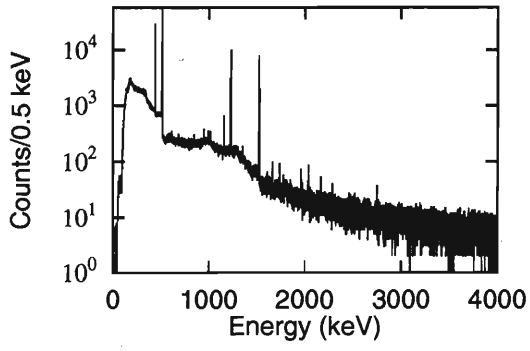

Fig. 1. γ-ray energy spectrum coincident with β-rays.

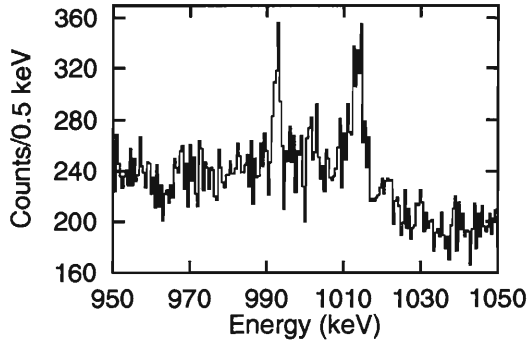

Fig. 2. γ-ray energy spectrum around 1 MeV.

*1 University of Tokyo
*2 Institut für Theoretische Physik, Universtät zu Köln, Germany
*3 Rikkyo University
*4 Tokyo Institute of Technology

References

1) P. van Isacker: Rep. Prog. Phys. **69**, 1661 (1999).
2) J. Zioni et al.: Nucl. Phys. A **181**, 465 (1972).
3) C. Friessner et al.: Phys. Rev. C **60**, 011304 (1999).
4) T. Kubo et al.: Nucl. Instrum. Methods Phys. Res. B **70**, 309 (1992).

$B(\mathrm{E2}; 0^+_{\mathrm{g.s.}} \rightarrow 2^+_1)$ measurement of the proton-rich $T = 1$ nuclei ^{46}Cr, ^{50}Fe, and ^{54}Ni

K. Yamada,[*1] T. Motobayashi, N. Aoi,[*2] H. Baba,[*1] K. Demichi,[*1] Z. Elekes, J. Gibelin,[*3] T. Gomi,[*1] H. Hasegawa,[*1] N. Imai,[*2] H. Iwasaki,[*4] S. Kanno,[*1] T. Kubo, K. Kurita,[*1] Y. U. Matsuyama,[*1] S. Michimasa,[*4] T. Minemura, M. Notani,[*4] T. Ohnishi,[*2] H. J. Ong,[*2] S. Ota,[*5] A. Ozawa, A. Saito,[*1] H. Sakurai,[*2] S. Shimoura,[*4] E. Takeshita,[*1] S. Takeuchi, M. Tamaki,[*4] Y. Togano,[*1] Y. Yanagisawa, K. Yoneda, and I. Tanihata

[Nuclear structure, B(E2), Coulomb excitation]

The electromagnetic matrix elements, M_{n} and M_{p}, are advantageous for studying the dynamical properties of nuclear states. In particular, the deviation of $M_{\mathrm{n}}/M_{\mathrm{p}}$ from N/Z is a good measure for a shell closure or a subshell closure, and provides information on the mechanism of core polarization.

Bernstein, Brown and Madsen[1] proposed to compare electromagnetic transitions in mirror nuclei to extract $M_{\mathrm{n}}/M_{\mathrm{p}}$ values. For electric quadrupole transitions, the relationship between the transition rates B(E2) and M_{p} is simply expressed as $B(\mathrm{E2}; 0^+ \rightarrow 2^+) = |\mathrm{M_p}|^2$. With the assumption of isospin symmetry, the matrix element M_{p} in a nucleus provides the value M_{n} in the mirror nucleus and *vice versa*. This method has been successfully applied to the pair of ^{26}Si and ^{26}Mg[2] or ^{38}Ca and ^{38}Ar.[3]

We performed the first measurement of $B(\mathrm{E2}; 0^+_{\mathrm{g.s.}} \rightarrow 2^+_1)$ for the proton-rich nuclei ^{46}Cr, ^{50}Fe, and ^{54}Ni to study unclear structures around the $Z = 20$–28 region systematically. Values of M_{n} for these $T_z = -1$ nuclei are obtained reliably, because their mirror nuclei ($T_z = +1$) are all stable and the B(E2) values are accurately determined.

A primary beam of ^{58}Ni accelerated by the RIKEN Ring Cyclotron was used for bombarding a 0.34-mm-thick Ni target at 95 A MeV with a typical beam intensity of 4.0 pnA. Projectile fragments were selected by RIPS with the help of a newly built RF deflector system[4] for purifying the secondary beam. The RF phase of the deflector was adjusted based on a primary beam measurement for calibrating the system. The momentum spread of the beam was set to be $\pm 0.7\%$, and a new vertical slit[4] for the deflector system was set so as to limit the beam intensity to about 5×10^3 counts per second. Secondary beams of ^{46}Cr and ^{50}Fe were focused on a 224 mg/cm^2 thick lead target, and a ^{54}Ni beam, on a 189 mg/cm^2 thick lead target. The averaged energies of the beams in the middle of the target were 45 A MeV, 42 A MeV, and 43 A MeV, respectively. Beam purities were improved respectively to 1.0%, 0.5%, and 0.2% by the RF deflector system. The factors of purity improvement were about twenty times.

The secondary beam was detected by three parallel-plate avalanche counters (PPACs) and by a plastic scintillator placed at the final focal plane (F3). Particle identification of the secondary beam was made by measuring the magnetic rigidity and time-of-flight (TOF) between the production target and the plastic scintillator. Independent runs were made in the intervals of coincidence runs with a 350-μm-thick Si detector to measure more precisely the fraction of the nucleus of interest in the beam.

We measured de-excitation γ-rays in coincidence with the scattered particles by using a subset of a new detector array[5] consisting of 116 NaI(Tl) scintillators with eleven layers. The scattered particles were detected by a PPAC with 150 mm × 150 mm size, and 3×3 matrices of Si detector telescopes with three layers. The thickness of each layer was 325 μm, 500 μm, and 500 μm. The particles were identified from energy deposits in the first and second layers of Si detectors, and the third layer was used as veto to reject light particles passing through the second layer.

Figure 1 shows the Doppler-corrected γ-ray energy spectrum obtained from ^{50}Fe + Pb scattering. A single distinct peak is seen at 765 keV. Analysis for extracting B(E2) values is in progress.

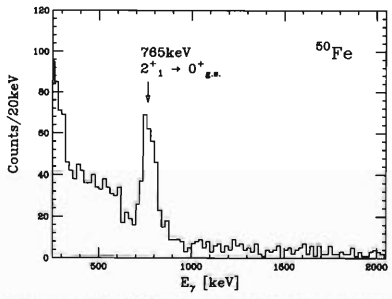

Fig. 1. Doppler-corrected γ-ray energy spectrum obtained from ^{50}Fe nuclei in flight with $\beta \approx 0.3$.

*1 Department of Physics, Rikkyo University
*2 Department of Physics, University of Tokyo
*3 Institut de Physique Nucléaire, Orsay, France
*4 Center for Nuclear Study, University of Tokyo
*5 Department of Physics, Kyoto University

References

1) A. M. Bernstein et al.: Phys. Rev. Lett. **42**, 425 (1979).
2) P. D. Cottle et al.: Phys. Rev. C **64**, 057304 (2001).
3) P. D. Cottle et al.: Phys. Rev. C **60**, 031301 (1999).
4) K. Yamada et al.: RIKEN Accel. Prog. Rep. **35**, 147 (2002).
5) H. Hasegawa et al.: RIKEN Accel. Prog. Rep. **35**, 169 (2002).

g Factor and oblate deformation of the $\frac{49}{2}^+$ isomer in ^{149}Dy

H. Watanabe, H. Ueno, D. Kameda,[*1] W. Sato, A. Yoshimi, H. Miyoshi,[*1] T. Kishida, Y. Kobayashi, J. Murata, J. Kaihara,[*1] K. Shimada,[*1] A. Odahara,[*2] Y. Gono,[*3] and K. Asahi

[NUCLEAR STRUCTURE, ^{149}Dy, g factor, high-spin isomer]

High-spin isomers have been observed systematically for $N = 83$ isotones.[1] It is well known that the excitation energies of these isomers with $60 \leq Z \leq 65$ are almost constant (8.5–9 MeV). Such characteristics are reproduced well in the framework of a deformed independent particle model (DIPM).[2,3] More detailed structural information of these isomers can be obtained by measuring nuclear moments which directly reflect microscopic nuclear structures. Among the high-spin isomers in $N = 83$ isotones, however, both the magnetic dipole and electric quadrupole moment have been measured only in ^{147}Gd so far; the configuration and the deformation parameter (β) are determined to be $[\pi(h^2_{11/2}(d^{-2}_{5/2})_0) \otimes \nu(f_{7/2}h_{9/2}i_{13/2}(d^{-2}_{3/2})_0)]_{49/2^+}$ [4] and -0.19,[5] respectively. These quantities can also be reproduced by the DIPM calculation. It is worth extending this kind of study to the other $N = 83$ isotones, particularly above $Z = 64$ sub-shell closure, in order to examine the mechanism producing the isomeric states at very high spin. In ^{149}Dy ($Z = 66$), a high-spin isomer with a half-life of 28 ns has been assigned at an excitation energy of 8.52 MeV in a recent work.[6] However, the spin-parity has not been yet estimated experimentally. According to the DIPM calculation, there are two possible candidates for this isomeric state, *i.e.*, $I^\pi = 47/2^-$ and $49/2^+$ (see Table 1). In the former case, the isomeric configuration is completely different from that in ^{147}Gd. Then a nearly spherical shape is expected for this isomeric state as well as for the lower-spin states in ^{149}Dy, which is attributable to the promotion of one proton across the $Z = 64$ shell gap. On the other hand, the latter has the same stretch-aligned configuration as the high-spin isomer in ^{147}Gd. This indicates that only neutrons excite beyond the $N = 82$ shell gap at this high-spin isomeric state because two valence protons already exist in the $h_{11/2}$ orbit, which is located just above the $Z = 64$ closed shell, at the ground state in ^{149}Dy. A large equilibrium oblate deformation is expected for this configuration as well as the high-spin isomer in ^{147}Gd.

In this work, the g factor of the high-spin isomer in ^{149}Dy has been measured using the γ-ray time-differential perturbed angular distribution (TDPAD) method with a pulsed beam of ^{132}Xe at RIKEN. Details of the experimental and analysis procedures are given in the last report.[7] The measurement of the g factor was carried out at two different temperatures, 328 K and 533 K, to confirm the temperature dependence of the paramagnetic effect in rare-earth elements. The results obtained in the present work are listed in Table 2. By taking an average of the values of g_{exp} derived for each temperature, the most reliable value, $\langle g_{exp} \rangle = 0.42 \pm 0.05$, could be obtained. This value is in good agreement with the calculated $g_{cal} = 0.46$ for the most likely configuration described in the spherical limit, $[\pi(h^2_{11/2}) \otimes \nu(f_{7/2}h_{9/2}i_{13/2})(d^{-2}_{3/2})_0]_{49/2^+}$. Therefore, we conclude that the spin-parity of the 28 ns high-spin isomer in ^{149}Dy is $49/2^+$.

Table 1. Probable spin-parity values and corresponding configurations predicted by the DIPM calculation for the $t_{1/2} = 28$ ns high-spin isomer in ^{149}Dy.

I^π	Configuration	g_{cal} [§]	β_{cal}
$\frac{47}{2}^-$	$\pi(h^3_{11/2}g^{-1}_{7/2}) \otimes \nu(i_{13/2})$	0.82	-0.041
$\frac{49}{2}^+$	$\pi(h^2_{11/2}) \otimes \nu((d^{-2}_{3/2})_0 f_{7/2}h_{9/2}i_{13/2})$	0.46	-0.166

§ g_{cal} is evaluated according to the simple additivity rule (Landé formula) with the following basic parameters; $g_\ell(\pi) = 1.1$, $g_\ell(\nu) = -0.03$, $g_s = 0.6 g_s$ (*free*).

Table 2. Summary of results obtained in the present work. For each temperature, the Larmor frequency, ω_L, was measured.

T [K]	ω_L [rad/ns]	$\beta(T)$ [§]	g_{exp}
328	0.182(34)	5.59	0.45(9)
533	0.103(11)	3.82	0.38(4)

§ calculated by Günther and Lindgen.[8]

*1 Tokyo Institute of Technology
*2 Nishinippon Institute of Technology
*3 Department of Physics, Kyushu University

References

1) A. Odahara et al.: Nucl. Phys. A **620**, 363 (1997), and references therein.
2) T. Døssing et al.: Phys. Scr. **24**, 258 (1981).
3) K. Neergård et al.: Phys. Lett. B **99**, 191 (1981).
4) O. Häusser et al.: Phys. Rev. Lett. **42**, 1451 (1979).
5) O. Häusser et al.: Nucl. Phys. A **443**, 135 (1985).
6) Y. Gono et al.: Eur. Phys. J. A **13**, 5 (2002).
7) H. Watanabe et al.: RIKEN Accel. Prog. Rep. **35**, 77 (2002).
8) C. Günther and I. Lindgen: in *Perturbed Angular Correlation*, edited by E. Karlsson, E. Matthias, and K. Siegbahn (North-Holland, Amsterdam, 1964), p. 357.

Recent improvements into the high spin isomeric beam line

T. Kishida, H. Watanabe, Y. Gono,[*1] T. Fukuchi,[*1] T. Sasaki,[*1] Y. Wakabayashi,[*1] M. Kibe,[*1] N. Hokoiwa,[*1] Q. Pan,[*2] and A. Odahara[*3]

[NUCLEAR REACTIONS, ^{16}O(^{136}Xe,7n)^{145m}Sm, Radioactive beams, Isomer]

Since 1993, the high-spin isomeric beam has been provided using RIKEN-RIPS based on the inverse kinematics of fusion-evaporation reactions. The intensity and purity of the secondary beam are 1–2 $\times$ 10^5 sec^{-1} and 10%, respectively, by using the production reaction of ^{16}O(^{136}Xe,7n)^{145m}Sm. However, when the secondary fusion reaction ^{13}C(^{145m}Sm,xn)$^{158-x}$Er experiment was performed, the purity of the high-spin isomeric beam became much worse due to a change in the primary beam condition.[1,2]

Recently, improvements for future experiments have been made in the primary beam handling system, gas target and recoil detector in order to reduce contaminations of the ^{136}Xe primary beam and to obtain a ^{145m}Sm secondary beam with a "good and stable" purity.

For the improvement of the primary beam handling system, a "V-shaped" movable collimating slit has been placed on the beam axis at 660 mm before the gas target system in order to limit the emittance of the primary beam and to make the downstream beam more stable and more insensitive to the operating conditions of the accelerator. This improvement prevents the irradiation of the target cell, thus reducing the primary beam component scattered by the target cell. By this improvement, the beam purity did not become worse even when the emittance of the primary beam changed largely, but this change could be detected as the decrease of the intensity of the secondary beam.

For the improvement of the gas target, the thickness of the apertures have been made thinner; the 14 mm-thick brass apertures of the gas cell have been replaced by 100 μm-thick tantalum, and the 10 mm-thick aluminum apertures of the outer chambers by 100 μm-thick tantalum. This improvement reduces the "scattered" primary beam component and prevents the precipitation of carbon inside the target cell.

In addition to the above improvements, a thin (2 μm-thick) plastic scintillation counter has been placed as a recoil detector at 460 mm after the secondary target position. The timing information of this counter can be used in off-line analysis to purify data. Since the distance from the gas target to the recoil detector is 30.87 m, the difference in time-of-flight between the primary beam and the secondary beam becomes large enough to separate the ^{145}Sm component from the other components. The time difference between the primary beam, ^{136}Xe, and the isomeric beam, ^{145m}Sm, is about 108 ns, and that between the primary beam and the reaction product, ^{142}Nd, is about 71 ns. (The ^{142}Nd's are produced by the fusion reaction between the primary beam and carbon in the CO_2 gas.) Figure 1 shows the time spectrum observed with the recoil detector. This counter can also be used as a monitor of beam purity.

However, as shown in Fig. 1, the time spectrum has a repetition cycle of 53 ns due to the 19 MHz frequency of the RF signal, so that the peak by the primary beam overlaps on the ^{145}Sm component accidentally. A beam-bunching method has been adopted in order to solve this problem, where the repetition cycle of the beam becomes (53 $\times$ n) ns (n: integer). The beam-bunching method can successfully separate the spectrum into ^{145}Sm, ^{142}Nd and ^{136}Xe components.

Our next experiment on the secondary fusion reaction ^{13}C(^{145m}Sm,xn)$^{158-x}$Er will be performed in the spring of 2003 with high-purity high-spin isomeric beam.

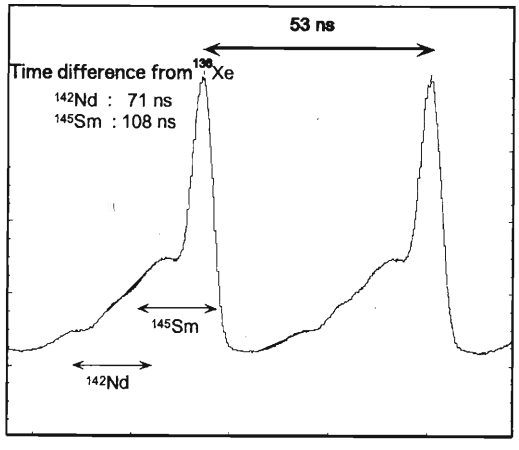

Fig. 1. Timing spectrum between plastic scintillation counter and RF signal.

References

1) T. Kishida et al.: Nucl. Instrum. Methods Phys. Res. A **484**, 45 (2002).
2) T. Kishida et al.: RIKEN Accel. Prog. Rep. **35**, 41 (2002).

*1 Department of Physics, Kyushu University
*2 Institute of Modern Physics, China
*3 Nishinippon Institute of Technology

Measurements of equilibrium charge state of heavy ions in helium gas using a RIKEN gas-filled recoil separator

D. Kaji,[*1], K. Morita, K. Morimoto, A. Yoneda, Y.-L. Zhao,[*2] H. Xu,[*3], E. Ideguchi, T. Ohnishi, H. Haba, K. Katori, H. Kudo,[*1] T. Suda, K. Sueki,[*4] A. Yoshida, T. Zheng,[*5] and I. Tanihata

[Equilibrium charge state, element 113, super-heavy element]

Equilibrium charge state of heavy elements in dilute helium gas was measured using a gas-filled recoil separator, GARIS, at RILAC facility.

The GARIS was designed for fast (in-flight) and effective collection of fusion reaction products, magnetically separating them from unwanted particles such as incident beams, light charged particles, target recoils and transfer reaction products.[1)] The GARIS will be used to search for new isotopes, including those of the heaviest elements whose atomic numbers are greater than 113.

One of the most important parameters of the separator is equilibrium charge state $\bar{q}$ of ions in helium gas. The magnetic rigidity of an ion is determined by the following equation:

$$B\rho = 0.0227 \times A \times \frac{(v/v_0)}{\bar{q}} \quad [\mathrm{T \cdot m}], \qquad (1)$$

where A, $\bar{q}$ and v are the mass number [amu], equilibrium charge state and velocity of an ion passing a trajectory with the radius ρ [m] through a homogenous magnetic field with a flux density B [T]. Here the velocity is expressed in the unit of the Bohr velocity $v_0 = c/137 = 2.19 \times 10^6$ [m/s], where c denotes the light speed.

We need to know the $\bar{q}$ values of the heavy elements, which are not yet observed, in order to properly set up the separator. To estimate the $\bar{q}$ values of such heavy elements, we need to have an empirical formula of the $\bar{q}$. Therefore, we measured the $B\rho$ distribution of heavy ions using 0 degree target recoils (^{208}Pb, ^{209}Bi and ^{169}Tm) and fusion reaction products (^{193}Bi, ^{196}Po, ^{200}At, ^{204,203}Fr, ^{212}Ac, ^{234}Bk, ^{245}Fm, ^{254}No, ^{255}Lr, ^{265}Hs and ^{271}[110]) produced by ^{40}Ar, ^{48}Ca, ^{58}Fe and ^{64}Ni-induced fusion reactions. For example, the $B\rho$ distribution of ^{245}Fm is shown in Fig. 1 together with their Gaussian fitting curve. The distribution is represented as a function of the collection efficiency of the GARIS. From the obtained curves, the $\bar{q}$ values for each recoil are deduced using Eq. (1). Obtained $\bar{q}$ values are plotted in Fig. 2. Values of $v/v_0 \times Z^{1/3}$ are taken as the horizontal axis. We have obtained the following empirical formula:

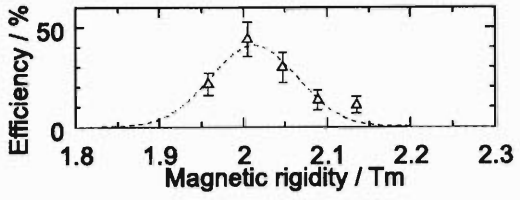

Fig. 1. $B\rho$ distribution for ^{245}Fm recoil measured by the GARIS with helium gas at the pressure of 76 Pa. The broken curve shows a fit to the data points with the Gaussian function.

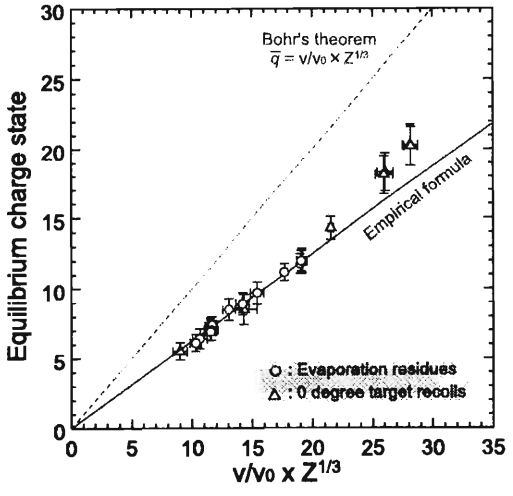

Fig. 2. Systematics of the measured $\bar{q}$ of heavy atoms in dilute helium gas as a function of $v/v_0 \times Z^{1/3}$. Circles represent the results of evaporation residues, and triangles indicate the ones of 0 degree target recoils. See text for details about the empirical formula.

$$\bar{q} = 0.625 \times (v/v_0) \cdot Z^{1/3}, \ [8 < (v/v_0) \cdot Z^{1/3} < 20].$$

The detailed discussion on $\bar{q}$ is described in Ref. 2. This formula will be applicable to the search for super-heavy elements with large atomic numbers over 110.

References

1) K. Morita et al.: Nucl. Instrum. Methods Phys. Res. B **70**, 220 (1992).
2) D. Kaji, K. Morita, K. Morimoto et al.: Nucl. Instrum. Methods Phys. Res. A, to be published.

*1 Department of Chemistry, Niigata University
*2 Institute of High Energy Physics, China
*3 Institute of Modern Physics, China
*4 University of Tsukuba
*5 Peking University, China

Identification of ^{234}Bk and ^{230}Am with RIKEN GARIS

K. Morimoto, K. Morita, D. Kaji,[*1] A. Yoneda, A. Yoshida, T. Suda, E. Ideguchi, T. Ohnishi, Y.-L. Zhao,[*2] H. Xu,[*3] T. Zheng,[*4] M. Haba, H. Kudo,[*1] H. Koura, K. Katori, and I. Tanihata

[New isotope, Bk, Am]

New neutron-deficient isotopes of ^{234}Bk and ^{230}Am produced by ^{197}Au(^{40}Ar, 3n)^{234}Bk reaction were identified using a RIKEN gas-filled recoil separator GARIS at the RILAC facility. The decay property of neutron-deficient actinide isotopes is interesting because many decay modes such as α, β^+ and electron capture (EC), and spontaneous fission decays coexist in this region.

An ^{40}Ar beam was accelerated by RILAC up to 188.4 MeV and irradiated gold targets. The targets were prepared by evaporation of metallic gold onto carbon foils of 30 μg/cm^2 thickness each. The thickness of the gold layer was 200 μg/cm^2. Eight target foils were mounted on a rotating wheel of 12.5 cm diameter at the target center. The wheel was rotated continuously at 600 rpm to prevent damage to the targets by heat from the intense primary beam. The GARIS was filled with He gas at 0.55 torr. Magnetic rigidity Bρ was set to 1.91 Tm, which was determined based on our empirical data[1] of the equilibrium charge state. Evaporation residues (ERs) were introduced into the GARIS, separated from the beam, target recoils and other unwanted particles, and transported to a detection chamber. ERs were then implanted into a position-sensitive semiconductor detector (PSD). All successive decays which started from the ERs after the implantation should take place at the same position in the detector. Identification of the products was based on the genetic correlations of mother and daughter nuclei. Because the ranges of ERs in a silicon detector were much shorter than those of decaying α particles, α particles emitted in the back hemisphere escaped from the detector. We could identify the products based on time, position, and energy correlation of decay signals.

We observed total four α decays followed by decay chains that started from ^{230}Pu. The average α energy was 7.85 $\pm$ 0.05 MeV and the mean decay time was 202 s. Possible candidates for the α decaying nuclei are ^{234}Cm and ^{234}Bk, where ^{234}Cm is a product of the p2n evaporation channel and ^{234}Bk is that of the 3n evaporation channel. It is known that ^{234}Cm emits α particles of 7.239 MeV with a half-life of 51 s,[2] and no α-decay chain after ^{230}Am has been observed. Therefore, we consider that the 7.8 MeV α is associated with the decay of ^{234}Bk to ^{230}Am. ^{230}Am is considered to have decayed to ^{230}Pu by EC decay. The average time between the α-decays of ^{234}Bk and ^{230}Pu has been determined to be 171 s, which corresponds to the sum of the lifetimes of ^{230}Am and ^{230}Pu. Using the known half-life of ^{230}Pu, 102 $\pm$ 10 s,[2] the half-life of ^{230}Am is estimated to be 17^{+119}_{-17} s. The decay chain is presented in Fig. 1.

In summary, we observed total four decay chains from ^{234}Bk after irradiating the production target with 2.37×10^{18} ions. The α-decay energy and half-life of ^{234}Bk have been determined to be 7850 $\pm$ 50 keV and 140^{+140}_{-47} s, respectively. The half-life of ^{230}Am is estimated to be 17^{+119}_{-17} s.

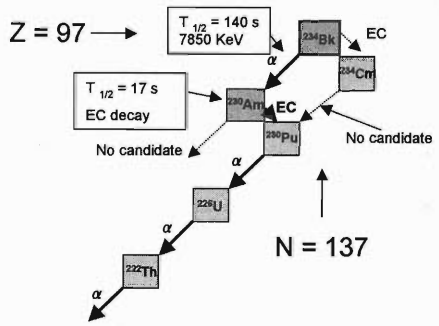

Fig. 1. Decay chain of new ^{234}Bk isotopes produced by ^{197}Au(^{40}Ar, 3n)^{234}Bk reaction. No decay to ^{234}Cm was observed. Another new ^{230}Am isotope shows no α-decay.

References

1) D. Kaji et al.: Nucl. Instrum. Methods Phys. Res. A, to be submitted.
2) P. Cagada et al.: GSI Sci. Rep. 2001, 15 (2002).

*1 Department of Chemistry, Niigata University
*2 Institute of High Energy Physics, China
*3 Institute of Modern Physics, China
*4 Peking University, China

Confirmation of the synthesis of isotope $^{271}110$ of the element 110

K. Morita, K. Morimoto, D. Kaji,* A. Yoneda, A. Yoshida, T. Suda, E. Ideguchi, T. Ohnishi, Y.-L. Zhao, H. Xu, T. Zheng, H. Haba, H. Kudo, K. Sueki, A. Ozawa, F. Tokanai, H. Koura, R. Kanungo, K. Katori, and I. Tanihata

[Nuclear reaction, Confirmation of element 110 synthesis, Gas-filled recoil separator]

The synthesis of isotope $^{271}110$ of the 110th element was confirmed by $^{208}Pb+^{64}Ni$ fusion measurement using the gas-filled recoil separator GARIS at the RIKEN Linear Accelerator (RILAC) Facility.

For element 110, productions of $^{269}110$,[1] $^{271}110$,[2] and $^{270}110$[3] were reported by a GSI group in Germany. Those of $^{273}110$[4] at FLNR of JINR in Russia and $^{267}110$[5] by an LBNL group in USA were also announced. However, no cross-check experiment was performed by any of those groups. Here, we performed experiments to confirm the production of $^{271}110$[2] at GSI, using the same reaction, $^{208}Pb+^{64}Ni \rightarrow {}^{271}110+n$, but with a different type of detection device. We used the gas-filled recoil separator GARIS, while the GSI group used the velocity filter type recoil separator SHIP.

A ^{64}Ni beam from the RILAC irradiated targets prepared by evaporating metallic ^{208}Pb onto carbon foil. The thicknesses of the ^{208}Pb layer and the carbon foil were 230 $\mu g/cm^2$ and 30 $\mu g/cm^2$, respectively. We performed the measurement using four beam energies from the RILAC: 310.2, 313.2, 316.3, and 320.7 MeV. Total beam dose was 4.4×10^{18}. The maximum event rate was observed at the energy of 316.3 MeV. Reaction products of interest produced in the target were separated from the beam, target recoils, and other unwanted particles by GARIS and transported to the detection area. Then the products were implanted into a position-sensitive silicon semiconductor detector (PSD), the effective area of which was 60 mm by 60 mm. All successive decays starting from the products after the implantation should occur at the same place. Identification of the products were based on genetic correlations of mother and daughter nuclei. We could use time, position, and energy correlations of decay signals. Transmission of GARIS was deduced to be 0.76 while that of SHIP was 0.4.

We observed 14 candidates of decay chains originating from $^{271}110$. The α energies detected using the PSD coincide well with the reported value of 10.72 MeV[6] for $^{271}110$. Almost all decays were followed by sequential decays of daughter (^{267}Hs), granddaughter (^{263}Sg), and/or grand-granddaughter (^{259}Rf) or even further. Measured decay times of isotope $^{271}110$, which were the time differences between the moment of implantation of the isotopes and the first α emission, were 0.057 ms, 0.92 ms, 1.31 ms, 1.36 ms, 1.69 ms, 1.74 ms, 2.22 ms, 3.80 ms, 4.63 ms, 6.59 ms, 7.54 ms, 46.0 ms, 87.14 ms, and 239.0 ms. They could be divided into two groups, one of decay times shorter than 10 ms (11 events), and another of decay times longer than 10 ms (3 events). The mean life time of the first group was calculated to be $2.90^{+3.0}_{-0.9}$ ms and that of the second was 124^{+646}_{-47} ms. The mean life times reported by the GSI group[6] were $1.8^{+1.8}_{-0.6}$ ms (11 events) and 65^{+452}_{-25} ms (2 events), respectively. The values obtained in the two independent experiments coincided well for both the short decay and long decay groups within the range of statistical error. The production cross section measured in the present experiment was $16.5^{+5.6}_{-5.3}$ pb, which agrees well with 15^{+9}_{-6} pb reported for the GSI experiment.

On the basis of the agreement of the two experimental results obtained using different setups in different operational principles, we conclude that the production of isotope $^{271}110$ of the 110th element was clearly confirmed. Furthermore, it also become clear that the isotope produced by the $^{208}Pb(^{64}Ni, 1n)$ reaction has at least two different decay half-lives. By combining the results of the two experiments, the new mean life with improved statistics are obtained as $2.35^{+1.35}_{-0.59}$ ms and 100^{+262}_{-36} ms. In terms of half-life, they are $1.62^{+0.94}_{-0.41}$ ms and $69.3^{+181.6}_{-25.0}$ ms, respectively.

Between the two modes of decay with different half-lives, no difference in energies of decay α s was observed. One of the possible explanations is as follows. An isomeric state exists in $^{271}110$ that decays *via* an isomeric transition with a half-life longer than that in the ground state. Both the isomeric state and the ground state are populated in the reaction, then the former decays by isomeric transition to the ground state. Subsequently, the ground state decays by α emission. To examine this possibility, the decay scheme should be clarified through further measurements, for example γ-ray detection.

References

1) S. Hofmann et al.: Z. Phys. A **350**, 277 (1995).
2) S. Hofmann et al.: Z. Phys. A **350**, 281 (1995).
3) S. Hofmann et al.: Eur. Phys. J. A **10**, 5 (2001).
4) Yu. A. Lazarev et al.: Rhys. Rev. C **54**, 620 (1996).
5) A. Ghiorso et al.: Nucl. Phys. A **583**, 861c (1995).
6) S. Hofmann: Rep. Prog. Phys. **61**, 639 (1998).

* Department of Chemistry, Niigata University

Measurement of an excitation function of production cross section of $^{271}110$ *via* $^{208}Pb + {}^{64}Ni \rightarrow {}^{271}110 + n$ reaction

K. Morita, K. Morimoto, D. Kaji,* A. Yoneda, A. Yoshida, T. Suda, E. Ideguchi, T. Ohnishi, Y.-L. Zhao, H. Xu, T. Zheng, H. Haba, H. Kudo, K. Sueki, A. Ozawa, F. Tokanai, H. Koura, A. V. Yeremin, R. Kanungo, K. Katori, and I. Tanihata

[Element 110, excitation function]

An excitation function of production cross section of $^{271}110$ *via* $^{208}Pb + {}^{64}Ni \rightarrow {}^{271}110 + n$ reaction was measured using a gas-filled recoil separator GARIS at RILAC facility.

An excitation function of a cross section for producing a very heavy system provides important information on the reaction mechanism as well as the optimum reaction energy giving the maximum yield for heavy element production.

From an experimental point of view, however, the measurement is rather difficult to carry out because the production cross sections are very small for producing isotopes of heavy elements such as those with atomic numbers greater than 110. Although there is a systematic study of the excitation function for heavy element production *via* cold-fusion reaction reported by Hofmann[1] at GSI in Germany, statistical error of the measured cross sections whose atomic number of the compound nuclei are greater than 110 is rather large because of the smallness of the cross section. We have tried to remeasure the excitation function for advancement of the research of a heavier system.

^{64}Ni ions were accelerated by RILAC. Cross sections were measured at the four energies listed in Table 1. The energy was determined by two methods. One was by measuring the magnetic rigidity $B\rho$ value by using a 90° bending magnet of which the ρ value is 1 m. The other was by measuring the time of flight of the beam. The difference between the two methods was 0.2% in energy. The beam was introduced to the target chamber in the gas region by passing through the differential pumping section to separate the vacuum region of the beam transport line from the gas region without using a foil.

Table 1. Summary of the measurements. a: Energy from the accelerator, b: Energy at the half-depth of the target.

E_{in}[a] (MeV)	E_c[b] (MeV)	Dose (10^{18})	Event	σ (pb)
310.2	308.2	1.45	1	$1.3^{+3.0}_{-0.9}$
313.2	311.3	0.86	4	$8.0^{+6.3}_{-3.8}$
316.3	314.4	1.07	9	$16.5^{+5.6}_{-5.3}$
320.7	318.8	1.01	0	< 3.7

* Department of Chemistry, Niigata University

The targets were prepared by evaporation of lead 208 metal (isotopically purified up to 97%) deposited in layers of 230 μg/cm^2 on carbon backing foils of 30 μg/cm^2. Additional carbon of 10 μg/cm^2 in thickness was deposited by evaporation on the target layers to protect the targets from sputtering. The beam hit the target from the 30 μg/cm^2 foil side. Eight targets were mounted on the rotating wheel, which was rotated during the irradiation by 1000 rpm. The diameter of the circle of which the beam center made was 12.5 cm. The pressure of the gas was set to 75 Pa. The $B\rho$ value of the product in GARIS was set to 2.04 Tm. The transmission of the GARIS was estimated to be 0.76.[2]

Results are listed in Table 1 together with energies from the accelerator (E_{in}) and energies at the half-depth of the target (E_c). Those are plotted in Fig. 1. The curve shown by a dotted line is Gaussian. The peak position of the curve is 313.8 MeV, and the full width at half maximum (FWHM) is 4.7 MeV. The obtained value of the peak position is 4 MeV higher than the one reported in Ref. 1.

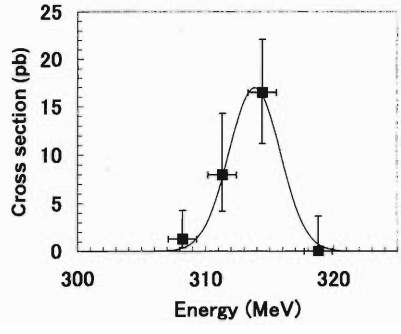

Fig. 1. Excitation function of production cross section of $^{271}110$. Horizontal axis indicates the energy at the half-depth of the target. Errors in cross sections have a 68% confidence level, and those in energies correspond to the energy losses in the targets.

References

1) S. Hofmann: Rep. Prog. Phys. **61**, 639 (1998).
2) K. Morita et al.: RIKEN Accel. Prog. Rep. **35**, 154 (2002).

γ-ray spectroscopy of hyperfragments with stopped K^-

K. Tanida for KEK-PS E509 collaboration

[HYPERNUCLEI, γ ray spectroscopy, Stopped kaon]

The success of high-resolution γ-ray spectroscopy of hypernuclei with germanium detectors[1-3] opened a new era of hypernuclear physics. These experiments revealed fine structures of light hypernuclei and provided valuable information on the underlying ΛN spin-dependent interaction. However, in these experiments, where direct reactions such as (π^+, K^+) and (K^-, π^-) were used to produce hypernuclei, beam times of more than a month were necessary. Therefore, systematic studies of hypernuclei were very difficult.

On the other hand, it is known that two orders of magnitude more hypernuclei can be produced as hyperfragments by stopped K^- reactions than by direct reactions. Furthermore, various species of hypernuclides lighter than target nucleus, including neutron (proton) rich ones, are available in stopped K^- reactions and thus a systematic study becomes possible.

Such studies are expected to extend capabilities of hypernuclear physics. For example, if data from many hypernuclei are available, we can discuss not only the two-body ΛN interaction, but also the three-body ΛNN interaction, which may play an important role in structures of hypernuclei because of the strong ΛN-ΣN coupling.[4,5] Also, charge symmetry breaking in the ΛN and ΛNN interactions can be investigated by comparing structures of mirror hypernuclei.

Motivated by the above discussions, we performed an experiment to measure γ rays from hyperfragments produced by stopped K^- reactions in April 2002 at KEK-PS K5 beamline. K^- beam was extracted at 650 MeV/c. We used three cherenkov counters (LC1-3) and three time-of-flight counters (B1-3) to identify kaons. Kaons were degraded by carbon blocks of $\sim 90\,\mathrm{g/cm^2}$ thick in total, and stopped at the targets. Non-stopping kaons were rejected by a veto counter (FV) placed downstream of the targets. We used five targets (Li, Be, ^{10}B, ^{11}B, and C) in order to see the target dependence of γ-ray yield.

We used Hyperball[6] for γ-ray detection. Hyperball consists of 14 germanium detectors (Ge), each surrounded by six bismuth germanate (BGO) counters. Total photo-peak efficiency of Hyperball was about 1% at 1 MeV including the effect of deadtime due to the high counting rate of Ge.

Now we are at the analysis stage. A preliminary analysis of full data shows that a γ ray from ${}^{7}_{\Lambda}\mathrm{Li}(5/2^+ \rightarrow 1/2^+)$ was observed at 2050 keV (see Fig. 1). This γ ray was observed for the ^{10}B and C targets, but not for the other targets, particularly, ^{11}B. This result cannot be explained by statistical decay of compound hypernucleus. Furthermore, since ^{11}B has $J^\pi = 3/2^-$ and ^{12}C has $J^\pi = 0^+$, high-spin states such as $5/2^+$ of ${}^{7}_{\Lambda}$Li are expected to be more favorably produced from ^{11}B than ^{12}C from naive discussions. Thus, the present result is interesting with respect to the production mechanism of hyperfragments.

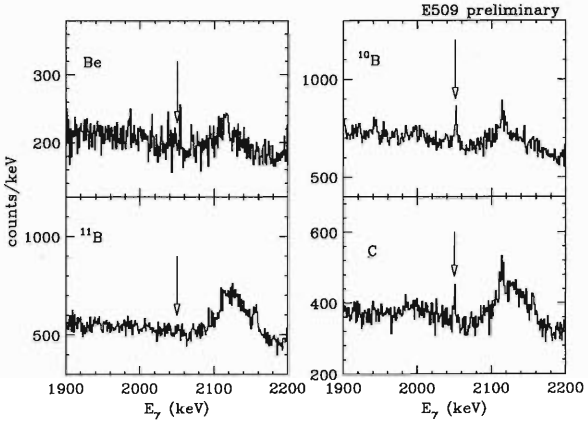

Fig. 1. γ-ray energy spectrum around 2 MeV for Be, ^{10}B, ^{11}B, and C targets. The 2050 keV γ ray from the ${}^{7}_{\Lambda}\mathrm{Li}(5/2^+ \rightarrow 1/2^+)$ transition was observed for the ^{10}B and C targets.

We also observed two more candidates for hypernuclear γ rays. One is at 1400 keV for the C target only, and the other is at 1303 keV for the ^{9}Be and ^{10}B targets. Identification of these γ rays, which is necessary to extract physics information, is not yet performed; they might be from ${}^{11}_{\Lambda}$B and ${}^{8}_{\Lambda}$Li, respectively.

These preliminary results indicate that γ-ray spectroscopy of hyperfragments with stopped K^- is sufficiently feasible. Further analysis is underway to determine the γ-ray intensity per stopped K^-. γ-γ coincidence analysis will also be performed.

We are planning to improve the experimental setups and acquire more statistics. Further experiments using heavier targets are being considered in future.

References

1) H. Tamura et al.: Phys. Rev. Lett. **84**, 5963 (2000).
2) K. Tanida et al.: Phys. Rev. Lett. **86**, 1982 (2001).
3) H. Akikawa et al.: Phys. Rev. Lett. **88**, 082501 (2002).
4) B. F. Gibson, I. R. Afnan, J. A. Carlson, and D. R. Lehman: Prog. Theor. Phys. Suppl. No. 117, 339 (1994).
5) Y. Akaishi, T. Harada, S. Shinmura, and Khin Swe Myint: Phys. Rev. Lett. **84**, 3539 (2000).
6) H. Tamura: Nucl. Phys. A **639**, 83c (1998).

Analysis of experiment KEK-PS E325 for the measurement of $\rho/\omega/\phi$ meson decays in nuclear matter

R. Muto,[*1] J. Chiba,[*2] H. En'yo, H. Funahashi,[*1] H. Hamagaki,[*3] M. Ieiri,[*2] M. Ishino,[*4] H. Kanda,[*5] M. Kitaguchi,[*1] S. Mihara,[*4] T. Miyashita,[*1] T. Murakami,[*1] M. Naruki,[*1] M. Nomachi,[*6] K. Ozawa,[*3] F. Sakuma,[*1] O. Sasaki,[*2] H. D. Sato,[*1] M. Sekimoto,[*2] T. Tabaru, K. H. Tanaka,[*2] S. Yamada,[*1] S. Yokkaichi, and Y. Yoshimura[*1]

[QCD, chiral symmetry, normal nuclear density, mass modification, vector meson]

In quantum chromodynamics, light quarks originally have only a few MeV/c^2 bare mass, but as a consequence of spontaneous chiral symmetry breaking, they obtain an effective mass of about a few hundred MeV/c^2. At a very high density and/or temperature, this symmetry will be restored and quark mass will return to its original value. Various theories suggest that even at a normal nuclear density, vector meson mass could be decreased as a precursor of chiral phase transition. For example, one model based on the QCD sum rule has been proposed by Hatsuda and Lee,[1] which predicted that the mass decrease at a normal nuclear density is about 120–180 MeV/c^2 for the ρ/ω mesons and about 20–40 MeV/c^2 for the ϕ meson. Since there has been only few lines of evidence to support such a theoretical concept, we have designed an experiment to detect a clear signature of vector-meson mass-modification in nuclear matter and to investigate the origin of the quark mass in hadron.

The experiment, KEK-PS E325, was designed to detect vector mesons, ρ, ω and ϕ, in the target nuclei produced in 12-GeV p+A interactions, and to measure the invariant mass spectrum of e^+e^- and K^+K^- pairs which are decay products of vector mesons. About 50 percent of the ρ mesons and several percent of the ω/ϕ mesons are expected to decay inside the nuclei. Thus, for example, we can expect the original ϕ meson peak decaying in vacuum with some tail or a second peak which consists of ϕ decaying in nuclei.

The data acquisition started in 1997 and ended in March 2002. In the last physics run that ended last March, we collected about 2.3 Tbytes raw data with upgraded drift chambers and electron identification counters. We accumulated statistics of about 100 times as large as our published result with 1998 data.[2] To analyze this large amount of data, particularly in the most time-consuming steps such as track reconstruction and track fitting, we used the excellent cpu power of RIKEN CC-J,[3] which is originally built for the RHIC spin physics. Thus far, we have analyzed half of these data in about 30,000 cpu·hours.

The recent analysis results of invariant mass spectra of e^+e^- pairs for the carbon target are shown in Fig. 1. The bold solid line is the best-fit result of the known hadronic sources with the combinatorial background, and the significant excess can be seen in the low mass side of the clear peak from decays of ω mesons in free space, which is located around 0.78 GeV/c^2. With this statistics, we are now able to determine the ρ/ω ratio from the tail of high-mass side of the ω peak. The obtained value is about 0.5, which is much smaller than the known ρ/ω ratio, unity, in pp interactions.[4] This fact implies that this excess mainly comes from ρ mesons, whose invariant mass shape is modified in nuclear matter. From the copper target data, we also obtained a similar result for ρ meson mass modification.

Now we are analyzing the rest of data. We will be able to obtain a dispersion relation for meson modification when all the statistics become available.

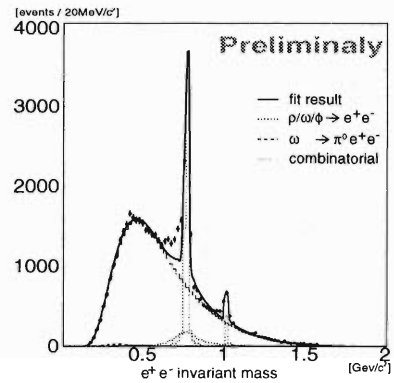

Fig. 1. Invariant mass spectrum of the e^+e^- pair for carbon target from 2002 data. The bold solid line shows the best-fit result of the known hadronic sources with the combinatorial background.

*1 Department of Physics, Kyoto University
*2 Institute for Particle and Nuclear Studies, High Energy Accelerator Research Organization (KEK)
*3 Center for Nuclear Study, University of Tokyo
*4 International Center for Elementary Particle Physics, University of Tokyo
*5 Tohoku University
*6 Research Center for Nuclear Physics, Osaka University

References

1) T. Hatsuda and S. H. Lee: Phys. Rev. C **46**, R34 (1992).
2) K. Ozawa et al.: Phys. Rev. Let. **86**, 5019 (2001).
3) T. Ichihara et al.: RIKEN Accel. Prog. Rep. **35**, 236 (2002); Y. Watanabe et al.: RIKEN Accel. Prog. Rep. **36**, 262 (2003).
4) V. Blobel et al.: Phys. Lett. B **48**, 73 (1974).

Precision spectroscopy of pionic 1s states of Sn nuclei and evidence for partial restoration of chiral symmetry in the nuclear medium

K. Suzuki,[*1] M. Fujita,[*2] H. Geissel,[*3] H. Gilg,[*4] A. Gillitzer,[*5] R. S. Hayano,[*1] S. Hirenzaki,[*2] K. Itahashi, M. Iwasaki, P. Kienle,[*4,*6] M. Matos,[*3] G. Münzenberg,[*3] T. Ohtsubo,[*7] M. Sato,[*8] M. Shindo,[*1] T. Suzuki,[*1] H. Weick,[*3] M. Winkler,[*3] T. Yamazaki, and T. Yoneyama[*8]

[pion, chiral symmetry]

It is important to study the isovector s-wave pion-nucleus interaction to deduce information on the possible reduction of the chiral order parameter in the nuclear medium.[1,2] Following a recent experiment[3] and analysis[4] of π^- in ^{205}Pb, deeply bound 1s states of π^- in ^{115,119,123}Sn were observed as dominant single peaks using the Sn$(d,{}^3\mathrm{He})$ pion-transfer reaction under the recoil-free condition at GSI, as shown in Fig. 1.[5] The 1s binding energies were determined to be 3.900 ± 0.020, 3.819 ± 0.013 and 3.749 ± 0.013 MeV for ^{115}Sn, ^{119}Sn and ^{123}Sn, respectively, with an additional systematic error of 0.015 MeV. The binding energies and widths were used to deduce the isovector potential parameter of the s-wave pion-nucleus interaction to be $b_1 = -0.115 \pm 0.007\, m_\pi^{-1}$ according to the procedure recently established.[4] This b_1 is observed to be enhanced compared with the free πN value ($-0.090\, m_\pi^{-1}$). This indicates a reduction of the chiral order parameter: $f_\pi^*(\rho)^2/f_\pi^2 = 0.78 \pm 0.04$ at an effective nuclear density $\rho \approx 0.60\,\rho_0$. This ratio can be expressed as $1 - \alpha\rho$, and the parameter $\alpha\rho_0$ is determined to be 0.37 ± 0.06. (See Fig. 2.) This value corresponds to a reduction of the quark condensate at the normal nuclear density: $\langle\bar{q}q\rangle_{\rho_0}/\langle\bar{q}q\rangle_0 \approx 0.66 \pm 0.06$, which is very close to a theoretical prediction from chiral dynamics.

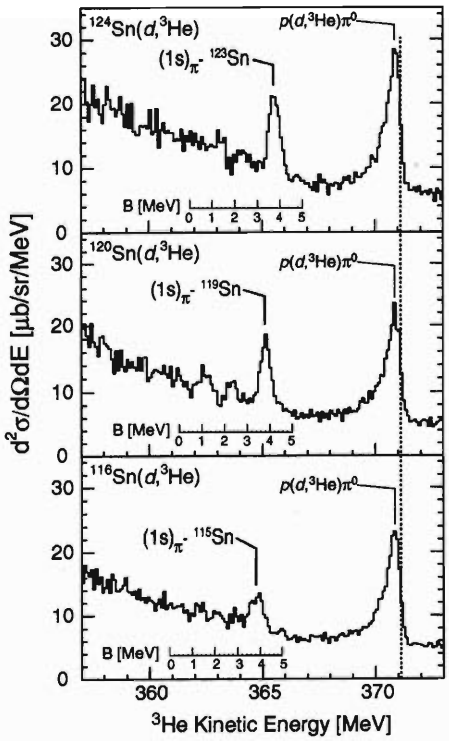

Fig. 1. Double differential cross sections versus the ^{3}He kinetic energy of the ^{124,120,116}Sn$(d,{}^3\mathrm{He})$ reaction measured at the incident deuteron energy (T_d) of 503.388 MeV. The scales of the π^- binding energies in ^{123,119,115}Sn are also indicated.

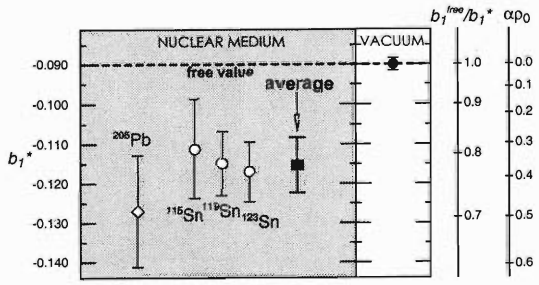

Fig. 2. Summary of the b_1^* values (in m_π^{-1}) deduced from the B_{1s} binding energies in ^{115,119,123}Sn together with the corresponding scales in $b_1^{\mathrm{free}}/b_1^*$ ($= f_\pi^*(\rho_e)^2/f_\pi^2$) and $\alpha\rho_0$. The previous ^{205}Pb data reanalyzed with Im B_0 ($= 0.046\, m_\pi^{-4}$) is shown for comparison.

*1 Department of Physics, School of Science, University of Tokyo
*2 Department of Physics, Nara Women's University
*3 GSI, Germany
*4 Physik-Department, Technische Universität München, Germany
*5 Institut für Kernphysik, Forschungszentrum Jülich, Germany
*6 Institute for Medium Energy Physics of the Austrian Academy of Sciences, Austria
*7 Department of Physics, Niigata University
*8 Department of Physics, Tokyo Institute of Technology

References

1) W. Weise: Acta Phys. Pol. **31**, 2715 (2000).
2) P. Kienle and T. Yamazaki: Phys. Lett. B **514**, 1 (2001).
3) H. Geissel et al.: Phys. Rev. Lett. **88**, 122301 (2002).
4) H. Geissel et al.: Phys. Lett. B **549**, 64 (2002).
5) K. Suzuki et al.: nucl-ex/0211023.

2. Atomic and Solid-State Physics

A unified treatment of positron annihilation and positronium formation near positronium formation threshold

A. Igarashi,[*1] M. Kimura,[*2] and I. Shimamura

In collisions of positrons (e^+) with atoms and molecules, if an incident positron shares the same space with one of the electrons (e^-) in the target, then there is a probability that the positron and electron will annihilate by emitting two or three gamma rays.[1] If the incident positron has a kinetic energy E above the threshold for the formation of the ground-state positronium (Ps) ($E_{th} = I - 6.8\,\mathrm{eV}$, where I is the ionization potential of the target), then the process that the positron captures an electron forming a Ps and escapes from the target field may be possible. This Ps eventually annihilates in the same manner. At any E lower than E_{th}, the positron can no more undergo a real capture process, but can virtually form a Ps in the closed channel and can annihilate with the electron in the Ps with some probability. This probability increases sharply as E approaches E_{th} continuously. Then, it is natural to speculate a close relationship between the annihilation and Ps formation cross sections across the threshold E_{th}. We provide a unified view and understanding of these two processes by taking an example of the hydrogen atom target.

In collisions of a positron and a hydrogen atom, surprisingly very few rigorous studies for annihilation have been reported. Earlier, Laricchia and Wilkin[2] and, Van Reeth and Humberston[3] have found the threshold divergence of the annihilation rate. Ryzhikh and Mitroy[4] have investigated the rate carefully, which is found to lie very close to that of Van Reeth and Humberston over the entire energy region. Humberston *et al.*[5] have investigated Ps formation, which shows a sharp threshold increase as $\sqrt{E - E_{th}}$. Thus, they found a discontinuity between the annihilation and Ps formation at the threshold E_{th}. All these theories for annihilation and Ps formation processes, however, stand based on no consideration of the finite lifetime of Ps. Very recently, however, Gribakin and Ludlow[6] have investigated the analytic behavior of the annihilation rate.

The hyperspherical close coupling (HSCC) method has been extensively employed to investigate electronic excitation and ionization in electron and positron collisions with atoms by several groups,[7] and has been successfully applied to observe new phenomena and to provide rationales to underlying physics. Within the HSCC formalism, we incorporate the imaginary potential to represent the finite lifetime of the (positron-electron) complex system.

In the present calculation, the adiabatic channel functions, which describe H ($n = 1, 2$) and Ps ($n = 1, 2$) where n represents the principal quantum number in the asymptotic region, are included in the expansion.

The present result in Fig. 1 shows the unified annihilation and Ps formation cross sections as a function of $(E - E_{th})$. Now the parts from annihilation and Ps formation smoothly join across the threshold, and the discontinuity no longer exists. Only a small structure, or change of the slope, in the unified cross section at the threshold is seen. Hence, within the present model, the Ps formation is just a part of the annihilation, and the origin of the dynamics for the two processes is the same, thus cannot be distinguished. The concept of Ps formation becomes meaningful only when the incident energy is sufficiently high so that the incident positron with a captured electron can travel far enough from the target. Therefore, for any more elaborate theory, these two processes are treated in equal-footing with inclusion of the finite lifetime of the (positron+electron) composite system.

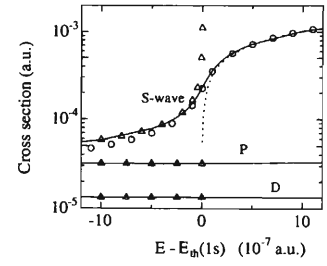

Fig. 1. Partial annihilation cross sections in $e^+ + H$ collisions near the Ps ($1s$) threshold. Solid curves: the HSCC calculations with the absorption potential. Δ: the HSCC calculations without the absorption potential. Dotted curves: Ps formation cross sections without the absorption potential.

*1 Department of Applied Physics, Miyazaki University
*2 Graduate School of Science and Engineering, Yamaguchi University

References

1) M. Charlton and J. W. Humberston: *Positron Physics* (Cambridge University Press, Cambridge, 2001).
2) G. Laricchia and C. Wilkin: Phys. Rev. Lett. **79**, 2241 (1997).
3) P. Van Reeth and J. W. Humberston: J. Phys. B **31**, L231 (1998).
4) G. G. Ryzhikh and J. Mitroy: J. Phys. B **33**, 2229 (2000).
5) J. W. Humberston, P. Van Reeth, M. S. T. Watts, and W. E. Meyerhoff: J. Phys. B **30**, 2477 (1997).
6) G. Gribakin and J. Ludlow: Phys. Rev. Lett. **88**, 163202 (2002).
7) A. Igarashi: Phys. Rev. A **50**, 232 (1994); Phys. Rev. A **50**, 4951 (1994).

Measurement of resonance coherent excitation of 94 MeV/u Ar^{17+} ion channeling through a Si crystal

Y. Nakai, T. Ikeda, Y. Kanai, T. Kambara, N. Fukunishi, T. Azuma,[*1] K. Komaki,[*2] Y. Takabayashi,[*3] and Y. Yamazaki[*2]

An ion channeling through a crystal experiences a periodic field. When the energy difference between two levels of the ion agrees with the energy of a "virtual-photon" of the periodic field, the ion is resonantly excited. Such a process is referred to as the "resonant coherent excitation (RCE)." In the case of ion channeling in the $(2\bar{2}0)$ plane of a Si crystal, the transition energy, E_{trans}, is uniquely associated with angle θ, which is the angle between the beam direction and the [001] axis, by the equation $k\cos\theta/a + l\sin\theta/(a/\sqrt{2}) = E_{trans}/hc\gamma\beta$, where k and l are integers, $c\beta$ is the ion velocity, $\gamma = 1/\sqrt{1-\beta^2}$, and h is the Planck constant. Recently, Azuma and coworkers have performed a series of RCE experiments using the planar-channeling of relativistic heavy ions.[1-4] It was found that the resonance was quite sharp, which suggests the possible use of RCE as a new tool for high-resolution spectroscopy of highly charged ions. Thus, we started the experiment on RCE toward a high-resolution spectroscopy at the RIKEN Ring Cyclotron (RRC).

As the first RCE experiment at RRC, we measured the RCE of the 1s-2p transition of 94 MeV/u Ar^{17+} ions. In order to improve the accuracy of the in-plane rotation angle of the crystal, a high-precision goniometer was developed. The total accuracy of the rotation angle is estimated to be as good as 0.0002° or better. The transport elements of the beamline were tuned so that the angular divergence of the beam was minimum. Beam optics calculation shows that the horizontal and vertical divergences were $\pm 5.4\,\mu$rad and $\pm 10.5\,\mu$rad, respectively. It also shows that the momentum spread of the incident beam was ~100 ppm in full width. The beam was collimated using a 3-mm-thick tungsten plate with a 0.5 mmϕ hole upstream of the Si target. A 7-μm-thick Si (001) crystal was used as a target, which was mounted on the high-precision goniometer. The ions emerging from the crystal were deflected by an analyzing magnet located downstream of the Si target in order to separate the final charge states. A two-dimensional position-sensitive detector (2D-PSD) was located 8 m downstream of the analyzing magnet, which detected Ar^{17+} and charge-changed Ar^{18+} ions.

Electrons in excited states are much more easily stripped in the target than those in the ground state. Therefore, the survival fraction of Ar^{17+}, $f(17+) = N(17+)/[N(17+) + N(18+)]$, should decrease when the Ar^{17+} ions are resonantly excited, where $N(q+)$ is the number of Ar^{q+} ions emerging from the crystal. The survival fraction $f(17+)$ was measured as a function of rotation angle θ. Figure 1 shows $f(17+)$ under the resonance condition with $(k,l) = (3,1)$. The two dips at approximately 7.3° and the dip at approximately 7.6° are associated with the transition to $(j = 1/2)$-like states and $(j = 3/2)$-like states, respectively. The width of the dip of the $(j = 3/2)$-like states is unexpectedly narrower than that of the $(k,l) = (1,1)$ RCE for 390 MeV/u Ar^{17+}.[3] The transition energy is also shown in Fig. 1, which was determined by assuming that the bottom of the resonance dip for the $(j = 3/2)$-like states corresponds to the energy of the $1s\text{-}2p_{3/2}$ transition in vacuum. The profile of the resonance dip is mainly attributed to (1) the position-dependent Stark effect, (2) the position-dependent transition probability, and (3) the position-dependent ionization probability of excited states.[3] The resonance dips will become sharper (especially for $(j = 1/2)$-like states) by selecting ions with small oscillating amplitudes of the channeling ion trajectories because the Stark splitting is small for ions near the channel center. It will become possible by measurement of the energy loss[1] in the target or the emerging angle from the target.

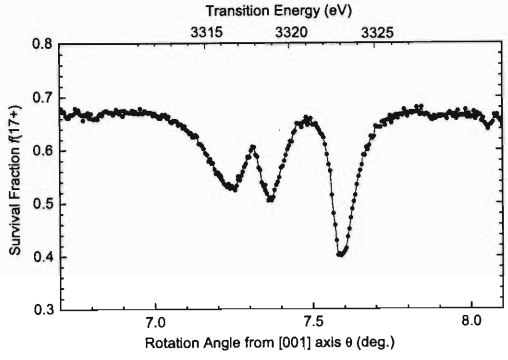

Fig. 1. Survival fraction $f(17+)$ under the resonance condition with $(k,l) = (3,1)$.

*1 Department of Physics, Tokyo Metropolitan University
*2 Institute of Physics, Graduate School of Arts and Sciences, University of Tokyo
*3 Venture Business Laboratory, Hiroshima University

References
1) T. Azuma at al.: Phys. Rev. Lett. **83**, 528 (1999).
2) T. Azuma: Phys. Scr. T **80**, 79 (1999).
3) T. Azuma et al.: Phys. Scr. T **92**, 61 (2001).
4) K. Komaki et al.: Nucl. Instrum. Methods Phys. Res. B **146**, 19 (1998).

Elastic wave from fast Ar- and Xe-ion irradiation on solids

T. Kambara, Y. Kanai, T. M. Kojima, Y. Nakai, Y. Yamazaki, A. Yoneda, and K. Kageyama*

For study of dynamical effects of heavy-ion irradiation in bulk solids, we have been measuring the elastic waves generated in various solids by irradiation of fast heavy ions.[1] The experiments have been performed at the RIKEN Ring Cyclotron with short-pulse beams of 95 MeV/nucleon ^{40}Ar and 26 MeV/nucleon ^{136}Xe ions.

The targets were 10-mm-thick square-shaped plates (40 mm × 40 mm) of polycrystalline Al and Cu, single crystals of KCl, LiF and BaF_2, fused silica (SiO_2), and polycrystalline Al_2O_3. The ions impinged perpendicularly on the square-shaped surface of the target.

The elastic waves were detected by two piezoelectric sensors (AE304 by Fuji-Ceramics) attached to the center of the surface opposite the beam injection (back sensor) and on the side surface. The target and the sensors were mounted on a movable feedthrough perpendicular to the beam, so that waveforms could be measured at different beam-spot positions.

Figure 1 shows elastic waveforms observed by the back sensor on the BaF_2 target irradiated with Ar ions, along with an example of the time structure of the beam at the top. The beam spot was about 4 mm × 4 mm. By moving the target setup by 1 mm steps, we measured the waveforms from different beam-spot positions within ±12 mm relative to the target center. On the right are shown the distances from the beam-spot centers to the target center, where 0 mm corresponds to the epicenter for the back sensor. The waveforms are normalized to 10^3 projectile ions and averaged over multiple beam pulses to reduce noise. The delay of the waveform after the beam pulse is attributed to the propagation of the elastic waves in the target. As described previously,[1] the onset of the wave is the bulk longitudinal wave generated at the end of the ion range. A dashed curve shows estimated arrival time of the longitudinal wave from the end of the range to the back sensor. In this estimation, we used an ion range of 3.11 mm calculated by TRIM code[2] and a wave velocity of 4280 m/s. The onset of the wave matches the estimated arrival time.

Figure 2 shows waveforms of the same BaF_2 sample irradiated with Xe ions with a beam spot of about 8 mm × 8 mm. A dashed curve shows estimated arrival time of longitudinal wave estimated with the ion range of 0.22 mm. Near the epicenter the estimated arrival time well matches the actual onset of the wave. Elsewhere it is later than the onset, which may be due to a large beam spot.

In the Ar irradiation, the waveform at the onset is quite similar regardless of the beam-spot position, which indicates that the elastic wave is almost isotropic. On the other hand, in the Xe irradiation, the waveform strongly depends on the beam-spot position: A sharp structure appears near the epicenter but it is not observed at other positions. Possibly different modes of wave are generated by the irradiation.

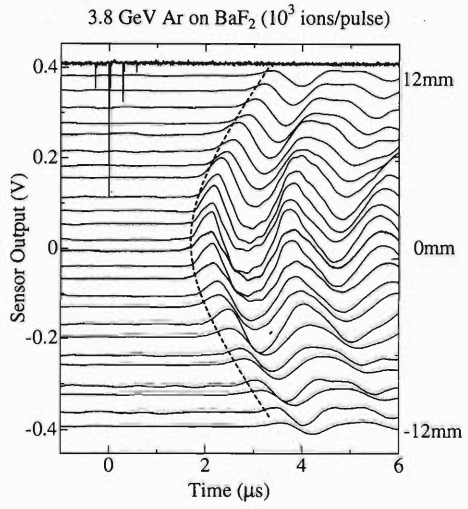

Fig. 1. Solid lines show elastic waveforms of BaF_2 from 3.8-GeV Ar-ion irradiation at different positions indicated on the right. The beam-pulse structure is at the top. The dashed curve shows the estimated arrival time of the longitudinal wave.

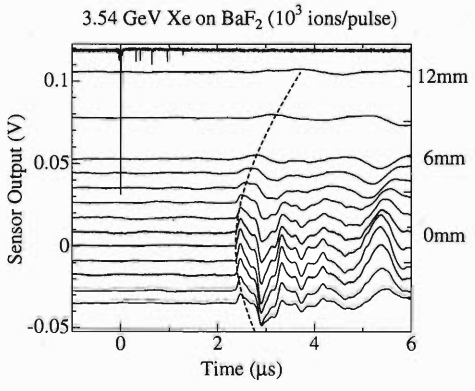

Fig. 2. Same as Fig. 1 for 3.54-GeV Xe-ion irradiation.

References

1) T. Kambara et al.: Nucl. Instrum. Methods Phys. Res. B **193**, 371 (2002).
2) J. F. Ziegler, J. P. Biersack, and U. Littmark: *The Stopping and Range of Ions in Solids* (Pergamon Press, New York, 1985).

* Department of Mechanical Engineering, Saitama University

Detector characteristics of piezoelectric lead-zirconate-titanate elements for heavy ions

T. Miyachi,* N. Hasebe,* H. Okada,* M. Fujii,* O. Okudaira,* N. Yamashita,* H. Ito,* H. Yoshioka,* A. Nagashima,* Y. Nakamura,* and T. Kambara

The aim of this study is to develop a radiation detector using a piezoelectric material. There are two detection methods;[1] the direct method and the indirect method. In the former method, an acoustic-sensitive detector is directly irradiated and outputs signals. On the other hand, by the latter method, a medium is irradiated and subsequently produced acoustic signals are detected by the acoustic-sensitive element. This note describes the first measurement with carbon ions using the direct method, and with argon ions using the indirect method with the RIKEN Ring Cyclotron.

A carbon beam, which was at 135 MeV/u and $\sim 10^{10}$ pps, was irradiated onto an array which was formed by stacking twenty lead-zirconate-titanate (PZT) elements; five 0.5 mm-thick and fifteen 0.6 mm-thick PZT elements. In front of the array, a plastic scintillation counter was placed, which served as a timing counter and an intensity monitor. Thus, we detected acoustic signals from each element generated by the carbon beam. Output signals observed in 15^{th}, 16^{th} and 17^{th} elements are shown in Fig. 1, from which we can observe that the PZT signals are at the maximum in the 16^{th} element, and disappear in the 17^{th} element.

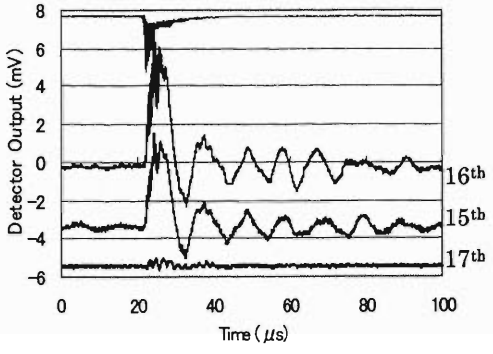

Fig. 1. Signals in PZT elements produced by C ions. From top to bottom, timing signal of the plastic counter, and signals of 16^{th}, 15^{th} and 17^{th} elements. The number of C ions of the pulsed beam is about 10^6.

It is noted that the integrated thickness up to the 16^{th} element is 9 mm, and the calculated range of carbon ions in PZT is 9.3 mm. That is, the carbon ions stop at the 16^{th} element and do not reach 17^{th} element.

When heavy ions are irradiated into water, acoustic signals are generated along the beam path. Consequently, we can observe the result of radiation as a pressure pulse. Five PZT rings (2 mm thick, and inner and outer diameters were 28 mm and 30 mm, respectively) were stacked to align each center on the beam line. The stacked elements were placed in a vessel filled with water. The plastic counter was placed as in the direct method. In Fig. 2, we show the signals detected using a 95 MeV/u argon beam directed at the center of the PZT rings. Two pulsed beams separated by $\sim 120\,\mu$s and subsequent acoustic signals in the first two elements are shown. The PZT signals were delayed by $\sim 10\,\mu$s, whose interval is consistent with the propagation time of sound in water through the distance of the ring radius, 14 mm.

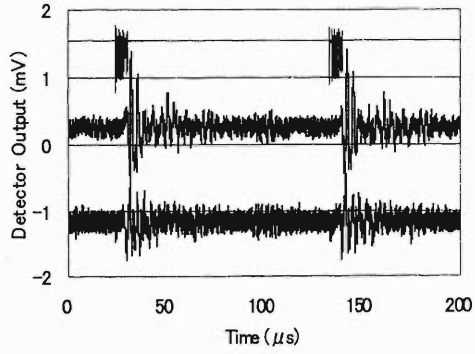

Fig. 2. Acoustic signals produced in water by Ar ions. From top to bottom, timing signal, and output signals of the first two elements. The number of Ar ions of each beam pulse is about 10^6.

References

1) T. Miyachi et al.: Jpn. J. Appl. Phys. **42**, (2003), in press.

* Advanced Research Institute for Science and Engineering, Waseda University

Modification of magnetic properties of FeNi invar alloys by GeV heavy ion irradiation†

A. Iwase,[*1] Y. Hamatani,[*1,*2] Y. Mukumoto,[*2] N. Ishikawa,[*1] Y. Chimi,[*1]
T. Kambara, C. Mueller,[*3] R. Neumann,[*3] and F. Ono[*2]

$Fe_{0.68}Ni_{0.32}$ Invar alloys were irradiated at room temperature with 3.54 GeV Xe ions using the RIKEN Ring Cyclotron, and with 2.71 GeV U ions using the GSI-UNILAC accelerator. Before and after irradiation, the magnetic moment of the specimens, M, was measured by using a specially designed system for rapid measurements, which was particularly useful for specimens such as the thermally unstable ones in the present ones. The Curie temperature of the specimens, Tc, was determined as the temperature at which the value of M changes from a finite value to zero.

Figure 1 indicates the value of Tc as a function of ion-fluence for Xe and U ion irradiations. The increase in Tc is observed even at low ion-fluence, implying that it can be attributed to ion-induced electronic excitation. As can be seen in the figure, the increase in Tc per unit fluence for U ion irradiation is an order of magnitude larger than for Xe ion irradiation. On the other hand, the calculation by the TRIM code shows that the average value of the electronic stopping power, Se, over the specimen for U ions is only twice as large as for Xe ions. This result suggests that the change in Curie temperature depends superlinearly on Se. It is well known that the Curie temperature of FeNi Invar alloys is quite sensitive to their lattice parameter.[1)] An external high pressure can contract the lattice, resulting in the decrease in Tc, while swift heavy ion irradiation induces a large lattice expansion in some materials.[2)] If such a lattice expansion is induced by GeV-ions also in Fe-Ni Invar alloys, we can explain the increase in Tc. Swift heavy ions also enhance a selective diffusion of constituent atoms in some alloys and vary their local atomic ratio.[3)] If such irradiation-enhanced diffusion makes a Ni rich zone in the specimen, Tc of this zone will increase, because even a small increase in Ni concentration from 32% can induce a large increase in Tc.[4)] To clarify the effect of swift heavy ion irradiation on the magnetic properties of FeNi Invar alloys in more details, measurements of the lattice parameter and spontaneous magnetization in GeV-ion irradiated Fe-Ni alloys are now in progress.

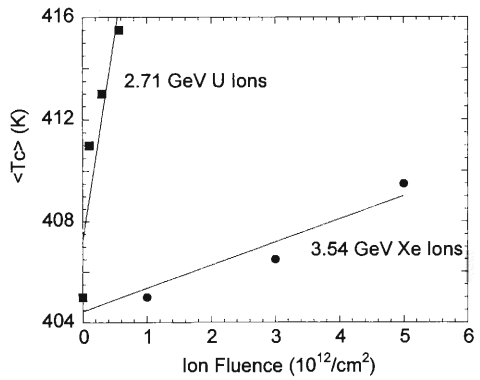

Fig. 1. Value of Curie temperature, Tc, as a function of ion-fluence for Xe ion irradiation and for U ion irradiation.

References

1) K. Hayashi and N. Mori: Solid State Commun. **38**, 1057 (1981).
2) N. Ishikawa, Y. Chimi, A. Iwase, H. Maeta, K. Tsuru, O. Michikami, T. Kambara, T. Mitamura, Y. Awaya, and M. Terasawa: Nucl. Instrum. Methods Phys. Res. B **135**, 184 (1998).
3) A. Iwase, T. Hasegawa, Y. Chimi, T. Tobita, N. Ishikawa, M. Suzuki, T. Kambara, and S. Ishino: Nucl. Instrum. Methods Phys. Res. B **195**, 309 (2002).
4) J. Crangle and G. C. Hallam: Proc. Phys. Soc. A **292**, 119 (1963).

† Codensed from the article in Nucl. Instrum. Methods Phys. Res. B (2002) in press.

*1 Japan Atomic Energy Research Institute
*2 Department of Physics, Okayama University
*3 Gesellschaft fuer Schwerionenforschung (GSI), Germany

Scanning tunneling microscopy and spectroscopy of individual ion tracks created in GaAs by GeV Xe ion irradiation

A. Hida,[*1] A. Iwase,[*2] Y. Mera,[*1] T. Kambara, and K. Maeda[*1]

Energetic ion irradiation, a technique for modifying the structures of solids and hence their physical properties, has a feature that the spatial extent of the modified area can be controlled by varying the species, the charge state, and the kinetic energy of ions. Irradiation with swift heavy ions generates linear defects called tracks. Although direct observations of individual ion tracks have been performed in some solids by optical microscopy,[1] transmission electron microscopy[2] and atomic force microscopy,[3] knowledge of the microscopic structures of individual ion tracks and of the associated electronic states is still quite limited. We investigated the structures and the electronic states of individual tracks created in GaAs by 3.54 GeV Xe^{31+} ion irradiation for the first time by scanning tunneling microscopy (STM)[4] combined with scanning tunneling spectroscopy (STS).

The samples used were Zn-doped p-type GaAs bulk crystals (hole density, $p \sim 10^{18}\,\mathrm{cm}^{-3}$) irradiated at an incidence normal to the (001) surface with 3.54 GeV Xe^{31+} ions up to a dose of 2.5×10^{11}–$5 \times 10^{11}\,\mathrm{cm}^{-2}$ at RIKEN Ring Cyclotron. After irradiation, clean cross-sectional (110) sample surfaces were prepared by cleaving in an ultrahigh-vacuum STM chamber (base pressure $< 2 \times 10^{-8}$ Pa) to bare the ion tracks. The individual tracks were probed with a mechanically sharpened Pt-Ir tip under various conditions of sample bias voltage (V_s) and tunneling current (I_t). The structural features were examined in the constant-current STM images obtained at $V_s = +2.1$ V and $I_t = 0.1$ nA, and the electronic properties were investigated by STS measurements of the local current-voltage (I-V) relation from which the approximate local density of states (LDOS) was deduced by calculating $(dI/dV)/(I/V)$. All experiments were performed at room temperature.

Figure 1 (a) shows a typical STM plan-view image of a single ion track observed in the cleavage (110) surface of the sample. Commonly, each track imaged in dark contrast is sheathed with a thin fringe in bright contrast. One may also notice a bright thin line running along the core of the track. Figure 1 (b) shows the average line profile of the tip height (giving the contrast in constant-current images) plotted across the track. The width of the track in dark contrast is ~5 nm, and the thickness of the bright sheath is ~2 nm on average. The tracks in dark contrast appear quite disordered, which is consistent with previous TEM observations of amorphous tracks of 5–8 nm diameter formed in heavy-ion-irradiated GaAs.[2] However, lattice contrasts were

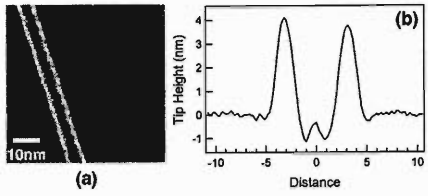

Fig. 1. (a) A typical STM image of a single track created in GaAs by 3.54 GeV Xe ion irradiation at room temperature. (b) The average line profile of the tip height across the ion track.

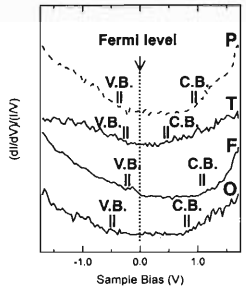

Fig. 2. LDOS spectra of characteristic sites around the track. The vertical double lines with letters V.B. and C.B. indicate the positions of the valence band top and the conduction band bottom, respectively.

clearly seen in the TEM image of the region outside the track, whereas the STM image exhibited no crystalline features extending over a distance of 40 nm from the track. The atomically resolved image beyond the disordered region indicates that the noncrystalline contrasts are not due to the poor resolution of the tip. Thus, our results indicate that the impact effect of an ion is not confined to the track but extends to a much larger area.

Figure 2 shows the spectra of LDOS deduced from the I-V relations measured at characteristic sites around the track. The zero energy in each spectrum indicates the Fermi level at the surface. At sites where atomic rows are observed, the spectrum ('P' in Fig. 2) shows features characteristic of p-type GaAs perfect crystals, a bandgap of ~1.4 eV and a Fermi level located near the valence band top. At the track in dark contrast ('T' in Fig. 2), however, the bandgap is considerably reduced. This is consistent with the well-known fact of band-tailing induced by amorphization of semiconductor crystals.[5] In contrast, at the bright fringe ('F') and the outskirts of the track ('O'), such reduction of the bandgap is not observed. This means that these regions retain the crystalline struc-

*1 Department of Applied Physics, University of Tokyo
*2 Japan Atomic Energy Research Institute

tures although they exhibit no crystalline contrasts in the STM images. The spectra at F sites and O sites differ from each other and those at the perfect sites ('P') in the relative position of the surface Fermi level with respect to the band edge and in the magnitude of the LDOS in the energy bands. Therefore, the main cause of the differences in the STM image contrasts can be attributed to the spatial variation of the electronic states probably influenced by some irradiation defects rather than the topographic features such as surface corrugation.

In conclusion, it was revealed by STM and STS that the effects of an ion passage in GaAs crystals are not confined to the track but extend to a much larger area. The amorphization was induced only inside individual tracks. On the other hand, the sheath and the surrounding retained crystalline structures although these structures electronically disordered.

The authors thank the technical staff of the RIKEN accelerator facility for their assistance with ion irradiation experiments. This work was supported by a Grant-in-Aid for Scientific Research on Priority Areas (B) "Manipulation of Atoms and Molecules by Electronic Excitation" from The Ministry of Education, Culture, Sports, Science and Technology of Japan.

References

1) D. A. Young: Nature **183**, 375 (1958).
2) M. W. Bench, I. M. Robertson, M. A. Kirk, and I. Jencic: J. Appl. Phys. **87**, 49 (2000).
3) A. Müller, R. Neumann, K. Schwartz, T. Steckenreiter, and C. Trautmann: Appl. Phys. A **66**, S1147 (1998).
4) G. Binnig and H. Rohrer: Helv. Phys. Acta **55**, 726 (1982).
5) S. Shigemori and T. Matsumori: Nucl. Instrum. Methods **182/183**, 719 (1981).

TDPAC studies using probes implanted in powder C_{60}

W. Sato, H. Ueno, H. Watanabe, H. Ogawa,[*1] H. Miyoshi,[*1] N. Imai,[*2] A. Yoshimi, K. Yoneda, D. Kameda,[*1] Y. Kobayashi, K. Sueki,[*3] Y. Ohkubo,[*4] and K. Asahi

Fullerene C_{60} is the third carbon allotrope having a unique molecular structure of a soccer-ball-like shape, and it has been reported that its bulk material shows intriguing physical properties such as semiconductivity and superconductivity when the molecules interact with adjacent atoms which are endohedrally or exohedrally doped. For studying the nature of those fullerene compounds, our interest was first directed to what sites of the molecules the doped atoms are likely to occupy when they are introduced by the ion implantation method. In order to obtain the site information, we adopted the time-differential perturbed angular correlation (TDPAC) method using implanted ions as the probes, because this method can provide information on the extranuclear field through the nuclear precession and/or fluctuation caused by electromagnetic interactions with the ambient surroundings. We have performed the probe implantation of ^{19}O and ^{140}Ce, which is a β-decay product of a fission fragment ^{140}Cs, at RARF and Kyoto University Research Reactor Institute (KURRI), respectively, to examine the sites occupied by them. As has already been reported,[1] a dynamic motion has been observed for the ^{19}O probes. For better understanding of the data, it is of importance to compare and contrast the data obtained for different probes. In the present report, we show the TDPAC time spectrum of ^{140}Ce and give it a preliminary interpretation.

Powder fullerene C_{60} of about 100 mg (99.95% purity) was pressed to form a disk of 7 mm$\phi \times$ 1 mm. The disk was stuck on a Teflon-sheet backing and then attached to the ion beam collector of KUR-ISOL.[2] The ion beam of a fission fragment, ^{140}Cs, was kept implanted in the sample at the acceleration voltage of up to 110 kV for 50 h. After radioactive equilibrium between ^{140}Ba and ^{140}La was achieved, TDPAC measurements were performed for the probe ^{140}Ce on the 329–487 keV cascade γ rays with the intermediate state of 4^+ having a mean life of 5.0 ns. A simplified decay scheme for the probe is shown in Fig. 1. A conventional four-detector system with BaF_2 scintillators was used for the γ-ray detection.

The TDPAC spectrum of ^{140}Ce in powder fullerene C_{60} at room temperature is shown in Fig. 2. One can see a slowly relaxing oscillatory structure in the spectrum that implies static perturbation from the extranuclear field. It is well known that C_{60} molecules have an isotropic thermal rotation at room temperature.[3] Considering this observation, it is difficult to interpret the present spectrum to suggest that the probe ^{140}Ce is encapsulated in the C_{60} cage. As experimentally demonstrated, it depends on the sizes of incident atoms whether they can enter the cages and be stably encaged.[4] We accordingly consider that the ^{140}Ce ions occupy interstitial sites of the fcc structure of the polycrystalline C_{60} without forming rigid bonds with the carbon cages. For more detailed discussion on the sites occupied by the implanted atoms, temperature dependence of TDPAC spectra should be examined.

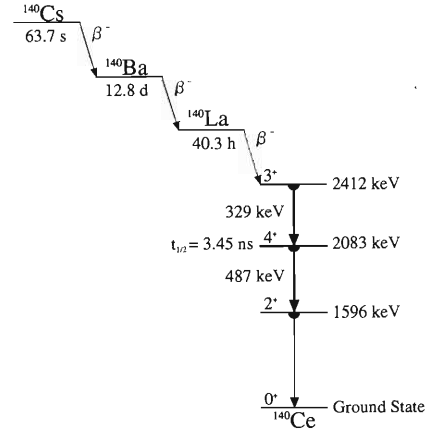

Fig. 1. Simplified decay scheme of ^{140}Ce.

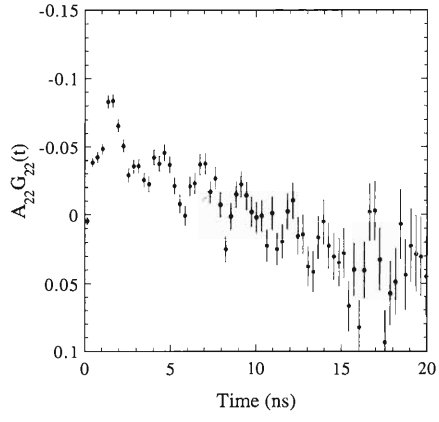

Fig. 2. TDPAC spectra of ^{140}Ce in powder C_{60}.

References

1) W. Sato et al.: J. Radioanal. Nucl. Chem. **255**, 183 (2003).
2) Y. Kawase et al.: Nucl. Instrum. Methods Phys. Res. A **241**, 305 (1985).
3) R. D. Johnson et al.: Science **255**, 1235 (1992).
4) T. Ohtsuki et al.: J. Chem. Phys. **112**, 2834 (2000).

*1 Department of Physics, Tokyo Institute of Technology
*2 Department of Physics, University of Tokyo
*3 Department of Chemistry, University of Tsukuba
*4 Research Reactor Institute, Kyoto University

Single-event effect in power MOSFETs caused by high-energy ions

S. Matsuda,[*1] S. Kuboyama,[*1] Y. Deguchi,[*1] S. Somekawa,[*1] N. Ikeda,[*1] H. Ohira,[*2] Y. Nagai,[*2] H. Otomo,[*2] K. Furuse,[*2] and M. Kase

A power MOSFET (metal oxide semiconductor field-effect transistor) is a key device in a power circuit which achieves low ON-resistance and fast switching. A MOSFET to be used in space is required to have radiation hardness so that radiation in space does not cause problems in its operation. Protons, heavy ions and other particles in space could cause single-event effects and lead to semiconductor device malfunction or failure. Single-event burnout (SEB) and single-event gate rupture (SEGR) are the main concern regarding power MOSFETs. SEB is triggered by a heavy ion passing through the device when it is off. Transient current by such ion turn on a parasitic bipolar transistor that results in burning out of the device, which could destroy it. SEGR is also caused by a heavy ion and destroys the device. Electrons and holes generated by a heavy ion passing through the area around the gate are collected near the gate oxide and a resultant high electric field causes breakdown of the gate.[1] Although SEB is the main concern regarding power MOSFETs, SEGR also needs to be considered. NASDA has developed SEB-hardened power MOSFETs, and has studied their SEGR hardness using the RIKEN Ring Cyclotron.

Two types of power MOSFETs were tested: one is 250 V MOSFETs which have two epi-layers with different resistivity to improve electric performance (TYPE-1), and the other is 250 V MOSFETs which have different cell structures to improve SEB hardness (TYPE-2). The structure is denoted by Δn-length. Samples were irradiated with a $^{58}Ni^{19+}$ beam of about 350 MeV at the surface. LET and the range were about 25 MeV/(mg/cm^2) and 57 μm, respectively. SEGR tolerance was determined by the breakdown voltage of V_{DS} and V_{GS} as parameters.

Figure 1 shows the SEGR tolerance of two TYPE-1 samples. The resistivity of the first epi-layer of each sample is different. Judging from the figure, SEGR hardness is not affected by the resistivity of the first epi-layer.

Figure 2 shows the SEGR tolerance of three TYPE-2 samples with different Δn-lengths. A sample indexed as 1c4, which is the closest candidate for space application (best SEB hardness), has good SEGR tolerance.

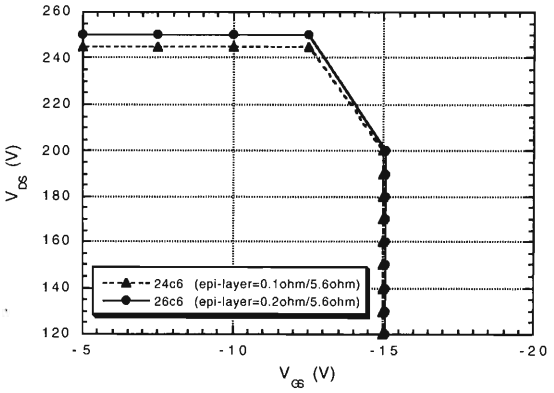

Fig. 1. SEGR tolerance of TYPE-1 (24c6 and 26c6). The area surrounded by plotted lines and x-y axes is SEGR-free.

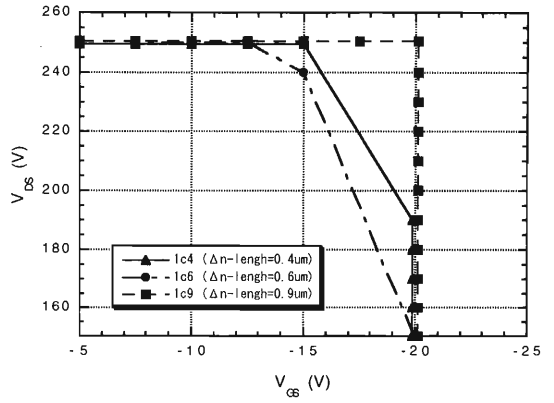

Fig. 2. SEGR tolerance of TYPE-2 (1c4, 1c6, and 1c9). The area surrounded by plotted lines and x-y axes is SEGR-free.

Although the 1c9 sample has the best SEGR tolerance, it has the lowest SEB hardness and is not practical for space use.

References

1) JAERI and NASDA Joint Research Report **2** (1999), II-9.

*1 National Space Development Agency of Japan
*2 Ryoei Technica Co., Ltd.

Charge state distribution of heavy ions through a plasma

A. Sakumi, T. Katayama, S. Ogawa,* and Y. Oguri*

The experimental investigation of the beam plasma interaction is the key issue of a heat up till hot dense plasma in the field of inertial confinement fusion-related topics, *e.g.*, the design of the fusion converters, and drivers,[1] and the fast ignition by proton beam.[2] We have experimentally investigated the mechanism of the interaction of heavy-ion beams with a partially ionized plasma, considered both contributions due to the free plasma particles and the bound electrons. These experiments are conducted at the e4-line in the RILAC facility.

We estimated the charge state distribution by integrating the rate equations:[3]

$$\frac{dP_q}{dt} = -(\alpha_{\mathrm{I}}(q) + \alpha_{\mathrm{C}}(q))P_q + \alpha_{\mathrm{C}}(q+1)P_{q+1} + \alpha_{\mathrm{I}}(q-1)P_{q-1},$$

where α_{I} and α_{C} are the rate coefficients of ionization and electron capture, respectively. P_q is the probability of the ions in charge state q ($0 \leq q \leq z_{\mathrm{p}}$, where z_{p} is the atomic number of projectile ions). We estimated the rate coefficients as described in Refs. 3 and 4 by considering the cross sections for ionization by ion collision, ionization by electron collision, bound electron capture, radiative recombination, dielectric recombination and three-body recombination. The ionization cross sections of the projectile are enhanced in the dense plasma by the density effect.[4] This effect is caused by the ladder-like excitation.[5] In the ladder-like excitation mechanism, an electron excited to an energy level with principal quantum number n_{t} (thermal limit) in a single collision is ionized by the dense plasma. The calculated charge state distribution of Kr ions in the plasma is shown in Fig. 1. The target is a plasma with a density of $10^{18}\,\mathrm{cm}^{-3}$ and a temperature of $\sim$15 eV.[6] The mean charge state (22.1, triangle) in the plasma is larger than that in the cold matter (19.1, circle).

For measuring the charge state distribution, we developed a magnetic spectrometer. The plasma lifetime was about 100 ns[3] so that the detector consists of MCP, plastic scintillator and Streak camera. The time resolution of this detector was about 2 ns. The experimental setup is shown in Fig. 2. At a preliminary experiment the signal is too weak to be detected because of the use of a conventional camera lens. Therefore we are planning to use taper fiber optics.

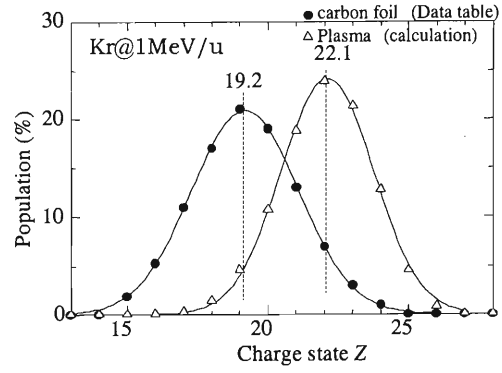

Fig. 1. Calculation of charge state distribution through the plasma (triangle). For comparisons, we denote the charge state distribution through a carbon foil (circle). The mean charge state in the plasma (22.1) is larger than that in a carbon foil (19.2).

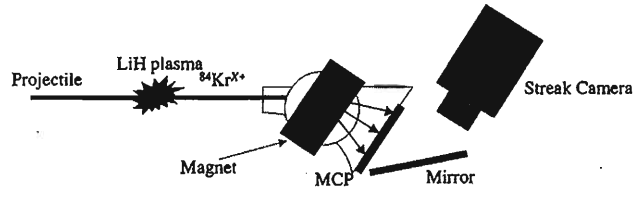

Fig. 2. Experimental setup for charge state distribution measurement.

References

1) HIBLIC-Heavy Ion Fusion Reactor, Nagoya University, IPPJ-663 (1984).
2) M. Gryzinski: Phys. Rev. A **138**, 305 (1965).
3) A. Sakumi et al.: Nucl. Instrum. Methods Phys. Res. A **464**, 231 (2001).
4) K. Shibata et al.: J. Appl. Phys. **91**, 4833 (2002).
5) T. Fujimoto and T. Kato: Phys. Rev. Lett. **48**, 1022 (1982).
6) A. Sakumi et al.: RIKEN Accel. Prog., Rep. **35**, 92 (2001).

* Research Laboratory for Nuclear Reactors, Tokyo Institute of Technology

Ultrafast plasma luminescence of heavy-ion tracks in insulators: Electron-hole plasma

K. Kimura,* M. Koshimizu,* K. Asai,* T. Kambara, and M. Kase

We have found the electron-hole plasma (e-h plasma) luminescence of incipient heavy-ion track cores in insulator crystals such as alkali halides, metal oxides, and alkaline-earth halides.[1,2] The e-h plasma is the first observed collective behavior of track cores of ions. Measurements of such e-h plasma luminescence require not only fast and sensitive detection techniques but also effective methods to discern the core part from the large secondary-electron effect. We have developed techniques for luminescence measurements with a time resolution of 85 ps.[1] To make the core effect prominent, the incident energies of projectiles were equalized to 2 MeV/nucleon. Ions of this energy have a maximum stopping power, but they cannot eject energetic secondary electrons; moreover, their track effects may be in similar extent because of the equal ion velocity. Time-resolved (TR) measurements revealed ultrafast and broad luminescence from ultraviolet to visible light. Its decay curve did not have a tail larger than the lifetime. Such short-lived luminescence assigned to e-h plasma[1,2] was observed over all crystals measured, although luminescence efficiency varied by 10000 times. Thus, the e-h plasma luminescence may be deduced to be a common phenomenon for many categories of insulators as well as semiconductors. In addition, their specific intensities increase super-linearly with increasing excitation density. Even at room temperature, we could observe similar luminescence intensities in spite of the fact that most excitons cannot exist at this temperature.

However, for a detailed characterization of the electron-hole plasma, some problems remain unsolved. The most basic problem is obtaining precise TR-spectra that are unaffected by ion current fluctuation. The second is to obtain systematic data to classify the sample dependence. For the first problem, we have developed a method for 8-channel (8-wavelength) time-correlated photon counting for each ion strike.[2] Figure 1a shows a 3D-plot of decay curves normalized for ion count *vs.* wavelength for Xe-ion-irradiated CsI at 6 K, Fig. 1b TR-spectra, and Fig. 1c 3D-decay curves at 300 K. One can discern easily fast luminescence due to e-h plasma as spikes in Fig. 1a. Much slower decays follow the spikes and have peaks at 290 and 340 nm that are evident in Fig. 1b. These two peaks are due to well-known on- and off-center self-trapped excitons (STEs). Their time profiles are distinct in Fig. 1c although superposed slightly by STEs. An envelope-joining spike, *i.e.*, the e-h plasma luminescence, has

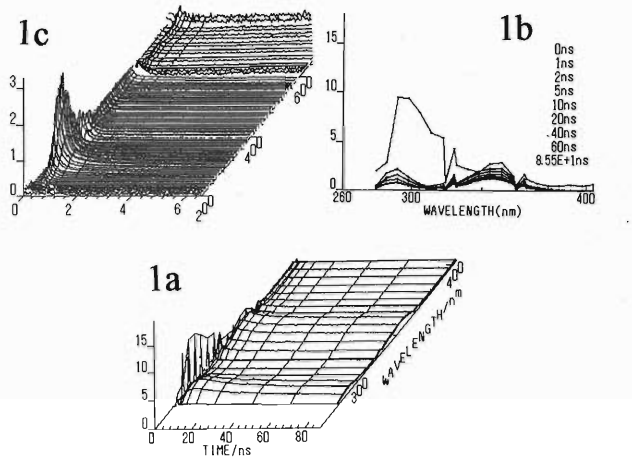

Fig. 1. 1a. 3D-plot of decay curves normalized for ion count *vs.* wavelength for Xe-ion-irradiated CsI at 6 K; 1b. TR-spectra; 1c. 3D-decay curves at 300 K.

broad peaks at wavelengths similar to that of STE luminescence and it also has an intensity in the range between STE bands, thereby forming a giant band covering from wavelengths shorter than the shorter limit given by STEs to wavelengths longer than the longer limit. Such shape could be also observed for the other crystals measured. Considering the present and previous results collectively, the present e-h plasma luminescence can be interpreted as follows. In the incipient track, ejected electrons expand radially. During their travel in the core, charge balance is destroyed completely, thus, metal ions (Me^+), halogen ions (X^-) and holes (X) can move rapidly resulting in aggregation: $X+X^- \rightarrow X_2^-$, $X+X \rightarrow X_2$, $X+X+X^- \rightarrow X_3^-$, and so forth. Namely, the self-trapping of holes starts. In that timescale, dense electrons return before self-trapping are completed (takes 100 ps). If an electron and a hot hole were isolated, the pair should relax into a STE. However, it can be estimated that many pairs are so dense to be adjacent. Many interacting pairs prefer to stabilize by emitting photons under nonstationary hole states rather than they relax to STEs of which formation takes about 100 ps. There are no other processes for releasing excess energy because ions and holes are in hot states and moreover crystal bonds for phonon propagation are destroyed.

References

1) K. Kimura, J. Kaneko, S. Sharma, W. Hong, and N. Itoh: Phys. Rev. B **60**, 12626 (1999).
2) K. Kimura, S. Sharma, and A. Popov: Radiat. Meas. **34**, 99 (2001); Nucl. Instrum. Methods Phys. Res. B **191**, 48 (2002).

* Department of Quantum Engineering and Systems Science, University of Tokyo

Time-resolved luminescence spectra of electron-hole plasma in ion-irradiated CdS

M. Koshimizu,* K. Kimura,* K. Asai,* and M. Kase

The irradiation effects of swift heavy ions in semiconductors and insulators are characterized by high-density electronic excitation along their paths. In order to understand the dynamics of high-density excitation states, we measured the time-resolved luminescence spectra using a SISP (single ion and single photon time correlation) system, with a time resolution of 80 ps. One of the authors (K. K.) observed the luminescence band due to the electron-hole plasma (EHP) in alumina and alkali halides.[1] In this study, we aim to compare the dynamics of the EHP produced by swift heavy ions to those produced by intense lasers. We chose CdS as a target, in which many researchers have investigated the property of the EHP using an intense laser field.

In the time-resolved luminescence spectrum of CdS at 15 K induced by 2 MeV/nucleon Xe ions, the broad luminescence band is observed at 485–520 nm, as is shown in Fig. 1 (a). The decay rate is about 300 ps in the entire band, which is much faster than that of the luminescence band due to free or bound excitons in CdS. Furthermore, the biexciton luminescence band, another candidate for the origin of this broad band, is very sharp. Therefore, we attribute this band to the spontaneous luminescence of EHP. We analyzed the shape of this band under the assumption that the k-selection rule does not hold in the recombination of electrons and holes in accordance with Goebel,[2] and we have obtained a carrier temperature and an electron-hole concentration of 15 K and $3 \times 10^{19}\mathrm{cm}^{-3}$, respectively. The obtained carrier concentration is about 10 times larger than that in the EHP produced by lasers with intensities of 2–25 $\mathrm{MW\,cm}^{-2}$.[3] In contrast, for the case of 2 MeV/nucleon Ar irradiation, a sharp luminescence band is observed at 12 K, as is shown in Fig. 1 (b). The shape of the luminescence band indicates that the density of the excited carriers is much lower for Ar-ion excitation than for Xe-ion irradiation.

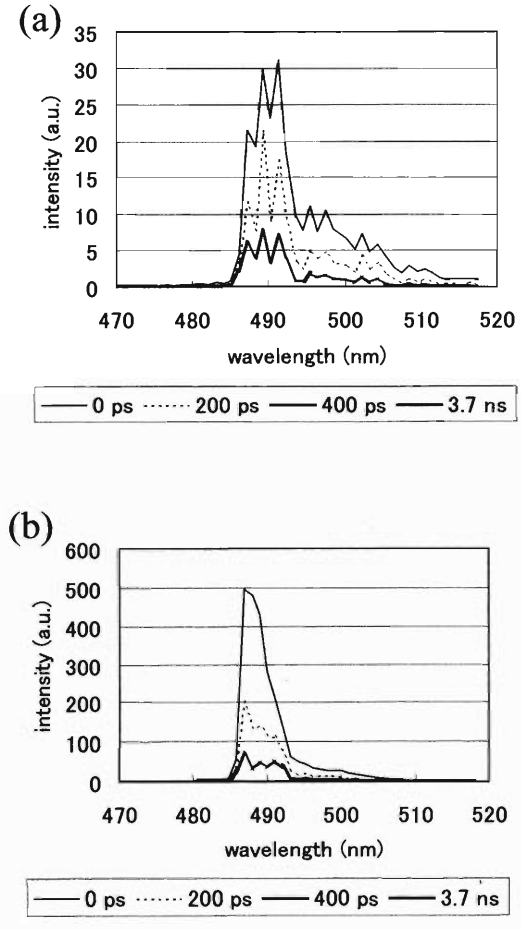

Fig. 1. Time-resolved luminescence spectrum of ion-irradiated CdS. (a) Xe, 15 K, (b) Ar, 12 K.

References

1) K. Kimura et al.: Phys. Rev. B **60**, 12626 (1999); Nucl. Instrum. Methods Phys. Res. B **191**, 48 (2002).
2) G. Goebel: Appl. Phys. Lett. **24**, 492 (1974).
3) H. Yoshida et al.: Solid State Commun. **33**, 161 (1980).

* Department of Quantum Engineering and Systems Science, University of Tokyo

Site occupancy change of hydrogen in Nb-Mo alloys with Mo concentration†

E. Yagi, S. Koike,*1 T. Matsumoto,*2 T. Urai, N. Tajima, and K. Ogiwara

The behaviour of hydrogen isotopes in metals is an important problem because of theoretical and technological interests, *e.g.*, quantum diffusion of hydrogen and hydrogen embrittlement. In order to elucidate the mechanism for such behaviour, knowledge on the state of hydrogen isotopes, especially their lattice location, is highly required. A number of experiments have been carried out on deuterium by a neutron diffraction method and also by a channelling method with a ^{3}He beam, whereas there have been only a few neutron experiments carried out on hydrogen because of their experimental difficulties and no channelling experiments in spite of their usefulness. The behaviour of hydrogen is not necessarily the same as that of deuterium as recognized, *e.g.*, from the difference in the phase diagram between metal-hydrogen and metal-deuterium systems. From this point of view, experiments on hydrogen are indispensable. To study the lattice location of hydrogen we have applied a nuclear reaction ^{1}H(^{11}B,α)α α with a ^{11}B beam of about 2 MeV to a channelling method, and demonstrated that this method is very useful.[1,2]

In the present study, the interaction between hydrogen and metal solutes in alloys is focused on, because microscopic information on such interactions in metallic alloys, even for deuterium, has been extremely limited. One example is the effect of alloying on the terminal solubility of hydrogen (TSH) in group V_a metals in the periodic table (V, Nb and Ta). It has been reported that, for undersized metal solutes, *e.g.*, Nb in Ta and Mo in Nb, the TSH increases rapidly with solute concentration up to a certain solute concentration, whereas, for oversized solutes, *e.g.*, Ta in Nb and Nb in V, the TSH increases less rapidly with solute concentration.[3] In order to understand the mechanism of this effect, the lattice location of hydrogen in such alloy systems is to be investigated. In the present study, an Nb-Mo alloy system has been chosen. This system forms a solid solution over the entire Mo concentration (C_{Mo}) range, and has a bcc crystal structure. The TSH in Nb at room temperature is about 3 at.%, whereas the TSH in Mo is very low. Therefore, systematic studies on the C_{Mo} dependence of the hydrogen site occupancy are desired. Previously we performed channelling studies to locate hydrogen in Nb-based Nb-Mo alloys with various Mo concentrations up to 20 at.% Mo.[4,5] In the present study, the lattice location of hydrogen in a more concentrated alloy with 26 at.% Mo is investigated.

The results on the site occupancy of hydrogen in the alloys with various Mo concentrations are summarized in Table 1. Generally speaking, the interaction between metal solutes and hydrogen consists of electronic and elastic interactions. Up to C_{Mo} = 20 at.%, the site change of hydrogen can be understood mainly by the elastic interactions and the change of interstitial volume due to reduction of lattice parameters on alloying with undersized Mo atoms. However, for 26 at.% Mo alloys, it cannot be explained in such a way. It may be inferred that, in the higher C_{Mo} region, the contribution of electronic interactions becomes important. It is considered that as the mechanism of the enhancement of TSH in the Nb-based Nb-Mo alloy system the trapping of hydrogen by Mo solute atoms is effective at least in the low C_{Mo} region.

Table 1. The summary of the results on the site occupancy of hydrogen in Nb-based Nb-Mo alloys.

Mo conc. C_{Mo} (at.%)	H conc. $C_H = [H]/[M]$	Sites of H atoms (R.T.)	(373 K)
0	0.023	T (§)	
3	0.02	T_{tr}	
	0.05	T_{tr}(40–60%) + T(40–60%)	T
10	0.06	T_{tr}(40–60%) + T(40–60%)	
20	0.026	T(70–80%) + O(20–30%)	
	0.042	T(70–80%) + O(20–30%)	
	0.08	T(90–100%) + O(0–10%)	
26	0.016	T (§)	
	0.026	T (§)	
	0.059	T (§)	

T; tetrahedral site, O; octahedral site, T_{tr}; trapped site (the site displaced from a T site by about 0.6 Å towards its nearest neighbour lattice point).
§ Possible fraction of O-site occupancy is less than 10%.

References

1) E. Yagi, T. Kobayashi, S. Nakamura, Y. Fukai, and K. Watanabe: J. Phys. Soc. Jpn. **52**, 3441 (1983); Phys. Rev. B **31**, 1640 (1985).
2) E. Yagi, T. Kobayashi, S. Nakamura, F. Kano, K. Watanabe, Y. Fukai, and S. Koike: Phys. Rev. B **33**, 5121 (1986).
3) D. G. Westlake and J. F. Miller: J. Less-Common Met. **65**, 139 (1979).
4) E. Yagi, S. Nakamura, F. Kano, T. Kobayashi, K. Watanabe, Y. Fukai, and T. Matsumoto: Phys. Rev. B **39**, 57 (1989).
5) E. Yagi and S. Koike: J. Phys. Soc. Jpn. **67**, 340 (1998).

† Condensed from the article in Phys. Rev. B **66**, 024026 (2002)

*1 Department of Physics, Science University of Tokyo
*2 National Institute for Materials Science

Energy-resolved angular distribution of product C^{2+} ions in C^{4+}-He collisions at 100 eV/q

M. Hoshino,* Y. Kanai, Y. Nakai, M. Kitajima,* H. Tanaka,* and Y. Yamazaki

Inelastic processes in C^{4+} + He collisions have been studied due to their possible applications to astrophysics and in the treatment of thermonuclear fusion plasmas. Several experimental[1] and theoretical[2] works on C^{4+} + He collisions have shown that the double-electron capture process is the most dominant at sufficiently low energy. As collision energy decreases, angular distribution of product ions becomes more sensitive to the shapes of interaction potential curves. Therefore, angular distribution measurements provide the information on the interaction potential, which is essential in term of gaining a detailed understanding of the two electron processes. Those for double-electron capture in C^{4+}-He collisions have been measured by Keller *et al.*[3] at impact energies of 100–200 eV/q, and by Danared and Barany[4] at 380 eV/q. However, these measurements have not clarified the final electronic state at very low energy. In this report, we present the recent result of an energy-resolved angular distribution measurement for product C^{2+} ions in C^{4+}-He collisions at the collision energy of 100 eV/q. We have successfully carried out the state-selective measurement of the oscillation pattern in double-electron capture. The result is shown as an energy-angle two-dimensional contour map of product ion intensity.

The experiment was carried out using a crossed-beam apparatus, which is set at the BL2 of the 14.5 GHz Caprice-type ECRIS in the RIKEN Experimental Hall for slow highly charged ions. Details of our experimental setup are described elsewhere.[5,6] The typical current and energy resolution of the monochromatized C^{4+} beam at 100 eV/q are 150 pA and 0.5 eV/q, respectively.

Angular-resolved energy gain spectra were measured by a scattered ion analyzer, which was set on the turntable and rotatable from $-10°$ to $+10°$ in 0.5° steps. From these energy gain spectra we constructed a 2-D contour map of the scattered ion intensity with respect to the energy difference ΔE of projectile and the scattering angle θ. The kinematics relation between ΔE and θ is derived from the energy and momentum conservation for a Q-value, where Q is an energy release of a reaction. When the Q-value is specified, a unique curve is drawn on the 2-D contour map. This curve shows the relation between ΔE and θ of the scattered ions in the a certain final channel.

Figure 1 shows the 2-D contour map of product C^{2+} ions in C^{4+} + He collisions at the energy of 100 eV/q.

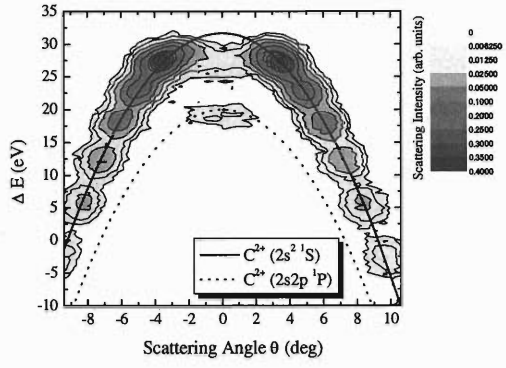

Fig. 1. 2-D contour map of product C^{2+} ions from double-electron capture for C^{4+}-He at the collision energy of 100 eV/q. Solid and dashed curves indicate the expected ΔE as a function of θ for the final channels specified by Q = 33.4 and 20.7 eV, respectively.

Solid and dashed curves show the relation between ΔE and θ for the final channels $C^{2+}(1s^22s^2\ ^1S)$ and $C^{2+}(1s^22s2p\ ^1P)$ corresponding to Q = 33.4 and 20.7 eV, respectively. On the 2-D contour map most of the signals exist on the solid curve for the $C^{2+}(1s^22s^2\ ^1S)$ channel. We conclude that the $C^{2+}(1s^22s^2\ ^1S)$ channel is a dominant final state at the collision energy of 100 eV/q. The oscillation pattern is clearly seen in the 2-D contour map. This oscillation structure, which is called Stueckelberg oscillation, results from the quantum interference effect between two different paths toward the same final state. The oscillation periods on the 2-D contour map are in good agreement with the results of Keller *et al.*[3] at the same collision energy. The advantage of our experiment is that the energy resolution is sufficiently high ($\Delta E/E \sim 1/150$) so that the state-selective angular distribution can be obtained at 100 eV/q.

The 2-D contour map representation of the scattered ion intensity allows us to show more clearly the state-selective angular distribution of product ions. This result shows that the energy-resolved angular distribution measurement using the 2-D contour map is a powerful tool to study the highly charged ion-atom collisions in a very low energy region.

* Department of Physics, Sophia University

References

1) K. Okuno et al.: Phys. Rev. A **28**, 127 (1983).
2) M. Kimura and R. E. Olson: J. Phys. B **17**, L713 (1984).
3) N. Keller et al.: Phys. Rev. A **48**, 3684 (1993).
4) H. Danared and A. Barany: J. Phys. B **19**, 3109 (1986).
5) M. Kitajima et al.: Phys. Scr. T **80**, 377 (1999).
6) M. Hoshino et al.: Phys. Scr. T **92**, 339 (2001).

Coincidence measurements of L X-ray and final charge state of Ar ions transmitted through a microcapillary

Y. Kanai, Y. Nakai, Y. Iwai, Y. Yamazaki, K. Nishio,* and H. Masuda,*

A slow highly charged ion passing through a microcapillary target resonantly captures target valence electrons into high-n orbitals with inner shell vacancies. The captured electrons cascade down via X-ray and/or Auger electron emissions. Using a N^{6+} beam, Ninomiya *et al.* showed that plural electrons stay in the L-shell or higher shell having a K-shell vacancy with nanosecond-order lifetime of K X-ray emission.[1] However, when ions have plural inner shell vacancies, the filling processes of the inner shell are not studied in detail. We have performed coincidence measurements of L X-rays of Ar ions transmitted through a Ni microcapillary with their final charge states for 2.8 keV/u Ar^{14+} ions, to study the filling processes of inner shell vacancies. In this report, we present the X-ray spectrum and the decay curve of X-ray yield for each final charge state.

A 2.8 keV/u Ar^{14+} beam was extracted from a 14.5 GHz Caprice type ECR ion source at RIKEN. The beam was collimated with an aperture and transported into a vacuum chamber. Ar ions impinge on a Ni capillary target along the capillary axis. The capillary diameter and the target thickness are about 150 nm and 1.1 μm, respectively. A Si(Li) detector is located at right angle on the beam axis. The shield located between the target and the Si(Li) detector is movable along the beam direction. A shield is used to limit the detection region of emitted X-rays. The charge states of emerging Ar ions are analyzed using an electrostatic charge state analyzer. The charge-analyzed Ar ions are detected using a channel electron multiplier (CEM).

The X-ray yields presented in this report are normalized by the transmitted beam current. The X-ray yield is measured as a function of shield position z. Roughly speaking, when the shield is located at z, the X-ray emitted at time t' is detected, where $14\,\text{ns} > t' > t = z/v$ (v: ion velocity). Typical coincidence X-ray spectra at $z = 0, 2, 4$ mm are shown in Fig. 1. The peak positions of coincidence L X-ray spectra shift to a lower energy side with decreasing final charge state (with increasing number of stabilized electrons s). This indicates that the number of L-shell vacancies when L X-rays are emitted decreases with decreasing final charge state. It is also found that the peak position of coincidence L X-ray spectra for each final charge state does not shift with shield position.

The shield position dependence of the coincidence X-ray yield for each final charge state is shown in Fig. 2.

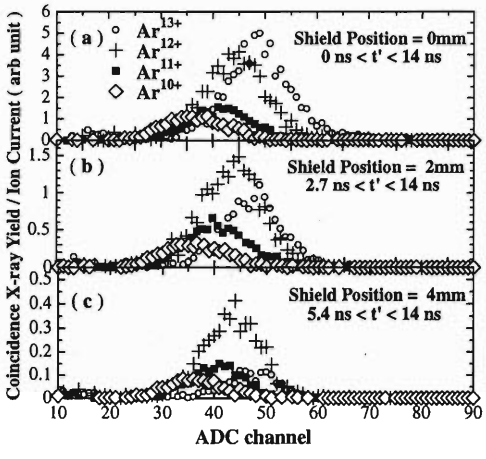

Fig. 1. X-ray spectra in coincidence with different final charge states. (a) Shield positions $z = 0$ mm, (b) $z = 2$ mm and (c) $z = 4$ mm.

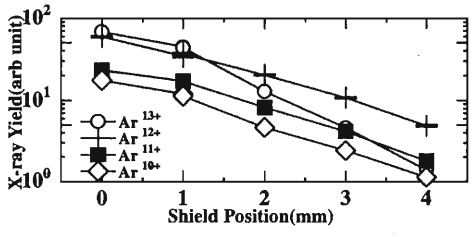

Fig. 2. Shield position dependence of the coincidence X-ray yield for each final charge state.

The shield position dependences of the coincidence X-ray yield for Ar^{q+} ($q = 10, 11, 12$) are similar to one another. On the other hand, the coincidence X-ray yield for Ar^{13+} decreases more rapidly than those for the other charge states. At a shield position of 4 mm, the X-ray from Ar^{12+} is dominant. Considering that the peak positions of the coincidence X-ray spectrum shift with the final charge state, as for Ar^{q+} ($q = 10, 11, 12$), it is thought that $(s-1)$ electrons rapidly fill the L-shell vacancies and that one electron is slowly de-excited via X-ray emission as shown in Fig. 2.

References

1) S. Ninomiya et al.: Phys. Rev. Lett. **78**, 4557 (1997).

* Department of Applied Chemistry, Tokyo Metropolitan University

High-resolution soft X-ray spectroscopy using a single photon counting method

Y. Iwai, Y. Kanai, Y. Nakai, T. Ikeda, H. Ohyama, K. Ando, H. Masuda,[*1]
K. Nishio,[*1] M. Nakao,[*2] H. A. Torii,[*3] K. Komaki,[*3] and Y. Yamazaki

In order to obtain X-ray spectra without background noise caused by cosmic rays and readout noise, a charge-coupled device (CCD) mounted on a high-resolution grating spectrometer was operated in a short exposure time, and the data analysis procedure was established to separate X-rays from the background noise because weak X-ray peaks cannot be distinguished from the fluctuation of the background noise. This procedure is referred to as the single event mode.

The present study was performed using a 14.5 GHz Caprice type electron cyclotron resonance ion source (ECRIS) at RIKEN.[1)] Details of a Ni microcapillary target and the soft X-ray spectrometer are given in Refs. 2 and 3, respectively. X-rays emitted from 2.3 keV/u N^{7+} and Ne^{9+} ions transmitted through the Ni microcapillary were measured with the spectrometer immediately downstream.

Figure 1 shows the "pulse height" distributions of the CCD signals of the 2p - 1s transition of N ions (500.3 eV) (the thin solid line) and the 1s2p - $1s^2$ transition of Ne ions (914.9 eV and 922.1 eV) (the thin dashed line).[4)] The thick solid and dashed lines show Gaussian fitting of the distributions of N and Ne ions, respectively. It is seen that the pulse height clearly reflects the X-ray energy, *i.e.*, the pulse height can be effectively used to discriminate background noise such as cosmic rays and readout noise.

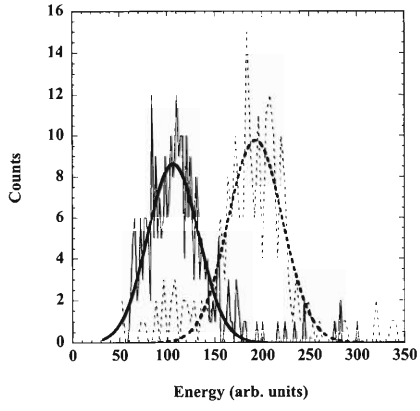

Fig. 1. Distribution of energy. The thin solid and dashed lines show distributions for H-like N ion 2p - 1s (500.3 eV) and He-like Ne ion 1s2p - $1s^2$ (914.9 eV and 922.1 eV) transition X-rays, respectively.[4)] The thick solid and dashed lines show Gaussian fitting curves for N and Ne ions, respectively.

Figure 2 shows K X-ray spectra from 2.3 keV/u N^{7+} ions transmitted through the Ni microcapillary. The solid and dashed lines show the X-ray spectra generated by the single event mode analysis and a raw spectra (the flat background has already been subtracted), which is plotted as a reference, respectively. These two spectra were accumulated under the same experimental condition. Only peaks corresponding to the 1s - 3p and 1s - 4p transitions are true X-ray peaks. It is found that the fluctuation of the baseline is decreased by the single event mode analysis. However, in the X-ray spectra of the single event mode, one can recognize some X-ray counts in the energy range where no X-rays should appear. These X-rays are considered to be stray X-rays because their pulse height distribution was almost the same as that of the X-rays at the true peaks. A modification, *e.g.*, the installation of a damper for 0th order light and more baffles, is in progress to reduce the amount of stray X-rays.

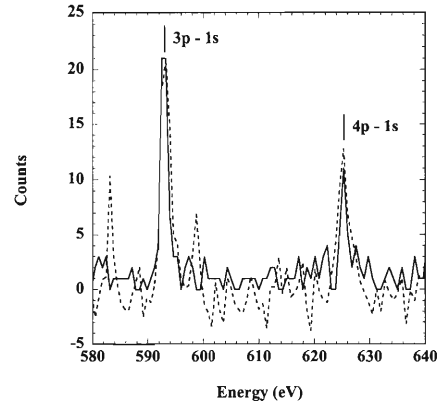

Fig. 2. K X-ray spectra measured with the spectrometer, for 2.3 keV/u N^{7+} transmission through a Ni microcapillary. The solid line shows the spectrum analyzed using the single event mode procedure. The dashed line is a raw spectrum. The bars with transition configurations show transition energies.[4)]

*1 Department of Applied Chemistry, Graduate School of Engineering, Tokyo Metropolitan University
*2 NTT Photonics Laboratories
*3 Institute of Physics, Graduate School of Arts and Sciences, University of Tokyo

References

1) Y. Kanai et al.: Phys. Scr. T **92**, 467 (2001).
2) H. Masuda et al.: Appl. Phys. Lett. **71**, 2770 (1997).
3) Y. Iwai et al.: Nucl. Instrum. Methods Phys. Res. B **193**, 504 (2002).
4) R. L. Kelly: J. Phys. Chem. Ref. Data **16**, Suppl. 1 (1987).

New method for positron accumulation in an ultrahigh-vacuum environment

N. Oshima,* T. M. Kojima, M. Niigaki,* A. Mohri, K. Komaki,* and Y. Yamazaki

For positron accumulation, a variety of techniques including trapping by collisions with buffer gas[1,2] and field ionization of high Rydberg positronium,[3] *etc.*,[4,5] have been studied intensively.

The buffer gas method can accumulate positrons with relatively high efficiency, but this is not compatible with an ultrahigh-vacuum (UHV) environment.[2] Other methods can accumulate positrons directly in UHV, but their accumulation rates are relatively low.[3–5]

We have been developing a new method which accumulates positrons directly in UHV with relatively high efficiency.[6]

The new method is schematically shown in Fig. 1. First, more than 10^{10} electrons are trapped in a multi-ring trap (MRT)[7] installed in a superconducting solenoid of 5 T (see Fig. 1 (a)). In the next step, a positron beam is injected into a tungsten re-moderator inside the trap and a certain fraction of it is re-emitted as slow positrons with a small energy of ~eV. The re-emitted positrons are injected into the electron plasma and lose their kinetic energy via collision with electrons. If the electron plasma density is maintained to be sufficiently high ($\geq 10^{10}/\mathrm{cm}^3$) the energy loss of positrons is larger than ~eV after a return trip through the electron plasma. Therefore, almost none of the re-emitted positrons can reach the re-moderator and they are confined in a trapping region (see Fig. 1 (b)). Such positrons are then self-cooled via synchrotron radiation, and eventually they are trapped at the bottom of the potential.

A ^{22}Na(22mCi)-based positron beam ($7 \times 10^5\,\mathrm{e}^+/\mathrm{s}$) was implanted into the re-moderator for 50 s and ~ 3.6×10^5 positrons were stored. This trapped positron number is deduced by counting their annihilation radiation emitted when they were extracted from the trap to a target and annihilated there. Storage time of the trapped positrons after the accumulation was changed in the range of 10–300 s and no remarkable decrease of the trapped positron number was observed. Roughly 1% of positrons implanted into the re-moderator were trapped with lifetimes much longer than ~300 s.

At present, the positron trapping rate normalized by the ^{22}Na source strength ($3.2 \times 10^2\,\mathrm{e}^+/\mathrm{mCi}$) is much higher than those obtained by other methods[3–5] which can accumulate positrons directly in UHV (see Fig. 2).

Optimization of the accumulation parameter is in progress.

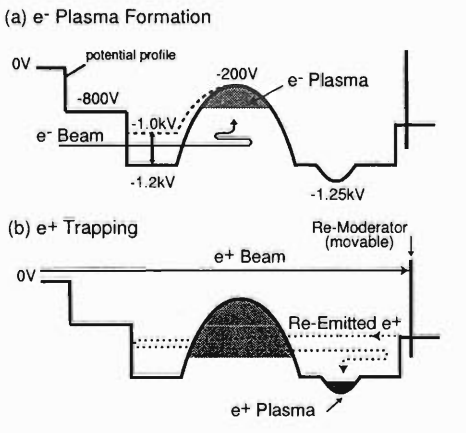

Fig. 1. Schematic procedure of positron trapping.

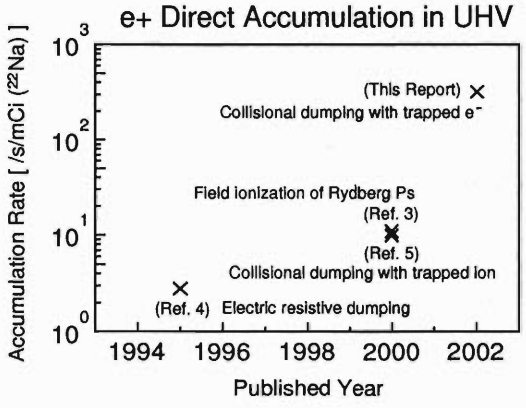

Fig. 2. Comparison of the positron accumulation rate normalized by the ^{22}Na positron source intensity.

References

1) C. M. Surko, M. Leventhal, and A. Passner: Phys. Rev. Lett. **62**, 901 (1989).
2) R. G. Greaves and C. M. Surko: Phys. Plasmas **4**, 1528 (1997).
3) J. Estrada, T. Roach, J. N. Tan, P. Yesley, and G. Gablielse: Phys. Rev. Lett. **84**, 859 (2000).
4) H. Haarsma, K. Abdullah, and G. Gablielse: Phys. Rev. Lett. **75**, 806 (1995).
5) A. S. Newbury, B. M. Jelenković, J. J. Bollinger, and D. J. Wineland: Phys. Rev. A **62**, 023405 (2000).
6) A. Mohri, T. M. Kojima, N. Oshima, M. Niigaki, and Y. Yamazaki: AIP Conf. Proc. **606**, 634 (2002).
7) A. Mohri, H. Higaki, H. Tanaka, Y. Yamazawa, M. Aoyagi, T. Yuyama, and T. Michishita: Jpn. J. Appl. Phys. **37**, 664 (1998).

* Institute of Physics, University of Tokyo

Measurement of inner shell electron ionization cross sections by low-energy positron impact

Y. Nagashima,* F. Saito, Y. Itoh, A. Goto, and T. Hyodo

When electrons, ions, or photons with energies higher than the threshold energy are incident on a target, characteristic X-rays are emitted by ionization of inner shell electrons. The inner shell ionization also occurs by positron impact. A positron, due to its positive charge, is decelerated while approaching the nuclei, whereas an electron is accelerated. Furthermore, exchange scattering does not occur in positron-atom scattering because of the distinguishability of a positron from an electron. A number of theoretical investigations have been performed in which absolute cross sections of the K-shell, L-shell and M-shell ionization cross sections of the atoms by the electron and positron impacts at the same incident energies are compared.[1] As expected, the positron-impact ionization cross sections at high impact energies are similar to those of electron impact. However, the cross sections near the threshold energies are lower than those by the electron impact.

The inner shell ionization cross sections can be measured by detecting the characteristic X-rays emitted from thin film samples. Experimental investigations for electron impact have been reported by many authors.[2] However, there are only a few reports on the absolute cross sections for positron impact. This is because a high background in the X-ray spectra is produced by the γ-rays emitted from positron annihilation in the films. The γ-rays deposit part of their energy in the X-ray detector crystal. For lower positron impact energies, the background becomes higher because more positrons stop and annihilate in the film. Therefore, the impact energies of the cross sections measured to date are restricted to those above 30 keV.[3]

Recently, we have found that the background is reduced if an X-ray detector with thin Si(Li) crystal is used.[4] In this work, we have measured the ionization cross sections of Cu K-shell and Ag L-shell electrons in the positron energy range below 30 keV using this detector.

The experimental system is a magnetically guided positron beam with a high-efficiency tungsten mesh moderator.[5] The beam intensity is 3.2×10^4 e^+/s. The beam energy is 0–30 keV. The diameter of the beam at the sample position is 3 mm. The samples are Cu film of 7.5 nm in thickness and Ag film of 7.2 nm in thickness. The thicknesses are similar to or smaller than the mean free path of positrons in the samples. The samples are vapor-deposited on 10 μg/cm^2 ($\sim$40 nm) carbon thin films supported with an aluminum holder with a hole of 8 mm in diameter. The samples are mounted at an angle of 30° with respect to the incident beam direction. The positron beam is controlled to be incident only on the film and not on the aluminum holder. The Si(Li) detector is oriented perpendicularly to the incident beam.

The inner shell ionization cross section Q is obtained from the following equation:

$$N_X = nlQN_0\varepsilon\omega, \tag{1}$$

where N_X is the X-ray count rate, n is the number density of the sample atoms, l is the thickness of the sample, N_0 is the beam intensity, ε is the detection efficiency of the X-ray, and ω is the fluorescence yield.[6] The determined values of Q are plotted in Fig. 1 against the positron impact energy. While the values for Cu-K shell are consistent with the theoretical calculation, the values for Ag-L shell are smaller than the theoretical prediction.[1]

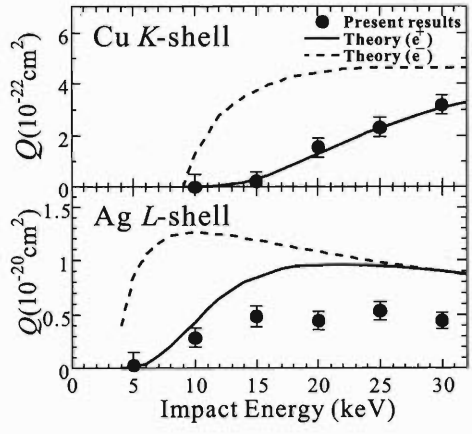

Fig. 1. Cu K-shell and Ag L-shell ionization cross sections plotted against the positron impact energy. Theoretical results for positron and electron impact[1] are also shown.

References

1) S. P. Khare and J. M. Wadehra: Can. J. Phys. **74**, 376 (1996).
2) C. J. Powell: Rev. Mod. Phys. **48**, 33 (1976).
3) H. Schneider, I. Tobehn, F. Ebel, and R. Hippler: Phys. Rev. Lett. **71**, 2707 (1993).
4) Y. Nagashima, F. Saito, Y. Itoh, A. Goto, and T. Hyodo: RIKEN Accel. Prog. Rep. **36**, 113 (2003).
5) F. Saito, Y. Nagashima, L. Wei, Y. Itoh, A. Goto, and T. Hyodo: Appl. Surf. Sci. **194**, 13 (2002).
6) W. Bambynek, B. Crasemann, R. W. Fink, H.-U. Freund, H. Mark, C. D. Swift, R. E. Price, and P. V. Rao: Rev. Mod. Phys. **44**, 716 (1972).

* Institute of Physics, Graduate School of Arts and Sciences, University of Tokyo

Si(Li) detector for measurement of characteristic X-rays by positron impact

Y. Nagashima,* F. Saito, Y. Itoh, A. Goto, and T. Hyodo

When electrons, ions, or photons with energies higher than the binding energy of inner shell electrons are incident on a target, characteristic X-rays are emitted by inner-shell ionization. These X-rays are widely used for elemental analysis of materials.

The characteristic X-ray emission by positron impact, however, is not used for elemental analysis because the background in the X-ray spectra is far higher than that in the case of impact of other particles. The background is produced by positron annihilation γ-rays which deposit part of their energy in the X-ray detector crystal.

The background is expected to be lower when the crystal is thinner. In the present work, we fabricated an X-ray detector with an Si(Li) crystal of 0.25 mm thickness, which is one order of magnitude thinner than the crystals of conventional Si(Li) detectors.

The effective area of the crystal must also be optimized because the energy resolution of the detector depends on the capacitance of the crystal. The effective area of the thin crystal was limited to be 20 mm^2. In order to obtain high efficiency, two crystals of 20 mm^2 area were placed in the detector and each crystal was connected to a separate pre-amplifier. The energy resolution was 300 eV at 5.9 keV.

The background caused in the newly developed detector by the positron annihilation γ-rays from the sample was tested by observing K X-rays from Ti (4.5 keV) induced by the γ-rays. A γ-ray standard source (^{22}Na) was attached to a Ti plate. (Positrons are not emitted from the source because ^{22}Na was encapsulated in a lucite plate of 2 mm thickness.) The spectra obtained from the detector and the conventional Si(Li) detector with a crystal of 3 mm thickness are shown in Fig. 1 (a) and (b), respectively. The characteristic X-ray peak in (a) is isolated clearly, while the peak in (b) is obscured by the background.

The L X-rays from the Ag target, K X-rays from the Ti target, and K X-rays from the Cu target emitted by positron impact were observed using the thin-crystal detector. The experimental system was a magnetically guided positron beam with a high-efficiency tungsten mesh moderator.[1] The beam intensity was 3×10^4 e^+/s. The beam energy was 0–30 keV. The samples were 0.1 mm in thickness.

The X-ray spectra are shown in Fig. 2. The background is sufficiently low to isolate characteristic X-rays. This shows that the use of the detector with a thin Si(Li) crystal is essential for the measurement of characteristic X-rays induced by positron impact.

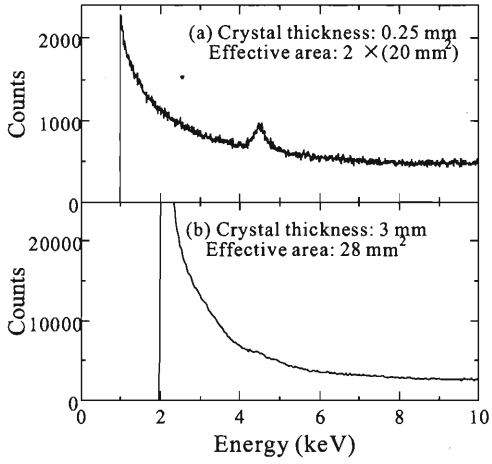

Fig. 1. Spectra of K X-rays from Ti induced by positron annihilation γ-rays for (a) the thin-Si(Li)-crystal detector and (b) a conventional Si(Li) detector.

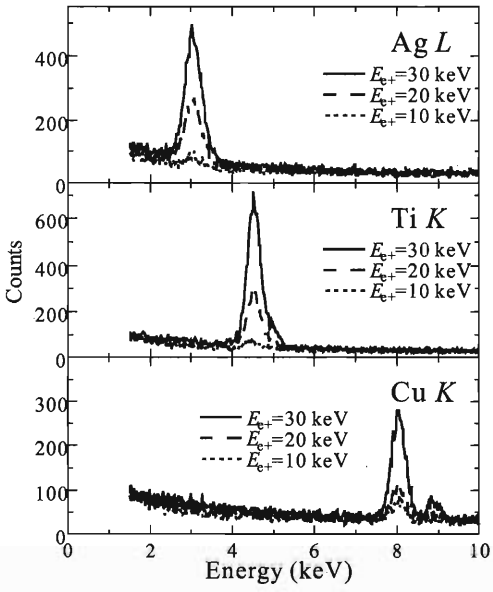

Fig. 2. X-ray spectra for Ag, Ti, and Cu targets induced by positron impact.

* Institute of Physics, Graduate School of Arts and Sciences, University of Tokyo

References

1) F. Saito, Y. Nagashima, L. Wei, Y. Itoh, A. Goto, and T. Hyodo: Appl. Surf. Sci. **194**, 13 (2002).

Precision spectroscopy of the Zeeman splittings of the $^9Be^+$ $2^2S_{1/2}$ hyperfine structure levels (II)

T. Nakamura,[*1] M. Wada, K. Okada,[*2] I. Katayama,[*1] S. Ohtani,[*3] and H. A. Schuessler[*4]

We have been working for precision measurements of the ground-state hyperfine structure of ions trapped in a combined trap.[1)] The main purpose of our project is to study the nuclear structure of unstable nuclei through the Bohr-Weisskopf effect which is deduced from a comparison of the hyperfine constant, which is normalized by the nuclear g-factor, among the isotopes. The isotope dependence is generally very small, so that we have been testing a precision measurement technique for the Zeeman splittings of the hyperfine structure of unstable nuclear ions trapped in the combined ion-trap, which is a superposition of a linear rf ion-trap with a strong magnetic field,[2)] to determine the hyperfine constant A and the nuclear g-factor, independently.

We have so far obtained the values of the hyperfine constant A and the nuclear g_I-factor, in units of the electronic g_J-factor, of $^9Be^+$ with our setup as $A = -625\,008\,835.23(75)$ Hz and $g'_I/g_J = 2.134\,780\,33(28) \times 10^{-4}$.[1)] They were obtained from two pairs of transition frequencies, the nuclear spin-flip transitions and the electron spin-flip transitions, at different optical pumping conditions, σ_+ and σ_-. The measurement was performed by repeating a short cycle of about 100 ms on a few hundreds of $^9Be^+$ ions. The accuracy and the sensitivity is already sufficient for application to our target nucleus, ^{11}Be. The on-line experiment for the investigation of ^{11}Be will be ready when another development for the accumulation of ^{11}Be ions produced at the cycloton facility is ready.[3)]

Although the present accuracy is sufficient for the primary purpose, we are still making efforts to improve the accuracy. Our measurement values are slightly inconsistent with the NIST results by about 2 σ. One reason for this disagreement could be a possible quadratic dependence of the hyperfine constant A and the nuclear g-factor on the strength of the external magnetic field.[4,5)] In order to confirm the theory, we need to measure the magnetic field dependence with greater accuracy.

The NIST group has demonstrated an ultimate accuracy of 10^{-11} in the determination of the A and of 10^{-9} in the g_I/g_J ratio.[6)] In their measurement, the particular strength of the magnetic field, where the nuclear spin flip transition is independent of the magnetic field strength in the first order, was used. Such a transition is called a *clock* transition. For their application to a frequency standard, such an ultra highly accurate transition at that particular condition of an arbitrary atom is required. However, for our purpose, various isotopic ions including short-lived isotopes are the objects to be studied. In this case, such adequate *clock* transitions are not always available. For instance, for the ^{11}Be ion, there is no *clock* transition, since the nuclear spin is $I = 1/2$, so that we have restricted ourselves to use an arbitrary fixed strength of the magnetic field.

Under such experimental conditions, a drift of the magnetic field strength was a significant effect on the accuracy limit. We modified the measurement sequence so as to measure the nuclear spin-flip transition and the electron spin-flip transition, simultaneously. The coherent time of each measurement cycle was also increased to decrease the line-width of the resonance curve. Figure 1 shows the present measurement spectrum of the nuclear spin-flip transition where the extended coherent time, $T = 80$ ms, was used. In this measurement, the homogeneity of the magnetic field over the ion-cloud limited the obtained accuracy. Due to an unknown reason, the ion-cloud was not located at the center of the magnetic field. We are currently adjusting the sim-coils to locate the trap center at the magnetic field center.

We expect to obtain better accuracy of at least one order of magnitude greater than the previous measurement. Then, we will vary the field strength to measure the field dependence with high accuracy.

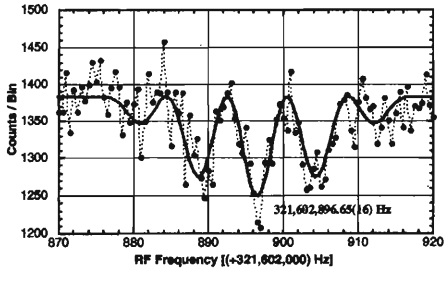

Fig. 1. Nuclear spin-flip resonance spectrum of the ground-state hyperfine structure of $^9Be^+$.

*1 Institute of Particle and Nuclear Studies, High Energy Accelerator Research Organization (KEK)
*2 Department of Physics, Sophia University
*3 Institute for Laser Science, University of Electro-Communications
*4 Department of Physics, Texas A&M University, USA

References

1) T. Nakamura et al.: Opt. Commun. **205**, 329 (2002).
2) T. Nakamura et al.: J. Appl. Phys. **89**, 2922 (2001).
3) M. Wada et al.: AIP Conf. Proc. **606**, 625 (2002).
4) N. P. Economou et al.: Phys. Rev. Lett. **38**, 1394 (1977).
5) N. Fortson: Phys. Rev. Lett. **59**, 988 (1987).
6) D. J. Wineland et al.: Adv. At. Mol. Phys. **19**, 135 (1983).

Chemical reaction of laser-excited Ca^{+*} with H_2O in an ion trap

K. Okada,[*1] M. Wada, L. Boesten,[*1] T. Nakamura,[*2] I. Katayama,[*2] and S. Ohtani[*3]

A study of the reactivity of laser-excited Ca^{+*} ions with H_2O molecules is an important subject in optical frequency standards using Ca^+, in addition to the fundamental studies of photochemical ion-molecule reactions with applications of trapped ions. Moreover, the hydration reaction of trapped ions is closely related to spectroscopic experiments conducted using a radioactive beam in our project.[1-3] In order to obtain detailed information on the reaction process, we have studied the laser-assisted reaction of $Ca^{+*}(D_J) + H_2O \rightarrow$ *products* by using the optical pumping technique.

The experimental setup is described elsewhere.[4,5] In order to detect the reaction product ions with H_2O, the laser-induced fluorescence (LIF) mass spectroscopy for trapped ions was developed as a combination method of the observation of LIF and secular motion excitation by a small perturbation rf voltage.[6] In the method, a small perturbation rf voltage V_s resonant with the motion of a selected ion species was applied to one of the trap electrodes for dipolar excitation. The perturbed ions, in turn, modify the intensity of the observed LIF from the laser-cooled Ca^+ ions through Coulomb interaction.

A mass spectrum can be obtained in the form of intensity changes in the fluorescence by scanning the perturbation rf frequency, as shown in Fig. 1. A mass signal of the product ions indicated by an arrow was observed only when the Ca^+ ions were pumped in the metastable $3D_{3/2}$ state, while there was no signal when the ions were in the ground $4S_{1/2}$ state. This gives clear evidence of the acceleration of the chemical reaction with H_2O by laser excitation to the metastable state. The reason for this phenomenon can be explained by the energy level structures of Ca^+ and $Ca^+(H_2O)$.[7] Since the $(2)^2B_1$ and $(2)^2B_2$ states of $Ca^+(H_2O)$ are energetically close to those of the $3D_J$ states of Ca^+ and the calculated electron populations of the lower $(1)^2A_2$ and $(2)^2A_1$ states in $Ca^+(H_2O)$ are concentrated at the $3d$ orbit of Ca^+,[8] $Ca^{+*}(D_J)$ may easily turn into these excited states of $Ca^+(H_2O)$ upon colliding with H_2O. Thus, new reaction channels are opened.

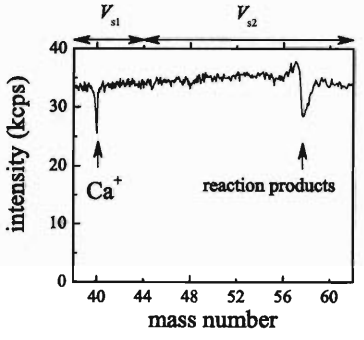

Fig. 1. Signal of the reaction-product ions strengthened by optical pumping into the $D_{3/2}$ state. The H_2O gas was intentionally introduced to a partial pressure of 1.1×10^{-6} Pa. The perturbation rf amplitudes were $V_{s1} = 0.5$ mV and $V_{s2} = 5$ mV. At present, we suppose that the product ions consisted of $CaOH^+$ and $HCaOH^+$ ions.

By using this strong state-dependence of the reactivity with H_2O, we measured the ion temperature dependence of the reaction rate coefficient for buffer-gas-cooled $^{40}Ca^+$ ions.[5] The order of the reaction rate coefficient was estimated to be $\sim 10^{-11}\,cm^3s^{-1}$ within this temperature range if room temperature ($T = 300$ K) was assumed for the H_2O gas. As seen in Fig. 2, the measured reaction rate tends to increase with decreasing ion temperature, which can be explained by the $1/\sqrt{T}$ dependence of the ion-dipole capture rate.[9]

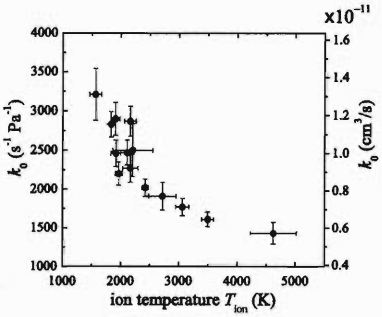

Fig. 2. Ion-temperature dependence of the reaction rate coefficient of $Ca^{+*}(D_J) + H_2O \rightarrow$ *products*. The ion temperature was evaluated by the Doppler widths of the LIF spectra measured at the the start and the end of each series of measurements.

*1 Department of Physics, Sophia University
*2 Institute of Particle and Nuclear Studies, High Energy Accelerator Research Organization (KEK)
*3 Institute of Laser Science, University of Electro-Communications

References

1) M. Wada et al.: RIKEN Rev., No. 31, p. 56 (2000).
2) M. Wada et al.: Nucl. Phys. A **626**, 365c (1997).
3) S. Fujitaka et al.: Nucl. Instrum. Methods Phys. Res. B **126**, 386 (1997).
4) K. Okada et al.: Jpn. J. Appl. Phys. **40**, 4221 (2001).
5) K. Okada et al.: J. Phys. B **36**, 33 (2003).
6) D. L. Larson, J. C. Bergquist, J. J. Bollinger, and W. M. Itano: Phys. Rev. Lett. **57**, 70 (1986).
7) M. Sanekata, F. Misaizu, and K. Fuke: J. Chem. Phys. **104**, 9768 (1996).
8) E. Kochanski and E. Constantin: J. Chem. Phys. **87**, 1661 (1987).
9) D. R. Bates: Astrophys. J. **270**, 564 (1983).

μSR study on the dynamics of the dynamical stripes in $La_{2-x}Sr_xCu_{1-y}Zn_yO_4$

I. Watanabe, T. Adachi,[*1] S. Yairi,[*1] Y. Koike,[*1] and K. Nagamine[*2]

The stripe correlations of spins and holes were suggested by Tranquada *et al.* to be important for understanding the mechanism of high-T_c superconductivity.[1] Recently, Koike *et al.*[2] and Adachi *et al.*[3] suggested on the basis of transport measurements that the dynamics of dynamical stripe correlations was affected by nonmagnetic impurities such as Zn. Thus, in order to confirm this suggestion, we have carried out zero-field (ZF) muon spin relaxation (μSR) measurements on $La_{2-x}Sr_xCu_{1-y}Zn_yO_4$ (LSCZO) with $x = 0.115$ and 0.13, changing y in fine steps.[4]

Polycrystalline samples of LSCZO with $y = 0$, 0.0025, 0.005, 0.0075, 0.01, 0.02, 0.03, 0.05, 0.07 and 0.10 were prepared for both systems with $x = 0.115$ and 0.13 by the ordinary solid-state-reaction method. ZF-μSR measurements were carried out at the RIKEN-RAL Muon Facility at the Rutherford-Appleton Laboratory in the UK using a pulsed positive surface-muon beam.

Figure 1 shows the Zn-concentration dependence of the magnetic transition temperature, T_N, which is obtained from the analysis of μSR time spectra, in the two systems with $x = 0.115$ and 0.13. In the case of $x = 0.115$, T_N slightly increases with increasing y and shows a peak at $y = 0.0075$. In the case of $x = 0.13$, on the other hand, the change of the magnetic state is very marked. The magnetically ordered state appears at $y = 0.0025$. T_N increases with increasing y and exhibits a peak at $y = 0.0075$, as in the case of $x = 0.115$. T_N decreases slowly with increasing y for $y > 0.0075$ in the two systems with $x = 0.115$ and 0.13. The y dependence of T_N for $y \geq 0.01$ is similar for both x values. No sign of the appearance of the static magnetically ordered state is observed down to 2 K for $y \geq 0.07$ in either system.

These results for systems with $x = 0.115$ and 0.13 can be understood as follows. Since the period of the stripe pattern of spins and holes at $x = 0.115$ is nearly commensurate with that of the crystal lattice,[1] the dynamical stripe correlations tend to be stabilized and form a static stripe order, even in the Zn-free sample ($y = 0$). The small increase in T_N, as a result of a 1% Zn-substitution in the $x = 0.115$ series of samples, can be explained as being due to the slight enhancement of the static stabilization of the dynamical stripe correlations owing to the pinning force of the substituted Zn. When the hole concentration increases from $x = 0.115$ to 0.13, excess holes destroy the commensurability between the periods of the stripe pattern and the crystal lattice, leading to the destabilization of the static stripe order. As the value of y increases for $x = 0.13$, the substituted Zn tends to pin a spin or hole domain of the dynamical stripe so as to suppress the Cu-spin fluctuations, and finally forces them to be statically stabilized, leading to the formation of the static stripe order and the increase in T_N. As a result, this result supports the suggestion by Koike *et al.*[2] and Adachi *et al.*[3] that a small concentration of nonmagnetic impurities tends to statically stabilize the dynamical stripe correlations forming the static long-range ordered state.

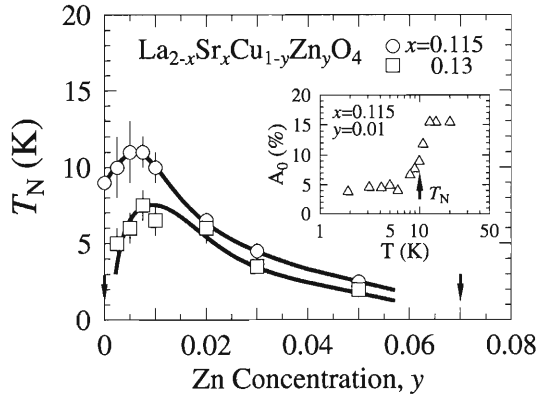

Fig. 1. Zn-concentration dependence of the magnetic transition temperature, T_N, of the Zn-substituted $La_{2-x}Sr_xCu_{1-y}Zn_yO_4$ with $x = 0.115$ and 0.13. Circles and squares show T_N's of the samples with $x = 0.115$ and 0.13, respectively. Solid lines are visual guides. Arrows at $y = 0$ and 0.07 mean that no sign of the appearance of the magnetic transition was observed down to 2 K for $x = 0.13$. Regarding $x = 0.115$, no sign of the appearance of the magnetic transition was observed down to 2 K for $y \geq 0.07$. The inset shows the temperature dependence of the initial asymmetry in the case of $x = 0.115$ and $y = 0.01$. T_N is indicated by an arrow in the inset as the midpoint of the transition.

References
1) J. M. Tranquada et al.: Nature **375**, 561 (1995).
2) Y. Koike et al.: J. Low Temp. Phys. **105**, 317 (1996).
3) T. Adachi et al.: J. Low Temp. Phys. **117**, 1151 (1999).
4) I. Watanabe et al.: Phys. Rev. B **65**, R180516 (2002).

*1 Department of Applied Physics, Tohoku University
*2 Meson Science Laboratory, High Energy Accelerator Research Organization (KEK)

Performance of an EBIS using high-T_c bulk superconductor

N. Nakamura, Y. Kanai, Y. Nakai, K. Komaki,* and Y. Yamazaki

An electron beam ion source (EBIS) is widely used as an effective source of highly charged ions. In an EBIS, ions are trapped in a magnetically confined electron beam and are successively ionized by electron impact. Thus, the current density of the electron beam is one of the most important parameters determining the maximum charge of produced ions. In order to realize a high-density beam, magnetic compression with a superconducting coil is commonly used. However, use of such a magnet usually entails high liquid helium consumption, and greatly increases the size and the running costs of the apparatus. Alternatively, we have developed an EBIS utilizing a permanent current on a high-T_c superconducting material to produce a strong magnetic field. It decreases the size of the EBIS and enables us to operate the EBIS at the liquid N_2 temperature with a sufficiently strong magnetic field.

The details of the present EBIS are given elsewhere.[1] Briefly, the EBIS mainly consists of three parts, an electron gun, a drift tube, and an electron collector. The electron beam emitted from the electron gun is accelerated toward the drift tube. The electron beam is compressed by the magnetic field produced by the high-T_c superconducting materials. After passing through the drift tube, the electron beam is decelerated to ~2 keV and collected by the water-cooled electron collector. Ions are confined within the center of the drift tube axially by an axial electrostatic well prepared by three successive electrodes and radially by the space charge potential of the compressed electron beam. Highly charged ions are thus produced by successive electron impact ionization of the trapped ions.

The high-T_c superconducting material used is YBa_2CuO_{7-x}, which has a high critical current density.[2] Three ring-shaped bulk materials are placed in series and sealed in a stainless-steel container which is in contact with the liquid N_2 reservoir wall. To magnetize the bulk materials, we used the so-called pulsed field magnetization technique,[3] where the magnetizing coil (182 turns of a wire with a cross section of $1.4 \times 3.0\,mm^2$) is installed in the liquid N_2 reservoir. By repeatedly applying pulsed magnetic field with a width of 11 ms and peak strength of 1–3 Tesla, we succeeded in magnetizing the bulk magnets up to 0.8 T at the liquid N_2 temperature.

In the first stage of test operation, the EBIS has been operated with electron energies below 12 keV. The maximum current achieved so far is 50 mA. Within these parameters, ~99% collection of the electron beam at the electron collector has been achieved. A preliminary ion extraction test has been performed recently. Figure 1 shows the typical charge spectra of extracted argon ions. Argon gas was injected through a small hole prepared in the middle electrode of the drift tube. Under the above-described parameters, argon can be fully ionized. However, in the present operation, the maximum charge state of the extracted ions was 17+ (H-like) as shown in the figure. This is probably due to the present vacuum condition. The base pressure in the test operation was $\sim 8 \times 10^{-8}$ Pa without an electron beam. However, the pressure increased as the electron beam current increased; finally it reached $\sim 7 \times 10^{-7}$ Pa with a 50 mA electron beam. We consider that higher charge states can be extracted after the vacuum condition is improved. In addition, it is noted that the present operation has been performed only in the DC mode, where ions with sufficient energy to pass over the well potential are accelerated. It is expected that the yield of ions with higher charge states will increase in the pulsed mode,[4] where the trapped ions are forcibly extracted by instantaneously reducing the well potential.

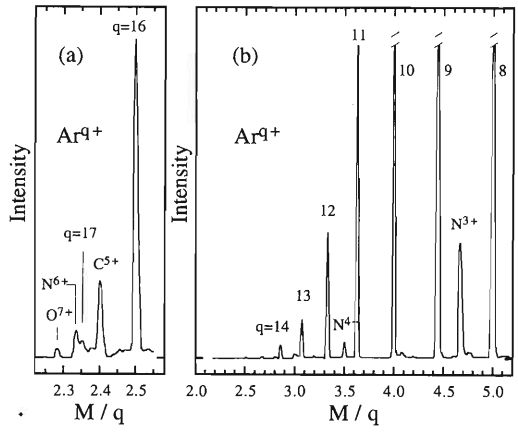

Fig. 1. Typical charge spectra of argon ions extracted from the present EBIS with electron beam parameters of (a) 11 keV–40 mA and (b) 7.5 keV–30 mA.

References

1) A. Endo et al.: RIKEN Accel. Prog. Rep. **34**, 116 (2001); Nucl. Instrum. Methods Phys. Res. B, in press (2003).
2) M. Morita et al.: Physica C **235/240**, 209 (1994).
3) T. Oka et al.: Physica C **335**, 101 (2000).
4) H. Shimizu et al.: Rev. Sci. Instrum. **71**, 681 (2000).

* Graduate School of Arts and Sciences, University of Tokyo

3. Radiochemistry and Nuclear Chemistry

In-beam Mössbauer spectroscopy of ^{57}Fe(← ^{57}Mn) implanted into graphite

Y. Kobayashi, M. K. Kubo,[*1] Y. Yamada,[*2] T. Saito,[*2] J. Murata, W. Sato, H. Watanabe, A. Yoshimi, D. Kameda,[*3] H. Miyoshi,[*3] K. Shimada,[*3] and H. Ueno

Graphite and its intercalation compounds have been of interest since 1960s, because of their characteristic physicochemical properties of displaying high electrical conductivity and high crystal anisotropy originating from their two-dimensional layered structure. However, graphite doped with transition metals have not yet been thoroughly studied, as compared with graphite doped with alkali and alkaline-earth metals, acids, halogens, and metal chlorides. The reason for this is that it is difficult to insert transition metals without forming ligands into an interlayer space by conventional chemical procedures. We have applied the in-beam Mössbauer technique using a ^{57}Mn beam to a sample of highly oriented pyrolytic graphite (HOPG), in order to elucidate the final lattice position of the implanted atoms and their dynamic jumping behavior between the two-dimensional layers in the graphite structure. The synthetic HOPG is characterized crystallographically as a graphite having c-axis angular spread of a few tenths of a degree and a randomly-oriented a-axis on the c-plane. However, since most properties of interest in graphite are isotropic within the hexagonal plane, HOPG is a very good substitute for the graphite single crystal. Recently, graphite crystals have been reconsidered again as an attractive material from the viewpoint of the anomalous magnetoresistance at low-temperature and the low-dimensional magnetism. The methods of the ion implantation Mössbauer spectroscopy is also thought to be effective for the study of the magnetic behavior described above.

^{57}Mn particles were produced as a RI beam following the nuclear projectile fragmentation of a ^{59}Co beam ($E = 80A$MeV) with a Be target using RIPS, and subsequently implanted into a sample of HOPG.[1,2] An in-beam ^{57}Fe(← ^{57}Mn) Mössbauer spectrum of HOPG obtained at 25 K is shown in Fig. 1. The total measuring time was 50 hr. The quality of the spectrum is still insufficient for detailed analysis because of the low intensity of the ^{59}Co primary beam. However, the resonance lines can be seen around −1 mm/s and small components corresponding to hyperfine magnetic splitting are observed.

For comparison, our previous data of the ^{57}Fe implantation into HOPG, which were obtained by the in-beam technique combined with the Coulomb excitation and recoil implantation at the VICKSI Accelerator in Hahn-Meitner-Institut-Berlin, are shown in Fig. 2.[3] The experimental parameters (implantation energy, stopping range, implantation dose, and the time scale for measurement after implantation) in the ^{57}Mn implantation experiment are much different from those of the Coulomb excited ^{57}Fe implantation. Nevertheless, the overall shape of ^{57}Fe(← ^{57}Mn) Mössbauer spectrum at 25 K seems to be almost similar to that of Coulomb excited implantation.

Detailed discussion on the observations by two different in-beam measurements will be reported elsewhere.

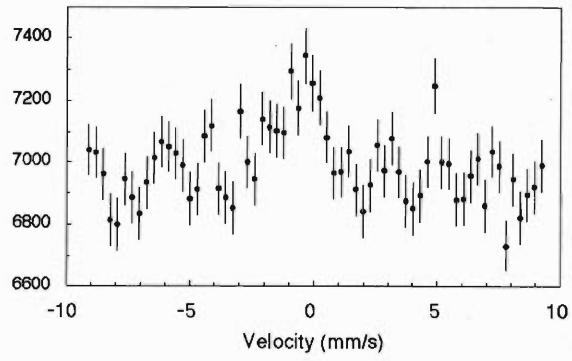

Fig. 1. In-beam Mössbauer spectrum of ^{57}Fe(← ^{57}Mn) implanted into HOPG at 25 K.

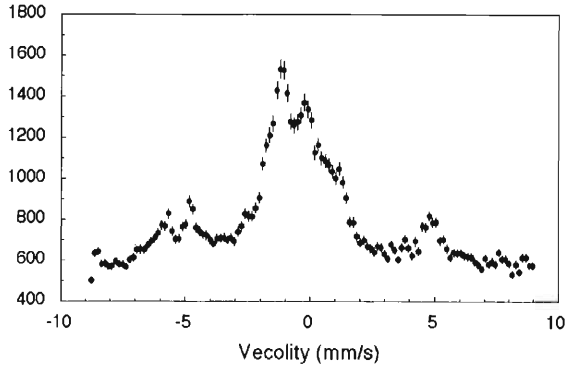

Fig. 2. In-beam Mössbauer spectrum of Coulomb excited ^{57}Fe implanted into HOPG at 13 K.[3]

References

1) Y. Kobayashi et al.: J. Radiochem. Nucl. Chem., **255**, 403 (2003).
2) Y. Kobayashi et al.: Euro. Phys. J. A **13**, 243 (2002).
3) Y. Kobayashi et al.: unpublished data (1997).

*1 International Christian University
*2 Department of Chemistry, Tokyo University of Science
*3 Tokyo Institute of Technology

Cadmium-resistant cells exhibit cross-resistance to manganese

T. Yanagiya and S. Enomoto

Environmental contamination by cadmium (Cd) is a serious problem because Cd has adverse effects on organisms. Metallothionein (MT) plays an important role in Cd detoxification.[1] Almost all Cd-resistant cell lines so far reported showed an increased amount of the cellular MT protein. Recently, we have established a Cd-resistant MT-null cell line (Cd-rB5), and found that its uptake rate of Cd was significantly reduced. Kinetic analysis revealed that Cd is taken up in cells partly through a high-affinity transport system for Mn, and that suppression of this pathway is one of the determinants of reduced susceptibility to Cd in Cd-rB5 cells.[2,3] Thus, to investigate whether the alterations of Cd and Mn transport are also observed in Cd-resistant cells that express MT-I and -II genes, we developed Cd-resistant cell lines (Cd-rA+ and Cd-rC+) from SV40-transformed embryonic fibroblasts derived from C57Bl/6 mice.

Cd-rA+ and Cd-rC+ cells exhibited a significant resistance to Cd compared with their parental cells as determined by MTT assay.[1,2] Although the IC_{50} value of Cd for parental cells was approximately 20 μM, the survival rates of Cd-resistant cells exposed to 100 μM $CdCl_2$ for 48 hr were more than 70–80% (data not shown). To investigate the determinants of tolerance to Cd in Cd-rA+ and Cd-rC+ cells, intracellular concentrations of MT were measured. The basal levels of cellular MT in Cd-rA+ and Cd-rC+ cells were 7.7- and 6.1-fold higher than those in parental cells, respectively. Then, we examined the sensitivity of Cd-rA+ and Cd-rC+ cells to $ZnCl_2$, $CuCl_2$ and $HgCl_2$. Although the concentrations of MT in Cd-rA+ and Cd-rC+ cells were significantly higher than those in their parental cells, Cd-rA+ and Cd-rC+ cells did not show any increase in resistance to these heavy metals (data not shown). These results suggest that the determinants of Cd resistance in Cd-rA+ and Cd-rC+ cells may be specific to Cd cytotoxicity.

Thus, we examined the accumulation of Cd and Mn in Cd-rA+ and Cd-rC+ cells after exposure to 0.03, 0.3, 3 or 10 μM $CdCl_2$ or $MnCl_2$ for 24 hr. As shown in Fig. 1 A, the accumulation of Cd in these cells was about 50% of that in parental cells. On the other hand, the accumulation of Mn in these cells was about 30% of that in parental cells (Fig. 1 B).

Since Cd-rA+ and Cd-rC+ cells exhibited a lowered accumulation of Mn, we examined the sensitivity of Cd-rA+ and Cd-rC+ cells to Mn by MTT assay. As shown in Fig. 2, Cd-rA+ and Cd-rC+ cells showed a significant resistance to Mn compared with parental cells. The IC_{50} values of Mn for Cd-rA+ and Cd-rC+ cells were 7.0- and 7.6-fold higher than that for parental cells, respectively.

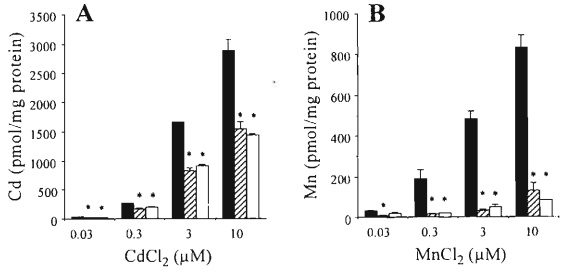

Fig. 1. Accumulation of Cd and Mn in Cd-resistant and parental cells. Cd-A+ (hatched columns), Cd-rC+ (open columns) and parental cells (closed columns) were exposed to 0.03, 0.3, 3 or 10 μM [^{109}Cd]-$CdCl_2$ (A) or [^{54}Mn]-$MnCl_2$ (B) for 24 hr. * Significantly different from parental cells ($p < 0.01$).

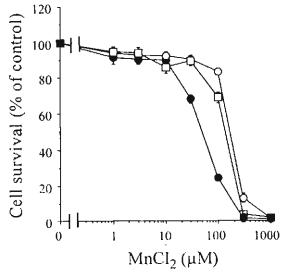

Fig. 2. Sensitivity of Cd-resistant and parental cells to $MnCl_2$. Cd-A+ (open circles), Cd-rC+ (open squares) and parental cells (closed circles) were exposed to various concentrations of $MnCl_2$ for 48 hr, and then the survival rates were estimated by MTT assay.

In this study, we showed that Cd-resistant cells that express the MT-I and II genes exhibit a reduced accumulation of Cd. These results suggest that the reduced accumulation of Cd may be a major factor involved in the tolerance of Cd-rA+ and Cd-rC+ to Cd. Additionally, Cd-rA+ and Cd-rC+ cell lines exhibited a lowered accumulation of Mn, suggesting that an increased resistance of Cd-rA+ and Cd-rC+ cells to Mn may be due to the reduced amount of Mn incorporated. Previously, we showed that the transport system for Mn may be used for the uptake of Cd in a Cd-resistant MT-null cell line, Cd-rB5 cells. Our findings in this study strongly suggest that there may be a relationship between transport of Cd and Mn. Further studies are needed to elucidate the mechanism of Cd and Mn transport.

References

1) Y. Kondo et al.: Life Sci. **64**, PL145 (1999).
2) T. Yanagiya et al.: Life Sci. **65**, PL177 (1999).
3) T. Yanagiya et al.: J. Pharmacol. Exp. Therap. **292**, 1080 (2000).

Investigation of intracellular kinetics of copper in HepG2 cell line

A. Nakayama, H. Haba, R. Hirunuma, and S. Enomoto

Copper is an essential redox active metal that serves as a cofactor in various enzymes such as cytochrome c oxidase, Cu, Zn superoxide dismutase, ceruloplasmin, and lysyl oxidase.[1] An excess of copper, however, induces cytotoxity due to its proclivity to participate in Fenton-like reactions that leads to the generation of highly reactive hydroxyl radicals.[2] It has been reported that copper stimulates proliferation and migration of human endothelial cells,[3] and also development of human cancer.[4]

Recently, it has been reported that organisms have developed sophisticated mechanisms of maintaining the balance between essential and toxic copper levels. Studies of copper uptake mechanism in human cells have shown that copper is transported by two-high affinity copper transport proteins, Ctr1 and Ctr3. Within cells, copper is distributed to specific subcellular components or proteins by copper chaperones that include Hah1, which delivers copper to ceruloplasmin, Cox17, which in turn delivers copper to mitochondrial cytochrome c oxidase, and CCS, which inserts copper into Cu, Zn superoxide dismutase.[5]

However, the molecular mechanisms underlying the alteration of intracellular copper distribution in diseased cells are poorly understood, because the utilization of radioactive copper isotope is generally difficult. Thus, we attempted to produce the ^{67}Cu which has the longest half-life ($t_{1/2} = 61.7$ hr) among the radioactive copper isotopes and to investigate the intracellular copper kinetics using ^{67}Cu.

^{67}Cu was introduced via the ^{70}Zn(p, α) reaction according to the method which was reported by D. J. Jamriska *et al.*[6] In brief, an enriched ^{70}Zn target (80%) was irradiated with 0.96 μA of a proton beam (proton energy: 12.8 MeV) for 1 hour and ^{67}Cu was separated from the unreacted target material and by-products, ^{67}Ga and ^{56}Co, by anion-exchange chromatography. The γ-ray spectrum is shown in Fig. 1. The resulting solution containing ^{67}Cu was heated to dryness and stocked until use. The dried ^{67}Cu was completely dissolved in a small amount of 1 M HCl, and diluted with Dulbecco's modified Eagle's medium (DMEM) supplemented with fetal bovine serum (FBS) at the time of use.

We used the human hepatocellular carcinoma cell line, HepG2, to investigate the kinetics of intracellular copper, because the characteristics of HepG2 cells has been well investigated. HepG2 cells were grown in

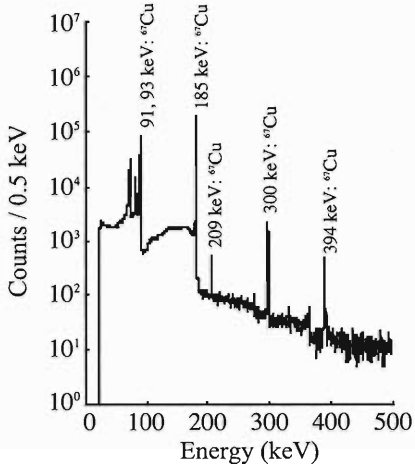

Fig. 1. γ-ray spectrum of refined tracer solution.

DMEM supplemented with 10% FBS. Then, 100 kBq of ^{67}Cu was added to the medium and the cells were incubated for 12 hours. After incubation, the cells were disrupted with lysis buffer (20 mM EDTA, 100 mM NaCl, and 1% SDS in 50 mM Tris-HCl buffer, pH 7.5) to obtain cytosols. The cytosols were analyzed by two-dimensional polyacrylamide gel electrophoresis (2D-PAGE) to evaluate the intracellular kinetics of copper. By this method, the proteins are quickly separated with a high resolution based on the isoelectric point and molecular mass. The radioactive copper was detected using a bioimaging analyzer BAS-2500 (Fuji Photo Film Co., Ltd, Japan).

Although useful information is not obtained at present, it is expected to obtain important information regarding copper cytotoxicity as well as the development and progression of cancer in the near future.

References

1) M. C. Linder: *Biochemistry of Copper* (Plenum Press, New York, 1991).
2) B. Halliwell and J. M. C. Gutteridge: Biochem. J. **219**, 1 (1984).
3) G. F. Hu: J. Cell. Biochem. **69**, 326 (1998).
4) A. Nakayama et al.: J. Trace Elem. Exp. Med. **15**, 31 (2002).
5) M. Marjorette et al.: J. Biol. Chem. **275**, 33244 (2000).
6) D. J. Jamriska et al.: J. Radioanal. Nucl. Chem. **195**, 263 (1995).

Affinity of trace elements to metal binding proteins in livers of Zn-deficient mice

T. Ohyama,[*1] T. Ogi,[*1] M. Yanaga,[*1] M. Noguchi,[*2] H. Suganuma,[*1] K. Ishikawa,[*2]
R. Hirunuma, and S. Enomoto

Zinc is a very important element for human health. More than 300 different enzymes in the body depend on Zn to work properly. This element concerns maintaining the immune system, synthesizing various hormones and so on.

Previously, we determined the concentrations of Zn and other trace elements, such as Mn, Fe, and Co, in various organs and tissues of mice fed with a Zn-deficient diet for adequate periods.[1] Their concentrations were different from those for mice raised under normal conditions. Furthermore, we examined in which fraction of the liver, that has important functions for protein syntheses, such variations in concentrations of trace elements would be recognized, and found the main variation in the supernatant fraction.[2] In the present work, we attempted to locate the Zn binding proteins which induce the variation of concentrations of trace elements under the Zn-deficient condition, and then, to analyze the affinity between the trace elements and those proteins, because Zn and other trace elements are bound to various proteins and cause them to possess different physiological functions in living organisms.

Eight-week old male mice of ICR strain were divided into two groups; one group was fed with a Zn-deficient diet and distilled water (Zn-def. mice), and the other group was fed with a control diet and distilled water (control mice). After 3 weeks of this treatment, their livers were removed and separated into two fractions, supernatant fraction (cytosol) and other fraction, by means of ultracentrifugation. Then, the cytosol was divided into 40 fractions (2 ml per a fraction) by gel filtration chromatography (Sephadex G-100) using Tris-HCl buffer (pH 7.4) as eluent at a flow rate of 10 ml/h. Concentrations of trace elements and protein amounts in each fraction were determined by ICP-MS and the BCA protein assay method, respectively. Assuming the high value of Zn concentration/protein amount ratio indicates the existence of protein which has a great affinity to Zn, 13, 15, 16, and 28th fractions were chosen and used in the following experiments. Affinities between trace elements and proteins existing in those fractions were examined by multitracer techniques. The solutions of the fractions were poured into centrifugal filter tubes, YM-3, which were purchased from Millipore Co., and a multitracer solution (10 μl per each tube) was added. Then, these tubes were centrifuged at 2500g for 240 min. Radioactivities in these samples were measured by HP Ge detectors. Radioactivities detected from filters indicate binding amounts and those from filtrates denote liberating amounts.

In the present experiment, the distribution of seven elements (Na, Mn, Fe, Co, Zn, Se, and Rb) was analyzed. The results for 15 and 16th fractions are summarized in Fig. 1. Zinc was completely bound to some proteins or other materials in the 15 and 16th fractions of both Zn-deficient and control mice. In the Zn-deficient mice, values of Mn and Co binding amounts in 15 and 16th fractions increased from 30 to 40% and 60 to 70% in comparison with control mice, respectively. This may suggest the existence of proteins which have a great affinity to Mn and/or Co in these fractions under the Zn-deficient condition.

As future work, we will once again perform this experiment in order to confirm the reproducibility.

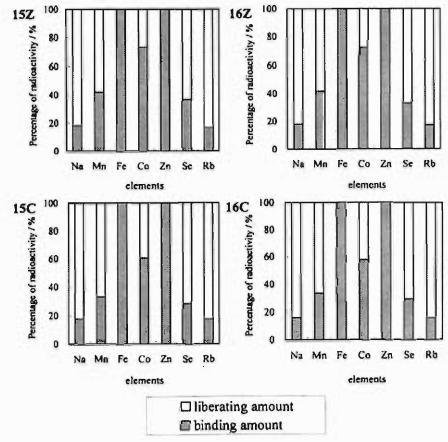

Fig. 1. Affinity between trace elements and proteins in fractions of Zn-deficient mice. (15z and 16z) and control mice (15c and 16c).

References

1) M. Yanaga et al.: J. Radioanal. Nucl. Chem. **231**, 187 (1998); J. Radioanal. Nucl. Chem. **243**, 661 (2000); J. Radioanal. Nucl. Chem. **245**, 255 (2000).
2) T. Ohyama et al.: Proc. Int. Symp. Bio-Trace Elem., Wako and Yamanashi, 2002-10~11, to be published (2003).

*1 Radiochemistry Research Laboratory, Faculty of Science, Shizuoka University
*2 Department of Biology and Geosciences, Faculty of Science, Shizuoka University

Multitracer screening in trace element delivery method: High rubidium uptake in mouse brain by intranasal administration†

Y. Kanayama,* T. Tsuji,* S. Enomoto, and R. Amano*

Tissue uptake of metal is closely related to the metal delivery means. To identify a new delivery system to the brain, our multitracer technique which enables a simultaneous tracing of various elements and their accurate comparisons was applied to the screening study of tracer uptake behaviors in the blood, plasma and brain of normal mice following administration by eight different means.

A radioactive multitracer (MT) solution was obtained from a Ag target irradiated with a ^{14}N beam of 135 MeV/nucleon accelerated in the RIKEN Ring Cyclotron, and was prepared as a physiological saline solution. The MT solution contained 18 radionuclides of 16 elements which are ^{7}Be, ^{46}Sc, ^{48}V, ^{51}Cr, ^{54}Mn, ^{56}Co, ^{58}Co, ^{59}Fe, ^{65}Zn, ^{74}As, ^{75}Se, ^{83}Rb, ^{84}Rb, ^{85}Sr, ^{95m}Tc, ^{88}Y, ^{88}Zr, and ^{103}Ru. Eighty-four 8-week-old ICR mice were administered an appropriate volume of the MT solution. Eight administration methods are listed as follows; intravenous injection (IV), intraperitoneal injection, intranasal administration (IN), intramuscular injection, subcutaneous injection, intracutaneous injection, percutaneous administration, and peroral administration (PO). All animals were sacrificed under ether anesthesia at several appropriate time intervals within 24 hours of each administration. After their blood was collected, the mice were transcardially perfused and then each brain was excised. Plasma samples were centrifugally separated from a half volume of the blood. The radionuclides and activities in the blood, plasma and brain were measured by γ-ray spectrometry using pure Ge detectors. The uptake behaviors were assessed in terms of the administered dose per wet weight (%dose/g).

Figure 1 shows typical simultaneous uptake rates within the 24 hours following the administrations of MT. Because of various patterns of the ^{54}Mn uptakes, it was apparent that the ^{54}Mn delivery manner is susceptible to administration routes. Among the six methods excepting the IV and PO methods, there were no differences in the brain uptake rates of ^{59}Fe. Concerning the brain uptake rates of ^{65}Zn and ^{75}Se, their delivery manners seem to have two patterns, *i.e.*, a fast accumulation pattern and a slow one, respectively. A difference between these two patterns may be due to the delivery route to the brain, that is, it depends on whether the tracers enter into the bloodstream directly or not.

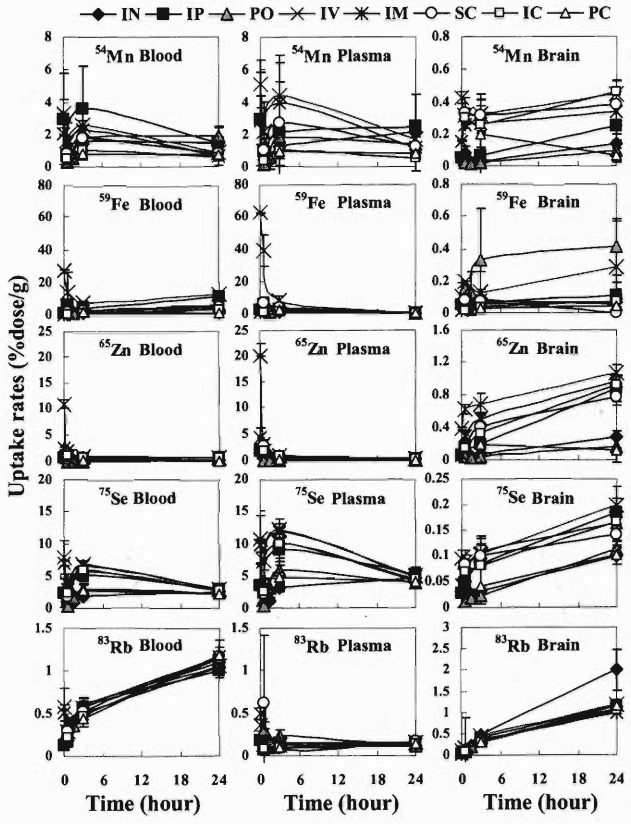

Fig. 1. Typical uptake rates of multitracer following administration by eight different methods. Abbreviations; IN: intravenous administration; IP: intraperitoneal injection; PO: peroral administration; IV: intravenous injection; IM: intramuscular injection; SC: subcutaneous injection; IC: intracutaneous injection; PC: percutaneous administration.

The ^{83}Rb uptake shows an anomalous behavior. Although there were no significant differences among the uptake rates of the blood and the plasma for all eight methods, the uptake rates in the brain for the IN method were approximately two times higher than those for the other seven methods. In addition, the ^{83}Rb uptake rates in the brain are the highest among those of all tracers for the IN method. This anomalous ^{83}Rb behavior may be related to the direct delivery pathway to the brain *via* nose.

In conclusion, the multitracer screening gives us a better understanding of the simultaneous delivery behavior of the 16 trace elements delivered by eight administration methods, and indicates the new discovery of a Rb delivery system to the brain which circumvents the systemic circulation.

† This report was presented at the 6th Conf. of the Int. Soc. for Trace Element Research in Humans (ISTERH), Quebec, Canada 2002-9

* School of Health Sciences, Faculty of Medicine, Kanazawa University

Tracer uptake behavior of manganese and other metals in the fetal, suckling and developing mice

T. Tsuji,* Y. Kanayama,* R. Hirunuma, S. Enomoto, and R. Amano*

Manganese (Mn) is an essential trace element in our life. In order to gain a better understanding the biological function and behavior of Mn, the tracer uptake behavior of Mn *in vivo* (in the brain and other organs of fetal, suckling and developing mice) has been studied using the multitracer technique (MT).[1] It yielded some useful information on Mn during developmental periods.

CD-1 mice were used in this experiment. Regarding the experiment concerning fetuses and suckling mice, the MT solution (0.1 ml) was injected intravenously (i.v.) into the 16-day-pregnant dams *via* tail. Forty-eight hours after injection, the dams were excised and maternal blood, placentas, fetuses and amniotic fluids were collected. The nine organs (parietal bone, brain, cardiac muscle, lung, thymus, liver, pancreas, spleen and kidneys) were collected from each fetus ($n = 3$). The MT transfer from dam to pups was studied using some 2 days suckling mice after birth. Nine organs were excised from each pup and endogastric milk was collected ($n = 3$). In order to examine the retention of MT in fetuses, one MT-injected radioactive pregnant mouse was used, and then after the birth the Radioactive-dam was exchanged for another non-radioactive-dam. Radioactive pups were bred by the non-radioactive-dam, and at the pup-ages of 1, 3, 6, 15 and 28 days, four organs (parietal bone, brain, liver and blood) were collected from each pup ($n = 3$). All samples were weighed immediately and freeze dried. The radioactivity of each dried sample was determined by γ-ray spectrometry using high-purity Ge detectors. The uptake behavior was evaluated in terms of the uptake percentage of the injected multitracer (%).

The results indicate that 8% Mn of the injected dose was transported to the fetuses *via* placenta from the maternal body. Figure 1 shows that the ^{54}Mn uptake levels in all organs of fetuses except brain were almost the same as those of suckling mice. The uptake rate of Mn in the organs was in the following order (except parietal bone, cardiac muscle and lung); liver > brain > thymus > kidneys > pancreas > spleen. A large amount of ^{54}Mn was, however, presented in the endogastric milk. Figure 2 shows the comparison of the retention percentages of ^{54}Mn and ^{65}Zn in some

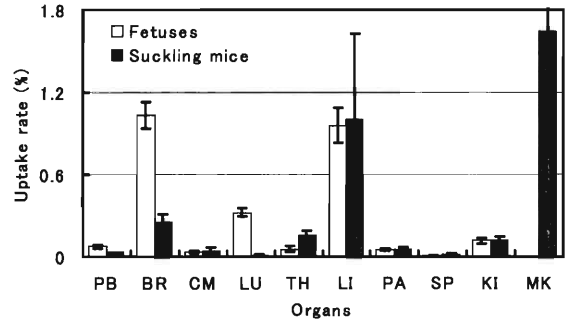

Fig. 1. Uptake of ^{54}Mn in the fetuses and suckling mice. (PB: parietal bone, BR: brain, CM: cardiac muscle, LU: lung, TH: thymus, LI: liver, PA: pancreas, SP: spleen, KI: kidneys and MK: endogastric milk.) Each mouse had 13 fetuses and suckling mice on average.

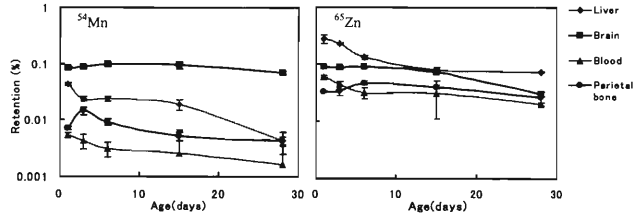

Fig. 2. Retention of ^{54}Mn and ^{65}Zn in parietal bone, brain, liver and blood of developing mice.

organs of developing mice. The ^{54}Mn was retained in the brain for 4 weeks after birth, whereas it was gradually decreased in the liver, parietal bone and blood. It is worth mentioning that the ^{54}Mn retention behavior is unique in the brain; the fetal retained-Mn remains there after birth and it redistributes heterogeneously in the brain. In conclusion, the multitracer technique gave some better understanding of the Mn distribution and its role in the developing brain.

References

1) T. Tsuji et al.: RIKEN Accel. Prog. Rep. **35**, 114 (2002).

* School of Health Sciences, Faculty of Medicine, Kanazawa University

Uptake of trace elements in cataractous rat lens

T. Nabekura,* T. Minami,* R. Hirunuma, S. Enomoto, and Y. Ito*

Transparency is a notable and unique characteristic of the lens, and is a basic prerequisite for normal visual acuity. Lens transparency relies on the cellular structure, protein structure and constitution, and electrolyte concentration. The UPL rat is a new dominant hereditary cataract model derived from Sprague-Dawley rats.[1] Mature cataracts are observed in a comparatively short time with an incidence of 100%.

Metals are known to act as activators and/or inhibitors of various enzyme reactions. However, the role of trace elements in lenses is not yet fully investigated. The multitracer technique was established at RIKEN and has been successfully applied to many biological systems for comparing the behavior of a number of elements under strictly identical experimental conditions. In the present study, the multitracer technique was applied to the determination of the uptake of trace elements in the lenses of normal and UPL cataract rats.

The radioactive multitracer solution was prepared from a silver foil irradiated with a ^{14}N beam of 135 MeV/nucleon from the RIKEN Ring Cyclotron. Lenses of normal and UPL rats were cultured in phosphate-buffered saline containing multitracers at 37°C under 5% CO_2/95% air atmosphere.[2] The radioactivities were determined by γ-ray spectrometry using a pure germanium detector.

Table 1 shows the uptake of trace elements in normal and UPL rat lenses exposed to multitracers for 24 hr. As, Be, Co, Cr, Fe, Mn, Na, Rb, Rh, Ru, Sc, Se, Sr, Tc, V, Y, Zn and Zr were detected in 24-hr-cultured lenses of normal and UPL cataract rats. However, the uptake rates of trace elements in the lens differed among the elements and between the normal and cataractous lenses. The uptakes of Sr and V were comparable in the lenses of normal and UPL rats. On the other hand, the uptakes of Co, Mn and Zn in UPL rat lenses were higher than those in normal rat lenses. The uptake of Zn was highest in normal rat lenses in comparison with the other trace elements. However, the uptake of Se was highest in the lenses of UPL cataract rats. In addition, the difference in Se uptake between the normal and cataractous lenses was greatest among the tested trace elements. Se is known to function as a cofactor of glutathione peroxidase and selenoproteins and is known to be essential for the protective mechanism against radical oxygen species. However, selenite is a strong sulfydryl oxidant and selenite-induced cataracts are widely used because they are a good model for other cataracts caused by oxidative stress. High concentrations of Se might have toxicity effects on lenses and Se participates in cataract development in UPL rats. Further studies are needed to reveal the mechanism for the increased accumulation of Se in UPL rat lenses.

Table 1. Uptake of trace elements in normal and UPL cataract rat lenses.

Element	Normal rat lens (%/mg lens)	UPL rat lens (%/mg lens)
As	0.01680 ± 0.0012	0.02257 ± 0.0012
Be	0.03453 ± 0.0047	0.05241 ± 0.0034
Co	0.01889 ± 0.0015	0.07885 ± 0.0045
Cr	0.03631 ± 0.0050	0.05645 ± 0.0045
Fe	0.04061 ± 0.0054	0.06120 ± 0.0058
Mn	0.02661 ± 0.0014	0.04283 ± 0.0014
Na	0.01395 ± 0.0007	0.01425 ± 0.0012
Rb	0.01298 ± 0.0002	0.01778 ± 0.0007
Rh	0.02507 ± 0.0016	0.05397 ± 0.0013
Ru	0.04953 ± 0.0043	0.06753 ± 0.0020
Sc	0.04231 ± 0.0065	0.06142 ± 0.0055
Se	0.01444 ± 0.0012	0.10617 ± 0.0044
Sr	0.02727 ± 0.0018	0.02445 ± 0.0005
Tc	0.02821 ± 0.0006	0.03107 ± 0.0005
V	0.04546 ± 0.0031	0.04172 ± 0.0021
Y	0.04080 ± 0.0062	0.05987 ± 0.0054
Zn	0.07126 ± 0.0060	0.09742 ± 0.0076
Zr	0.04426 ± 0.0071	0.06372 ± 0.0066

Lenses of normal and UPL rats were exposed to a multitracer for 24 hr. Data represent mean ± S.E. of five determinations.

References

1) T. Nabekura et al.: Curr. Eye Res. **22**, 446 (2001).
2) T. Nabekura et al.: Toxicology **163**, 101 (2001).

* Kinki University

Multitracer study on the intestinal absorption of various trace elements: Effect of NaFeEDTA as a food fortificant

K. Igarashi, R. Hirunuma, S. Enomoto, and S. Kimura*

Iron deficiency is the major nutritional problem in developing countries, primarily affecting women of childbearing age, children and infants. The main causative factor is the poor absorption of iron from their foodstuffs. Staple foods such as grains, vegetables and legumes contain non-heme iron, which has a low intestinal absorption efficiency compared with heme iron. Furthermore, the staple foods also contain inhibitors of iron absorption such as phytic acid and polyphenols. Since the inhibitors bind to non-heme iron, the bioavailability of iron is extremely low. Food fortification is generally considered to be a beneficial long-term strategy for improving iron deficiency in developing countries.[1] Sodium iron ethylenediaminetetra-acetic acid (NaFeEDTA) as a fortificant has been recommended for food fortification programs. NaFeEDTA causes fewer organoleptic problems than most other fortificants and its relative bioavailability appears to be greater in food with a high content of inhibitors.[2] On the other hand, it is possible that EDTA may bind to metals other than iron and influence their absorption because of its strong chelating property.

In this study, to investigate the effect of NaFeEDTA on the intestinal absorption of trace elements, we determined the uptake rates of various trace elements into the serosal site of everted intestinal segments of rats using a multitracer technique. We further determined the effect of tannic acid, a polyphenol, on the incorporation of trace elements.

We modified the methods described by Schümann *et al.* and Yoshida *et al.*[3,4] Seven-week-old male Wistar rats were fasted overnight and then their abdomen was opened under anesthesia. The duodenum, jejunum and ileum (6 cm long each) were removed and everted. The segments were filled with 0.6 ml of a buffer (pH 7.2), and then immersed in 10 ml of a buffer containing an Ag-derived multitracer solution, and NaFeEDTA or ferrous sulfate ($FeSO_4$) as a control. The segments were incubated with bubbling 95% O_2 and 5% CO_2 at 37°C for 1 h. After incubation, the solution in the serosal site was collected. The samples were placed in a Ge-detector, and the radioactivities of the multitracers were measured.

Table 1. The incorporation of various trace elements into serosal site of everted intestinal segments of rats.

		NaFeEDTA[1]	$FeSO_4$[1]	NaFeEDTA+TA[2]	$FeSO_4$+TA[2]
V	Duodenum	0.067±0.025	0.028±0.024	0.033±0.025	0.036±0.026
	Jejunum	0.028±0.028	0.026±0.011	0.143±0.086	0.028±0.019
	Ileum	0.099±0.099	0.023±0.011	0.082±0.066	0.005±0.005
Co	Duodenum	0.099±0.006	0.249±0.049[a]	0.082±0.005[b]	0.137±0.010[ab]
	Jejunum	0.135±0.004	0.146±0.032	0.121±0.009[a]	0.072±0.004[b]
	Ileum	0.214±0.028[a]	0.088±0.021	0.193±0.024[a]	0.056±0.003
Zn	Duodenum	0.046±0.004	0.026±0.006	0.043±0.003[a]	0.012±0.004
	Jejunum	0.094±0.006[a]	0.020±0.003	0.087±0.007[a]	0.006±0.002[b]
	Ileum	0.178±0.031[a]	0.037±0.015	0.154±0.019[a]	0.006±0.003
As	Duodenum	0.023±0.014	0.154±0.031[a]	0.024±0.015	0.089±0.011[a]
	Jejunum	0.027±0.014	0.176±0.024[a]	0.061±0.021	0.136±0.017[a]
	Ileum	0.086±0.030	0.218±0.026[a]	0.146±0.033	0.194±0.029
Se	Duodenum	0.087±0.011	0.063±0.008	0.078±0.005	0.072±0.006
	Jejunum	0.156±0.014	0.139±0.015	0.137±0.009	0.133±0.016
	Ileum	0.481±0.132	0.498±0.118	0.581±0.105	0.333±0.043

[1] The segments were incubated with buffer containing multitracer solution, and NaFeEDTA or $FeSO_4$.

[2] The segments were incubated with buffer containing multitracer solution, and NaFeEDTA or $FeSO_4$ with tannic acid.

[a] Significant differences were observed between NaFeEDTA- and $FeSO_4$-incubated segments ($P < 0.05$).

[b] Significantly different from the value obtained in the absence of tannic acid ($P < 0.05$).

* Graduate School of Human Life Sciences, Showa Women's University

Table 1 shows the incorporation of various trace elements into the serosal site of everted intestinal segments of rats. The Zn uptake rates in NaFeEDTA-incubated segments were higher than those in $FeSO_4$-incubated segments, suggesting that the intestinal absorption of Zn in the buffer containing NaFeEDTA is higher than that in the buffer containing $FeSO_4$. Although NaFeEDTA increased the uptake rate of Co into the serosal site of ileum, the uptake rate of Co into the NaFeEDTA-incubated segment of the duodenum was lower than that in the $FeSO_4$-incubated segment. No significant difference in Se and V uptake rates was observed between NaFeEDTA- and $FeSO_4$-incubated segments, suggesting that NaFeEDTA does not influence the intestinal absorption of Se and V. The uptake rates of As in NaFeEDTA-incubated segments were lower than those in $FeSO_4$-incubated segments. This result suggests that NaFeEDTA reduces the incorporation of As into the serosal site of everted intestinal segments. It is possible that NaFeEDTA inhibits the intestinal absorption of As only.

However, staple foods in developing countries contains inhibitors of iron absorption. It is important to investigate the effect of interaction between inhibitors and NaFeEDTA on the intestinal absorption of trace elements. Thus, we further determined the effect of tannic acid on the absorption of various trace elements in everted intestinal segments. The inhibitory effect was observed in term of the incorporation of Zn and Co in $FeSO_4$-incubated segments. On the other hand, tannic acid affected the incorporation of Co only in NaFeEDTA-incubated segments, suggesting that the intestinal absorption of various trace elements in the buffer containing NaFeEDTA is negligibly affected by tannic acid compared with that in the buffer containing $FeSO_4$.

The uptake rates of Zn and Co in NaFeEDTA-incubated segments were higher than those in $FeSO_4$-incubated segments. The As uptake rates for NaFeEDTA-incubated segments were lower than those for $FeSO_4$-incubated segments. These results suggest that NaFeEDTA also influences the intestinal absorption of Zn, Co and As in the presence of tannic acid.

In this study, the results demonstrated that NaFeEDTA reduces the incorporation of As only into the serosal site of everted intestinal segments with or without tannic acid, indicating that NaFeEDTA does not affect the intestinal absorption of essential trace elements. The uptake of trace elements in the buffer containing NaFeEDTA was not inhibited by tannic acid, in contrast to that in the buffer containing $FeSO_4$, indicating that NaFeEDTA may protect the intestinal absorption of various trace elements in the presence of inhibitors. Our findings indicate that NaFeEDTA is suitable for use in the iron fortification program in developing countries.

References

1) J. D. Cook and M. Reusser: Am. J. Clin. Nutr. **38**, 648 (1983).
2) T. H. Bothwell: Arch. Latinoam. Nutr. **49**, 23S (1999).
3) K. Schümann, E. Bernd, and F. Wolfgang: Am. J. Physiol. (Gastrointest. Liver Physiol.) **276**, G431 (1999).
4) S. Yoshida, M. Masuda, M. Nakayama, M. Yamasaki, H. Morikawa, R. Hirunuma, and S. Enomoto: RIKEN Rev., No. 35, p. 67 (2001).

Multitracer study on the adsorption of Re and Os on sediments from artificial seawater

M. Ito,* Y. Takahashi,* H. Mouri,* R. Hirunuma, S. Enomoto, and H. Shimizu*

The nuclide ^{187}Re is radioactive and decays to stable ^{187}Os by emission of a β-particle with a half-life of 4.23×10^{10} years. The Re-Os system has been thought to be highly suitable for the dating of iron meteorites and some sulfide minerals as a geochronometer and useful as a geochemical tracer. In oceans, it is well known that Re and Os accumulate in the sediments under anoxic conditions such as black shales, in which Re and Os are strongly correlated with organic carbon.[1] However, their behavior in seawater is not well known and basic laboratory experiments on chemical processes of Re and Os behavior in the marine environment have not been conducted. In this study, the adsorption of Re and Os was examined on sediments from artificial seawater using a multitracer technique.

The nuclides ^{183}Re and ^{185}Os were obtained from a Au target irradiated with ^{12}C or ^{14}N ions by the RIKEN Ring Cyclotron. Both nuclides decay by electron capture, with a half-life of 70 days and 93.6 days, respectively. It is well known that Os is easily oxidized to Os(VIII)O_4 in a weakly oxic condition, which characterized by high volatility. The Au target was dissolved with aqua regia in a closed system and Os was distilled under vacuum from the solution as OsO_4 at 60–90°C for about two hours. Rhenium was extracted from the residue with a cation exchange resin (AG50-WX8). The extracted solution containing ^{183}Re and ^{185}Os was diluted with artificial seawater, and adjusted to pH 8 with a NaOH solution. Rhenium and Os were retained in artificial seawater and not excluded from the aqueous phase. In order to compare the behavior of other ions with Re and Os, some radioisotopes were added to the ^{183}Re and ^{185}Os solution.

In order to understand the chemical property of Re and Os in seawater, we examined the adsorption of Re and Os on several adsorbents such as anion exchange resin (AG1-X8), cation exchange resin (Bio-Rex70), hematite, ferromanganese nodule and Tokyo Bay sediments from artificial seawater at pH 8 (Fig. 1). It is clear that Re and Os are adsorbed on the anion exchange resin to a larger degree than those on the cation exchange resin, which suggests that Re and Os are dissolved as anions in artificial seawater. Recently, it has been observed that mobile Os was partly adsorbed on Fe-oxyhydroxides under oxidative conditions during weathering,[2] which is not the case with Re. In our experiments, Os was partly adsorbed onto hematite, and Re was completely dissolved in artificial seawater under oxidative conditions. This result

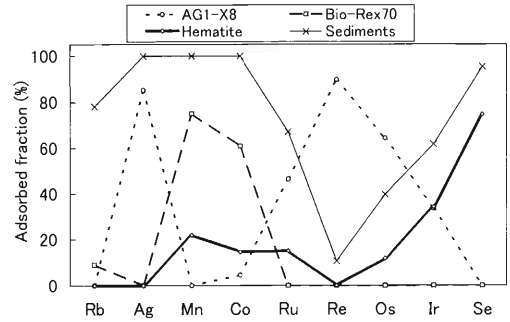

Fig. 1. Adsorbed fraction of Re and Os onto each adsorbent.

is consistent with the significant enrichments of Os in oxic metalliferous marine sediments.[3] In the case of Tokyo Bay sediments, which contain organic carbon (1.85 wt%) to produce anoxic conditions ($Eh < 0$ V), both Re and Os were partly removed from artificial seawater into sediments. In order to consider the interaction between Os and organic matter, humic acid was added to artificial seawater to examine the effect of humic acid on the adsorption of Os on kaolinite (Fig. 2). It is expected that adsorption of metal ion on kaolinite is partly prevented if the ion forms a complex with humic acid. In our experiments, adsorption of Os on kaolinite was promoted, indicating that Os does not form a complex with humic acid. This suggests that adsorption of Os may be promoted by humic acid resulting in anoxic conditions.

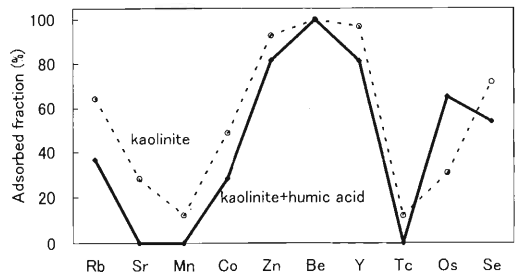

Fig. 2. Adsorbed fraction of Os and other elements onto kaolinite in the presence and absence of humic acid. (kaolinite: 4 g, artificial seawater: 13.5 ml, humic acid (10 g/l): 100 μl).

References

1) G. Ravizza et al.: Geochim. Cosmochim. Acta **55**, 3741 (1991).
2) L. A. Jaffe et al.: Earth Planet. Sci. Lett. **198**, 339 (2002).
3) G. Ravizza et al.: Earth Planet. Sci. Lett. **138**, 105 (1996).

* Department of Earth and Planetary Systems Science, Hiroshima University

Acylpyrazolones with crown ether moiety as intramolecular synergist

S. Umetani,[*1] Y. Komatsu,[*2] H. Yamada,[*3] and S. Enomoto

Macrocyclic ligands such as crown ethers and cryptands have been utilized in metal ion separations. It was shown that macrocyclic ligands can enhance separability when they are added in the aqueous phase as ion-size-selective masking reagents in the extraction of alkali, alkaline earth and lanthanide metal ions with chelate extraction reagents.[1] On the contrary, macrocyclic ligands can work as synergists when they are added in the organic phase. In both cases, unique separability can be expected since the selectivity of the macrocyclic ligands and the chelating reagents is quite different. It can also be expected that the unique extractability is applicable to the separation of multitracers produced by an accelerator.

Novel 4-acyl-5-pyrazolones with the crown ether moiety as the intramolecular synergist (Fig. 1) have been synthesized and solvent extraction of various metal ions is examined. It is expected that the crown ether moiety behaves as the intramolecular synergist and that the selectivity is governed by the acylpyrazolone and the crown ether parts. These ligands are powerful and selective extracting reagents for alkali, alkaline earth and divalent transition metal ions, and selectivity is quite unique depending on the intramolecular synergist.

The synthesis of **1a-b** are described in the literature.[2] **2a-c** were also prepared from 1-phenyl-3-methyl-4-chloroacetyl-5-pyrazolone and commercially available hydroxy crown ethers in a similar manner.

Alkali metal ions were extracted in the order $Li^+ > Na^+ > K^+ > Rb^+ > Cs^+$ with **2a**, that is, Li^+ was extracted in the lowest pH region, $Na^+ > K^+ > Rb^+ > Cs^+ > Li^+$ with **2b** and $K^+ > Na^+ > Rb^+ > Cs^+ > Li^+$ with **2c**. The separability and the extractability with these ligands are notable. It is clear that the crown ether moiety works as an intramolecular synergist. The extraction reaction was found to follow Eq. (1) according to the slope analysis.

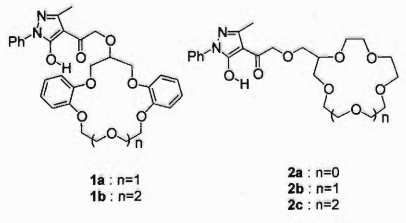

Fig. 1. Acylpyrazolones with crown ether moiety.

$$M^{n+} + nHA_o = MA_{n,o} + nH^+, \quad (1)$$

where M and HA stand for the metal ion and the extraction reagent, and the subscript o denotes the species in the organic phase.

The log K_{ex} values for the extraction of alkali metal ions with **2a-c** are plotted against the log K values which are the formation constants for alkali metal ions with 12-crown-4, 15-crown-5 and 18-crown-6 in methanol measured by conductmetric titration. A fairly good linear relationship was obtained between log K_{ex} and log K values indicating that the extraction selectivity with **2a-c** for the extraction of alkali metal ions is governed primarily by the crown ether moiety depending on the cavity size.

Alkaline earth metal ions were extracted in the order $Mg^{2+} > Ca^{2+} > Sr^{2+} > Ba^{2+}$ with **2a**, $Ca^{2+} > Mg^{2+} > Sr^{2+} > Ba^{2+}$ with **2b** and $Sr^{2+} > Ba^{2+} > Ca^{2+} > Mg^{2+}$ with **2c**. No good linear relationship was obtained unlike the case of alkali metal ions, indicating that the selectivity is governed by both the acylpyrazolone and the crown ether parts.

Divalent transition metal ions were extracted in the order, $Pb^{2+} > Mn^{2+} > Cd^{2+} > Cu^{2+} > Zn^{2+} > Co^{2+} > Ni^{2+}$ with **1a** and $Pb^{2+} > Cu^{2+} > Mn^{2+} > Zn^{2+} > Co^{2+} > Cd^{2+} > Ni^{2+}$ with **1b**. The extraction orders with the present ligands are unique. Among the divalent transition metal ions, an extraordinarily high extractability was observed for Mn^{2+}, Cd^{2+} and Pb^{2+}. It is well known that the extractability for these metal ions is much lower than those for the other divalent transition metal ions with the conventional chelating extractants. The adduct formation constants (β), defined as Eq. (2), were obtained by examining the effect of the benzo-crown ether (L) concentration in the organic phase.

$$MA_{n,o} + L_o = MA_nL_o. \quad (2)$$

The log β values for Mn^{2+}, Cd^{2+} and Pb^{2+} with both benzo-15-crown-5 and benzo-18-crown-6 are considerably larger than those for the other divalent transition metal ions, which cannot be rationalized considering the formation constants (K) as described above. The extraordinarily high extractability of Mn^{2+}, Cd^{2+} and Pb^{2+} is attributable to the specific adduct formation reaction presumably based on the complex structure.

*1 Institute for Chemical Research, Kyoto University
*2 Faculty of Engineering, Kanazawa Institute of Technology
*3 Advanced Materials Laboratory, National Institute for Materials Science

References

1) S. Tsurubou, M. Mizutani, Y. Kadota, T. Yamamoto, S. Umetani, T. Sasaki, Q. T. H. Le, and M. Matsui: Anal. Chem. **67**, 1465 (1995).
2) S. Yamazaki, M. Hanada, Y. Yanase, C. Fukumori, K. Ogura, T. Saeki, and S. Umetani: J. Chem. Soc., Perkin Trans. 1, 693 (1999).

Development of a gas-jet-coupled multitarget system for multitracer production

H. Haba, R. Hirunuma, and S. Enomoto

Since 1991,[1] the RIKEN multitracer technique has been successfully applied to investigations of behavior of various elements in the fields of chemistry, biology, medicine, engineering, and environmental science. Radionuclides of a large number of elements were simultaneously produced from metallic targets such as Ti, Ag, and Au irradiated with a 135 MeV/nucl. ^{14}N (or ^{12}C, ^{16}O) beam from the RIKEN Ring Cyclotron (RRC). After the irradiations, these radionuclides were chemically separated from the target material.[1,2] Thus, carrier-free and salt-free multitracer solutions were applied to various experiments. Recently, a few technical developments for the preparation of the multitracer were reported.[3,4] Takamiya *et al.*[3] produced multitracers using the thermal neutron fission of ^{235}U at the Kyoto University Reactor (KUR). They separated the fission products from the UO_2 target using NaCl as a catcher material. On the other hand, Shibata *et al.*[4] found that the multitracer solution is obtained quickly and easily by amalgamating the Au target irradiated with RRC.

We plan to develop a gas-jet-coupled multitarget system as a novel technique for multitracer production. A schematic of this system is shown in Fig. 1. The 135 MeV/nucl. ^{14}N (or ^{12}C, ^{16}O) beam from RRC passes through 30 multiple targets of about 1 μm thickness with 10 mm spacings. The recoiling multitracers are stopped in He (or Ar) gas, attached to aerosols such as NaCl, KCl, and C, and are continuously transported through a capillary tube to a chemistry room, where the multitracers are collected on a glass filter. Thus, the multitracer solutions are obtained only by washing the filter with a suitable solution. The ^{14}N beam finally enters the thick metallic targets such as Ti, Ag, and Au of about 200 μm thickness. After the irradiation, the long-lived multitracers were chemically separated based on the same procedure as applied previously.[1,2]

Advantages of the gas-jet-coupled multitarget system are as follows. (1) The multitracers are separated from the target material without chemical separation and transported to the chemistry room within a few seconds. Thus, radionuclides with short half-lives of less than 1 minute are available for tracer experiments. (2) The targets with various chemical forms are prepared by electrodeposition or vacuum-evaporation techniques. The composition of the radionuclides in the multitracer can be optimized by changing the target material and its array. (3) The radionuclides of interest are concentrated by using a liquid chromatography apparatus based on ion exchange or solvent extraction. (4) All of the targets are continuously cooled with He gas during the irradiation. Thus, a beam intensity of more than 1 pμA will be acceptable, though the present maximum is approximately 0.1 pμA due to the irradiation in a vacuum chamber.

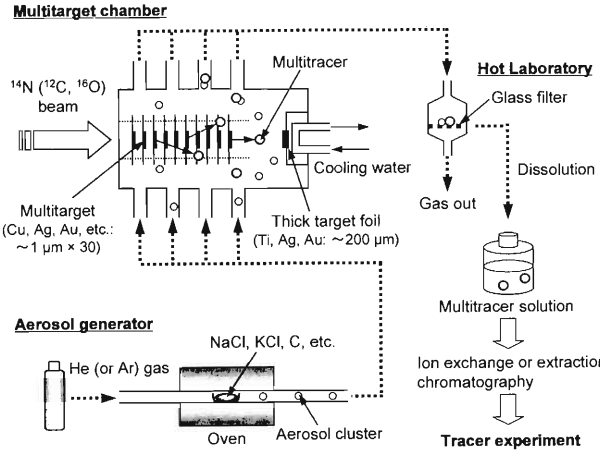

Fig. 1. Schematic of the gas-jet-coupled multitarget system for multitracer production.

References

1) S. Ambe et al.: Chem. Lett. **1991**, 149.
2) S. Ambe: RIKEN Rev., No. 13, 3 (1996).
3) K. Takamiya et al.: RIKEN Rev., No. 35, 107 (2001).
4) S. Shibata et al.: RIKEN Rev., No. 35, 115 (2001).

4. Radiation Chemistry and Radiation Biology

Effects of heavy-ion beams on human lymphoblastoid cells

T. Tsukada, S. Goto,* M. Tomita, S. Morimoto, N. Fukunishi, and F. Yatagai

The tumor suppressor gene *p53*, encodes a nuclear phosphoprotein of 393 amino acids that promotes cell cycle arrest or apoptosis after DNA damage.[1] Mutations or deletions in *p53*, which frequently occur in human cancers, lead to a diminished capacity of malignant lymphocytes to undergo apoptosis in response to ionizing radiation such as X-ray or cytotoxic agents and therefore to enhanced resistance to chemotherapy or radiotherapy. Recently, high-LET (Linear Energy Transfer) radiation has been used as the radiotherapy tool for cancer treatment,[2] but the basic mechanisms of cellular responses after exposure to heavy ion beams are still not well understood.

In this study, we examined the involvement of *p53* in cellular responses after irradiation of heavy ion beams. We used two human B-lymphoblast cell lines derived from the same donor but differing in *p53* status: TK6 (wild-type *p53*), and NH32 (*p53* deficient). Cells were exposed to X rays or to heavy ion beams (C ions: 22 keV/μm, Fe ions: 1000 keV/μm) at doses of 1, 2, 3, 5, 10 Gy (X rays) and 3 Gy (C ions) and 1, 3, 5 Gy (Fe ions). Apoptosis was determined by the externalization of phosphatidylserine that was measured as annexin V positive cells by flow cytometry. 3 Gy is chosen for the comparison of X-ray, C-ion and Fe-ion exposure because the extent of survival ratio measured by colony formation ability is similar at that dose in both TK6 and NH32 (below 10%). X rays induced extensive apoptosis in TK6 (wild-type *p53*) cells, as shown by the formation of hypodiploid particles and the externalization of phosphatidylserine (Fig. 1 (A)), In contrast, cell death was triggered at a significantly

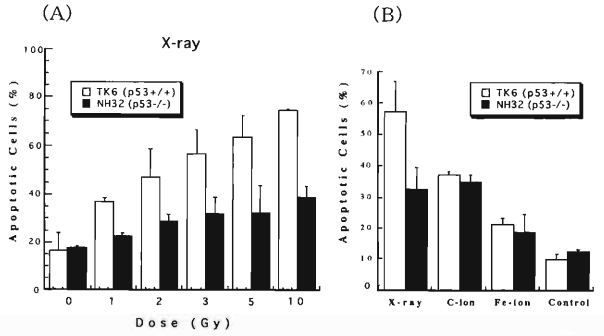

Fig. 1. Phosphatydylserine externalization in TK6 (*p53*+/+) and NH32 (*p53*−/−) cells 24 hour after irradiation with X rays, C ions (22 keV/μm) or Fe ions (1000 keV/μm). 5×10^5 cells were labeled with annexin V-FITC and propidium iodide, and analyzed by flow cytometry. Apoptosis is expressed as the percentage of cells positive to annexin V-FITC staining. Each column in the histogram consists of both single positive annexin V-FITC cells and double positive annexin V-FITC and propidium iodide cells. (A) Proportion of dose response apoptotic cells after X-ray irradiation. (B) Comparison of proportion of apoptotic cells after irradiation of X rays, and C ions (22 keV/μm) and Fe ions (1000 keV/μm) at 3 Gy.

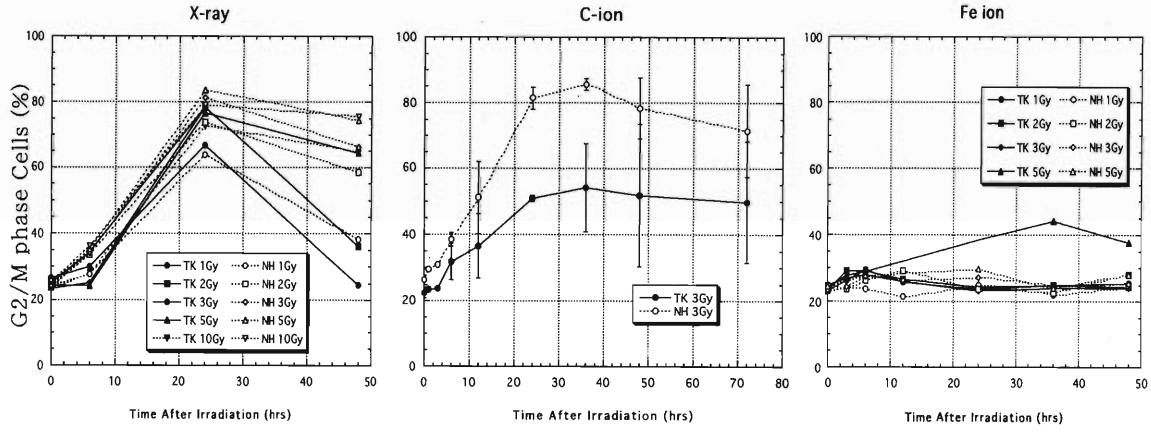

Fig. 2. Cell cycle progression in TK6 and NH32 after irradiation of X rays, C ions (22 keV/μm) and Fe ions (1000 keV/μm). Following the irradiation, cells were fixed with ice-cold 70% ethanol at each post irradiation time and stained by propidium iodide. Cell cycle distributions were analyzed by flow cytometry.

* Department of Radiation Biology, Graduate School of Medical Science, Nagasaki University

lower rate in NH32 (*p53* deficient). However, C ion and Fe ion also cause apoptosis in TK6, there are no significant differences in an apoptotic rate between TK6 and NH32 (Fig. 1 (B)). Heavy ion beams may cause *p53*-independent cell death that also expressed the biochemical hallmarks of apoptosis. This result suggests that irradiation with heavy ion beams might be useful for tumor treatment especially for tumors lacking functional *p53*.

We also examined cell cycle progression after heavy-ion exposure by flow cytometry (Fig. 2). G2/M-phase cells accumulated after irradiation of X rays (at 1 to 10 Gy) and C ions (at 3 Gy) but not by Fe ions (at 1 and 3 Gy). In X-ray irradiation, the absence of functional *p53* only delays cell cycle progression of G2/M-phase to G0/G1-phase, but in C-ion irradiation, it delays cell cycle progression longer than that of X-ray irradiation, and causes G2/M-phase accumulation more efficiently. This result suggests that *p53* is involved in the pathways of repair for DNA damage caused by C-ion irradiation. On the other hand, Fe ions cause clustered DNA damage and irradiated cells arrested in the S-phase and did not proceed to the G2/M-phase.[3] The *p53* may not be involved in the repairing process of such kind of severe DNA damage.

References

1) T. Jacks, L. Remington, B. O. Williams, E. M. Schmitt, S. Halachmi, R. T. Bronson, and R. A. Weinberg: Curr. Biol. **4**, 1 (1994).
2) T. Nakano, M. Suzuki, A. Abe, Y. Suzuki, S. Morita, J. Mizoe, S. Sato, T. Miyamoto, T. Kamada, H. Kato, and H. Tsujii: Caner J. Sci. Am. **5**, 362 (1999).
3) S. Goto, S. Morimoto, M. Kase, and F. Yatagai: RIKEN Accel. Prog. Rep. **35**, 133 (2002).

Effect of heavy ions on the activation of DNA double-strand break repair proteins

M. Tomita, T. Tsukada, N. Fukunishi, and F. Yatagai

DNA double-strand break (DSB) is induced by ionizing radiation, as well as the process of DNA replication, and is particularly the most lethal damage. In mammalian cells, DSB is repaired by mainly two distinct and complementary mechanisms, namely, nonhomologous end-joining (NHEJ) and homologous recombination (HR).

NBS1 is a responsible gene for Nijmegen breakage syndrome (NBS), which is known to be a rare autosomal recessive disorder and a chromosome breakage syndrome. Cells from NBS patients show chromosomal instability, cancer predisposition, hypersensitivity to ionizing radiation and abnormal cell cycle regulation after irradiation.[1,2] NBS1 was known to form nuclear foci after irradiation. Recently, Tauchi *et al.*[3] reported that NBS1 is essential for DNA repair by HR in higher vertebrate cells.

Histone H2AX is phosphorylated at ser139 (named γ-H2AX) after irradiation and forms nuclear foci at the site of DSB as well as that of NBS1 foci formation.[4] Recently, Celeste *et al.*[5] reported that H2AX knock out cells show a high radiation sensitivity, chromosomal instability, DSB repair defects and impaired recruitment of NBS1 to nuclear foci induced by ionizing radiation.

Accelerated heavy ions have been known to induce clustered DNA damage, which is two or more DNA damages induced within a few helical turns. It has been considered that the higher biological effectiveness of higher LET heavy ions would be determined predominantly by a complex clustered DNA damage that leads to a non-repairable DSB. To elucidate the physiological consequence of clustered DNA damages induced by heavy-ions, we examined the response of DSB repair proteins on heavy ions-induced clustered DNA damage.

Figure 1 shows the ionizing radiation-induced nuclear foci formation of NBS1 and γ-H2AX by immunofluorescent staining in human cervical carcinoma HeLa cells. In Fig. 1 (A), NBS1 was distributed uniformly in the cell nuclei of unirradiated cells. After X-irradiation, NBS1 formed discrete foci at the sites of DSB. On the other hand, NBS1 formed large foci after Fe-ion irradiation, which was not observed after X-irradiation. Additionally, γ-H2AX also formed large foci after Fe-ion irradiation (Fig. 1 (B)). These results suggest that NBS1 and γ-H2AX can be used as molecular marker of DNA clustered damage induced by heavy ions.

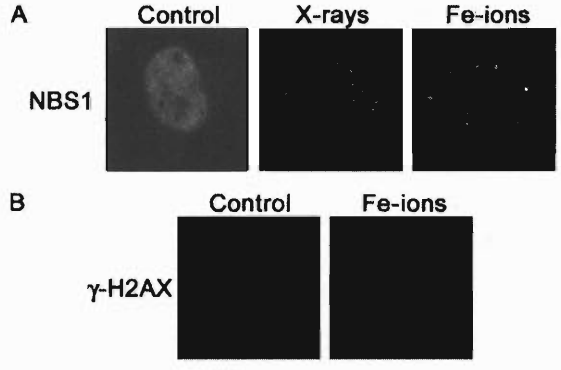

Fig. 1. IR-induced foci formation of NBS1 (A) and γ-H2AX (B) in HeLa cells. HeLa cells were irradiated with 5 Gy of X-rays or Fe ions (LET = 1000 keV/μm) and were fixed 8 h after irradiation. Immunofluorescent staining with anti-NBS1 or anti-γ-H2AX antibody was performed.

DNA-dependent protein kinase (DNA-PK) is Ser/Thr kinase composed of catalytic subunit (DNA-PKcs) and DNA-binding heterodimer (Ku70 and Ku86). DNA-PK acts as a sensor of DSB during NHEJ, since DNA-PK is activated to bind to the ends of double-strand DNA. We have recently observed that DNA-PKcs forms nuclear foci after X-irradiation. Examination of the DNA-PKcs foci formation after irradiation of heavy ions can be expected to provide new insights into the physiological consequence of clustered DNA damage.

References

1) A. Ito et al.: Biochem. Biophys. Res. Commun. **265**, 716 (1999).
2) H. Tauchi et al.: J. Biol. Chem. **276**, 12 (2001).
3) H. Tauchi et al.: Nature **420**, 93 (2002).
4) E. P. Rogalu et al.: J. Cell. Biol. **146**, 905 (1999).
5) A. Celeste et al.: Science **296**, 922 (2002).

Effect of *Fusarium* expressing yeast phytochelatin synthase gene on the uptake of radionuclides by tomato plants

T. Soshi, S. Enomoto, and I. Yamaguchi

It has been proposed that the use of plants to remove toxic materials such as toxic metals and radionuclides, from land (phytoremediation) is a cost-effective and ecologically compatible technology for reducing the risks of toxicity to humans. But the removal efficiency of phytoremediation is lower than that of the conventional method (soil washing and soil dumping). To enhance the uptake and accumulation of toxic materials by plants, several approaches were reported such as administering a chemical chelater to soil, genetic engineering of plants[1] and using microorganisms.[2,3] The introduction and overexpression of metal-binding peptides, such as phytochelatins (PCs), have been exploited to increase metal accumulation by plants and yeasts.[4,5] We introduced the phytochelatin synthase (PCS) gene isolated from *Schizosaccharomyces pombe* to nonpathogenic strains of *Fusarium oxysporum* F. spio *rycopersici* (N.P.F.), which enhanced the uptake of some nuclides by tomato plants through infection, and analyzed nuclides accumulation in tomato plants infected by the transformant.[6] However the effect of the PCS-expressing transformant on the uptake of radionuclides by tomato plants was not monitored. In this study, we analyzed the influence of the transgenic N.P.F., in which the yeast PCS gene was expressed, on the uptake of radionuclides by tomato plants using the multitracer technique.

The *S. Pombe* PCS gene was cloned and introduced into N.P.F. by transformation. Tomato seeds were sown in plastic pots containing 150 g of sterilized horticultural soil (Kureha engei baido, Kureha Chemical Industry Co., Tokyo). The tomato plants were cultivated in a greenhouse at 25–30°C and under 15,000 to 1,700 lux light for 12 hrs a day. Two weeks after seeding, a mixture of diluted multitracer and radioactive cesium (^{137}Cs) was applied to each pot. The same amount of solution was absorbed by filter paper for comparison. Liquid cultures of N.P.F.s were poured directly on the soil for inoculation. In the following two weeks, aerial parts of the plants were collected and dried at 50°C overnight. Then the radioactivity was measured using a hyperpure Ge detector (SEIKO EG&G).

Figure 1 shows the uptake of radionuclides (Mn, Co, Zn, Se, Rb, Sr and Cs) by tomato plants inoculated with N.P.F. strains. Wild type N.P.F. enhanced Rb and Sr uptake by tomato plants and there was no effect

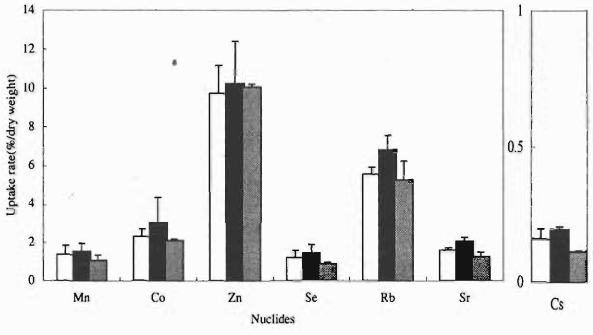

Fig. 1. Radionuclides uptake by tomato plants inoculated with PCS expressed transformant. Data of the activity to the control per gram dry weight of the plant is expressed in percentage. Error bar shows standard deviation derived from 4 replicates.

on Mn, Zn, Se, Co and Cs uptake. In tomato plants infected by the PCS-expressing transformant, the uptake of Mn, Co, Se, Rb, Sr and Cs was less compared with the wild-type-N.P.F.-infected plants. Furthermore Se, Sr and Cs uptake was lower than that by noninfected tomato plants. We have reported that accumulation of Mn and Cs in the hyphae of N.P.F. increased by PCS expression but that of Co and Se decreased.[6] This cannot be simply explained by the modification of metal existence in hyphae by PCS expression. The transformant may change the metal availability to plants by modifying the soil characteristics or the chemical forms of metals. For further clarification, soil characterization and determination of chemical forms of metals in soil is required.

References

1) M. Mejare and L. Bulow: Trends Biotechnol. **19**, 67 (2001).
2) T. Soshi et al.: RIKEN Accel. Prog. Rep. **34**, 165 (2001).
3) N. S. Whiting et al.: Environ. Sci. Technol. **35**, 3144 (2001).
4) O. K. Vatamaniuk et al.: Proc. Natl. Acad. Sci. USA **96**, 7110 (1999).
5) S.-B. Ha et al.: Plant Cell **11**, 1153 (1999).
6) T. Soshi et al.: RIKEN Accel. Prog. Rep. **35**, 127 (2002).

Effects of heavy-ion beam irradiation in rose (*Rosa hybrid cv.* 'Bridal Fantasy') (II)

Y. Hara,* T. Abe, K. Sakamoto, Y. Miyazawa, and S. Yoshida

In recent years, the heavy-ion beam has been used as a new plant breeding method that causes mutation in various plant species. In our previous study, irradiating the buds by a heavy-ion beam effectively yielded new mutants of roses. The values of LD_{50} were found to be 10–20 Gy for ^{20}Ne ion and 20–50 Gy for ^{14}N ion. In the present experiment, we investigated in detail about the relationships between the exposure dose and the survival of buds, and shoot elongation from the grafted buds, as well as the characteristics of mutated flowers.

The spray-type rose cultivar with white flowers, namely 'Bridal Fantasy' was used. Ten offshoots (approximately 70 mm long) were used for each treatment. Irradiation treatments were conducted at the doses of 10, 15, and 20 Gy for ^{20}Ne ions and 20, 30, 40, and 50 Gy for ^{14}N ions at an energy of 135 MeV/u and compared with the control (0 Gy) buds. Then the buds were grafted on the rose stock 2–3 days after irradiation. Survival of the buds, lengths of shoots elongated from the grafted buds, and the characteristics of mutated flowers were recorded 1–3 months after the grafting.

Frequencies of survival of the buds and length of the shoots decreased with the increase of exposure dose. In the ^{20}Ne ion treatment, 20 Gy irradiation delayed the growth of buds, and shortened the shoot length. In the ^{14}N ion treatment, 40 Gy irradiation decreased the number of elongated shoots, while 50 Gy irradiation inhibited the growth of almost all the plants (Table 1). High mutation rates for the flowers were obtained at the 15 or 20 Gy exposures for ^{20}Ne ion, and 30 or 40 Gy exposures for ^{14}N ion (Table 2). The phenotypes of the mutated flowers were categorized as follows; mutations for color of petals, and number of petals as well as for shapes, sizes, and greening of outer tips. Although there seemed to be no relationships between the altered characteristics and the irradiation dose, some plants yielded malformed flowers, which did not bloom normally (Table 3).

From these results, it was suggested that the optimum irradiation dose of the heavy-ion beam which cause mutations of the offshoot of the rose shoot was 10–15 Gy for ^{20}Ne ion, and around 30 Gy for ^{14}N ion. As numerous mutants were obtained easily, heavy-ion beam irradiation is proved to be an efficient way for breeding of rose cultivars. However, in order to establish more effective breeding method, further investigations are necessary to overcome the chimera state of flower, and sustaining and fixation of the mutant characteristcs.

Table 2. Effects of heavy-ion beam irradiation on rose flowers.

Ion	Dose (Gy)	No. of flowers	No. of mutants	Frequency (%)
Ne	10	63	12	19.0
	15	58	30	51.7
	20	25	10	40.0
N	20	56	0	0.0
	30	58	25	43.1
	40	29	19	65.5
	50	0	nd	nd
Control		26	0	0.0

Table 3. Effects of heavy-ion beam irradiation on flower characteristics.

Ion	Dose (Gy)	Number of mutants				
		Color	Petal number	Shape	Size	Greening
Ne	10	9	3	5	1	0
	15	3	21	1	0	12
	20	1	4	0	2	7
N	30	8	16	3	4	10
	40	6	9	9	10	3

Table 1. Effects of heavy-ion beam irradiation on the growth of rose 'Bridal Fantasy.'

Ion	Dose (Gy)	No. of plants	number and length of survived shoots			
			70 days after irradiation		100 days after irradiation	
			number	length (cm)	number	length (cm)
Ne	10	10	10	70.0	10	81.0
	15	10	7	47.4	7	82.7
	20	10	7	10.0	7	53.0
N	20	10	10	68.7	10	78.0
	30	10	9	18.0	9	49.0
	40	10	2	1.5	4	30.3
	50	10	0	0.0	2	1.0
Control		10	9	61.0	9	72.7

* Kanagawa Prefectural Agricultural Research Institute

Effect of heavy-ion beam irradiation on the survival and growth of Sastuma mandarin

H. Kagami,* T. Abe, K. Sakamoto, Y. Miyazawa, I. Sawano,* and S. Yoshida

'Aoshima unshiu' is a leading variety of sastuma mandarin due to good taste, early maturity. Several handreds of nucellar seedlings (somatic origin) of 'Aoshima unshiu' were investigated in the Shizuoka Citrus Experiment Station to isolate an early maturing spontaneous mutant. Only few lines, such as S1152, were earlier maturing than the original variety. Therefore, we conducted an experiment using heavy-ion beams for the induction of mutation in the S1152 line.

Irradiation treatments of heavy-ion beams were conducted on the axillary buds of hard branches. The buds were irradiated in the dose range of 10 to 50 Gy of ^{20}Ne ions (135 MeV/u) and 20 to 100 Gy of ^{12}C ions (135 MeV/u) in March and September 2001 and March 2002. Branches were cut approximately 6 cm in length and fixed with adhesive tape to align the buds. Twenty branches were used for each treatment. These branches were grafted on 2-year-old *Poncirus trifoliate*. The frequencies of plants that survived were recorded 6 months after grafting. The length of branches and the number of axillary buds were investigated one year after grafting.

The survival rate decreased with the increase in exposure dose. Plants irradiated with doses higher than 50 Gy survived (Fig. 1). The values of LD_{50} were found to be less than 20 Gy of the C ions and 20–30 Gy of the Ne ions (Fig. 1). All plants that survived showed abnormal shape in the first leaves after treatment and continued to grow normally and produce normal leaves. After one year, there was no difference in the length of branches and the number of axillary buds between normal trees and trees irradiated with 20 Gy of C ions, 10 or 20 Gy of Ne ions (Fig. 2). The frequencies of morphologically abnormal trees (Fig. 3) were 10% (2 plants/20 plants that survived) and 3.3% (1/30) with 20 Gy of C ions and 10 Gy of Ne ions, respectively. These results clearly demonstrate that heavy-ion beams are effective for the induction of abnormal leaf formation in Sastuma mandarin. Further observations are needed to determine the change of phenotype in the flowering stage after 3 years.

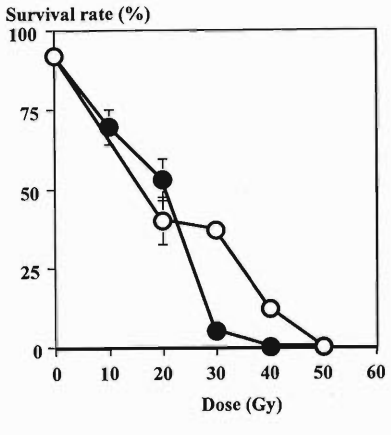

Fig. 1. Effect of irradiated ions and exposure dose on the survival rate of the S1152 plants. ○: C ion, ●: Ne ion.

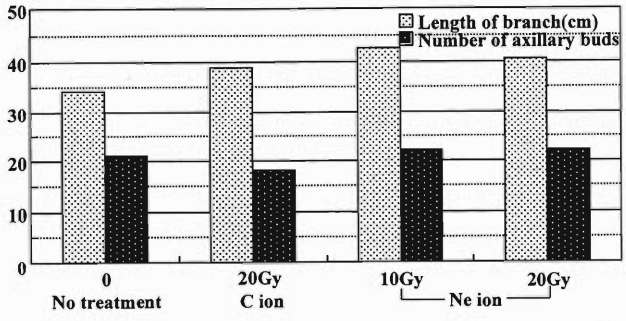

Fig. 2. Effect of irradiation of 20 Gy for C ion and 10, 20 Gy for Ne ion on the growth of S1152.

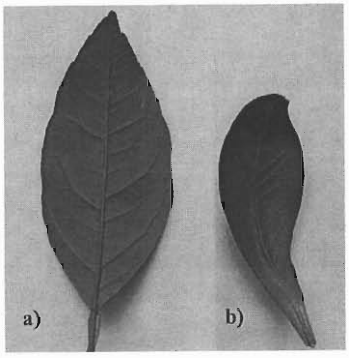

Fig. 3. Effects of heavy-ion beam irradiation on the leaf shape of Sastuma mandarin. a) Wild-type leaf, b) abnormal leaf.

* Shizuoka Citrus Experiment Station

Biological effects of ion beams on buckwheat

T. Morishita,* T. Abe, N. Fukunishi, Y. Miyazawa, K. Sakamoto, and S. Yoshida

Recently, heavy-ion beams have been regarded as a new mutagen because such high-LET (linear energy transfer) irradiation provides higher RBE (relative biological effectiveness) for various endpoints, compared with gamma rays. In this study, the biological effects of ion beams were investigated in buckwheat.

Dry seeds of common buckwheat (var: *Botansoba* (Bot)) and tartary buckwheat (var: *Rotundatiem* (Rot)) were used in this study. The seeds were about 5 mm in size. The seeds were fixed as a single layer on a 6 cm plastic petri dish, and irradiated with $^{12}C^{6+}$ (135 MeV/u), $^{20}Ne^{10+}$ (135 MeV/u), $^{40}Ar^{17+}$ (95 MeV/u, 305 keV/μm), and $^{56}Fe^{24+}$ (90 MeV/u, 630 keV/μm) ions. For adjusting the LET of $^{12}C^{6+}$ and $^{20}Ne^{10+}$-ions at the surface of seed, an absorber was inserted before reaching the sample. A gamma ray from 44 TBq ^{60}Co was used as the low LET ionizing radiation control. The irradiated seeds were sown in nursing soil. After 7–10 days, the capability of germination was measured. After 3 weeks, the survival capability was determined by the existence of a growing point. Survival rates were represented as a percentage of the surviving plants to that of the germinated seeds. The lethal dose 50 (LD_{50}) and mean lethal dose (D_{37}) of each buckwheat variety were obtained from a dose-response curve.

The survival curves for various ions are shown in Fig. 1. The relative lethal effect per dose increased with the increasing LET in both C and Ne ions. The effects of Ar and Fe ions were higher than those of the C and Ne ions. From these dose-response curves, the LD_{50} ranged from 30–500 Gy (Rot) and 10–300 Gy (Bot). Bot was more sensitive than Rot with these ions.

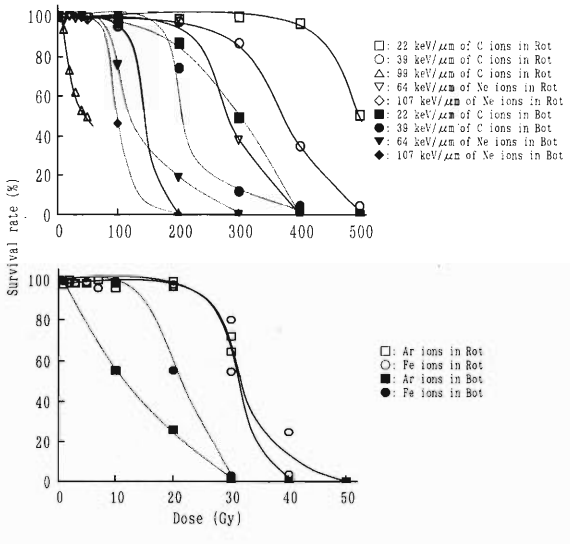

Fig. 1. Survival curves for various ion beams. Upper figure shows the effect of C and Ne ions and lower one that of Ar and Fe ions. Solid line is Rot and dotted line is Bot.

The relationship between the RBE and the LET is shown in Fig. 2. The RBE was estimated as the D_{37} of gamma ray (standard radiation) divided by the obtained D_{37} value in Rot and Bot. Clear peaks of the RBE of D_{37} with values of 17.7 and 22.5 were observed at 305 keV/μm in Rot and Bot, respectively. The maximum value of the RBE of Bot was higher than that of Rot. This shows that the RBE reached a maximum at 305 keV/μm, which is higher than 74–172 keV/μm.[1] and 252 keV/μm.[2]

The effective cross sections for D_{37} of Rot and Bot are shown in Fig. 3. The effective cross sections increased with the LET, and the maximum values were 2.7 (Rot) and 3.0 μm^2 (Bot). Other studies have reported that the cross sections increased with the LET.[2,3] In this study, similar results were obtained. Further study will be necessary to define the mutagen effect of ion beams.

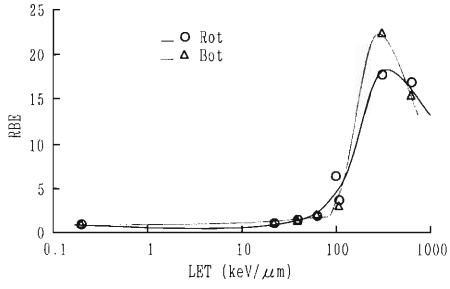

Fig. 2. The relationship between the RBE (D_{37}) and the LET (surface) for irradiated intact seeds.

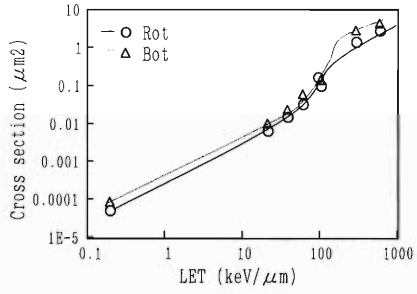

Fig. 3. The relationship between the LET (surface) and the effective cross section for D_{37} in intact seeds.

References

1) Y. Hirono et al.: Radiat. Res. **44**, 204 (1970).
2) A. Tanaka et al.: Int. J. Radiat. Biol. **72**, 121 (1997).
3) M. Mei et al.: Adv. Space Res. **14**, 363 (1994).

* National Institute of Agrobiological Sciences

Effects of heavy-ion beam irradiation on seeds of Eustoma during imbibition

M. Miyasaka,* T. Abe, Y. Miyazawa, K. Sakamoto, T. Usui,* and S. Yoshida

We have released many varieties of Eustoma with new colors of flowers and early- or late-flowering time using pure line breeding and cross breeding in Nagano Vegetable and Ornamental Crops Experiment Station from 1977. Producing an F_1 hybrid has been recently adapted in our breeding program. Mutation breeding is considered to be an effective method for many plant species. In this paper we report the effect of heavy-ion beams on imbibition in seeds, and on growth of M_1 plants.

Eustoma (*Eustoma Grandiflorum Shinn*) seeds; R664-1, S951 and Shinano Orchid (SO) of pure-bred varieties, R341 and T925 of F_1 hybrid varieties, were soaked for 3 to 4 days in water with 1.0% agar at 25°C under continuous light. Seeds during imbibition were irradiated with Ne-ion beams (135 MeV/u, LET; 63 KeV/μm) within a dose range from 5 to 100 Gy. After the irradiation, seeds were transplanted in soil in cell trays and grown in a greenhouse at 15–25°C. One month after irradiation, germinated plants were counted. Three months after irradiation, the fresh weight of the plants were measured. Plant growth and flowering time were investigated 9 months after irradiation.

Germination frequencies decreased when irradiated at 30 Gy and 50 Gy, and the germinated plants died at 50 Gy (Table 1). The LD_{50} value of T925 was 30–50 Gy. The LD_{50} values of other varieties were 20–30 Gy. In the case of F_1 hybrid varieties, such as T925 and R341, they showed higher germination frequencies than other varieties, because of their heterosis, or the frequencies were the same as those of one selfed line. While the growth of plants irradiated at 20 Gy and 30 Gy was retarded in the early stage (Fig. 1), their growth recovered after 9 months (Fig. 2). Abnormal leaf shapes were observed in plants exposeed to 5–30 Gy, however, almost all of these plants had produced normal leaves after 3 months. Some morphological abnormalities were needle leaves, corrugated leaves, or heart-shape leaves in the M_1 plants. Irradiation had little effect on the time of flowering.

Further observation is required to determine the mutated phenotype in M_2 progenies. And further experimentation should be conducted to select strains with a promising commercial value, and to evaluate the stability of these promising strains.

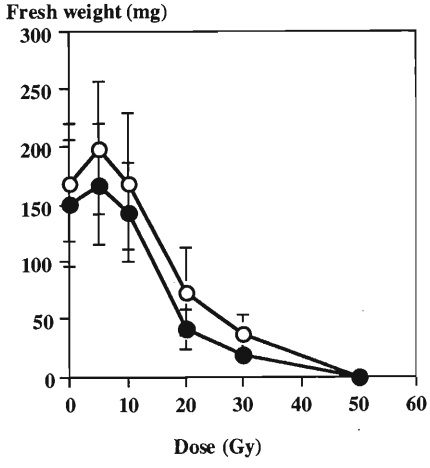

Fig. 1. Effects of irradiation of seeds during imbibition with Ne-ion beams on the plant growth. Fresh weight on above-ground part (○) and underground part (●).

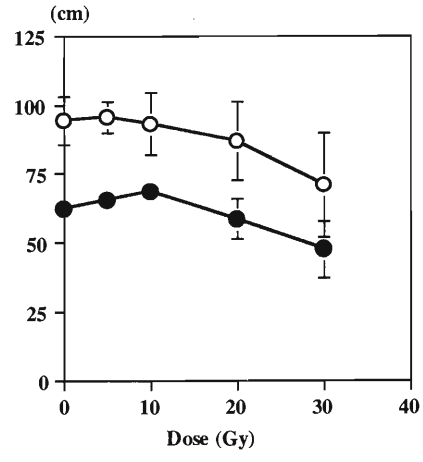

Fig. 2. Effects of irradiation of seeds during imbibition with Ne-ion beams on the plant growth after 9 months. Plant height (○) and stem length (●).

Table 1. Effects of Ne-ion irradiation on germination percentage of Eustoma.

Dose (Gy)	Germination (%)				
	R644-1	S951	SO	R341	T925
0	70	95	70	100	90
5	60	85	60	95	89
10	50	75	65	90	65
20	60	80	70	95	73
30	20	30	10	40	70
50	0	0	0	0	2
100	0	0	0	0	0

* Nagano Vegetable and Ornamental Crops Experiment Station

Effects of heavy-ion beam irradiation on the pollen of *Cannabis sativa* L.

K. Sakamoto, T. Abe, and S. Yoshida

A few species of flowering plants are dioecious, for example, *Actinidia* (kiwi plant), *Asparagus*, *Silene latifolia* (*Melandrium album*), and *Cannabis* (hemp). In a dioecious plant, *Cannabis sativa*, the two genotypes are XX (female) and XY (male), and the Y chromosome is twice the size of the X chromosome.[1] It is reported that the X and Y chromosomes of *C. sativa* carry female- and male-determining genes, respectively. In order to obtain a mutation of the Y chromosome in *C. sativa*, we applied the heavy-ion beam irradiation method, which has been reported to be an effective method for obtaining mutagenic pollens.[2]

Buds of male flowers were irradiated with a ^{20}Ne-ion beam at dosage rates of 0.1, 1.0, 5.0, and 10 Gy. The irradiated pollens were used to pollinate the non-irradiated female flower, and the seeds were harvested three weeks after pollination. Morphologically normal shape flowers which were lower part of the male plants irradiated at a dosage rate of 10 Gy, were used as a control (in Table 1, 0 Gy). They were set on outside of the irradiation area. One hundred seeds were used for the experiment. The germination percentage was counted after two weeks. DNA was extracted from the leaf of the germinated seedling, and the sex of the seedling was distinguished using the polymerase chain reaction (PCR) method. The primer used for the PCR was produced on the basis of the DNA sequence which was specific for the male plant of *C. sativa*.[3]

The morphological features of each male flower after irradiation are shown in Fig. 1. The anthers irradiated with 5.0 Gy had abnormal shapes such as bent shape and were smaller than these observed with the normal male flower. The anther irradiated with 10 Gy withered. The germination rate decreased with increasing dose of exposure (Table 1). The discrimination between male and female germinated plants was performed by PCR using male-specific primers. The size of the fragment responsible for the male-specific band was 600 bp (Fig. 2). The dose range of 0.1 to 1.0 Gy produced a slightly higher number of female plant than male plant. In contrast, the male plants were observed in 41 out of 59 plants with 0 Gy irradiation, which was 69.5% of appearance frequency (Table 1).

Table 1. Effects of ^{20}Ne heavy-ion beam irradiation in *C. sativa*.

Irradiation does (Gy)	No. of cultured seeds	No. of germinated seeds (%)	No. of male plants	No. of female plants
0	100	59	41	18
0.1	100	11	4	7
1.0	100	7	3	4
5.0	100	3	2	1
10	100	—	—	—

Fig. 1. Morphological features of male flowers of *C. sativa* induced by ^{20}Ne heavy-ion beam irradiation. The dosage rates are 0.5 (A), 1.0 (B), 5.0 (C), and 10 (D) Gy.

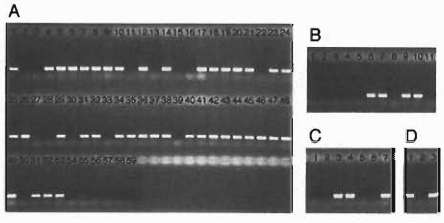

Fig. 2. Discrimination of male and female plants by PCR. PCR was carried out using the male-specific primer. The bands indicates male plants. The dosage rates are 0 (A), 0.5 (B), 1.0 (C), and 5.0 (D) Gy.

Results of our previous research on distinguishing male and female plant of *C. sativa* using 850 specimens confirmed that 370 specimens (43.5%) are male. This indicates that the prevalence of male plants is slightly higher than that of female plants. The result of this research contradicts our knowledge. It is not clear why there was a high prevalence of male plants in *C. sativa*. One possibility is that the upper damage by the ^{20}Ne-ion beam was transmitted to the male flower of the downward. These results demonstrate that the X-chromosome might be affected by heavy-ion beam irradiation. At present, the effect of the prevalence of male and female is being examined by supplementary experiments.

References

1) K. Sakamoto, Y. Akiyama, K. Fukui, H. Kamada, and S. Satoh: Cytologia **63**, 459 (1998).
2) C. H. Bae, T. Abe, T. Matsuyama, T. Nakano, K. Miyoshi, and S. Yoshida: Breed. Sci. **48**, 327 (1998).
3) K. Sakamoto, N. Ohmido, K. Fukui, H. Kamada, and S. Satoh: Plant Mol. Biol. **44**, 723 (2000).

5. Instrumentation

Optimization of the performance of a CsI(Tl) scintillator + Si pin photodiode detector for medium-energy light-charged-particle hybrid array

Z. Elekes,[*1] Zs. Fülöp,[*2] J. Gál,[*2] Gy. Hegyesi,[*2] G. Kalinka,[*2] J. Molnár,[*2] T. Motobayashi, A. Saito,[*3] and Y. Yanagisawa

NaI(Tl), BGO and CsI(Tl) crystals in compact arrays will be used at RIKEN RI Beam Factory in the near future. NaI(Tl) detectors are designed to detect gamma rays from fast moving nuclei produced in nuclear reactions with radioactive beams. However, from highly excited states, high-energy photons are also expected which can be monitored by BGO scintillators exploiting their higher efficiencies for energetic photons. For the reactions with a light target, in addition to the gamma-ray measurement, recoil particle detection allows for the determination of the scattering angle which is difficult from the laboratory angle of the heavy product due to the nature of reversed kinematics. Detection of the recoil particles is also useful in identifying the reaction channel. For this purpose, we intend to employ CsI(Tl) crystals coupled to photodiodes (Fig. 1).

From considerations on nuclear reactions to be investigated, the individual CsI(Tl) crystal size was chosen as $16 \times 16 \times 55\,\mathrm{mm}^3$ in order to stop light particles with approximately 110 MeV/u. Actually one squared end is tapered to 5 mm length to fit the $10 \times 10\,\mathrm{mm}^2$ Si pin photodiode (PD). Coupling the untapered end either directly, or via a tapered plexi lightguide to the PD, gave inferior light collection.

A glue to bond together scintillator and PD must possess high transparency, matched refractive index, optimum bond strength to accomodate thermal expansion difference, chemical inertness against modestly reactive CsI, and easy handling. Although neither of the three epoxies and three silicones preselected and eventually evaluated glues met all the requirements, Epotek 302, a two-component epoxy, was chosen for its best overall performance.

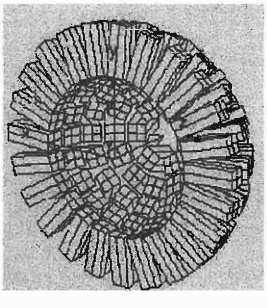

Fig. 1. Schematic view of CsI(Tl) ball made by GEANT.

The selection of an appropriate light reflector around the optical part, in order to maximize the amount of detected (collected) light, is crucial for the quality of the detector. Equally important is the precise geometry and accurate assembly of the entire detector, since the latter is the basis of a good performance. Numerous combinations of diffferent surface conditions (polished, lightly painted, and matted) and of various wrapping materials (Teflon, Tyvek, Lumirror, VM2000 mirror films obtained from 3M company,[1)] and Aluminised Mylar (AlMy) films) for the sides and front face were tested to find the best solution(s) (VM2000 foil is a multilayer interference film based on giant birefringent optics,[2)] a promising new alternative in scintillation detection to the presently overwhelmingly applied diffuse reflectors). Parallel with these experiments Monte Carlo calculations[3)] were made to simulate light collection, and to find the best set of empirical constants for matching of measured and calculated results.

Two combinations turned out particularly good: (i) all surfaces highly polished, the sides wrapped loosely with ≥ 25 turns of 60 μm soft Teflon tape, (ii) front face polished, side surfaces specially depolished and covered with ≥ 2 layers of 60 μm 3M mirror film. For the front face Lumirror (180 μm), 3M foil or AlMy foils (2–12 μm My, 0.2–1 μm Al) can be used, depending on the type and energy of the particles to be detected. The performances are approximately the same: for 5.5 MeV α particles tested, the light collection efficiency is $\approx 70\%$, energy resolution is $\leq 2.5\%$ and low energy background continuum is $\leq 3\%$, whereas for γs, the light yield is ≈ 30 photon/keV with $\leq 0.3\%$ nonuniformity along crystal length and the energy resolution for 511 keV is $\leq 10\%$.

An accelerated (long term) stability test at 60°C revealed the superiority of Epotek 302 among glues and the 3M film among wrapping materials (Fig. 2). This fact and space limitations were the basis for the selection of 3M foil for final production. Similar solutions in the third-generation Diamant detector system in conjunction with Euroball,[4)] or in the GLAST space detector system under construction,[5)] also support the excellenc use and justifies the choice of VM2000 3M foil.

A beam test for particle identification of four detectors was performed at RIKEN Accelerator Re-

*1 On leave from Institute of Nuclear Research (ATOMKI), Hungary
*2 ATOMKI, Hungary
*3 Rikkyo University

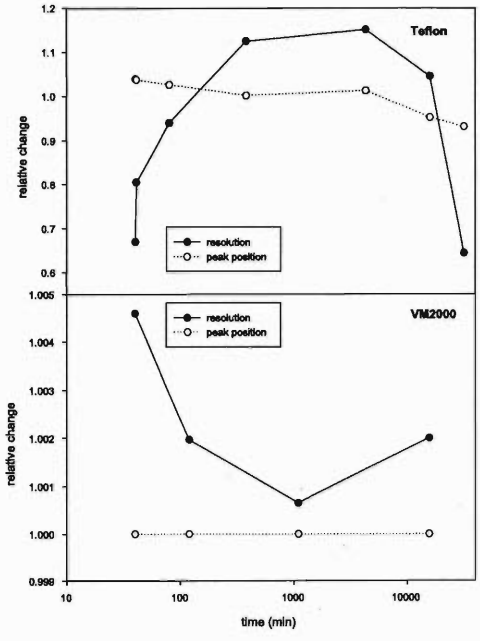

Fig. 2. Heating test of detectors glued with EPOTEK-302 and wrapped with Teflon and VM2000 foils. Note the different y scale of figures.

search Facility using a high-energy deuteron beam (50 MeV/A). The sides of the detectors were wrapped with VM2000 foil while the front faces of two detectors were wrapped with VM2000 and two front faces with Aluminized Mylar. The primary beam was degraded by a 0.5-cm-thick Al plate in which other light-charged particles were created at a maximum energy of 43.3 MeV/A which means 9.6 mm range for protons, 5.9 mm for deuterons, 4.5 mm for tritons, 1.1 mm for ^{3}He and 0.9 mm for ^{4}He in CsI(Tl). Particle identification was carried out by using a ballistic deficit method: two electronic channels for each detector with low (10 μs shaping time) and high (2 μs shaping time)

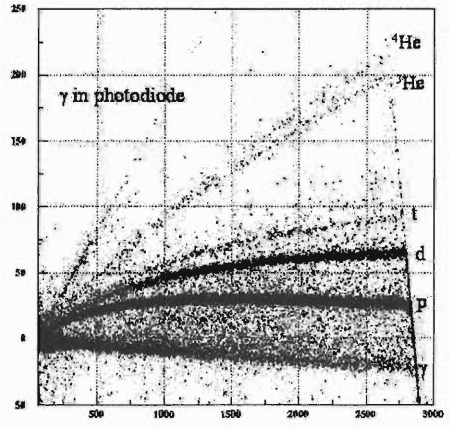

Fig. 3. Particle identification test with detector No.3. Spectra obtained with different shaping times are plotted against each other (X: low ballistic deficit, *i.e.*, energy (the end of spectrum represents 95 MeV), Y: high ballistic deficit, *i.e.*, particle type). The axes are slightly rotated.

ballistic deficits respectively gave energy and particle data, as well. Clear separation of gamma, proton, deuteron, triton, and ^{3}He and ^{4}He particles above 5–10 MeV was observed (Fig. 3). No significant difference in particle identification by different detectors was seen. Further improvements can be expected with the application of newly developed and tested dedicated electronics.[6)]

References

1) http://www.3m.com/lightmanagement
2) M. F. Weber et al.: Science **287**, 2451 (2000).
3) E. Frlež, B. K. Wright, and D. Počanić: Comput. Phys. Commun. **134**, 110 (2001).
4) G. Kalinka et al.: ATOMKI Ann. Rep. **2002**, 64.
5) http://glast.stanford.edu
6) J. Gál et al.: RIKEN Accel. Prog. Rep. **36**, 143 (2003).

Development of analog signal processing channel for CsI(Tl) scintillation detector array

J. Gál,[*1] J. Molnár,[*1] D. Novák,[*1] G. Kalinka,[*1] G. Hegyesi,[*1] J. Végh,[*1] Zs. Fülöp,[*1] Z. Elekes,[*2] T. Motobayashi, and A. Saito[*3]

An analogue signal processing channel has been developed for analyzing the signals supplied by photodiodes coupled to individual detectors of the CsI(Tl) scintillation detector array to be used at the RIKEN RI Beam Factory.[1,2)]

As it is well known the CsI(Tl) scintillation crystal has a unique feature: the decay time of the scintillation light is highly dependent on the ionization density of the incident radiation. This phenomenon can be applied determining the type of radiation, *e.g.*, if the radiation is composed of different types of particle it can be used for particle identification.

During the construction of the analogue signal processing channel, the following solutions, which were based on previous results obtained from EUROBALL detectors, were realized:

For deriving a proper energy signal, a semi-Gaussian prefilter with a 1.2 μs time constant is used, which is followed by a delay-switched gated integrator. The peaking time is adjustable from 3 μs to 12 μs.

For timing purposes, two different shaping methods are used. A bipolar signal is shaped from the semi-Gaussian prefiltered unipolar signal by a second 1.2-μs-time-constant CR filter. The zero-crossing time of this signal is amplitude-independent, but rise-time (particle type) dependent. A tripolar signal is also shaped by the subtraction of two bipolar signals shaped by different time constants. The first zero crossing of this signal is amplitude independent and almost rise time independent. Timing signals are generated from the first zero crossings of the tripolar signal and the zero crossing of the bipolar signal.

For signal recognition a leading edge discriminator is applied. Its input is the bipolar signal and its threshold is controllable. The leading edge discriminator gates both of the above-mentioned timing discriminators.

For particle discrimination, three techniques are used: the ballistic deficit method,[3,4)] the zero-crossing method,[5)] and the combination of these: the mixed method. Switching between the discrimination modes is controllable. In the case of the ballistic deficit method, the particle-type information is given by the ratio of the amplitude of the gated integrator output and the amplitude of the first lobe of the bipolar signal. The zero-crossing technique is realised using a time-to-amplitude converter (TAC). The start signal can be the timing signal derived from the first zero crossing of the tripolar signal or an external timing signal, if it is available from other detectors. The stop signal is the timing signal extracted from the bipolar signal. In the mixed methods, the particle-type information is obtained by the weighted summation of the outputs produced by the ballistic deficit and the zero-crossing methods.

Time reference information is produced by a TAC. The start signal is the timing pulse generated from the tripolar signal and the stop signal is the delayed external timing signal. The stop signal is common for all the channels.

The input signal polarity of the signal processor is jumper selectable and the decay time constant is 50 μs. It has three analogue outputs: energy, particle type and time reference. Their shape is rectangular having a width of 2 μs. They can be connected directly to the input of peaking ADCs, and no additional control pulse for the ADC is required.

The main parameters of the channel (*e.g.*, gain, pole zero, delays) are designed to be software controllable. Moreover, the analogue channel has several analogue and digital inspection points, which can be connected to inspection lines in order to check them by an oscilloscope. The selection of the inspection points is software controllable.

The analogue channel has been tested using an alpha

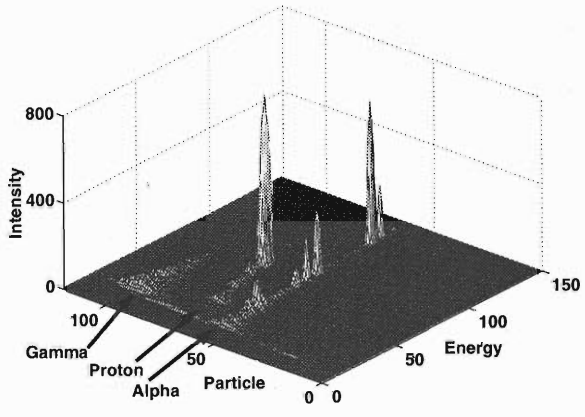

Fig. 1. Two-dimensional plot of data taken by the above-described setup. In the experiment 20 MeV alpha beam hits the mylar target. The energy scale in the figure is uncalibrated. The particle scale was deduced using the ballistic deficit method, therefore, it is basically the ratio of the faster component to the total decay time of the scintillation light.

*1 ATOMKI, Hungary
*2 On leave from ATOMKI, Hungary
*3 Rikkyo University

beam and a mylar target in the Cyclotron Laboratory of the Institute of Nuclear Research, Debrecen, Hungary. A typical result of this measurement is shown in Fig. 1.

References

1) T. Motobayashi: Proposal at International Advisory Committee Meet., for RI Beam Factory, RIKEN, June (2001).
2) Z. Elekes et al.: RIKEN Accel. Prog. Rep. **36**, 141 (2003).
3) J. Gál et al.: Nucl. Instrum. Methods Phys. Res. A **366**, 120 (1995).
4) J. Gál et al.: Nucl. Instrum. Methods Phys. Res. A **399**, 407 (1997).
5) T. K. Alexander et al.: Nucl. Instrum. Methods **13**, 244 (1961).

Responses of inorganic scintillators to energetic heavy-ion beam

T. Suda, M. Chiba,[*1] E. Ideguchi, I. Tanihata, T. Izumikawa,[*2] T. Suzuki,[*2] and M. Takahashi[*2]

Excellent energy resolution of inorganic scintillators, such as NaI(Tl), for energetic heavy ions has been previously reported,[1,2] which was a key for good particle identification capability in several experiments involving RI beams at the RIPS facility.[3]

In this report, we present the results of a study on the Z- and A-dependence of the light output of a NaI(Tl) crystal for energetic heavy ions, 100 MeV/u, which has been little known to date. In addition, the energy dependence of the NaI(Tl) light output to a heavy ion higher energy, up to 300 MeV/u, measured at HIMAC is also presented.

The NaI(Tl) responses for eight radioactive isotopes have been measured at the RIPS facility of RIKEN using a ^{22}Ne beam of 110 MeV/u. Isotopes whose A/Z ratio is close to 3 were transported to the final focus, F3, where a NaI(Tl) detector was placed. Since no degrader was used at the dispersive focal plane, F1, the responses for eight isotopes, ^{8,9}Li, ^{11,12}Be, ^{14,15}B and ^{17,18}C, could be measured simultaneously, which minimizes systematic errors for the light output determination. Particle identification was performed based on the standard Bρ-ΔE-TOF method.

Figure 1 (a) shows the NaI(Tl) light output for the eight isotopes as a function of their total kinetic energy, which is deduced from the Bρ measurement with a correction for energy loss inside detectors placed upstream of the NaI(Tl) detector. Solid lines in the figure are guides for the eye. The Z-quenching of light output is clearly observed; larger Z particles produce less light output compared to smaller Z particles having the same total kinetic energy. This is due to the difference of energy loss density for particles with different Z. A similar phenomenon has also been reported for a CsI(Tl) crystal at similar energies.[4]

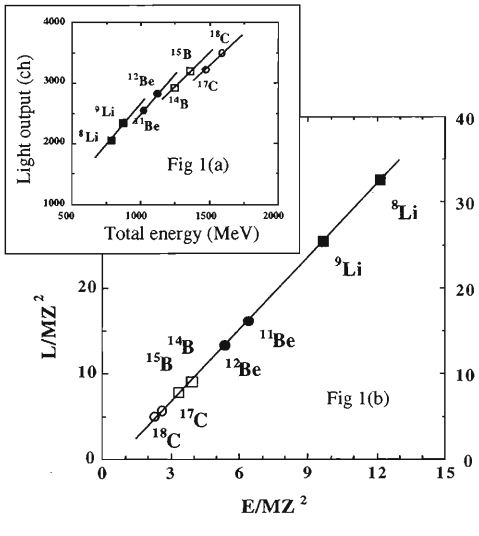

Fig. 1. Light output and total kinetic energy of several isotopes. See text for details.

How can we understand this Z-dependence of the light output? We start from an assumption that dL/dE, the light output per unit energy loss, is a function of dE/dx, the energy loss per unit length.[5]

$$dL/dE = f(dE/dx). \tag{1}$$

One can integrate Eq. (1) over x using the relationship, $dE/dx \propto Z^2M/E$. Here, M denotes the mass, which is proportional to the mass number A. Then, it is easy to deduce,

$$L/MZ^2 = g(E/MZ^2). \tag{2}$$

This shows that L/MZ^2 is a (common) function of E/MZ^2 for particles having different Z and A. In Fig. 1 (b), the corrected light outputs, L/MZ^2, for the measured isotopes are plotted as a function of the corrected total energy, E/MZ^2. All the data points are found to be on a common function of E/MZ^2. Furthermore, the function appears, in a good approximation, to be a linear relationship between L/MZ^2 and E/MZ^2; $L/MZ^2 = aE/MZ^2+b$, where a and b denote the slope and intercept, respectively.

In this case, one can rewrite Eq. (2) as,

$$L = aE + bMZ^2. \tag{3}$$

The Z- and A-dependence of the light output comes up only in the intercept, but not in the slope. It is worth pointing out that, as observed in Fig. 1 (b), the sign of b is negative. The reason why the light output, L, is smaller for larger Z ions at a fixed energy is due to the negative contribution of bMZ^2, attributed to a well-known nonlinear effect of the light output at lower energy. To establish a general relationship between L and E applicable for a wider A- and Z-range and wider energy range, further studies are called for.

The measurements of the response of several inorganic scintillators, NaI(Tl), CsI(Tl), GSO and LSO, have been extended to a higher beam energy up to 290 MeV/u to investigate the energy dependence of the light output. Very little has been previously reported for this energy region, except for one measurement for a BGO crystal to heavy ions.[6] The measurement was performed using a ^{20}Ne beam at the heavy-ion synchrotron facility of Heavy Ion Medical Accelerator in Chiba (HIMAC), National Institute for Radiation Study (NIRS).

*1 Tohoku University
*2 Niigata University

In Fig. 2, the light output of NaI(Tl), as an example, is plotted as a function of the beam energy. Although the data points are limited to be only three, the light output is confirmed to be proportional to the energy deposit. The light output L, thus, can be given by;

$$L = aE + b, \tag{4}$$

where a and b are, again, the slope parameter and the intercept, respectively. The intercept obtained by fitting has a negative value, which is due to the nonlinear effect at lower energy, as observed for light ions at low energies.

In addition to the light output, the energy resolution, $\Delta E/E$, is also plotted as a function of the beam energy in Fig. 2(b). The resolution changes from 0.25% to 0.19% in sigma. The data are well fitted with a function of $1/\sqrt{E}$ + constant, instead of the expected $1/\sqrt{E}$ form. The constant offset, determined to be 0.08% by fitting, may be due to contributions from inelastic scattering of the incoming beam inside the crystal and electric noise.

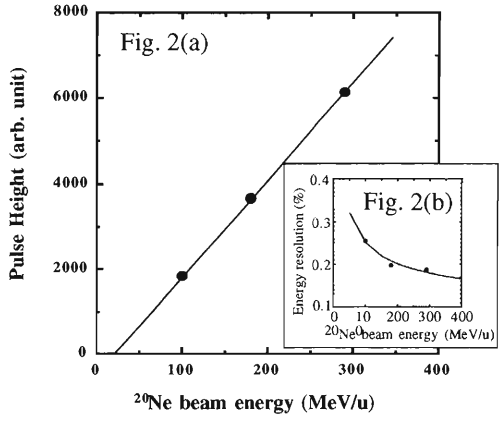

Fig. 2. (a) Light output, and (b) the energy resolution, as a function of the beam energy.

In this report, the Z- and A-dependence of the light output of a NaI(Tl) detector has been discussed. The light outputs of ^{8,9}Li, ^{11,12}Be, ^{14,15}B and ^{17,18}C have been measured at once at the RIPS facility. By correcting the light output and the energy deposit by a factor of MZ^2, the light output for a different Z nucleus is found to be reduced to a common function of the energy deposit.

The energy dependence of the NaI(Tl) light output to a heavy ion (^{20}Ne) beam has been extended to the energy of 300 MeV/u at HIMAC. No nonlinear effect of the light output is found, and the light output is confirmed to be proportional to the energy deposit in this energy region.

References

1) T. Suda et al.: RIKEN Accel. Prog. Rep. **35**, 171 (2002).
2) T. Suda et al.: RIKEN Accel. Prog. Rep. **35**, 42 (2002).
3) R. Kanungo et al.: Phys. Rev. Lett. **88**, 142502 (2002); T. Suzuki et al.: Phys. Rev. Lett. **89**, 012501 (2002).
4) M. Kurokawa et al.: RIKEN Accel. Prog. Rep. **24**, 42, (1991).
5) R. B. Murray and A. Meyer: Phys. Rev. **122**, 815 (1961).
6) N. Matsufuji et al.: Nucl. Instrum. Methods Phys. Res. A **430**, 60 (1999).

A novel position-sensitive detector using a pair of wedge-shaped scintillators

T. Suda, B. Louis,*1 R. Kanungo, T. Ohnishi, I. Tanihata, and Y. Yamaguchi*2

The performance of a pair of wedge-shaped plastic scintillators as a novel position-sensitive detector for intermediate-energy heavy-ion beams has been studied. Figure 1 shows a schematic view of the wedge-shaped detector. Both ends of the wedge plastic scintillator are viewed using two phototubes, HAMAMATSU 6533.

Two wedge scintillators are arranged as shown in Fig. 1, to obtain a constant thickness for particles passing through the detectors. Since the energy loss of a particle in one of the wedge detector depends linearly on the vertical (y) position while maintaining the total energy deposit constant, one is able to determine the y position by comparing the energy loss between both wedge detectors.

The horizontal (x) position is determined by the time difference of signals from the two phototubes.

The performance of the detector has been studied using a ^{20}Ne beam of 70 MeV/A at the E1C beam line of the RIKEN Ring Cyclotron (RRC). The beam size at the focus, where the wedge detector was placed, was tuned to be large enough to cover the vertical size of the detector. A 1-mm slit was used to define the horizontal position of the beam on the wedge scintillator.

The horizontal position resolution determined by the time difference of phototubes is 1.3 mm in sigma. The effective light velocity, determined by changing the horizontal position of the slit, is 37% of the speed of light. The reason for this small light velocity in the wedge-shaped scintillator is not yet clear. The intrinsic time resolution of each wedge detector is found to be 28 ps in sigma.

Figure 2 shows the pulse height correlation of the two wedge detectors. Here, pulse height is obtained by multiplying the pulse heights of the two phototubes after correcting for pedestals, then taking its square root.

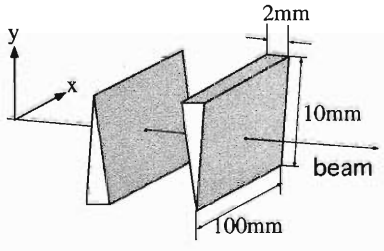

Fig. 1. A pair of wedge-shaped plastic scintillators.

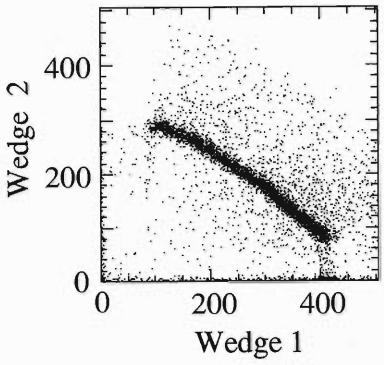

Fig. 2. Energy loss correlation between two wedge detectors.

As seen in Fig. 2, there is a clear correlation between the energy losses in the wedge detectors, showing a constant energy loss of 197 MeV in the two wedge scintillators. by knowing the minimum and maximum pulse heights corresponding to the detector height of 10 mm one can determine the vertical position. The resolution of the vertical position estimated from this correlation is 300 μm in sigma.

It is interesting to note here that the energy-loss correlation in Fig. 2 shows a small zigzag structure if observed carefully. This zig-zag structure may be attributed to the non-uniform surface of the wedge detector, generated during a polishing process. Since the vertical resolution is 300 μm, this system is sensitive to a surface uniformity of a few 10 μm.

As conclusions of this study, we have studied the performance of a new position-sensitive detector using a pair of wedge-shaped plastic scintillators. The position resolutions were 1.3 mm and 300 μm for horizontal and vertical positions from the time difference of phototubes at both ends, and the pulse height correlation of the two wedge detectors, respectively.

Since this detector having a good position resolution in addition to a good timing characteristic is easy to fabricate and operate at a high counting rate, several applications can be foreseen for experiments involving energetic heavy ions.

*1 Ecole des Mines de Nantes, France
*2 Niigata University

Development of NaI(Tl) detector array for in-beam γ-ray spectroscopy

S. Takeuchi, T. Motobayashi, H. Murakami,* K. Demichi,* and H. Hasegawa*

A new array of NaI(Tl) detectors is under development to be used in studying structures of unstable nuclei by in-beam γ-ray spectroscopy. A similar array has been successfully applied to studies of unstable nuclei such as Coulomb excitation, proton and alpha inelastic scattering, and fragmentation reactions.[1–4] In the present facility and the RI beam factory (RIBF), unstable nuclei are provided as fast secondary beams, and γ rays emitted from fast-moving residual nuclei of secondary reactions with appropriate targets are to be detected. One is able to determine the transition probability, excitation energy, and level scheme of the nuclei by detecting γ rays coincident with residual nuclei.

The present development is aimed at improving the detection efficiency and energy resolution, which are crucial for detailed spectroscopy of very unstable nuclei under a very-low-intensity beam, such as that with γ-γ coincidence. Since the γ-ray energy is Doppler-shifted depending on the emission angle with respect to the direction of the residual nuclei, a high angular resolution of the detection system is necessary for a high energy resolution after Doppler-correction.

We have designed a detection system with improved angular resolution and γ-ray detection efficiency.[5] It consists of 160 NaI(Tl) scintillators surrounding the target. Each scintillator is of rectangular shape with a size of $40 \times 80 \times 160\,\mathrm{mm}^3$, coupled to a 38-mm-$\phi$ photomultiplier tube, and its intrinsic resolution is around 8–9% at 662 keV (^{137}Cs). Sixteen layers, each of which consists of 5–12 scintillators, are arranged coaxially with respect to the beam axis, and are closely packed to cover the angular range of 16–164°. The distance from the target is 35 cm for the layer around 90°. Each detector is supported by a 5-mm-thick aluminum plate which is mounted at 5 cm intervals. The angular resolution of γ-ray detection is about 7° at 90°, where the Doppler effect is largest, which is much better than that of about 20° for the previous NaI(Tl) array.

The efficiency and the γ-ray energy resolution were estimated by means of the GEANT code[6] to be 21% and 7.5% (FWHM), respectively, at $E_\gamma = 1\,\mathrm{MeV}$ with $\beta = v/c = 0.3$ for the full array. These values are better than those for the previous array consisting of 68 NaI(Tl) scintillators, which were about 15% and 11% (FWHM) at $E_\gamma = 1\,\mathrm{MeV}$ with $\beta = 0.3$.

Half of the NaI(Tl) array has already been completed (see Fig. 1) and used in several experiments. The improvement of the energy resolution for the present array is demonstrated in γ-ray energy spectra

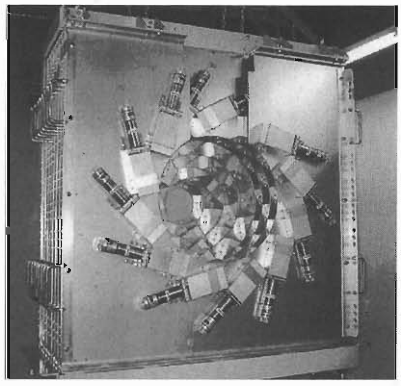

Fig. 1. Half of the NaI(Tl) array.

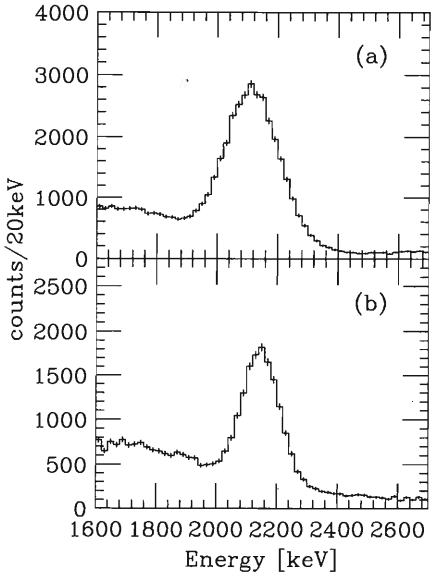

Fig. 2. Doppler-corrected spectra of γ-rays coincident with ^{12}Be in the inelastic scattering of ^{12}Be with a liquid-helium target. (a) Spectrum obtained with the previous NaI(Tl) array. (b) Spectrum obtained with the present NaI(Tl) array.

obtained in two independent experiments as shown in Fig. 2. The conditions of the two experiments are almost the same, (secondary beams of ^{12}Be with $\beta \simeq 0.3$ on a liquid helium target), except for the γ-ray detectors. Figure 2 (a) and (b) shows the Doppler-corrected γ-ray spectra taken with the previous and new NaI(Tl) arrays,[3] respectively. Full energy peaks are observed at around 2.1 MeV corresponding to the $2^+ \rightarrow 0^+$ transition in ^{12}Be. A difference in the energy resolution

* Department of Physics, Rikkyo University

is clearly seen. The widths of the peaks are around 200 keV (FWHM) and 140 keV (FWHM) for the previous and the new array, respectively.

The other half of the array will be built during the year 2003 to form a complete setup. We plan to reduce the thickness of the aluminum supports to increase efficiency. This will lead to a total efficiency of about 5% for 1 MeV photons from moving sources with $\beta = 0.3$.

References

1) H. Iwasaki et al.: Phys. Lett. B **522**, 227 (2001).
2) H. Iwasaki et al.: Phys. Lett. B **481**, 7 (2000).
3) Y. U. Matsuyama et al.: RIKEN Accel. Prog. Rep. **35**, 53 (2002).
4) K. Yoneda et al.: Phys. Lett. B **499**, 233 (2001).
5) H. Hasegawa et al.: RIKEN Accel. Prog. Rep. **35**, 169 (2002).
6) GEANT3: *Detector Description and Simulation Tool* (CERN, Geneva, 1993).

Position extraction from a segmented Ge-detector with planar geometry

M. Kurokawa,[*1] S. Shimoura,[*1] H. Iwasaki,[*1] H. Baba,[*2] S. Michimasa,[*1] S. Ota,[*3] M. Tamaki,[*1] H. Murakami,[*2] and H. Sakai[*1]

In the γ-ray spectroscopy with Ge-detectors, the energy correction of Doppler-shifted γ-rays has been performed using the granularity of a detector array. Recent progress in the spectroscopy with fast radioactive-isotope (RI) beams requires higher granularity than that has ever been achieved in order to obtain an energy resolution higher than a few tens of keV for a moving source with around 30% of the light velocity. The higher granularity is accomplished by extracting the position information from a Ge-detector. In this article, the method of extracting the position information is introduced and the expected resolution obtained by the method is discussed for the detector adopted in the array of Center for Nuclear Study (CNS), the University of Tokyo.

As seen in the schematic view of the detector (Fig. 1), the detector has a planar structure and the front side is divided into nine segments. Each segment is identified with the number given in the figure. The signal from a segment is called net charge signal or transient signal, depending on whether the segment contains the interaction point or not. The analog sum of all of the nine signals is defined as total signal. The cylindrical coordinate system (r, ϕ, z) is applied to express the position within the detector of cylindrical shape with the thickness of 2.0 cm and the diameter of 7.0 cm.

The position information with a smaller unit than the segment size is obtained by analyzing the pulse shapes. The method of analysis is determined based on the simulated relationship between the interacting point and the pulse shapes. The accuracy of the prediction was experimentally confirmed.[1)]

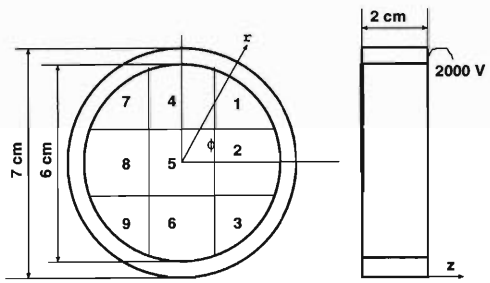

Fig. 1. Schematic view of the segmented Ge detector adopted in the array of CNS. Each segment is identified with the number indicated in the figure. Position within the detector is expressed by the cylindrical coordinate system (r, ϕ, z).

The simulated relationship is that the maximum amplitude of the transient signal is correlated with the distance between the interacting point and the segment border, as shown in Fig. 2. For the interactions in segment #2 with $\phi = 0°$, the maximum amplitude of the transient signal from segment #5 is given as a function of r both for the simulated and the experimental results in the figure. The simulated results are well reproduced by the experimental data. Based on the simulated correlation seen in the figure, the present noise level, which is almost comparable to the size of the symbol, corresponds to the position resolution higher than 1 mm in the region of $r < 2.0$ cm. On the other hand, in the edge region of the detecor and in the vicinity of $z = 6$ mm, extraction of the position information seems difficult due to the weak correlation.

Another simulated relationship is the rise time dependence on z, as shown in Fig. 3, where the interval of the time of 10% and 90% charge collection T_{19} is given as a function of z both for the simulated and observed pulse shapes of the total signals. To exclude the dependence on r and ϕ, the interacting points for the signals were restricted to be $r < 2.0$ cm.[1)] Simulated parabolic dependence is supported by the experimental results. However, the dependence is different from what is seen in the planar detector with a large number of strip electrodes both for the front and the back side of the detector. In the detector, the rise times obtained from the two sides exhibits a monotonic increase and decrease as a function of z due to the small

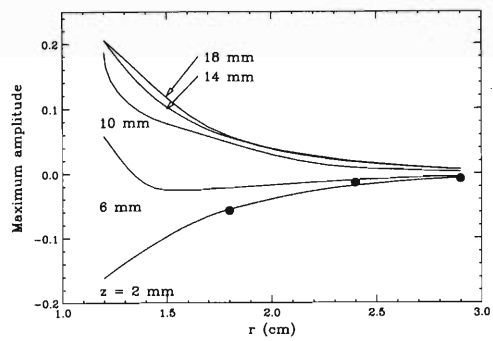

Fig. 2. Measured maximum amplitude of the signal from the segment #5 is plotted as a function of r together with the simulated results (solid curves) for the interactions in the segment #2 with $\phi = 0°$.

*1 Center for Nuclear Study, University of Tokyo
*2 Department of Physics, Rikkyo University
*3 Department of Physics, Kyoto University

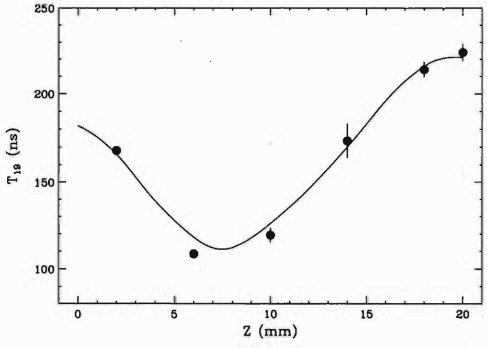

Fig. 3. Rise time T_{19} (see text) is plotted as a function of z for the observed pulse shapes of the total signals together with that obtained from the simulation (solid curve).

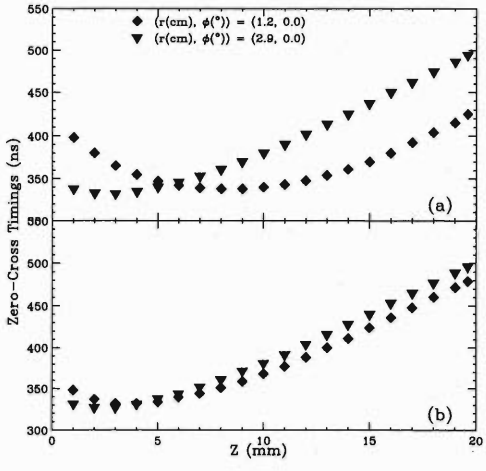

Fig. 4. Simulated zero-cross timings (see text) are plotted for the total signals (a) and the net charge signals (b).

pixell effect.[2] Hence the difference of the two timings extracted from the front and the back side gives a good measure of z.[3] For the present detector, on the contrary, the difference of the two timings for the total signal and the net charge signal is not appropriate for the evaluate of the z value due to the disappearance of the effect in the total signal, though the behaviour of the total signals from the region of $r < 2.0\,\mathrm{cm}$ is the same with that of the signals extracted from the back side of the detector except for their polarities. Two timings should be recorded simultaneously for the detector of the present type.

In Fig. 4, the two timings are plotted as a function of z for the total signals (upper panel) and the net charge signals (lower panel). In the figure, the zero-cross timing after $(CR)^2 - (RC)^4$ shaping of each signal[4] is simulated instead of T_{19} to examine the performance of the analog processing. Here, CR and RC denote the differential and the integration, respectively. Both of the shaping times are set to be 50 ns by considering the range of the rise time. The parabolic shape for the total signal is well reproduced by the timing in the case of $r = 1.2\,\mathrm{cm}$. For the net charge signals, the small pixell effect appears as an increasing function in a wider range of z than that for the total signals. Thus, the rise time dependence on z is well reflected in the timing obtained by the shaping.

Each timing information allows the spread of the extracted z value for the events with $\phi = 0°$ as seen from the figure, and the resultant z value obtained by applying the two timings has still a finite width of around a few millimeters. Hence, the two timings give rough position information on z. In order to eliminate the ambiguity, position information on r is useful. Therefore, the resultant resolution along the direction of z is expected to be improved up to the grade of that along the direction of r for the events with $\phi = 0°$.

References

1) M. Kurokawa et al.: Conf. Rec. of the 2002 IEEE Nucl. Science Symp. and Medical Imaging Conf., Norfolk, USA, 2002-11, to be published.
2) H. L. Malm et al.: Appl. Phys. Lett. **26**, 344 (1975).
3) M. Momayeji et al.: Proc. SPIE **3768**, 530 (1999).
4) G. F. Knoll: *Radiation Detection and Measurement*, 2nd ed., (John Wiley & Sons, New York, 1989).

Position sensitivity of a segmented planar Ge detector

E. Ideguchi, B. Cederwall,[*1] T. Bäck,[*1] L. Milechina,[*1] Y. Gono,[*2] Y. Yang,[*2] T. Teranishi,[*3] N. Aoi,[*4] D. Bucurescu,[*5] and T. Kishida

In the measurement of γ-rays emitted in a nuclear reaction, energy resolution is often deteriorated by the Doppler-broadening effect. In order to reduce and correct the effect, a Ge telescope system consisting of a segmented planar Ge detector[1] and a clover Ge detector[2] has been developed.[3] The planar Ge crystal of 5 cm × 5 cm with 2 cm thickness is used as a transmission-type ΔE counter. It has a 25-fold electrically segmented cathode electrode and one anode electrode on the opposite side of the Ge crystal. The size of each segment is 1 cm × 1 cm. The clover Ge detector was used as an E counter. Doppler broadening is reduced due to the small solid angle of each segment of the planar Ge placed in front. By applying a tracking technique recently developed for highly segmented Ge detectors[4–7] to the current detector systems, we aim to obtain a higher effective granularity and therefore a better Doppler correction. A necessary feature is that a sufficiently high position sensitivity for γ-ray interactions in the detector volume can be obtained. In this report we present results from a preliminary study of pulse shape measurements on the segmented planar Ge detector and the deduced position sensitivity for single γ-ray interactions.

In order to determine how the pulse shapes of signals produced in the Ge detector depend on the location of the interaction points, it was necessary to create experimental conditions where primarily single-interaction events are considered. This was achieved by irradiating the segmented planar Ge detector with a collimated ^{137}Cs γ-ray source and requiring coincidence between this detector and another (coaxial) Ge detector. The spot size of the ^{137}Cs source was approximately 1 mm across. The coaxial detector was also collimated by a Pb slit collimator in order to detect only γ-rays scattered at 90° to the segmented detector. Energy gates were then applied to the detector signals in order to select single-Compton-scattering events. The segmented planar detector was placed in a fixed position and the collimators were fixed on a Cu plate. The irradiation depth was determined by changing the distance between the collimator setup and the planar Ge (see Fig. 1). In this case, the energy of the Compton-scattered γ-rays is 288 keV and the energy deposited in the planar Ge detector is 374 keV. The hole size of the

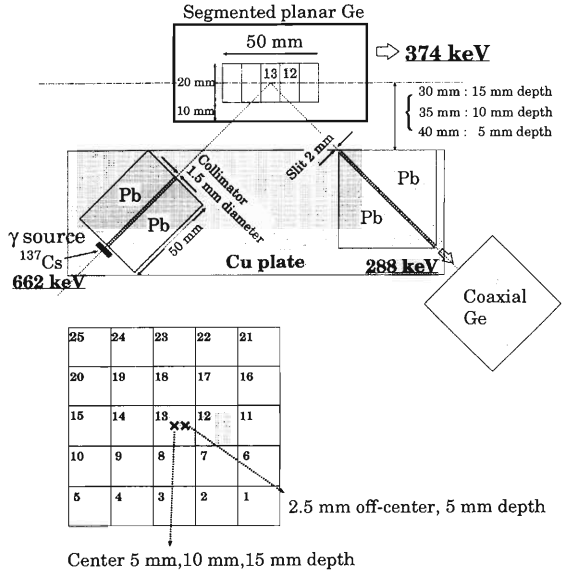

Fig. 1. Setup with segmented planar Ge detector, Pb collimator and slit. The four irradiation points are indicated.

Pb collimator and the width of the slit were chosen to be 1.5 mm and 2 mm, respectively. The event rate was about one event per twenty minutes. The uncertainty in the position determination of the γ-ray interactions due to the collimator setup was extracted from simulations. Gamma rays were irradiated to the central segment (# 13) of the crystal, and the output signals from the cathode element # 13 and the adjoining cathode element # 12 were used to obtain the net-charge and mirror-charge pulse shapes. In the measurement, three different interaction depths of 5 mm, 10 mm, and 15 mm in the center of the segment # 13 were chosen as well as one interaction point at 5 mm depth but 2.5 mm off-center.

We define T_{50} as the earliest time at 50% of the maximum amplitude of the pulse, and it was used as a measure of the arrival time of the charge at the anode relative to the timing of the CFD output of cathode segment # 13. The experimental T_{50} values for different interaction points are plotted in Fig. 2, and clear differences of T_{50} values are seen for three different interaction depths.

The uncertainties in the T_{50} values are primarily a combination of the geometrical uncertainty due to the Pb collimators and effects intrinsic to the detector such as electronic noise, charge trapping *etc.* The intrinsic position sensitivity of the detector (for single interactions) can therefore be unfolded by removing the geometrical contribution as estimated from the

*1 Department of Physics, Royal Institute of Technology, Sweden
*2 Department of Physics, Kyushu University
*3 Center for Nuclear Study, University of Tokyo
*4 Department of Physics, University of Tokyo
*5 Horia Hulubei National Institute of Physics and Nuclear Engineering, Romania

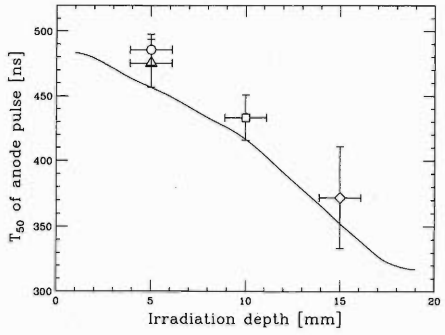

Fig. 2. Plots of T_{50} as a function of depth of interaction. The solid curve corresponds to the simulation. Error bars in the transverse direction are geometrical uncertainty estimated by simulations and those in the longitudinal direction are measured T_{50} distribution.

simulations. In Table 1, ΔZ_{T50} indicates the width of the T_{50} distribution, which is converted to that of depth based on the relation between T_{50} and interaction depth shown in Fig. 2, and ΔZ shows the estimated position sensitivity after removing the geometrical contribution. The large ΔZ_{T50} value, $\sim$2.5 mm, for the case of 15 mm depth arises from the large spread in the T_{50} distribution. From Table 1, we may conclude that an intrinsic position sensitivity for single interactions is $\sim$2 mm on average for the depth direction.

In order to gain an understanding of the measured signals from the segmented Ge detector and the relations between pulse shape and the interaction position, we have performed simple model calculations. Signals are produced by the movements of charge carriers, produced by the ionization from Compton interactions. The charge carriers induce image charges on the electrodes and the measured signals correspond to the image charge currents flowing into or out of the electrodes. In the present case of a planar segmented detector, the induced charges can readily be calculated using the method of imaginary charges. The induced charge on a given electrode will be formed by an infinite series of imaginary charges at increasing distances. A calculated T_{50} curve as a function of interaction depth reproduces well the experimental distribution of T_{50} values for different interaction points as seen in Fig. 2.

The present measurement was also carried out at two irradiation points for the transverse direction, *i.e.* at the center and at 2.5 mm from the center towards segment # 12. Since the signals from only two of the adjoining segments were acquired, limited information on the dependence of mirror charge pulses on the transverse position was obtained.

Table 1. Position sensitivity for 374 keV single γ-ray interactions at different depths deduced from the measured T_{50} distributions (second column) and after unfolding the geometrical uncertainty from the collimators (third column).

Depth(Z) [mm]	ΔZ_{T50} [mm]	ΔZ [mm]
5	1.8 (7)	1.4 (9)
5 (2.5 mm right)	2.7 (11)	2.5 (12)
10	1.7 (6)	1.1 (10)
15	3.0 (7)	2.7 (8)

The amplitudes of induced pulses in neighboring segments are strongly dependent on the transverse position of the irradiation point and less affected by the depth of interaction. Figure 3 shows the absolute value of the maximum amplitude of mirror-charge pulses as a function of interaction depth. The error bars for the experimental data points arise from the geometrical uncertainty and from fluctuations of the pulse heights due to electronic and statistical noise. The calculated curves are in fair agreement with the experimental data. The change of curvature around 5 mm depth arises from the change of polarity of the pulses in this region.

From this study, we may conclude that the transverse position can be determined from these signals, probably with similar accuracy as the depth of interaction. In order to determine systematic trends of the mirror charge signals, our present investigation needs to be complemented by further studies for this type of detector geometry.

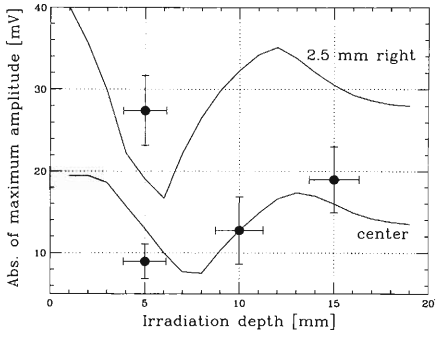

Fig. 3. Absolute values of the maximum amplitudes of mirror-charge pulses plotted as a function of interaction depth. Experimental data and corresponding calculated curves are shown.

References

1) E. Ideguchi et al.: RIKEN Accel. Prog. Rep. **27**, 121 (1994).
2) P. M. Jones et al.: Nucl. Instrum. Methods Phys. Res. A **362**, 556 (1995).
3) Y. Gono et al.: Nucl. Phys. A **588**, 241c (1995).
4) M. A. Deleplanque et al.: Nucl. Instrum. Methods Phys. Res. A **430**, 292 (1999).
5) G. J. Schmid et al.: Nucl. Instrum. Methods Phys. Res. A **430**, 69 (1999).
6) J. van der Marel and B. Cederwall: Nucl. Instrum. Methods Phys. Res. A **437**, 538 (1999).
7) K. Vetter et al.: Nucl. Instrum. Methods Phys. Res. A **452**, 223 (2000).

DOI measurement performance of segmented planar germanium detector for MT-GREI

S. Motomura, Q. Y. Pan, M. Kibe,* Y. Gono, S. Enomoto, Y. Yano, and K. Asahi

Development of a Compton camera for multitracer γ ray emission imaging (MT-GREI) is being carried out in order to realize noninvasive and simultaneous imaging of various radioisotopes distributed in a sample.[1] The Compton camera consists of two segmented planar germanium (Ge) detectors which are placed in parallel. If an incident γ ray is Compton scattered in the first detector and then the scattered γ ray is fully absorbed in the second detector, a cone can be defined from the energy and position of the interactions which are measured by each detector. The cone indicates the incident angle of the γ ray. Then the image of the radioisotopes is reconstructed from the cones collected over many Compton scattering events. Thus the precision of measuring the position of the interaction points seriously affects the quality of the reconstructed image.

We have simulated the pulse shapes of the output signals obtained by the existing segmented planar Ge detector, in order to investigate the dependence of the pulse shape on the depth of interaction point (DOI). The dimensions of the detector are 50 mm × 50 mm × 20 mm, and the cathode is segmented into 25 square pixels whose dimensions are 10 mm × 10 mm. The cathode is grounded and bias voltage of +3000 V is applied between the anode and the cathode.

As a result of the interaction of a γ ray in Ge crystalline material, electron-hole pairs are excited. Those charge carriers drift according to the electric field generated by the bias voltage. The electric field in the crystal is altered by the movement of the charge carriers, and charges are induced on each electrode. Those induced charges are amplified by the charge-sensitive preamplifiers.

The amount of the induced charges on each electrode is deduced by the summation of the separately calculated charges for electrons and holes. In order to calculate the amount of charges induced by a point charge, the electrical potential made by the point charge was calculated by numerically solving the Poisson's equation (Fig. 1). The electric field was deduced from the gradient of the electric potential. Then the amount of the charges induced by the point charge was calculated by integrating the electric field on the surface of each electrode. Positions of the electron and hole were calculated every 2 ns and the amount of induced charges on each electrode was calculated as a function of time. Then the pulse shape of the output signal was calculated by including the response of the preamplifier.

The results of calculations presented in this report

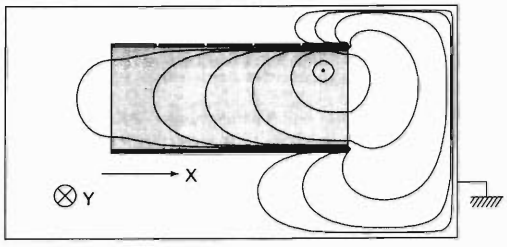

Fig. 1. Calculated electrical potential made by a point charge located in the Ge crystal.

were obtained when the interaction position in X- and Y-direction was fixed at: (1) $X = 0$ mm, $Y = 0$ mm (center) or (2) $X = 20$ mm, $Y = 0$ mm (edge), where the origin of the coordinate axes was the center of the crystal. Furthermore, only the signal from the segment containing the interaction point was considered.

When the interaction position was fixed at the edge, we calculated the time taken until the amplitude of the signal reaches x % of the maximum since occurrence of the interaction (T_x). The dependence of T_x on DOI is shown in Fig. 2. If the bigger x is taken for the T_x of anode, the dependence of the T_x on DOI becomes clearer. However, due to the turnover observed at the

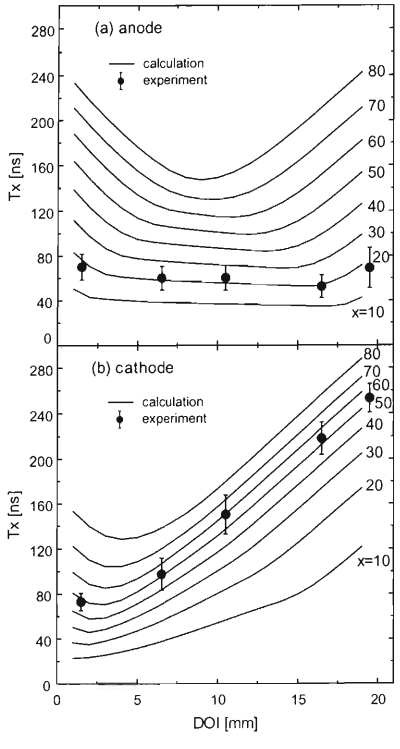

Fig. 2. DOI dependence of T_x.

* Graduate School of Science, Kyushu University

middle depth, DOI can not be deduced directly from T_x of anode. On the other hand, one-to-one correspondence of DOI to T_x of cathode can be obtained except at the shallow DOI region. Then $T_{x,y}$ was introduced, where $T_{x,y}$ is the time difference calculated by subtracting T_y of anode from T_x of cathode. It was found that the clearest one-to-one correspondence of DOI to $T_{x,y}$ is obtained if 50 and 20 are chosen for x and y, respectively. DOI as a function of $T_{50,20}$ is shown in Fig. 3. DOI can be measured using this curve.

The performance of DOI measurement using $T_{x,y}$ was tested by a test experiment using the existing segmented planar Ge detector. The geometry of the experimental setup is shown in Fig. 4. The γ rays emitted from the ^{137}Cs γ-ray source were collimated in order to irradiate only one segment at the edge of the crystal. DOI of the γ ray entering the coaxial Ge detector was limited by the lead slit placed between the segmented Ge detector and the coaxial Ge detector. Single Compton scattering events were collected by coincidence measurement between the irradiated segment and the coaxial Ge detector. Five measurements were carried out at various depths of the slit position:

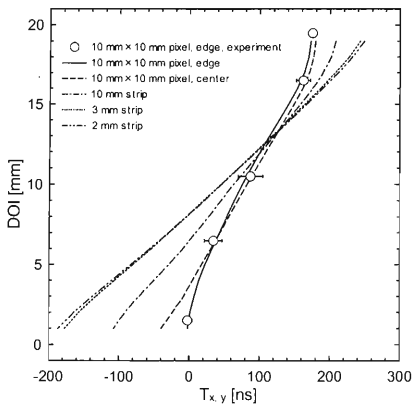

Fig. 3. DOI vs. $T_{x,y}$. The experimental values were fitted by adjusting the zero point.

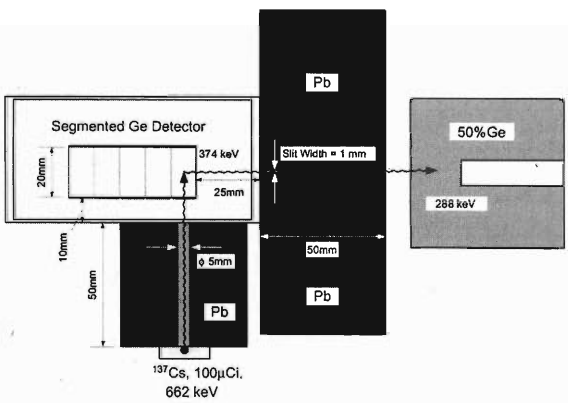

Fig. 4. Experimental setup used to investigate the performance of DOI measurement.

1.5 mm, 6.5 mm, 10.5 mm, 16.5 mm and 19.5 mm.

The experimental T_x was extracted by the constant fraction triggering method. The x for the cathode was fixed at 50, and the x for the anode was adjusted so that the widest distribution of $T_{x,y}$ could be obtained. T_x was measured taking the timing signal of the coaxial Ge detector as the reference. The measured data agreed well with the calculated curves of T_{20} for anode and T_{50} for cathode (Fig. 2).

The experimental $T_{x,y}$ was deduced from the experimental T_x. The experimental values were fitted to the calculated curve by taking the zero point of the $T_{x,y}$ as a parameter. The fit of the experimental values to the calculated curve is very good as shown in Fig. 3. Precision of DOI measurement attained by the experiment was deduced by using the calculated curve and the result of the simulation performed using GEANT3[2] (Table 1).

$T_{x,y}$ was also calculated when the interaction position was fixed at the center. In this case, the slope of the curve is preserved even at the shallow DOI region. If the time resolution of the system is constant, uncertainty of DOI measurement is proportional to the slope of the curve. Therefore, it is expected that the precision of $\sim$2 mm is obtained even at the shallow DOI region in this case.

Moreover, $T_{x,y}$ was calculated for double-sided orthogonal-strip Ge detectors with the strip widths of 10 mm, 3 mm, and 2 mm. The calculation was carried out when the interaction position was fixed at the center. The result of this calculation is shown in Fig. 3. In the 10-mm-strip case, the precision of DOI measurement is expected to be 1.5 times better than in the 10 mm × 10 mm-pixel case considering the slope of the curve, even though the number of segments is the same. This is because one-to-one correspondence of DOI to T_x can be obtained from both anode and cathode. In the 2-mm-strip case, precision of DOI measurement is expected to be less than 1 mm, and in the 3-mm-strip case, almost the same precision of DOI measurement as in the 2-mm-strip case is expected.

Table 1. Deduced precision of DOI measurement attained by the experiment.

DOI (mm)	Precision of DOI in FWHM (mm)
1.5	3.1
6.5	1.5
10.5	2.2
16.5	1.5
19.5	3.7

References

1) Y. F. Yang et al.: IEEE Trans. Nucl. Sci. **48**, 656 (2001).
2) GEANT3: *Detector Description and Simulation Tool* (CERN, Geneva, 1993).

Performance study of the strip germanium telescope

M. K. Suzuki,* N. Aoi,* N. Imai,* and H. Sakurai*

The Strip Germanium Telescope (SGT) is a γ-ray spectrometer designed by our group to have high position and energy resolutions with a reasonable efficiency even for high-energy γ-rays around 1–2 MeV. The SGT is capable of in-beam γ-ray spectroscopy using fast RI beams (β = 0.3–0.5) in which an accurate Doppler shift correction is required. For the Doppler shift correction, the polar angle of the γ-ray emission, or the detection position along the beam axis is necessary. The SGT has been developed to realize this requirement with a simple configuration. In this article, we report on the performance study of the SGT using a ^{12}Be beam provided by RIPS as well as that using a standard γ-ray source.

The major design concept for the SGT stems from the combination of the position-sensitive detector (the planar crystal) and the energy measurement detector (the coaxial crystal). As shown in Fig. 1, these crystals have dimensions of 50 mm × 50 mm × 20 mm (planar) and ϕ 70 mm × 70 mm (coaxial). The coaxial crystal is placed behind the planar crystal in the same cryostat. The planar crystal has twenty-five 2-mm-wide strip electrodes, and each signal is read out individually. A sum amplifier is used to sum up all the signals including all the strips and the coaxial.

The thickness of the planar crystal is chosen to be comparable to the Compton absorption length of 1 MeV γ-rays so that the γ-rays are mostly Compton-scattered once in the planar crystal and the scattered γ-rays can escape from the planar crystal. The Compton scattering has a forward-peaked angular distribution, and thus, the scattered γ-rays mostly hit the coaxial crystal. The volume of the coaxial crystal is large enough to absorb the scattered γ-rays with high probability. In this process, the position of the first hit is determined from the position of the electrodes which have a signal, and the total energy from the sum of the energy deposits in the two crystals. Compared with more sophisticated detectors, such as γ-ray tracking arrays,[1] this method has an advantage of simplicity by omitting the capability of full γ-ray-tracking, which is not necessary for the Doppler shift correction. The good position resolution of the SGT allows us to use the detector in in-beam experiments even at angles around 90 degrees with respect to the beam axis, where the angular resolution dominates the accuracy of the Doppler shift correction.

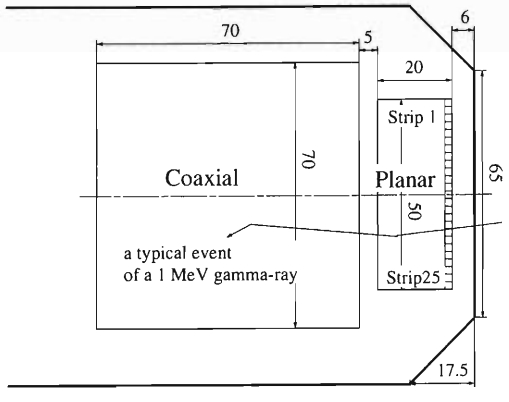

Fig. 1. The Strip Germanium Telescope.

Basic performances of the SGT were obtained using a ^{152}Eu source. The source was placed 15 cm away from the surface of the can. The 1408 keV γ-rays were used to determine the energy resolutions, and the efficiency for each strip in the planar as well as that of the coaxial crystal. Relatively high-energy γ-rays were used to create many Compton scattering events in the planar.

The detection efficiency was determined for the following cases; (a) a γ-ray is absorbed in the planar, (b) a γ-ray is Compton-scattered in the planar and then absorbed in the coaxial, and (c) a γ-ray is absorbed only in the coaxial. Cases a and b are further classified according to the hit pattern of the strips; (a-1 and b-1) only one strip has a signal, and (a-2 and b-2) neighboring two strips have signals. The efficiency for the cases a-1, a-2, b-1, b-2, and c are 1.2×10^{-5}, 1.6×10^{-4}, 9.4×10^{-5}, 2.7×10^{-4}, and 3.5×10^{-4}, respectively. The sum of the efficiency for the cases a and b, which can be used for position determination, is 7.4×10^{-4}.

The intrinsic energy resolutions of individual the strips and coaxial are typically 2.5 keV (FWHM) for single-hit events. For multi hit events, the resolution of the energy sum is typically 10 keV. The bad resolution for multihit events is due to cross-talk between neighboring strips or between the coaxial and one of the strips. The cross-talk is not due to the so-called mirror charge effect, but probably due to a problem of the integrated cabling around the pre-amplifier, which is now under investigation. Although the resolution is not very good, it is acceptable for in-beam experiments, in which other factors may dominate the resolution.

To demonstrate the performances of the SGT for the actual in-beam experiment, we have tested the SGT in an inelastic scattering of ^{12}Be (E = 45.7A MeV, β = 0.30) with a 1-mm-thick plastic target at RIPS. Figure 2 shows the preliminary spectra of γ-rays with (top) and without (bottom) the Doppler shift correc-

* University of Tokyo

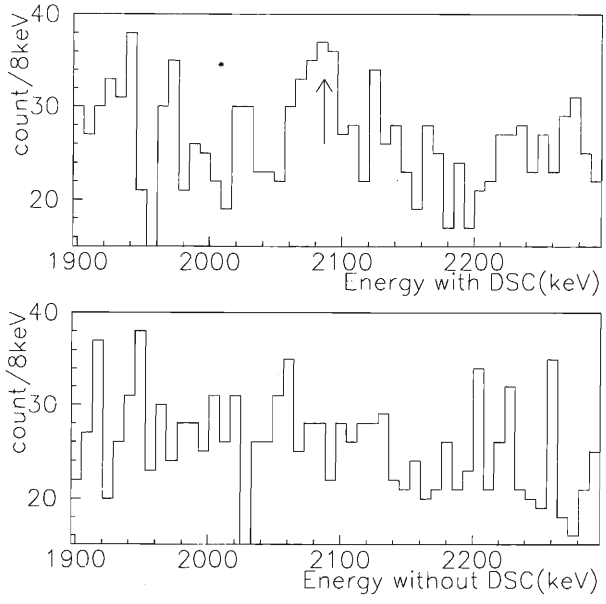

Fig. 2. γ-rays energy spectrum with (top) and without (bottom) the Doppler shift correction, observed by the Strip Germanium Telescope.

tion. The detected point used in the Doppler shift correction was assumed to be the center of the hit strips. The 2.1 MeV peak due to the ground state transition from the first excited state in ^{12}Be is clearly seen in the top panel, whereas no peaks are observed in the bottom panel. This shows that the Doppler shift correction is appropriately performed. The width of the peak is approximately 30 keV, which is broader than the one estimated from the basic performance mentioned above. The unexpected energy resolution is due to insufficient parameter-tuning performed in the analysis.

The validity of the position sensitivity and reasonable detection efficiency of the SGT are shown in the above measurements. In future experiments, better energy resolution should be obtained by improving the electronic circuits and the analysis procedure. Owing to the good position resolution, the SGT can be placed very close to the target keeping the capability of the accurate Doppler shift correction, which makes the detection efficiency significantly larger. For example, the detection efficiency of 0.7% with the energy resolution of approximately 1% would be obtained by placing the SGT 5 cm from the target.

References

1) GRETA: Nucl. Phys. A **582**, 286 (2001).

Responses of HPGe detectors to high-energy charged particles

T. Yakushiji,[*1] R. Taki,[*2] T. Kobayashi,[*1] Y. Seki,[*1] H. Okamura,[*3] H. Akiyoshi, K. Sekiguchi, N. Sakamoto, and A. Goto

Two types of high purity Ge (HPGe) detectors for charged particles have been studied: a stack-type planar HPGe detector for protons and a semiplanar HPGe detector for heavy ions.

The stack-type detector consists of six planar HPGe crystals in a cryostat, each of which has a 60 mm sensitive diameter and 20 mm thickness, separated by 3 mm, and a Be entrance window of 400 μm thickness. This detector was fabricated for the purpose of measuring protons from the $(p, 2p)$ reaction. Protons up to 260 MeV can be stopped in the detector.

The test experiment was carried out using protons accelerated up to 210 MeV by the RIKEN Ring Cyclotron (RRC). Protons elastically scattered by a gold strip target were momentum-analyzed at $\theta = 7°$ by the magnetic spectrograph SMART. Passing through a vacuum window (50-μm Kapton), they were detected at the second focal plane by a multiwire drift chamber, which determines the proton momentum, and by HPGe located downstream of the drift chamber (Fig. 1 (a)). This setup allows us to determin the proton energy better than the energy spread of the primary beam from RRC. The observed energy resolution of HPGe is 0.082 MeV (rms); the main contribution is the energy-loss straggling in the Be window, which is estimated to be 0.06 MeV (rms). The spread of time difference between the first and second crystals is 0.20 ns (rms), which corresponds to the time resolution of 0.14 ns (rms) for one crystal. It proves that the timing signal from HPGe, if it detects protons, can be used as a trigger.

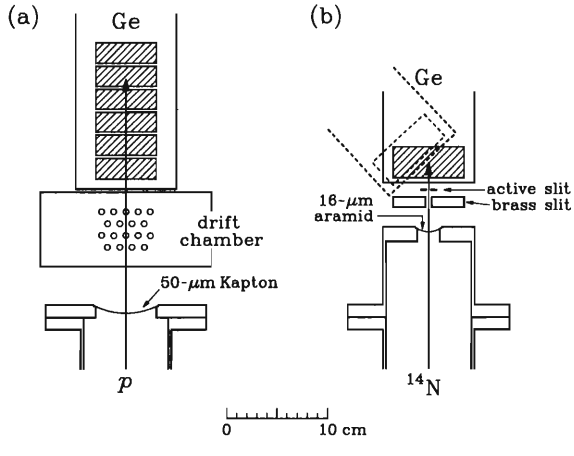

Fig. 1. Detector setup for (a) the stack-type and (b) semiplanar HPGe detectors.

The second type of HPGe detectors, consisting of a semiplanar HPGe crystal with 30 mm thickness and 70 mm sensitive diameter and a Be entrance window of 300 μm thickness, was used to test its response to ^{14}N at 135 MeV/nucleon as a typical heavy ion beam. Since its range is about 1 cm, this type of HPGe detectors can serve as compact energy detectors for the measurement of longitudinal emittance of the RRC beam, which is important for the operation of RI-beam factory. However, the energy resolution of HPGe to energetic heavy ions is not well known.

^{14}N of 1890 MeV was elastically scattered by a gold strip target and momentum-analyzed at $\theta = 2°$ by SMART. In the case of heavy ions, the energy-loss straggling in the drift chamber is not negligible. Thus, after passing through a vacuum window (16-μm aramid), ^{14}N was collimated by a scintillator active slit with a 1-mm aperture, which corresponds to a momentum width of 0.01%, and detected by HPGe at the second focal plane (Fig. 1 (b)). The injection angle to HPGe was either normal or 43°, expecting to see the influence of the plasma effect on the charge collection. The observed energy resolution is 0.56 and 0.65 MeV (rms) at normal and 43° injection, respectively, after subtracting contributions from the energy-loss straggling in the Be window. Improvement of the charge collection expected for the inclined injection was not observed. Further study is in progress.

*1 Department of Physics, Tohoku University
*2 Department of Physics and Astronomy, Michigan State University, USA
*3 Department of Physics, Saitama University

Development of an RI-ion stopping gas chamber with the ion counting capability for RIAB

K. Shimada,[*1] K. Asahi, T. Ito,[*1] J. Kaihara,[*1] D. Kameda,[*1] Y. Kobayashi, H. Miyoshi,[*1] J. Murata, T. Okada,[*2] T. Saito,[*3] W. Sato, S. Suda,[*1] H. Ueno, H. Watanabe, and A. Yoshimi

A new method for the polarization of radioactive nuclei, which we call the Atomic Beam Method on Radioactive Isotopes (RIAB),[1)] is under development. In the RIAB method, a slow beam of neutral radioactive atoms is subjected to a sextuple magnetic field, under which those atoms with their spins parallel to the field (low field seekers) feel a focusing force while those with antiparallel spins (high field seekers) are diverged out from the beam line. After this spin-selection stage, atoms enter a region of a low, a homogeneous dipole field, a the magnetic resonance transition is induced between a particular pair of Breit-Rabi levels of an atom in flight. Finally, a second spin selection is carried out in a sextupole or a quadrupole field so that only those atoms whose spins are flipped by the magnetic resonance are transmitted through a slit located after it. In order for spin selection stages to be effective, a low energy of the atomic beam is essential. The radioactive nuclei produced by projectile fragmentation (PF) reactions, however, inevitably have high energies and wide energy distributions. We therefore adopt the following scheme to obtain a low-energy beam of neutral RI beams: RI ions produced by PF and separated by RIPS are stopped in a high-pressure He stopping gas which has a high first ionization potential, so that almost all the incident ions could not neutralize, and then are guided by a static electric field into an orifice region. There the ions are neutralized and the resulting atoms are transported by a gas flow to form a gas jet into vacuum.

In the present work, we fabricated and tested a stopping gas chamber which is also furnished with a function of a gas ionization chamber, so that direct counting of the ions stopped in the gas stopping chamber. The direct counting of the incident ions allows high-accuracy determination of the efficiency of the ion collection and jet formation processes.

A schematic of the gas stopping and counting chamber with the Frisch grid[2)] is shown in Fig. 1. The chamber is filled with a noble gas at a pressure as high as about 44 kPa. High voltages are supplied to the eight ring electrodes to form a static electric field distribution for the collection of the incident ions that are stopped in the stopping gas.[3)]

The anode collects electrons produced by incident ions in the stopping process in the gas chamber. From the measured anode signal, we estimate the number

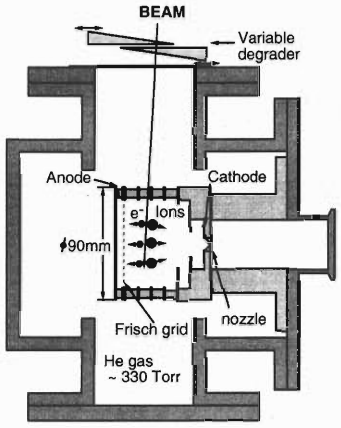

Fig. 1. The gas stopping ionization chamber.

of incident ions. In addition, we distinguish between the stopping and the passing-through events by observing the pulse corresponding to the Bragg curve which has a maximum near the end of the range, so that the pulse shape information is deduced from the comparison of the outputs of two shaping amplifiers with different shaping times. The pulse height of a signal after the short-time shaping essentially represents the Bragg peak height B, while the other signal with the long shaping time represents the integrated charge E.

A test experiment was carried out at RIPS. A beam of radioactive ions ^{12}B was produced from the fragmentation of ^{22}Ne projectiles on a 0.74 g/cm^2 thick ^{9}Be target at an energy of E/A = 94.2 MeV/u. The stopping gas was a He with the pressure of 42 kPa, and the voltages applied to the anode and the Frisch grid were 235 V and 180 V, respectively. The shaping times for E and B signals are chosen to be 6 μs and 3 μs, respectively. The correlation between the observed B and E signals is shown in Fig. 2. In this run, the

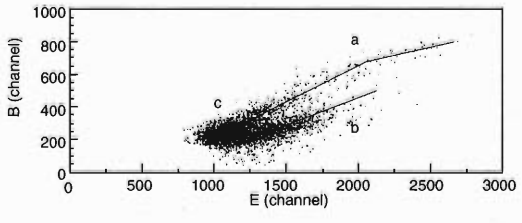

Fig. 2. The correlation between the observed B and E signals. The thin lines drawn along the ridges are guides for the eyes.

*1 Department of Physics, Tokyo Institute of Technology
*2 Gakushuin University
*3 Department of Chemistry, Tokyo University of Science

thickness of the variable degrader inserted upstream of the chamber was tuned so as to have most of the ions stopped in the gas chamber. In this two ridge lines labelled as "a" and "b" in Fig. 2 are observed. The line with a larger inclination ("a") represents the incident ions that are stopped in the working volume of the detector. The line with a smaller inclination ("b") represents events of the incident ions that passed through the working volume of the detector. In the experiment, the RI beam has a width of the energy, thus we tune the variable degrader to stop the incident ions that have the center of energy at an edge of the detector. Hence, the events of these ions show the dense spot "c". The insufficient separation obtained between lines "a" and "b" is ascribed to the shaping time for B which was longer than the width of the Bragg peak because of the presence of electrical noises.

We also tested Ne and Ar gasses as a stopping substance. They are known to have superior properties as gasses for the ionization chamber with lower working voltages, higher gains, better proportionalities and higher rate capabilities. In addition, they have better stopping powers. A drawback to employ these gasses is that the stopped ions might suffer from neutralization such that the collection by an electric field may not work. The data analysis is now under way.

References

1) H. Miyoshi et al.: RIKEN Accel. Prog. Rep. **35**, 143 (2002).
2) O. Frisch: British Atomic Energy Report BR-**49** (1944).
3) J. Kaihara et al.: RIKEN Accel. Prog. Rep. **36**, 192 (2003).

Development of ion chamber

Y. Yamaguchi,[*1] K. Kimura,[*2] A. Ozawa, T. Ohnishi, T. Suzuki,[*1] T. Izumikawa,[*1] T. Yamaguchi, T. Zheng,[*3] C. Wu,[*3] D. Fang, S. Watanabe,[*1] and I. Tanihata

We have been developing a new type of ion chamber (IC), as a detector for energy-loss measurements, which can be stably used under a high counting rate at the forthcoming RI Beam Factory. Construction of the new IC is basically the same as that of the previous one,[1)] except for its effective length of 60 cm for obtaining better energy resolution. Figure 1 shows the inside of the new IC. When a relativistic heavy ion beam passes through the effective area of the IC, which contains a counting gas (P–10), it generates an ionization track consisting of electrons and positive ions. This chamber has no grid, so both electrons and slowly moving positive ions contribute to anode signals. Anode signals are summed per four layers, thus six anode signals were separately amplified by conventional charge sensitive preamplifier and spectroscopy amplifier systems. Contributions from slow positive ion tails could be completely rejected using bipolar signals of the spectroscopy amplifier.

This type of gas counter is known to be strong against a high counting rate. On the other hand, the energy resolution from a single layer itself is worse than that from a semiconductor detector. However, we may overcome is problem by increasing the number of layers n, as

$$\sigma = \sigma_{parent}/n, \tag{1}$$

where σ_{parent} and σ denote the width of the distribution of the energy deposited in a single anode ($ic1$) and that in n samples anode layers ($icsum$), respectively, and $n = 6$. Figure 2 demonstrates the situation

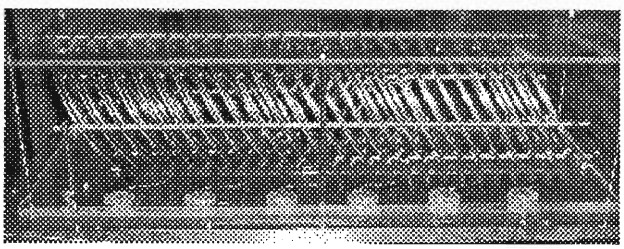

Fig. 1. Side view of IC. It consists of several anodes and cathodes made of thin foils tilted 30 degrees to the center axis in order to protect recombination between electrons and positive ions. Twenty-four layers of anode and cathode pairs separated by 20 mm are stacked together. It is operated using P–10 gas at a pressure of 740 Torr.

*1 Niigata University
*2 Nagasaki Institute of Applied Science
*3 Peking University, China

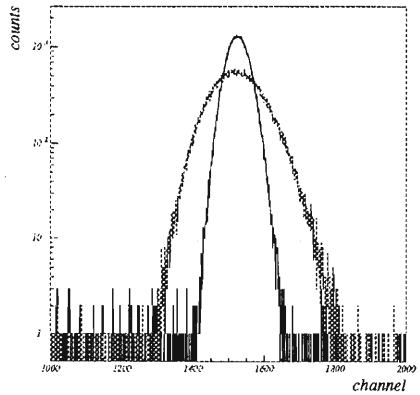

Fig. 2. Pulse height spectra for $ic1$ and $icsum$. The wider curve indicate $ic1$ signal, whereas the narrower one indicate $icsum$ signal.

of improvement.

The resolution of the $icsum$ signal became about 2.5 times better than that of $ic1$ signal. We report the results of two experiments performed at the E1C beam line.[2)] We arranged the IC to be adjacent to the F2 chamber, and also a plastic counter put on behind the IC. The particles were identified by a standard method based on the energy loss (ΔE), time-of-flight (TOF) and magnetic rigidity ($B\rho$) measurement for each fragment. The TOF of each fragment was determined using signals from the plastic counter and the accelerator (rf signal). The IC and a Si detector, the thickness of which is 150 μm, provided independent energy loss values (ΔE). The magnetic field at the dipole was monitored using a hall probe.

The first experiment was carried out in November 2001, in which each fragment ($Z = 12$ to $Z = 25$) was produced through the projectile fragmentation of the ^{56}Fe primary beam (90 MeV/u). The purpose of this experiment was to determine the energy resolution as a function of Z number. Figure 3 shows a two-dimensional plot of what constructed from the IC signal where each fragment appears as a spot. A contamination is observed due to the scattered primary particles and a fluctuation in the rf signal. However, each fragment was separated well enough to determine the resolution. The energy resolution of the Si detector was also measured at the same time. Figure 4 shows the comparison of the energy resolution between the IC and the Si detector as a function of Z number. It is clearly seen that the energy resolution obtained from the IC is satisfactory compared with Si detector. It should be noted that the energy resolution is better

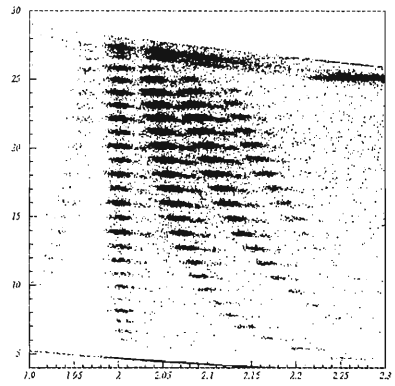

Fig. 3. The vertical axis indicates the Z number deduced from energy loss of the IC. The horizontal axis indicate A/Z calculated using the TOF signal. Counting rate was 500 Hz.

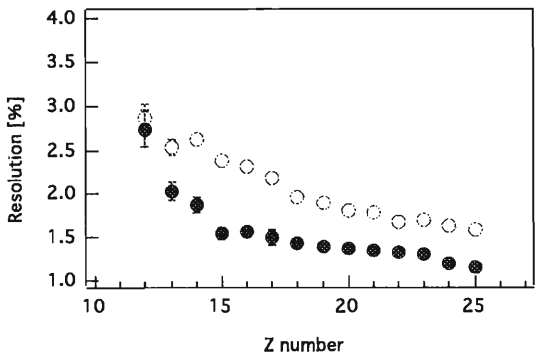

Fig. 4. Comparison of energy resolution between the IC and the Si detector as a function of Z number. The open and closed circles indicate the energy resolutions (FWHM) from the Si detector and the IC. Counting rate was 500 Hz.

for larger Z numbers.

The second experiment was carried out in September 2002. Each fragment ($Z = 5$ to $Z = 9$) was produced through the projectile fragmentation of the ^{20}Ne primary beam (110 MeV/u). The objective was to determine the counting rate dependence of the energy resolution up to approximately 450 kHz. Pile-up rejection at such a counting rate was performed using two signals (*normal* and *delayed* signals) from the plastic counter. In a two-dimensional plot of the above two quantities, events without pile-up should appear along a linear line while background events, not only pile-up events but also scattered primary particles, appear out of the line. We eliminated pile-up events in this way. Figure 5 shows the counting rate dependence of the energy resolution for ^{16}O ($A/Z = 2$) particles. It is apparent that the pile-up rejection works quite effectively over a wide range of counting rate up to 450 kHz. Thus, it is proved that the IC has sufficient energy resolution ($\sim 3\%$) and is strong against a high counting rate.

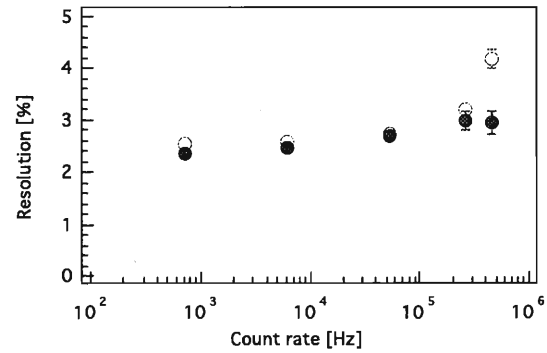

Fig. 5. Energy resolution of IC as a function of counting rate. The open and closed circles indicate the energy resolutions (σ) without and with the pile-up rejection, respectively. Counting rate was up to 452 kHz.

References

1) K. Kimura et al.: RIKEN Accel. Prog. Rep. **33**, 176 (2000).
2) T. Yamaguchi et al.: RIKEN Accel. Prog. Rep. **34**, 179 (2001).

Response of the *ASTRO-E2* hard X-ray detector for accelerated ions

Y. Okada,[*1] M. Kawaharada,[*1] M. M. Murakami,[*1] J. Kotoku,[*1] M. Kokubun,[*1] K. Makishima,[*1] S. Hong,[*2] M. Mori,[*3] Y. Terada, K. Yamaoka, H. Miyasaka, S. Kawasoe,[*4] M. Ohno,[*4] Y. Fukazawa,[*4] Y. Kobayashi,[*5] T. Mitani,[*5] H. Inoue,[*5] K. Nakazawa,[*5] and T. Takahashi[*5]

ASTRO-E2 is the fifth X-ray astronomy satellite of Japan, which carries three experiments on board with the energy range of 0.1–600 keV. The Hard X-ray Detector (HXD) on board *ASTRO-E2* consists of 16 modular assembly of well units, which is a combination of well-type GSO (Gd_2SiO_5:Ce)/BGO ($Bi_4Ge_3O_{12}$) phoswich counters and surrounding 20 BGO anti units.[1] The most attractive feature of the HXD is its low background in the energy range of 10–600 keV, and resultant high sensitivity. The key to the excellent sensitivity of HXD is achieved by the accurate estimation of the background spectrum irradiated by cosmic particles in the orbit. Therefore it is very important to know the response of HXD to the accelerated ions before the launch.

One of the purposes of this experiment is to measure the background spectrum of well and anti units, which originates from an activation induced by cosmic rays in the orbit of the satellite. Although the launch of *ASTRO-E* failed in the year 2000, we have already studied the activation experiment of the *single* BGO and GSO crystal.[2,3] Thus we will be able to compare the obtained spectrum with the simulation utilizing the radioactive isotopes that have already been identified from the previous experiment.[2]

Another purpose of this experiment is to monitor the response of the electronic system in the HXD when it is irradiated with high-energy cosmic rays ($\sim$ GeV). Although we have designed the electronic system to have fast recovery against the charged particles,[4] we actually need to confirm its performance by irradiating it with heavy ions.

The first experiment was executed on 29 September 2002 at RIKEN Ring Cyclotron. We irradiated one well unit, including the GSO main detector, and one anti unit simultaneously with 210 MeV/nucleon H_2^+ particles. The intensity of the beam which had penetrated the plastic scintillator located perpendicular to the beam upstream of the target was set to ~ 2.8 MHz. A total dose of 2.96×10^9 H_2^+ was irradiated and this corresponds to the amount to which one GSO should be irradiated for about 150 days in orbit. The internal background was measured by well and anti unit themselves, and external background was also measured by the CdTe diode detector, which is placed near the GSO detector after the beam irradiation.

Figure 1–left shows the relationship between the count rate and the time after the irradiation, and Fig. 1–right shows the CdTe spectrum, which is the background spectrum near the GSO crystal, obtained 3.0 hours after the irradiation. The decay properties of well and anti detectors show nearly consistent results with those of the past experiment utilizing single BGO crystal.[2,3] Currently the analysis of all sets of the data and simulation using GEANT4 code are in progress.

The second experiment was executed on 24 November 2002 at RIKEN Ring Cyclotron. We irradiated one well unit and one anti unit with 90 MeV/nucleon $^{56}Fe^{24+}$ particles. We monitored the output signal of the PMT directly and some points in the electric system for both well and anti units during the irradiation. The beam intensity was a few counts/sec for well unit and a few, 10^2, 10^3 for anti unit in order to obtain the signal response induced by one charged particle to avoid a pile-up of the signal. For the output signal of the PMT, we did not obtain any anomalous signal and confirmed the good performance of BGO crystal for the charged particles. We also measured the signals at various points in the electronic system, the analysis of which is currently in progress. We can say that the electronic system in HXD will not present any problem in the use for high-energy cosmic rays.

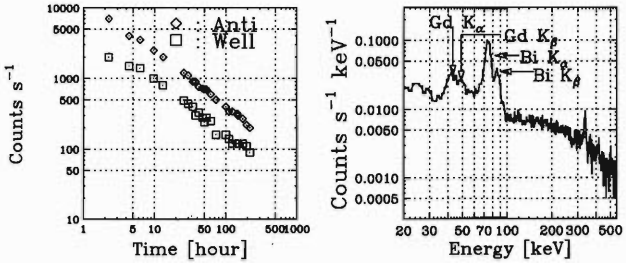

Fig. 1. (left) Decay time profile of anti and well units. (right) CdTe spectrum obtained 2.5–3.0 hours after the irradiation.

*1 Department of Physics, University of Tokyo
*2 College of Science and Technology, Nihon University
*3 Department of Physics, Saitama University
*4 Department of Physics, Hiroshima University
*5 Institute of Space and Astronautical Science

References
1) T. Kamae et al.: Proc. SPIE **2806**, 314 (1996).
2) M. Kokubun et al.: RIKEN Accel. Prog. Rep. **31**, 161 (1998).
3) M. Kokubun et al.: IEEE Trans. Nucl. Sci. **46**, 371 (1999).
4) C. Tanihata et al.: Proc. SPIE **3765**, 645 (1999).

Development of neutron counter for $^{16}O(d, d^*_{singlet})^{16}O^*$ (SDR) reaction measurement

H. Kumasaka,[*1] H. Okamura,[*1] T. Uesaka,[*3] K. Suda,[*1] R. Suzuki,[*1] T. Ikeda,[*1] K. Itoh,[*1]
H. Sakai,[*3] A. Tamii,[*2] M. Hatano,[*2] Y. Maeda,[*2] T. Saito,[*2] H. Kuboki,[*2]
N. Sakamoto, K. Sekiguchi, Y. Satou,[*3] and K. Yako[*3]

Langanke *et al.*[1] suggested a possibility for identification of μ and τ neutrinos at Super Kamiokande. The scenario is that the neutrinos excite the spin-flip dipole resonance (SDR) of ^{16}O in the neutral current reaction $^{16}O(\nu, \nu')^{16}O^*$, and are identified by detecting a gamma ray after the decay from excited SDR. To realize such a scenario, it is desirable to experimentally determine all of the values relevant to SDR in ^{16}O and its decay. However, SDR has not been studied as well as the Gamow-Teller resonance. The $(d, d^*_{singlet})$ reaction can be a powerful probe for such a study. Since $d_{singlet}$ is measured by the coincidence detection of protons and neutrons, we have developed a neutron counter to establish this reaction as a probe for selective excitation of SDR in ^{16}O.

In order to select $d_{singlet}$, which is a proton and neutron pair in the $^1S_0$ state, the energy and angular resolution of the neutron counter must be better than 0.5 MeV (FWHM) and 3 mrad (FWHM), respectively. The newly fabricated neutron counter is layered with eight planes, each of which consists of six plastic scintillators (Bicron BC-408) with a size of $10 \times 60 \times 3\,cm^3$ (Fig. 1). The thickness of 3 cm is determined to satisfy the above resolution at the flight length of 21 m. Moreover the height of 10 cm is determined to satisfy the angular resolution. Charged particle veto scintillators are installed in front of the neutron counter.

The neutron detection efficiency and the energy resolution were measured using the $^7Li(p, n)^7Be$[g.s.+0.43 MeV] reaction at $E_p = 135$ MeV. The proton beam was generated by accelerating H_2^+, the single charged hydrogen molecule. The time width of the beam bunch and the intrinsic time resolution of the neutron counter were measured by injecting a faint beam directly to the counter. The experiment was carried out in the E4 experimental area at the RIKEN Accelerator Research Facility. The neutron counter was placed at a distance of 21 m from the target. The primary beam was swept by SMART and stopped in the first dipole magnet for the (p, n) measurement.

The ^7Li target had a thickness of $0.127\,g/cm^2$. The scattering cross section in the laboratory system was estimated to be 39.49 ± 1.35 mb/sr at $E_p = 135$ MeV and $\theta_n = 0°$.[2] The detection efficiency was found to be $9.65 \pm 0.53\%$ at a threshold of 10 MeV_{ee}. This relatively high threshold was chosen considering the effect of wrap around of the beam and the room background.

The time-of-flight (TOF) was obtained from the RF pulse of the cyclotron. Figure 2 shows the TOF spectrum of the $^7Li(p, n)^7Be$[g.s.+0.43 MeV] reaction. The width of the peak was 1.27 ns (FWHM), which corresponds to the energy resolution of 2.76 MeV. It is considered that the spread of flight time due to energy loss in the target Δt_{target}, the time width of beam bunch Δt_{beam}, and the time resolution of the neutron counter Δt_{NC} contributes to this measured resolution Δt_{exp}. These are summarized in Table 1. Δt_{target} was estimated from the energy loss and the flight length. The intrinsic time resolution of the detector Δt_{int} was obtained from the width of time dif-

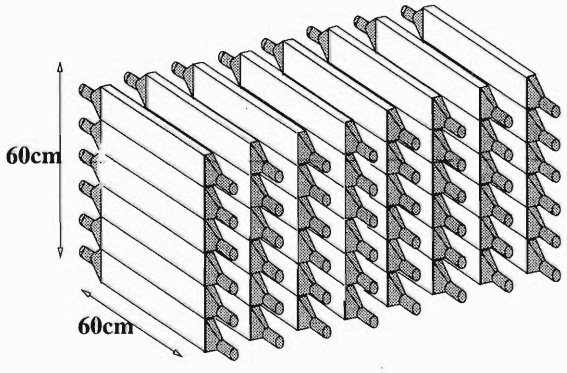

Fig. 1. Specification of the neutron counter. The scintillator is $10 \times 60 \times 3\,cm^3$ in size.

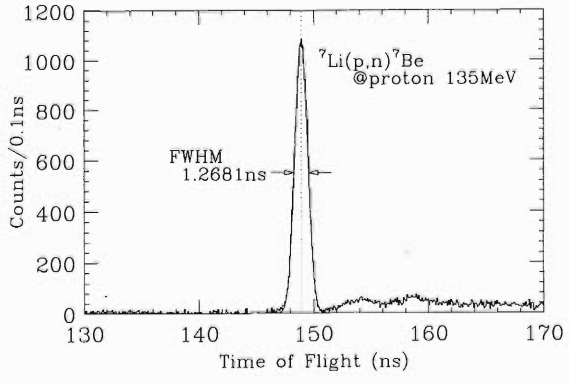

Fig. 2. TOF spectrum of the $^7Li(p, n)^7Be$[g.s.+0.43 MeV] reaction at $E_p = 135$ MeV, $\theta_n = 0°$.

*1 Department of Physics, Saitama University
*2 Department of Physics, University of Tokyo
*3 Center for Nuclear Study, University of Tokyo

Table 1. Time and energy resolution.

i	Δt_i (ns)	ΔE_i (MeV)
target	0.290	0.631
int	0.189	0.411
beam	1.012	2.203
NC	0.542	1.179
exp	1.27	2.76

ference between two adjacent planes in the faint beam measurement. $\Delta t_{\rm beam}$ was obtained by quadratically subtracting $\Delta_{\rm int}$ from the width of the peak in the faint-beam TOF spectrum. Finally, $\Delta t_{\rm NC}$ was deduced from $\Delta t^2_{\rm NC} = \Delta t^2_{\rm exp} - \Delta t^2_{\rm beam} - \Delta t^2_{\rm target}$. $\Delta t_{\rm NC}$ includes $\Delta t_{\rm int}$ as well as the effect from ambiguities of the reaction point in a 3-cm thick scintillator.

The resolution $\Delta t_{\rm exp}$ does not satisfy the required resolution. A possible method for improving the resolution is to determine the TOF not by using RF signals but by using proton timing signals. We are now attempting to analyze the proton orbit in the spectrograph, calculate the TOF for each proton by the orbit and the proton velocity, trace the timing signal back to the target, and deduce the precise reaction time.

References

1) K. Langanke, P. Vogel, and E. Kolbe: Phys. Rev. Lett. **76**, 2629 (1996).
2) T. N. Taddeucci: Phys. Rev. C **41**, 2548 (1990).

High-efficiency position-sensitive scintillation detector for beta ray

S. Nishimura, M. Kurata-Nishimura, M. A. Famiano,* Y. Nishi, and I. Tanihata

The neutron-rich nuclei far from stability are expected to play a key role in the r-process nucleosynthesis. Sufficiently accurate estimation of elemental abundances in the network calculations requires the lifetime information for a wide range of neutron-rich nuclei. At present, however, the study of these nuclei as far as from the stability region is limited by their low production rates. Therefore, detecting the decay events of such rare isotopes requires the efforts of improving the detection efficiencies of the beta-ray detector as well as reducing the sensitivities to the gamma-ray background.

In general, there are two methods to measure the half-lives of radioactive isotopes (RI). One is a direct measurement method, where identified isotopes are directly implanted into position-sensitive detectors (SSD)[1] or a gas detector in a chamber. This method greatly facilitates identifying incident RIs with weak beams. Here, we will report the detector system using an indirect measurement reported in Ref. 2. Our system is designed for operating detectors without pulsing the incident beam with relatively high beam intensity, where the incident RIs are implanted into an intermediate material, and then these stopped RIs are transferred from the beam line to the beta-ray detection system mechanically. The advantage of this indirect measurement is its possibility of reducing backgrounds from the accumulated RIs in the materials by moving the intermediate material. Thus, it becomes possible to operate the detector system for long time periods with less background and radiation damage in the detector. An accurate event matching, *i.e.* association of the implanted RIs with the decay events, is necessary to deduce the half-life of decaying species after a certain amount of time. In our system, the event matching is performed by reconstructing both the position of implanted RIs and that for the beta decays using the position sensitive detectors in the beam line and out of the beam line, respectively. Since the distance between the intermediate material and the beta-ray detector is less than 1 mm, it is not necessary to have a tracking system for beta rays. The possibilities of energy measurement of beta-rays as well as the identification of beta rays from gamma rays identification are under consideration.

A high-efficiency position-sensitive scintillation detector (HEPSS) based on scintillator and photomultiplier tubes is developed as a beta-ray detection system. This device consists of one layer of a thin plastic scintillator directly coupled to a position-sensitive photomultiplier tube (PMT: Hamamatsu R8520). Thus, it is relatively insensitive to the gamma rays compared to the SSD. The R8520 is a metal-package PMT with position sensitivity, which has recently been developed by Hamamatsu Co. Ltd. A schematic view of HEPSS is shown in Fig. 1. The R8520 consists of 6 sensitive anodes orthogonally placed along horizontal and vertical axies, respectively. Thus, the PMT has 12 channels of anode signals in addition to a signal from its last dynode. In order to reduce the channel of readout electronics, a resistive divide network is applied from each channel to produce a signal that provides an output proportional to its position.[3] The centroid position of each event is calculated by measuring the pulse heights, where the crosstalk at the PMT window becomes negligible. The advantages of the HEPSS is seen in its simple structure, easy treatment, and its radiation hardness relative to other detectors such as the scintillating fiber detectors and a silicon detector.

First of all, the characteristics of the R8520 are investigated by irradiating a spotlight on the PMT window, where light from a blue-LED is transferred to the PMT via an optical fiber with the diameter of 0.5 mm. The system is installed in the light shield box to perform systematic studies. The position of the fiber relative to the window of the R8520 is controlled by an X-Y-Z table precisely. The light yield and its duration time of LED light is adjusted by the combination of ND filters and the conditions of the LED driver to demonstrate the response of the PMT for various types of scintillation light. Irradiated positions of fiber are reconstructed from the pulse height information of the signals from the R8520, where the irradiated position of blue-LED light is scanned with a step size of 2 mm. The result is shown in Fig. 2. An excellent position resolution of below 0.2 mm is obtained at the bias voltage of -750 V. The structure of the spots in the reconstructed X-Y map in Fig. 2 shows a slight structure caused by the non-linearity of the PMT. Thus, the position calibration of the PMT itself would be required,

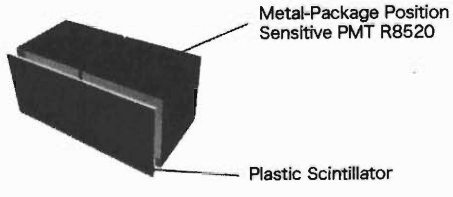

Fig. 1. Schematic view of the HEPSS for the half-life measurement. A thin scintillator is coupled on the PMT window directly for beta-ray detection. This device of PMT R8520 is applied for a position-sensitive photon detector.

* National Superconducting Cyclotron Laboratory, USA

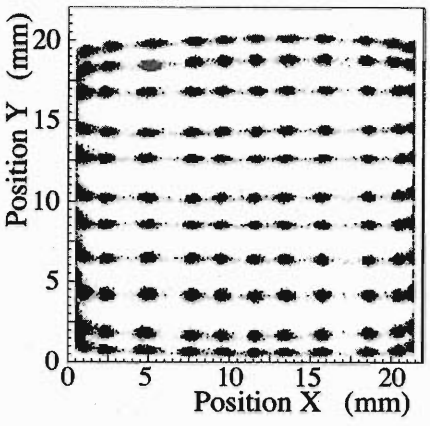

Fig. 2. Reconstructed position information of spot light scanned by a 2 mm step size on the R8520.

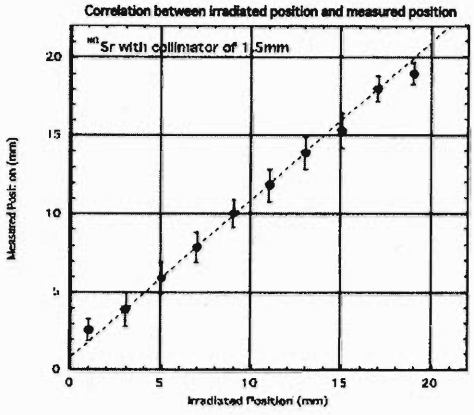

Fig. 3. Correlation between irradiated position of beta ray and the reconstructed position using radioactive source ^{90}Sr with a collimator having a hole of 1.5 mm diameter.

if one needs to obtain absolute position information.

Maximum multiplicity of stopped ions including the background, which we can treat, depend on the precision of position measurement of beta-ray emission points as well as the implanted points of ions. The performance of the HEPSS is investigated using a radioactive source ^{90}Sr instead of LED light to estimate the realistic performance for the beta rays.[4] An Al collimator with a 1.5 mm diameter hole is used to investigate the position sensitivity of HEPSS, where a plastic scintillator (BC422) with a thickness of 0.5 mm is used for the beta-ray detection. Figure 3 shows the correlation between the irradiated position and the measured position in the range of 20 mm. The averaged position resolution is confirmed to be below 0.7 mm. Such high position resolution allows us to operate the device in a high multiplicity environment under a mixed-beam condition. The efficiency of the HEPSS is also estimated by attaching another PMT on the other side of a scintillator and is confirmed to be above 98%. Because of the characteristics of low noise of the PMT below 0.5 Hz at the bias voltage of -750 V, the HEPSS can be operated under a self-trigger mode without extra coincidence.

Additional upgrade of the HEPSS is planned by inserting a different type of scintillator (2nd layer) between the current scintillator (1st layer) and the PMT. This idea is based on identification of beta-ray from gamma-ray background and possibly measuring the total energy of the beta ray. For example, BC444 is one of the candidates for the second layer of the scintillator. It has a two-order-of-magnitude slower timing response compared to the normal plastic scintillator. Therefore, the position of the beta ray can be determined by the 1st layer using shorter gate width and the energy deposited at the 2nd layer can be determined by measuring the pulse height of the last dynode with wider gate width. Such coincidence could enable use to distinguish the beta rays from the gamma rays, which is known as a phoswich detector. In addition, there would be a possibility to measure the total energy of the beta ray using a pixel type of BC444 (or $CaF_2(Eu)$) instead of a thin plastic scintillator in the 2nd layer. The idea is to stop the beta rays in the thick scintillation material without losing the position information from the 1st layer of scintillation light.

Similar application is also considered in the energy measurement of the incident ions for the measurement of E (ΔE/bx) which will help us to identify the incident ions. Here, the scintillator BC418 will be attached on the rotating wheel as an ion catcher foil instead of Al-foil. In the beam line, the scintillation light emitted from the BC418 will be directly collected by the downstream R8520 PMTs to measure the position of the incident RI precisely. In addition, a thin plastic scintillator BC444 will be attached on the R8520 PMTs to veto the incident RIs passed thought the BC418 by requiring no slow component of the scintillation light from the BC444. Here, the BC418 are rotated by a stepping motor and are sandwiched by the HEPSS detectors surrounding the scintillation wheel.

References

1) J. I. Prisciandaro et al.: Phys. Lett. B **510**, 17 (2001).
2) M. Famiano et al.: RIKEN Accel. Prog. Rep. **35**, 32 (2002).
3) K. Inoue et al.: Nucl. Instrum. Methods Phys. Res. A **423**, 364 (1999).
4) S. Nishimura et al.: Nucl. Phys. A, to be published.

Simulation of detector response for the $^{8}Li(\alpha, n)^{11}B$ reaction at the energy of 0.25 MeV per nucleon using Geant4

M. Kurata-Nishimura, S. Nishimura, I. Tanihata, S. Kubono,* and T. Teranishi*

The $^{8}Li(\alpha, n)^{11}B$ reaction is considered to be an important for reproducing an abundance of light elements by nucleosynthesis in the inhomogeneous big bang model.[1,2] Recently, it has also been identified to play an important role in r-process nucleosynthesis occurring in supernova explosion.[3] In the both environments, it is claimed to determine the reaction cross section in the direct reaction with the center of mass energy less than 1 MeV. Some previous experiments were conducted to determine this reaction cross section;[4-6] however, the results of such experiments were not in qualitative agreement with each other. Moreover, the measurements of the low-energy cross section below 1 MeV/n, where it is the most important energy region, have not been conducted yet due to difficulty of handling low-energy beams.

We have also performed such measurements with a beam energy of 0.6 MeV/n at the ISAC facility in the TRIUMF cyclotron in summer 2001.[7] A target cell was stuffed with He gas with a pressure of around 25 Torr. Neutrons were detected by 48 slats of plastic neutron counters covering the polar angle from 20° to 140° 1.5 m away from the target. As a result, it was difficult to separate neutron peaks from the background. We found that neutron peaks are buried by a huge γ ray background produced at the He gas target window in which most of ^{8}Li beams stopped.

In order to overcome the problem, we propose a new setup as shown in Fig. 1. There are three modifications from the previous setup. The first is that the window of the gas target is removed by applying a new technique developed by Sagara *et al.*[8] They proved that the pressure of 10 Torr was attainable using He gas at a low flow rate compared to a usual differential pumping system. The second is that a position-sensitive silicon detector (SSD) is installed inside the gas target. This detector enables to detect ^{11}B produced by the reaction and to put this signal into a trigger logic. The third is that the plastic scintillation counter is replaced by a liquid scintillation counter (LQS). By managing the signal from the LQS through a pulse shape discriminator (PSD), the signals of neutrons could be distinguished from those of γ rays.

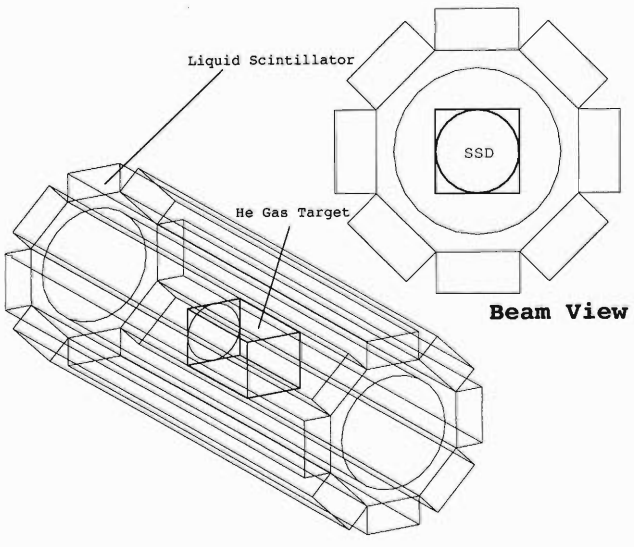

Fig. 1. Schematic picture of experimental setup.

In this paper, the neutron separation ability determined in a bench test using a ^{252}Cf. source is reported. Moreover, the current status for the optimization of SSD and LQS geometries is discussed obtained using the Geant4[9] simulation code.

The liquid scintillator is stuffed in the glass box with dimensions of $100 \times 50 \times 1000\ mm^3$. The signal from the LQS is read through two PMTs (Hamamatsu R1250-03) attached to both ends of the glass box of the LQS. The PMT signals are divided into three lines. One is fed into the PSD and the others are fed into two ADCs which are read with a wide gate of 400 ns width and a delayed gate of 33 ns delay. The neutron source of ^{252}Cf is placed on an NaI counter 90 cm away from the LQS. In a time of flight spectrum between the NaI and the LQS, the neutron peak is clearly separated from the sharp γ peak. In this spectrum, the percentage of γ rays is apparently reduced by requiring that PSD detected a neutron like signal. Consequently, the usage of the PSD with the LQS eliminates 90% γ rays while 20% neutron is lost. Additionally, 5% more γ rays can be eliminated by applying a Pb shield which covers the LQS.

Geant4 is a tool kit for the full and fast Monte Carlo simulation of the passage of particles through matter. Originally, Geant4 is developed for the simulation of detectors in the high energy physics. They are extending the validity range of particle interactions down to a lower energy. Currently, the low-energy processes of electromagnetic interactions implemented in Geant4, *e.g.*, compton scattering, Rayleigh effect, γ conversion, Bremsstrahlung, and ionisation are valid for energies down to 250 eV and can be used up to approximately 100 GeV. The details are described elsewhere.[9]

As shown in Fig. 1, the gas target with a length of 20 cm is sitting at the center of the detectors and the LQS is established covering an almost full azimuthal

* Center for Nuclear Study, University of Tokyo

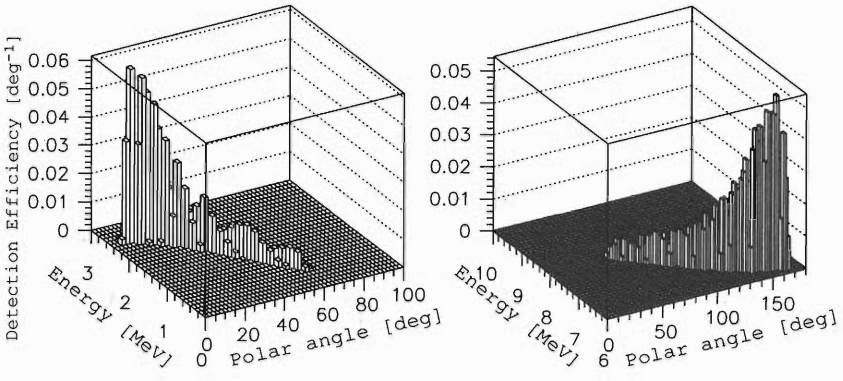

Fig. 2. Kinematics of (a) ^{11}B and (b) neutron accepted by SSD and LQS.

angle. The disk-shaped position-sensitive SSD with a diameter of 10 cm and a thickness of 300 μm is installed in the exit end inside the gas target.

In the current version of Geant4, nuclear reactions are not implemented in the physics process, thus, ^{8}Li$(\alpha, \mathrm{n})^{11}$B is generated manually. The reaction point is arranged to be 0 cm in the x and y axes and is randomly distributed in the z axis inside the target. The kinematics of ^{11}B and neutron detected by the SSD and the LQS are shown in Fig. 2 (a) and (b), respectively. The SSD dimension limits the ^{11}B acceptance.

Finally, the detection efficiency is estimated to be around 12% including the geometrical acceptance and neutron detection efficiency. Therefore, even if we have a 1×10^6 cps (counts per second) intensity beam and assume a 100 mbarn reaction cross section, approximately 0.18 cps events can be recorded. It is possible to improve this detection rate by a factor of 2–3 by installing the SSD not only at the end but on the side of the target according to increasing acceptance of ^{11}B.

Furthermore, since the total energy deposit in the SSD are well correlated to the emitted kinematic energy, the reaction point and emitted angle can be determined with a resolution of 3 mm and 3 degree in sigma, respectively, using the information on the total energy deposit and hit position of the SSD.

The optimization can be completed using the Geant4 simulation code before the construction of the detector.

References

1) M. J. Balbes et al.: Phys. Rev. Lett. **71**, 3931 (1993).
2) N. Hata et al.: Phys. Rev. Lett. **75**, 3977 (1995).
3) M. Terasawa et al.: Astrophys. J. **562**, 470 (2001).
4) X. Gu et al.: Phys. Lett. B **343**, 31 (1995).
5) R. N. Boyd et al.: Phys. Rev. Lett. **68**, 1283 (1992).
6) Y. Mizoi et al.: Phys. Rev. C **62**, 065801 (2000).
7) M. K-Nishimura et al.: RIKEN Accel. Prog. Rep. **35**, 80 (2002).
8) K. Sagara et al.: Nucl. Instum. Methods Phys. Res. A **378**, 392 (1996).
9) Geant4 collaborations: http://geant4.web.cern.ch/geant4/

Beam calibration of radiation monitor onboard French-Brazilian microsatellite

H. Miyasaka, H. Kato, U. B. Jayanthi,[*1] T. Tamagawa, K. Yamaoka, I. Sakurai, S. Hong,[*2] M. Nakajima,[*2] M. Kohama, Y. Terada, J. Kotoku,[*3] Y. Uchihori,[*4] A. Ozawa, Y. Yamaguchi,[*5] F. Daging, and T. Ohnishi

An international collaboration to monitor the radiation belt with a French-Brazilian microsatellite (FBM) is now being pursued. The satellite is planned to be launched at the end of 2003 at an orbital altitude of ~750 km and an inclination of ~7°. The radiation monitor, named APEX for "Alpha, Proton and Electron fluxes monitoring experiments in the inner magnetosphere," is being developed by RIKEN and INPE[*1].[1,2] APEX will enable observation of the continuous particle fluxes in the equatorial region of the inner magnetosphere and the main focus is to study the dynamical phenomena of particle diffusion and precipitation during a magnetic disturbance.

APEX consists of four silicon PIN diodes (D1 – D4) with two Al absorbers of different thicknesses. Each of the PIN diode has a 1 cm × 1 cm effective area with 0.4 mm thickness and the Al absorbers are 2 and 5 mm thick, which are placed in front of D2 and D4, respectively. Figure 1 shows the cross-sectional view of the APEX telescope. Two Al absorbers are employed to increase the dynamic range of the particle energies for detection. APEX will observe the counts of electron, proton and He with several energy bands by setting the threshold at each detector energy deposit. Observable energy ranges of APEX are listed in Table 1. This covers the typical energy range of the radiation belt and the relativistic energy populations during magnetic disturbances.

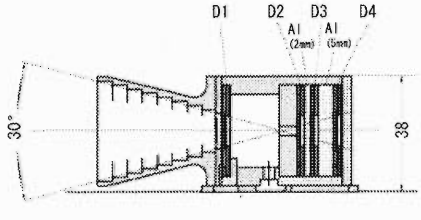

Fig. 1. Cross-sectional view of APEX telescope. D1 to D4 are PIN diodes.

Table 1. Observable energy range of APEX telescope.

Particle	Energy range	Energy band
Electron	0.15 – 3.1 MeV	4
Proton	1.5 – 70 MeV	5
Helium	3.1 – 50 MeV	4

*1 Instituto Nacional de Pesquisas Espaciais, Brazil
*2 Nihon University
*3 University of Tokyo
*4 National Institute of Radiological Sciences
*5 Niigata University

We performed two calibration tests at the E3A and E1C facilities at RIKEN Ring Cyclotron. For the first test, we used a H_2^+ beam with 135 MeV/nucleon and put Al plates of various thicknesses in front of the APEX to produce protons of various energies. For the second test, we used secondary particles which were produced by bombarding a ^{12}C beam with 70 MeV/nucleon on a Be target and selected using a $B\rho$ magnet. The particle energy of those test covered the APEX observable energy ranges, which are shown in Table 1.

Figure 2 shows an example of the above results with a scatter plot of D1 versus D2 output in MeV. Note that the incident particle energy adjusted to produce particles that can penetrate D1 but not D3 for this test. Dashed lines in the figure represent the expected energy deposit of each particle (H, ^{3}He or ^{4}He). Features of this curve correspond to the incident particle which stopped at D2 (I) and penetrate D2 but stopped at the 2-mm-thick Al absorbers (II). The left panel of Fig. 2. shows the result of the first test where the thickness of the Al plate was 60 mm and the right panel shows a secondary-particle response (^{3}He, ^{4}He) which was evoked by a 1 mm Be target and 0.4 T for the selection magnet. As shown in figures, APEX has sufficient performance for identifying even ^{3}He and ^{4}He where we count both particles as He in actual observation in space. From all of these results, we verified that the APEX performance meets our expectation.

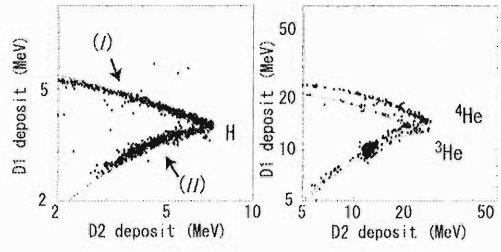

Fig. 2. Scatter plots of D1 versus D2 deposit in MeV. Left panel shows the response of direct irradiation of proton 135 MeV + Al (60 mm). Right panel shows the response of ^{3}He and ^{4}He produced by Be target.

References

1) U. B. Jayanthi: submitted to Adv. Space Res.
2) T. Kohno et al.: RIKEN Accel. Prog. Rep. **31**, 168 (1998).

High nuclear polarization in aromatic molecule with a cw Ar-ion laser

T. Wakui,[*1] M. Hatano,[*2] H. Sakai,[*1,*2] T. Uesaka,[*1] and A. Tamii[*2]

A polarized solid proton target using a crystal of naphthalene doped with pentacene is being developed for experiments with RI beams.[1] The target is well suited for the RI beam experiments that will be carried out under the so-called inverse kinematic condition, because protons in the crystal can be polarized in the magnetic field lower than 0.3 T and at the temperature higher than 77 K by means of pulsed dynamic nuclear polarization (DNP).[2] The polarization procedure is described in Ref. 3.

In this method, pentacene molecules have been excited by using a mercury lamp, a nitrogen laser, and recently a flush-lamp-pumped dye laser. Iinuma *et al.* obtained the highest proton polarization of 32% with the dye laser,[4] which can irradiate an appropriate wavelength of 600 nm. However, the dye laser is not suited for scattering experiments because of the lifetime of the dye. It is necessary to change the dye once a day during the experiments to maintain the laser power; the polarizing process is interrupted by the changing of the dye for a few hours.

Pentacene molecules can also be excited by using an Ar-ion laser. The wavelength of its main mode is 514 nm, which corresponds to the energy of transition to the third excited state, as shown in Fig. 1. The laser beam has to be pulsed to obtain a large population difference, because the lifetime of the most populated sublevel, $m_s = 0$, is shorter than that of other levels, $m_s = \pm 1$, as shown in Fig. 1. The energy of one pulse for an Ar-ion laser is 14 times smaller than that for the dye laser, when the laser beam with the power of 25 W is pulsed to the width of 20 μs. However, the repetition rate for the Ar-ion laser can be increased to a few kHz as long as the pulse separation is much longer than the lifetime of the triplet state, although the repetition rate for the dye laser is typically 50 Hz. Thus, we expected that the Ar-ion laser can provide proton polarization comparable to that obtained with the dye laser. Moreover, the Ar-ion laser has advantages such as long lifetime and easy operation.

A prototype proton polarizing system was constructed and used to study the effectiveness of Ar-ion laser as a light source for excitation of pentacene.[1] The power of the Ar-ion laser used in this study was 4.2 W and the laser beam was mechanically pulsed by an optical chopper. The pulse width and the repetition rate were 20 μs and 1 kHz, respectively. The resulting average power of the laser was 84 mW. Last year, we obtained proton polarization of $18.4 \pm 3.9\%$ in 0.3 T at 100 K with the pulsed laser beam.[5] The limiting factor of proton polarization was the laser power. Figure 2 shows the measured proton polarization as a function of the average laser power. It is evident that proton polarization increases almost linearly with increasing laser power below 84 mW. Thus, we have decided to introduce a high-power Ar-ion laser into the polarized proton target system.

The newly installed Ar-ion laser has the maximum power of 25 W that corresponds to the average power of 500 mW for the pulsed laser beam. Figure 3 shows a result of proton polarization as a function of time during the buildup process. We have succeeded in polarizing protons up to $36.8 \pm 4.3\%$ in 0.3 T at 100 K by using the high-power Ar-ion laser.

On the basis of the result, we have started to construct the polarized proton target system that will be used in beam irradiation experiments. The target system and preliminary result of proton polarization with the system are described in Ref. 6.

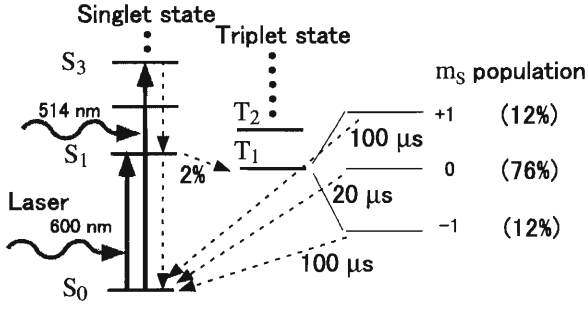

Fig. 1. Energy levels of pentacene. Pentacene molecules are excited to the third excited state by using the Ar-ion laser. The lifetime of the $m_s = 0$ level is shorter than that of other levels, $m_s = \pm 1$.

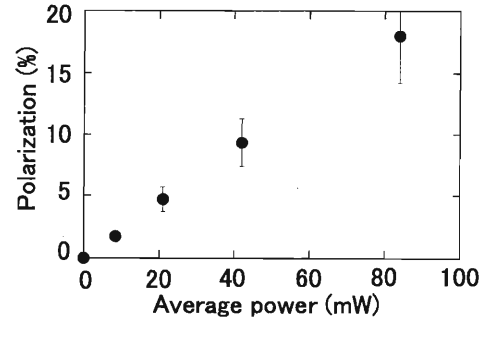

Fig. 2. Proton polarization as a function of the average laser power. Proton polarization increases almost linearly with increasing laser power.

*1 Center for Nuclear Study, University of Tokyo
*2 Department of Physics, University of Tokyo

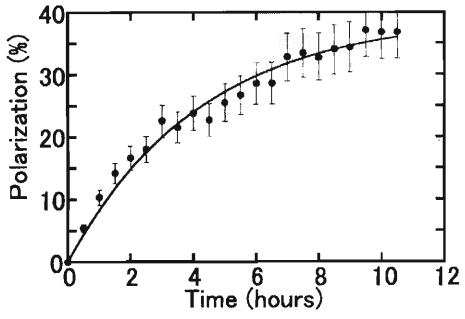

Fig. 3. Proton polarization as a function of time in the magnetic field of 0.3 T at 100 K. The obtained proton polarization is $36.8 \pm 4.3\%$ and the extrapolated maximum proton polarization is $39.3 \pm 4.6\%$.

References

1) T. Wakui et al.: RIKEN Accel. Prog. Rep. **34**, 194 (2001).
2) A. Henstra et al.: Phys. Lett. A **134**, 134 (1988).
3) M. Hatano et al.: RIKEN Accel. Prog. Rep. **33**, 182 (2000).
4) M. Iinuma et al.: Phys. Rev. Lett. **84**, 171 (2000).
5) T. Wakui et al.: RIKEN Accel. Prog. Rep. **35**, 149 (2002).
6) M. Hatano et al.: RIKEN Accel. Prog. Rep. **36**, 48 (2003).

Frequency characteristics of the nuclear spin oscillator with ^{129}Xe

A. Yoshimi and K. Asahi

We investigated the frequency characteristics of the nuclear spin oscillator which has been developed in our laboratory.[1] The device, where the nuclear spin precession is preserved beyond the intrinsic transverse relaxation time by the feedback magnetic field, has been developed for the detection of the small energy shift of 10^{-24} eV in the nucleus, aiming at fundamental physics experiments.

The ^{129}Xe nucleus, confined in a spherical glass cell and then located in a 3-layer magnetic shield to eliminate the external magnetic perturbation, was polarized by the hyperfine interaction with the optically polarized Rb atoms. The homogeneous static field of $B_0 = 28.3\,\mathrm{mG}$, which corresponds to the precession frequency of ^{129}Xe nuclei $\nu_0 = 33.5\,\mathrm{Hz}$, was produced by a solenoid coil wound inside the magnetic shield. The nuclear precession of ^{129}Xe was detected by the transmission of a probe laser beam tuned to the Rb D1 absorption line which was affected by the transverse polarization of ^{129}Xe through the hyperfine interaction between the ^{129}Xe nuclei and Rb atoms.[1] The transmitted signal, modulated by the precession frequency of ^{129}Xe nuclei, was phase sensitively detected with the bandwidth of 0.8 Hz to suppress the noise components. The low-frequency signal thus obtained was then processed with the reference signals to produce the feedback signal of 33.5 Hz to operate the spin oscillator.

The Fourier spectrum obtained by the continuous operation of the nuclear spin oscillator with the observation time of 1000 seconds is shown in Fig. 1 (a). The absolute line width of the observed spectrum was narrower by a factor of 30 than that of the obtained spectrum (Fig. 1 (b)) by the conventional nuclear spin 'maser' operated at the frequency 3.5 kHz where the nuclear spin was detected by the NMR pickup-coil. This improvement was accomplished by the realization of the low-frequency operation of the spin maser, which should be called a spin oscillator due to its lower frequency than the micro wave range.

The frequency stability in the oscillator on the time scale of 100 seconds is of the order of 1 mHz as shown in Fig. 2 (a). The instability mainly comes from the current fluctuation in the solenoid coil producing the static field B_0. The solenoid current measured simultaneously by a high-precision ammeter is shown in Fig. 2 (b) and its instability was found to be 0.1 μA. At present, the above frequency instability is considered to limit the long-term determination precision of precession frequency to the order of 1 μHz during 10^4 second observation time.

To improve the frequency stability, we are in the process of preparing a new experimental layout in two ways; i) installing the ultra high-precision current source, ii) utilizing the Rb atoms coexisting with the ^{129}Xe gas in the glass cell as the magnetometer which is expected to have a sensitivity of $10^{-12}\,\mathrm{G}/\sqrt{\mathrm{Hz}}$.[2]

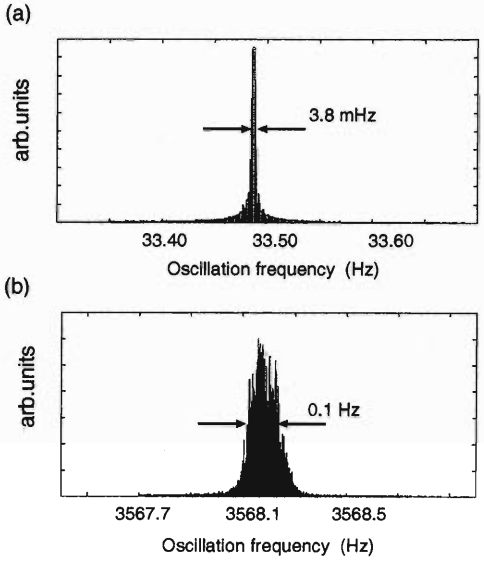

Fig. 1. Fourier spectrums obtained from (a) the present nuclear spin oscillator and (b) the conventional nuclear spin 'maser.'

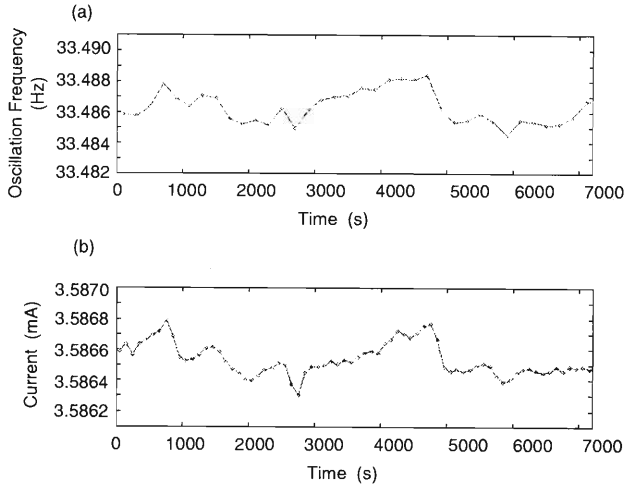

Fig. 2. (a) Measured frequency instability of the nuclear spin oscillator on the time scale of 100 seconds. (b) Measured current instability in the solenoid coil producing the static field.

References

1) A. Yoshimi et al.: RIKEN Accel. Prog. Rep. **35**, 151 (2002).
2) D. Budker et al.: Phys. Rev. A **62**, 043403 (2000).

Development of a Wien filter system in CNS

J. J. He,* S. Kubono,* T. Teranishi,* M. Notani,* and N. Yamazaki*

A low-energy in-flight type RI beam separator CRIB[1] has been running at RARF for a few years under the CNS-RIKEN joint project, providing two main criteria for the separation of reaction products. The first one is the magnetic rigidity ($B\rho = Av/Z$) given by the first analyzing magnetic dipole D1, the second one is the energy loss of ions in materials, by means of a thin flat degrader located in the intermediate focal plane F1 of the separator. The combination of these two methods provides a selection proportional to $A^{2.5}/Z^{1.5}$. However, the problem of contaminants is very serious in the RI beam at the achromatic focal plane (F2) in many cases, and these contaminants limit the purity and the intensity of the aimed RI beam. If we examine the bi-dimensional plot (E, TOF) in Ref. 2, it can be seen clearly that the nuclides in the F2 focal plane have different energies, *i.e.* different nuclides with different velocities. So an aimed nuclide can be selected by a velocity separator with high purity. In CNS, we have designed and constructed a Wien filter,[1] in which an electrostatic and a magnetic field are crossed. The high voltages (±200 KV maximum) can be applied to the electrodes to form a horizontal electric field (50 KV/cm maximum), which is combined with the vertical magnetic field (2.9 kG maximum).

The ion optics of the Wien filter has been reinvestigated by using GIOS code,[3,4] which allows the calculation of the motion of charged particles through electrostatic fields, multipoles as well as the Wien filter. All effects of the main fields as well as of the fringing fields can be taken into account up to the third order.

In the Wien filter, the high voltages for the electrodes will limit the velocity dispersions of particles. The maximum velocity dispersions (dx/dv) were calculated by GIOS and are listed in Table 1 for $A/q = 2$ particles at different energies. The results indicate that if a particle has a 2.5% velocity deviation with respect to the reference energy of 4 MeV/nucleon, it cannot be detected within a $5 \times 5\,cm^2$ Si detector. Considering the combination of CRIB and the Wien filter, and taking the 6.94-MeV/nucleon $^{14}O^{8+}$ radioactive ion as the reference particle, the maximum velocity dispersion at the exit of Wien filter (F3) was calculated to be 0.63 cm/% that is comparable to the value obtained in GANIL.[5] The beam transmission efficiency of the whole system can reach to about 30% under the assumption of the $^{14}O^{8+}$ RI beam emittance of $\Delta x = \Delta y = \pm 1.5$ mm, $\Delta\theta_x = \Delta\theta_y = \pm 30$ mrad and $\Delta p/p = 0$. The beam envelopes for the above given $^{14}O^{8+}$ particles are shown in Fig. 1.

Table 1. The calculated maximum velocity dispersions (dx/dv) for $A/q = 2$ particles at different energies.

E (AMeV)	dx/dv (cm/%)	B (Tesla)	E (KV/cm)
2.0	2.38	0.253	49.6
4.0	1.00	0.180	49.8
8.0	0.48	0.128	49.9

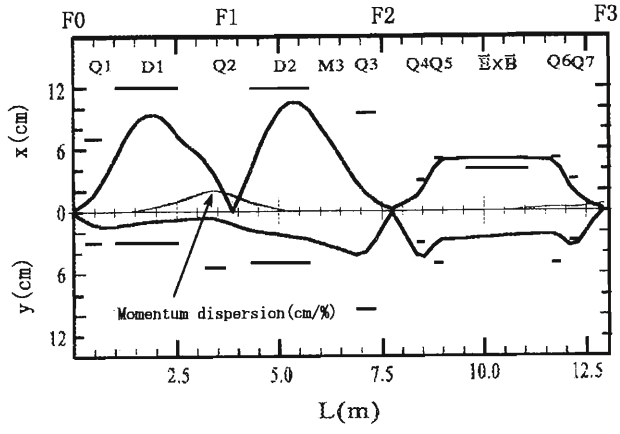

Fig. 1. Beam envelopes for 6.94-MeV/nucleon $^{14}O^{8+}$ beam passing through CRIB and Wien filter system calculated by GIOS code. The solid lines indicate envelopes in x and y directions, and the thin line around the central axis indicates the horizontal momentum dispersion (in units of cm/%, the scale is the same as that of the envelope). The short bars around the envelopes indicate the gaps of the elements.

Now, a test experiment using an α source is being prepared, in which the velocity dispersion (dx/dv), the beam transmission efficiency and the typical solid angle for the Wien filter will be measured and compared to the theoretical estimations.

References

1) T. Teranishi et al.: CNS-REP-39 (2001) p. 1.
2) J. J. He et al.: RIKEN Accel. Prog. Rep. **36**, 81 (2003).
3) H. Wollnik et al.: Proc. 7th Int. Conf. on Atomic Masses and Fundamental Constants (AMCO-7), Darmstadt-Seeheim, Germany, 1984-9, edited by O. Klepper (Lehrdruckerei, Darmstadt, 1984) p. 705; GSI Report, THD-26, 679 (1984).
4) H. Wollnik: *Optics of Charged Particles*, (Academic Press, Orlando, 1987).
5) R. Anne et al.: Nucl. Instrum. Methods Phys. Res. B **70**, 276 (1992).

* Center for Nuclear Study, University of Tokyo

Detector design for β decay experiments

J. Murata, K. Asahi, H. Miyoshi,* K. Shimada,* H. Ueno, A. Yoshimi, H. Watanabe, D. Kameda,* and J. Kaihara*

Precision nuclear β decay experiments are planned using the radioactive atomic beam apparatus.[1] The present project aims to discover time reversal symmetry violation (T-Violation) in a nuclear system,[2] which is predicted by a number of theoretical models on physics beyond the standard model. All experimental evidence of the T-Violation and the related CP-Violation can be explained within the framework of the Cabbibo-Kobayashi-Maskawa quark mixing matrix (CKM) included in the standard model. The CKM predictions on the T-Violation of the nuclear weak decay are negligible compared to the current experimental sensitivity. Therefore, observation of a non-zero T-Violation in the nuclear β decay implies discovery of the physics beyond the standard model, which predicts visible T-Violation effects on the nuclear β decay. RIBF has a strong discovery potential for such precision measurements on the nuclear β decay because of its huge RI beam intensity.

The authors designed a prototype experimental setup for the β decay experiments, consisting of an RI beam buffering gas cell, an atomic beam polarizer, electron-tracking detectors and recoil ion detectors. The T-Violation experiments require the polarization of the cold RI beam, therefore, such experiments have to wait for the completion of the atomic-beam-polarizing apparatus. A similar β decay experiment using an unpolarized cold RI beam is planned, which can be performed as soon as possible without the polarizer. In the unpolarized case, we aim to perform a precision measurement of the β-ν correlation coefficient a, defined as $W(\theta_{\beta\nu}) = 1 + a\cos(\theta_{\beta\nu})$, where $W(\theta_{\beta\nu})$ is the angular correlation function between electron and ν, and $\theta_{\beta\nu}$ is the angle between them. The precision measurement of a is also sensitive to physics beyond the standard model, such as the existence of the right-handed charged current. A single measurement of the recoil energy spectra is sensitive to on a; in fact, all the modern experimental attempts are made and planned using the recoil energy spectrum.[3] However, a direct determination of a by measuring both the electrons and the recoil ions has advantages for such precision measurements although it presents experimental difficulties.

A detector design for determining the β-ν correlation is shown in Fig. 1. The cold radioactive atomic beams, which have low velocities of about 400 m/s, are injected into the long decay volume, about 2 m. When β decay occurs inside the effective region, the emitted electron (positron) is detected by the electron detectors

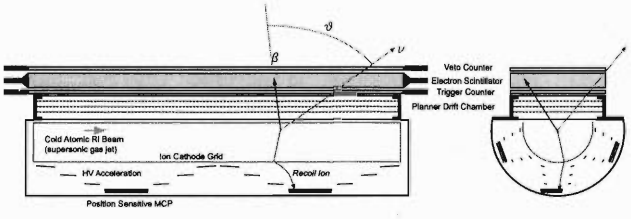

Fig. 1. Possible detector setup design for β-ν correlation measurement.

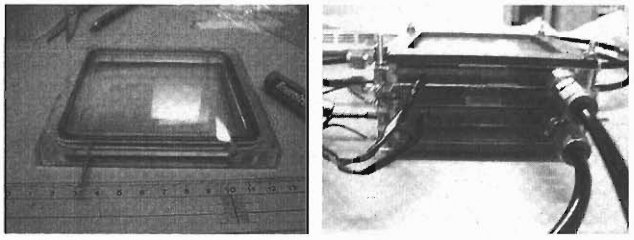

Fig. 2. The prototype single-wire drift chamber. A layer (left) and the combined view (right) is shown.

that consist of a scintillation counter and a drift chamber. The kinetic energy of the electron is measured using the scintillation counter and the electron track is determined using the planner drift chamber. Then by assuming the nearly parallel profiles of the cold RI atomic beam, the decay vertex can be roughly estimated. The recoil ion is measured using microchannel plates (MCPs) with an electrical acceleration field. By using position-sensitive MCPs, ion-emitted directions are also determined by reconstructing the ion drifting tracks inside the acceleration field. Together with the timing information of the electron detectors, the kinetic energies of the recoil ions can be determined by time-of-flight measurements.

This year, the authors started the R&D of the detector components. As the first step, a special drift chamber called a "single-wire drift chamber (SWDC)" is built. The very cost-effective simple device contains only a single sense wire without any field shaping wires.[4] The SWDC is not directly applicable to the β decay experiments, however, we built this simple chamber to learn the properties of the drift chambers. The prototype chamber is shown in Fig. 2, consisting of two X layers and two Y layers. Each layer has a single sense wire of 20 μm gold-plated tungsten wire, sandwiched by two ground planes coated with insulator sheets. The gas volume has an 8.9 mm $\times$ 8.9 mm

* Department of Physics, Tokyo Institute of Technology

wide area and a gap width of 10 mm. In order to avoid the so-called left-right ambiguity and to keep a larger effective area, the sense wire is placed at a 34.5 mm off-centered position. Cathode strips at ground level are located at edges parallel to the wire. According to Ref. 4, very homogeneous field can be obtained automatically after the insulator panels are sufficienty charged up. Test measurements using P-10 gas (90% Ar + 10%CH_4) at a wire voltage of about 1700 V are under way. We expect to finish the SWDC test and start building the real multiwire drift chamber soon.

References

1) H. Miyoshi et al.: RIKEN Accel. Prog. Rep. **36**, 193 (2003) and the references therein.
2) A. L. Hallin et al.: Phys. Rev. Lett. **52**, 337 (1984).
3) C. H. Johnson et al.: Phys. Rev. **132**, 1149 (1963).
4) J. Allinson et al.: Nucl. Instrum. Methods Phys. Res. **201**, 341 (1982).

DPOL: A vector and tensor polarimeter for intermediate-energy deuterons

Y. Satou,[*1] S. Ishida, H. Sakai,[*2] H. Okamura,[*3] N. Sakamoto, H. Otsu,[*4] T. Uesaka,[*3] T. Wakasa,[*5] A. Tamii,[*2] T. Ohnishi, K. Sekiguchi, K. Yako,[*2] K. Suda,[*3] M. Hatano,[*2] H. Kato,[*2] Y. Maeda,[*2] T. Ichihara, and T. Niizeki[*6]

To study the isoscalar spin excitations in nuclei for low-lying levels as well as in the continuum through the measurement of single- and double-spin-flip probabilities, S_1 and S_2, in the $(\vec{d}, \vec{d'})$ reaction,[1] we have developed an intermediate-energy focal-plane deuteron polarimeter DPOL at the RIKEN Accelerator Research Facility (RARF). The determination of S_1 and S_2 relies on the ability to measure both vector and tensor components of the scattered deuterons in the polarimeter. To fulfill this requirement, DPOL was designed to utilize, as analyzer reactions, $\vec{d}+{}^{12}$C elastic scattering and the ${}^1\mathrm{H}(\vec{d}, 2p)$ charge exchange reaction, which are expected to have large vector and tensor figures of merit, respectively, in the energy range of our interest: $E_d = 200$–300 MeV.

Figure 1 shows the counter arrangement of DPOL. It comprised three parts: the multiwire drift chamber for track reconstruction, the secondary CH_2 target, and the counter hodoscope for detecting charged particles. The counter hodoscope consisted of a front plastic scintillator wall (HOD), a rear wall (CM) and an iron absorber in between. The configuration of the hodoscope allowed it to distinguish between protons and deuterons using their energy loss characteristics in matters. Shown in the inset of Fig. 1 are measured missing mass spectra of the analyzer reactions. For elastic scattering a ^{12}C recoil was assumed, while for the charge exchange reaction a ^{1}H recoil was assumed. We see clear peaks due to the desired reactions. In order to eliminate contributions from parasitic components, such as those arising from the $d + p$ and ${}^{12}\mathrm{C}(d, 2p)$ reactions, cuts were applied on the missing-mass spectra in the off-line analysis.

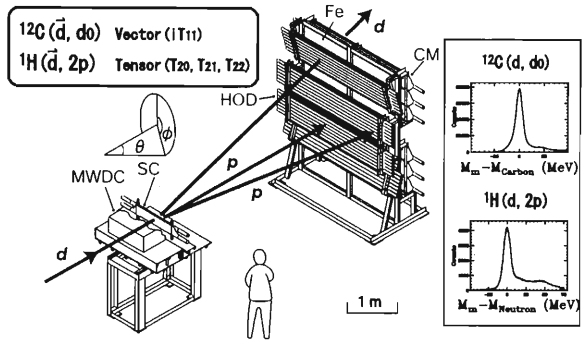

Fig. 1. Layout of the polarimeter DPOL.

Figure 2 summarizes the results of the calibration experiment, which was performed to determine the unpolarized cross sections ϵ and the effective analyzing powers T_{kq}. The obtained figure-of-merit values, defined by $F_{kq} = \sqrt{\int \epsilon T_{kq}^2 \mathrm{d}\Omega}$, are plotted versus E_d as open circles. The data are compared with those of the vector polarimeter POMME[2] (open squares) and the tensor polarimeter POLDER[3] (open diamonds) calibrated at SATURNE. Although the tensor figure-of-merit values F_{20} and F_{22} of DPOL are slightly lower than those of POLDER, which employed a liquid hydrogen target for the scatterer, almost comparable values to those of POMME are obtained for the vector figure-of-merit values F_{11}. The feature of DPOL of having large figure-of-merit values for both vector and tensor components in a single counter configuration helps reduce uncertainties associated with the measured polarization observables than would be achieved using different polarimeters in separate measurements, and makes DPOL a unique apparatus for nuclear spectroscopy using intermediate-energy polarized deuterons.

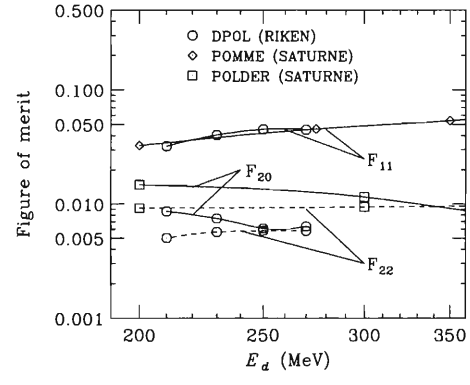

Fig. 2. Summary of the calibration experiment of DPOL.

*1 Department of Physics, Tokyo Institute of Technology
*2 Department of Physics, University of Tokyo
*3 Department of Physics, Saitama University
*4 Department of Physics, Tohoku University
*5 Research Center for Nuclear Physics, Osaka University
*6 Faculty of Home Economics, Tokyo Kasei University

References

1) Y. Satou et al.: Phys. Lett. B **521**, 153 (2001).
2) B. Bonin et al.: Nucl. Instrum. Methods Phys. Res. A **288**, 389 (1990).
3) S. Kox et al.: Nucl. Instrum. Methods Phys. Res. A **346**, 527 (1994).

Development of laser spectroscopic detection for RI atoms trapped in superfluid helium

Y. Fukuyama, Y. Matsuo, T. Furukawa,* T. Kobayashi, T. Shimoda,* and I. Tanihata

High-resolution laser spectroscopy of atoms reveals the nuclear properties through the interaction between nuclear moments and electrons (hyperfine interaction). Among nuclear properties, charge radii are related to isotope shifts (Is), and spin and electromagnetic moments are related to hyperfine structures (HFs). For laser spectroscopy of a limited number of atoms such as RI atoms that are generated at accelerator facilities, trapping atoms in a spatially limited area would be essential. Well-known techniques possibly being applied for this purpose are the electromagnetic ion trap and laser trapping/cooling of atoms. However, atoms that can be trapped and cooled are mostly limited to alkali, alkali-earth, and rare-gas atoms, and alkali-earth ions because these trapping and cooling techniques utilize closed cycles in the electronic energy structure of atoms. Very few attempts have been made to trap high-energy ion beams over 1 MeV/u and to combine them with laser spectroscopy, such as, the development of the rf-ion guide technique using He buffer gas is in progress in RIKEN.[1)]

To overcome the limitation of trapping methods that rely on the internal energy structure of atoms, we propose a *new* type of trap, which is a superfluid He trap where RI atoms are directly injected and trapped. For this purpose two major advantages are expected in the superfluid He trap. One is that any nuclide species are stopped and trapped in superfluid He as neutral atoms or singly charged ions. When the ion beam is injected to the superfluid He with a kinetic energy of 25 MeV/u, injected atoms stop after traveling 10–30 mm depending on nuclear species. The other is that superfluid He is a highly transparent medium from the region of RF to UV, so that it is possible to perform ion beam injection and laser spectroscopy at the same time. In particular, an optical pumping technique and a laser-microwave double-resonance technique are powerful tools for measuring hyperfine structures precisely. In vacuum, these techniques require multiple lasers of different wavelengths except for alkali atoms and alkali-earth ions. Atoms in superfluid He stay in a different environment from those in vacuum. Since electronic transition wavelengths of atoms in superfluid He are affected by the interaction between electrons and surrounding He atoms, the linewidths of electronic transitions are broadened. It is expected that the optical pumping of various atoms will be made possible using a single laser line owing to such line broadening. The aim of this work is to develop the system to trap and carry out laser spectroscopy of RI atoms using a superfluid He trap and to deduce information on the nuclear structure such as electromagnetic moments of nuclei.

The specific aim of this research is to determine the electromagnetic moment of proton-rich unstable ^{21}Mg atoms. To achieve our goals of trapping Mg atoms in superfluid He and deducing electromagnetic moments, the following three steps are required. (1) Injection of an ion beam to a liquid He chamber and optical detection of trapped atoms. (2) Optical pumping of atoms other than alkali atoms in superfluid He. (3) Measurement of electromagnetic moments of ^{21}Mg using a laser-microwave double-resonance technique. In order to start with step (1), it is important to confirm that trapped atoms are in the region of optical detection. First we would like to perform position-sensitive detection of ^{23}Mg using beta-ray counters and optical detection with LIF simultaneously. The reasons for choosing ^{23}Mg as the starting material are that Mg is the atom that has been optically observed atom in superfluid He and the lifetime of ^{23}Mg, 11.3 s, is comparable to the trapping time of the injected ion beam.

For the preparation of step (1), we have constructed a laser spectroscopic detection system for RI atoms using a superfluid He cryostat. The overview is shown in Fig. 1. The system consists of three parts, the details of which are as follows.

(a) A superfluid He cryostat
A newly constructed cryostat has a 77 K liquid nitrogen bath, a 4.2 K liquid He bath, and a superfluid He bath, as depicted in Fig. 2. Liquid He is transferred from a container to the 4.2 K liquid He bath using a transfer tube, then transferred from the 4.2 K bath to the superfluid He bath through a needle valve. Thus, the condition of the superfluid He bath is not affected by that of the 4.2 K He bath. ^{23}Mg atoms of 25 MeV/u are directly injected into the superfluid He bath and stop after traveling about 25 mm. Since the

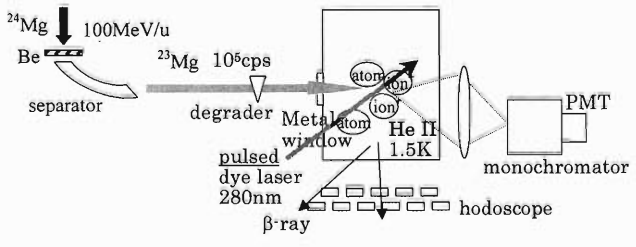

Fig. 1. Overview of the RI ion beam injection and trapping in the superfluid He cryostat.

* Department of Physics, Osaka University

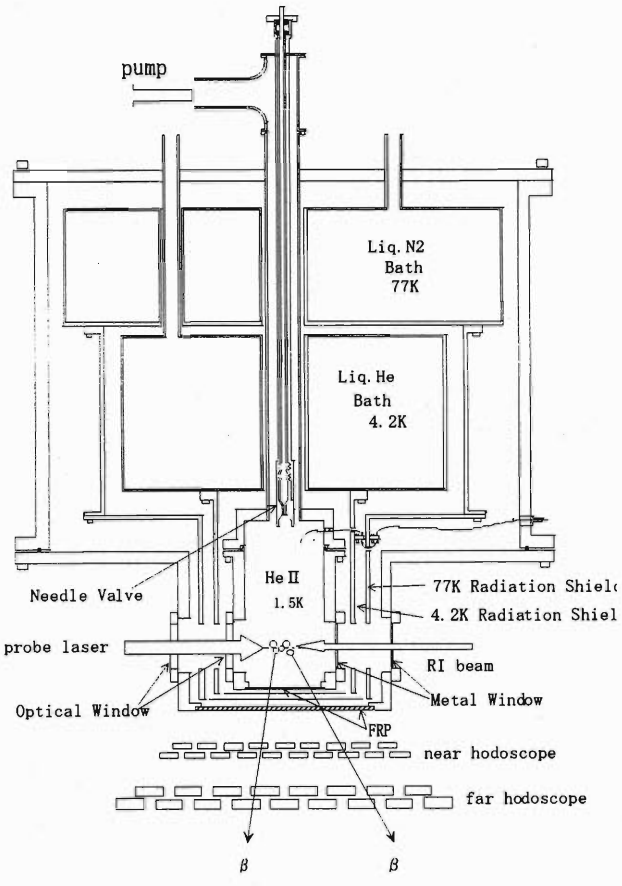

Fig. 2. Cross-sectional view of the superfluid He cryostat.

stop position of injected atoms linearly depends on the density of liquid He, the temperature of liquid He in the superfluid He bath is required to be stable within 5 percent during the experiment. At present, the new cryostat has achieved stability at the temperature of 2.01 ± 0.05 K for a few hours.

(b) Beta-ray hodoscopes
The beta-ray which is generated by trapped RI atoms in superfluid He is observed underneath the cryostat using a hodoscope. The hodoscope consists of two layers of plastic scintillators that are 30 cm apart. The position of the trapped RI atoms can be determined by monitoring the beta-ray trace through the two layers. The position resolution of this hodoscope system is approximately 5 mm. The stop position of RI atoms can be adjusted by putting a degrader of proper thickness in front of the cryostat so that the RI atom is stopped and trapped at the center of the cryostat.

(c) Laser spectroscopic detection system
The trapped RI atoms in superfluid He are irradiated by pulsed dye laser radiation and LIF spectra are observed. The power and the diameter of the pulsed dye laser are 20 μJ/pulse and 5 mm, respectively. The correction solid angle of fluorescence is 0.7 sr (5.5%). The transmittance of monochrometer and the quantum efficiency of the photomultiplier at 285 nm, which is the resonance wavelength of a ^{23}Mg atom, are 20% and 25%, respectively. The LIF spectrum of ^{24}Mg atoms produced by laser ablation observed in liquid He using the new cryostat is shown in Fig. 3.

We are planning to perform the step (1) experiment of using the RIKEN Ring Cyclotron facility. The ^{23}Mg beam is produced by the bombardment of the primary beam of 100 MeV/u ^{24}Mg to the ^{9}Be target of 0.6 g/cm^2. Since injected atoms stay at the same position for the order of 10 s, if 10^5 cps atoms are generated, we expect 10^6 atoms in the detection region that is estimated to be sufficient for optical detection according to the experiment at the laser laboratory. The preparation for the experiment is now in progress.

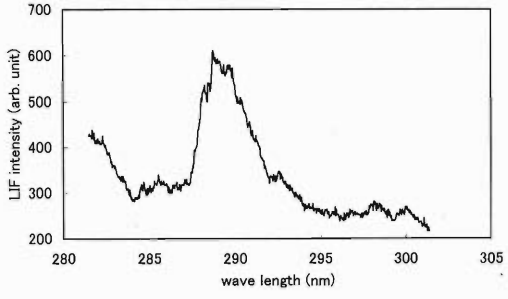

Fig. 3. LIF spectrum of ^{24}Mg atoms in liquid He.

References

1) M. Wada et al.: RIKEN Rev. No. 31, p. 56 (2000).

Development of MSTPC at a high-injection rate

T. Hashimoto,[*1,*2] T. Kawamura,[*1] H. Ishiyama,[*3] T. Ishikawa,[*1] M. H. Tanaka,[*3] T. Furukawa,[*4] N. Yoshikawa,[*3] Y. X. Watanabe,[*3] H. Miyatake,[*3] S. C. Jeong,[*3] T. Nomura,[*3] Y. Mizoi, T. Komatsubara,[*5] Y. Tagishi,[*5] and K. Nakai[*1]

A multiple-sampling tracking proportional chamber (MSTPC)[1] was constructed for experiments with radioactive nuclear beams (RNB) at the low-energy region.

Figure 1 shows the cross-sectional view of the MSTPC. The MSTPC is installed in a vacuum chamber made of aluminum and is operated at a pressure of a few hundred Torr or less. The gas in the chamber (90% He and 10% CO_2) works both as a counter gas and as a gas target. The MSTPC can measure a three-dimensional track of a multiple charged particle and the energy loss along its trajectory. Electrons produced by the charged particles are drifted through the three types of grid (gating grid, shield grid and ground grid as shown in Fig. 1) toward the proportional region, which consists of 24 cathode PAD cells with anode wires. The detection solid angle completely covers 4π.

The experimental program, which aims at determining the astrophysical reaction rate of (α, n) and (p, n) is in progress using the MSTPC. In this experiment, it is necessary that the MSTPC has the same performance at a RNB injection rate of less than 10^4 pps. However, large peak shifts of the energy-loss signals from cathode PADs were observed at a high injection rate. Figure 2 shows the systematic change of the peak shift at various injection rates of ^{15}N particle ($E = 2$ [MeV/nucleon]).

The horizontal axis shows the cathode PAD number. The pulse height is normalized to the one obtained at a injection rate about 200 pps. The sudden changes of the pulse height at both edges of the MSTPC were caused by the charge-up on the G-10 frames of the grids. In order to avoid this effect, we covered these frames with metal plates.

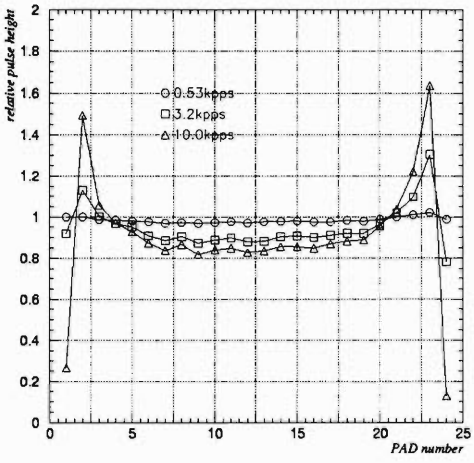

Fig. 2. Peak shift of the MSTPC.

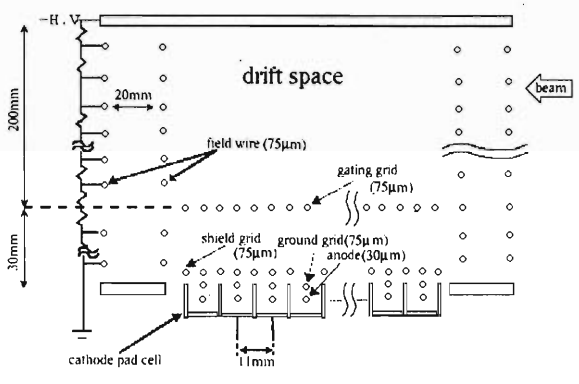

Fig. 1. Schematic cross-sectional view of the MSTPC.

Due to the space-charge gain limitation near the anode wire, a additional pulse height defect can be seen around the center of the MSTPC. As a solution to this problem, we have installed a gating grid[2] as shown in Fig. 1. Alternate wires of the gating grid are connected to two independent high-voltage power supplies and the electric transparency for drifting electrons is controlled by changing the potential difference between alternate wires. Normally, the gating grid works to absorb all electrons before the anode wires. If a trigger signal is received, the gating grid passes all electrons to reach anode wires. For example, in our experiment, the trigger signal is generated from the coincidence between the signal from PPAC, placed upstream the MSTPC, and one from the neutron counter, placed around the MSTPC.

We tested the gating grid experimentally using a sample beam of ^{14}N ions ($E = 30$ MeV) from Tandem accelerator at University of Tsukuba. The gating grid was triggered by the signal from SSD at the end of the MSTPC. By scaling down the numbers of SSD signals, various trigger rates can be set independent of the injection rate.

Figure 3 shows the peak shift as a function of the injection rate without the gating grid operation. The sudden change of the pulse height in Fig. 2 disappears. When the injection rate is 3.6 kpps, the pulse height

*1 Department of Physics, Tokyo University of Science
*2 The Japan Society for The Promotion of Science
*3 High Energy Accelerator Research Organization (KEK)
*4 Department of Physics, Osaka University
*5 Department of Physics, University of Tsukuba

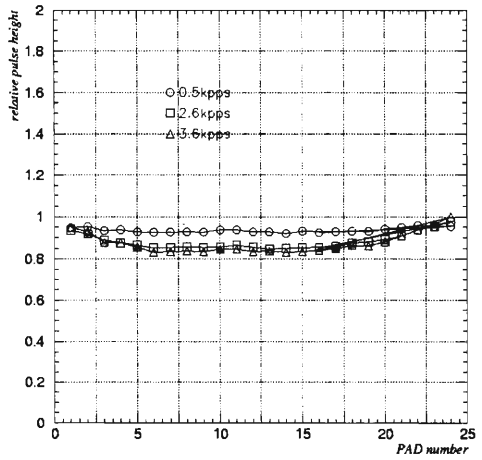

Fig. 3. Peak shift without the gating grid.

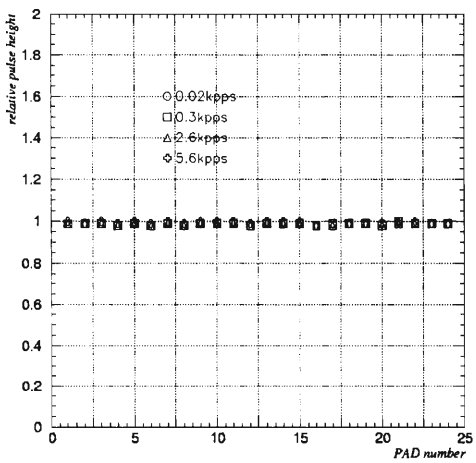

Fig. 4. Peak shift using the gating grid.

defect becomes 15% around the center of the MSTPC. The value is nearly the same as that shown in the Fig. 2.

Figure 4 shows the peak shift using the gating grid operation. The trigger rate was kept constant at 20 cps at various injection rates from 20 pps to 5.6 kpps. This trigger rate is the realistic value in our experiment. The energy-loss signals are unchanged within 2% accuracy at the injection rates from 20 pps to 5.6 kpps. This result shows a sufficiently small peak shift for our experimental requirements.

We performed quantitative evaluation of the pulse height defect around the center of the MSTPC. The sheath of positive ions, which grows rapidly near the anode wire, acts so that the local electric field is reduced. Therefore, multiplication becomes small (space-charge gain limitation). Following the formula by Hendricks,[3] we evaluate the pulse height defect numerically under the assumption of using the cylindrical cathode. As a result, it is estimated that the pulse height defect becomes 9% when the injection rate is 3.6 kpps. This value is consistent with the measured value.

After the improvement mentioned above, we carried out the measurement of the $^{16}\mathrm{N}(\alpha,n)^{19}\mathrm{F}$ reaction cross section. The injection rate of $^{16}\mathrm{N}$ ions is 3.0 kpps. The typical event of this experiment is shown in Fig. 5.

The left side figure shows the energy loss (dE/dx) spectrum in the PAD length. A sudden change of the dE/dx signal indicates that the $^{16}\mathrm{N}$ beam really reacts with the $^{4}\mathrm{He}$ nucleus. The right side figures show the horizontal and vertical projections of the three-dimensional particle trajectory. The vertical axes of each spectra represent the horizontal and vertical positions, respectively. The arrows in these figures show the direction of the neutron detected simultaneously. Hence, from these signals, *i.e.*, energy losses and direction of charged particles together with emitted neutrons, the true event can be assigned unambiguously. Further analysis is in progress.

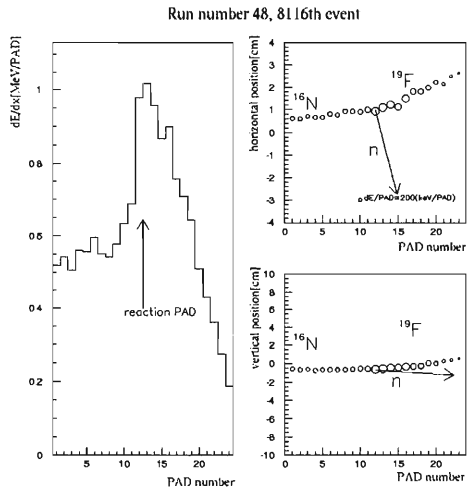

Fig. 5. Typical event of $^{16}\mathrm{N}(\alpha,n)^{19}\mathrm{F}$.

Measurement of the $^{8}\mathrm{Li}(\alpha,n)^{11}\mathrm{B}$ reaction cross section will be carried out at JAERI this winter.

References

1) Y. Mizoi et al.: Nucl. Instrum. Methods Phys. Res. A **431**, 112 (1999).
2) P. Nemethly et al.: Nucl. Instrum. Methods Phys. Res. **212**, 112 (1983).
3) R. W. Hendricks: Rev. Sci. Instrum. **40**, 1216 (1969).

Development of time-of-flight detector with streak camera III

T. Ohnishi, K. Morimoto, F. Tokanai,* and I. Tanihata

A high-resolution time-of-flight (ToF) detector using a streak camera has been developed for particle identification of the radioactive-isotope (RI) beam at RI Beam Factory.[1,2] At this factory, heavy ions are accelerated up to 400 MeV/A. To measure the mass (A) of a heavy ion at such high energies using the conventional detector system ($\Delta t \sim 150$ ps), a long flight length is required for the ToF method. For example, to measure a mass of around 60 amu with $\Delta A = 0.7$, the required flight length is about 11 m. Therefore, a new ToF detector system using a streak camera with short flight length ($\sim$1 m) and good time resolution ($\sim$10 ps) has been constructed.

The schematic view of this ToF detector system is shown in Fig. 1. Two streak cameras are tilted at 45 degrees with respect to the beam line. The target foil is mounted at the center of the detector. Each emitted electrons from the target are accelerated and measured by the wedge-and-strip (W&S) detector located at the end of the streak camera. These electrons are swept by RF signals while passing through the streak camera. Therefore, the difference in positions measured using two streak cameras gives the flight time of the beam. The time resolution is related to the position resolution of the W&S detector. To obtain a good time resolution ($\sim$10 ps), a position resolution better than 50 μm is required.

The test experiment was performed at the E1C beam line using a ^{20}Ne beam, whose energy is equal to 135 MeV/A. Two streak cameras were placed after the second focal plane. The result of the previous experiment[3] indicated the detection efficiency of this system to be about 50%. This was due to the low secondary electron emission probability from the thin Al foil target with evaporated Au. To improve this low efficiency, the CsI-evaporated target is used in this experiment.

The target thickness dependence of the detection efficiency is shown in Fig. 2. When the thickness is greater than 20 μg/cm^2, the detection efficiency is found to be almost 99%. This means that the total number of emitted electrons become very large, due to the low binding energy of CsI ions.

Measurement with the RI beam was also performed. For particle identification, a silicon detector for ΔE measurement and plastic counter for ToF measurement were used. The Z-dependence of the detection efficiency is shown in Fig. 3. The efficiency is higher than 90% when Z is greater than 6. Figure 4 shows the Z-dependence of the sum of the electrons emitted from the target. The solid line shows the result of fitting. This dependence ($\sim Z^2$) is explained by energy loss in the target.

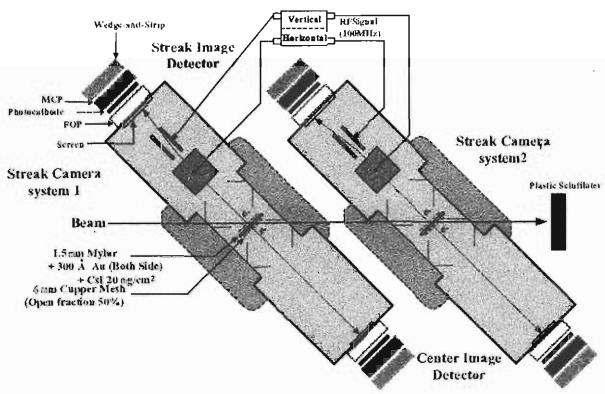

Fig. 1. Schematic view of experimental setup.

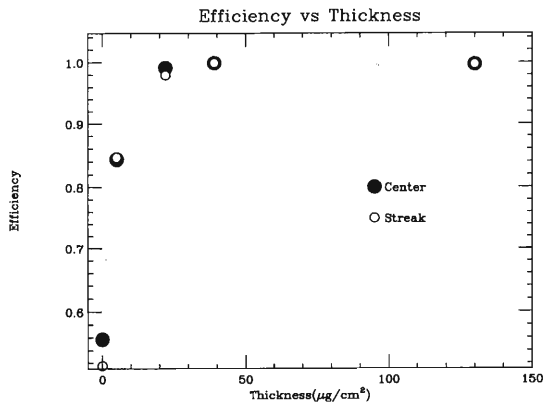

Fig. 2. Target thickness dependence of detection efficiency. "Streak" and "Center" denote streak cameras with and without RF signal, respectively.

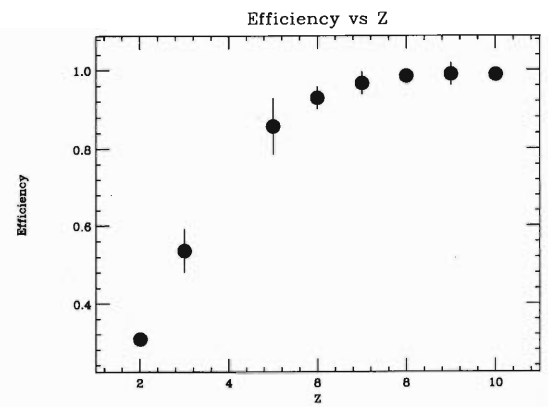

Fig. 3. Z dependence of detection efficiency.

* Department of Physics, Yamagata University

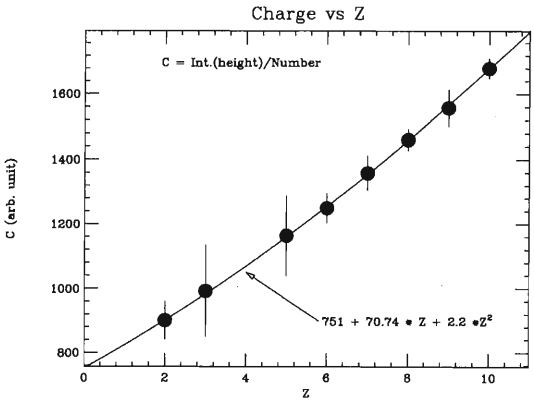

Fig. 4. Z dependence of total charge. The solid line shows the result of fitting.

The ToF resolution was measured using this system. The obtained value was 1.5 ns (FWHM). Although the number of secondary electrons emitted from the target evaporated with CsI was much larger than we expected, the time resolution was not as good as expected. One reason is that the electrical setting (amplifier or MCP gain) in the online measurement was probably different from that in an offline calibration with a source.

In future, we plan to calibrate the total system including the above-mentioned electronics with a beam. We expect to obtain a good time resolution.

References

1) F. Tokanai et al.: IEEE Trans. Nucl. Sci. **47**, 1753 (2000).
2) F. Tokanai et al.: RIKEN Accel. Prog. Rep. **33**, 159 (2000).
3) K. Morimoto et al.: RIKEN Accel. Prog. Rep. **35**, 161 (2002).

Off-line test using a multiple-reflection time-of-flight mass spectrometer

Y. Ishida, M. Wada, Y. Matsuo, I. Tanihata, A. Casares,* and H. Wollnik*

The masses of nuclei in regions far from β-stability are an interesting research subject because they play an important role in astrophysical processes, and because the predictions of various mass models greatly differ from each other. However, mass measurements with good accuracy are scarce in such regions due to experimental difficulty.

We plan to measure the masses of very short lived nuclei far from stability using a multiple-reflection time-of-flight mass spectrometer (MR-TOF). A large variety of exotic nuclei can be produced and separated in-flight using the RIKEN projectile fragment separator (RIPS) or Big RIPS in the RIKEN RI-beam factory project. Those energetic ions are injected into an RF ion-guide system and thermalized.[1] The ions are extracted from this system and guided to the MR-TOF for mass spectrometry.

As we have reported,[2] the MR-TOF has been constructed in RIKEN as a coaxial system with two pulsed grid-free ion mirrors and two einzel lenses. We placed an electron-impact ion source on one side and microchannel plates on the other side for an off-line test. The ions produced in the ion source by the 70-eV electron impact are accelerated to an energy of 1.5 keV, and extracted into the MR-TOF at a 0.3–5 kHz repetition frequency. By switching the electric voltages of the ion mirrors on and off, the ions can move back and forth between the ion mirrors repeatedly. The more energetic ions penetrate deeper into the repeller fields of the ion mirrors, thus the system can become energy-isochronous, that is, the flight time of the ions does not depend on ion energy although it vary with ion mass.[3]

The MR-TOF has been improved to achieve high mass-resolving power and transmission. A sample gas mixture of 50% N_2 and 50% CO was used for the off-line test because the molecules of N_2 and CO have same mass number, so that a high mass-resolving power can be demonstrated. The mass difference of these molecules is 10.46 MeV/c^2. Typical spectra with different numbers of reflections are shown in Fig. 1. As seen in Fig. 1, while the FWHM in (c) is as narrow as that in (a), the flight-time difference between N_2 and CO increases to 400 ns, which is 15 times larger than that in (a). Therefore, the mass-resolving power, $m/\Delta m = t/2FWHM$, increases to more than 40,000 and a mass accuracy of 10 keV/c^2 is achieved.

The mass-resolving power as a function of flight time is indicated in Fig. 2 (a). It is shown that the mass-resolving power increases almost linearly with flight time up to 1 ms. That is, the MR-TOF satisfies the

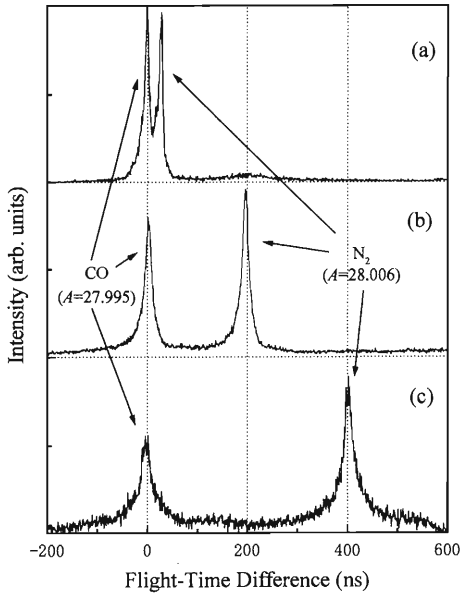

Fig. 1. Measured mass spectra of the N_2 and CO gas mixture with (a) 36 reflections, (b) 246 reflections, and (c) 510 reflections. Mass values in atomic mass units are indicated in parentheses. All spectra are aligned with the center of the CO peak.

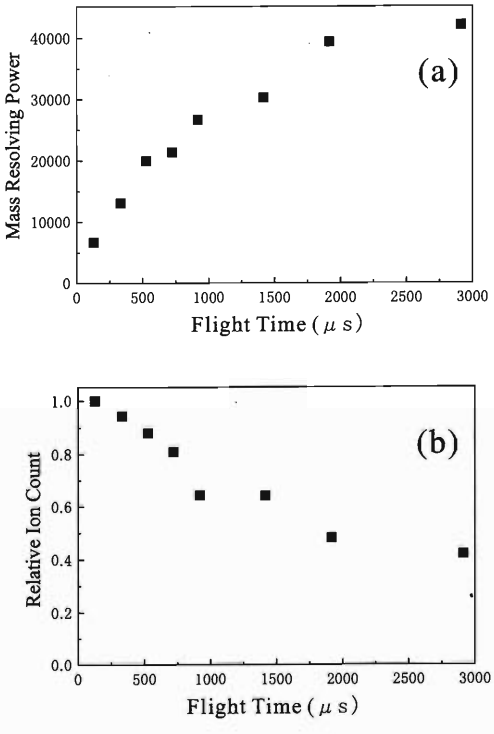

Fig. 2. Flight-time dependences of (a) mass-resolving power and (b) ion count relative to that of a 130-μs flight time.

* Oak Ridge National Laboratory, USA

energy-isochronous conditions for any numbers of reflections chosen, thus the increase in the mass-resolving power depends only on the overall flight time of the ions. However, it becomes constant at a mass-resolving power of approximately 40,000. This is due to the ripple of the high-voltage power supply and the second-order aberrations of energy and position dispersions at the ion source.

Figure 2 (b) shows the flight-time dependence of ion count relative to that of a 130-μs flight time. The ion count slightly decreased with flight time. In this measurement, the lens strength did not change while the flight time increased. The lens strength was optimal for the short flight-time measurement but not for the long flight-time measurement. This means that the beam halo caused by lateral aberrations grows every reflection.

The higher the resolving power of a mass spectrometer, the more information on nuclei we can obtain. In order to reach a high mass-resolving power of more than 10^5, it is necessary to elongate the MR-TOF because the resolving power of the MR-TOF is mainly limited by the stability of the power supply for the electrodes.[4] For on-line measurements, modification of the ion source is necessary.

References

1) M. Wada et al.: RIKEN Accel. Prog. Rep. **35**, 141 (2002).
2) Y. Ishida et al.: RIKEN Accel. Prog. Rep. **35**, 157 (2002).
3) H. Wollnik and M. Przewloka: Int. J. Mass Spectrom. Ion Processes **96**, 267 (1990).
4) A. Casares, A. Kholomeev, and H. Wollnik: Int. J. Mass Spectrom. **206**, 267 (2001).

Preparation of boron target for projectile fragmentation

S. Ozawa and M. Hamagaki

In order to use boron as a target for projectile fragmentation in nuclear physics experiments, we developed a new method of preparing self-supporting boron films by sputtering with an electron-beam-excited plasma (EBEP).[1] For example, ^{11}B(^{18}O, ^{17}N)^{12}C and ^{11}B(d, ^{2}He)^{11}Be reactions[2] require the boron target.

In general, it is difficult to prepare self-supporting boron films and high-quality boron films are quite important for the target. There are three commonly used methods of preparing boron films; vapor deposition,[3] pressing, and sputtering.[4] Vapor deposition has an advantage in terms of deposition rate, but it is difficult to prepare self-supporting films because the films prepared by this method are low-density and porous. Pressing enables preparation of high-purity films easily, but the method is only effective for a thick target (more than 10 mg/cm^2). Sputtering enables preparation of high-density films, however the deposition rate of sputtering is lower than that of vapor deposition. Moreover, this method requires an external heater for heating the boron target in order to apply a bias voltage because boron has electrical resistivity of 4×10^6 Ωcm at room temperature (20°C), which decreases considerably with an increase in temperature. For example, an infrared lamp or a laser is used for this method.

EBEP has the potential to increase the deposition rate and temperature of the boron target because of high-density ions and energetic electrons. It is very important for EBEP sputtering that the energy of the high-density electron beam leads to an increase in the plasma density and temperature of the boron target in the plasma. The deposition rate increases with ion current to bombard the target. The boron target changes from insulator to conductor by electron beam bombardment without an external heater such as a lamp or a laser.

A schematic view of the experimental setup is shown in Fig. 1. The setup consists of three regions: discharge plasma region, electron accelerating region, and EBEP region. The entire vacuum chambers are made of Pyrex glass for insulation. The target is a boron tablet (ϕ40 mm × 5 mm) with a purity of 99%, and covered by carbon which has a 30 mm aperture (see Fig. 2). The feedthrough made of copper is covered by an insulator to prevent sputtring, because the material with an applied bias voltage is sputtered by argon ions when it comes in contact with a plasma. The substrate is Pyrex glass with a thickness of 1 mm and placed on the copper table which is cooled by water. A shutter is located above the table, which can do open-close movement by rotating the rod outside the vacuum chamber. A carbon chip (10 mm × 10 mm), the mass of which has been measured beforehand, is placed on the substrate to measure the thickness of the boron film. The distance from the target to the substrate is 30 mm. The tilt angle of the target is about 20 degrees. The typical parameters of the EBEP system are shown in Table 1. Before the experiment, the EBEP region was pumped up to 7×10^{-4} Pa. Then the region was filled up with Ar gas of 0.1 Pa. The electron beam injected into the EBEP region produces a high-density plasma, and then bombards the boron target. The boron target was heated sufficiently to be a conductor (~1000°C) by the electron beam. The bias voltage was applied to the boron target when the target became a conductor, and the shutter was opened. The target was sputtered by Ar ions with the energy of the applied voltage. At this time, the boron target maintained a high temperature by high-power ion bombardment. The diameter of the electron beam was about 30 mm.

Deposited films normally have the internal stress.

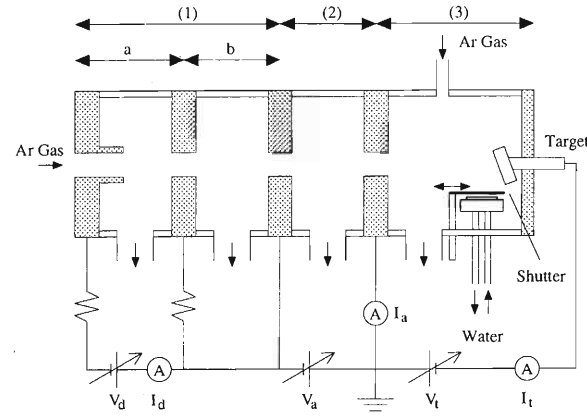

Fig. 1. Layout of the experimental setup. The apparatus consists of three region: discharge plasma region (1), electron accelerating region (2) and EBEP region (3).

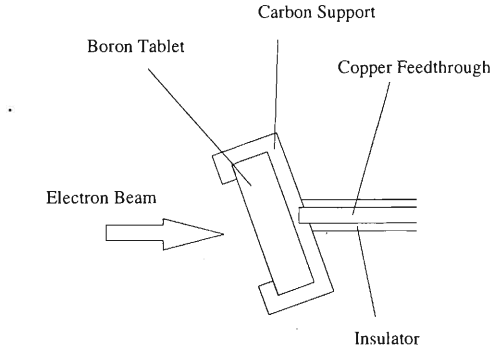

Fig. 2. Schematic view of the target.

Table 1. Typical parameters of the EBEP system. Refer to Fig. 1 for the gas pressure of each region.

Discharge voltage (V_d)	40 V
Discharge current (I_d)	6 A
Acceleration voltage (V_a)	100 V
Electron beam current (I_a)	5 A
Target bias voltage (V_t)	−280 V
Target current (I_t)	0.6 A
Gas pressure of (1)-a region	10 Pa
Gas pressure of (1)-b region	1 Pa
Gas pressure of (2) region	0.01 Pa
Base pressure of (3) region	7×10^{-4} Pa
Gas pressure of (3) region	0.1 Pa

A large stress causes mechanical failure to the films during deposition. In the present experiment, a boron film of 140 μg/cm^2 was obtained by deposition for an hour, and the thickness being the limiting factor was controlled under the present conditions. The deposition rate was 0.17 nm/s. Hechtl reported that boron films of more than 120 μg/cm^2 start flaking due to the internal stress.[5] On the other hand, Satomi *et al.* reported that the internal stress in the boron films on Mo substrates changed from compressive stress to large tensile stress by varying deposition rate and substrate temperature.[6] We would determine stress-free conditions and prepare boron films of more than 140 μg/cm^2 by optimization of these parameters.

The deposited boron films must be separated from the substrate to be self-supporting films. In general, water-soluble materials are deposited on the substrate before the boron films are deposited. However, self-supporting boron films are obtained without water-soluble materials on the substrate by EBEP sputtering.

According to scanning electron microscope (SEM) micrographs, the surface of the films is very clean and smooth as observed in the image magnified to 500 diameters. The films are analyzed by an electron probe micro analyzer (EPMA). Table 2 shows the result of EPMA analysis. Boron, carbon, nitrogen and oxygen were detected. To use boron as a target in nuclear physics experiments, more than 90% purity is necessary. Impurity of carbon will be decreased easily by enveloping the target support made of carbon with an isolator. To reduce the contamination of nitrogen and oxygen, we should improve the base pressure of the vacuum chamber.

Table 2. Components of boron films.

Element	Atomic percent
Boron	39.0
Carbon	33.3
Nitrogen	20.9
Oxygen	6.8

References

1) M. Hamagaki et al.: Jpn. J. Appl. Phys. **33**, 4369 (1994).
2) T. Ohnishi et al.: Nucl. Phys. A **687**, 38c (2001).
3) K. Kamimura et al.: J. Solid State Chem. **154**, 153 (2000).
4) Y. Itoh et al.: Jpn. J. Appl. Phys. **33**, 5959 (1994).
5) E. Hechtl: J. Nucl. Mater. **196/198**, 713 (1990).
6) N. Satomi et al.: Fusion Engineering and Design **39/40**, 493 (1998).

Development of a solid oxygen target for $^{16}O(d, d^*_{singlet})^{16}O^*(SDR)$ reaction measurement

R. Suzuki,[*1] H. Okamura,[*1] T. Uesaka,[*3] K. Suda,[*1] H. Kumasaka,[*1] T. Ikeda,[*1] K. Itoh,[*1]
H. Sakai, A. Tamii,[*2] M. Hatano,[*2] Y. Maeda,[*2] T. Saito,[*2] H. Kuboki,[*2]
N. Sakamoto, K. Sekiguchi, Y. Satou,[*3] and K. Yako[*3]

The ^{16}O nucleus is the lightest double-magic nucleus, except for ^4He, and therefore is one of the most important subjects to be studied in nuclear physics. Recently, it has also interested astrophysicists since Langanke *et al.*[1] suggested the use of ^{16}O nuclei, which are abundant in the water tank of Super Kamiokande, as a detector material for detection of ν_μ and ν_τ. For the purpose of determining the response of the ^{16}O nucleus to neutral current, we measured the cross section of spin dipole resonance (SDR) in ^{16}O via the $(d, d^*_{singlet})$ reaction.[2] We have developed a solid oxygen target for the measurement.

Possible candidates for the ^{16}O target are compounds such as H_2O, Li_2O, a gas target, a liquid target, and a solid target. Since spin-isospin flip reactions of hydrogen and other spin-unsaturated nuclei in there compounds have much larger cross sections than those of oxygen nuclei, these compounds are not appropriate for the target material. A gas target, which necessarily accompanies window foils, is also not appropriate for the same reason. On the other hand, a liquid target is excluded because of its luminosity: Since the measurement of the $(d, d^*_{singlet})$ reaction requires coincidence detections of two nucleons, the luminosity should be less than 10^3/mb·s to maintain an appropriate S/N ratio. Supposing that the beam intensity is larger than 0.1 nA to make the effect of dark current negligible, it is necessary to prepare a target with a thickness of less than several tens of mg/cm^2. This thickness is impossible to achieve for a liquid target. Thus we decided to develop a windowless solid oxygen target of high purity and suitable thickness.

The target was prepared in the form of an oxygen "foil" on a thin gold backing. The gold backing of 1 μm thickness was mounted on a refrigerator and cooled to $\sim$20 K. Oxygen gas was sprayed slowly from a diffuser onto the backing and frozen. The diffuser end was covered with a mesh which was 250 μm thick and had 300 μm diameter holes spaced at 750 μm intervals (Fig. 1.)

Measurement of a thickness was carried out with two independent methods. One method is based on a scattering loss of β-ray. A β source (^{90}Sr) is placed in front of the oxygen target and a scintillator ($5 \times 5 \times 5$ mm^3) detects β-rays passing through the oxygen target. Collimators are located at both side of the target. Then we have compared the counting rate of β-ray before and after spraying oxygen gas. To transform the scattering loss to the thickness of oxygen, we used the β attenuation length estimated by interpolating ^{12}C and ^{27}Al data. With this measurement we optimized spraying parameters. It is found that oxygen accumulates at a rate of 2 mg/cm^2 in every one minute when the flow rate is 5 cc/min.

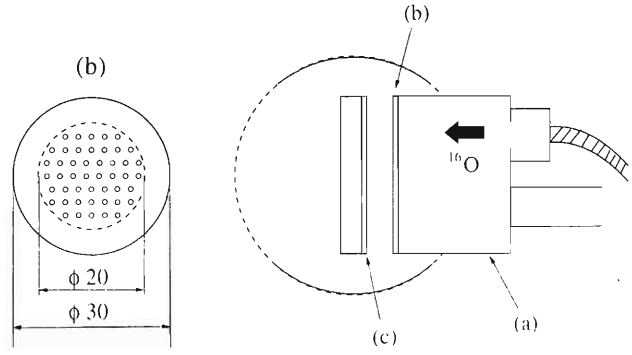

Fig. 1. (a) is a diffuser and oxygen gas is sprayed from there. (b) is a mesh which was 250 μm thick and had 300 μm diameter holes spaced at 750 μm intervals. (c) is a 1 μm gold backing.

As the other method, an elastic scattering experiment which use 270 MeV deuteron beam was carried out using the spectrometer at RIKEN Accelerator Research Facility, SMART. The solid oxygen, Mylar and carbon were used as a target. Thicknesses of Mylar and carbon were both 35 mg/cm^2. Mylar was used to calibrate the oxygen thickness. Carbon was used to subtract a contribution of carbon in Mylar. As a result from the measurement of elastic scattering, the thickness of the oxygen target was found to be 43.4 ± 1.3 mg/cm^2, when we sprayed oxygen gas for 20 minutes at the flow rate 5 cc/min. This is consistent with the β ray measurement. It is also found that thickess has non-uniformity, which has not been found in the β ray measurement. When we measured the thickness at an interval of 2 mm, we found it varied from 26.9 mg/cm^2 to 49.6 mg/cm^2 in the region of $\pm$5 mm from center of the target. It may be caused by the mesh structure of the diffuser.

We also carried out measurement of the $(d, ^2He)$ reaction to estimate the S/N ratio of the $(d, d^*_{singlet})$ reaction because the $(d, ^2He)$ reaction could excite spin-isospin flip state as well as the $(d, d^*_{singlet})$ reaction.

*1 Department of Physics, Saitama University
*2 Department of Physics, University of Tokyo
*3 Center for Nuclear Study, University of Tokyo

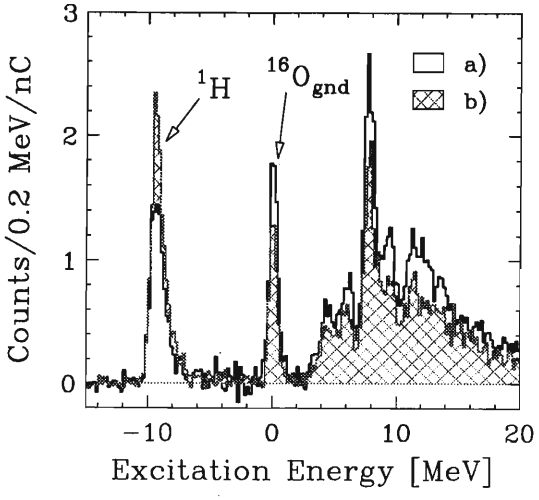

Fig. 2. Time-dependent change of ^{16}O and ^{1}H. (a) is for the first 10 min of a normal run of 105 min and (b) is for the last 10 minutes.

^{16}O peaks were clearly observed although ^{1}H peak was found at low excitation energy. This small contamination of ^{1}H is a consequence of water molecules in the residual gas stacking on the target surface continuously during the measurement. The stacking rate is 0.02 mg/cm^2/h.

It is found that ^{16}O decreased with time as shown in Fig. 2. In a typical run of 105 min and 0.3 nA, it was found that ^{16}O decreased to 7.2 mg/cm^2 and ^{1}H increased to 0.04 mg/cm^2. It is supposed that the decrease of ^{16}O is due to sublimation.

However, since the luminosity can be monitored continuously with the $(d, ^2\mathrm{He})$ reaction, the observed non-uniformity and time-dependent change in thickness do not lead to a large uncertainty in the cross section of $(d, d^*_{\mathrm{singlet}})$ reaction.

References

1) K. Langanke et al.: Phys. Rev. Lett. **76**, 2629 (1996).
2) K. Suda et al.: RIKEN Accel. Prog. Rep. **36**, 54 (2003).

RF deflector system for proton-rich RI beams (III)

K. Yamada,[*1] T. Motobayashi, N. Aoi,[*2] H. Baba,[*1] K. Demichi,[*1] Z. Elekes, H. Iwasaki,[*3] S. Kanno,[*1] T. Kubo, H. Kumagai, K. Kurita,[*1] Y. U. Matsuyama,[*1] S. Michimasa,[*3] M. Notani,[*3] A. Ozawa, A. Saito,[*1] E. Takeshita,[*1] S. Takeuchi, Y. Togano,[*1] Y. Yanagisawa, and I. Tanihata

The RF deflector system reported previously[1,2] was completed. The cavity resonator part including parallel-electrodes was installed between the Quadrupole-Magnet-9 (Q9) and the second focal plane (F2) chamber of RIPS.[3] The switching magnet which had been located in that place was removed, and a new straight beam duct would be attached when the deflector system is in the offline state. All setup of the system is shown in Fig. 1.

Figure 2 shows a picture of the main part of the RF deflector system connected to the beam line. The cylindrical part is the coaxial cavity resonator, and the square box seen in front of the cavity contains a 20 kW main amplifier. The cavity is evacuated by an 800 litter compound molecular pump and an oil-free scroll pump. Figure 3 shows the copper electrodes in the beam line. The electrodes are cooled by water, and their gap size is fixed to be 40 mm. The width of the electrodes, 120 mm, is sufficiently large to accept secondary beams with the maximum angular acceptance of RIPS, though the gap of 40 mm accepts only 70–80% of the full emittance of RIPS.

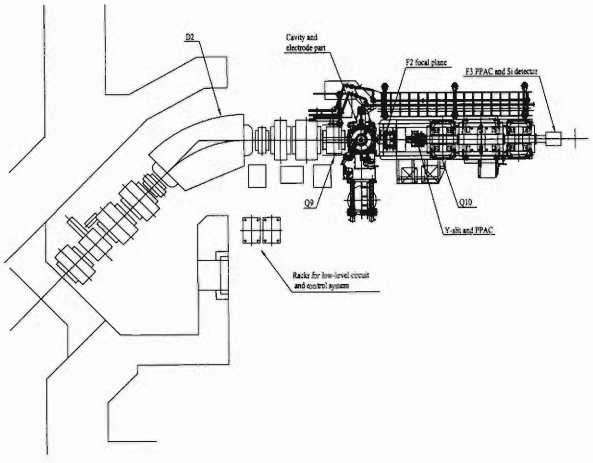

Fig. 1. All setup of RF deflector system.

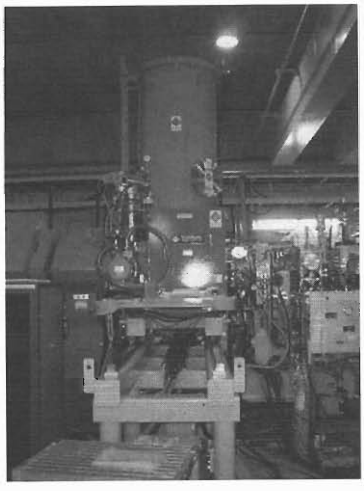

Fig. 2. An outward appearance of RF deflector system.

A high-voltage DC power supply for the main amplifier was set in the power source room E. High-voltage lines of 10 kV for the plate of the vacuum tube, 1 kV for the screen grid, 300 V for the control grid, the filament power supply, and control signal cables were wired from the power supply to the main amplifier via the beam distribution room D. Two racks for the low-level circuit and control system were placed on the side of the cavity. A personal computer (PC) for control was put in the RIPS control room, and was connected directly to the control system by an Ethernet twist-pair cable. We can operate the deflector system by a touch panel on the control system or the control PC exclusively.

A cubic chamber for a vertical-slit system (Y-slit) was also inserted between the F2 chamber and Q10 lens. The slit consists of two 120 mm × 115 mm copper plates of 25 mm thickness, and its aperture is changed from ±1 mm to ±100 mm by remote control.

We performed a test experiment using a ^{20}Ne beam at 135 MeV/nucleon accelerated by Riken Ring Cyclotron with an RF frequency of 32.6 MHz. The voltage applied to the RF deflector system was set to be 100 kV with a frequency of 16.3 MHz. Since the vacuum pres-

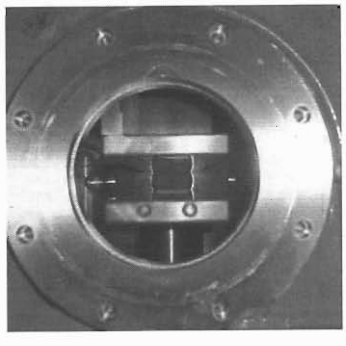

Fig. 3. The copper electrodes in the main vacuum chamber.

*1 Department of Physics, Rikkyo University
*2 Department of Physics, University of Tokyo
*3 Center for Nuclear Study, University of Tokyo

sure must be lower than 2×10^{-4} Pa in order to operate the deflector system, a 12-μm-thick Mylar film was inserted between the deflector and the F2 chamber for vacuum separation. Two NaI(Tl) scintillators and four CsI(Tl) scintillators were mounted after F3 to check the influences of RF noise and X-rays from the RF deflector system. The incident beam was identified by the TOF-ΔE method with a 0.5-mm-thick plastic scintillator and a 350-μm-thick silicon detector set at F2. A PPAC was installed after the Y-slit to measure the beam deflection from the central orbit. Another PPAC set at F2 was resistant to the possible effects of RF noise, by the use of dual sealed cables, gold evaporated windows, and so on. However, this PPAC could not be used because of the influence of X-rays. Other detectors mounted downstream could be used without a problem.

An attenuated primary beam was focused on a 10-mm-thick ^{9}Be target, and was degraded to 82 MeV/nucleon to be analyzed by RIPS. The momentum spread was maintained to be $\pm 0.05\%$. The parameters of RIPS were adjusted to focus the beam on F2 in the horizontal direction and on the Y-slit in the vertical direction. Figure 4 shows the beam profile measured at the position of the Y-slit as a function of the RF phase

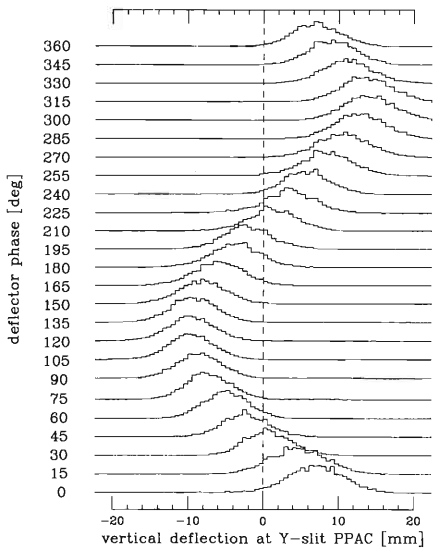

Fig. 4. The central orbit deflection for each phase of the deflector system.

of the deflector, demonstrating correct performance of the system.

In order to examine its capability of purifying secondary beams, "cocktail" beams of ^{16}O, ^{17}F, ^{18}Ne were injected into the RF deflector. Figure 5 shows TOF spectra measured for the beam with $\pm 1.0\%$ momentum spread. When the Y-slit is open to 200 mm, the spectrum shown in Fig. 5 (a) is free from the effect of the deflector, and events for ^{16}O, ^{17}F, and ^{18}Ne are all seen. On the other hand, by adjusting the oscillation phase so as to maximize the ^{18}Ne intensity, the spectrum with a narrow slit (Fig. 5 (b)) exhibits a large reduction of unwanted ^{16}O and ^{17}F. Consequently, the purity of ^{18}Ne in the beam is improved from 17% to 86% by the use of the RF deflector. The RF deflector system has already been successfully employed in Coulomb excitation experiments on ^{46}Cr, ^{50}Fe, ^{54}Ni.[4] The system worked stably during the experiment. The RF deflector system opened up new possibilities of experiments by purifying secondary beams.

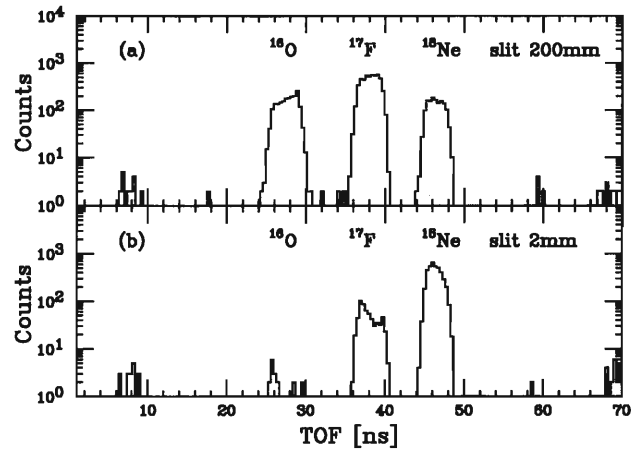

Fig. 5. An example of the effect of RF deflector system.

References

1) K. Yamada et al.: RIKEN Accel. Prog. Rep. **34**, 201 (2001).
2) K. Yamada et al.: RIKEN Accel. Prog. Rep. **35**, 147 (2002).
3) T. Kubo et al.: Nucl. Instrum. Methods Phys. Res. B **70**, 309 (1992).
4) K. Yamada et al.: RIKEN Accel. Prog. Rep. **36**, 85 (2003).

RI beam extraction using electric transportation in gas cell stopper

J. Kaihara,[*1] K. Asahi, T. Ito,[*1] D. Kameda,[*1] Y. Kobayashi, H. Miyoshi,[*1] J. Murata, T. Saito,[*2] W. Sato, K. Shimada,[*1] S. Suda,[*1] H. Ueno, H. Watanabe, and A. Yoshimi

As a part of the plan for building a radioactive atomic beam (RIAB) apparatus with the goal of producing highly polarized radioactive nuclei,[1] we performed R&D of an ion-stopping gas cell, for the purpose of stopping the RI beam produced by the projectile fragmentation reaction and separated by the RIPS (**RI**KEN **P**rojectile-Fragment **S**eparator) at RIKEN. In order to use the RI beam as an ion beam incident to the RIAB, the beam momentum must be degraded, and also, electrically neutralized. We confirmed by a simulation study that the RIAB has extensive potential for the study using polarized RI and will be able to obtain nearly 100% polarization, which allows us to have precise measurements of nuclear moments in a wide range of the nuclear chart, application to surface materials science, and also a test of fundamental symmetries such as time-reversal invariance.

The RI beam gas cell stopper is the most challenging technical part of the RIAB. A low-pressure (about 1 Torr) gas cell ion stopper (LPGS) is located immediately in front of the RIAB magnets, providing a supersonic cold flow with a Laval-type nozzle. For a sufficient stopping power and resultant transportation efficiency, another high-pressure gas cell stopper (HPGS) is located immediately in front of the LPGS. The incident ions are stopped inside the gas volume (He, Ne or Ar gas), and then transported from the HPGS to the LPSG by a gas flow and an electric field.

We have developed a new HPGS chamber apparatus from the previous HPGS (used in the experiment in October 2001[2]), which is shown in Fig. 1. The field pattern was optimized to achieve a maximum transportation efficiency, in order to obtain a strong focusing force at the nozzle. We performed the second test experiment, using the RI beam at RIKEN in November 2002. We used ^{12}B ions produced by a projectile fragmentation reaction of 110 MeV/u ^{22}Ne beam on a 740 mg/cm^2 ^{9}Be target, separated by RIPS. The incident beam energy at the HPGS is about from 0 to approximately MeV/u after the degradation. The ions stopped inside the HPSG and penetrated through it are counted by the anode electrode, which detects currents of electrons scattered by the incident ions. These signals have different time profiles, and hence we can estimate the number of the stopped ions.[3] The transported ions by an electric field and gas flow are counted by plastic scintillation counters (PS) combined with photomultipliers (PM) on the left and right sides, which detect β particles emitted from the β-unstable ion. By observing the field strength dependence on the β counting rate, we can estimate the transportation rate.

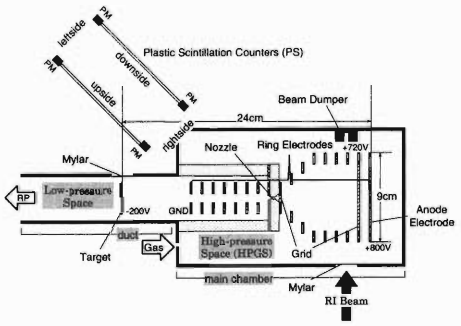

Fig. 1. Schematic view of the setup.

From the results of the measurement, we detected a part of the incident ions stopped in the HPSG.[3] The analysis of the transportation rate from the HPSG to the target in the low-pressure space is now in progress. The typical data of the PS (using He at 300 Torr) is shown in Fig. 2. The spectrum [a] and [b] respectively show $(V_R - V_L)/(V_R + V_L)$ vs β counts of the upside PS and of the downside PS, where $V_{L(R)}$ represents the pulse height detected by the left (right) PM. The spectrum [a] indicates that the upside PS detected β particles at the rightside, and [b] indicates the downside PS did at the leftside, and hence β particles are considered to originate from the duct of the apparatus. We are going to analize these data, and determine the origin of the ions.

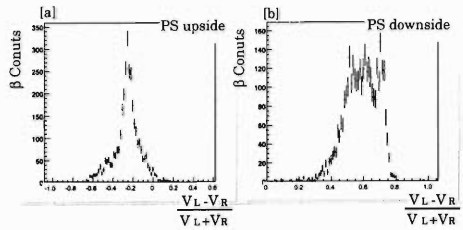

Fig. 2. $(V_R - V_L)/(V_R + V_L)$ *vs.* β particle counts of the PS.

*1 Tokyo Institute of Technology
*2 Tokyo University of Technology

References

1) H. Miyoshi et al.: RIKEN Accel. Prog. Rep. **34**, 181 (2001).
2) J. Kaihara et al.: RIKEN Accel. Prog. Rep. **35**, 146 (2002).
3) K. Shimada et al.: RIKEN Accel. Prog. Rep. **36**, 159 (2003).

Construction of sextupole magnet for RI atomic beam

H. Miyoshi,* J. Murata, K. Asahi, H. Ueno, A. Yoshimi, H. Watanabe, D. Kameda,* J. Kaihara,* K. Shimada,* W. Sato, K. Sakai,* and Y. Kobayashi

The low-energy radioactive isotope (RI) beam is useful in material physics and surface physics. The radioactive projectile fragment separator (RIPS) at RIKEN provides high-energy beams. In addition, the β-NMR method, with which we have measured a number of nuclear moments, requires a polarized RI beam. We are developing an *RI atomic-beam resonance method* to produce and handle a low-energy spin-polarized RI atomic beam, which we call RIABR.

The RIABR system is described elsewhere.[1,2] A high-energy RI beam from the accelerator is decelerated and stopped in a gas volume filled with rare gas. Using an electric field and then a gas flow, the RI ions are transported to a gas nozzle and extracted from the nozzle. Then, the RI ions are neutralized by interaction with gas or electrons from an electron gun and transported to a target sample or an RF cavity. Because the gas jet diverged from the nozzle, we have to converge the RI atomic beam. The required distribution size of the RI is smaller than several centimeters, when we converge the RI atomic beam for the target samples or an RF cavity.

We designed sextupole magnets to converge the RI atomic beam by using a calculation code OPERA.[3] The sextupole magnets will be installed 10 cm in front of the RF cavity.

The sextupole magnets shown in Fig. 1 have been constructed this year. To converge the RI atomic beam efficiently, we install three sextupole magnets. The inner diameter is increased over a region 12–30 mm. Each sextupole magnet consists of 24 segments of permanent magnet (NEOMAX-44H). The magnetic field at the pole tip is about 1.3 T.

The field strength of the sextupole magnet is shown in Fig. 2. The field strength is measured by a hole

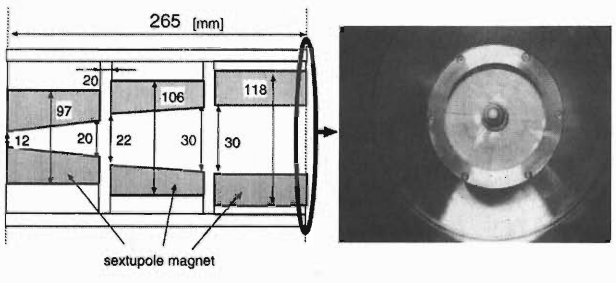

Fig. 1. Schematic view of the constructed sextupole magnet. The shadow zones are drawn as the sextupole magnet in this figure. The RI ions are transported from the left side to the right side. The right picture shows the view of the constructed magnet from the right side.

* Tokyo Institute of Technology

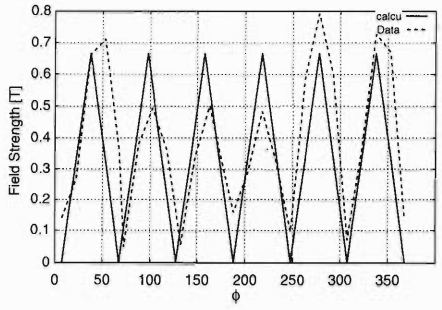

Fig. 2. Comparison of $B(\boldsymbol{r})$ field obtained from calculation[4] (solid line) with the measured values from the sextupole magnet (dotted line). ϕ denotes the angle.

probe. The measured absolute values are in agreement with the model calculation[4] within 18%. The focusing power of the sextupole magnet is simulated assuming that the mass of RI is 20 unit mass, and the drift velocity is about 600 m/s. The results are shown in Fig. 3. When the entrance size of the RF cavity is about 2 cm, the efficiency of RI which enters the RF cavity is improved by 1.8 with the magnet. This efficiency is good enough for our plan. If a lighter mass or slower RI is assumed, the focusing power becomes more efficient.

Next year, we plan to produce a low-energy RI beam using the sextupole magnet.

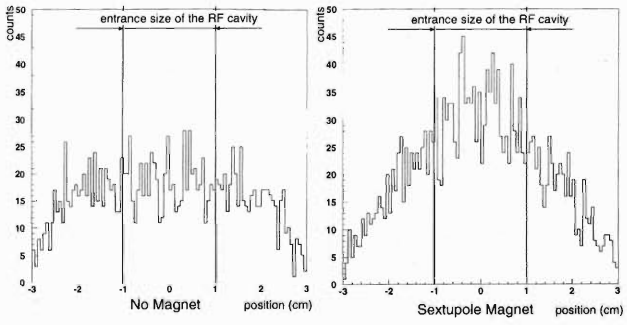

Fig. 3. Simulation result for distribution of transmitted RI at 10 cm behind the magnet. The left data is without magnet; the right one is with the sextupole magnet.

References

1) J. Kaihara et al.: RIKEN Accel. Prog. Rep. **36**, 192 (2003).
2) K. Shimada et al.: RIKEN Accel. Prog. Rep. **36**, 159 (2003).
3) OPERA-2d and OPERA-3d/TOSCA, Vector Field, Ltd., Oxford, UK.
4) K. Halbach: Nucl. Instrum. Methods **169**, 1 (1980).

On-line collection of ^{8}Li ions from the projectile fragment separator using an rf ion guide system (II)

M. Wada, Y. Ishida, T. Nakamura,[*1] A. Takamine,[*2] Y. Yamazaki, T. Kambara, H. Ohyama, Y. Kanai, T. M. Kojima, Y. Nakai, A. Yoshida, T. Kubo, Y. Matsuo, Y. Fukuyama, K. Okada,[*3] T. Sonoda,[*4] K. Noda,[*5] S. Ohtani,[*6] H. Kawakami,[*1] and I. Katayama[*1]

The projectile fragment separator provides a wide variety of short-lived RI ions with less restrictions on their chemical property or lifetime limit. The beam energy and quality, however, are not adequate for low-energy beam experiments, particularly for trapping experiments. We have been working on technical developments for obtaining slow or trapped RI ions provided by the fragment separator using a large gas-catcher cell and an rf ion guide system.[1,2] The energetic ions are stopped and thermalized in a He gas catcher where a large fraction of them are maintained in a singly charged state. The stopped ions are transported by electric fields in the cell which enables us to use a large cell for collecting large-spread beams behind an energy degrader. Since the ion motion in the gas cell simply follows the line of the electric field, all ions are collected on the cathode electrode. In the rf ion guide, the cathode electrode is composed of many ring electrodes to which rf voltages are applied in addition to dc potentials with the idea that the average force due to the rf gradient field drives the ions away from the electrodes. The ions move on the surface of the electrode toward the exit nozzle (Fig. 1). Then they are transferred to the experimental setup located under uhv by another type of rf beam guide through differential pumping sections.

On-line tests of the rf ion guide system have been performed at the present facility which provides a 70-MeV/u ^{8}Li ion beam with a typical intensity of $\sim 10^6$ atoms/s. With the first proof-of-principle model consisting of a 10 cmϕ × 70 cm cell filled with 30 Torr He gas and two-*rf-funnel* structures, an overall efficiency of 10^{-4} was obtained.[2,3] This limited efficiency was evaluated such that the stopping efficiency of the cell was 0.5% and the ion-guide efficiency was 2%. In order to improve the performance of the system, a larger cell with higher pressure, higher rf voltage and finer interval of the electrode structure is required. With this in mind, a new large gas cell of 40 cmϕ × 2 m with a newly designed planer rf electrode assembly (*rf-carpet*) was constructed. The rf carpet electrode is composed of two layers of planer printed circuit boards.

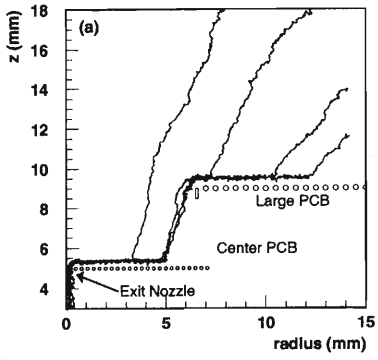

Fig. 1. Typical ion trajectories in the two-layer rf carpet as determined by microscopic particle simulation for ^{8}Li ions in 90 Torr He gas. The rf voltage between adjacent electrode rings is 190 V at 26 MHz. The superimposed dc field at the surface of the nozzle carpet and the upper carpet are 8 V/cm and 10 V/cm, respectively.

The upper board is a disk of 29 cmϕ with 280 ring electrodes and a central hole of 10 mmϕ. The bottom board is a disk of 3 cmϕ with 43 ring electrodes and an exit nozzle of 0.6 mmϕ. A typical rf voltage between adjacent ring electrodes was 150 V_{pp} at 15 MHz. This rf condition enables us to use a high-pressure He gas, typically 100 Torr, which corresponds to a stopping efficiency of about 7% for the present incoming ^{8}Li beam. Figure 2 shows the overall efficiency of the new setup as a function of the primary beam intensity. A maximum overall efficiency of 0.2% was achieved when the gas pressure was 100 Torr at low beam intensity while a decrease was observed as the beam intensity was increased. This phenomenon is also known in conventional IGISOL systems as a serious problem.[4,5] We also measured with a collimated beam to confirm that the effect is mainly dependent on the energy deposition density rather than on the total energy loss. This result suggests that it is better for high-intensity beams to use low pressure in a large cell.

One of the possible reasons for this phenomenon is the presence of impurity molecules which may cause the formation of molecular clusters. The present rf gradient field condition does not enable manipulation of such cluster ions, since the mobility of the cluster ions is not as large as that of atomic ions. An effective way to eliminate such molecules in the gas is to put a cold trap in the cell. Although it is difficult to maintain a low temperature in He gas, the obtained improvement in the performance due to this cold trap

*1 Institute of Particle and Nuclear Studies, High-Energy Accelerator Research Organization (KEK)
*2 Graduate School of Arts and Sciences, University of Tokyo
*3 Department of Physics, Sophia University
*4 Cyclotron RI Center, Tohoku University
*5 National Institute for Radiological Science
*6 Institute for Laser Science, University of Electro-Communications

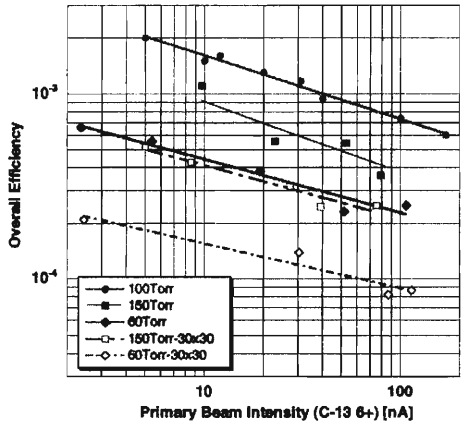

Fig. 2. Overall efficiency for the collection of ^{8}Li ions as a function of the primary beam intensity. A maximum efficiency of 0.2% was obtained when the gas pressure was 100 Torr. The data shown by dashed lines correspond to measurements with a collimated beam. Such a collimated beam reduces the total energy loss but preserves the energy deposition density. The dependence curves are almost parallel for the corresponding pairs.

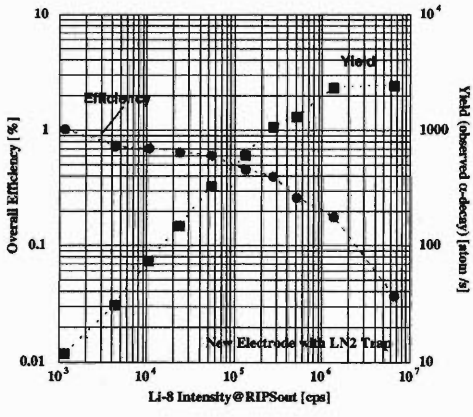

Fig. 3. Overall efficiency and yield of slow ^{8}Li ions with LN_2 trap as functions of incoming ^{8}Li beam intensity. A maximum efficiency of 1% was obtained when the intensity was weak.

is excellent. The experimental result of efficiency with a liquid-nitrogen trap is shown in Fig. 3. The maximum overall efficiency finally reached a milestone value of 1%. Although a decrease in efficiency with increasing beam intensity was still observed, the dependence was not as steep as that in the previous case.

The extraction time of the stopped ions from the cell is also an important concern, particularly when very short lived nuclei are concerned. The stopped ions are transported by the static field in the cell. The static field at a place far from the exit in the present setup is very weak, since the field is exclusively due to a penetration from the rf carpet electrode assembly. Note that an additional static field gradient obtained by applying different dc potentials on the cell itself further enhances the loss process, since part of the field lines are terminated at the surface of the cell. We measured the time spectra of the delayed α decay of ^{8}Li as a function of the time phase of the pulsed primary beam. The profile of the time spectrum shows a convolution of the time profile of the ^{8}Li ion beam and the exponential decay with the intrinsic lifetime of ^{8}Li, $T_{1/2} = 838$ ms, so that the time profile of the ^{8}Li ion beam can be deduced by the deconvolution of the measured time spectrum with the exponential response function. The pulsed primary beam with a time profile of 50 ms duration at a 0.09 Hz repetition frequency was used for the measurement. Figure 4 shows the time spectrum of the delayed α-decay of ^{8}Li with the deduced deconvolution result. This measurement was performed under the conditions that the He gas pressure was 150 Torr and the dc electric field at the surface of the electrode was 2 V/cm. The obtained time profile of the ^{8}Li ion beam showed that a 20% fraction was extracted within 100 ms while a 50% fraction within 450 ms. The last 20% fraction took more than 1.4 s to extract which is considered to come from the corner of the cell. Further investigation of the time profile analysis is in progress.

The so far obtained yield for ^{8}Li is more than 2000 atoms per second, which is sufficient for many applications. A similar yield is expected for ^{11}Be ions in the present setup. We plan to perform a precision hyperfine structure measurement in a nuclear structure study.

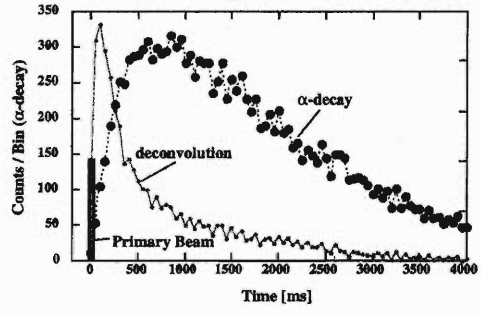

Fig. 4. Time spectra of the delayed-α decay and deconvoluted time profile of the ^{8}Li ion beam. Pulse profile of the primary beam is also indicated as a solid line.

References

1) M. Wada et al.: AIP Conf. Proc. **606**, 625 (2002).
2) M. Wada et al.: Nucl. Instrum. Methods Phys. Res. B (2002), in press.
3) M. Wada et al.: RIKEN Accel. Prog. Rep. **34**, 141 (2001).
4) K. Morita et al.: Nucl. Instrum. Methods Phys. Res. B **26**, 406 (1987).
5) P. Dendooven: Nucl. Instrum. Methods Phys. Res. B **126**, 182 (1997).

Performance of a gas-filled recoil separator GARIS

K. Morita, K. Morimoto, D. Kaji,* A. Yoneda, A. Yoshida, T. Suda, E. Ideguchi, T. Ohnishi, Y.-L. Zhao, H. Xu, T. Zheng, H. Haba, H. Kudo, K. Sueki, K. Katori and I. Tanihata

A gas-filled recoil separator GARIS for heavy-element research was installed at an experimental hall of the RIKEN (The Institute of Physical and Chemical Research) Linear Accelerator (RILAC) facility. One of the most interesting applications of the separator is the discovery of nuclei of superheavy elements whose atomic number is greater than 110. The production cross sections tend to decrease in logarithmic manner with the increase of the atomic number of the nucleus. The small production cross section is limiting farther research of nuclei with greater atomic numbers. To overcome this difficulty, more intense primary beams must be extracted from an accelerator, and recoil separator with high efficiency and high background reduction must be used. We propose a series of experiments to search for unknown nuclei of very heavy elements with the use of the GARIS and intense beams from RILAC.

We performed series of experiment to study the performance of the GARIS. Ion optical characteristics, transmissions, and background reduction rates were studied. The first separation method using a gas-filled separator was developed by Cohen and Fulmer in 1958.[1] The principle of operation of this separator is given in many references.[2–4] The most characteristic feature of this gas-filled recoil separator is that the trajectory of ions does not depend roughly on the velocity or on the initial charge state of the ions. The ions are separated and collected according only to their mass and atomic number in the first-order approximation. Therefore, this gas-filled separator has a large efficiency.

The GARIS consists of four magnets in a D1-Q1-Q2-D2 configuration, where D and Q denote the dipole and quadrupole magnets, respectively. The geometrical setup of the magnets is shown in Fig. 1. Typical beam envelops for both reaction products of interest and the primary beam are also shown in the figure. The primary beam is stopped at the tantalum plate set on the wall of the vacuum chamber of the D1 magnet. The total length of the central trajectory is 5.76 m.

The ion-optical characteristics of the system were studied by using computer code TRANSPORT.[5] The system has a double focusing condition in the horizontal and vertical directions. The horizontal magnification is -0.76, the vertical magnification is -1.99, and the dispersion is 0.97 in unit of cm/%. The acceptance of the GARIS was measured using alpha rays from an ^{241}Am source whose intensity was calibrated separately. The source was set at the target position

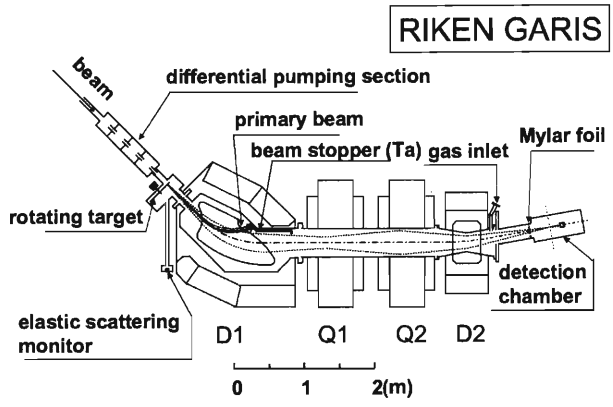

Fig. 1. Plane view of the RIKEN GARIS. The shapes of dipole magnets are shown in the figure. Envelops as in text of reaction products and the primary beam are also shown.

of the separator. The alpha particles were detected at the focal plane by using a semiconductor detector whose effective area was 60 mm × 60 mm. A helium gas was not filled in this measurement. The measured value was 12.2 msr.

In order to separate a gas region of the GARIS from a vacuum region on the accelerator side without using any foil we installed a differential pumping system. Under typical operating condition, the pressure of helium gas in GARIS is 76 Pa, while that at accelerator side nearest to the GARIS is 1×10^{-2} Pa.

The inner part of the detection chamber is separated from the gas-filled region by 1 μm Mylar foil and is kept in vacuum (3×10^{-4} Pa).

The focal plane detection system consists of two microchannel plate (MCP) assemblies and a silicon semiconductor detector (SSD) box. A schematic view of the detection system is shown in Fig. 2.

The MCP assemblies are used for two purposes. One is to measure the time-of-flight (ToF) of the particles coming into the SSD box to obtain their mass information. The other is to distinguish decay signals in the SSD box used in the anticoincidence mode. The signals from the SSD box are identified to be the decay events when both of MCP assemblies give no signal. The active area of the MCP was 78 mm in diameter. The typical timing resolution of the detectors is 500 ps in FWHM.

The stop detector array (SSD box) consists of five 16-strip silicon detectors. The active area of each detector is (60×60) mm^2. Each strip is 3.75 mm wide. In one of the detector (PSD), each strip is

* Department of Chemistry, Niigata University

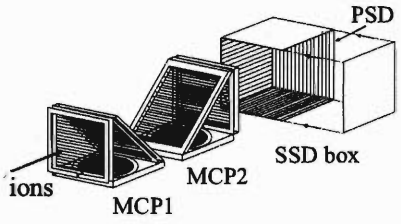

Fig. 2. Detection system at the focal plane of GARIS.

position-sensitive in the vertical direction. In the other four detectors (side detectors), strips are not position-sensitive. The side detectors are set in the backward direction to the stop detector in order to detect decay particles escaping from the implanted nuclei in the stop detector. They cover a solid angle of 70% of 2π.

Transmissions of the GARIS for low-energy ions were measured using target recoils and fusion-evaporation reaction products.

Target recoils (^{208}Pb and ^{209}Bi), which correspond to near 180 degree elastic scattering of incident beams (^{40}Ar) from the RILAC, were used as the low-energy ions. Their cross sections become those of the Rutherford scattering in the present case. These target recoils were detected at the focal plane of the GARIS with the same detector mentioned above.

Transmissions were measured also by using fusion-evaporation products. Yields of the products detected using the focal plane detector were compared with those deduced from the production cross sections reported in literatures. The reactions used were
$^{169}\mathrm{Tm}(^{40}\mathrm{Ar}, 5n)^{204}\mathrm{Fr}(E(^{40}\mathrm{Ar}) = 191.\,\mathrm{MeV})$,[6]
$^{208}\mathrm{Pb}(^{48}\mathrm{Ca}, 2n)^{254}\mathrm{No}(E(^{48}\mathrm{Ca}) = 218.4\,\mathrm{MeV})$,[7]
$^{209}\mathrm{Bi}(^{48}\mathrm{Ca}, 2n)^{255}\mathrm{Lr}(E(^{48}\mathrm{Ca}) = 218.4\,\mathrm{MeV})$,[7] and
$^{208}\mathrm{Pb}(^{58}\mathrm{Fe}, 1n)^{265}\mathrm{Hs}(E(^{58}\mathrm{Fe}) = 282.3\,\mathrm{MeV})$.[8]
The results are plotted in Fig. 3 using solid diamonds together with the results obtained using the target recoils plotted using open diamonds. In the figure, the value of v/v_0, which denotes ion velocity normalized to the Bohr velocity (= c/137), is taken as the abscissa where c denotes the light velocity. As is shown by the figure, the transmission of GARIS increases with the increase of the velocity of the ions. This phenomenon is well explained quantitatively by multiple scattering of ions with helium gas atoms.

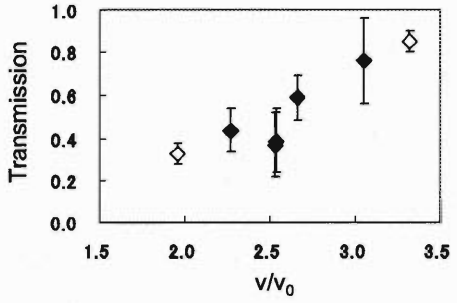

Fig. 3. Transmission of GARIS for heavy ions. Open diamonds: results measured with target recoils, solid diamonds: results measured with evaporation residues. Ion velocity normalized to the Bohr velocity (v_0) is taken as the abscisa.

References

1) B. L. Cohen and C. B. Fulmer: Nucl. Phys. **6**, 547 (1958).
2) H. Lawin et al.: Nucl. Instrum. Methods **137**, 103 (1976).
3) P. Armbruster et al.: Nucl. Instrum. Methods **91**, 499 (1971).
4) A. Ghiorso et al.: Nucl. Instrum. Methods Phys. Res. A **269**, 192 (1988).
5) K. L. Brown et al.: SLAC-91, Rev. 1 (1974).
6) D. Vermeulen et al.: Z. Phys. A **318**, 157 (1984).
7) H. W. Gäggeler et al.: Nucl. Phys. A **502**, 561c (1989).
8) S. Hofmann: Rep. Prog. Phys. **61**, 639 (1998).

Direct simulation Monte-Carlo for supersonic gas jet

J. Murata, K. Asahi, H. Miyoshi,* and K. Shimada*

A precision computer simulation is necessary for the planned supersonic gas jet system, which produces a neutral atomic beam towards the radio-isotope atomic-beam magnetic resonance apparatus.[1] A specially shaped nozzle called the Laval-type nozzle is used to produce the required cold and parallel atomic beams. A precision knowledge of the output gas flow is a key issue in designing the atomic beam magnetic resonance apparatus. The requirements for the gas flow are that it be as slow, and as parallel; as is reasonably achievable. In order to fulfill these requirements, an elementary fluid dynamics based calculation was performed previously.[1] There are existing simulation tools for the gas flow, for example, VarJET.[2] However, all such calculations are based upon the Navier-Stokes equation of the classical fluid dynamics which assumes a continuum fluid. The output gas density of the current case of approximately 10^{-3}–10^{-4} Torr is too low to assume the classical continuum fluid dynamics. Such a gas pressure region requires a theoretical treatment which considers a molecular gas flow with small molecular collisions. A direct Monte-Carlo-type calculation satisfies this requirement, and which fulfills the Boltzmann equation. In the case that only a small number of molecules participates, the well-known molecular dynamics which directly follows the movements and collisions of every molecule can be applicable. However, considering the limited computer power available, we cannot apply this molecular dynamics for a large number problems including the current case. The direct simulation Monte-Carlo (DSMC) method introduced by Bird is often used for the treatment of such intermediate rarefaction gas flows.[3] In general, the Knudsen number defined as K_n = (mean free path)/(typical system length) is used to classify the gas density. The Navier-Stokes equation requires $K_n \ll 1$; on the other hand, in the case of $K_n \gg 1$, a free molecular gas assumption can be applicable, enabling an analytical treatment. Because the DSMC method does not have applicable limits on K_n, it is the only tool which can be used to solve the present problem in the intermediate K_n region. The DSMC treats a molecular group as a single particle, following their movements and collisions in the same manner as molecular dynamics.

The author developed a DSMC-based gas jet simulation tool for the simulation of the gas jet from the Laval nozzle. This is the first explicit application of the DSMC on the gas flow simulation inside a vacuum chamber in the field of nuclear physics. Particularly in the current case, we must treat not only the output thin gas but also the initial gas buffering volume before the nozzle neck, of which the pressure is typically order of 1 Torr. The DSMC is a powerful tool for treating such problems that include very different pressure scales. In addition to the advantage of its the wide pressure dynamic range, the DSMC has the powerful potential to provide an exact treatment of a mixed gas with a highly asymmetric mixing ratio. In fact, we must treat a mixed gas which is dominated by a carrier gas with a negligible fraction of the target radioactive atoms as an impurity. It cannot be treated by any Navier-Stokes based calculation. In Fig. 1, sample results obtained with different shaped nozzles are shown. Currently, mixed gas is not able to be treated yet. Conditions such as initial gas pressure, temperature, surface reflection, and the nozzle geometries have not yet been optimized, however, we can see the differences in the output gas jet shape. The development of the simulation code has just begun. It will be completed, including mixing gas treatment, within 2003 and will then start to be used in designing gas jet systems.

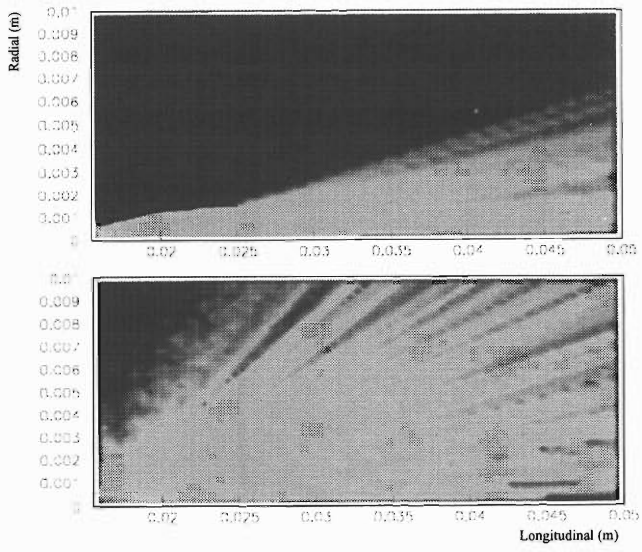

Fig. 1. Sample results of the DSMC calculation for a Lavar nozzle (top) and for a simple window (bottom). Different properties of the output supersonic gas jet flows can be found.

References

1) H. Miyoshi et al.: RIKEN Accel. Prog. Rep. **36**, 193 (2003) and references therein.
2) V. L. Varentsov and A. A. Ignatiev: Nucl. Instrum. Methods Phys. Res. A **413**, 447 (1998).
3) G. A. Bird: *Molecular Gas Dynamics and the Direct Simulation of Gas Flows* (Oxford University Press, New York, 1994).

* Department of Physics, Tokyo Institute of Technology

Advanced computer network for RIKEN accelerator research facility

T. Ichihara, Y. Watanabe, K. Yoshida, and A. Yoshida

The plan of the migration to the Advanced Computer Network of RIKEN Accelerator Research Facility (RARF) was considered in the beginning of 2001. The actual migration was started in December 2001 and completed in February 2002. After the migration, the very stable and secure operation of the RARF Advanced Computer Network has been successfully achieved.

Recently, the security of the computer network has become a very important issues in all places. For example, many personal computers are connected to the Internet *via* the LAN. However, it is not easy to maintain the security of each personal computer at a certain level, because they are managed by individual users who are not interested in security so much. Many security holes have been discovered one after another for various operating systems and application softwares and it is necessary to update or apply patches to close security holes each time.

The network Intrusion Detecting System (IDS) had been installed at the boundary of the RARF LAN in order to monitor unauthorized access in 2000. The IDS consists of the free-software SNORT,[1] mySQL,[2] ACID[3] and RedHat 7.1 Linux pc. The IDS detects IP packets of unauthorized access to the RARF LAN and logs them through the mySQL database. The IDS is very helpful in improving the security of RARF LAN, however, security is still insufficient. The IDS records security-related events but it does not prevent unauthorized access itself.

Under these circumstances, we decided to introduce a new advanced network to the RARF, where the security of all computers is maintained at a sufficient level with minimum effort from individual user.

Figure 1 shows the current configuration of the RARF Advanced Computer Network.

The RARF Advanced Computer Network consists of two components, the RARF private LAN as shown in the lower part of the figure and the RARF global LAN in the upper part.

All computers connected to the RARF private LAN are assigned private addresses statically or dynamically. To access the Internet, these private addresses are translated dynamically to global addresses by a firewall machine (PIX 535). Most personal computers managed by individuals are connected to this private LAN. These private LANs are divided into several groups (subnets) categorized by buildings and laboratories. The routing of the IP and Apple-Talk protocols between these subnets is carried out for convenience.

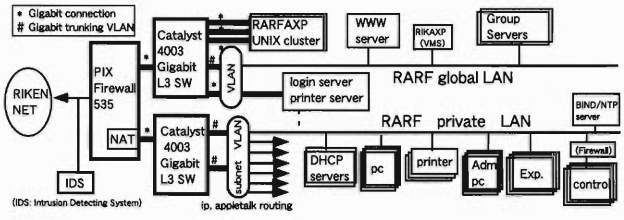

Fig. 1. Configuration of the RARF Advanced Network.

All computers connected to the global LAN are assigned global addresses. We assume that server computers such as those with Web servers are connected to the global LAN. The global LAN is connected to the Internet *via* the firewall machine (PIX 535). At the firewall, access limitation rules are applied to all computers. By default setting, no access into the computers from the Internet is allowed.

Virus infection *via* E-mail has been a very serious problem recently. In order to prevent virus infections *via* E-mail, a virus-detecting and -eliminating system has been installed to the central mail server computer (RARFAXP) of the RARF in the summer of 2001. This system has been working very stably thus far.

With all the above features, a very secure and stable operation of the RARF computing network was established in February 2002.

References

1) http://www.snort.org/
2) http://www.mysql.org/
3) http://www.cert.org/kb/acid/

RIKEN-RAL Port 4 beam line: Construction and beam characteristics

K. Ishida, P. Strasser, Y. Matsuda, K. Nagamine,[*1] T. Matsuzaki, I. Watanabe, M. Iwasaki, and G. H. Eaton[*2]

Due to an increase of beam time demand at the RIKEN-RAL Muon Facility,[1,2] a new experimental area (Port 4) has become necessary in order to promote further studies of muon science. In 2000, RIKEN and RAL agreed to extend the R55 experimental hall to make the loading bay area, which sits along existing RIKEN beam lines, available for a new muon beam line. After the hall extension was completed in the summer of 2001, the installation of Port 4 beam line components started. The first beam was delivered to Port 4 on November 22, 2001.

The schematic layout of the new beam line is shown in Fig. 1. The beam line is composed of a pion production target in the 800 MeV proton beam line, a pion injection part, a superconducting solenoid for pion-to-muon decay, and a muon extraction part. The Port 4 muon beam line is designed to be able to deliver both surface muon beam and decay muon beam, whose momentum can be 100 MeV/c at maximum. The same beam optics as Port 3 (QQQ-K-D-QQQ-D-QQQ) was chosen for the muon extraction, where Q and D represent a quadrupole magnet and dipole magnet, respectively, and K represents a pulsed kicker system for separating the bunches of two-bunched muon beams. A drift-space just after B4 was kept for the installation in the near future of a cross-field separator to remove electron/positron contamination in the muon beam. Figure 2 (a) shows the typical results of beam optic calculation by TRANSPORT.

This new beam line is used for the experiment to measure muonic X-rays from nuclei which are implanted into a hydrogen/deuterium film.[3]

After the beam line was completed, we noted a serious problem. Since the beam line of Port 4 was common until the last dipole magnet (B4), we had anticipated that we could easily obtain the same beam intensity as that at Port 3 by only tuning the last dipole magnet and the last triplet quadrupoles (Q21–Q23). However, we found that the beam intensity was only 1/3 of that obtained by us at Port 3. After an intensive tuning work, during which we tuned all the magnet currents carefully, we accumulated more information for understanding of each magnet component. During the optimization, we attempted also other polarity settings of the magnets, and found that, with the reversed polarity of one of the triplet quadrupoles

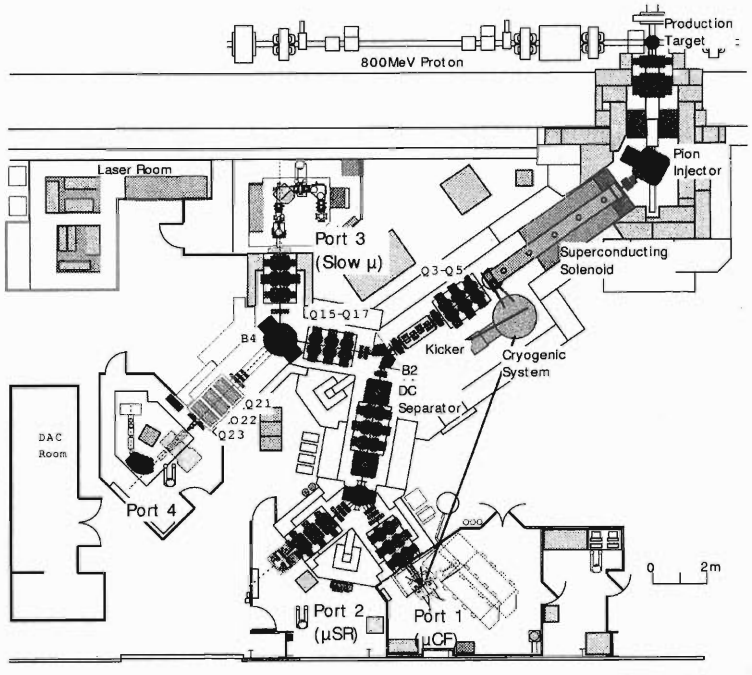

Fig. 1. Schematic layout of the RIKEN-RAL Muon Facility with a new Port 4 beam line and a new experimental area.

*1 Meson Science Laboratory, Institute of Materials Structure Science, High-Energy Accelerator Research Organization (KEK)
*2 Rutherford Appleton Laboratory, UK

(a) (b)

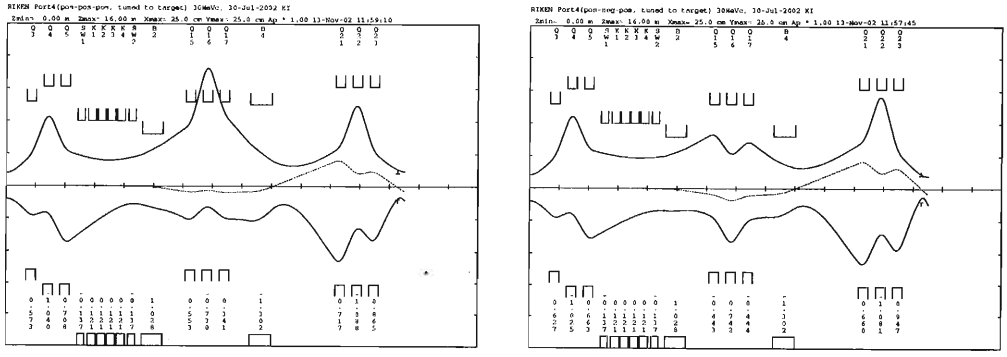

Fig. 2. Typical results of beam optic calculation for the muon extraction part of Port 4: (a) original design and (b) new optimized design with reversed polarities of Q15--Q17. The lower curve is the horizontal beam envelope, the upper curve the vertical envelope, and the dashed curve the horizontal momentum dispersion. The position of the beam collimator is shown by ⊤ and ⊥.

(Fig. 2 (b)), we were able increase the muon beam intensity by 20%. After this work, we were able to recover the intensity to 60% of that at Port 4. However, this was still small and the lack of intensity in Port 4 remained as a puzzle. Thus, we decided to investigate the problem by introducing a beam profile monitor as reported in another article.[4)]

Due to the geometrical interference with the experimental setup, the profile monitor could be placed only at about 25 cm upstream of the real target. However, this was exactly the position where the beam collimator was planned to be placed, and it is important that the muon beam is well focussed at this position. As soon as the profile monitor was placed in the beam, we found that the beam center was shifted by about 2 cm both horizontally and vertically from the geometrical center. It took sometime to find the origin of this shift, but we finally found that it was due to an external short circuit of a coil in one of the magnetic poles of the Q21 magnet. A part of the insulation tape had been damaged during installation. This produced a tilted dipole field superimposed over the normal quadrupole field, and thus the beam axis started to deviate from the center line.

After fixing the problem, we finally obtained a muon beam intensity twice that at Port 3, as a result of a better tuning. The typical beam size for surface muon beams at the beam profile monitor was 3.5 cm (H) × 3.5 cm (V) (FWHM), while the beam size was slightly larger (4.0 cm × 4.0 cm) for backward decay muon beams of the same momentum (27 MeV/c).

References

1) K. Nagamine et al.: Hyperfine Interact. **101/102**, 521 (1996).
2) T. Matsuzaki et al.: Nucl. Instrum. Methods Phys. Res. A **465**, 365 (2001).
3) P. Strasser et al.: Hyperfine Interact. **119**, 317 (1999).
4) P. Strasser et al.: RIKEN Accel. Prog. Rep. **36**, 202 (2003).

A beam profile monitor for RIKEN-RAL pulsed muon beam

P. Strasser, K. Ishida, Y. Matsuda, and M. Iwasaki

The need of a beam profile monitor for the RIKEN-RAL pulsed muon beam facility[1,2] was urgent in order to complete the commissioning of a newly constructed experimental area (Port 4). Normally, the tuning of a muon beamline is performed by optimizing the number of muons stopped in a target (*e.g.*, graphite) by detecting positrons or electrons. This procedure, which is quite laborious and time-consuming, only gives the total number of muons arriving within a defined area. However during the commissioning of Port 4, as reported in another article,[3] we encountered a serious problem that we could not easily solve using this standard procedure. We decided to investigate further this problem by introducing a muon beam profile monitor.

The objective for the design of this beam profile monitor was to be able to obtain both horizontal and vertical beam profiles simultaneously using surface muons (μ^+), which have a momentum of only 27 MeV/c. At this energy, the range of a muon in a scintillator (NE-102) is only about 1 mm. This profile monitor should also be able to operate with pulsed beams and reject positron or electron contamination in the muon beam. Finally, it should work with high-intensity surface muon beams as well as with low-intensity backward decay muon (μ^+ and μ^-) beams.[2]

The schematic view of the beam profile monitor is shown in Fig. 1. Each axis comprises nine scintillators (4 mm wide and 0.5 mm thick, with 10-mm steps) mounted on 1/2" photomultipliers (Hamamatsu type H3165-01), which were recycled from the muon g-2 experiment at BNL. Each scintillator is wrapped with two layers of 10-μm-thick Aluminium-Mylar. In addition, the front and the back of the central area are also covered with an additional layer. This proved to be sufficient to reduce light leaks to an acceptable level without significantly slowing down the incoming muons. Each photomultiplier output was sent to a charge ADC (LeCroy model 2249SG) with a time gate of 200 ns to be digitized. The data acquisition program EXP[4] was used to process the data and fill the histograms.

Figure 2 shows a typical photomultiplier output signal (counter X5) when the profile monitor was placed in the surface μ^+ beam at RIKEN-RAL muon facility Port 4. It should be noted that at ISIS-RAL the proton beam has a two-bunch pulse structure, 70 ns wide and separated by 320 ns. The signal on the left corresponds to the first positron pulse that arrives just before the first muon pulse (same momentum), the broad signal in the middle to the first muon pulse followed closely by the second positron pulse, and the peak on the right to the second muon pulse, respectively. Each pulse is followed by a positron tail with a 2.2-μs lifetime. By adjusting the gate of the ADC accordingly, we can select only the second muon pulse. Before the profile monitor can be used, the gain of each counter should be calibrated. Each of the horizontal and vertical counters was placed successively at the center position, and the high voltage of the photomultipliers was adjusted (about 450 V) to obtain the same ADC values.

With low-energy decay muons (μ^+ or μ^-), the counters must be recalibrated (about 800 V) since the beam intensity is smaller by more than two orders of magnitude. Figure 3 shows a typical photomultiplier output signal (counter X5) obtained with 27 MeV/c decay μ^-. Due to the low intensity and the small scintillator

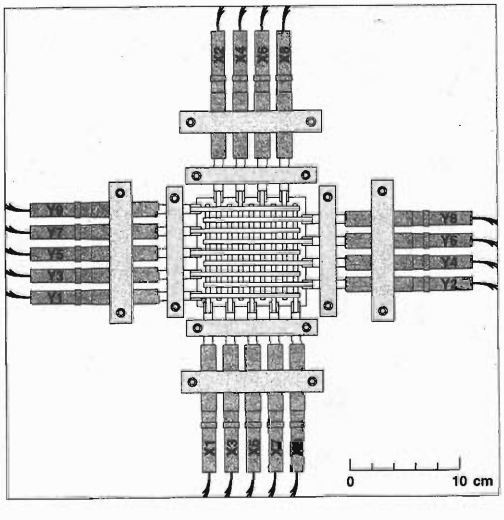

Fig. 1. Schematic view of the muon beam profile monitor.

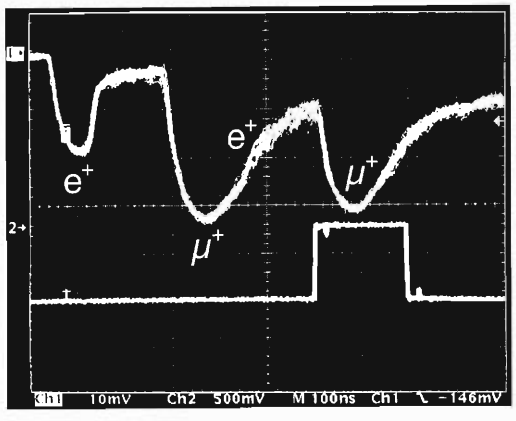

Fig. 2. Typical photomultiplier output signal (counter X5) with a surface muon and positron beam of 27 MeV/c (upper curve), and the corresponding ADC gate signal (lower curve). See text for explanation.

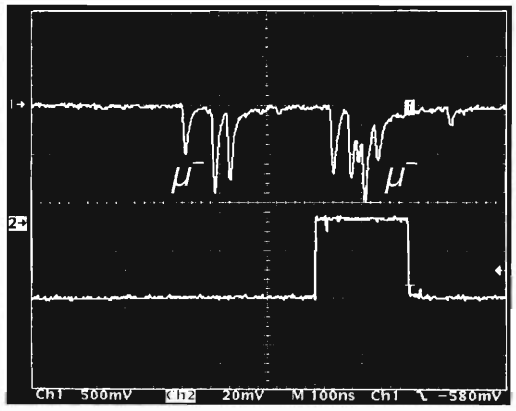

Fig. 3. Typical photomultiplier output signal (counter X5) with 27 MeV/c decay μ^- (upper curve), and the corresponding ADC gate signal (lower curve).

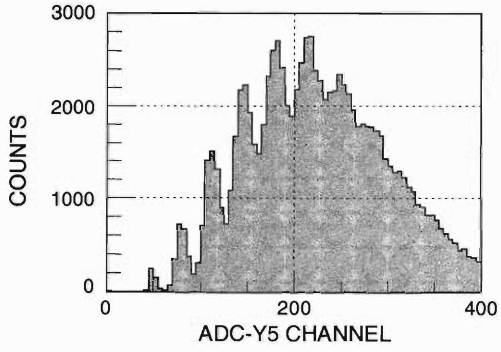

Fig. 4. ADC output with 27 MeV/c decay μ^-.

size, a single muon can be observed. Electron contamination is also significantly suppressed because muons are produced from pion decay in flight in the solenoid (pions and muons have different momentums), rather than at the production target in the primary proton beam like surface μ^+. The ADC output (see Fig. 4) also clearly shows distinct peaks for each number of muons passing through the scintillator per spill, the first one being the pedestal.

As an example of the performance of this beam profile monitor, the horizontal and vertical muon beam profiles obtained with surface muons at Port 4 for different B4 dipole magnet settings are shown in Fig. 5. Each profile can be obtained with just 1000 spills or about 20 sec. Figure 6 shows the different beam profile parameters that are generated automatically after each profile is completed. This graphical interface was found to be very useful in rapid visualization of the response of the beam to each magnet and for optimization of the beamline parameters.

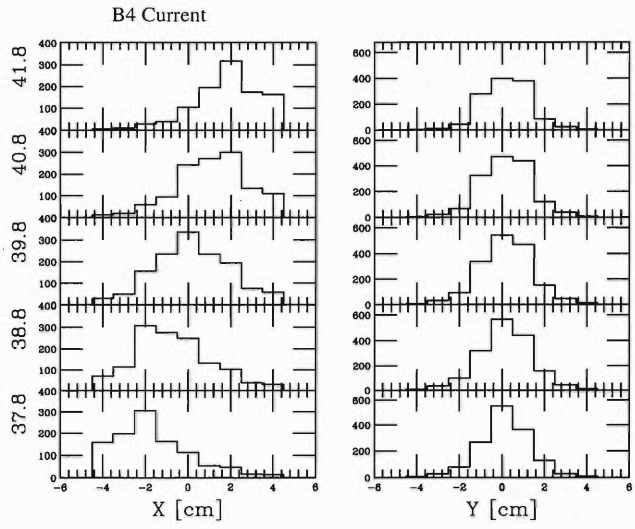

Fig. 5. Horizontal and vertical muon beam profiles as a function of B4 dipole magnet settings measured with surface muons at Port 4.

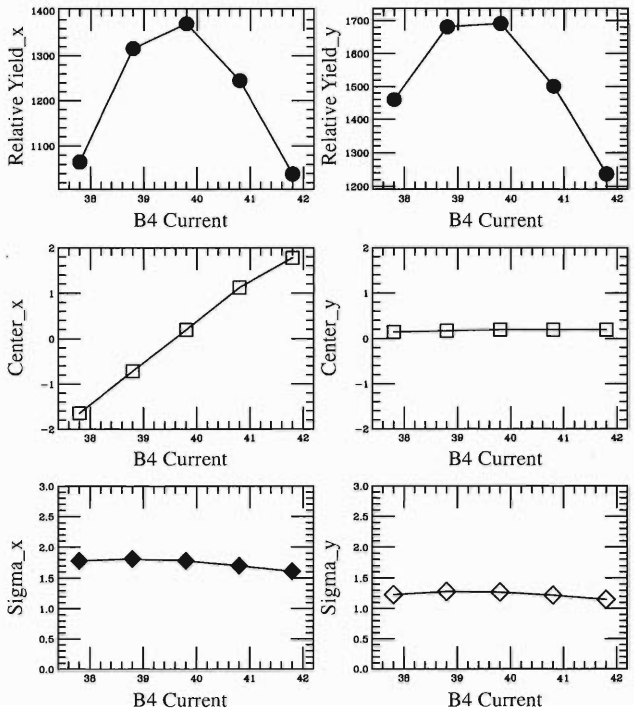

Fig. 6. Beam profile parameters of Fig. 5.

References

1) K. Nagamine et al.: Hyperfine Interact. **101/102**, 521 (1996).
2) T. Matsuzaki et al.: Nucl. Instrum. Methods Phys. Res. A **465**, 365 (2001).
3) K. Ishida et al.: RIKEN Accel. Prog. Rep. **36**, 200 (2003).
4) S. N. Nakamura and M. Iwasaki: Nucl. Instrum. Methods Phys. Res. A **388**, 220 (1997).

6. Material Analysis

Development of a highly sensitive high-resolution in-air particle-induced X-ray emission (PIXE) System: III

K. Maeda, K. Hasegawa,[*1] K. Ogiwara, M. Maeda,[*2] and H. Hamanaka[*1]

Particle-induced X-ray emission (PIXE) analysis with high energy resolution is one of the most effective tools for direct investigation of chemical bonding states of atoms in target materials. We have developed a compact crystal spectrometer system for high-resolution PIXE measurements in air of atmospheric pressure.[1] The system is composed of a flat analyzing crystal and a position-sensitive proportional counter (PSPC). The utility of the system for direct chemical state analysis was demonstrated by measuring K X-ray spectra of third-period elements.

In order to realize more rapid and more sensitive analysis, we have adopted two approaches to the improvement of the detection efficiency of the spectrometer system. One is the development of a multistacked PSPC assembly with a large sensitive area.[2,3] The other is the construction of a focusing-type spectrometer which consists of a cylindrically curved crystal and a single PSPC. We report here the latter approach.

The geometry of focusing is schematically shown in Fig. 1. The radius of curvature of the analyzing crystal is denoted by r. When an X-ray source is located at a point S, X-rays diffracted by the crystal converge to the center axis F_A-F_B. The practical experimental setup is illustrated in Fig. 2. A target sample is placed in air and bombarded with a 2.1 MeV proton beam of 3 mm diameter. A curved crystal and a PSPC are set on parallel long-stroke stages ST1 and ST2, respectively. A narrow entrance slit of 0.4 mm width is placed between the target and the crystal, at a position very close (around 7 mm) to the proton beam spot on the target. The position of the entrance slit is considered to be the origin of dispersing X-rays in the spectrometer system.[4] When changing the energy

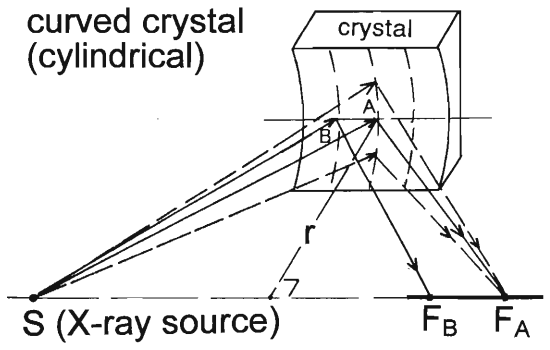

Fig. 1. Geometry of focusing.

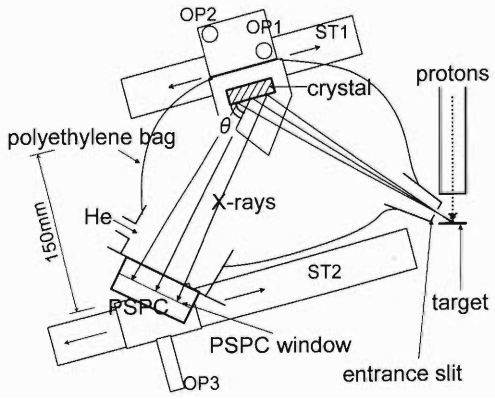

Fig. 2. Experimental setup of the focusing spectrometer.

range of measurements, that is, when changing the angle θ, the crystal and the PSPC should be moved in parallel on stages ST1 and ST2. The X-ray path length is given by $\sim 2r/\sin\theta$.

A cylindrical Ge (111) crystal with r of 150 mm, 50 mm in height and 30 mm in width was used. The interplanar spacing $d = 0.327$ nm of Ge (111) is suitable for sulfur and phosphorus K X-ray measurements. The crystal is mounted on a double-tilt stage (OP1 and OP2). The stage is adjusted by remote control so as to obtain the maximum detection efficiency. A PSPC of 7.4 mm in sensitive height and 30 mm in sensitive width is mounted on stage OP3 and placed perpendicular to the direction of the X-ray path. The PSPC employs a 7-μm-diameter carbon fiber as the anode; mixed gas of $Ar:CH_4$ (9:1) or $Kr:CO_2$ (9:1) is used as the counter gas. The X-ray path from the entrance slit to the PSPC is enclosed within a polyethylene bag filled with helium gas.

Using the same setup as shown in Fig. 2, but changing the analyzing crystal from flat Ge (111) to curved Ge (111), S Kα spectra of MoS_2 were measured to determine the enhancement factor of the detection efficiency after focusing. The efficiency of detecting S Kα with the curved crystal was increased by one order of magnitude compared to that with the flat crystal; no degeneration of energy resolution was observed.

In addition to the absolute detection efficiency, the signal-to-background (S/B) ratio was greatly improved using the focusing system. This is seen in Fig. 3 where S Kβ spectra of elementary sulfur are shown. The ratio of the Kβ_1 peak height to background (around $\theta = 49.7°$) obtained with the curved crystal-single PSPC system was five times higher than that obtained with the flat crystal-stacked PSPC system.

*1 Faculty of Engineering, Hosei University
*2 Tokyo University of Fisheries

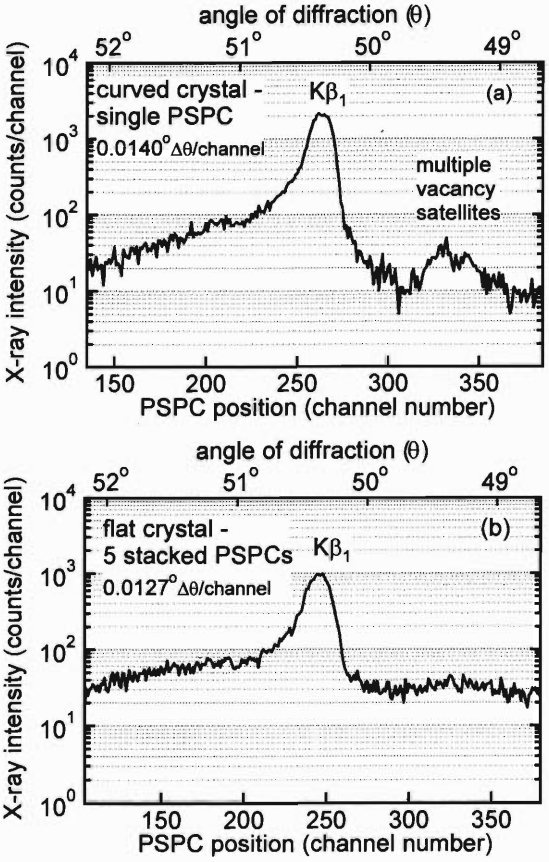

Fig. 3. Comparison of S Kβ spectra of elementary sulfur measured with (a) the curved crystal-single PSPC system and (b) the flat crystal-stacked PSPC system.

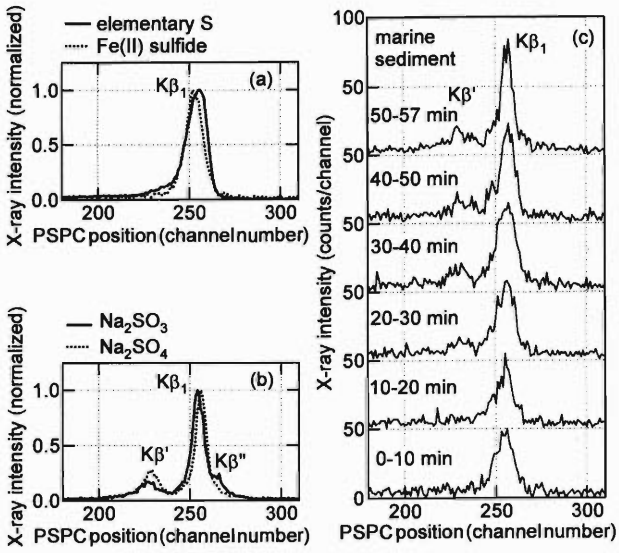

Fig. 4. S Kβ spectra of (a) elementary S and Fe(II) sulfide, (b) Na_2SO_3 and Na_2SO_4, and (c) time-resolved S Kβ spectra of a marine sediment sample: proton beam current 30–50 nA; 0.50 eV/channel. The sediment sample was collected from Tokyo Bay in Nov. 2000, kept frozen until PIXE measurement, defrosted and deposited on a Millipore filter. The filter loaded with the sample was taken out of a container charged with N_2 gas immediately before the measurement started.

Like the flat crystal-stacked PSPC system,[2] the new system is useful for rapid chemical state analysis through K$\alpha_{1,2}$ chemical shift measurements within a few seconds to one minute.

The Kβ spectra reflect the nature of chemical bonding more prominently than the Kα spectra. However, for the third-period elements, the production cross sections of Kβ are only 1–10 percent of those of Kα. Using the new system, measurements of the Kβ spectra can also be carried out in a short time. Figure 4 (a) and (b) shows examples of the S Kβ spectra obtained in 5 to 12 minutes of measuring time. Differences in the fine structures of Kβ spectra from elementary sulfur, iron (II) sulfide, Na_2SO_3 and Na_2SO_4 are clearly recognized.

The improvement of the S/B ratio made it possible to determine the fine structures in Kβ spectra from minor component elements, which had been hidden by the background in the previous systems. Along with the Kβ spectra from known targets, time-resolved Kβ spectra of S from a marine sediment sample (S concentration = 2 weight%) are shown in Fig. 4 (c). The Kβ spectra of the sediment sample from the early stage of measurement (0–20 minutes) resemble those of elementary S or sulfide S. After 20 minutes, a low-energy satellite peak Kβ', evidence of S-O bonds, appeared. The intensity ratio of Kβ'/Kβ_1 in the spectrum obtained after 50 minutes was much smaller than that of sulfate S, and similar to that of sulfite S. However, the high-energy shoulder Kβ'', a characteristic of sulfite S, was not detected in this spectrum. This indicates that a portion of S atoms in the sediment sample was oxidized by air, and once the oxidation had started, the portion quickly reached the highest oxidation state.

Both absolute and relative detection efficiencies of in-air high-resolution PIXE analysis were considerably improved by adopting the focusing geometry. However, not all kinds of analyzing crystals can be formed into curved crystals of good quality. The flat crystal-stacked PSPC system or the curved crystal-single PSPC system should be used case by case.

References

1) K. Maeda et al.: Nucl. Instrum. Methods Phys. Res. B **134**, 418 (1998).
2) K. Maeda et al.: Nucl. Instrum. Methods Phys. Res. B **190**, 704 (2002).
3) K. Hasegawa et al.: Trans. Soc. Instrum. Control Eng., **39**, 11 (2003).
4) K. Maeda et al.: Int. J. PIXE **11**, 35 (2001).

Separation of potassium and calcium by centrifugal partition chromatograph system

Y. Komatsu,[*1] M. Sekita,[*2] R. M. Fujii,[*1] H. Yamada,[*2] S. Umetani,[*3] and S. Enomoto

The ring cyclotron of the RIKEN Accelerator produces radioactive elements called multitracers which include about 50 radioactive elements useful in the fields of biotechnology, medical technology, and other applications. The accelerator enables us to obtain information simultaneously using multiple elements; however, if all elements are used for the tracer technique, some of them will have negative effects on the specimen or it will become very difficult to analyze the results. Thus, it is necessary to separate chemically only the desirable elements from the produced tracer elements. Techniques such as the ion-exchange techniques and the solvent extraction techniques have been tried to separate the elements of the same group elements in the periodic table to date. The column method is commonly used in the ion-exchange techniques. In the case of the solvent extraction techniques, there is rather a disadvantage in that the separation of metal ions may be insufficient and the extracted ions are determined by the extraction agents themselves. In order to improve the separation of metal ions, we applied the centrifugal partition chromatography (CPC) technique to separating the metal ions. The CPC technique is also called as the "multistage solvent extraction method" which possibly improves the separation of the metal elements through multistage separation in more than one hundred steps, based on the finding the separation is insufficient by the conventional one-stage with one-step separation technique. In this study, we will report the results of the separation of potassium ions of the alkali metal ions and calcium ions of the alkaline earth metal ions by this CPC technique, which we have obtained during the course of developing the automation technique for the chemical separation.

After cyclohexane containing thenoyltrifluoroacetone (TTA) was filled in the CPC device with aqueous solution without containing any metal ion for the stationary phase, the second aqueous solution containing potassium and calcium ions for the mobile phase was flowed into the CPC device. By applying the centrifugal force within the CPC device, the calcium ions in the mobile phase were moved into the stationary phase by forming a metal complex with TTA. Using this procedure, only potassium ions in the mobile phase were directly moved to the fraction collector, while calcium ions were in the stationary phase within the CPC device. At every 5 minutes, each 10 cm^3 solution was flowed to the sampling tubes in the fraction collector to monitor the amount of metal ions during experiments. The measured amounts of the potassium and calcium ions (ppm) versus CPC time (min) are shown in Fig. 1. One can observe in Fig. 1 that only the potassium ions were extracted as the aqueous solution after passing through the CPC device at about 115 min.

In the next stage, hydrochloric acid solution was used as the mobile phase for the CPC device. Since the pH of the solution in the CPC device was changed to the acid region at this stage, calcium ions forming the TTA chelate in the stationary phase were back-extracted into the mobile phase by exchanging the proton in the aqueous solution of the mobile phase within the CPC device. As can be seen in Fig. 1, the peak of the concentration of calcium ions appeared at about 310 min from the beginning of sampling. As the result, the potassium ions moved to the fraction collector at the first stage at an early time, then the calcium ions were transferred in the next stage at a later time. As can be seen in the figure, this method highly improves the separation and two metal ions can be separated completely by the CPC time compared with the conventional solvent extraction techniques. This enables separation of metal ions in a mixture of metal ions.

In conclusion, we successfully separated the potassium and calcium ions with a very high efficiency using the CPC technique. This method will be one of possible techniques for the automation of the chemical separation of multitracer elements.

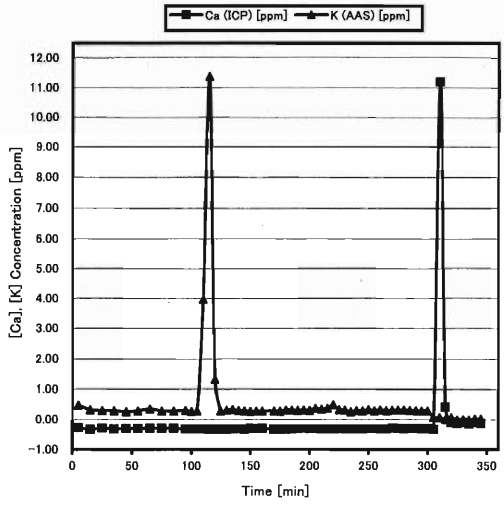

Fig. 1. Measured amounts of K and Ca ions in ppm versus CPC time (min).

*1 Department of Environmental Systems Engineering, Kanazawa Institute of Technology
*2 Advanced Materials Laboratory, National Institute for Materials Science
*3 Institute for Chemical Research, Kyoto University

7. RIKEN-BNL Collaboration on Spin Physics Program

Next-to-leading order QCD corrections to A_{LL}^{π}

B. Jäger,* M. Stratmann,* and W. Vogelsang

Very inelastic pp collisions with longitudinally polarized beams at RHIC will open up unequaled possibilities to measure the polarized gluon density Δg. RHIC operates at high energies ($\sqrt{S} = 200$ and $500\,\mathrm{GeV}$), where the underlying theoretical framework, *i.e.*, perturbative QCD, is expected to be under good control.

The basic concept that underlies most of spin physics at RHIC is the factorization theorem. It states that large momentum-transfer reactions may be factorized into long-distance pieces that contain the desired information on the spin structure of the nucleon in terms of its *universal* parton densities, such as Δg, and parts that are short-distance and describe the hard interactions of the partons. The latter can be evaluated using perturbative QCD.

In the following, we consider the spin-dependent cross section

$$d\Delta\sigma \equiv \frac{1}{2}\left[d\sigma^{++} - d\sigma^{+-}\right], \tag{1}$$

(the superscripts denoting the helicities of the protons in the scattering) for the reaction $pp \to \pi X$, where the pion is at high transverse momentum p_T, ensuring large momentum transfer. The statement of the factorization theorem is then

$$d\Delta\sigma = \sum_{a,\,b,\,c} \Delta f_a \otimes \Delta f_b \otimes d\Delta\hat{\sigma}_{ab}^{c} \otimes D_c^{\pi}, \tag{2}$$

where $\otimes$ denotes a convolution and where the sum is over all contributing partonic channels $a + b \to c + X$, with $d\Delta\hat{\sigma}_{ab}^{c}$ the associated partonic cross section. It is planned for the upcoming RHIC run to attempt a first measurement of the spin asymmetry for this reaction.

In general, a leading-order (LO) estimate of (2) merely captures the main features, but does not usually provide a quantitative understanding. Only with knowledge of the next-to-leading order (NLO) QCD corrections to the $d\Delta\hat{\sigma}_{ab}^{c}$ can one reliably extract information on the parton distribution functions from the reaction. For the case of high-p_T pions, these corrections have been computed very recently.[1,2] We briefly sketch here our calculation; for details, see Ref. 1.

The partonic cross sections $d\Delta\hat{\sigma}_{ab}^{c}$ in (2) have to be summed over all final states (excluding c which fragments) and integrated over the entire phase space of X. The LO results, which have been known for a long time, are obtained from evaluation of all tree-level $2 \to 2$ QCD scattering diagrams. At NLO, we have $\mathcal{O}(\alpha_s)$ corrections to the LO reactions, and also additional new processes, giving rise to 16 different channels in total. At intermediate stages the NLO calculation will necessarily show singularities. We chose dimensional regularization to make these singularities manifest. For those processes that are already present at LO, real $2 \to 3$ and virtual one-loop $2 \to 2$ contributions will individually have infrared poles that cancel in their sum. Virtual diagrams will also produce ultraviolet poles that must be removed by the renormalization of the strong coupling constant. Finally, there are collinear divergencies which are factored into the bare parton distribution and fragmentation functions. In this way one eventually arrives at the finite partonic hard-scattering cross sections $d\Delta\hat{\sigma}_{ab}^{c}$ at NLO. We note that we have simultaneously computed the NLO corrections for the unpolarized case, where we fully agree at an *analytical level* with results available in the literature.[3]

Figure 1 shows our results for the unpolarized and polarized cross sections at NLO and LO. The lower part of the figure displays the "K-factor," $K = d(\Delta)\sigma^{\mathrm{NLO}}/d(\Delta)\sigma^{\mathrm{LO}}$. One can see that in the unpolarized case the corrections are roughly constant and about 50% over the p_T-region considered. In the polarized case, we generally find smaller corrections with similar size to those for the unpolarized case only at the high-p_T end.

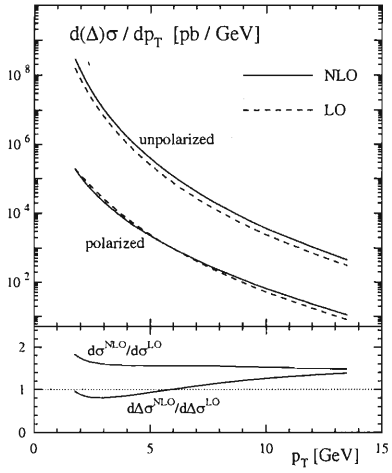

Fig. 1. Unpolarized and polarized π^0 production cross sections in NLO (solid lines) and LO (dashed lines) at $\sqrt{S} = 200\,\mathrm{GeV}$. The lower panel shows the K-factors.

References

1) B. Jäger, A. Schäfer, M. Stratmann, and W. Vogelsang: hep-ph/0211007, to appear in Phys. Rev. D.
2) D. de Florian: hep-ph/0210442.
3) F. Aversa et al.: Nucl. Phys. B **327**, 105 (1989).

* University of Regensburg, Germany

New analysis of polarized parton distribution functions

M. Hirai, for the Asymmetry Analysis Collaboration

We study the influence of precise experimental data on the determination of polarized parton distribution functions (polarized PDF's). Polarized PDF's have so far been optimized by χ^2 analysis using the polarized deep inelastic scattering (polarized DIS) world data.[1] In the present analysis, we re-analyzed polarized PDF's including the precise measurements of the SLAC-E155 proton target.[2] Four distributions ($\Delta u_v(x)$, $\Delta d_v(x)$, $\Delta\bar{q}(x)$, and $\Delta g(x)$) are determined by χ^2 analysis, and their uncertainties are estimated by the Hessian method.

The best-fit result is $\chi^2(/d.o.f.) = 346.33(0.90)$. The correlation coefficient $\rho_{\bar{q}g}$ between the first moments of the antiquark and gluon distributions becomes $\rho_{\bar{q}g} = -0.836$, which indicates a strong correlation between the two distributions. The obtained first moments of the antiquark and gluon distributions are $\Delta\bar{q} = -0.062 \pm 0.023$ and $\Delta g = 0.499 \pm 1.268$, respectively. The spin content $\Delta\Sigma$ ($= \Delta u_v + \Delta d_v + 6\Delta\bar{q}$) becomes $\Delta\Sigma = 0.213 \pm 0.138$. The valence quark contributions are fixed by assuming the antiquark $SU(3)_f$ flavor symmetry and by using the hyperon β-decay constants, then their uncertainties become zero. The spin content $\Delta\Sigma$ is therefore subject to the antiquark uncertainty. The gluon distribution and spin content still have large uncertainties.

Figure 1 shows the PDF uncertainties of the new results and the previous ones (AAC00, NLO set2).[1] There is no significant improvement of the valence quark uncertainties. In the $SU(3)_f$ symmetry assumption, fixing of the first moments strongly restricts the behavior of the valence quark distributions. In contrast, the antiquark and gluon uncertainties are reduced in the range $0.01 < x < 0.5$, where E155 proton data exist. Precise polarized DIS data can reduce mainly the antiquark uncertainty. On the other hand, the gluon uncertainty changes in response to the reduction of the antiquark uncertainty due to the strong correlation between the two distributions. The gluon contribution to the structure function $g_1(x)$, which appears with a non-zero coefficient function ΔC_g in the NLO calculation, is less than the quark and antiquark contributions. We can extract only a small amount of information on the gluon distribution. Actually, the gluon uncertainty is still large. This indicates the difficulty of determining the gluon distributions from the polarized DIS data. Therefore, uncertainty reduction of the gluon distribution is due to the strong correlation rather than the NLO contribution.

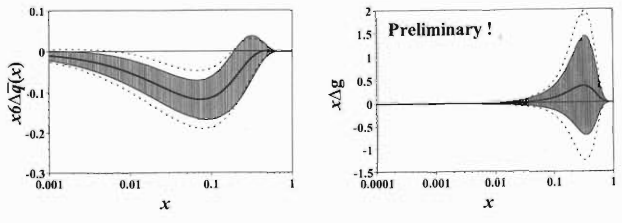

Fig. 1. Polarized PDF's with uncertainties at $Q^2 = 1\,\mathrm{GeV}^2$. Dashed curves are the uncertainties of previous results (AAC00 NLO-2).

In order to examine the correlation effect on parameterization, we re-analyzed the case of $\Delta g(x) = 0$ in which the fixed gluon distribution does not have uncertainty. Figure 2 shows the polarized PDF uncertainties of the $\Delta g(x) = 0$ and $\Delta g(x) \neq 0$ cases. The gluon distribution appears at high-Q^2 due to Q^2 evolution of the singlet-type DGLAP equation. The change of the valence quark uncertainties is negligible. The considerable improvement of the antiquark uncertainty is due to the vanishing gluon uncertainty. The obscure gluon distribution brings about a large antiquark uncertainty through the strong correlation. If the gluon distribution is determined well by RHIC-Spin experiments, the uncertainty of the antiquark distribution can be reduced to some extent. Similarly, the complementary relation can lead to reduction in the large uncertainty of the spin content $\Delta\Sigma$. We can then understand the spin structure of the nucleon in greater detail.

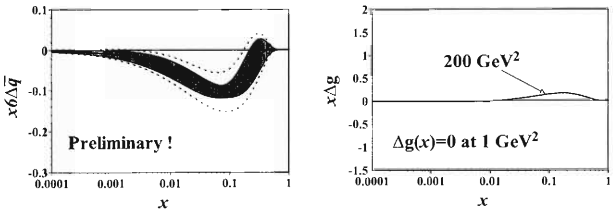

Fig. 2. Polarized antiquark and gluon distributions with uncertainties at $Q^2 = 1\,\mathrm{GeV}^2$. The shaded portion shows the uncertainty of $\Delta g(x) = 0$ results, and the dashed curves are the uncertainties of new results ($\Delta g(x) \neq 0$).

References

1) Asymmetry Analysis Collaboration, Y. Goto et al.: Phys. Rev. D **62**, 034017 (2000); M. Hirai: hep-ph/0211190.
2) E155 Collaboration, P. L. Anthony et al.: Phys. Lett. B **493**, 19 (2000).

Semi-inclusive D meson production in neutrino deep inelastic scattering

K. Sudoh

The flavor structure of sea quark distributions has been actively studied in recent years. The semi-inclusive deep inelastic scattering (DIS) is a promising way to access the flavor decomposed parton distribution functions (PDFs) in the nucleon. In particular, the charged current DIS using neutrino beams is effective in extracting the strange quark distribution.

Supposing a future neutrino factory, we investigated semi-inclusive $D/\bar{D}$ production including $\mathcal{O}(\alpha_s)$ corrections in neutrino-polarized proton scattering; $\nu + \vec{p} \to l^- + D + X$, $\bar{\nu} + \vec{p} \to l^+ + \bar{D} + X$. The leading order process is due to $W^{\pm}$ boson exchange $W^+ s(d) \to c$. In addition, several processes are taken into account in $\mathcal{O}(\alpha_s)$ next-to-leading order (NLO) calculations, *i.e.*, gluon radiation processes $W^+ s(d) \to cg$, virtual gluon corrections to remove singularity coming from soft gluon radiation, and boson-gluon fusion processes $W^+ g \to c\bar{s}(\bar{d})$.

The spin asymmetry for D production is written as

$$A^D = \frac{[d\sigma_{--} - d\sigma_{-+}]/dx}{[d\sigma_{--} + d\sigma_{-+}]/dx} = \frac{d\Delta\sigma/dx}{d\sigma/dx}, \qquad (1)$$

where $d\sigma_{hh'}$ denotes the spin-dependent cross section with definite helicities h and h' for the neutrino and target proton, respectively. Similar analyses have been performed by several people, in which charged current charm quark production at NLO in ep and νp scattering is discussed.[1)]

In numerical calculations, we adopted four kinds of parametrizations for the polarized PDFs, being AAC,[2)] BB,[3)] GRSV,[4)] and LSS,[5)] which were recently proposed. We show the parametrization model dependence of the spin asymmetry in Fig. 1 as a function of Bjorken x at neutrino beam energy $E_\nu = 200\,\mathrm{GeV}$. The upper panel and lower panel in Fig. 1 represent the asymmetries for D production and $\bar{D}$ production, respectively. For D production, s, d quark and gluon distributions contribute to the asymmetry A^D. A^D is dominated by a valence d_v quark at large x ($x > 0.3$), though the d quark component is highly suppressed by CKM. On the contrary, for $\bar{D}$ production, $\bar{s}$, $\bar{d}$ quark and gluon components contribute to the asymmetry $A^{\bar{D}}$. The $\bar{d}$ quark contribution, however, is almost negligible, and therefore, the asymmetry is directly affected by the shape of the $\bar{s}$ quark distribution.

As shown in both figures, the spin asymmetries strongly depend on parametrization models. We see that the case of the LSS parametrization is quite different from the cases of other parametrizations. In particular, the asymmetry due to the LSS parametrization in $\bar{D}$ production goes over 1 at $x \sim 0.3$, though the asymmetry should be less than 1. This is because the

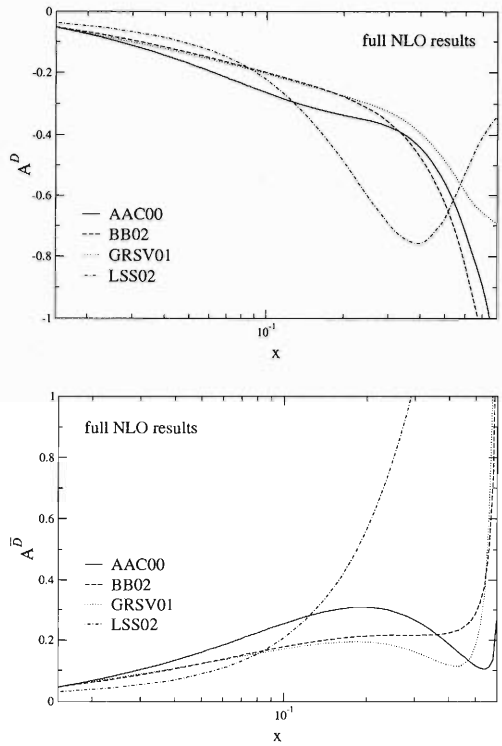

Fig. 1. Comparison of the spin asymmetries in NLO for D production (upper) and $\bar{D}$ production (lower) with various parametrization models of the polarized PDFs.

polarized s quark distribution in their parametrization badly violates the positivity condition at $x \sim 0.3$.

In semi-inclusive DIS, an additional ambiguity originates from the fragmentation function. However, the ambiguity can be neglected in the x distribution of A^D, since the kinematical variable related to fragmentation is integrated out in this distribution. Measurement of $\bar{D}$ production in neutrino DIS is promising not only for testing the parametrization models of the polarized PDFs but also for directly extracting the strange quark distribution in the nucleon.

References

1) M. Glück, S. Kretzer, and E. Reya: Phys. Lett. B **398**, 381 (1997); S. Kretzer and M. Stratmann: Eur. Phys. J. C **10**, 107 (1999).
2) Asymmetry Analysis Collaboration, Y. Goto et al.: Phys. Rev. D **62**, 034017 (2000).
3) J. Blümlein and H. Böttcher: Nucl. Phys. B **636**, 225 (2002).
4) M. Glück, E. Reya, M. Stratmann, and W. Vogelsang: Phys. Rev. D **63**, 094005 (2001).
5) E. Leader, A. V. Sidorov, and D. B. Stamenov: Eur. Phys. J. C **23**, 479 (2002).

Status of the QCDOC computer project

P. A. Boyle,[*1,*2] D. Chen,[*3] N. H. Christ,[*2] C. Cristian,[*2] Z. Dong, A. Gara,[*3] B. Joó,[*1] C. Jung,[*2,*4] C. Kim,[*2] L. Levkova,[*2] X. Liao,[*2] G. F. Liu,[*2] R. D. Mawhinney,[*2] S. Ohta,[*4,*5] K. Petrov,[*2,*4] T. Wettig,[*2,*6] and A. Yamaguchi[*2]

The QCDOC (QCD On a Chip) project started in 1999 as a joint effort of RIKEN, Columbia University and IBM Research to design a massively parallel super computer optimized for numerical calculations in lattice quantum chromodynamics (QCD). The architecture combines a state-of-the-art system-on-a-chip technology with a custom-designed logic specially optimized for lattice QCD calculations to provide computing power in the tens of TFlops range at a price/performance ratio of 1 US$ per sustained MFlops.[1–3] The British UKQCD collaboration and the US lattice gauge theory community later endorsed the project. Both RIKEN-BNL Research Center (RBRC) and the UKQCD collaboration will build configurations with 10-TFlops peak speed at the end of 2003. The US community is in a process of deciding the size of their QCDOC computer.

The QCDOC computer is a multiple-instruction, multiple-data (MIMD) machine with distributed memory, just like its predecessor, the QCDSP at Columbia University and RIKEN-BNL Research Center. While a single processing node of the QCDSP consists of seven chips assembled on a credit-card-sized board, now it is possible to integrate the components that make up a single node on a single chip, creating an application-specific integrated circuit (ASIC). The QCDOC chip is such an ASIC, consisting of a) a 500 MHz, 32-bit PowerPC 440 processor core, b) a 64-bit, 1 GFlops floating-point unit, c) a 4 MByte embedded-DRAM memory, d) controllers for embedded and external memories, e) a nearest-neighbor serial communication unit (SCU) with latencies of 120 ns (300 ns) for send (receive), overlapped between the 12 independent directions and an aggregate bandwidth of 12 Gbit/s, and f) other components such as an Ethernet controller, etc. The power consumption of the chip will be approximately 5 W. Two such ASICs will be mounted on a daughter board, together with two industry-standard double data rate (DDR) SDRAM modules (one per ASIC). Thirty-two daughter boards will be mounted on a mother board, and eight mother boards in a crate with a single backplane. The final machine consists of a certain number of such crates.

There are two separate networks: the physics network and the Ethernet-based auxiliary network. The physics network consists of high-speed serial links between nearest neighbors with a bandwidth of 2 × 500 Mbits/s per link. The nodes are arranged in a six-dimensional torus which allows efficient partitioning of the machine in software. The SCU in the ASIC provides direct memory access, single-bit error detection with automatic resend, and a low-latency store-and-forward mode for global operations. The Ethernet-based 100 Mbit/s auxiliary network is used for booting, diagnostics, and I/O over Ethernet, with an Ethernet controller integrated on the ASIC. Hubs on the mother board will provide a bandwidth of 1.6 Gbit/s off a mother board to commercial switches and the host workstation.

The ASIC logic design has been completed and the final net list was accepted by IBM in November. VHDL simulations of various lattice QCD numerical programs have been running on the design for many months. Based on these simulations we estimate the efficiency of the QCDOC systems as 50% or better of their peak speed. The physical design of the ASIC is now under way at IBM with release-to-manufacture expected by the end of the year. Production of the chip will start immediately following that. Daughter board and mother board designs are also being finalized. Their production will begin in the spring of 2003. The host computer configuration, both hardware and software, is being discussed. The first production-scale machine with a peak speed of 2 TFlops and all functionalities will be built during the summer. The 10 TFlops peak RBRC QCDOC machine will be completed near the end of 2003.

References

1) D. Chen et al.: Nucl. Phys. B, (Proc. Suppl.), **94**, 825 (2001); hep-lat/0011004.
2) P. A. Boyle et al.: Nucl. Phys. B, (Proc. Suppl.), **106**, 177 (2002); hep-lat/0110124.
3) P. A. Boyle et al.: Nucl. Phys. B, (Proc. Suppl.), to be published; hep-lat/0210034.

*1 School of Physics, University of Edinburgh, UK
*2 Department of Physics, Columbia University, USA
*3 IBM T. J. Watson Research Center, USA
*4 Department of Physics, Brookhaven National Laboratory, USA
*5 Institute of Particle and Nuclear Studies, High-Energy Accelerator Research Organization (KEK)
*6 Department of Physics, Yale University, USA

Light quark masses from domain wall fermions†

C. Dawson

The up, down and strange quark masses are fundamental parameters of quantum chromodynamics. Here we report the results of a calculation of the values of the strange quark mass, and the average of the up and down quark masses using lattice QCD with domain wall fermions[1] in the quenched approximation.

Our approach is to calculate the mass of the pseudo-scalar and vector meson on the lattice for several input bare lattice quark masses. This dependence on the quark mass is compared to theoretical expectations. For the pseudo-scalar meson mass we use the predictions of first order chiral perturbation theory, which for the pion and kaon masses read

$$m_\pi^2 a^2 = B_\pi a\overline{m}\,, \tag{1}$$

$$m_K^2 a^2 = B_\pi a(m_s + \overline{m})/2\,, \tag{2}$$

where $\overline{m}$ is the averages of the up and down quark masses, m_s is the strange quark mass, a is the lattice spacing and B_π is a constant. For the vector meson mass the leading quark mass dependence should be linear, and so for the rho meson mass we have

$$m_\rho a = A_\rho + B_\rho \overline{m}\,. \tag{3}$$

Here A_ρ and B_ρ are constants. To determine the quark masses we fit the lattice data to Eqs. (1) to (3), extracting B_π, A_ρ and B_ρ. Then using the values of m_π, m_K and m_ρ from experiment we calculate a and the bare quark masses. For our final extraction of the constants we also took into account the leading corrections to Eqs. (1) and (2) due to the quenched approximation (more details and the exact form of these corrections can be found in Ref. 1).

This bare quark mass is then converted into a renormalised quark mass in the $\overline{MS}$ scheme using a two-step procedure: First, a renormalisation factor connecting the lattice bare quark mass to a renormalised mass in the RI-scheme is calculated using the nonperturbative renormalisation method of the Rome/Southampton group.[2] Secondly, this is converted into an $\overline{MS}$-scheme mass using a matching factor calculated in continuum perturbation theory.[3] This approach is taken to avoid using lattice perturbation theory which is extremely time-consuming.

Domain wall fermions[4] provide a lattice discretisation of QCD that avoids the problems of explicitly broken chiral symmetry on the lattice, while preserving exact vector symmetry. They do this by adding a fifth dimension to the problem; as the extent of this fifth dimension tends to infinity the explicit chiral symmetry tends to zero. As practical simulations have $O(10)$ points along the fifth dimension, there will be some residual chiral symmetry breaking which must be small for this approach to work. In Ref. 5, it is shown that the form of the discretisation of the gauge action has a large effect on the size of this effect. In particular, the DBW2 action[6] exhibits excellent chiral symmetry breaking, even for relatively large lattice spacings. However, when using an unusual discretisation for a gauge action, unforeseen complications may arise and so an important aspect of the work reported here is the comparison of the DBW2 results with those from the more traditional Wilson gauge action.

Figure 1 shows the pseudo-scalar mass versus the renormalised quark mass (in the $\overline{MS}$ scheme at 2 GeV) for the DBW2 gauge action at inverse lattice spacings of approximately 2 GeV and 1.3 GeV and the Wilson gauge action with $a^{-1} \approx 2$ GeV (for simulation details see Ref. 1). As can be seen the Wilson and DBW2 gauge actions at $a^{-1} = 2$ GeV agree very well with each other and also with the DBW2 action at $a^{-1} = 1.3$ GeV, evidence that the DBW2 action has impressively small lattice artifact corrections. The final numbers for the quark masses are $m_s \approx 130$ MeV and $\overline{m} = 5$ MeV (see Ref. 1 for the precise numbers for each action).

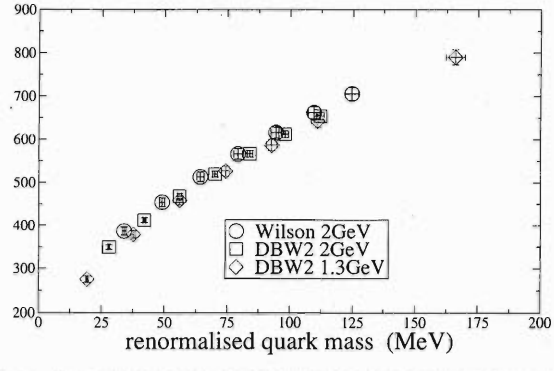

Fig. 1. Comparison of the pseudo-scalar meson mass versus renormalised quark mass for the different gauge actions used.

† This work was done in collaboration with Y. Aoki, T. Blum, N. Christ, C. Cristian, T. Izubuchi, G. Liu, R. Mawhinney, S. Ohta, K. Orginos, A. Soni and L. Wu. We thank RIKEN, Brookhaven National Laboratory and the U.S. Department of Energy for providing the facilities essential for this work.

References

1) RBC Collaboration, C. Dawson et al.: hep-lat/0210005 (2002).
2) G. Martinelli et al.: Nucl. Phys. B **445**, 81 (1995).
3) K. G. Chetyrkin and A. Retey: Nucl. Phys. B **583**, 3 (2000).
4) V. Furman and Y. Shamir: Nucl. Phys. B **439**, 54 (1995).
5) Y. Aoki et al.: hep-lat/0211023 (2002).
6) QCD-TARO, P. de Forcrand et al.: Nucl. Phys. B **577**, 263 (2000).

Nucleon matrix elements with domain wall fermions

K. Orginos, for the RBC Collaboration

The structure of the nucleon is one of the fundamental problems that lattice QCD can address. In the last few years, substantial efforts have been made by several groups[1–3] in calculating the non-perturbative matrix elements relevant to the nucleon structure. To date only Wilson fermions, both improved and unimproved, have been used in both the quenched approximation and in full QCD. In this study, we examine the feasibility of studying nucleon matrix elements with domain wall fermions in the quenched approximation. Domain wall fermions have only $\mathcal{O}(a^2)$ lattice artifacts, thus non-perturbative renormalization works very well, and have no problem with exceptional configurations.[4] Furthermore, the chiral symmetry they preserve on the lattice eliminates mixings with lower dimensional operators, rendering the renormalization of certain matrix elements significantly simpler. For these reasons, the study of the nucleon structure with domain wall fermions is important.

We study the nucleon matrix elements relevant to the leading twist contributions to the moments of the nucleon structure functions.[3] Our current results are restricted only to those matrix elements that can be computed with zero momentum nucleon states. We use the DBW2 gauge action which is known to improve the domain wall fermion chiral properties. These results are for 416 lattices of size $16^3 \times 32$ at $\beta = 0.870$ with lattice spacing $a^{-1} = 1.3\,\mathrm{GeV}$. This provides us with a physical volume ($\sim (2.4fm)^3$) large enough to reduce finite size effects known to affect some nucleon matrix elements such as g_A. For more technical details of the calculation see Ref. 5. Here we present some interesting results from our calculations.

First, Fig. 1 presents our results for the non-singlet quark density distribution $\langle x \rangle_{u-d}$. This is related to the lowest moment of the unpolarized structure functions F_1 and F_2. Down to 380 MeV pion mass no significant curvature within statistical errors can be seen. Lighter quark masses and higher statistics are needed in order to resolve the expected chiral log behavior near the chiral limit.[6] The ratio $\langle x \rangle_u / \langle x \rangle_d$ linearly extrapolated to the chiral is 2.41(4), in agreement with the quenched Wilson fermion result.[2,3]

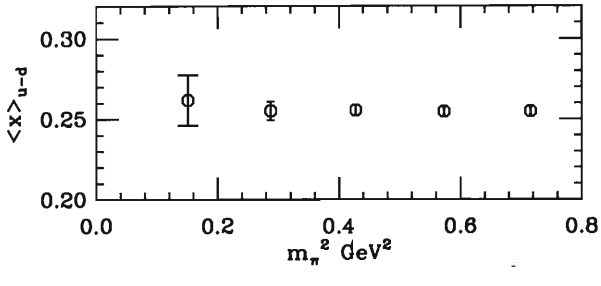

Fig. 1. Flavor non-singlet quark density $\langle x \rangle_{u-d}$ *vs.* pion mass squared.

Second, we computed the d_1 matrix element which is a twist 3 contribution to the first moment of g_2. If chiral symmetry is broken, the operator

$$\mathcal{O}_{34}^{[5]q} = \frac{1}{4}\bar{q}\gamma_5 \left[\gamma_3 \overleftrightarrow{D}_4 - \gamma_4 \overleftrightarrow{D}_3\right] q$$

which is used to measure d_1 mixes with the lower dimensional operator $\mathcal{O}_{34}^{\sigma q} = \bar{q}\gamma_5\sigma_{34}q$. Hence in Wilson fermion calculations, a non perturbative subtraction has to be performed.[1] With domain wall fermions, this kind of mixing is proportional to the residual mass which in our case is negligible. Thus, we expect that a straight forward computation of d_1 with domain wall fermions provides directly the physically interesting result. In Fig. 2, we present our unrenormalized results for d_1 as a function of the quark mass. For comparison, we also plot the unrenormalized quenched Wilson results for $\beta = 6.0$ from Ref. 3. The fact that our result almost vanishes at the chiral limit is an indication that the power divergent mixing is absent for domain wall fermions. The behavior we find for the d_1 matrix element is consistent with that of the non-perturbatively renormalized d_2 calculated by QCDSF[1] with Wilson fermions. The matrix element d_2 is a twist 3 contribution to the second moment of g_2 and has similar renormalization properties with d_1.

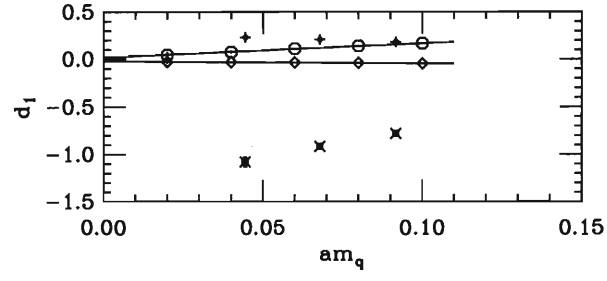

Fig. 2. Connected d_1 matrix element *vs.* quark mass for the up (octagons) and down (diamonds) quarks. The up (fancy squares) and down (fancy diamonds) quarks for Wilson fermions.[3]

References

1) M. Gockeler et al.: Phys. Rev. D **63**, 074506 (2001).
2) M. Gockeler et al.: Phys. Rev. D **53**, 2317 (1996).
3) LHPC, D. Dolgov et al.: hep-lat/0201021 (2002).
4) T. Blum et al.: Phys. Rev. D **66**, 014504 (2002).
5) RBC, K. Orginos: Lattice 2002, hep-lat/0209137.
6) W. Detmold et al.: Phys. Rev. Lett. **87**, 172001 (2001).

Nucleon axial charge from lattice QCD†

T. Blum,[*1] S. Ohta,[*1,*2] K. Orginos,[*1] and S. Sasaki[*3]

Domain wall fermions (DWFs)[1] preserve chiral symmetry on the lattice by introducing a fictitious fifth dimension in which the symmetry violation is exponentially suppressed. The DBW2 ("doubly blocked Wilson 2") improved gauge action[2] improves the approach to the continuum by adding rectangular (2×1) Wilson loops to the action. By combining the two, the "residual mass," which controls low-energy chiral behavior, is driven to as low as $am_{\rm res} < O(10^{-4})$, or $\ll 1\,\mathrm{MeV}$. Successful numerical lattice calculations for the investigation of chiral symmetry and the ground-state hadron mass spectrum,[3] Kaon matrix elements,[4] and negative-parity excited nucleon (N^*) mass[5] have been reported. Here we apply the method to the axial charge, g_A, the simplest of nucleon electroweak matrix elements.

From neutron β decay, we know that $g_V = G_F \cos\theta_c$ and $g_A/g_V = 1.2670(30)$.[6] These quantities are defined as $q^2 \to 0$ limits of the form factors $g_V(q^2)$ and $g_A(q^2)$ in the relevant vector and axial current matrix elements. On the lattice, in general, we calculate the matrix elements of these currents with a lattice cutoff, $a^{-1} \sim 1$–$2\,\mathrm{GeV}$, and extrapolate to the continuum, $a \to 0$, introducing lattice renormalization: $g^{\rm ren}_{V,A} = Z^{\rm lat}_{V,A} g^{\rm lat}_{V,A}$. Also, unwanted lattice artefacts may result in unphysical mixing of chirally distinct operators. DWFs make the calculation particularly easy, because the chiral symmetry is almost exact; the relation $Z_A = Z_V$ is maintained, thus the lattice ratio $(g_A/g_V)^{\rm lat}$ directly yields the renormalized ratio.

The calculations are performed on two lattices: $8^3 \times 24 \times 16$ ($\sim (1.2\,\mathrm{fm})^3$) and $16^3 \times 32 \times 16$ ($\sim (2.4\,\mathrm{fm})^3$). Nucleon source-sink separation is set at about 1.5 fm, and quark mass values of $m_f = 0.02$, 0.04, 0.06, 0.08 and 0.10 are used. The pion mass is as low as $m_\pi \geq 390\,\mathrm{MeV}$ and satisfies $m_\pi L \geq 4.8$ and 2.4, respectively. The residual mass at this cutoff is about $0.8\,\mathrm{MeV}$ or $am_{\rm res} \sim 6 \times 10^{-4}$. Clear volume dependence is observed between $V \sim (2.4\,\mathrm{fm})^3$ and $V \sim (1.2\,\mathrm{fm})^3$. The large volume results show a very mild m_f dependence and linearly extrapolate to a value of $(g_A/g_V)^{\rm ren} = 1.21(3)(+4)$. The first error is statistical and is obtained by the linear fit, and the second is systematic and is a result of the preliminary finite-size analysis. In Fig. 1 the data are presented in physical units together with the small-volume Wilson gauge action results. The smaller volume results with Wilson ($16^3 \times 32$ at $a \sim 0.1\,\mathrm{fm}$) and DBW2 ($8^3 \times 24$ at $a \sim 0.15\,\mathrm{fm}$) actions are mutually consistent. In summary, we confirmed a lattice-volume dependence of the nucleon axial charge, g_A/g_V.

We thank RIKEN, Brookhaven National Laboratory and the U.S. Department of Energy for providing the facilities essential for the completion of this work.

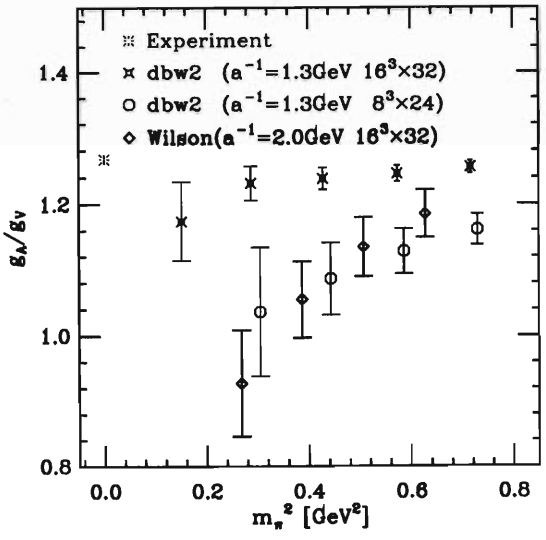

Fig. 1. $(g_A/g_V)^{\rm ren}$: m_π^2 and volume dependence in a physical scale set by ρ meson mass.

References

1) D. B. Kaplan: Phys. Lett. B **288**, 342 (1992); Y. Shamir: Nucl. Phys. B **406**, 90 (1993); V. Furman and Y. Shamir: Nucl. Phys. B **439**, 54 (1995).
2) QCD-TARO Collaboration, P. de Forcrand et al.: Nucl. Phys. B **577**, 263 (2000).
3) RBC Collaboration, T. Blum et al.: to appear in Phys. Rev. D, hep-lat/0007038.
4) RBC Collaboration, T. Blum et al.: RBRC Scientific Articles 4; hep-lat/0110075, submitted for publication in Phys. Rev. D.
5) S. Sasaki, T. Blum, and S. Ohta: Phys. Rev. D **65**, 074503 (2002).
6) The Particle Data Group, K. Hagiwara et al.: Phys. Rev. D **66**, 010001 (2002).

† Condensed from the contribution to the Int. Symp. on Lattice Field Theories "Lattice 2002," (Cambridge, MA, USA, 2002), Nucl. Phys. (Proc. Suppl.) to be published; hep-lat/0210006

*1 Brookhaven National Laboratory, USA
*2 Institute of Particle and Nuclear Studies, High-Energy Accelerator Research Organization (KEK)
*3 Department of Physics, University of Tokyo

Nucleon decay matrix elements for domain-wall fermions†

Y. Aoki

Nucleon decay is one of the most important aspects that any (SUSY) GUT model has. In low-energy effective theories it is represented by dimension six operators made of one lepton field and three quark fields. In the decay of $p \to \pi^0 + e^+$, for example, we must calculate the hadronic matrix element of the three-quark operator $\mathcal{O}^{\not B}_{R/L;L} = \epsilon^{ijk}(u^{iT}CP_{R/L}d^j)P_L u^k$ with initial proton and final pion states, where i, j, and k are the color indices. C is the charge conjugation matrix. $P_{R/L}$ represents the right or left projection matrix, respectively. The matrix element has a tensor structure,[2]

$$\langle \pi; \vec{p}|\mathcal{O}^{\not B}_{R/L;L}|p;\vec{k}\rangle = P_L[W_0 - i\not{q}W_q]u_p, \tag{1}$$

where u_p is the proton spinor, $q = k - p$, with k and p being the four momenta of a proton and a pion, respectively. The relevant form factor W_0 is what we need since $\not{q}$ can be replaced with the lepton mass after multiplying the lepton spinor, and is negligible in our precision.

In this study we try to calculate nucleon decay matrix elements with domain-wall fermions in the quenched approximation. Using DBW2 gauge action makes chiral symmetry breaking particularly small compared to the other actions.[3] With this good chiral symmetry one expects good properties for calculating hadronic matrix elements: 1) prevention of operator mixing with different chiral structure, and 2) good scaling, even down to the $1/a \simeq 1\,\mathrm{GeV}$ region.[3,4] We restrict ourselves to the case of a degenerate quark mass in the meson. In this case, one can calculate $p \to \pi^0 + l^+$ and $p \to \pi^+ + \bar{\nu}$ decay amplitudes. The latter is obtained by multiplying the former by $\sqrt{2}$ under the exact SU(2) symmetry of u and d quarks.

We use 100 independent gauge configurations with a size of $16^3 \times 32$ generated by the DBW2 gauge action at $\beta = 0.87$. The domain wall height and the size of the fifth direction are $M_5 = 1.8$ and $L_s = 12$. An estimate of the inverse lattice spacing from the ρ mass is $a^{-1} = 1.23(5)\,\mathrm{GeV}$. The results of W_0 obtained from the direct calculation of the three-point function with the bare operator $\mathcal{O}^{\not B}_{L;L}$ are shown in Fig. 1. The solid diamond show the result after taking an appropriate limit for the quark mass m_f and q^2. We also calculate the chiral Lagrangian parameters α and β defined as

$$\alpha P_L u_p \equiv \langle 0|\mathcal{O}^{\not B}_{R;L}|p\rangle, \tag{2}$$

$$\beta P_L u_p \equiv \langle 0|\mathcal{O}^{\not B}_{L;L}|p\rangle. \tag{3}$$

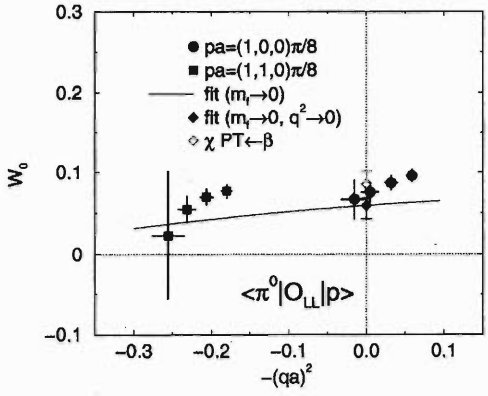

Fig. 1. W_0 for $p \to (\pi^0, l^+)$ decay with $\mathcal{O}_{L;L}$ as a function of invariant mass squared of lepton.

By the tree-level chiral perturbation theory,[5] the relevant part of the matrix element is obtained:

$$\langle \pi^0|\mathcal{O}^{\not B}_{L;L}|p\rangle_{\mathrm{rel}} \simeq \beta(1 + D + F)P_L u_p/\sqrt{2}f, \tag{4}$$

where $D = 0.47$ and $F = 0.80$ from the experiment,[6] and f is $f_\pi = 0.131\,\mathrm{GeV}$. The open diamond in Fig. 1 represents this indirect estimation. There is no significant difference between direct and indirect results in the current statistics. However, 40% excess for the central value determined by the indirect method is quite similar to the JLQCD result.[2] A similar result is also obtained for $\langle \pi^0|\mathcal{O}^{\not B}_{R;L}|p\rangle$.

The above results must be renormalized for the value in the $\overline{MS}$ scheme in continuum theory. We expect these operators are multiplicatively renormalized since chiral symmetry breaking is small ($m_{\mathrm{res}} \sim 1.5\,\mathrm{MeV}$). The nonperturbative renormalization[7] will be carried out in the near future by employing a RI-MOM scheme, which works well in the domain-wall fermion.[8]

† This work has been done in the RBC collaboration. See Ref. 1 for the more detailed article

References

1) RBC Collaboration, Y. Aoki et al.: hep-lat/0210008 (2002).
2) JLQCD Collaboration, S. Aoki et al.: Phys. Rev. D **62**, 014506 (2000).
3) Y. Aoki et al.: hep-lat/0211023 (2002).
4) T. Blum et al.: hep-lat/0007038 (2000).
5) M. Claudson, M. B. Wise, and L. J. Hall: Nucl. Phys. B **195**, 297 (1982).
6) S. Y. Hsueh et al.: Phys. Rev. D **38**, 2056 (1988).
7) G. Martinelli et al.: Nucl. Phys. B **445**, 81 (1995).
8) T. Blum et al.: Phys. Rev. D **66**, 014504 (2002).

Lattice QCD calculation of the lowest order hadronic contribution to the muon anomalous magnetic moment†

T. Blum

The magnetic moment of the muon is defined through the vertex function

$$\Gamma^{\mu}(p',p) = \left(\gamma^{\mu} F_1(q^2) + \frac{i\,\sigma^{\mu\nu} q_{\nu}}{2m} F_2(q^2)\right), \qquad (1)$$

where $q = p' - p$ is the photon momentum, and p, p' are the incoming and outgoing momenta of the muon. Form factors F_1 and F_2 contain all information about the muon's interaction with the electromagnetic field. In particular, $F_1(0) = 1$ is the electric charge of the muon in units of e, and

$$g = 2(F_1(0) + F_2(0)), \qquad (2)$$

is the Landé g-factor proportional to the magnetic moment. It is conventional to define the anomaly

$$a_{\mu} \equiv \frac{g-2}{2} = F_2(0), \qquad (3)$$

as the difference of g from its tree level value. Corrections to $F_2(0)$, and therefore a_{μ}, start at $\mathcal{O}(\alpha)$, where α is the fine structure constant.

The most precise measurement ever of the muon's anomalous magnetic moment was recently carried out at Brookhaven National Laboratory.[1] Comparison of the experimental value with the Standard Model yields a difference of 2.7 standard deviations[1] where the theoretical and experimental uncertainties are roughly the same. The dominant theoretical uncertainty arises in hadronic corrections which begin at $\mathcal{O}(\alpha^2)$ through the hadronic vacuum polarization. In Table 1 we summarize the hadronic contributions. Presently, the $\mathcal{O}(\alpha^2)$ hadronic contribution is calculated by using dispersion relations and the experimental value of the total cross-section for $e^+e^- \to$ hadrons to relate the imaginary part of the vacuum polarization to the real part. Thus a purely theoretical, first principles, calculation has been lacking. The aim of this work is to perform such a calculation.

Table 1. Hadronic contributions to a_{μ}.

$a_{\mu}^{\rm had}$(vac.pol. $\mathcal{O}(\alpha^2)$)	$692(6) \times 10^{-10}$
$a_{\mu}^{\rm had}$(light $-$ light $\mathcal{O}(\alpha^3)$)	$8.6(3.2) \times 10^{-10}$
$a_{\mu}^{\rm had}$(other $\mathcal{O}(\alpha^3)$)	$-10.0(0.6) \times 10^{-10}$
$a_{\mu}^{\rm had}$(total)	$690.4(7) \times 10^{-10}$
Theory total	$11\,659\,177(7) \times 10^{-10}$
Experiment	$11\,659\,204(7)(5) \times 10^{-10}$

† We thank RIKEN, Brookhaven National Laboratory, and the U.S. Department of Energy for providing the facilities essential for this work. All computations were done on the RIKEN BNL QCDSP supercomputer.

The vacuum polarization is given by the Fourier transform of the two-point function

$$\Pi^{\mu\nu}(q) = \int d^4x\, e^{i\,q\,(x-y)} \langle J^{\mu}(x) J^{\nu}(y)\rangle = (q^2 g^{\mu\nu} - q^{\mu}q^{\nu})\Pi(q^2), \qquad (4)$$

where J^{μ} is the electromagnetic current, the last line results from Lorentz and gauge invariance, and $\Pi^{\mu\nu}(q)$ clearly satisfies the Ward-Takahashi identity.

Using domain wall fermions and the associated conserved vector current, the vacuum polarization tensor is computed non-perturbatively. In Fig. 1 we show $\Pi(\hat{q}^2)$ computed in the quenched approximation at $a^{-1} \approx 1.3\,\text{GeV}$, spatial volume $(2.4\,\text{fm})^3$, and quark mass $(\overline{MS},\ \mu = 1/a = 1.3\,\text{GeV}) \approx 90\,\text{MeV}$ ($\hat{q}^{\mu} \equiv 2/a \sin(\pi\, n_{\mu}/L_{\mu})$, $n_{\mu} = 0, \ldots, L_{\mu} - 1$)). The agreement with perturbation theory[2] is impressive, even when $|\hat{q}| < 1$ (since $\Pi(q^2)$ is logarithmically divergent, the perturbation theory curve has been shifted by a constant). At very high momenta, the curves do not agree because of lattice artifacts.

To obtain the $\mathcal{O}(\alpha^2)$ hadronic correction, the polarization $\Pi(q^2)$ must be inserted into the usual one-loop vertex function, and the loop integral computed numerically. For $q^2 \gg 1$ perturbation theory can be used, while for $q^2 \ll 1$ the lattice result is required. Once the above procedure is completed, an investigation of the uncertainties due to quenching and unphysical quark mass can be undertaken.

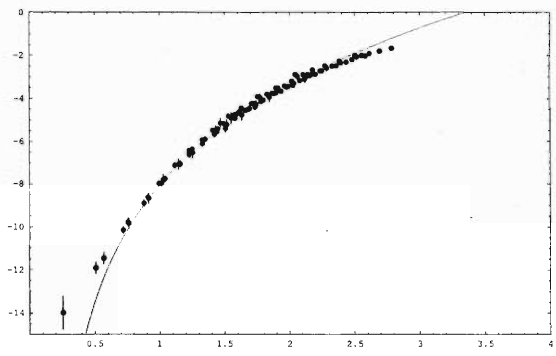

Fig. 1. The polarization function $12\pi^2\Pi(\hat{q}^2)$ *vs.* $|\hat{q}|$ (GeV). The solid line is from Ref. 2.

References

1) G. W. Bennett et al.: Phys. Rev. Lett. **89**, 101804 (2002).
2) K. Chetyrkin et al.: Nucl. Phys. B **482**, 213 (1996).

Polemass reduction and thermal width of glueball at $T \neq 0$ in SU(3) anisotropic lattice QCD†

N. Ishii, H. Suganuma,*1 and H. Matsufuru*2

Hadrons are relativistic bound states of quarks and gluons. Hence, at nonzero temperature/density, even in the confinement phase, we expect them to change their properties reflecting the changes of the QCD vacuum such as the reduction of the string tension and partial chiral restoration. In fact, a number of effective models predict the polemass reduction of various hadrons of more than a few hundred MeV near the critical temperature T_c of QCD phase transition.[1–4] Recently, motivated by these studies, quenched anisotropic lattice QCD has been used to measure the polemass of various hadrons at finite temperatures,[5–7] revealing profound results that for both light and heavy $q\bar{q}$-mesons, no significant change is observed below T_c, while for the glueball, a significant polemass reduction of about 300 MeV is observed near T_c. In all of these studies, the narrowness of the peak is assumed. However, since at $T \neq 0$, each bound state peak acquires a finite thermal width through the interaction with the heat bath, it is desirable that the finite width is taken into account. Here, we report the advanced analysis of the thermal 0^{++} glueball based on SU(3) quenched anisotropic lattice QCD, taking into account the effect of thermal width.

Generally, to extract physical observables such as mass and width, we have to resort to the spectral representation of the two-point correlator $G(t) \equiv Z(\beta)^{-1}\mathrm{tr}\left\{e^{-\beta H}\phi(t)\phi(0)\right\}$ as

$$G(t) = \int_{-\infty}^{\infty} \frac{d\omega}{2\pi} \frac{\rho(\omega)}{2\sinh(\beta\omega/2)} \cosh\left(\omega(\beta/2-t)\right), \quad (1)$$

where H is the QCD Hamiltonian, $Z \equiv \mathrm{tr}(e^{-\beta H})$, $\phi(t) \equiv e^{tH}\phi(0)e^{-tH}$ is the zero-momentum projected glueball operator in the imaginary-time Heisenberg picture, and $\rho(\omega)$ is the spectral function. Appropriate smearing on $\phi(t)$ is adopted to maximize the overlap with the glueball state. To extract the physical observables, we parameterize $\rho(\omega)$ and use Eq. (1) to fit $G(t)$ generated by lattice QCD. In Refs. 5–7 the narrow-peak ansatz has been adopted, where $\rho(\omega)$ is parameterized as $\rho(\omega) = 2\pi A\left(\delta(\omega - m) - \delta(\omega + m)\right) + \cdots$ with the two fit parameters A and m corresponding to the overlap and the polemass, respectively.

To consider the thermal width, we recall that $\rho(\omega)$ is the imaginary part of the retarded Green function $G_R(\omega)$, *i.e.*, $\rho(\omega) = -2\mathrm{Im}\left(G_R(\omega)\right)$. At $T = 0$, bound state poles of $G_R(\omega)$ are located on the real ω-axis. With increasing T, they begin to deviate from the real axis into the complex ω-plane. Thus the contribution of each complex pole to $\rho(\omega)$ can be parameterized with a Lorentzian as $\rho(\omega) = 2\pi A\left(\delta_\Gamma(\omega - \omega_0) - \delta_\Gamma(\omega + \omega_0)\right) + \cdots$, where A, ω_0 and Γ are the fit parameters corresponding to the overlap, the center and the thermal width, respectively. $\delta_\epsilon(x) \equiv \frac{1}{\pi}\mathrm{Im}\left(\frac{1}{x-i\epsilon}\right)$ denotes a smeared delta function. We refer to the corresponding fit function as the Breit-Wigner type.

The numerical results are shown in Fig. 1. We use 5000 to 9900 gauge configurations generated by the Wilson action with $\beta = 6.25$ and the renormalized anisotropy $\xi \equiv a_s/a_t = 4$. Although the narrow-peak ansatz indicates the significant polemass reduction of about 300 MeV, the Breit-Wigner ansatz indicates the significant thermal width broadening of more than 300 MeV with a slight reduction in the peak center. These two analyses thus lead to two different physical implications. Note that, due to the biased factor "$\sinh(\beta\omega/2)$" in Eq. (1) which enhances the smaller ω region of $\rho(\omega)$, thermal width is effectively seen as the reduced polemass in the narrow-peak ansatz. Hence, in the case of the glueball, the thermal effect is most probably the thermal width broadening.

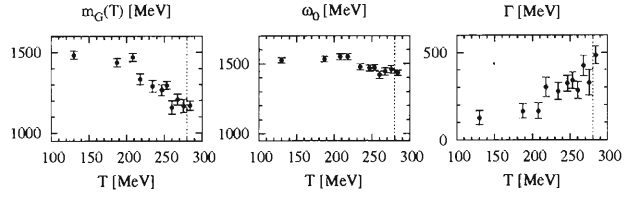

Fig. 1. Polemass $m_G(T)$ from the narrow-peak ansatz, and the center $\omega_0(T)$ and the thermal width $\Gamma(T)$ from the Breit-Wigner ansatz. Vertical dotted lines indicate the critical temperature $T_c \simeq 280$ MeV. Appropriate smearings are adopted in the glueball operator.

References
1) T. Hatsuda et al.: Phys. Rev. Lett. **55**, 158 (1985).
2) T. Hashimoto et al.: Phys. Rev. Lett. **57**, 2123 (1986).
3) T. Hatsuda et al.: Phys. Rev. D **47**, 1225 (1993).
4) H. Ichie et al.: Phys. Rev. D **52**, 2944 (1995).
5) QCD-TARO Collab.: Phys. Rev. D **63**, 054501 (2001).
6) T. Umeda et al.: Int. J. Mod. Phys. A **16**, 2215 (2001).
7) N. Ishii et al.: Phys. Rev. D **66**, 014507 (2002).

† Condensed from the article in Phys. Rev. D **66**, 094506 (2002)

*1 Faculty of Science, Tokyo Institute of Technology
*2 Yukawa Institute for Theoretical Physics, Kyoto University

Universality, the QCD critical/tricritical point and the quark number susceptibility

Y. Hatta* and T. Ikeda

Recently, phase transitions of QCD at finite temperature and density have been extensively studied both theoretically and experimentally. We investigate the quark number susceptibility χ_q near the QCD critical end-point (CEP), the tricritical point (TCP) and the O(4) critical line at finite temperature T and quark chemical potential μ.

χ_q is a response of the quark number density to the variation of the quark chemical potential and is one of the key quantities characterizing the phase change from hadronic matter to quark gluon plasma (QGP). Therefore, it would be important to study its critical behavior with and without the quark masses to see whether it can provide a new method of detecting the TCP/CEP in the lattice simulations as well as in the heavy-ion collision experiments.

At the QCD critical end-point, the sigma meson becomes massless and the phase transition belongs to the Ising universality class. Signatures of the end-point arising from the critical fluctuation have been discussed in the literatures. Here we extend the analyses from the viewpoint of universality with particular emphasis on the behavior of χ_q.[1] The universality argument predicts that the critical region of CEP is small. If the critical region of CEP is small, we are naturally led to consider the mean field region around the critical region. TCP also has its mean field region. Then, an interesting possibility arises; the mean field region may survive in the physical (T, μ) plane. Indeed, the universality argument based on the Ginzburg-Landau potential suggests that TCP is as important as CEP at least in the small quark mass limit.[1]

In order to complement the general universality argument, we made a semiquantitative study of the quark number susceptibility near CEP/TCP for several quark masses on the basis of the Cornwall-Jackiw-Tomboulis (CJT) potential for QCD in the improved-ladder approximation. Figure 1 is the quark number susceptibility with the quark mass $m_q = 5\,\mathrm{MeV}$ in the (T, μ) plane. As expected, it diverges at CEP and is enhanced in a wide region around CEP. We also calculated the critical exponents. The result shows that the critical exponent gradually changes from that of CEP to that of TCP.[1] This indicates that a crossover of different universality classes (tricritical universality class to Ising universality class via the mean field region of CEP) occurs. We expect that, although we adopted a specific model, the qualitative behavior of χ_q is model independent. Thus we propose a possibility that the hidden TCP strongly affects the physics around CEP.

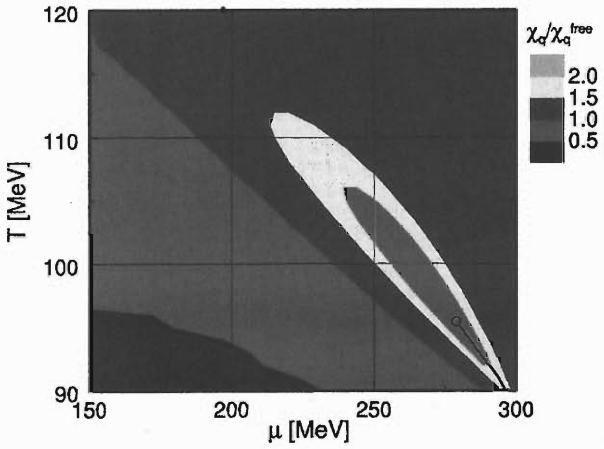

Fig. 1. The quark number susceptibility in the (T, μ) plane with the quark mass $m_q = 5\,\mathrm{MeV}$. The value of the susceptibility is divided by that of the massless free theory. The open circle is the critical end point.

Our results have some implications on the heavy-ion collision experiments. The divergence of χ_q is directly related to an anomaly in the event-by-event fluctuation of baryon number B (divided by the entropy S)

$$\frac{\langle (\Delta B)^2 \rangle}{S}.$$

We expect that the event-by-event fluctuation of the *proton number* is relatively enhanced for collisions which have passed 'near' CEP/TCP. Also, if the effect of TCP turns out to be large, we must take into account the long-wavelength fluctuations of the *pions* as well as the sigma meson because the pions are no longer the 'environment' but participate in the critical fluctuations around the trace of TCP.

References

1) Y. Hatta and T. Ikeda: Phys. Rev. D **67**, 014028 (2003).

* Department of Physics, Kyoto University

Geometric scaling and Froissart bound from gluon saturation

E. Ferreiro,[*1] E. Iancu,[*2] K. Itakura, and L. McLerran[*3]

The problems we have been concerned about are extreme situations in QCD with high gluon density. In the past few years, we have obtained better understanding of such high density gluonic matter ("Color Glass Condensate"). At very high energies, the cross sections for hadronic processes are dominated by the small-x gluons in the hadron wavefunction. These gluons form a high-density matter which is believed to reach saturation, and become a Color Glass Condensate. Roughly speaking, the saturation is realized under the balance between the creation of small x gluons ("gain") and their recombination ("loss") which becomes significant at high gluon density. Note that the cross section of recombination, at the level of the fundamental process $gg \to g$, is proportional to the *square* of the gluon density, which introduces non-linearity in the evolution equation. However, as the density increases, multiple scattering among gluons, which induces higher-order non-linearity, becomes increasingly important, and eventually the partonic description is replaced by the coherent field description. This dense gluonic matter is relevant for various high-energy processes such as the deep inelastic scattering (DIS) of leptons on a nucleon (ep) or a nucleus (eA) and the relativistic heavy-ion collisions (AA). We have provided two important things: natural interpretation of the new phenomenon "geometric scaling"[1)] and the computation of the hadronic cross section at high energy.[2)] We work in a regime where the typical momentum scale is larger than the confinement scale $\Lambda_{\rm QCD}$ so that we can use weak-coupling techniques. However, this is not a simple perturbative regime because we need non-perturbative calculations such as resummation of log enhanced factors.

Geometric scaling is a novel scaling phenomenon in DIS at small x which was found by Staśto, Golec-Biernat and Kwieciński. Namely, the total cross sections of virtual-photon and proton scattering in DIS at $x < 0.01$, which are a priori functions of two independent variables, namely, the photon virtuality Q^2 and the Bjorken variable x, are consistent with scaling in terms of the variable $\xi = Q^2 R_0^2(x)$, where $R_0^2(x) = (x/x_0)^\lambda/Q_0^2$ with the parameters $\lambda = 0.3 \div 0.4$, $Q_0 = 1\,\mathrm{GeV}$, and $x_0 \sim 3 \times 10^{-4}$. This has been observed in the kinematical regime $0.045 < Q^2 < 450\,\mathrm{GeV}^2$.

At sufficiently low Q^2, below the saturation scale $Q_s^2(x)$ ($\sim$ a few GeV^2), this phenomenon finds a natural explanation as a property of the Color Glass Condensate. Indeed, in the saturation regime, the saturation momentum $Q_s(x)$ is the only one relevant scale, and any dimensionless quantity should be expressed as a function of $Q^2/Q_s^2(x)$. Therefore, this naturally leads to the identification of $Q_s^2(x)$ with the function $1/R_0^2(x)$. However, we have to also explain why the geometric scaling holds even above the saturation scale. To explain the experimental observation of geometric scaling up to much higher values of Q^2, of the order of $100\,\mathrm{GeV}^2$, we studied the solution to the BFKL equation subjected to a *saturation boundary condition* at $Q^2 \sim Q_s^2(x)$. We found that through the saturation boundary condition, the information of the saturation, and thus the scaling, is persistent even above the saturation scale, within a window $1 \lesssim \ln(Q^2/Q_s^2) \ll \ln(Q_s^2/\Lambda_{\rm QCD}^2)$, or $Q^2 < Q_s^4/\Lambda_{\rm QCD}^2$. This upper bound is in good agreement with the phenomenologically observed upper limit.

Another important problem is to understand the energy dependence of the hadronic cross section. Since it is claimed that the linear evolution equation such as the BFKL equation violates the unitarity bound (so called "Froissart bound"), it is interesting how this can be cured from the viewpoint of gluon saturation.

We have demonstrated that the dipole-hadron cross section computed from the non-linear evolution equation (the Balitsky-Kovchegov equation) for the Colour Glass Condensate indeed saturates the Froissart bound in the case of a fixed coupling and for a small dipole ($Q^2 \gg \Lambda_{\rm QCD}^2$). That is, the cross section increases as

$$\sigma \approx \frac{\pi}{2} \frac{(\omega \bar{\alpha}_s)^2}{m_\pi^2} \ln^2 s \qquad (\bar{\alpha}_s = \alpha_s N_c/\pi,\ \omega = 4\ln 2)\,.$$

The pion mass enters through the non-perturbative initial conditions at low energy. The BFKL equation emerges as a limit of the non-linear evolution equation valid in the tail of the hadron wavefunction. In Ref. 2), we provided a physical picture for the transverse expansion of the hadron with increasing energy, and emphasized the importance of colour correlations among the saturated gluons in suppressing non-unitary contributions due to long-range Coulomb tails. We also presented the impact parameter dependence of the saturation scale.

References

1) E. Iancu, K. Itakura, and L. McLerran: Nucl. Phys. A **708**, 327 (2002); hep-ph/0205198.
2) E. Ferreiro, E. Iancu, K. Itakura, and L. McLerran: Nucl. Phys. A **710**, 373 (2002).

*1 Universidad de Santiago de Compostela, Spain
*2 Service de Physique Théorique, CEA Saclay, France
*3 Brookhaven National Laboratory, USA

Hadronic probes of matter under extreme conditions

S. Jeon*

Charge balance functions and charge fluctuations have been proposed as a means of gaining insight into the dynamics of hadronization in relativistic heavy-ion collisions. As a quark-gluon plasma scenario entails a large production of new charges late in the reaction, a tight correlation between the balancing charge/anti-charge pairs would provide evidence of the creation of a novel state of matter.

Using such correlation functions, it can be shown that the charge fluctuation and the balance function are related as[1)]

$$\frac{\langle (Q - \langle Q \rangle)^2 \rangle}{\langle N_{\rm ch} \rangle} = 1 - \int_0^Y d\Delta y \, B(\Delta y | Y) + O\left(\frac{\langle Q \rangle}{\langle N_{\rm ch} \rangle}\right), \qquad (1)$$

where $Q = N_+ - N_-$ and $N_{\rm ch} = N_+ + N_-$. If a QGP is formed, then charge fluctuation is reduced due to the fact that quarks have $Q = \pm 1/3, \pm 2/3$ and gluons contribute to $\langle N_{\rm ch} \rangle$. This also implies that the balance function must become sharper if a QGP is formed.

In this work,[2)] we study the generation of η' mesons by a gluon fusion process in proton-nucleus '(pA)' collisions. In particular, we argue that measuring the η' meson momentum spectrum enables us to have direct access to the gluon density in the small x region of the heavy nucleus.

In Fig. 1 we show the ratio of pA to pp η' production cross sections for two representative values of nuclear intrinsic momenta. As shown, this ratio is quite sensitive to the intrinsic momenta and shadowing.

The aim of this study[3)] is to show that the observed suppression can be described using a perturbative next-to-leading order, $O(\alpha_s^3)$, calculation of inclusive π^0 production, with the nuclear shadowing effect and parton energy loss being energy-dependent.

In Fig. 2 we show the ratio of π^0 production in Au-Au collisions to the one in pp collisions. We find that for a constant energy loss and for an LPM energy-dependent energy loss, the ratio increases with p_T, while for the BH case, the ratio decreases with p_T in agreement with recent PHENIX data.

Understanding π^0 production at RHIC is also important because large-p_T π^0 mesons form a significant background for prompt photons.

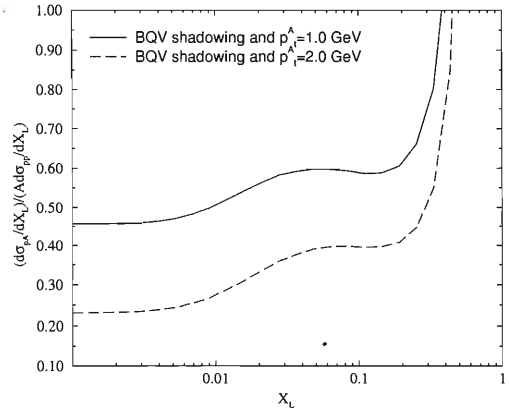

Fig. 1. Ratio of pA to pp η' production cross sections at $\sqrt{s} = 200$.

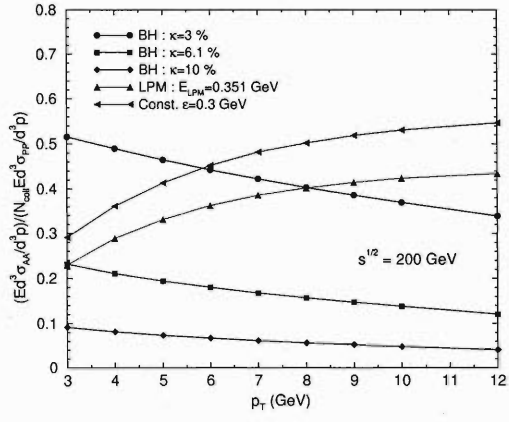

Fig. 2. Ratio of inclusive π^0 cross sections in Au-Au collision to those in pp at $\sqrt{s} = 200\,\text{GeV}$.

References

1) S. Jeon and S. Pratt: Phys. Rev. C **65**, 044902 (2002).
2) J. Jalilian-Marian and S. Jeon: Phys. Rev. C **65**, 065201 (2002).
3) S. Jeon, J. Jalilian-Marian, and I. Sarcevic: nucl-th/0208012.

* Department of Physics, McGill University, Canada

Chiral and color superconducting phase transitions with vector interaction using a simple model

M. Kitazawa,[*1] T. Koide,[*2] T. Kunihiro,[*2] and Y. Nemoto

We investigated the effects of vector interaction on chiral and color superconducting phase transitions at a finite density and temperature using the Nambu-Jona Lasinio (NJL) model. The vector interaction we take into account here is of the type

$$\mathcal{L}_{\mathcal{V}} = -G_V(\bar{\psi}\gamma^{\mu}\psi)^2. \tag{1}$$

Many works on color superconductivity (CSC) have not taken into account this interaction to date. Our point, however, is that it is chiral invariant and a universal feature of effective models derived from microscopic theories as well as the NJL model.

The effect of the vector interaction is less known, although it is important for the chiral and CSC phase transitions. Indeed, the vector coupling weakens the phase transition and delays the chiral restoration. According to the thermodynamics, when phases I and II are in the equilibrium state, the temperatures $T_{I,II}$, pressures $P_{I,II}$ and chemical potentials $\mu_{I,II}$ should be the same,

$$T_I = T_{II}, \quad P_I = P_{II}, \quad \mu_I = \mu_{II}. \tag{2}$$

When I and II are, respectively, the chirally broken (χSB) and restored phases with quark masses $M_I > M_{II}$, the chirally restored phase is at a higher density than the broken phase from the last equation of (2), since $\mu_{I,II}$ at $T = 0$ are given by $\mu_i = \sqrt{M_i^2 + p_F^2}$, $(i = I,\ II)$, and hence $p_{F_I} < p_{F_{II}}$, where p_F is the Fermi momentum of the i-th phase. Thus the chiral restoration at a finite density is necessarily accompanied with a density jump to a higher density state with a large Fermi surface, which favors the formation of Cooper instability leading to CSC. The vector coupling, however, includes the term $(\bar{\psi}\gamma^0\psi)^2$ which gives rise to a repulsive energy proportional to the squared density. This effect is greater in the chirally restored phase than in the broken phase. Therefore, the vector coupling weakens and delays the phase transition of chiral restoration at a low temperature. This is an assumption on why the existence of the vector coupling delays the chiral restoration and the formation of color superconductivity at higher chemical potentials, and possibly may alter the nature of the transition from the χSB phase to the CSC phase drastically.

We showed in our study[1)] that the inclusion of the vector coupling actually induces a novel interplay between χSB and CSC through the difference in the finite baryon density and changes the nature of the phase transition and the phase structure at a low temperature.

We show numerical results in the phase diagrams in the T-μ_B plane and in the T-ρ_B plane without G_V (Fig. 1) and with a reasonable value of G_V (Fig. 2), where μ_B and ρ_B are the baryon chemical potential and density, respectively. G_S represents the coupling of scalar-pseudoscalar 4-fermi interaction. One can observe that the order of the phase transition from χSB to the Wigner or CSC phase weakens and the phase transitions delay at finite G_V.

Although our analysis is based on a simple effective model, our finding that the vector interaction enhances the competition between the χSB and CSC phase transitions is a universal feature. Therefore, it is interesting and important to confirm this using more realistic models.

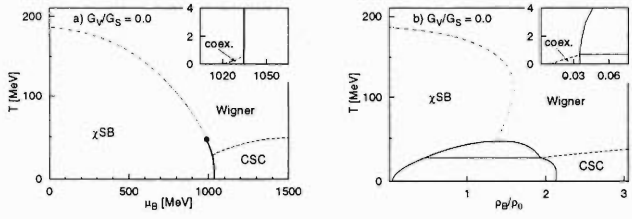

Fig. 1. (a) Phase diagrams in the T-μ_B plane (a) and in the T-ρ_B plane (b) with $G_V = 0$. The solid line represents the critical line of the first-order phase transition, the dashed line the second-order, and the dot-dashed line a crossover. ρ_0 is the nuclear density.

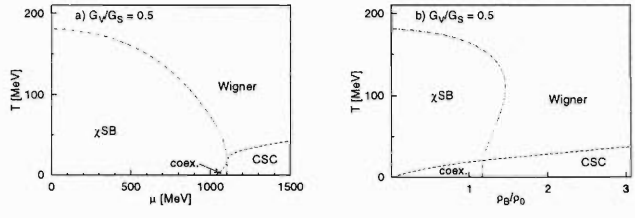

Fig. 2. Phase diagrams in the T-μ_B plane (a) and in the T-ρ_B plane (b) with $G_V/G_S = 0.5$.

References

1) M. Kitazawa, T. Koide, T. Kunihiro, and Y. Nemoto: Prog. Theor. Phys. **108**, 929 (2002).

*1 Department of Physics, Kyoto University
*2 Yukawa Institute for Theoretical Physics, Kyoto University

Precursor of color superconductivity in hot quark matter

M. Kitazawa,[*1] T. Koide,[*2] T. Kunihiro,[*2] and Y. Nemoto

We investigate possible precursory phenomena of color superconductivity (CSC) in hot quark matter.[1] We will show that a large fluctuation of the quark-quark pair (diquark) field of CSC exists even above the critical temperature T_C, *i.e.*, in the Wigner phase, which might affect observables to be detected by the heavy ion collisions with large baryon stopping.

Since we are interested in a relatively low temperature and density region, we adopt a low-energy effective theory of QCD, the two-flavor Nambu-Jona-Lasinio (NJL) model, which is a simplified version of the instanton-induced interaction. By fixing parameters so that experimental values of relevant quantities are reproduced, we obtain the phase diagram in the mean field approximation shown in Fig. 1. Since we consider the chiral limit, the second order phase transition takes place at high temperature.

We now examine the fluctuation of the color Cooper pairs in the Wigner phase at $T > T_C$. We can obtain possible collective states and their strength functions based on the linear response theory. The basic quantity which measures the excitation strength of the fluctuating pair field is the spectral function. We show the numerical results of the spectral function for the scalar diquark channel in Fig. 2. The temperature dependence of the spectral function at $\mu = 400\,\mathrm{MeV}$ and zero momentum transfer is shown in Fig. 2 (a). One can see that a prominent peak moving toward the origin grows as the temperature is lowered and approaches T_c as indicated by the arrow in Fig. 1. From an experimental point of view, it is interesting that the peak survives at T even well above T_c with $\epsilon \equiv (T - T_c)/T_c \sim 0.2$. This means that the precritical region of CSC is one to two

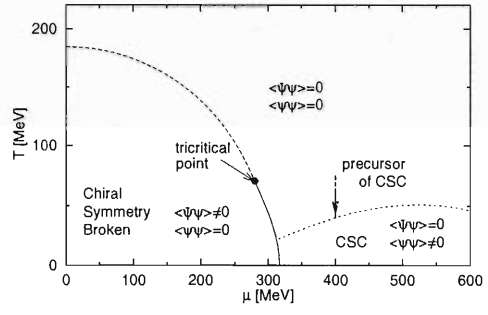

Fig. 1. The phase diagram in temperature *vs.* quark chemical potential plane. The solid and dashed lines denote the critical lines of the first and second order phase transitions, respectively.

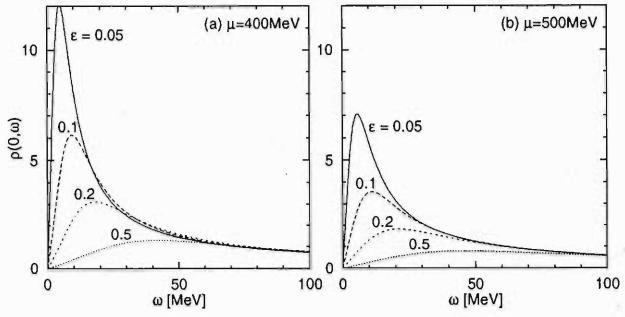

Fig. 2. Spectral function for the scalar diquark at $T > T_c$ with $\epsilon \equiv (T - T_c)/T_c = 0.05$, 0.1, 0.2 and 0.5 at $\mu = 400\,\mathrm{MeV}$ (a) and $\mu = 500\,\mathrm{MeV}$ (b).

orders larger in the unit of T_c than that in electric superconductors. For $\mu = 500\,\mathrm{MeV}$ (Fig. 2 (b)), although the growth of the peak becomes relatively moderate, the qualitative features do not change.

The existence of the peak with the narrow width suggests the existence of a well-defined collective mode as an elementary excitation in the Wigner phase. The collective mode is examined by searching possible poles of the response function. Such a pole $\omega = \omega(k)$ means that the system admits spontaneous excitation of the collective mode with the dispersion relation $\omega = \omega(k)$. A numerical calculation shows that there indeed exists a pole in the lower-half plane of ω for $T > T_c$, which approaches the origin as T decreases toward T_c. Such a mode whose energy tends to vanish as the system approaches the critical point is called a soft mode. Thus we have found the pole for the soft mode for CSC in hot quark matter. The significance of such a soft mode lies in the fact that it causes a long-range correlation for the color Cooper pairs in the Wigner phase, which will lead to singular behavior of various observables such as the transport coefficients.

In short, we have studied precursory phenomena for the color superconductivity (CSC) in hot quark matter. The fluctuating pair field exists with a prominent strength even well above T_c. Such a large fluctuation enables us to observe CSC by heavy ion collision with large baryon stopping analogous to the precritical phenomena in metal and cuprate superconductors.

References

1) M. Kitazawa, T. Koide, T. Kunihiro, and Y. Nemoto: Phys. Rev. D **65**, 091504 (2002).

*1 Department of Physics, Kyoto University
*2 Yukawa Institute for Theoretical Physics, Kyoto University

Detailed analysis of the three-quark potential in SU(3) lattice QCD

T. T. Takahashi,[*1] H. Suganuma,[*2] Y. Nemoto, and H. Matsufuru[*3]

The static three-quark (3Q) potential (V_{3Q}) is studied in detail using SU(3) lattice QCD.[1] The quark-antiquark ($Q\bar{Q}$) potential, which is responsible for the meson properties, has been well studied in lattice QCD, while there is almost no reliable formula to describe V_{3Q}. V_{3Q} is directly responsible for the baryon properties and is obtained by measuring the so-called 3Q Wilson loop on the lattice as shown in Fig. 1.

At present the arguments regarding the 3Q potential seem to be quite controversial. In a recent lattice study, our previous analysis has supported the so-called Y-type flux-tube picture,[2] whereas some authors express V_{3Q} by a sum of two-body potentials between any two quarks, which supports the so-called Δ-type flux tube picture[3] (Fig. 2). These controversial results may be due to the difficulty of an accurate measurement of the 3Q ground-state potential in lattice QCD. For example, Alexandrou *et al.* showed a result only for the equilateral triangle case without the fit analysis.[3]

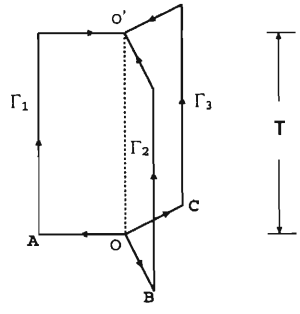

Fig. 1. The 3Q Wilson loop.

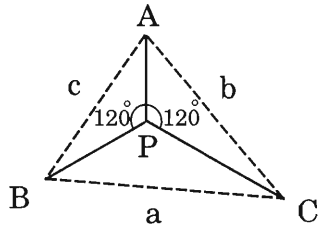

Fig. 2. The flux-tube configuration of the 3Q system. Quarks are placed on the vertices, A, B and C. Solid lines represent the Y-type picture and dashed lines the Δ-type one.

Here we perform an accurate measurement of the static 3Q potential for more than 300 different pattern of the 3Q system in lattice QCD at $\beta = 5.7, 5.8$ and 6.0. We also use the smearing method to remove the excited-state contaminations and obtain the true ground-state potential.

Our numerical results and the fit analysis on V_{3Q} show that the lattice QCD data of V_{3Q} are well reproduced within a few percent deviation by the sum of a constant, the two-body Coulomb term and the three-body linear confinement term, *i.e.*, the Y-type ansatz is favored. From the comparison with the $Q\bar{Q}$ potential, we have found a universality of the string tension, $\sigma_{3Q} \simeq \sigma_{Q\bar{Q}}$, and the one-gluon exchange result for the Coulomb coefficients, $A_{3Q} \simeq 1/2A_{Q\bar{Q}}$.

We also perform various fit analyses. We investigate the fit analysis with the lattice Coulomb potential instead of the Coulomb potential and have found a better fit with a similar result for the parameters. The fit with the Δ ansatz is worse than that with the Y-ansatz in the confinement part in V_{3Q}, although V_{3Q} seems to be approximated by the Δ ansatz with $\sigma_\delta \simeq 0.53\sigma$. We also perform the fit analysis with the Yukawa potential instead of the Coulomb potential and have found that there is no definite evidence that the short-distance potential is of the Yukawa type. Finally we consider a more general ansatz including the Y and Δ ansatze in some limits and have found that the Y-type flux-tube picture is more favorable than the Δ-type one. Therefore all of these detailed fit analyses for the lattice QCD data of the 3Q potential support the Y-type ansatz.

References

1) T. T. Takahashi, H. Suganuma, Y. Nemoto, and H. Matsufuru: Phys. Rev. D **65**, 114509 (2002).
2) T. T. Takahashi, H. Matsufuru, Y. Nemoto, and H. Suganuma: Phys. Rev. Lett. **86**, 18 (2001); Proc. Int. Symp. on Dynamics of Gauge Fields, Tokyo, 1999-12, edited by A. Chodos et al. (Universal Academy Press, 2000), p. 179; T. T. Takahashi, H. Suganuma, H. Matsufuru, and Y. Nemoto; AIP Conf. Proc. **594**, 341 (2001).
3) C. Alexandrou, Ph. de Forcrand, and A. Tsapalis: Phys. Rev. D **65**, 054503 (2002); Nucl. Phys. B (Proc. Suppl.) **106**, 403 (2002).

*1 Research Center of Nuclear Physics, Osaka University
*2 Faculty of Science, Tokyo Institute of Technology
*3 Yukawa Institute for Theoretical Physics, Kyoto University

Color-flavor transformation and application to lattice QCD

B. Schlittgen* and T. Wettig*

Current state-of-the-art algorithms for lattice simulations of QCD evaluate the determinant of the lattice Dirac operator indirectly by inverting the matrix representing this operator. While this matrix is sparse it is very large (dimension = 12 × lattice volume) and has many entries away from the diagonal, making its inversion very costly, in particular for realistically small quark masses. This constitutes the bottleneck in simulations with dynamical fermions. The quest for new algorithms, possibly based on alternative formulations of lattice QCD, is therefore a pressing issue.

A few years ago, Zirnbauer[1] presented and proved a color-flavor transformation for gauge group $\mathrm{U}(N_c)$. This transformation is a mathematical identity which relates an integral over $\mathrm{U}(N_c)$ gauge fields to an integral over $N_f \times N_f$ complex matrices, where N_f denotes the number of quark flavors. While the transformation was derived for applications to disordered systems in condensed matter physics, it owes its name to the observation that certain indices in the integrand are coupled in the same way as in lattice gauge theory. Most interestingly, when the transformation is applied to the lattice partition function of a $\mathrm{U}(N_c)$ gauge theory, one obtains a fermion matrix which is diagonal in the lattice site and color indices, and therefore block-diagonal overall with blocks of dimension $4N_f$. Evaluating the determinant of such a block-diagonal matrix comes at a cost negligible compared to that of the conventional approach. Therefore, in addition to its mathematical elegance, this new formulation has the potential to speed up numerical simulations by orders of magnitude, making it possible to use realistic quark masses and to reach the continuum limit.

In order to apply this alternative approach to QCD with gauge group $\mathrm{SU}(N_c)$, the first step is to derive such a color-flavor transformation for the special unitary group. This is a much harder problem than for $\mathrm{U}(N_c)$, but we succeeded to obtain the full result[2]

$$\int_{\mathrm{SU}(N_c)} dU \exp\left(\bar\psi_a^i U^{ij} \psi_a^j + \bar\varphi_a^i U^{\dagger ij} \varphi_a^j\right) = C \int_{\mathrm{Gl}(N_f,\mathbb{C})} \frac{dZ dZ^\dagger}{\det(\mathbb{1} + ZZ^\dagger)^{2N_f+N_c}} \times \exp\left(\bar\psi_a^i Z_{ab} \varphi_b^i - \bar\varphi_a^i Z_{ab}^\dagger \psi_b^i\right) \sum_{Q=0}^{N_f} \chi_Q,$$

where

$$\chi_0 = 1, \qquad \chi_{Q>0} = \mathcal{C}_Q \left[\det(\mathcal{M})^Q + \det(\mathcal{N})^Q\right],$$
$$\mathcal{M}^{ij} = \bar\psi_a^i (\mathbb{1} + ZZ^\dagger)_{ab} \psi_b^j, \quad \mathcal{N}^{ij} = \bar\varphi_a^i (\mathbb{1} + Z^\dagger Z)_{ab} \varphi_b^j,$$

$$C = \frac{1}{\pi^{N_f^2}} \prod_{n=0}^{N_f-1} \frac{(N_c+N_f+n)!}{(N_c+n)!},$$

$$\mathcal{C}_Q = \frac{1}{(Q!)^{N_c} (N_c!)^Q} \prod_{n=0}^{Q-1} \frac{(N_c+n)!(N_f+n)!}{n!(N_c+N_f+n)!}.$$

Here, $i,j = 1,\ldots,N_c$ and $a,b = 1,\ldots,N_f$ with N_c (N_f) the number of colors (flavors). The integral over U corresponds to a single link of the lattice.

Subsequently, this transformation was applied to lattice QCD. Note that the Dirac indices of the quark fields can be treated as additional flavors. While the color-flavor transformation applies to lattice QCD in the strong-coupling limit, the inclusion of auxiliary heavy quark flavors leads to a dynamically generated plaquette term in the action. Combining this idea of "induced QCD" with our $\mathrm{SU}(N_c)$ color-flavor transformation, we reformulated lattice QCD to find a theory of baryon loops in a mesonic background.[3]

There is one remaining problem that stands in the way of a numerical implementation of this approach. Because the integration on the flavor-side of the transformation is over complex matrices, the resulting action is complex so that a sign problem arises. In an attempt to overcome this problem, we considered integrating out some of the degrees of freedom analytically, retaining only hermitian matrices in the numerical path integral. This led us to the explicit calculation of generalizations of several integrals over the unitary group to the case where general complex matrices appear in the integrand. These results were obtained in Ref. 4 using the character expansion method, and they are also of interest in other areas of mathematical physics. Unfortunately, the complex action problem could only be resolved in this manner for $N_f = 1$. We are currently exploring other mathematical approaches. Contrary to the case of QCD at nonzero density, there is no physical argument leading to a sign problem, therefore a solution should be possible. The complex $N_f \times N_f$ matrices that appear in the color-flavor transformation parameterize the coset space $\mathrm{U}(2N_f)/[\mathrm{U}(N_f)\times\mathrm{U}(N_f)]$, and we are investigating whether an alternative parameterization of this coset space could lead to a real action.

* Yale University, USA

References

1) M. R. Zirnbauer: J. Phys. A **29**, 7113 (1996).
2) B. Schlittgen and T. Wettig: Nucl. Phys. B **632**, 155 (2002).
3) B. Schlittgen and T. Wettig: hep-lat/0208044, to appear in Nucl. Phys. B (Proc. Suppl.).
4) B. Schlittgen and T. Wettig: math-ph/0209030, to appear in J. Phys. A.

Calculation of kaon weak matrix elements on the lattice†

J. Noaki

Numerical simulation in lattice QCD is the most promising method of non perturbative calculation of weak matrix elements. In this article, we present an outline of the ongoing project of RBC Collaboration to perform quenched calculation of B_K and $K \to \pi\pi$ matrix elements using domain-wall fermion (DWF) as an extension of previous works.[1,2]

The DBW2 gauge action that we used to promote chiral behavior on the lattice is a kind of renormalization group (RG) improved action and has been recognized to generate topological charge $Q_{\rm top}$ that evolves very slowly by standard Monte Carlo techniques. In order to obtain a well-distributed $Q_{\rm top}$, we generate gauge configurations using the standard Wilson gauge action in steps of 10,000 sweeps and use each of these as the initial configuration for DBW2 evolution. In the DBW2 evolution starting from initial Wilson configurations, we observed that while the pseudo-scaler meson mass equilibrated after about 5,000 sweeps, $Q_{\rm top}$ rarely changed from its initial value.[3] Assuming that the global property of the gauge configuration such as $Q_{\rm top}$ does not change with RG improvement, our method allows us to obtain DBW2 gauge configurations with a well-distributed $Q_{\rm top}$. With 50 initial Wilson configurations, we obtain $\langle Q_{\rm top}\rangle = -0.32\pm3.36$ with $-10 < Q_{\rm top} < +7$.

We generated gauge configurations with a lattice scale $a^{-1} \approx 3\,\mathrm{GeV}$. Because it is well known that DWF fails to localize to the four-dimensional domain walls in the 5th dimension for $m_f a$ close to 1.0, a smaller lattice spacing allows us to take a larger m_f without spoiling of the mechanism of DWF. Through the behavior of eigenvectors of five-dimensional Hamiltonian, we observed that DWF worked for $m_f a$ that corresponds to $m_c a$.

The simulation parameters used for spectrum calculation for basic study are summarized in the middle column of Table 1. We studied meson masses and determined the lattice scale a^{-1} to be 2.89(12) GeV based on the rho meson mass at the chiral limit. The chiral symmetry breaking due to finite 5th width L_s was calculated to be $m_{\rm res} = 1.011(35)\,\mathrm{MeV}$ with $M_5 = 1.7$, $L_s = 8$, and $0.276(10)\,\mathrm{MeV}$ with $M_5 = 1.65$, $L_s = 10$. The latter set of parameters will be used in the calculation of matrix elements as listed in the right column of Table 1. After the estimation of the equilibration mentioned above, we calculated matrix elements every 5,000 sweeps.

Kaon B-parameter is defined as the ratio of matrix elements:

Table 1. Simulation parameters for observables.

	spectrum	matrix elements
size	$24^3 \times 48$	
M_5	1.7	1.65
L_s	8	10
$m_f a$	0.02, 0.03, 0.04	0.008 – 0.040 in step of 0.008
#sweep	every 1,000	every 5,000
#config.	120	53

$$B_K \equiv \frac{\left\langle \bar{K}^0 \left| [\bar{s}\gamma_\mu(1-\gamma_5)d]^2 \right| K^0 \right\rangle}{\frac{3}{8}\left\langle \bar{K}^0 \left| \bar{s}\gamma_4\gamma_5 d \right| 0 \right\rangle \left\langle 0 \left| \bar{s}\gamma_4\gamma_5 d \right| K^0 \right\rangle}$$

The numerator is proportional to $B_K \times (m_\pi a)^2$ and should have a chiral property. By fitting our data to the polynomial $a_0 + a_1(m_f a) + a_2(m_f a)^2$, we obtain a_0 consistent with zero.

Figure 1 shows our results of the bare value on the lattice as a function of $m_f a$ and a fit to the function $B_K(m_f a) = \xi_0[1 + C m_f a \ln(m_f a)] + \xi_1 m_f a$. We carried this fit with the value of C taken from the chiral perturbation theory and obtained $\chi^2/\mathrm{dof} = 0.084$, which is comparable with $\chi^2/\mathrm{dof} = 0.034$, in the case of free C. Employing the perturbative renormalization,[4] the value of B_K in the $\overline{\rm MS}$, NDR scheme can be estimated. Our result is found to be consistent with a previous result[5] using similar simulation parameters.

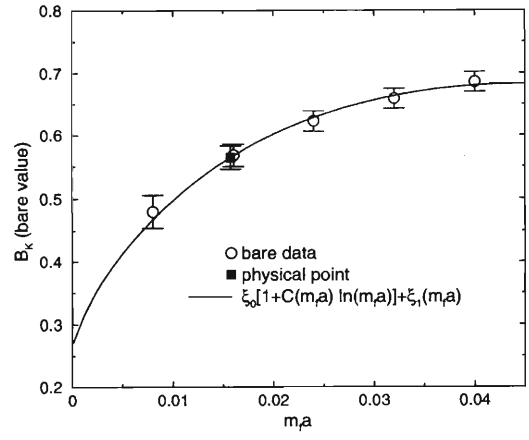

Fig. 1. Lattice value of B_K as a function of $m_f a$ (open symbol). The interpolated point (filled symbol) indicates the value at $m_f a = m_s a/2$.

† This work was carried out in RBC Collaboration. We thank RIKEN, BNL, and the U.S. DOE for providing the facilities essential for the completion of this work.

References

1) CP-PACS Collaboration, J. Noaki et al.: hep-lat/0108013.
2) RBC Collaboration, T. Blum et al.: hep-lat/0110075.
3) RBC Collaboration, J. Noaki et al.: hep-lat/0211013.
4) S. Aoki et al.: hep-lat/0206013.
5) CP-PACS Collaboration, S. Aoki et al.: Phys. Rev. D **64**, 114506 (2001).

Overview of RIKEN and RIKEN BNL Research Center activities

H. En'yo and G. Bunce, for the RIKEN BNL Research Center

The past year has been a very exciting and successful one for our spin program, with the first collisions of polarized protons at high energy, and solid and also surprising new spin results. This first run, at $\sqrt{s} = 200\,\mathrm{GeV}$, was an order of magnitude higher energy than any previous polarized proton collisions. RIKEN and RBRC played a major role in the success of this first run, and we are also preparing for the first run, in 2003, with spin rotators around the PHENIX and STAR experiments, to be able to observe the first collisions of longitudinally polarized protons. For the longer term, we are developing new triggering for PHENIX, new detectors to allow us to observe heavy quarks and jets, and we are studying the sensitivity of scattering quarks to spin at the BELLE experiment at KEK. For the very long term, we are studying and promoting colliding polarized electrons and polarized protons in RHIC, to follow the polarized proton collision program.

For the 2001–2002 polarized proton run, RBRC and RIKEN, along with other important collaborators, developed the polarimetry used to measure the beam polarization in RHIC, we set up the triggering used for the proton run for PHENIX, improving the collection of high transverse momentum data by orders of magnitude. This resulted in data for π^0s out to $p_T = 12\,\mathrm{GeV/c}$. This important data set was very well described by the standard theory, pQCD, supporting our plans for interpreting our future data at RHIC in terms of the scattering of polarized quarks and gluons. Data for high p_T hadrons and for forward muons were collected, also using triggers developed by our groups. Both dimuon and dielectron data gave the first measurements at RHIC for J/Ψ production in proton-proton scattering. We developed methods of measuring the luminosity for the proton collisions, both for absolute cross sections, and high precision relative luminosity for the different spin combinations in the collisions, as well as monitoring the data during the run. A study was just completed of the spin sensitivity of the beam-beam counters in PHENIX, showing excellent stability and insensitivity to spin. The alignment system for the muon tracking chambers was developed and worked well. An important analysis of transverse energy for gold collisions was done. Finally, for this run a lead-tungstate crystal electromagnetic calorimeter was built to study sensitivity to spin for very forward production. This showed surprisingly strong sensitivity to the proton spin direction for neutron production. The Computer Center in Japan, CCJ, was central to much of this work.

Activities of the RIKEN and RBRC groups for the future include upgrades for RHIC polarimetry, storing more information for analysis. New "local polarimeters" will be installed at PHENIX to measure the polarization at collision, based on the neutron result of this year. These will be able to calibrate the spin rotators at PHENIX, which will give us longitudinal polarization for this run. There has been considerable work to install the north muon arm for PHENIX for the coming run, which completes the baseline detector. A new beam counter system is being installed, compatible with a vertex chamber which is also being installed. A trigger connecting the RICH and electromagnetic calorimeters will be in place. A new polarimeter based on the RHIC polarimeter, has been installed in the AGS. It is a central device in efforts to improve the polarization from the AGS, which was low this past year. The RHIC spin running plan for this coming year is to first study the AGS, using the new polarimeter. In April and May, 2003, we will collide polarized protons in RHIC with longitudinally polarized protons. This will give us the first data sensitive to the gluon polarization in the proton. At PHENIX, this will be done with π^0s, $\pi^{\pm}$, and μ. No other facility has the sensitivity of RHIC to measure the gluon polarization, and this begins a major focus of the RHIC spin program.

For the future runs, we are developing a new partial Siberian Snake for the AGS, and RIKEN is playing a major role in the magnet design for this. This summer we studied several triggering ideas for the future W-boson physics. We have promising methods to improve our selection of the Ws, and we are developing a plan. We have a program to build a silicon inner tracking detector for PHENIX, and prototypes are being built and tested, in collaboration with BNL Instrumentation Division and with CERN. This new tracking detector will help us identify heavy quarks and jets (the spray of particles from a scattered quark or gluon). In the BELLE experiment at KEK we are measuring the sensitivity of the spray of particles generated from scattered quarks to find out whether we can identify the polarization of the quark from this spray of particles. The result will be used by PHENIX and STAR at RHIC to study the transverse spin structure of the proton. Most of the above work depends on the excellent computer facility at RIKEN, CCJ, to analyze data, to simulate detector performance, and for simulations to develop new triggers and detectors.

For the very long term, we have been leading studies for a polarized electron-polarized proton and electron-heavy ion collider at RHIC.

Finally, the workshops held by RBRC in both theory and experiment have been crucial to develop and define the RHIC spin program.

Single muon production at $\sqrt{s} = 200\,\mathrm{GeV}$ in the PHENIX experiment

A. Taketani, A. Al-Jamel,[*1] D. S. Brown,[*1] H. Kobayashi, N. Kamihara,[*2] and H. D. Sato,[*3]
for the PHENIX Collaboration

We collected the proton-proton collision data at $\sqrt{s} = 200\,\mathrm{GeV}$ by using the PHENIX detector in run 2 during December 2001 to January 2002. Both beams had 17 to 20 percent transverse polarization in average. Events which include single muons have been analyzed in this report.

The muon is expected to be an excellent probe for investigating nucleon spin structure. Heavy flavor bound states, such as J/ψ and Υ, open heavy flavors, and W boson decay into single or pair muons. These processes can be factorized into (1) nucleon structure, (2) hard parton scattering, and (3) fragmentation. (2) can be calculated by the perturbative QCD. (3) is taken from e^+e^- collider experiments. Even single muons from charged π and K decay, are expected to carry leading particle information from the original parton fragmentation.

The PHENIX muon arm consists of a Muon Tracker (MuTr) and a Muon Identifier (MuId). The MuTr sits in the Muon Magnet and measures the momentum. The MuId acts as an range counter to distinguish muons from a large hadron background. Also it works as a trigger counter. We operated the south PHENIX muon arm in run 2,[1,2] and confirmed its performance.[3,4] The data which corresponds to 0.15 pb^{-1} was taken and analyzed. The muon trigger and minimum bias trigger were required for muon events.[5] 981,024 events out of all the triggered events were selected by requiring more than one reconstructed track in the MuId. There were three groups of selection criteria. (1) The event vertex along the beam direction, identified by a beam-beam counter (BBC) which covers $3 < |eta| < 4$, must be $-20\,\mathrm{cm}$ to $50\,\mathrm{cm}$ to ensure the muon penetrates the full length of absorber materials, (2) good track fit quality, and (3) track matching cut between MuTr and MuId track segments. 203,196 tracks survived these selections.

Major sources of these muons are charged π and K decay in our observation at $0.5\,\mathrm{GeV} < p_t < 2.5\,\mathrm{GeV}$. Even the most optimistic model predicts that a muon from heavy flavor decay is significant at $p_t > 3\,\mathrm{GeV}$. Decay yield should depend on the flight length before reaching to a first absorber material. Since decay kink angles are relatively small, 0.005 and 0.05 radian for π and K, respectively, muon direction should be the same as the original π/K direction at the observed muon momentum range. The decay length L is defined as $L = Z/\cos\theta$, where Z is the length from the event vertex, measured by the BBC, to the first absorber material, and θ is the polar angle of the muon direction. Figure 1 shows the decay length dependence of single-muon yield. The yield is normalized by the raw coincidence rate between forward and backward BBC which correspond to the luminosity. The Monte Carlo (MC) points are generated by a PYTHIA event generator with an *ad hoc* π/K decay routine. The integrated yield for the MC is normalized to the experimental data. Since the shape of the L dependency agrees well, these selected particles are confirmed to be good muons.

Zero value of transverse single-spin asymmetry is expected from the leading order pQCD calculation. However, the E704 experiment at FERMI-LAB reported a large asymmetry value[6] for forward pion at $\sqrt{s} = 20\,\mathrm{GeV}$. The Qiu-Sterman model[7] predicts $A_N = 0.015$ at $\langle x_f \rangle \sim 0.4$ and $p_t \sim 1.5\,\mathrm{GeV}$. The expected measurement error from our event statistics and beam polarization is similar size. We are working to obtain the asymmetry as well as the p_t spectrum.

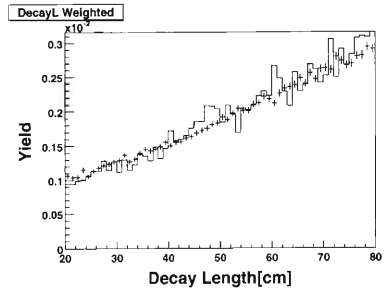

Fig. 1. Decay length dependence of single muon yield. Plus signs indicate the luminosity normalized yield with error bar and the solid line is the Monte Carlo simulation result.

*1 New Mexico State University, USA
*2 Tokyo Institute of Technology
*3 Kyoto University

References

1) A. Taketani et al.: RIKEN Accel. Prog. Rep. **35**, 224 (2002).
2) H. Kobayashi et al.: RIKEN Accel. Prog. Rep. **35**, 232 (2002).
3) H. D. Sato et al.: RIKEN Accel. Prog. Rep. **35**, 225 (2002).
4) N. Kamihara et al.: RIKEN Accel. Prog. Rep. **35**, 231 (2002).
5) H. D. Sato et al.: RIKEN Accel. Prog. Rep. **36**, 231 (2003).
6) D. L. Adams et al.: Phys. Lett. B **264**, 462 (1991).
7) J. Qiu and G. Sterman: Phys. Rev. D **59**, 014004 (1999).

Measurement of single spin asymmetry of charged particles for $3.0 < |\eta| < 3.9$ by PHENIX BBC in polarized pp collision at $\sqrt{s} = 200\,\mathrm{GeV}$

K. Tanida, T. Kawabata,* V. L. Rykov, and Y. Goto, for the PHENIX Collaboration

In FY2001, the first collision of transversely polarized protons at $\sqrt{s} = 200\,\mathrm{GeV}$ was observed at RHIC. Using the data taken in FY2001, the PHENIX experiment[1] is looking into the single spin asymmetry (A_N) in various channels. Among them, A_N of forward particles are of interest since the discovery of large A_N in forward pions at $\sqrt{s} = 20\,\mathrm{GeV}$ by FNAL E704.[2]

Beam-Beam Counter (BBC) is the most forward detector in PHENIX except for Zero Degree Calorimeter, which has no capability to measure A_N. BBC consists of two identical detectors (BBC-north and BBC-south) of 64 quartz Cherenkov counters ($n \sim 1.4$) and covers pseudorapidity range of $3.0 < |\eta| < 3.9$. With BBC, only inclusive fast charged particles can be measured as it does not measure momentum, energy, or charge sign of particles.

In RHIC, both of the colliding protons (denoted "blue" and "yellow" hereafter, according to the standard RHIC notation) are polarized. Therefore, we have two single spin asymmetries, namely, A_B and A_Y.[a] On the other hand, a beam bunch in each beam has spin up ($\uparrow$) or down ($\downarrow$), and we have four types of bunch crossing, namely, $(S_B, S_Y) = (\uparrow\uparrow)$, $(\uparrow\downarrow)$, $(\downarrow\uparrow)$, and $(\downarrow\downarrow)$. We found that if the integrated luminosity is different among these crossings, particularly if the sum for $(\uparrow\uparrow)$ and $(\downarrow\downarrow)$ crossings is different from that for $(\uparrow\downarrow)$ and $(\downarrow\uparrow)$ crossings, A_B and A_Y are no longer independent so that commonly used methods, such as the square root formula does not give impartial estimation for A_B and A_Y.

In order to avoid this problem, we developed a new method to obtain the two single spin asymmetries. We calculated left-right asymmetry for each crossing $[a_{LR}(i)]$ by

$$a_{LR}(i) = \frac{N_L(i) - N_R(i)}{N_L(i) + N_R(i)},$$

where $N_L(i)$ $[N_R(i)]$ is the number of counts detected in the left-side (right-side) of BBC (-north or -south) for crossing number i. A_B and A_Y were obtained by fitting this to a function

$$a_{LR}(i) = \frac{D + A_B P_B S_B(i) + A_Y P_Y S_Y(i)}{1 + D A_B P_B S_B(i) + D A_Y P_Y S_Y(i)},$$

where D is a fitting parameter for detector asymmetry caused by the difference in acceptance and detection efficiency of left-side and right-side counters. P_B and P_Y are bunch number independent constants for beam polarizations, and their typical value was 0.2 in the present analysis.[b] $S_B(i)$ and $S_Y(i)$ are $+1$ (-1) for bunches of spin up (down).

Analytical studies and Monte-Carlo simulations show that this method is at least as good as the square root formula and is even better from a point of view that it can take the correlation of A_B and A_Y into account correctly. Furthermore, fitting χ^2 gives some indication of systematic errors, *e.g.*, bunch-by-bunch variation of beam polarization.

In the present BBC analysis, we used $\epsilon_{B(Y)} = A_{B(Y)} P_{B(Y)}$ instead of $A_{B(Y)}$ for fitting parameter in order to avoid uncertainties in beam polarization measurements. Figure 1 shows the obtained ϵ_B and ϵ_Y for each beam fill. While STAR reported that finite ϵ of $O(10^{-3})$ is observed in their preliminary analysis in a more forward region $(3.4 < \eta < 5.0)$,[3] finite asymmetry is not observed at this level in the present analysis. Fitting χ^2 was consistent with unity. Detector asymmetry, D, was found to be resonably small (~ 0.1 or smaller) and stable for these fills. Further analysis to understand systematic errors is still in progress.

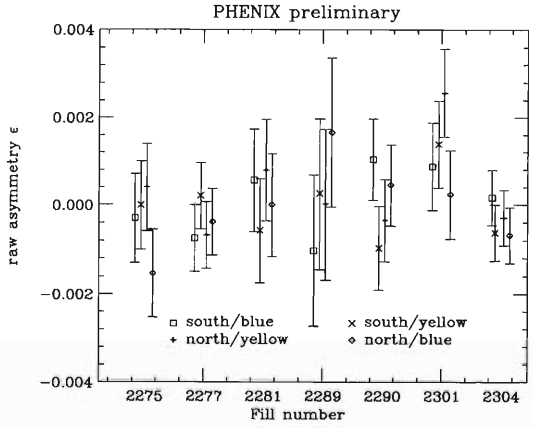

Fig. 1. Fill by fill raw asymmetries, ϵ_B and ϵ_Y, of BBC-north and BBC-south. Error bars are for statistical error only.

References

1) G. P. Morrison et al.: Nucl. Phys. A **638**, 565c (1998).
2) D. L. Adams et al.: Phys. Lett. B **264**, 462 (1991).
3) J. Kiryluk et al.: Proc. 15th Int. Spin Physics Symp. (SPIN 2002), Upton, USA, 2002-9, in press.

* Center for Nuclear Study, University of Tokyo

a) In the case of BBC-north, A_B is the asymmetry for forward particles and A_Y is that for backward particles.

b) If bunch-by-bunch beam polarization is given, we can use $P_B(i)$ as signed polarization of a bunch instead of $P_B S_B(i)$.

Measurement of the neutral pion cross section in proton-proton collisions at $\sqrt{s} = 200\,\mathrm{GeV}$ with PHENIX

H. Torii,* A. Bazilevsky, B. Fox, Y. Goto, K. Imai,* T. Kawabata, K. Okada, N. Saito,* and H. D. Sato*

This study used the PHENIX electromagnetic calorimeters (EMCal), which have an azimuthal coverage of $90° + 90°$ and pseudo-rapidity coverage of ± 0.35. The data were collected during the proton-proton run in 2001–2002 at RHIC using the minimum bias (MB) from beam–beam counters (BBC) and newly installed EMCal triggers. The EMCal trigger was essential in enhancing the sample of neutral pions at high p_T. This trigger has two types: 2×2 non-overwrapping tower sum (0.8 GeV threshold) and 4×4 overwrapping tower sum (2 and 3 GeV thresholds). For higher p_T, this work is based upon the data collected via the 2×2 trigger whose rejection factor was 90. We will report only the measurement performed with the lead scintillator sampling calorimeter.

Figure 1 shows sample invariant mass spectra for two photons. Above a p_T of $\sim 3\,\mathrm{GeV/c}$, the ratio of the combinatorial background to the signal was $\sim 10\%$. To extract the number of π^0 in each p_T bin, several functions were used to fit to the combinatorial background over a variety of fit ranges. The systematic error was estimated from the variation of these fits and the run-to-run stability of the yield.

The acceptance, efficiency, and smearing correction was obtained by a Monte Carlo simulation which was tuned using results from the test beam measurements and the data itself. The systematic error was estimated from the change in the correction factor when the parameters were varied within their errors. Using the MB data, the π^0 efficiency of the 2×2 trigger was determined to plateau at 80% above a p_T of $\sim 3\,\mathrm{GeV/c}$. A systematic error of 10% was assigned to this quantity by comparing it to the result from a Monte Carlo simulation which included the measured efficiencies for the tiles in the trigger. The bias for π^0 detection arising from the MB trigger condition was measured to be 75%, independent of p_T up to a p_T of $\sim 5\,\mathrm{GeV/c}$ using the sample data collected with a 4×4 trigger which, unlike the 2×2 trigger, did not impose the MB requirement. The MB trigger efficiency of 51% was obtained from a PYTHIA + GEANT simulation. We assigned a normalization error of 30% based on the difference between the cross section measured from a van der Meer/vernier scan and the total (elastic+inelastic) $p + p$ cross section.

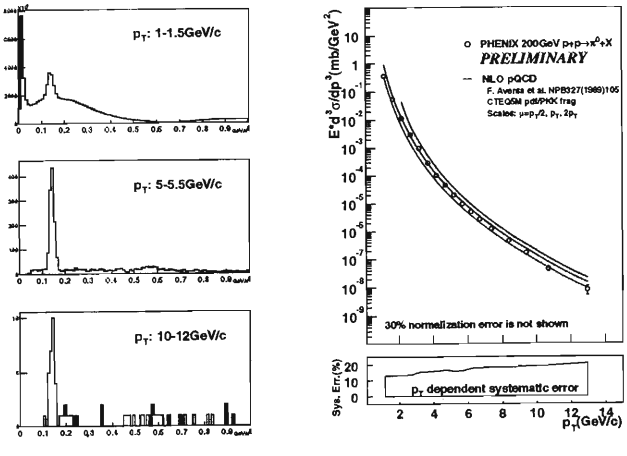

Fig. 1. [left] Invariant mass spectrum for p_T ranges of 1 to 1.5 GeV/c (top), 5 to 5.5 GeV/c (middle), and 10 to 12 GeV/c (bottom). [right] The inclusive neutral pion cross section (open circle) and comparison of NLO pQCD calculation using $p_T/2$ (top line), p_T (middle line), and $2p_T$ (bottom line) renormalization and factorization scales.

Figure 1 shows a comparison of an NLO pQCD calculation[1] using the formalism of Adversa *et al.*[2] with the CTEQ5M parton distribution functions[3] and the PKK fragmentation functions.[4] The data for the lower p_T range is shown from the MB trigger samples to avoid the larger systematic error of the 2×2 trigger samples. Over the full p_T range, this calculation is consistent with our measurement within the systematic errors. The UA1 collaboration measured the $(h^+ + h^-)/2$ production cross section in the $p - \bar{p}$ collisions at $\sqrt{s} = 200\,\mathrm{GeV}$ in the ± 2.5 rapidity range.[5] When scaled to our rapidity range and corrected for the particle composition using ISR results,[6] our measurement is consistent with the UA1 measurement over their measured p_T range of 1 to 6 GeV/c.

The NLO pQCD calculation with a set of parton distribution and fragmentation function is consistent with our measurement over the full p_T range of 1 to 13 GeV/c within the systematic error and the scale selection.

References

1) Private communication with W. Vogelsang.
2) F. Aversa, P. Chiappetta, M. Greco, and J.-Ph. Guillet: Nucl. Phys. B **327**, 105 (1989).
3) H. L. Lai et al.: Eur. Phys. J. C **12**, 375 (2000).
4) B. A. Kniehl, G. Kramer, and B. Potter: Nucl. Phys. B **582**, 514 (2000).
5) C. Albajar et al.: Nucl. Phys. B **335**, 261 (1990).
6) B. Alper et al.: Nucl. Phys. B **100**, 237 (1975).

* Department of Physics, Kyoto University

Measurement of J/ψ in p+p collisions at $\sqrt{s} = 200\,\mathrm{GeV}$

H. D. Sato,[*1] V. Cianciolo,[*2] Y. Akiba,[*3] J. L. Nagle,[*4] and X. Wei[*5]

The PHENIX experiment at the Relativistic Heavy Ion Collider (RHIC) detects J/ψ particles in the rapidity range $|y| < 0.35$ using the electron-pair decay channel and in $1.2 < y < 2.2$ using the muon-pair decay channel. Differential cross sections for the J/ψ production in those ranges have been measured in p+p collisions at $\sqrt{s} = 200\,\mathrm{GeV}$ in the RHIC Run 2001–2002 period (Run-2). The total cross section extracted is $\sigma_{J/\psi} = 3.8 \pm 0.6$ (stat.) $\pm$ 1.3 (syst.) μb, consistent with prediction of perturbative-QCD based models.

Measurements of J/ψ in p+p collisions at RHIC are vital to: (1) testing theoretical models for the production mechanism and (2) providing the reference point for the measurements in heavy ion collisions. In this paper, the preliminary results of the production cross section for J/ψ in p+p collisions at $\sqrt{s} = 200\,\mathrm{GeV}$ are presented.

In Run-2, both Central Arms, West and East Arms, which cover $|\eta| < 0.35$, $\Delta\phi$ (azimuthal coverage) $= \pi$, and the South Muon Arm, which covers $1.2 < \eta < 2.2$ with a full azimuth were operational. In p+p collisions, J/ψ particles have been successfully identified with the invariant mass of e^+e^- pairs measured in the Central Arms and $\mu^+\mu^-$ pairs measured in the South Muon Arm as shown in Fig. 1 (a) and (b) respectively.

Using the detection efficiencies for $J/\psi \rightarrow \mu^+\mu^-(e^+e^-)$ events and integrated luminosities used for each analysis, rapidity-differential cross sections $Br(J/\psi \rightarrow \mu^+\mu^-)d\sigma_{J/\psi}/dy|_{y=1.7} = 37 \pm 7$ (stat.) $\pm$ 11 (syst.) nb and $Br(J/\psi \rightarrow e^+e^-)d\sigma_{J/\psi}/dy|_{y=0} = 52 \pm 13$ (stat.) ± 18 (syst.) nb have been obtained including the branching fractions for the J/ψ decays. The average transverse momentum of the J/ψ's, 1.66 ± 0.18 (stat.) $\pm$ 0.09 (syst.) GeV/c ($1.2 < y < 2.2$), is slightly higher than low-energy results.

The rapidity distribution, which is sensitive to gluon distribution in the Bjorken-x range $0.002 < x < 0.2$, is consistent with appropriate parton distribution functions (PDFs). The total cross section extracted is $\sigma(p + p \rightarrow J/\psi X) = 3.8 \pm 0.6$ (stat.) $\pm$ 1.3 (syst.)μb using $Br(J/\psi \rightarrow l^+l^-) = 0.059$.[1)] Figure 2 shows center-of-mass energy dependence of the total cross section for the J/ψ production in nucleon-nucleon collisions including the results of low-energy experiments. The solid and dotted lines show the color-evaporation model predictions with two different sets of PDFs, QCD scales and charm quark masses described in Ref. 2, which agree with both the PHENIX and low-energy results.

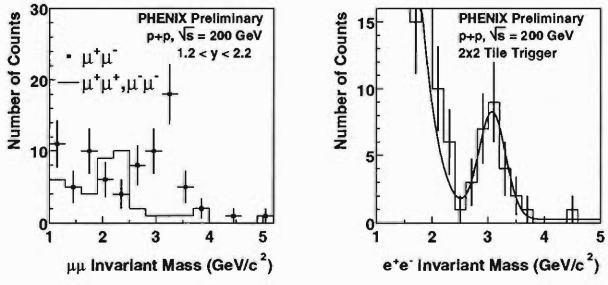

(a) (b)

Fig. 1. (a) Invariant mass spectra for unlike-sign and like-sign muon pairs. (b) Invariant mass spectrum for e^+e^- pairs with a Gaussian fit to the J/ψ peak. The error bars include statistical errors only.

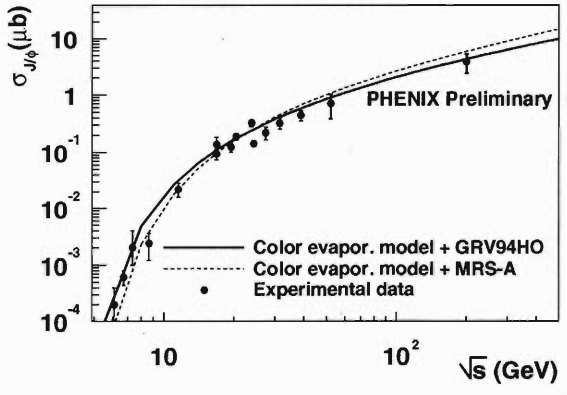

Fig. 2. Center-of-mass energy dependence of the total production cross section for J/ψ in nucleon-nucleon collisions. The error bars include both statistical and systematic errors added in quadrature. The two curves show the color-evaporation model predictions described in Ref. 2.

References

1) K. Hagiwara et al.: Phys. Rev. D **66**, 010001 (2002).
2) J. F. Amundson et al.: Phys. Lett. B **390**, 323 (1997).

*1 Department of Physics, Kyoto University
*2 Oak Ridge National Laboratory, USA
*3 Institute for Particle and Nuclear Studies, High-Energy Accelerator Research Organization (KEK)
*4 Columbia University, USA
*5 University of California at Riverside, USA

Measurement of single transverse-spin asymmetries in forward production of photons and neutrons in pp collisions at $\sqrt{s} = 200\,\mathrm{GeV}$

Y. Fukao,[*1] A. Bazilevsky, L. C. Bland,[*2] A. Bogdanov,[*3] G. Bunce, A. Deshpande, H. En'yo, B. Fox, Y. Goto, J. Haggerty,[*2] K. Imai,[*1] W. Lenz,[*2] D. von Lintig,[*2] M. Liu,[*4] Y. Makdisi,[*2] R. Muto,[*1] S. Nurushev,[*5] E. Pascuzzi, M. L. Purschke,[*2] N. Saito,[*1] F. Sakuma,[*1] S. Stoll,[*2] K. Tanida, M. Togawa,[*1] J. Tojo, Y. Watanabe, and C. Woody[*2]

BNL RHIC was commissioned for polarized proton-proton collisions at the center of mass energy $\sqrt{s} = 200\,\mathrm{GeV}$ during RUN-2 in 2001–2002. We measured single transverse-spin asymmetries ($\mathcal{A}_N$) for production of photons, neutral pions (π^0) and neutrons. Such asymmetries were observed in the E704 experiment at Fermilab for example[1,2] and stimulated many theoretical studies.[3] We are interested in these asymmetries for their possible use in the development of a polarimeter for measuring beam polarization at RHIC collision points together with experiments.

In this study, two detector systems were placed 1800 cm east and west of the collision point, between the two beam pipes behind the dipole magnet for bending beams (see Fig. 1). The magnet swept away the charged particles. One of the detector systems is an electromagnetic-calorimeter-based system (EM-Cal polarimeter) for photon, π^0 and neutron detection, which comprises an EM calorimeter segmented in an array of five and twelve, and scintillation counters for particle identification. The other is hadron-calorimeter-based system (H-Cal polarimeter) for neutron detection which consists of an H calorimeter,[4] postshower counter for measuring the horizontal position of the particle hits and a scintillation counter for photon veto. To separate the beam-gas interaction, two sets of hodoscopes were placed at $z = \pm 2\,\mathrm{m}$ covering the pseudorapidity range of $2.3 < |\eta| < 4.0$.

Asymmetry results are summarized in Fig. 2 for positive and negative x_F's, and only statistical errors are shown. Figure 2 a) and b) shows asymmetries for an inclusive photons and π^0's, respectively, and are consistently zero within systematic error. Neutron asymmetry plots obtained using an EM-Cal polarimeter and an H-Cal polarimeter are shown in Fig. 2 c) and d), respectively. Average analyzing powers, $\mathcal{A}_N$, are

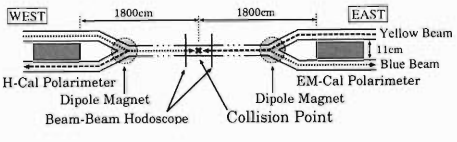

Fig. 1. Top view of the experimental setup.

*1 Department of Physics, Kyoto University
*2 Brookhaven National Laboratory, USA
*3 Moscow Engineering Physics Institute, State University, Russia
*4 Los Alamos National Laboratory, USA
*5 Institute of High Energy Physics, Russia

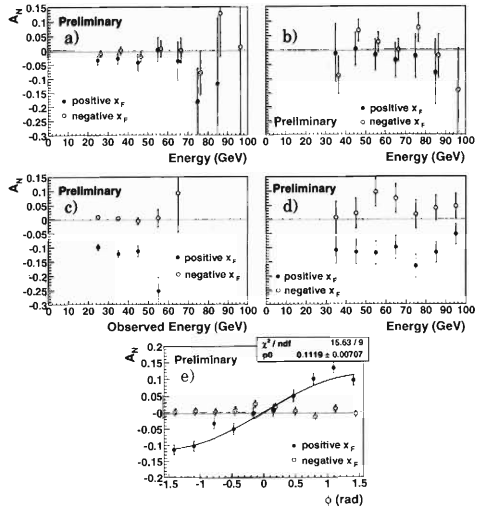

Fig. 2. Asymmetry plots for a) photon, b) π^0 and c), d), e) neutron.

-0.109 ± 0.007 and -0.110 ± 0.015, respectively, and these are consistent each other. The plots in Fig. 2 a)–d) show asymmetries as functions of energy except for c), where the observed energy is used instead. Another asymmetry plot for a neutron is shown in Fig. 2 e), as a function of the azimuthal angle (ϕ) of the produced neutron with respect to the beam polarization. The asymmetries are fitted to a sine curve and the result is -0.112 ± 0.007 with a reduced χ^2 of 1.7, which shows consistency with the projected spin component.

While the cross section for forward neutron production is known to be well described by the one-pion-exchange model at lower energies ($< \sqrt{s} = 63\,\mathrm{GeV}$), a nonzero asymmetry might suggest contribution from interference between pion and Pomeron exchange processes.[5] Further investigation especially to identify the event structure is needed to quantitatively estimate such contributions. The observed neutron asymmetry will be utilized to analyze the spin direction at the RHIC PHENIX collision point in Run-3.

References

1) D. L. Adams et al.: Phys. Lett. B **264**, 462 (1991).
2) A. Bravar et al.: Phys. Rev. Lett. **77**, 2626 (1996).
3) M. Anselmino, M. Boglione, and F. Murgia: Phys. Lett. B **362**, 164 (1995).
4) C. Adler et al.: Nucl. Instrum. Methods Phys. Res. A **470**, 488 (2001).
5) B. Kopeliovich: http://spin.riken.bnl.gov/rsc/write-up/Kopeliovich/kopeliovich.pdf

Charged particle analysis in polarized p-p collisions at 200 GeV/c

F. Messer, F. Bauer,* A. Deshpande, B. Fox, Y. Goto, and K. Okada, for the PHENIX Collaboration

During its second year of operation, the PHENIX experiment, originally designed to study penetrating probes in Au-Au collisions at the Relativistic Heavy Ion Collider (RICH), has successfully collected transversely polarized proton-proton collisions at $\sqrt{s_{NN}} = 200\,\mathrm{GeV/c}$.

PHENIX is composed of two central arms (EAST and WEST) and two muon arms (NORTH and SOUTH). Each of the two central arms covers 90 degrees in azimuth and $\Delta\eta = 0.7$ around mid-rapidity (Fig. 1).

Charged particles are detected using drift chambers (DC) positioned at roughly 2 m from the collision vertex. The drift chambers track particle trajectory in the main bend plane of the PHENIX axial magnetic field and allow the reconstruction of momentum with a resolution of $\delta p/p \simeq 1\%\ p$ (GeV/c) in the high momentum limit. Several multi-wire proportional chambers with pad readout (PC1, PC2 and PC3) positioned between 2.5 m and 5 m in a field-free region, are used to confirm the trajectory and, together with the knowledge of the vertex location, they provide polar angle information. Due to the lack of information regarding the original direction of the track at the vertex, non-primary particles, *i.e.*, decay and shower products in the magnetic poles, which feel only a fraction of the total magnetic field, are falsely reconstructed at high transverse momentum. To suppress the non-vertex contribution, a stringent two-dimensional cut in the plane defined by the azimuthal angle ϕ and the position along the beam axis Z must be applied for the distance between the extrapolated position of the track at PC3 (PC2) and the actual measurement. This cut reduces substantially the background at p_T larger than 3 GeV/c. The remaining background (10% at 5 GeV/c) can be measured statistically and subtracted from the data.

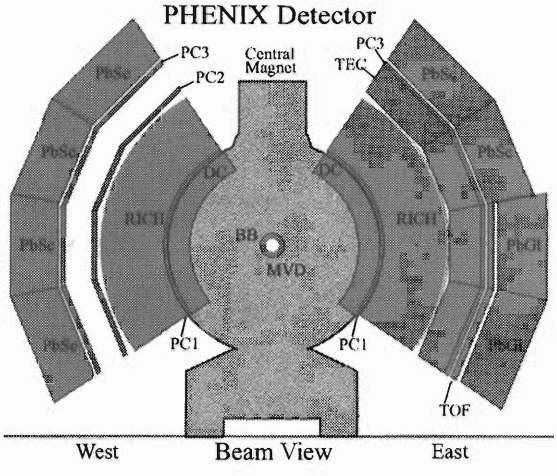

Fig. 1. PHENIX experimental setup during the second year of operation.[1)]

Using a minimum-bias sample composed of 100 million proton-proton collisions, we can study charged particle cross sections up to 5 GeV/c. In addition, another substantial sample of high-p_T triggered events can permit us to extend the measured range up to 10 GeV/c. Together with the cross-section results, PHENIX is using the transversely polarized beams, to analyze the left-right asymmetry (single transverse-spin asymmetry), $A_N = (\sigma_L - \sigma_R)/(\sigma_L + \sigma_R)$ of charged particles over a wide momentum range.

In addition, the cross section and transverse spin asymmetry can be studied for different particle species due to the excellent identification capabilities of PHENIX which permit the separation of kaons and pions up to 2 GeV/c and protons up to 4 GeV/c using a time of flight detector (TOF).[2)] Above $p = 5$ GeV/c, the PHENIX RICH detectors allow us to study charged pions.[3)]

References

1) PHENIX Collaboration, D. Morrison et al.: Nucl. Phys. A **638**, 565 (1998).
2) PHENIX Collaboration, J. Velkovska et al.: Nucl. Phys. A **698**, 507c (2002).
3) PHENIX Collaboration, F. Messer et al.: RIKEN Accel. Prog. Rep. **36**, 235 (2003).

* University of Riverside, USA

Transverse energy measurements in Au+Au collisions in PHENIX at RHIC

A. Bazilevsky, for the PHENIX Collaboration

Transverse energy (E_T) is a global variable which gives excellent characterization of the high-energy nucleus-nucleus collisions, thus providing information about the initial conditions.[1)]

First results for E_T at midrapidity in Au-Au collisions at $\sqrt{s_{NN}} = 130\,\mathrm{GeV}$ measured with the PHENIX detector were reported in Ref. 2. The same experimental techniques were used to analyze data obtained at $\sqrt{s_{NN}} = 200\,\mathrm{GeV}$. In order to more precisely compare the results at the two beam energies, both data samples were processed through the same analysis procedure using a more restrictive event selection criteria. The trigger required the coincidence of two beam-beam counters and two zero-degree calorimeters. The minimum bias trigger efficiency was found to be the same within 0.7% at $\sqrt{s_{NN}} = 130\,\mathrm{GeV}$ and 200 GeV, equal to $91.4^{+2.5}_{-3.0}\%$.

The part of the PbSc electromagnetic calorimeter used for the E_T measurements covers the pseudorapidity range $|\eta| \leq 0.38$ with azimuthal apertures of $\Delta\phi = 44.4°$ in $\sqrt{s_{NN}} = 130\,\mathrm{GeV}$ data and $\Delta\phi = 112°$ in $\sqrt{s_{NN}} = 200\,\mathrm{GeV}$ data.

The results at $\sqrt{s_{NN}} = 130\,\mathrm{GeV}$ presented in this paper and reported earlier in Ref. 2 are consistent within systematic errors (excluding the 4% scale shift in E_T due to its new definition[a)]).

The ratio of the pseudorapidity densities ($dE_T/d\eta|_{\eta=0}$) measured at $\sqrt{s_{NN}} = 130\,\mathrm{GeV}$ and 200 GeV ($R_{200/130}$) for each centrality bin, corresponding to 5% of the nuclear interaction cross section, is shown in Fig. 1. For the most central bin, the transverse energy increases by $14 \pm 2\%$ and remains nearly unchanged with centrality.

E_T and charge particle multiplicity (N_{ch}) behave very similarly such that the mean E_T per charged particle remains unchanged over a broad range of centralities (see Fig. 2, left). The same behavior of $\langle E_T \rangle / \langle N_{ch} \rangle$ with centrality was observed by the WA98 Collaboration at $\sqrt{s_{NN}} = 17.2\,\mathrm{GeV}$.[3)] The ratio remains unchanged also as a function of $\sqrt{s_{NN}}$ (see Fig. 2, right).

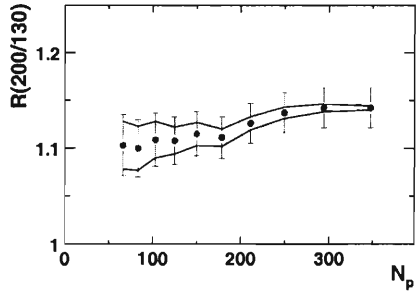

Fig. 1. $R_{200/130}$ versus centrality. The number of participants N_p is taken from data at $\sqrt{s_{NN}} = 200\,\mathrm{GeV}$. The lines represent the effect of the $\pm 1\sigma$ centrality-dependent systematic errors, the error bars are the total systematic errors.

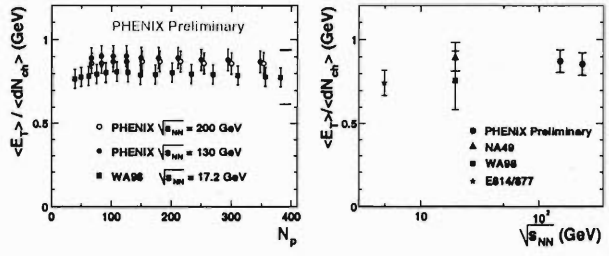

Fig. 2. Ratio of transverse energy and charge particle pseudorapidity densities versus N_p (left) and $\sqrt{s_{NN}}$ (right) for the most central collisions. SPS and AGS data are taken from WA98,[3)] NA49[4)] and E814/E877.[5)]

References

1) Proc. Quark Matter 1984, edited by K. Kajantie (Springer, Berlin, 1985); Proc. Quark Matter 1987, edited by H. Satz, H. J. Specht, and R. Stock (Springer, Berlin, 1988).
2) PHENIX Collaboration, K. Adcox et al.: Phys. Rev. Lett. **87**, 052301 (2001); A. Bazilevsky: RIKEN Accel. Prog. Rep. **35**, 219 (2002).
3) WA98 Collaboration, M. M. Aggarwal et al.: Eur. Phys. J. C **18**, 651 (2001).
4) J. Bächler et al.: Nucl. Phys. A **661**, 45 (1999); T. Alber et al.: Phys. Rev. Lett. **75**, 3814 (1995).
5) J. Barrette et al.: Phys. Rev. C **51**, 3309 (1995); Phys. Rev. Lett. **70**, 2996 (1993).

a) In our previous publications,[2)] E_T was defined using the kinetic energy for nucleons and the total energy for all other particles. This approach does not take into account the mass of nucleons resulting from pair production. In this paper, E_T was defined with $E - M_N$ for baryons, $E + M_N$ for antibaryons, and E for all other particles, where E is the total energy of the particle and M_N is the nucleon mass. The revised definition of E_T increases its value by about 4%, independent of centrality.

Charged pion identification at high p_t using the PHENIX RICH detector

F. Messer, for the PHENIX Collaboration

During the second year of operation, the Relativistic Heavy Ion Collider at BNL has collided Au as well as transversely polarized proton beams at the center-of-mass energy of 200 GeV. The PHENIX experiment[1] registered more than 100 million min-bias events in Au-Au as well as proton-proton collisions. This high statistics data sample together with the good momentum resolution furnished by two drift chambers $\delta p/p^2 \simeq 1\%\,(\mathrm{GeV/c})$ permit us to measure charged particles over a large dynamic range.[2] In addition, with the use of two large-acceptance Ring Imagine Cherenkov detectors (RICH) each of which covers 90 degrees in azimuth and 0.7 unit of pseudo-rapidity, PHENIX is in the unique position to efficiently identify charged pions at a high transverse-momentum region. Originally designed for electron and positron identification, the RICH detectors are sensitive to pions above the Chrenkov threshold of 4.7 GeV/c. The number of photoelectrons emitted is strongly dependent on momentum (Fig. 1).

The largest background in this analysis is represented by low-energy photon conversions in the front window of the drift chamber (roughly at a radius of 200 cm) where bending due to the residual magnetic field is very small. To suppress this kind of background, we require that the charged particle tracks which fire the RICH, undergo nuclear interactions in the electromagnetic calorimeter (EMC), thereby depositing a large amount of energy (Fig. 2).

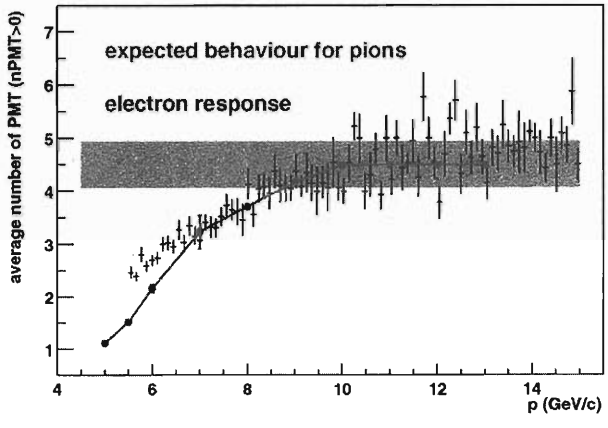

Fig. 1. Strong momentum dependence of light emission for pions. Comparision between measurements (points) and expectation (line). The shaded area represents the response of the detector to electrons.

Raw data have been corrected for geometrical acceptance of the detector, for track reconstruction efficiency, decay in flight and limited momentum resolution using a single-track Monte-Carlo simulation which includes all the PHENIX dectectors. To study the effect of the high particle environment in central collision, the simulated single tracks were embedded in real data events.

The charged pion yields have been measured as a function of the violence of the collision, and they indicate that in the most central reaction, the charged pions are suppressed by a factor of 4.5 ± 2 in comparison to a simple binary scaling expectation of peripheral collisions. The ratio π^-/π^+ is constant at 1 and it is, within statistical and systematic errors, independent of momentum and centrality.

Much larger statistics of such data are expected in the coming runs for p-p, d-Au and Au-Au collisions.

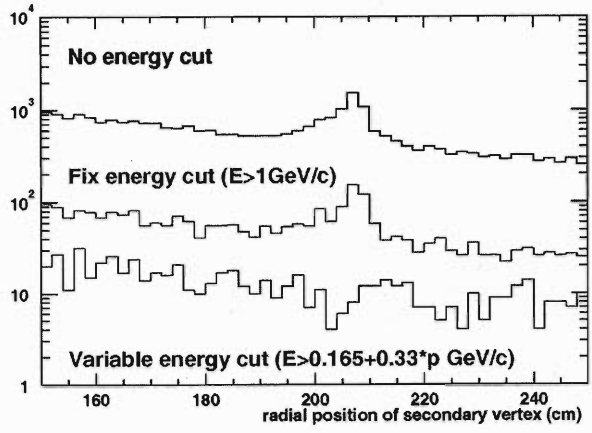

Fig. 2. Radial position of the secondary vertex is plotted for every pair of charged tracks. If no energy cut is required a large peak due to conversion in the drift chamber window is observed. The peak is reduced and disappears with increasing energy cut as function of momentum (p).

References

1) D. Morrison, PHENIX Collaboration: Nucl. Phys. A **638**, 565 (1998).
2) F. Messer et al., PHENIX Collaboration: RIKEN Accel. Prog. Rep. **36**, 233 (2003).

Spin monitoring for the polarized proton collisions at PHENIX

Y. Goto, A. Bazilevsky, G. Bunce,[*1] A. Deshpande, B. Fox, M. Grosse Perdekamp, O. Jinnouchi, M. Kaneta, H. Kobayashi, K. Okada, N. Saito,[*2] H. D. Sato,[*2] and A. Taketani

The RHIC started operation as a polarized proton–proton collider in December, 2001. In this run, which is called run-2, we measured single transverse-spin asymmetries (A_N) with transverse-spin collisions. In addition, we have performed many systematic studies to measure the double longitudinal-spin asymmetry (A_{LL}),

$$A_{LL} = \frac{1}{P_B \cdot P_Y} \cdot \frac{N_{++} - R \cdot N_{+-}}{N_{++} + R \cdot N_{+-}},$$

for the gluon polarization measurement in the proton with longitudinal-spin collisions in 2003 (run-3). In this formula, P_B and P_Y denote the polarization of colliding beams in the RHIC rings which are called the Blue ring and the Yellow ring, respectively. The number of events or yields from collisions with parallel (antiparallel) beam helicity is represented by N_{++} (N_{+-}). The ratio of luminosity for collisions with parallel beam helicity to that with antiparallel beam helicity is expressed by $R = L_{++}/L_{+-}$. One of the important systematic studies is that of R, so-called relative luminosity.[1)]

From run-3, we will start the gluon polarization measurement with many channels at PHENIX. We will measure A_{LL} of neutral pions, charged hadrons, and heavy flavor channels like J/ψ and single electrons. In the measurement of neutral pions and charged hadrons, our goal is to measure 0.3% level asymmetry with the A_{LL} measurement. In order to achieve this, we will develop an online monitoring system:

- to monitor stability of the relative luminosity measurement, which is required to be a sub-0.1%-level measurement, and
- to analyze the A_{LL} of neutral pions with reduced precision for the monitoring purpose.

In run-2, we could achieve the relative luminosity measurement within 0.3% systematic error as a preliminary value when each bunch in the RHIC ring had very similar "characteristics." There were 55 beam bunches in one ring in run-2, and there will be 110 bunches in run-3. Each bunch in the RHIC rings is filled independently so that the pattern of polarization direction for the bunches can be arranged to give all possible spin combinations for the colliding bunch-crossings. This enables successive measurements of parallel and antiparallel yields in the A_{LL} measurement. It greatly reduces time-dependent uncertainty. We investigated some "characteristics" of the beam bunch in run-2. One of them was the collision vertex distribution. We found that we could achieve 0.3%-level measurement when the vertex distribution in each bunch had similar width (RMS).

In run-3, we need further investigation of how other accelerator parameters (*e.g.*, emittance, collision angle) in each bunch affects the relative luminosity measurement by using the online monitoring system. The online monitoring system needs to collect information from both the RHIC accelerator and the PHENIX experiment. At RHIC in run-3, the polarization pattern of collisions will be changed in one fill by "recogging" (changing the collision combination of crossing bunches in each ring) and flipping the polarization direction with the spin flipper rf-dipole magnet. These accelerator operations will reduce uncertainty of the relative luminosity measurement. By monitoring the correlation between the stability of the relative luminosity measurement and the accelerator parameters, and the effect of the "recogging" and the "flipping" to the measurement, we plan to achieve the sub-0.1%-level measurement.

After we get the required precision of the relative luminosity by monitoring it properly, we plan to monitor the A_{LL} of neutral pions. If there is sufficient gluon polarization in the proton, we should be able to monitor non-zero A_{LL} in the neutral pion measurement. The neutral pion cross section measurement has already been carried out in run-2,[2)] and it has to be established in the online monitoring process. We will make a relative luminosity database in the online monitoring process to be used in the online A_{LL} monitor of neutral pions. The database will include the relative luminosity information and the evaluation of uncertainties.

References

1) T. Kawabata et al.: RIKEN Accel. Prog. Rep. **36**, 239 (2003).
2) H. Torii et al.: RIKEN Accel. Prog. Rep. **36**, 230 (2003).

*1 Brookhaven National Laboratory, USA
*2 Kyoto University

RHIC pC CNI polarimeter: Results from the first collider run

O. Jinnouchi, I. G. Alekseev,[*1] A. Bravar,[*2] G. Bunce,[*2] R. Cadman,[*3] A. Deshpande, S. Dhawan,[*4] H. En'yo, D. E. Fields,[*5] H. Huang,[*2] V. Hughes,[*4] G. Igo,[*6] K. Imai,[*7] V. P. Kanavets,[*1] J. Kiryluk,[*6] K. Kurita,[*8] Z. Li,[*2] W. Lozowski,[*9] W. W. MacKay,[*2] Y. Makdisi,[*2] S. Rescia,[*2] T. Roser,[*2] N. Saito,[*7] H. Spinka,[*4] B. Surrow,[*2] D. N. Svirida,[*1] J. Tojo, D. Underwood,[*4] and J. Wood[*6]

Polarimeters using the proton-carbon scattering process in the Coulomb Nuclear Interference (CNI) region were installed in the Relativistic Heavy Ion Collider (RHIC) at Brookhaven National Laboratory (BNL). Polarization measurements were successfully carried out with the high-energy polarized proton beams during the first polarized pp collision run in 2001/2. This article briefly reports their performance.

The polarimeters serve as both fast monitors of the beam polarization for the accelerator, and as the primary polarimeters for the normalization of the physics asymmetries at the experiments. Based on the experience of a successful commissioning in 2000,[1] the polarimeters were expected to demonstrate their maximum capability in 2001/2. The run started on 11/29/01 and took place over 8 weeks; this breaks down to 3 weeks for commissioning and 5 weeks for the physics run. The beam in each ring was in 55 bunches with alternating polarization signs and with 8×10^{10} protons per bunch. Measurements were made at injection (24.3 GeV) and every two hours at the collision energy of 100 GeV. Measurements to 10% error were made within a minute during the 2001/2 run. In addition to the fast operation, the results of measurements must be broadcast to the experiments immediately.

The experimental setup consists of an ultrathin carbon target (3.5-μg/cm^2 thick) and six silicon strip detectors (SSDs). The readout system using waveform digitizers (WFDs) was adopted in order to permit very high-rate measurements. The WFD system selects the carbon event without dead time.

Figure 1 shows a number of polarization measurements for a typical fill. The intensity decreased during the storage, the physics asymmetries (closed points) were stable. The false asymmetries (open points), which should be zero, fluctuated around zero.

The polarization values at injection energy averaged over the long storage (> 4 hours) fills are investigated. The analyzing power at the RHIC injection energy was determined from an experiment[2] which measured the pC CNI process at a beam energy of 21.6 GeV. 15–

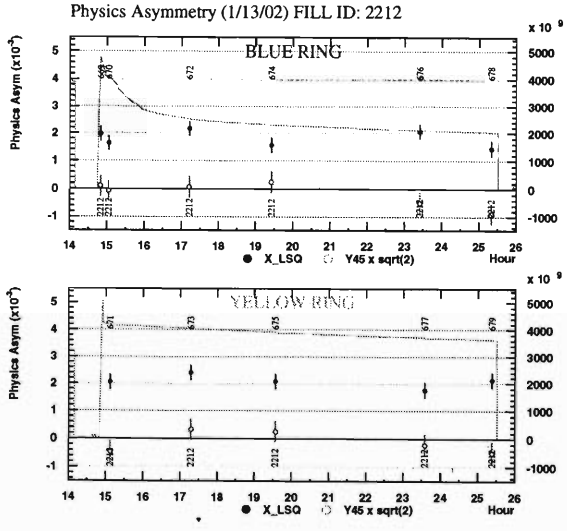

Fig. 1. Measured physics asymmetries along with the polarized proton intensity as a function of time for a typical fill. The upper (Lower) figure shows the Blue (Yellow) ring. Closed points represent the vertical asymmetry and open points show the horizontal components. All measurements are taken at 100 GeV except for the first Blue measurement, *i.e.*, run 669 was taken at injection energy. Solid curves represent the number of total protons in each ring.

27% polarization at injection energy was observed for both rings.

The RHIC pC CNI polarimeter provided reliable polarization values in the first successful polarized pp collision run in 2001/2. It worked beautifully throughout the period, and high statistics (20×10^6 events) measurements were carried out in one minute, owing to the newly adopted waveform digitizer modules. Stable proton polarizations at 100 GeV were measured with little or no loss in magnitude over the storage. Detailed off-line analysis was carried out, and the major systematic errors were estimated. Several interesting challenges are expected for the upcoming run.

*1 Institute for Theoretical and Experimental Physics, Russia
*2 Brookhaven National Laboratory, USA
*3 Argonne National Laboratory, USA
*4 Yale University, USA
*5 University of New Mexico, USA
*6 University of California, Los Angeles, USA
*7 Kyoto University
*8 Rikkyo University
*9 Indiana University Cyclotron Facility, USA

References

1) O. Jinnouchi et al.: RIKEN Accel. Prog. Rep. **35**, 228 (2002).
2) J. Tojo et al.: Phys. Rev. Lett. **89**, 052302 (2002).

Luminosity measurement of RHIC polarized proton collisions at PHENIX

Y. Goto, S. Belikov,[*1] G. Bunce,[*2] A. Drees,[*2] B. Fox, T. Kawabata,[*3] N. Saito,[*4] and H. D. Sato[*4]

In all the cross-section measurements at PHENIX[1)] we need to determine the luminosity, $\mathcal{L}_{\rm PHENIX}$. One way to obtain the luminosity is:

$$\mathcal{L}_{\rm PHENIX} = \frac{N_{\rm BBC}}{\sigma_{pp} \cdot \epsilon_{\rm BBC}},$$

where $N_{\rm BBC}$ is the number of the Beam-Beam Counter (BBC) trigger, σ_{pp} is the proton-proton inelastic cross section, and $\epsilon_{\rm BBC}$ is the efficiency of the BBC in the proton-proton inelastic events. In order to understand the systematic uncertainties of the luminosity measurement, we utilized the vernier (van der Meer) scan based on the BBC detector. The vernier scan is the method used to obtain the absolute cross section which was performed at the RHIC accelerator. In the process of the analysis of the vernier scan data, we checked all systematic uncertainties which were common to the cross-section measurement, and, as a result of the analysis, we confirmed that σ_{pp} obtained by the vernier scan was consistent with the world average value (42 mb) within the systematic uncertainties.

The vernier scan measured collision rates as a function of beam displacement by stepwise sweeping of one beam across the other. The proton-proton inelastic cross section is obtained by:

$$\sigma_{\rm BBC}^{|z|<75} = \frac{N_{\rm BBC}^{|z|<75}}{\mathcal{L}_{\rm RHIC}} = \sigma_{pp} \cdot \epsilon_{\rm BBC}^{|z|<75},$$

where $\sigma_{\rm BBC}^{|z|<75}$ is the "raw" proton-proton inelastic cross section with the BBC signal, $N_{\rm BBC}^{|z|<75}$ is the scaler count of the BBC signal, and $\mathcal{L}_{\rm RHIC}$ is the instantaneous luminosity which was also given by the vernier scan. The vertex position is denoted by z. A vertex position cut $|z| < 75$ cm was applied to the BBC signal. Figure 1 shows the BBC signal counts as a function of the beam displacement. The preliminary result based on a total of 3 scans is:

$$\sigma_{\rm BBC}^{|z|<75} = 12.6 \pm 0.1({\rm stat}) \pm 1.0({\rm syst}){\rm mb}.$$

The proton-proton inelastic cross section was derived by evaluating the BBC efficiency, $\epsilon_{\rm BBC}^{|z|<75}$. The BBC efficiency was evaluated by dividing it into the BBC coincidence efficiency and the BBC z-vertex cut efficiency. The former was obtained by the simulation. Figure 2 shows the simulated BBC coincidence efficiency. In the vertex position region $|z| <$ 150 cm, it was 44%. The latter was evaluated by using the PHENIX data in the vernier scan period, which was 66%. By correcting the BBC coincidence efficiency (44%) and the BBC z-vertex efficiency (66%) on the vernier scan cross section (12.6 mb) the proton-proton inelastic cross section measured at PHENIX is 12.6 mb/0.44/0.66 = 43.4 mb, which shows good agreement with the world average value, 42 mb.

In the cross-sectional measurements at PHENIX in Ref. 1, the narrower vertex position cut ($|z| < 30$ cm or 35 cm) was applied, and the vertex position dependence was negligible. The BBC efficiency, $\epsilon_{\rm BBC}$, was evaluated to be 51% without z-dependence. The absolute normalization scale of the luminosity measurement, $\sigma_{pp} \cdot \epsilon_{\rm BBC}$, is 43.4 mb × 0.51. We are now finalizing the systematic errors of this measurement.

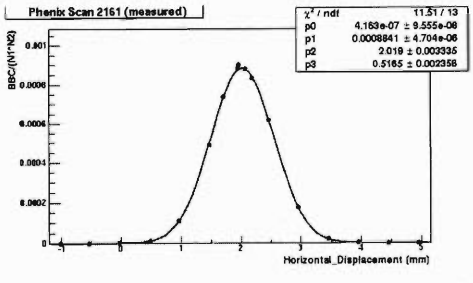

Fig. 1. BBC counts as a function of the beam displacement in the vernier scan.

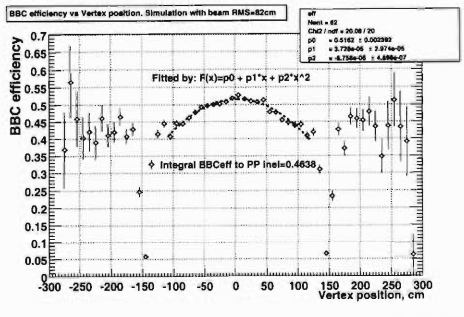

Fig. 2. Simulated BBC coincidence efficiency.

*1 Iowa State University, USA
*2 Brookhaven National Laboratory, USA
*3 Center for Nuclear Study, University of Tokyo
*4 Kyoto University

References

1) H. Torii et al.: RIKEN Accel. Prog. Rep. **36**, 230 (2003); H. D. Sato et al.: RIKEN Accel. Prog. Rep. **36**, 231 (2003); F. Messer et al.: RIKEN Accel. Prog. Rep. **36**, 233 (2003).

Relative luminosity measurement at PHENIX

T. Kawabata, B. Fox, G. Bunce, and Y. Goto

We have begun asymmetry measurements for polarized proton collisions at RHIC. In the first physics run (run 2), 60-beam bunches were stored in the blue and yellow rings at RHIC. The lifetime of these beam bunches in RHIC was typically ~8 hours. Once the beam condition worsened, the old fill was aborted and new bunches were stored again. The bunch-by-bunch pattern for the signs of the beam-polarization axis was arranged for each of the blue and yellow rings to yield all possible spin combinations of the colliding bunches. The left-right spin asymmetry A_N was measured using vertically polarized beams in run 2. In the next run (run 3), we will measure the longitudinal double spin asymmetry A_{LL} using longitudinally polarized beams. A_{LL} is obtained from the asymmetry between the spin-parallel and antiparallel collisions, as defined by

$$A_{LL} = \frac{1}{P_B P_Y} \frac{N_{++}/L_{++} - N_{+-}/L_{+-}}{N_{++}/L_{++} + N_{+-}/L_{+-}},$$

where N_{++} (N_{+-}) and L_{++} (L_{+-}) are yields and luminosities in bunch collisions with the parallel (antiparallel) polarization. P_B and P_Y are the beam polarizations for the blue and yellow rings, respectively. The 0.1%-level precision for the relative luminosity $r = L_{++}/L_{+-}$ is required for sub-% level asymmetry measurement.

The PHENIX detector complex has several luminosity monitors. The zero-degree calorimeters (ZDCs), beam-beam counters (BBCs), and normalization trigger counters (NTCs) are located at 18 m, 1.4 m, and 0.4 m from the collision point, respectively. The ZDCs, BBCs, and NTCs are located at both north and south sides. We can measure the luminosity by counting the coincidence signals of the north and south detectors. We can also determine the vertex position along the beam direction (Z-vertex position) by using the differences in the time of flight of emitted particles. The information on the Z-vertex position enables us to eliminate background events due to the collision of the beam with residual gas in the beam pipe.

The coincidence signals were counted by the GL1-P scalers. The GL1-P scalers are capable of counting four kinds of signals with 32-bit depth for each crossing (240 channels in run 2). In run 2, the GL1-P scalers were arranged to count the minimum bias trigger (MB), NTC narrow (NTCn), BBC local level 1 (BBCLL1), and ZDC signals. The BBCLL1 and NTCn signals were created by applying the Z-vertex cut with $|Z_{BBC}| < 75$ cm and $|Z_{NTC}| < 40$ cm for the BBC and NTC coincidence signals, respectively. The MB signal was generated when the BBCLL1 or NTC fired. The BBCLL1 is expected to be the best measure of luminosity among the four channels in the GL1-P scalers, since the contamination from the beam-gas background is small (less than 10^{-4}). The ZDC signal is also not affected by the beam-gas background. The statistical uncertainty is not, however, negligible because the acceptance is very small due to the long distance from the collision point.

We deduced the relative luminosity r^x (x = NTCn, ZDC, BBCLL1, and MB) from the GL1-P counts for each fill. The ratio between these relative luminosities $R_y^x \equiv r^x/r^y$ is useful for studying the stability of the luminosity monitors. As an example, R_{ZDC}^{BBCLL1} is plotted as a function of the fill number (serial number for fills in RHIC) by the solid circles in Fig. 1. The solid lines indicate the statistical errors. In order to estimate the systematic error, we randomly sorted beam bunches into two groups A and B, estimated R_y^x using L_A and L_B instead of L_{++} and L_{+-}, and repeated the procedure 400 times. The width of the distribution for R_y^x can be considered as the total error that includes both statistical and systematic contributions. The shaded bars in Fig. 1 show the total error in R_{ZDC}^{BBCLL1}. The systematic errors are less than 0.2% for good fills after subtracting the statistical effect, but there are still poor fills with 0.5%-level systematic errors.

Since there are differences in the acceptance for the Z-vertex position between the luminosity monitors, the crossing-by-crossing variation of the Z-vertex width may cause the systematic error in the relative luminosity. In fact, crossing-by-crossing fluctuation of the Z-vertex width was observed in several fills with large systematic errors. The systematic errors, however, are not reduced even if tight Z-vertex cuts are applied to the luminosity monitors. The origin of the systematic errors is still unclear. Further investigation, including an approach from the accelerator side, is in progress.

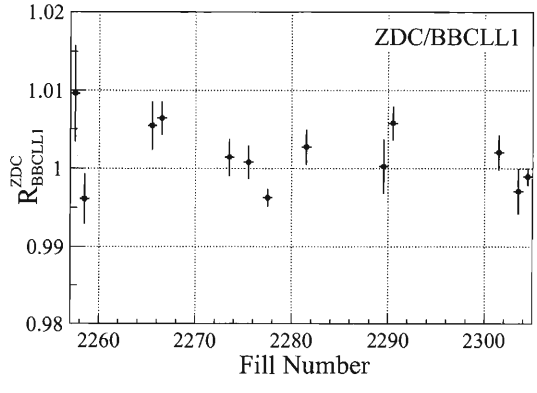

Fig. 1. R_{ZDC}^{BBCLL1} as a function of fill number.

Triggering muons in Run-2 and Run-3 p+p collisions at RHIC

H. D. Sato,[*1] N. Saito,[*1] H. En'yo, A. Taketani, V. Cianciolo,[*2] and A. Drees[*3]

A simple trigger system, called the blue-logic trigger, was introduced to trigger single muons and muon pairs in p+p collisions during the RHIC Run-2 (2001–2002) period. Its performance and perspective for the next run (Run-3) are described.

Triggering is essential for p+p collisions at RHIC because of their high interaction rates (300 times larger than in Au+Au collisions). A coarse-segmented trigger system called the MuID blue-logic trigger (BLT)[a] was constructed using the Muon Identifier (MuID) in PHENIX and used to trigger muons in the South Muon Arm during the Run-2 p+p period.

Figure 1 shows a schematic view of the system. All MuID planes, or gaps, are divided into four regions (called quadrants) by horizontal and vertical lines through the middle. The coincidence of fired gaps of each quadrant, caused by a muon track, gives a quadrant trigger. The chance for a muon to cross more than one quadrant is negligible. Because of the limited number of input channels of the trigger circuit, only four gaps (gap 1, 3, 4 and 5) out of five were used. Each quadrant is further divided into two sectors for both horizontal and vertical tube orientations. In total, 16 pseudo-trigger output signals from each sector, grand OR of all individual signal-channels inside, are sent to the trigger algorithm. Trigger decisions are made by the LeCroy 2372 Memory Lookup Units (MLUs) for each quadrant. Two MLUs are prepared for each quadrant for both "deep" and "shallow" triggers. A deep trigger requires hits in all the gaps and a shallow trigger requires hits up to the third gap. Hit patterns are required to point to the event vertex, as shown in Fig. 2. To minimize the loss of trigger efficiency due to finite chamber efficiencies, the algorithm allows some gaps to miss hits. For a deep trigger, 6 out of 8 gaps (including both orientations) are required to have a hit and 3 out of 4 gaps for a shallow trigger. Extra hits are allowed, which means no efficiency loss due to background hits.

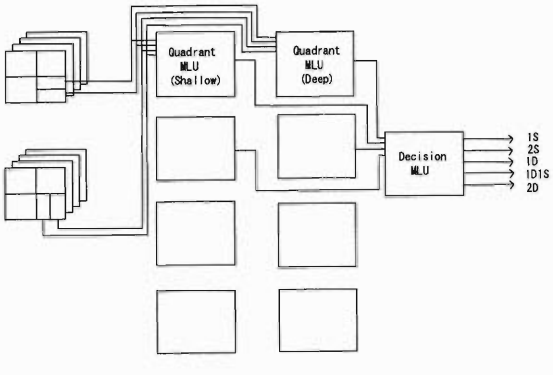

Fig. 1. Schematic diagram of the MuID blue-logic trigger. Each "Quadrant" MLU takes 16 (4 for each gap) output signals from the MuID Front-End Electronics. The "Decision" MLU takes output signals of all the "shallow" and "deep" quadrant MLUs and generates final trigger bits, which are 1S to 2D, as described in the text.

Another MLU, called the "Decision MLU," counts the number of fired quadrants and issues five trigger signals:

(1) single shallow (1S) – one shallow quadrant is fired,
(2) double shallow (2S) – two or more shallow quadrants,
(3) single deep (1D) – one deep quadrant,
(4) deep-shallow (1D1S) – One deep quadrant and one or more shallow quadrants and
(5) double deep (2D) – two or more deep quadrants, which are sent to Global Level-1.

The level-1 triggers of PHENIX are issued by the Global Level-1 (GL1) module, whose input is Local Level-1 and blue-logic triggers from various subsystems. The maximum DAQ rate (about 1 kHz) and the number of triggers (10 or more) limit the rates for each GL1 trigger to about 100 Hz or less. Two kinds of muon-related triggers were prepared for physics triggers:

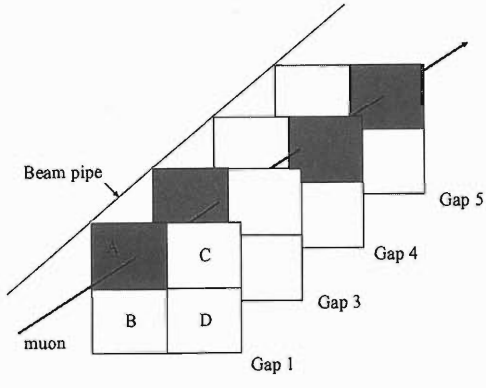

Fig. 2. An accepted pattern of the MuID blue-logic trigger. Only one quadrant is shown. Capital letters represent each segment. Gap 2 was not used because of the limitation of input channels of trigger logic.

*1 Department of Physics, Kyoto University
*2 Oak Ridge National Laboratory, USA
*3 Brookhaven National Laboratory, USA

a) So named because the trigger circuit is constructed using NIM- and CAMAC-standard electronics.

(A) MB ⊗ 1D for the single muon trigger and
(B) MB ⊗ 1D1S for the dimuon trigger,

where MB stands for the minimum-bias trigger and ⊗ for logical AND.

The rate of the single muon trigger was usually less than 100 Hz and consistent with that of the irreducible hadron-decay background before the nosecone (1/1500 of the minimum bias rate) within a factor of two. However, we sometimes observed abnormally high (∼1 kHz) rates. To understand this, we performed a dedicated study where beams are cogged, mis-steered and collimated while monitoring the changes in trigger rates including other triggers such as Beam-Beam Counters. As a result, we found that the high rate was due to blown-up beams which hit the beam pipe and produced high-energy secondary particles (including muons) sailing through the MuID. For physics analyses offline, this background can be rejected with a vertex cut. We used this trigger with a prescale factor of 4, abandoning 4/5 of all events, when the trigger rate was high. The rate of the dimuon trigger was typically about 1/10 that of the single muon trigger and never beyond 100 Hz. Therefore no prescale factor was applied to the dimuon trigger.

Figure 3 shows trigger circuit (TC) efficiencies for 34 randomly selected p+p runs. TC efficiencies reflect the inefficiency of the hardware trigger circuit. It is defined as

$$\frac{\#\text{ of events with both hardware and software triggers}}{\#\text{ of events with software triggers}}$$

using MB-triggered events, where a hardware trigger means the BLT output (GL1 input) and a software trigger is a result of the software which emulates the trigger algorithm. On average, an efficiency of 96.8% has been obtained for the single muon trigger and 98.7% for the dimuon trigger with small satistical errors (< 0.1%). Inefficiencies are ascribed to hardware dead time which depends on the trigger rate. A simple model calculation, in which all efficiency loss is assumed to be due to the dead time, reproduces TC efficiencies for the single muon trigger well, as shown in Fig. 4. This consistency ensures that both hardware and software triggers worked as expected.

In Run-3, BLT will be used for triggering muons in the North Arm. The dimuon trigger rate will be sufficiently low even with 10 times higher luminosity. For the single muon trigger, we may need prescale factors, depending on its rate. BLT is also confirmed to work moderately in d+Au collisions planned in Run-3. For the South Arm, a more sophisticated trigger system, MuID Local-Level-1, will be implemented with a better background rejection. Also, several ideas for triggering high-p_T single muons are being developed for the later runs, for example, a Cherenkov detector just in front of the MuID to reject low-momentum muons.

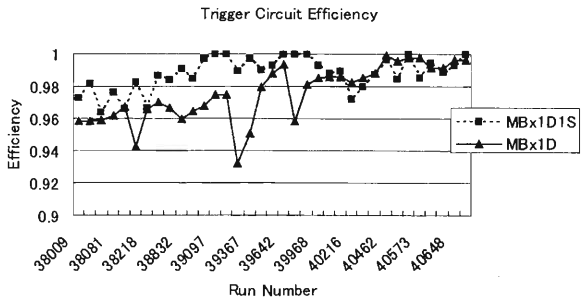

Fig. 3. Trigger circuit efficiency (defined in the text) as a function of the run number for the single muon (MB ⊗ 1D) and dimuon (MB ⊗ 1D1S) triggers.

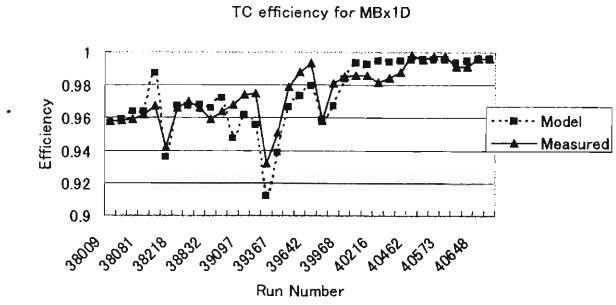

Fig. 4. Trigger circuit efficiency (defined in the text) as a function of the run number for the single muon trigger, with that determined by a simple model calculation.

Construction and commissioning of the PHENIX north muon tracker: The gas system

H. Kobayashi, W. Sondheim,[*1] D. S. Brown,[*2] D. M. Lee,[*1] J. Murata, and N. Kamihara[*3]

The PHENIX north muon tracker is a subsystem of the north muon arm which consists of a muon identifier and a muon tracker. The muon tracker consists of three stations of cathode strip chambers situated in the radial field magnet.

After the successful data collecting period[1] that ended at the end of February 2002, integration of the PHENIX north muon tracker was started and it was completed in November 2002. Figure 1 shows a picture of the north muon tracker taken after chamber installation was completed when the scaffoldings inside the magnet were being built, which was followed by installation of other parts, namely, electronic cables, gas tubes, optical fibers, optical alignment cameras and so forth.

The muon tracker gas system has been designed[2] and constructed[3] for the south tracker in year 2000 and operated[4] from year 2001 to 2002. It uses 50%Ar+30%CO_2+20%CF_4 mixed gas, which is non-flammable and it gives a good gain and a small Lorentz angle. It consists of a gas distribution panel at the front end of each arm and components in the gas mixing house. The components in the gas mixing house are the main control rack and the compressor panel.

In order to use the existing gas system for both the south and the north muon trackers, two hardware upgrades were developped and completed during the shutdown period.

- The gas distribution panel for the north muon tracker was newly built.
- A new branch path to and from the north muon tracker was added in the main control rack in the gas mixing house.

Figure 2 shows the newly built north gas distribution panel. It is located at the north east bottom of the

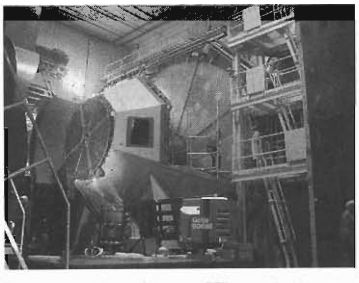

Fig. 1. North muon tracker. The picture was taken on June 21, 2002 after all chambers were installed when the scaffoldings were being built.

*1 Los Alamos National Laboratory, USA
*2 New Mexico State University, USA
*3 Tokyo Institute of Technology

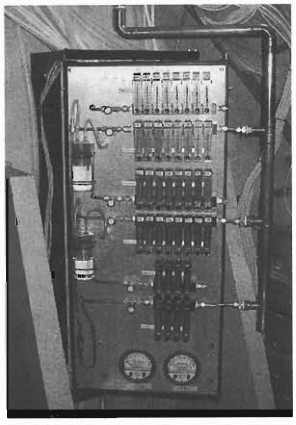

Fig. 2. Gas distribution panel for the north muon tracker.

north muon tracker. It's basic design is the same as that of the gas distribution panel built for the south muon tracker but the mechanical structure is made more compact in order to fit it in the narrow space. The distribution panel consists of twenty flow meters, two safety babblers, two pressure gages and five mass flow meters. Each of the pressure gages and the flow meters has an electrical read out to allow remote monitoring. The twenty flow meters are used to measure and adjust the flow rate to and from each chamber. One of the two safety babblers guarantees the pressure between inlet and outlet lines of less than 2.5 inches WC and the other bubbler guarantees the pressure between outlet and ventilation lines of less than 1.0 inches WC. The two pressure gages monitor the inlet pressure and the outlet pressure relative to the atmospheric pressure.

After chamber installation and gas tube routing were completed, gas flow to and from each chamber was checked. Using a gas leak detector, several gas leak points were identified where loose pipe connections were found in some chambers and they were all fixed.

During the commissioning of the gas system, it was found that a very high impedance in the main rack in the gas-mixing house prevents a smooth flow from the chamber to the main rack. Thus it has been decided to replace the thin pipes used in the main rack with thicker pipes. The replacement work is in progress.

References

1) D. F. Fields: RIKEN Accel. Prog. Rep. **35**, 229 (2002).
2) J. Murata et al.: RIKEN Accel. Prog. Rep. **33**, 165 (2000).
3) J. Murata et al.: RIKEN Accel. Prog. Rep. **34**, 237 (2001).
4) H. Kobayashi et al.: RIKEN Accel. Prog. Rep. **35**, 232 (2002).

Geometry alignment calibration of the PHENIX muon tracker

H. Kobayashi, N. Kamihara,[*1] S. Batsouri,[*2] M. Brooks,[*3] N. Bruner,[*4] M. Leitch,[*3]
P. L. McGaughey,[*3] H. D. Sato,[*5] and A. Taketani

Muon measurement at RHIC energies provides a means of studying the physics of both the heavy ion and the spin program. Particularly in the spin program, heavy flavor (charm and bottom) quark production is considered as a good probe for the study of gluon polarization in the proton. Dimuons originated from quarkonium (J/Ψ, Υ, *etc.*) production give a clear signal which identifies heavy flavor production. Single muons originated from open heavy flavor production are dominant over the π/K decay backgrounds at high transverse momentum.

The PHENIX muon arms were designed for the measurement of the muons. They consist of the north arm and the south arm, and cover the pseudo rapidity range of $1.1 < |\eta| < 2.4$ and the full azimuthal angle range. The south arm was operational during the years 2001–2002. The north arm will become operational in the years 2002–2003. Each arm consists of a muon tracker (MuTr) and a muon identifier (MuID). The MuID is five sandwiches of plastic tubes and steel absorbers and provides an event trigger with muon identification. The MuTr is a spectrometer which consists of three stations of cathode strip readout chambers situated in the radial magnetic field around the beam axis. Each station is mechanically separated into a number of individual chambers: station-1 consists of four chambers and station-2 and -3 each consist of eight chambers. Each station-1 chamber is further segmented in the azimuthal direction into four. Each station-2 and -3 chamber is segmented in the azimuthal direction into two. The smallest segment in the azimuthal direction is $\Delta\phi = 2\pi/16$ units in each station which is conventionally called a "half-octant."

Geometry alignment calibration of the muon tracker is important for obtaining optimum momentum resolution out of a given chamber resolution. Obtaining the best momentum resolution contributes to the achievement of a good separation of quarkonium mass peaks from the background. Having a high momentum resolution also enables us to classify single muon production according to the transverse momentum spectra. An optical survey for the measurement of the initial chamber position in the experimental hall was carried out by BNL technicians with a 1 mm uncertainty. The result of the survey is used in the tracking software as the preliminary real location of the chamber. However, the precision of the initial survey is not sufficient, because it is necessary to know the alignment with precision better than 150 μm in order for the J/Ψ mass peak to be visible.[1)]

Three kinds of data under the zero magnetic field were recorded for the study of alignment: (a) Cosmic ray data triggered by the MuID, (b) Au-Au collision data, and (c) p-p collision data. The number of straight tracks in data (a) were not sufficient to get a obtain high precision. Data (b) could not be used for the study of alignment because many ghost tracks were found due to the high multiplicity in the heavy ion collisions and a large number of high-voltage channels were inoperable when the zero magnetic field data was collected, although these problems were later fixed. Finally, data (c) was used since it easily showed clean tracks. A total of 46 k straight tracks out of 4800 k minimum bias triggered events was selected by requiring that the residual at station-2 be within 1 cm from the centroid of the distribution. These straight tracks may not always be muons because the selection of track hits in the MuID was not required in the alignment study, since it reduces the number of straight tracks down to 1/20.

Since the smallest segment of the alignment study is the half-octant, the "half-octant frame" and the "body centered frame" are defined in each half octant. Figure 1 shows the definition of the half-octant frame and Fig. 2 shows the definition of the body centered frame. The half-octant frame is defined such that the y-axis direction matches the direction of a strip in the straight plane. The z-axis is same as the accelerator beam direction which runs from south to north. The x-axis direction is perpendicular to both y- and z-axes. The body centered frame is defined such that three axis has

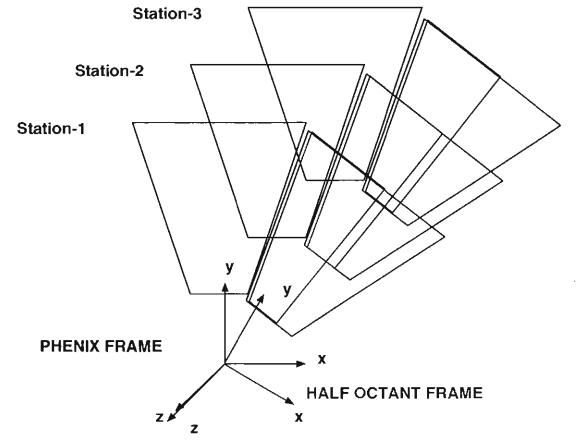

Fig. 1. Half octant frame.

*1 Tokyo Institute of Technology
*2 Columbia University, USA
*3 Los Alamos National Laboratory, USA
*4 University of New Mexico, USA
*5 Kyoto University

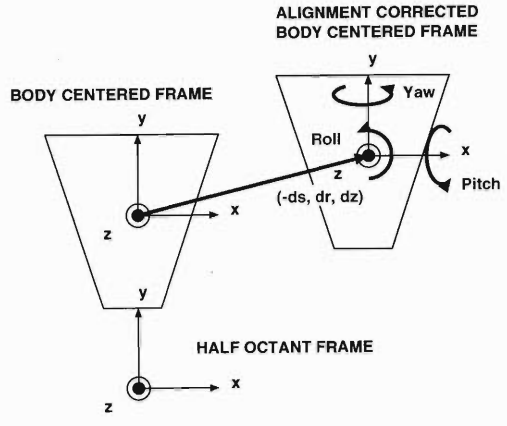

Fig. 2. Alignment parameters.

same direction as the half-octant frame but the origin of the frame is set at the body center of the half-octant, which is defined at the middle of the center strip.

The alignment parameters are defined using the half-octant frame for the translation and the body centered frame for the rotation. The alignment constants for translation, $(dx, dy, dz) = (-ds, dr, dz)$, are defined as the difference between the half octant body centers for the survey position and the true position. The alignment constants for the rotation, $(\theta_x, \theta_y, \theta_z) =$ (Pitch, Yaw, Roll), are defined as the angle difference of half octant body direction between the translation corrected chamber orientation and the true orientation.

Straight line fitting of tracks was performed through taking combinations of hits in station-1, -2 and -3. Geometry alignment of the muon tracker was studied by looking at the residuals in each station or in each gap. A residual is defined by difference between a measured hit position and a projected position at the i-th layer (station or gap).

$$\begin{pmatrix} R_{xi} \\ R_{yi} \\ R_{zi} \end{pmatrix} = \begin{pmatrix} x_i - (\alpha_x z_i + \beta_x) \\ y_i - (\alpha_y z_i + \beta_y) \\ 0 \end{pmatrix}, \quad (1)$$

where (α_x, β_x), (α_y, β_y) are the slope and offset parameters, respectively, for the straight line fit of hit points. Alignment correction is applied according to the following formula.

$$\vec{x}_m^{(1)} = \mathcal{R}_{\mathrm{BodyCenter}} \left(\vec{x}_m^{(0)} + \Delta\vec{X} \right), \quad (2)$$

where $\Delta\vec{X} = (dx, dy, dz)$ is the vector of translation correction and $\mathcal{R}_{\mathrm{BodyCenter}} = \mathcal{R}_{\mathrm{Yaw}}\mathcal{R}_{\mathrm{Pitch}}\mathcal{R}_{\mathrm{Roll}}$ is the matrix for the rotation correction.

Assume that the rotation correction is small compared to the translation correction. Redefining the residual for the corrected position $(R_x^{(1)}, R_y^{(1)})$ and requiring that the residual for the corrected position be small yields the following formula that shows the relationship between alignment constants and the residual before alignment correction.

$$R_x^{(0)} = \alpha_x^{(0)} dz - dx, \quad (3)$$

$$R_y^{(0)} = \alpha_y^{(0)} dz - dy. \quad (4)$$

According to these formulae the translation dz can be determined by considering the correlation between $R_x^{(0)}$ versus α_x and $R_y^{(0)}$ versus α_y. Then subsequently dx and dy can be determined by taking the average of the residuals and the slopes from all tracks.

The analysis according to formulae (3) and (4) gave a systematic difference of $dz \sim 2\,\mathrm{mm}$ for all segments and it was corrected in the code describing the station-1 z position. Alignment constants dx and dy to correct the position of the station-3 half octants were determined after the dz correction. The alignment constants at each gap in station-2 are summarized in the reference.[2)]

The ds $(= -dx)$ correction was determined in each half octant at station-3. The determined values of ds show a values spread in the range of $40 < |ds| < 3070\,\mu\mathrm{m}$ which corresponds to the range of $15 < |ds| < 1228\,\mu\mathrm{m}$ at station-2 because the distance between station-1 and -2 is 2/5 of that between station-1 and -3. The dr $(= dy)$ correction is distributed in the range of $100 < |dr| < 9500\,\mu\mathrm{m}$ at station-3 in most half octants. In some half octants, alignment constants were not determined because there were insufficient number of tracks due to inoperable high-voltage or electronics channels. It was confirmed that the residual distribution is more converged around zero if the translation alignment correction is applied. The result was used in the Run2 pp version 1 data production. The J/Ψ mass peak after alignment correction is found in the reference.[3)]

Alignment constants for the rotation were looked at but not released for the production because there were insufficient statistics to determine them.

Recently, track reconstruction software has been improved in order to reduce ghost tracks in heavy ion collision data. The tracking efficiency has been improved from 20% to 29%. It is worth while to re-examine the alignment again using the zero field Au-Au collision data with the improved reconstruction software. It is also worth while to reconsider p-p data again because it may yield more number of tracks for the determination of the rotation alignment constants.

References

1) N. Kamihara et al.: RIKEN Accel. Prog. Rep. **35**, 231 (2002).
2) H. Kobayashi et al.: PHENIX Technical Note, to be submitted.
3) H. D. Sato et al.: RIKEN Accel. Prog. Rep. **36**, 231 (2003).

Operation and upgrade of optical alignment system for PHENIX muon tracker

N. Kamihara,[*1] H. Kobayashi, A. Al-Jamel,[*2] R. L. Armendariz,[*2] T. Horaguchi,[*1] M. Leitch,[*3] D. M. Lee,[*3] J. Murata, W. Sondheim,[*3] T.-A. Shibata,[*1] and A. Taketani

The PHENIX detector complex has two muon arms, the south and north arms. Each arm consists of a muon tracker (MuTr), a muon identifier (MuId) and a muon magnet. The MuTr measures muon momentum in the magnetic field. The MuId is located downstream of the MuTr and without the magnetic field. The MuID identifies muons as by their range in a stack of counters and absorbers. MuTr consists of three layers of cathode strip readout chambers. Each layer is called a station and is divided into eight octants in the ϕ direction. The MuTr detectors are described in detail elsewhere.[1)] The momentum is determined by measuring the curvature of a muon track. It is very crucial to align the second station position relative to the other two stations for a precise momentum measurement. Our physics-driven goal is a position resolution of 100 μm.

Straight tracks from proton-proton collisions with zero magnetic field are used to determine the initial alignment.[2)] Due to the magnetic field and temperature excursions, the station position may vary. We built Optical Alignment System (OASys) to monitor the time dependence of the position. Straight tracks can provide the initial alignment while the OASys gives deviations versus time. A unit of the OASys consists of a light source at the first station, a focusing convex lens at the second station, and a CCD camera (640 × 480 pixels and each pixel size is 11.0 μm × 13.0 μm) at the third station. The latter monitors the spot image from the light source through the lenses. When the second station moves relative to the other stations, the image position on the CCD moves. Each octant has seven units, thus the total number of units per arm is 56. The images are captured by the computer through a video capture board and stored for analysis every one hour.

We operated the OASys on the south arm during the entire RUN 2 period which ran from August 1st 2001 to January 23rd 2002.

Two 1-dimensional histograms are obtained by projecting to the horizontal and vertical axes. Each histogram was fitted by the following function which has Gaussian and constant terms.

$$f(x) = Const + \alpha \cdot \exp\left(-\frac{(x - \langle x \rangle)^2}{2\sigma^2}\right),$$

where $\langle x \rangle$ and σ represent the center position and the width of the focused image, respectively. In addition, *Const* and α are free parameters for the fit.

All of the fit results were examined. The failed fits were rejected based on the following.

(1) Standard deviations and average values of each fit parameter over the entire period were calculated. If the value for any fit exceeded a standard deviation of more than five from the average, this fit result was removed from the data set.
(2) The above process was then repeated until all data satisfy the five-standard deviation cut.

The reasons for the failures will be described later.

We analyzed the remaining data to monitor the time dependent movement among the stations. All movements among the three stations can approximately be considered as the result of a displacement of the second station from the viewpoint of the momentum measurement.

Figure 1 shows a correlation between displacement and temperature. The thermometer was placed on the middle of the second station support structure which is close to the chamber surface. The temperature showed gradual changes between day and night in a one day periods. The displacement shared the following behavior. The size of the displacement was about 35 μm per 0.5°C temperature change. This value is fairly close to the G10 thermal expansion value.

Figure 2 shows the displacement when the magnetic field was turned on and that when it was turned off. When the magnet was turned on, the station displacement was about 100 μm. When turned off, the station position was restored to almost its original position within the variations due to temperature excursions.

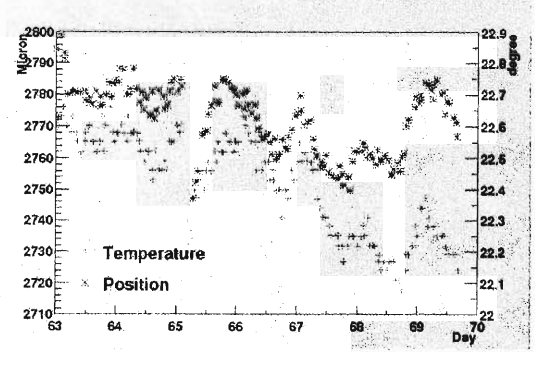

Fig. 1. The correlation between displacement and temperature. The star-shaped dots and cross-shaped dots are the fitted positions and temperature, respectively.

*1 Tokyo Institute of Technology
*2 Department of Physics, New Mexico State University, USA
*3 Los Alamos National Laboratory, USA

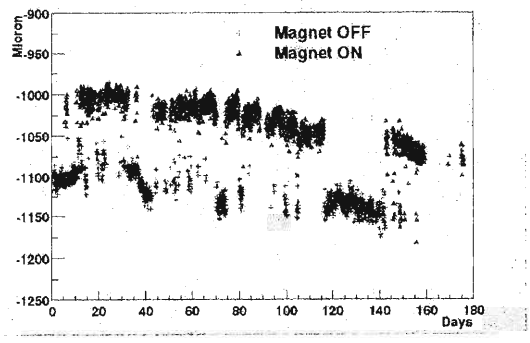

Fig. 2. The station displacement when the magnetic field is on and that when it is off. The cross-shaped dots and triangular-shaped dots are the data when the muon magnet of the south arm was off and on, respectively. There was about a 100 μm displacement when the muon magnet condition was changed.

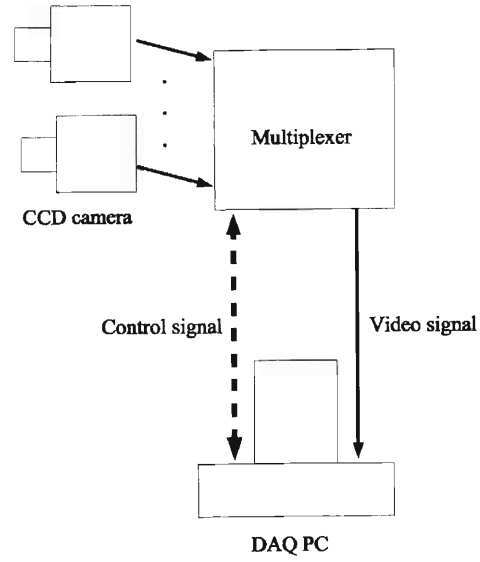

Fig. 3. The schematic of the data acquisition system.

We can obtain the chamber movement. But the implementation of the analysis code to include this movement is in progress.

We found eight units that moved more than 500 μm during the RUN 2 period. These motions came from mechanical problems. The lenses were glued on the mounting brackets and the CCD cameras were fixed to camera blocks by two screws. These eight problematic units mechanically moved in their mounting fixtures. For the next run we decided to improve the mounting scheme for all south and north units. All the lenses were fixed by a screw and the cameras were fixed by four screws.

The OASys for the north arm was newly constructed along with the entire north MuTr detector system. Dedicated convex lenses with suitable focal length were used for the north arm in order to obtain sharper images.

The video signals from each unit were multiplexed by a Keithly Model 7001 multiplexer and fed to the video capture board on a PC. Each arm has one multiplexer and one PC. The camera and the multiplexer are located near the detector and the PC is located in the counting house. Figure 3 shows the schematic of the data acquisition system.

The video signal line was isolated by using an optical transmitter, fiber and receiver, in order to eliminate a potential ground loop between the PHENIX detector and counting house. A dedicated TTL line was used to synchronize multiplexing and video capturing during RUN 2, but there was no confirmation of the switch to the next unit after sending this synchronizing signal. This system eventually failed and the associated data could not be analyzed correctly. Therefore, after RUN 2, GPIB interfaces were also installed to control the multiplexers. Software switches the multiplexer to the next camera, and confirms the status of the multiplexer. Then it takes the video image from video capture board. The image files are then sent to a LINUX PC for each of the two arms, and analyzed by the ROOT framework.[3] Analysis of the data for all the 56 cameras takes 15 minutes.

The OASys for both arms is now ready for RUN 3.

References

1) J. Murata et al.: RIKEN Accel. Prog. Rep. **33**, 165 (2000).
2) H. Kobayashi et al.: RIKEN Accel. Prog. Rep. **35**, 232 (2002).
3) http://root.cern.ch/

South muon arm operation in 2001/2 and north muon arm construction

D. E. Fields*

Muons are an important physics probe for both the heavy-ion physics program (focusing on the generation, detection, and subsequent characterization of the quark-gluon plasma (QGP)) and the spin physics program (measuring the helicity distributions of flavor-separated quarks and antiquarks, as well as the first *direct* measurement of the gluon polarization in the nucleon). For these purposes, the most interesting muons originate from vector meson (J/Ψ, Y, *etc.*) decays, Drell-Yan decays, W-decay, and heavy flavor (c and b) meson decays. PHENIX has implemented a two-arm (North and South) muon spectrometer at high rapidity to supplement the photon, electron and hadron identification at mid-rapidity. More details and current information on the PHENIX experiment can be found in Ref. 1, a concise recent summary of the planned RHIC spin program can be found in Ref. 2, and a detailed description of the muon spectrometer design can be found in Ref. 3.

The South Muon Arm was completed in the spring of 2000, and operated well during Run-02 for RHIC where the first 200 GeV Au-Au and 200 GeV $\vec{p}$-$\vec{p}$ data were recorded. For the Au-Au portion of the run, PHENIX recorded a total luminosity of $24\,\mathrm{mb}^{-1}$. Preliminary analysis of this data showed a low track-finding efficiency due primarily to the high multiplicity in the heavy-ion collision environment. Intense software and alignment work has been ongoing, much of which involves first looking at the relatively low multiplicity environment of the p-p data. During the p-p part of RHIC Run-02, RHIC delivered $700\,\mathrm{nb}^{-1}$ to PHENIX, which, after a relatively restrictive vertex cut, left PHENIX with $150\,\mathrm{nb}^{-1}$ of data to analyze. Preliminary analysis of this data clearly shows a J/Ψ peak at the correct di-muon invariant mass (Fig. 1). Details of this analysis can be found in Ref. 4. Additional analysis on the single muon spectra as a function of vertex position (and hence decay length before the absorber) shows agreement with Monte Carlo simulations.

The South Muon Arm chambers had some high voltage (frequent tripping on some channels) and electronics read-out (unresponsive channels) problems during Run-02. During the post-run shutdown, the South Arm was partially disassembled in order to gain access for repairs. This represented a monumental effort by the Muon Arm collaboration, who was simultaneously installing the North Muon Arm chambers and electronics. As of this writing, the South Arm high-voltage is functional at the 90% level, and the read-out is fully functional.

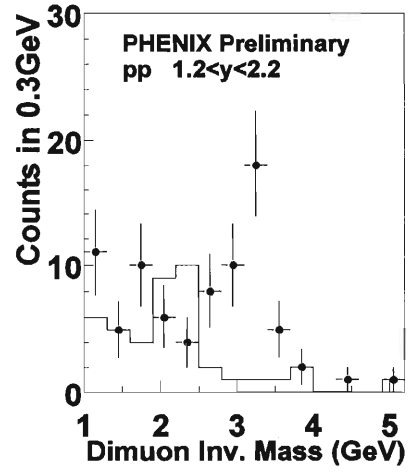

Fig. 1. Minbias pp muon invariant mass spectrum (points), with unlike-sign pair background (histogram).

The North Muon Arm chambers were completed in the spring of 2002. In October, all chambers, read-out electronics and alignment systems were functional and ready for RHIC Run-03 operation. This second arm will more than double the acceptance for high transverse momentum muon pairs.

References

1) http://www.phenix.bnl.gov
2) G. Bunce et al.: hep-ph/0007218.
3) PHENIX-NIM: Accepted for publication in Nucl. Instrum. Methods Phys. Res. A Special Issue.
4) A. D. Frawley: nucl-ex/0210013.

* University of New Mexico, USA

EMCal-RICH level-1 trigger performance at PHENIX RUN2

K. Okada, A. Bazilevsky, B. Fox, Y. Goto, M. Grosse Perdekamp, H. Torii,*1 and W. Xie*2

In particle physics, electrons and photons are important probes since they appear without affecting strong interactions. Leading hadrons also provide us with information on the initial stage of parton collisions. For example in spin physics, we expect the polarized gluon signal on the double-spin asymmetry of the direct photon yield and the hadron yield. π^0 and $\pi^{\pm}$ would have different effects because of the polarization of the target quark. Electrons will be used for tagging heavy particles such as charm, beauty and W-boson. W-bosons can distinguish between collided quark species. For these purposes, an electro-magnetic calorimeter (EMCal) and a Ring Image Cherenkov Counter (RICH) level-1 trigger (ERT) have been installed in PHENIX during the RUN2 proton run (2001-02). The PHENIX detector[1] is one of the detectors at the Relativistic Heavy Ion Collider (RHIC) at Brookhaven National Laboratory (BNL).

In EMCal, an energy threshold was set as a trigger unit. There are two kinds of trigger units, one fabricated from 4 PMTs (2 × 2) which covers an area of about $10 \times 10\,[\mathrm{cm}^2]$ perpendicular to the particle direction, and the other fabricated from 16 PMTs (4 × 4). 36 trigger signals made up one trigger module which was called Super Module (SM). EMCal consists of 172 SMs. RICH was also segmented in 256 trigger modules. Each module has a threshold on the number of photo-electrons. The coincidence between EMCal and RICH granules is used for electron trigger. Photons and hadrons are collected using EMCal.

There are two check points on the performance. One is the live channel ratio and the other is the trigger turn-on curve. The dead trigger tiles directly introduce the acceptance reduction. The lower tail of the trigger turn-on curve limits the rejection power, because the number of particles increases exponentially in the low-energy region.

The RICH live channel ratio was 15% in RUN2. EMCal performance will be described here. Most dead channels were due to the mask of hot channels. If a noisy trigger tile existed in a SM, we had to mask this SM which corresponds to 36 trigger tiles. The ratio of masked channels was about 30%.

The width of the trigger turn-on curve was determined by both the gain variance of the photomultipliers and the noise (or mistuning) of the trigger circuit. The gain variance was extracted from the calibration parameters, which was 18% for the lead-scintillator-type (PbSc) and 11% for the lead-glass-type (PbGl). By plotting the trigger turn-on curve on the ADC value, we can extract the trigger circuit noise (or mistuning) effect (Fig. 1). From the comparison with the gain variance, we can conclude that trigger circuit noise (or mistuning) is the dominant contribution to the turn-on curve width in the 4 × 4 triggers, and the two sources are comparable in the 2 × 2 trigger.

The 2 × 2 trigger had rejection powers of 15 with a threshold of 0.4 GeV per trigger unit and 90 with a threshold of 0.8 GeV per trigger unit. The 4 × 4 trigger had a rejection power of 600 with threshold of 2.1 GeV per trigger unit. The estimation of the rejection power based on the PYTHIA event generator[2] and GEANT[3]-based simulation with a sharp turn-on curve agrees with results for the 2 × 2 trigger, while the rejection power of the 4 × 4 trigger is low because of the dull turn-on curve.

We got much gain in the physics results with EMCal 2 × 2 triggered events. J/ψ cross sections at mid-rapidity were obtained, π^0 transverse momentum spectra reached about $12\,\mathrm{GeV}/c$ and the yield of charged hadrons increased by a factor of 20.

The ERT will play a more important role in future high-luminosity runs (which needs more rejection powers). We already fixed the problems of RICH trigger tiles and the tuning of EMCal is going on both in the live channel ratio and the turn-on curve. The coincidence between RICH and EMCal trigger granules will be functioned for electrons.

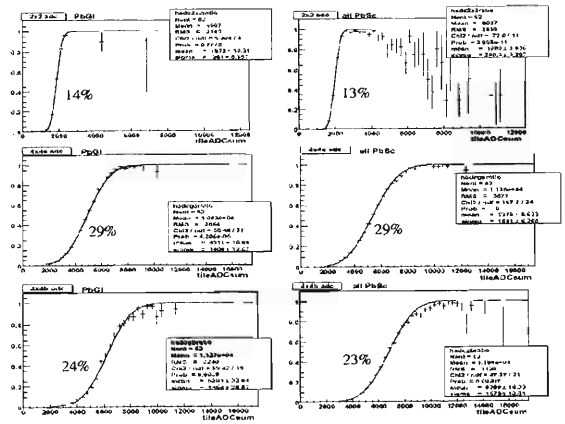

Fig. 1. ERT turn-on curve with ADC value. (left) Lead-glass-type (right) Lead-scintillator-type. (top) 2 × 2 (middle) 4 × 4a (bottom) 4 × 4b.

*1 Kyoto University
*2 University of California, USA

References

1) D. P. Morrison et al.: Nucl. Phys. A **638**, 565c (1998).
2) T. Sjöstrand: Comput. Phys. Commun. **82**, 74 (1994).
3) CERN Program Library Long Writeup W5013 (1993).

Overview and physics of PHENIX silicon upgrades

Y. Goto, H. En'yo, J. M. Heuser, T. Kawabata,[*1] Z. Li,[*2] H. Ohnishi, V. Radeka,[*2] V. L. Rykov, K. Tanida, and J. Tojo

We started a project to develop silicon detectors for precise vertex finding and tracking. The goal of this project is to build a silicon vertex tracker subsystem for the PHENIX detector upgrade.

A strawman design of the silicon detector at PHENIX consists of barrel detectors and endcap detectors as shown in Table 1. The barrel part has four layers and covers pseudorapidity, $|\eta| < 1$, and almost full azimuthal angle. The endcap part is designed to match with the muon arms which cover $1.2 < |\eta| < 2.4$.

We have been considering the design of the detector to maximize our capability in both the spin physics and the heavy-ion physics at PHENIX. The momentum resolution and displaced vertex resolution of the detector are required to be sufficient for our physics scope as follows.

For the spin physics, the gluon polarization measurement[1)] is a major topic. The prompt photon is one of the most clear signals of the gluon polarization. The silicon tracker enables us to detect the jet at the opposite side of the photon to reconstruct the kinematics. For this purpose, the design covers wide pseudorapidity and azimuthal angle, and has a good jet axis direction resolution. Figure 1 shows the simulated momentum resolution of the barrel detector with various detector configurations.

The heavy-flavor measurement is also sensitive to the gluon polarization. The silicon tracker enables us to identify the bottom quark by detecting the displaced decay vertex. Figure 2 shows the simulated vertex resolution of the endcap detector, which shows the z-vertex resolution of 190 μm. This performance is sufficient to clearly identify J/ψ from B-meson decay.

For this upgrade, we are developing strip sensor chips,[2)] pixel detectors,[3)] and mechanical structures.

Table 1. Strawman layout of the silicon detector at PHENIX.

part	detector	position	#channel
barrel-1	pixel	$r = 2$ cm, $\|z\| < 15$ cm	1.3 M
barrel-2	strip	$r = 6$ cm, $\|z\| < 15$ cm	90 K
barrel-3	strip	$r = 8$ cm, $\|z\| < 15$ cm	120 K
barrel-4	strip	$r = 10$ cm, $\|z\| < 15$ cm	150 K
endcap-1	pixel	$2.5 < r < 18$ cm, $\|z\| = 20$ cm	250 K
endcap-2	pixel	$2.5 < r < 18$ cm, $\|z\| = 26$ cm	250 K
endcap-3	pixel	$2.5 < r < 18$ cm, $\|z\| = 32$ cm	250 K
endcap-4	pixel	$2.5 < r < 18$ cm, $\|z\| = 38$ cm	250 K

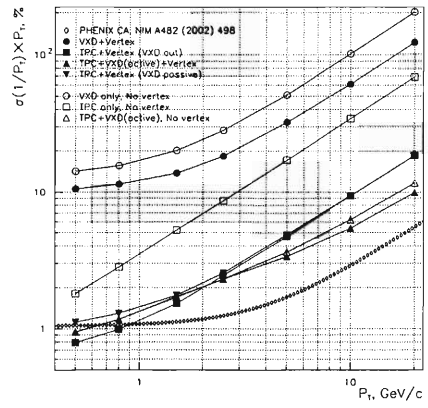

Fig. 1. Simulated momentum resolution of the barrel detector.

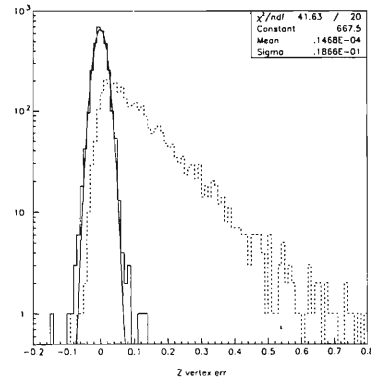

Fig. 2. Simulated z-vertex distribution for J/ψ from B-meson decay (solid line) and vertex resolution (dashed line) reconstructed for the endcap detector.

In addition, electronics to readout signals and an interface with the PHENIX DAQ system are other large elements of the development.

References

1) A. Bazilevsky et al.: RIKEN Accel. Prog. Rep. **34**, 243 (2001); H. D. Sato et al.: RIKEN Accel. Prog. Rep. **34**, 244 (2001).
2) Z. Li et al.: RIKEN Accel. Prog. Rep. **36**, 250 (2003); J. Tojo et al.: RIKEN Accel. Prog. Rep. **36**, 252 (2003).
3) J. M. Heuser et al.: RIKEN Accel. Prog. Rep. **36**, 253 (2003); H. Ohnishi: RIKEN Accel. Prog. Rep. **36**, 254 (2003).

*1 Center for Nuclear Study, University of Tokyo
*2 Brookhaven National Laboratory, USA

Novel silicon strip detector for the PHENIX upgrade†

Z. Li,*1 H. En'yo, Y. Goto, V. Radeka,*1 T. Kawabata,*2 V. L. Rykov, K. Tanida, and J. Tojo

A novel strip detector developed at BNL has been applied in the development of a prototype Si strip detector for the PHENIX upgrade at RHIC. This novel detector type can generate X-Y two-dimensional position sensitivity with single-sided processing and readout. The prototype Si strip detector has an active area of about 3 cm×6 cm, which is divided into two identical halves. Both X and Y pitches are 80 μm, with a stereo angle of 4.6°. There are 384 X strips and 384 Y strips on each half of the detector. The first batch of prototype Si strip detectors has been produced at BNL. The initial tests of detector electrical properties have yielded satisfactory results. Charge collection tests on test-structure strip detectors have shown both X and Y position sensitivities to laser light.

The schematic of the prototype Si strip detector for the PHENIX upgrade is shown in Fig. 1.

The chip size is 3 cm × 6 cm, and the detector is divided into two identical halves. In the left half, there are 384 Y strips with 80 μm pitch and bonding pads for readout on the left side and there are 384 X strips with 80 μm pitch and bonding pads for readout in the middle of the wafer. The stereo angle between the X and Y strips is about 4.6°. The right half is a mirror copy of the left one with respect to the middle line of the detector chip. Using BNL's novel detector structure,[1)] both the X and Y strips can be read out from the same side of the wafer.

Figure 2 shows the ACAD design layout of the mask set for the prototype Si strip detector to be processed on 4"-diameter Si wafers. The mask set has five layers, with each layer representing one mask lithography step. There are two detector chips on each wafer, which are denoted A and B for detector chip #1, and C and D for detector chip #2. On the same wafer, there

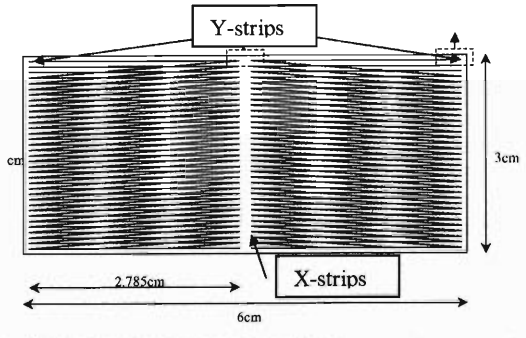

Fig. 1. Schematic of the prototype Si strip detector for the PHENIX upgrade.

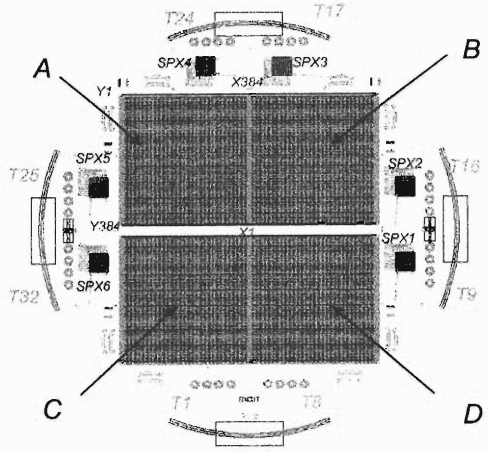

Fig. 2. Mask design layout for the prototype Si strip detectors.

are also many test structures: 1) there are 32 circular test diodes (T1 to T32) of 2 mm diameter, used for testing the wafer processing quality; 2) there are six test strip detectors (SPX1 to SPX6) with a similar strip design for that of the prototype but a much smaller area (about 16 mm^2) and strip number (14), used to test the X-Y sensitivity with a laser testing system; and 3) there are a number of resistor-type test structures used for testing the contact qualities between different metal contacts.

Prototype detectors have been processed on 4"-diameter high-resistivity (4–6 kΩ-cm) Si wafers with thicknesses of 400 μm and 250 μm. The processing is a single-sided process with five mask steps. The detector structure is of $p^+/n/n^+$ diode configuration. The main difference between this novel process and the conventional single-sided strip detector process is the addition of a second metal process (double-metal process) to the detector fabrication. The second metal is used to connect the Y strips (with the first metal connecting the X strips). The two metals, which are both Al in our case, are separated by a polyamide layer of 2–4 μm.

The fabrication of the first prototype batch of four 400 μm wafers was completed in May 2002.

Figure 3 shows details of the detector near the Y-strip bonding pad area, where the bonding pads, guard rings (2), and Al lines for the X-strip and Y-strip are clearly seen. Details of the middle area between area A and B, where the bonding pads of X-strips in both areas are located, are shown in Fig. 4. In Fig. 4, in addition to the bonding pads for the X-strips, the Al lines for the X-strips and the guard ring (one in each area) can be clearly seen.

The second prototype Si strip detectors fabricated on 250-μm-thick Si wafers were completed in October

† This research was supported in part by the U.S. Department of Energy: Contract No. DE-Ac02-98CH10886
*1 Brookhaven National Laboratory, USA
*2 Center for Nuclear Study, University of Tokyo

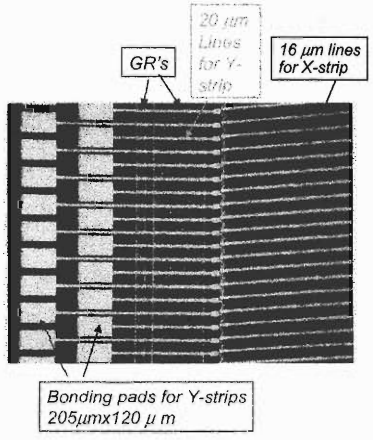

Fig. 3. Photograph of the first batch prototype Si strip detectors: area near the Y-strip bonding pads.

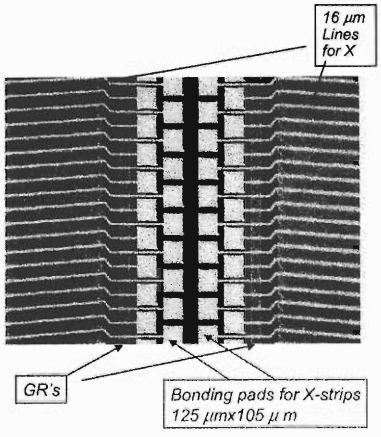

Fig. 4. Photograph of the first batch prototype Si strip detectors: area near the X-strip bonding pads.

2002. Similar results to those measured in the first batch of detectors have been obtained from electrical measurements on this batch of detectors.

Systematic electrical tests have been performed on all structures, the test diodes, the test resistors, the test strip detectors, and prototype strip detectors, on the wafers. I-V tests have been conducted on the test resistors with results showing very good contacts between the first and second Al layers, as well as good continuity of the Al strip over the SiO_2 steps and polyamide steps that can be as high as 4 μm. Both I-V and C-V tests have been carried out on all other structures to check the leakage current, full depletion voltage, and the capacitance at full depletion.

Both I-V and C-V characteristics of single strips have been measured on prototype strip detectors, without grounding the neighboring strips. The strip current stays at 2–3 nA up to 400 volts (Fig. 5). The C-V characteristic of the same strip is shown in Fig. 6. The full depletion is reached at about 80 volts when the capacitance becomes flat. The strip capacitance

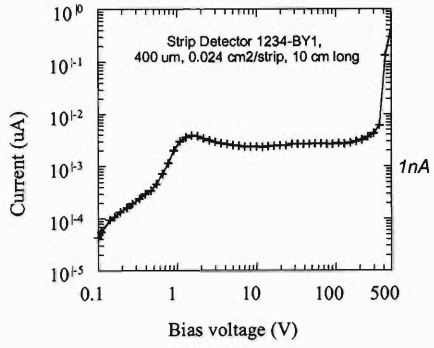

Fig. 5. I-V characteristic of a single, typical strip on a prototype strip detectors.

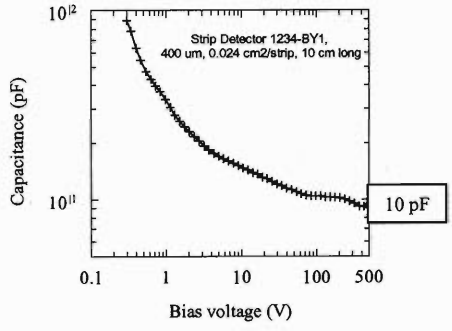

Fig. 6. C-V characteristic of a single, typical strip on a prototype strip detectors.

at full depletion is about 10 pF. Although the novel strip detector has a higher strip capacitance than a conventional strip detector with the same strip area and length, the measured strip capacitance may be an overestimation of the real strip capacitance since none of its neighboring strips are grounded during the measurements. The same can be true also for the strip current due to the fact that the neighboring strips are grounded during the I-V measurements. The actual leakage current of a single strip may therefore be lower than the measured value shown in Fig. 5 and Fig. 6.

Test strip detectors (SPX#, as shown in Fig. 2) have been tested on the charge collection property and position sensitivity using a setup called the Transient Current Technique (TCT) with a red laser to generate free carriers. The laser spot is 500 μm, slightly smaller than the pitch (560 μm) of the test strip detector.

Signals from both the X-strip and Y-strip can be detected, giving a two-dimensional position sensitivity.

Two batches of prototype Si strip detectors for the PHENIX upgrade have been produced using BNL's novel detector structure. Charge collection measurements, using TCT and a red laser, have demonstrated that two-dimensional position sensitivity can be obtained.

References

1) Z. Li: BNL Internal Report, BNL Rep. No. 67527 (2000).

Development of silicon strip telescope for PHENIX upgrade

J. Tojo, H. En'yo, Y. Goto, J. M. Heuser, Z. Li,[*1] H. Ohnishi, V. L. Rykov, N. Saito,[*2] F. Sakuma,[*2] M. Sekimoto,[*3] K. Tanida, M. Togawa,[*2] and Y. Watanabe

The PHENIX experiment at Relativistic Heavy Ion Collider (RHIC) in Brookhaven National Laboratory (BNL) has shown the capability of the baseline detector system for both spin physics and heavy ion physics since its operation started in 2000. To enhance its physics capability, upgrades of the PHENIX detector system have been proposed. One of the major upgrades is to develop a silicon vertex tracker in the inner region of the detector system.[1] We developed a silicon strip detector as a candidate for two or three outer layers in the barrel part of the silicon vertex tracker.

A single-sided silicon strip sensor with a two-dimensional readout capability was newly developed.[2] The sensor has a $p^+/n/n^+$ diode structure with two sets of aluminum readout strips with a pitch of 80 μm and a stereo angle of 4.6°. The active area is 3 cm × 6 cm. Two models of the sensor with thicknesses of 400 μm and 250 μm were fabricated and applied to the silicon strip detector.

The silicon strip detector was designed to read out a half of the sensor to evaluate the detector performance. Figure 1 shows a picture of the detector. The detector consisted of the sensor, six analog readout chips, a base board, a fanout board and two SMT boards.

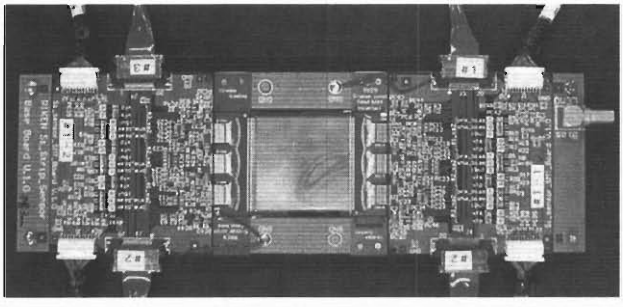

Fig. 1. A picture of the silicon strip detector.

The sensor was mounted on the base board made of BT Regin with a thickness of 1650 μm for the 400 μm sensor or 1570 μm for the 250 μm sensor. A part of the sensor back plane was glued with a conductive epoxy (Loctite 3888) to one of layers of the base board to apply a bias voltage. The sensor was wire-bonded to the fanout board with aluminum wires (30 μm in diameter). The fanout board was made of BT Regin with a thickness of 190 μm. It was designed to electrically connect the sensor and the readout chips with a gold wire (23 μm in diameter) by matching the difference between the pitch of the sensor (80 μm) and that of the readout chip (45.6 μm). The VA2 chip[3] was used to read out a signal from the sensor. The chip is a type of analog multiplexor with 128-channel charge sensitive preamplifier-shaper circuit. The preamplifier has a 1–3 μm peaking time and a nominal gain of 30 mV/pC. Three VA2 chips were wire-bonded to the four-layer SMT board with the thickness of 610 μm with aluminum wires (30 μm in diameter). The SMT board was designed to operate the VA2 chips and read out multiplexed analog signals through an interface with a VME data acquisition system.

The detector is being bench-tested with cosmic rays and a radioactive source. A beam test at KEK-PS is planned to evaluate the detector performance particularly for position resolution, detection efficiency and two-hit separation efficiency dependent on the bias voltage applied to the sensor and the incident angle of charged particles. A telescope of seven silicon strip detectors will be constructed for the beam test.

References

1) Y. Goto et al.: RIKEN Accel. Prog. Rep. **36**, 249 (2003).
2) Z. Li et al.: RIKEN Accel. Prog. Rep. **36**, 250 (2003).
3) http://www.ideas.no/

*1 Brookhaven National Laboratory, USA
*2 Department of Physics, Kyoto University
*3 High Energy Accelerator Research Organization (KEK)

Progress with the NA60 pixel detector telescope

J. M. Heuser, for the PHENIX/NA60/ALICE Collaboration

The NA60[1] collaboration constructs a vertex spectrometer that comprises a silicon pixel detector[2] technology developed at CERN for an upcoming application in the inner tracking system of the ALICE[3] experiment at CERN's Large Hadron Collider. The vertex spectrometer augments the di-muon spectrometer previously used in the NA50 experiment at CERN's Super Proton Synchrotron and enables the measurement of prompt di-muon and charm production with proton and heavy-ion beams in a fixed target environment.

In ultra relativistic heavy-ion collisions above a critical temperature or density, a phase transition is expected to occur from a confined hadronic matter to a deconfined partonic system. The observed centrality-dependent suppression pattern of charmonia states (J/Ψ, χ_c, Ψ') provides a signal for the onset of color deconfinement. Also, the measured enhancement of intermediate mass (1–3 GeV/c^2) di-lepton production is compatible with the formation of a quark gluon plasma phase. Thermal di-leptons from electromagnetic radiation emitted by free quarks are a direct evidence for a deconfined phase in thermal equilibrium. The measurement of muon track offsets in the NA60 pixel detector vertex spectrometer will, for the first time, allow us to distinguish between thermal radiation and other mechanisms as a cause of the intermediate mass di-muon excess.

The NA60 silicon pixel tracking telescope (see Fig. 1) will be located in a 2.5 T dipole magnet between the target and the muon spectrometer. The full tracking telescope comprises 16 detector planes between 7 and 35 cm downstream of the target. Its angular acceptance $3 < \eta < 4$ matches the muon spectrometer. This allows the first six planes to cover a smaller area than the last eight planes. A detector plane consists of several single-chip pixel detector assemblies mounted on a thick-film bus on a planar ceramic support. An assembly is made of an ALICE1LHCb[4] front-end chip, containing nearly 8 200 pixels of $50 \times 425\,\mu$m^2 size, bump-bonded to a sensor chip of a matching design. The 10 planes close to the target comprise four assemblies, the six planes further downstream are built from eight assemblies. The ceramic support itself is glued and wire-bonded onto a printed circuit board that provides mechanical support when mounted in a support box and routes all signals between the front-end electronics and the data acquisition and control systems. A water cooling structure is attached to the ceramics to remove about 1 W per chip and to keep the detectors at an operating temperature of about 20°C. The full NA60 pixel detector telescope comprises 88 detector assemblies with a total of about 720 000 pixel cells.

Fig. 1. The NA60 silicon pixel tracking telescope comprises 16 detector planes (10 small, 6 large) between 7 and 35 cm downstream of the target (seen on the left).

The first detector plane was constructed in spring of 2002 and successfully operated in a microstrip detector telescope during a run with 400 GeV/c protons in June 2002.[5–7] Three detector planes were available for a run with 20 and 30 AGeV/c Pb ion beams in October 2002, preparing the experiment for the physics runs in 2003 with the expected full telescope. Figure 2 shows beam profiles in those pixel detector arrays.

Besides the interest in the physics that will be accessible with this device, the RIKEN group gains experience with the CERN pixel detector technology in NA60 and aims in collaboration with ALICE at its application in a vertex spectrometer upgrade of the PHENIX experiment at BNL's Relativistic Heavy Ion Collider.

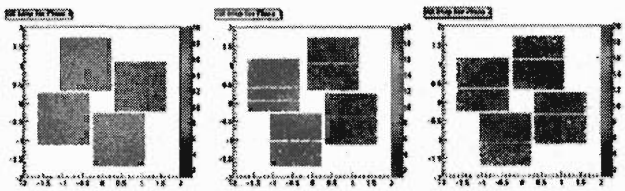

Fig. 2. Pb-ion beam profiles in the first three constructed pixel detector planes (October 2002).

References

1) NA60 Collaboration: SPSC/P316, 7 March 2000.
2) E. H. M. Heijne: Nucl. Instrum. Methods Phys. Res. A **465**, 1 (2001).
3) ALICE Collaboration: CERN/LHCC 99-12, 18 June 1999.
4) W. Snoeys et al.: Nucl. Instrum. Methods Phys. Res. A **465**, 176 (2001).
5) NA60 Collaboration: CERN/SPSC 2002-009, SPSC/M679, 12 March 2002.
6) NA60 Collaboration: NA60 Note 2002-3, 11 March 2002.
7) NA60 Collaboration: CERN/SPSC 2002-024, SPSC-M-689, 15 May 2002 and CERN/SPSC 2002-025, SPSC-M-690, 12 July 2002; new memorandum in preparation.

Performance of the NA60 silicon pixel telescope

H. Ohnishi

Ultra relativistic heavy-ion collisions offer a unique opportunity of producing a highly condensed QCD matter, which may undergo a phase transition from a normal nuclear matter to a state of deconfined interacting partons. The observed J/ψ suppression pattern in high energy heavy-ion collisions at the CERN SPS seems to provide the first signal of color deconfinement through parton condensation. However, this observation does not imply that the produced deconfined system existed for a sarfficiently long period to reach thermalization, forming a Quark Gluon Plasma (QGP). The best signal that can be used to probe the temperature of the system is thermal dilepton production. However, this signal has not been clearly studied to date, due to experimental limitations. The observed enhancement of intermediate mass dimuons ($1.5 < M < 2.5\,\mathrm{GeV}$) in nuclear collisions could be due to the production of thermal dimuons, but other explanations are equally possible, like a bigger contribution from semileptonic decays of open charm mesons.

The NA60[1] experiment will measure the J/ψ suppression pattern in high energy In-In collisions. By comparing this new measurement to the pattern measured in Pb-Pb collisions, we should be able to determine the critical scale for the onset of deconfined parton condensation, and distinguish between a parton percolation transition (that should occur as a function of the number of nucleons participanting in the collision) and a thermal transition (that should depend on the reached local energy density). Moreover, NA60 is designed to measure muons arising from displaced positions with respect to the primary collision vertex, thereby identifying open charm meson decays and allowing a first clear measurement of the open charm production cross section in heavy ion collisions.

Past experiments have not been able to reveal open charm decays in heavy-ion collisions because the secondary vertices are immersed in very high particle densities and because charm production is a rare process, requiring high luminosity experiments, which have to cope with rather high levels of radiation damage. Recently, radiation-tolerant silicon pixel readout chips have been developed, opening the opportunity to measure secondary vertices in heavy-ion collisions. A detailed description of the NA60 silicon pixel detector is reported elsewhere.[2]

In October 2002 we performed a test experiment using beams of 20 and 30 GeV/nucleon Lead ions. In order to have their transverse coordinates measured, the incident Lead ions were passed through a radiation hard beam tracker, the beamscope, made of four silicon microstrip cryogenic detectors, operated at 130 K. Then, the beam particles went through three lead targets of 1.5, 1.0 and 0.5 mm thickness. Three planes of silicon pixel detectors[1] were installed immediately behind the target box at 7.7, 10.1 and 13.1 cm from the centre of the target system. The noninteracting beam ions and the beam fragments were detected using a zero degree calorimeter (ZDC), allowing us to measure the collision centrality.

The run conditions were as follows. The beam intensity varied between $\sim 3\times10^4$ and $\sim 3\times10^5$ ions per burst, with a spill of 10 seconds. The triggers were generated by the ZDC; some runs with a beam trigger and some with an interaction trigger, which rejects events with a ZDC signal around the Pb ion peak, in order to increase the relative number of interactions written to tape. The trigger rate was generally between 2000 and 4000 triggers per burst, depending on the run.

Figure 1 (a) shows the distribution of the vertices reconstructed with the three pixel planes, in the beam axis. The three lead targets can be clearly observed. The small peak at -4 cm is caused by the reaction of lead ions in the exit window of the beam scope cryostat box. Figure 1 (b) shows the anti-correlation between the number of reconstructed tracks associated with the third target and the forward energy deposited in the ZDC. The detailed evaluation of the performance of the pixel planes is in progress.

In summary, three NA60 pixel detector planes were successfully constructed and operated in the experiment during the low energy lead ion run in October 2002. The detectors worked very well both in standalone and when fully integrated in the DAQ. The data analysis is in progress, while work is continuing to complete the full silicon pixel telescope for the physics run with indium beam in September-October 2003.

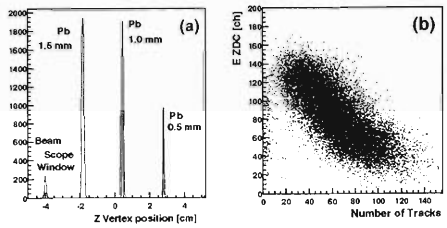

Fig. 1. (a) Z-vertex distribution reconstructed by three silicon pixel planes. (b) Correlation between energy deposit in ZDC and number of tracks.

References

1) NA60 Collaboration: SPSC/P316, 7 March 2000.
2) J. M. Heuser: RIKEN Accel. Prog. Rep. **36**, 253 (2003).

Superconducting snake for AGS

M. Okamura, T. Katayama, T. Tominaka, and T. Ohkawa

The AGS synchrotron at Brookhaven National Laboratory (USA) is equipped with a partial snake,[1] that helps in overcoming the imperfection resonances that appear during the acceleration of polarized protons. The existing partial snake is a solenoid magnet located in the C10 straight section of the AGS, with a field that rises at the same rate as that of the AGS main magnets. The longitudinal (Bz) component of the solenoidal partial snake introduces linear coupling of the transverse coordinates of the beam, and consequently additional intrinsic resonances which affect the final polarization of the beam. In order to reduce the coupling caused by the solenoid magnet, an alternative partial snake composed by a helical dipole magnet, has been proposed.[2] The basic structure is similar to that of RHIC snake magnets,[3] but more complicated. The desired rotation angle of spin is 30 degrees. To achieve high polarization in RHIC, overcoming intrinsic resonance in the AGS is indispensable.

A 3D view generated by OPERA-3D[4] is shown in Fig. 1. In order to increase the spin rotation angle in the limited space in AGS, the helix has dual pitches as shown in Fig. 2 and Table 1. Both sides of the magnet has a rapid pitch. The effective magnetic length is 2.028 m and the warm bore radius is 150 mm. The required magnetic field strength for the 30 degree spin rotation at $G_\gamma = 8.68$ beam is 3 T. Due to the use of a symmetric helical magnetic field, the overall beam deflection is canceled. The extracted beam is parallel to the injected beam, on a different line. This beam shift in the horizontal plane will be canceled by trim coils installed at the main dipole magnets of the AGS on both sides of the new AGS snake magnet. The structure of the magnet is complicated, so that 3D field analysis is needed. Figure 3 shows a cross-sectional view of the magnet. Each current block is supported by a machined cylinder made of aluminum or stainless steel, and has 12 by 9 cable layers. Only the top current block in the inner layer has 5 layers of cable windings. To induce a magnetic field of 3 T, 340 A of current is

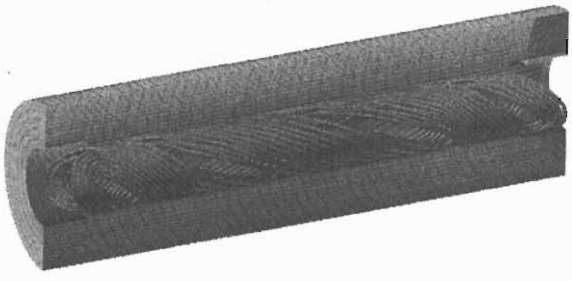

Fig. 1. 3D view of the partial helical snake.

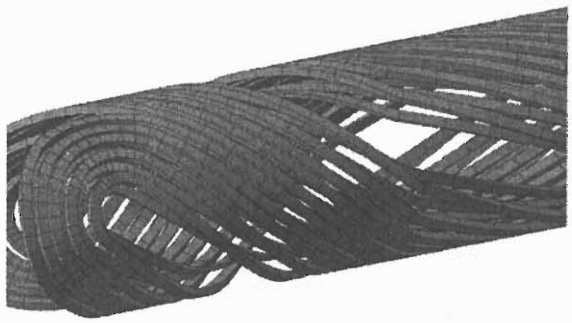

Fig. 2. Coil structure.

Table 1. Design parameters.

	Parameter	Value
Coils		
	Current density (A/mm^2)	567
	Operating current (A)	340
	Total turns	2064
	O.D. of Cable (mm) (6 around 1 type)	1.0
	Copper ratio	2.5
	Total turns	1728
	Inductance (H)	7.7
	Stored energy (MJ)	0.45
	Magnetic length (mm)	431, 1166, 431
	Total angle (degree)	180, 243.5, 180
	Helical pitch (deg./mm)	0.4176, 0.2088, 0.4176
Yoke		
	I.D. (mm)	300
	O.D. (mm)	740
	Length (mm)	24000
	Packing factor (%)	99

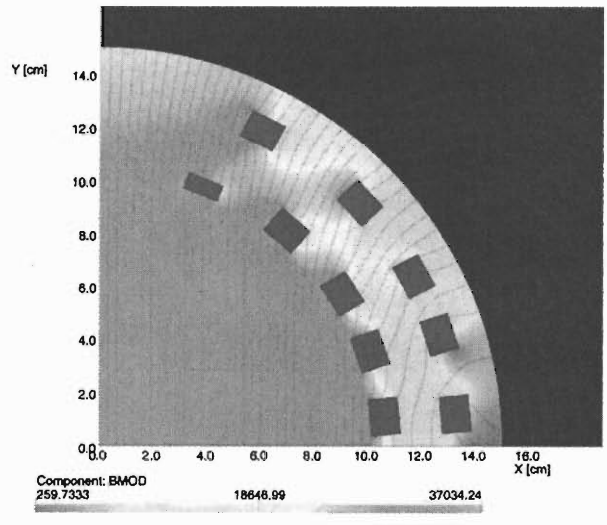

Fig. 3. Cross-sectional view of the helical snake.

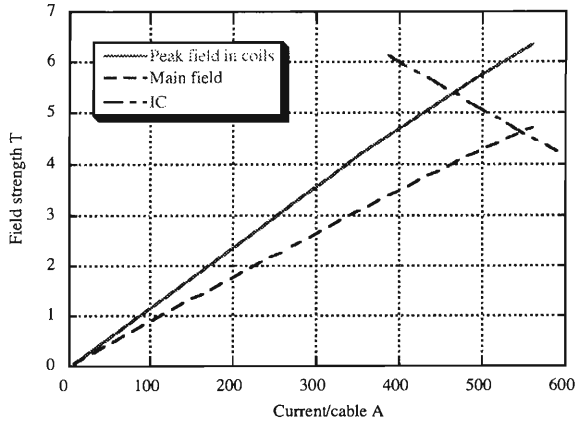

Fig. 4. Peak field and IC curve.

Table 2. Multipole components.

	2D	3D (azim.)	3D (vert.)
Dipole (T)	3.168	3.078	3.091
Sextupole/Dipole	5.6×10^{-4}	6.1×10^{-4}	-3.6×10^{-3}
Decapole/Dipole	-5.1×10^{-5}	-3.6×10^{-5}	-3.8×10^{-5}

Reference radius is set at 50 mm. All the values are based on normal components.

needed. Considering 3D effects, the length and outer diameter of the yoke were determined not to exceed 1.4 T of the field strength in the outer surface region. The field excitation curve predicted by 3D calculation is indicated in Fig. 4.

The field shape of the helical partial snake has unique distortions and then multipole components were computed using 2D and 3D codes. Table 2 shows results with the 2D and 3D calculation models. In 3D case, these values are obtained at the center of the magnet. The assumed current was 350 A/cable. Discrepancies between 2D analysis and 3D (azim.) analysis, derived from azimuthal field component expansion, are due to 3D effects. The magnetic field flux in the iron runs not only in the transverse plane but also in the longitudinal direction in the 3D structure and the saturated regions of the yoke are slightly different between the 2D and 3D cases. The vertical component of the field is not the same as that derived from an expansion of the azimuthal field component, due to the presence of a longitudinal field component in the magnet.[5] The field shape along the beam axis is shown in Fig. 5. The center of the magnet corresponds to $z = 0$. Major multipole components are indicated in

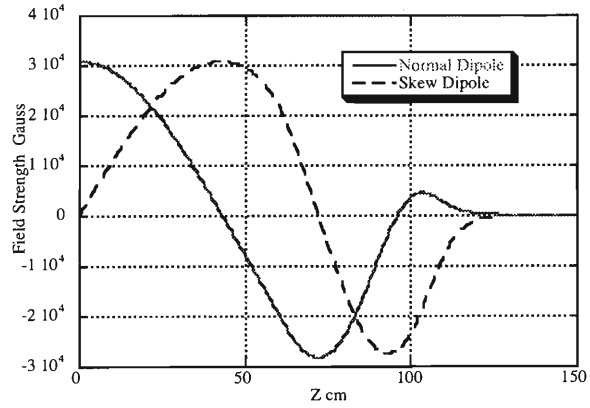

Fig. 5. Dipole component.

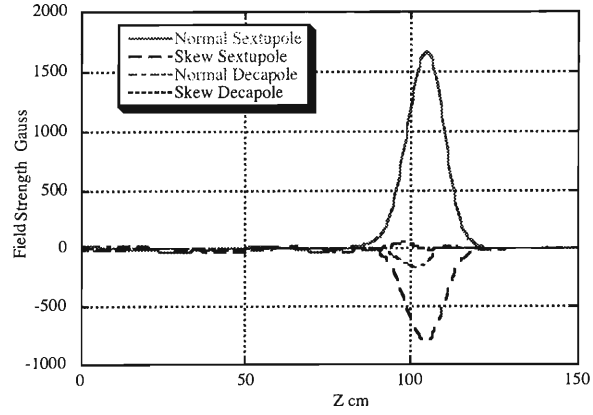

Fig. 6. Sextupole and decapole components.

Fig. 6. In the body of the magnet, these sextupole and decapole components are within ±23 gauss. In order to suppress the sextupole component in the end regions, a pair of additional correction sextupole windings will be designed based on results of magnetic field measurement performed at a test bench and installed. This magnet will be fabricated in 2003.

References

1) H. Huang et al.: Phys. Rev. Lett. **73**, 2982 (1994).
2) T. Roser et al.: AGS/RHIC/SN-72/BNL (1998).
3) M. Syphers et al.: Proc. PAC97, Vancouver, Canada, 1997-5 (IEEE, Piscataway, 1997), p. 3359.
4) Vector Fields Limited, Oxford, UK.
5) T. Tominaka et al.: Proc. PAC97, Vancouver, Canada 1997-5 (IEEE, Piscataway, 1997), p. 3437.

Cooling system study of AGS partial snake

M. Okamura, T. Katayama, T. Tominaka, and T. Ohkawa

A superconducting helical dipole magnet, which will help preserve the polarization of a proton beam in the Alternate Gradient Synchrotron (AGS), has been proposed. By replacing an existing solenoid-type Siberian Snake with a helical magnet, the strength of the remaining intrinsic resonances, which are due to transverse coupling, can be reduced. This magnet has a field of 3 T and an effective length of 2 m. The cooling system for this magnet is studied.

For cryostat cooling, three systems (conduction cooling, recondensation and pool cooling) were compared. We calculated the thermal load of the systems and estimated their annual costs. The comparison of the cooling systems is shown in Table 1.

The advantages and disadvantages of each system are summarized as follows.

(1) Conduction cooling

(advantages)

- There is no need for liquid helium.
- Running cost entails only the cost of required electricity to drive the cryocooler, thus annual cost is low.

(disadvantages)

- It takes about 175 days to cool the cold mass from room temperature (300 K) to 4.2 K.
- Even if the cold mass is precooled using liquid nitrogen, it takes about 60 days to cool the coil from 77 K to 4.2 K.
- If the stored energy, for example 0.45 MJ, is released in a quench, it takes about 5 days to recover the superconducting state.
- The cryocooler requires maintenance every 10,000 hours.

(2) LHe Re-condensation

(advantages)

- A liquid helium recondensation system provides long-run operation of equipment for the elimination of liquid helium evaporated from the cryostat.
- Running cost is only electricity to drive the cryocooler, so annual cost is low.

(disadvantages)

- About 5700 L of liquid helium is needed for the initial cooling.
- About 170 L of liquid helium evaporates if the stored energy, for example 0.45 MJ, is released in a quench.
- The cryocooler requires maintenance every 10,000 hours.
- Local backup systems for electricity and cooling water are needed.

(3) Pool cooling

(advantages)

- Highly reliable.
- Simplicity.

(disadvantages)

- Running cost is high.
- About 5700 L of liquid helium is needed for the

Table 1. Comparison of cooling systems.

Item		Unit	Conduction Cooling	LHe Recondensation	Pool Cooling
Thermal load	to 4 K	W	1.8	2.3	3.3
	to 20 K	W	11.8	11.8	–
	to 80 K	W	89	89	90
4 K Cryocooler	Refrigeration capacity	W	1.5 (4.2 K) 35 (50 K)	1.5 (4.2 K) 35 (50 K)	–
	Number		2	2	–
	Power requirement	kW/unit	6.5	6.5	–
Loss of LHe		L/h	–	–	4.6
Requirement of LHe for initial cooling		L	–	5700	5700
Initial cooling time	from 300 K to 4 K	day	175	10	10
	from 80 K to 4 K	day	60	5	5
Initial cost (cryocooler and LHe)		$1000s	154	179	90
Running cost		$1000s/year	43	43	150
Annual Cost		$1000s/year	58	60	159

initial cooling.

- About 170 L of liquid helium evaporates if the stored energy, for example 0.45 MJ, is released in aquench.

Conduction cooling systems present two serious problems. One is a very long initial cooling time, the other is a long quench recovery time. In conclusion, conduction cooling systems are not suitable for this cryostat. Both of the liquid helium recondensation system or the pool cooling system are acceptable. The evaporated volume of liquid helium at a coil quench is reduced by about one third if the coil is protected with an external resistor of 4 Ω. Even if the coil quenches three times a day, only 170 L of liquid helium in the reservoir tank evaporates and there is no need for additional liquid helium injection. From the point of view of reliability, a liquid helium recondensation system is slightly inferior to the pool cooling system, but its annual cost is lower. It seems reasonable to choose a liquid helium recondensation system for the cooling system of this cryostat.

Physics & status of the Electron Ion Collider

A. Deshpande, for the EIC Collaboration

Addition of a high-intensity highly polarized electron beam facility to the Relativistic Heavy-Ion Collider (RHIC) complex will significantly enhance RHIC's capability to study fundamental and universal aspects of QCD. We propose to build a $\approx 10\,\mathrm{GeV}$ polarized electron beam facility at BNL.[1] Collisions of such electrons with the heavy-ion beams of 100 GeV per nucleon energy will result in deep inelastic collisions with $\sqrt{s} \sim 63\,\mathrm{GeV}$. When collided with the polarized protons at 250 GeV in RHIC, this will result in a $\sqrt{s} = 100\,\mathrm{GeV}$ in CM energy for polarized DIS off protons. Furthermore, the luminosity planned for the EIC for e-p collisions is of the order of $10^{33}\,\mathrm{cm}^{-2}\,\mathrm{sec}^{-1}$ which is about 100 times more than the HERA luminosity after its planned luminosity upgrade. The CM energy *vs.* luminosity plot of past and future DIS facilities is plotted in Fig. 1.

The proposed electron beam facility is expected to deliver a highly polarized ($\sim$70%) electron beam. With the polarized proton beam already available at RHIC, one could perform polarized DIS with $\sqrt{s} \approx 100\,\mathrm{GeV}$.[1] The highest CM energy at which polarized DIS has been performed so far is $\approx 20\,\mathrm{GeV}$. As such, at EIC, one would be able to make the spin structure function measurements in a new low-x region which today remains completely unexplored. A comprehensive list of polarized DIS inclusive and semi-inclusive physics measurements that could be performed at EIC is given in Ref. 2. In addition to those, it is now clear, based on studies performed since then, that many more exclusive measurements could also be performed[1] with an appropriately designed detector integrated with the beam line design.

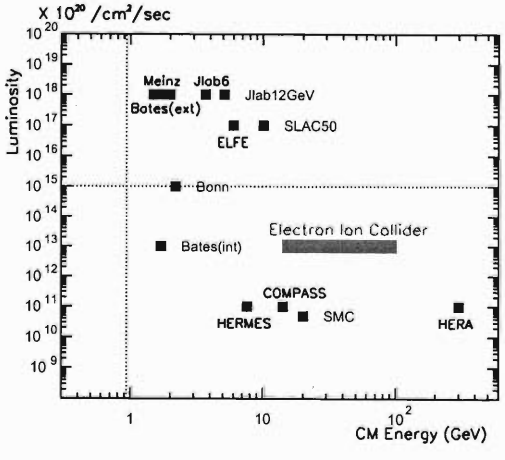

Fig. 1. The center of mass energy *vs.* the e-p luminosity plot for past and some future DIS facilities.

With the EIC, one can also perform unpolarized DIS using the heavy ions in RHIC. The most interesting kinematic region indicating unusual nuclear phenomena is at low x.[3] In the last decade, experiments at HERA have provided hints of saturation of unpolarized F_2 structure functions at low x. However, exploration of even higher gluonic density kinematics is necessary to confirm these observations. With EIC's lower CM energy, this is not possible with protons, however, one could use a heavy ion to enhance the gluon densities and expect to see saturation phenomena using the RHIC beams in e-A DIS. Experimental signatures for this kind of unusual phenomena have been predicted in various recent publications.[3] The EIC will be a unique place to study this physics in detail as a function of A (*e.g.* the atomic number) of the beam. Also, the variable energies for each nuclear beam will allow a study of the onset of saturation physics. Other unpolarized DIS phenomena which have been studied in the past in the fixed target environment have been mainly related to color transparency, EMC effect and other intermediate low-x related phenomena. These could also now be studied at EIC.

Various subgroups are now being formed to realize the EIC project and its physics.[4] The activities of the accelerator working group formed principally by the collaboration of MIT/Bates and BNL have resulted in a preliminary design for the electron ring that could realize the EIC at BNL. A small group of people met recently at BNL to discuss the electron beam polarimetry and its into the electron ring accelerator design. Physics groups have continued their activities in smaller subgroups and are expected to present their investigations at regular intervals. EIC collaborations meetings are presently planned at a frequency of once a year. The detector development activity is about to start. Integration of the detector with the accelerator lattice is one of the issues of particular interest to the EIC community because of the particular interest in low x physics and the demanding particle ID requirements posed by exclusive physics interests.[1,4]

References

1) A. Deshpande, R. Milner, and R. Venugopalan: BNL Internal Report, BNL Rep. No. 68933 (2002).
2) A. Deshpande et al.: RIKEN Accel. Prog. Rep. **34**, 251 (2001).
3) E. Iancu, A. Leonidov, and L. McLerran: hep-ph/0202270.
4) EIC Home Page: http://www.bnl.gov/eic

Fragmentation function analysis at Belle

K. Hasuko, M. Grosse Perdekamp,[*1] J. S. Lange,[*2] A. Ogawa,[*1] and V. Siegle[*1]

In the study of transverse spin phenomena, it is very interesting and important to understand the spin dependence in the fragmentation of a polarized quark. Particularly, nontrivial azimuthal angle asymmetries may arise from the non-perturbative dynamics in the fragmentation of a transversely polarized quark.[1] To extract these fragmentation functions, we became involved in the Belle collaboration (an e^+e^-collider experiment)[2] at the KEK B factory.[3] In addition to these new fragmentation functions being interesting, they can be a strong tool for accessing the quark transversity distributions in proton, δq, which are completely unknown and their knowledge is essential for a complete understanding of the nucleon structure.[4] We intend to study the following relevant fragmentation functions: the Collins-Heppelmann function $H_1^\perp$ and the hadron-pair interference fragmentation functions $\delta\hat{q}^{h_1,h_2}$.

Measurements of the Collins-Heppelmann function $H_1^\perp$ require two-jet events originating from light quarks and the azimuthal correlations of well-identified pions in each jet as shown in Fig. 1 (a).[5]

Another fragmentation function of interest, $\delta\hat{q}^{h_1,h_2}$, describes quark fragmentation to a $\pi^+\pi^-$pair active in the ρ-σ invariant mass region, where the s-waves and p-waves interfere with each other.[6] Due to the interference, the angle between the two planes defined by the two pion pairs, as shown in Fig. 1 (b), distributes proportionally to $f(z_{12}, m_{12}, Q^2) \times f(z_{34}, m_{34}, Q^2)$, where m_{12} and m_{34} are the invariant masses of the two pion pairs; z_{12} and z_{34} are the longitudinal momentum fractions of the pairs.[7]

This year we have studied the event topology of $e^+e^- \longrightarrow q\bar{q}$ in the continuum region 60 MeV below the Υ(4S) resonance. In Fig. 2 (a), we compare the distribution of the angles between two unlike-sign tracks using a sample of Belle data and Monte Carlo (MC) simulation. One can see a well-defined jet structure and a good agreement in the results between the use of Belle data and MC simulation. The jet axis can be defined by using the thrust axis, and three- or more-jet

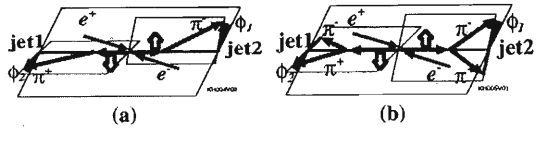

Fig. 1. Kinematics of (a) $e^+e^- \longrightarrow \pi^+_{jet1}\pi^-_{jet2}X$ and (b) $e^+e^- \longrightarrow (\pi^+\pi^-)_{jet1}(\pi^+\pi^-)_{jet2}X$.

*1 Brookhaven National Laboratory, USA
*2 University of Frankfurt, Germany

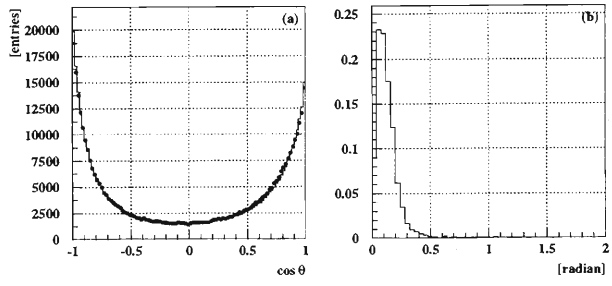

Fig. 2. (a) The distribution of the angle between two unlike-sign tracks from the Belle data (circle) and MC simulation (histogram). (b) The distribution of the angle between the thrust axis and the q ($\bar{q}$) direction with $T > 0.8$.

events are rejected by applying the thrust $T > 0.8$. After applying $T > 0.8$, the difference between the thrust axis and the initial q ($\bar{q}$) direction in MC is shown in Fig. 2 (b).

The essential experimental requirements for the fragmentation analysis are good particle identification in a wide momentum region and momentum resolution of about 100 MeV; these requirements are easily within the reach of the Belle detector.[2,8] The fragmentation functions scale as $\log Q^2$. Subsequently, analyzing powers at Belle (at Υ(4S), $Q^2 \approx 10^2\,\mathrm{GeV}^2$) are expected to be four times larger than ones at LEP (at Z^0, $Q^2 \approx 91^2\,\mathrm{GeV}^2$). By taking into account the difference in luminosity, the sensitivity $\Delta H_1^\perp / H_1^\perp$ will be higher by a factor of 20 at Belle than at LEP.

Analysis has started using 32 million $q\bar{q}$ off-resonance events in the Belle experiment. Significance in the testing asymmetries will be at the level of a few percent. First results are expected within one year.

References

1) J. C. Collins: Nucl. Phys. B **396**, 161 (1993); J. C. Collins, S. F. Heppelmann, and G. Ladinsky: Nucl. Phys. B **420**, 563 (1994).
2) Belle Collaboration, S. Mori et al.: Nucl. Instrum. Methods Phys. Res. A **479**, 117 (2002).
3) KEK B Factory Design Report, KEK Rep. 95-7 (1995) (unpublished).
4) M. Grosse Perdekamp, A. Ogawa, K. Hasuko, J. S. Lange, and V. Siegle: Nucl. Phys. A **711**, 69 (2002).
5) D. Boer, R. Jakob, and P.J. Mulders: Phys. Lett. B **424**, 143 (1998).
6) R. L. Jaffe et al.: Phys. Rev. Lett. **80**, 1166 (1998).
7) X. Artru and J. Collins: Z. Phys. C **69**, 277 (1996).
8) Belle Collaboration, A. Gordon et al.: Phys. Lett. B **542**, 183 (2002).

Development of SVD2.0 DAQ system for Belle

K. Hasuko

The Silicon Vertex Detector (SVD) plays an important role in the Belle experiment[1] at the KEK B factory.[2] Although the basic performance of current SVD is satisfactory,[3] further improvements in vertex resolution, acceptance and radiation tolerance will be achieved in the next version of SVD, SVD2.0, being installed in February 2003. The data acquisition (DAQ) system has been developed and first integration tests are in progress.

SVD2.0 consists of four concentric cylindrical layers ($2.2 < r < 8.0$ cm) of 216 double-side silicon strip detectors (DSSDs) with two orthogonal-coordinate readouts (100K channels in total). The polar angle coverage is extended to be the nominal angular coverage of Belle, $17 < \theta < 150$ degrees. The layers are formed with "ladders," each of which consists of DSSDs connected to aluminum nitride hybrids *via* kapton flex circuits. A picture of SVD2.0 is shown in Fig. 1.

Figure 2 shows a block diagram of the overall trigger and DAQ system. Signals from DSSDs are received with VA1TA chips mounted in hybrids. The VA1TA is a dedicated, radiation hard 128-channel chip, containing preamplifiers, shapers and track-and-hold circuits. In the track-to-hold mode, the analog signals are sequentially routed *via* a multiplexer and repeater system (REBO) to a system of fast analog-to-digital converters (FADCs) located in the electronics hut. The data are then sent to the DAQ system by triggers *via* a distributor system (TTM).

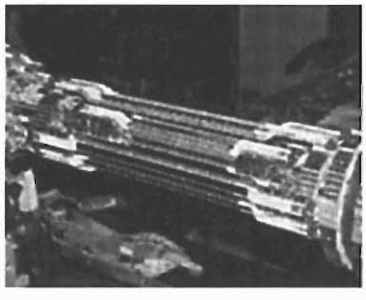

Fig. 1. Belle SVD2.0.

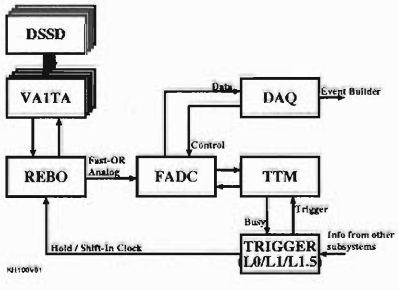

Fig. 2. Block diagram of SVD2.0 trigger/DAQ system.

For easier implementation, handling and maintenance, we have employed a DAQ scheme for SVD2.0 base on standard PCs, instead of Motorola DSPs on the FADC modules in the current version. The SVD2.0 DAQ system consists of PCs using PCI/32-bit LVDS[a] parallel interfaces. The PCI interface (P-PCI board) contains an ALTERA FPGA and external FIFO. The FPGA handles PCI/external buses and the FIFO. The external bus is a synchronous bus strobed by a clock signal, and connected with FADC output. The PCs receive event data from the FADC system, and perform data compression and formatting based on the following algorithm: 1) calculate pedestal, the common mode noise and S/N ratio from the noise, 2) find the cluster from the S/N ratio and 3) provide information on the position of the cluster. The PCs then send the hit information to the event builder *via* 100BaseT TCP/IP. One PC can handle up to three P-PCI boards; 36 FADC boards and at least 12 PCs are required for the full DAQ system.

Before integration, P-PCI boards were tested using the FADC emulator, which is implemented using a 6U-VME general-purpose FPGA module to check the link connection, link protocol, correctness of data transfer and so on. Long-term tests were also performed to check stability. The data transfer rate of the PCI bus for three P-PCIs to one PC connections was measured to be 20 Mbytes/sec. The FADC boards were then tested using the tested P-PCI boards and most of all the functionalities of FADC have been checked.

The data-compression procedure is performed in a slice of integrated DAQ system. For the events with typical 8 % occupancy, it works properly up to 1.3 kHz of event rate using dual Xeon Pentium IV (2.4 GHz) processors. The throughput is dominated by the performance of software, but it satisfies the requirements.

The DAQ system also has been included in the first half-system test and cosmic-ray events have been detected. These initial performances significantly contribute to the desired goal of SVD2.0 and physics studies at Belle. Detailed studies of its performance are in progress.

References

1) Belle Collaboration, S. Mori et al.: Nucl. Instrum. Methods Phys. Res. A **479**, 117 (2002).
2) KEK B Factory Design Report, KEK Rep. 95-7 (1995) (unpublished).
3) R. Abe et al.: Nucl. Instrum. Methods Phys. Res. A **478**, 296 (2002).

a) Low-Voltage Differential Signal.

Computing center in Japan for RHIC physics (CC-J)

Y. Watanabe, T. Ichihara, S. Yokkaichi, O. Jinnouchi, A. Kiyomichi, Y. Goto, H. Hamagaki,* and H. En'yo

The RIKEN CC-J,[1] which serves as the computing center in Japan for RHIC[2] physics, started operation in June 2000. The CC-J aims to become the principal site of computing for PHENIX[3] simulation, a regional PHENIX Asian computing center, and a center for the analysis of RHIC spin physics. The size of the CC-J reached the planned full scale in March 2002.

The second period of RHIC experiment was carried out between August 2001 and January 2002 including the world's first polarized p + p collisions. The PHENIX detector produced about 50 TB data during this period and about 35 TB data were transferred from the RHIC Computing Facility (RCF)[4] at BNL to the CC-J with many tape cartridges using airplane transport.[5] Figure 1 shows the growth of HPSS[a] data storage at the CC-J for a period of 19 months.

Over the last year, about 13 analysis/simulation projects were carried out.

(1) Fast analysis for spin
(2) Electron/photon analysis
(3) Fluctuation analysis
(4) BBC trigger study
(5) pi0 analysis
(6) Photon polarimeter analysis
(7) Simulation for silicon vertex detector
(8) pp muon
(9) EMCal photon analysis
(10) Hadron analysis
(11) Lambda simulation
(12) Alignment study of muon arm
(13) Belle simulation

The biggest project was the official DST[b] production of pp collision data. The CC-J processed about 70% of the pp collision data. This is described in another article.[6] The results/status of other projects are also reported in this volume.

Figure 2 shows the configuration of the current CC-J system, which shows that there were three major hardware upgrades over the last year.

(1) 108 more CPUs
(2) One more data server with 4 TB FC RAID
(3) One more silo to increase the storage capacity

Figure 3 shows the photograph of the CPU farm. Two tall racks on the right side of the photograph are newly installed clusters. The right rack has 72 Pentium-III (1.4 GHz) and the other has 36 Pentium-4 (2.0 GHz). After adding these new clusters, the CPU farm consisted of 332 CPUs and total CPU performance reached 378 GHz. The operating system is RedHat LINUX running on all of the CPU farms. It was upgraded to RedHat7.2 and Kernel 2.4.7 from

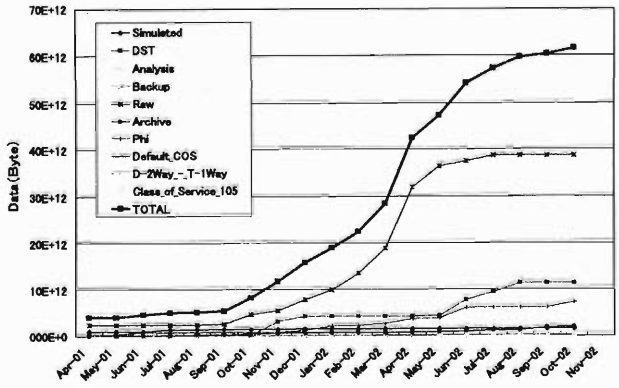

Fig. 1. Total bytes used for HPSS tape storage classes on a monthly basis.

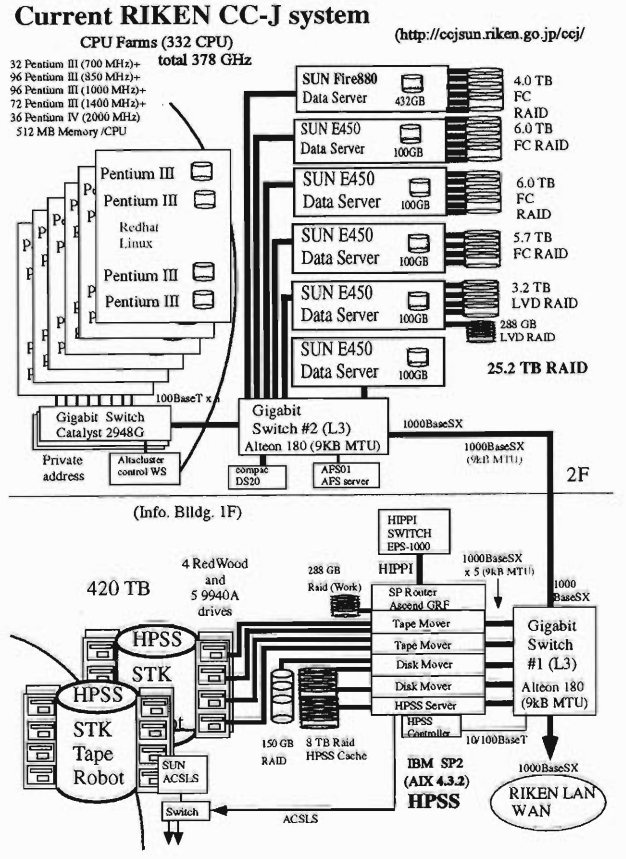

Fig. 2. Current configuration of the CC-J system.

* Center for Nuclear Study, University of Tokyo

a) High Performance Storage System
b) Data Summary Tape

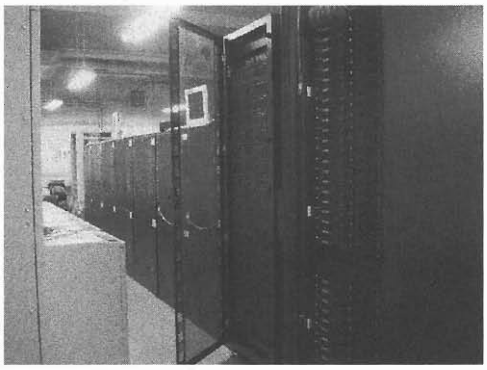

Fig. 3. LINUX CPU farm: Two tall racks on the right are newly installed. They consist of 36 Pentium-4 2.0 GHz (left) and 72 Pentium-III 1.4 GHz (right).

RedHat6.1 and Kernel 2.2.19, right after pp production has been completed. Moreover the CPU farms installed before this year (so called Alta Cluster) were needed to upgrade the Kernel to 2.4.18. Figure 4 shows a newly installed data server, which consists of a SUN Fire880 and 4 TB FC RAID. After installation, the total disk capacity of data servers increased to 25.4 TB. The SUN Fire880 is much more powerful than previous SUN E450 and capacity will further increase 8 TB soon. The right-hand silo in Fig. 5 is the newly installed STK Powderhorn 9310 which is to be used only in the CC-J, in contrast, the other one is shared between RIKEN supercomputer and the CC-J. As a result, the CC-J can handle up to 7,000 cartridges. Thus means that 420 TB data can be stored in the silos with 60 GB/cartridge. Moreover, five more tape drives (STK 9940A) were installed. The 9940A drives are a replacement of the previous RedWood's, but each data cartridge is not compatible with the other one. It took about one month to transfer all data to 9940A from RedWood. We are planning to install six more powerful tape drives soon. Then aggregate data capacity and transfer rate will reach about 1.4 PB (1,400 TB) and 200 MB/s, respectively.

The authors are grateful to Professor Bruce Gibbard and the staff of the RCF for their earnest cooperation and discussion.

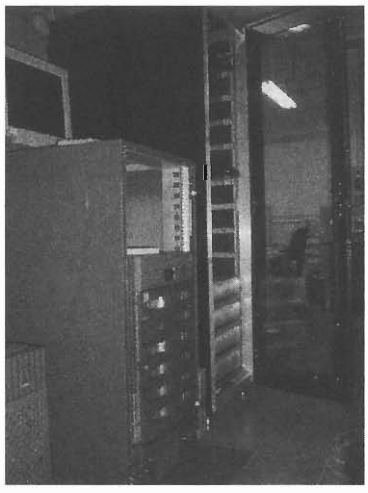

Fig. 4. SUN Fire880 and FC RAID.

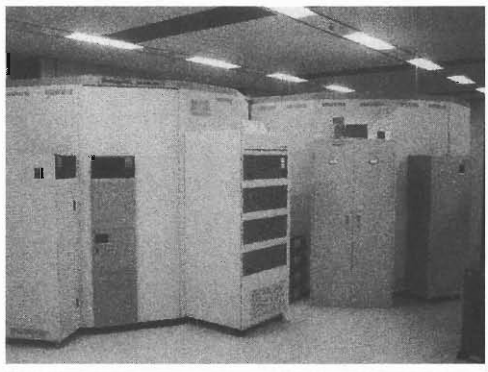

Fig. 5. Two StorageTek 9310 Powderhorns: The right one is for use only in the CC-J and the left one is shared between RIKEN Supercomputer and the CC-J.

References

1) T. Ichihara et al.: RIKEN Accel. Prog. Rep. **35**, 236 (2002): http://ccjsun.riken.go.jp/ccj/
2) http://www.bnl.gov/rhic/
3) http://www.bnl.gov/RHIC/PHENIX.htm
4) http://www.rhic.bnl.gov/RCF/
5) Y. Watanabe et al.: RIKEN Accel. Prog. Rep. **34**, 254 (2001).
6) A. Kiyomichi et al.: RIKEN Accel. Prog. Rep. **36**, 264 (2003).

Large-scale DST production at CC-J for PHENIX $p + p$ collisions run

A. Kiyomichi, T. Chujo,* Y. Goto, T. Ichihara, O. Jinnouchi, Y. Watanabe, and S. Yokkaichi

In the 2001–2002 run, the Relativistic Heavy Ion Collider (RHIC) at BNL started operation as a polarized proton collider. All devices for measuring the transversely polarized proton collisions were successfully operated at $\sqrt{s} = 200\,\mathrm{GeV}$. The PHENIX experiment[1] stored more than 180 million events of minimum bias trigger. The total data size was approximately 26 TB.

RIKEN CC-J (Computing Center in Japan, Fig. 1)[2] has taken charge of official DST (Data Summary Tapes) production for the PHENIX $p + p$ collisions data. We selected 22 TB of available raw data and processed at RCF (RHIC Computing Facility) and CC-J. The PRDF (PHENIX Raw Data Format) files were transferred from BNL to RIKEN by air using tape media and they were archived into the HPSS (High-Performance Storage System). The DST production at CC-J was performed from May to July 2002 and about 70% of available raw data was processed. All generated data were transferred to BNL.

The procedure for the DST production is described as follows.

(1) The PRDF data was transferred on a local disk of Linux client from the HPSS.
(2) The event reconstruction program analyzed this PRDF and recorded the result data onto DST.
(3) The QA (Quality Assurance) program was processed on DST. To reduce the data size, we created microDST which were recorded with the result data directly from DST.
(4) Several calibration parameters were tuned by DST or microDST analysis, such as run dependence of timing offset and gain correction. We reproducted microDST using more tuned calibration parameters. We called this process "after-burner."
(5) We created nanoDST from burned microDST. The nanoDST stored their information as a list of particles for each event.
(6) All generated data were archived into the HPSS.

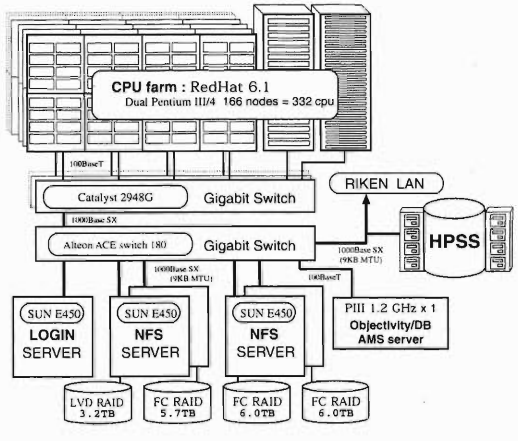

Fig. 1. RIKEN CC-J system configuration.

The event reconstruction software is built daily at RCF and placed in the AFS (Andrew File System) repository. To access AFS from the Linux farms stably, mirroring of the AFS contents to a local data server is carried out daily using the *rsync* utility. For event reconstruction, we use the Objectivity/DB as a calibration database. In CC-J, we also operate the Objectivity/DB. The daily mirroring script for the DB has been previously developed.[3] We tagged and used the fixed version of the reconstruction software and DB, independently of the daily update.

Table 1 shows typical parameters of a job (30,000 events). This represents 100,000 hours of CPU time and 8.0 TB of data volume to process about 15 TB of raw data. To make them quickly available to all PHENIX collaborations, microDST and nanoDST files (about 1.5 TB) were archived onto a disk and transferred to BNL by the APAN network. We also used tape media to transport DST files (about 6.5 TB) from CC-J to BNL.

Table 1. Typical CPU time and data size for a job. Presented CPU time is for the Pentium III (1 GHz) processor.

Number of event in PRDF	30000 events
Data size of PRDF	1500 MB
Data size of output (Total)	800 MB
DST size	500 MB
microDST size	115 MB
nanoDST size	15 MB
others (QA, calibration files)	170 MB
Total CPU time	9.5 hours
reconstruction	7.5 hours
others (data reduction, overhead)	2.0 hours

* Brookhaven National Laboratory, USA

References
1) PHENIX Collaboration: to be published to Nucl. Instrum. Methods Phys. Res. A.
2) Y. Watanabe et al.: RIKEN Accel. Prog. Rep. **36**, 262 (2003).
3) S. Yokkaichi et al.: RIKEN Accel. Prog. Rep. **35**, 238 (2002).

Measurement of identified charged hadrons in Au+Au collisions at $\sqrt{s_{NN}} = 200\,\mathrm{GeV}$

A. Kiyomichi and T. Chujo,* for the PHENIX Collaboration

The purpose of the ultra relativistic heavy-ion program at the Relativistic Heavy Ion Collider (RHIC), from a physics point of view, is to study nuclear matter at extremely high temperature and energy density with the hope of observing a new form of matter called quark gluon plasma (QGP). Since hadrons contain basic information about collision dynamics, the production of hadrons is one of the important probes of QGP.

PHENIX[1] is one of the major experiments performed at RHIC for measuring a variety of signals from heavy-ion collisions. We have measured the transverse momentum distributions for $\pi^{\pm}$, $K^{\pm}$, p and $\overline{p}$ at mid-rapidity in Au+Au collisions at $\sqrt{s_{NN}} = 200\,\mathrm{GeV}$ over a broad momentum range with various centrality selections. To identify charged particles, the high-resolution TOF counter[2] is used in this analysis. The data are classified into 11 centrality bins expressed as a percentage of the total inelastic cross section. The spectra for each particle species are corrected for geometrical acceptance, decay in flight, multiple scattering, and tracking efficiency using single particle Monte Carlo simulation. Multiplicity-dependent track reconstruction efficiency is also determined and applied by embedding simulated tracks into real events.

Figure 1[3] shows the p_T distributions for the identified hadrons in the most central events (0–5%) and the most peripheral events (60–91.4%). In each panel, the data are presented up to $1.8\,\mathrm{GeV}/c$ for charged pions and kaons, and $3.8\,\mathrm{GeV}/c$ for p and $\overline{p}$. In the low p_T region of the most central events, the data indicate that the inverse slope increases with particle mass. Also, the p and $\overline{p}$ spectra have a shoulder-arm shape while the pion spectra have a concave shape. On the other hand, in the most peripheral events, the spectra are almost parallel to each other. This mass dependence of the slopes and shapes of the spectra for protons in the central events can be explained by a radial flow picture. At approximately $2.0\,\mathrm{GeV}/c$ in central events, the proton yield becomes comparable to the pion yield. A similar behavior is also observed for negatively charged particles.

Figure 2[3] shows the centrality dependence of $\langle p_T \rangle$ for the identified charged hadrons together with the 130 GeV data points.[4] In both the 200 GeV and 130 GeV data, $\langle p_T \rangle$ for all particle species increases from the most peripheral to the most central events and also increases with particle mass. The dependence of $\langle p_T \rangle$ on particle mass suggests the existence of a collective hydrodynamical expansion.

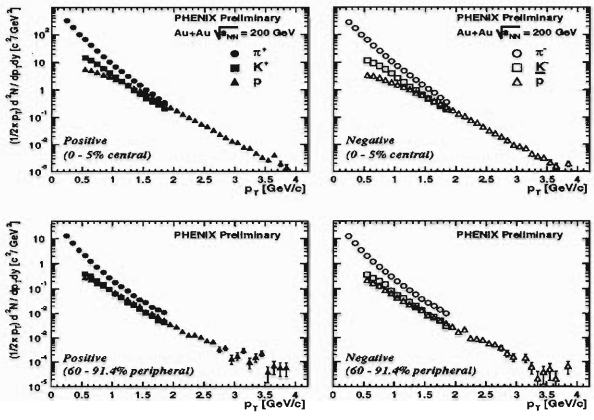

Fig. 1. Transverse momentum distributions for pions (circles), kaons (squares) and p, $\overline{p}$ (triangles) in 0–5% most central events (upper panels) and 60–91.4% most peripheral events (lower panels) at $\sqrt{s_{NN}} = 200\,\mathrm{GeV}$ in Au+Au collisions. The left panels show positive particles and the right panels show negative particles.

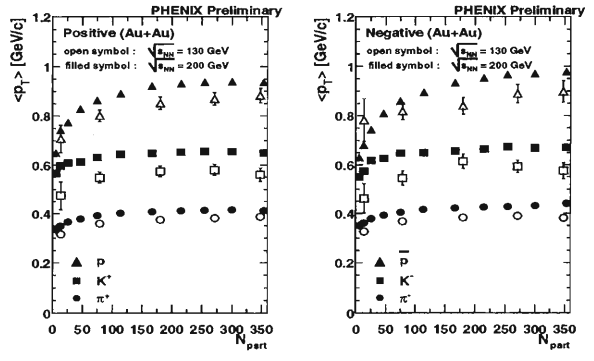

Fig. 2. Mean transverse momenta as a function of N_{part} for pions (circles), kaons (squares) and p, $\overline{p}$ (triangles). The left panel shows positive particles and the right panel shows negative particles. The open symbols indicate the data for 130 GeV[4] while the filled symbols indicate the data for 200 GeV in Au+Au collisions.

References

1) PHENIX Collaboration: to be published to Nucl. Instrum. Methods Phys. Res. A.
2) A. Kiyomichi et al.: RIKEN Accel. Prog. Rep. **35**, 244 (2002).
3) T. Chujo et al.: Proc. Quark Matter 2002 (QM2002) Nantes, France, 2002-7; Nucl. Phys. A, to be published.
4) K. Adcox et al.: Phys. Rev. Lett. **88**, 242301 (2002).

* Brookhaven National Laboratory, USA

Searching for non-hadronic sources of photons in Au + Au collisions at $\sqrt{s_{NN}} = 130\,\mathrm{GeV}$ at RHIC-PHENIX

T. Sakaguchi,[*1] X. Camard,[*2] G. David,[*3] D. d'Enterria,[*2] H. Hamagaki,[*1] S. Kametani,[*1] K. Kato,[*4] T. Matsumoto,[*1] S. Mioduszewski,[*3] K. Oyama,[*1] K. Ozawa,[*1] M. L. Purschke,[*3] M. Tamai,[*4] H. Torii,[*5] and C. Woody,[*3] for the PHENIX Collaboration

It is predicted from lattice QCD calculation that at high energy density, a phase transition from hadronic matter to a plasma of deconfined quarks and gluons (QGP) may occur, which is believed to have existed in the early universe a few microseconds after the Big Bang. Relativistic heavy ion collisions at the Relativistic Heavy Ion Collider (RHIC) at Brookhaven National Laboratory (BNL) are expected to produce such a phase transition. The photon has long been considered an excellent probe of the early stages of the collisions because photons have a long mean free path compared to the size of the nuclear volume involved in the collisions.

To extract the component of thermal photons, the background γ's from known hadronic sources must be subtracted. Of several hadronic sources, π^0 and η are the major contributors to the background γ's, and the sum of the contributions from all other sources is $\sim 4\%$ of the total. Thus, π^0 and η contributions must be correctly evaluated and subtracted from measured inclusive photons. In the RHIC Year-1 RUN, PHENIX[1)] has succeeded in measuring π^0's[2)] using EMCal.[1)] This report evaluates the contribution of γ's from hadronic sources using the π^0 spectrum, and looks for any additional sources of photons for central collision events.

The transverse momentum spectra for central (0–10%) and peripheral (60–80%) events are shown in the literature.[1)] Events are classified in accordance with the impact parameters of two colliding gold ions. 0% corresponds to an impact parameter of 0, and 100% to that of the diameter of a gold ion. The spectra for both the peripheral and central events are fitted with a power-law function. The systematic error on the fitted π^0 is estimated to be 20–35% depending on p_T. Since the acceptance of PHENIX EMCal was not sufficient to measure η with transverse momentum of $p_T \leq 1.5\,\mathrm{GeV}$ in Year-1 RUN, m_T scaling is used to estimate the spectrum of η. The spectrum is normalized relative to π^0 at infinite p_T as $\eta/\pi^0|_{(p_T=\infty)} = 0.55$ with the systematic uncertainty of 50%. The total systematic error on the sum of the yield of π^0 and η is estimated to be 22–37%.

The Fast Monte Carlo[3)] was utilized to generate the γ's from π^0 and η, to accumulate all γ's entered in the acceptance, and to smear its energy according to the smearing function. The photon identification and clustering efficiency as well as the background contribution are evaluated using HIJING simulation events reconstructed through a GEANT simulation code. The efficiency numbers are used for obtaining the γ spectrum from measured cluster energy distributions. Figure 1 shows the ratios of the measured γ distributions to those calculated from the contribution of π^0, η both for peripheral (60–80%) and central (0–10%) events. The gray bands show the systematic errors originating from π^0 measurement, η/π^0 ratio, photon idenditification and clustering efficiency, and the estimate of the background contributions. The measured distributions are consistent with the calculated distributions for both peripheral and central events within the current statistical and systematic errors.

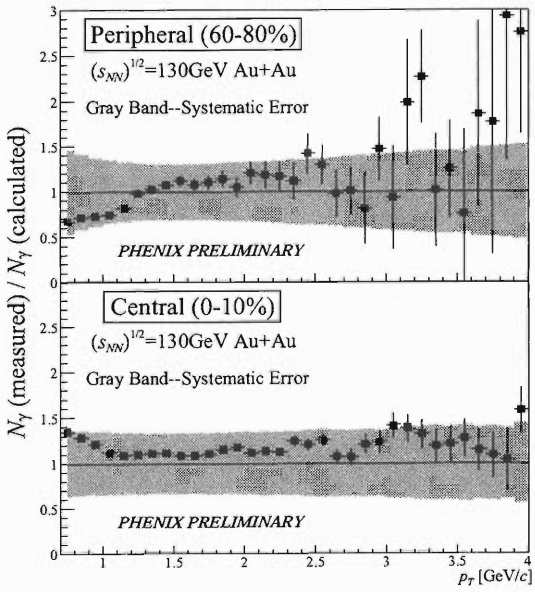

Fig. 1. Ratios of measured and calculated γ distributions for peripheral (upper) and central (lower) events, shown with systematic error bands.

*1 Center for Nuclear Study, University of Tokyo
*2 Groupe Photons, SUBATECH, France
*3 Brookhaven National Laboratory, USA
*4 Advanced Research Institute for Science and Engineering, Waseda University
*5 Department of Physics, Kyoto University

References

1) PHENIX Collaboration: Nucl. Instrum. Methods Phys. Res. A, to be submitted.
2) K. Adcox et al.: Phys. Rev. Lett. **88**, 022301 (1998).
3) T. Sakaguchi et al.: CNS Ann. Rep. 2000; CNS-REP-36, 35 (2001).

Measurement of electrons and photons at RHIC-PHENIX

T. Hachiya*[1] and Y. Akiba*[2]

Single electrons and photons are direct probes for studying hot and dense matter created in high energy heavy-ion collisions, because they do not have strong interaction with the surrounding medium and they can provide information on the initial stage of collisions. The measurement of single electrons at high transverse momentum (p_T) is a useful way to study heavy-flavor production, mainly charm quark, which is sensitive to the initial gluon density. Thermal photon radiation at 1–3 [GeV/c] in p_T is a signal of quark gluon plasma, a phase of high density nuclear matter consisting of deconfined quarks and gluons. The measurement of direct photons allows us to study the characteristics of the matter created in the collisions.

We have studied single electron production and inclusive photon production in Au+Au collisions at $\sqrt{s_{NN}}$ = 130 and 200 GeV. The data is obtained by the PHENIX experiment at RHIC.[1] Charged particle tracks are reconstructed with drift chambers and pad chambers. Electron identification is performed with ring imaging Cherenkov detectors and electromagnetic calorimeters.

The source of electrons can be divided into 2 categories, *photonic* sources, *e.g.*, Dalitz decays of light mesons and conversions of photons in the detector, and *non-photonic* sources, *e.g.*, semi-leptonic decays of heavy quarks. The contributions are estimated by different methods in 130 GeV[2] and 200 GeV[3] data. Electrons from the *photonic* source are subtracted from inclusive electrons to extract electrons from the *non-photonic* source. Figure 1 shows invariant p_T spectra of electrons from *non-photonic* sources in minimum bias Au+Au collisions at $\sqrt{s_{NN}}$ = 130 GeV and 200 GeV. The spectra are fully corrected for geometrical acceptance and reconstruction and particle identification efficiencies. The dotted and solid curves in Fig. 1 correspond to predictions of electron spectra from semi-leptonic charm decays at $\sqrt{s_{NN}}$ = 130 GeV and 200 GeV. They are calculated with PYTHIA[4] for pp collisions and are scaled with the number of binary collisions in Au+Au collisions. The electron yields and the spectral shape are in reasonable agreement with the expectation from charm decays.

Inclusive photons are measured by their conversion to low mass e^+e^- pairs.[5] In part of Au+Au running at $\sqrt{s_{NN}}$ = 200 GeV, a photon converter was added to the standard PHENIX setup. The converter was a thin brass tube (1.7% radiation length) with 29 cm radius from collision vertex. Raw p_T spectrum of conversion pairs from only the converter is extracted by comparing the data sets with and without the converter. The raw p_T spectrum is corrected for the acceptance and the conversion probability determined by a detailed GEANT simulation. Figure 2 shows the p_T spectrum of inclusive photons in minimum bias Au+Au collisions at $\sqrt{s_{NN}}$ = 200 GeV. The analysis for searching thermal photons in the photon spectrum is in progress.

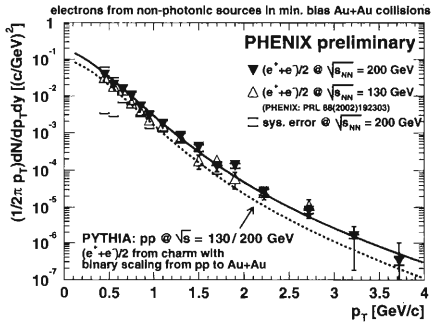

Fig. 1. p_T spectra of electrons from *non-photonic* sources in minimum bias Au+Au collisions at $\sqrt{s_{NN}}$ = 130 GeV and 200 GeV (open and closed symbol, respectively) compared with the expected contributions from semi-leptonic decay of charms at $\sqrt{s_{NN}}$ = 130 GeV (dot) and 200 GeV (solid).

We would like to thank RIKEN CC-J. The excellent computing environment of the facility is helpful for our analysis.

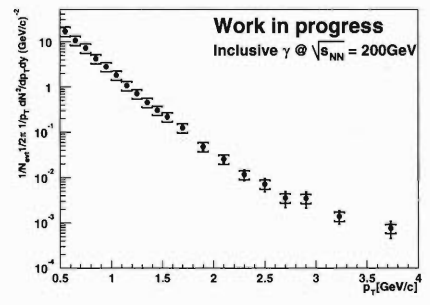

Fig. 2. p_T spectrum of inclusive photons in minimum bias Au+Au collisions at $\sqrt{s_{NN}}$ = 200 GeV. Error bars and brackets show statistical and systematic errors, respectively. Geometrical acceptance and reconstruction efficiencies are corrected by a detailed GEANT simulation.

*1 Department of Physics, Hiroshima University
*2 High Energy Accelerator Research Organization (KEK)

References

1) PHENIX Collaboration, H. Hamagaki et al.: Nucl. Phys. A **698**, 412 (2002).
2) K. Adcox et al.: Phys. Rev. Lett. **88**, 192303 (2002).
3) PHENIX Collaboration, R. Averbeck et al.: to be published; nucl-ex/0209016.
4) T. Sjostrand: Comput. Phys. Commun. **82**, 74 (1994).
5) PHENIX Analysis Note, AN158 (2002).

Study of neutral pion production in PHENIX first year Au+Au run at $\sqrt{s_{NN}} = 130\,\mathrm{GeV}$

K. Oyama,* for the PHENIX Collaboration

At the Relativistic Heavy Ion Collider (RHIC) in the Brookhaven National Laboratory (BNL), the first run of Au + Au collisions at $\sqrt{s_{NN}} = 130\,\mathrm{GeV}$ was performed in year 2000. The π^0 measurement using the electromagnetic calorimeter (EMCal) of the PHENIX detector[1] resulted in the discovery of the strong suppression of the π^0 yield at a high transverse momentum (p_T). This phenomenon is considered as a consequence of the jet quenching effect caused by the parton energy loss in the quark gluon plasma phase (QGP). The CCJ Linux computing farm at the RIKEN Radiation Laboratory was used for the analysis.

In $p + p$ collisions, hard-scattered partons fragment into hadron jets. These fragments are the primary source of high-p_T hadrons, typically above $2\,\mathrm{GeV}/c$. In Au + Au collisions, hard scattering occurs at the earliest stage of the collision, before a thermalized system is formed. The partons which lost their energy in the hot medium through gluon bremsstrahlung, could effectively quench the jet. A direct observation of such an effect would be a depletion in the yield of high-p_T hadrons, since a larger energy loss is theoretically expected in the QGP than in a typical hadronic matter.[2]

To quantify such a depletion, the obtained p_T spectra are to be compared to those theoretically predicted under the condition where no medium effect is expected. Given that hard scatterings have a small cross section, one can regard the nucleon as an incoherent superposition of partons, and Au + Au collisions are modeled as a sum of independent $N + N$ collisions (binary scaling). For a given event class of $A+A$ collisions specified by an impact parameter, $\langle N_{\mathrm{bin}} \rangle$ can be determined theoretically as the average number of $N + N$ collisions per event, and the nuclear modification factor is defined as

$$R_{AA}(p_T) = \frac{d^2 n^{A+A}/dp_T d\eta}{\langle N_{\mathrm{bin}} \rangle \cdot d^2 n^{N+N}/dp_T d\eta}, \qquad (1)$$

where n^{A+A} is the π^0 yield in the Au+Au collision, and n^{N+N} is the π^0 yield in the $N + N$ collision estimated from the past experiments at $S\bar{p}pS$ and Tevatron.[3] In the absence of the nuclear effect, $R_{AA} = 1$. Previous measurements at a lower energy indicate that $R_{AA} > 1$ at $p_T > 2\,\mathrm{GeV}/c$ due to the Cronin effect.[4]

Experimentally, π^0's are identified by detecting the $\pi^0 \to \gamma\gamma$ decay using the EMCal. Hadronic showers are suppressed by applying arrival time and shower shape cuts. The combinatorial background is estimated by mixing γ's from different events. The mixed invariant mass distribution is subtracted from the true distribution after the normalization. The π^0 yield in each p_T bin is determined by integrating the subtracted mass distribution in a window determined by a Gaussian fit to the π^0 peak. From the Monte-Carlo simulation, the correction factors for the p_T spectra were determined by taking into account the effects of energy resolution, cluster overlaps, analysis cuts, and detector acceptance.

Event classification is provided by the two beam-beam counters and the two zero-degree calorimeters.[1] The total geometrical Au + Au cross sections were divided into five centrality classes, 0–10% ("most central" fraction of the cross section), 10–20%, 20–40%, 40–60%, and 60–80% ("most peripheral"). A Glauber calculation gives $\langle N_{\mathrm{bin}} \rangle = 905 \pm 96$ for the central and $\langle N_{\mathrm{bin}} \rangle = 20 \pm 6$ for the peripheral.[5]

This analysis was performed at CCJ and 62,000 CPU hours was used. The most dominant usage of the CPU power was the combinatorial background calculation and the Monte-Carlo simulation because these required large statistics to minimize their statistical errors compared to the experimental data.

As the results, the binary scaling prediction agrees with the data in the peripheral collisions at $2 < p_T < 5\,\mathrm{GeV}/c$ region, while for the central collisions, the data systematically lie below the binary scaling prediction and R_{AA} was found to be 0.4 ± 0.15. It was found that the depletion begins at the mid-centrality (20–40%) and gets stronger as one goes to the central collisions. The data implicates that the unusual energy loss of partons in dense matter is seen in the central collisions, and this phenomenon takes place even at the mid-centrality collisions. The result from the most central class was published[6] and analysis of the centrality dependence of R_{AA} is to be published soon.[7]

References

1) W. Zajc et al.: Nucl. Phys. A **698**, 39c (2002).
2) R. Baier et al.: Ann. Rev. Nucl. Part. Sci. **50**, 37 (2000).
3) A. Drees: Nucl. Phys. A **698**, 331c (2002).
4) D. Antreasyan et al.: Phys. Rev. D **19**, 764 (1979).
5) K. Adcox et al.: Phys. Rev. Lett. **86**, 3500 (2001).
6) K. Adcox et al.: Phys. Rev. Lett. **88**, 22301 (2002).
7) K. Oyama: Doctoral Thesis, University of Tokyo, (2003).

* Center for Nuclear Study, Graduate School of Science, University of Tokyo

Λ and $\overline{\Lambda}$ production in $\sqrt{s_{NN}} = 130\,\mathrm{GeV}$ Au+Au collisions at RHIC PHENIX experiment†

H. Ohnishi, for the PHENIX Collaboration

Measurement of strange particle production is one of the important tool for studying nuclear matter produced by ultra relativistic nucleus-nucleus collisions. Furthermore, the net baryon number such as $(\Lambda - \overline{\Lambda})$ at midrapidity is directly connected with the particle production mechanism in the interaction region.

The present analysis relies on the PHENIX west arm spectrometer which covers an angular range of $\Delta\phi = \pi/4$ and pseudorapidity range of $|\eta| < 0.35$. Tracks of charge particles are reconstructed using the drift chamber (DC) and two layers of the pad chamber (PC1), with associated hit on a lead-scintillator electromagnetic calorimeter (EMCal). Signals from two sets of beam-beam counters (BBC) and two zero degree calorimeters (ZDC) used to derive the trigger which covered 92% of the 6.8 barn total Au+Au cross section, and the analogue signal are used for the centrality selection.

For this analysis, 1.3 M minimum-bias events with a vertex position of $|z| < 20\,\mathrm{cm}$ are used. To reconstruct Λ and $\overline{\Lambda}$, their weak decays $\Lambda \to p\pi^-$ and $\overline{\Lambda} \to \overline{p}\pi^+$ are used. Momenta of the particles are reconstructed using DC and PC1, with a momentum resolution of $\delta p/p \simeq 0.6\% \oplus 3.6\% p$ [GeV/c]. The particle is identified by the time-of-flight (ToF) signal of the EMCal with a time resolution of $\sim$700 ps. Particle mass is calculated using momentum from DC-PC1 and ToF information from EMCal, then a 2σ momentum-dependent cut on mass squared distribution is applied to identify pion, proton and antiproton. To provide clean particle selection, upper momentum cuts of 0.6 GeV/c and 1.4 GeV/c for pions and protons are applied, respectively. Then each proton/antiproton is combined with each pion in the same event and invariant mass is calculated. To estimate background from combinations of particles and short-lived resonances, the mass distribution with the combinations of protons and pions from different events with same centrality class is used. Moreover, the decayed proton energy within $E_p^{min} < E_p < E_p^{max}$ is required for each proton, where E_p^{min} and E_p^{max} are calculated from the two-body decay kinematics in the Λ center-of-mass system. A similar cut is used for the pions. The final value of S/B for both Λ and $\overline{\Lambda}$ is 1/2 and we obtained $\sim$ 12000 Λ and $\sim$ 9000 $\overline{\Lambda}$, in the mass range of $1.05 < m_{p\pi} < 1.20\,\mathrm{GeV/c^2}$.

To obtain correction factors, *i.e.*, the acceptance of Λ and $\overline{\Lambda}$, pion decay-in-flight, the effect of the measured mass smeared by its resolution and reconstruction efficiency, single-particle MC events were generated over the full azimuth ϕ ($0 < \phi < 2\pi$) and one unit rapidity ($-0.5 < y < 0.5$). Then generated particles were passed through the PHENIX GEANT simulator. Production of these single-particle MC events is carried out at the RIKEN PHENIX-CCJ[1] facility. The correction function is defined as the ratio of the input (generated) transverse momentum (p_T) distribution to the p_T distribution of the particle reconstructed in the spectrometer. Furthermore, to estimate the efficiency drop due to the high-multiplicity environment, we use a single-particle MC track embedded into real events and analyze the merged events with the same analysis code. We found that the reconstruction efficiency decreases from 90% for minimum-bias to 70% for central events, independent of the p_T.

Figure 1 shows invariant yields of Λ and $\overline{\Lambda}$ as a function of the transverse momentum for minimum-bias and for the most central events. The absolute yield of dN/dy at mid rapidity are determined by extrapolating to all p_T range. The average $\overline{\Lambda}/\Lambda$ is found to be $[0.75 \pm 0.09 \pm 0.17]$. Figure 2 shows ratio $\overline{\Lambda}/\Lambda$ as a function of p_T and centrality (the number of participating nucleons). The ratio is constant over the measured p_T range with no significant variation in a function of centrality. It is notable that the measured net Λ is significantly larger than that predicted by models based on hadronic strings (*e.g.* HIJING[2]).

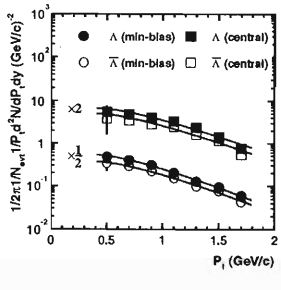

Fig. 1. Transverse momentum spectra of Λ and $\overline{\Lambda}$ for minimum bias and top 5% central events.

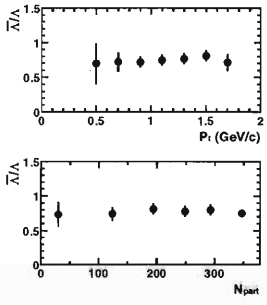

Fig. 2. The ratio of Λ and $\overline{\Lambda}$ as a function of p_T and centrality (number of participants).

† Condensed from the article in Phys. Rev. Lett. **89**, 092302 (2002)

References

1) Y. Watanabe et al.: RIKEN Accel. Prog. Rep. **36**, 262 (2003).
2) X. N. Wang and M. Gyulassy: Phys. Rev. D. **44**, 351 (1991).

Study of the PHENIX Beam-Beam Counter trigger efficiency based on the simulation for the RHIC run-2 analysis

T. Hachiya,* K. Homma,* T. Nakamura,* and N. Sugita*

In the heavy-ion collisions such as those in the Relativistic Heavy Ion Collider (RHIC), it is a key issue to determine the impact parameter or the centrality of each collision to classify the collision dynamics. The centrality is supposed to be related to the number of participants or the number of wounded nucleons per nucleus-nucleus collision based on the Glauber Model.[1] The extraction of the number of participants is the most basic and crucial measurement in order to obtain a baseline by which we can discuss whether produced many-body system is only a sum of individual nucleon-nucleon scatterings or a non trivial collective system.

The Beam-Beam Counter (BBC) in the PHENIX detector is one of the most important devices that trigger collision events, measure the Z-vertex along the heavy ion beam, provide starting time for the time-of-flight system and to determine the collision centrality by the observed charge sum. The BBC consists of two assembled components each with 64 Cerenkov counters, which are symmetrically located at ± 145 cm from the nominal collision point along the colliding beam axis. Each Cerenkov element consists of a quartz radiator and a photomultiplier. The intrinsic time resolution of each element was estimated as about 40 ps.[2] As another important trigger device, a Zero Degree Calorimeter (ZDC) measures spectator neutrons that are not bound in the fragment nucleus. The ZDC also consists of two components located at ± 18 m from the interaction point. Since the ZDC measures spectator neutrons while the BBC measures charged tracks from the participants, an anticorrelation exists between the BBC and ZDC in the observed charge sums. As the minimum bias trigger, the PHENIX experiment required at least two hits: $N_{hit} \geq 2$ for each BBC side and hits for both of the two ZDC components in Au + Au collisions at $\sqrt{S_{NN}} = 200$ GeV during the 2001 runs (PHENIX run-2).

In the following, we will briefly report on how the trigger biases were evaluated by the BBC in run-2 based on simulated events by a HIJING event generator.[3] In order to estimate the trigger biases as accurate as possible, we have implemented all of the BBC responses and the BBC level-1 trigger board logic (BBCLL1) in the simulation with exactly the same constants as those used in the real data taking. We have generated events by HIJING 1.35 with default options with the impact parameter b < 25 fm at $\sqrt{S_{NN}} = 200$ GeV. These generated events were further simulated by detector simulation and reconstructions were made by the tuned BBC response. Trigger efficiencies have been classified into two types: the efficiency that requires only BBCLL1 and the efficiency that requires both BBCLL1 and offline vertex cut. As the trigger efficiency of the offline analysis, the latter efficiency is necessary. Since the Z-vertex reconstruction efficiency is slightly dependent on the vertex positions, we defined those two efficiencies as weighted efficiencies with respect to Z-vertex positions. Since this study is based on Monte Carlo events, the trigger biases would be affected by the multiplicity distribution in the model. However, we estimated systematic variations of the trigger efficiencies by modifying dN/dy in HIJING events, and evaluated systematic uncertainties on the efficiencies due to different inputs of dN/dy in several cut criteria. We also estimated systematic errors due to different shapes of Z-vertex distributions and the uncertainty of threshold values of TDC channels which could affect definitions of hit PMTs in the BBCLL1 board.

As a conclusion, the estimated trigger efficiency by HIJING events with 10% increased multiplicity as its central value was $93.1\% \pm 0.4\%$ (stat.) $\pm 1.6\%$ (syst.), when $N_{hit} \geq 2$ and the vertex cut of ± 75 cm in the BBCLL1 logic and the offline vertex cut of ± 30 cm were imposed.[4] The systematic error was estimated as the quadratic sum of errors on input multiplicities, trigger threshold (hardware threshold and variation of PMT gains) and Z-vertex shape dependence. The quoted systematic error included the change of PMT gains due to different operational conditions through the run-2 Au + Au run period. This result was widely used for the determination of the number of participants as the basic PHENIX analysis.[5]

We would like to thank RIKEN CC-J for providing excellent environments to support this simulation work.

References

1) A simple geometrical model with Woods-Saxon nuclear density distribution.
2) PHENIX Technical Note TN393 (2001).
3) M. Gyulassy and X. N. Wang: Comput. Phys. Commun. **83**, 307 (1994).
4) PHENIX Analysis Note AN107 (2002). The central value is slightly different from the quoted value in the note due to updates after the note release.
5) PHENIX Analysis Note AN113 (2002).

* Graduate School of Science, Hiroshima University

Study of event-by-event fluctuations on isospin symmetry at RHIC-PHENIX

T. Nakamura* and K. Homma,* for the PHENIX Collaboration

In the 1970's high energy cosmic ray experiments[1] anomalous events that had a large asymmetry between the numbers of charged and photon clusters on emulsions were observed. These events, named "Centauro Event," could be explained by the formation of disoriented chiral condensates (DCC) at the chiral phase transition based on effective theories of QCD.[2] As a result, domains with large fluctuations in the neutral-to-charged pion ratio could be created event-by-event. From this perspective, such an event is a signature of the chiral symmetry restoration. However, events of this nature have never been observed in the past accelerator experiments.[3,4] There is a feasibility that RHIC achieves the chiral symmetry restoration followed by DCC creation. A search for Centauro type events has been performed in Au+Au collisions at $\sqrt{S_{NN}} = 200\,\mathrm{GeV}$ in the PHENIX[5] experiment.

The PHENIX detector has a two-arm structure, each of which covers 90 degrees in azimuth (ϕ) and ± 0.35 in pseudo rapidity (η), and it can detect charged tracks using tracking detectors and photon clusters using electromagnetic calorimeters in the phase space. Photon clusters were selected by requiring timing, shower profile and no association with charged tracks to increase the photon purity. We measured the position of each charged track and photon cluster in η-ϕ space in an event-by-event basis, and searched for a domain that has a large asymmetry between the number of charged tracks and photon clusters in various locations and sizes in the phase space. Data samples used were minimum bias events taken without magnetic field for momentum measurement to maintain the sensitivity to the low p_T phenomena such as DCC.

In this study a novel multi-resolution analysis (MRA) technique[6] has been developed to specify possible locations and sizes of such anomalous domains contained in an event.[7] This technique can efficiently extract the most anomalous domain on the asymmetry in the variable η and ϕ subdivided spaces. The fluctuation on this asymmetry, δA_{I_3} normalized to one standard deviation is defined as a function of subdivided space points and the sizes as follows:

$$\delta A_{I_3}(\eta,\phi,\Delta\eta\Delta\phi) \equiv \frac{N_{\pi^\pm}(\eta,\phi,\Delta\eta\Delta\phi) - N_\gamma(\eta,\phi,\Delta\eta\Delta\phi)}{\sqrt{\langle N_{\pi^\pm}(\Delta\eta\Delta\phi)\rangle + \langle N_\gamma(\Delta\eta\Delta\phi)\rangle}} \simeq \frac{N_{ch}(\eta,\phi,\Delta\eta\Delta\phi) - N_\gamma(\eta,\phi,\Delta\eta\Delta\phi)}{\sqrt{\langle N_{ch}(\Delta\eta\Delta\phi)\rangle + \langle N_\gamma(\Delta\eta\Delta\phi)\rangle}};$$

where $N_{\pi^\pm}$, N_γ, and N_{ch} denote the number of charged pions, photons and unidentified charged tracks for a given event, respectively, and $\langle N(\Delta\eta\Delta\phi)\rangle$ denotes an average number expected from the total numbers observed in the whole detector acceptance for a given subdivided space size.

Figure 1 shows the maximum δA_{I_3} among all subdivided space per event. The absolute scale of the distribution is expressed in an arbitrary unit on purpose at this analysis stage. As a baseline distribution, binomial samples were created by randomly distributing charged tracks and photon clusters into the whole acceptance of the PHENIX detector, which is plotted with a shaded histogram in the figure. The same event-by-event multiplicity sets (N_{ch}, N_γ) obtained in the real data were reproduced in the binomial sample. In order to reflect detector biases, binomial samples were produced according to hit maps obtained from the real data with 100 times larger statistics.

In summary, we have performed two-dimensional MRA on the asymmetry between the number of charged tracks and photon clusters in the η and ϕ space. Although it is too premature to draw any conclusions, it seems that there are obvious deviations from the binomial sample. As possible sources of additional fluctuations, at least thermal fluctuations, flow effect and jets must be taken into account. In the future analysis we will search for anomalous fluctuations beyond those known sources of fluctuations.

We would like to thank RIKEN CC-J for providing the excellent environment to produce high statistics of the binomial samples in this study.

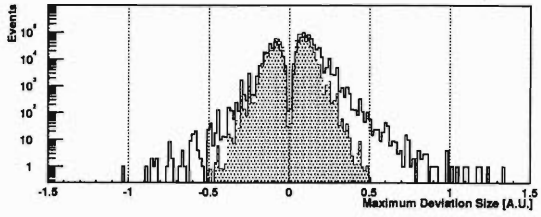

Fig. 1. Event-by-event maximum δA_{I_3} distribution in minimum bias magnetic field-off events (solid) and binomial samples with hit map with 100 times larger statistics than the data (shaded). The binomial distribution was normalized to the number of events in the data.

References

1) G. M. G. Lattes, Y. Fujimoto, and S. Hasegawa: Phys. Rep. **65**, 151 (1980).
2) K. Rajagopal, and F. Wilczek: Nucl. Phys. B **379**, 395 (1993).
3) G. Arnison et al.: Phys. Lett. B **122**, 189 (1983).
4) T. C. Brooks et al.: Phys. Rev. D **61**, 032003 (2000).
5) G. P. Morrison et al.: Nucl. Phys. A **638**, 565 (1998).
6) C. K. Chui: *Introduction to Wavelets* (Academic Press, New York, 1992).
7) PHENIX Collaboration, K. Homma and T. Nakamura et al.: Poster at 16th Int. Conf. PaNic02 (2002).

* Hiroshima University

Monte Carlo production for Belle experiment

K. Hasuko and V. Siegle*

Studies of spin-dependent fragmentation functions are performed in an unpolarized e^+e^- experiment, using the Belle detector[1] at the KEK B factory.[2] The Belle detector collected experimental data, corresponding to integrated luminosities of more than $100\,\mathrm{fb}^{-1}$. The fragmentation function analysis of Belle requires a detailed study of possible detector acceptance effects. It is necessary to produce three times the number of actual Belle physics data events as Monte Carlo (MC) simulation including a full simulation of the Belle detector response. A part of the MC production is performed at RIKEN CCJ.[3]

For the MC production, full set of Belle software and libraries was installed at CCJ. The software codes are written in C++ and use standard libraries. They are compiled and run under the Linux OS. Parameters, such as detector configurations, are supplied by a database server using PostgreSQL.[4] MC production jobs run on Redhat 7.2 (RH7.2) nodes of CCJ under the "Belle MC-production management system." This system consists of system scripts and interactive scripts. The system scripts are written in csh and scheduled by Linux standard scheduling daemon (cron). The interactive scripts are also written in csh. The system scripts manage the following tasks:

(1) generate event files
(2) prepare beam background files
(3) make batch script files
(4) submit batch jobs
(5) check log files
(6) copy files to main storage
(7) update database

Event files are generated using the QQ event generator[5] at CCJ or picked up from KEK (task 1). Beam background files are generated by a random trigger in the Belle experiment; these files are picked up from KEK (task 2). Batch script files for the GEANT3-based detector simulation[6] and Belle standard reconstruction procedure are made using the event files and beam background files (task 3). After making batch script files, they are submitted to the LSF batch queuing system of CCJ. When the jobs are completed, all log files are checked and simple data quality check is performed for output files (task 5). After all the jobs in a set are completed, the output files are transferred to the main storage at KEK (task 6). The status of MC production is recorded in the database every ten minutes and updated information is also shown on a web page (task 7).

The system scripts monitor each job submitted and give warning messages for several error levels. The interactive scripts are used to solve such problems.

The MC production at CCJ has started in June 2002 and is running very stably. The management system works properly to leverage the resources and to minimize manpower for maintenance. The total number of MC events is 112 million, corresponding to $9.3\,\mathrm{fb}^{-1}$ of beam equivalent luminosity. The production history is shown in Fig. 1. We plan to produce a total of $20\,\mathrm{fb}^{-1}$ by March 2003.[7]

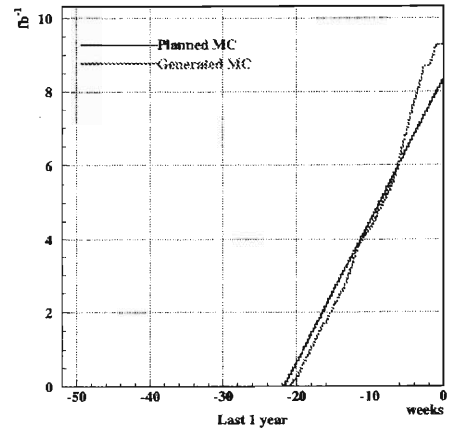

Fig. 1. Production history. The curve shows generated number of events; the straight line shows planned number of events. 0 week is November 1, 2002.

References

1) Belle Collaboration, S. Mori et al.: Nucl. Instrum. Methods Phys. Res. A **479**, 117 (2002).
2) KEK B Factory Design Report, KEK Rep. 95-7 (1995) (unpublished).
3) T. Ichihara et al.: RIKEN Accel. Prog. Rep. **35**, 236 (2002); RIKEN Accel. Prog. Rep. **34**, 252 (2001); http://ccjsun.riken.go.jp/ccj/
4) http://www.postgresql.org/
5) CLEO's QQ program; http://www.lns.cornell.edu/public/CLEO/soft/QQ
6) GEANT 3.21, CERN Rep. DD/EE/84-1 (1984).
7) Proposal for CCJ; http://ccjsun.riken.go.jp/ccj/proposals/sim/matthias020311.txt

* Brookhaven National Laboratory, USA

Toward the design of the electron pair spectrometer at JHF 50-GeV PS

S. Yokkaichi and K. Ozawa*

The spontaneous braking of chiral symmetry plays an essential role in QCD. The constituent-quark mass in hadrons is due to this braking. In hot/dense matter, the symmetry is expected to be restored and the spectral properties of hadrons such as the mass and the decay width could be modified. There have been many theoretical approaches to this problem[1] and some experiments have already observed the modification of hadrons in nuclear matter. One such experiment, KEK-PS E325, is reported in this volume.[2]

Here we intend to discuss the feasibility of a next-generation experiment, the measurement of electron pairs from the decay of vector mesons in nuclear matter at JH[3] 50-GeV PS. Higher statistics than E325 enable us to discuss the precise structure and kinematical/nuclear-size dependence of the hadron spectra in the e^+e^- channel.

In the JHF project, the first beam will be available in 2007. One of the planned beam lines in the 50 GeV proton synchrotron, the high momentum multipurpose beam line, is designed to provide 10^9–10^{10} primary protons per pulse. With the insertion of a production target, various secondary beams ($\pi^{\pm}$, $K^{\pm}$, *etc.*) will also become available in this beam line.

As the first step toward designing the new experiment, we estimated a yield of ϕ mesons in the e^+e^- decay mode. We used the nuclear cascade code JAM[4] to estimate the production cross section and the kinematical distribution of the ϕ meson in p + A reactions. It should be noted that the predictions by JAM are consistent with the results of the 12 GeV p+A reaction measured by E325, in the kinematical distribution of the ϕ meson and even in the absolute production cross section within a factor of 2. It was also confirmed that the incident-energy dependence of the predicted cross section by JAM is consistent with the available data in the pp reaction.[5] RIKEN-CCJ[6] is used for the JAM calculation and the detector simulation.

Here, we discuss the p + Cu reaction at 12 GeV, 30 GeV and 50 GeV of incident kinetic energies. The beam energy 30 GeV is planned for Phase 1 of the JHF project, while 50 GeV is available for Phase 2. Cross sections are scaled by the measured value at 12 GeV.

Two detector geometries are considered. 'Case A' is the same as E325, which covers ±23° vertically and from ±12° to ±90° horizontally in the left and right side. In 'case B' the vertical acceptance is enlarged to ±45°, the horizontal acceptance is 0°–±90° except for the very forward region of 0°–±12° both vertically and horizontally.

* Center for Nuclear Study, University of Tokyo

The results are shown in Table 1. At 30 or 50 GeV the cross sections are 3–5 times larger than those at 12 GeV, but the Lorentz boost decreases the detector acceptances for $\phi \rightarrow e^+e^-$ detection. Therefore, the effective yields are only 2–2.5 times larger when we use case A, the same setup as E325. However, the yield increases by 13-fold when we introduce case B.

An other consideration was made to use secondary beams, *e.g.* ~10 GeV/c K^-, which may have a larger production cross section than the proton-induced reaction. If the available intensity is around 10^9/pulse, the same as E325, a larger cross section means a higher yield of the ϕ meson. To estimate the intensity of the secondary beam, we used the Sanford-Wang[7] formula for the secondary particle production. We have assumed the beam-line parameter for Phase 1 as 30 GeV 1×10^{14} proton/pulse, 2% beam loss at the production target and the beam line at the production angle is 4.7° with an acceptance of 0.2 msr·%. The length of the beam line was assumed to be 120 m to take particle decays into account. We confirmed that for 3 GeV/c–12 GeV/c K^- the available intensity is only about 10^5/pulse. In Phase 2, the higher intensity and energy of the 50 GeV primary beam will result in about 10 times larger secondary intensity.

In conclusion, it is possible to collect about 13 times more ϕ mesons than E325 using case B acceptance and the 50 GeV proton beam with an intensity of 1×10^9/pulse, which is the same as E325. For the secondary beams, however, the available intensity needs to be 10^2–10^3 times higher to be useful.

Table 1. ϕ meson yield.

beam energy		12 GeV	30 GeV	50 GeV
cross section		1.0 mb	3.0 mb	5.1 mb
detector acceptance	case A	8.8%	6.0%	4.5%
	case B	45%	31%	23%
normalized yield by current E325	case A	1	2.0	2.6
	case B	5.1	10.0	12.7

References

1) T. Hatsuda and T. Kunihiro: Phys. Rep. **247**, 221 (1994), etc.
2) K. Ozawa et al.: Phys. Rev. Lett. **86**, 5019 (2001); R. Muto et al.: RIKEN Accel. Prog. Rep. **36**, 93 (2003).
3) http://jkj.tokai.jaeri.go.jp/
4) Y. Nara et al.: Phys. Rev. C **61**, 024901 (1999).
5) D. Drijard et al.: Z. Phys. C **9**, 293 (1981).
6) Y. Watanabe et al.: RIKEN Accel. Prog. Rep. **36**, 262 (2003).
7) J. L. Sanford and C. L. Wang: BNL Rep. No. 11299, 1 (1967); BNL Rep. No. 11479, 1 (1967).

8. Miscellaneous

Global anisotropy *vs.* small-scale fluctuation of neutrino flux in supernova explosion

H. Madokoro, T. Shimizu, and Y. Mochizuki

Multidimensional simulations of supernova explosions have been performed by several groups. Shimizu *et al.*[1] carefully investigated the effects of anisotropic neutrino radiation on the explosion. They found that locally intense neutrino radiation along the pole is sufficient for reviving a stalled shock wave. They assumed, however, that anisotropy takes a global form, that is, no fluctuation in the neutrino flux is considered. In this work, we study the effects of small-scale fluctuation in the neutrino flux. Note that Burrows *et al.*[2] pointed out that the neutrino flux can fluctuate with angle and time due to gravity waves around the neutrino sphere.

We have solved the two-dimensional hydrodynamical equations in the polar coordinate. A generalized Roe's method is used to solve the general equations of motion.[1] The local neutrino flux is assumed as

$$l_\nu(r,\theta) = \frac{7}{16}\sigma T_\nu^4 c_1 \left(1 + c_2 \cos^2(n_\theta \theta)\right) \frac{1}{r^2}, \qquad (1)$$

where σ is the Boltzmann constant, and $T_\nu = 4.70\,\mathrm{MeV}$ is the temperature on the neutrino sphere. In Eq. (1), the parameter c_2 represents the magnitude of anisotropy, and n_θ the number of waves in the θ direction. The case of $n_\theta = 1$ corresponds to the global anisotropy (no fluctuation). Note that c_2 is a function of n_θ. For each value of n_θ, c_2 is calculated by estimating the degree of anisotropy for an observer far from the neutrino sphere.[3] We obtain the following values: $c_2 = 0.100$ for $n_\theta = 1$, $c_2 = 0.051$ for $n_\theta = 3$, and $c_2 = 0.035$ for $n_\theta = 5$. c_1 is calculated from c_2 and n_θ so as to adjust the total neutrino luminosity to that in the spherical model.

Figure 1 shows the contour maps of the entropy distribution with the velocity fields. We can see that the shock front for the case of $n_\theta = 1$ (crowded contour lines at $r \sim 1700$–$2500\,\mathrm{km}$) displays large asymmetry. That for the case of $n_\theta = 3$ is also anisotropic although less deformed, while the shock wave becomes almost spherical when n_θ is increased to 5. It is seen that the larger the value of n_θ is, the less the shock wave extends. This is related to the difference of the energy gain rate. Figure 2 shows the evolution of explosion energy, as well as the thermal, kinetic, and gravitational energies. The explosion energy for the case of $n_\theta = 1$ (global anisotropy) is higher than those of the cases with the fluctuation. The rate of energy gain is also the largest for the case of $n_\theta = 1$, and decreases when fluctuation is included. Thus we found that the case of global anisotropy shows the most energetic explosion. The effects of time fluctuation in the neutrino flux[2] on the explosion energy will be examined in the future.

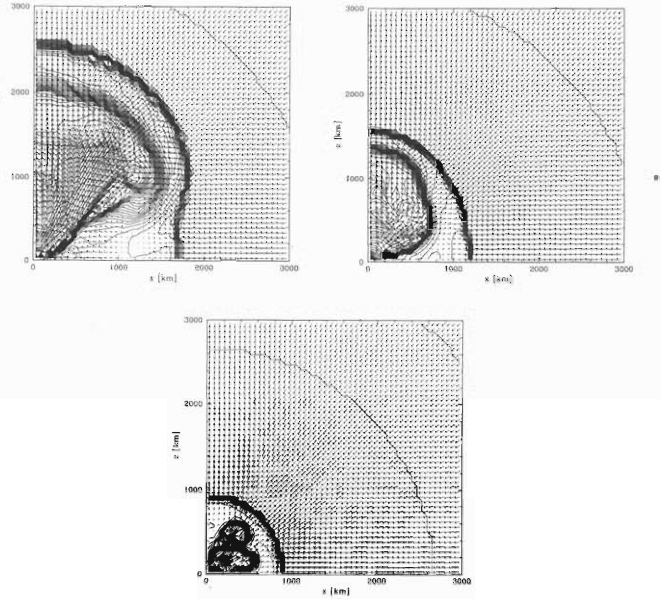

Fig. 1. Contour maps of the entropy distribution with the velocity fields. Top-left: $n_\theta = 1$ ($c_2 = 0.105$) at $t = 210\,\mathrm{ms}$, Top-right: $n_\theta = 3$ ($c_2 = 0.051$) at $t = 219\,\mathrm{ms}$, Bottom: $n_\theta = 5$ ($c_2 = 0.035$) at $t = 215\,\mathrm{ms}$.

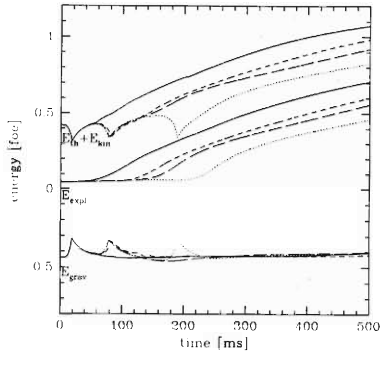

Fig. 2. Evolution of thermal and kinetic energies ($E_{\mathrm{th}} + E_{\mathrm{kin}}$), gravitational energy (E_{grav}) and explosion energy (E_{expl}). Solid line corresponds to the case of $n_\theta = 1$ ($c_2 = 0.105$), short-dashed line $n_\theta = 3$ ($c_2 = 0.051$), long-dashed line $n_\theta = 5$ ($c_2 = 0.035$), and dotted line $c_2 = 0$ (spherical).

References

1) T. M. Shimizu et al.: Astrophys. J. **552**, 756 (2001).
2) A. Burrows et al.: Astrophys. J. **450**, 830 (1995).
3) H. Madokoro, T. Shimizu, and Y. Mochizuki: submitted to Astrophys. J.

Application of multitracer γ-ray emission imaging (MT-GREI) to cognitive brain science

H. Takeichi, S. Motomura, S. Enomoto, and Y. Yano

MT-GREI (multitracer γ-ray emission imaging) is a tracer imaging technique recently developed at RIKEN and Kyushu University.[1,2] It enables nondestructive and simultaneous imaging of multiple trace elements at a high spatial resolution.

The basic principle of MT-GREI is as follows. A multitracer consisting of many radioisotopes is generated by high-energy heavy-ion reactions and administered to the sample. The tracer emits γ rays, which are detected by a pair of segmented Ge detectors placed parallel to each other, forming a Compton camera. The γ rays from individual radioactive nuclides are distinguished from each other by their energies. If a γ ray emitted from the sample scatters in the front detector and then the scattered γ ray deposits its full energy in the back detector, the two consecutive interaction positions and energy losses define the cone on which the γ-ray source lies, following Compton kinematics. By direct summation of several such cones produced by a number of events, the spatial distribution or images of the individual tracer elements are reconstructed. An early prototype was fabricated using $50 \times 50\,\mathrm{mm}^2$ planar Ge detectors divided into 25 segments of equal size. Its spatial resolution was 2 mm. The latest system was fabricated using $30 \times 30\,\mathrm{mm}^2$ strip Ge detectors divided into 169 segments. Its spatial resolution was 0.2 mm.

MT-GREI can be applied to many fields. In this article, an application of MT-GREI to cognitive brain science is described. Cognitive brain science is a discipline in which mechanisms of brain functions are studied as information processing. Recent progress in cognitive brain science owes much to noninvasive measurement techniques of human brain activation such as PET (positron emission tomography)[3] and fMRI (functional magnetic resonance imaging).[4] However, neural activity cannot be directly measured by these techniques because of their principle and limited spatial resolution.

For example, rCBF (regional cerebral blood flow) is measured by the $H_2{}^{15}O$ PET technique and glucose metabolism is measured by the ^{18}F-FDG (^{18}F-labeled fluorodeoxyglucose) PET technique. Although rCBF and glucose metabolism correlate with neural activity, the rCBF image or the glucose metabolism image may not match the spatial distribution of the neural activity precisely.

Blood oxygenation is measured by the BOLD (blood-oxygenation-level-dependent) fMRI technique and rCBF is measured by the perfusion-based fMRI technique. The exact relation between blood oxygenation level and neural activity is controversial. The problem with rCBF measurement is described above.

Unlike PET and fMRI, MT-GREI can probe the behavior of a wide variety of elements directly related to neural activity, such as Na, K, Ca, Mn, and Zn. Therefore, it opens a possibility of direct noninvasive measurement of neural activity or even plasticity at high spatial resolution for the first time. Thus, MT-GREI may be free from limitations associated with the techniques currently used in indirect measurement of brain activation. Because the multitracer technique has serendipity, namely, a multitracer may contain elements which are not intended to be included, it is also expected that an unprecedented element is involved in neural activity.

As our primary goal, we plan to measure the activation of barrels in the somatosensory cortex of a rat *in vivo* using MT-GREI, because rat barrel activation can be used as a robust pilot paradigm. More complex paradigms such as the activation of place cells in the hippocampus or the activation of amygdala in fear conditioning may be used in the future. These paradigms are also robust and related to learning and plasticity. As steps toward achieving our primary goal, we plan to (1) improve the spatial resolution of the MT-GREI system up to 0.02 mm or higher, (2) confirm the system performance using an inorganic test sample, (3) examine the system performance using rat slices *in vitro*, and (4) examine the system performance using rats *in vivo* in the resting state without stimulation, before conducting the final experiment.

Ultimately, we want to pursue the possibility of applying MT-GREI to humans. The impact of noninvasive direct measurement of human brain activation will not be small. It provides a novel technique not only for medical diagnosis of brain disorders but also for precise understanding of human-specific brain functions such as consciousness, creative thinking, or language processing.

In conclusion, by further improvement of its spatial resolution, MT-GREI is expected to be a novel approach in cognitive brain science. PET, fMRI, and MT-GREI will altogether form a new foundation for noninvasive measurement of brain activation.

References

1) Y. F. Yang et al.: IEEE Trans. Nucl. Sci. **48**, 656 (2001).
2) S. Motomura et al.: RIKEN Rev., No. 35, 116 (2001).
3) P. T. Fox et al.: J. Cereb. Blood Flow Metab. **4**, 329 (1984).
4) S. Ogawa et al.: Proc. Natl. Acad. Sci. USA **87**, 9868 (1990).

IV. DEVELOPMENT OF ACCELERATOR FACILITIES

Production of highly charged Ar ions from RIKEN 18 GHz ECRIS

Y. Higurashi, T. Nakagawa, M. Kidera, E. Ikezawa, T. Aihara,* M. Kase, and Y. Yano

At RIKEN, the intense beams of multicharged heavy ions, such as Ar^{8+}, Kr^{13+}, Xe^{20+} and U^{35+}, are highly sought after the radioisotope beam (RIB) factory project.[1] For this reason, we constructed the RIKEN 18 GHz electron cyclotron resonance ion source (RIKEN 18 GHz ECRIS) in the middle of the 1990s and successfully produced an intense beam of heavy ions. However, to meet the requirement of the RIB factory project, we still need to further improve RIKEN 18 GHz ECRIS.[1]

In the experiments using the liquid-He-free superconducting ECRIS at RIKEN,[2] we recognized that it is important not only to increase the magnetic field strength, but also to optimize the magnetic field configuration for increasing the beam intensity.[3,4] Especially, the minimum magnetic field strength of the mirror magnetic field (B_{min}) and the beam extraction side of the mirror magnetic field (B_{ext}) play essential roles increasing the beam intensity. In these experiments, we found an optimum B_{min} value that maximizes the beam intensity. The optimum B_{min} value was 0.48–0.5 T for production of various heavy ions.[3,4] In the case of B_{ext}, the optimum value was strongly dependent on the charge state of the heavy ions.[5] If we apply it to RIKEN 18 GHz ECRIS, we may increase the beam intensity of heavy ions.

The detailed description of RIKEN 18 GHz ECRIS and it's current performance are described in Ref. 2. Figure 1 shows the cross-sectional view of RIKEN 18 GHz ECRIS and the magnetic field configuration of the mirror magnetic field for production of an Ar^{8+} ion beam.

To increase the transmission efficiency of the intense heavy-ion beam, the numerical simulation of the beam trajectory between the ECRIS and RFQ linac has been performed using the particle-in-cell model.[6] Based on this result, we set the solenoid coil between the ECRIS and the analyzing magnet.

For RIKEN 18 GHz ECRIS, we set $B_{min} = 0.48$ T. Unfortunately, RIKEN 18 GHz ECRIS has only two sets of solenoid coils for producing mirror magnetic field as shown in Fig. 1 (a). It means that when choosing the optimum B_{min} value, the magnetic field strength at the beam extraction side (B_{ext}) may not be optimum for production of Ar^{8+}. For plasma confinement, the effective B_{ext} should not be the maximum magnetic field at the beam extraction side, but the magnetic field at the plasma electrode position as shown in Fig. 1 (b). The magnetic field near the plasma electrode position also affects the condition of beam extraction. For optimizing the B_{ext} and extraction conditions for Ar^{8+} ion, we changed the plasma electrode position to maximize the beam intensity. In this experiment, the plasma electrode was set 4 cm from the edge of the ECR zone as shown in Fig. 1 (b). B_{inj}, B_{min} and effective B_{ext} were 1.32, 0.48 and 0.95 T, respectively. The extraction voltage was 17 kV. Figure 2 shows the beam intensity of Ar^{8+} as a function

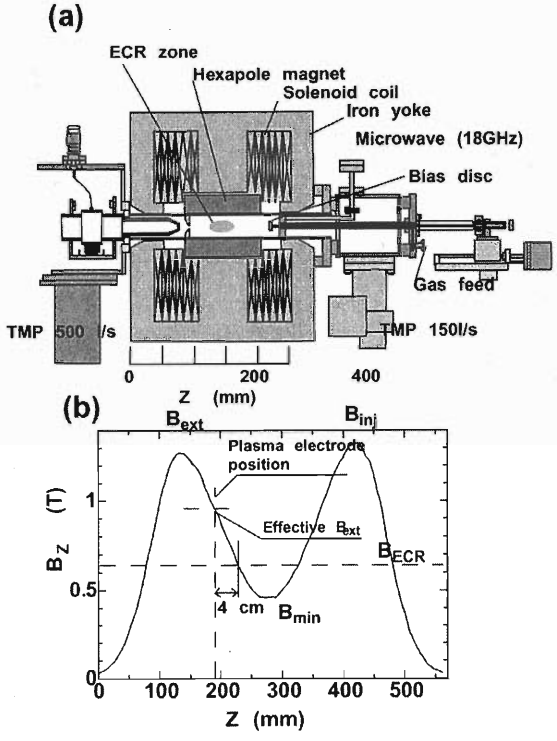

Fig. 1. (a) Cross-sectional view of RIKEN 18 GHz ECRIS (b) Mirror magnetic field configuration to produce Ar^{8+}.

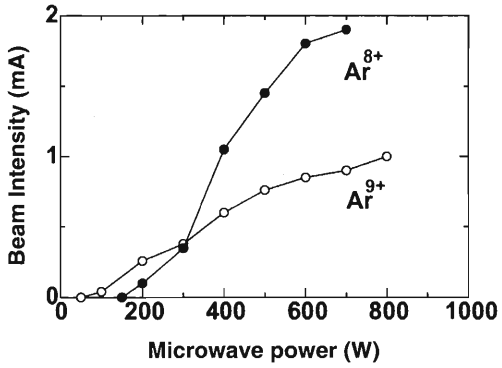

Fig. 2. Beam intensities of $Ar^{8+,9+}$ ion as a function of microwave power. The ion source was tuned at a microwave power of 600 W.

* SHI Accelerator Service, Ltd.

of microwave power. The ion source was tuned at a microwave power of 600 W. In this experiment, we changed microwave power without changing the other parameters (gas pressure, magnetic field strength, extraction voltage and so on). It should be noted that the beam intensity was not saturated at the highest microwave power of 700 W in this experiment. This means that we may obtain higher beam current at higher microwave power. Using this configuration, we successfully produced 1.90 mA of Ar^{8+} at 700 W of microwave power.

Using the solenoid coil, we successfully increased the beam intensity. The increase in beam intensity using the solenoid coil was 20–30% under this condition. However, the effect of the solenoid coil was strongly dependent on the beam intensity, the condition of the ion source and ion species. In order to maximize the transmission efficiency, we need further investigation.

References

1) Y. Yano, A. Goto, M. Kase, and T. Katayama: AIP Conf. Proc. **600**, 161 (2001).
2) T. Nakagawa and Y. Yano: Rev. Sci. Instrum. **71**, 637 (2000).
3) H. Arai et al.: Nucl. Instrum. Methods Phys. Res. A **491**, 9 (2002).
4) T. Kurita et al.: Nucl. Instrum. Methods Phys. Res. B **192**, 429 (2002).
5) M. Imanaka et al.: Jpn. J. Appl. Phys. **41**, 3926 (2002).
6) V. Alexandrov et al.: Rev. Sci. Instrum. **71**, 1091 (2000).

First beam injection from the Hyper ECR ion source to the RIKEN AVF cyclotron

Y. Ohshiro,* S. Watanabe,* Y. Higurashi, T. Kageyama, M. Kidera, T. Nakagawa, M. Kase, S. Kubono,* and T. Katayama

The installation of the CNS Hyper ECR ion source at the RARF, and the construction of new beam line[1] for the injection of ions to the K70 AVF cyclotron were completed on February 25, 2002. Thus far, several kinds of ions (see Table 1) have already been used for nuclear and biological experiments.

The present performance of the Hyper ECR ion source is described below:

First, the power test of a 14.2 GHz RF power system was carried out by driving the RF amplifier. The RF power was tested up to 800 W because the range of 200 W to 800 W is required for multicharge ion production.

Second, the magnetic mirror field was measured along the axis of the ion source. Two peaks of 12.5 kG were generated with a current of 600 A. A schematic drawing of the ion source is shown in Fig. 1 together with the mirror field distribution used for $^{12}C^{5+}$ and $^{14}N^{6+}$ production. In this case, the excitation currents were 450 A and 550 A for the two solenoid coils, as shown in the figure. The mirror ratio is about 2.7 ($B_{max} \sim 11$ kG and $B_{min} \sim 4$ kG). The length of the ECR zone is about 7 cm. The electrical power consumption is nearly 40 kW.

Third, we searched for the optimum position of the anode electrode for extraction of intense stable beams from the ion source, by moving it in 0.5 cm increments along the axis. It was found that the optimum position was at 6.5 cm from the median plane of the sextupole magnet (see Fig. 1).

Fourth, we investigated the extraction voltage dependence on the beam intensity. In the case of $^{14}N^{5+}$ and $^{14}N^{6+}$, the beam intensity extracted at 20 kV was found to increase nearly 3 times more than that at 10 kV. Figure 2 shows the yield of the nitrogen ion

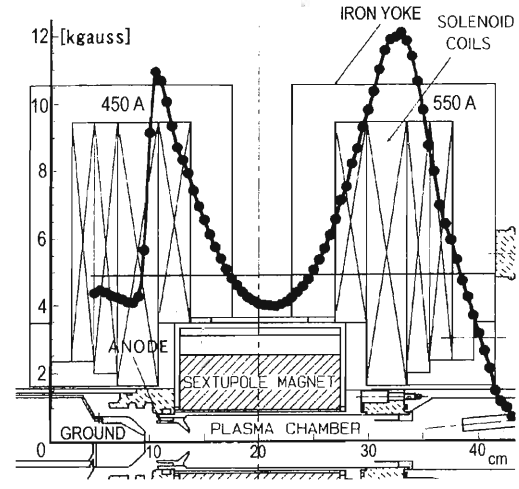

Fig. 1. A schematic drawing of Hyper ECR ion source together with the mirror field distribution used for production of ions such as $^{12}C^{5+}$ and $^{14}N^{6+}$.

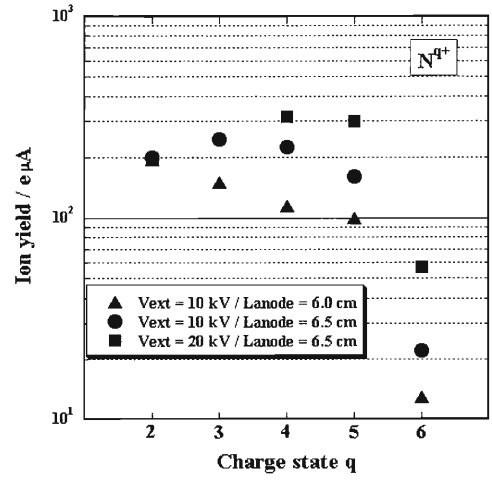

Fig. 2. The yields of the nitrogen ions for each charge state extracted from the Hyper ECR ion source.

Table 1. Some results of the beams extracted from the AVF cyclotron. For the meanings of i_1 and i_3, see Fig. 3.

Ion Species	Acceleration Energy [MeV/u]	Analyzed beam intensity i_1 [eμA]	Transmission efficiency i_3/i_1 [%]
H^+	9.9	56	14
$^{12}C^{4+}$	7.0	28	19
$^{13}C^{4+}$	4.0	16	11
$^{14}N^{5+}$	7.0	33	13
$^{14}N^{6+}$	6.4	6	29
$^{20}Ne^{7+}$	6.3	12	25

* Center for Nuclear Study, Graduate School of Science, University of Tokyo

for each charge state. The distribution was obtained under the following conditions of the extraction voltage, V_{ext}, and anode position: (10 kV, 6 cm), (10 kV, 6.5 cm) and (20 kV, 6.5 cm).

A schematic diagram of the ion transport system is presented in Fig. 3. Ion beams from the ion source are transported horizontally (see I in the figure) and vertically injected through the upper hole of the main magnet into the cyclotron by means of a series of a bending magnet, a quadrupole quartet and five solenoid magnets (see II in the figure). An RF buncher is placed immediately in front of the upper magnetic yoke of the cyclotron, 2 m upstream of the cyclotron center. Details of the design of the axial injection line have already been described in Ref. 2.

We have studied the beam transmission, that is, the ratio of the beam intensity at the extraction position of the AVF cyclotron (i_3 at FC-3) to that at the injection position (i_1 at FC-1), as shown in Fig. 3. Table 1 shows some results so far obtained. As shown in the table, a maximum transmission of about 29% has been achieved. The merits of using flat-top acceleration were examined using a $^{14}N^{6+}$ ion beam.[3,4] The results are shown in Table 2.

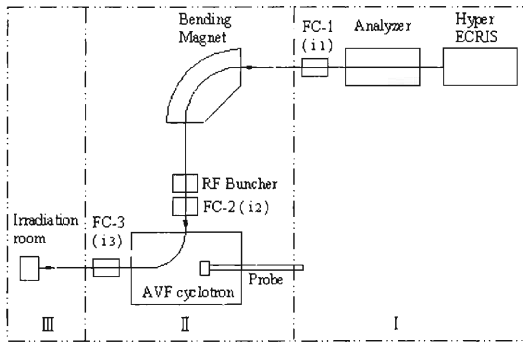

Fig. 3. Schematic diagram of transport system.

Table 2. Comparison of the beam transmission efficiencies with the flat-top acceleration for the $^{14}N^{6+}$ ion beam. The radius of 82.5 cm is the position on the extraction orbit after the deflector.

Measuring position	Transmission efficiency (%)	
	FT off	FT on
Probe at radius of 7.5 cm on median plane	31.3	32.0
Probe at radius of 64.5 cm on median plane	26.3	26.8
Probe at radius of 82.5 cm on median plane	19.6	21.4

References

1) Y. Ohshiro et al.: RIKEN Accel. Prog. Rep. **35**, 256 (2002).
2) N. Nakanishi et al.: RIKEN Accel. Prog. Rep. **20**, 188 (1987).
3) S. Watanabe et al.: CNS Ann. Rep. **2001**, 47 (2002).
4) A. Goto et al.: RIKEN Accel. Prog. Rep. **36**, 287 (2003).

Improvement of the control system for RRC, AVF and RILAC

M. Kobayashi-Komiyama, I. Yokoyama, M. Nagase, E. Ikezawa, M. Fujimaki,
A. Uchiyama,* T. Tanabe, and M. Kase

The old control system with M60 for the RIKEN Accelerator Research Facility (RARF) was completely removed in the summer of 2002, after a long-term use of more than sixteen years. It has been replaced with a new control system using the Experimental Physics and Industrial Control System (EPICS)[1] since April, 2001. The details of the system are described in Ref. 2. After the system replacement, however, unknown troubles sometimes occurred during the beam operation. In those cases, an operator had to change the control system back to the M60 system frequently. By investigating these troubles, it was clarified that they were caused mainly by bugs in the control programs we developed and mismatching among the programs or between a program and the system. After fighting with some bugs for several months, the number of troubles was reduced markedly in 2002. Thus the previous control system with M60 was not needed any longer as a backup. The two sets of main computers in the M60 system were scrapped in the summer.

Most of the basic operations of RILAC, AVF, RRC, RIPS, SMART, and their beam lines are currently carried out by the EPICS without any serious problems. The EPICS already includes two sets of CAMAC-CIM/DIM interfaces (one for RILAC, the other for RRC and AVF) and the old GP-IB interface for twenty-year-old power supplies in RILAC. On the other hand, it has always been required that the system is extended not only in the RIBF project but even in the existing machines. New components have been introduced into the cases such as the upgrade project of RILAC, the extension of the AVF beam line, renewals of very old power supplies in RILAC, and renewal of the vacuum control for RRC. There is a demand that the system expansion should be carried out only by adding the parameters of new components into the database of the EPICS, if they are controlled by either the CAMAC or the GP-IB. However, both the interfaces were already old and it is not a good idea to employ such old ones for the control of new components. Then it was decided to introduce two types of new control interfaces, which will be used in the RIBF project, into the EPICS. One is the network IO (NIO) interface used for new magnet power supplies. The other is a programmable logic controller (PLC) used for a new RF system, charge-state multiplier (CSM) system and new vacuum system in cyclotrons.

The first power supplies controlled by the NIO system were installed last year for the magnets in the new RILAC beam line. After their original driver software and control programs were developed in the EPICS, we could use them in the beam operation basically. The development of software programs for the NIO interface is still under way, and a test of their actual operation in a total system is carried out in the EPICS.

Although there are at least four kinds of interfaces for magnet power supplies in RARF, an operator can control all the magnets without taking into consideration the difference of control devices of their power supplies. He can set currents of different kinds of magnet power supplies through one kind of control window in which all magnets are arranged in sequence from the upstream of the beam. Furthermore, we can record all values of current of magnet power supplies in one file and we can monitor the status of magnet power supplies by using the common alarm system. That is, we succeeded in making the control of the magnet power supplies very simple and very convenient for an operator.

On the other hand, Fig. 1 shows the structure of the PLC control system in RARF. All of the PLC control systems were stand alone systems. Then, we took only their reading function in the EPICS to monitor the status remotely on one PC at the control room. We selected the RRC vacuum control system with the OMRON PLC (CS1), which has been replaced with a new one in the summer of 2002, as the first target to be introduced into the system. We developed the original driver software for the CS1 in the same manner as the GP-IB devices. Currently, an operator can always monitor the vacuum status at the control room. The new RF control system and the CSM system also have the CS1. Thus, the gathering of data from these systems in the EPICS is under way.

For advanced controls, we newly installed some effective tools for operations in 2002. One of them is the program for recording and retrieving the data obtained

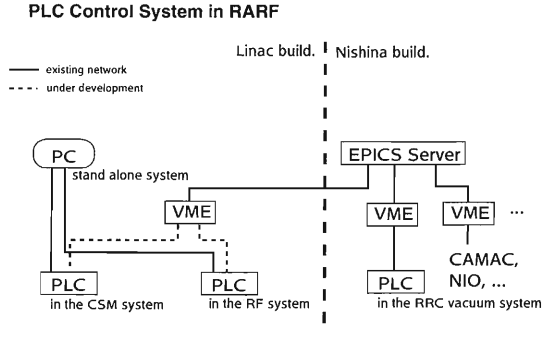

Fig. 1. Structure of the PLC system in RARF.

* SHI Accelerator Service, Ltd.

by beam profile monitors. By using this program, an operator can retrieve a previous good data whenever he wants to refer to it on the same PC during beam tuning. Another new effective tool is the program for writing all actions of an operator during the beam operation and all system errors onto log files. This is very effective in determining the event before an accident happened or in retrieving the good operation by referring to a log file. The log file contains the following parameters for each operator's action: date, time, the name of device, the action, the current measured by the Faraday cup which stops a beam, and the name of the Faraday cup. By recording the current measured by the Faraday cup with each action, we can determine the beam condition after the beam tuning by checking the log files.

One objective of developing the recording program of operation log is to enable to check a previous data as mentioned above. The other objective is to produce an automatic beam tuning program to be applied to some parts of RARF. It would significantly help an operator particularly in some routine patterns in an operation. Automatic beam tuning can be realized by carrying out the program including many complex calculations about the beam transport, however, it can also be realized by that the program sets a variety of tuning parameters to each device by following the operator's action recorded in the log file. The program which is applied to beam transportation in the straight beam line inside room A is under development to determine whether we can perform the beam tuning automatically by this method or not.

On the other hand, we started to test the upgrading of our EPICS version by using a linux machine. Although many convenient tools are prepared by the EPICS collaboration, most of them correspond to an upgraded EPICS base software, which we cannot use in our system in the present status. For using their convenient tools and for following the change of hardwares which compose our system, we will continue an investigation for upgrading the system in 2003.

References

1) http://www.aps.anl.gov/epics/
2) M. Kobayashi-Komiyama et al.: RIKEN Accel. Prog. Rep. **35**, 266 (2002).

Renewal of the rf feedback control system for RILAC

N. Sakamoto, O. Kamigaito, S. Kohara, T. Ohki,* Y. Chiba, and M. Kase

The performance of the new rf feedback control system is reported. The new rf control devices have been developed and were installed in the RILAC (variable-frequency heavy-ion linac) rf feedback control system. After careful tuning of the devices, stability of the rf voltage of the RILAC cavities (18–42 MHz) was significantly improved. The new rf control devices, phase controller (Thamway A081-1067B) and level controller (Thamway A081-1067B) were designed and made for the booster ring cyclotrons of IRC (intermediate-stage ring cyclotron) and SRC (superconducting ring cyclotron) at RIBF (Radioactive Beam Factory). At RIBF, the final beam current of heavy-ion beams on a production target is as high as 1 particle μA. To achieve this target intensity, it is crucial to reduce the beam loss as much as possible. The instability of the rf voltage of the cavities, *e.g.*, amplitude deviation, phase excursion and so on, causes emittance growth during acceleration and consequently beam loss increases particularly at injection and extraction points of the cyclotron.

For IRC and SRC, required amplitude and phase stabilities are typically

$$\Delta V_p/V_p \leq \pm 5 \times 10^{-4}$$

$$\Delta\theta \leq \pm 0.1^\circ. \quad (1)$$

To achieve this requirement, the feedback control devices must be stable themselves. The main parts of the electric circuit of the feedback control are packed in a temperature controlled aluminum box so that the circuit works stably under a constant temperature and is electrically well shielded. The aluminum box and other elements such as dividers and power source are put together into an outer case. The new devices, phase controller and level controller, were installed in the RILAC #5 and #6 cavities whose power amplifiers are the same as those for IRC and SRC.[1] A simplified block diagram of the rf feedback control system is shown in Fig. 1. Cavity voltage sampled with a capacitive voltage divider is fed into a 50 ohm attenuator so as to make the input level of the feedback control system +30 dBm for the maximum cavity voltage of 300 kV_p at 37.75 MHz. A gas arrester tube is inserted at the output of the divider to protect the system from surge voltage due to discharge inside the cavity.

To determine the stability of an rf signal, it is convenient to use a spectrum analyzer. Ripples such as amplitude and phase modulation appear as side-band signals. For example, an amplitude modulation of

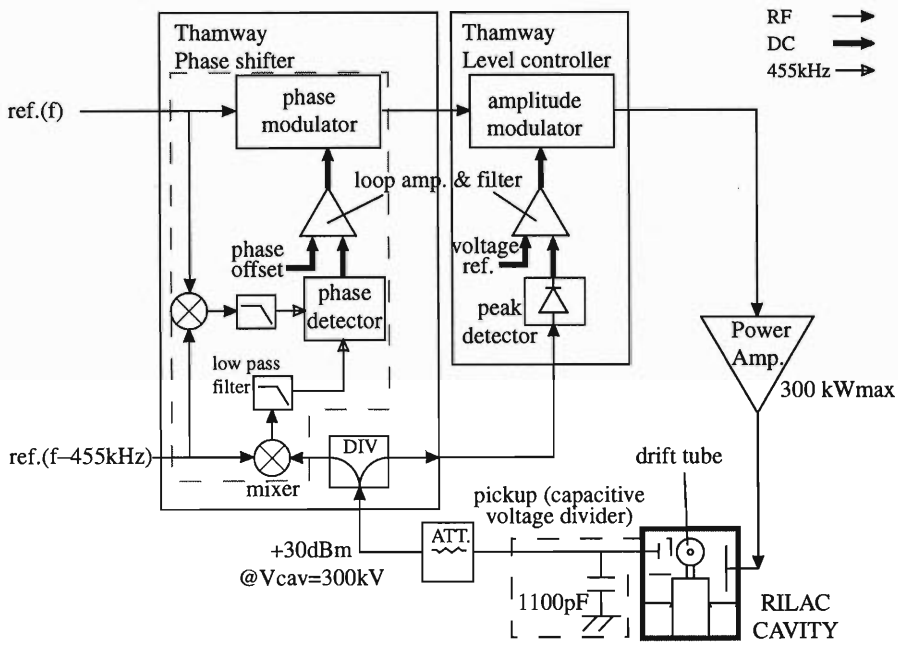

Fig. 1. Simplified block diagram of the new rf feedback control system for RILAC #5 and #6 cavities. $\Delta\phi$: phase shifter, ΔV: amplitude modulator, REG: regulator, DIV: signal divider, ATT: attenuator, GTA: gas tube arrester T08-90.

* SHI Accelerator Service, Ltd.

$\pm 5 \times 10^{-4}$ and a phase modulation of $\pm 0.1°$ correspond to the spectrum levels of -72 dB and -61 dB, respectively. The pickup signal spectrum of #5 cavity is shown in Fig. 2. Ripples caused by the power source occasionally appear as side-bands of 50 Hz, 150 Hz, and 300 Hz. Response of the feedback loop was tailored to satisfy simultaneously side band suppression and loop stability at an rf frequency. In Fig. 2, ripples at the operation frequencies of 18.33 MHz and 32.00 MHz are suppressed to -75 dB and -66 dB, respectively, and are sufficiently small to fulfill the requirement (1). In comparison with the old system, the ripple level was improved by -15–-25 dB.

Long term stability was measured using a vector voltmeter. The amplitude and phase deviations of #5 pickup signal were monitored with an interval of approximately 1 hour and are plotted in Fig. 3. The voltage deviation was much smaller than the vector voltmeter resolution limit of 1.5×10^{-3} and the phase

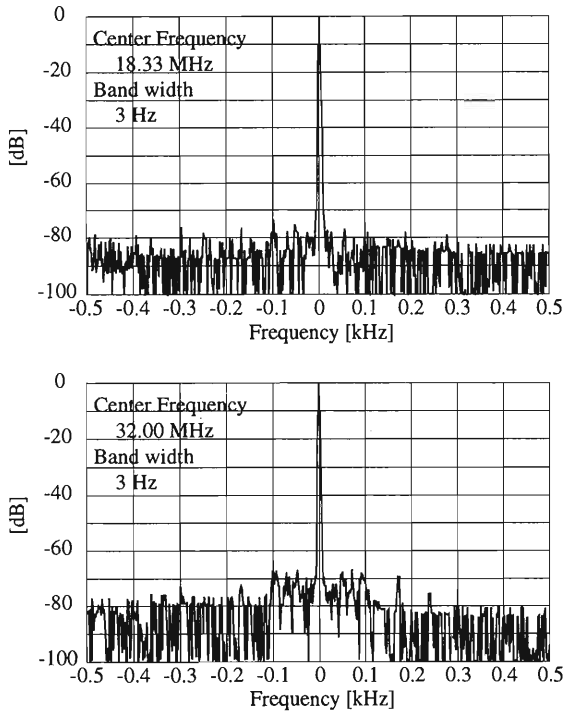

Fig. 2. Frequency spectrums of the pickup signal of RILAC #5 cavity at the operation frequencies of 18.33 MHz (upper) and 32.00 MHz (lower). The amplitude is normalized with a peak level at center frequency.

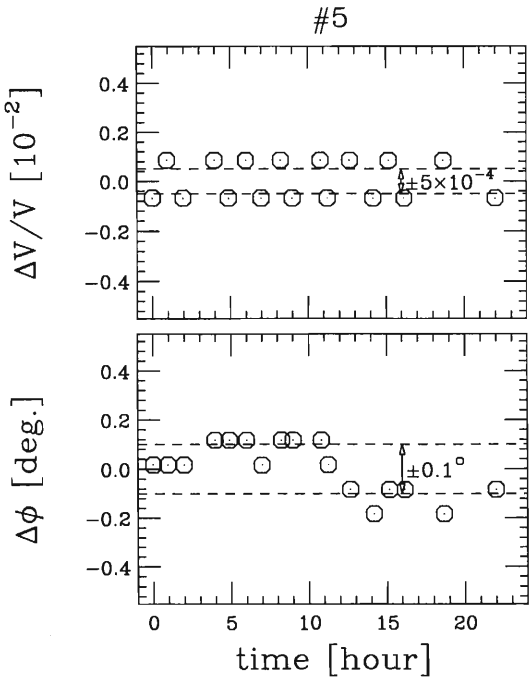

Fig. 3. The voltage and the phase stability of the RILAC #5 cavity at 32.00 MHz. The dashed lines indicate the target stabilities of Eq. (1).

excursion was about $\pm 0.1°$ so that the required stability (1) was successfully achieved. As for #6 cavity the stability was also largely improved.

For #1–#4 cavities, only the phase controllers were replaced by new ones. Then oscillation of old level controller occurred with a side-band frequency of 2–3 kHz. Therefore we made the time constant of the level controller slower. Finally, the oscillation was disappeared and the stability of the rf voltage became the same as those of #5 and #6.

After the renewal of the rf feedback control system, the energy spread of the beam from RILAC is much smaller than before and the longitudinal excursion observed by a phase probe at the exit of RILAC has almost disappeared. This is a great advantage for nuclear experiments, such as superheavy-ion search, which require high energy resolution.

References

1) E. Ikezawa et al.: RIKEN Accel. Prog. Rep. **33**, 6 (2000).

High power operation of CSM cavities

O. Kamigaito, H. Hasebe,* T. Aihara,* T. Ohki,* H. Yamauchi,* A. Uchiyama,* K. Oyamada,*
S. Kohara, N. Sakamoto, E. Ikezawa, M. Kase, and Y. Yano

The accelerator section of the Charge-State Multiplier system (CSM)[1] has been successfully operated as the booster of the RIKEN heavy ion linac (RILAC) since March 2002. In the high-power test before the commissioning, however, we encountered a serious problem of intensive X-ray radiation from the CSM cavities, which was generated by energetic electrons emitted from the electrodes under the high rf-electric field. The origin of the emission was finally found to be carbon dust produced by the teflon components in the cavities. In this paper, the analysis of the X-ray radiation and the remedy for it are given.

The booster of RILAC consists of six cavities, each of which has six or eight rf-gaps, as shown in Fig. 1. Almost all the components are made of oxygen-free copper (C1100). The rf-power is fed through the capacitive feeder, and the rf-voltage is monitored by two capacitive pickups. The vacuum pressure in the cavities remains around 4×10^{-6} Pa when the rf-power is off.

During the high-power test performed in the winter of 2001–2002, very strong X-rays were radiated from the cavities, especially from the first tank (A1), when the gap voltage exceeded 230 kV. The radiation dose exceeded 100 mSv/h on the cavity surface in the worst case. At the same time, the power consumption of the cavity increased. We also found that the beam pipes on both sides of the cavity were heated up to 50 degrees, which increased the vacuum pressure up to 5×10^{-5} Pa. Finally it became impossible to raise the voltage beyond 290 kV, irrespective of the amount of power fed into the cavity; rf-breakdown also occurred frequently. These were considered to be typical phenomena of the field emission of electrons in the cavities.

Figure 2 shows the relationship between the rf-power consumption and the cavity voltage. The relationship in the case of normal operation is expressed by the

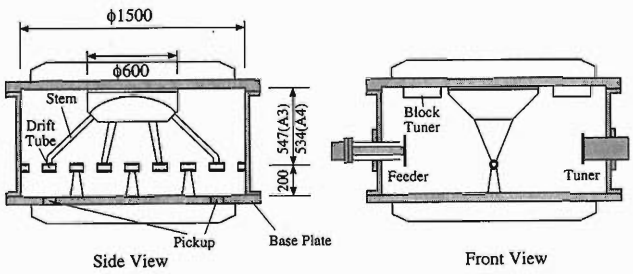

Fig. 1. Schematic drawing of a CSM cavity. All the cavities have a similar structure.[1]

* SHI Accelerator Service, Ltd.

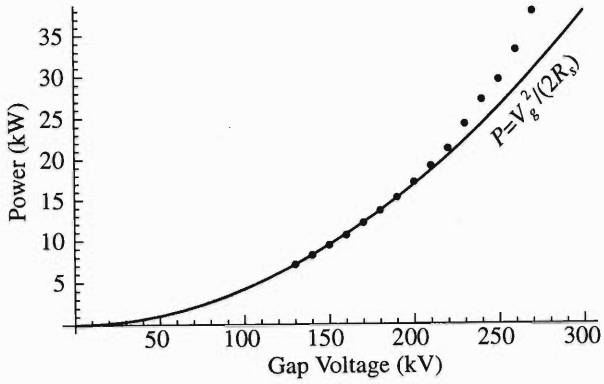

Fig. 2. Power dissipation measured for the CSM-A1 cavity at various gap voltages. The solid curve represents the normal relationship.

quadratic curve whose curvature is proportional to the inverse of the shunt impedance. When the X-rays were radiated, the power dissipation deviated upwards from the curve, as shown in Fig. 2. In the worst case, the difference was 20 kW at 270 kV; about 40 percent of the rf-power was consumed for the electron acceleration.

For the field-emission of electrons, Fowler-Nordheim analysis is applicable.[2] It relates the rms current of emitted electrons in A, $\bar{I}_{FE}$, to the so-called surface enhancement factor β, which represents the field enhancement due to the surface conditions such as protrusions and dust, through the following equation;

$$\frac{d[\log_{10}(\bar{I}_{FE}/E^{2.5})]}{d(1/E)} = -\frac{-2.84 \times 10^9 \phi^{1.5}}{\beta}, \qquad (1)$$

where E and ϕ are the macroscopic surface field (V/m) and the work function of copper (eV), respectively. In other words, the factor β can be determined from the slope of a semi-log plot of $\bar{I}_{FE}/E^{2.5}$ against $1/E$.

We assume that the emitted electrons are accelerated between the rf gaps on the top phase, and the rms current is calculated as follows;

$$\frac{1}{2}\left(\sqrt{2}\bar{I}_{FE}\right) V_g = P_{in} - \frac{V_g^2}{2R_s}, \qquad (2)$$

where V_g, P_{in}, and R_s are the gap voltage, power consumption, and the shunt impedance, respectively. Another assumption was made that the emission took place on the edge of the drift tube where the electric field is the highest. The macroscopic field was estimated by the MAFIA calculations; it is 10.7 MV/m at the gap voltage of 300 kV.

The result is plotted in Fig. 3. In the calculation, ϕ was set to be 5 eV. The slope of the fitted line shows

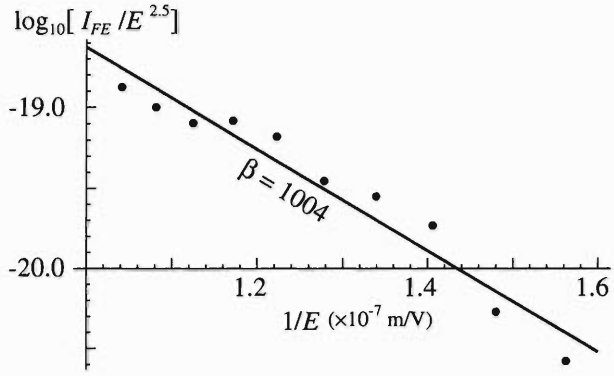

Fig. 3. Fowler-Nordheim plot deduced from the measurement in Fig. 2. The solid line is the fitted one to the data.

that β is about 1000, which means that the surface was heavily polluted.

The inside of the cavity did not appear to be significantly polluted on observation; there were no dark spots nor melted points in spite of the frequent breakdown of the rf voltage. However, we found that very fine, black dust was attached to the entire area of the inner surface, when we wiped it. In addition, the teflon insulators used in the pickups were heavily damaged. A small portion of the insulator, which had been directly exposed to the electron radiation, hardened and decomposed to the thickness of 2 mm, as shown in Fig. 4. It was clear that some amount of the teflon had been missing. We also found that the teflon rings in the feeder and the tuner, which had been used as the positioning guide, were damaged in the same way.

The black dust taken from the inner surface was analyzed by several microanalysis methods: ESCA (electron spectroscopy for chemical analysis), EPMA (electron probe micro analyzer), and XF (X-ray fluorescence spectrometer). Each analysis method showed that the main components of the dust were carbon and copper. In addition, a small amount of fluorine was detected. According to the ESCA analysis, some of the fluorine forms C-F bonds, and some is combined with metal (probably with copper).

The mechanism of the X-ray radiation can be explained in the following way. First, the emitted electrons struck against the teflon surface. The teflon decomposed into small pieces which flew into the cavity, where they further decomposed into carbon and fluorine due to the emitted electrons. When a dust particle hit the electrode, secondary electrons were emitted. Moreover, the fine dust attached on the surface is a source of electron emission. This process enhanced

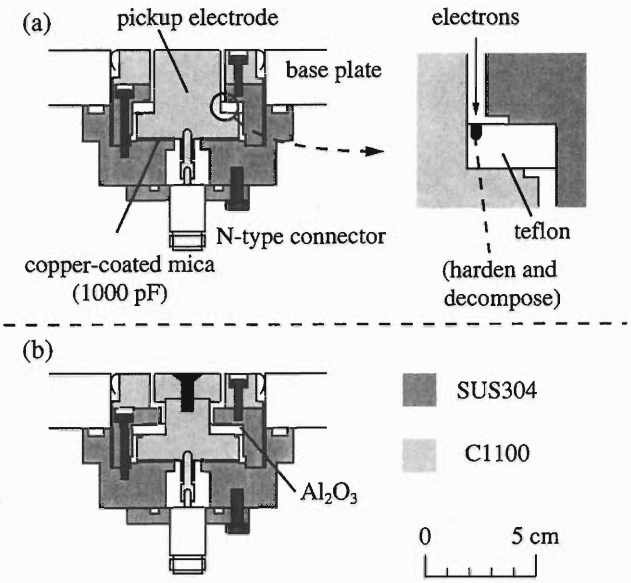

Fig. 4. Schematic drawing of the pickup. The top figure (a) shows the original configuration with a detailed diagram of the teflon insulator damaged by the emitted electrons. The bottom one (b) shows the modified pickup.

the number of emitted electrons, and accordingly, the X-ray dose became higher.

On the basis of the above explanation, we modified the pickups as shown in Fig. 4. The insulator was changed to an aluminum oxide one (Mitsui mining material MA-PL), which is more stable against the radiation. Moreover, the pickup electrode was modified so that the insulator could be shielded from the emitted electrons. The teflon rings in the feeder and the tuner were removed at the same time.

After the above modifications, it has become possible to operate the cavities quite stably. The power is proportional to the square of the rf-voltage up to 320 kV within the acceptable range of measurement accuracy. The vacuum pressure is less than 1×10^{-5} Pa during the operation. Conditioning at higher voltages is in progress.

References

1) O. Kamigaito et al.: Proc. 26th Linear Accelerator Meeting in Japan, Tsukuba, 2001-8 (High Energy Accelerator Research Organization (KEK), 2001), p. 43; http://conference.kek.jp/LAM26/LAM26PDF/1C-5web.PDF
2) G. A. Loew and J. W. Wang: in *Handbook of accelerator physics and engineering* (World Scientific, Singapore, 1999), p. 390.

Beam test and operation of the flattop acceleration system in the RIKEN AVF cyclotron

A. Goto, N. Sakamoto, S. Kohara, K. Takahashi,[*1] P. R. Sarma, O. Kamigaito, R. Taki, M. Kase, S. Watanabe,[*2] T. Teranishi,[*2] H. Iwasaki,[*2] Y. Yanagisawa,[*2] Y. Ohshiro,[*2] T. Katayama, and Y. Yano

Since the installation of the flattop acceleration system in 2001,[1] we conducted a beam acceleration test and have been using it in routine operation.

We measured the longitudinal emittance (phase width and momentum spread) of a beam from the AVF cyclotron by using the CRIB spectrometer.[2] In the measurement, a beam of $^{14}N^{6+}$ ions was accelerated up to 6.4 MeV/u at a fundamental rf frequency of 15.6 MHz and focused at the object point F0 of the CRIB by 2–3 mm in diameter. The positions of particles were measured one by one with a parallel plate avalanche counter (PPAC), which was placed at the image point F1, with the beam intensity being reduced using a beam attenuator placed upstream of the cyclotron. Position and time resolutions of the PPAC were 0.8 mm and 0.6 ns, respectively. The measurement with the flattop system was carried out for four combinations of QM1 and QM2 parameters. Figure 1 shows examples of the beam size (momentum) spectrum and phase-momentum distribution with and without the flattop system. By simultaneously fitting the four beam profiles measured at F1 as well as that at F0 with a single value of transverse beam emittance, the momentum spread when using the flattop system was deduced to be about 0.1% (FWHM). Because the measurement was carried out in only one QM combination for the flattop off, the momentum spread was estimated by assuming that the transverse beam emittance was the same as that for the flattop on and was about 0.3% (FWHM). The phase widths (time spreads) were about 1.2 ns (FWHM) and 1.8 ns (FWHM) for the flattop on and off, respectively.

Beam tuning using the flattop system was carried out with the following procedures. At first, the cyclotron was tuned only with the fundamental rf-frequency system. The third-harmonic frequency system was then excited with the voltage of the fundamental frequency being kept unchanged. The voltage and phase of the third-harmonic frequency were adjusted so as to obtain the flattop signal on an oscilloscope. The reason why the fundamental-frequency voltage was kept unchanged was to obtain a constant orbit in the central region; the central region of the cyclotron was designed to accelerate particles passing through the first and second acceleration gaps at the rf phase of about −30 degrees in order to obtain the beam focused.[3] The beam could have the same energy gain at these two gaps as that with the fundamental-frequency system only, because the contribution of the third-harmonic frequency is zero at this phase. Finally, the phase and voltage were finely adjusted in order to obtain the beam profile immediately after the cyclotron symmetrical and as narrow as possible. We found that the single-turn extraction was achieved more easily with the flattop system. Figure 2 shows an example of beam profiles for both cases.

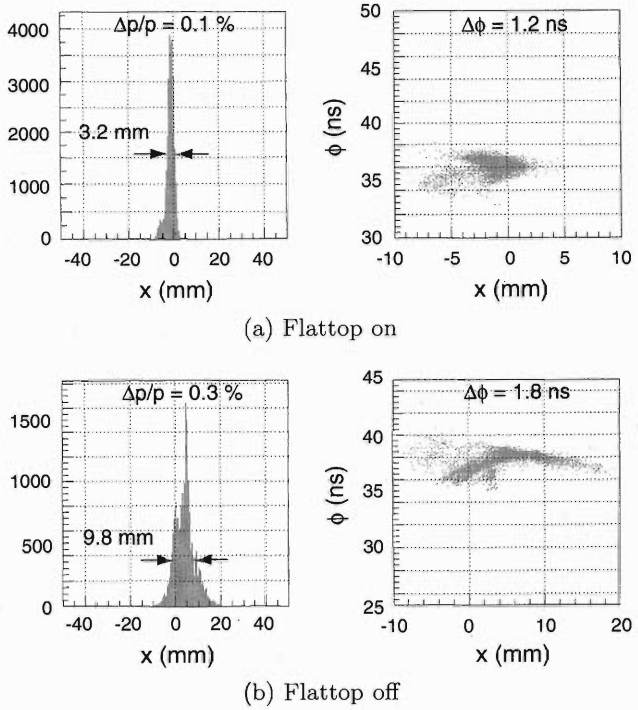

Fig. 1. Beam size (momentum) spectrum and phase-momentum distribution measured with a PPAC placed at F1 of the CRIB: (a) with and (b) without the flattop system.

In routine operation, beam transmission has been improved not only through the AVF cyclotron but also through the RRC. For example, we obtained a transmission of 85% through the RRC compared with that of 75% that had usually been obtained for 70 MeV/u ^{13}C ion beams; the beam intensity of 330 pnA was increased to 490 pnA on target.

Although the flattop system has thus been operated successfully, a problem on the flattop system to be figured out remains, that is, an electric breakdown occurs

*1 SHI Accelerator Service, Ltd.
*2 Center for Nuclear Study, Graduate School of Science, University of Tokyo

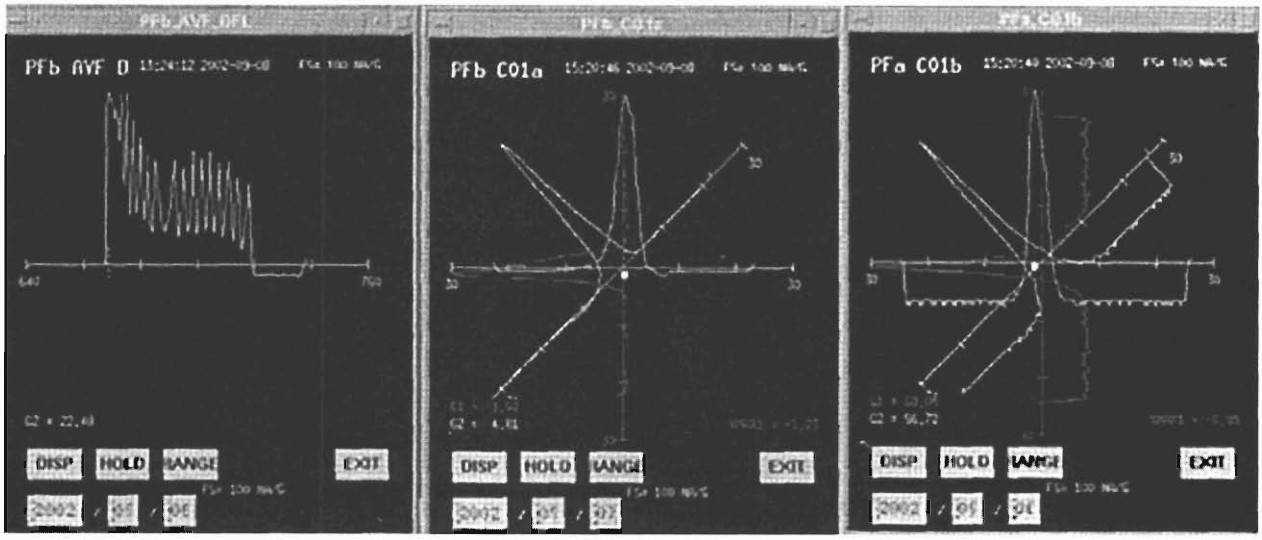

(a) Flattop on

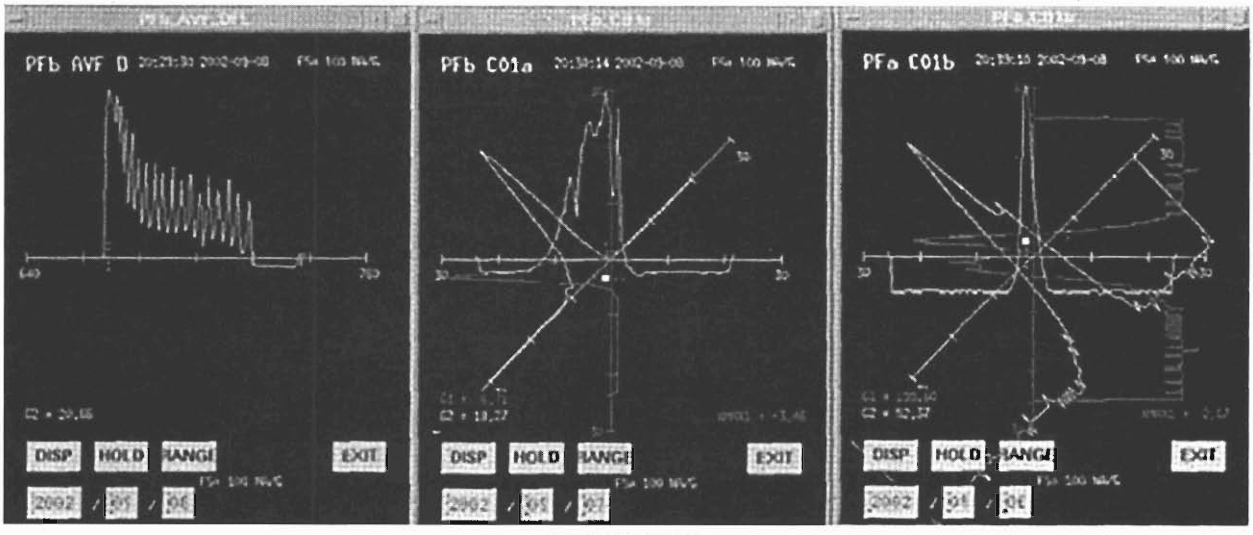

(b) Flattop off

Fig. 2. Beam profiles: (a) with and (b) without the flattop system. For both cases, the profiles at the entrance of the electrostatic deflector and at 3.5 m and 4.5 m downstream from the exit of the cyclotron are shown at the left, middle and right, respectively. The profile after the cyclotron was measured with a set of three thin wires, which were placed along the horizontal, vertical, and slanted lines, respectively.

at the flattop voltage of above approximately 40 kV, while no such breakdown occurs for the fundamental-frequency alone even at the voltage of 50 kV. The cause of that is being investigated.

The flattop system has been constructed in collaboration with the CNS (Center for Nuclear Study, Graduate School of Science, the University of Tokyo).

References

1) S. Kohara et al.: RIKEN Accel. Prog. Rep. **35**, 272 (2002).
2) Y. Yanagisawa et al.: RIKEN Accel. Prog. Rep. **34**, 183 (2001).
3) A. Goto et al.: RIKEN Accel. Prog. Rep. **22**, 205 (1988).

Improvement of momentum resolution: Conventional method and a new scheme

P. R. Sarma,* A. Goto, and Y. Yano

In the standard technique of beam momentum resolution, one uses the property of momentum dispersion by dipole magnets. The resolving power of the dispersive system, which consists of bending magnets and optional quadrupole magnets, depends not only on the dispersive power of the bending magnet, but also on the beam size at the image slit. The various parameters of the resolving system, *viz.*, the magnetic field strengths and lengths of the magnets, the magnet apertures and also the various drift lengths can be optimized for maximizing the resolving power.

The resolving power is $\Delta p/p = R_{16}/2S$. Here, R is the beam transport matrix and S is the size of the beam in the dispersive plane. We have written a code ROBOT (Random Optimization of Beam Optics and Transport)[1] which transports the beam and also performs the optimization by using the random search method. In this method, one chooses the parameters at random from given ranges and tests whether the resolving power (or any other objective function) increases. One subsequently chooses the parameters around this set and gradually reduces the range so that the convergence becomes faster. Figure 1 shows an example of the maximization of resolving power.

Recently we used the CRIB spectrometer[2] for measuring the longitudinal emittance of a $^{14}N^{6+}$ beam with an energy of 7.1 MeV/nucleon extracted from the AVF cyclotron. Only one of the bending magnets of the spectrometer was used for measuring the momentum of the particles coming out at different RF phases.

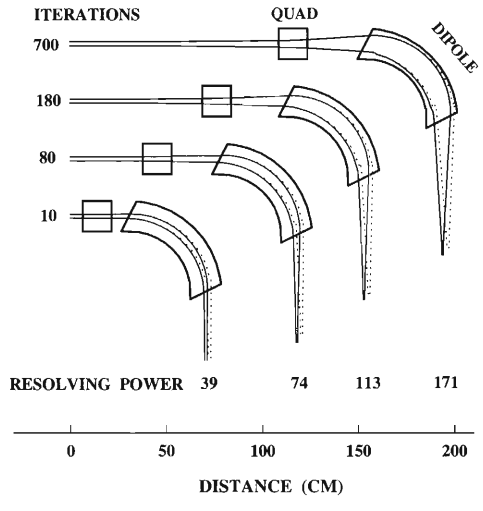

Fig. 1. Resolving power after various iterations.

* Variable Energy Cyclotron Centre, India

Table 1. Typical quadrupole settings for CRIB.

	Gradient in Q1 (kG/cm)	Gradient in Q2 (kG/cm)	R_{16}	Size (mm)
Unoptimized	−.473	.273	157	4.40
Optimized	−.391	.203	182	1.05

The momentum-dispersed beam was detected with a position-sensitive detector (PPAC). We used the code ROBOT for enhancing the resolving power. As the various drift spaces and lengths of the magnetic elements were already fixed, we optimized only the fields of the quadrupoles placed before and after the 90° bending magnet. Table 1 gives typical results of optimization for a beam with an initial size of ±1 mm and a divergence of ±30 mrad. As a result of the optimization, the reduction in the emittance with the flattop on could clearly be seen.

The momentum dispersion by dipole magnets can be understood in terms of the transfer matrices. It is the dependence of the matrix on the beam energy or momentum which causes the dispersion. Thus, in principle, any beam line element, whose transfer matrix depends on the beam energy, can separate the beam energy.

Quadrupole magnets are important beam line elements whose transfer matrices depend on the beam energy. We have investigated the possibility of using only quadrupole magnets (and no dipole magnet) for energy selection. The quadrupoles can be arranged so that they focus the particles of the central energy and defocus the particles of other energies. After passing through a slit, the final beam will contain more particles of the central energy. With one or two quadrupoles, the above-mentioned energy resolution is too small to be useful. However, with three qaudrupoles, the energy selection becomes comparable to that with dipole magnets. We have calculated the design parameters of the quadrupoles and the final drift space for a beam with a central momentum of 0.2698 GeV/c ($^{14}N^{6+}$ beam of energy 7.1 MeV/nucleon) and an emittance of 30π mm.mrad.

Let the beam matrix for a beam line with three consecutive quadrupoles followed by drift spaces D be $\sigma(p)$ which depends on the momentum p. At the target, the half-sizes x_f and y_f of the beam in the x- and y-directions are then $x_f = \sqrt{\sigma_{11}}$ and $y_f = \sqrt{\sigma_{33}}$. It is obvious that the beam size will be different for different momenta and so the density of particles inside a slit will be at its highest for the central momentum and will be lower for different momenta (Fig. 2).

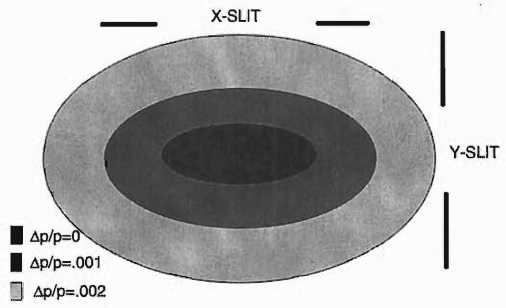

Fig. 2. Dependence of beam size on Δp.

x_f and y_f have hyperbolic dependence on the momentum deviation Δp.

$$x_f^2 - \alpha^2 \Delta p^2 = 1 \quad \text{and} \quad y_f^2 - \beta^2 \Delta p^2 = 1, \tag{1}$$

where α and β give the strengths of momentum dependence on the beam size in the x-direction and y-direction, respectively. Thus, the number of particles N ($< \Delta p$) having momentum deviation within $|\Delta p|$ passing through a given rectangular slit is

$$N\ (< \Delta p) = \int_{-\Delta p}^{\Delta p} \frac{g(\mu) d\mu}{\sqrt{(1+\alpha^2\mu^2)(1+\beta^2\mu^2)}}, \tag{2}$$

where μ represents the momentum deviation Δp and $g(\mu)$ is the momentum dependence of the initial beam. The system will have a high resolution if α and β are large. For finding these out, one has to calculate the beam size for two different momenta, and for maximizing the momentum dependence, it is necessary to optimize the beam line parameters such as the field gradients and lengths of the three quadrupoles and the drift space between them. We have suitably modified the code ROBOT for this purpose. Figure 3 shows the beam envelopes of the beam. Table 2 gives the optimized design parameters. The optinization process reduces the drift spaces between the quadrupoles to zero, *i.e.*, the field changes abruptly between them. In a practical case, there will always be an edge field and so the resolving power obtained will be somewhat less than that calculated.

In this triplet quadrupole scheme, the beam size of off-momentum particles is magnified. Thus one can use a cascade of triplets where the beam size and hence the resolving power will be multiplied after each triplet. In the case of dipoles, one can use only two bending magnets to double the resolving power; the resolving power in this case is additive. Figure 4 shows the resolving power for various numbers of quadrupoles. The fine tuning between two triplets may be carried out by observing the beam current after the second triplet. When the current is maximum, the matching is complete. It is noted here that the resolving power above is the one obtained for the zero distance between the adjacent quadrupoles, and that if the distance is taken

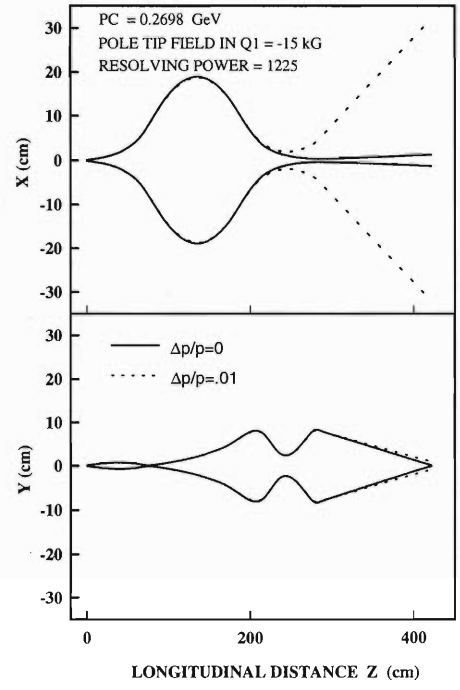

Fig. 3. Beam envelope for two different Δp.

Table 2. Design parameters of a typical system.

Element	Length (cm)	Field grad. (kG/cm)
Quadrupole 1	75.2	−1.5
Quadrupole 2	119.8	0.324
Quadrupole 3	92.2	−1.5
Final drift	135	-

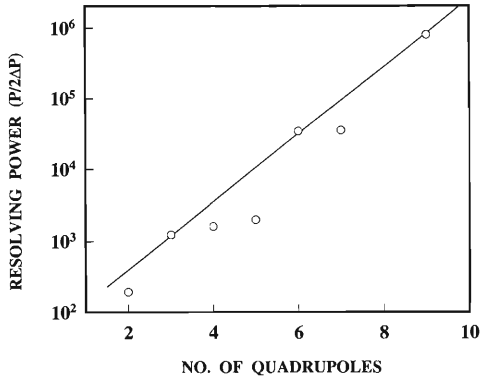

Fig. 4. Increase in resolving power by using cascades of triplets.

to be 10 cm the resolving power decreases by about 40%.

References

1) S. S. Rao: in *Optimization—Theory and Applications*, (Wiley Eastern, New Delhi, 1978) Ch.6.2.
2) S. Kubono et al.: Eur. Phys. J. A **13**, 207 (2000).

Automated irradiation system for radiation biology experiments

H. Akiyoshi, N. Fukunishi, M. Kase, Y. Yano, T. Abe, and S. Yoshida

Radiation biology experiments are frequently performed in the RIKEN Accelerator Research Facility. A new automated irradiation system for radiation biology experiments was constructed. The irradiation system allows automatic irradiation of multiple biological samples with ions at different energies without entering the experimental room or reaccelerating ions to different energies. Hitherto, an automated system was used.[1] However, the system still largely requires manual operation, long-term-radiation damage made the plastic parts fragile, and the control computer of the older system is superannuated without much hope of upgrading the malfunctioning parts due to chronic use. The newly constructed automated irradiation system consists of three sections with a control circuit box and a control computer. Figure 1 shows the schematic of the system.

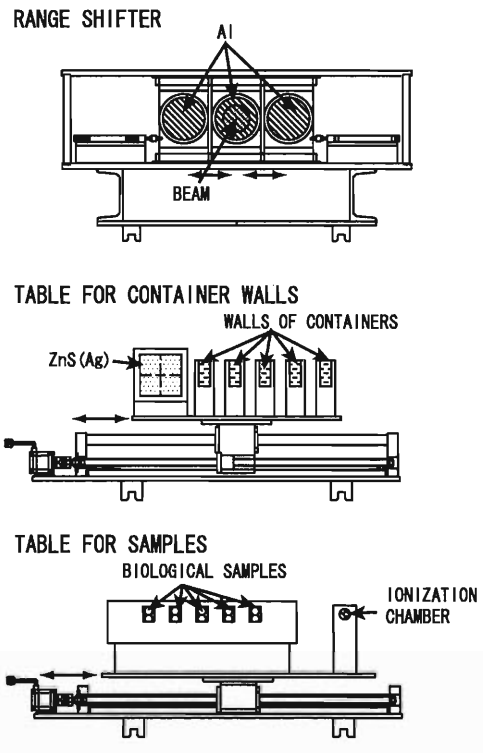

Fig. 1. Schematic of automated irradiation system. All of the three sections of the system are presented on their side view for easy understanding. The figure at the topmost part is the range shifter. The figure in the middle is the table for container walls. The table for samples is drawn at the lowest position. The beam comes from the upper part of the figure, passes through the system, and stops at a beam dump downstream.

The first section is a range shifter section that is placed most upstream of the system. The energy of ions is decreased at the range shifter section by passing the ions through a set of absorbers according to the desired energy for irradiation. The range shifter of the old system uses two rotating wheels on which seven absorbers for each wheel are attached with holes without an absorber. This old range shifter allows only sixty-three combinations of total absorber thicknesses, so absorber reattachment is required each time according to the kind of ion and the incident beam energy. The range shifter of the new system does not require the reattachment of the absorbers because it allows 821 possible total thicknesses of absorbers; this is the first merit of the new system. Combinations of one 0.05-, one 0.1-, two 0.2-, one 0.5-, one 1-, two 2-, one 5-, one 10-, and one 20-mm-thick Al foils and plates are selected to obtain a total thickness of absorbers from 0.05 mm to 41.05 mm at increments of 0.05 mm. The absorbers are placed into the beam position by air cylinders attached to the foils and plates one by one. The thicknesses of Al foils and plates are measured using a micrometer with an accuracy of $\pm 2\,\mu$m, and are used in calibration.

The middle section is a table for container walls. A beam viewer and several plates made by cutting walls of the containers for biological samples are set on the table. The plates are used to calibrate the ionization chamber readout to the previously measured dose curve, adjusting the energy difference caused by the container wall. The table is another merit of the new system, thus manual changing of container walls after opening the heavy shield door and entering the experimental room are no longer necessary. The last section is a table for samples. The tables move to their reference points automatically when the system is turned on.

A sequencer in the control circuit box controls the air cylinders and two AC servo motors for tables according to a command file on the control computer which is connected through a serial cable. The codes for calibration, making the command file, and control of wobbler magnets are written in Java language for easy translation to the other computers running on other operating systems.

The debut of the new automated irradiation system will be in January, 2003.

References

1) T. Kanai et al.: RIKEN Accel. Prog. Rep. **25**, 103 (1992).

Charge strippers for the RI-Beam Factory

H. Akiyoshi, N. Inabe, N. Fukunishi, H. Hasebe,* T. Chiba, M. Kase, and Y. Yano

Charge strippers play an essential role in heavy ion accelerators because high charge-states allow small machines which require low construction costs or allow extended application of existing accelerators. Three stripper sections in the RI-Beam Factory (RIBF) at five typical kinds of energies for the intense heavy ion beams are under investigation at present. Figure 1 shows the schematic of the RIBF. The first section is located between the accelerating and decelerating parts of the charge-state multiplier (CSM). The second section is located between the RIKEN Ring Cyclotron (RRC) and the fixed-frequency ring cyclotron (fRC). The third section is located between the fRC (or the RRC) and the Intermediate-stage Ring Cyclotron (IRC). Three energies are considered for the case with the fRC, and two energies for the case without the fRC that will be actualized immediately after the setting up of the IRC and the Superconducting Ring Cyclotron (SRC). Uranium and xenon ions are considered as typical ions in the case with the fRC, and xenon ions are considered as typical ions in the case without the fRC. In the following discussion, the incident beam currents on the strippers are selected in order to achieve 1 pμA uranium beams and 1.5 pμA xenon beams at 350 MeV/nucleon accelerated with the fRC, and 0.2 pμA xenon beams at 276 MeV/nucleon accelerated without the fRC at the exit of the SRC. The parameters of the strippers for the RIBF in consideration are tabulated in Table 1.

A number of experiments to measure the equilibrium charge-states of various ions at various energies were performed for decades. By fitting these data

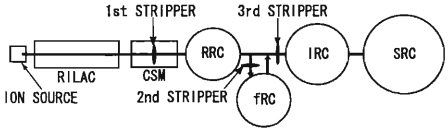

Fig. 1. Schematic of the RIBF.

several semi-empirical global formulae were developed, (*e.g.*, Refs. 1–4). Some semi-empirical formulae, which provide the equilibrium carbon foil[5,6] or gas[5] thickness, were also developed. In the case of ions higher than 30 MeV/nucleon, a numerical calculation code GLOBAL,[7] which provides pre-equilibrium charge-state distribution, was developed. However, the predictions obtained using the formulae and the code vary significantly. On the other hand, we need to know the exact equilibrium charge-states and the equilibrium thicknesses in order to design an accelerator because the required magnetic fields are inversely proportional to the charge of the ions, and a passage of ion beams through the strippers causes energy loss and the increase of the longitudinal and transverse beam emittances due to the energy struggling and multiple scattering. Therefore experiments to obtain such information have been planned. As an outset, the charge-state distribution of ^{136}Xe at 11 MeV/nucleon, which corresponds to the energy at the second section, was measured with strippers of various thicknesses.

The three stripper sections are mainly characterized by the incident energy of the ions. We will present an overview of these three stripper sections.

At the first stripper section, a 15 pμA $^{238}U^{35+}$ beam at 0.9 MeV/nucleon and a 0.9 pμA $^{136}Xe^{38+}$ beam at 2.9 MeV/nucleon are expected. According to Ref. 2 incident uranium and xenon beam currents should be as high as 90 pμA and 10 pμA, respectively. The distinctive features of the first stripper section are thus the high beam intensity and the low energies. Both features cause the short lifetime of carbon foils which are most commonly used charge strippers. For example, when 90 pμA uranium ions at 0.9 MeV/nucleon are focused on a carbon foil with 5-mm-diameter circular shape, using Baron's formula[6] it is predicted that the lifetime of the carbon foil is about 4 seconds. In the case of the 10 pμA xenon beam at 2.9 MeV/nucleon,

Table 1. Parameters of the strippers for the RIBF.

		with the fRC					without the fRC	
Ion		^{238}U			^{136}Xe		^{136}Xe	
Stripper section		1st	2nd	3rd	2nd	3rd	1st	3rd
Energy (MeV/nucleon)		0.9	11	46	11	46	2.9	39
Required charge-state		35+	72+	88+	42+	51+	38+	45+
Thickness (mg/cm^2)	C foil	0.025[6]	0.5[8]	14[7]	0.15	20[7]	0.061[6]	0.25[7]
Expecting charge-state	C foil	36+	72+	88+	44+	52+	38+	45+
Fraction	C foil	17%[2]	19%[8]	34%[7]	30%	52%[7]	9%[2]	23%[7]
Thickness (mg/cm^2)	N gas			0.09,[5] 14[7]	0.03[5]	0.09[5]		0.08[5]
Expecting charge-state	N gas			88+	43+	52+		51+
Fraction	N gas			2%,[1] 30%[7]	20%[1]	30%[1]		28%[1]

* SHI Accelerator Service, Ltd.

the lifetime of the carbon foil is predicted to be 5 minutes. The lifetimes of the carbon foils produced in the RIKEN Accelerator Research Facility are more than ten times longer than those predicted using Baron's formula. A rotating carbon foil may have a greater lifetime because it decreases the energy density deposited to the carbon foil by the beam. For example, when we bombard the 5-mm-diameter beam at the spot between the 15 mm and 20 mm radiuses of the rotating carbon foil, the energy density deposited to the carbon foil by the beam is 1/28 of that of still carbon foil.

Another possible method of improving the resistance to the beam for the xenon case is the use of a liquid film stripper[9] because the temperatures of the carbon foils are well below the evaporating temperature, thus breakage is not expected to be caused by the heat.

At the second stripper section, 3 pμA $^{238}U^{72+}$ and $^{136}Xe^{42+}$ beams at 11 MeV/nucleon are expected. The charge-state distribution of ^{136}Xe was measured with strippers of various thicknesses. The xenon beam was bombarded on carbon foils, aramid films, and a polyimide film with thicknesses from 40 μg/cm^2 to 2.2 mg/cm^2. Figure 2 shows the charge-state fractions of ^{136}Xe at 11 MeV/nucleon. We can use, for example, a 0.15 mg/cm^2 thick foil to obtain $^{136}Xe^{44+}$ with 30% fraction. In the uranium case, an experimental data[8] exists, that the equilibrium charge-state at 11.4 MeV/nucleon stripped by a 0.49 mg/cm^2 thick carbon foil is 73+ with a fraction of 19%. The carbon foil receives 1 kW power when a 15 pμA $^{238}U^{35+}$ beam is stripped by a 0.5 mg/cm^2 thick carbon foil. Again the rotating carbon foil is expected to facilitate the situation. We cannot use a gas stripper for uranium here in order to gain a high charge-state, although according to the prediction by the semi-empirical formula[1] $^{136}Xe^{43+}$ can be achieved by a gas stripper with a fraction of 20%.

Behind the third stripper section 1 pμA $^{238}U^{88+}$ and 1.5 pμA $^{136}Xe^{51+}$ beams at 46 MeV/nucleon, and a 0.2 pμA $^{136}Xe^{45+}$ beam at 39 MeV/nucleon

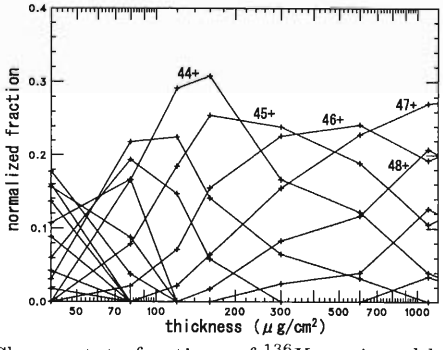

Fig. 2. Charge-state fractions of ^{136}Xe stripped by carbon foils, aramid films, and polyimide film, that were obtained in the present experiment. The charge-state fraction is normalized by the area of Gaussian fitted to the measured charge-state distribution. Numbers on the figure indicates the charge-states of the stripped ^{136}Xe.

are expected. According to the GLOBAL calculation, 34%, 52% and 23% fractions of $^{238}U^{88+}$ at 46 MeV/nucleon, $^{136}Xe^{52+}$ at 46 MeV/nucleon and $^{136}Xe^{45+}$ at 39 MeV/nucleon can be obtained by 14 mg/cm^2, 20 mg/cm^2 and 0.25 mg/cm^2 thick carbon foils, respectively. The thicknesses of the former two cases are selected to obtain 46 MeV/nucleon beams behind the strippers, and the thickness of the last case, without the fRC, is selected to minimize the energy loss due to the stripper foil. The stripper foils as thick as 14 mg/cm^2 or 20 mg/cm^2 receive high power, so it is clearly indispensable to use a rotating carbon foil. The possibility to utilize other solid strippers thinner than the carbon foils was also examined by the GLOBAL calculation. According to the calculation, for example, we can obtain $^{238}U^{83+}$, the required charge-state by the IRC, at 46 MeV/nucleon with 18% fraction by a 1 mg/cm^2 thick tantalum foil receiving a low amount of heat deposit. However, it requires another stripper before injecting into the SRC because the required charge-state by the SRC is 88+. Multiplying the fractions at the strippers downstream of the fRC and the IRC, we obtain 1/6 fraction of the case stripped by a 14 mg/cm^2 thick carbon foil downstream of the fRC, so we will not discuss the other materials further here. The heat problem may be solved if we would use a gas stripper. According to the semi-empirical formulae[1,4] we can obtain sufficiently high charge-states of xenon ions using a gas stripper. However it is a delicate situation in the case of uranium ions at 46 MeV/nucleon. We must obtain $^{238}U^{88+}$ to accelerate with the SRC. The predicted equilibrium charges are 86+ by Schiwietz's formula and 88+ by the GLOBAL calculation, but 84+ by Sayer's formula, so the fractions of 88+ are fifteen times different as 30% by the GLOBAL calculation compared with 2% by Sayer's formula. An experiment with uranium beam will clarify the uncertainty, but we cannot obtain a uranium beam at present. Therefore, some experiments using available beams are being planned to compare the predictions obtained using the formulae and the calculation.

References

1) R. O. Sayer: Rev. Phys. Appl. **12**, 1543 (1977).
2) K. Shima et al.: Phys. Rev. A **40**, 3557 (1989).
3) A. Leon et al.: At. Data Nucl. Data Tables **69**, 217 (1998).
4) G. Schiwietz and P. L. Glande: Nucl. Instrum. Methods Phys. Res. B **175/177**, 125 (2001).
5) M. A. McMahan: *Handbook of Accelerator Physics and Engineering*, edited by A. W. Chao and M. Tigner (World Scientific, Singapore, 1999).
6) E. Baron: IEEE Trans. Nucl. Sci. **26**, 2411 (1979).
7) GLOBAL in C. Scheidenberger et al.: Nucl. Instrum. Methods Phys. Res. B **142**, 441 (1998).
8) Experimental data in Ref. 7.
9) H. Akiyoshi et al.: Proc. 13th Symp. on Accelerator Science and Technology, Osaka, 2001-10 (2001), p. 331.

Conceptual design of the RIKEN fRC

T. Mitsumoto,* A. Goto, N. Inabe, O. Kamigaito, N. Sakamoto, N. Fukunishi, H. Akiyoshi, S. Yokouchi, M. Kase, and Y. Yano

A fixed-frequency ring cyclotron (fRC) is proposed for the RIKEN RI Beam Factory Project.[1] The fRC is used between the RIKEN Ring Cyclotron (RRC) and the Intermediate-stage Ring Cyclotron (IRC). The fRC will enable us to obtain a 350 MeV/nucleon uranium beam with the intensity of 1 pμA at the exit of the Superconducting Ring Cyclotron (SRC). The first conceptual design was reported last year.[2] Some fundamental parameters are modified so that the fRC can be used for the RI beam Factory Project.

The new parameters of the fRC are listed in Table 1. The major modification of the previous design were in terms of the injection and extraction radius. In the new design, energy losses through two charge strippers placed upstream and downstream of the fRC are taken into account. In the case of uranium ions, energy losses by the upstream and downstream charge strippers are considered to be 0.4 and 4.5 MeV/nucleon, respectively.[3] The injection and extraction energies are reduced/increased to be 10.54 MeV/nucleon and 50.72 MeV/nucleon, respectively. The major ions to be accelerated are considered to be $^{238}U^{71+}$ and $^{136}Xe^{45+}$. The maximum magnetic rigidity of the extraction beam is 3.47 Tm.

RF frequency and harmonics are also modified. In the new design, the RF frequency is 54.99 MHz instead of 36.66 MHz. This new value is three times the frequency of the injector linacs. With this modification, the efficiency of the resonators will be much better than that of the previous design. The reduction of phase acceptance will be compensated by a new rebuncher installed between the RRC and the fRC.

The sector magnet of the fRC will be equipped with 10 pairs of trimcoils. The total trimcoil current for one sector is 3 kA, which is much less than that of the IRC of 18 kA. By the reduction of the total current, the structure of the trimcoil will be simplified. Table 2 shows the main parameters of the sector magnets.

Figure 1 shows the layout of the fRC in the E4 experimental room of RIKEN Accelerator Research Facility (RARF).[4] The main components of the fRC will be installed in 10.8 m square area. The weight of the fRC is considered to be 1400 tons.

Table 1. Main parameters of the fRC.

K-b value		570 MeV
Number of sectors		4
Mean radius	Injection	1.55 m
	Extraction	3.30 m
Injection energy		10.54 MeV/nucleon
Extraction energy		50.72 MeV/nucleon
Velocity gain factor		2.126
Number of cavities		2
Harmonics		12
RF frequency		54.99 MHz

Table 2. Main parameters of the sector magnets.

Pole gap	50 mm
Sector angle	58.4 degree
Total height	3.34 m
Weight	330 tons/sector
Maximum magnetic field	1.68 T
Main coil	
Maximum current	650 A
Maximum excitation current	91 kA/sector
Power consumption	60 kW/sector

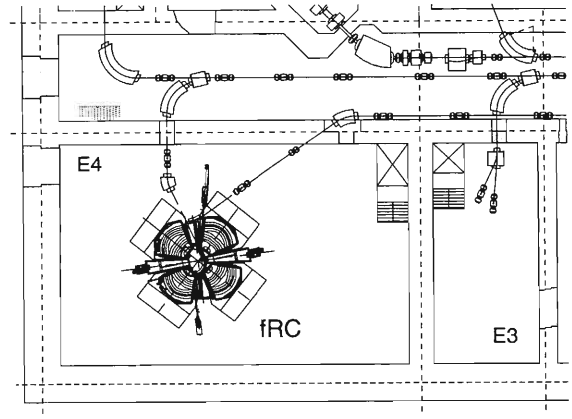

Fig. 1. Layout of the fRC.

References
1) Y. Yano et al.: RIKEN Accel. Prog. Rep. **34**, 301 (2001).
2) T. Mitsumoto et al.: RIKEN Accel. Prog. Rep. **35**, 277 (2002).
3) H. Akiyoshi et al.: RIKEN Accel. Prog. Rep. **36**, 292 (2003).
4) http://www.rarf.riken.go.jp/

* Sumitomo Heavy Industries, Ltd.

Magnetic field measurements of the beam injection and extraction elements for the IRC

J. Ohnishi, T. Mitsumoto,* A. Goto, and Y. Yano

A series of magnetic field measurements of the intermediate-stage ring cyclotron (IRC) had been performed in the factory of Sumitomo Heavy Industries Ltd. since 2000. These results have been already reported.[1,2] This report describes the results of the magnetic field measurements of the beam injection and extraction elements.

Figure 1 shows a schematic of the IRC injection and extraction elements. The injection system consists of one bending magnet (BM), two magnetic channels (MIC1, MIC2), and one electrostatic inflection channel (EIC). The extraction system consists of one electrostatic deflection channel (EDC), two magnetic channels (MDC1 and MDC2), and two bending magnets (EBM1, EBM2).[3]

Figure 2 shows cross sections of the magnetic channels. The magnetic channels are placed in the pole gap (80 mm) of the sector magnets. Coils are made of 7 mm × 7 mm hollow conductors with a hole of 4 mm in diameter for cooling water. Iron shims are used for the MIC1 and MIC2 to increase magnetic field strength. Their thicknesses are 2.2 mm and 5 mm, respectively. The magnetic channels except for the MIC2 have compensation coils for reducing the leakage magnetic fields on the circulation orbit of the beam.

Figure 3 shows the magnetic field strength of the MIC2 as an example. The abscissa is the magnetic field strength of the sector magnets and the ordinate is the MIC2 magnetic field, indicating an increase in the sector fields. As shown in Fig. 3, the MIC2 can increase the sector field, which produces the MIC2 field,

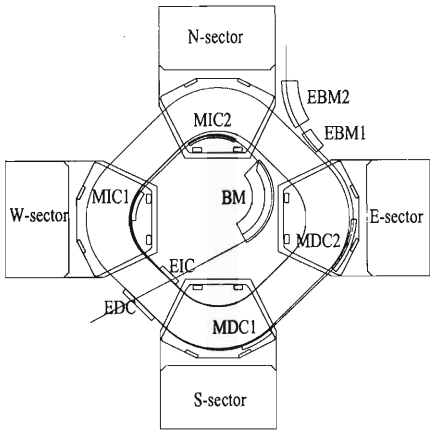

Fig. 1. Schematic of the injection and extraction elements for the IRC.

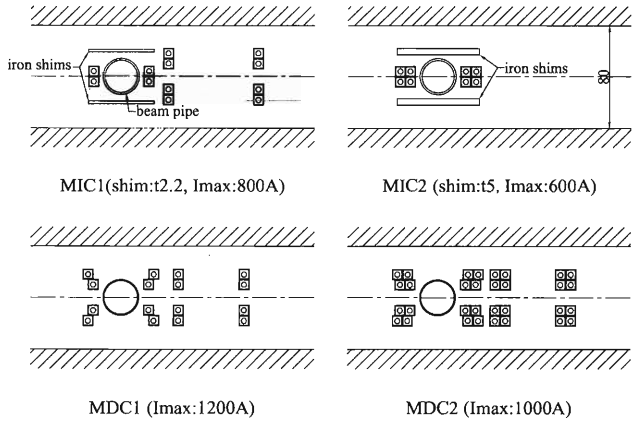

Fig. 2. Cross sections of the magnetic channels. The magnetic channels are placed in the pole gap (80 mm) of the sector magnets.

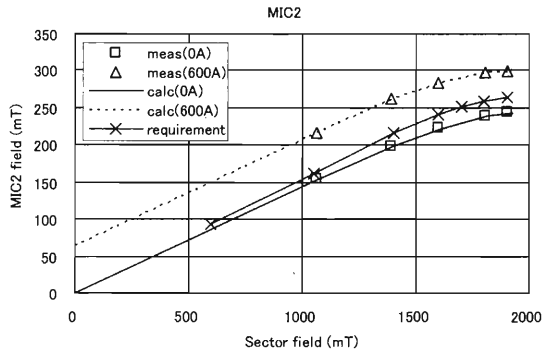

Fig. 3. Calculated and measured magnetic field strengths of the MIC2.

by the iron shims even when the current of the MIC2 is 0 A. Magnetic field calculations were carried out by two-dimensional code "POISSON." The measured data are in good agreement with the calculation results, considering the poles of the sector magnets. It was found that the magnetic field strengths required for the injection of the real beams are within the adjustable limits of the coil current. It was confirmed that other magnetic channels also satisfy the design requirements.

Magnetic field mapping was performed to measure the magnetic perturbation from the injection and extraction elements. Figure 4 shows the perturbation of the magnetic field on the first equilibrium orbit from the E-sector to the N-sector as an example, which is the largest perturbation. The abscissa indicates the

* Sumitomo Heavy Industries, Ltd.

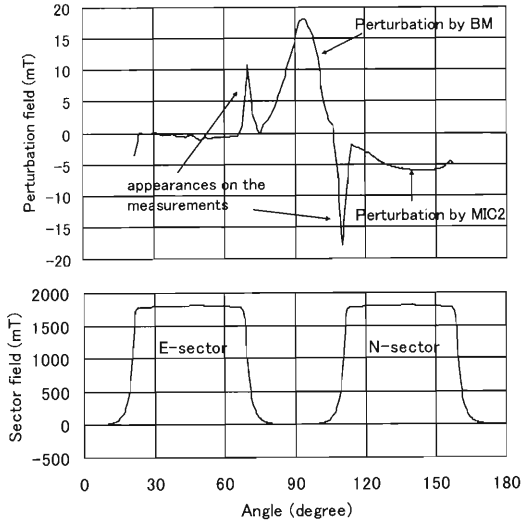

Fig. 4. Perturbation of the magnetic field on the most inside circulation orbit of the cyclotron. Lower graph shows the magnetic field on the same orbit. Apparent peaks are due to the positional error of the hall probes in the field-changing region.

azimuth angle of 90 degrees for the valley center between E- and N-sector magnets. These data were obtained from the difference between the field mapping data with BM, MIC2, EBM1, and EBM2 and without these elements. In field mapping, the sector magnets, BM, EBM1 and EBM2, were excited at the magnetic field strength required for the beam with a $B\rho$ of 2.92 Tm which is near the maximum value. Although the MIC2 could not be excited due to a shortage of cooling capacity in this field mapping, it has been confirmed that the perturbation field generated by a coil current of the MIC2 is small in another measurement. Figure 4 shows that the maximum strengths of the perturbation field are 18 mT and −6 mT for the BM and the MIC2, respectively.

The perturbation of the magnetic field from other injection and extraction elements has been also measured by field mapping. Based on the results of the magnetic field measurements, these perturbations will be cancelled by using trim coils of the sector magnets in the beam operation of the cyclotron. For the magnetic perturbation field produced by the BM, we will try to reduce it by adding a magnetic shield to the BM.

References

1) J. Ohnishi et al.: Proc. 16th Int. Conf. on Cyclotrons and Their Applications, East Lansing, USA, 2001-5 (AIP, 2001), p. 351.
2) J. Ohnishi et al.: RIKEN Accel. Prog. Rep. **35**, 279 (2002).
3) T. Mitsumoto et al.: Proc. 16th Int. Conf. on Cyclotrons and Their Applications, East Lansing, USA, 2001-5 (AIP, 2001), p. 167.

Status of the SRC for the RIKEN RI Beam Factory

A. Goto, H. Okuno, J. Ohnishi, N. Fukunishi, S. Fujishima,[*1] T. Tominaka, K. Ikegami, N. Sakamoto, Y. Miyazawa, S. Yokouchi, T. Fujinawa,[*2] T. Mitsumoto,[*3] O. Kamigaito, H. Akiyoshi, M. Kase, and Y. Yano

This year, fabrication of each component of the SRC has been progressing for completion in the spring of 2003.

For the sector magnet,[1] winding of the superconducting main coils and trim coils has been underway; nine of the twelve main coils and seven of the twenty-four trim coils have already been completed as of November 2002 (see Figs. 1 and 2). Errors of positions of the center of the main coil's cross section, which come from the fabrication errors of the coil vessel, the winding errors of the coils, and the change of shape due to welding of the seal covers, turned out to be within the tolerance of ±1 mm. Errors for the trim coils were also within the tolerance of ±2 mm. Among the six cryostats, two pairs of side wall and beam chamber wall have been welded to each other. A set of the side wall and beam chamber wall is shown in Fig. 3. Also carried out was the trial fabrication of the normal-conducting trim coil that is made of double tubes, which consist of a copper conductor tube of 10 mm in diameter covered with stainless steel tube of 17 mm in diameter with an insulator in between. The normal-conducting trim coils will be attached to the surface of the beam chamber wall. The poles have been completed (see Fig. 4), and the yokes and magnetic shields are being fabricated. By considering the radiation vulnerability of normally used Mylar films of the multilayer insulator, we have decided to adopt

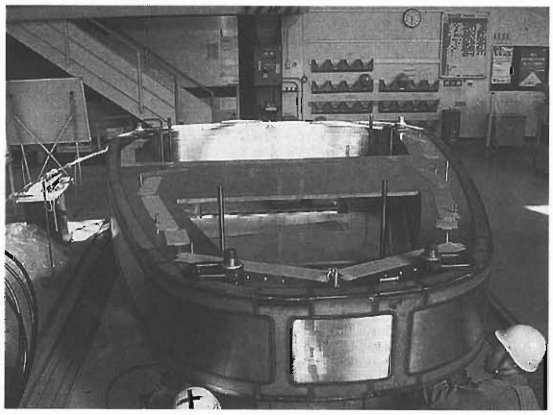

Fig. 1. Completed main coil covered with its vessel. Welding lines for sealing can be seen.

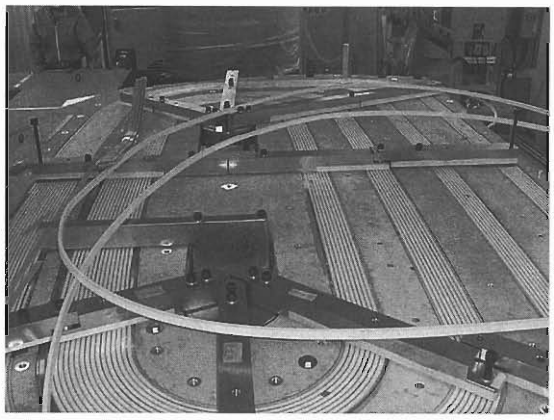

Fig. 2. Winding of the trim coils.

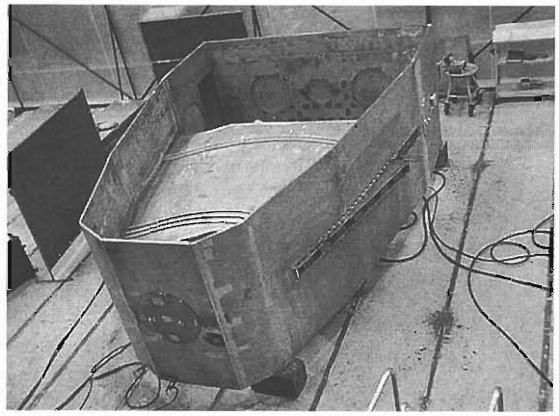

Fig. 3. Side wall and beam chamber wall of the cryostat. Three normal-conducting trim coils are attached to the surface of the beam chamber wall.

Fig. 4. Completed poles.

*1 Ishikawajima-Harima Heavy Industries Co., Ltd.
*2 Mitsubishi Electric Corporation
*3 Sumitomo Heavy Industries, Ltd.

polyimide films for one third of their total areas that would be exposed to high radiation levels, with the remaining two thirds being covered with the Mylar films.

The detailed mechanical design of the He control Dewar vessel for the main and trim coils has been finalized. The outer cryostat vessel measures 2.5 m in diameter by 3.7 m in height; the volume of the helium vessel is about 2.4 m^3. The connection of the main and trim coils among the six sector magnets is made inside the control Dewar vessel. The design of the helium transfer line between the refrigerator and the control Dewar vessel has also been finalized by analyzing the pressure drop in the line. Three compressors have been completed and a refrigerator TCF200S is under fabrication.[2] The arrangement of instrumentations such as temperature sensors, strain gauges, and so forth. has been finalized. About 350 temperature sensors and about 260 strain gauges are attached onto various places of the low-temperature part of the sector magnet.

Two important R&D tests were made on the helium vapor-cooled current leads for use in correction the currents of the main and trim coils and for the SBM,[3] and on the irradiation effect on cryogenic temperature sensors.[4] Two types of current leads for currents of 500 A, 400 A and 100 A (cable-in-conduit type and groove type) were designed, fabricated and tested. Both types were experimentally confirmed to be reliable for use in the SRC. In order to determine the effects of irradiation on temperature sensors such as Cernox^{TM}, CGR and PtCo, their samples were irradiated using 210 MeV proton beams from the RRC. It was experimentally confirmed that Cernox^{TM} was more resistant to radiation than CGR and that PtCo was strongly resistant at least up to the equivalent dose of 10^4 Gy.

Thirty-eight sets of power supplies for the normal-conducting trim coils have been completed. The power supplies for the main coils and superconducting trim coils are in near completion.[5]

Three of the four main rf resonators have already been completed (see Fig. 5). The fourth resonator and a flattop resonator, both of which are attached to each other, are in the course of fabrication; the outer chambers for both have been completed. A new rf feedback control device for better phase and voltage stability has been developed for the RILAC cavities whose power amplifiers are the same as those for the SRC.[6] The new device has allowed us to obtain markedly improved stability resulting in a more stable beam from the RILAC. It will also be introduced into the rf system of the SRC.

The other components of the SRC such as injection and extraction channels, valley chambers, vacuum pumps, beam diagnostics devices, and so forth. are also under fabrication. For the electrostatic inflection channel (EIC) and electrostatic deflection channel (EDC), the detailed design was finalized.[7] The extraction bending magnet (EBM) has been completed and was found to produce a magnetic field of 2.2 T according to the design.

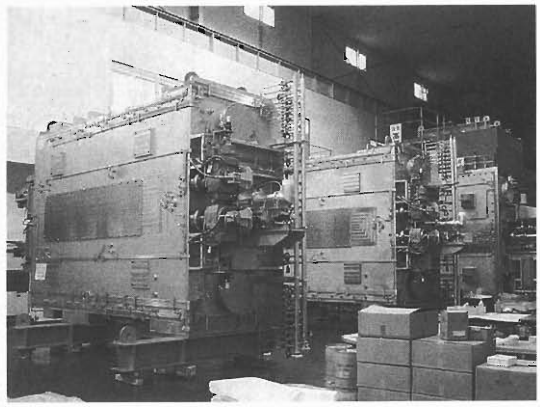

Fig. 5. Completed main rf resonators.

A contract will be placed on the fabrication of the components of the injection and extraction beam lines within this fiscal year.

Figure 6 shows the photograph of the SRC vault that was taken in December 2002.

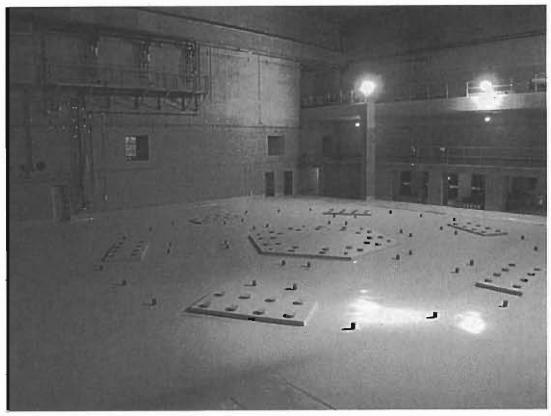

Fig. 6. Photograph of the SRC vault taken in December 2002.

References

1) A. Goto et al.: AIP Conf. Proc. **600**, 319 (2001).
2) K. Ikegami et al.: RIKEN Accel. Prog. Rep. **36**, 303 (2003).
3) T. Tominaka et al.: RIKEN Accel. Prog. Rep. **36**, 304 (2003).
4) T. Tominaka et al.: RIKEN Accel. Prog. Rep. **36**, 306 (2003).
5) N. Sakamoto et al.: RIKEN Accel. Prog. Rep. **36**, 283 (2003).
6) J. Ohnishi et al.: RIKEN Accel. Prog. Rep. **36**, 301 (2003).
7) S. Fujishima et al.: RIKEN Accel. Prog. Rep. **36**, 308 (2003).

Beam space charge simulation in the RIKEN SRC

S. B. Vorojtsov,[*1] A. S. Vorozhtsov,[*1] T. Mitsumoto,[*2] A. Goto, and Y. Yano

The present investigation is a numerical simulation study focused on the longitudinal space charge (LSC) effects of heavy-ion beams in the RIKEN SRC.[1] Detailed description of the simulation is given elsewhere.[2]

Three-dimensional multi-particle simulation code "NAJO",[3] which has recently been modified, was used to simulate the beam dynamics under rather realistic conditions. Simulations were made mainly for $^{16}O^{8+}$ ions because of their large number of turns and small turn separation at the extraction radius. Simulations were also made for $^{238}U^{88+}$ ions.

Machine parameters of the SRC given in Refs. 1, 4, 5, and 6 were used in the present calculations with some modifications. Radial dependence of the energy gain per turn was derived from the recently measured data for the rf resonator of the IRC, which is similar to that of the SRC. Radial distribution of the RF voltage in the flattop (FT) resonator (the third harmonic) was assumed to be analogous to that of the main RF resonator. The magnetic field map given in the SRC design[5] was used in the simulations.

The closed-equilibrium orbit code was used to calculate the properties related to the beam dynamics, which were determined by the magnetic field map. Figure 1 shows the tune diagram for the $^{16}O^{8+}$ and $^{238}U^{88+}$ beams.

In the present simulations the starting point for particles was set at the innermost radius and center of the valley where the SBM is placed. The central particle of the beam was given initial parameters corresponding to the accelerated equilibrium orbit (AEO). Ions were accelerated to the desired final beam energy with ~276 turns for the $^{16}O^{8+}$ beam. The radial turn pattern given by a differential probe was simulated. The probe had a radial position sensitivity of 0.5 mm with a finger attached behind the block of the main electrode. The turn separation for the central beam was ~4.5 mm at the EDC. In order to get larger turn separation at the extraction radius, a precessional motion was introduced by initially giving the beam a small angle at the starting point. The off-centered beam (with the deviation of +6 mrad from the AEO at the starting point) yielded the turn separation of 10.6 mm at the extraction radius. Under these conditions the beam clearance between the last two turns was 2.3 mm at the level of 0.1% as shown in Fig. 2.

In order to get an idea of the LSC effects, the dependence of beam widening on the number of neighboring turns which would contribute to the space charge force was investigated. Figure 3 shows the beam widening as a function of the number of neighboring turns for the beam intensity of 6 pμA. It can be seen that the increase in the radial beam width due to the LSC effects is ~15% for a single turn and approaches 22–23% as the number of neighboring turns increases. We con-

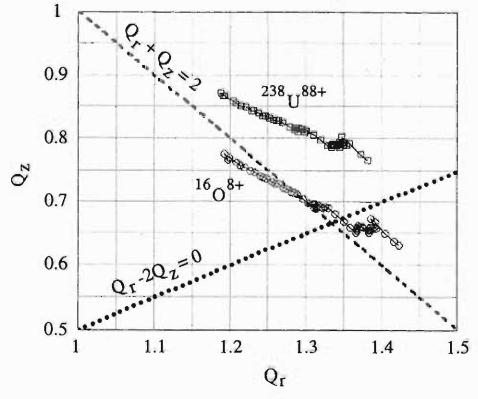

Fig. 1. Tune diagrams for the $^{16}O^{8+}$ and $^{238}U^{88+}$ ions.

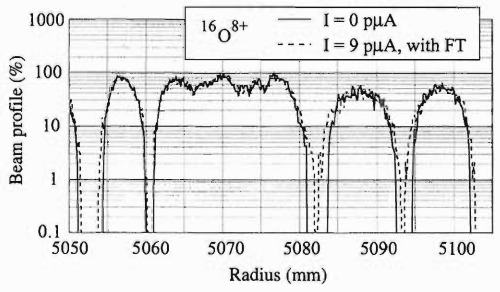

Fig. 2. Radial turn patterns for the $^{16}O^{8+}$ ions obtained with off-centering. Solid line: $I = 0\,\mathrm{p}\mu\mathrm{A}$, and dash line: $I = 9\,\mathrm{p}\mu\mathrm{A}$ and FT phase = 180°.

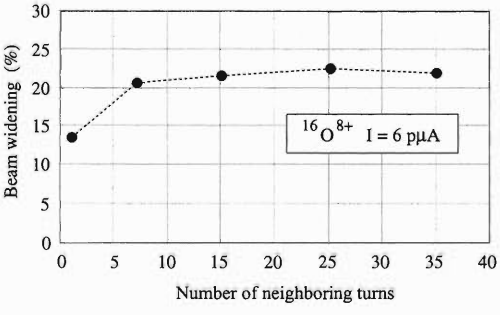

Fig. 3. Dependence of beam widening on the number of neighboring turns that would contribute to the space charge force.

*1 Joint Institute for Nuclear Research, Russia
*2 Sumitomo Heavy Industries, Ltd.

cluded that 25 turns in total (12 turns upstream and 12 turns downstream) were sufficient to estimate the LSC effect with an accuracy of ~1%.

The maximum allowable intensity for the $^{16}O^{8+}$ ion beam was estimated to be ~9 pμA as shown in Fig. 4. The intensity limit is defined by the beam intensity when the particle losses due to the radial widening of the SC dominated beam is 1%. While the thickness of the septum of the EDC is ~0.5 mm, the beam clearance between the last two turns should be larger than the thickness because of the shadow of the septum. Compensation of the LSC effect by the FT phase shift in the range of 180°–181.25° allowed us to increase this intensity limit up to ~20 pμA as shown in Fig. 4.

For the $^{238}U^{88+}$ ion beam, it was necessary to perform 321 turns to reach the desired final energy. Corresponding tunes for this ion are given in Fig. 1. The turn separation of the centered beam was 3.6 mm at the extraction radius. Off-centered injection with the deviation of −2 mm and +6 mrad from the AEO allowed us to get the turn separation of 10.8 mm at the extraction radius. Under these conditions the beam clearance between the last two turns was ~3 mm at the level of 0.1%. The maximum allowable intensity for the $^{238}U^{88+}$ ion beam was estimated to be ~1.8 pμA as shown in Fig. 5. Compensation of the LSC effect by the FT phase shift allowed us to increase this intensity limit up to ~2.1 pμA.

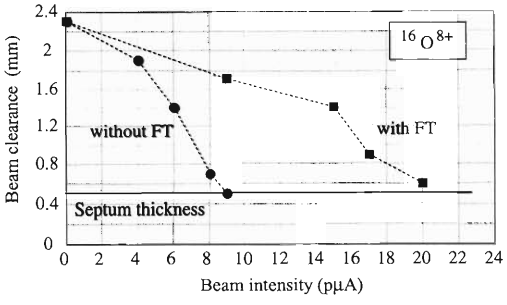

Fig. 4. Beam clearance between the last two turns as a function of beam intensity for the $^{16}O^{8+}$ beam.

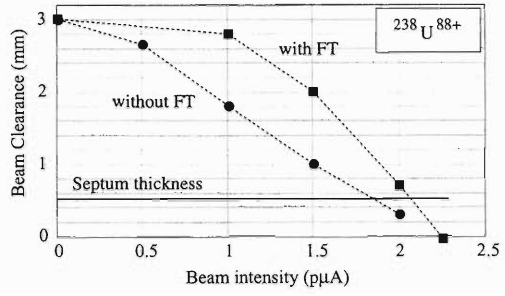

Fig. 5. Beam clearance between the last two turns as a function of beam intensity for the $^{238}U^{88+}$ beam.

References

1) Y. Yano et al.: Proc. 2001 Particle Accelerator Conf., Chicago, USA, 2001-6 (IEEE, 2001), p. 575
2) S. B. Vorojtsov et al.: RIKEN-AF-AC-36 (2002).
3) A. Chabert et al.: Proc. Conf. on Accelerator Design and Operation, Berlin, Germany, 1983-9 (Springer-Verlag, 1984), p. 164.
4) N. Sakamoto et al.: Proc. 12th Symp. on Accelerator Science and Technology, Wako, 1999-10 (1999), p. 221.
5) A. Goto et al.: RIKEN Accel. Prog. Rep. **35**, 285 (2002).
6) J. W. Kim et al.: Proc. 1999 Particle Accelerator Conf., New York, USA, 1999-3~4 (IEEE, 1999), p. 2268.

Power supply system for SRC superconducting coils

J. Ohnishi, T. Tominaka, M. Nagase, H. Okuno, and A. Goto

The Superconducting Ring Cyclotron (SRC) is composed of six sector magnets. Each sector magnet has a pair of superconducting main coils and four pairs of superconducting trim coils as well as 22 pairs of normal-conducting trim coils.[1)]

Figure 1 shows a connection diagram of the power supply system for the SRC superconducting coils. The power supplies of the main coils are composed of one main power supply (P0) with the maximum current of 5200 A and six auxiliaries (P01–P06) with that of 100 A which are used to adjust differences of magnetic fields among the sector magnets. The trim coils have four main power supplies (P1–P4) with the maximum current of 3200 A, two auxiliaries (P11, P12) with that of 400 A, and six auxiliaries (P21–P42) with that of 100 A. Each power supply for the trim coils can change its current direction by a switch. The auxiliary power supplies for the trim coils are used for correction of the magnetic field perturbations produced by the injection and the extraction elements. The current leads of the trim coils, which connect the room-temperature cable to the coils at liquid helium temperature, are also shown in Fig. 1 (T1–T5). The current leads between adjacent coils are used commonly as shown in Fig. 1 in order to reduce the heat loss in the current leads. As a result, the power supply system for the trim coils is grounded at one point. Parameters of the power supplies for the SRC superconducting coils are listed in Table 1. All power supplies operate in constant current mode with very high stability as shown in Table 1.

Each superconducting coil has a strong magnetic coupling in the same sector magnet. The inductance matrix is shown in Table 2. It was deduced from the magnetic energy calculated with the 3D magnetic field calculation code "TOSCA," assuming no magnetic coupling among the sector magnets. The inductance of each coil changes with excitation level because of the existence of the iron yokes. In Table 2, two values corresponding to low and high excitation levels are

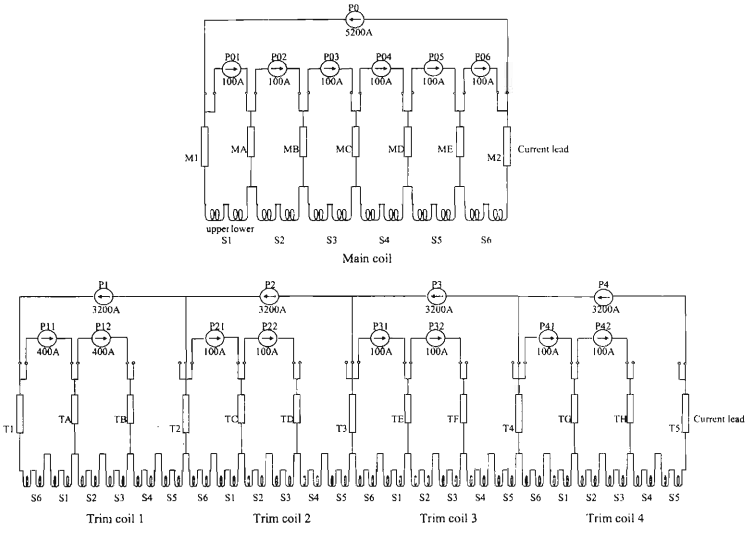

Fig. 1. Connection diagram of SRC power supply system. S1–S6 denote the number of the sector magnet and M1, M2, MA–ME, T1–T5, TA–TH denote the current leads.

Table 1. Parameters of the power supplies for SRC superconducting coils.

	Main coil		Trim coil		
	Main	Auxiliary	Main	Auxiliary 1	Auxiliary 2
	P0	P01–P06	P1–P4	P11, P12	P21–P42
No.	1	6	4	2	6
Nominal current [A]	5200	100	3200	400	100
Max. voltage [V]	35	16	8	10	16
Max. power [kW]	182	1.6	25.6	4	16
Ramp rate [A/s]	0.1–1.5	0.1–1.5	0.1–5.0	0.1–5.0	0.1–5.0
Dump resistor [Ω]	0.3/0.015	2	0.05	0.1	0.3
8 hours stability [ppm]	5	20	5	20	100

Table 2. Inductance matrix for the SRC superconducting coils at low and high excitation levels. The former is the value at low excitation level. For the self-inductance of the main coil, the value is given from the stored energy of the maximum current.

	Main	Trim1	Trim2	Trim3	Trim4
Main	18782				
Trim1	−51/−18	1.8/1.3			
Trim2	−1180/−364	9.7/4.2	188/88		
Trim3	813/273	0.0/0.1	0.1/3.5	89/42	
Trim4	445/139	0.0/0.0	0.0/1.3	46/18	52/31

given for the inductances except for the self-inductance of the main coil, for which the value is calculated from the stored energy at the maximum current. Two values for the inductances of the trim coils were calculated from the energies in cases where iron yokes exist and do not exist. On the other hand, two values for the mutual inductances between the main and the trim coils were calculated from energies where the iron yokes exist and currents of the main coil are 1000 A and 5000 A, respectively.

Figure 2 shows a simplified circuit diagram of the main coil power supply. It consists of a converter, a chopper using the insulated gate bipolar transistor (IGBT) and a coil protection circuit. When a quench of a superconducting coil occurs, power supplies are required to discharge the stored energy of the coil and to decrease the coil currents rapidly such that the temperature rise of the coil by Joule heating is maintained at an acceptable value. The time constant of the main coil was designed to be 60 seconds considering the temperature rise and the insulating voltage of the coil.[2] The coil protection sequence is as follows: a) The IGBT chopper is turned off and the thyristor THY1 is turned on; b) The coil current is commutated to THY1; c) Two high-speed circuit breakers (HSCB) SW1and SW2 are opened; and d) The coil current is commutated to a pair of dump resistors R1's of 0.3 Ω and decays at a time constant of about 60 seconds. Two HSCBs are used for redundancy. On the other hand, when a problem with either the cryogenic cooling system or the power supply itself occurs, the thyristor THY2 is turned on and only HSCB SW2 is opened. Then the stored energy is discharged slowly at a time constant of 1200 seconds in the dump resistor R2 of 0.015 Ω. This slow-discharge scheme is adopted in order to avoid evaporation of a large quantity of liquid

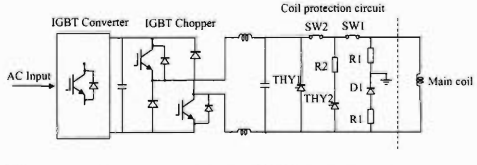

Fig. 2. Circuit diagram of the SRC main coil power supply.

helium due to the eddy current loss in the fast discharge. The dump resistors R1 and R2 are made of steel with a weight of about 2.5 tons and air-cooled.

Since, in general, the fast discharge of one coil sometimes causes unallowably large induced voltage and/or current increase to the other coils due to the magnetic coupling in the complex coil system such as the SRC, the order of discharge and the selection of each dump resistor is very important. When the SRC main coil is dumped at fast discharge, the main power supplies for the trim coils and all the auxiliary power supplies must be switched to corresponding dump resistors in advance. The resistance for each power supply is listed in Table 1. Figure 3 shows the calculated currents and voltages of the main and the trim coils during the fast discharge. In this calculation, the steps of the fast discharge are as follows: First, the main and the trim coils are excited at the maximum current of 5200 A and 3200 A, respectively; Next, four trim coils are cut off at $t = 1$ sec. and their discharge starts; Last, the main coil is cut off at $t = 2$ sec and its discharge starts. The maximum induced voltages were calculated to be 780 V and 300 V for the main and the trim coils, respectively, which are within the design values of the insulated resistant voltage. Besides, there is no increase in all coil currents. Though the auxiliary power supplies are not surveyed in this calculation, the simulations for various cases including the auxiliary power supplies were carried out and the safety of the coil protection system was confirmed.

The power supplies for the SRC superconducting coils are being manufactured and will be completed in the spring of 2003.

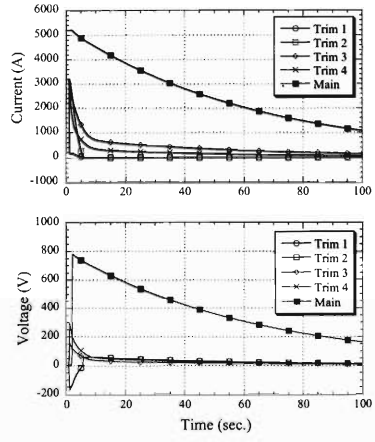

Fig. 3. Calculated currents and voltages of the main and the trim coils during the fast discharge.

References

1) A. Goto et al.: AIP Conf. Proc. **600**, 319 (2001).
2) T. Tominaka et al.: RIKEN Accel. Prog. Rep. **35**, 295 (2002).

Status of helium cooling system for the RIKEN SRC

K. Ikegami, H. Okuno, J. Ohnishi, T. Tominaka, M. Ohtake, A. Goto, and Y. Yano

This year we have completed the whole design of the helium cooling system for the RIKEN superconducting ring cyclotron (SRC) and placed an order for the system with a maker. Figure 1 shows a diagram of the helium cooling system. A superconducting bending magnet (SBM) is also operated by the same system. The system is a closed-circut system without liquid nitrogen; it consists of a control dewar connected to the six cryostats of the sector magnets and the cryostat of the SBM, a refrigerator, three compressors, four reservoir tanks and other parts. The cold mass weight of the six sector magnets have been decreased from 360 tons to 162 tons according to the design change.[1] It will take 21 days to cool them from room temperature to 4.5 K.

The refrigerator has a cooling power of 620 W at 4.5 K for the coils, 4000 W at 70 K for the thermal shields, and 4 g/sec for the current leads. The total equivalent refrigeration capacity at 4.5 k is approximately 1100 W. The refrigerator is of TCF 200S type made by LINDE. The specifications of the refrigerator are listed in Table 1. Three compressors are connected in parallel for the cooling system; two of them are used in regular operation and the other one is a spare. After operating for 8000 hours, the flow line is switched from one of the two compressors, previously operated, to the spare for maintenance. Each of the three compressors, which are made by MAEKAWA Co., has an electric power of 315 KW and a gas flow rate of 74.2 g/sec. The specifications of the compressor are listed in Table 2.

The total amount of liquid helium contained in both the coil vessels and the control dewar has been decreased from about 5000 l to 3000 l in the new design. The number of reservoir tanks has accordingly been reduced to four. Each tank has a volume of 100 m^3; its size is 15 m in height and 3 m in diameter. One of the four reservoir tanks is used as a buffer tank in regular operation, and the other three are used to recover evaporated helium gas through a recovery tube line when the coils quench. The gas analyzer, which is made by LINDE, has a measuring range from 1 to 100 vpm for gases such as water vapor, nitrogen and oxygen in pure helium. The vacuum pump has a pumping speed of 450 m^3/h made by Osaka Vac. Co.

The helium cooling system is controlled with the computer system developed by Nippon Sanso Co. The control system consists of Windows PC, Versa Module Europe (VME) and a Local Area Network (LAN). Information pertaining to temperature, pressure, gas flow, liquid level, on/off status of the devices and open/close status of the valves for the refrigerator, compressors, reservoir tanks and the control dewar of the SRC and the SBM is sent to the VME controller through the input/output station and is graphically displayed on the CRT. This information is also sent to the main accelerator control room connected *via* LAN.

Each of the above components is scheduled to be installed in the accelerator building during the spring to summer priod of 2003. The entire helium cooling system is scheduled to be completed by 2005.

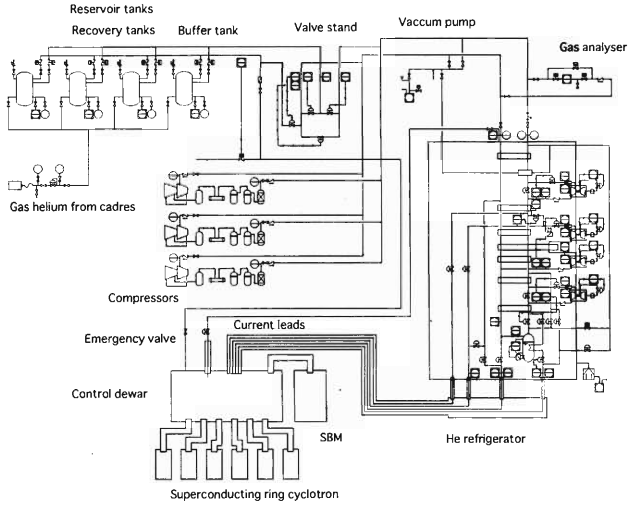

Fig. 1. Design of the helium cooling system for the SRC.

Table 1. Specifications of the refrigerator for the SRC.

Capacity of the refrigerator	
Cooling power at 4.5 K	620 W 4 g/sec (Current leads)
Cooling power at 70 K	4000 W
Inlet gas flow	148 g/sec
Equivalent cooling capacity at 4.5 K	1100 W

Table 2. Specifications of the compressor for the SRC.

Outlet Pressure	1.85 Mpa
Inlet Pressure	0.10 Mpa
Gas flow rate	74.2 g/sec 1496 Nm^3/h
AC voltage	6600 V, 3 ϕ
Electric power/each	315 kW

References

1) A. Goto et al.: AIP Conf. Proc. **600**, 319 (2001).

Helium vapor-cooled current leads for the RIKEN SRC

T. Tominaka, H. Okuno, S. Fujishima,* M. Ohtake, T. Chiba, J. Ohnishi,
K. Ikegami, A. Goto, and Y. Yano

Conventional vapor-cooled current leads are to be used in the RIKEN Superconducting Ring Cyclotron (SRC).[1,2] Six types of leads are required to satisfy the various requirements for the RIKEN SRC Superconducting magnet. These are listed in Table 1. Current leads are designed to minimize the total heat load on the cryogenic system. This is realized by choosing a shape factor defined as LI/A (L: length, A: cross-section, I: current) and a flow rate.[3–6] A 20% operating mass flow, 0.060 g/sec/kA (1.2 W/kA) above the theoretical minimum flow and heat input of 0.050 g/sec/kA (1.0 W/kA), is expected for the SRC current leads. An additional requirement for the 5200 A leads is that the leads must sustain the operating current for 10 minutes after interruption of cooling flow. It is also postulated that the frost buildup be kept to a minimum.

During the cutoff process of the current supply, the current through leads is expressed as follows

$$I(t) = I_0 e^{-\frac{t}{\tau}} = I_0 e^{-\frac{R}{L}t}, \tag{1}$$

where R is the dump resistance and L is the inductance of coil. Therefore, the total energy dissipated on the current lead with resistance of r_L is expressed as follows

$$E = r_L \int_0^\infty \{I(t)\}^2 dt = r_L \int_0^\infty {I_0}^2 e^{-\frac{2t}{\tau}} dt$$
$$= \frac{\tau}{2} r_L {I_0}^2. \tag{2}$$

As a result, it is realized that the half-time of the time constant corresponds to the interruption time of cooling flow. The time constant, $\tau = L/R = 18.8/0.015 = 1250$ sec, of slow cutoff of the current supply of the SRC main coil results in the interruption time of about 10 minutes. In addition, the interruption times of 10 minutes is sufficient for current leads of other coils with the short time constant due to small inductances.

Table 1. Power leads for SRC.

Type	Quantity	Length	Function
5200 A	2	≈ 1670 mm	Main coil
4200 A	3	≈ 1670 mm	Trim coil
3200 A	2	≈ 1670 mm	Trim coil
500 A	2	≈ 760 mm	SBM§
400 A	2	≈ 1270 mm	Correction for trim coil
100 A	11	≈ 1270 mm	Correction for main and trim coil

§ SBM: Superconducting Bending Magnet for the injection of SRC.

* Ishikawajima-Harima Heavy Industries Co., Ltd.

The current leads with relatively large current capacities, 5200, 4200 and 3200 A leads, were not newly developed. These current leads of cable-in-conduit-type are obtained from an experienced company with the required specifications for the maximum voltage and the sustainable interruption time of cooling flow.

The cable-in-conduit-type leads, which consist of 2 mmϕ phosphorous deoxidized copper wires are applied for leads with the relatively small current capacities of 500 A, 400 A, and 100 A. The electric resistivity of phosphorous deoxidized copper (C1220BD-H) is measured from room temperature to 4.2 K; the obtained results are 2.1×10^{-9} Ωm at 4.2 K and 1.77×10^{-8} Ωm at 273 K. This measured electric resistivity of the phosphorous deoxidized copper is much smaller than that stated in some textbooks, which 6.7×10^{-9} Ωm at 4.2 K, corresponding to $LI/A = 286 \times (\rho_{4.2\,\mathrm{K}})^{-0.5} = 3.5 \times 10^6$ A/m.[3,5] This means that the phosphorous deoxidized copper (C1220BD-H) made in Japan is different from that made in other countries. Then, the shape factor LI/A of 7.6×10^6 A/m is applied for these current leads. The experimental setup for the quality measurement of the current leads is shown in Fig. 1. The cross section of 500 A leads for a superconducting bending magnet (SBM) which are fabricated by the Mitsubishi Electric Company, is shown in Fig. 2. In addition, soldering is applied with the Ag solder which has a high melting temperature of about 700°C for safety.

The heat input, pressure drop, voltage drop, among others as functions of the GHe mass flow are mea-

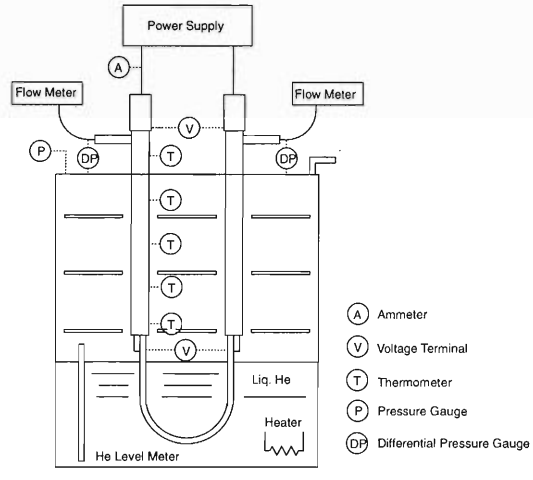

Fig. 1. Schematic layout of experimental setup for the quality measurement of the current leads.

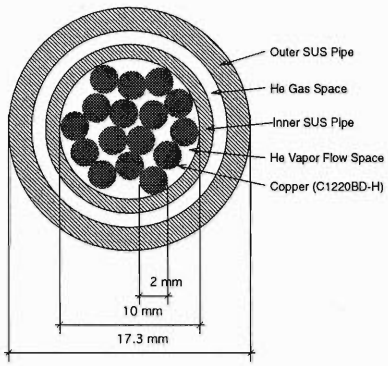

Fig. 2. Cross-sectional view of 500 A leads SBM (cable-in-conduit-type).

sured. In particular, the heat input is estimated from the decreasing rate of the LHe level, using the measured relation between the LHe decreasing rate and the heater power. The measured results are listed in Table 2. Measured heat input characteristics are shown in Fig. 3, together with the self-cooling line expressed by $w = C_L m$, where w is the heat input, C_L is the latent heat of evaporation of liquid helium, and m is the mass flow. It is also implied that the efficiency of heat transfer (or exchange) to He vapor gas is about 50%. Furthermore, the sustainable time of 10 min after interruption of cooling flow is confirmed experimentally.

As another candidate, fin-type leads, which have straight threads cut into a conductor, are applied. The 100 A leads with the length of 760 mm, which are fabricated at RIKEN, are shown in Fig. 4. The shape factor LI/A of about $1.2 - 1.5 \times 10^6$ A/m is applied for these current leads made of brass (C1220BD-H).

Similar measurements are made, as shown in Table 3. However, the measured results are scattered due to the small heat input compared to the background heat input of the cryostat of about 1 W. The sustainable time of 10 minutes after interruption of cooling flow is also confirmed experimentally.

Both types of current leads are experimentally confirmed to be reliable for use in the SRC, and less sensitive to excess current with sufficient safety margin in the event of cooling gas flow stoppage. Unfortunately, it is implied that the heat leak is larger than the expected one. The measurement accuracy for the heat input has to be improved.

Table 2. 500 A current leads for SBM.

Type	Measured	Measured
Heat input	1.9 W	1.6 W
@ mass flow	@ 0.052 g/s	@ 0.059 g/s
Pressure drop	0.7, 1.7 kPa	0.7, 1.7 kPa
Voltage drop	62 mV	62 mV

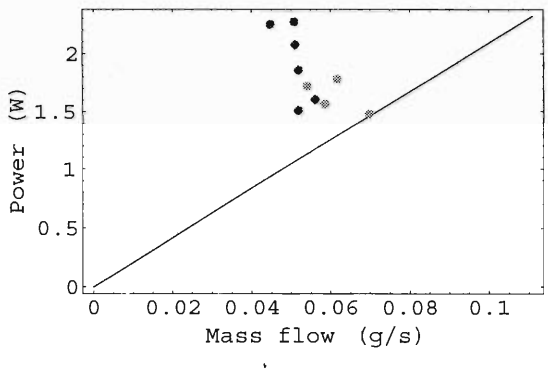

Fig. 3. Measured heat input characteristics for a pair of 500 A current leads.

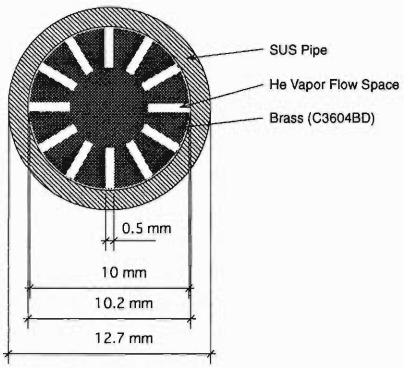

Fig. 4. Cross-sectional view of 100 A leads (fin-type).

Table 3. 100 A current leads for SRC.

Type	Measured @ 103 A	Measured @ 155 A
Heat input	0.3 W	0.38 W
@ mass flow	@ 0.015 g/s	@ 0.018 g/s
Pressure drop	0.55 kPa	0.8 kPa
Voltage drop	70 mV	120 mV

References

1) Y. Yano et al.: AIP Conf. Proc. **600**, 161 (2001).
2) A. Goto et al.: AIP Conf. Proc. **600**, 319 (2001).
3) M. N. Wilson: in *Superconducting Magnets* (Oxford University Press, Oxford, 1983), p. 256.
4) Y. Iwasa: in *Case Studies in Superconducting Magnets* (Plenum Press, New York, 1994), p. 125.
5) J. G. Weisend II ed.: in *Handbook of Cryogenic Engineering* (Taylor & Francis, Philadelphia, 1998), p. 399.
6) A. Nicoletti and M. L. F. Rehak: Adv. Cryog. Eng. **43**, 261 (1998).

Irradiation effects on cryogenic temperature sensors

T. Tominaka, H. Okuno, J. Ohnishi, N. Fukunishi, H. Akiyoshi, A. Goto, and Y. Yano

The beam losses in the Superconducting Ring Cyclotron (SRC) are estimated to be 10 pnA.[1,2] In principle, the cryogenic sensors will be mounted at the periphery of the cold masses, where the integrated dose for 30 years of operation of the accelerator is 20 MGy. About 300 temperature sensors listed in Table 1 will be installed, and most of them will be exposed to high radiation doses during the operation of the accelerator. During the lifetime of the accelerator, several warm-up cycles for maintenance have to be considered, and generally the annealing effect of the damaged sensors can be expected. The radiation effects of cryogenic sensors including Cernox^{TM} and Carbon-Glass^{TM} resistor (CGR) have been tested at different doses up to 10^{15} neutrons/cm^2 (20 kGy).[3–5] The aim of this work was to estimate the accumulated radiation effects due to irradiation at room temperature up to 100 kGy.

The superconducting magnet of SRC will be operated at temperatures ranging from 4.4 K to 4.5 K, their absolute values of which should be measured at an accuracy higher than 100 mK.

For the measurement of the temperature characteristics of resistance before and of about 108 days after irradiation, the cryogenic temperature sensors mounted in the OFHC sample holder, which is mountable to five sensors including a calibrated sensor, are located at various positions or heights of different temperatures in the LHe dewar vessel, as shown in Fig. 1. Furthermore, five sensors are also immersed in the LN_2 vessel. The measurement system consists of an Agilent Technologies (AT) 3458A DVM, a Yokogawa 2792 standard resistor, an Advantest R6243 current source, and an AT 34970 scanner with an HP 34901A two-wire scanner card. The temperature sensors are measured in a four-wire configuration (10 μA for Cernox^{TM} and CGR, 2 mA for PtCo). For four different radiation doses, the cryogenic sensors at room temperature have been irradiated with 210 MeV proton beams (beam size: 1 cm^2) of various intensities for various irradiation times, as shown in Table 2. It is estimated that the radiation dose of 10 kGy is approximately equivalent to 210 MeV proton beams of 1 nA for 1 hour.

Table 1. Cryogenic thermometry in the SRC.

	Coil	Joint box	Control dewar	Total
Cernox^{TM}	30	2	0	32
CGR	6	4	18	28
PtCo	96	0	12	108
CC*	130	0	45	175

* Copper-Constantan thermocouple mainly for radiation shield.

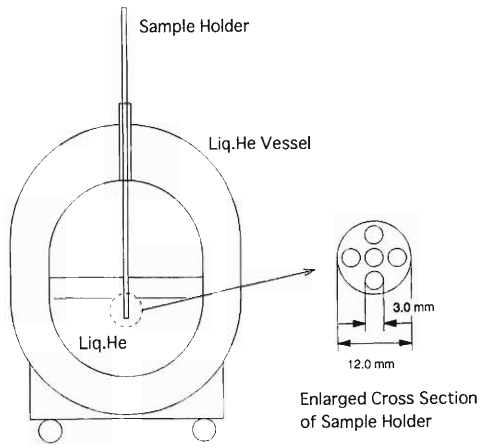

Fig. 1. Schematic layout of an experimental setup.

Table 2. Equivalent radiation dose of proton beam.

Radiation Dose (kGy)	Beam Current (nA)	Irradiation Time (min)
0.1	0.075	8
1	0.075	80
10	1.0	60
100	9.8–12	60

Five Cernox^{TM} sensors of the size of 3 mm diameter × 8.5 mm length (Model: CX-1070-AA of Lake Shore Cryotronics, USA) including one calibrated sensor have been tested. The calibrated sensor has no radiation, but the other four sensors have four different radiation doses. Measured results are shown in Fig. 2, for $\Delta R/R = (R' - R)/R$, where R' and R are resistances after and before irradiation, respectively, which are listed in Table 3, including the estimation

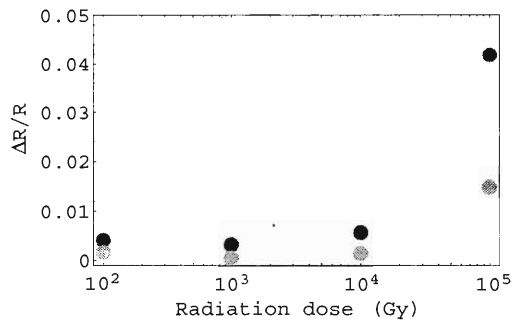

Fig. 2. Radiation effect for Cernox^{TM} (dark: 4.2 K and light gray: 77 K).

Table 3. Measured results of cryogenic temperature sensors.

Gy	0	10^2	10^3	10^4	10^5
Cernox					
$\Delta R/R$@4.2 K (%)	0.30	0.41	0.32	0.57	4.2
ΔT@4.2 K (K)	−0.0065	−0.0090	−0.0070	−0.012	−0.087
$\Delta R/R$@77 K (%)	0.044	0.17	0.065	0.016	1.5
ΔT@77 K (K)	−0.034	−0.13	−0.050	−0.12	−1.1
CGR					
$\Delta R/R$@4.2 K (%)	0.77	0.84	1.7	5.3	20
ΔT@4.2 K (K)	−0.0084	−0.0092	−0.018	−0.056	−0.19
$\Delta R/R$@77 K (%)	−0.054	0.18	0.20	0.040	3.8
ΔT@77 K (K)	0.076	−0.25	−0.28	−0.056	−4.9
PtCo					
$\Delta R/R$@4.2 K (%)	—	—	0.0043	0.0056	—
ΔT@4.2 K (K)	—	—	0.0021	0.0027	—
$\Delta R/R$@77 K (%)	—	—	0.23	0.23	—
ΔT@77 K (K)	—	—	0.16	0.16	—

of the temperature difference, ΔT. In Fig. 2, the dark points correspond to the results at 4.2 K, otherwise, the light gray points correspond to those at 77 K. It seems that the variation of the sensor without radiation was mainly due to the effect of thermal cycle. The results of small radiation effect up to 10^4 Gy are consistent with those reported previously.[3–5)]

Similarly, five CGR sensors of the size of 3 mm diameter × 8.5 mm length (Carbon-Glass^{TM}, Model: CGR-1-1000 of Lake Shore) including one calibrated sensor have been tested. The calibrated sensor has no radiation, but the other four sensors have four different radiation doses. Measured results are listed in Table 3, and are shown in Fig. 3.

Two PtCo sensors of the size of 2 mm diameter × 23 mm long (Model: R800-6, Pt-Co 0.5 at % of Chino, Japan) with relatively uniform sensitivity in the whole range from 4 to 300 K have been tested. Two sensors have different radiation doses. Measured results are listed in Table 3, and are shown in Fig. 4.

Between two sensors, Cernox^{TM} and CGR, with high sensitivity at the 4 K region, it is experimentally shown that the Cernox^{TM} sensor is more resistant to radiation than CGR. Similarly, it becomes also clear that the PtCo sensor is strongly resistant to radiation at least up to the equivalent dose of 10^4 Gy. It seems that our results are roughly consistent with those reported previously.

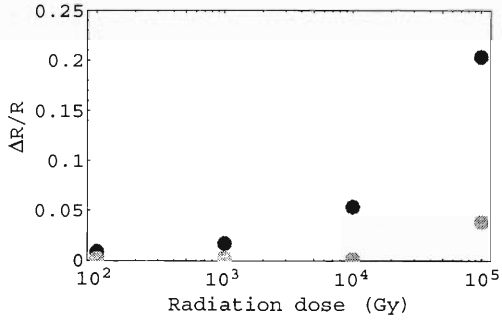

Fig. 3. Radiation effect for CGR (dark: 4.2 K and light gray: 77 K).

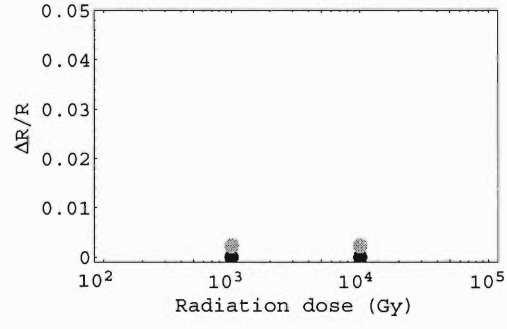

Fig. 4. Radiation effect for PtCo (dark: 4.2 K and light gray: 77 K).

References
1) Y. Yano et al.: AIP Conf. Proc. **600**, 161 (2001).
2) A. Goto et al.: AIP Conf. Proc. **600**, 319 (2001).
3) S. Scott Courts and D. Scott Holmes: Adv. Cryog. Eng. **41**, 1707 (1996).
4) T. Junquera et al.: CERN-LHC Project Rep. 153 (1997).
5) J-F. Amand et al.: CERN-LHC Project Rep. 209 (1998).

Design of electrostatic channels for the RIKEN SRC

S. Fujishima,* H. Okuno, A. Goto, and Y. Yano

The RIKEN Superconducting Ring Cyclotron (SRC) is one of the main accelerators for the RIKEN RI Beam Factory.[1] Fabrication of the injection and extraction systems[2] for the SRC is in progress.

Figure 1 shows a schematic layout of the injection and extraction elements and trajectory of the beam. The injection system consists of one superconducting bending magnet (SBM), two normal-conducting magnetic inflection channels (MIC1 and MIC2), and one electrostatic inflection channel (EIC). The extraction system consists of one electrostatic deflection channel (EDC), three normal-conducting magnetic deflection channels (MDC1, MDC2 and MDC3), and one normal-conducting extraction bending magnet (EBM).

The basic structures of EIC and EDC are similar. Each electrostatic channel mainly consists of a cathode and a thin septum (ground), and generates a high electrostatic field of 100 kV/cm in the electrode gap of 12 mm. Hereafter, EC stands for EIC or EDC.

Figure 2 shows a schema of EDC as an example. The fringe field of the sector magnets depends nonlinearly on the excitation levels, so the field profile changes and trajectories of the beams differ from each other. Therefore, not only EC should be movable in the radial direction, but also the curvature of EC should be variable. For this purpose, EC consists of three arcs connected by two hinges, and can be rotated around the hinges by motors. The motors are covered with iron shells to shield background magnetic fields. EC has a crossing hole of ϕ50 mm to introduce the beams from preaccelerators into the central region of SRC.

Figure 3 shows a cross-sectional outline around the electrodes of EDC as an example. In Table 1, the basic specifications of EIC and EDC are listed.

The energy of the extracted beam is expected to be 100 kW at the maximum. To cut off such a high-energy beam from the accelerating orbit with minimum

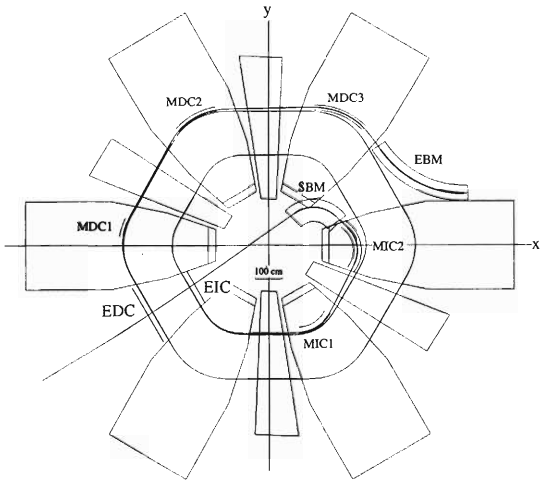

Fig. 1. Schematic layout of the injection and extraction elements and trajectory of the beam.

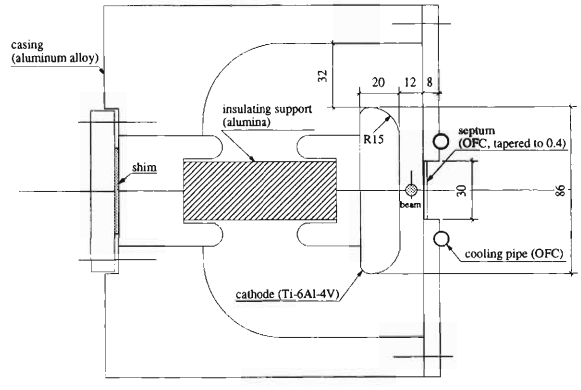

Fig. 3. Cross-sectional outline around the electrodes of EDC.

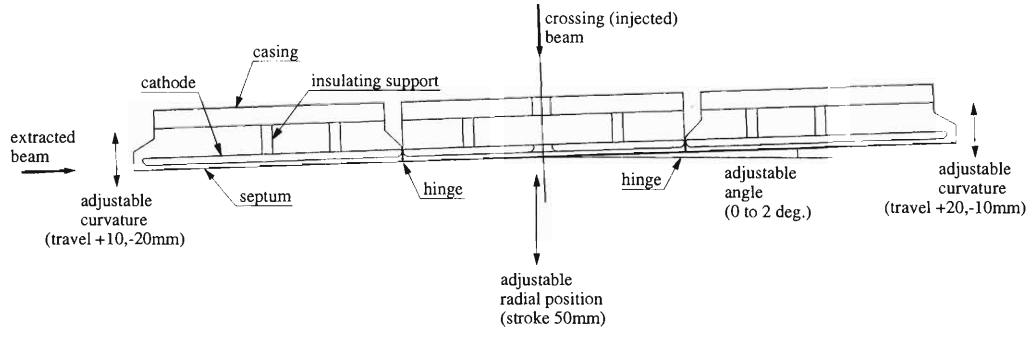

Fig. 2. Schema of EDC.

* Ishikawajima-Harima Heavy Industries Co., Ltd.

Table 1. Specifications of EIC and EDC.

	EIC	EDC
Arc length [mm]	1300	2250
Curvature	variable	variable
Radial stroke [mm]	40	50
Max. field [kV/cm]	100	100
Electrode gap [mm]	12	12
Septum thickness [mm]	1.0	tapered to 0.4
Cathode height [mm]	82	86

beam loss and suppress heating on the front edge of the septum of EDC, the septum is tapered as sharp as possible. Considering not to deform with machining, the thickness of the front edge was selected to be 0.4 mm. On the other hand, in the case of EIC, the septum is not required to be as thin as that of EDC, thus the thickness is 1.0 mm throughout the septum of EIC. The maximum attracting electorostatic force between electrodes is about 5 g·force/cm^2, both septums have sufficient stiffness against the force.

Oxygen-free copper was adopted as a material of the septum because of its good thermal conductivity, and water cooling pipes are soldered near the septum. Titanium alloy (Ti-6Al-4V) was adopted as a material of the cathodes because of its high nondischarge property and light weight.

To suppress the peak electrostatic field on the cathodes, the curvature of the corner was set to be sufficiently large with adjusting the length of the vertical straight section related to field uniformity. Field uniformity in the beam region is about 3×10^{-3}.

The weight of each partial cathode of EDC is 5.5 kg and sufficiently light to be held by hands at the maintenance. The light weight of the cathode also contributes to suppressing the field nonuniformity caused by the flexure of the supporting insulators.

The supporting insulator is made of alumina, and placed far from the entrance of the channel to avoid spatter by beam bombardment. The gap between electrodes can be adjusted from 10 mm to 14 mm by changing the interfacial shims between supporting insulators and casing. EC is installed with suspensory arms from the top frange of a vacuum chamber.

High-voltage power supplies for the EIC and EDC are specified as 130 kV and 2.3 mA. Although EDC itself can withstand a maximum voltage of 150 kV, in preparation for a boost up of the power supply if needed in the future.

A preaccelerator of SRC, the RIKEN Intermediate Ring Cyclotron (IRC)[3] has similar electrostatic channels to those of SRC. In a demonstration test of the electrostatic channels of IRC, a voltage of 120 kV or an electrostatic field of 100 kV/cm was impressed successfully. Therefore we confirmed adequacy of the design of EC for SRC also.

Not only an adequate design, but also a quality control in fabrication is very important to realize stable electrostatic channels. Even a little bit of oil blot and/or dust deposit by machining should be completely eliminated to prevent a discharge.

In addition, a lot of care should be taken for workability and efficiency at the maintenance, because EIC and EDC will be extremely radioactivated and may need frequent maintenance. Cleaning of the cathodes to remove stain on the surface and exchange of deteriorated supporting insulators are mainly needed at the maintenance. The maintenace must be carried out with simplicity and speed to reduce exposure of workers, even though, before the maintenance, the channel is replaced with a spare and left until radiation decay sufficiently.

For this purpose, the following items were modified or adopted by considering of the design and workability of existing cyclotrons in RIKEN. Foothold for installation and disinstallation of EIC and EDC, that is, the top surface of the vacuum chamber was flattened to afford an efficient working space, and in addition, cables and vacuum gauges were laid out so as not to be a hindrance. A rubber O-ring was adopted as a gasket for the frange hanging EC. From the aspect of resistance against irradiation and airtightness, a metal gasket has better property than the rubber O-ring. However, in the case of the metal gasket, more bolts are necessary, and it is more difficult to screw up and seal vacuum tightly. As a consequence, the working time becomes longer and exposure of the worker increases. Therefore, the rubber O-ring was adopted to put the health of the workers above the performance of the metal gasket. The cathodes were lightened to be handled easily by oneself. The supporting insulators are designed to be compatible with those of IRC to share the spares.

References

1) A. Goto et al.: RIKEN Accel. Prog. Rep. **36**, 297 (2003).
2) S. Fujishima et al.: AIP Conf. Proc. **600**, 449 (2001).
3) T. Mitsumoto et al.: RIKEN Accel. Prog. Rep. **34**, 331 (2001).

Cogeneration system for RI beam factory

T. Fujinawa, Y. Sekiguchi, K. Yamaguchi, H. Tokuoka, Y. Takuma,* H. Ueno,* and Y. Yano

In the RI Beam Factory (RIBF) project, accelerators, magnets and other devices will consume huge electrical power. The estimated value of the energy consumption is 18 MW, which does not include the energy consumption in the existing facility used as a preinjection system for the RIBF. Most of the electrical power will be converted to heat thus cooling systems with big capacity will be required. The cooling water system with cooling towers is planned to remove 8 MW of heat. A 4.2 Mwpower- class (1200 USRT) refrigerator will also be used. In addition a 2.1 Mwpower-class (600 USRT) air-conditioner unit is required to remove the heat exhausted to the air. Note that 1 USRT (United States ton of refrigeration) corresponds to 3.6 kW. If we choose an electrical chiller system, an additional 1.9 MW of electrical power is necessary the accelerators and other devices are planned to work more than 7000 hours in a year and it is an important issue how efficient power supply systems and cooling systems are.

Our answer to this problem is to introduce a so-called cogeneration system shown in Fig. 1. The cogeneration system supplies 5 MW of electrical power and 13 tons per hour of saturated steam. Our system consists mainly of a turbine, a compressor, a generator, a steam generator and absorption chillers. In Fig. 1, G, C and T denote the generator, the compressor and the turbine, respectively. The turbine is rotated by the energy obtained by burning of fuel. The turbine is connected to the generator, the power output of which is 5 MW. This cycle is called the Brayton cycle.

The exhaust heat of the turbine will be used to generate saturated steam. A part of the saturated steam will be injected into the turbine. An additional 1.3 MW electrical power will be obtained by the injection of 8 tons per hour of steam. This cycle is the Rankine cycle. The maximum electrical output is 6.3 MW but the efficiency is somewhat less than its maximum value in this case. Hence our cogeneration system is a so-called combined cycle (the Brayton and Rankine cycle). The energy efficiency in total is 60.9% (at 6 MW+2000USRT), which is 1.5 times larger than that of a usual thermal power station.[1] The remaining saturated steam will be send to the absorption chillers. The absorption chillers provide us chilled water of 7°C like a gas cooling machine. The total capacity of absorption chillers is 2000 USRT. The main part of it (1800 USRT) will be used in a cooling water system in the RIBF and the remaining part (190 USRT) will be used in the intake air cooler shown in Fig. 1. The intake air cooler is necessary to keep air density in the summer.

The reason why we chose this type of cogeneration system is as follows. An alternative candidate was the gas engine type, which is more efficient in generating electrical power. It does not provide sufficient exhaust heat to the absorption chillers and mechanical vibration is very serious. We also investigated the system with an adsorption chiller, which utilizes the exhaust heat of accelerators and magnets. However, the temperature of the cooling water used for the magnets is not sufficiently high for the adsorption chiller to work effectively.

The cogeneration system is cost-effective. If we operate the cogeneration system 8400 hours in a year with 6 MW and 1800 USRT output, we can save 100 millions of yen per year. In addition, our system is an ecologically friendly system. The fuel chosen here is liquid natural gas which is very clean energy. The SO_2 emission is zero and the NOx emission is 42 ppm which

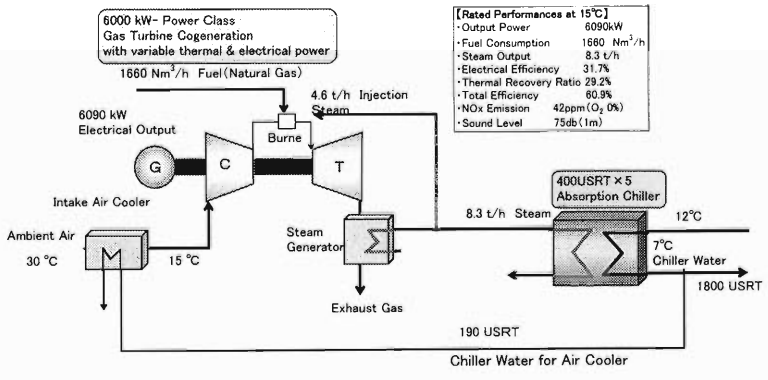

Fig. 1. Cogeneration system flow diagram.

* Mitsubishi Electric Corporation

corresponds to 75% of that of a conventional thermal power station.[2] The cogeneration system is set in the first floor of the RIBF building and hence the energy loss in transmission in electricity is negligible. By collecting these effects, we can suppress the CO_2 emission by 1100 tons per year, which corresponds to 220 ha, of forest. The absorption chillers do not use greenhouse-effect gases like chlorofluorocarbons (CFC). These aspects of the cogeneration system are very suited to the spirit of the Kyoto Protocol (COP3) for the battle against global warming.[3]

Another merit due to the installation of the cogeneration system is that two types of power supply systems support several machines. One is the usual commercial one and the other is the cogeneration system. In the RIBF, super-conducting magnets will be cooled by the helium cryogenic system, for which we require the non-stop operation because very expensive liquid helium will be lost without cooling. Hence, the helium cryogenic systems and other important loads will be doubly supported.

Both the cogeneration system and commercial power as shown in Fig. 2 usually support all loads. When the cogeneration system stops, commercial electrical power immediately supports all loads. On the contrary, when the commercial power supply suddenly stops the high-speed circuit breaker works within 20 milliseconds and the cogeneration system supports only these essential loads such as the helium cryogenic systems and other important loads.[2]

The cogeneration system is now under construction and power supply will start in March 2003. We plan the improvement (250 kW) of the cogeneration system after the commissioning of the RIBF facility by utilizing the exhaust heat of the magnets.

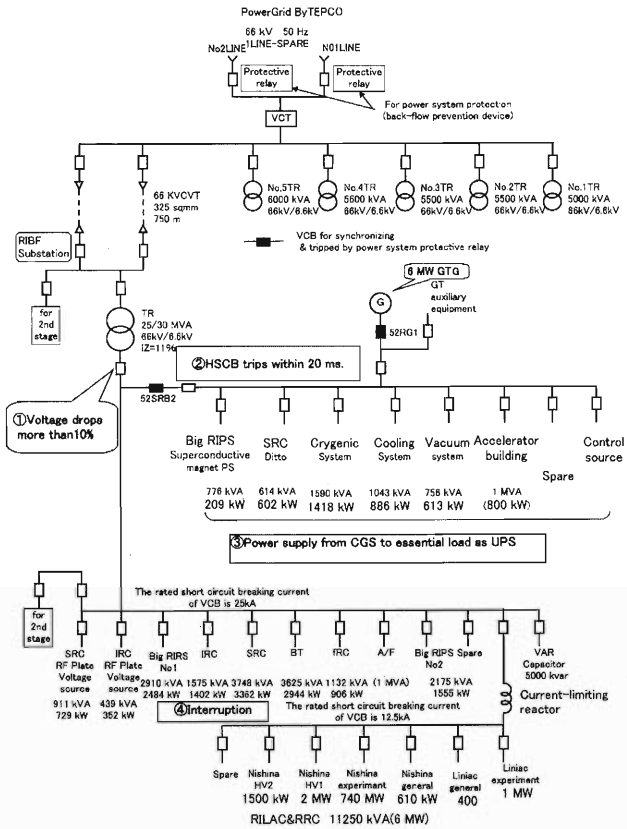

Fig. 2. Single Line diagram.

References

1) Institute of Research and Innovation: Report for Diversified Type Energy System (1998).
2) Mitsubishi Electr. Tech. Rep., **75**, No. 9 (2001).
3) Tokyo Gas Co., Ltd.: Gas Cogeneration System.

Magnetic field measurement of superconducting quadrupole magnet for BigRIPS

K. Kusaka, T. Kubo, Y. Mizoi, K. Yoshida, N. Kakutani,*
T. Tsuchihashi,* H. Kamikubo,* and K. Sato*

A prototype of the superconducting quadrupole triplet for the BigRIPS separator[1] has been successfully fabricated and tested for R&D studies.[2] It has been disassembled and the three quadrupole magnets inside it have been reinstalled in a newly built cryostat with small refrigerators.[3] This report describes the magnetic field measurement system for the superconducting quadrupole magnets for the BigRIPS separator and preliminary results of measurement.

Although the operation of beamline quadrupole magnets generally requirs only knowledge of their field integral, a detailed space distribution of their multipole components is needed for that of BigRIPS quadrupoles. This is due to the large bore/length ratio of the quadrupoles, in other words, to the large acceptance of the BigRIPS separator. The beam trajectories in the BigRIPS quadrupoles have a strong curvature and software tracking is essential to achieve high resolution. Moreover, the BigRIPS quadrupole is a superconducting magnet installed in a cryostat, so that its axis can be defined only by measuring its magnetic field.

We adopted a cylindrical field map with Hall sensors for the measurement of BigRIPS quadrupoles, since it is the most straightforward way of decomposing the measured field distribution into multipole components. The magnetic center is easily calculated from the dipole component of the field distribution on the cylinder.

Figure 1 shows the top view of the field measuring apparatus, which is a two-axis stage driven by stepping motors. The Hall sensors are mounted on the arm which moves along the beamline axis (z-direction) in the warm bore of the magnet. The arm is driven by a feed screw along the stainless-steel guide pipe. The guide pipe, the screw, and the arm rotate as a whole in azimuthal direction (θ-direction). The entire apparatus in the warm bore is driven by non-backlash spur gears mounted outside the magnet. The axis of the azimuthal rotation is fixed by cross-roller bearings are mounted on the magnet flanges. Basic parameters for the mapping stage are listed in Table 1.

We used three Hall sensors (HHP-MU, AREPOC Ltd.) for each magnetic field component, B_r, B_θ, and B_z. These sensors are mounted on a circle, as shown in Fig. 2, such that all three components of the magnetic field are measured at each measuring point when the sensors are rotated at a step of 9°.

Figure 3 shows a block diagram of the control and measurement systems. Two stepping motors are driven by the pulse generator of the motor controller board (PCI7209, Interface Corporation) installed in a control PC. While the azimuthal position of the stage is measured using the rotary encoder, the z-position of the Hall sensor arm is calculated based on the z-encoder pulse and the pitch of the feed screw. The resolution of the azimuthal position is 0.06°. In addi-

Table 1. Parameters for the magnetic field mapping stage.

	Stroke	Minimal Step	Max. Speed
z	2800 mm	0.01 mm	1 cm/sec
θ	360° CW/CCW	0.03°	8 sec/rev

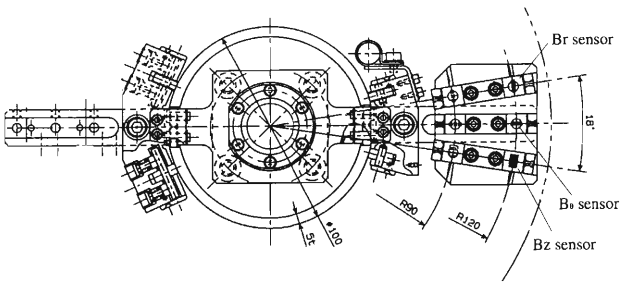

Fig. 2. Three Hall sensors mounted on the arm of the field mapping stage.

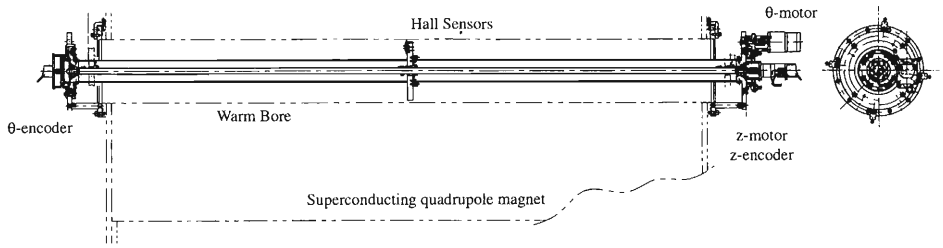

Fig. 1. Top view of the magnetic field measuring apparatus.

* Toshiba Corporation

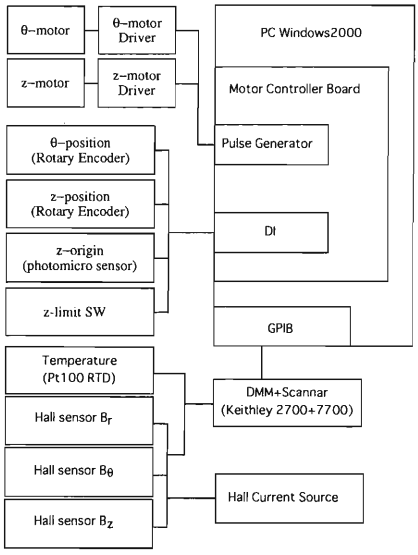

Fig. 3. Schematic diagram of the control and measurement systems.

tion to the Hall voltage, a digital multimeter (DMM), (Keithley 2700) with a scanner unit (7700) monitors the Hall current and the temperature by Pt100 RTD. The data from the DMM are stored in PC via a GPIB interface.

The motion of the Hall sensor arm was measured using a height gauge before being installed in the magnet and the positional accuracy of the Hall sensor motion was estimated. The estimated accuracies are ± 0.1 for in the radius and 2 mrad for the azimuthal angle, caused by the bend and torsion of the guide pipe, respectively. Considering the size of the Hall sensor and a possible error of mounting, the positional accuracy of the measurement is about 0.4 mm in the radial direction. This can be improved by a calibration with the reference quadrupole magnet. The center of the Hall sensor rotation also moves vertically depending on the z-position of the arm, which is due to the deflection of the guide pipe.

We show in Fig. 4 an example of the spatial distribution of the quadrupole component of B_θ. The

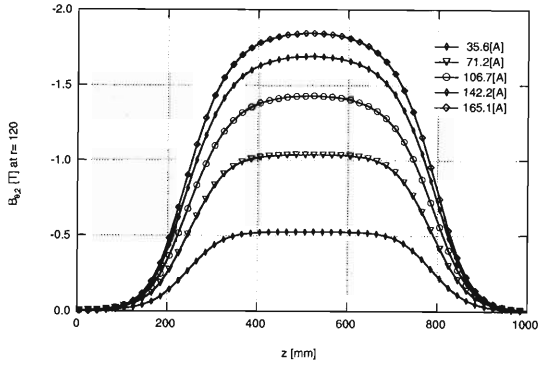

Fig. 4. Distribution of the quadrupole field component of the Q500A magnet along the beam line axis z.

quadrupole component of the Q500A magnet at a radius $r = 120$ mm is plotted as a function of z, which is the distance from the flange of the magnet to the Hall sensor position. Only the Q500A magnet was excited at the current of 35.6 A, 71.2 A, 106.7 A, 142.2 A and 165.1 A, for each mapping. The measurement took 130 minutes for each mapping. The stroke and the step of the z-motion were 1080 mm and 20 mm, respectively. At each z, the Hall sensors were rotated 360° at a step of 9°. The direction of rotation was maintained in one direction in order to avoid possible backlash. The Hall voltage was sampled ten times and their average was recorded. We decompose the measured B_θ field using the fast Fourier transform (FFT). The use of FFT is advantageous in extracting the multipole component from the data with a positioning error. The center of the Q500A magnet in the beam direction is calculated to be 497.5 mm, while its design value is 495 mm. The mapping time for the Q800 magnet was 1656 minutes at a z-stroke of 1360 mm. The steps of z- and θ-motions were same as those for the Q500A magnet.

Figure 5 shows an example of an excitation curve. The magnitude of the quadrupole component of B_θ of the Q500A magnet at the magnet center is plotted as a function of excitation current. Figure 5 also shows the 3D calculation by TOSCA.[2] The data are corrected using the data of the stage motion measurement. The deviation from the calculation was -0.14–0.23%, which is within the positional accuracy of 0.4 mm for the radius for the quadrupole component.

Detailed analysis of measured data and comparison with 3D calculation will be reported in the near future.

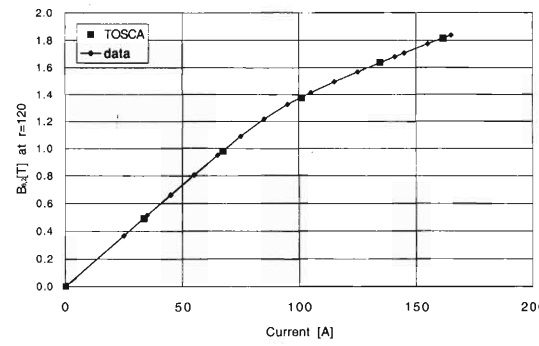

Fig. 5. Excitation curve for the Q500A magnet.

References

1) T. Kubo et al.: RIKEN Accel. Prog. Rep. **35**, 301 (2002); T. Kubo: Nucl. Instrum. Methods Phys. Res. B, in press.
2) T. Hirumachi et al.: IEEE Trans. Appl. Supercond. **10**, 238 (2000); T. Kubo et al.: RIKEN Accel. Prog. Rep. **33**, 238 (2000); H. Kouzu et al.: RIKEN Accel. Prog. Rep. **34**, 350 (2001); T. Tominaka et al.: RIKEN Accel. Prog. Rep. **34**, 353 (2001).
3) K. Kusaka et al.: RIKEN Accel. Prog. Rep. **35**, 303 (2002); K. Kusaka et al.: RIKEN Accel. Prog. Rep. **36**, 314 (2003).

Superconducting quadrupole magnet with small refrigerators II

K. Kusaka, T. Kubo, T. Tominaka, Y. Mizoi, K. Yoshida, Y. Yano,
N. Kakutani,* T. Tsuchihashi,* and K. Sato*

Superconducting quadrupole magnets are to be used for the BigRIPS separator[1] in the RI-beam factory project.[2] Two types of cryogenic system for the quadrupoles are planned. One is a large cryoplant system in which a single refrigerator supplies liquid He (LHe) to a number of magnets through transfer lines. The quadrupoles located close to the production targets and beam dumps are cooled in this manner. A detailed report on the cryoplant for the BigRIPS quadrupoles can be found elsewhere.[3] Another system is a stand-alone-type superconducting magnet equipped with small refrigerators on its cryostat.[4] The stand-alone-type magnets are to be used in the analyzing section of the BigRIPS where a possible radiation level is reasonably low. Here we report the results of cooling tests and the long term continuous operation of small refrigerators.

A prototype of the superferric quadrupole triplet has been fabricated and tested for R&D studies.[5] Three quadrupole magnets are installed in a dewar-type cryostat. Based on the prototype cryostat a new cryostat with small refrigerators was designed, reducing the heat load as much as possible.[4] It was fabricated by Toshiba in 2002 and cooling and excitation tests together with magnetic field measurements were performed at the factory. Figure 1 shows an image of the superconducting quadrupole magnet with small refrigerators together with a field mapper.

In Fig. 2 we show a schematic diagram of the cryogenic system of the superconducting quadrupole magnet with two small refrigerators. One is a Gifford-McMahon cooler using a Joule-Thomson expansion (GM/JT) to cool the He vessel in which three superconducting quadrupoles are installed and cooled by the LHe bath cooling method. It liquifies He gas that evaporates in the He vessel with the recondensing heat exchanger unit. The cooling capacity of the GM/JT cooler is 2.5 W at 4.3 K. The other is a Gifford-McMahon (GM) cooler which cools, by heat conduction, high-T_c superconducting current leads and a shield surrounding the He vessel, with the cooling capacity of 90 W at 80 K. Both refrigerators operate using separate water-cooled compressors.

Since the cold mass of the magnet (~8.4 ton) is too large for small refrigerators to cool from room temperature to 4 K, precooling with liquid N_2 (LN2) and LHe is necessary. The cooling test was performed in March, 2002. It took 8 days to cool the magnet from room temperature to ~100 K with ~3800 L of LN2. The cool-down from ~100 K to 4 K took 7 days. About 3000 L of LHe was transferred during this period and ~210 L of LHe remained in the He vessel after precooling. The shield was constantly cooled by the GM cooler.

The heat load of the cryostat was measured before mounting the GM/JT cooler. We have measured the

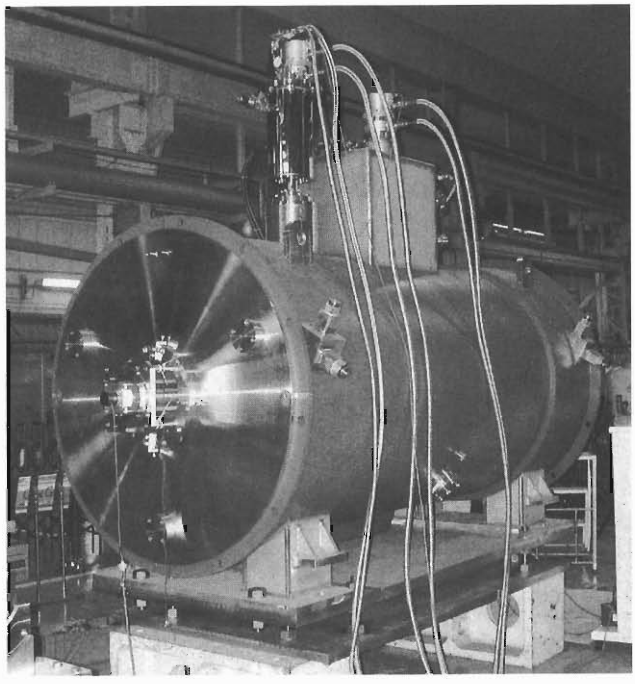

Fig. 1. Superconducting quadrupole magnet with small refrigerators. A magnetic field mapping device is installed.

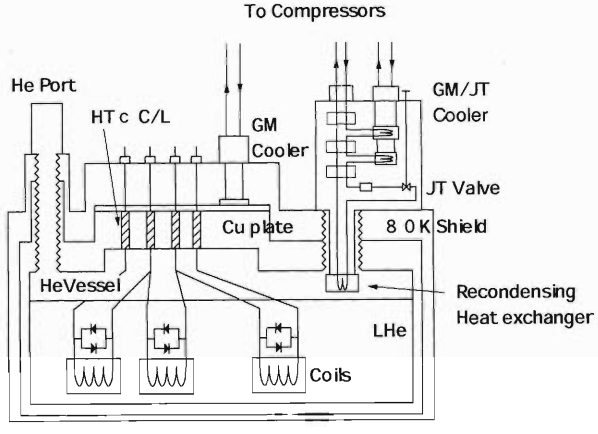

Fig. 2. A schematic diagram of the cryogenic system of the superconducting quadrupole magnet with small refrigerators.

* Toshiba Corporation

change of the LHe level leaving the cryostat untouched for 5 days. The pressure of the LHe was kept constant by leaving the GM/JT port open. The consumption rate of the LHe was 1.72 L/hour, which corresponds to 1.23 W of the heat load of the He vessel when the magnets are not energized. The design value of the heat load of the He vessel is 1.82 W. We also tried to measure the heat load for a current ramping period by measuring the He gas flow evaporating from the He vessel, since the change of the LHe level is too small to be measured by the LHe level meter in a short period. The measurement of the gas flow was not successful, since the pressure loss from the He vessel to the gas flow meter is too large, so that the pressure in the LHe vessel could change and the gas flow never became constant. We are now planning a different method of measuring the heat load of the ramping period.

After the heat load measurement the GM/JT cooler was mounted and the following excitation and cut-off tests were performed. Since the cooling capacity of the GM/JT cooler is too low to compensate for the AC loss of coils during ramping periods, the pressure of the He vessel would exceed the relief pressure of safety valves, if the rampings were repeated many times. Several excitation patterns with realistic ramping speeds were tested and no significant increase of the pressure ($>$ 0.01 Mpa) was observed. Two cut-off tests were performed successfully. One is the test of a sudden refrigerator stop when the magnets are excited. The other is the one which simulates a quench of high T_c superconducting current lead. By imposing external voltage to the current lead we activated the interlock system against an abnormal voltage drop of the current lead. In both tests the stored energy was safely transferred from the magnet to power supplies with the current decedent rate of 1 A/sec. Neither magnet quench nor gas He release occurred. We have confirmed that the pressure of the He vessel seldom exceeds its relief pressure in a standard operation of the fragment separator. We have also tested the coil protection diode installed in the He vessel. While all three magnets were excited, we artificially operated the current lead protection switch to detach one of the power supplies from the circuit. While the stored energy in the magnet with the power supply detached was dissipated in the diodes, the energy stored in the other magnets were safely transferred to each power supply.

In addition to the series of excitation and cut-off tests, a magnetic field measurement was performed at the factory. A preliminary result of the magnetic field measurement is reported elsewhere.[6] After this measurement the magnet has been brought into RIKEN, being kept cooled. During the transport the GM/JT cooler was dismounted from the cryostat and reinstalled in RIKEN. The period of the refrigerator stop was about two days and the LHe of $\sim$250 L was lost. After refills of LHe, the GM/JT cooler together with the GM cooler has since been operating for three months. The LHe level has stayed constant except during periods when power and/or water supply was suspended.

The superconducting quadrupole magnet with small refrigerators has been successfully fabricated and tested. A detailed analysis of heat load measurement and magnetic field measurement will be reported in the near future.

References

1) T. Kubo et al.: RIKEN Accel. Prog. Rep. **35**, 301 (2002); T. Kubo: Nucl. Instrum. Methods Phys. Res. B, in press.
2) Y. Yano et al.: AIP Conf. Proc. **600**, 161 (2001).
3) T. Kubo et al.: RIKEN Accel. Prog. Rep. **36**, 316 (2003).
4) K. Kusaka et al.: RIKEN Accel. Prog. Rep. **35**, 303 (2002).
5) H. Kouzu et al.: RIKEN Accel. Prog. Rep. **34**, 350 (2001); T. Tominaka et al.: RIKEN Accel. Prog. Rep. **34**, 353 (2001).
6) K. Kusaka et al.: RIKEN Accel. Prog. Rep. **36**, 312 (2003).

Basic design of a liquid-helium cryogenic system for the BigRIPS separator

T. Kubo, N. Kakutani,* K. Kusaka, Y. Mizoi, K. Yoshida, A. Yoshida, T. Tominaka, K. Ikegami, T. Tsuchihashi,* M. Shimada,* and K. Sato

The in-flight RI beam separator BigRIPS[1] to be used for the production of radioactive-isotope (RI) beams is being built in the RI-beam factory.[2] Superconducting quadrupole magnets with large apertures (ϕ180–240 mm) and high fields (14.1–24 T/m) are employed, allowing a high acceptance in the ion-optical system of BigRIPS. The main magnetic components of the BigRIPS are fourteen superconducting quadrupole triplets and six room-temperature dipoles. The superconducting quadrupole triplet consists of three superconducting quadrupoles that are rigidly linked to each other, being installed in a liquid-helium vessel in a single cryostat.[3] The first five quadrupole triplets of the BigRIPS are cooled by an integrated, closed cryogenic system with large cooling capacity, in which a single refrigerator supplies the five cryostats with liquid helium through a low-temperature transfer line. This scheme has been adopted because those quadrupole triplets are exposed to high neutron-radiation from the production target and beam dump, which gives rise to significant additional heat load to the cryogenic system. Moreover the radiation heat load changes considerably depending on the intensity, energy and kind of primary beam, and it suddenly disappears when the beam stops. The cryogenic system has been designed taking into account these situations. On the other hand, the rest of the quadrupole triplets to be placed downstream are cooled by a small GM-JT cooler, which is mounted on each cryostat. In this report, we present design features of the integrated cryogenic system. The small refrigeration system is described elsewhere.[4]

Figure 1 shows a schematic diagram of the cryogenic system. Its main components are as follows: a main refrigerator/liquefier called a cold box, a liquid-helium dewar vessel, a low-temperature transfer line with five valve boxes and a joint box, a main compressor unit, a valve unit, three gas-helium buffer tanks, a recovery compressor unit, a low temperature gas-helium recovery line equipped with a heater, and a room temperature gas helium return line from current leads. It is also equipped with a gas analyzer and a gas purifier. Each cryostat of the superconducting quadrupole triplets is connected to the transfer line through the valve box. The system supplies the cryostats with gas helium at 70–80 K as well as liquid helium at 4.5 K. The gas helium is used to cool 80-K thermal shields in the cryostats and transfer line. Most of the 4.5-K gas helium evaporating in the cryostats is returned to the return path of the refrigerator through the transfer line as shown in Fig. 1. The 80-K gas helium is

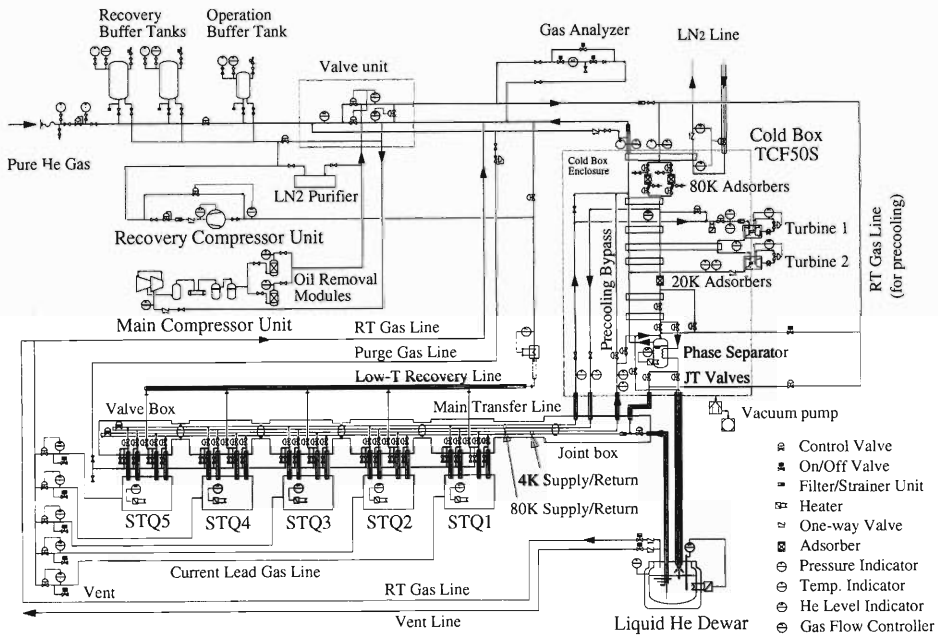

Fig. 1. A schematic diagram of the cryogenic system for the BigRIPS separator. The first five superconducting quadrupole triplets are cooled by using this system.

* Toshiba Corporation

also returned to the refrigerator. Part of the 4.5-K gas helium is used to cool current leads which connects superconducting coils to power supplies. The gas helium coming out of the current leads is returned to the main compressor through the return line. The low temperature gas-helium recovery line is used only when the refrigerator stops. In this case evaporating gas helium is returned to the recovery compressor after being heated by the heater, and then stored in the buffer tanks.

The main refrigerator/liquefier, TCF50S, is being fabricated by Linde Kryotechnik. Its main components are two stages of expansion turbines with gas bearing, seven stages of heat exchangers, two JT valves, a phase separator, and two kinds of low-temperature adsorbers. The cooling capacity of the cryogenic system shown in Fig. 1 is designed to be 320 W for refrigeration at 4.5 K, 0.91 g/s (or 27 liters/hour) for current lead cooling, and 700 W at 80 K for thermal shield cooling. The first heat exchanger in the refrigerator is equipped with a liquid-nitrogen heat exchanger. When liquid nitrogen is supplied to this heat exchanger, the cooling capacity at 4.5 K goes up to 420 W. In designing the system, the cooling capacity was determined on the basis of estimated heat loads to the superconducting quadrupoles and the transfer line. The additional heat load due to the neutron radiation was also taken into account. The system can stand the radiation heat load up to 270 W at 4.5 K when the liquid nitrogen is supplied, while it can stand the load up to 170 W when the liquid nitrogen is not supplied. In order to cope with the change of the radiation heat load, the cryostats are equipped with a heater, which can compensate the change of the heat load. This allows stable operation of the cryogenic system under the high neutron radiation. The summary of the cooling capacity is listed in Table 1.

The low-temperature transfer line accommodates the following four lines: a 4.5-K liquid-helium line, a 4.5-K gas-helium return line, an 80-K gas-helium line, and an 80-K gas-helium return line. Each cryostat is connected to the transfer line through a valve box by using four U-shaped pipes with bayonet joints. The valve box is equipped with low-temperature (Low-T) valves by which the flow to and from the cryostat is controlled. It also accommodates a valve which controls the flow to the recovery line. The valve box is equipped with room-temperature (RT) valves connected to gas purging lines, which are used for the case that a quadrupole triplet has to be removed and replaced by a new one due to some troubles. The outlet of current leads is also equipped with a valve, which controls the flow rate.

Table 1. Cooling capacity and requirement of the cryogenic system.

	Supply quantity	Requirement
Refrigerator load @ 4.5K	320 W without Liq. N_2 420 W with Liq. N_2	150 W + radiation load (~100 W)
Liquefier load @ 4.5K	0.91 g/s (or 27 liters/hour)	0.91 g/s (or 27 liters/hour)
Heat intercept load @ 80K	700 W	698 W

The main compressor is designed to have a discharge flow rate of 73.5 g/sec, its power consumption being 315 kW. Its suction and discharge pressure are 0.1 MPa and 1.7 MPa, respectively. The recovery compressor has a discharge pressure of 1.8 MPa, allowing a flow rate of 70 Nm^3/hour, which is sufficiently large to recover the evaporating gas helium (58 Nm^3/hour). The heater installed in the low-temperature recovery line warms cold gas helium from 4.5 K to room temperature with a heating capacity of 8 kW. The buffer tanks are designed to have a maximum allowable pressure of 2 MPa. Two of the buffer tanks, which have a volume of 100 m^3 each, are used for the recovery of gas helium, while another one, which has a volume of 10 m^3, is used to stabilize the gas pressure during the operation. The liquid helium dewar vessel has a volume of 2000 liters, usually storing liquid helium of about 1000 liters. When some helium is lost due to quenching of superconducting coils, liquid helium is supplied from the dewar vessel to the cryostats.

The cold mass weight of each cryostat is about 10 tons and its helium vessel can contain about 600 liters of liquid helium at maximum. The cooling-down time of the whole system is estimated to be about 14.5 days and 18.5 days with and without the liquid nitrogen precooling, respectively. It is possible to cool down one quadrupole triplet from room temperature while others are kept at low temperature. This situation happens when a quadrupole triplet has to be replaced by new one. In this case the cooling time is estimated to be about 10 days and 12.5 days with and without the liquid nitrogen precooling, respectively.

Fabrication of the cryogenic system will be completed by March, 2004 and stand-alone test operation of the refrigerator will be carried out until then. Test operation of the whole system is scheduled for a later date.

References

1) T. Kubo et al.: RIKEN Accel. Prog. Rep. **35**, 301 (2002); T. Kubo: Nucl. Instrum. Methods Phys. Res. B, in press.
2) Y. Yano et al.: AIP Conf. Proc. **600**, 161 (2001).
3) T. Hirumachi et al.: IEEE Trans. Appl. Supercond. **10**, 236 (2000); T. Kubo et al.: RIKEN Accel. Prog. Rep. **33**, 238 (2000); H. Kouzu et al.: RIKEN Accel. Prog. Rep. **34**, 350 (2001); T. Tominaka et al.: RIKEN Accel. Prog. Rep. **34**, 353 (2001); K. Kusaka et al.: RIKEN Accel. Prog. Rep. **35**, 303 (2002).
4) K. Kusaka et al.: RIKEN Accel. Prog. Rep. **36**, 314 (2003).

Design study of a beam dump for BigRIPS

Y. Mizoi, T. Kubo, K. Kusaka, A. Yoshida, and K. Yoshida

The primary beams from SRC will be stopped at beam dumps inside the first dipole magnet of BigRIPS. The maximum heat load deposited by the beams will reach up to 83.3 kW in the case of a ^{238}U beam with an energy of 350 MeV/nucleon and an intensity of 1 particle μA. The heat-flux density of the beams becomes 380 MW/m^2 by perpendicular injection which cause critical damage to the beam dump or even burnout. However, because the beams are injected to the beam dump with moderate angles due to the bending curvature along the dipole magnet, the projected beam-spot size is magnified horizontally by a factor of 3–4. In addition, the beam-spot size can be also magnified vertically by a factor of 5–7 by tilting the beam-dump walls. By magnifying the beam-spot size both horizontally and vertically, the heat-flux density of the beams can be attenuated to 16 MW/m^2, but it is still difficult to remove by an ordinary cooling system. However, according to recent techniques of the cooling system developed by plasma fusion-reactor groups, the heat load of above 10 MW/m^2 can be cooled safely by adopting their present techniques.

The essential methods to remove such a high-density heat flux are water-flow cooling systems with improved heat-transfer coefficient due to the use of a swirl tube or a screw tube.[1)] The swirl tube has a twisted ribbon along the inside of a tube, and the screw tube has a notched inner surface like a nut. Figures 1 and 2 show the schematic views of the swirl tube and the screw tube, respectively. Their characteristic shapes improve the heat-transfer coefficient arising from forced-convection cooling by a factor of 2–3, compared to an ordinary smooth tube, while the temperature of the inner surface of the tube is below the boiling point of water. Increasing its temperature to above the boiling point of water, the cooling mechanism shifts from simple forced convection to mixed-phase cooling, in other words, subcooled boiling. In subcooled boiling, water flows involve locally boiling water, whose bulk temperature is below the boiling point, and heat is mainly removed by latent heat of evaporation of water. In addition, a temperature margin can be obtained by pressurizing the water flow, because the boiling point of water increases with pressure.

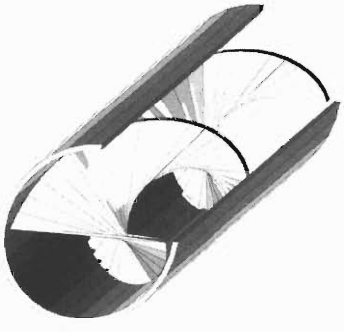

Fig. 1. Schematic view of the swirl tube.

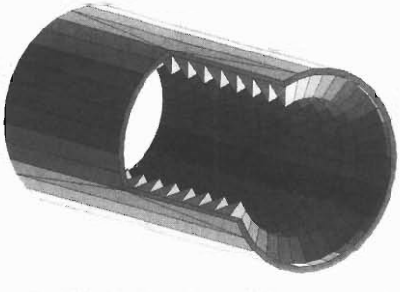

Fig. 2. Schematic view of the screw tube.

We will choose the swirl tube as a candidate for the beam dump for BigRIPS because it is easy to make a long size one (~3 m), and to make a vertically tilted wall with bending along the curvature of the dipole magnet. Figures 3 and 4 show the schematic views of the beam dump made of swirl tubes. The beam dump will be installed inside the vacuum chamber set between the upper and lower poles of the dipole magnet.

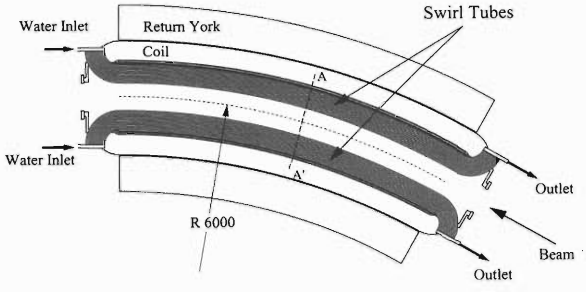

Fig. 3. Horizontal cross-sectional view of the dipole magnet and the beam dump. Cross-sectional view of the line A–A′ is shown in Fig. 4.

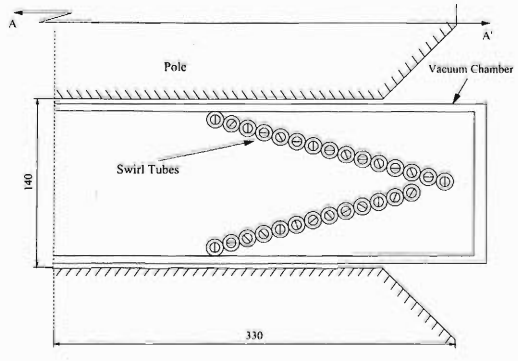

Fig. 4. Vertical cross-sectional view of the beam dump.

Although a thinner wall of the beam dump is preferable for heat conduction, the beam dump should have an sufficient wall thickness so that no heavy-ion beams reach the cooling water, in order to avoid radio activation and chemical activation of water. For example, the range of the ^{12}C with an energy of 400 MeV/nucleon through copper is about 4.5 cm, however, because the beams hit the beam dump obliquely, it is sufficient that the thickness of the beam-dump wall is more than 3 mm.

For a more safe operation of BigRIPS, we are designing the beam dump for the heat load of 100 kW and the heat-flux density of 20 MW/m^2.

Taking these conditions into account, we chose the swirl tube with an inner diameter of 8 mm and an outer diameter of 14 mm, which is made of copper, for first-trail calculation. It is assumed in this calculation that the water-flow speed is 10 m/s and the pressure is 10 atm where the boiling point of water is about 180°C. Figure 5 shows the result performed by ANSYS which is a software of finite-element method. This result shows that the present model is feasible for cooling a 20 MW/m^2 heat load, because the maximum temperature is sufficiently lower than the melting point of copper (1083°C). The design of the prototype beam dump based on the present result is in progress.

For the next step, we will research the materials which have not only good heat conductivity, but also sufficient strength and long endurance, and study the structures for easy maintenance and easy repair, because the place of the first dipole magnet will be hardly radioactivated.

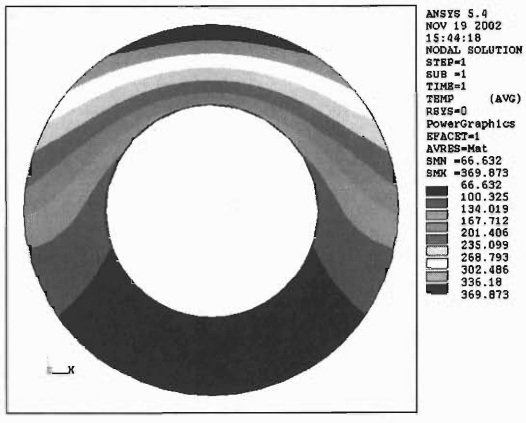

Fig. 5. Result of the finite-element method calculation. The heat flux with 20 MW/m^2 is irradiated to the upper half of the tube. The temperature distribution is shown in Celsius. Though this model looks like the smooth tube, the simulation is performed assuming that this tube is a swirl tube.

References

1) J. Boscary et al.: Fusion Eng. Des. **43**, 147 (1998).

CORBA GPIB-object

T. Tanabe and T. Masuoka*

In any accelerator control system, the General Purpose Interface Bus (GPIB)-based equipment is difficult to integrate into the main controls due to the fact that each equipment has different set of commands and the GPIB standard itself is not entirely respected by all manufacturers. Even if these limitations are accepted, different manufacturers of the GPIB controller offer different methods to remotely use a GPIB equipment over ethernet LAN. Those products are expensive and can be used only on a certain operating system (OS). Therefore, we have developed a common object request broker architecture (CORBA)[1] wrapper program which has unified interfaces for other parts of the control system running in various OSs. It is designed with the extensible markup language (XML) setup file for each type of equipment produced from a relational database management system (RDBMS) in mind.

Figure 1 shows the system configuration for this developed program. The Linux PC is fairly old one with Pentium Pro 200 MHz CPU and 128 MB memory running RedHat Linux Ver7.2. We deliberately chose an old PC in order to ensure that this package can be used in old recycled PC. The host PC, in which interoperable naming service (INS) is running, is the Sun Ultra10 workstation with Solaris 2.6. However, this INS program runs in a Java Virtual Machine (JVM) and any PC or WS with JVM support can be used for this purpose. The ORB used in this server is TAO1.2.1 compiled by ACE5.2.[2] The XML parser is Libxml 2.3.9.[3] The GPIB-PCI board used is the model PCI-4301 by Interface Inc.[4] and its driver is provided by the manufacturer. The equipment tested is the Gmacs 7523 controller.[5]

The procedural explanation of the software package is as follows:

(1) Obtain the information on the initial setup of the GPIB board from XML data.
  (a) Obtain the information on the CORBA server object for the XML data provider, which is registered in interoperable naming service (INS).
  (b) Obtain XML file with the initial setting of the GPIB board from this object.
  (c) Read a file that is used to compare the tags in two XML files.
  (d) Compare this file with the obtained XML to extract the setting using a Simple API for XML (SAX) parser.
  (e) Set the GPIB board.

(2) Register the CORBA object reference to INS.
  (a) Instantiate an object that is capable of communicating with the GPIB equipment whose data was obtained in the above procedures.
  (b) Register this object to INS.

(3) Manipulate the equipment through GPIB.
  (a) CORBA client receives the server object reference through INS.
  (b) Now one can supply GPIB command from the client to the equipment via the server object.

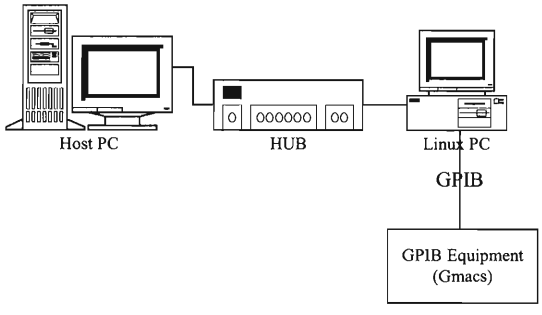

Fig. 1. CORBA-GPIB object test system configuration.

A typical initial setting file is shown in Table 1 and the description for each line is as follows:
Line 1: XML version and character encoding
Line 2: General GPIB board opening/closing tags
Line 3: Specific GPIB board opening/closing tags
Line 4: Object name, Max 31 characters
Line 5: Board name, Max 31 characters
Line 6: Group name, Max 31 characters
Line 7: Block name, Max 31 characters

Table 1. GPIBInitInfo.xml.

```
1  <?xml version="1.0" encoding="UTF-8"?>
2    <gpibboards>
3    <gpibboard>
4  <objectname>GPIB_PCI4301[1]_OBJ</objectname>
5        <boardname>GPIB_PCI4301[1]</boardname>
6        <groupname>IRC</groupname>
7        <blockname>TRIM</blockname>
8        <boardno>0</boardno>
9        <sdrvtime>50</sdrvtime>
10       <eventtime>33</eventtime>
11       <comntime>2</comntime>
12       <gpibmode>IF_MASTER</gpibmode>
13       <asyncmode>ASYNC_ON</asyncmode>
14       <nrfd>NRFD_ON</nrfd>
15       <senddelimiter>DELM_CRLF</senddelimiter>
16       <recvdelimiter>DELM_CRLF</recvdelimiter>
17       <sendchardelimiter>A</sendchardelimiter>
18       <recvchardelimiter>Z</recvchardelimiter>
19   </gpibboard>
20 </gpibboards>
```

* Nichizo Denshi-Seigyo Co., Ltd.

Line 8: Board number, 0–15
Line 9: Send/receive time-out, 1–65535 (in 100 ms)
Line 10: Event change time-out, 1–65535 (in 100 ms)
Line 11: Handshake time-out, 0 (2 μs), 1 (500 ns) 2 (350 ns)
Line 12: GPIB mode setting, IF_MASTER (master mode), IF_SLAVE (slave mode)
Line 13: Asynchronous/synchronous mode setting, ASYNC_ON (asynchronous mode), ASYNC_ON (synchronous mode)
Line 14: Not ready for data (NRFD) setting, NRFD_ON, NRFD_OFF
Line 15: Delimiter setting,

GPIB_NONE	: none
GPIB_NULL	: NULL
GPIB_EOI	: EOF
GPIB_LF	: EOI
GPIB_CR	: CR
GPIB_LF_EOI	: LF+EOI
GPIB_CR_EOI	: CR+EOI
GPIB_CRLF	: CRLF
PIB_CRLF_EOI	: CRLF+EOI
GPIB_CHAR	: Arbitrary ASCII character following "!"

The interface definition language (IDL) defined for this object is in the following.

```
module RIKEN_ACI {
  typedef sequence<char> charSeq;
  typedef sequence<short> shortSeq;
  typedef sequence<string> stringSeq;
  enum GPIB_MODE { GPIB_MASTER,
  GPIB_SLAVE };
  enum GPIB_ASYNC_MODE { GPIB_ASYNC,
  GPIB_SYNC };
  enum GPIB_DELM { GPIB_NONE, GPIB_NULL,
  GPIB_EOI, GPIB_LF, GPIB_CR, GPIB_LF_EOI,
  GPIB_CR_EOI, GPIB_CRLF, GPIB_CRLF_EOI,
  GPIB_CHAR };
  interfaceXML_DB {stringretGPIB_XML(); };
interfaceGPIB: Device {
  short retGPIBReset( in short sBd );
  oneway void nretGPIBReset( in short sBd );
  short retPutBus( in short sBd, in long lData );
  oneway void nretPutBus( in short sBd, in long
  lData );
  long retGetBus( in short sBd );
  short retPutDevClear( in short sBd, in shortSeq
  tAddr );
  oneway void nretPutDevClear( in short sBd, in
  shortSeq tAddr );
  short retPutDevReset( in short sBd, in shortSeq
  tAddr );
  oneway void nretPutDevReset( in short sBd, in
  shortSeq tAddr );
  short retPutRemote( in short sBd, in shortSeq
  tAddr );
  oneway void nretPutRemote( in short sBd, in
  shortSeq tAddr );
  short retPutLocal( in short sBd, in shortSeq
  tAddr );
  oneway void nretPutLocal( in short sBd, in
  shortSeq tAddr );
  short retPutTrigger( in short sBd, in shortSeq
  tAddr );
  oneway void nretPutTrigger( in short sBd, in
  shortSeq tAddr );
  short retPutRENON( in short sBd );
  oneway void nretPutRENON( in short sBd );
  short retPutRENOFF( in short sBd );
  oneway void nretPutRENOFF( in short sBd );
  short retPutSendDelimiter( in short sBd, in
  GPIB_DELM tDelim, in char cDelim );
  oneway void nretPutSendDelimiter( in short sBd,
  in GPIB_DELM tDelim, in char cDelim );
  short retPutRecvDelimiter( in short sBd, in
  GPIB_DELM tDelim, in char cDelim );
  oneway void nretPutRecvDelimiter( in short sBd,
  in GPIB_DELM tDelim, in char cDelim );
  short retPutNRFDON( in short sBd );
  oneway void nretPutNRFDON( in short sBd );
  short retPutNRFDOFF( in short sBd );
  oneway void nretPutNRFDOFF( in short sBd );
  short retWrite( in short sBd, in shortSeq tAddr, in
  charSeq tData );
  oneway void nretWrite( in short sBd, in shortSeq
  tAddr, in charSeq tData );
  charSeq retRead( in short sBd, in short sAddr );
  short retPutSRQ( in short sBd, in shortSeq
  tAddr );
  oneway void nretPutSRQ( in short sBd, in shortSeq
  tAddr );
  long retGetSRQ( in short sBd, in short sAddr );
  short retPutSDRVTimeout( in short sBd, in long
  lTime );
  oneway void nretPutSDRVTimeout( in short sBd,
  in long lTime );
  short retPutEVENTTimeout( in short sBd, in long
  lTime );
  oneway void nretPutEVENTTimeout( in short sBd,
  in long lTime ); }; };
```

We have experienced various errors associated with the time-out setting of the Linux driver for the GPIB board. This problem occurs when the repetition rate of data taking exceeds a certain value. There is no general solution to solve the problem other than to set the data-taking rate sufficiently low.

It should be noted that this framework only gives a common CORBA interface to various GPIB devices. A client program must be developed to accommodate necessary commands and logic. If a different GPIB board is used in the Linux PC, board-dependent class files should be modified accordingly.

References

1) http://www.omg.org/
2) http://www.cs.wustl.edu/~schmidt/TAO.html
3) http://xmlsoft.org/
4) http://www.interface.co.jp/
5) http://www.taiyo.co.jp/

An electron ring for e-RI collider of MUSES

T. Koseki, N. Inabe, and T. Katayama

Since April 2002, construction of a new experimental building of the RIKEN RI Beam Factory has been started. The design of the accelerator complex of the MUSES projects[1] has been updated to accommodate the experimental building. Figure 1 shows a magnetic layout of the newly designed electron and RI (e-RI) collider. The ion ring has a beam energy of 204.5 MeV/nucleon, a circumference of 112.3 m and an emittance of 0.1 mm·mrad. The collision frequency is 36.67 MHz, which is determined by the rf frequency of the Accumulator Cooler Ring, a pre-accelerator of the ion ring.

The electron ring has two arc sections and two long straight sections. Each arc section consists of 8 FODO cells and two matching sections. Figures 2 and 3 show the structure of the unit FODO cell and the optics of the colliding section, respectively. Although the required beam energy for the collision experiment ranges between 0.5 and 0.7 GeV, the ring is designed to be variable from 0.3 GeV to 1.0 GeV. An energy of 0.3 GeV is used for beam injection from an injector linac (or microtron) and an energy of 1.0 GeV for intensive X-ray production using an undulator to carry out a collision experiment of X-ray and RI beam. For e-RI collision, an emittance of 40 nm·rad and a stored

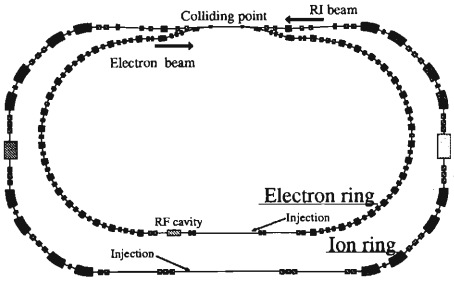

Fig. 1. Magnetic layout of the e-RI collider.

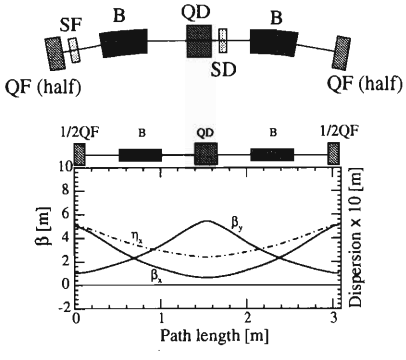

Fig. 2. Structure and optics of the unit FODO cell.

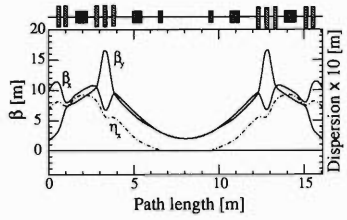

Fig. 3. Optics of the colliding section.

Table 1. Main parameters of the electron ring.

Energy [GeV]	0.5	0.7
Circumference [m]	89.98	
Emittance [nm·rad]	24.63	48.28
Energy spread	2.57×10^{-4}	3.59×10^{-4}
Momentum compaction	1.78×10^{-2}	
Betatron tune	7.07/6.15	
Chromaticity	−9.55/−9.29	
Energy loss/turn [keV]	2.0	7.6
Damping time, trans/longi [ms]	151 / 75.5	55.0 / 27.5
RF frequency [MHz]	476.71	
Harmonic number	143	
No. of beam bunches	11	

current of 0.5 A are required to obtain sufficient luminosity.[1] A small energy spread is also important to perform the experiments with a good energy resolution. The parameters of the electron ring are summarized in Table 1. One of the features of the ring is to store a large beam current of 0.5 A at the low energy operation less than 1 GeV. This means that the single- and multi-bunch collective effects influence significantly the performance of the electron ring and the luminosity of the collider. In the following parts of this report, some of the typical collective effects in the electron ring are briefly discussed.

The coupled-bunch instability, one of the most serious instabilities in circulating accelerators, gives stored current limitation and large emittance growth. We estimated the growth rate of the coupled-bunch instability using the Wang formalism for Gaussian bunches.[2] Figure 4 shows the longitudinal and transverse critical impedances, which are calculated from the balance between growth time and radiation damping time at a beam current of 0.5 A. As the radiation damping times are quite long, some additional damping schemes are necessary to suppress the instability. The bunch-by-bunch feedback system using digital signal processors

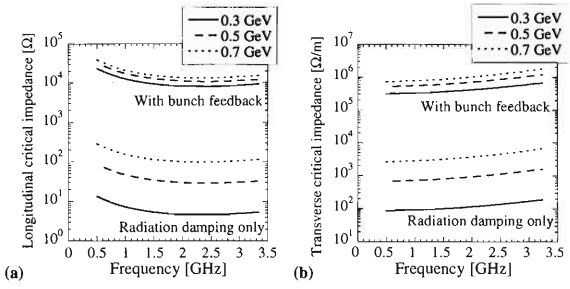

Fig. 4. (a) Longitudinal and (b) transverse critical impedances of coupled-bunch instability for 0.5 A.

is an effective device for curing the instability and is operated satisfactorily at some flavour factories and synchrotron light sources.[3] The critical impedances, when the bunch feedback system having a damping time of 0.2 ms switches on, are also given in these figures. They, however, are still not large enough compared with typical resonator impedances, so that an rf cavity with a damping structure of higher-order modes (HOMs) should be adopted for the ring. The HOM damped cavity with a SiC beam duct[4] is a promising candidate for this purpose.

Broadband impedances in the storage ring excite short-range wake field on the vacuum chamber and contribute to single-bunch coherent effects. The microwave instability occurs when a bunch current exceeds a critical threshold value and induces bunch lengthening and energy spread widening. We estimated the threshold current using the Boussard criterion[5] and behavior above the threshold using the Chao-Gareyte scaling law.[6] Figure 5 shows the current dependences of bunch length and energy spread at 0.5 GeV. Here, the effective impedance is assumed to be 0.5 Ω or 1.0 Ω and it has no frequency dependence. Although the effect of bunch lengthening is large, it does not affect the luminosity because the bunch length of the ion beam is about 10 cm. On the other hand, the energy spread σ_E becomes larger than that required from the collision experiment at high current. Appropriate care is needed to reduce the energy spread. The vacuum components of the ring should be

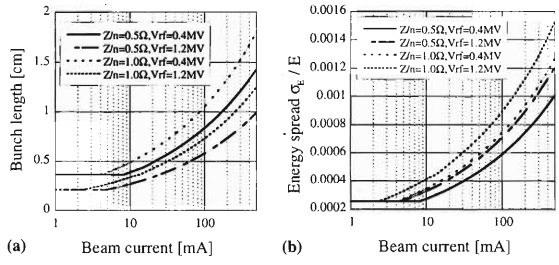

Fig. 5. (a) Bunch lengthening and (b) energy spread due to microwave instability.

carefully designed to make the broadband impedance as small as possible.

Figure 6 shows the current dependence of emittance growth due to intrabeam scattering calculated using the computer code ZAP.[7] κ is the coupling of emittance between the horizontal and vertical directions. The optimum emittance for the collision experiment is about 40 nm·rad, therefore the emittance growth does not reduce the luminosity significantly.

Beam lifetime is mainly determined by the Touschek effect and residual gas scattering.[7] Figure 7 shows the accelerating voltage dependence of the half-lifetimes due to the Touschek effect and residual gas scattering. In the calculation, the effects of microwave instability and intrabeam scattering are taken into account. The gas scattering lifetime is estimated with the following assumptions: vacuum pressure is 4×10^{-8} Pa (CO equivalent) and limited acceptance is determined by a septum magnet. For a standard rf system, the maximum rf voltage per single cavity is 0.5–0.7 MV. If a lifetime of much more than 1 hour is required, a two-cavity system is preferable.

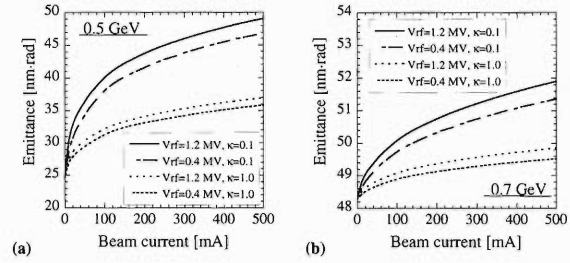

Fig. 6. Current dependence of emittance growth due to intrabeam scattering at (a) 0.5 GeV and (b) 0.7 GeV.

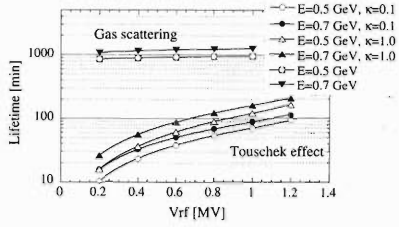

Fig. 7. Rf voltage dependence of the Touschek and residual gas scattering lifetimes.

References

1) T. Katayama et al.: MUSES Conceptual Design Report (2000).
2) J. M. Wang: BNL Report No. BNL-51302 (1980).
3) For example, E. Kikutani et al.: Proc. EPAC02, (2002) p.2085.
4) T. Koseki et al.: Rev. Sci. Instrum. **66**, 1926 (1995).
5) D. Boussared: CERN/Lab,11/RF/Int.75-2 (1975).
6) A. W. Chao and J. Gareyto: SLAC Note SPEAR-197/PEP-224 (1976).
7) M. S. Zisman et al.: LBL Report No. LBL-21270 (1986).

Study on electron cooler at RIKEN

M. Nishiura, T. Tanabe, T. Katayama, E. Syresin,[*1] and I. Watanabe[*2]

The Electron Cooler (EC) of an Accumulator Cooler Ring (ACR)[1,2] consists of a Gun, a toroidal, and a collector section. A magnetic shield is placed outside the guiding solenoid and covers it from the Gun section to the collector section. The magnetic shield affects the magnetic field inside the guiding solenoids. A high magnetic field uniformity (the ratio of the transverse field to the longitudinal field, $B_\perp/B$, of the order of 10^{-5}) is required in the cooling section of the ACR-EC. Moreover, strictly speaking, the EC does not use an axially symmetric solenoid, and a more realistic model should be examined for better understanding of magnetic fields and electron beam trajectories. The toroidal section, which is the connecting part between the Gun and the cooling section, plays an important role in guiding the electron beam and merging it with the ion beam by keeping the electron-beam temperature as low as possible.

The three-dimensional magnetic field is calculated[3] using the TOSCA with finite element method. The finite element mesh data was constructed close to the original drawing for the ACR-EC proposed by Tanabe *et al.*[2] In the Gun section, two solenoids situated coaxially are used to produce the magnetic field for adiabatic expansion. The toroidal section with the angle of 90 degrees is divided into two regions at the angle of 53 degrees. The toroidal section with the radius of 1.5 m consists of 30 solenoids placed with a 0.9-degree interval between them. The second toroidal magnet has a radius of 1.72 m, and consists of 20 racetrack conductors placed with the same interval as the first toroidal. The solenoid length at the cooling section is 3.6 m, and both ends are connected to the toroidal sections. The magnetic shield with 5-cm thickness covers all the solenoids.

In a typical case of $B_{\mathrm{Gun}} = 4\,\mathrm{kG}$ and $B_{\mathrm{Cool}} = 500\,\mathrm{G}$, the magnetic field along the solenoid axis, B, and the adiabatic parameter, $\xi = (\lambda_c/B)\,|dB/ds|$, are shown in Fig. 1, where λ_c is the spiral length of the cyclotron motion and s is the position on the solenoid axis. The cathode of electron Gun is placed at $s = 1.57\,\mathrm{m}$. The adiabatic parameter has a reasonable value of 5×10^{-2} at most. Although the correction coils for the field compensation are placed near the connection between sections, the required uniformity of the magnetic field $\delta B/B$ has not yet been achieved at the edge of the cooling section. In the present design, it is found that this field disturbance reduces the effective length of the cooling section to 2.2 m.

Figure 2 shows the magnetic flux lines are superimposed on the cross-sectional view of the EC. A

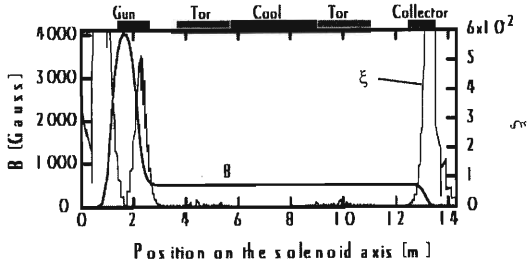

Fig. 1. Magnetic field and adiabatic parameter along the solenoid axis. Gun indicates Gun section, Tor toroidal section, Cool cooling section, and Collector collector section.

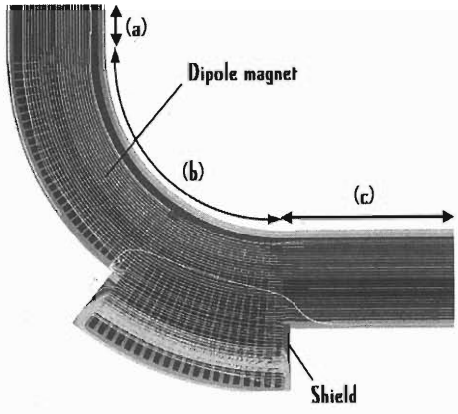

Fig. 2. Magnetic flux lines of the cooling solenoid and the large diameter solenoids. Notations of (a), (b), and (c) correspond to Gun, Tor, Cool, respectively, in Fig. 1.

dipole magnet bent by 90 degrees is installed inside the guiding solenoids at the toroidal section in order to suppress the drift motion of the electron-beam across the magnetic fields and control the electron beam orbit. Single-particle tracking has been carried out using this structure. An electron with the energy of 220 keV is emitted from the cathode position of the electron Gun. After passing through the toroidal section, the displacement of the electron position from the design orbit became about 4.38×10^{-4} cm by optimizing the line-integrated Bl value of the dipole field.

The transverse temperature of an electron beam less than 1 eV has not yet been achieved. The tolerance of the disturbed magnetic field and the field shapes should be investigated using beam tracking with synthetic magnetic field distributions.

*1 Joint Institute for Nuclear Research, Russia
*2 Toshiba Corporation

References

1) T. Katayama et al.: Proc. EPAC '98, (1998) p. 529.
2) T. Tanabe et al.: Nucl. Instrum. Methods Phys. Res. A **441**, 104 (2000).
3) M. Nishiura et al.: Proc. EPAC '02, (2002) p. 1377.

Measurement of rf characteristics of magnetic material (FINEMET) for an rf cavity of MUSES-ACR

M. Watanabe, Y. Chiba, K. Ohtomo,* T. Koseki, and T. Katayama

As the second phase of the RIBF (RI Beam Factory) project, MUSES (Multi-USe Experimental Storage rings), a complex of a synchrotron and storage rings for radioactive ion experiments is being studied. In the ACR (Accumulation Cooler Ring), an rf system having a frequency sweep width of less than 0.4 MHz in the frequency range from 22 to 38 MHz, period of 100 msec pulse operation with 5 Hz cycling and a gap voltage of 50 kV are required for rf stacking.[1)]

Ferrite-loaded cavities have been used widely in synchrotrons. They are tuned cavities and therefore they need the complex frequency tracking system by modulating the dc magnetic bias field. Rapid deterioration of rf characteristics with increase of rf magnetic flux density is intrinsic to ferrite and causes serious problems in a high-gradient cavity.

A magnetic alloy (FINEMET, developed by HITACHI Metal Co. Ltd) is made of Fe-based nanocrystalline alloy. FINEMET has the following features; the magnetic Q value is very low in the rf frequency range above 1 MHz, low dependence on rf magnetic flux density up to high magnetic flux density (until 2000 Gauss) and Curie temperature of 840 K makes working operation possible at high temperatures.[2)] These are contrary features to those of usual ferrite material and considered to be applicable to a high-gradient synchrotron cavity.

Recently, rf accelerating cavities[3,4)] using this material have been developed in the frequency range below 15 MHz. They have inherently very wide band features due to low Q value of FINEMET and do not need a complex tuning system at the expense of high rf excitation power.

In order to investigate the feasibility of FINEMET-loaded rf cavity for the MUSES-ACR, we measured its rf characteristics in the frequency range up to 40 MHz, named FT-3M. The sample is made of thin tape, which is approximately 18 μm thick, and wound into a troidal shape having a size of 140 mm (I.D.), 200 mm (O.D.) and 25.4 mm (width). The tape is coated with SiO_2 for insulation. We need the data of μ'_pQf in the frequency range from 22 to 38 MHz. The μ'_pQf data above 15 MHz have not been published.

Figure 1 shows a schematic of the cross section of a test vessel. The painted area shows the FINEMET core. It has a coaxial structure made of copper as the outer conductor and aluminum as the inner one.

The equivalent circuit of the test vessel can be expressed as a parallel circuit of cores and capacitance. The input admittance Y of the test vessel was measured in the form of real part G and imaginary part B. Using equivalent inductance Lc, geometric capacitance Cp and angular frequency ω, Y is expressed as,

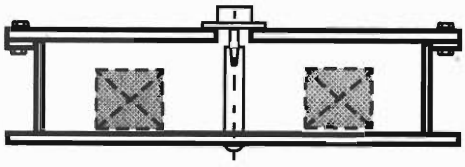

Fig. 1. Cross section of test vessel.

$$Y = G + jB = 1/j\omega Lc + j\omega Cp, \tag{1}$$

where Lc is given by

$$Lc = \mu_0\mu d/2\pi \times \ln(Ro/Ri), \tag{2}$$

where Ri, Ro, and d are inner diameter, outer diameter and height of the core respectively. μ_0 is permeability of vacuum and μ is relative permeability of the vessel. It has a complex value and the imaginary part represents rf loss in the vessel. The loss in the FINEMET is so large that the rf losses due to the other parts of the test vessel can be neglected in Eq. (1). Permeability is usually defined as

$$\mu = \mu'_s - j\mu''_s, \tag{3}$$

where suffix s denotes an expression corresponding to a series connection of reactance and resistance elements.

Generally, permeability is expressed as the series expression. The parallel permeability[5)] (suffix p) often used in an accelerating cavity is derived from the series expression of μ as

$$1/\mu = 1/\mu'_p - 1/j\mu''_p. \tag{4}$$

Using these expressions, the relationships between μ'_s and μ'_p, μ''_s and μ''_p are given in Eqs. (5) and (6),

$$\mu'_p = \mu'_s(1 + 1/Q^2), \tag{5}$$

$$\mu''_s = \mu''_p/(1 + Q^2), \tag{6}$$

where Q is the magnetic quality factor. The Q value can also be expressed using a complex permeability;

$$Q = \mu'_s/\mu''_s = \mu''_p/\mu'_p. \tag{7}$$

It should be noted from Eqs. (5) or (6) that in the case of high Q, μ'_s is nearly equal to μ'_p but in the case of low Q, both expressions give different values.

Shunt resistance (Rp) is expressed as,

$$Rp = 1/G = \mu'_pQf \times \mu_0 d \times \ln(Ro/Ri), \tag{8}$$

* Sumitomo Heavy Industries, Ltd.

where f is frequency. As shown in this equation, $\mu'_p Qf$ is proportional to Rp, which decides the accelerating voltage.

The admittance of the test vessel was measured using a network analyzer (HP4195A) in the frequency range from 100 kHz to 40 MHz.

The typical result of measured admittance (G, B) is shown in Fig. 2. Effective permeability (μ'_s, μ''_s) of the core volume and $\mu'_p Qf$ values, calculated using the measured admittance, are shown in Figs. 3 and 4, respectively. As shown, the μ'_s and the μ''_s become

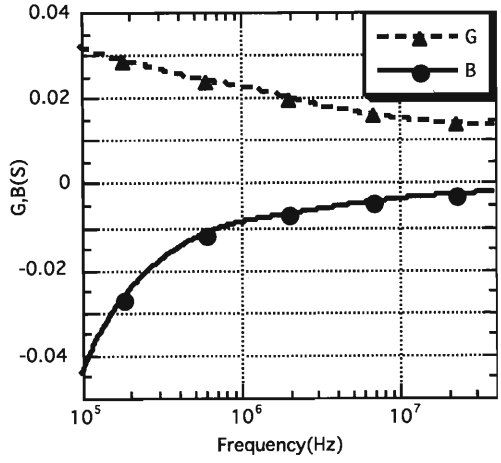

Fig. 2. Admittance of rf test vessel.

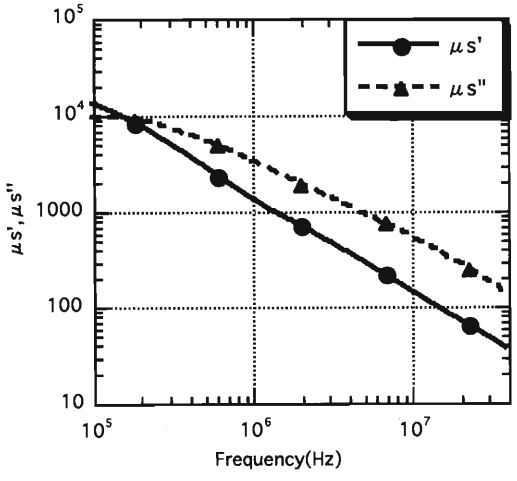

Fig. 3. Permeabiity of FINEMET.

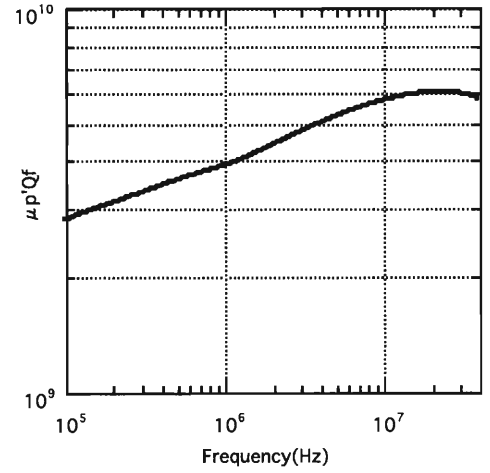

Fig. 4. $\mu'_p Qf$ of FINEMET.

lower as the frequency increases and the $\mu'_p Qf$ becomes higher as the frequency increases up to approximately a few tens MHz.

In this measurement, the input power to the vessel was about 0.3 mW. Other measurements at several high input power levels up to 30 W were carried out using an external high-power directional coupler and an external high-power rf source together with the network analyzer. The measured results were almost the same at the two power levels. As mentioned above, since the characteristics of FINEMET are stable up to the high rf magnetic flux density, the obtained data can be utilized for designing an actual cavity used at a high power level.

Since the measured μ''_s is larger than μ'_s, Q values are less than 1, as shown in Eq. (7). The Q values are somewhat too small for the rf cavity of the ACR. Cutting the ring core and introducing air gaps increase the Q value of a cavity.[6] We have plans to investigate this method as the next step.

References

1) T. Katayama et al.: MUSES Conceptual Design Report (2000).
2) Y. Mori et al.: Proc. EPAC98, (1998), p. 299.
3) M. Aiba et al.: Proc. EPAC2000, (2000), p. 581.
4) Z. Fang et al.: Proc. EPAC2002, (2002), p. 2145.
5) Y. Tanabe et al.: Proc. APAC98 (1998), p. 390.
6) J. Day et al.: Proc. PAC2001, (2001), p. 882.

Study of ion beam ordered state

H. Tsutsui,[*1] T. Katayama, I. Meshkov,[*2] A. Sidorin,[*2] A. Smirnov,[*2] E. Syresin,[*2] and D. Möhl[*3]

An anomalously small momentum spread[1] has been observed in several storage rings with electron cooling (EC) since the early 1980s. This phenomenon was explained as the crystallisation of the ion beam, and theoretical and simulation studies of it have been conducted.[2] The experimental possibilities of MUSES can be substantially enhanced if this ordered state is achieved. Particularly, it allows one to measure isotope masses with high precision. Also, high luminosity in e-RI colliding experiments can be expected. For designing an ion ring optimised for these experiments, a simulation code was developed which is described in this article. Also some theoretical investigation on the condition necessary to achieve the 1D chain state is explained.

The Hamiltonian for the coasting beam is

$$\begin{aligned} H &= H_1 + H_2, \\ H_1 &= -\frac{x\delta_p}{\rho} + \frac{\delta_p^2}{2\gamma_0^2} + \frac{p_x^2+p_y^2}{2} \\ &\quad + \left(\frac{1}{\rho^2}+K\right)\frac{x^2}{2} - \frac{K}{2}y^2, \\ H_2 &= \frac{\lambda}{6}\left(x^3-3xy^2\right) + \frac{r_{ion}}{\gamma_0^2\beta_0^2}\sum_{i=1}^{N}[(x-x_i)^2 \\ &\quad + (y-y_i)^2 + \gamma_0^2(z-z_i)^2]^{-1/2}, \end{aligned} \tag{1}$$

where (x, y, z), $(p_x, p_y, \delta_p = \Delta p/p)$, ρ, γ_0, β_0, K, λ, and r_{ion} are the coordinate, momentum, curvature radius, relativistic factor, normalised velocity, quadrupole field strength, sextupole field strength, and classical radius of the ion, respectively.

For the integration, a second-order symplectic method[3]

$$\begin{aligned} \mathcal{M} &\equiv Te^{-:\int_{s_1}^{s_2} ds' H(s'):} \\ &\approx \prod_{\Delta s}\left[e^{-:H_1(s)\frac{\Delta s}{2}:}e^{-:H_2(s)\Delta s:}e^{-:H_1(s)\frac{\Delta s}{2}:}\right], \end{aligned} \tag{2}$$

is applied in order to avoid nonphysical (in)stabilities. Also in order to reduce the calculation time of the space-charge interaction ($\propto N^2$), the periodic boundary condition is used.[4]

The momentum after every passage of EC is approximated as

$$\delta_p \leftarrow (1-\eta_l)\delta_p,\ p_x \leftarrow (1-\eta_t)p_x,\ p_y \leftarrow (1-\eta_t)p_y, \tag{3}$$

where η_l and η_t are the longitudinal and the transverse cooling coefficients, respectively.

*1 Sumitomo Heavy Industries, Ltd.
*2 Joint Institute for Nuclear Research, Russia
*3 CERN, Switzerland

The simulation code was checked with the Hasse-Schiffer (HS) model,[5] where the linear Hamiltonian is

$$H_1 = \frac{\delta_p^2}{2\gamma_0^2} + \frac{p_x^2+p_y^2}{2} + K\frac{x^2+y^2}{2}. \tag{4}$$

They defined a dimensionless linear density as

$$\lambda_{ion} = \frac{N}{C}\left(\frac{3r_{ion}}{2K\gamma_0^5\beta_0^2}\right)^{\frac{1}{3}} = \left(\frac{3N^3 r_{ion}}{8\pi^2 Q^2 C\gamma_0^5\beta_0^2}\right)^{\frac{1}{3}}, \tag{5}$$

where C and Q are the circumference and the betatron tune, respectively, to classify the ordered states ($0 < \lambda_{ion} < 0.709$: 1D chain, $0.709 < \lambda_{ion} < 0.964$: zig-zag, $\cdots$). Figure 1 shows the simulated beam distributions after 50000 turns. They are consistent with the theory. The initial momentum spread and the emittance are $\sigma_p = 5\times10^{-5}$ and $\epsilon = 10\,\pi$ nm-rad, respectively.

Next, the ESR experiment[1] was simulated with

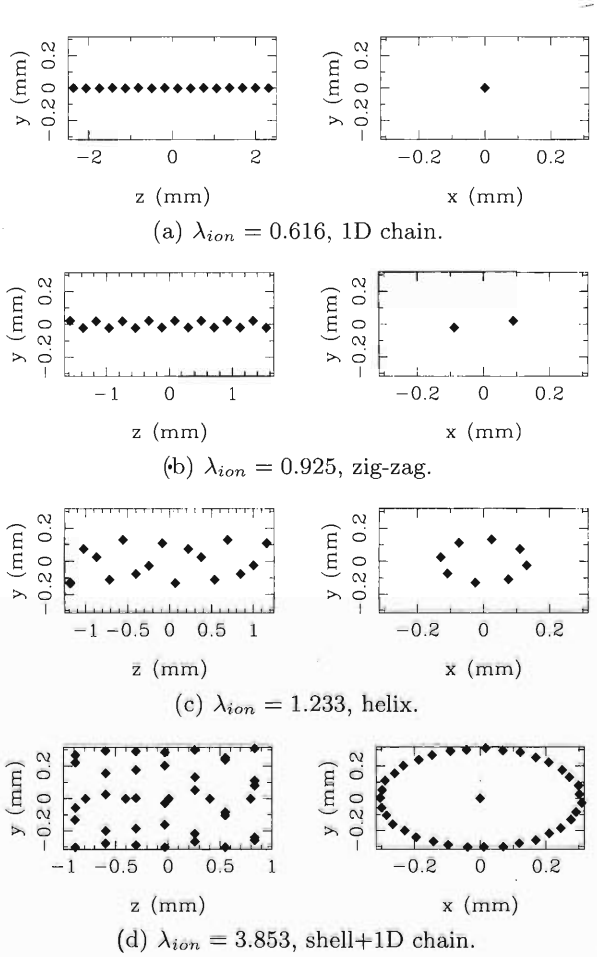

(a) $\lambda_{ion} = 0.616$, 1D chain.

(b) $\lambda_{ion} = 0.925$, zig-zag.

(c) $\lambda_{ion} = 1.233$, helix.

(d) $\lambda_{ion} = 3.853$, shell+1D chain.

Fig. 1. Simulated beam distributions after 50000 turns with the HS model.

this code. In the experiment, anomalous momentum spread reduction of the beam was observed when the number of ions in the ring was less than 10^3–10^4, depending on the ion species and the cooling rate by EC. The typical cooling rate is approximately 10 Hz for the longitudinal direction and 0.1–1 Hz for the transverse direction, which correspond to $\eta_l \approx 10^{-5}$ and $\eta_t \approx 10^{-6}$–10^{-7}, respectively. Since a simulation run with these values takes so long (typically a few days with Alpha CPU) to reach an equilibrium, larger η_l, η_t were used. Figure 2 shows the result for the 360 MeV/nucleon $^{197}Au^{79+}$ case when $\eta_l = \eta_t = 10^{-4}$. The phase transition from the random distribution to the 1D chain can be seen. Figure 3 shows the σ_p as a function of N for various cooling coefficients. It is interesting that the threshold becomes larger as the transverse cooling rate becomes smaller. The reason may be that the effective two body interaction is small when the transverse oscillation amplitude is large.

In this case $\lambda_{ion} = 1.1 \times 10^{-3}$ when $N = 10^4$, which means that the phase transition occurs in the 1D chain region. The momentum spread is determined by the

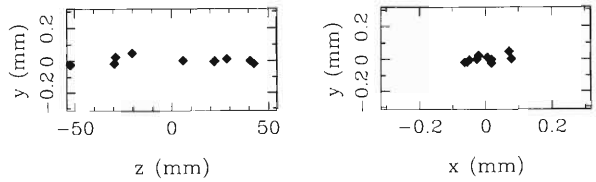

(a) $N = 10^4$. Above transition.

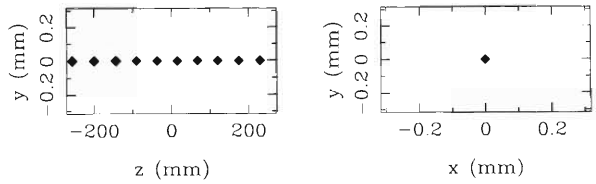

(b) $N = 10^3$. Below transition.

Fig. 2. Simulated beam distributions for the ESR experiment. $\eta_l = \eta_t = 10^{-4}$.

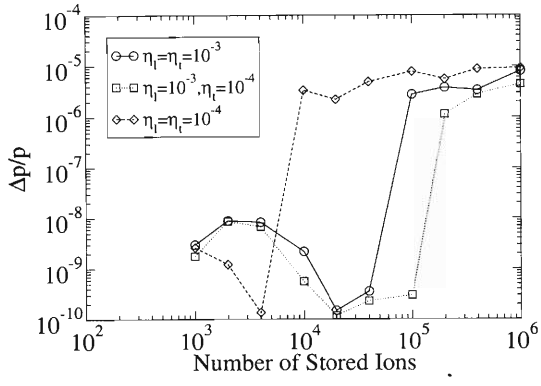

Fig. 3. Simulated σ_p as a function of N for various cooling coefficients for 360 MeV/u $^{197}Au^{79+}$ in ESR.

balance of the EC and the heating by the intrabeam scattering (IBS). Usually the heating rate by IBS becomes larger as the longitudinal temperature $T_\parallel = mc^2\beta_0^2\sigma_p^2/k$ becomes smaller. However, when $T_\parallel$ is considerably low, there is a small chance for the interactions to occur, and the heating rate becomes small. Hence a phase transition occurs. The analytical formulas of the IBS heating rate at low temperature are as yet unknown. But one can see from Fig. 3 that the threshold number of the ions is almost proportional to the cooling rate, and that in order to obtain $N = 10^6$ particles in the 1D chain state η_l should be larger than 10^{-2}, which corresponds to the cooling rate of 1–10 kHz.

The coherent tune of the μ-th mode Q_μ ($\mu = 0, 1, \cdots, N-1$) for the 1D chain state is

$$\frac{Q_\mu^2}{Q^2} = 1 - \frac{4\lambda_{ion}^3}{3}\sum_{l=1}^{\infty}\frac{1-\cos(2\pi(Q_\mu+\mu)l/N)}{l^3}, \quad (6)$$

which is plotted in Fig. 4. Assuming that all coherent tune shifts should be less than 0.25 to avoid some coherent mode hitting a fourth-order resonance, N should be less than, for 360 MeV/u $^{197}Au^{79+}$ in ESR,

$$N_{sc} = \left(\frac{4\pi^2 QC\gamma_0^5\beta_0^2}{7\zeta(3)r_{ion}}\right)^{\frac{1}{3}} = 3.9 \times 10^6, \quad (7)$$

where $\zeta(n)$ is the Riemann zeta function. This threshold does not depend significantly on the lattice structure. Other conditions for the 1D chain were derived by Meshkov *et al.*[6]

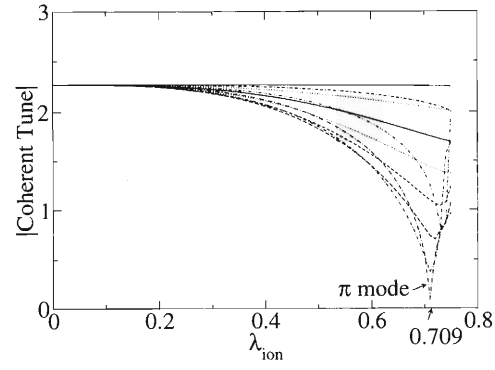

Fig. 4. Coherent tune as a function of linear density.

References

1) M. Steck et al.: Phys. Rev. Lett. **77**, 3803 (1996), and references therein.
2) D. M. Maletić and A. G. Ruggiero (eds.): *Crystalline Beams and Related Issues* (World Scientific, Singapore, 1996).
3) E. Forest: *Beam Dynamics, A New Attitude and Framework* (Harwood, Amsterdam, 1998).
4) V. V. Avilov: Solid State Commun. **44**, 555 (1982).
5) R. W. Hasse and J. P. Schiffer: Ann. Phys. **203**, 419 (1990).
6) I. Meshkov et al.: RIKEN-AF-AC-34 (2002).

Cures for instabilities during electron-cooling bunching

M. Takanaka

In performing particles-tracking simulations, we have studied the electron-cooling (EC) bunching of ion beams at low energies in a ring in order to satisfy ion-beam requirements for electron-RI beam colliding experiments planned at the Radioisotope Beam Factory.[1,2] The simulation results have shown that the ion beam meets a transverse and a longitudinal instability during EC bunching. We describe cures for the instabilities here.

The source of the transverse instability is the gradient field of toroids at both ends of the EC section, that not only bends a beam but also twists it. The analysis of the amplitude and phase equation for a particle[2] has shown that a repetition of the twist causes resonances of $Q_x \pm Q_y = n$ (n = integer) in the bunched beam which has a betatron-tune spread due to the space-charge effects. The resonances are characterized by the following resonant invariants:

$$\epsilon_x = C,$$
$$(Q_x \pm Q_y - n)\epsilon_y \mp \frac{1}{\pi}\sqrt{\epsilon_x \epsilon_y} A_y \cos(\Phi + n\theta_y^{eff}) = C,$$

where $\Phi = (Q_x \pm Q_y - n)\theta + \phi_x \pm \phi_y$, ϵ is a transverse emittance, A_y an effective twist strength, θ_y^{eff} an effective action position of the twist, θ the azimuth position of an ion, and ϕ the initial phase advance of the ion. The above equations show that ions trapped in the emittance-increasing resonances are lost through hitting the chamber wall at large emittance. We install skew quadrupole magnets (or SQs) in the ring to change the emittance-increasing resonance to an emittance-beating one which is characterized by the following resonant invariants:

$$\epsilon_x + \epsilon_y = \epsilon = C,$$
$$(Q_x \pm Q_y - n)\epsilon_y \mp \frac{1}{\pi}\sqrt{(\epsilon - \epsilon_y)\epsilon_y} A_y \times \cos(\Phi + n\theta_y^{eff}) = C.$$

The above equations show that ions trapped in the emittance-beating resonance can remain within a transverse limited space. The simulation result shown in Fig. 1 shows that the resonance control is effective for stabilizing the beam transversely.

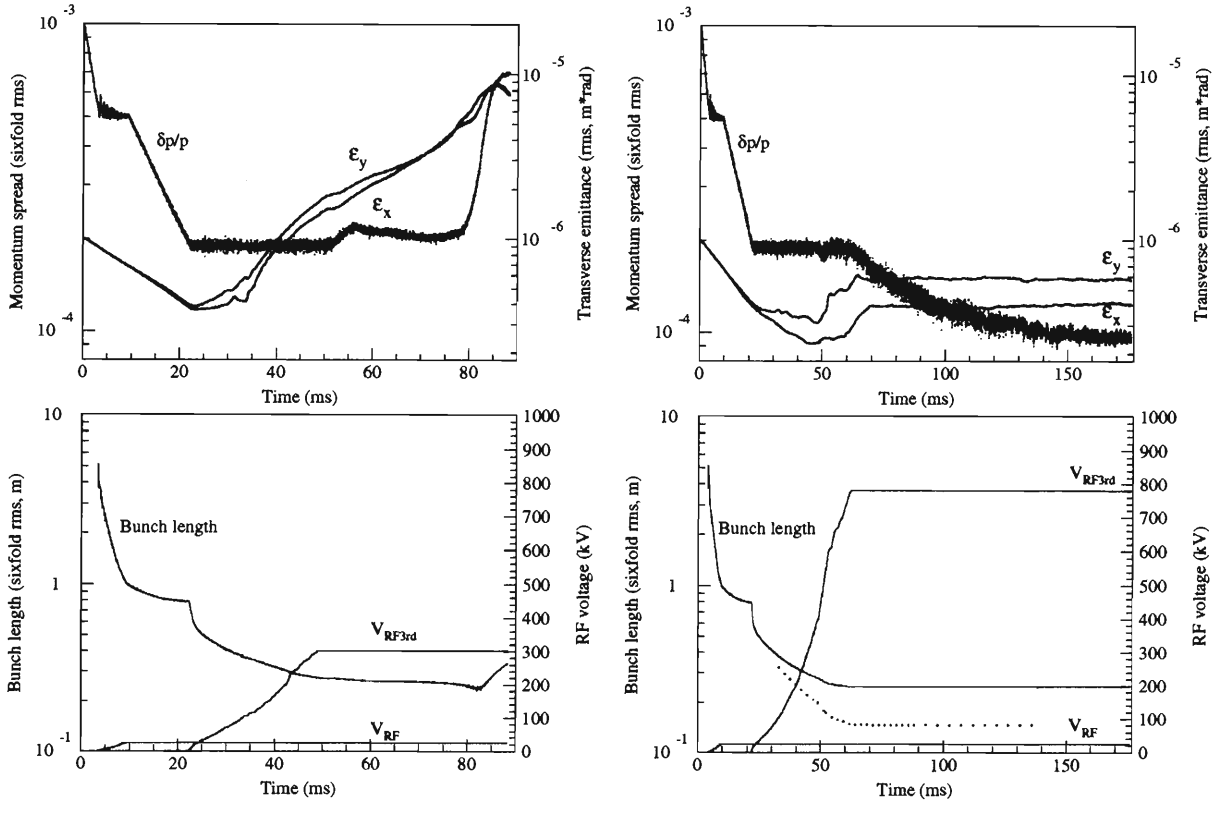

Fig. 1. Time evolutions of EC bunching of a $^{238}U^{92+}$ beam of 4 mA. The right-hand figures are for the case where the resonance source is controlled using SQs. In the lower figure on the right the dotted curve indicates the sixfold rms bunch length without counting the ions far from the bunch.

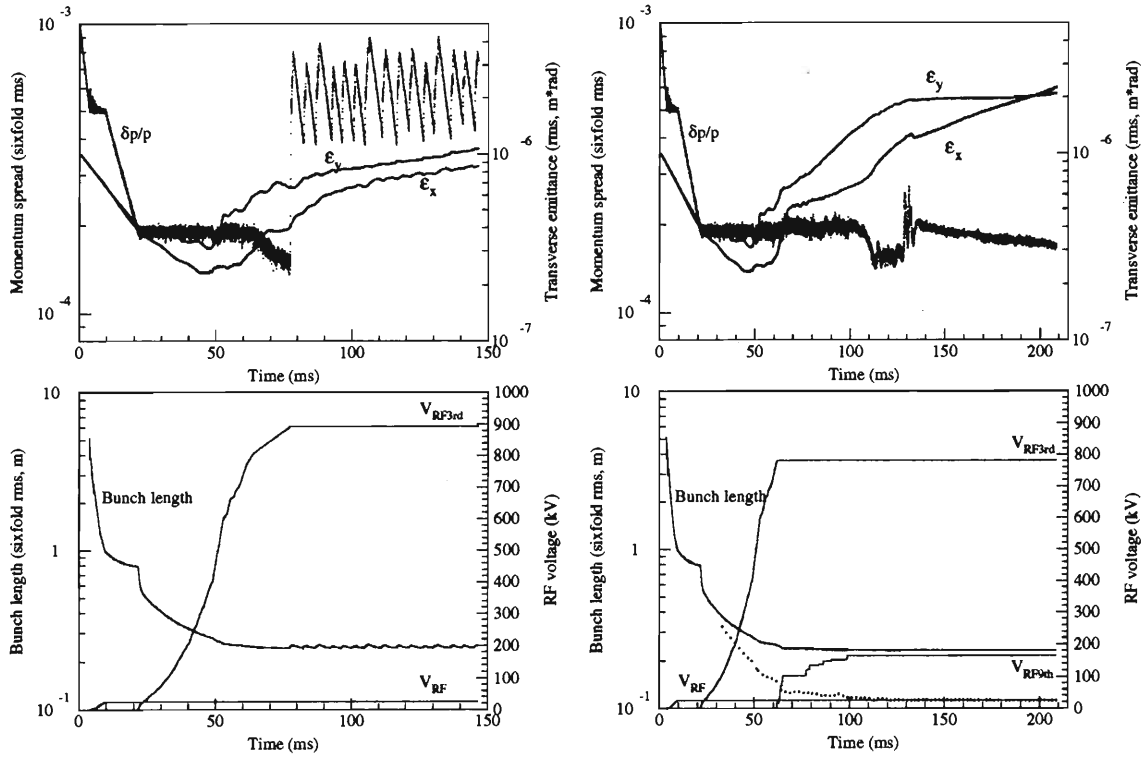

Fig. 2. Time evolutions of EC bunching of a $^{238}U^{92+}$ beam of 4 mA in the case where the resonance source is controlled using SQs. The figures on the right are for the case where additional 9th-harmonic RF voltage is supplied. In the lower figure on the right the dotted curve indicates the sixfold rms bunch length without counting the ions far from the bunch.

When we increase the 3rd-harmonic RF voltage to 0.9 MV under the resonance control in order to make the bunch shorter, the beam becomes unstable longitudinally, as shown on the left-hand side of Fig. 2.

At the 3rd-harmonic RF voltage of 780 kV we start to supply the 9th-harmonic RF voltage at the same azimuth as we supply the 3rd-harmonic one. The simulation result of supplying the 9th-harmonic RF voltage shown on the right-hand side of Fig. 2 shows that the beam is stable longitudinally up to at least the 9th-harmonic RF voltage of 160 kV which corresponds to an addition of 480 kV to the 3rd one of 780 kV, while the sum of the two voltages is beyond the longitudinal-instability threshold of 0.9 MV for the current case.

A line density λ of a stable space-charge-dominated bunched beam has the following approximate relation with a kth-harmonic RF voltage under the dominance of the space-charge impedance when the other RF voltages are not supplied:

$$\lambda \propto 1 - \frac{4z^2}{l_0^2} + \frac{(hk)^2 4z^4}{12R^2 l_0^2},$$

where l_0 is the bunch length when the nonlinearity of the voltage around the zero cross is negligibly small, R the ring radius, h the RF harmonics, and z the longitudinal displacement from the bunch center. The nonlinearity has the effect of making the bunch confinement loose on the head and the tail side. The effect due to the 9th-harmonic RF voltage is nine times stronger at the bunch ends than that due to the 3rd one when the 9th-harmonic voltage is one-third of the 3rd-harmonic voltage, or when the l_0 is equal under both voltages. As the simulation result, the nonlinearity of the 9th-harmonic RF voltage is seen to play a role in cure for the longitudinal instability.

After the longitudinal cure, however, the beam is seen to meet the weak transverse instability. We have checked that the instability occurs as ever without the transverse broad-band impedance or without consideration of image charges reflected from the chamber in the simulation. We guess that the weak instability for the shorter bunch is due to the imperfection of the resonance control.

In conclusion, performing the simulations we have clarified that the two proposed cures are effective ones for the transverse and the longitudinal instability during EC bunching, respectively.

References

1) M. Takanaka: Proc. PAC2001 (2001), p. 3897; RIKEN Accel. Prog. Rep. **35**, 312 (2002).
2) M. Takanaka: Proc. EPAC2002 (2002), p. 1410.

Prototype of highly -sensitive cryogenic current comparator with HTS SQUID and HTS magnetic shield

T. Watanabe, S. Watanabe, T. Ikeda, M. Kase, T. Kawaguchi,* Y. Sasaki, and T. Katayama

A prototype of a highly -sensitive Cryogenic Current Comparator (CCC) for the measurement of the intensity of faint beams, such as a radioisotope beam, was developed for the RIKEN RI beam factory.[1,2] The HTS CCC comprises a high-temperature superconducting (HTS) magnetic shield and an HTS Superconducting QUantum Interference Device (SQUID), because a high-accuracy and nondestructive measurement is required. Recently, the prototype of the HTS CCC system was completed and the first measurement using a simulated beam was carried out. This paper describes the present status of the prototype of the HTS CCC system and the results of the measurement.

A cylindrical HTS magnetic shield based on Bi_2-Sr_2-Ca_2-Cu_3-O_x (Bi-2223) with sizes of 148 mm in diameter and 250 mm in length was fabricated by dip-coating (300 μm) on a 99.9% MgO ceramic substrate.[1] An HTS magnetic shield has an advantage in that the magnetic shielding effect is independent of the frequency of environmental magnetic noise, even in the low-frequency band.[3] The critical current (I_c) of 4500 A/cm^2 and the critical temperature (T_c) of 106 K of the Bi-2223 cylindrical HTS shield were obtained by a DC four-probe method using a small sample of Bi-2223. Furthermore, in order to measure the field distribution inside the HTS shield and to obtain the attenuation factor, we constructed a measurement system.[4] The system is composed of an X-Y-Z stage driven by stepping motors, G10-rod which is fixed on the X-Y-Z stage and attaches two probes of HTS-SQUIDs, LN_2 dewar vessel and Helmholtz coil that supplies an external field. Hereafter, we define the direction of the cylindrical axis as the z-direction and the direction perpendicular to the axis as the r-direction. If external fields B_{z0} and B_{r0} exist, the attenuation factors $S_z(z)$ and $S_r(z)$ are defined as

$$S_z(z) = B_z(z)/B_{z0},$$
$$S_r(z) = B_r(z)/B_{r0},$$

where $B_z(z)$ and $B_r(z)$ are z and r components of the magnetic field at position z, respectively. Figure 1 shows the measurement results of the attenuation factors $S_z(z)$ and $S_r(z)$, where the directions of the external magnetic field B_0 (3.5 μT, 1 Hz) are the z-direction (•) and r-direction (○), respectively. From these measurement results, the attenuation factors of $S_z(0) = 5 \times 10^{-4}$ and $S_r(0) = 8 \times 10^{-2}$ were obtained.

In order to confirm the shielding effect by adding permalloy shields, we calculated the attenuation factors using the finite element method program OPERA-3d[5] and Fig. 2 shows one example of the calculated results. It was found that the shielding effect is 3 times improved when a chimney-like cylinder shield is added. In this figure, a beam chamber penetrates the holes of both right- and -left ends, and a cold head penetrates the upper hole. The magnetic field at the radius of 10 cm from the center was calculated and the field strength is expressed as the length at each point in Fig. 2. As seen in Fig. 3, the magnetic shields are composed of the HTS shield, permalloy 1, permalloy 2 (disk) and permalloy 2 (cylinder). From the measured and calculated results, it is expected that the geomagnetism of 3×10^{-5} T can be decreased to 3.6×10^{-13} T in the z-direction and 5.6×10^{-11} T in the x-direction, respectively.

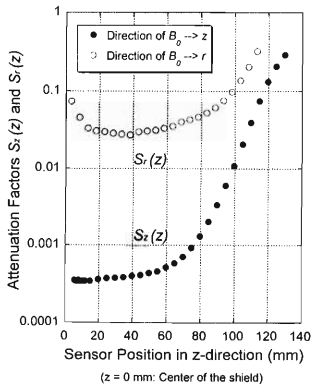

Fig. 1. Measurement results of the attenuation factors $S_z(z)$ and $S_r(z)$, where the directions of the external magnetic field B_0 (3.5 μT, 1 Hz) are the z-direction (•) and r-direction (○), respectively.

A photograph and a schematic of the prototype of the HTS CCC system are shown in Fig. 4 (a) and (b), respectively. The HTS magnetic shield and the HTS current sensor including the HTS SQUID are cooled by a pulse-tube refrigerator which is a low vibration

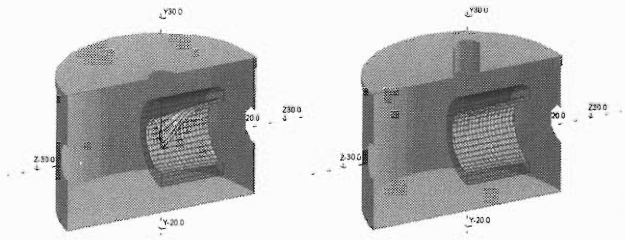

Fig. 2. Calculated results in which the shielding effect is improved when a chimney-like cylinder shield is added.

* KT Science Ltd.

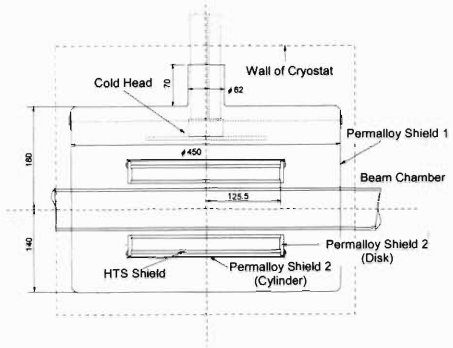

Fig. 3. Magnetic shields are composed of the HTS shield, permalloy 1, permalloy 2 (disk) and permalloy 2 (cylinder).

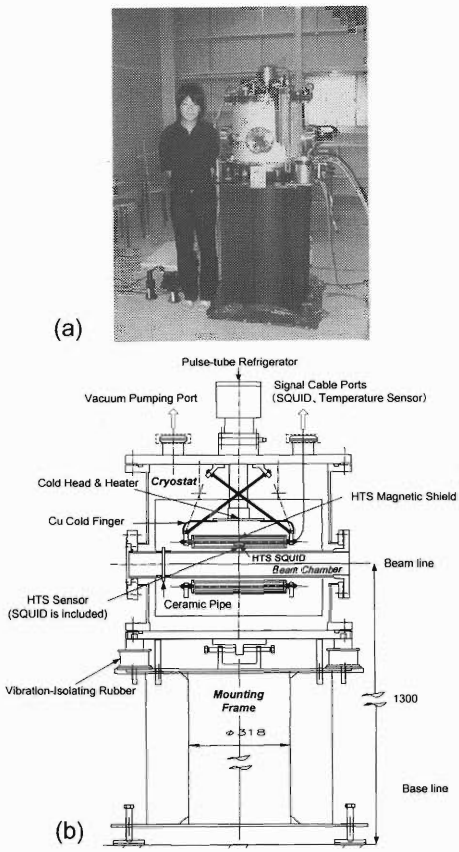

Fig. 4. Photograph (a) and a schematic (b) of the prototype of the HTS CCC system.

type and has a refrigeration power of 11 W at the temperature of 77 K. The operation temperature can be selected between 64 K to 90 K (critical temperature of the HTS SQUID) using a heater, since the pulse-tube refrigerator is capable of cooling down to lower temperatures than the case of using liquid nitrogen. Furthermore, it is possible to stabilize the temperature of the HTS SQUID with the accuracy of 5 mK using a PID feedback controller which has four thermometers and a heater.

In order to investigate the noise source, not only the vibration coming from the ground but also that generated by the pulse-tube refrigerator itself had been analyzed using accelerometers and an FFT on a time and frequency domain. Next, the first output signal was observed by feeding 100 nA square waves of 200 Hz into a Cu -rod which were set in a beam chamber (Fig. 5). Futhermore, the plotted output voltage of the SQUID electronics as a function of the simulated beam current is presented in Fig. 6. Although the output voltage should be proportional to the beam current, the deviation from the solid line at each point is due to an electric and a vibration noise.

Presently, we are examining the characteristics of the prototype of the HTS CCC system in the CNS experimental hall. Then we are planning to install it for the measurement of the beam current in the beam transport line of the RIKEN Ring Cyclotron (RRC).

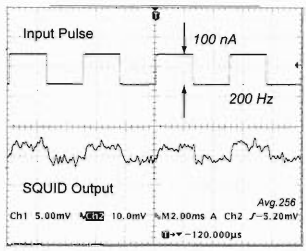

Fig. 5. The first output signal was observed by feeding 100 nA square waves of 200 Hz into a Cu -rod which were set in a beam chamber, recently.

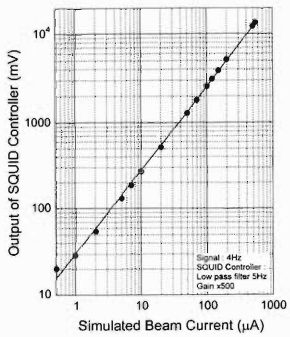

Fig. 6. Plotted output voltage of the SQUID electronics as a function of the simulated beam current.

References
1) T. Watanabe et al.: RIKEN Accel. Rep. **35**, 314 (2002).
2) T. Watanabe et al.: Proc. of EPAC 2002, Paris, France, 2002-6 (CERN, Geneva, 2002), p. 1995.
3) Y. Ishikawa et al.: Proc. 4th Int. Symp. Superconductivity (ISS '91), Tokyo, 1991-10 (Springer, Tokyo, 1992), p. 1073.
4) S. Watanabe et al.: Proc. of EPAC 2002, Paris, France, 2002-6 (CERN, Geneva, 2002), p. 1992.
5) Vector Fields Inc., UK.

V. RADIATION MONITORING

Routine work for radiation safety in the ring cyclotron facility

Y. Uwamino, S. Fujita, S. Ito, H. Sakamoto, T. Ito,[*1] N. Hirao,[*2] T. Nakamura,[*2] and M. Kase

We report here the residual radioactivity and leakage radiation level at the Ring Cyclotron Facility.

Residual radioactivities in the Ring Cyclotron Facility were measured at various locations using ionization-chamber survey meters.

The measurements were performed almost after every beam experiment as well as during the routine overhaul period. The routine overhaul period started immediately after the experiment which was carried out with the ^{59}Co beam of 80 MeV/nucleon in the E6 experimental vault from Aug. 5–10, 2002.

The dose rates observed in the injector AVF cyclotron on Aug. 21 in this overhaul period were 1.9 mSv/h at the deflector, 2.2 mSv/h at the magnetic channel, 2.5 mSv/h at the gradient corrector and 1.6 mSv/h at the main probe. The Ring Cyclotron vacuum chamber was opened very briefly, and the dose rates in it were not measured.

During the period from Oct. 1, 2001 to Sept. 30, 2002, the dose rates were measured along the beam lines. Spots **a**–**y**, marked by bullets in Fig. 1, are the places where the dose rates exceeded 20 μSv/h. Table 1 summarizes the observed dose rates and gives the dates when the measurements were performed.

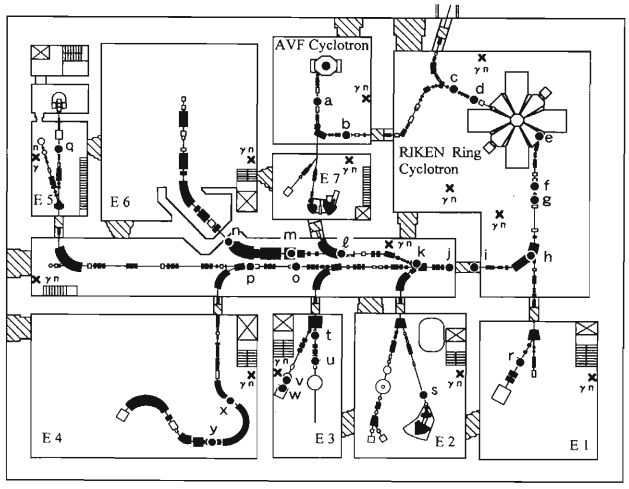

Fig. 1. Layout of the RIKEN Ring Cyclotron Facility as of 2002. Measured locations of residual radioactivities along the beam lines are shown by bullets **a**–**y**.

Table 1. Summary of the dose rates measured along the beam lines with ionization-chamber survey meters. Detection points **a**–**y** indicate the measured locations shown in Fig. 1.

Detection point	Measured dose rate (μSv/h)	Date	Particle	Energy (MeV/u)	Intensity (enA)	Period (days)
a	60	Apr 19, '02	C-12	135	1	2
b	65	Dec 28, '01	d	270	70	3
c	75	Apr 19, '02	C-12	135	1	2
d	40	Dec 28, '01	d	270	70	3
e	800	Nov 21, '01	Ne-22	110	2000	6
f	950	Apr 19, '02	C-12	135	1	2
g	3000	Apr 19, '02	C-12	135	1	2
h	140	Apr 19, '02	C-12	135	1	2
i	50	Nov 21, '01	Ne-22	110	2000	6
j	160	Dec 28, '01	d	270	70	3
k	180	Aug 12, '02	Co-59	80	180	5
l	4500	Aug 12, '02	Co-59	80	180	5
m	1550	Nov 21, '01	Ne-22	110	2000	6
n	150	Aug 12, '02	Co-59	80	180	5
o	90	Dec 28, '01	d	270	70	3
p	80	Dec 28, '01	d	270	70	3
q	20	Oct 29, '01	C-12	135	1	2
r	20	Dec 28, '01	d	270	70	3
s	33	Mar 18, '02	He-4	20	23	2
t	25	Jul 11, '02	P	135	200	1
u	45	Jul 11, '02	P	135	200	1
v	2500	Aug 5, '02	N-14	135	1000	2
w	2600	Nov 26, '01	N-14	135	1000	2
x	24	Jun 17, '02	d	270	300	2
y	40	Dec 28, '01	d	270	70	3

*1 Science Service, Inc.
*2 Tokyo University of Science

The maximum dose rate was found to be 4.5 mSv/h (4500 μSv/h) at the beam duct in the beam distribution corridor denoted by 1 in Fig. 1. Whenever we observed a high dose rate, we roped off the area and posted a sign warning that it was dangerous to remain for a long time in that place.

We also continuously monitored the leakage radiation from the Ring Cyclotron Facility. Having analyzed the collected data of leakage neutrons, we found that the radiation levels in the controlled area were much lower than the allowable dose limit. The leakage of γ-rays and neutrons was below the detection limit of the environmental monitors. We evaluated the radiation level at the boundary of the accelerator facility using the monitor which was installed in the computer room on the ground floor immediately above a bending magnet which guided the beams from the ring cyclotron vault to the distribution corridor. As a result, we obtained a radiation level of approximately 5 μSv/year which was much lower than the allowable dose limit (1 mSv/year).

The routine operation of the Ring Cyclotron was started in April, 1987, and many experimenters, workers and visitors have entered the Nishina radiation controlled area. The annual total numbers of persons and visitors that entered the area are shown in Figs. 2 and 3, which are about 30000 and about 1000, respectively; their grand total numbers since 1987 are 459919 and 18610.

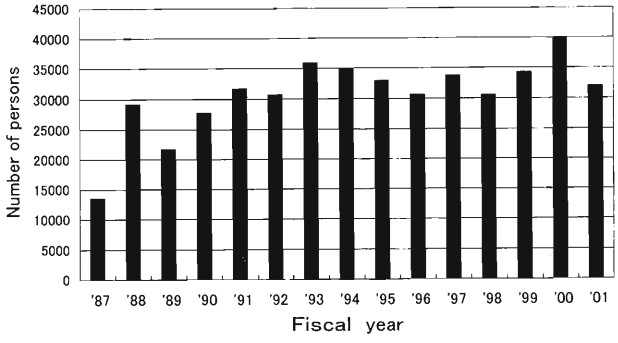

Fig. 2. Annual total number of persons who entered the Nishina radiation controlled area.

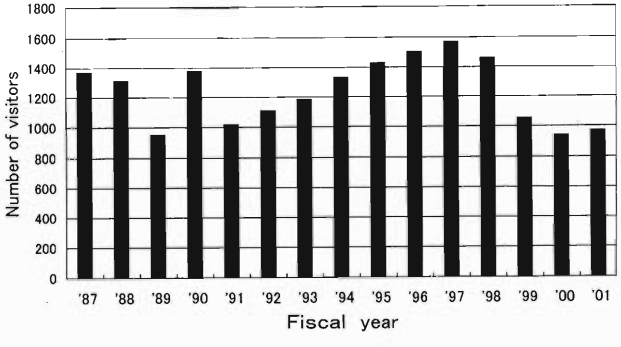

Fig. 3. Annual total number of visitors to Nishina radiation controlled area. "Visitors" do not include experimenters and workers.

VI. LIST OF PUBLICATIONS

1. Accelerator development and accelerator physics

M. Kase, A. Goto, T. Kageyama, I. Yokoyama, M. Nagase, S. Kohara, T. Nakagawa, N. Inabe, K. Ikegami, O. Kamigaito, M. Kidera, J. Fujita, A. Yoneda, M. Kobayashi, and Y. Yano: "Present status of the RIKEN Accelerator Research Facility (RARF)", Proc. 15th Int. Conf. on Cyclotrons and Their Applications 98, Caen, France, 1998–6, IOP Publishing, London, pp. 629–631 (1998).

M. Kase, A. Goto, T. Kageyama, M. Nagase, S. Kohara, T. Nakagawa, K. Ikegami, J. Fujita, N. Inabe, O. Kamigaito, M. Kidera, M. Kobayashi, A. Yoneda, I. Yokoyama, H. Isshiki, H. Akagi, R. Abe, N. Tsukiori, K. Takahashi, T. Maie, T. Homma, K. Kobayashi, and R. Ohta: "Present status of the RIKEN Ring Cyclotron (RRC)", Proc. 12th Symp. on Accelerator Science and Technology, Wako, 1999–10, RIKEN, Wako, pp. 28–30 (1999).

Y. Yano, A. Goto, M. Kase, and T. Katayama: "RI beam factory project at RIKEN", AIP Conf. Proc. **600**, 161–166 (2001).

T. Mitsumoto, A. Goto, M. Kase, J. Ohnishi, O. Kamigaito, N. Sakamoto, K. Ikegami, H. Okuno, Y. Miyazawa, Y. Yano, T. Hiasa, and Y. Kumata: "Construction of the RIKEN IRC", AIP Conf. Proc. **600**, 167–169 (2001).

N. Sakamoto, O. Kamigaito, Y. Miyazawa, T. Mitsumoto, A. Goto, and Y. Yano: "Construction of the RF-resonator for the RIKEN intermediate-stage ring cyclotron (IRC)", AIP Conf. Proc. **600**, 306–308 (2001).

A. Goto, H. Okuno, J. Ohnishi, N. Fukunishi, T. Mitsumoto, S. Fujishima, T. Tominaka, K. Ikegami, Y. Miyazawa, and Y. Yano: "Progress on the sector magnets for the RIKEN SRC", AIP Conf. Proc. **600**, 319–323 (2001).

J. Ohnishi, T. Mitsumoto, A. Goto, and Y. Yano: "Magnetic field measurement of RIKEN IRC sector magnets", AIP Conf. Proc. **600**, 351–353 (2001).

S. Fujishima, H. Okuno, T. Tominaka, A. Goto, and Y. Yano: "Design of the injection and extraction systems for the RIKEN SRC", AIP Conf. Proc. **600**, 449–451 (2001).

M. Kidera, T. Nakagawa, S. Enomoto, K. Takahashi, H. Baba, R. Hirunuma, T. Ohyama, K. Igarashi, M. Fujimaki, E. Ikezawa, O. Kamigaito, M. Kase, A. Goto, and Y. Yano: "Development of new analytical system using the electron cyclotron resonance ion source and heavy ion linear accelerator", Anal. Sci. **17**, Suppl., pp. i17–i20 (2001).

M. Kase, T. Kageyama, M. Nagase, S. Kohara, T. Nakagawa, E. Ikezawa, M. Fujimaki, N. Fukunishi, S. Numata, O. Kamigaito, M. Kidera, A. Yoneda, M. Komiyama, I. Yokoyama, H. Isshiki, H. Akagi, R. Abe, N. Tsukiori, K. Takahashi, T. Maie, R. Ohta, K. Kobayashi, M. Nishida, T. Aihara, T. Ohki, H. Hasebe, H. Yamauchi, A. Uchiyama, A. Goto, and Y. Yano: "Present status of the RIKEN Accelerator Research Facility (RARF)", Proc. 13th Symp. on Accelerator Science and Technology, (RCNP, Osaka University), Suita, 2001–10, RCNP, Osaka University, Osaka, pp. 43–45 (2001).

S. Fujishima, H. Okuno, N. Fukunishi, A. Goto, and Y. Yano: "Design of an extraction bending magnet for the RIKEN SRC", Proc. 13th Symp. on Accelerator Science and Technology, (RCNP, Osaka University), Suita, 2001–10, RCNP, Osaka University, Osaka, pp. 274–276 (2001).

M. Komiyama, I. Yokoyama, M. Nagase, E. Ikezawa, M. Fujimaki, R. Abe, T. Tanabe, and M. Kase: "New control system for the RIKEN Ring Cyclotron using EPICS", Proc. 13th Symp. on Accelerator Science and Technology, (RCNP, Osaka University), Suita, 2001–10, RCNP, Osaka University, Osaka, pp. 411–413 (2001).

M. Takanaka: "Characteristics of electron-cooled bunched beams predicted by a simulation", Proc. 2001 Particle Accelerator Conf., Chicago, USA, 2001–6, IEEE, Piscataway, pp. 3897–3899 (2001).

S. Fujishima, A. Goto, H. Okuno, and Y. Yano: "Design of the magnetic channels for the RIKEN Superconducting Ring Cyclotron", IEEE Trans. Appl. Supercond. **12**, 63–66 (2002).

T. Tominaka, N. Fukunishi, A. Goto, J. Ohnishi, H. Okuno, and Y. Yano: "Quench analysis of RIKEN superconducting Ring Cyclotron", IEEE Trans. Appl. Supercond. **12**, 1587–1590 (2002).

T. Tominaka: "Chapter 4.2: Electromagnet", Jiki Kagaku, IPC, Tokyo, pp. 99–108 (2002).

D. Cortina-Gil, K. Markenroth, F. Attallah, T. Baumann, J. Benlliure, M. J. B. Borge, L. V. Chulkov, U. D. Pramanik, J. Fermandez-Vazquez, C. Forssen, L. M. Fraile, H. Geissel, J. Gerl, F. Hammache, K. Itahashi, R. Janik, B. Jonson, S. Karlsson, H. Lenske, S. Mandal, M. Meister, X. Mocko, G. Munzenberg, T. Ohtsubo, A. Ozawa, Y. Parfenova, V. Pribora, K. Riisager, H. Scheit, R. Schneider, K. Schmidt, G. Schrieder, H. Simon, B. Sitar, A. Stolz, P. Strmen, K. Summerer, I. Szarka, S. Wan, H. Weick, and M. Zhukov: "Experimental evidence for the ^{8}B ground state configuration", Phys. Lett. B **529**, 36–41 (2002).

M. Kidera, Y. Higurashi, T. Aihara, M. Kase, and Y. Yano: "Development of RIKEN 18GHz RCRIS", Proc. 15th Int. Workshop on ECR Ion Sources (ECRIS'02), Jyväskylä, Finland, 2002–6, University of Jyväskylä, Jyväskylä, pp. 74–76 (2002).

Y. Yano, A. Goto, M. Kase, and T. Katayama:

"RIKEN RI Beam Factory Project: Progress report", Proc. 2001 Particle Accelerator Conf., (ANL and others), Chicago, USA, 2001–6, IEEE, New York, pp. 575–579 (2002).

M. Niimura, A. Chutjian, S. Smith, M. Lamoureaux, A. Goto, and Y. Yano: "Physics and control of the afterglow HCI-beam pulsewidths for synchrotoron and atomic physics", Proc. 2001 Particle Accelerator Conf., (ANL and others), Chicago, USA, 2001–6, IEEE, New York, pp. 2141–2143 (2002).

M. Nishiura, T. Katayama, T. Tanabe, S. Anatori, E. Syresin, and I. Watanabe: "Design of the ACR Electron Cooler RIKEN", Proc. 8th European Particle Accelerator Conf. (EPAC 2002), Paris, France, 2002–6, EPAC, Geneva, pp. 1377–1379 (2002).

M. Kidera, T. Nakagawa, Y. Higurashi, M. Kase, and Y. Yano: "Effect of plasma chamber surface for production of highly charged ions from ECRIS", Rev. Sci. Instrum. **73**, 611–613 (2002).

M. Bacal, M. Nishiura, M. Sasao, M. Hamabe, M. Wada, and H. Yamaoka: "Effect of argon additive in negative hydrogen ion sources", Rev. Sci. Instrum. **73**, 903–905 (2002).

M. Nishiura, M. Sasao, Y. Matsumoto, M. Hamabe, M. Wada, H. Yamaoka, and M. Bacal: "Influence of filament materials on vacuum ultraviolet emission in H^- ion source", Rev. Sci. Instrum. **73**, 949–951 (2002).

M. Nishiura, M. Sasao, Y. Matsumoto, M. Hamabe, M. Wada, H. Yamaoka, and M. Bacal: "Cooling effect of hydrogen negative ions in argon gas mixture", Rev. Sci. Instrum. **73**, 973–975 (2002).

2. Nuclear physics and nuclear instrumentation

K. Naito: "Introduction of chiral symmetry and its spontaneous breaking", Nucl. Study **44**, 123–141 (1999).

H. Iwasaki, T. Motobayashi, H. Akiyoshi, Y. Ando, N. Fukuda, H. Fujiwara, Z. Fulop, K. I. Hahn, Y. Higurashi, M. Hirai, I. Hisanaga, N. Iwasa, T. Kijima, T. Minemura, T. Nakamura, M. Notani, S. Ozawa, H. Sakurai, S. Shimoura, S. Takeuchi, T. Teranishi, Y. Yanagisawa, and M. Ishihara: "Quadrupole deformation of ^{12}Be studied by proton inelastic scattering", Phys. Lett. B **481**, 7–13 (2000).

K. Suda, H. Okamura, N. Sakamoto, A. Tamii, T. Uesaka, Y. Sato, T. Ohnishi, K. Sekiguchi, K. Yako, S. Sakoda, J. Nishikawa, H. Kato, M. Hatano, Y. Maeda, and H. Sakai: "Absolute calibration of the deuteron beam polarization at intermediate energies via the $^{12}C(\vec{d},\alpha)^{10}B^*(2^+)$ reaction", AIP Conf. Proc. **570**, 806–810 (2001).

K. Nomoto, K. Maeda, Y. Mochizuki, S. Kumagai, H. Umeda, T. Nakamura, and I. Tanihata: "Gamma-ray signatures of supernovae and hypernovae", AIP Conf. Proc. **587**, 487–497 (2001).

Y. X. Watanabe, A. Yoshida, T. Fukuda, T. Sekine, Y. Watanabe, H. Ikezoe, Y. Nagame, T. Ikuta, I. Nishinaka, Y. Mizoi, J. Nakano, M. Hirai, H. Sakurai, H. Kobinata, Y. H. Pu, K. Kimura, and M. Ishihara: "Measurement of fusion excitation functions of ^{27,29,31}Al + ^{197}Au", Eur. Phys. J. A **10**, 373–379 (2001).

Y. Mochizuki: Genso Tanjyo no Nazo ni Semaru (Video), edited by I. Tanihata and Y. Yano, Image Scinence, Inc., Tokyo, (2001).

K. Nagamine: "Review of muon catalyzed fusion experiments - activities after EXAT98 and future perspectives", Hyperfine Interact. **138**, 5–13 (2001).

K. Ishida, K. Nagamine, T. Matsuzaki, N. Kawamura, S. Nakamura, Y. Matsuda, M. Kato, H. Sugai, M. Tanase, K. Kudo, N. Takeda, and G. H. Eaton: "Review of measurements of fusion neutrons and x-rays in muon catalyzed d-t fusion at RIKEN-RAL: Details of the detection system", Hyperfine Interact. **138**, 225–234 (2001).

N. Kawamura, K. Nagamine, T. Matsuzaki, K. Ishida, S. Nakamura, Y. Matsuda, M. Tanase, M. Kato, K. Kurosawa, H. Sugai, K. Kudo, N. Takeda, and G. H. Eaton: "The first observation of the temperature-dependent phenomenon of muoon catalyzed fusion in solid D-T mixtures", Hyperfine Interact. **138**, 235–240 (2001).

T. Matsuzaki, K. Nagamine, K. Ishida, N. Kawamura, S. Nakamura, M. Kato, H. Sugai, M. Tanase, K. Kudo, N. Takeda, and G. H. Eaton: "Recent result of muon catalyzed t-t fusion at RIKEN-RAL", Hyperfine Interact. **138**, 295–305 (2001).

A. Toyoda, K. Ishida, K. Simomura, Y. Matsuda, W. Higemoto, S. Nakamura, T. Matsuzaki, and K. Nagamine: "Study of muon-catalyzed fusion in ortho-para controlled solid deuterium", Hyperfine Interact. **138**, 307–312 (2001).

S. Nakamura, D. Tomono, Y. Matsuda, G. Mason, M. Iwasaki, K. Ishida, T. Matsuzaki, I. Watanabe, S. Sakamoto, and K. Nagamine: "The precise measurement of the μ^+ lifetime", Hyperfine Interact. **138**, 445–450 (2001).

A. A. Korsheninnikov, M. S. Golovkov, E. Y. Nikolskii, A. Ozawa, K. Yoshida, I. Tanihata, Z. Fulop, K. Kusaka, K. Morimoto, H. Otsu, H. Petrascu, F. Tokanai, A. M. Rodin, A. S. Fomichev, S. I. Sidorchuk, S. V. Stepantsov, M. L. Chelnokov, V. A. Gorshkov, D. D. Bogdanov, R. Wolski, G. M. Ter-Akopian, Y. T. Oganessian, W. Mittig, P. Roussel-Chomaz, H. Savajols, E. A. Kuzmin, B. G. Novatskii, and A. A. Ogloblin: "Studies of transfer reactions with exotic beams. Superheavy hydrogen ^{5}H", Int. Symp. on Exotic Nuclei, (JINR, RIKEN, and others), Lake Baikal, Russia, 2001–7, edited by Y. Penionzhkevich and E. A. Cherepanov, World Scientific, Singapore, pp. 317–333 (2001).

T. Matsuzaki, K. Ishida, K. Nagamine, I. Watanabe, G. H. Eaton, and G. W. Williams: "The RIKEN-RAL pulsed Muon Facility", Nucl. Instrum. Methods Phys. Res. A **465**, 365–383 (2001).

T. Ohnishi, H. Sakai, H. Okamura, T. Niizeki, K. Ito, T. Uesaka, Y. Sato, K. Sekiguchi, K. Yako, S. Fukusaka, N. Sakamoto, and H. Ohnuma: "Study of spin-isospin excitation in ^{11}Be via the (d,^{2}He) reaction at 270 MeV", Nucl. Phys. A **687**, 38c–43c (2001).

K. Asahi and K. Matsuta: "Nuclear electromagnetic moments. β-NMR and its applications", Nucl. Phys. A **693**, 63–76 (2001).

F. A. Ivanyuk and S. Yamaji: "The effect of nuclear rotation on the collective transport coefficients", Nucl. Phys. A **694**, 295–311 (2001).

M. S. Golovkov, A. A. Korsheninnikov, I. Tanihata, D. D. Bogdanov, M. L. Chelnokov, A. S. Fomichev, V. A. Gorshkov, Y. T. Oganessian, A. M. Rodin, S. I. Sidorchuk, S. V. Stepantsov, G. M. Ter-Akopian, R. Wolski, W. Mittig, P. Roussel-Chomaz, H. Savajols, E. A. Kuzmin, E. Y. Nikolsky, B. G. Novatsky, and A. A. Ogloblin: "Spectroscopy of ^{7}He and superheavy hydrogen isotope ^{5}H", Phys. At. Nucl. **64**, 1244–1248 (2001).

S. Takeuchi, S. Shimoura, T. Motobayashi, H. Akiyoshi, Y. Ando, N. Aoi, Z. Fulop, T. Gomi, Y. Higurashi, M. Hirai, N. Iwasa, H. Iwasaki, Y. Iwata, H. Kobayashi, M. Kurokawa, Z. Liu, T. Minemura, S. Ozawa, H. Sakurai, M. Serata, T. Teranishi, K. Yamada, Y. Yanagisawa, and M. Ishihara: "Isobaric analog state of ^{14}Be", Phys. Lett. B **515**, 255–260 (2001).

H. Iwasaki, T. Motobayashi, H. Sakurai, K. Yoneda, T. Gomi, N. Aoi, N. Fukuda, Z. Fulop, U. Futakami, Z. Gacsi, Y. Higurashi, N. Imai, N. Iwasa, T. Kubo, M. Kunibu, M. Kurokawa, Z. Liu, T. Minemura, A. Saito, M. Serata, S. Shimoura, S. Takeuchi, Y. Watanabe, K. Yamada, Y. Yanagisawa, and M. Ishihara: "Large collectivity of ^{34}Mg", Phys. Lett. B **522**, 227–232 (2001).

H. Sagawa and K. Asahi: "N/Z dependence of core polarization charges and quadrupole moments of B isotopes", Phys. Rev. C **63**, 064310-1–064310-9 (2001).

N. Dinh Dang and V. Zelevinsky: "Improved treatment of ground-state correlations: Modified random phase approximation", Phys. Rev. C **64**, 064319-1–064319-10 (2001).

I. Nakagawa, J. Shaw, S. Churchwell, X. Jiang, B. Asavapibhop, M. C. Berisso, P. E. Bosted, K. Burchesky, F. Casagrande, A. Cichocki, R. S. Hicks, A. Hotta, T. Kobayashi, R. A. Miskimen, G. A. Peterson, S. E. Rock, T. Suda, T. Tamae, W. Turchinetz, and K. Wang: "Measurement of the elastic magnetic form factor of ^{3}He at high momentum transfer", Phys. Rev. Lett. **86**, 5446–5449 (2001).

A. A. Korsheninnikov, M. S. Golovkov, I. Tanihata, A. M. Rodin, A. S. Fomichev, S. I. Sidorchuk, S. V. Stepantsov, M. L. Chelnokov, V. A. Gorshkov, D. D. Bogdanov, R. Wolski, G. M. Ter-Akopian, Y. T. Oganessian, W. Mittig, P. Roussel-Chomaz, H. Savajols, E. A. Kuzmin, E. Y. Nikolskii, and A. A. Ogloblin: "Superheavy hydrogen ^{5}H", Phys. Rev. Lett. **87**, 092501-1–092501-4 (2001).

T. Ohtsuka, M. Honma, T. Mizusaki, N. Shimizu, and Y. Utsuno: "Monte carlo shell model for atomic nuclei", Prog. Part. Nucl. Phys. **47**, 319–400 (2001).

H. Sakai, K. Sekiguchi, Y. Maeda, W. Glöckle, M. B. Greenfield, K. Hatanaka, M. Hatano, D. Hirooka, H. Kamada, J. Kamiya, H. Kato, T. Ohnishi, H. Okamura, J. Rapaport, T. Saito, N. Sakamoto, S. Sakoda, Y. Sato, K. Suda, A. Tamii, N. Uchigashima, T. Uesaka, T. Wakasa, H. Witała, and K. Yako: "Clear signature of three-nucleon force effects via the precise measurements of $\vec{d}\vec{p}$ and $\vec{n}d$ scatterings", AIP Conf. Proc. **610**, 643–647 (2002).

K. Yoneda, H. Sakurai, T. Gomi, T. Motobayashi, N. Aoi, N. Fukuda, U. Futakami, Z. Gacsi, Y. Higurashi, N. Imai, N. Iwasa, H. Iwasaki, T. Kubo, M. Kunibu, M. Kurokawa, Z. Liu, T. Minemura, A. Saito, M. Serata, S. Shimoura, S. Takeuchi, Y. X. Watanabe, K. Yamada, Y. Yanagisawa, K. Yogo, A. Yoshida, and M. Ishihara: "Deformation of the neutron-rich isotope ^{34}Mg studied via in-beam gamma-ray spectroscopy using two-step fragmentation", AIP Conf. Proc. **610**, 766–770 (2002).

A. Ozawa, T. Suzuki, and I. Tanihata: "Measurements of interaction cross-section as a tool for the study of unstable nuclei", Butsuri **57**, 90–100 (2002).

K. Iida: "Color superconductivity", Butsuri **57**, 883–890 (2002).

Y. Mochizuki: Element Genesis: Solving the Mystery (Video), edited by I. Tanihata, Y. Yano, and R. Boyd, Image Scinence, Inc., Tokyo, (2002).

H. Iwasaki, T. Motobayashi, H. Akiyoshi, Y. Ando, N. Fukuda, H. Fujiwara, Z. Fulop, K. I. Hahn, Y. Higurashi, M. Hirai, I. Hisanaga, N. Iwasa, T. Kijima, A. Mengoni, T. Minemura, T. Nakamura, M. Notani, S. Ozawa, H. Sagawa, H. Sakurai, S. Shimoura, S. Takeuchi, T. Teranishi, Y. Yanagisawa, and M. Ishihara: "Inelastic scattering on ^{12}Be and disappearance of the N=8 magic number", Eur. Phys. J. A **13**, 55–58 (2002).

A. Ozawa: "Measurement of the interaction cross-section and related topics", Eur. Phys. J. A **13**, 163–167 (2002).

S. Kubono, Y. Yanagisawa, T. Teranishi, S. Kato, T. Kishida, S. Michimasa, T. Ohshiro, S. Shimoura, K. Ue, S. Watanabe, and N. Yamazaki: "New low-energy RIB separator CRIB for nuclear astrophysics", Eur. Phys. J. A **13**, 217–220 (2002).

M. Kato, T. Ito, H. Sugai, Y. Kawamura, T. Hayashi, M. Nishi, M. Tanase, T. Matsuzaki, K. Ishida, and

K. Nagamine: "Development of electrochemical hydrogen pump under vacuum condition for a compact tritium gas recycling system", Fusion Sci. Technol. **41**, 859–863 (2002).

T. Matsuzaki, K. Nagamine, K. Ishida, M. Kato, H. Sugai, M. Tanase, and G. H. Eaton: "An in-situ tritium-deuterium gas-purification system for muon catalyzed fusion experiments at the RIKEN-RAL Muon Facility", Fusion Sci. Technol. **41**, 993–997 (2002).

Y. Mochizuki: Genso Tanjyo no Nazo ni Semaru (Video), revised and enlarged ed., edited by I. Tanihata and Y. Yano, Image Scinence, Inc., Tokyo, (2002).

D. Beaumel, S. Fortier, H. Laurent, J. Maison, S. Pita, T. Kubo, T. Teranishi, H. Sakurai, T. Nakamura, N. Aoi, N. Fukuda, M. Hirai, N. Imai, H. Iwasaki, H. Kumagai, K. Yoneda, M. Ishihara, A. Mengoni, T. Motobayashi, H. Ohnuma, and S. M. Lukyanov: "Some applications of an indirect method to determine direct radiative cross-sections at astrophysical energies", Ind. J. Phys. **76S**, 145–147 (2002).

K. Ishida: "μCF experiments at RIKEN-RAL (1): introduction and muon loss processes", International Workshop on Future of Muon Science on Future of Muon Science, (KEK and RIKEN), Tsukuba and Wako, 2002–3, edited by Y. Miyake and K. Nagamine, KEK, Tsukuba, pp. 81–82 (2002).

H. Koura: "Alpha-decay half-lives and fission barriers for superheavy nuclei predicted by a nuclear mass formula", J. Nucl. Radiochem. Sci. **3**, 201–203 (2002).

H. Koura, T. Tachibana, and T. Yoshida: "Estimation of alpha-decay half-lives and fission barriers from the viewpoint of a new mass formula", J. Nucl. Sci. Technol., Suppl. 2, pp. 774–777 (2002).

N. Nakao, T. Kurosawa, T. Nakamura, and Y. Uwamino: "Development of a quasi-monoenergetic neutron field and measurements of the response function of an organic liquid scintillator for the neutron energy range from 66 to 206 MeV", Nucl. Instrum. Methods Phys. Res. A **476**, 176–180 (2002).

S. Ishimoto, T. Kobayashi, K. Morimoto, I. Nomura, A. Ozawa, S. Suzuki, Y. Takahashi, I. Tanihata, and T. Tsuru: "Windowless solid hydrogen target", Nucl. Instrum. Methods Phys. Res. A **480**, 304–314 (2002).

T. Matsuzaki, K. Nagamine, M. Tanase, M. Kato, K. Kurosawa, H. Sugai, K. Ishida, S. Nakamura, I. Watanabe, and G. H. Eaton: "A tritium gas-handling system for muon catalyzed fusion research at the RIKEN-RAL Muon Facility", Nucl. Instrum. Methods Phys. Res. A **480**, 814–827 (2002).

Y. Yang, Y. Gounou, S. Motomura, S. Enomoto, and Y. Yano: "Monte Carlo simulations of the performance of a Compton camera consisting of position-sensitive germanium detectors", Nucl. Instrum. Methods Phys. Res. A **482**, 806–813 (2002).

T. Kishida, H. Watanabe, E. Ideguchi, T. Kubo, Y. Yang, M. Ishihara, S. Yamamoto, Y. Gounou, T. Morikawa, T. Tsutsumi, T. Fukuchi, S. Motomura, H. Tsuchida, O. Kashiyama, K. Saitoh, M. Shibata, A. Odahara, Y. Zhang, X. Zhou, B. Cederwall, T. Back, and D. Bucurescu: "High spin isomeric beam line", Nucl. Instrum. Methods Phys. Res. A **484**, 45–55 (2002).

T. Baumann, H. Ikeda, M. Kurokawa, M. Miura, T. Nakamura, Y. Nishi, S. Nishimura, A. Ozawa, T. Sugimoto, I. Tanihata, and M. Thoennessen: "Improving neutron detection efficiency by using passive converters", Nucl. Instrum. Methods Phys. Res. B **192**, 339–344 (2002).

S. Momota, M. Notani, S. Ito, A. Ozawa, T. Suzuki, I. Tanihata, N. Aoi, H. Sakurai, T. Teranishi, Y. Watanabe, A. Yoshida, N. Inabe, T. Kubo, H. Okuno, N. Fukuda, H. Iwasaki, K. Yoneda, H. Ogawa, A. Kitagawa, M. Kanazawa, M. Torikoshi, M. Suda, and A. Ono: "Production of projectile-like fragments at intermediate energies", Nucl. Phys. A **701**, 150c–155c (2002).

K. Yoneda, H. Sakurai, T. Gomi, T. Motobayashi, N. Aoi, N. Fukuda, U. Futakami, Z. Gacsi, Y. Higurashi, N. Imai, N. Iwasa, H. Iwasaki, T. Kubo, M. Kunibu, M. Kurokawa, Z. Liu, T. Minemura, A. Saito, M. Serata, S. Shimoura, S. Takeuchi, Y. X. Watanabe, K. Yamada, Y. Yanagisawa, K. Yogo, A. Yoshida, and M. Ishihara: "Gamma-ray spectroscopy of ^{34}Mg via RI beam fragmentation", Nucl. Phys. A **701**, 437c–440c (2002).

H. Sakurai: "Nuclear spectroscopy on unstable nuclei at RIKEN", Nucl. Phys. A **704**, 27c–36c (2002).

A. Ozawa, T. Baumann, L. Chulkov, D. Cortina, U. Datta, J. Fernandez, H. Geissel, F. Hammache, K. Itahashi, M. Ivanov, R. Janik, T. Kato, K. Kimura, T. Kobayashi, K. Markenroth, M. Meister, G. Munzenberg, T. Ohtsubo, S. Ohya, T. Okuda, A. A. Ogloblin, V. Privora, M. Sekiguchi, B. Sitar, P. Strmen, S. Sugimoto, K. Summerer, T. Suzuki, I. Tanihata, and Y. Yamaguchi: "Measurements of the interaction cross sections for Ar and Cl isotopes", Nucl. Phys. A **709**, 60–72 (2002).

T. Zheng, T. Yamaguchi, A. Ozawa, M. Chiba, R. Kanungo, T. Kato, K. Katori, K. Morimoto, T. Ohnishi, T. Suda, I. Tanihata, Y. Yamaguchi, A. Yoshida, K. Yoshida, H. Toki, and N. Nakajima: "Study of halo structure of ^{16}C from reaction cross section measurement", Nucl. Phys. A **709**, 103–118 (2002).

M. Sasaki, E. Kim, T. Nunomiya, T. Nakamura, N. Nakao, T. Shibata, Y. Uwamino, S. Ito, and A. Fukumura: "Measurements of high-energy neutrons penetrated through concrete shields using self-TOF, NE213, and activation detectors", Nucl. Sci. Eng. **141**, 140–153 (2002).

A. A. Korsheninnikov, M. Golovkov, A. Ozawa, K. Yoshida, I. Tanihata, Z. Fulop, K. Kusaka, K. Morimoto, H. Otsu, H. Petrascu, F. Tokanai, D. D. Bogdanov, M. L. Chelnokov, A. S. Fomichev, V. A. Gorshkov, Y. T. Oganessian, A. M. Rodin, S. I. Sidorchuk, S. V. Stepantsov, G. M. Ter-Akopian, R. Wolski, W. Mittig, P. Roussel-Chomaz, H. Savajols, E. A. Kuzmin, E. Y. Nikolskii, B. G. Novatskii, and A. A. Ogloblin: "Superheavy hydrogen ^{5}H. Spectroscopy of ^{7}He", Phys. At. Nucl. **65**, 664–668 (2002).

S. Ishimoto, T. Kobayashi, k. Morimoto, I. Nomura, A. Ozawa, S. Suzuki, Y. Takahashi, I. Tanihata, and T. Tsuru: "Topological phase transition in solidification of confined liquids", Phys. Lett. A **299**, 622–627 (2002).

T. Matsuzaki, K. Nagamine, K. Ishida, N. Kawamura, S. Nakamura, Y. Matsuda, M. Tanase, M. Kato, K. Kurosawa, H. Sugai, K. Kudo, N. Takeda, and G. H. Eaton: "First observation of radiative photons associated with the μ^- transfer process from $(t\mu^-)$ to ^{3}He through an intermediate $(t^{3}He\mu^-)$ mesomolecule", Phys. Lett. B **527**, 43–49 (2002).

M. Notani, H. Sakurai, N. Aoi, Y. Yanagisawa, A. Saito, N. Imai, T. Gomi, M. Miura, S. Michimasa, H. Iwasaki, N. Fukuda, M. Ishihara, T. Kubo, S. Kubono, H. Kumagai, S. M. Lukyanov, T. Motobayashi, T. Onishi, Y. E. Penionzhkevich, S. Shimoura, T. Teranishi, K. Ue, V. Ugryumov, and A. Yoshida: "New neutron-rich isotopes, ^{34}Ne, ^{37}Na and ^{43}Si, produced by fragmentation of a 64A MeV ^{48}Ca beam", Phys. Lett. B **542**, 49–54 (2002).

K. Sekiguchi, H. Sakai, H. Witała, W. Glöckle, J. Golak, M. Hatano, H. Kamada, H. Kato, Y. Maeda, J. Nishikawa, A. Nogga, T. Ohnishi, H. Okamura, N. Sakamoto, S. Sakoda, Y. Sato, K. Suda, A. Tamii, T. Uesaka, T. Wakasa, and K. Yako: "Complete set of precise deuteron analyzing powers at intermediate energies: Comparison with modern nuclear force predictions", Phys. Rev. C **65**, 034003-1–034003-16 (2002).

N. Dinh Dang: "Strength of the double-phonon state within an exactly solvable model", Phys. Rev. C **65**, 034325-1–034325-7 (2002).

K. Tanabe, S. Yamaji, and A. Arima: "Spin symmetry and pseudospin symmetry in the relativistic mean field with a deformed potential", Phys. Rev. C **65**, 054313-1–054313-9 (2002).

N. Aoi, K. Yoneda, E. Ideguchi, T. Kishida, T. Nakamura, M. Notani, H. Sakurai, T. Teranishi, Y. Watanabe, H. Wu, A. Yoshida, H. Miyatake, Y. Yamamoto, H. Ogawa, S. Yamamoto, and M. Ishihara: "Anomaly of $N = 8$ shell closure in neutron-rich Be and B isotopes studied via delayed neutron emitting ^{14}Be β decay", Phys. Rev. C **66**, 014301-1–014301-11 (2002).

K. Iida and G. Baym: "Superfluid phases of quark matter. II. Phenomenology and sum rules", Phys. Rev. D **65**, 014022-1–014022-7 (2002).

K. Iida and G. Baym: "Superfluid phases of quark matter. III. Supercurrents and vortices", Phys. Rev. D **66**, 014015-1–014015-15 (2002).

T. Yamazaki: "Deeply bound 1s and 2p pionic states in ^{205}Pb and determination of the s-wave part of the pion-nucleus interaction", Phys. Rev. Lett. **88**, No. , pp. 122301-1–122301-4 (2002).

T. Suzuki, Y. Ogawa, M. Chiba, M. Fukuda, N. Iwasa, T. Izumikawa, R. Kanungo, Y. Kawamura, A. Ozawa, T. Suda, I. Tanihata, S. Watanabe, T. Yamaguchi, and Y. Yamaguchi: "Momentum distribution of ^{15}B fragments from the breakup of ^{17}B", Phys. Rev. Lett. **89**, 012501-1–012501-4 (2002).

T. Ichihara, M. Ishihara, H. Ohnuma, T. Niizeki, Y. Sato, H. Okamura, S. Kubono, M. Tanaka, and Y. Fuchi: "Isovector quadrupole resonance observed in the ^{60}Ni(^{13}C,^{13}N)^{60}Co reaction at $E/A =$ 100 MeV", Phys. Rev. Lett. **89**, 142501-1–142501-4 (2002).

K. Iida: "Color superconductivity at asymptotically high densities", Soryushiron Kenkyu **105**, A105–A112 (2002).

K. Iida: "Quark stars and color superconductivity", Parity **18**, 36–38 (2003).

3. Atomic and solid-state physics

Y. Nakai, T. Kambara, Y. Yamazaki, A. Ito, and H. Tsuchida: "Time-of-flight profiles of singly charged fullerence-like fragment ions produced in fast He^{2+}-C_{60} collision", At. Collision Res. Jpn., No. 27, pp. 26–27 (2001).

F. B. Rosmej, Y. Kanai, Y. Iwai, Y. Morishita, M. Wada, H. Oyama, T. Kambara, Y. Nakai, and Y. Yamazaki: "Application of soft x-ray spectromicroscopy methods at experiments with slow Ne^{9+} beams interacting with surfaces", At. Collision Res. Jpn., No. 27, pp. 35–36 (2001).

Y. Iwai, Y. Kanai, H. Oyama, K. Ando, H. Masuda, K. Nishio, K. Komaki, and Y. Yamazaki: "High-resolution soft x-ray measurements in 2.3 keV/u $^{15}N^{7+}$ ions transmitted through a microcapillary", At. Collision Res. Jpn., No. 27, pp. 37–38 (2001).

Y. Yamazaki: "Control of non-neutral plasmas and generation of ultra-slow antiproton beam", Hyperfine Interact. **138**, 141–152 (2001).

T. Yamazaki: "Antiprotonic helium: An exotic hydrogenic atom", The Hydrogen Atom: Precision Physics of Simple Atomic Systems (Lecture Notes in Physics, Vol. 570), Springer, Berlin, pp. 246–265 (2001).

A. Mohri, T. M. Kojima, N. Oshima, M. Niigaki, and Y. Yamazaki: "System of slow highly charged ion beam generation using a cold positron plasma trap at RIKEN", Non-Neutral Plasma Phyiscs IV,

San Diego, USA, 2001–7~8, edited by F. Anderegg, American Institute of Physics, Melville, pp. 634–640 (2002).
M. Tachikawa, I. Shimamura, R. Buenker, and M. Kimura: "Positron binding by molecules", Nucl. Instrum. Methods Phys. Res. B **192**, 40–41 (2002).
R. Whitehead, J. McCann, Y. Teranishi, and I. Shimamura: "Antihydrogen formation in collisions of antiprotons with positronium: The effects of a strong laser field", Nucl. Instrum. Methods Phys. Res. B **192**, 42–43 (2002).
T. Kambara, K. Kageyama, Y. Kanai, T. M. Kojima, Y. Nakai, A. Yoneda, and Y. Yamazaki: "Elastic wave from fast heavy ion irradiation on solids", Nucl. Instrum. Methods Phys. Res. B **193**, 371–375 (2002).
Y. Iwai, D. Murakoshi, Y. Kanai, H. Oyama, K. Ando, H. Masuda, K. Nishio, M. Nakao, T. Tamamura, K. Komaki, and Y. Yamazaki: "High-resolution soft X-ray spectroscopy of 2.3 keV/u N^{7+} ions through a microcapillary target", Nucl. Instrum. Methods Phys. Res. B **193**, 504–507 (2002).
Y. Yamazaki: "A microcapillary target as a metastable hollow ion source", Nucl. Instrum. Methods Phys. Res. B **193**, 516–522 (2002).
T. Kuroki, H. Torii, K. Komaki, and Y. Yamazaki: "Proton sputtering from H-terminated Si(100) surfaces with slow highly charged ions", Nucl. Instrum. Methods Phys. Res. B **193**, 804–808 (2002).
A. Iwase, T. Hasegawa, Y. Chimi, T. Tobita, N. Ishikawa, M. Suzuki, T. Kambara, and S. Ishino: "Hardening of Fe-Cu alloys by swift heavy ion irradiation", Nucl. Instrum. Methods Phys. Res. B **195**, 309–314 (2002).
T. Nakamura, M. Wada, K. Okada, I. Katayama, S. Ohtani, and H. A. Schuessler: "Precision spectroscopy of the Zeeman splittings of the $^9Be^+2^2S_{1/2}$ hyperfine structure for nuclear structure studies", Opt. Commun. **205**, 329–336 (2002).
E. Yagi, S. Koike, T. Matsumoto, T. Urai, N. Tajima, and K. Ogiwara: "Site occupancy change of hydrogen in Nb-Mo alloys with Mo concentration", Phys. Rev. B **66**, 024206-1–024206-7 (2002).
A. Igarashi, M. Kimura, and I. Shimamura: "Unified treatment of positron annihilation and positronium formation", Phys. Rev. Lett. **89**, 123201-1–123201-4 (2002).
T. Ikeda, Y. Nakai, C. Otani, H. Sato, H. Oyama, Y. Kanai, Y. Takizawa, Y. Iwai, Y. Morishita, T. Oku, N. Ohshima, H. Watanabe, H. Miyasaka, K. Kawai, H. Kato, H. Shimizu, and Y. Yamazaki: "X-ray spectroscopy in atomic collision experiment using superconducting tunnel junctions", Physica C **372/376**, 391–394 (2002).
S. Okayasu, M. Sasase, K. Hojou, Y. Chimi, A. Iwase, H. Ikeda, R. Yoshizaki, T. Kambara, H. Sato, Y. Hamatani, and A. Maeda: "Irradiation effects on MgB_2 bulk samples and formation of columnar defects in high-T_C superconductor", Physica C **382**, 104–107 (2002).

4. Radiochemistry, radiation chemistry, and radiation biology

T. Abe, C. Bae, T. Ozaki, J. Wang, and S. Yoshida: "Stress-tolerant mutants induced by heavy-ion beams", Gamma Field Symp., No. 39, pp. 45–56 (2000).
T. Yanagiya, N. Imura, S. Enomoto, Y. Kondo, and S. Himeno: "Suppression of a high-affinity transport system for manganese in cadmium-resistant metallothionein-null cells", J. Pharmacol. Exp. Ther. **292**, 1080–1086 (2000).
J. Furukawa, R. Hirunuma, S. Enomoto, and T. Nakanishi: "A study of multitracer to measure the binding affinity to an apoplast protein of the root in the presence of Al", Anal. Sci. **17**, Suppl., pp. i1479–i1481 (2001).
K. Matsumoto, I. Ui, R. Hirunuma, S. Enomoto, and K. Endo: "*In vivo* detection of dynamics of elements in a living rats using multitracer technique", Anal. Sci. **17**, Suppl., pp. i1487–i1490 (2001).
R. Hirunuma and S. Enomoto: "Application of the multitracer technique: Metabolic study of various elements in Se-deficient rats", Anal. Sci. **17**, Suppl., pp. i1495–i1498 (2001).
K. Igarashi, H. Inage, Y. Nakakoshi, T. Yanagiya, R. Hirunuma, S. Enomoto, and S. Kimura: "Multitracer study on behavior of various trace elements in anemic rats: Effect of sodium iron ethylenediaminetetraacetic acid and ferrous sulfate as food additives", Anal. Sci. **17**, Suppl., pp. i1519–i1522 (2001).
S. Enomoto and R. Hirunuma: "The Multitracer technique: Manufacturing and application to bio-trace elemental research", Anal. Sci. **17**, Suppl., pp. i617–i620 (2001).
Y. Takahashi, Y. Minai, C. Egawa, T. Mifune, R. Hirunuma, and S. Enomoto: "Application of multitracer technique to the studies on migration of trace elements in geosphere", Anal. Sci. **17** , Suppl., pp. i621–i624 (2001).
T. Ozaki, S. Ambe, Y. Minai, S. Enomoto, F. Yatagai, T. Abe, S. Yoshida, and Y. Makide: "Effects of ionic valency of interacting metal elements in ion uptake by carrot (*Daucas carota* cv. U.S. harumakigosun)", Biol. Trace Elem. Res. **84**, 197–211 (2001).
K. Igarashi, H. Inage, Y. Nakakoshi, T. Yanagiya, R. Hirunuma, S. Enomoto, and S. Kimura: "Influence of sodium iron ethylenediaminetetraacetic acid and ferrous sulfate on the absorption of trace elements in anemic rats using multitracer technique", Biomed. Res. Trace Elements **12**, 305–306 (2001).
K. Igarashi, A. Sasaki, Y. Yoda, H. Inage, Y.

Nakakoshi, R. Hirunuma, S. Enomoto, and S. Kimura: "Influence of tannic acid on iron absorption of ethylenediaminetetraacetic acid in rats", Biryo Eiyouso Kenkyu Dai 18 Syu, pp. 25–28 (2001).

Y. Hama, T. Oka, J. Uchiyama, H. Kanbe, K. Nabeta, and F. Yatagai: "Long-term oxidative degradation in polyethylene irradiated with ion beams", Rad. Phys. Chem. **62**, 133–139 (2001).

K. Kimura, S. Sharma, and A. I. Popov: "Novel ultrafast luminescence from incipient ion tracks of insulator crystals: electron-hole plasma formation in the track core", Radia. Meas. **34**, 99–103 (2001).

K. Kimura, S. Sharma, and A. I. Popov: "Novel ultrafast luminescence from incipient ion tracks of insulator crystals: electron-hole plasma formation in the track core", Radia. Meas. **34**, 99–103 (2001).

T. Abe and K. Suzuki: "The use of Heavy-ion irradiation for mutation breeding", Agric. Hortic. **77**, 580–586 (2002).

R. G. Weginwar, S. Enomoto, R. Hirunuma, and S. Anbe: "Correlation between serum cholesterols and trace element uptake in liver, kidney, and blood of hypercholesterolemic mice", Biol. Trace Elem. Res. **86**, 249–268 (2002).

T. Abe, S. Yoshida, K. Suzuki, and T. Kusumi: "A new method for mutation breeding using heavy-ion beams.", Brain Techno News, No. 90, pp. 14–17 (2002).

K. Masumura, K. Kuniya, T. Kurobe, M. Fukuoka, F. Yatagai, and T. Nomi: "Heavy-ion-induced mutations in the *gpt* delta transgenic mouse: Comparison of mutation spectra induced by heavy-ion, X-ray, and γ-ray radiation", Environ. Mol. Mutagen. **40**, 207–215 (2002).

F. Yatagai, T. Kurobe, T. Nomi, K. Masumura, T. Tsukada, H. Yamaguchi, K. Kasai, and N. Fukunishi: "Heavy-ion-induced mutations in the *gpt* delta transgenic mouse: Effect of *p53* gene knockout", Environ. Mol. Mutagen. **40**, 216–225 (2002).

T. Ohyama, M. Yanaga, T. Yoshida, H. Maetsu, M. Noguchi, H. Suganuma, T. Omori, R. Hirunuma, and S. Enomoto: "Uptake of trace elements in Zn-deficient mice", J. Radioanal. Nucl. Chem. **251**, 393–398 (2002).

S. Anbe, O. Katayama, and F. Ambe: "Multitracer studies on the permeation of various elements through a supported liquid membrane containing TBP", J. Radioanal. Nucl. Chem. **253**, 351–355 (2002).

H. Tamano, S. Enomoto, N. Oku, and A. Takeda: "Preferential uptake of zinc, manganese, and rubidium in rat brain tumor", Nucl. Med. Biol. **29**, 505–508 (2002).

F. Yatagai: "A development in detection system for gene and chromosome aberrations", Radiat. Biol. Res. Commun. **37**, 189–203 (2002).

F. Yatagai: "Development in detection systems for gene mutations and chromosomal aberrations", Radiat. Biol. Res. Commun. **37**, 189–203 (2002).

F. Yatagai, S. Morimoto, S. Goto, T. Kato, M. Honma, and F. Hanaoka: "Mutation induction in human cells after low dose X ray exposure", Radiat. Prot. Dosim. **99**, 241–243 (2002).

S. Morimoto, T. Kato, M. Honma, M. Hayashi, F. Hanaoka, and F. Yatagai: "Detection of genetic alterations induced by low-dose X rays: analysis of loss of heterozygosity for *TK* mutation in human lymphoblastoid cells", Radiat. Res. **157**, 533–538 (2002).

T. Ozaki, S. Anbe, S. Enomoto, Y. Minai, S. Yoshida, and Y. Makide: "Multitracer study on the uptake mechanism of yttrium and rare earth elements by autumn fern", Radiochim. Acta **90**, 303–307 (2002).

S. Himeno, T. Yanagiya, S. Enomoto, Y. Kondo, and N. Imura: "Cellular cadmium uptake mediated by the transport system for manganese", Tohoku J. Exp. Med. **196**, 43–50 (2002).

K. Matsumoto, H. Kawahigashi, R. Hirunuma, S. Enomoto, and K. Endo: "Noninvasive detection of dynamics of various elements in the upper abdomen of selenium-deficient rats using multitracer technique", Yakugaku Zasshi **122**, 277–282 (2002).

5. Material Analysis

K. Maeda, A. Tonomura, H. Hamanaka, and K. Hasegawa: "Improvement in the precision and the facility of chemical shift measurements using a position sensitive crystal spectrometer for PIXE", Int. J. PIXE **11**, 35–44 (2001).

K. Maeda, K. Hasegawa, H. Hamanaka, M. Maeda, S. Yabuki, and K. Ogiwara: "Rapid chemical state analysis by a highly sensitive high-resolution PIXE system", Nucl. Instrum. Methods Phys. Res. B **190**, 704–708 (2002).

H. Hamanaka, K. Hasegawa, and K. Maeda: "Application of a laser displacement sensor to high resolution PIXE measurements", Rep. Res. Cen. Ion Beam Technol., Hosei Univ., Suppl. No. 20, pp. 111–114 (2002).

6. RIKEN-BNL Collaboration on Spin Physics Program

S. Ohta and M. Wingate: "SU(4) pure-gauge phase structure and string tensions", Nucl. Phys. B (Proc. Suppl.) **83/84**, 381–383 (2000).

T. Schaefer: "Kaon condensation in high-density quark matter", Phys. Rev. Lett. **85**, 5531–5534 (2000).

Y. Goto and PHENIX Collaboration: "Measurement of the gluon polarization in the proton at the PHENIX", AIP Conf. Proc. **570**, 442–446 (2001).

J. Schaffner-Bielich: "Effect of in-medium properties on heavy-ion collisions", J. Phys. G **27**, 337–347 (2001).

D. Zschiesche, L. Gerland, S. Schramm, J. Schaffner-Bielich, H. Stocker, and W. Greiner: "Critial review of quark gluon plasma signals", Nucl. Phys. A **681**, 34c–40c (2001).

J. Schaffner-Bielich: "Strange dibaryons in neutron stars and in heavy-ion collisions", Nucl. Phys. A **691**, 416c–422c (2001).

D. Chen, N. H. Christ, C. Cristian, Z. Dong, A. Gara, K. Garg, B. Joo, C. Kim, L. Levkova, X. Liao, R. D. Mawhinney, S. Ohta, and T. Wettig: "QCDOC: A 10-teraflops scale computer for lattice QCD", Nucl. Phys. B (Proc. Suppl.) **94**, 825–832 (2001).

L. McLerran and J. Schaffner-Bielich: "Intrinsic broadening of the transverse momentum spectra in ultrarelativistic heavy-ion collisions?", Phys. Lett. B **514**, 29–32 (2001).

T. Schaefer, D. T. Son, M. A. Stephanov, D. Toublan, and J. Verbaarschot: "Kaon condensation and Goldstone's theorem", Phys. Lett. B **522**, 67–75 (2001).

D. Zschiesche, P. Papazoglou, S. Schramm, J. Schaffner-Bielich, H. Stöcker, and W. Greiner: "Hadrons in dense resonance matter: A chiral SU(3) approach", Phys. Rev. C **63**, 025211-1–025211-10 (2001).

C. Hanhart, G. A. Miller, F. Myhrer, T. Sato, and U. van Kolck: "Toy model for pion production in nucleon-nucleon collisions", Phys. Rev. C **63**, 044002-1–044002-7 (2001).

L. Diaconescu, R. Schiavilla, and U. van Kolck: "Parity-violating electron-deuteron scattering", Phys. Rev. C **63**, 044007-1–044007-11 (2001).

E. S. Fraga, R. D. Pisarski, and J. Schaffner-Bielich: "Small, dense quark stars from perturbative QCD", Phys. Rev. D **63**, 121702-1–121702-5 (2001).

R. Venugopalan and J. Wirstam: "Hard thermal loops and beyond in the finite temperature world-line formulation of QED", Phys. Rev. D **63**, 125022-1–125022-15 (2001).

C. Bernard, T. Burch, K. Originos, D. Toussaint, T. A. DeGrand, C. DeTar, S. Datta, S. Gottlieb, U. M. Heller, and R. Sugar: "QCD spectrum with three quark flavors", Phys. Rev. D **64**, 054506-1–054506-15 (2001).

T. Burch, K. Originos, and D. Toussaint: "Measurement of hybrid content of heavy quarkonia using lattice nonrelativistic QCD", Phys. Rev. D **64**, 074505-1–074505-5 (2001).

T. Blum, N. Christ, C. Cristian, C. Dawson, X. Liao, G. Liu, R. D. Mawhinney, L. Wu, and Y. Zhestkov: "Chirality correlation within Dirac eigenvectors from domain wall fermions", Phys. Rev. D **65**, 014504-1–014504-10 (2001).

G. Policastro, D. T. Son, and A. O. Starinets: "Shear viscosity of strongly coupled N = 4 supersymmetric Yang-Mills plasma", Phys. Rev. Lett. **87**, 081601-1–081601-4 (2001).

A. Ramos, J. Schaffner-Bielich, and J. Wambach: "Kaon condensation in neutron stars", Physics of Neutron Star Interiors, edited by D. Blaschke, N. K. Glendenning, and A. Sedrakian, Springer, Berlin, pp. 175–202 (2001).

J. Murata and PHENIX Collaboration: "Construction of the PHENIX south muon arm", AIP Conf. Proc. **610**, 947–951 (2002).

T. Tominaka, M. Okamura, and T. Katayama: "Contribution of iron yoke on helical coils", IEEE Trans. Appl. Supercond. **12**, 1479–1482 (2002).

S. A. Bass: "Strongness production in microscopic transport models", J. Phys. G **28**, 1543–1551 (2002).

T. Tominaka, M. Okamura, and T. Katayama: "Analytical field calculation of helical magnets with an axially symmetric iron yoke", Nucl. Instrum. Methods Phys. Res. A **484**, 36–44 (2002).

S. Jeon, V. Koch, K. Redlich, and X. N. Wang: "Fluctuations of rare particles as a measure of chemical equilibration", Nucl. Phys. A **697**, 546–562 (2002).

S. A. Bass: "Microscopic reaction dynamics at SPS and RHIC", Nucl. Phys. A **698**, 164c–170c (2002).

A. Krasnitz and R. Venugopalan: "Small X physics and the initial conditions in heavy ion collisions", Nucl. Phys. A **698**, 209c–216c (2002).

U. van Kolck: "Recent developments in nuclear effective field theory", Nucl. Phys. A **699**, 33c–40c (2002).

S. R. Beane, P. F. Bedaque, M. J. Savage, and U. van Kolck: "Towards a perturbative theory of nuclear forces", Nucl. Phys. A **700**, 377–402 (2002).

K. Kurita: "Proton-carbon CNI polarimeter for RHIC", Nucl. Phys. B (Proc. Suppl.) **105**, 164–167 (2002).

Y. Aoki and RBC Collaboration: "Hadron spectrum for quenched domain-wall fermions with DBW2 gauge action", Nucl. Phys. B (Proc. Suppl.) **106**, 245–247 (2002).

T. Blum and RBC Collaboration: "Im A_0, Im A_2, and ε' from lattice QCD", Nucl. Phys. B (Proc. Suppl.) **106**, 317–319 (2002).

N. Ishii, H. Suganuma, and H. Matsufuru: "Glueball properties at finite temperature", Nucl. Phys. B (Proc. Suppl.) **106**, 516–518 (2002).

K. Originos: "Chiral properties of domain wall fermions with improved gauge actions", Nucl. Phys. B (Proc. Suppl.) **106**, 721–723 (2002).

Y. Nara, S. Vance, and P. Csizmadia: "A study of parthon energy loss in Au + Au collisions at RHIC using transport theory", Phys. Lett. B **531**, 209–215 (2002).

S. Cheng, S. Pratt, P. Csizmadia, Y. Nara, D. Molnár, M. Gyulassy, S. E. Vance, and B. Zhang: "Effect of finite-range interactions in classical transport theory", Phys. Rev. C **65**, 024901-1–024901-12 (2002).

M. Stratmann and W. Vogelsang: "Next-to-leading order QCD evolution of transversity fragmentation functions", Phys. Rev. D **65**, 057502-1–057502-4

(2002).
H. Abuki, T. Hatsuda, and K. Itakura: "Strucutural change of Cooper pairs and momentum-dependent gap in color superconductivity", Phys. Rev. D **65**, 074014-1–074014-14 (2002).
S. Sasaki, T. Blum, and S. Ohta: "Lattice study of the nucleon excited states with domain wall fermions", Phys. Rev. D **65**, 074503-1–074503-14 (2002).
M. A. Stephanov: "Thermal fluctuamons in the interacting pion gas", Phys. Rev. D **65**, 096008-1–096008-7 (2002).
T. Blum, N. Christ, C. Cristian, C. Dawson, G. Fleming, G. Liu, R. D. Mawhinney, A. Soni, P. Vranas, M. Wingate, L. Wu, and Y. Zhestkov: "Nonperturbative renormalization of domain wall fermions: Quark bilinears", Phys. Rev. D **66**, 014504-1–014504-19 (2002).
N. Ishii, H. Suganuma, and H. Matsufuru: "Scalar glueball mass reduction at finite temperature in SU(3) anisotropic lattice QCD", Phys. Rev. D **66**, 014507-1–014507-5 (2002).
N. Ishii, H. Suganuma, and H. Matsufuru: "Glueball properties at finite temperature in SU(3) anisotropic lattice QCD", Phys. Rev. D **66**, 094506-1–094506-22 (2002).
D. T. Son and M. A. Stephanov: "Pion propagation near the QCD chiral phase transition", Phys. Rev. Lett. **88**, 202302-1 –202302-4 (2002).

VII. LIST OF PREPRINTS

2002

RIKEN-AF-NP

414 Y. Yamazaki and Y. Akaishi: "Nuclear $\bar{\mathrm{K}}$ bound states in proton-rich systems to be produced by (K^-, π^-) reactions through Λ^* as a doorway"

415 R. Kanungo, M. Chiba, N. Iwasa, S. Nishimura, A. Ozawa, C. Samanta, T. Suda, T. Suzuki, Y. Yamaguchi, T. Zheng, and I. Tanihata: "The first experimental evidence of core modification in near drip-line nucleus ^{23}O"

416 D. Kaji, K. Morita, K. Morimoto, Y. L. Zhao, A. Yoneda, T. Suda, A. Yoshida, H. Kudo, K. Katori, and I. Tanihata: "Status of heavy element synthesis in RIKEN"

417 H. Kurasawa and T. Suzuki: "Relativistic vs. Non-relativistic nuclear models"

418 N. Dinh Dang, N. Sandulescu, and A. Arima: "Transition from the superfluid phase to the normal phase in nuclei far from stability"

419 T. Zheng: "Study of anamalous structure of ^{16}C from reaction cross section measurement"

420 T. Yamazaki and Y. Akaishi: "(K^-, π^-) production of nuclear K^- bound states in proton-rich systems via Λ^* doorways"

421 H. Toki, S. Sugimoto, and K. Ikeda: "Relativistic mean field theory with the pion in finite nuclei"

422 H. Geissel, H. Gilg, A. Gillitzer, R. S. Hayano, S. Hirenzaki, K. Itahashi, M. Iwasaki, P. Kienle, M. Munch, G. Munzenberg, W. Schott, K. Suzuki, D. Tomono, H. Weich, T. Yamazaki, and T. Yoneyama: "Experimental indication of a reduced chiral order parameter from the 1s pai- state in ^{205}Pb"

423 M. Notani, H. Sakurai, N. Aoi, Y. Yanagisawa, A. Saito, N. Imai, T. Gomi, M. Miura, S. Michimasa, H. Iwasaki, N. Fukuda, M. Ishihara, T. Kubo, S. Kubono, H. Kumagai, S, M. Lukyanov, T. K. Onishi, Yu. E. Penionzhkevich, S. Shimoura, T. Teranishi, K. Ue, V. Ugryumov, and A. Yoshida: "New neutron-rich isotopes, ^{34}Ne, ^{37}Na and ^{43}Si, produced by fragmentation of a 64A MeV ^{48}Ca beam"

424 A. Ozawa, T. Baumann, L. Chulkov, D. Cortina, U. Datta, J. Fernandez, H. Geissel, F. Hammache, K. Itahashi, M. Ivanov, R. Janik, T. Kato, K. Kimura, T. Kobayashi, K. Markenroth, M. Meister, G. Munzenberg, T. Ohtsubo, S. Ohya, T. Okuda, A. A. Ogloblin, V. Privora, M. Sekiguchi, B. Star, P. Strmen, S. Sugimoto, K. Summerer, T. Suzuki, I. Tanihata, and Y. Yamaguchi: "Measurements of the interaction cross sections for Ar and Cl isotopes"

425 A. Dote, Y. Akaishi, H. Horiuchi, and T. Yamazaki: "High-density K^- nuclear systems with isovector deformation"

426 N. Dinh Dang and A. Arima: "Modified quasiparticle random-phase approximation and charge-exchange transitions"

427 T. Ichihara, M. Ishihara, H. Ohnuma, T. Niizeki, Y. Satou, H. Okamura, S. Kubono, M. Tanaka, and Y. Fuchi: "Isovector quadrupole resonance observed in the ^{60}Ni(^{13}C, ^{13}N)^{60}Co reaction at E/A = 100 MeV"

428 B. Abu-Ibrahim, Y. Ogawa, Y. Suzuki, and I. Tanihata: "Cross section calculations in glauber model: I. core plus one-nucleon case"

429 T. Zheng, T. Yamaguchi, A. Ozawa, M. Chiba, R. Kanungo, T. Kato, K. Katori, K. Morimoto, T. Ohnishi, T. Suda, I. Tanihata, Y. Yamaguchi, A. Yoshida, K. Yoshida, H. Toki, and N. Nakajima: "Study of halo

structure of ^{16}C from reaction cross section measurement"

430 Y. Satou, S.Ishida, H. Sakai, H. Okamura, N. Sakamoto, H. Otsu, T. Uesaka, A. Tamii, T. Wakasa, T. Ohnishi, K. Sekiguchi, K. Yako, K. Suda, M. Hatano, H. Kato, Y. Maeda, J. Nishikawa, T. Ichihara, T. Niizeki, H. Kamada, W. Glockle, and H. Witata: "Three-body dN interaction in the analysis of the $^{12}\mathrm{C}(\vec{d},d')$ reaction at 270 MeV"

431 E. Widmann, R. S. Hayano, T. Ishikawa, J. Sakaguchi, T. Tasaki, H. Yamaguchi, J. Eades, M. Hori, H. A. Torii, B. Juhasz, D. Horvath, and T. Yamazaki: "Hyperfine structure of antiprotonic helium revealed by a laser-microwave-laser resonance method"

432 I. Hisanaga, T. Motobayashi, H. Akiyoshi, Y. Ando, H. Fujikawa, N. Fukuda, Zs. Fülöp, T. Gomi, K. I. Hahn, Y. Higurashi, M. Hirai, M. Ishihara, N. Iwasa, H. Iwasaki, Y. Iwata, T. Kijima, S. Kubono, T. Minemura, T. Nakamura, M. Notani, S. Ozawa, H. Sakurai, S. Shimoura, S. Takeuchi, T. Teranishi, and Y. Yanagisawa: "Determination of the astrophysical $^{8}\mathrm{B}(\mathrm{p},\gamma)^{9}\mathrm{C}$ cross section from the ^{9}C dissociation"

433 T. Motobayashi: "Nucler astrophysics experiments with high energy RI beams"

434 S. Nishimura, M. Kurata-Nishimura, K. Morimoto, Y. Nishi, and I. Tanihata: "Systematic studies of scientillation detector with timing resolution of 10 ps for heavy ion beam"

435 S. Shimoura, A. Saito, T. Minemura, Y. U. Matsuyama, H. Baba, H. Akioyoshi, N. Aoi, T. Gomi, Y. Higurashi, K. Ieki, N. Imai, N. Iwasa, H. Iwasaki, S. Kanno, S. Kubono, M. Kunibu, S. Michimasa, T. Motobayashi, T. Nakamura, H. Sakurai, M. Serata, E. Takeshita, S. Takeuchi, T. Teranishi, K. Ue, K. Yamada, Y. Yanagisawa, M. Ishihara, and N. Itagaki: "Isomeric 0^+ state in ^{12}Be"

436 N. Dinh Dang: "Energies of the ground state and first excited 0^+ state in an exactly solvable pairing model"

437 T. Katayama, T. Suda, and I. Tanihata: "Status of MUSES project and electron RI collider at RIKEN"

438 A. Ozawa, Y. Yamaguchi, M. Chiba, R. Kanungo, K. Kimura, S. Momota, T. Suda, T. Suzuki, I. Tanihata, T. Zheng, S. Watanabe, T. Yamaguchi, and K. Yoshida: "Search for ^{21}B"

439 H. Geissel, H. Gilg, A. Gillitzer, R. S. Hayano, S. Hirenzaki, K. Itahashi, M. Iwasaki, P. Kienle, M. Munch, G. Munzenberg, W. Schott, K. Suzuki, D. Tomono, H. Weich, T. Yamazaki, and T. Yoneyama: "Experimental indication of a reduced chiral order parameter from the 1 s pai- state in ^{205}Pb"

440 T. Yamazaki and S. Hirenzaki: "Transposition of a local-density-dependent pion-nucleus potential to an effective density-linear potential-generalized Seki-Masutani relations"

441 K. Suzuki, M. Fujita, H. Geissel, H. Gilg, A. Gillitzer, R. S. Hayano, S. Hirenzaki, K. Itahashi, M. Iwasaki, P. Kienle, M. Matos, G. Munzenberg, T. Ohtsubo, M. Sato, M. Shindo, T. Suzuki, H. Weick, M. Winkler, T. Yamazaki, and T. Yoneyama: "Precision spectroscopy of pionic 1s states of Sn nuclei and evidence for partial restoration of chiral symmetry in the nuclear medium"

RIKEN-AF-AC

33 I. Meshkov, A. Sidorin, A. Smirnov, E. Syresin, and T. Katayama: "Luminosity of an experiment with internal gas target at MUSES"

34 I. Meshkov, A. Sidorin, A. Smirnov, E. Syresin, and T. Katayama: "Ordered state of ion beams"

35 A. Goto: "Collected papers on the RIKEN RI Beam Factory project"

36 S. B. Vorojtsov, A. S. Vorozhtsov, T. Mitsumoto, A. Goto, and Y. Yano: "Beam space charge simulation in RIKEN SRC"

37 P. R. Sarma: "Design of improved magnetic channel for superconducting cyclotrons by random search method"

38 P. R. Sarma: "A new technique of beam energy resolution by using only quadrupole magnets"

39 D. Mohl and T. Katayama: "Luminosity of an electron-ion collider with an ordered ion beam"

40 D. Mohl and T. Katayama: "On the transverse space charge limit of 1D crystalline beams"

VIII. PAPERS PRESENTED AT MEETINGS

1. Accelerator development and accelerator physics

N. Sakamoto, O. Kamigaito, Y. Miyazawa, T. Mitsumoto, A. Goto, and Y. Yano: "Construction of the RF-resonator for the RIKEN intermediate-stage ring cyclotron (IRC)", 16th Int. Conf. on Cyclotrons and Their Applications, East Lansing, USA, May (2001).

H. Okuno, S. Fujishima, T. Tominaka, A. Goto, and Y. Yano: "Design and construction of the superconducting bending magnet for the injection system of the RIKEN SRC", 16th Int. Conf. on Cyclotrons and Their Applications, East Lansing, USA, May (2001).

S. Fujishima, H. Okuno, T. Tominaka, A. Goto, and Y. Yano: "Design of the injection and extraction systems for the RIKEN SRC", 16th Int. Conf. on Cyclotrons and Their Applications 2001, East Lansing, USA, May (2001).

Y. Yano: "RI beam factory project at RIKEN", 16th Int. Conf. on Cyclotrons and Their Applications 2001, East Lansing, USA, May (2001).

H. Okuno, S. Fujishima, T. Tominaka, A. Goto, and Y. Yano: "Design and fabrication of the superconducting bending magnet for the injection system of the RIKEN SRC", 17th Int. Conf. on Magnet Technology, (CERN), Geneve, Switzerland, Sept. (2001).

S. Fujishima, A. Goto, H. Okuno, and Y. Yano: "Design of the magnetic channels for the RIKEN Superconducting Ring Cyclotron", 17th Int. Conf. on Magnet Technology, (CERN), Geneva, Switzerland, Sept. (2001).

T. Tominaka, N. Fukunishi, A. Goto, J. Ohnishi, H. Okuno, and Y. Yano: "Quench analysis of RIKEN Superconducting Ring Cyclotron", 17th Int. Conf. on Magnet Technology, (CERN), Geneva, Switzerland, Sept. (2001).

T. Koseki: "Development of HOM damped cavity with SiC beam duct", Shanghai Symp. on Intermediate-Energy Light Source, (Shanghai National Synchrotron Radiation Center and others), Shanghai, China, Sept. (2001).

M. Nishiura, M. Sasao, Y. Matsumoto, M. Hamabe, M. Wada, H. Yamaoka, and M. Bacal: "Influence of filament materials on vacuum ultraviolet emission in H^- ion source", 9th Int. Conf. on Ion Sources (ICIS 2001), (Lawrence Berkeley National Laboratory and others), Oakland, USA, Sept. (2001).

S. Kohara, A. Goto, O. Kamigaito, M. Kase, N. Sakamoto, S. Watanabe, and T. Katayama: "Construction of the flat-top acceleration system in the RIKEN AVF cyclotron", 13th Symp. on Accelerator Science and Technology, (RCNP and ISIR, Osaka University), Suita, Oct. (2001).

S. Fujishima, H. Okuno, N. Fukunishi, A. Goto, and Y. Yano: "Design of an extraction bending magnet for the RIKEN SRC", 13th Symp. on Accelerator Science and Technology, (RCNP and ISIR, Osaka University), Suita, Oct. (2001).

H. Okuno, J. Ohnishi, N. Fukunishi, T. Mitsumoto, S. Fujishima, T. Tominaka, N. Sakamoto, O. Kamigaito, M. Fujimaki, K. Ikegami, Y. Miyazawa, M. Kase, A. Goto, and Y. Yano: "Status of the RIKEN SRC", 13th Symp. on Accelerator Science and Technology, (RCNP and ISIR, Osaka University), Suita, Oct. (2001).

H. Okuno, J. Ohnishi, N. Fukunishi, T. Mitsumoto, S. Fujishima, T. Tominaka, K. Ikegami, Y. Miyazawa, A. Goto, and Y. Yano: "Superconducting magnets for the RIKEN SRC", 13th Symp. on Accelerator Science and Technology, (RCNP and ISIR, Osaka University), Suita, Oct. (2001).

T. Koseki: "Electron ring for the e-RI collider of MUSES", Int. Workshop on Rare Isotope Physics at Storage Rings, (GSI and RIKEN), Hirschegg, Austria, Mar. (2002).

A. Sakumi, T. Katayama, and Y. Oguri: "Beam-plasma experiments at RIKEN", 14th Int. Symp. on Heavy Ion Inertial Fusion, (Institute for Theoretical and Experimental Physics), Moscow, Russia, May (2002).

M. Kidera, T. Nakagawa, Y. Higurashi, T. Aihara, M. Kase, and Y. Yano: "Development of RIKEN 18 GHz ECRIS: Production of metallic ions", 15th Int. Workshop on ECR Ion Sources (ECRIS'02), Jyväskylä, Finland, June (2002).

M. Takanaka: "Cure for the transverse instability during electron-cooling bunching with skew quadrupole magnets", 8th European Particle Accelerator Conf. (EPAC 2002), (CEA/DSM and others), Paris, France, June (2002).

T. Watanabe, S. Watanabe, T. Ikeda, M. Kase, T. Katayama, and T. Kawaguchi: "Design of highly-sensitive current monitor with HTS SQUID and HTS magnetic shield", 8th European Particle Accelerator Conf. (EPAC 2002), (CEA/DSM and others), Paris, France, June (2002).

T. Tanabe, T. Masuoka, and M. Kase: "XML-based integration for VMEs, an application server and RDBMS", 8th European Particle Accelerator Conf. (EPAC 2002), (CEA/DSM and others), Paris, France, June (2002).

M. Kidera, T. Nakagawa, S. Enomoto, K. Takahashi, T. Ohyama, K. Igarashi, M. Fujimaki, E. Ikezawa, O. Kamigaito, M. Kase, A. Goto, and Y. Yano: ""ECRIS-AMS" method and its application", Int. Symp. on Bio-Trace Elements 2002 (BITREL2002); Joint Symp. of RIKEN and Yamanashi Institute of Environmental Sciences, Wako, Fujiyoshida, Oct.–Nov. (2002).

T. Saito, V. P. Ladygin, T. Uesaka, M. Hatano, A. Y. Isupov, H. Kato, K. Kumasaka, Y. Maeda, N. B. Ladygina, M. H. Malakov, J. Nishikawa, T. Ohnishi, H. Okamura, S. G. Reznikov, H. Sakai, N. Sakamoto, S. Sakoda, K. Sekiguchi, R. Suzuki, K. Suda, A. Tamii, N. Uchigashima, and K. Yako: "Study of the spin structure of ^{3}He(^{3}H) via $\vec{d}\vec{d} \rightarrow {}^3\mathrm{He}\, n\, ({}^3\mathrm{H}\, p)$ reaction at intermediate energies", Kyudai-RCNP Int. Mini-Symp. on Nuclear Many-Body and Medium Effects in Nuclear Interactions and Reactions (MEDIUM02), Fukuoka, Oct. (2002).

2. Nuclear physics and nuclear instrumentation

K. Asahi: "Development of highly polarized radioactive ion beams and their application", Workshop at Tohoku University, Sendai, July–Aug. (2000).

T. Suzuki and GSI-RIKEN-Kurchatov-Comenius Collaboration: "Measurements of interaction cross sections for nuclei far from stability at relativistic energies", Tours Symp. on Nuclear Physics IV (TOURS 2000), (IN2P3), Tours, France, Sept. (2000).

T. Suda: "Electron-RI collider at RIKEN RI Beam Factory", LNS Int. Workshop on Physics with GeV Electrons and Gamma-rays, (LNS, Tohoku University), Sendai, Feb. (2001).

H. Miyoshi, K. Asahi, H. Ogawa, H. Ueno, D. Kameda, K. Yoneda, H. Watanabe, N. Imai, W. Sato, A. Yoshimi, K. Sakai, Y. Kobayashi, A. Yoshida, T. Kubo, and M. Ishihara: "Magnetic moment of a neutron-rich nucleus ^{17}C and its ground-state spin", 56th Ann. Meet. of the Physical Soc. of Japan, Hachioji, Mar. (2001).

N. Kawamura, K. Nagamine, T. Matsuzaki, K. Ishida, S. Nakamura, Y. Matsuda, M. Tanase, M. Kato, K. Kurosawa, H. Sugai, K. Kudo, N. Takeda, and G. H. Eaton: "First observation of temperature-dependent phenomenon of muon catalyzed fusion in solid D-T mixtures", Int. RIKEN Conf. on Muon Catalyzed Fusion and Related Exotic Atoms (μCF01), Shimoda, Apr. (2001).

K. Ishida, K. Nagamine, T. Matsuzaki, N. Kawamura, S. Nakamura, Y. Matsuda, M. Kato, H. Sugai, M. Tanase, K. Kudo, N. Takeda, and G. H. Eaton: "Measurement of fusion neutrons and X-rays in muon catalyzed d-t fusion at RIKEN-RAL", Int. RIKEN Conf. on Muon Catalyzed Fusion and Related Exotic Atoms (μCF01), Shimoda, Apr. (2001).

A. Toyoda, K. Ishida, K. Simomura, Y. Matsuda, W. Higemoto, S. Nakamura, T. Matsuzaki, and K. Nagamine: "Study of muon-catalyzed fusion in ortho-para controlled solid deuterium", Int. RIKEN Conf. on Muon Catalyzed Fusion and Related Exotic Atoms (μCF01), Shimoda, Apr. (2001).

T. Suda: "Nuclear physics at RIKEN RI beam factory", 7th Int. Spring Seminar on Nuclear Physics, Challenges of Nuclear Structure, (Universita di Napoli), Maiori, Italy, May (2001).

H. Koura, T. Tachibana, and M. Yamada: "Estimation of alpha-decay half-lives and fission barriers in the superheavy nuclidic region from the viewpoint of a new mass formula", 3rd Int. Conf. on Exotic Nuclei and Atomic Masses (enam 2001), (Dept. Phys., University of Jyväskylä), Hämeenlinna, Finland, July (2001).

T. Wakui, M. Hatano, H. Sakai, A. Tamii, and T. Uesaka: "A polarized solid proton target for a radioisotope beam facility", Int. Nuclear Physics Conf. (INPC2001), (University of California and Lawrence Berkeley National Laboratory), Berkeley, USA, July–Aug. (2001).

K. Yoneda, H. Sakurai, T. Gomi, T. Motobayashi, N. Aoi, N. Fukuda, U. Futakami, Z. Gacsi, Y. Higurashi, N. Imai, N. Iwasa, H. Iwasaki, T. Kubo, M. Kunibu, M. Kurokawa, Z. Liu, T. Minemura, A. Saito, M. Serata, S. Shimoura, S. Takeuchi, Y. X. Watanabe, K. Yamada, Y. Yanagisawa, K. Yogo, A. Yoshida, and M. Ishihara: "Deformation of the neutron-rich isotope ^{34}Mg studied via in-beam gamma-ray spectroscopy using two-step fragmentation", Int. Nuclear Physics Conf. (INPC2001), (University of California and Lawrence Berkeley National Laboratory), Berkeley, USA, July–Aug. (2001).

H. Ueno, K. Asahi, K. Yoneda, H. Watanabe, W. Sato, A. Yoshimi, Y. Kobayashi, A. Yoshida, T. Kubo, M. Ishihara, H. Ogawa, H. Miyoshi, D. Kameda, T. Suga, K. Ohno, K. Sakai, K. Yogo, and N. Imai: "Measurement of g-factor for the ground state of ^{17}C", Int. Nuclear Physics Conf. (INPC2001), (University of California and Lawrence Berkeley National Laboratory), Berkeley, USA, July–Aug. (2001).

H. Ueno, W. Sato, H. Ogawa, K. Yoneda, Y. Kobayashi, D. Kameda, H. Miyoshi, H. Watanabe, N. Imai, A. Yoshimi, J. Kaihara, and K. Asahi: "Development of a detector system for transient magnetic field experiments with radioactive-isotope beams and a test experiment", 12th Int. Conf. on Hyperfine Interactions, Park City, USA, Aug. (2001).

K. Asahi, H. Ogawa, H. Ueno, Y. Kobayashi, W. Sato, A. Yoshimi, D. Kameda, H. Miyoshi, K. Sakai, H. Watanabe, N. Imai, Y. Watanabe, K. Yoneda, N. Fukuda, N. Aoi, A. Yoshida, T. Kubo, and M. Ishihara: "Nuclear moments and hyperfine interactions studies with polarized radioactive nuclear beams at RIKEN", 12th Int. Conf. on Hyperfine Interactions, Park City, USA, Aug. (2001).

K. Asahi, Y. Kobayashi, H. Ueno, A. Yoshimi, W. Sato, H. Watanabe, H. Miyoshi, and D. Kameda: "Radioactive ion beams as microscopic probes into matter", Int. Congr. on Analytical Sciences 2001, (Japan Society for Analytical Chemistry), Tokyo, Aug. (2001).

T. Suda: "Electron-RI collider at RIKEN RI Beam Factory", Workshop on Electromagnetic Nuclear Reactions at Low Momentum Transfer, (Saint Mary's University), Halifax, Canada, Aug. (2001).

A. Yoshimi and K. Asahi: "Nuclear spin maser with an external feedback mechanism and its application", 2001 Fall Meet. of the Physical Soc. of Japan, Tokushima, Sept. (2001).

H. Ueno, W. Sato, H. Ogawa, K. Yoneda, Y. Kobayashi, D. Kameda, H. Miyoshi, H. Watanabe, N. Imai, A. Yoshimi, K. Asahi, A. Yoshida, M. Ishihara, K. Yogo, K. Sakai, and K. Ohno: "Magnetic moment of the ground state of ^{17}C", 4th Italy-Japan Symp. on Heavy Ion Physics, Tokyo, Sept. (2001).

T. Wakui, M. Hatano, H. Sakai, A. Tamii, and T. Uesaka: "Development of polarized solid proton target for RI Beam experiment", 9th Int. Workshop on Polarized Sources and Targets (PST 2001), (Indiana University Cyclotron Facility), Nashville, USA, Sept.–Oct. (2001).

H. Ogawa, K. Asahi, H. Ueno, H. Miyoshi, D. Kameda, N. Imai, K. Yoneda, H. Watanabe, A. Yoshimi, W. Sato, J. Kaihara, K. Sakai, Y. Kobayashi, A. Yoshida, T. Kubo, T. Suga, and K. Yogo: "Assignment of the ground-state spin-parity for ^{17}C through g-factor measurement", Yukawa Int. Seminar 2001 (YKIS01): Physics of Unstable Nuclei, (Yukawa Institute for Theoretical Physics, Kyoto University), Kyoto, Nov. (2001).

A. Kohama: "Density distributions of unstable nuclei by proton elastic scattering", RIKEN Gensikaku-Riron Group-Kenkyuukai: Reaction of Unstable Nuclei, Wako, Jan. (2002).

A. Ozawa: "Recent experiments for interaction cross-section measurements", RIKEN Gensikaku-Riron Group-Kenkyuukai: Reaction of Unstable Nuclei, Wako, Jan. (2002).

A. Ozawa: "Measurements of interaction cross-sections and related topics", RIKEN Winter School, Niigata, Jan. (2002).

K. Ishida: "Production and application of high-intensity low-energy muon beams: Recent development", FFAG Accelerator Workshop (FFAG02), (KEK), Tsukuba, Feb. (2002).

A. Ozawa: "Measurements of interaction cross-sections for Ar-isotopes", 57th Ann. Meet. of Physical Soc. of Japan, Shigaken Kusatsu, Mar. (2002).

K. Sekiguchi, H. Sakai, H. Okamura, A. Tamii, T. Uesaka, K. Suda, N. Sakamoto, T. Wakasa, Y. Sato, T. Ohnishi, K. Yako, S. Sakoda, H. Kato, Y. Maeda, M. Hatano, T. Saito, N. Uchigashima, N. Nayestanaki, and K. Ermisch: "Polarization transfer measurement for d-p elastic scattering and three nucleon force", 57th Ann. Meet. of Physical Soc. of Japan, Shigaken Kusatsu, Mar. (2002).

H. Koura and T. Tachibana: "Properties of neutron-rich nuclei from nuclear mass formulas", 57th Ann. Meet. of Physical Soc. of Japan, Shigaken Kusatsu, Mar. (2002).

S. Sugimoto: "Relativistic mean field theory with pion for finite nuclei", 57th Ann. Meet. of Physical Soc. of Japan, Shigaken Kusatsu, Mar. (2002).

Y. Yamaguchi: "Search for 21B", 57th Ann. Meet. of Physical Soc. of Japan, Shigaken Kusatsu, Mar. (2002).

K. Iida and G. Baym: "Superfluid phases of quark matter: Phenomenology and sum rules", 57th Ann. Meet. of Physical Soc. of Japan, Shigaken Kusatu, Mar. (2002).

T. Ito, T. Matsuzaki, M. Kato, and H. Sugai: "Development of high-purity hydrogen isotope gas supplying system", Ann. Meet. of Atomic Energy Soc. of Japan, Kobe, Mar. (2002).

K. Ishida, N. Kawamura, and T. Matsuzaki: "μCF experiments at RIKEN-RAL", Int. Workshop on Future of Muon Science, (KEK and RIKEN), Wako, Mar. (2002).

T. Matsuzaki: "μCF experiments at RIKEN-RAL (t-t μCF)", Int. Workshop on Future of Muon Science, (KEK and RIKEN), Wako, Mar. (2002).

K. Ishida: "Frontier of muon catalyzed fusion study", RIKEN Symp. on Studies on Condensed Matter Physics, Atomic Physics, Hyperfine Interactions and Biomedical Science Using RIKEN Accelerators VI, Wako, Mar. (2002).

K. Ishida: "Muon catalyzed fusion", Workshop on High Intensity Secondary Beam with Phase Rotation (V), (Kyoto University), Uji, Mar. (2002).

Y. Mochizuki: "Supernovae and nucleosynthesis (invited)", Joint Meet. of Earth and Planetary Science, Tokyo, May (2002).

Y. Mochizuki: "Video "Element Genesis" and some points when researchers make a scientific video (invited)", Seminar of Dept. of Science at Josai Univ., Sakado, May (2002).

T. Matsuzaki: "Muon catalyzed fusion", 21st Tritium Focus Group Meet., (Laboratory for Laser Energetics, University of Rochester), Rochester, USA, May (2002).

A. A. Korsheninnikov: "Recent studies of exotic nuclei in Dubna and RIKEN", HALO '02: Study Weekend on Dripline Nuclei, Göteborg, Sweden, June (2002).

A. A. Korsheninnikov: "Some recent studies of exotic nuclei", 52nd Meet. on Nuclear Spectroscopy and Nuclear Structure (NUCLEUS-2002), (Russian Academy of Science and Others), Moscow, Russia, June (2002).

K. Ishida: "Muon catalyzed fusion", 4th NuFact '02 Workshop: Neutrino Factories based on Muon Storage Rings, (Imperial College and others), London, UK, July (2002).

Y. Mochizuki: "Element genesis-Solving the mystery (Video Presentation)", 7th Int. Symp. on Nuclei

in the Cosmos, (CNS, RIKEN), Fuji-Yoshida, July (2002).

K. Iida and G. Baym: "Magnetic and rotational vortices in superfluid quark matter", 7th Int. Symp. on Nuclei in the Cosmos, Fujiyoshida, July (2002).

T. Motobayashi: "Nuclear astrophysics experiments with high energy RI beams", 7th Int. Symp. on Nuclei in the Cosmos, (CNS, University of Tokyo and RIKEN Accelerator Research Facility), Fujiyoshida, July (2002).

K. Iida and G. Baym: "Magnetic and rotational vortices in superfluid quark matter", 16th Int. Conf. on Ultrarelativistic Nucleus-Nucleus Collisions (Quark Matter 2002), (SUBATECH), Nantes, France, July (2002).

A. Ozawa: "Researches on Unstable Nuclear Structure at RIKEN", Workshop on Nuclear Synthesis and Radioactive Nuclei, (Tandem Accelerator Center, University of Tsukuba), Tsukuba, July (2002).

A. Ozawa: "Physics for unstable nuclei", 16th Hokkaido Kaku-riron Group Kenkyu-kai, (Hokkaido University), Sapporo, Aug. (2002).

A. Ozawa: "Recent measurements of reaction cross section and related topics", 1st CNS Int. Summer School (CISS02), (CNS, University of Tokyo), Wako, Aug. (2002).

H. Sakurai: "Spectroscopy on very neutron-rich nuclei at RIKEN", 224th ACS Natl. Meet., (American Chemical Society), Boston, USA, Aug. (2002).

H. Sakai: "Nd scattering at intermediate energy and three-nucleon force effects", 2nd Asia Pacific Conf. on Few-Body Problems in Physics (APFB02), Shanghai, China, Aug. (2002).

T. Saito, V. P. Ladygin, T. Uesaka, M. Hatano, A. Y. Isupov, H. Kato, K. Kumasaka, Y. Maeda, N. B. Ladygina, M. H. Malakov, J. Nishikawa, T. Ohnishi, H. Okamura, S. G. Reznikov, H. Sakai, N. Sakamoto, S. Sakoda, K. Sekiguchi, R. Suzuki, K. Suda, A. Tamii, N. Uchigashima, and K. Yako: "Measurement of the analyzing powers for the $\vec{d}\vec{d} \rightarrow {}^3\mathrm{He}\,n$ and $\vec{d}\vec{d} \rightarrow {}^3\mathrm{H}\,p$ reactions at intermediate energies", 2nd Asia Pacific Conf. on Few-Body Problems in Physics (APFB02), Shanghai, China, Aug. (2002).

K. Sekiguchi, H. Sakai, H. Okamura, A. Tamii, T. Uesaka, K. Suda, N. Sakamoto, T. Wakasa, Y. Sato, T. Ohnishi, K. Yako, S. Sakoda, H. Kato, Y. Maeda, M. Hatano, T. Saito, N. Uchigashima, N. Nayestanaki, and K. Ermisch: "Polarization transfer measurement for d-p elastic scattering to search for three nucleon force effects", 2nd Asia Pacific Conf. on Few-Body Problems in Physics (APFB02), Shanghai, China, Aug. (2002).

K. Iida: "Compact stars: from observations to dense matter", YITP Workshop on Thermal Quantum Field Theories and Their Application, (Yukawa Institute for Theoretical Physics, Kyoto University), Kyoto, Aug. (2002).

T. Motobayashi: "Coulomb dissociation studies for explosive hydrogen burning", 17th Int. Nuclear Physics Divisional Conf. of the European Physical Soc. (NPDC-17), (ATOMKI), Debrecen, Hungary, Sept.–Oct. (2002).

Y. Ishida, M. Wada, Y. Matsuo, I. Tanihata, A. Casares, and H. Wollnik: "Development of a multiple reflection time-of-flight mass spectrometer for short-lived nuclei", 2002 Fall Meet. of the Physical Soc. of Japan, Tokyo, Sept. (2002).

A. Ozawa: "Momentum Distributions of 14C and 15C fragments for 16C breakup at 83 A MeV", 2002 Fall Meet. of the Physical Soc. of Japan, Tokyo, Sept. (2002).

N. Kawamura, K. Nagamine, T. Matsuzaki, K. Ishida, S. Nakamura, Y. Matsuda, H. Imao, M. Tanase, M. Kato, H. Sugai, K. Kudo, N. Takeda, and G. H. Eaton: "Muon catalyzed fusion experiment for D-T mixture at RIKEN-RAL Muon Facility: Temperature-dependent phenomana on μCF", 2002 Fall Meet. of the Physical Soc. of Japan, Tokyo, Sept. (2002).

K. Ishida, K. Nagamine, T. Matsuzaki, N. Kawamura, Y. Matsuda, H. Imao, M. Tanase, M. Kato, H. Sugai, K. Kudo, N. Takeda, and G. H. Eaton: "Muon catalyzed fusion experiment in D-T mixture at RIKEN-RAL Muon Facility: Nonequilibrium molecular composition effect", 2002 Fall Meet. of the Physical Soc. of Japan, Tokyo, Sept. (2002).

K. Iida: "Quark matter and color superconductivity", 2002 Fall Meet. of the Physical Soc. of Japan, Tokyo, Sept. (2002).

K. Sekiguchi, H. Sakai, H. Okamura, T. Uesaka, K. Suda, N. Sakamoto, T. Wakasa, Y. Sato, T. Ohnishi, K. Yako, S. Sakoda, H. Kato, Y. Maeda, M. Hatano, T. Saito, N. Uchigashima, N. Nayestanaki, and K. Ermisch: "Polarization transfer measurement for d-p elastic scattering: a probe for three nucleon force properties", 15th Int. Spin Physics Symp. (SPIN 2002), (Brookhaven National Laboratory), Long Island, USA, Sept. (2002).

T. Saito, V. P. Ladygin, T. Uesaka, M. Hatano, A. Y. Isupov, H. Kato, K. Kumasaka, Y. Maeda, N. B. Ladygina, M. H. Malakov, J. Nishikawa, T. Ohnishi, H. Okamura, S. G. Reznikov, H. Sakai, N. Sakamoto, S. Sakoda, K. Sekiguchi, R. Suzuki, K. Suda, A. Tamii, N. Uchigashima, and K. Yako: "Study of ${}^3\mathrm{He}({}^3\mathrm{H})$ spin structure via $\vec{d}\vec{d}$ *to* ${}^3\mathrm{He}\,n\,({}^3\mathrm{H}\,p)$ reaction", 15th Int. Spin Physics Symp. (SPIN 2002), (Brookhaven National Laboratory), Long Island, USA, Sept. (2002).

K. Sekiguchi, H. Sakai, H. Okamura, A. Tamii, T. Wakasa, T. Uesaka, K. Suda, N. Sakamoto, Y. Sato, T. Ohnishi, K. Yako, S. Sakoda, H. Kato, Y. Maeda, M. Hatano, T. Saito, N. Uchigashima, N. Nayestanaki, and K. Ermisch: "Polarization transfer measurement for d-p scattering and three nucleon

force effects", 16th Int. Conf. on Particles and Nuclei (PANIC02), Osaka, Sept.–Oct. (2002).

K. Sekiguchi, H. Sakai, H. Okamura, A. Tamii, T. Uesaka, K. Suda, N. Sakamoto, T. Wakasa, Y. Sato, T. Ohnishi, K. Yako, S. Sakoda, H. Kato, Y. Maeda, M. Hatano, T. Saito, N. Uchigashima, N. Nayestanaki, and K. Ermisch: "Measurement of d-p elastic scattering at intermediate energies and three-nucleon force", Kyudai-RCNP Int. Mini-Symp. on Nuclear Many-Body and Medium Effects in Nuclear Interactions and Reactions (MEDIUM02), Fukuoka, Oct. (2002).

H. Koura: "Nuclear mass formulas and its application for astrophysics", 2002 Symp. on Nuclear Data, (Japan Atomic Energy Research Institute), Tokaimura, Nov. (2002).

K. Iida: "Compact stars and quark matter", CNS/RIKEN Joint Int. Workshop on Physics of QCD Many Body System - Future Perspective Based upon RHIC -, Wako, Nov. (2002).

A. Ozawa: "Measurements of interaction cross sections for Ar and Cl isotopes", Int. Symp. on Physics of Unstable Nuclei (ISPUN02), (INST, Hanoi and IOP, Hanoi), Halong Bay, Vietnum, Nov. (2002).

K. Ishida: "Highlights of μCF experiments at RIKEN/RAL", Int. Workshop on Exotic Atoms—Future Perspectives (EXA 2002), (Institute for Medium Energy Physics of Austrian Academy of Sciences), Vienna, Austria, Nov. (2002).

Y. Mochizuki: "^{44}Ti: its initial abundance in Cas A and its detection possibility in SN 1987A with INTEGRAL", 19th Meet. between Nuclear Astrophysicists and Nuclear Physicists, (Universite Libre de Bruxelles), Brussels, Belgium, Dec. (2002).

3. Atomic and solid-state physics

R. H. Scheicher, U. N. Roy, T. P. Das, K. Ishida, T. Matsuzaki, S. Nakamura, N. Kawamura, and K. Nagamine: "Theory for relative strengths of trapping of He^+ ions in solid, liquid and gaseous hydrogen", Int. RIKEN Conf. on Muon Catalyzed Fusion and Related Exotic Atoms (μCF01), Shimoda, Apr. (2001).

K. Ishioka, M. Hase, K. Ushida, and M. Kitajima: "Coherent Phonon in ion-irradiated graphite", 44th Symp. on Radiation Chemistry, (Japanese Society of Radiation Chemistry), Higashiosaka, Sept. (2001).

Y. Iwai: "The formation and relaxation process of hollow atoms", Workshop on Plasma and X-ray Spectroscopy, (Kansai Research Establishment, Japan Atomic Energy Research Institute), Kyoto, Nov. (2001).

I. Shimamura and Y. Teranishi: "Diabatic-ionization model of antiproton capture by atoms", 9th Symp. on the Theory of Atomic and Molecular Processes: Antimatter Science by Using Antiprotons, Hayama, Jan. (2002).

M. Wada: "On-line test of an rf ion-guide for collection of energetic Li-8 ion beam", Workshop on Collaboration Studies Using Particle Accelerator for Cancer Therapy 2001, (National Institute of Radiological Sciences), Chiba, Feb. (2002).

H. Shimada, Y. Nakai, H. Oyama, K. Ando, T. Kambara, and Y. Yamazaki: "Construction of a TOF spectrometer for ions created by intense laser", 57th Ann. Meet. of Physical Soc. of Japan, Shigaken Kusatsu, Mar. (2002).

Y. Iwai, Y. Kanai, H. Oyama, K. Ando, H. Masuda, K. Nishio, M. Nakao, T. Tamamura, K. Komaki, and Y. Yamazaki: "High-resolution soft X-ray spectroscopy of 2.3 keV/u $N^{6,7+}$ ions through microcapillary targets", 57th Ann. Meet. of Physical Soc. of Japan, Shigaken Kusatsu, Mar. (2002).

R. Saneto, Y. Fukuyama, I. Tanihata, H. Sasada, and Y. Matsuo: "LIF detection of alkali earth ions introduced into liquid helium by electric field", 57th Ann. Meet. of Physical Soc. of Japan, Shigaken Kusatsu, Mar. (2002).

M. Wada, Y. Ishida, T. Nakamura, Y. Nakai, T. M. Kojima, Y. Kanai, N. Oshima, H. Oyama, T. Kambara, Y. Yamazaki, A. Yoshida, T. Kubo, Y. Matsuo, Y. Fukuyama, K. Okada, T. Sonoda, K. Noda, H. Kawakami, S. Ohtani, and I. Katayama: "On-line collection of energetic ^{8}Li ions from RIPS using an rf ion-guide system", 57th Ann. Meet. of Physical Soc. of Japan, Shigaken Kusatsu, Mar. (2002).

M. Niigaki, T. M. Kojima, N. Oshima, A. Mohri, and Y. Yamazaki: "Optimizaiton of plasma conditions stored in a multi-ring trap", 57th Ann. Meet. of Physical Soc. of Japan, Shigaken Kusatsu, Mar. (2002).

M. Hoshino, M. Kitajima, Y. Kanai, Y. Nakai, H. Tanaka, and Y. Yamazaki: "The study of double-electron capture processes using 2D-mapping in C^{4+}-He collision at the collision energy range below 100 eV/q", 57th Ann. Meet. of Physical Soc. of Japan, Shigaken Kusatsu, Mar. (2002).

M. Wada: "Slow and trapped RI-beams from projectile fragment separators", JAERI Fundamental Science Seminar on Nuclear Structure Study: Experimental Technique Toward New Horizon, Tokaimura, Mar. (2002).

N. Oshima, T. M. Kojima, M. Niigaki, A. Mohri, T. Kambara, Y. Kanai, Y. Nakai, H. Oyama, M. Wada, and Y. Yamazaki: "Development of an intense slow positron source and a positron cooling technique for multi charged ions", RIKEN Symp. on Studies on Condensed Matter Physics, Atomic Physics, Hyperfine Interactions and Biomedical Science Using RIKEN Accelerators VI, Wako, Mar. (2002).

T. Ikeda: "Study of hollow atoms with STJ X-ray detector", RIKEN Symp. on Studies on Condensed

Matter Physics, Atomic Physics, Hyperfine Interactions and Biomedical Science Using RIKEN Accelcrators VI, Wako, Mar. (2002).

N. Nakamura, A. Endo, Y. Kanai, H. Torii, K. Komaki, and Y. Yamazaki: "Electron beam ion source equipped with a bulk high Tc superconductor solenoid: Construction and experimental plans", 27th Ann. Meet. of the Soc. for Atomic Collision Research, Kyoto, Aug. (2002).

Y. Iwai, Y. Kanai, Y. Nakai, T. Ikeda, H. Oyama, K. Ando, H. Masuda, K. Nishio, M. Nakao, H. Torii, K. Komaki, and Y. Yamazaki: "High-resolution soft X-ray spectroscopy of 2.3 keV/u $N^{6,7+}$ ions through a microcapillary target", 27th Ann. Meet. of the Soc. for Atomic Collision Research, Kyoto, Aug. (2002).

M. Niigaki, T. Kojima, N. Oshima, A. Mohri, S. Letout, and Y. Yamazaki: "Production of ultraslow HCI beams sympathetically cooled by a cold positron plasma in a multi-ring linear penning trap-II", 27th Ann. Meet. of the Soc. for Atomic Collision Research, Kyoto, Aug. (2002).

Y. Nakai: "The collisions between fast ions and C_{60} in MeV region", 27th Ann. Meet. of the Soc. for Atomic Collision Research, Kyoto, Aug. (2002).

M. Hoshino, Y. Kanai, M. Kitajima, Y. Nakai, H. Tanaka, and Y. Yamazaki: "Two-dimensional representation of multi-electron capture processes for highly charged ion-atom collisions in the energy range below 100 eV/q", 27th Ann. Meet. of the Soc. for Atomic Collision Research, Kyoto, Aug. (2002).

Y. Yamazaki: "Production of ultraslow antiproton beam and its application to atomic collisions", Int. Workshop on Atomic Physics Researches at Storage Rings, (Institute of Modern Physics, CAS), Lanzhou, China, Aug. (2002).

N. Nakamura, A. Endo, E. Noguchi, K. Komaki, and Y. Yamazaki: "A compact electron beam ions source equipped with a bulk high Tc superconductor solenoid", 11th Int. Conf. on the Physics of Highly Charged Ions (HCI 2002), Caen, France, Sept. (2002).

Y. Takabayashi, T. Azuma, C. Kondo, T. Ito, K. Komaki, Y. Yamazaki, E. Takada, and T. Murakami: "Anisotropic X-ray emission from resonant coherently excited highly-charged heavy ions", 11th Int. Conf. on the Physics of Highly Charged Ions (HCI 2002), Caen, France, Sept. (2002).

T. Ikeda, Y. Nakai, Y. Kanai, T. Kambara, N. Fukunishi, T. Azuma, K. Komaki, Y. Takabayashi, and Y. Yamazaki: "Development of a 5-axis high-precision goniometer for crystal assisted high-resolution spectroscopy of highly charged ions", 11th Int. Conf. on the Physics of Highly Charged Ions (HCI 2002), Caen, France, Sept. (2002).

N. Oshima, T. Kojima, M. Niigaki, A. Mohri, K. Komaki, and Y. Yamazaki: "Development of a cold MCI source for ultra-slow collisions", 11th Int. Conf. on the Physics of Highly Charged Ions (HCI 2002), Caen, France, Sept. (2002).

M. Hoshino, Y. Kanai, M. Kitajima, Y. Nakai, H. Tanaka, and Y. Yamazaki: "Energy gain-scattering angle 2d representation of highly charged ion-atom collisions in the energy region of 50–100 eV/q", 11th Int. Conf. on the Physics of Highly Charged Ions (IICI 2002), Caen, France, Sept. (2002).

Y. Takabayashi, C. Kondo, T. Ito, T. Azuma, K. Komaki, Y. Yamazaki, E. Takada, and T. Murakami: "High resolution spectroscopy of highly charged heavy ions using resonant coherent excitation phenomena", 11th Int. Conf. on the Physics of Highly Charged Ions (HCI 2002), Caen, France, Sept. (2002).

Y. Iwai, Y. Kanai, Y. Nakai, T. Ikeda, H. Oyama, K. Ando, H. Masuda, K. Nishio, M. Nakao, H. Torii, K. Komaki, and Y. Yamazaki: "High-resolution soft X-ray spectroscopy of slow highly charged ion transmitted through a microcapillary target", 11th Int. Conf. on the Physics of Highly Charged Ions (HCI 2002), Caen, France, Sept. (2002).

N. Yamanaka: "Mass polarization effect in He-like and Li-like ions", 11th Int. Conf. on the Physics of Highly Charged Ions (HCI 2002), Caen, France, Sept. (2002).

Y. Kanai, Y. Iwai, H. Masuda, K. Nishio, M. Nakao, and Y. Yamazaki: "Measurement of L X-ray of Ar ions transmitted through a microcapillary target", 11th Int. Conf. on the Physics of Highly Charged Ions (HCI 2002), Caen, France, Sept. (2002).

A. Ito, T. Majima, Y. Nakai, and H. Tsuchida: "Multiple electron emission from C_{60} in charge-changing collisions with fast projectile ions", 11th Int. Conf. on the Physics of Highly Charged Ions (HCI 2002), Caen, France, Sept. (2002).

H. Shimada, Y. Nakai, T. Kambara, H. Oyama, K. Ando, and Y. Yamazaki: "Production of multiply charged Ar ions with a TW laser", 11th Int. Conf. on the Physics of Highly Charged Ions (HCI 2002), Caen, France, Sept. (2002).

Y. Nakai, T. Ikeda, Y. Kanai, T. Kambara, N. Fukunishi, T. Azuma, K. Komaki, Y. Takabayashi, and Y. Yamazaki: "Resonant coherent excitation of 95 MeV/u Ar^{17+} ions channeling through a Si crystal", 11th Int. Conf. on the Physics of Highly Charged Ions (HCI 2002), Caen, France, Sept. (2002).

Y. Zou, M. Huang, R. Hutton, K. Ando, and H. Oyama: "The continuing saga of the Si-like intercombination lines in highly charged ions, Si-like Rhodium", 11th Int. Conf. on the Physics of Highly Charged Ions (HCI 2002), Caen, France, Sept. (2002).

Y. Morishita, R. Hutton, Y. Kanai, K. Ando, T. Brage, F. B. Rosmej, H. Masuda, K. Ishii, H. Torii, K. Komaki, and Y. Yamazaki: "Visible light spec-

troscopy of Ar^{6+} ions in high Rydberg states produced with microcapillary target", 11th Int. Conf. on the Physics of Highly Charged Ions (HCI 2002), Caen, France, Sept. (2002).

Y. Kanai, Y. Nakai, Y. Iwai, Y. Yamazaki, H. Masuda, and K. Nishio: "Measurement of L X-ray of Ar ions transmitted through a microcapillary target", 2002 Fall Meet. of the Physical Soc. of Japan, Kasugai, Sept. (2002).

4. Radiochemistry, radiation chemistry, and radiation biology

J. Furukawa, R. Hirunuma, S. Enomoto, and T. Nakanishi: "Analysis of the binding affinity of multitracer to an apoplast protein extracted from soybean root", Ann. Meet. of Japanese Soc. of Soil Science and Plant Nutrition, Kochi, Apr. (2001).

T. Nabekura, T. Minami, R. Hirunuma, S. Enomoto, R. Hori, and Y. Ito: "Transport of trace elements in rat lens", 9th Int. Congr. of Toxicology, (ASCEPT, IUTOX), Brisbane, Australia, July (2001).

S. Motomura, Y. Yang, Q. Pan, Y. Gounou, S. Enomoto, Y. Yano, and K. Asahi: "Compton camera for multitracer", 4th Italy-Japan Symp. on Heavy Ion Physics, (RIKEN and others), Wako, Tokyo, Sept. (2001).

S. Enomoto: "Multi-tracer technology in biology", 4th Italy-Japan Symp. on Heavy Ion Physics, (RIKEN and others), Wako, Tokyo, Sept. (2001).

W. Ding, S. Enomoto, R. Hirunuma, T. Ohyama, and K. Igarashi: "An in vivo evaluation of multitracer transport and absorption in everted duodenum-jejunum sacs of control and streptozotocin -diabetic rats", RIKEN Symp. on Development and Application of the Multitracer Technique, Wako, Dec. (2001).

A. Nakayama, H. Yasui, R. Hirunuma, S. Enomoto, and H. Sakurai: "Behavior of elements in partially hepatectomized rats", RIKEN Symp. on Development and Application of the Multitracer Technique, Wako, Dec. (2001).

T. Nabekura, T. Minami, R. Hirunuma, S. Enomoto, and Y. Ito: "Behavior of metals and metallothionein in lens of rats", RIKEN Symp. on Development and Application of the Multitracer Technique, Wako, Dec. (2001).

Y. Takahashi, C. Egawa, T. Mifune, R. Hirunuma, and S. Enomoto: "Effect of surface diffusion on the diffusivity of elements through porewater of granite", RIKEN Symp. on Development and Application of the Multitracer Technique, Wako, Dec. (2001).

H. Yasui, T. Takino, J. Fugono, A. Nakayama, K. Kawabe, H. Sakurai, R. Hirunuma, and S. Enomoto: "Effect of vanadium treatment on tissue distribution of multitracer in streptozotocin induced diabetic rats", RIKEN Symp. on Development and Application of the Multitracer Technique, Wako, Dec. (2001).

K. Igarashi, Y. Nakakoshi, R. Hirunuma, S. Enomoto, and S. Kimura: "Influence of iron compound on the transport of various trace elements in everted intestinal segments of rats", RIKEN Symp. on Development and Application of the Multitracer Technique, Wako, Dec. (2001).

T. Ohyama, M. Yanaga, H. Maetsu, T. Yoshida, M. Noguchi, H. Suganuma, K. Ishikawa, R. Hirunuma, S. Enomoto, and T. Omori: "Investigation of biobehavior of trace elements in the Zn-deficient mice", RIKEN Symp. on Development and Application of the Multitracer Technique, Wako, Dec. (2001).

J. Furukawa, R. Hirunuma, S. Enomoto, and T. Nakanishi: "Measurement of binding affinity of multitracer to plant apoplast protein in root tips", RIKEN Symp. on Development and Application of the Multitracer Technique, Wako, Dec. (2001).

T. Yanagiya, S. Enomoto, N. Imura, and S. Himeno: "Reduction of Cd cytotoxicity by Mn", RIKEN Symp. on Development and Application of the Multitracer Technique, Wako, Dec. (2001).

K. Matsumoto, R. Hirunuma, S. Enomoto, and K. Endo: "Relationship between mineral oxidative in rat: Noninvasive and simultaneous measurement of dynamics of biotrace elements using in vivo multitracer technique", RIKEN Symp. on Development and Application of the Multitracer Technique, Wako, Dec. (2001).

S. Enomoto: "Research of multitracer production on RIKEN Ring Cyclotron and development of new multitracer production system at RIKEN RI beam factory facility", RIKEN Symp. on Development and Application of the Multitracer Technique, Wako, Dec. (2001).

H. Haba, S. Enomoto, R. Hirunuma, Y. Nagame, and A. Shinohara: "Research of the nuclear chemistry of transactinide: Development of a gas-jet coupled multitarget system and an automated rapid chemistry apparatus", RIKEN Symp. on Development and Application of the Multitracer Technique, Wako, Dec. (2001).

S. Yoshida, M. Yamasaki, S. Enomoto, and H. Morikawa: "Study on the absorption of divalent cations in the intestinal loop using the multitracer technique", RIKEN Symp. on Development and Application of the Multitracer Technique, Wako, Dec. (2001).

R. Hirunuma and S. Enomoto: "Uptake of various trace elements in Se-excessive rats", RIKEN Symp. on Development and Application of the Multitracer Technique, Wako, Dec. (2001).

F. Yatagai, S. Morimoto, T. Kato, and M. Honma: "Sensitive detection of chromosome changes by heavy-ion irradiation", 18th Space Utilization Symp., (Institute of Space and Astronautical Sci-

ence), Sagamihara, Jan. (2002).

F. Yatagai: "Biological characterization of DNA double-strand break produced by ion-irradiation", RIKEN Symp. on Structure and Property Modifications of Solids by GeV Heavy Ions, Wako, Mar. (2002).

H. Tamano, A. Takeda, S. Enomoto, and N. Oku: "Behavior of Zn in rat brain tumor", 122nd Ann. Meet. of the Pharmaceutical Soc. of Japan, Chiba, Mar. (2002).

S. Enomoto, R. Hirunuma, S. Motomura, and Y. Gounou: "Development of multitracer γ-ray emission imaging (MT-GEI): A new detection system for multitracer", 122nd Ann. Meet. of the Pharmaceutical Soc. of Japan, Chiba, Mar. (2002).

R. Hirunuma, M. Kidera, T. Ohyama, K. Takahashi, S. Enomoto, and T. Nakagawa: "Development of new trace elements analytical system using the electron cyclotron resonance ion source and heavy ion linear accelerator", 122nd Ann. Meet. of the Pharmaceutical Soc. of Japan, Chiba, Mar. (2002).

T. Abe: "Effective mutation method for plant breeding using heavy-ion beams", 29th Workshop for Biotechnology in Nagano, (Nagano Agricultural Research Center), Nagano, Mar. (2002).

S. Goto, S. Morimoto, T. Tsukada, M. Watanabe, and F. Yatagai: "Densely located DNA damage caused a delay in cell-cycle progression in human lymphoblastoid cells exposed to Fe-ion", 2nd Int. Workshop on Space Radiation Research (IWSSRR-2), (National Institute of Radiological Sciences and others), Nara, Mar. (2002).

T. Abe, C. Bae, M. Fujiwara, T. Matsuyama, and S. Yoshida: "Effective mutation method for plants using heavy-ion beams", 2nd Int. Workshop on Space Radiation Research (IWSSRR-2), (National Institute of Radiological Sciences and others), Nara, Mar. (2002).

T. Kato, M. Honma, S. Morimoto, and F. Yatagai: "Fine mapping of LOH events in spontaneous tk^- mutants of the human lymphoblastoid cell line TK6", 2nd Int. Workshop on Space Radiation Research (IWSSRR-2), (National Institute of Radiological Sciences and others), Nara, Mar. (2002).

M. Hamatani, Y. Iitsuka, T. Abe, K. Miyoshi, M. Yamamoto, and S. Yoshida: "Mutant flower of dahlia (*Dahlia pinnata cav.*) induced by heavy-ion beams", 2nd Int. Workshop on Space Radiation Research (IWSSRR-2), (National Institute of Radiological Sciences and others), Nara, Mar. (2002).

K. Suzuki, Y. Yomo, T. Abe, Y. Katsumoto, K. Miyazaki, S. Yoshida, and T. Kusumi: "Mutational breeding of verbena with large number of flowers using heavy-ion beams irradiation", 2nd Int. Workshop on Space Radiation Research (IWSSRR-2), (National Institute of Radiological Sciences and others), Nara, Mar. (2002).

T. Takanami, Y. Zhang, H. Aoki, H. Takahashi, A. Takahashi, T. Ohnishi, T. Abe, S. Yoshida, and A. Higashitani: "Repair system for DNA damages in meiotic cells of Caenorhabditis elegans", 2nd Int. Workshop on Space Radiation Research (IWSSRR-2), (National Institute of Radiological Sciences and others), Nara, Mar. (2002).

S. Enomoto, R. Hirunuma, R. Amano, F. Yatagai, and Y. Yano: "Research in metabolic physiology on space field by using the multitracer technology", 2nd Int. Workshop on Space Radiation Research (IWSSRR-2), (National Institute of Radiological Sciences and others), Nara, Mar. (2002).

F. Yatagai, S. Morimoto, M. Honma, F. Hanaoka, and Y. Yano: "The development in sensitive detection of genetic alterations caused by space environmental radiation", 2nd Int. Workshop on Space Radiation Research (IWSSRR-2), (National Institute of Radiological Sciences and others), Nara, Mar. (2002).

T. Abe: "Mutation breeding using heavy-ion beams", Workshop for Mutation Breeding with Ion Beams, (Shisuoka Citrus Experimant Station), Shizuoka, Mar. (2002).

S. Goto, S. Morimoto, T. Tsukada, M. Watanabe, F. Hanaoka, Y. Yano, and F. Yatagai: "Densely located DNA damage caused a delay in cell-cycle progression in human lymphoblastoid cells", 33rd Ann. Meet. on Frontiers Beyond the Human Genome, (Environmental Mutagen Society), Anchorage, USA, Apr.–May (2002).

T. Kato, M. Honma, S. Morimoto, and F. Yatagai: "Fine mapping of LOH events in spontaneous TK^- mutants of the human lymphoblastoide cell line TK6", 33rd Ann. Meet. on Frontiers Beyond the Human Genome, (Environmental Mutagen Society), Anchorage, USA, Apr.–May (2002).

W. Ding, S. Enomoto, R. Hirunuma, T. Ohyama, and K. Igarashi: "An in vivo evaluation of multitracer transport and absorption in everted duodenum-jejunum sacs of coctrol and streptozotocin-diabetic rats", 12th Symp. on the Role of Metals in Biological Reactions, Biology and Medicine, (The Pharmaceutical Society of Japan), Kyoto, May (2002).

S. Enomoto, R. Hirunuma, T. Ohyama, K. Igarashi, K. Takahashi, M. Kidera, T. Nakagawa, S. Motomura, and Y. Gounou: "Developments of the new simultaneous multi-elements analysis: multitracer gamma-ray emission imaging (MT-GREI) and high sensitive analyzing system using the electron cyclotron resonance ion source and heavy ion linear accelerator", 12th Symp. on the Role of Metals in Biological Reactions, Biology and Medicine, (The Pharmaceutical Society of Japan), Kyoto, May (2002).

T. Ohyama, M. Kidera, T. Nakagawa, M. Yanaga, K. Takahashi, R. Hirunuma, and S. Enomoto: "High sensitive trace elements analysis by ECRIS-AMS", 12th Symp. on the Role of Metals in Biological Re-

actions, Biology and Medicine, (The Pharmaceutical Society of Japan), Kyoto, May (2002).

K. Igarashi, Y. Nakakoshi, R. Hirunuma, S. Enomoto, and S. Kimura: "Influence of NaFeEDTA and ferrous sulfate on the absorption of trace elements in rats everted intestinal segments", 19th Symp. of Trace Nutrients Research, Kyoto, May (2002).

T. Abe, M. Hamatani, Y. Iitsuka, N. Fukunishi, K. Miyoshi, M. Yamamoto, and S. Yoshida: "Flower mutants of dahlia (*Dahlia pinnata* Cav.) induced by heavy-ion beams", 10th IAPTC&B Congr. on Plant Biology 2002 and Beyond, Orlando, USA, June (2002).

S. Yoshida, K. Suzuki, Y. Yomo, T. Abe, . Katsumoto, K. Miyazaki, and T. Kusumi: "Isolation of sterile mutants of *Verbena hybrida* using heavy-ion beams irradiation", 10th IAPTC&B Congr. on Plant Biology 2002 and Beyond, Orlando, USA, June (2002).

S. Yoshida, T. Abe, T. Tanaka, T. Kusumi, and K. Suzuki: "A new method of plant mutagenesis using heavy-ion beams", 19th Ann. Meet. and Symp. of Japanese Soc. of Plant Cell and Molecular Biology, Nara, July (2002).

T. Abe, K. Suzuki, Y. Miyazawa, S. Yoshida, T. Kusumi, and T. Tanaka: "Isolation of mutants of tobacco using heavy-ion beams irradiation", 20th Ann. Meet. and Symp. of Japanese Soc. for Plant Cell and Molecular Biology, Nara, July (2002).

T. Abe: "A new technology of mutation breeding using the RIKEN Ring Cyclotron", 3rd Workshop for Plant Breeding in Kagoshima, (Kagoshima Biotechnology Institute), Kagoshima, July (2002).

T. Tsuji, Y. Yabushita, Y. Kanayama, R. Hirunuma, S. Enomoto, and R. Amano: "Behaviour of Mn and various elements in the fetal mice", 13th Ann. Meet. of the Japan Soc. for Biomedical Research on Trace Elements, Kisarazu, July (2002).

T. Ohyama, M. Koike, T. Ogi, Y. Kawamoto, H. Maetsu, H. Suganuma, M. Noguchi, K. Ishikawa, R. Hirunuma, S. Enomoto, and M. Yanaga: "Determination of trace elements in liver of Zn-deficient mice by INAA", 13th Ann. Meet. of the Japan Soc. for Biomedical Research on Trace Elements, Kisarazu, July (2002).

W. Ding, S. Enomoto, and R. Hirunuma: "Effect of vanadium and several hormones on the tolerance to glucose and distribution of trace elements in the prediabetic stage and diabetic stage of KK mice", 13th Ann. Meet. of the Japan Soc. for Biomedical Research on Trace Elements, Kisarazu, July (2002).

K. Igarashi, Y. Nakakoshi, R. Hirunuma, S. Enomoto, and S. Kimura: "Influence of NaFeEDTA and ferrous sulfate on the absorption of trace elements in everted intestinal segments of rats", 13th Ann. Meet. of the Japan Soc. for Biomedical Research on Trace Elements, Kisarazu, July (2002).

T. Abe, T. Matsuyama, and S. Yoshida: "The use of heavy-ion irradiation for mutation induction", Workshop for Plant Ultraviolet-B Radiation, (Graduate School of Life Sciences, Tohoku University), Sendai, Aug. (2002).

T. Abe: "Plant mutation breeding using ion-beam irradiation", 19th Fukui Agricultural Experiment Station Workshop, Fukui, Sept. (2002).

H. Kagami, I. Sawano, T. Abe, and S. Yoshida: "Effect of heavy-ion beams irradiation on the survival and tree growth of sastuma mandarin", 2002 Ann. Meet. of Tokai Shibu in Japanese Soc. for Horticultural Science, Tsu, Sept. (2002).

M. Honma, W. Wang, M. Sakuraba, M. Izumi, F. Yatagai, and M. Hayashi: "A fate of DNA double strand breaks in mammalian cells", 45th Ann. Meet. of the Japan Radiation Research Soc., Sendai, Sept. (2002).

K. Masumura, M. Hoshino, F. Yatagai, M. Ochiai, O. Ueda, H. Suzuki, H. Nakagama, M. Fukuoka, and T. Nomi: "DNA PKcs-independent error-prone DNA end-joining pathway and its role in radiation-induced mutagenesis", 45th Ann. Meet. of the Japan Radiation Research Soc., Sendai, Sept. (2002).

K. Igarashi, H. Inage, Y. Nakakoshi, R. Hirunuma, S. Enomoto, and S. Kimura: "Influence of sodium iron ethylenediaminetetraacetic acid on the absorption of iron and other trace elements in rats", 6th Conf. of the Int. Soc. for Trace Element Research in Humans (ISTERH), Quebec, Canada, Sept. (2002).

T. Tsukada, S. Goto, and F. Yatagai: "Apoptosis induction after exposure to heavy-ions", 34th COSPAR Scientific Assembly; 2nd World Space Congr., Houston, USA, Oct. (2002).

S. Goto, M. Tomita, S. Morimoto, and F. Yatagai: "Cellular responses and genetic consequences by DSBs induced after heavy-ion exposure", 34th COSPAR Scientific Assembly; 2nd World Space Congr., Houston, USA, Oct. (2002).

S. Yoshida, T. Abe, and Y. Yano: "Development of plant mutagenesis using ion-beam irradiation", 1st Workshop on Application for Ion Beam Biology, (TIARA), Takasaki, Nov. (2002).

F. Yatagai, S. Morimoto, T. Kato, and M. Honma: "Speculation of DNA double-strand break repair pathway from changes in LOH pattern caused by p53 defect", 31th Ann. Meet. of the Japan Environmental Mutagen Research Soc., Tokyo, Nov. (2002).

T. Takeyumi, Y. Ito, T. Abe, and H. Yamanouchi: "Effect of acute irradiation on regrow in tea", Ann. Meet. for Tea Research, 2002, Shizuoka, Nov. (2002).

F. Yatagai, S. Morimoto, T. Kato, and M. Honma: "Availability of LOH analysis: Estimation of genetic influences of space environment", 16th Ann. Meet. of Japanese Soc. for Biological Sciences in Space, Toyama, Nov. (2002).

S. Goto, S. Morimoto, T. Tsukada, M. Watanabe, and F. Yatagai: "Delayed cell cycle progression by clus-

tered damage", 25th Ann. Meet. of the Molecular Biology Soc. of Japan, Yokohama, Dec. (2002).

5. Material Analysis

M. Iwaki: "Methods of determining the atomic density of amorphous carbon using ion implantation", 17th Symp. on Surface Layer Modification by Ion Implantation, Tokyo, Nov. (2001).

T. Kobayashi, A. Nakao, and M. Iwaki: "Mechanical properties of amorphous carbon films produced from polymers by ion implantation", 28th Ann. Conf. of the Carbon Soc. of Japan, Kiryu, Dec. (2001).

M. Maeda, K. Maeda, and K. Hasegawa: "Direct chemical specification of S in marine sediments by in-air high-resolution PIXE", 2002 Spring Meet. of the Oceanographic Soc. of Japan, Tokyo, Mar. (2002).

K. Maeda, K. Hasegawa, H. Hamanaka, M. Maeda, and K. Ogiwara: "A highly sensitive high-resolution in-air PIXE system using a curved crystal in von Hamos geometry", 4th Int. Symp. on BioPIXE, (Instituto Nacional de Investigaciones Nucleares Mexico), Mexico City, Mexico, Apr. (2002).

K. Maeda, K. Hasegawa, K. Ogiwara, M. Maeda, and H. Hamanaka: "Improvement in the sensitivity of in-air high-resolution PIXE - II", 19th PIXE Symp., Akita, Oct. (2002).

6. RIKEN-BNL Collaboration on Spin Physics Program

Y. Goto: "PHENIX spin plans in year-1", Spin Physics at RHIC in Year-1 and Beyond, New York, USA, Mar. (2001).

S. A. Bass, A. Dumitru, P. Danielewicz, and S. Pratt: "Probing hadronization with strangeness", Int. Symp. on Non-Equilibrium and Nonlinear Dynamics in Nuclear and Other Finite Systems, Beijing, China, May (2001).

J. Schaffner-Bielich: "Who needs flow anyway?", RHIC/INT Workshop 2001 on Ultra-relativistic Heavy Ion Collisions in the RHIC era, (Lawrence Berkeley National Laboratory), Berkeley, USA, May–June (2001).

S. A. Bass: "Microscopic reaction dynamics in ultra-relativistic heavy-ion collisions at SPS and RHIC", 6th Workshop on Non-Perturbative QCD, (American University of Paris), Paris, France, June (2001).

M. H. Reno, I. Sarcevic, G. Sterman, M. Stratmann, and W. Vogelsang: "Ultrahigh-energy neutrinos, small x and unitarity", Snowmass 2001: A Summer Study on the Future of Particle Physics, (American Physical Society and others), Snowmass, USA, June–July (2001).

J. Murata: "Beyond the standard model physics at RHIC in polarized pp collision", Advanced Study Institute: Symmetries and Spin, Praha-SPIN-2001, (Charles University), Praha, Czech, July (2001).

J. Murata: "Construction of the PHENIX south muon arm", Int. Nuclear Physics Conf. (INPC2001), (University of California and the Lawrence Berkeley National Laboratory), Berkeley, USA, July–Aug. (2001).

D. T. Son: "Confinement and domain walls in high density quark matter", Conf. on Compact Stars in the QCD Phase Diagram (CSQCD), Copenhagen, Denmark, Aug. (2001).

Y. Aoki: "Hadron spectrum for quenched domain-wall fermions with DBW2 gauge action", Lattice 2001: 19th Int. Symp. on Lattice Field Theory, (DESY Zeuthen and Humboldt-Universitat zu Berlin), Berlin, Germany, Aug. (2001).

M. A. Stephanov: "Novel phenomena in high-density QCD", Lattice 2001: 19th Int. Symp. on Lattice Field Theory, (DESY Zeuthen and Humboldt-Universitat zu Berlin), Berlin, Germany, Aug. (2001).

T. Tominaka, M. Okamura, and T. Katayama: "Contribution of iron yoke on helical coils", 17th Int. Conf. on Magnet Technology, (CERN), Geneva, Switzerland, Sept. (2001).

J. Noaki: "Calculation of non-leptonic kaon decay amplitudes from K to π matrix elements in quenched domain-wall QCD", Lattice QCD and Hadron Phenomenology, (Institute for Nuclear Theory), Seattle, USA, Sept.–Dec. (2001).

Y. Aoki: "Hadron spectrum for quenched clomain-wall fermions with DBW2 gauge action", Lattice QCD and Hadron Phenomenology, (Intitute for Nuclear Theory, University of Washington), Seattle, USA, Sept.–Dec. (2001).

C. Dawson: "Non-perturbative renormalization with domain wall fermions", Lattice QCD and Hadron Phenomenology, (Institute for Nuclear Theory, Washington University), Seattle, USA, Sept.–Dec. (2001).

S. A. Bass: "Microscopic reaction dynamics at SPS and RHIC", Int. Workshop on the Physics of the Quark-Gluon Plasma, Palaiseau, France, Sept. (2001).

C. Dawson: "Localisation of chirality for domain wall fermion eigenvectors", 1st Joint Meet. of the Nuclear Physicists of the American and Japanese Physical Soc. (HAW01), Maui, USA, Oct. (2001).

M. A. Stephanov: "Phase diagram of QCD", 1st Joint Meet. of the Nuclear Physicists of the American and Japanese Physical Soc. (HAW01), Maui, USA, Oct. (2001).

Y. Aoki: "Quenched domain wall QCD with DBW2 gauge action toward nucleon decay matrix element calculation", 1st Joint Meet. of the Nuclear Physicists of the American and Japanese Physical Soc. (HAW01), Maui, USA, Oct. (2001).

S. A. Bass: "QGP-theory: Status and perspectives", 4th Int. Conf. on the Physics and Astrophysics of

the Quark-Gluon Plasma (ICPAQGP-2001), (Variable Energy Cyclotron Centre), Jaipur, India, Nov. (2001).

S. Jeon: "Particle ratio fluctuations in heavy ion collisions", RHIC Winter Workshop 2002 (RWW02), (Institute of Nuclear Theory), Seattle, USA, Jan. (2002).

O. Jinnouchi, K. Kurita, J. Tojo, N. Saito, H. Enyo, K. Imai, I. Alekseev, D. Svirida, D. Fields, G. Bunce, T. Roser, H. Spinka, H. Huang, Z. Li, W. W. Mackay, G. Mahler, Y. Makdisi, W. McGahern, S. Rescia, A. Deshpande, G. Igo, W. Lozowski, V. Kanavets, S. Dhawan, and V. Hughes: "pC CNI polarimeter at RHIC spin project", 57th Ann. Meet. of Physical Soc. of Japan, Shigaken Kusatsu, Mar. (2002).

Y. Aoki: "Nucleon decay matrix elements for domain-wall fermions", LATTICE 2002: 20th Int. Symp. on Lattice Field Theory, (Massachusetts Institute of Technology), Cambridge, USA, June (2002).

N. Ishii, H. Matsufuru, and H. Suganuma: "The thermal width of the glueball at non-zero temperature", LATTICE 2002: 20th Int. Symp. on Lattice Field Theory, (Massachusetts Institute of Technology), Cambridge, USA, June (2002).

M. Hirai: "Polarized parton distribution functions: AAC analysis", 4th Int. Workshop on Neutrino Factories based on Muon Storage Rings (NuFACT'02), (Imperial College of Science, Technology and Medicine), London, UK, July (2002).

K. Sudo: "Polarized parton distribution in neutrino induced heavy flavor production", 4th Int. Workshop on Neutrino Factories based on Muon Storage Rings (NuFACT'02), (Imperial College of Science, Technology and Medicine), London, UK, July (2002).

N. Ishii, H. Matsufuru, and H. Suganuma: "Glueball properties at finite temperature in SU(3) anisotropic Lattice QCD", YITP Workshop on Thermal Quantum Field Theories and Their Application, (Yukawa Institute for Theoretical Physics, Kyoto University), Kyoto, Aug. (2002).

A. Kiyomichi: "Study of identified charged hadron spectra in Au+Au collisions at $\sqrt{s_{NN}} = 200\,\mathrm{GeV}$ measured by the RHIC-PHENIX experiment", 2002 Fall Meet. of the Physical Soc. of Japan, Tokyo, Sept. (2002).

T. Ikeda, T. Hatsuda, Y. Hatta, and T. Kunihiro: "The quark-number susceptibility near the critical line of the chiral transition in the T-μ plane", 2002 Fall Meet. of the Physical Soc. of Japan, Tokyo, Sept. (2002).

N. Ishii, H. Matsufuru, and H. Suganuma: "The thermal glueball at finite temperature in SU(3) anisotropic lattice QCD", 5th Int. Conf. on Quark Confinement and the Hadron Spectrum, (National Institute for Nuclear Physics and Milano University), Gargnano, Italy, Sept. (2002).

K. Sudo: "D meson production in neutrino DIS as a probe of polarized strange quark distribution", 15th Int. Spin Physics Symp. (SPIN 2002), (Brookhaven National Laboratory), New York, USA, Sept. (2002).

M. Hirai: "Recent status of polarized parton distributions", 15th Int. Spin Physics Symp. (SPIN 2002), Long Island, USA, Sept. (2002).

IX. LIST OF SYMPOSIA

(Jan.–Dec. 2002)

1) RIKEN Winter School - RIB Experiments in the New Millennium
6–11 Jan., Tsunan, RI Beam Science Lab., RIKEN

2) Theory Studies for RHIC-Spin
12 Jan.–5 Apr., New York, USA, RBRC, RIKEN

3) Development and Application of Superconductor Radiation Detector (3rd STJ Workshop)
16–17 Jan., Wako, Image Information Div., RIKEN

4) Reactions of Unstable Nuclei
23–25 Jan., Wako, RI Beam Science Lab., RIKEN

5) 9th RIKEN Symp. on the Theory of Atomic and Molecular Processes: Antimatter Science Using Antiprotons
26–27 Jan., Hayama, Atomic Physics Lab., RIKEN

6) Rare Isotope Physics at Storage Rings
3–8 Feb., Hirschegg, Austria, Beam Physics and Engineering Lab., GSI and RIKEN

7) FFAG Accelerator Workshop: FFAG 02-Versatile Applications and Future Prospects of FFAG Accelerator
13–15 Feb., Tsukuba, Wako, RIKEN and KEK

8) Condensed Matter Studies with Radioactive Ion Beams
21–22 Feb., Wako, Applied Nuclear Physics Lab., RIKEN

9) RHIC Spin Collaboration Meeting VII
22 Feb., New York, USA, RBRC, RIKEN

10) Structure and Property Modifications of Solids by GeV Heavy Ions
4 Mar., Wako, Atomic Physics Lab., RIKEN

11) 6th Studies on Condensed Matter Physics, Atomic Physics, Hyperfine in Biomedical Science Using RIKEN Accelerators
5 Mar., Wako, Applied Nuclear Physics Lab., RIKEN

12) Int. Workshop on Future of Muon Science
7–9 Mar., Tsukuba and Wako, Muon Science Lab., KEK and RIKEN

13) Hadron Structure from Lattice QCD
18–22 Mar., New York, USA, RBRC, RIKEN

14) Baryon Dynamics at RHIC
28–30 Mar., New York, USA, RBRC, RIKEN

15) RIKEN Winter School, Quark-Gluon Structure of the Nucleon & QCD
29–31 Mar., Wako, RBRC and Radiation Lab., RIKEN

16) RHIC Spin Collaboration Meeting VIII
12 Apr., New York, USA, RBRC, RIKEN

17) RHIC Spin Collaboration Meeting IX
22 May, New York, USA, RBRC, RIKEN

18) RHIC Spin Collaboration Meeting X

17 June, New York, USA, RBRC, RIKEN

19) Nuclei in Cosmos
8–12 July, Fujiyoshida, RI Beam Science Lab., CNS and RIKEN

20) New Developments of Radioisotope Tomography Technology in Nuclear Medicine
19 July, Wako, Cyclotron Center, RIKEN

21) RHIC Spin Collaboration Meeting XI
29 July, New York, USA, RBRC, RIKEN

22) Summer Program: Current and Future Directions at RHIC
5–23 Aug., New York, USA, RBRC, RIKEN

23) RHIC Spin Collaboration Meeting XII
16 Sept., New York, USA, RBRC, RIKEN

24) Large-Scale Computations in Nuclear Physics using the QCDOC
26–28 Sept., New York, USA, RBRC, RIKEN

25) RHIC Spin Collaboration Meeting XIII
22 Oct., New York, USA, RBRC, RIKEN

26) Int. Symp. on Bio-Trace Elements 2002
28 Oct.–2 Nov., Wako and Fujiyoshida, Cyclotron Center, RIKEN and Yamanashi Institute of Environmental Sciences

27) Int. Symp. on Frontiers of Collective Motions (CM2002)
6–9 Nov., Aizu, RI Beam Science Lab., RIKEN, University of Aizu, and CNS

28) EIC Workshop Electron Beam Polarimetry for the Electron Ion Collider at BNL
8 Nov., New York, USA, RBRC, RIKEN

29) Int. Symp. on Physics of Unstable Nuclei (ISPUN02)
20–25 Nov., Halong Bay, Vietnum, RI Beam Science Lab., RIKEN and Institute for Nuclear Science & Technique, Vietnum

30) High Energy Density Matter and Beam Physics/Engineering
13 Dec., Wako, Beam Physics and Engineering Lab., University of Tokyo

31) Joint Workshop on Resonances in Physics, Chemistry and Biology
18–20 Dec., Hayama, Atomic Physics Lab., JSPS-NSF and RIKEN

32) RHIC Spin Collaboration Meeting XIV
20 Dec., New York, USA, RBRC, RIKEN

X. LIST OF SEMINARS

(Jan.–Dec. 2002)

Radiation Lab., RI Beam Science Lab., Applied Nuclear Physics Lab., and Beam Technology Div.

1) P. Ring, Technische Universität München (Germany), 14 Feb.
"Relativistic mean field description of exotic nuclear structure"

2) U. Garg, University of Notre Dame (USA), 22 Feb.
"Compressional-mode giant resonances and the nuclear incompressibility"

3) B. A. Brown, Michigan State University (USA), 9 Apr.
"Spectroscopic factors in light nuclei-building blocks of the shell model"

4) Z. Li, RBRC (USA), 6 June
"Novel Si strip detectors for the PHENIX upgrade"

5) Y. Akaishi, KEK (Tsukuba), 17 June
"Nuclear $\overline{\mathrm{K}}$ bound states in light nuclei: A new paradigm in nuclear physics"

6) W. Shen, Shanghai Institute of Nuclear Research (China), 28 June
"Possible exotic structure in light proton rich nuclei around A $\sim$ 30"

7) Z. Fülöp, ATOMKI (Hungary), 2 July
"Anomalies in ultra-low energy collisions between nuclei"

8) M. Ozima, University of Tokyo (Tokyo), 23 July
"Suggestions from meteorite science to nuclear physics"

9) M. Akaogi, Gakushuin University (Tokyo), 23 July
"Phase transition of mantle minerals under very high pressure"

10) T. Ohtsubo, Niigata University (Niigata) 25 July
"Direct observation of bound state beta decay of bare 207Tl at FRS-ESR in GSI"

11) S.A. Bass, Duke University/RBRC (USA), 12 Sept.
"Physics of relativistic heavy ion collisions with the parton cascade model"

12) Y. Ye, Peking University (China), 26 Sept.
"Experimental nuclear and particle physics in Peking University"

13) S. Hofmann, GSI (Germany), 1 Oct.
"Synthesis and properties of superheavy elements"

14) I. Johnson, Lawrence Berkeley National Laboratory (USA), 16 Oct.
"Photon production and detection techniques in heavy ion collisions"

15) T. Koike, SUNY Stony Brook (USA), 12 Nov.
"Spontaneous symmetry breaking in rotating nuclei: Chiral doublet bands"

16) V. I. Zagrebaev, JINR/FLNR (Russia), 16 Dec.
"Fusion-fission dynamics of heavy nuclear systems and perspectives of superheavy element formation"

17) A. Mengoni, CERN-EP (Switzerland)/ENEA-Bologna (Italy), 18 Dec.
"Performance and experimental programme of the new neutron time-of-flight facility (n_TOF) at CERN"

18) K. Tatsumi, Stanford Linear Accelerator Center (USA), 24 Dec.
"GEANT4: A toolkit for the simulation of the passage of particles through matter"

Radiation Lab.

1) M. Ishida, Tokyo Institute of Technology (Tokyo), 22 Jan.
"Confirmation of σ (450–600) in excited Υ-decays and other $\pi\pi$-production processes"

2) H. Suganuma, Tokyo Institute of Technology (Tokyo), 26 Feb.
"Hadron physics based on lattice QCD"

3) K. Sudoh, RIKEN (Wako), 9 Apr.
"Charmed hadron production in charged current DIS and polarized PDF's"

4) D. Yu-Bing, Institute of High Energy Physics (China), 16 Apr.
"Meson cloud effect on resonance transition properties"

5) T. Hirano, University of Tokyo (Tokyo), 21 May
"Hydrodynamic analysis of relativistic heavy-ion

collisions at the RHIC energy"

6) Y. Tsue, Kochi University (Kochi), 28 May
"Variational approach to collective isospin rotations of a quantum meson field"

7) H. Fujii, University of Tokyo (Tokyo), 4 June
"Penetration of a high energy QQ-bar bound state through random SU(N) color field"

8) K. Itakura, RBRC (USA), 18 June
"Geometric scaling at small x"

9) N. Ukegawa, University of Tsukuba (Tsukuba), 18 June
"Recent status of tevatron CDF"

10) C. Nonaka, RIKEN (Wako), 9 July
"Study of the finite density state based on SU(2) lattice QCD"

11) N. Ishii, RIKEN (Wako), 18 July
"Glueballs at finite temperature from anisotropic lattice QCD: Mass reduction and/or thermal width"

12) H. Akimoto, Waseda University (Tokyo), 18 July
"Physics from the polarized positron-electron collider at SLAC"

13) A. Bass, Duke University/RBRC (USA), 12 Sept.
"Physics of relativistic heavy ion collisions with the parton cascade model"

14) W. Vogelsang, RBRC (USA), 24 Sept.
"QCD and the spin structure of the nucleon"

15) T. Sugihara, RBRC (USA), 15 Oct.
"Introduction to density matrix renormalization group"

16) K. Fukushima, University of Tokyo (Tokyo), 26 Nov.
"Spectral functions in the sigma channel near the critical end point"

17) A. Hosaka, RCNP, Osaka University (Suita), 29 Nov.
"Chiral symmetry in baryon physics"

18) T. Mibe, RCNP, Osaka University (Suita), 29 Nov.
"Measurement of polarization observables in the ϕ-meson photoproduction with linearly polarized photons"

19) K. Yokokawa, University of Tokyo (Tokyo), 3 Dec.
"Simultaneous softening of σ and ρ mesons associated with chiral restoration"

20) Y. Sumino, Tohoku University (Sendai), 20 Dec.
"Understanding heavy quarkonium systems in perturbative QCD"

21) T.-A. Shibata, Tokyo Institute of Technology (Tokyo), 20 Dec.
"HERMES results on generalized GDH sum rule and quark-hadron duality"

22) T. Abe, Colorado University/Stanford Linear Accelerator Center (USA), 24 Dec.
"Electroweak physics at SLD"

23) K. Hagiwara, KEK (Tsukuba), 24 Dec.
"On electroweak precision measurements at SLC and LEP"

RI Beam Science Lab.

1) K. Ikeda, RIKEN (Wako), 23 Feb.
"Pion-nucleon coupling and the mean-field theory"

2) H. Toki, RCNP, Osaka University (Suita), 23 Feb.
"Surface pion condensation in finite nuclei"

3) S. Hirenzaki, Nara Women's University (Nara), 6 Mar.
"Pionic atoms on unstable nuclei"

4) K.Itahashi, Tokyo Institute of Technology (Tokyo), 6 Mar.
"Experiments on exotic atoms and nuclei"

5) N. Tajima, Fukui University (Fukui), 18 Mar.
"Hartree-Fock + BCS approach to unstable nuclei with the Skyrme force"

6) Y. Akaishi, KEK (Tsukuba), 1 June
"Neutron-rich nuclei including hyperons"

7) I. Hamamoto, Lund University (Sweden), 8 Aug.
"Some topics in the ground-state density of unstable nuclei"

8) T. Tatsumi, Kyoto University (Kyoto), 24 Aug.
"Modern aspect of pion condensation"

Applied Nuclear Physics Lab.

1) H. Akai, Osaka University (Suita), 4 Oct.
"Magnetic semiconductor and hyperfine interaction"

2) T. Ohono, Computational Materials Science Cen-

ter, NIMS (Tsukuba), 3 Oct.
"Quantum mechanical analysis of adatoms dynamics on silicon surfaces"

3) N. Takahashi, Osaka Gakuin University (Suita), 4 Dec.
"Extraction of radioactive ions from superfluid He: A novel method for the RI beam production"

Atomic Physics Lab.

1) R. H. Schuch, Stockholm University (Sweden), 18 Jan.
"Recombination for tests of QED and diagnostics of solar flares"

2) T. Meguro, RIKEN (Wako), 5 Feb.
"Nanoscale modification of surface electronics states by HCI impact"

3) L. Ratliff, National Institute of Standards and Technology (USA), 6 Mar.
"Modification of mica and graphite surfaces by highly charged ion impact"

4) S. Tomita, Institute of Physics and Astronomy, University Aarhus (Denmark), 21 May
"Fragmentation of biomolecules and clusters"

5) R. Shimizu, Osaka Institute of Technology (Osaka), 20 June
"Development of cathodes as an origin of surface science"

6) Y. Huang, Institute of High Energy Physics, Chinese Academy of Sciences (China), 23 July
"Pulsed ultrasound excited by heavy ion: A first experiment and a preliminaly theoretical consideration"

7) T. Nishimura, University of Rome (Italy), 27 Aug.
"Vibration excitation of methane by positron impact"

8) H. Suno, Kansas State University (USA), 13 Sept.
"Three-body recombination of ultracold atoms"

9) J.-M. Li, Chinese Academy of Sciences/Tsinghua University (China), 9 Oct.
"Basic study in cluster physics"

10) M. Inokuti, Argonne National Laboratory (USA), 21 Oct.
"Principles of radiation physics: A monograph in preparation"

11) K. Tokesi, ATOMKI (Hungary), 20 Nov.
"Hollow stoms in microcapillaries"

12) R. Srivastava, Indian Institute of Technology Roorkee (India), 27 Nov.
"Electron excitation of the D states in alkaline earth atoms"

13) C. M. Surko, University of California (USA), 16 Dec.
"Physics with low-energy positron plasmas and trap-based beams"

Muon Science Lab.

1) M. Ericson, Institut de Physique Nucléaire de Lyon (France), 11 Oct.
"Chiral symmetry in a dense medium"

Beam Physics and Engineering Lab.

1) H. Okamoto, Hiroshima University (Higashi-hiroshima), 17 Jan.
"Crystal beam"

2) M. Hamagaki, RIKEN (Wako), 24 Jan.
"Development of electron-beam-excited plasma and its application"

3) T. Hara, Toyota Technological Institute (Nagoya), 5 Apr.
"Development of small scale X-ray laser"

4) A. Sakumi, RIKEN (Wako), 28 June
"Experimental study for the interaction with heavy ion beam and laser-produced plasma"

5) D. Möhl, CERN (Switzerland), 25 Oct.
"An electron-ion collider using a 1D ordered ions"

6) A. Smirnov, JINR (Russia), 20 Dec.
"Simulation study of beam ordering"

RIBF Project Office, Beam Dynamics Div., and Beam Tecnology Div.

1) G. Berg, Kernfysisch Versneller Instituut (The Netherlands), 13 Feb.
"Electro-magnetic devices in nuclear experiments and facilities"

2) T. Mito, National Institute for Future Science (Toki), 15 May
"He cooling system for the LHD"

3) S. B. Vorojtsov, JINR (Russia)/RIKEN (Wako), 2 July
"Beam space charge simulation in RIKEN SRC"

4) J. Nolen, Argonne National Laboratory (USA), 28 Aug.
"Overview of the U.S. rare isotope accelerator proposal"

5) P. R. Sarma, Variable Energy Cyclotron Centre (India)/RIKEN (Wako), 30 Sept.
"Improvement of momentum resolution-conventional method and a new technique"

6) M. Kumada, National Institute of Radiological Sciences (Chiba), 17 Oct.
"Applications of the recently developed super-high field permanent magnets to accelerators"

7) K. Sato, RCNP, Osaka University (Suita), 8 Nov.
"A new method to solve motions of particles using spiral acceleration orbits in isochronous cyclotrons"

Radioisotope Technology Div.

1) N. Suzuki, University of Tokyo (Tokyo), 18 Jan.
"Radiosensitive mechanisms in radiation induced rapid cell death"

2) K. Suzuki, Nagasaki University (Nagasaki), 18 Jan.
"Molecular mechanism of radiation stress response"

3) E. Drobetsky, University de Montreal (Canada), 24 Apr.
"The role of the p53 tumour suppressor in the cellular response to UV-induced genotoxic stress"

4) M. Durante, University of Naples Federico II (Italy), 7 May
"Kinetics of formation of chromosome aberrations"

5) Y. Ogra, Chiba University (Chiba), 21 June
"Speciation of bio-trace elements by mass spectrometry"

6) K. Matsumoto, BSI, RIKEN (Wako), 16 Aug.
"Prefrontal mechanisms for controlled behavior"

RIKEN BNL Research Center

1) F. Braghin, University of Sao Paulo (Brasil), 11 Jan.
"Expanding configurations in the $\lambda\phi^4$ model"

2) H.-C. Chen, University of Chicago (USA), 15 Jan.
"Universal extra dimensions"

3) V. Kazakov, L'Ecole Normal Superieure (France), 16 Jan.
"Berezinskii-Kosterlitz-Thouless vortices on random surfaces and integrable matrix quantum mechanics"

4) D. Son, Columbia University (USA), 17 Jan.
"Pion propagation near the QCD chiral phase transition"

5) C. Anastasiou, Stanford Linear Accelerator Center (USA), 23 Jan.
"Two-loop corrections for QCD scattering"

6) U. Trittmann, Ohio State University (USA), 25 Jan.
"Simulation of dimensionally reduced SYM-Chern-Simons theory"

7) J. Kalinowski, Warsaw University (Poland), 30 Jan.
"Determination of SUSY parameters at $e^+ e^-$ linear colliders"

8) B. Schlittgen, Yale University (USA), 31 Jan.
"Colour-flavour transformation for the special unitary group"

9) K. Tuchin, Institute for Nuclear Theory (USA), 1 Feb.
"Inclusive gluon production in DIS at high parton densities"

10) C. Oleari, Madison University (USA), 6 Feb.
"Higgs + 2 jets via gluon fusion: LHC and VLHC"

11) M. Gyulassy, Columbia University (USA), 7 Feb.
"HBT at RHIC"

12) G. Nayak, Los Alamos National Laboratory (USA), 8 Feb.
"Non-equilibrium QCD phase at RHIC"

13) F. Berruto, Boston University (USA), 20 Feb.
"A study of the 't Hooft model with the overlap Dirac operator"

14) O. Philipsen, Laboratory for Nuclear Science, MIT (USA), 22 Feb.
"Non-perturbative gluon mass and heavy quark physics"

15) I. Campos, Center for Data Intensive Computing, BNL (USA), 6 Mar.
"Numerical investigation of the 3D Hubbard model in a PC cluster"

16) E. Shuryak, SUNY Stony Brook (USA), 7 Mar.
"How quantum mechanics of the glue can help us with the RHIC puzzles"

17) H. Weigert, University of Regensburg (Germany), 14 Mar.
"Energy dependence of QCD cross sections: Saturation effects from HERA to RHIC & LHC"

18) T. Hirano, University of Tokyo (Tokyo), 15 Mar.
"The effect of early chemical freeze out on radial & elliptic flow from a full 3D hydrodynamic model"

19) H.-J. Drescher, New York University (USA), 22 Mar.
"Highest energy cosmic rays"

20) D. Rainwater, Fermi National Accelerator Laboratory (USA), 27 Mar.
"LHC Higgs physics: Recent developments"

21) J. Kodaira, Hiroshima University (Higashi-hiroshima), 11 Apr.
"B meson light-cone distribution amplitudes in heavy quark effective theory"

22) U. M. Heller, School of Computational Science & Information Technology, Florida State University (USA), 12 Apr.
"QCD thermodynamics with improved staggered quarks"

23) K. Itakura, RBRC/BNL (USA), 18 Apr.
"Geometric scaling above the saturation scale"

24) S. Gottlieb, Indiana University/Fermi National Accelerator Laboratory (USA), 1 May
"Spectrum and f_B with three dynamical flavors from the MILC Collaboration"

25) A. Signer, University of Durham (UK), 8 May
"Unstable particles: An effective field theory approach"

26) B. Gelman, University of Maryland (USA), 17 May
"What can we learn about the nucleon-nucleon interaction from large N_c QCD"

27) G. Landsberg, Brown University (USA), 22 May
"Black hole production at future colliders and beyond"

28) P. Levai, RMKI (Hungary), 24 May
"Diagnostics of hot dense matter in URHIC"

29) T. Csorgo, KFKI (Hungary), 28 May
"Inflation of fireballs and the mt scaling of HBT Radii"

30) G. Aarts, Ohio State University (USA), 31 May
"Transport coefficients from the lattice?"

31) J. Lenaghan, Niels Bohr Institute (Denmark), 7 June
"Pion production and saturation in proton-nucleus collisions"

32) Y. Shamir, Tel Aviv University (Israel), 19 June
"Non-perturbative BRST invariance and what it might be good for"

33) C. Nonaka, RIKEN (Wako), 20 June
"Study of the finite density state based on SU(2) lattice QCD"

34) S. Aoki, University of Tsukuba (Tsukuba), 10 July
"Non-perturbative determination of c_SW in three-flavor dynamical QCD"

35) A. Kusenko, UCLA (USA), 11 July
"CP violation and baryogenesis"

36) S. J. Brodsky, Stanford Linear Accelerator Center (USA), 12 July
"The novel physics of ultraperipheral collisions"

37) C. Kao, University of Oklahoma (USA), 12 July
"Indirect search for neutralino dark matter with high energy neutrinos"

38) V. Serbo, Novosibirsk State University (Russia), 26 July
"Strong field effects in lepton pair production from relativistic nuclear collisions"

39) E. Mottola, Los Alamos National Laboratory (USA), 2 Aug.
"Gravitational condensate stars: An alternative to black holes"

40) Y. Hatta, BNL (USA), 19 Sept.
"Universality, the QCD critical point and the quark number susceptibility"

41) B. Kopeliovich, Max-Plank-Institut (Germany), 20 Sept.
"Collisions at RHIC: View from the light cone"

42) K. Fujikawa, University of Tokyo (Tokyo), 25 Sept.
"Supersymmetry on the lattice and the Leibniz

rule"

43) D. Kosower, RBRC (USA), 10 Oct.
"Quark number susceptibility near tricritical and critical end points"

44) J. Kapusta, University of Minnesota (USA), 22 Oct.
"Baryon/anti-baryon production at high energy density and at RHIC"

45) F. Sannino, NORDITA (Denmark), 23 Oct.
"Relativistic massive vector condensation"

46) S. Thomas, Stanford University (USA), 30 Oct.
"Gauge mediation with split messengers"

47) A. Freund, University of Regensburg (Germany), 31 Oct.
"Saturation and the EIC: Looking for good observables"

48) A. Belitsky, University of Maryland (USA), 1 Nov.
"Parton distributions are parton densities"

49) W. Skiba, Yale University (USA), 6 Nov.
"Little Higgses from an antisymmetric condensate"

50) K. Splittorff, SUNY Stony Brook (USA), 8 Nov.
"Fluctuation induced critical behavior and explicit breaking of Lorentz invariance"

51) V. Koch, Lawrence Berkeley National Laboratory (USA), 13 Nov.
"Fluctuations and equilibration"

52) D. Pirjol, Johns Hopkins University (USA), 13 Nov.
"Factorization in B decays from the soft-collinear effective theory"

53) G. Carter, University of Washington (USA), 15 Nov.
"Axial coupling of the quark"

54) T. DeGrand, University of Colorado (USA), 20 Nov.
"The kaon B parameter using overlap fermions"

55) D. Lin, University of Southampton (UK), 4 Dec.
"$K \to 2\pi$ decays at next-to-leading order in the chiral expansion on finite volumes"

56) T. Sugihara, RBRC (USA), 5 Dec.
"Introduction to density matrix renormalization group"

57) S. Fortunato, Bielefeld University (Germany), 6 Dec.
"Percolation and critical behaviour in spin models and SU(N) gauge theories"

58) R. Kitano, Institute for Advanced Study (USA), 11 Dec.
"Calculation of muon electron conversion rate in nuclei"

59) M. Strickland, Vienna Technical University (Austria), 13 Dec.
"Two-loop hard thermal loop perturbation theory"

60) K. Orginos, RBRC (USA), 17 Dec.
"Nucleon structure functions on the lattice"

61) M. Oswald, Niels Bohr Institute (Denmark), 19 Dec.
"Effective Yang-Mills theory at high temperatures"

62) D. Teaney, BNL (USA), 20 Dec.
"Impact dependence of saturation scale"

XI. LIST OF PERSONNEL

RARF/RIBF Project Head Office

Yorinao INOUE (Director)
Masayasu ISHIHARA (Project Adviser)

Cyclotron Group

Yasushige YANO*1

Beam Dynamics Team

Nobuhisa FUKUNISHI
Osamu KAMIGAITO
Naruhiko SAKAMOTO
Akira GOTO*2
Jun-ichi OHNISHI
Masanori WAKASUGI

Beam Technology Team

Masaki FUJIMAKI
Eiji IKEZAWA
Tadashi KAGEYAMA
Shigeo KOHARA
Makoto NAGASE
Kiyoshi OGIWARA
Jiro FUJITA
Naohito INABE
Masayuki KASE*2
Kosuke MORITA
Takahide NAKAGAWA
Toshiya TANABE

RIB Generator Team

Toshiyuki KUBO*2
Atsushi YOSHIDA
Toshimi SUDA

Bio-medical Applications Team

Shuichi ENOMOTO
Kuniko MAEDA
Fumio YATAGAI*2
Masako IZUMI
Kazuya TAKAHASHI

Cryogenics Team

Kumio IKEGAMI*2
Hiroki OKUNO
Masao OHTAKE

Storage Ring Team

Takeshi KATAYAMA*2
Keiko KUMAGAI
Masahiro OKAMURA
Tadashi KOSEKI
Masato NAKAMURA
Tamaki WATANABE

Experimental Sytem Group

Isao TANIHATA*1

Nuclear Reaction Team

Eiji IDEGUCHI
Toshiyuki KUBO
Shunji NISHIMURA
Toshimi SUDA
Koichi YOSHIDA
Alexei A. KORCHENINNIKOV
Kouji MORIMOTO
Akira OZAWA
Isao TANIHATA*2
Atsushi YOSHIDA

Nuclear Structure Team

Takashi ICHIHARA
Tohru MOTOBAYASHI*2
Takashi KISHIDA
Yasushi WATANABE

Low Energy Team

Koichiro ASAHI*2
Hirohiko SHIMIZU
Jiro MURATA
Yoshio KOBAYASHI
Hideki UENO

Atomic and Other Science Team

Tomoko ABE
Tokihiro IKEDA
Yasuyuki KANAI
Takao KOJIMA
Yoichi NAKAI
Michiharu WADA
Shuichi ENOMOTO
Tadashi KAMBARA
Yoshio KOBAYASHI
Yukari MATSUO
Hitoshi OYAMA
Yasunori YAMAZAKI*2

Experiment Support Team

Tadashi KAMBARA*2
Teiichiro MATSUZAKI
Yasuyuki KANAI
Kosuke MORITA

Network Support Team

Takashi ICHIHARA*2
Atsushi YOSHIDA
Yasushi WATANABE
Koichi YOSHIDA

Safety Group

Yoshitomo UWAMINO*1
Sachiko ITO
Shin FUJITA

Planning and Coordination Group

Norio OJIMA*1

Planning and Coordination Office

Takashi EMOTO
Shouko MATSUDA
Shigeo NUMATA
Kenji SATO
Mieko KOGURE
Toshiko NAKAMURA
Norio OJIMA*3
Haruhiro TOKUOKA

Steering Committee

Koichiro ASAHI
Akira GOTO
Takashi ICHIHARA
Tadashi KAMBARA
Takeshi KATAYAMA
Teiichiro MATSUZAKI
Isao TANIHATA
Yasunori YAMAZAKI*4
Fumio YATAGAI
Hideto EN'YO
Fumio HANAOKA
Masahiko IWASAKI
Masayuki KASE
Kazuo MAKISHIMA
Tohru MOTOBAYASHI
Yoshitomo UWAMINO
Yasushige YANO
Shigeo YOSHIDA

*1 Group Director, *2 Team Leader, *3 Head, *4 Chairperson

Cosmic Radiation Laboratory

Head

Kazuo MAKISHIMA

Members

Hiroshi KATO
Hiromasa MIYASAKA*1
Mitsuhiro KOHAMA*2
Kazutaka YAMAOKA*2
Toru TAMAGAWA
Yukikatsu TERADA*1
Ikuya SAKURAI*2

*1 Special Postdoctoral Researcher
*2 Contract Researcher

Visiting Members

Yasushi FUKAZAWA (Dept. Phys., Hiroshima Univ.)
Tateo GOKA (NASDA)
Soojing HONG (Coll. Sci. Technol., Nihon Univ.)
Hokuto INOUE (ISAS)
Madoka KAWAHARADA (Dept. Phys., Univ. Tokyo)
Satoshi KAWASOE (Dept. Phys., Hiroshima Univ.)
Yoshihito KOBAYASHI (ISAS)
Motohide KOKUBUN (Dept. Phys., Univ. Tokyo)
Hideki KOSHIISHI (NASDA)
Jun'ichi KOTOKU (Dept. Phys., Univ. Tokyo)
Haruhisa MATSUMOTO (NASDA)
Takefumi MITANI (ISAS)
Masanori MORI (Dept. Phys., Saitama Univ.)
Mio MURAKAMI (Dept. Phys., Univ. Tokyo)
Motoki NAKAJIMA (Coll. Sci. Technol., Nihon Univ.)
Kazuhiro NAKAZAWA (ISAS)
Masanori OHHO (Dept. Phys., Hiroshima Univ.)
Yuu OKADA (Dept. Phys., Univ. Tokyo)
Tadayuki TAKAHASHI (ISAS)

Radiation Laboratory

Head

Hideto EN'YO

Members

Takashi ICHIHARA
Atsushi TAKETANI
Yasushi WATANABE
Satoshi YOKKAICHI*1
Masanori HIRAI*2
Osamu JINNOUCHI*2
Kenichi NAITO*2
Tsuguchika TABARU*2
Vladimir RYKOV*2
Kazumi HASUKO*2
Kazutaka SUDO*2
Yoshie OTAKE
Kiyoshi TANIDA
Jiro MURATA*1
Junji TOJO*1
Noriyoshi ISHII*2
Yutaka MIZOI*2
Kensuke OKADA*2
Hiroaki ONISHI*2
Johann HEUSER*2
Akio KIYOMICHI*2

*1 Special Postdoctoral Researcher
*2 Contract Researcher

Visiting Members

Minoru ADACHI (Fac. Sci., Tokyo Inst. Technol.)
Yasuyuki AKIBA (KEK)
Igor ALEKSEEV(Phys. Dept., BNL, USA)
Yoshiaki ANDO (Coll. Sci., Rikkyo Univ.)
Nori AOI (Dept. Phys., Grad. Sch. Sci., Univ. Tokyo)

Masato ASAI (JAERI)
Hiroyasu ASAMI (KEK)
Masayuki ASAKAWA (Fac. Sci., Kyoto Univ.)
Thomas BAUMANN (Natl. Supercond. Cycl. Lab., Michigan State Univ., USA)
Daniel BAZIN (Natl. Supercond. Cycl. Lab., Michigan State Univ., USA)
F. A. BECK (CRN, France)
Wolfgang BENTZ (Dept. Phys., Grad. Sch. Sci., Univ. Tokyo)
Hyong Chan BHANG (Dept. Phys., Seoul Natl. Univ., Korea)
R. BROGLIA (Univ. Milano, Italy)
Melynda BROOKS (LANL, USA)
Muriel Jane BURWARD-HOY (Dept. Phys., State Univ. New York, Stony Brook, USA)
Rick CASTEN (Phys. Dept., BNL, USA)
Tatsuya CHUJO (Phys. Dept., BNL, USA)
Gianluca COLO (Univ. Milano, Italy)
Norman CRIST (Columbia Univ., USA)
Zsolt DOMBRÁDI (Inst. Nucl. Res., Hung. Acad. Sci., Hungary)
Zoltan ELEKES (Inst. Nucl. Res., Hung. Acad. Sci., Hungary)
Hubert FLOCARD (Div. Phys. Theor., Inst. Phys. Nucl., France)
Yoshihide FUCHI (KEK)
Hirotsugu FUJII (Grad. Sch. Arts Sci., Univ. Tokyo)
Kazuo FUJIKAWA (Fac. Sci., Univ. Tokyo)
Mitsunori FUKUDA (Grad. Sch. Sci., Osaka Univ.)
Tomokazu FUKUDA (KEK)
Zsolt FÜLÖP (Inst. Nucl. Res., Hung. Acad. Sci., Hungary)
Kazuyoshi FURUTAKA (JAERI)
Janos GAL (Inst. Nucl. Res., Hung. Acad. Sci., Hungary)
Adrian GELBERG (Köln Univ., Germany)
Yasuyuki GONO (Fac. Sci., Kyushu Univ.)
Ikuko HAMAMOTO (Lund Inst. Technol., Univ. Lund, Sweden)
Tetsuo HATSUDA (Fac. Sci., Univ. Tokyo)
Naoki HAYASHI (JAERI)
Arata HAYASHIGAKI (Dept. Phys., Grad. Sch. Sci., Univ. Tokyo)
Kenichi HIKASA (Grad. Sch. Sci., Tohoku Univ.)
Tesufumi HIRANO (Dept. Phys., Grad. Sch. Sci., Univ. Tokyo)
Kensuke HOMMA (Fac. Sci., Hiroshima Univ.)
Hisashi HORIUCHI (Dept. Fund. Sci., Fac. Integr. Human Stud., Kyoto Univ.)
Tomohiro HOTTA (Grad. Sch. Arts Sci., Univ. Tokyo)
Munetake ICHIMURA (Grad. Sch. Arts Sci., Univ. Tokyo)
Kazuo IEKI (Coll. Sci., Rikkyo Univ.)
Kenichi IMAI (Fac. Sci., Kyoto Univ.)
Michiko IMOTO (Lab. Phys., Coll. Sci. Technol., Nihon Univ.)
Tetsuro ISHII (JAERI)
Kenta ITABASHI (Tokyo Inst. Technol.)
Masahiko IWASAKI (Tokyo Inst. Technol.)
Hideaki IZUMI (Grad. Sch. Sci., Osaka Univ.)
Genming JIN (Inst. Modern Phys., Chin. Acad. Sci., China)
Kaori KAKI (Fac. Sci., Shizuoka Univ.)
Gabor KALINKA (Inst. Nucl. Res., Hung. Acad. Sci., Hungary)
Jirota KASAGI (Lab. Nucl. Sci., Tohoku Univ.)
Seigo KATO (Fac. Ed., Yamagata Univ.)
Jong Chan KIM (Dept. Phys., Seoul Natl. Univ., Korea)
Edouard KISTENEV (Phys. Dept., BNL, USA)
Yuichiro KIYO (Grad. Sch. Sci., Tohoku Univ.)
Jirou KODAIRA (Fac. Sci., Hiroshima Univ.)
Yuji KOIKE (Fac. Sci., Niigata Univ.)
Shunzo KUMANO (Fac. Sci. Eng., Saga Univ.)
Teiji KUNIHIRO (YITP, Kyoto Univ.)
Hideshige KUSAKARI (Fac. Ed., Chiba Univ.)
Guanhua LIU (Inst. Modern Phys., Chin. Acad. Sci., China)
Zhong LIU (Inst. Modern Phys., Chin. Acad. Sci., China)

Earle LOMON (Massachusetts Inst. Technol., USA)
Serguei LOUKIANOV (Flerov Lab. Nucl. React., JINR, Russia)
Yajun MAO (Phys. Dept., BNL, USA)
Satoshi MATSUDA (Dept. Fund. Sci., Fac. Integr. Human Stud., Kyoto Univ.)
Tetsuo MATSUI (Grad. Sch. Arts Sci., Univ. Tokyo)
Kenichi MATSUYANAGI (Fac. Sci., Kyoto Univ.)
Alberto MENGONI (Phys. Div., ENEA, Italy)
Yasuo MIAKE (Inst. Phys., Univ. Tsukuba)
Shoichi MIDORIKAWA (Fac. Eng., Aomori Univ.)
Byung-Joo MIN (Korea Atom. Energy Res. Inst., Korea)
Shiro MITARAI (Fac. Sci., Kyushu Univ.)
Masanori MIYAMA (Fac. Sci., Tokyo Metrop. Univ.)
Hiroari MIYATAKE (KEK)
Peter MOLLER (LANL, USA)
Toshiyuki MORII (Fac. Human Dev., Kobe Univ.)
Tsuneyasu MORIKAWA (Fac. Sci., Kyushu Univ.)
Shunpei MORINOBU (Fac. Sci., Kyushu Univ.)
Ben R. MOTTELSON (NORDITA, Denmark)
Ludwig MUELLER (Phys. Dept., Univ. Padoba, Italy)
Takeshi MURAKAMI (Natl. Inst. Radiol. Sci.)
Hiroyuki MURAKAMI (Coll. Sci., Rikkyo Univ.)
Ryotaro MUTO (Fac. Sci., Kyoto Univ.)
Tomofumi NAGAE (KEK)
Yasuki NAGAI (RCNP, Osaka Univ.)
Shoji NAGAMIYA (KEK)
Mitsuo NAKAJIMA (Interdiscip. Grad. Sch. Sci. Eng., Tokyo Inst. Technol.)
Shogo NAKAMURA (Fac. Ed., Yokohama Natl. Univ.)
Takashi NAKAMURA (Tokyo Inst. Technol.)
Masanobu NAKAMURA (Fac. Sci., Kyoto Univ.)
Shintaro NAKAYAMA (Fac. Integr. Arts Sci., Univ. Tokushima)
Takashi NIIZEKI (Tokyo Kasei Univ.)
Jun NISHIMURA (Cen. Integr. Res. Sci. Eng., Nagoya Univ.)
Chiho NONAKA (Fac. Sci. Hiroshima Univ.)
Tetsuo NORO (RCNP, Osaka Univ.)
Atsuko ODAHARA (Nishinippon Inst. Technol.)
Masao OGAWA (Tokyo Inst. Technol.)
Akio OGAWA (Phys. Dept., BNL, USA)
Kazuto OSHIMA (Gunma Natl. Coll. Technol.)
Shigemi OHTA (KEK)
Hiroyuki OKAMURA (Fac. Sci., Saitama Univ.)
Ryutaro OOISHI (Inst. Phys., Univ. Tsukuba)
Hikonojo ORIHARA (Cycl. Radioisot. Cen., Tohoku Univ.)
Masumi OSHIMA (JAERI)
Haruhiko OUTA (KEK)
Qiangyan PAN (Inst. Modern Phys., Chin. Acad. Sci., China)
Edward PASCUZZI (Phys. Dept., BNL, USA)
Iouri PENIONZHKEVICH (Flerov Lab. Nucl. React., JINR, Russia)
Dimitra PIERROUTSAKOU (Sezione Napoli (INFN), Italy)
Zhongzhou REN (Nanjing Univ., China)
Koichi SAITO (Tohoku Pharm. Univ.)
Akito SAITO (Coll. Sci., Rikkyo Univ.)
Naohito SAITO (Fac. Sci., Kyoto Univ.)
Harutaka SAKAGUCHI (Fac. Sci., Kyoto Univ.)
Fuminori SAKUMA (Fac. Sci., Kyoto Univ.)
Hiroyuki SAKURAGI (Fac. Sci., Osaka City Univ.)
Hiroyoshi SAKURAI (Dept. Phys., Grad. Sch. Sci., Univ. Tokyo)
Shoichi SASAKI (Fac. Sci., Univ. Tokyo)
Hikaru SATO (KEK)
Hiroki SATO (Fac. Sci., Kyoto Univ.)
Susumu SATO (Inst. Phys., Univ. Tsukuba)

Shinya SAWADA (KEK)
Markus SCHAEFER (Phys. Inst., Univ. Goettingen, Germany)
Andreas SCHAFER (Inst. Theor. Phys., Univ. Regensburg, Germany)
Wolf-Dieter SCHMIDT-OTT (Phys. Inst., Univ. Goettingen, Germany)
Bo SEDERWALL (Royal Inst. Technol., Sweden)
Michiko SEKIMOTO (KEK)
Toshiaki SHIBATA (Tokyo Inst. Technol.)
Kenta SHIGAKI (KEK)
Hajime SHIMIZU (Fac. Ed., Yamagata Univ.)
Yoshifumi SHIMIZU (Fac. Sci., Kyushu Univ.)
Tadashi SHIMODA (Grad. Sch. Sci., Osaka Univ.)
Cosimo SIGNORINI (Phys. Dept., Univ. Padoba, Italy)
Lucian STROE (Phys. Dept., Univ. Padoba, Italy)
Masahiko SUGAWARA (Chiba Inst. Technol.)
Toru SUGITATE (Fac. Sci., Hiroshima Univ.)
Yasuyuki SUZUKI (Fac. Sci., Niigata Univ.)
Katsuhiko SUZUKI (Dept. Phys., Grad. Sch. Sci., Univ. Tokyo)
Toshio SUZUKI (Fac. Eng., Fukui Univ.)
Yasuhisa TAJIMA (Cycl. Radioisot. Cen., Tohoku Univ.)
Eiichi TAKADA (Natl. Inst. Radiol. Sci.)
Tadayuki TAKAHASHI (Inst. Space Astronaut. Sci.)
Hiroki TAKEMOTO (JAERI)
Noboru TAKIGAWA (Grad. Sch. Sci., Tohoku Univ.)
Makoto TAKIZAWA (Showa Coll. Pharm. Sci.)
Atsushi TAMII (Fac. Sci., Univ. Tokyo)
Masahiko TANAKA (KEK)
Atsushi TANOKURA (Fac. Sci. Technol., Sophia Univ.)
Atsuki TERAKAWA (Cycl. Radioisot. Cen., Tohoku Univ.)
Takeshi TOYAMA (KEK)
Hidenori TOYOKAWA (JASRI)
Tsuneo UEMATSU (Dept. Fund. Sci., Fac. Integr. Human Stud., Kyoto Univ.)
Masahiro UNO (MEXT)
Masashi WAKAMATSU (Lab. Nucl. Stud., Fac. Sci., Osaka Univ.)
Tomotsugu WAKASA (RCNP, Osaka Univ.)
Sebastian WHITE (Phys. Dept., BNL, USA)
Shuwei XU (Inst. Modern Phys., Chin. Acad. Sci., China)
Teruya YAMANISHI (Fac. Eng., Fukui Univ. Technol.)
Yoshiki YAMASHITA (Hirosaki Univ.)
Yoshiaki YASUI (KEK)
Koichi YAZAKI (Tokyo Women's Chr. Univ.)
Koji YOSHIMURA (Int. Cen. Element. Part. Phys., Univ. Tokyo)
Naotaka YOSHINAGA (Fac. Sci., Saitama Univ.)
Masaru YOSOI (Fac. Sci., Kyoto Univ.)
Yu-Hu ZHANG (Inst. Modern Phys., Chin. Acad. Sci., China)
Xiaohong ZHOU (Inst. Modern Phys., Chin. Acad. Sci., China)
Lihua ZHU (China Inst. Atom. Energy, China)

Trainees
Kazuya AOKI (Fac. Sci., Kyoto Univ.)
Yoshinori FUKAO (Fac. Sci., Kyoto Univ.)
Takashi HACHIYA (Fac. Sci., Hiroshima Univ.)
Yoshiaki KUROKI (Inst. Phys., Univ. Tsukuba)
Kentarou MAWATARI (Fac. Human Dev. Kobe Univ.)
Tomoaki NAKAMURA (Fac. Sci., Hiroshima Univ.)
Miwako NARA (Inst. Phys. Univ. Tsukuba)
Satoshi OYAMA (Fac. Human Dev. Kobe Univ.)
Noriyuki SUGITA (Fac. Sci., Hiroshima Univ.)
Hisayuki TORII (Fac. Sci. Kyoto Univ.)
Hiroshi TSURUOKA (Inst. Phys. Univ. Tsukuba)

RI Beam Science Laboratory

Head

Isao TANIHATA

Members

Alexei A. KORSHENINNIKOV
Toshimi SUDA
Koichi YOSHIDA
Kouji MORIMOTO
Eiji IDEGUCHI
Yoshimitsu FUKUYAMA*1
Masaaki KIMURA*1
Mizuki NISHIMURA*1
Satoshi SUGIMOTO*1
Deging FANG*2
Yoshihisa ISHIDA*2
Kensuke KUSAKA*2
Tetsuya OHNISHI*2
Yukari MATSUO
Atsushi YOSHIDA
Akira OZAWA
Shunji NISHIMURA
Akihisa KOHAMA
Kei IIDA*1
Yuji NISHI*1
Noritaka SHIMIZU*1
Takayuki YAMAGUCHI*1
Kiyomi IKEDA*2
Rituparna KANUNGO*2
Yuko MOCHIZUKI*2
Toshimitsu YAMAZAKI*2

*1 Special Postdoctoral Researcher
*2 Contract Researcher

Visiting Members

Yasuhisa ABE (Yukawa Inst. Theor. Phys., Kyoto Univ.)
Shizuko ADACHI (ICFD)
Mohammad AHMADY (Univ. Western Ontario, Canada)
Yoran ALHASSID (Yale Univ., USA)
Yasuo AOKI (Fac. Sci., Univ. Tsukuba)
Shigeyoshi AOYAMA (Kitami. Inst. Technol.)
Michi ARATANI (Inst. Enviromental Sci.)
Yoshihiro ARITOMO (JINR, Russia)
Michael BOLBOT (Sci., Notre Dame Univ., USA)
Richard BOYD (Ohio Univ., USA)
Roff BROCKMANN (Inst. Phys., Univ. Mainz., Germany)
Antonio CASARES (Oak Ridge Lab., USA)
Masami CHIBA (Fac. Sci., Tohoku Univ.)
Llie CRUCCERU (Horia Inst. Eng., Romania)
Vivek DATAR (Bhabha Atom. Res. Cen., India)
Dean J. DAVID (CALTEC, USA)
Alla S. DEMIYANOVA (Kurchatov Inst. Atom. Energy, Russia)
Tadayoshi DOKE (Sci. Eng. Res Lab., Waseda Univ.)
Yoshiko ENYO (Inst. Nucl. Study, Univ. Tokyo)
Michael FAMIANO (Ohio Univ., USA)
Andrei FOMITCHEV (JNRF, Russia)
Takaaki FUKUOKA (Taisho Univ.)
Mamoru FUJIWARA (RCNP, Osaka Univ.)
Zsolt FÜLÖP (ATOMKI, Hungary)
Zoltan GACSI (ATOMKI, Hungary)
Yu-Cheng GE (Peking Univ., China)
Hans GEISSEL (GSI, Germany)
Mircea GIURGIU (Inst. Phys. Nucl. Eng., Romania)
Mikheil S. GOLOVKOV (Kurchatov Inst., Russia)
Sergei A. GONCHAROV (Kurchatov Inst., Russia)
Stephanoe GORIELY (Inst. Astron., Belgium)
Alexander GORINE (IHEO, Russia)
Ranjana GOSWAMI (Variable Energy Cycl. Cen. Calcutta, India)
Syuichi GUNJI (Yamagata Univ.)
Zhenhui HAN (Fudan Univ., China)
Toru HARADA (Fac. Sci. Inf., Sapporo Gakuen Univ.)
Nobuyuki HASEBE (Sci. Eng. Res. Lab., Waseda Univ.)

Jun HASEGAWA (Fac. Eng., Tokyo Inst. Technol.)
Michio HATANO (Fac. Sci., Univ. Tokyo.)
Nguyen Thuc HIEN (Hanoi Univ., Vietnam)
Satoru HIRENZAKI (Fac. Sci., Nara Women's Univ.)
Michio HONMA (Univ. Aizu)
Takatoshi HORIBATA (Fac. Sci., Aomori Univ.)
Shen HONG (Dept. Phys., Nankai Univ.)
Masakatu HORIGUCHI (Horiguchi Ironworks)
Hisashi HORIUCHI (Fac. Sci., Kyoto Univ.)
Akitsu IKEDA (Shizuoka Inst. Sci. Technol.)
Nobumichi ISHIDA (Seikei Univ.)
Shigeru ISHIMOTO (KEK)
Naoyuki ITAGAKI (Fac. Sci., Univ. Tokyo)
Kenta ITAHASHI (Fac. Sci., Tokyo Inst. Technol.)
Makoto ITO (Fac. Sci., Hokkaido Univ.)
Akira IWAMOTO (JAERI)
Naohisa IWASA (Fac. Sci., Tohoku Univ.)
Aiichi IWASAKI (Nishogakusha Univ.)
Takuji IZUMIKAWA (Fac. Sci., Niigata Univ.)
Takeo IZUYAMA (Fac. Sci., Toho Univ.)
Dang-Xing JIANG (Peking Univ. China)
Masayasu KAMIMURA (Fac. Sci., Kyushu Univ.)
Toshiki KAJINO (Natl. Astron. Obs.)
Kazuya KANEKO (Kyushu Sangyo Univ.)
Kiyoshi KATO (Fac. Sci., Hokkaido Univ.)
Toshiyuki KATO (Fac. Eng. Res., Waseda Univ.)
Jun KIKUCHI (Sci. Eng. Res. Lab., Waseda Univ.)
Kikuo KIMURA (Fac. Sci., Nagasaki Inst. Appl. Sci.)
Syunichi KITAHARA (Jumonji Women's Univ.)
Masanori KOBAYASHI (Sci. Eng. Res. Lab., Waseda Univ.)
Toshio KOBAYASHI (Fac. Sci., Tohoku Univ.)
James KOLATA (Notre Dame Univ., USA)
Grigori KOSSENKO (OMSK State Univ., Russia)
Hiroyuki KOURA (Fac. Sci. Eng., Waseda Univ.)
Evgueni KOUZMINE (Kurchatov Inst., Russia)
Attila KRASZNAHORKAY (ATOMKI, Hungary)
Hidekazu KUMAGAI
Suresh KUMARU (Bhabha Atom. Res. Cen., India)
Khiem LE HONG (Inst. Phys., Natl. Cen. Sci. Technol., Vietnam)
Xing-Qing LI (Peking Univ., China)
Zhi-Huan LI (Peking Univ., China)
Hongfeng LU (Peking Univ., China)
Takahiro MIZUSAKI (Fac. Sci., Univ. Tokyo)
Koichi MARUYAMA (Inst. Nucl. Study, Univ. Tokyo)
Tomoyuki MARUYAMA (Nihon Univ.)
Toshiki MARUYAMA (JAERI)
Nobuyuki MATSUOKA (RCNP, Osaka Univ.)
Kensaku MATSUTA (Fac. Sci., Osaka Univ.)
Yoshitaka MATSUYAMA (Inst. Nucl. Study, Univ. Tokyo)
Kenichi MATSUYANAGI (Grad. Sch. Sci., Kyoto Univ.)
Masayuki MATSUZAKI (Fac. Ed., Fukuoka Univ.)
Jie MENG (Peking Univ., China)
Souichi MIDORIKAWA (Fac. Eng., Aomori Univ.)
Kei MINAMISONO (Fac. Sci., Osaka Univ.)
Tadanori MINAMISONO (Fac. Sci., Osaka Univ.)
Wolfgang MITTING (GANIL, France)
Mototugu MIHARA (Fac. Sci., Osaka Univ.)
Tanu Ekanath MIRGULE (Bhabha Atom. Res. Cen., India)
Takashi MIYACHI (Fac. Sci. Eng., Waseda Univ.)
Yasuo MIYAKE (Fac. Sci., Univ. Tsukuba)

Osamu MIYAMURA (Fac. Sci., Hiroshima Univ.)
Sadao MOMOTA (Kochi Univ. Technol.)
Hiroaki MORITA (Horiguchi Ironworks)
Mitsuo MURAOKA (Fac. Sci., Aomori Univ.)
Atsushi MUTA (Inst. Phys., Univ. Tsukuba)
Kazuo MUTO (Inst. Sci., Chiba Univ.)
Hitoshi NAKADA (Fac. Sci., Chiba Univ.)
Takashi NAKATSUKASA (Fac. Sci., Tohoku Univ.)
Yoichi NOJIRI (Kochi Univ. Technol.)
Izumi NOMURA (Natl. Inst. Fusion Sci.)
Kengo OGAWA (Coll. Arts Sci., Chiba Univ.)
Masao OGAWA (Fac. Eng., Tokyo Inst. Technol.)
Yoko OGAWA (Fac. Sci., Osaka Univ.)
Alexei A. OGLOBLIN (Kurchatov Inst., Russia)
Akira OHNISHI (Fac. Sci., Hokkaido Univ.)
Naoki OHNISHI (Fac. Eng., Yamanashi Univ.)
Masahisa OHTA (Fac. Sci., Konan Univ.)
Hideaki OHTSU (Fac. Sci., Tohoku Univ.)
Takashi OHTSUBO (Fac. Sci., Niigata Univ.)
Narito OKABE (Fac. Sci., Hokkaido Univ.)
Hiroyuki OKADA (Sci. Eng. Res. Lab., Waseda Univ.)
Kazuo OMATA (Inst. Nucl. Study, Univ. Tokyo)
Akira ONO (Fac. Sci., Tohoku Univ.)
Makito OOI (Dept. Phys., Sch. Sci., Univ. Tokyo)
Shinsho ORYU (Fac. Sci. Technol., Tokyo Univ. Sci.)
Takaharu OTSUKA (Fac. Sci., Univ. Tokyo)
Diane REITZNER (Ohio Univ., USA)
Kazuhiro OYAMATSU (Aichi Shukutoku Univ.)
Emmanuel ROLACCO (EAC, France)
Zhou Zhang REN (Nanjing Univ., China)
Chamanz. P. ROUSSEL (GANIL, France)
Hiroyuki SAGAWA (Univ. Aizu)
Harutaka SAKAGUCHI (Grad. Sch., Kyoto Univ.)
Hideyuki SAKAI (Fac. Sci., Univ. Tokyo)
Hirohisa SAKURAI (Yamagata Univ.)
Chhanda SAMANTA (Sala Inst. Nucl. Phys., Calcutta, India)
Badawy SARHAN (Cairo Univ., Egypt)
Hiromasa SASA (Horiguchi Ironworks)
Hiroshi SATO (Seikei Univ.)
Kazuhiro SATO (Tokyo Fire Dept.)
Kenichi SATO (Dept. Phys., Tohoku Coll. Pharm)
Lee S. SCHROEDER (Laurence Berkeley Lab., USA)
Ryoichi SEKI (California Univ., USA)
Milena SERRA (Tech. Munich Univ., Germany)
Bradley M. SHERRIL (Michigan State Univ., USA)
Caiwan SHEN (Dept. Nucl. Phys., China Inst. At. Energy, China)
Michihiro SHIBATA (Nagoya Univ.)
Toru SHIBATA (Sci. Eng., Aoyama Gakuin Univ.)
Cosimo SIGNORINI (INEN, Italy)
Mickael SMITH (Inst. Oak Ridge, USA)
Koonin STEVEN (CALTEC, USA)
Hideo SUGANUMA (RCNP, Osaka Univ.)
Masahiko SUGAWARA (Fund. Sci., Chiba Inst. Technol.)
Kohsuke SUMIYOSHI (Numazu Coll. Technol.)
Summerer KLAUS (GSI, Germany)
Akihiro SUZUKI (Shinshu Univ.)
Hideyuki SUZUKI (KEK)
Takeshi SUZUKI (Fac. Sci., Niigata Univ.)
Tsuneo SUZUKI (Fac. Sci., Kanazawa Univ.)
Toshio SUZUKI (Coll. Hum. Sci., Nihon Univ.)

Toshio SUZUKI (Fukui Univ.)
Yasuyuki SUZUKI (Fac. Sci., Niigata Univ.)
Takahiro TACHIBANA (Sen. High Sch., Waseda Univ.)
Koji TAKAHASHI (Inst. Max Plank, Germany)
Yutaka TAKAHASHI (Fac. Sci., Osaka Univ.)
Masatoshi TAKANO (Sci. Eng. Res. Lab., Waseda Univ.)
Tadashi TAKEMASA (Kyoto Univ. Ed.)
Noboru TAKIGAWA (Fac. Sci., Tohoku Univ.)
Naoki TAJIMA (Fac. Sci., Fukui Univ.)
Kazuko TANABE (Otsuma Women's Univ.)
Kazuhiro TANAKA (Med. Dept., Juntendo Univ.)
Takaya TANAKA (Fac. Sci., Saitama Univ.)
Kazuhiro TERASAWA (Fac. Sci. Eng., Waseda Univ.)
Hirokazu TEZUKA (Dept. Liberal Arts., Fac. Literature, Toyo Univ.)
Peter SHIROLF (Univ. Munich, Germany)
Mitsuru TOHYAMA (Kyorin Univ.)
Fuyuki TOKANAI (Fac. Sci., Yamagata Univ.)
Hiroshi TOKI (RCNP, Osaka Univ.)
Toshiaki TOMODA (Fac. Sci., Aomori Univ.)
Baeck TORBJOEN (Phys. Dept. Frescat., Sweden)
Jeffrey A. TOSTEVIN (Univ. Surry, India)
Yukio UCHIBORI (NIRS)
Yutaka UTSUNO (Tokai Res. Estab., JAERI)
Hiroaki UTSUNOMIYA (Fac. Sci., Konan Univ.)
Kalman VARGA (Inst. Oak Ridge, USA)
Takahiro WADA (Fac. Sci., Konan Univ.)
Masamiti WAKAI (Grad. Sch. Sci., Osaka Univ.)
Quanjin WANG (Peking Univ., China)
Martin WINKLER (GSI, Germany.)
Cuie WU (Peking Univ., China.)
Herman WOLLNIK (Oak Ridge. Lab., USA)
Kazuhiro YABANA (Fac. Sci., Univ. Tsukuba)
Hirosuke YAGI (Fac. Sci., Univ. Tsukuba)
Kazunari YAMADA (Fac. Sci., Rikkyo Univ.)
Syoichi YAMADA (Fac. Sci., Univ. Tokyo)
Yoshitaka YAMAGUCHI (Fac. Sci., Niigata Univ.)
Yoshio YAMAGUCHI (Inst. Nucl. Study, Univ. Tokyo)
Yanlin YE (Peking Univ., China.)
Alhassid YORANN (Yale Univ., USA)
Nobuaki YOSHIDA (Fac. Inf., Konan Univ.)
Naotaka YOSHINAGA (Fac. Sci., Saitama Univ.)
Akira YUNOKI (Toshiba Co.)
Tao ZHENG (Peking Univ., China)
Shan-Gi ZHOU (Peking Univ., China)

Trainees

Youhei ARAKAWA (Fac. Sci., Osaka Univ.)
Takeshi FURUKAWA
Yohei ASHIE (Fac. Sci. Eng., Waseda Univ.)
Cholsong CHONG (Fac. Sci. Eng., Waseda Univ.)
Takeshi FURUKAWA (Fac. Sci., Osaka Univ.)
Naoki FUKUDA (Fac. Sci. Eng., Waseda Univ.)
Tetsuhito FUSE (Fac. Sci. Eng., Waseda Univ.)
Izumi HASHIMOTO (Fac. Sci., Osaka Univ.)
Kazuaki HASHIZUME (Fac. Sci., Konan Univ.)
Masamichi HARUKI (Fac. Sci. Eng., Waseda Univ.)
Masaru HIBINO (Fac. Sci. Eng., Waseda Univ.)
Hiroshi HIGASHI (Fac. Sci. Eng., Waseda Univ.)
Takuji HIRAMOTO (Fac. Sci. Eng., Waseda Univ.)
Tsutomu IGARASHI (Fac. Sci. Eng., Waseda Univ.)

Akifumi IHARA (Fac. Sci. Eng., Waseda Univ.)
Hiroshi ITO (Fac. Sci. Eng., Waseda Univ.)
Tomomi KATO (Fac. Sci., Niigata Univ.)
Yoshie KAWAMURA (Fac. Sci., Niigata Univ.)
Eiichi KIHIRA (Fac. Sci. Eng., Waseda Univ.)
Takao KITANI (Fac. Sci. Eng., Waseda Univ.)
Atushi KIYAMU (Ibaraki Univ.)
Shingo KOBAYASHI (Fac. Sci. Eng., Waseda Univ.)
Satoshi KODAIRA (Fac. Sci. Eng., Waseda Univ.)
Takayuki KOIKE (Fac. Sci. Eng., Waseda Univ.)
Yohei MATSUDA (Fac. Sci., Tohoku Univ.)
Makoto MATSUNAGA (Fac. Sci. Eng., Waseda Univ.)
Takahiro MASUMURA (Fac. Sci. Eng., Waseda Univ.)
Howard MEREDITH (Ohio Univ., USA)
Daisuke MIKI (Fac. Sci. Eng., Waseda Univ.)
Satoshi MURASAWA (Fac. Sci. Eng., Waseda Univ.)
Atsushi NAGASHIMA (Fac. Sci. Eng., Waseda Univ.)
Yusuke NAKAMURA (Fac. Sci. Eng., Waseda Univ.)
Fumihiko NISHIKIDO (Fac. Sci. Eng., Waseda Univ.)
Masako OGURA (Fac. Sci., Osaka Univ.)
Kazuki OHZEKI (Fac. Sci., Tohoku Univ.)
Akihiro OKA (Fac. Sci. Eng., Waseda Univ.)
Takashi OKUDA (Fac. Sci., Tohoku Univ.)
Osamu OKUDAIRA (Fac. Sci. Eng., Waseda Univ.)
Kiminori OZAKI (Fac. Sci. Eng., Waseda Univ.)
Hisanori SAKABA (Fac. Sci. Eng., Waseda Univ.)
Takao SAKAGUCHI (Fac. Sci. Eng., Waseda Univ.)
Makoto SASAKI (Fac. Sci., Osaka Univ.)
Kazunori SATO (Fac. Sci., Niigata Univ.)
Yoko SEKI (Fac. Sci., Tohoku Univ.)
Masatugu SEKIGUCHI (Fac. Sci., Tohoku Univ.)
Atsuhito SHIINA (Fac. Sci. Eng., Waseda Univ.)
Noritaka SHIMIZU (Fac. Sci., Univ. Tokyo)
Hirofumi SOURI (Fac. Sci. Eng., Waseda Univ.)
Edward SMITH (Ohio Univ., USA)
Atsushi TAKEMURA (Fac. Sci., Osaka Univ.)
Haruyuki TAKEMURA (Fac. Sci. Eng., Waseda Univ.)
Sunao TAKENAKA (Fac. Sci. Eng., Waseda Univ.)
Masatoshi TAKENOUCHI (Fac. Sci. Eng., Waseda Univ.)
Motoyuki TANAKA (Fac. Sci. Eng., Waseda Univ.)
Shinya TAZAWA (Fac. Sci., Tohoku Univ.)
Kazuhiro TERASAWA (Fac. Sci. Eng., Waseda Univ.)
Mariko TERASAWA (Natl. Astron. Obs.)
Shigeru TERUHI (Fac. Sci. Eng., Waseda Univ.)
Toru UZIIE (Fac. Sci., Tohoku Univ.)
Kiwamu WATANABE (Fac. Sci., Tohoku Univ.)
Shigeo WATANABE (Fac. Sci., Niigata Univ.)
Takashi YAKUSHIJI (Fac. Sci., Tohoku Univ.)
Masaki YAMASHITA (Fac. Sci. Eng., Waseda Univ.)
Naoyuki YAMASHITA (Fac. Sci. Eng., Waseda Univ.)
Junichi YASHIRO (Fac. Sci. Eng., Waseda Univ.)
Jun YASUTANI (Fac. Sci. Eng., Waseda Univ.)
Eriko YOKOYAMA (Fac. Sci. Eng., Waseda Univ.)
Hideki YOSHIOKA (Fac. Sci. Eng., Waseda Univ.)

Applied Nuclear Physics Laboratory

Head

Koichiro ASAHI

Members

Yoshio KOBAYASHI
Jiro MURATA
Akihiro YOSHIMI*1
Hiroshi WATANABE*2
Hideki UENO
Wataru SATO*1
Ken-ichiro YONEDA*1

*1 Special Postdoctoral Researcher
*2 Contract Researcher

Visiting Members

Minoru ADACHI
Yasuaki EINAGA (Fac. Sci. Eng., Keio Univ.)
Nobuaki IMAI (Dept. Phys., Grad. Sch. Sci., Univ. Tokyo)
Kenya M. KUBO (Div. Nat. Sci., Int. Chr. Univ)
Hisanori MIYOSHI (Grad. Sch. Sci. Eng., Tokyo Inst. Technol.)
Hiromichi NAKAHARA (Grad. Sch. Sci., Tokyo Metrop. Univ.)
Hiroshi OGAWA (Nat. Inst. Adv. Ind. Sci. Technol.)
Takuya OKADA (Fac. Sci., Gakushuin Univ.)
Hiroyuki SAGAWA (Math. Sci., Univ. Aizu)
Kenji SAKAI (Grad. Sch. Sci. Eng., Tokyo Inst. Technol.)
Suguru SHIMIZU (Grad. Sch. Sci. Eng., Osaka Univ.)
Toru SHIMOURA (Grad. Sch. Sci., Univ. Tokyo)
Masahiko UTSURO (Res. Cen. Nucl. Phys., Osaka Univ.)
Yasuhiro YAMADA (Fac. Sci., Tokyo Univ. Sci.)
Eiichi YAGI (Fac. Sci. Eng., Waseda Univ.)
Jin NAKAMURA (Dept. Appl. Phys. Chem., Univ. Electro-Commun.)
Masaki MURATA (Grad. Sch. Sci., Univ. Tokyo)

Trainees

Daisuke KAMEDA (Grad. Sch. Sci. Eng., Tokyo Inst. Technol.)
Jou KAIHARA (Fac. Sci., Tokyo Inst. Technol.)
Kenji SHIMADA (Fac. Sci., Tokyo Inst. Technol.)
Takashi ITO (Fac. Sci., Tokyo Inst. Technol.)
Shinichi SUDA (Fac. Sci., Tokyo Inst. Technol.)
Keiichi KATSUMATA (Fac. Sci., Tokyo Univ. Sci.)
Takako FUJITA (Fac. Sci., Tokyo Univ. Sci.)
Mami YAMADA (Grad. Sch. Sci., Univ. Tokyo)
Takaaki KOIKE (Fac. Sci., Tokyo Inst. Technol.)
Jun MIYAZAKI (Grad. Sci., Tokyo Univ. Sci.)
Takashi SAITO (Fac. Sci., Tokyo Univ. Sci.)
Tetsuya NAKAGAWA (Fac. Sci., Tokyo Univ. Sci.)
Akira KUMAKURA (Fac. Sci., Tokyo Univ. Sci.)
Kohei KOJIMA (Grad. Sch. Sci., Univ. Tokyo)
Atsushi SAITO (Fac. Sci., Tokyo Univ. Sci.)
Takahiro OHTSUKA (Div. Nat. Sci., Int. Chr. Univ)
Jyunko SUDA (Div. Nat. Sci., Int. Chr. Univ)
Hiroshi MATSUBA (Fac. Sci., Waseda Univ.)
Kazuya MIYAHARA (Fac. Sci., Waseda Univ.)
Yoshiki OKADA (Fac. Sci., Waseda Univ.)
Shinichi HAGIWARA (Fac. Sci., Waseda Univ.)
Katsuhito MORI (Fac. Sci., Waseda Univ.)
Kiwamu SAKUMA (Fac. Sci., Waseda Univ.)
Motoyasu YOSHII (Fac. Sci., Waseda Univ.)

Atomic Physics Laboratory

Head

Yasunori YAMAZAKI

Members

Isao SHIMAMURA
Tadashi KAMBARA

Yasuyuki KANAI
Hitoshi OYAMA
Takao M. KOJIMA
Takane KOBAYASHI
Masaki OURA
Yoshio IWAI*
Nobuhiro YAMANAKA*
Masami NISHIDA
Michiharu WADA
Yoichi NAKAI
Tokihiro IKEDA
Yuichiro MORISHITA*
Nobuyuki NAKAMURA*

* Special Postdoctoral Reseacher

Visiting Members

Kozo ANDO
Yohko AWAYA (Coll. Art Design Gen. Ed., Musashino Art Univ.)
Toshiyuki AZUMA (Dept. Phys., Tokyo Metrop. Univ.)
Li CHEN (LASIM, Lyon Univ., France)
Yasuhiro CHIMI (Tokai Res. Estab., JAERI)
Kazumi FUJIMA (Fac. Eng., Yamanashi Univ.)
Shunsuke HARA (Dept. Gen. Ed., Tsukuba Coll. Tech.)
Atsushi HATAKEYAMA (Grad. Sch. Arts Sci., Univ. Tokyo)
Kazuo HAYAKAWA (Shizuoka Inst. Sci. Technol.)
Hiroyuki HIGAKI (Inst. Appl. Phys., Univ. Tsukuba)
Akira HITACHI (Kochi Med. Sch.)
Jiri HORACEK (Charles Univ., Czech)
Masamitsu HOSHINO (Grad. Sch. Sci. Eng., Sophia Univ.)
Roger HUTTON (Dept. Phys., Univ. Lund, Sweden)
Atsushi ICHIMURA (Inst. Space Astro. Sci.)
Akinori IGARASHI (Fac. Eng., Miyazaki Univ.)
Hiroshi IKEDA (Inst. Appl. Phys., Cryogen. Cen., Univ. Tsukuba)
Mitio INOKUTI (Argonne Natl. Lab., USA)
Keishi ISHII (Fac. Sci. Eng., Ritsumeikan Univ.)
Norito ISHIKAWA (Tokai Res. Estab., JAERI)
Akio ITOH (Fac. Eng., Kyoto Univ.)
Yoh ITOH (Fac. Sci., Josai Univ.)
Akihiro IWASE (Tokai Res. Estab., JAERI)
Kensuke KAGEYAMA (Fac. Eng., Saitama Univ.)
Kenji KIMURA (Fac. Eng., Kyoto Univ.)
Mineo KIMURA (Fac. Eng., Yamaguchi Univ.)
Masashi KITAJIMA (Fac. Sci. Tech., Sophia Univ.)
Nobuo KOBAYASHI (Dept. Phys., Tokyo Metrop. Univ.)
Tetsuo KOIZUMI (Dept. Phys., Rikkyo Univ.)
Ken-ichiro KOMAKI (Grad. Sch. Arts Sci., Univ. Tokyo)
Kenichi KOWARI (Dept. Appl. Phys. Chem., Univ. Electro-Commun.)
Kenro KUROKI (Natl. Res. Inst. Police Sci.)
Takashi MATSUO (Dept. Pathol., Tokyo Med. Den. Univ.)
Michio MATSUZAWA (Dept. Appl. Phys. Chem., Univ. Electro-Commun.)
Koichiro MITSUKE (Inst. Mol. Sci.)
Akihiro MOHRI
Takeshi MUKOYAMA (Kansai Gaidai Univ.)
Kanetada NAGAMINE (Inst. Mater. Struc. Sci., KEK)
Takashi NAKAMURA (KEK)
Megumi NIIGAKI (Dept. Phys., Grad. Sch. Sci., Univ. Tokyo)
Tamio NISHIMURA (Dept. Chim., Univ. Roma, Italy)
Shunsuke OHTANI (Inst. Laser Sci., Univ. Electro-Commun.)
Nagayasu OSHIMA (Grad. Sch. Arts Sci., Univ. Tokyo)
Norio OKABAYASHI (Grad. Sch. Arts Sci., Univ. Tokyo)
Kunihiro OKADA (Fac. Sci. Technol., Sophia Univ.)
Satoru OKAYASU (Tokai Res. Estab., JAERI)
Kazuhiko OKUNO (Dept. Phys., Tokyo Metrop. Univ.)
Fumihisa ONO (Fac. Sci., Okayama Univ.)
Yi-Zhi QU (Univ. Sci. Technol. China, China)
Frank B. ROSMEJ (GSI, Germany)

Akio SAKAI (Vacuum Products Co.)
Hiroshi SATO (Fac. Sci., Ochanomizu Univ.)
Reinhold SCHUCH (Phys. Dept., Stockholm Univ., Sweden)
Hans A. SCHUESSLER (Texas A & M Univ., USA)
Noriyuki SHIMAKURA (Fac. Sci., Niigata Univ.)
Michiya TAKEKAWA (Grad. Sch. Arts Sci., Univ. Tokyo)
Karoly TOKESI (ATOMKI, Hungary)
Tadao TONUMA (Adv. Res. Inst. Sci. Eng., Waseda Univ.)
Hiroyuki TORII (Grad. Sch. Arts Sci., Univ. Tokyo)
Nobuyuki TOSHIMA (Inst. Appl. Phys., Univ. Tsukuba)
Hidetsugu TSUCHIDA (Fac. Sci., Nara Women's Univ.)
Kiyoshi UEDA (Res. Inst. Sci. Meas., Tohoku Univ.)
Akira YAGISHITA (KEK)
Yutaka YOSHIDA (Shizuoka Inst. Sci. Technol.)
Ken YOSHIKI FRANZÉN (Grad. Sch. Arts Sci., Univ. Tokyo)
Yaming ZOU (Shanghai Jiao Tong Univ., China)

Trainees

Fanfu CHEN (Dept. Phys., Grad. Sch. Sci., Rikkyo Univ.)
Rina KAJITA (Grad. Sch. Sci. Eng., Sophia Univ.)
Atsushi HIROSE (Fac. Eng., Iwate Univ.)
Premysl KOLORENC (Charles Univ., Czech)
Seiji KOMATSU (Dept. Phys., Okayama Univ.)
Chikara KONDOU (Dept. Phys., Grad. Sch. Sci., Univ. Tokyo)
Naofumi KURODA (Dept. Phys., Grad. Sch. Sci., Univ. Tokyo)
Simon LETOUT (Univ. Paris XI-Orsay, France)
Takuya MAJIMA (Grad. Sch. Eng., Kyoto Univ.)
Francois MALLET (Univ. Paris XI-Orsay, France)
Eiichiro NOGUCHI (Dept. Phys., Grad. Sch. Sci., Univ. Tokyo)
Syuiti SAKAGUTI (Grad. Sch. Sci. Eng., Saitama Univ.)
Hiroyuki SHIMADA (Dept. Phys., Grad. Sch. Sci., Univ. Tokyo)
Tetsu SONODA (Grad. Sch. Sci., Tohoku Univ.)
Yuichi TAKABAYASHI (Dept. Phys., Grad. Sch. Sci., Univ. Tokyo)
Aiko TAKAMINE (Dept. Phys., Grad. Sch. Sci., Univ. Tokyo)
Satoko WATANABE (Grad. Sch. Sci. Eng., Saitama Univ.)
Masanori YANAGISAWA (Grad. Sch. Sci. Eng., Sophia Univ.)

Heavy Ion Nuclear Physics laboratory

Head

Tohru MOTOBAYASHI

Members

Takashi ICHIHARA
Yasushi WATANABE
Yoshiyuki YANAGISAWA*1
Satoshi TAKEUCHI*2
Takashi KISHIDA
Naoki FUKUDA*1
Ken-ichiro YONEDA*1

*1 Special Postdoctoral Researcher
*2 Contract Researcher

Visiting Members

Vinodkumar Mayyan ATTUKALATHIL (Fac. Sci., Tokyo Inst. Technol.)
Zsolt DOMBRADI (Inst. Nucl. Res., Hung. Acad. Sci., Hungary)
Zoltan ELEKES (Inst. Nucl. Res., Hung. Acad. Sci., Hungary)
Zsolt FÜLÖP (Inst. Nucl. Res., Hung. Acad. Sci., Hungary)
Adrian GELBERG (Koln Univ., Germany)
Nobuaki IMAI (Dept. Phys., Grad. Sch. Sci., Univ. Tokyo)
Gabor KALINKA (Inst. Nucl. Res., Hung. Acad. Sci., Hungary)
Kazuyoshi KURITA (Coll. Sci., Rikkyo Univ.)

Takashi NAKAMURA (Fac. Sci., Tokyo Inst. Technol.)
Akito SAITO (Coll. Sci., Rikkyo Univ.)
Hiroyoshi SAKURAI (Dept. Phys., Grad. Sch. Sci., Univ. Tokyo)
Yoshiteru SATO (Fac. Sci., Tokyo Inst. Technol.)
Peter von BRENTANO (Koln Univ., Germany)

Trainees

Hidetada BABA (Coll. Sci., Rikkyo Univ.)
Kimihiko DEMICHI (Coll. Sci., Rikkyo Univ.)
Tomonori FUKUCHI (Fac. Sci., Kyushu Univ.)
Julien Didier GIBELIN (Inst. de Phys. Nucl., France)
Hirokazu HASEGAWA (Coll. Sci., Rikkyo Univ.)
Naho HOKOIWA (Fac. Sci., Kyushu Univ.)
Yuichi ICHIKAWA (Dept. Phys., Grad. Sch. Sci., Univ. Tokyo)
Tomoyuki ISHIDA (Dept. Phys., Grad. Sch. Sci., Univ. Tokyo)
Kazuhiro ISHIKAWA (Fac. Sci., Tokyo Inst. Technol.)
Emi KANEKO (Coll. Sci., Rikkyo Univ.)
Shouko KANNO (Coll. Sci., Rikkyo Univ.)
Shoko KAWAI (Coll. Sci., Rikkyo Univ.)
Michiya KIBE (Fac. Sci., Kyushu Univ.)
Yosuke KONDO (Fac. Sci., Tokyo Inst. Technol.)
Hironori KUBOKI (Dept. Phys., Grad. Sch. Sci., Univ. Tokyo)
Naoya KUBOSHIMA (Coll. Sci., Rikkyo Univ.)
Yukie MAEDA (Dept. Phys., Grad. Sch. Sci., Univ. Tokyo)
Yuuichi MATSUYAMA (Coll. Sci., Rikkyo Univ.)
Kathleen Louise MILLER (Natl. Superconduct. Cycl. Lab., Michigan State Univ., USA)
Motooki MIURA (Fac. Sci., Tokyo Inst. Technol.)
Hooi Jin ONG (Dept. Phys., Grad. Sch. Sci., Univ. Tokyo)
Takeo ONISHI (Dept. Phys., Grad. Sch. Sci., Univ. Tokyo)
Mituhito OSADA (Dept. Phys., Grad. Sch. Sci., Univ. Tokyo)
Takaaki SAITO (Dept. Phys., Grad. Sch. Sci., Univ. Tokyo)
Hazuki SAKAI (Coll. Sci., Rikkyo Univ.)
Takafumi SASAKI (Fac. Sci., Kyushu Univ.)
Masaki SASANO (Dept. Phys., Grad. Sch. Sci., Univ. Tokyo)
Shigenori SIMIZU (Coll. Sci., Rikkyo Univ.)
Takashi SUGIMOTO (Fac. Sci., Tokyo Inst. Technol.)
Hiroshi SUZUKI (Dept. Phys., Grad. Sch. Sci., Univ. Tokyo)
Masaru SUZUKI (Dept. Phys., Grad. Sch. Sci., Univ. Tokyo)
Eri TAKESHITA (Coll. Sci., Rikkyo Univ.)
Yasuhiro TOGANO (Coll. Sci., Rikkyo Univ.)
Koji UE (Dept. Phys., Grad. Sch. Sci., Univ. Tokyo)
Yasuo WAKABAYASHI (Fac. Sci., Kyushu Univ.)

Magnetic Materials Laboratory

Head

Hidenori TAKAGI

Members

Masayuki HAGIWARA
Hiroki YAMAZAKI
Tetsuya MUTO*
Hiroko KATORI
Kenji KAMISHIMA*
Ken YOKOYAMA*

* Special Postdoctoral Researcher

Visiting Members

Olivier CADOR (Inst. Chim. Mat. Cond. Bordeaux, France)
Andrew HARRISON (Univ. Edinburgh, UK)
Zentaro HONDA (Fac. Eng., Saitama Univ.)
Corine MATHONIERE (Inst. Chim. Mat. Cond. Bordeaux, France)

Hans-Jürgen MIKESKA (Univ. Hannover, Germany)
Kazuhiko MINAMI (Fac. Sci., Nagoya Univ.)
Junko SATOOKA (Fac. Eng., Yokohama Natl. Univ.)
Stephen SHAPIRO (BNL, USA)
Michael STEINER (Hahn-Meitner Inst., Germany)

Muon Science Laboratory

Head

Kanetada NAGAMINE (~March)
Masahiko IWASAKI (April~)

Members

Teiichiro MATSUZAKI
Katsuhiko ISHIDA
Yasuyuki MATSUDA
Toshifumi OKAMOTO*1
Patrick STRASSER*2
Akio KOYAMA
Isao WATANABE
Kenta ITAHASHI
Hiroyuki YAMASE*1
Vemuru KRISHNAMURTHY*2

*1 Special Postdoctoral Researcher
*2 Contract Researcher

Visiting Members

Tadashi ADACHI (Fac. Eng., Tohoku Univ.)
Yoshitami AJIRO (Fac. Sci., Kyushu Univ.)
Jun AKIMITSU (Coll. Sci. Eng., Aoyama Gakuin Univ.)
Juichiro ARAI (Tokyo Univ. Sci.)
Kunio AWAGA (Grad. Sch. Arts Sci., Univ. Tokyo)
Pavel BAKULE
Ludmila Nikolaevna BOGDANOVA (Inst. Theor. Exp. Phys., Russia)
Tina M. BRIERRE (Inst. Metal Sci., Tohoku Univ.)
Tara Prasad DAS (State Univ. New York, USA)
Don FLEMING (TRIUMF, Canada)
Yutaka FUJII (Fac. Eng., Fukui Univ.)
Masaki FUJITA (Inst. Chem. Res., Kyoto Univ.)
Atsuko FUKAYA (Inst. Chem. Res., Kyoto Univ.)
Makoto HAGIWARA (Fac. Eng. Design, Kyoto Inst. Technol.)
Wataru HIGEMOTO (KEK)
Emiko HIYAMA (KEK)
Susumu IKEDA (KEK)
Shigeru ISHIMOTO (KEK)
Atsuko ITO
Ryosuke KADONO (KEK)
Masayasu KAMIMURA (Fac. Sci., Kyushu Univ.)
Mineo KATO (Tokai Res. Estab., JAERI)
Naritoshi KAWAMURA (KEK)
Yasushi KINO (Fac. Sci., Tohoku Univ.)
Akihiro KODA (KEK)
Takahisa KOIKE (KEK)
Youji KOIKE (Fac. Eng., Tohoku Univ.)
Andrey KRAVTOV (Russ. Fed. Nucl. Cen., Russia)
Yoshitaka KUNO (Fac. Sci., Osaka Univ.)
Hong LI (Michigan State Univ., USA)
Roderick MACRAE (Notre Dame Radiat. Lab., USA)
Syunsuke MAKIMURA (KEK)
Goro MARUTA (Fac. Sci., Hokkaido Univ.)
Yasuhiro MIYAKE (KEK)
Satoshi N. NAKAMURA (Fac. Sci., Tohoku Univ.)
Takashi NAKAMURA (Fac. Sci., Tokyo Inst. Technol.)
Takehito NAKANO (Fac. Sci., Osaka Univ.)
Nobuhiko NISHIDA (Fac. Sci., Tokyo Inst. Technol.)

Kusuo NISHIYAMA (KEK)
Yasuo NOZUE (Fac. Sci., Osaka Univ.)
Vassili V. PEREVOZCHIKOV (Russ. Fed. Nucl. Cen., Russia)
Leonid I. PONOMAREV (Kurchatov Inst., Russia)
Francis L. PRATT (RAL, UK)
Shinichi SAKAMOTO (Tokai Res. Estab., JAERI)
Ryoichi SEKI (California State Univ., USA)
Koichiro SHIMOMURA (KEK)
Evgeni SOLOVJEW (Univ. Skopja, Russia)
Vyacheslav G. STORCHAK (Kurchatov Inst., Russia)
Hiroyuki SUGAI (Tokai Res. Estab., JAERI)
Keiji TAKEDA (Fac. Sci., Hokkaido Univ.)
Masashi TAKIGAWA (Inst. Solid State Phys.)
Masakazu TANASE (Takasaki Res. Estab., JAERI)
Eiko TORIKAI (Fac. Eng., Yamanashi Univ.)
Akihisa TOYODA (KEK)
Kazuo UEDA (Inst. Solid State Phys.)
Eiichi YAGI
Kazuyoshi YAMADA (Inst. Chem. Res., Kyoto Univ.)
A. A. YUKHIMCHUK (Russ. Fed. Nucl. Cen., Russia)

Trainees
Dai TOMONO (Fac. Sci., Tokyo Inst. Technol.)
Hiroyuki TANAKA (Fac. Sci., Nagoya Univ.)
Haruo MIYADERA (Fac. Sci., Univ. Tokyo)

Beam Physics and Engineering Laboratory

Head
Takeshi KATAYAMA

Members
Moritake TAMBA
Tamaki WATANABE
Masahiro OKAMURA
Tadashi KOSEKI
Masaki NISHIURA*1
Akira SAKUMI*1
Masao TAKANAKA*2
Manabu HAMAGAKI
Masato NAKAMURA
Keiko KUMAGAI
Naoki FUKUDA*1
Shuichi OZAWA*1
Yoshiyuki YANAGISAWA*1
Masao WATANABE*2

*1 Special Postdoctoral Researcher
*2 Contract Researcher

Visiting Members
Robert A. JAMESON (Los Alamos Natl. Lab., USA)
Dieter MOEHL (CERN, Switzerland)
Nori AOI (CNS, Univ. Tokyo)
Alexander BOLSHAKOV (ITEP, Russia)
Yoshihide FUCHI (KEK)
Zsolt FÜLÖP (ATOMKI, Hungary)
Hideki HAMAGAKI (CNS, Univ. Tokyo)
Tamio HARA (Toyota Technol. Inst.)
Yuichi HASHIMOTO (Canon Inc.)
Toshiyuki HATTORI (Res. Lab. Nucl. React., Tokyo Inst. Technol.)
Midori HIRANO (CNS, Univ. Tokyo)
Masahide INUDUKA (CNS, Univ. Tokyo)
Hironori IWASAKI (CNS, Univ. Tokyo)
He JIANJUN (CNS, Univ. Tokyo)
Seigo KATOU (Univ. Yamagata)
Shigeki KATO (KEK)
Takahiro KAWABATA (CNS, Univ. Tokyo)

Hahn Kevin INSIK (Ewha Woman's Univ., Korea)
Kiyoji KOHNO (CNS, Univ. Tokyo)
Shigeru KUBONO (CNS, Univ. Tokyo)
Shogo KUBOTA (CNS, Univ. Tokyo)
Igor MESHKOV (JINR, Russia)
Hirofumi MIYAZAKI (Sumitomo Heavy Ind. Ltd.)
Masahiro NOTANI (CNS, Univ. Tokyo)
Masao OGAWA (Tokyo Inst. Technol.)
Yun Chong CHEOUL (Chung-Ang Univ., Korea)
Yoshiyuki OGURI (Res. Lab. Nucl. React., Tokyo Inst. Technol.)
Yukimitsu OHSHIRO (CNS, Univ. Tokyo)
Ken OYAMA (Univ. Tokyo)
Kyoichiro OZAWA (CNS, Univ. Tokyo)
Takao SAKAGUCHI (CNS, Univ. Tokyo)
Takeshi SAKAKIBARA (Chuo Univ.)
Yuichi SAKAMOTO (Nichimen Co.)
Yoshiteru SATO (CNS, Univ. Tokyo)
Boris SHARKOV (ITEP, Russia)
Fumio SHIMOKOSHI (CNS, Univ. Tokyo)
Susumu SHIMOURA (CNS, Univ. Tokyo)
Anatoly SIDORIN (JINR, Russia)
Alexander SKRINSKY (ITEP, Russia)
Alexandre SMIRNOV (JINR, Russia)
Kazuo SUGII (Osaka Vacuum, Ltd.)
Masaharu SUZUKI (CNS, Univ. Tokyo)
Evgeny SYRESIN (JINR, Russia)
Seisaku TAKAKU (CNS, Univ. Tokyo)
Masahiko TANAKA (KEK)
Takashi TERANISHI (CNS, Univ. Tokyo)
Masao TSUCHIYA (Ishikawajima-Harima Heavy Ind. Co. Ltd.)
Hiroshi TSUTSUI (Sumitomo Heavy Ind., Ltd.)
Meiko UESAKA (CNS, Univ. Tokyo)
Tomohiro UESAKA (CNS, Univ. Tokyo)
Takashi WAKUI (CNS, Univ. Tokyo)
Shin-ichi WATANABE (CNS, Univ. Tokyo)
Meiqin XIAO (Fermi Natl. Accel. Lab., USA)
Kentaro YAKO (CNS, Univ. Tokyo)
Shoichi YAMAKA (CNS, Univ. Tokyo)
Koji YAMAKAWA (Irie Kouken Co.)
Norio YAMAZAKI (CNS, Univ. Tokyo)
Pavel ZENKEVITCH (ITEP, Russia)
Takeshi TAKEUCHI (CNS, Univ. Tokyo)
Masaki SERATA (Coll Sci., Rikkyo Univ.)
Takashi MATSUMOTO (CNS, Univ. Tokyo)
Shin-ichiro MICHIMASA (Univ. Tokyo)
Souichiro KAMETANI (Waseda Univ.)
Kazuo YAMAMOTO (Tokyo Inst. Technol.)
Hiroshi AMEMIYA
Yoshiaki CHIBA
Kiyohiko OKAZAKI
Motonobu TAKANO
Katsuki YANO

Trainees

Tadaaki ISOBE (Waseda Univ.)
Ju Hahn LEE (Chung-Ang Univ., Korea)
Fukutaro KAJIWARA
Kouichi KATOU (Waseda Univ.)
Shigemi KURIHARA
Hajime NANJOU (Univ. Tokyo)
Takeshi NISHIMOTO (Tokyo Inst. Technol.)

Shinsuke OOTA (Kyoto Univ.)
Munetaka TAMAI (Waseda Univ.)
Kouji UE (CNS, Univ. Tokyo)

Semiconductors Laboratory

Head
Yoshinobu AOYAGI

Visiting Members
Akira HIDA (Dept. Appl. Phys., Sch. Eng., Univ. Tokyo)

Cellular Physiology Laboratory

Head
Fumio HANAOKA

Members
Fumio YATAGAI

Visiting Members
Koichi ANDO (Natl. Inst. Radiol. Sci.)
Yoshiya FURUSAWA (Natl. Inst. Radiol. Sci.)
Yoshimasa HAMA (Sci. Eng. Inst., Waseda Univ.)
Nobutoshi ITOH (Fac. Sci., Univ. Tokyo)
Tatsuaki KANAI (Natl. Inst. Radiol. Sci.)
Kiyomi KASAI (Natl. Inst. Radiol. Sci.)
Yasuhiko KOBAYASHI (JAERI)
Hiroshi WATANABE (JAERI)
Masami WATANABE (Fac. Pharm. Sci., Nagasaki Univ.)
Shoji YAMASHITA (Natl. Saitama Hospital)

Plant Functions Laboratory

Head
Shigeo YOSHIDA

Members
Tomoko ABE
Makoto FUJIWARA*1
Koichi SAKAMOTO*1
Yoshiharu YAMAMOTO*2
Tomoki MATSUYAMA
Yutaka MIYAZAWA*1
Hiroyuki SAITO*2

*1 Special Postdoctoral Researcher
*2 Contract Researcher

Visiting Members
Ryuuichi ITO (Fac. Sci., Univ. Ryukyus)
Koji FURUKAWA (Mukoyama Orchids Co. Ltd.)
Misako HAMATANI (Hiroshima City Agr. Forest. Promot. Cen.)
Yasuhide HARA (Kanagawa Inst. Agr. Sci.)
Ichiro HONDA (Natl. Agr. Res. Cen., Min. Agr. Forest. Fish.)
Mitsugu HORITA (Hokkaido Green-bio Inst.)
Hiroshi KAGAMI (Shizuoka Citrus Exp. Station)
Takeo KITAURA (Kanagawa Inst. Agr. Sci.)
Kazumitsu MIYOSHI (Fac. Bioresource Sci., Akita Pref. Univ.)
Toshikazu MORISHITA (Inst. Rad. Breeding, Natl. Inst. Agr. Res.)
Takiko SHIMADA (Res. Inst. Agr. Resources, Ishikawa Agr. Coll.)
Masao SUGIYAMA (Hokko Chemical Ind. Co., Ltd.)
Kenichi SUZUKI (Suntory Flowers Ltd.)
Ken TOKUHARA (Dogashima Orchid Cen.)

Takuji YOSHIDA (Takii Seed Co., Ltd.)
Hisashi TSUJIMOTO (Fac. Agr., Tottori Univ.)
Masao WATANABE (Fac. Agr., Iwate Univ.)

Trainees

Masanori HATASHITA (Wakasa Wan Energy Res. Cen.)
Akio IWASAKI (Kochi Agr. Res. Cen.)
Tetsuji KINOSHITA (Miyazaki Agr. Exp. Station)
Tomojiro KOIDE (RIKEN Vitamin Co., Ltd.)
Yuki KOMOMI (Fac. Sci. Tech., Tokyo Univ. Sci.)
Mitsuo MATSUMOTO (Kochi Agr. Res. Cen.)
Masuo NITTA (Kochi Agr. Res. Cen.)
Keiichi TAKAGI (Wakasa Wan Energy Res. Cen.)
Sei TAKATA (Kochi Agr. Res. Cen.)
Tetsuya UMEKI (Miyazaki Agr. Exp. Station)

CYCLOTRON CENTER

Chief Scientist

Yasushige YANO

RIBF Project Office

Head

Yasushige YANO

Members

Toshiyuki KUBO
Hiroshige TAKEICHI
Shinichiro FUJII[*1]
Hideki MADOKORO[*1]
Nguyen DINH DANG[*2]
Masanori WAKASUGI
Naohito INABE
Ka-hae KIM[*1]
Toshiyuki MINEMURA[*1]

[*1] Special Postdoctoral Researcher
[*2] Contract Researcher

Visiting Members

Kazuo ARAKAWA (Takasaki Rad. Chem. Res. Estab., JAERI)
Alok CHAKRABARTI (Var. Ener. Cycl. Cen., India)
Tadashi FUJINAWA (Mitsubishi Electric Co., Ltd.)
Shiro FUJISHIMA (I.H.I.)
Mitsuhiro FUKUDA (Takasaki Res. Estab., JAERI)
Toshikazu HIASA (Sumitomo Heavy Ind., Ltd.)
Tamiko HIRUMACHI (Toshiba Corp.)
Toshihiro HONMA (N.I.R.S.)
Nobukazu KAKUTANI (Toshiba Corp.)
Syuuichi KIDO (Hitachi Ltd.)
Masayuki KUMADA (N.I.R.S.)
Kazuo KUNO (Mitsubishi Electric Co., Ltd.)
Shin-ichi MASUNO (Mitsubishi Electric Co., Ltd.)
Toshikatu MASUOKA (Hitachi Zosen Corp.)
Ju-Mei MATSUI (Mitsubishi Electric Co., Ltd.)
Toshinori MITSUMOTO (Sumitomo Heavy Ind., Ltd.)
Shoushichi MOTONAGA
Tomohiro OHKAWA (Mitsubishi Res. Inst. Inc.)
Kiyotaka OHTOMO (Sumitomo Heavy Ind., Ltd.)
Mutsuko SASAKI
Shuhei YAMAJI (Kanagawa Inst. Technol.)

Beam Technology Division

Head

Masayuki KASE

Members

Jiro FUJITA
Shin FUJITA
Tadashi KAGEYAMA
Kosuke MORITA
Kiminori USHIDA
Toshiya TANABE
Sachiko ITO
Masatake HEMMI
Tsutomu YAMAKI
Akiko MASUDA*1
Yoshihide HIGURASHI*2
Misaki KOMIYAMA*2
Tadashi YOKOUCHI*2
Kiyoshi OGIWARA
Makoto NAGASE
Shigeo KOHARA
Takahide NAKAGAWA
Eiji IKEZAWA
Masaki FUJIMAKI
Toshiya CHIBA
Yoshitoshi MIYAZAWA
Ichiro YOKOYAMA
Hiromichi AKIYOSHI*2
Masanori KIDERA*2
Hisao SAKAMOTO*2
Akira YONEDA*2

*1 Special Postdoctoral Researcher
*2 Contract Researcher

Visiting Members

Takashi ABURAYA (NASDA)
Keisuke ASAI (Grad. Sch. Eng., Univ. Tokyo)
Shinji BABA (NASDA)
Yasushi DEGUCHI (NASDA)
Kaoru FURUSE (NASDA)
Yasuyuki FUTAMI (N.I.R.S.)
Tateo GOKA (NASDA)
Kichiji HATANAKA (RCNP, Osaka Univ.)
Yuichi HATSUKAWA (Tokai Res. Estab., JAERI)
Ryugo S. HAYANO (Fac. Sci., Univ. Tokyo)
Teruo HIROTA (Toyo Denshi Keisoku Co., Ltd.)
Masanori IDESAWA (Univ. Electro-Commun.)
Yoshiya IIDE (NASDA)
Seiji IIO (Sumitomo Heavy Ind. Ltd.)
Naomi IKEDA (NASDA)
Hiroshi IKEZOE (Tokai Res. Estab., JAERI)
Takashi INAMURA (Warsaw Univ., Poland)
Masayuki ITO (Adv. Res. Inst. Sci. Eng., Waseda Univ.)
Sung Chang JEONG (KEK)
Takashi KANAMORI (NASDA)
Ichiro KATAYAMA (KEK)
Jyun KAWAI (Grad. Sch. Eng., Kyoto Univ.)
Kazuie KIMURA
Osamu KOYAMA (Katagiri Eng. Co., Ltd.)
Satoshi KUBOYAMA (NASDA)
Hisaaki KUDO (Fac. Sci., Niigata Univ.)
Tadahiro KUROSAWA (Electrotechn. Lab., Agency Ind. Sci. Tech.)
San-mu LEE (Inst. Phys., Univ. Tsukuba)
Sumio MATSUDA (NASDA)
Kiyoshi MATSUNO (Fujiden Eng. Co., Ltd.)
Takehiro MATSUSE (Fac. Textile Sci. Tech., Shinshu Univ.)
Tadanori MINAMISONO (Grad. Sch. Sci., Osaka Univ.)
Hiroari MIYATAKE (KEK)
Tetsuya MURAKAMI (Grad. Sch. Sci., Kyoto Univ.)
Yuki NAGAI (NASDA)
Noriaki NAKAO (KEK)
Takashi NAKAMURA (Cycl. Radioisot. Cen., Tohoku Univ.)
Norio NEMOTO (NASDA)

Mechtchriakov NIKOLAI (Inst. Theor. Phys., China)
Toru NOMURA (KEK)
Hideharu OHIRA (NASDA)
Tsutomu OHTSUKI (Lab. Nucl. Sci., Tohoku Univ.)
Hironobu OHZONO (NASDA)
Koji OISHI (Shimizu Construction Co., Ltd.)
Hiromitsu OOTOMO (NASDA)
Kenshi SAGARA (Fac. Sci., Kyushu Univ.)
Hideyuki SAKAI (Dept. Phys., Sch. Sci., Univ. Tokyo)
Eido SHIBAMURA (Saitama Pref. Jr. Coll.)
Osamu SHIMADA (NASDA)
Hiroyuki SHINDO (NASDA)
Tsutomu SHINOZUKA (Cycl. Radioisot. Cen., Tohoku Univ.)
Shuji SOMEKAWA (NASDA)
Keisuke SUEKI (Inst. Chemi., Univ. Tsukuba)
Isao SUGAI (KEK)
Masami SUZUKI (Irie Koken Co. Ltd.)
Norio TAKADA (NASDA)
Noriyuki TSUBAKI (NASDA)
Hiroaki UTSUNOMIYA (Fac. Sci., Konan Univ.)
Ryoichi WADA (Texas A&M Univ., USA)
Masakazu WASHIO (Adv. Res. Inst. Sci. Eng., Waseda Univ.)
Yuji YAMAKAWA (Shimizu Construction Co., Ltd.)
Hirohito YAMAZAKI (Lab. Nucl. Sci., Tohoku Univ.)

Trainees

Hideyuki ARAI (Inst. Phys., Univ. Tsukuba)
Rintaro FUJIMOTO (Dept. Phys., Sch. Sci., Univ. Tokyo)
Tomoko GOMI (Coll. Sci., Rikkyo Univ.)
Masashi IMANAKA (Inst. Phys., Univ. Tsukuba)
Atsushi IWAI (Fac. Sci., Tohoku Univ.)
Hiroshi IWASE (Fac. Sci., Tohoku Univ.)
Daiya KAJI (Fac. Sci., Niigata Univ.)
Masataka KOBAYASHI (Adv. Res. Inst. Sci. Eng., Waseda Univ.)
Masanori KOSHIMIZU (Dept. Eng., Grad. Sch. Eng., Univ. Tokyo)
Erika MIHARA (Fac. Sci., Tohoku Univ.)
Masakazu MORI (Adv. Res. Inst. Sci. Eng., Waseda Univ.)
Masayoshi NOMURA (Grad. Sch. Eng., Tokyo Univ.)
Tomoya NUNOMIYA (Fac. Sci., Tohoku Univ.)
Kazutaka TERUNUMA (Fac. Sci., Tohoku Univ.)
Rei UMEBAYASHI (Dept. Eng., Grad. Sch. Eng., Univ. Tokyo)
Hiroshi YASHIMA (Fac. Sci., Tohoku Univ.)
Shunsuke YONAI (Fac. Sci., Tohoku Univ.)

Beam Dynamics Division

Head

Akira GOTO

Members

Nobuhisa FUKUNISHI
Jun-ichi OHNISHI
Fuminori SAITO
Kimiko SEKIGUCHI*
Osamu KAMIGAITO
Hiroki OKUNO
Naruhiko SAKAMOTO

* Special Postdoctoral Researcher

Visiting Members

Takashi FUJISAWA (N.I.R.S.)
Toshio HYODO (Grad. Sch. Arts Sci., Univ. Tokyo)
Yoshiko ITOH (Adv. Res. Inst. Sci. Eng., Waseda Univ.)

Kazuya ITOH (Tandem Accel. Cen., Univ. Tsukuba)
Toshikazu KURIHARA (KEK)
Shinji MACHIDA (KEK)
Yoshiharu MORI (KEK)
Yasuyuki NAGASHIMA (Grad. Sch. Arts Sci., Univ. Tokyo)
Hiroyuki OKAMURA (Dept. Phys., Saitama Univ.)
Katsuhiko SAITO (Sumitomo Heavy Ind., Ltd.)
Serguei VOROJTSOV (J.I.N.R., Russia)

Trainees

Takahiro AKIYAMA (Dept. Phys., Saitama Univ.)
Motooki HOSOI (Dept. Phys., Saitama Univ.)
Takuichiro IKEDA (Dept. Phys., Saitama Univ.)
Keisuke ITOH (Dept. Phys., Saitama Univ.)
Hirokazu KUMASAKA (Dept. Phys., Saitama Univ.)
Kenji SUDA (Dept. Phys., Saitama Univ.)
Kousuke SUGAWARA (Dept. Phys., Saitama Univ.)
Ryoko SUZUKI (Dept. Phys., Saitama Univ.)
Sunao TAKEDA (Dept. Phys., Saitama Univ.)
Reiko TAKI (Michigan State Univ., USA)
Yoshimitsu WADA (Dept. Phys., Saitama Univ.)

Radioisotope Technology Division

Head

Fumio YATAGAI

Members

Kuniko MAEDA
Shuichi ENOMOTO
Teruyo TSUKADA
Takahiro YANAGIYA*1
Rieko HIRUNUMA*2
Shigeko MORIMOTO*2
Akihiro NAKAYAMA*2
Takayuki SOSHI*2
Kazuya TAKAHASHI
Masako IZUMI
Hiromitsu HABA*1
Wenjun DING*2
Kaori IGARASHI*2
Shinji MOTOMURA*2
Qiangyan PAN*2
Masanori TOMITA*2

*1 Special Postdoctoral Researcher
*2 Contract Researcher

Visiting Members

Ryohei AMANO (Fac. Med., Kanazawa Univ.)
Sachiko AMARI (Washington Univ., USA)
Elliot DROBETSKY (Univ. Montreal, Canada)
Kazutoyo ENDO (Showa Pharm. Univ.)
Mika FUKUOKA (Tokyo Univ. Fish.)
Sachiko GOTO (Sch. Pharm. Sci., Nagasaki Univ.)
Ken-ichi HASEGAWA (Fac. Eng., Hosei Univ.)
Hiroshi HIDAKA (Fac. Sci., Hiroshima Univ.)
Seiichiro HIMENO (Sch. Pharm. Sci., Kitasato Univ.)
Masamitsu HONMA (Natl. Inst. Health Sci.)
Naoko IKEDA (Showa Women's Univ.)
Hiroko INAGE (Int. Life Sci. Inst.)
Hiroyuki KAGI (Grad. Sch. Sci., Univ. Tokyo)
Takesi KATO
Kenji KAWABE (Kyoto Pharm. Univ.)
Osamu KAWAGUCHI (Sch. Med., Keio Univ.)
Tetsuya KAWATA (Fac. Med., Chiba Univ.)
Hideaki MAEKAWA (Natl. Inst. Infect. Dis.)
Hiroshi MAEZAWA (Fac. Med. Technol., Univ. Tokushima)
Ken-ichiro MATSUMOTO (Showa Pharm. Univ.)

Yoshitaka MINAI (Cen. Art. Sci., Musashi Univ.)
Takeshi MINAMI (Dept. Life Sci., Sch. Sci. Eng., Kinki Univ.)
Tomohiro NABEKURA (Sch. Pharm. Sci., Kinki Univ.)
Yuichiro NAGAME (JAERI)
Tomoko NAKANISHI (Grad. Sch. Agr. Life Sci., Univ. Tokyo)
Yukiko NAKANISHI (Int. Life Sci. Inst.)
Nguyen van CHUYEN (Jpn. Women's Univ.)
Takehiko NOHMI (Natl. Inst. Health Sci.)
Yasumitsu OGURA (Grad. Sch. Pharm. Sci., Chiba Univ.)
Takeo OHNISHI (Fac. Biol., Nara Med. Univ.)
Takuya OHYAMA (Fac. Sci., Shizuoka Univ.)
Hiromu SAKURAI (Kyoto Pharm. Univ.)
Sadao SHIBATA (Natl. Inst. Radiol. Sci.)
Hiroshi SHIMIZU (Fac. Sci., Hiroshima Univ.)
Atsushi SHINOHARA (Dept. Chem., Grad. Sch. Sci., Osaka Univ.)
Hiroyuki SUZUKI (RI Res. Cen., Chiba Univ.)
Kazuo T. SUZUKI (Grad. Sch. Pharm. Sci., Chiba Univ.)
Keiko TAGAMI (Natl. Inst. Radiol. Sci.)
Akihisa TAKAHASHI (Fac. Biol., Nara Med. Univ.)
Masaaki TAKAHASHI (Grad. Sch. Agr. Biol. Sci., Osaka Pref. Univ.)
Miho TAKAHASHI (Tokyo Univ. Fish.)
Yoshio TAKAHASHI (Fac. Sci., Hiroshima Univ.)
Kaoru TAKAKURA (Div. Natural Sci., Int. Chr. Univ.)
Atsushi TAKEDA (Sch. Pharm. Sci., Univ. Shizuoka)
Haruna TAMANO (Sch. Pharm. Sci., Univ. Shizuoka)
Shigeo UCHIDA (Natl. Inst. Radiol. Sci.)
Kohshin WASHIYAMA (Fac. Med., Kanazawa Univ.)
Honglu WU (Johnson Space Cen., NASA, USA)
Mineo YAMASAKI (Nara Med. Univ.)
Makoto YANAGA (Fac. Sci., Shizuoka Univ.)
Hiroyuki YASUI (Kyoto Pharm. Univ.)
Akihiko YOKOYAMA (Fac. Sci., Kanazawa Univ.)
Shigekazu YONEDA (Natl. Sci. Museum)
Shozo YOSHIDA (Nara Med. Univ.)

Trainees

Jun FUGONO (Kyoto Pharm. Univ.)
Jun FURUKAWA (Grad. Sch. Agr. Life Sci., Univ. Tokyo)
Hiroko IHARA (Sch. Med., Keio Univ.)
Yoshiyuki KAJITA (Fac. Sci., Shizuoka Univ.)
Yousuke KANAYANA (Fac. Med., Kanazawa Univ.)
Nobuyuki KINUGAWA (Fac. Sci., Shizuoka Univ.)
Tsutomu MATSUO (Fac. Sci. Eng., Waseda Univ.)
Takanori OGI (Fac. Sci., Shizuoka Univ.)
Toshitaka OKA (Fac. Sci. Eng., Waseda Univ.)
Momoko TAKAHASHI (Div. Natural Sci., Int. Chr. Univ.)
Ta Thi Tuyet MAI (Jpn. Women's Univ.)
Takae TSUJI (Fac. Med., Kanazawa Univ.)
Hideaki YOSHIDA (Fac. Sci. Eng., Waseda Univ.)

Liquid Helium Service Division

Head

Yasushige YANO

Members

Kumio IKEGAMI
Kazushiro NAKANO
Toshiharu TOMINAKA*
Ken-ichi KATO
Masao OTAKE

---

* Contract Researcher

Visiting Members
Toshiyuki MITO (Jpn. Nucl. Cycl. Dev. Inst.)

ADVANCED ENGINEERING CENTER

Research Instruments Development Division

Head
Katsumi SENOO

Members
Yuji IKEGAMI
Yoshio NOMIYA
Susumu SHIMODA
Seigo SUGAHARA
Teruo URAI
Yutaka YAMADA
Tokuji KITSUNAI
Tsunenobu SHIGA
Akira SHIRAISHI
Norio TAJIMA
Shogo YAMADA

Contract Members
Naoe KANEKO
Akira MATSUMOTO
Tetsuji SASAMOTO
Saburo TOKIWA
Tokuji WATANABE
Ushizo KUBO
Yuzo NIIOKA
Kiyoji TAKAHASHI
Sumio YAMAMOTO

CHARACTERIZATION CENTER

Surface Characterization Division

Head
Masaya IWAKI

Members
Tomohiro KOBAYASHI
Kowashi WATANABE
Aiko NAKAO

ADVANCED COMPUTING CENTER

Image Information Division

Head
Hirohiko M. SHIMIZU

Members
Hiromi SATO
Shigetomo SHIKI*1
Takayuki OKU*2
Tomohiro ADACHI*2
Kazuaki IKEDA*2
Yoshiya KAWASAKI*1
Masahiro TAKEDA*1
Yoshiyuki TAKIZAWA*2
Takahiro MORISHIMA*2

*1 Special Postdoctoral Researcher
*2 Contract Researcher

Visiting Members
Kenji SAKAI (Dept. Phys., Tokyo Inst. Technol.)
Fuyuki TOKANAI (Dept. Phys., Yamagata Univ.)
Tadashi KIFUNE (Fac. Eng., Shinshu Univ.)
Tohru TAINO (Fac. Eng., Saitama Univ.)
Hiroaki MYOREN (Fac. Eng., Saitama Univ.)

RIKEN BIORESOURCE CENTER

Department of Biological Systems
Experimental Animal Division

Head
Yuichi OBATA

Members
Noriko HIRAIWA
Chikako YOSHIDA-NORO
Fumio IKE
Atsushi YOSHIKI

RIKEN BNL Research Center

Head
Tsung-Dao LEE (Director)
Nicholas P. SAMIOS (Deputy Director)
Hideto EN'YO (RBRC Associate Director)

Experimental

Group Leader
Hideto EN'YO

Deputy Group Leader
Gerry M. BUNCE

Members
Yuji GOTO
Atsushi TAKETANI
Alexander BAZILEVSKY*1
Douglas Edward FIELDS *2
Matthias GROSS PERDEKAMP*2
Takahiro KAWABATA*4
Federica MESSER*1
Takashi ICHIHARA
Yasushi WATANABE
Abhay DESHPANDE*1
Brendan FOX*1
Masashi KANETA*3
Hideyuki KOBAYASHI*4
Satoshi YOKKAICHI*4

Visiting Members
Yoshinori FUKAO (Kyoto Univ.)
Takuma HORAGUCHI (Tokyo Inst. Technol.)
Kazuyoshi KURITA (Rikkyo Univ.)
Jens Soren LANGE (Univ. Frankfurt, Germany)
Akio OGAWA (BNL, USA)
Naohito SAITO (Kyoto Univ.)
Viktor SIEGLE (Univ. Heiderberg, Germany)
Manabu TOGAWA (Kyoto Univ.)

Theory

Group Leader
Tsung-Dao LEE

Deputy Group Leader
Anthony J. BALTZ

Members
Yasumichi AOKI*3
Thomas BLUM*1
Takashi IKEDA*4
Sangyong JEON*2
Yasushi NARA*3
Jun-ichi NOAKI*3
Steffen A. BASS*2
Christopher DAWSON*1
Kazunori ITAKURA*3
Alexander KUSENKO*2
Yukio NEMOTO*3
Konstantinos ORIGINOS*3

Thomas SCHAEFER*2
Takanori SUGIHARA*4
Rajagopal VENUGOPALAN*2
Tilo WETTIG*2
Mikhail A. STEPHANOV*2
Ubirajara van KOLCK*2
Werner VOGELSANG*1
Norikazu YAMADA*3

Visiting Members

Miklos GYULASSY (Columbia Univ., USA)
Yoshitaka HATTA (Kyoto Univ.)
Robert L. JAFFE (Massachusetts Inst. Technol., USA)
Robert MAWHINNEY (Columbia Univ., USA)
Shigemi OHTA (KEK)
Edward SHURYAK (State Univ. New York, Stony Brook, USA)

Administration

Pamela ESPOSITO (Secretary)
Rae GREENBERG (Assistant)
Tammy Anne HEINZ (Assistant)
Taeko ITO (Secretary)

Administrative Manager

Motohide YOKOTA

Deputy Administrative Manager

Chiharu SHIMOYAMADA

---

*1 RIKEN BNL Fellow, *2 RHIC Physics Fellow,
*3 Research Associate, *4 Special Postdoctoral Researcher

RIKEN PLANT SCIENCE CENTER

Laboratory for Remediation Research

Head

Isamu YAMAGUCHI

Members

Makoto KIMURA
Takayuki SOSHI

SAFETY DIVISION

Head

Hiroshi SAWA

Laboratory Safety Section

Head

Yoshitomo UWAMINO

Members

Makoto MIYAGAWA
Hiroko KATOU
Nobuyasu YAMAGISHI
Shigemi SHINOHARA
Hajime YOSHIKI
Kunio FUKASAWA

Research Ethics Section

Head

Satoru KAGAYA

Members

Akira OZAKI
Mika SUZUKI

AUTHOR INDEX

RIKEN Accelerator Progress Report Vol. 36

理化学研究所加速器年次報告　第36巻（2003）

印　刷　平成15年（2003）3月17日
発　行　平成15年（2003）3月24日

発行者　理化学研究所
代表者　小林俊一
〒351-0198　埼玉県和光市広沢2番1号
電話（048）462－1111

編集者　理化学研究所加速器研究施設
運営委員会

印刷所　三美印刷株式会社
〒116-0013　東京都荒川区西日暮里5－9－8

定価5,000円
（消費税別）

理化学研究所

埼玉県　和光市　広沢